

# 中草藥研究中心

2018 年 9 月 1 日~2019 年 8 月 31 日

## 論文集(上)



CHANG GUNG UNIVERSITY OF SCIENCE AND TECHNOLOGY

長庚科技大學  
中草藥研究中心  
2018年9月1日~2019年8月31日  
論文集  
目 錄

(上冊)

序號	期刊論文	學校主要 負責教師	頁碼
1.	Chen, C. Y.; Tsai, Y. F.; Huang, W. J.; Chang, S. H.; Hwang, T. L. Propofol inhibits endogenous formyl peptide-induced neutrophil activation and alleviates lung injury. <i>Free Radic Biol Med</i> 129:372-382; 2018. DOI: 10.1016/j.freeradbiomed.2018.09.048.	黃聰龍	1
2.	Chen, P. J.; Ko, I. L.; Lee, C. L.; Hu, H. C.; Chang, F. R.; Wu, Y. C.; Leu, Y. L.; Wu, C. C.; Lin, C. Y.; Pan, C. Y.; Tsai, Y. F.; Hwang, T. L. Targeting allosteric site of AKT by 5,7-dimethoxy-1,4-phenanthrenequinone suppresses neutrophilic inflammation. <i>EBioMedicine</i> 40:528-540; 2019. DOI: 10.1016/j.ebiom.2019.01.043.	黃聰龍	12
3.	Lai, H. C.; Chang, C. J.; Lin, C. S.; Wu, T. R.; Hsu, Y. J.; Wu, T. S.; Lu, J. J.; Martel, J.; Ojcius, D. M.; Ku, C. L.; Young, J. D.; Lu, C. C. NK Cell-Derived IFN-gamma Protects against Nontuberculous Mycobacterial Lung Infection. <i>J Immunol</i> 201:1478-1490; 2018. DOI: 10.4049/jimmunol.1800123.	賴信志	25
4.	Chen, T. H.; Chiu, C. T.; Lee, C.; Chu, Y. Y.; Cheng, H. T.; Hsu, J. T.; Wu, R. C.; Yeh, T. S.; Lin, K. H. Circulating microRNA-22-3p Predicts the Malignant Progression of Precancerous Gastric Lesions from Intestinal Metaplasia to Early Adenocarcinoma. <i>Dig Dis Sci</i> 63:2301-2308; 2018. DOI: 10.1007/s10620-018-5106-4.	林光輝	38
5.	Kabary, D. M.; Helmy, M. W.; Abdelfattah, E. A.; Fang, J. Y.; Elkhodairy, K. A.; Elzoghby, A. O. Inhalable multi-compartmental phospholipid enveloped lipid core nanocomposites for localized mTOR inhibitor/herbal combined therapy of lung carcinoma. <i>Eur J Pharm Biopharm</i> 130:152-164; 2018. DOI: 10.1016/j.ejpb.2018.06.027.	方嘉佑	46
6.	Kabary, D. M.; Helmy, M. W.; Elkhodairy, K. A.; Fang, J. Y.; Elzoghby, A. O. Hyaluronate/lactoferrin layer-by-layer-coated lipid nanocarriers for targeted co-delivery of rapamycin and berberine to lung carcinoma. <i>Colloids Surf B Biointerfaces</i> 169:183-194; 2018. DOI: 10.1016/j.colsurfb.2018.05.008.	方嘉佑	59
7.	Lee, C. W.; Wu, C. H.; Chiang, Y. C.; Chen, Y. L.; Chang, K. T.; Chuang, C. C.; Lee, I. T. Carbon monoxide releasing molecule-2 attenuates <i>Pseudomonas aeruginosa</i> -induced ROS-dependent ICAM-1 expression in human pulmonary alveolar epithelial cells. <i>Redox Biol</i> 18:93-103; 2018. DOI: 10.1016/j.redox.2018.07.001.	李江文	71



8.	Wang, L. J.; Lee, S. Y.; Chou, M. C.; Yang, K. C.; Lee, T. L.; Shyu, Y. C. Impact of Drug Adherence on Oppositional Defiant Disorder and Conduct Disorder Among Patients With Attention-Deficit/Hyperactivity Disorder. <i>J Clin Psychiatry</i> 79; 2018. DOI: 10.4088/JCP.17m11784.	徐于喬	82
9.	Liao, H. T.; Tsai, M. J.; Brahmayya, M.; Chen, J. P. Bone Regeneration Using Adipose-Derived Stem Cells in Injectable Thermo-Gelling Hydrogel Scaffold Containing Platelet-Rich Plasma and Biphasic Calcium Phosphate. <i>Int J Mol Sci</i> 19; 2018. DOI: 10.3390/ijms19092537.	陳志平	89
10.	Huang, C. H.; Chang, L. C.; Hu, S.; Hsiao, C. Y.; Wu, S. J. Spilanthol inhibits TNF-alpha-induced ICAM1 expression and proinflammatory responses by inducing heme oxygenase1 expression and suppressing pJNK in HaCaT keratinocytes. <i>Mol Med Rep</i> 18:2987-2994; 2018. DOI: 10.3892/mmr.2018.9245.	蕭千祐、 吳淑如	107
11.	Peng, K. T.; Chiang, Y. C.; Ko, H. H.; Chi, P. L.; Tsai, C. L.; Ko, M. I.; Lee, M. H.; Hsu, L. F.; Lee, C. W. Mechanism of Lakoochin A Inducing Apoptosis of A375.S2 Melanoma Cells through Mitochondrial ROS and MAPKs Pathway. <i>Int J Mol Sci</i> 19; 2018. DOI: 10.3390/ijms19092649.	李江文	115
12.	Wei, C. Y.; Wang, S. W.; Ye, J. W.; Hwang, T. L.; Cheng, M. J.; Sung, P. J.; Chang, T. H.; Chen, J. J. New Anti-Inflammatory Aporphine and Lignan Derivatives from the Root Wood of <i>Hernandia nymphaeifolia</i> . <i>Molecules</i> 23, pii: E2286; 2018. DOI: 10.3390/molecules23092286.	黃聰龍	130
13.	Elgohary, M. M.; Helmy, M. W.; Abdelfattah, E. A.; Ragab, D. M.; Mortada, S. M.; Fang, J. Y.; Elzoghby, A. O. Targeting sialic acid residues on lung cancer cells by inhalable boronic acid-decorated albumin nanocomposites for combined chemo/herbal therapy. <i>J Control Release</i> 285:230-243; 2018. DOI: 10.1016/j.jconrel.2018.07.014.	方嘉佑	142
14.	Lin, Y. C.; Lin, C. F.; Alalaiwe, A.; Wang, P. W.; Fang, Y. P.; Fang, J. Y. UV filter entrapment in mesoporous silica hydrogel for skin protection against UVA with minimization of percutaneous absorption. <i>Eur J Pharm Sci</i> 122:185-194; 2018. DOI: 10.1016/j.ejps.2018.07.013.	林傳福、 方嘉佑	156
15.	Liu, C. C.; Lin, C. C.; Hsiao, Y. C.; Wang, P. J.; Yu, J. S. Proteomic characterization of six Taiwanese snake venoms: Identification of species-specific proteins and development of a SISCAPA-MRM assay for cobra venom factors. <i>J Proteomics</i> 187:59-68; 2018. DOI: 10.1016/j.jprot.2018.06.003.	余兆松	166
16.	Chung, H. M.; Wang, Y. C.; Tseng, C. C.; Chen, N. F.; Wen, Z. H.; Fang, L. S.; Hwang, T. L.; Wu, Y. C.; Sung, P. J. Natural Product Chemistry of Gorgonian Corals of Genus <i>Junceella</i> (-)Part III. <i>Mar Drugs</i> 16, pii: E339; 2018. DOI: 10.3390/md16090339.	黃聰龍	176
17.	Chen, J. T.; Liu, C. C.; Yu, J. S.; Li, H. H.; Lai, M. C. Integrated omics profiling identifies hypoxia-regulated genes in HCT116	余兆松	186

- colon cancer cells. *J Proteomics* 188:139-151; 2018. DOI: 10.1016/j.jprot.2018.02.031.
18. Chen, P. H.; Shyu, Y. C.; Tsai, M. Y.; Lee, S. Y.; Yang, K. C.; Yang, C. J.; Lee, T. L.; Wang, L. J. Correlation between attention-deficit/hyperactivity disorder, its pharmacotherapy and thyroid dysfunction: A nationwide population-based study in Taiwan. *Clin Endocrinol (Oxf)*; 2018. DOI: 10.1111/cen.13817. 徐于喬 199
  19. Abdelmoneem, M. A.; Mahmoud, M.; Zaky, A.; Helmy, M. W.; Sallam, M.; Fang, J. Y.; Elkhodairy, K. A.; Elzoghby, A. O. Decorating protein nanospheres with lactoferrin enhances oral COX-2 inhibitor/herbal therapy of hepatocellular carcinoma. *Nanomedicine (Lond)* 13:2377-2395; 2018. DOI: 10.2217/nmm-2018-0134. 方嘉佑 208
  20. Xu, J. H.; Chang, Y. C.; Li, G. Q.; Wen, Z. H.; Wu, Y. C.; Sung, P. J. Briaviolides O and P, new briaranes from a cultured octocoral *Briareum violaceum*. *Phytochemistry Letters* 27:129-133; 2018. DOI: 10.1016/j.phytol.2018.07.016. 張祐嘉 227
  21. Cho, R. L.; Yang, C. C.; Tseng, H. C.; Hsiao, L. D.; Lin, C. C.; Yang, C. M. Haem oxygenase-1 up-regulation by rosiglitazone via ROS-dependent Nrf2-antioxidant response elements axis or PPARgamma attenuates LPS-mediated lung inflammation. *Br J Pharmacol* 175:3928-3946; 2018. DOI: 10.1111/bph.14465. 楊春茂 232
  22. Liou, C. J.; Wei, C. H.; Chen, Y. L.; Cheng, C. Y.; Wang, C. L.; Huang, W. C. Fisetin Protects Against Hepatic Steatosis Through Regulation of the Sirt1/AMPK and Fatty Acid beta-Oxidation Signaling Pathway in High-Fat Diet-Induced Obese Mice. *Cell Physiol Biochem* 49:1870-1884; 2018. DOI: 10.1159/000493650. 劉倩君、鄭靜宜、黃文忠 251
  23. Huang, W. C.; Wu, L. Y.; Hu, S.; Wu, S. J. Spilanthol Inhibits COX-2 and ICAM-1 Expression via Suppression of NF-kappaB and MAPK Signaling in Interleukin-1beta-Stimulated Human Lung Epithelial Cells. *Inflammation* 41:1934-1944; 2018. DOI: 10.1007/s10753-018-0837-0. 黃文忠、吳淑如 266
  24. Lam, S. H.; Chen, P. H.; Hung, H. Y.; Hwang, T. L.; Chiang, C. C.; Thang, T. D.; Kuo, P. C.; Wu, T. S. Chemical Constituents from the Stems of *Tinospora sinensis* and Their Bioactivity. *Molecules* 23, pii: E2541; 2018. DOI: 10.3390/molecules23102541. 黃聰龍 278
  25. Abdelmoneem, M. A.; Mahmoud, M.; Zaky, A.; Helmy, M. W.; Sallam, M.; Fang, J. Y.; Elkhodairy, K. A.; Elzoghby, A. O. Dual-targeted casein micelles as green nanomedicine for synergistic phytotherapy of hepatocellular carcinoma. *J Control Release* 287:78-93; 2018. DOI: 10.1016/j.jconrel.2018.08.026. 方嘉佑 290
  26. Yu, S. Y.; Wang, S. W.; Hwang, T. L.; Wei, B. L.; Su, C. J.; Chang, F. R.; Cheng, Y. B. Components from the Leaves and Twigs of Mangrove *Lumnitzera racemosa* with Anti-Angiogenic and Anti-Inflammatory Effects. *Mar Drugs* 16, pii: E404; 2018. DOI: 10.3390/md16110404. 黃聰龍 306

27. Chan, Y. Y.; Wang, C. Y.; Hwang, T. L.; Juang, S. H.; Hung, H. Y.; Kuo, P. C.; Chen, P. J.; Wu, T. S. The Constituents of the Stems of *Cissus assamica* and Their Bioactivities. *Molecules* 23, pii: E2799; 2018. DOI: 10.3390/molecules23112799. 黃聰龍 314
28. Tsai, M. H.; Yang, C. M.; Chang, K. T.; Chuang, C. C.; Lin, W. N.; Jiang, R. S.; Wu, C. H.; Lee, I. T. Carbon monoxide ameliorates *Staphylococcus aureus*-elicited COX-2/IL-6/MMP-9-dependent human aortic endothelial cell migration and inflammatory responses. *Immunol Lett* 203:40-49; 2018. DOI: 10.1016/j.imlet.2018.09.010. 楊春茂 323
29. Alalaiwe, A.; Hung, C. F.; Leu, Y. L.; Tahara, K.; Chen, H. H.; Hu, K. Y.; Fang, J. Y. The active compounds derived from *Psoralea corylifolia* for photochemotherapy against psoriasis-like lesions: The relationship between structure and percutaneous absorption. *Eur J Pharm Sci* 124:114-126; 2018. DOI: 10.1016/j.ejps.2018.08.031. 方嘉佑 334
30. Yang, S. C.; Huang, T. H.; Chiu, C. H.; Chou, W. L.; Alalaiwe, A.; Yeh, Y. C.; Su, K. W.; Fang, J. Y. The atopic dermatitis-like lesion and the associated MRSA infection and barrier dysfunction can be alleviated by 2,4-dimethoxy-6-methylbenzene-1,3-diol from *Antrodia camphorata*. *J Dermatol Sci* 92:188-196; 2018. DOI: 10.1016/j.jdermsci.2018.09.002. 方嘉佑 347
31. Tsai, M. H.; Wu, C. H.; Lin, W. N.; Cheng, C. Y.; Chuang, C. C.; Chang, K. T.; Jiang, R. S.; Hsu, J. F.; Lee, I. T. Infection with *Staphylococcus aureus* elicits COX-2/PGE2/IL-6/MMP-9-dependent aorta inflammation via the inhibition of intracellular ROS production. *Biomed Pharmacother* 107:889-900; 2018. DOI: 10.1016/j.biopha.2018.08.096. 鄭靜宜 356
32. Lu, C. W.; Hsieh, H. L.; Lin, T. Y.; Hsieh, T. Y.; Huang, S. K.; Wang, S. J. Echinacoside, an Active Constituent of *Cistanche Herba*, Exerts a Neuroprotective Effect in a Kainic Acid Rat Model by Inhibiting Inflammatory Processes and Activating the Akt/GSK3 $\beta$  Pathway. *Biol Pharm Bull* 41:1685-1693; 2018. DOI: 10.1248/bpb.b18-00407. 謝喜龍、王素珍 368
33. Thabet, A. A.; Youssef, F. S.; Korinek, M.; Chang, F. R.; Wu, Y. C.; Chen, B. H.; El-Shazly, M.; Singab, A. N. B.; Hwang, T. L. Study of the anti-allergic and anti-inflammatory activity of *Brachychiton rupestris* and *Brachychiton discolor* leaves (Malvaceae) using in vitro models. *BMC Complement Altern Med* 18:299; 2018. DOI: 10.1186/s12906-018-2359-6. 黃聰龍 377
34. Lin, Y. H.; Wu, M. H.; Huang, Y. H.; Yeh, C. T.; Chi, H. C.; Tsai, C. Y.; Chuang, W. Y.; Yu, C. J.; Chung, I. H.; Chen, C. Y.; Lin, K. H. Thyroid hormone negatively regulates tumorigenesis through suppression of BC200. *Endocr Relat Cancer* 25:967-979; 2018. DOI: 10.1530/ERC-18-0176. 林光輝 392
35. Liu, C. C.; Yu, J. S.; Wang, P. J.; Hsiao, Y. C.; Liu, C. H.; Chen, Y. C.; Lai, P. F.; Hsu, C. P.; Fann, W. C.; Lin, C. C. Development of sandwich ELISA and lateral flow strip assays for diagnosing clinically significant snakebite in Taiwan. *PLoS Negl Trop Dis* 12:e0007014; 2018. DOI: 10.1371/journal.pntd.0007014. 余兆松 405



- |     |  |                             |     |
|-----|--|-----------------------------|-----|
| 36. | Gaber, M.; Mabrouk, M. T.; Freag, M. S.; Khiste, S. K.; Fang, J. Y.; Elkhodairy, K. A.; Elzoghby, A. O. Protein-polysaccharide nanohybrids: Hybridization techniques and drug delivery applications. <i>Eur J Pharm Biopharm</i> 133:42-62; 2018. DOI: 10.1016/j.ejpb.2018.10.001.   | 方嘉佑                         | 428 |
| 37. | Lee, K. M.; Gong, Y. N.; Hsieh, T. H.; Woodman, A.; Dekker, N. H.; Cameron, C. E.; Shih, S. R. Discovery of Enterovirus A71-like nonstructural genomes in recent circulating viruses of the Enterovirus A species. <i>Emerg Microbes Infect</i> 7:111; 2018. DOI: 10.1038/s41426-018-0107-0.   | 施信如                         | 449 |
| 38. | Lin, Z. C.; Hsieh, P. W.; Hwang, T. L.; Chen, C. Y.; Sung, C. T.; Fang, J. Y. Topical application of anthranilate derivatives ameliorates psoriatic inflammation in a mouse model by inhibiting keratinocyte-derived chemokine expression and neutrophil infiltration. <i>FASEB J</i> :fj201800354; 2018. DOI: 10.1096/fj.201800354. | 謝佩文、<br>黃聰龍、<br>陳琦媛、<br>方嘉佑 | 463 |
| 39. | Tseng, T. H.; Lin, W. L.; Chang, C. K.; Lee, K. C.; Tung, S. Y.; Kuo, H. C. Protective Effects of Morus Root Extract (MRE) Against Lipopolysaccharide-Activated RAW264.7 Cells and CCl4-Induced Mouse Hepatic Damage. <i>Cell Physiol Biochem</i> 51:1376-1388; 2018. DOI: 10.1159/000495555.  | 郭星君                         | 476 |
| 40. | Tseng, H. C.; Lin, C. C.; Wang, C. Y.; Yang, C. C.; Hsiao, L. D.; Yang, C. M. Lysophosphatidylcholine induces cyclooxygenase-2-dependent IL-6 expression in human cardiac fibroblasts. <i>Cell Mol Life Sci</i> 75:4599-4617; 2018. DOI: 10.1007/s00018-018-2916-7.  | 楊春茂                         | 489 |



## Original article

## Propofol inhibits endogenous formyl peptide-induced neutrophil activation and alleviates lung injury



Chun-Yu Chen<sup>a,b</sup>, Yung-Fong Tsai<sup>a,b</sup>, Wei-Ju Huang<sup>a</sup>, Shih-Hsin Chang<sup>a,d</sup>,  
Tsong-Long Hwang<sup>a,b,c,e,f,\*</sup>

<sup>a</sup> Graduate Institute of Natural Products, College of Medicine, Chang Gung University, Taoyuan 333, Taiwan

<sup>b</sup> Department of Anesthesiology, Chang Gung Memorial Hospital, Taoyuan 333, Taiwan

<sup>c</sup> Chinese Herbal Medicine Research Team, Healthy Aging Research Center, Chang Gung University, Taoyuan 333, Taiwan

<sup>d</sup> Graduate Institute of Health Industry Technology, College of Human Ecology, Chang Gung University of Science and Technology, Taoyuan 333, Taiwan

<sup>e</sup> Research Center for Chinese Herbal Medicine, Research Center for Food and Cosmetic Safety, and Graduate Institute of Health Industry Technology, College of Human Ecology, Chang Gung University of Science and Technology, Taoyuan 333, Taiwan

<sup>f</sup> Department of Chemical Engineering, Ming Chi University of Technology, New Taipei City 243, Taiwan

## ARTICLE INFO

## Keywords:

Acute lung injury

Formyl-peptide receptor

Mitochondrial-derived formyl peptides

Neutrophil

Propofol

## ABSTRACT

Critically ill patients have a high risk of sepsis. Various studies have demonstrated that propofol has anti-inflammatory effects that may benefit critically ill patients who require anesthesia. However, the mechanism and therapeutic effect remain incompletely understood. Our previous data suggest that propofol can act as a formyl peptide receptor 1 (FPR1) antagonist. Here, we hypothesize that propofol mitigates sepsis-induced acute lung injury (ALI) by inhibiting mitochondria-derived *N*-formyl peptide-mediated neutrophil activation. Oxidative stress caused by activated neutrophils is involved in the pathogenesis of ALI. In human neutrophils, propofol competitively reduced the release of superoxide and associated reactive oxygen species induced by fMMYALF, a human mitochondria-derived *N*-formyl peptide, suggesting that propofol effectively suppresses neutrophilic oxidative stress. In addition, propofol significantly inhibited fMMYALF-induced elastase release, chemotaxis, calcium mobilization, and phosphorylation of protein kinase B and mitogen-activated protein kinases. These results indicate that propofol suppresses neutrophil activation by blocking the interaction between endogenous *N*-formyl peptide and its receptor, FPR1, thus inhibiting downstream signaling. Furthermore, propofol alleviated alveolar wall disruption, edematous changes, and neutrophil infiltration in lipopolysaccharide-induced ALI in mice. Noticeably, propofol improved the survival of sepsis mice. This study indicates that the anti-neutrophil effects of propofol may benefit critically ill septic patients.

## 1. Introduction

Propofol (2,6-Diisopropylphenol) is a commonly used anesthetic drug that is administered intravenously for the induction and maintenance of anesthesia. The favorable pharmacokinetic characteristics of propofol make it a rapid-onset and short-acting agent. In addition, the anti-inflammatory and antioxidant effects of propofol [1–3] increase the advantage of its use in clinical practice. Several studies have indicated that propofol can moderate many aspects of inflammatory

responses. Propofol suppresses the immune activities of monocytes/macrophages [2–7] and neutrophils [2,8–10], including chemotaxis, extravasation, migration, phagocytosis, and production of reactive oxygen species (ROS). Moreover, propofol attenuates proinflammatory cytokine generation [2,3,11,12] and reduces the biosynthesis of nitric oxide [2–4,13–15] both in vitro and in vivo.

The risk of systemic inflammatory response syndrome (SIRS) and infection is higher among critically ill patients who have experienced trauma or cardiac arrest or have undergone surgery. Endogenous

**Abbreviations:** ALI, acute lung injury;  $[Ca^{2+}]_i$ , intracellular calcium concentration; DAMPs, damage-associated molecular patterns; DHR 123, dihydrorhodamine 123; DMSO, dimethylsulfoxide; ERK, extracellular-signal-regulated kinase; fluo-3/AM, fluo-3 acetomethoxyester; fMLF, formyl methionyl-leucyl phenylalanine; FPR1, formyl peptide receptor 1; HBSS, Hank's balanced salt solution; HE, hematoxylin and eosin; ICUs, intensive care units; JNK, c-Jun N-terminal kinase; LDH, lactate dehydrogenase; LPS, Lipopolysaccharide; MPO, myeloperoxidase; NADH, the reduced form of nicotinamide adenine dinucleotide; PIP3, phosphatidylinositol (3,4,5) P3; Propofol, 2,6-diisopropylphenol; ROS, reactive oxygen species; SIRS, systemic inflammatory response syndrome

\* Correspondence to: Graduate Institute of Natural Products, College of Medicine, Chang Gung University, 259 Wenhwa 1st Road, Kweishan, Taoyuan 333, Taiwan.

E-mail address: [htl@mail.cgu.edu.tw](mailto:htl@mail.cgu.edu.tw) (T.-L. Hwang).

<https://doi.org/10.1016/j.freeradbiomed.2018.09.048>

Received 30 June 2018; Received in revised form 27 September 2018; Accepted 29 September 2018

Available online 10 October 2018

0891-5849/© 2018 Elsevier Inc. All rights reserved.

damage-associated molecular patterns (DAMPs), which are released in large amounts from damaged cells or tissues in critically ill patients, activate the innate immune system, and make a contribution to the pathogenesis of septic shock, acute lung injury (ALI), and multi-organ failure. Moreover, once the immune system cannot restrain an invading pathogen sufficiently, the overwhelming inflammatory responses may further deteriorate the immune system's antimicrobial function, engendering a vicious cycle. Recently published protocols for managing critically ill patients proposed that continuous or intermittent sedation should be minimized [16]. However, treating some critically ill patients, such as those who suffer from hypersensitive airway or increased intracranial pressure, requires the use of sedatives for providing bronchodilation [17,18] and neuroprotective effects [19,20] as well as minimizing stress responses. Moreover, anesthesia is an essential measure for inducing unconsciousness and analgesia in critically ill patients who required surgery. In summary, sedative agents should be selected cautiously for anesthetizing patients who are severely ill and at high risk of secondary infection and sepsis. The antioxidant and anti-inflammatory properties of propofol may benefit critically ill patients with SIRS.

Our previous study demonstrated that propofol is a competitive inhibitor of formyl methionyl-leucyl phenylalanine (fMLF) that functions by blocking formyl peptide receptor 1 (FPR1) [8]. In this study, we hypothesized that propofol has a therapeutic effect through competitive inhibition of human neutrophil activation induced by an endogenous *N*-formylated peptides. Mitochondria-derived *N*-formylated peptides are quickly released following tissue or cell damage [21–23]. These *N*-formylated peptides are strong chemoattractants and can initiate and aggravate inflammation, resulting in SIRS; thus, they can be considered as DAMPs. We executed the current study with the aim of ascertaining whether propofol inhibits fMMYALF, a human mitochondria-derived *N*-formylated peptide [21,23], induced neutrophil activities, including respiratory burst, degranulation, and chemotaxis. Additionally, the pharmacological effects of fMMYALF were analyzed to evaluate whether the inhibitory effects of propofol are attributable to blocking of the interaction between fMMYALF and its receptor, FPR1, which interrupts receptor-mediated downstream signaling. Sepsis is the most common cause of ALI [24], which results in increased lung permeability, enhanced neutrophil recruitment, respiratory failure, and mortality. We further investigated the protective effects of propofol in a murine model of ALI induced by endotoxin.

## 2. Material and methods

### 2.1. Reagents

Propofol (2,6-Diisopropylphenol) was obtained from Sigma–Aldrich (St. Louis, MO, USA). Dihydrorhodamine 123 (DHR 123) and fluo-3 acetomethoxyester (fluo-3/AM) were purchased from Molecular Probes (Eugene, OR). Antibodies directed against phospho-extracellular-signal-regulated kinase (ERK), ERK, phospho-c-Jun N-terminal kinase (JNK), JNK, phospho-protein kinase B (AKT) (ser-473), and AKT were purchased from Cell Signaling (Beverly, MA, USA). An anti-p38 antibody was obtained from Santa Cruz Biotechnology (Santa Cruz, CA, USA). All other pharmacologic agents were purchased from Sigma–Aldrich.

### 2.2. Preparation of human neutrophils

The research protocol was granted approval by the institutional review board of Chang Gung Memorial Hospital. After obtaining written informed consent, human neutrophils were isolated from heparinized venous blood donated by healthy participants aged 20–30 years who had reported no systemic disease within 1 week before blood collection. The procedures used for human neutrophil isolation have been described previously [8]. Briefly, the blood samples were subjected to dextran sedimentation and Ficoll–Hypaque centrifugation,

followed by hypotonic lysis of contaminating red blood cells. The segregated neutrophils were suspended and stored in pH 7.4  $\text{Ca}^{2+}$ -free Hank's balanced salt solution (HBSS) at 4 °C prior to the experiments. We employed the Wright–Giemsa stain to confirm the purity of neutrophil suspension. Trypan blue exclusion was applied, and a viability of > 98% was established.

### 2.3. Assessment of the elastase release

We measured elastase release to determine the degranulation function of activated neutrophils [25]. The elastase substrate was methoxysuccinyl-Ala-Ala-Pro-Val-p-nitroanilide. Human neutrophils ( $6 \times 10^5$  cells/mL) were mixed with the substrate (0.1 mM) in HBSS with  $\text{CaCl}_2$  (1 mM) at 37 °C. The neutrophils were treated with dimethylsulfoxide (DMSO) or propofol (5–100  $\mu\text{M}$ ) for 5 min. They were then activated by different concentrations of fMMYALF (30–30,000 nM) in pretreatment with cytochalasin B (0.5  $\mu\text{g/mL}$ ). A spectrometer (Hitachi U-3010, Tokyo, Japan) was employed to continuously record the change in absorbance at 405 nm.

### 2.4. Determination of superoxide release

We used ferricytochrome *c*, which can be reduced by superoxide, to evaluate the superoxide release in human neutrophils [26]. Briefly, neutrophils ( $6 \times 10^5$  cells/mL) were incubated in HBSS containing ferricytochrome *c* (0.5 mg/mL) and  $\text{CaCl}_2$  (1 mM) at 37 °C. Afterward, they were treated with DMSO or propofol (5–100  $\mu\text{M}$ ) for 5 min. Neutrophils activation was achieved by adding fMMYALF (0–30,000 nM) with pretreatment of cytochalasin B (1  $\mu\text{g/mL}$ ). We continuously monitored the changes in absorbance at 550 nm resulting from a ferricytochrome *c* reduction with a double beam spectrophotometer (Hitachi U-3010) with stirring. We calculated the superoxide release as the difference between the reaction with superoxide dismutase (100 U/mL) and that without superoxide dismutase divided by the extinction coefficient for ferricytochrome *c*'s reduced form [26].

### 2.5. Assay of intracellular ROS production

Nonfluorescent DHR 123 can be converted to fluorescent rhodamine 123 by ROS; therefore, we determined the intracellular ROS concentration by measuring the fluorescence of rhodamine 123. We mixed human neutrophils ( $1 \times 10^6$  cells/mL) with DHR 123 (2  $\mu\text{M}$ ) at 37 °C for 15 min. They were subsequently treated with DMSO or propofol (50  $\mu\text{M}$ ) for 5 min. Activation of neutrophils was performed by adding fMMYALF (30–3000 nM) for another 5 min with pretreatment of cytochalasin B (0.5  $\mu\text{g/mL}$ ). Subsequently, the reaction was terminated by putting the samples on ice. Flow cytometry was applied to ascertain the change in fluorescence.

### 2.6. Measurement of total ROS release

We used the luminol-enhanced chemiluminescence method to measure the total ROS concentration. We incubated human neutrophils ( $7 \times 10^5$  cells/mL) with luminol (37.5  $\mu\text{M}$ ) and horseradish peroxidase (6 U/mL) for 5 min at 37 °C. Subsequently, they were treated with DMSO or propofol (50  $\mu\text{M}$ ) for 5 min. Activation of neutrophils was executed using fMMYALF (30–3000 nM). Chemiluminescence was detected using a Tecan Infinite F200 Pro 96-well chemiluminometer (Tecan Group, Männedorf, Switzerland).

### 2.7. Determination of lactate dehydrogenase (LDH) release

In order to exclude the possible cytotoxic effect of the combination of propofol and fMMYALF, LDH activity was assessed with a commercial LDH assay kit (Promega, Madison, WI, USA). Briefly, human neutrophils ( $6 \times 10^5$  cells/mL) were treated with propofol (50  $\mu\text{M}$ ) for



5 min and fMMYALF (10–3000 nM) for another 10 min. The LDH assay reagents were then added to the supernatant and incubated for another 30 min. The OD<sub>490</sub> signal was assessed and compared with the total LDH activity, which was defined by measuring the OD<sub>490</sub> of lysed neutrophils treated with lysing solution (0.1% Triton X-100) for 30 min.

## 2.8. Evaluation of cell migration

The chemotaxis of human neutrophils was evaluated using a microchemotaxis chamber with a 3- $\mu$ m filter (Millipore, Darmstadt, Germany). Neutrophils ( $2.5 \times 10^6$  cells/mL) were treated with DMSO or propofol (50  $\mu$ M) for 5 min at 37 °C in the upper chamber. The lower chamber contained various concentrations of fMMYALF (30–300 nM). After incubation in 5% CO<sub>2</sub> for 120 min, a cell counter (Moxi, Orflo, Ketchum, ID, USA) was used to ascertain the number of migrating neutrophils.

## 2.9. Determination of intracellular calcium concentration

We cocultured neutrophils ( $3 \times 10^6$  cells/mL) with fluo-3/AM (2  $\mu$ M) for 45 min at 37 °C. The neutrophils were then centrifuged and resuspended in HBSS with CaCl<sub>2</sub> (1 mM). We then treated these labeled cells with DMSO or propofol (50  $\mu$ M) for 5 min. The cytosolic calcium levels in response to fMMYALF (10–300 nM) were obtained using a spectrophotometer (Hitachi F-4500). The excitation and emission wavelengths were 488 and 520 nm, respectively. In each experiment, 20 mM ethylene glycol tetraacetic acid and 0.05% Triton X-100 were added to obtain the minimum and maximum fluorescence values, respectively.

## 2.10. Immunoblotting analysis

Human neutrophils were treated with DMSO or propofol (50  $\mu$ M) for 5 min and subsequently stimulated with fMMYALF (10–300 nM) for 30 s, followed by placing the cells on ice to stop the reaction. Cells were then centrifuged at 4 °C, and the precipitated pellet was lysed in lysis buffer (150  $\mu$ L) containing NaCl (100 mM), EDTA (1 mM), HEPES (50 mM, pH 7.4), Na<sub>3</sub>VO<sub>4</sub> (2 mM), p-nitrophenyl phosphate (10 mM), 2-mercaptoethanol (5%), phenylmethanesulfonyl fluoride (1 mM), protease inhibitor cocktails (1%, Sigma–Aldrich), and Triton X-100 (1%). Following sonication, the lysates underwent centrifugation (14,000 rpm at 4 °C for 20 min) and were subjected to sodium dodecyl sulfate–polyacrylamide gels (12%) to separate the proteins. The proteins separated through electrophoresis were transferred onto nitrocellulose membranes, followed by blocking the membrane with 5% nonfat milk in a mixture of Tris-buffered saline and Tween 20. The membranes were incubated in solution containing relevant primary and horseradish peroxidase-conjugated secondary antibodies (Cell Signaling Technology, Beverly, MA). An enhanced chemiluminescence solution (Amersham Biosciences) was added to the membranes, and proteins were detected and quantified using the BioSpectrum Imaging System (UVP, Upland, CA, USA).

## 2.11. Lipopolysaccharide (LPS)-induced sepsis model

All animal experiments were approved by the Institutional Animal Care and Use Committee of Chang Gung University. BALB/c mice (male, 20–25 g, 7–8 weeks old) were acquired from BioLASCO (Taipei, Taiwan). They were housed in an air-conditioned room under a 12-h light–dark cycle. They were provided with 1 week to adapt to the housing environment prior to the experiment. Mice were randomly divided into four groups as follows: Group 1, sham-operated mice treated with DMSO (50  $\mu$ L, 10%); Group 2, sham-operated mice treated with propofol (50  $\mu$ L, 20 mg/Kg and 40 mg/Kg); Group 3, septic mice treated with DMSO (50  $\mu$ L, 10%); and Group 4, septic mice treated with propofol (50  $\mu$ L, 20 mg/Kg and 40 mg/Kg). Propofol was dissolved in

DMSO and then diluted 10-fold using normal saline. Three doses of DMSO or propofol were administered to the mice intraperitoneally every 30 min. Following the second administration of DMSO or propofol, the mice were challenged with a single 200- $\mu$ L dose of LPS (10 mg/Kg, *Escherichia coli*, serotype O111:B4, Sigma–Aldrich, USA) or 0.9% saline (sham operation) administered intraperitoneally. The mice were humanely sacrificed under isoflurane inhalation–administered anesthesia 20 h after LPS administration. Two segments of the right upper lobe of the lung were fixed in 10% neutral buffered formalin. They were subsequently set in paraffin blocks, and then cut into 5- $\mu$ m-thick sections for histological and immunohistochemical analysis. The other tissues were frozen at –80 °C until the assay. In survival study, septic mice were challenged with a single 200- $\mu$ L dose of LPS (10 mg/kg) with or without three doses of 50  $\mu$ L propofol (10, 20, or 40 mg/kg). The survival rate was monitored for 7 days.

## 2.12. Myeloperoxidase (MPO) activity assay

To measure the MPO activity, lung tissues were homogenized in phosphate buffered saline containing 0.5% hexadecyltrimethylammonium bromide (Sigma–Aldrich, USA) by using the MagNA Lyser Instrument (Roche, Germany). After being centrifuged (12,000  $\times$  g) at 4 °C for 20 min, the supernatant fluids were incubated with 0.2 mg/mL o-dianisidine dihydrochloride containing 0.001% H<sub>2</sub>O<sub>2</sub>. The absorption was spectrophotometrically determined at 405 nm. The MPO activity was normalized to the protein concentration. The total protein concentration in the homogenate was ascertained by employing the Bradford method (Bio-Rad, USA).

## 2.13. Histology and immunohistochemistry

The paraffin-embedded sections were deparaffinized and stained using hematoxylin and eosin (HE). For immunohistochemical staining, the sections were incubated with a Ly6G antibody (eBiosciences, USA) and MPO antibody (Abcam, UK). Secondary labeling was achieved using the SuperPicture Polymer Detection kit (Thermo Fisher, USA). We observed the sections by using an Olympus BX51 microscope. Additionally, a DP12 digital camera was used to record images.

## 2.14. Statistical analysis

Data are presented from four to seven samples used for each specific experiment. The data are expressed as means  $\pm$  standard error of the mean. Statistical analysis was executed using Student's *t*-test. The SigmaPlot (Systat Software, San José, CA, USA) software was used for all computation. A *p*-value of 0.05 was considered statistically significant.

# 3. Results

## 3.1. Propofol competitively inhibits fMMYALF-induced elastase and superoxide release in human neutrophils

To assess whether propofol affects neutrophil function and inflammatory activities induced by endogenous mitochondrial-derived formyl peptide, we first evaluated its effect on elastase and superoxide release in fMMYALF-activated human neutrophils. Our results revealed that propofol (5–100  $\mu$ M) dose-dependently reduced elastase release and superoxide release with IC<sub>50</sub> values of  $6.00 \pm 1.02 \mu$ M and  $15.09 \pm 3.65 \mu$ M, respectively (Figs. 1A and 2A). Furthermore, the addition of propofol caused a parallel right shift in the dose–response curves of fMMYALF for elastase and superoxide release (Figs. 1B and 2B), suggesting that propofol has a competitive effect with endogenous mitochondrial-derived formyl peptide.

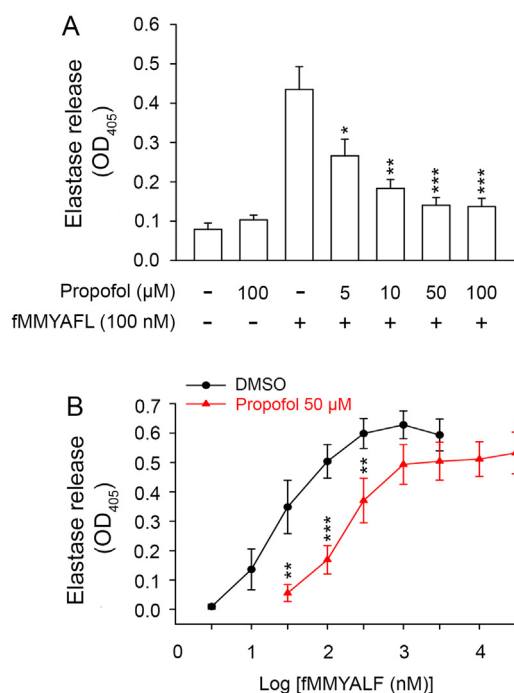


**Fig. 1. Propofol competitively inhibits fMMYALF-induced elastase release in human neutrophils.** Human neutrophils ( $6 \times 10^5$  cells/mL) were pre-incubated with dimethylsulfoxide (0.1% DMSO) or propofol and then activated with fMMYALF. (A) The concentration of propofol ranged from 5 to 100  $\mu$ M, and the concentration of fMMYALF was 100 nM. Elastase release were detected spectrophotometrically using elastase substrate. (B) As the concentration of fMMYALF increased (30–30,000 nM), the inhibition effect of propofol (50  $\mu$ M) decreased. The addition of propofol causes a parallel right shift in the dose-response curves of fMMYALF for superoxide release. Data are expressed as the mean  $\pm$  standard error of the mean,  $n = 5-7$ , \* $p < 0.05$ , \*\* $p < 0.01$ , \*\*\* $p < 0.001$ , as compared to the control assay.

### 3.2. Propofol competitively reduces fMMYALF-induced ROS release in human neutrophils

In human neutrophils, the NADPH-oxidase-produced superoxide anion can be converted to many ROS that have strongly germicidal effects but are concomitantly harmful to tissues. Our results revealed that intracellular ROS production in fMMYALF-activated neutrophils was inhibited by propofol (50  $\mu$ M). Propofol (50  $\mu$ M) did not affect the basal ROS production in unstimulated neutrophils (Fig. 3). Moreover, our data showed that propofol reduced the level of total ROS, which was measured using luminol-enhanced chemiluminescence method (Fig. 4). Furthermore, the mixture of fMMYALF and propofol (50  $\mu$ M) did not increase the release of LDH (data not shown), which suggests that the combined use of fMMYALF and propofol was not cytotoxic to human neutrophils.

### 3.3. Propofol inhibits chemotaxis of human neutrophils

The extravasation and migration of neutrophils into inflammatory sites is a critical response in FPR1-mediated immunological events. For investigating whether propofol reduces neutrophil migration, we examined the chemotactic response of neutrophils to fMMYALF. Our results demonstrated that propofol (50  $\mu$ M) significantly reduced the fMMYALF-stimulated migration of neutrophils (Fig. 5).

### 3.4. Propofol decreases intracellular $Ca^{2+}$ mobilization and phosphorylation of protein kinase B and MAPKs

Notably,  $Ca^{2+}$  acts as an essential second messenger in neutrophil

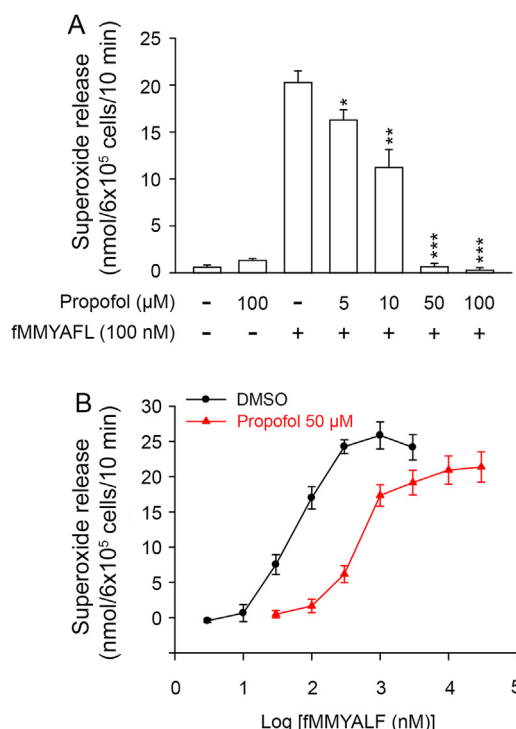


**Fig. 2. Propofol competitively inhibits fMMYALF-induced superoxide release in human neutrophils.** Human neutrophils ( $6 \times 10^5$  cells/mL) were pre-incubated with dimethylsulfoxide (DMSO) or propofol and then activated with fMMYALF. (A) The concentration of propofol ranged from 5 to 100  $\mu$ M, and the concentration of fMMYALF was 100 nM. Superoxide release were detected spectrophotometrically using ferricytochrome c. (B) As the concentration of fMMYALF increased (30–30,000 nM), the inhibition effect of propofol (50  $\mu$ M) decreased. The addition of propofol causes a parallel right shift in the dose-response curves of fMMYALF for superoxide release. Data are expressed as the mean  $\pm$  standard error of the mean,  $n = 6$ , \*\* $p < 0.01$ , \*\*\* $p < 0.001$ , as compared to the control assay.

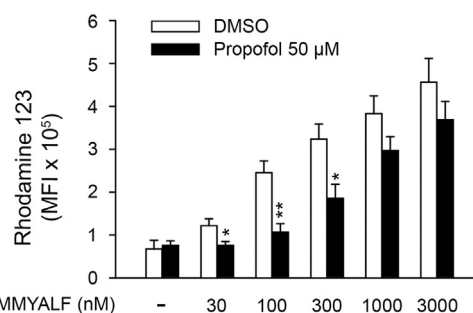


**Fig. 3. Propofol inhibits fMMYALF-induced intracellular reactive oxygen species (ROS) production in human neutrophils.** Human neutrophils ( $1 \times 10^6$  cells/mL) were labeled with DHR 123 (2  $\mu$ M) and then were treated with DMSO or propofol (50  $\mu$ M). The neutrophils were activated with fMMYALF (30–3000 nM). Intracellular ROS was determined as intracellular fluorescence intensity measured by flow cytometry. Data are expressed as the mean  $\pm$  standard error of the mean,  $n = 6$ , \* $p < 0.05$ , \*\* $p < 0.01$ , as compared to the control group.

activations. Neutrophil stimulation with fMMYALF resulted in a prompt increase in the intracellular  $Ca^{2+}$  concentration ( $[Ca^{2+}]_i$ ). Our results showed that propofol (50  $\mu$ M) reduced the magnitude of the increase in  $[Ca^{2+}]_i$  (Fig. 6). The activation of phosphatidylinositol 3-kinase (PI3K) and subsequent triggering of AKT and mitogen-activated protein kinase (MAPK) pathways are involved in the FPR1 downstream signaling [27]. Propofol (50  $\mu$ M) significantly reduced the phosphorylation of ERK, p38, JNK, and AKT in human neutrophils treated with various

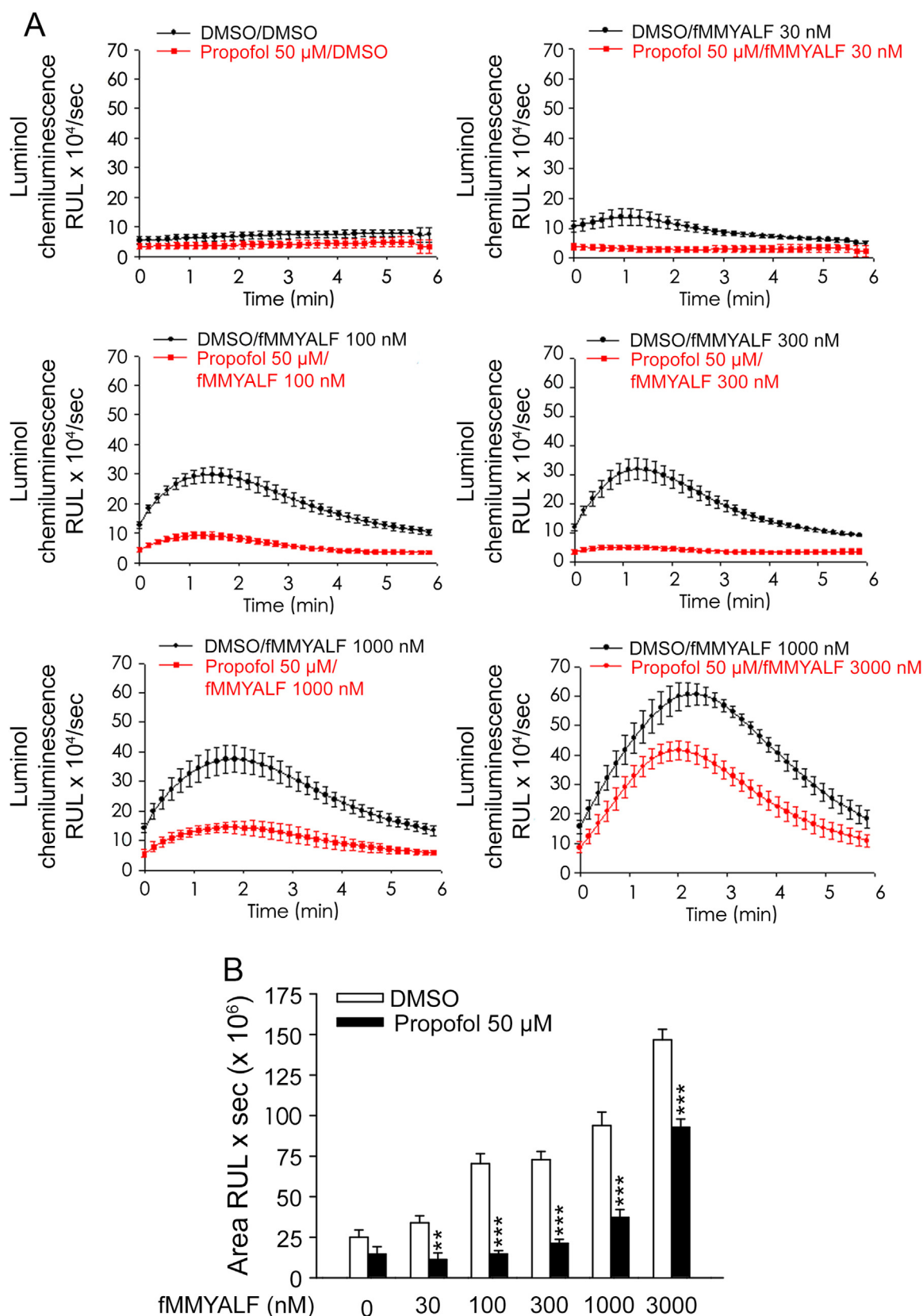


**Fig. 4. Propofol reduces total ROS release in fMMYALF-induced human neutrophils.** Total ROS formation was induced by fMMYALF and measured using the luminol–peroxidase system. Human neutrophils ( $7 \times 10^5$  cells/mL) were incubated with  $37.5 \mu\text{M}$  luminol and  $6 \text{ U/mL}$  horseradish peroxidase and subsequently treated with DMSO or propofol ( $50 \mu\text{M}$ ). Cells were activated using fMMYALF (30–3000 nM). The chemiluminescence was detected with a 96-well chemiluminometer. Representative images from one of five independent experiments are shown in (A). Data are expressed as the mean  $\pm$  standard error of the mean,  $n = 5$ ,  $**p < 0.01$ ,  $***p < 0.001$ , as compared to the control group.



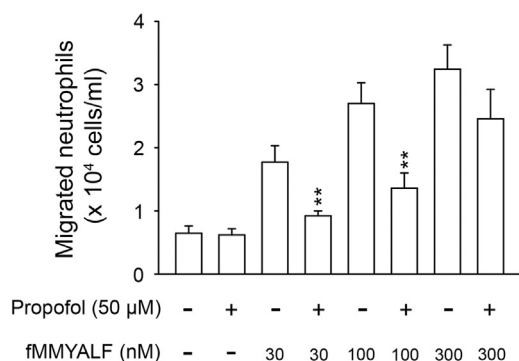


**Fig. 5. Propofol reduces fMMYALF-induced neutrophil migration.** Human neutrophils ( $2.5 \times 10^6$  cells/mL) were pre-incubated with DMSO or propofol (50  $\mu$ M) in the upper chamber. The lower chamber contained various concentrations of fMMYALF (30–300 nM). Migrated neutrophils were counted after 120 min. Data are expressed as the mean  $\pm$  standard error of the mean,  $n = 5$ , \*\* $p < 0.01$ , as compared to the control group.

concentrations of fMMYALF (Fig. 7). Moreover, the reduction effect of propofol was reversed when the concentration of fMMYALF was increased.

### 3.5. Propofol attenuates sepsis-induced ALI and improves survival of septic mice

We used a sepsis-induced ALI murine model to evaluate whether propofol reduces the inflammation-associated lung impairment during sepsis. The lungs of mice with sepsis induced by intraperitoneally administered LPS were collected and subjected to HE staining, immunohistochemical staining with MPO and Ly6G, and an assay for MPO activity. The results of the lung injury assessment are presented for sham-operated mice treated with DMSO; 50  $\mu$ L, 10%, Group 1) or propofol (50  $\mu$ L, 20 mg/Kg and 40 mg/Kg, Group 2), and mice with sepsis-induced ALI treated with DMSO (Group 3) or propofol (Group 4). As shown in Fig. 8, sepsis resulted in alveolar wall disruption and edematous changes, which were alleviated by propofol. Sepsis also increased neutrophil infiltration, as evidenced by an increase in immunohistochemical MPO and Ly6G expression. Intraperitoneal administration of propofol effectively reduced the increase in pulmonary neutrophil infiltration (Fig. 8). Additionally, MPO activity, which is a quantitative indicator of neutrophil infiltration, exhibited a significantly increased in the lungs of septic mice. Administration of intraperitoneal propofol (20 and 40 mg/kg) significantly inhibited the rise in MPO activity in the lungs of septic mice (Fig. 8A). Furthermore, a survival study was conducted, in which septic mice were challenged with 10 mg/kg LPS with or without propofol (50  $\mu$ L; 10, 20 or 40 mg/kg). The survival rate was monitored for 7 days to evaluate overall survival ( $n = 6$  for each group). Ultimately, within 3 days of the LPS challenge, all mice in control group perished; by contrast, 80% of mice treated with propofol (40 mg/kg) survived more than 7 days after the LPS challenge (Fig. 9).

## 4. Discussion

Propofol is commonly used in operation rooms or intensive care units (ICUs) for critically ill patients. Various clinical trials have demonstrated that the antioxidant, anti-inflammatory, and free-radical-scavenging properties of propofol can provide clinical benefits. For examples, the use of propofol has been reported to reduce the incidence of postoperative cognitive dysfunction, maintain an appropriate hemodynamic status, shorten ICU stays, and increase the lung compliance of patients who underwent major surgery or cardio-pulmonary bypass [28–32]. Nevertheless, the detailed molecular mechanism that governs these protective effects of propofol is still incompletely understood. In a

previous study, we demonstrated that propofol inhibits fMLF-induced neutrophil activation by blocking FPR1 [8]. However, fMLF, which is an exogenous bacterial formylated peptide, is rarely involved in the early stage of sterile tissue injury. The present study illustrated that propofol competitively inhibits the interaction between FPR1 and fMMYALF, which is a mitochondria-derived DAMP released from damaged cells [22,33,34]. Therefore, propofol can reduce superoxide production and associated ROS formation, elastase release, and cell migration, which are all inflammatory responses of neutrophils that can be observed in critically-ill patients caused by traumatic or surgical-associated injury.

The human immune is a complex system whose primary aim is to protect human the body from invading pathogens. To achieve this aim, recognition of pathogenic microbes is the first and most critical step, followed by the initiation of a series of responses required for eliminating the invading pathogens. Nevertheless, while invading pathogens that cause tissue injury must be eliminated, the commensal microorganisms that are required for host survival should be tolerated. In addition, the immune system plays a crucial role in maintaining hemostatic tissue function. Sterile tissue injury arising from traumatic or surgery-associated injury must be detected and repaired. In other words, with the emergence of the “danger model” in the scientific community, researchers have come to understand that the immune system depends on various pattern-recognition receptors to distinguish danger and nondanger patterns, rather than self and nonself patterns [35]. The common causes of critical illness, including sepsis, trauma, surgery-related cell damage, hypoxia, and ischemia, also cause uncontrolled cell or tissue damage. Consequently, intracellular molecules, some of which are considered as DAMPs, are either actively or passively discharged into the surrounding tissue and circulation [35,36]. Moreover, because critically ill patients exhibit immune-associated complications, DAMPs have crucial implications in the prognosis of these patients and are considered possible therapeutic targets for anti-inflammatory compounds.

In the past decade, studies have demonstrated that the mitochondrial molecules released into circulation act as DAMPs [37]; therefore, they contribute to DAMP-mediated immune stimulation [22,33,37]. Mitochondria originated from engulfed prokaryotic cells [38,39]. Mitochondrial protein synthesis is similar to that of their prokaryotic ancestor and begins with the *N*-formyl methionine residue [22,40], which is absent in the cytosol. The fMMYALF is an *N*-formyl peptide that corresponds to the *N* terminus of mitochondrial NADH dehydrogenase subunit 6. Prior studies have reported that fMMYALF, similar to fMLF of prokaryotic origin, is a potent activator that stimulates immune effector cells via FPRs [21,22,41]. It induces p38, p44, and p42 MAPK phosphorylation, resulting in the release of proinflammatory signals, including matrix metalloproteinase-8 and interleukin 8 [22,37]. Moreover, recent studies found that the level of mitochondria-derived formylated peptides is increased in bronchoalveolar lavage fluid and serum of patients with acute respiratory distress syndrome (ARDS) [23]. Considering the importance of mitochondrial *N*-formylated peptides in ARDS, we used the fMMYALF for human neutrophil stimulation in this study. Our results suggest that propofol may have therapeutic benefits to attenuate endogenous *N*-formylated peptides-mediated inflammatory diseases.

The receptor binding assay used in our previous study demonstrated that propofol competitively binds to FPR1, thus blocking the downstream signal transduction of FPR1 and inhibiting neutrophil immune activities [8]. In this study, we assessed the pharmacological action of fMMYALF in the presence of propofol. Cellular inflammatory responses, including ROS generation, elastase release, and cell migration were assessed at different concentrations of the stimulant (fMMYALF) and constant concentration of the inhibitor (propofol). The addition of propofol (50  $\mu$ M) causes a parallel rightward shift of the fMMYALF response curve, which represents an increase in the  $EC_{50}$  of the agonist (fMMYALF). In other words, propofol reduces the potency but not the

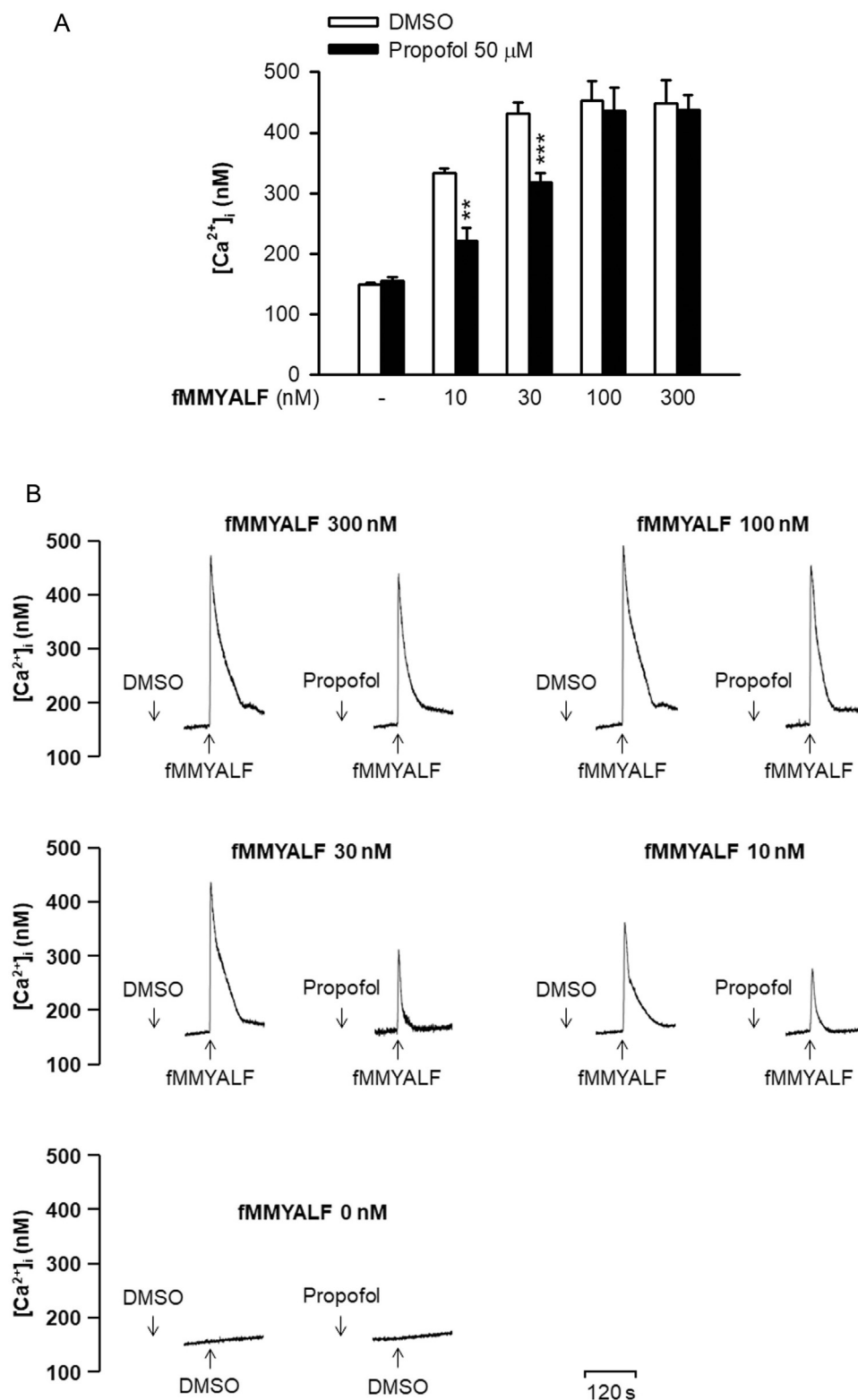


**Fig. 6. Propofol competitively reduces Ca<sup>2+</sup> mobilization in fMMYALF-activated human neutrophils.** Fluo 3-loaded neutrophils were incubated with DMSO (as control) or propofol (50 μM) for 5 min. Cells were then activated by fMMYALF. Mobilization of Ca<sup>2+</sup> was determined in real time in a spectrofluorometer. (A) Data are expressed as the mean ± standard error of the mean, n = 7, \*\*p < 0.01, \*\*\*p < 0.001 as compared with the corresponding control. (B) Representative traces are shown.

maximal response of fMMYALF. In clinical condition, the plasma concentration of propofol is kept between 1 μg/mL to 30 μg/mL [42]. the dosage of propofol used in our in vitro studies ranges from are 5 μM (about 0.891 μg/mL) to 100 μM (about 17.83 μg/mL). Therefore, the

propofol dosage used in our in vitro studies are corresponding to clinical practice.

FPRs is a member of Gi/o protein-coupled receptor. Ligand interaction with FPRs initiates the dissociation of the Gα subunit from the

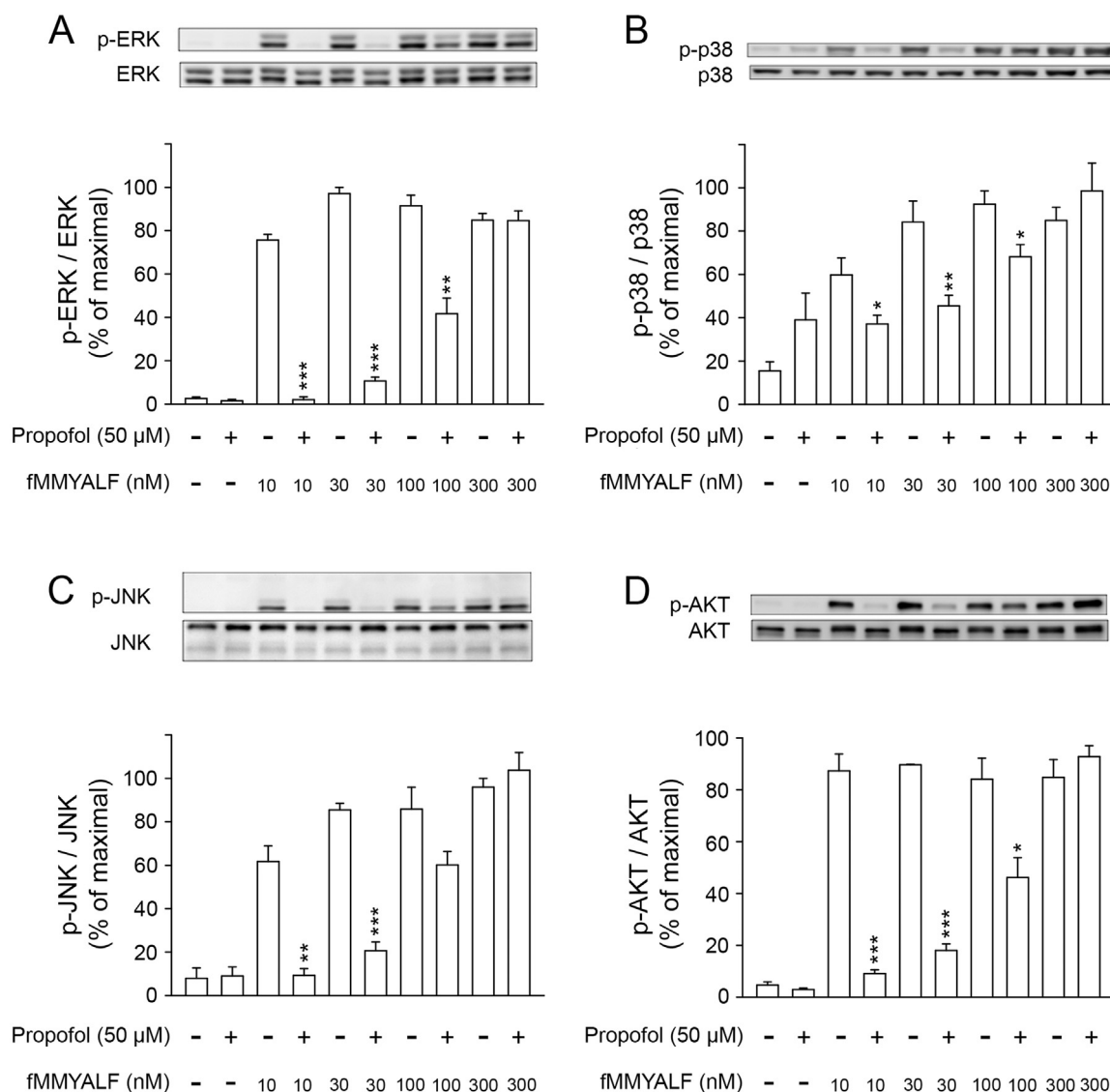


**Fig. 7. Propofol inhibits the phosphorylation of protein kinase B (AKT) and mitogen-activated protein kinases in fMMYALF-activated human neutrophils.** Human neutrophils were pre-incubated with DMSO or propofol (50 μM) before stimulation with fMMYALF (10–300 nM). All the Western blotting experiments were performed under the same condition. After transferring the blots onto nitrocellulose membranes, we immediately cropped the targeted blots according to referenced indicating markers, and then targeted proteins were immunoblotted with its specific monoclonal antibody. Representative images from one of four independent experiments of Western blotting using anti-phospho antibodies directed against extracellular-signal-regulated kinase (ERK), p38, c-Jun N-terminal kinase (JNK), and AKT were shown. Bands on the blots were analyzed using a densitometer, and the quantitative ratios for all samples were normalized to the corresponding total protein. Data are expressed as the mean ± standard error of the mean, n = 6, \**p* < 0.05, \*\**p* < 0.01, \*\*\**p* < 0.001, as compared to the control group.

Gβγ subunit. Intracellular Ca<sup>2+</sup> mobilization occurs downstream of G-protein activation and is crucial to respiratory burst in human neutrophils [43,44]. Our data demonstrated that propofol reduced the fMMYALF-induced mobilization of intracellular Ca<sup>2+</sup>. The activation of PI3K and the subsequent production of phosphatidylinositol (3,4,5) P3 (PIP3) and AKT are other major signal transduction event associated with FPRs and mediated by Gβγ dimers [45]. Furthermore, the p38 and ERK MAPKs are downstream mediators of the FPR signaling pathway [46,47]. They are strongly activated on neutrophil stimulation with FPR1 agonists. The p38 promotes the chemotactic migration of neutrophils [48]. Western blot analysis in our experiments revealed that propofol reduced fMMYALF-induced phosphorylation of ERK, p38, JNK, and AKT. Taken together, the preceding evidence demonstrates that propofol can effectively reduce fMMYALF-induced human neutrophil inflammatory responses by directly interfering with the binding of fMMYALF to FPR1, thereby blocking the subsequent signal transduction.

Despite considerable progress in elucidating the mechanisms of sepsis and sepsis-associated ALI as well as the development of novel intervention therapies in ICUs, sepsis and sepsis-induced ALI remain leading causes of mortality in critically ill patients [49]. Oxidative stress is a dangerous pathogenic factor in sepsis and sepsis-associated ALI [50]. Oxidative burst by neutrophil NADPH oxidase can produce huge amounts of superoxide and associated ROS at the site of inflammation. Prolonged and uncontrolled oxidative stress by activated neutrophils impairs surrounding cells and results in inflammatory disorders [51]. Recruitment and infiltration of neutrophils is considered as a critical process in ALI [52,53]. Because FPR1 plays a vital role in the process of neutrophil migration during acute and chronic inflammation [54], researchers have carefully investigated the importance of FPR1 in neutrophil recruitment during the development of LPS-induced ALI [55]. Specifically, a prior study demonstrated that the lung infiltration of neutrophils was markedly reduced in the FPR1<sup>-/-</sup> mice [56]. Moreover, we and other researchers have shown that cyclosporine H, an



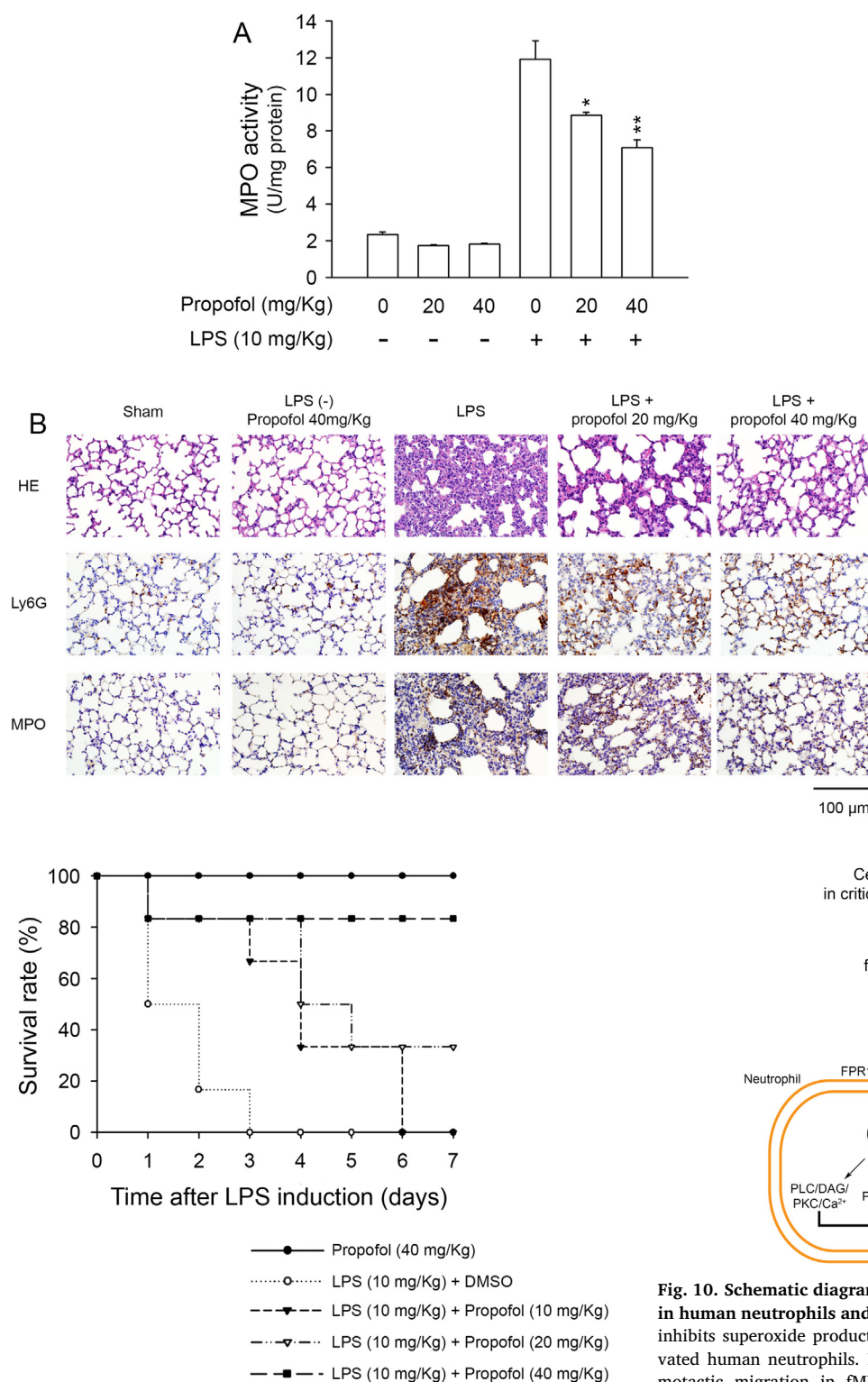


**Fig. 9. Propofol ameliorates LPS-induced mortality in mice.** Mice were challenged with LPS (10 mg/kg) with or without propofol (10, 20 or 40 mg/kg). The survival rate was monitored for 7 days to evaluate overall survival ( $n = 6$  for each group). 100% of the mice died within 3 days after the LPS challenge, whereas 80% of mice treated with propofol survived for 7 days after the LPS challenge.

FPR1 antagonist, can pharmacologically reduce the neutrophils recruitment, thus affording protection effect against LPS-induced ALI [56,57]. In the present study, propofol was shown to reduce pulmonary edema, neutrophil infiltration, and MPO activity in our experimental

**Fig. 8. Effects of propofol on myeloperoxidase (MPO) level and histopathologic examination of mouse lungs in sepsis-induced acute lung injury (ALI).** Mice were pretreated with three doses of DMSO (50  $\mu$ L, 10%) or propofol (50  $\mu$ L, 20 mg/Kg and 40 mg/Kg) intraperitoneally. Following the second administration of DMSO or propofol, the mice were challenged with single dose of 200  $\mu$ L of LPS (10 mg/Kg) or 0.9% saline (sham operation) administered intraperitoneally. Twenty hours after LPS or 0.9% saline administration, mouse lungs were resected and subjected to (A) an assay for MPO activity, (B, upper) hematoxylin and eosin (HE) staining, (B, middle) immunohistochemical detection for neutrophilic Ly6G proteins, and (B, lower) MPO proteins. All sections were observed at an original magnification of  $\times 200$ . Data are expressed as the mean  $\pm$  standard error of the mean,  $n = 7$ , \* $p < 0.05$ , \*\* $p < 0.01$ , \*\*\* $p < 0.001$ , as compared to the control group.

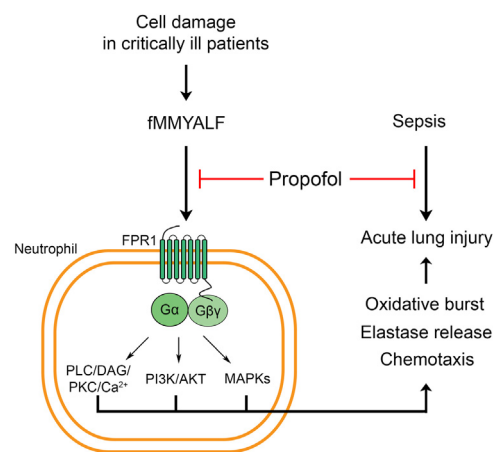


**Fig. 10. Schematic diagram illustrating the therapeutic effects of propofol in human neutrophils and sepsis-induced acute lung injury (ALI).** Propofol inhibits superoxide production and associated ROS release in fMMYALF-activated human neutrophils. Propofol also suppresses elastase release and chemotactic migration in fMMYALF-induced human neutrophils. The anti-inflammatory effects of propofol in human neutrophils are mediated by interfering with the binding of fMMYALF to FPR1, which inhibits the downstream signaling of receptors. Furthermore, propofol attenuates sepsis-induced ALI and mortality in mice.

murine model of LPS-induced ALI. Additionally, propofol reduces the mortality rate of mice with endotoxemic ALI. Taken together, this evidence shows that FPR1 is an important target of anti-inflammatory strategies and provides protection against LPS-induced ALI. We suggest that the mechanism of action of propofol in animal model is mediated through blocking the interaction of mitochondria formylated peptide

and FPR.

## 5. Conclusions

We concluded that the inhibitory effects of propofol on fMMYALF-induced neutrophil activation are mediated by competition with FPR1, which inhibits receptor-mediated downstream signaling and inflammatory responses such as oxidative burst, elastase release, and chemotactic migration (Fig. 10). Our experiments performed using a septic mouse model revealed that propofol, an FPR1 antagonist, may be beneficial for treating patients who are critically ill with sepsis and sepsis-associated ALI.

## Acknowledgments

This work was supported by the grants from the Ministry of Science and Technology (MOST 106-2320-B-255-003-MY3 and MOST 104-2320-B-255-004-MY3), Ministry of Education (EMRPD1G0231 and EMRPD1H0381), and Chang Gung Memorial Hospital (CMRPF1F0011~3, CMRPF1F0061~3, CMRPF1G0241~3, and BMRP450), Taiwan.

## References

- [1] W. Fan, X. Zhu, L. Wu, Z. Wu, D. Li, F. Huang, H. He, Propofol: an anesthetic possessing neuroprotective effects, *Eur. Rev. Med. Pharmacol. Sci.* 19 (8) (2015) 1520–1529.
- [2] P.E. Marik, Propofol: an immunomodulating agent, *Pharmacotherapy* 25 (5 Pt 2) (2005) 28S–33S.
- [3] C. Vanlersberghe, F. Camu, Propofol, *Handb. Exp. Pharmacol.* 182 (2008) 227–252.
- [4] R.M. Chen, G.J. Wu, Y.T. Tai, W.Z. Sun, Y.L. Lin, W.C. Jean, T.L. Chen, Propofol reduces nitric oxide biosynthesis in lipopolysaccharide-activated macrophages by downregulating the expression of inducible nitric oxide synthase, *Arch. Toxicol.* 77 (7) (2003) 418–423.
- [5] J. Tang, X. Chen, W. Tu, Y. Guo, Z. Zhao, Q. Xue, C. Lin, J. Xiao, X. Sun, T. Tao, M. Gu, Y. Liu, Propofol inhibits the activation of p38 through up-regulating the expression of annexin A1 to exert its anti-inflammation effect, *PLoS One* 6 (12) (2011) e27890.
- [6] D.W. Wheeler, A.J. Thompson, F. Corletto, J. Reckless, J.C. Loke, N. Lapaque, A.J. Grant, P. Mastroeni, D.J. Grainger, C.L. Padgett, J.A. O'Brien, N.G. Miller, J. Trowsdale, S.C. Lummis, D.K. Menon, J.S. Beech, Anaesthetic impairment of immune function is mediated via GABA(A) receptors, *PLoS One* 6 (2) (2011) e17152.
- [7] C.H. Li, R.P. Lee, Y.L. Lin, C.S. Lin, B.G. Hsu, F.J. Tseng, Y.C. Chen, K.W. Liao, F.L. Yang, The treatment of propofol induced the TGF- $\beta$ 1 expression in human endothelial cells to suppress endocytosis activities of monocytes, *Cytokine* 52 (3) (2010) 203–209.
- [8] S.C. Yang, P.J. Chung, C.M. Ho, C.Y. Kuo, M.F. Hung, Y.T. Huang, W.Y. Chang, Y.W. Chang, K.H. Chan, T.L. Hwang, Propofol inhibits superoxide production, elastase release, and chemotaxis in formyl peptide-activated human neutrophils by blocking formyl peptide receptor 1, *J. Immunol.* 190 (12) (2013) 6511–6519.
- [9] H.F. Galley, A.M. Dubbels, N.R. Webster, The effect of midazolam and propofol on interleukin-8 from human polymorphonuclear leukocytes, *Anesth. Analg.* 86 (6) (1998) 1289–1293.
- [10] K. Mikawa, H. Akamatsu, K. Nishina, M. Shiga, N. Maekawa, H. Obara, Y. Niwa, Propofol inhibits human neutrophil functions, *Anesth. Analg.* 87 (3) (1998) 695–700.
- [11] T. Taniguchi, H. Kanakura, K. Yamamoto, Effects of posttreatment with propofol on mortality and cytokine responses to endotoxin-induced shock in rats, *Crit. Care Med.* 30 (4) (2002) 904–907.
- [12] F. Liu, M.R. Chen, J. Liu, Y. Zou, T.Y. Wang, Y.X. Zuo, T.H. Wang, Propofol administration improves neurological function associated with inhibition of pro-inflammatory cytokines in adult rats after traumatic brain injury, *Neuropeptides* 58 (2016) 1–6.
- [13] W. Fan, Q. Liu, X. Zhu, Z. Wu, D. Li, F. Huang, H. He, Regulatory effects of anesthetics on nitric oxide, *Life Sci.* 151 (2016) 76–85.
- [14] H. Yagmurdu, K. Binnetoglu, H.M. Astarci, M.C. Yagmurdu, Propofol attenuates cytokine-mediated upregulation of expression of inducible nitric oxide synthase and apoptosis during regeneration post-partial hepatectomy, *Acta Cir. Bras.* 32 (5) (2017) 396–406.
- [15] Z. Xu, Y. Lu, J. Wang, X. Ding, J. Chen, C. Miao, The protective effect of propofol against TNF- $\alpha$ -induced apoptosis was mediated via inhibiting iNOS/NO production and maintaining intracellular Ca(2+) homeostasis in mouse hippocampal HT22 cells, *Biomed. Pharmacother.* 91 (2017) 664–672.
- [16] A. Rhodes, L.E. Evans, W. Alhazzani, M.M. Levy, M. Antonelli, R. Ferrer, A. Kumar, J.E. Sevransky, C.L. Sprung, M.E. Nunnally, B. Rochwerf, G.D. Rubenfeld, D.C. Angus, D. Annane, R.J. Beale, G.J. Bellingham, G.R. Bernard, J.D. Chiche, C. Coopersmith, D.P. De Backer, C.J. French, S. Fujishima, H. Gerlach, J.L. Hidalgo, S.M. Hollenberg, A.E. Jones, D.R. Karnad, R.M. Kleinpell, Y. Koh, T.C. Lisboa, F.R. Machado, J.J. Marini, J.C. Marshall, J.E. Mazuski, L.A. McIntyre, A.S. McLean, S. Mehta, R.P. Moreno, J. Myburgh, P. Navalesi, O. Nishida, T.M. Osborn, A. Perner, C.M. Plunkett, M. Ranieri, C.A. Schorr, M.A. Seckel, C.W. Seymour, L. Shieh, K.A. Shukri, S.Q. Simpson, M. Karnad, B.T. Thompson, S.R. Townsend, T. Van der Poll, J.L. Vincent, W.J. Wiersinga, J.L. Zimmerman, R.P. Dellinger, Surviving sepsis campaign: international guidelines for management of sepsis and septic shock, *Crit. Care Med.* (2016) 486–552.
- [17] K.J. Grim, A.J. Abcejo, A. Barnes, V. Sathish, D.F. Smelter, G.C. Ford, M.A. Thompson, Y.S. Prakash, C.M. Pabelick, Caveolae and propofol effects on airway smooth muscle, *Br. J. Anaesth.* (2012) 444–453.
- [18] L. Calzetta, A. Soggiu, P. Roncada, L. Bonizzi, E. Pistocchini, A. Urbani, B. Rinaldi, M.G. Matera, Propofol protects against opioid-induced hyperresponsiveness of airway smooth muscle in a horse model of target-controlled infusion anaesthesia, *Eur. J. Pharmacol.* 765 (2015) 463–471.
- [19] F. Ulbrich, L. Eisert, H. Buerkle, U. Goebel, N. Schallner, Propofol, but not ketamine or midazolam, exerts neuroprotection after ischaemic injury by inhibition of Toll-like receptor 4 and nuclear factor kappa-light-chain-enhancer of activated B-cell signalling: a combined in vitro and animal study, *Eur. J. Anaesthesiol.* 33 (9) (2016) 670–680.
- [20] G. De Cosmo, E. Congedo, A. Clemente, P. Aceto, Sedation in PACU: the role of propofol, *Curr. Drug Targets* 6 (7) (2005) 741–744.
- [21] M.J. Rabiet, E. Huet, F. Boulay, Human mitochondria-derived N-formylated peptides are novel agonists equally active on FPR and FPR1, while *Listeria* monocytes-derived peptides preferentially activate FPR, *Eur. J. Immunol.* 35 (8) (2005) 2486–2495.
- [22] M. Raoof, Q. Zhang, K. Itagaki, C.J. Hauser, Mitochondrial peptides are potent immune activators that activate human neutrophils via FPR-1, *J. Trauma* 68 (6) (2010) 1328–1332 (discussion1332–1334).
- [23] D.A. Dorward, C.D. Lucas, M.K. Doherty, G.B. Chapman, E.J. Scholefield, A. Conway Morris, J.M. Felton, T. Kipari, D.C. Humphries, C.T. Robb, A.J. Simpson, P.D. Whitfield, C. Haslett, K. Dhaliwal, A.G. Rossi, Novel role for endogenous mitochondrial formylated peptide-driven formyl peptide receptor 1 signalling in acute respiratory distress syndrome, *Thorax* 72 (10) (2017) 928–936.
- [24] A.A. Fowler, R.F. Hamman, J.T. Good, K.N. Benson, M. Baird, D.J. Eberle, T.L. Petty, T.M. Hyers, Adult respiratory distress syndrome: risk with common predispositions, *Ann. Intern. Med.* 98 (5 Pt 1) (1983) 593–597.
- [25] T.L. Hwang, Y.L. Leu, S.H. Kao, M.C. Tang, H.L. Chang, Viscolin, a new chalcone from *Viscum coloratum*, inhibits human neutrophil superoxide anion and elastase release via a cAMP-dependent pathway, *Free Radic. Biol. Med.* 41 (9) (2006) 1433–1441.
- [26] C.Y. Chen, C.C. Liaw, Y.H. Chen, W.Y. Chang, P.J. Chung, T.L. Hwang, A novel immunomodulatory effect of ugonin U in human neutrophils via stimulation of phospholipase C, *Free Radic. Biol. Med.* 72 (2014) 222–231.
- [27] K. Futosi, S. Fodor, A. Mocsai, Reprint of Neutrophil cell surface receptors and their intracellular signal transduction pathways, *Int. Immunopharmacol.* 17 (4) (2013) 1185–1197.
- [28] R.C. Landis, J.R. Brown, D. Fitzgerald, D.S. Likosky, L. Shore-Lesserson, R.A. Baker, J.W. Hammon, Attenuating the systemic inflammatory response to adult cardiopulmonary bypass: a critical review of the evidence base, *J. Extra Corpor. Technol.* 46 (3) (2014) 197–211.
- [29] K. An, H. Shu, W. Huang, X. Huang, M. Xu, L. Yang, K. Xu, C. Wang, Effects of propofol on pulmonary inflammatory response and dysfunction induced by cardiopulmonary bypass, *Anaesthesia* 63 (11) (2008) 1187–1192.
- [30] Z. Huang, X. Zhong, M.G. Irwin, S. Ji, G.T. Wong, Y. Liu, Z.Y. Xia, B.A. Finegan, Z. Xia, Synergy of isoflurane preconditioning and propofol postconditioning reduces myocardial reperfusion injury in patients, *Clin. Sci.* 121 (2) (2011) 57–69.
- [31] S. Sayed, N.K. Idriss, H.G. Sayyidf, A.A. Ashry, D.M. Rafat, A.O. Mohamed, A.D. Blann, Effects of propofol and isoflurane on haemodynamics and the inflammatory response in cardiopulmonary bypass surgery, *Br. J. Biomed. Sci.* 72 (3) (2015) 93–101.
- [32] Y. Qiao, H. Feng, T. Zhao, H. Yan, H. Zhang, X. Zhao, Postoperative cognitive dysfunction after inhalational anesthesia in elderly patients undergoing major surgery: the influence of anesthetic technique, cerebral injury and systemic inflammation, *BMC Anesthesiol.* 15 (2015) 154.
- [33] D.V. Krysko, P. Agostinis, O. Krysko, A.D. Garg, C. Bachert, B.N. Lambrecht, P. Vandenabeele, Emerging role of damage-associated molecular patterns derived from mitochondria in inflammation, *Trends Immunol.* 32 (4) (2011) 157–164.
- [34] T. Eleftheriadis, G. Pissas, V. Liakopoulos, I. Stefanidis, Cytochrome c as a potentially clinical useful marker of mitochondrial and cellular damage, *Front. Immunol.* 7 (2016) 279.
- [35] P. Matzinger, Tolerance, danger, and the extended family, *Annu. Rev. Immunol.* 12 (1994) 991–1045.
- [36] J.J. Oppenheim, D. Yang, Alarmins: chemotactic activators of immune responses, *Curr. Opin. Immunol.* 17 (4) (2005) 359–365.
- [37] Q. Zhang, M. Raoof, Y. Chen, Y. Sumi, T. Sursal, W. Junger, K. Brohi, K. Itagaki, C.J. Hauser, Circulating mitochondrial DAMPs cause inflammatory responses to injury, *Nature* 464 (7285) (2010) 104–107.
- [38] M.W. Gray, G. Burger, B.F. Lang, Mitochondrial evolution, *Science* 283 (5407) (1999) 1476–1481.
- [39] C. Zimmer, Origins. On the origin of eukaryotes, *Science* 325 (5941) (2009) 666–668.
- [40] K. Marcker, The formation of N-formyl-methionyl-sRNA, *J. Mol. Biol.* 14 (1) (1965) 63–70.
- [41] E.D. Crouser, G. Shao, M.W. Julian, J.E. Macre, G.S. Shadel, S. Tridandapani, Q. Huang, M.D. Wewers, Monocyte activation by necrotic cells is promoted by

- mitochondrial proteins and formyl peptide receptors, *Crit. Care Med.* 37 (6) (2009) 2000–2009.
- [42] M.S. Khan, E.L. Zetterlund, H. Green, A. Oscarsson, A.L. Zackrisson, E. Svanborg, M.L. Lindholm, H. Persson, C. Eintrei, Pharmacogenetics, plasma concentrations, clinical signs and EEG during propofol treatment, *Basic Clin. Pharmacol. Toxicol.* 115 (6) (2014) 565–570.
- [43] S. Brechard, E.J. Tschirhart, Regulation of superoxide production in neutrophils: role of calcium influx, *J. Leukoc. Biol.* 84 (5) (2008) 1223–1237.
- [44] M.J. Berridge, P. Lipp, M.D. Bootman, The versatility and universality of calcium signalling, *Nat. Rev. Mol. Cell Biol.* 1 (1) (2000) 11–21.
- [45] L. Stephens, A. Smrcka, F.T. Cooke, T.R. Jackson, P.C. Sternweis, P.T. Hawkins, A novel phosphoinositide 3 kinase activity in myeloid-derived cells is activated by G protein beta gamma subunits, *Cell* 77 (1) (1994) 83–93.
- [46] A. Mocsai, Z. Jakus, T. Vantus, G. Berton, C.A. Lowell, E. Ligeti, Kinase pathways in chemoattractant-induced degranulation of neutrophils: the role of p38 mitogen-activated protein kinase activated by Src family kinases, *J. Immunol.* 164 (8) (2000) 4321–4331.
- [47] B. Heit, L. Liu, P. Colarusso, K.D. Puri, P. Kubes, PI3K accelerates, but is not required for, neutrophil chemotaxis to fMLP, *J. Cell Sci.* 121 (Pt 2) (2008) 205–214.
- [48] M.O. Hannigan, L. Zhan, Y. Ai, A. Kotlyarov, M. Gaestel, C.K. Huang, Abnormal migration phenotype of mitogen-activated protein kinase-activated protein kinase 2-/- neutrophils in Zigmond chambers containing formyl-methionyl-leucyl-phenylalanine gradients, *J. Immunol.* 167 (7) (2001) 3953–3961.
- [49] M.A. Matthay, L.B. Ware, G.A. Zimmerman, The acute respiratory distress syndrome, *J. Clin. Investig.* 122 (8) (2012) 2731–2740.
- [50] G. Hong, D. Zheng, L. Zhang, R. Ni, G. Wang, G.C. Fan, Z. Lu, T. Peng, Administration of nicotinamide riboside prevents oxidative stress and organ injury in sepsis, *Free Radic. Biol. Med.* 123 (2018) 125–137.
- [51] L. Glennon-Alty, A.P. Hackett, E.A. Chapman, H.L. Wright, Neutrophils and redox stress in the pathogenesis of autoimmune disease, *Free Radic. Biol. Med.* 125 (2018) 25–35.
- [52] J. Grommes, O. Soehnlein, Contribution of neutrophils to acute lung injury, *Mol. Med.* 17 (3–4) (2011) 293–307.
- [53] R.L. Zemans, M.A. Matthay, What drives neutrophils to the alveoli in ARDS? *Thorax* 72 (1) (2017) 1–3.
- [54] Y.F. Tsai, S.C. Yang, T.L. Hwang, Formyl peptide receptor modulators: a patent review and potential applications for inflammatory diseases (2012–2015), *Expert Opin. Ther. Pat.* (2016) 1–18.
- [55] C.F. Wenceslau, T. Szasz, C.G. McCarthy, B. Baban, E. NeSmith, R.C. Webb, Mitochondrial N-formyl peptides cause airway contraction and lung neutrophil infiltration via formyl peptide receptor activation, *Pulm. Pharmacol. Ther.* 37 (2016) 49–56.
- [56] J. Grommes, M. Drechsler, O. Soehnlein, CCR5 and FPR1 mediate neutrophil recruitment in endotoxin-induced lung injury, *J. Innate Immun.* 6 (1) (2014) 111–116.
- [57] S.C. Yang, S.H. Chang, P.W. Hsieh, Y.T. Huang, C.M. Ho, Y.F. Tsai, T.L. Hwang, Dipeptide HCH6-1 inhibits neutrophil activation and protects against acute lung injury by blocking FPR1, *Free Radic. Biol. Med.* 106 (2017) 254–269.



Contents lists available at ScienceDirect

EBioMedicine

journal homepage: [www.ebiomedicine.com](http://www.ebiomedicine.com)

EBioMedicine

Published by THE LANCET

## Targeting allosteric site of AKT by 5,7-dimethoxy-1,4-phenanthrenequinone suppresses neutrophilic inflammation

Po-Jen Chen<sup>a,b</sup>, I-Ling Ko<sup>b</sup>, Chia-Lin Lee<sup>c,d</sup>, Hao-Chun Hu<sup>e</sup>, Fang-Rong Chang<sup>e</sup>, Yang-Chang Wu<sup>e</sup>, Yann-Lii Leu<sup>b,f,g</sup>, Chih-Ching Wu<sup>h,i</sup>, Cheng-Yu Lin<sup>b</sup>, Chang-Yu Pan<sup>b</sup>, Yung-Fong Tsai<sup>b,j</sup>, Tsong-Long Hwang<sup>b,f,j,k,l,\*</sup>

<sup>a</sup> Department of Cosmetic Science, Providence University, Taichung 433, Taiwan

<sup>b</sup> Graduate Institute of Natural Products, College of Medicine, Chang Gung University, Taoyuan 333, Taiwan

<sup>c</sup> Chinese Medicine Research and Development Center, China Medical University Hospital, Taichung 404, Taiwan

<sup>d</sup> Department of Cosmeceutics, China Medical University, Taichung 404, Taiwan

<sup>e</sup> Graduate Institute of Natural Products, College of Pharmacy and Research Center for Natural Products & Drug Development, Kaohsiung Medical University, Kaohsiung 807, Taiwan

<sup>f</sup> Chinese Herbal Medicine Research Team, Healthy Aging Research Center, Chang Gung University, Taoyuan 333, Taiwan

<sup>g</sup> Center for Traditional Chinese Medicine, Chang Gung Memorial Hospital, Taoyuan 333, Taiwan

<sup>h</sup> Department of Medical Biotechnology and Laboratory Science, College of Medicine, Chang Gung University, Taoyuan 333, Taiwan

<sup>i</sup> Department of Otolaryngology – Head & Neck Surgery, Chang Gung Memorial Hospital, Taoyuan 333, Taiwan

<sup>j</sup> Department of Anaesthesiology, Chang Gung Memorial Hospital, Taoyuan 333, Taiwan

<sup>k</sup> Research Center for Chinese Herbal Medicine, Research Center for Food and Cosmetic Safety, Graduate Institute of Health Industry Technology, College of Human Ecology, Chang Gung University of Science and Technology, Taoyuan 333, Taiwan

<sup>l</sup> Department of Chemical Engineering, Ming Chi University of Technology, New Taipei City 243, Taiwan

### ARTICLE INFO

#### Article history:

Received 21 December 2018

Received in revised form 22 January 2019

Accepted 22 January 2019

Available online xxxxx

#### Keywords:

Acute lung injury

AKT

5,7-dimethoxy-1,4-phenanthrenequinone

Inflammation

Neutrophil

### ABSTRACT

**Background:** Acute lung injury (ALI) is a severe life-threatening inflammatory disease. Neutrophil activation is a major pathogenic factor in ALI. Protein kinase B (PKB)/AKT regulates diverse cellular responses, but the significance in neutrophilic inflammation and ALI remains unknown.

**Methods:** Human neutrophils and neutrophil-like differentiated HL-60 (dHL-60) cells were used to examine the anti-inflammatory effects of 5,7-dimethoxy-1,4-phenanthrenequinone (CLLV-1). The therapeutic potential of CLLV-1 was determined in a mouse model of lipopolysaccharide (LPS)-induced ALI.

**Findings:** CLLV-1 inhibited respiratory burst, degranulation, adhesion, and chemotaxis in human neutrophils and dHL-60 cells. CLLV-1 inhibited the phosphorylation of AKT (Thr308 and Ser473), but not of ERK, JNK, or p38. Furthermore, CLLV-1 blocked AKT activity and covalently reacted with AKT Cys310 *in vitro*. The AKT<sub>309–313</sub> peptide-CLLV-1 adducts were determined by NMR or mass spectrometry assay. The alkylation agent-conjugated AKT (reduced form) level was also inhibited by CLLV-1. Significantly, CLLV-1 ameliorated LPS-induced ALI, neutrophil infiltration, and AKT activation in mice.

**Interpretation:** Our results identify CLLV-1 as a covalent allosteric AKT inhibitor by targeting AKT Cys310. CLLV-1 shows potent anti-inflammatory activity in human neutrophils and LPS-induced mouse ALI. Our findings provide a mechanistic framework for redox modification of AKT that may serve as a novel pharmacological target to alleviate neutrophilic inflammation.

© 2019 The Authors. Published by Elsevier B.V. This is an open access article under the CC BY-NC-ND license (<http://creativecommons.org/licenses/by-nc-nd/4.0/>).

### 1. Introduction

Neutrophils are the first line of host defense in the innate immune response. They are chemoattracted to inflammatory regions in response to infection, and they subsequently eliminate invading pathogens

through respiratory burst, degranulation, and neutrophil extracellular traps (NETs). However, overwhelming neutrophil activation plays a critical role both in infective and sterile inflammation [1–4]. The reactive oxygen species (ROS) and proteases released by activated neutrophils can damage healthy surrounding tissues, resulting in deleterious inflammatory lung diseases, such as acute lung injury (ALI), chronic obstructive pulmonary disease, or asthma [5–8].

Pathogen recognition or an inflammatory environment triggers many critical intracellular signal processes through surface receptors

\* Corresponding author at: Graduate Institute of Natural Products, Chang Gung University, 259 Wen-Hwa 1<sup>st</sup> Road, Kweishan, Taoyuan 333, Taiwan.  
E-mail address: [htl@mail.cgu.edu.tw](mailto:htl@mail.cgu.edu.tw) (T.-L. Hwang).



**Research in context***Evidence before this study*

Acute lung injury (ALI) is a severe life-threatening disease with high mortality. Neutrophil infiltration and activation play a critical role in ALI. Protein kinase B (PKB)/AKT controls diverse cellular responses. However, the role of AKT in regulating neutrophil functions is not well understood, and the targeting AKT for ALI remains unknown.

*Added value of this study*

We identify that 5,7-dimethoxy-1,4-phenanthrenequinone (CLLV-1) acts as a covalent allosteric AKT inhibitor by targeting AKT Cys310. CLLV-1 showed anti-inflammatory effects by suppressing neutrophil respiratory burst, degranulation, adhesion, and chemotaxis. Significantly, CLLV-1 ameliorated neutrophil infiltration, AKT activation, and lung injury in LPS-induced mouse ALI model. These results demonstrated that the targeting AKT in human neutrophils has the potential to treat ALI, and CLLV-1 may serve as a novel AKT inhibitor by targeting redox regulatory site of AKT.

*Implications of all the available evidence*

This study has provided evidences that AKT Cys310 is a pharmacological target for treating neutrophilic inflammatory diseases. CLLV-1 is a novel allosteric AKT inhibitor. CLLV-1 could act as a lead compound for treating ALI.

in neutrophils [9–12]. The serine/threonine-specific protein kinase, protein kinase B (PKB)/AKT, has been reported to regulate the neutrophil immune responses, including respiratory burst, degranulation, and chemotaxis [13–15]. In human neutrophils, activated AKT phosphorylates p47<sup>phox</sup>, a component of nicotinamide adenosine dinucleotide phosphate (NADPH) oxidase, to initiate respiratory burst [16–18]. Pharmacological inhibition of phosphoinositide 3-kinase (PI3K)/AKT signaling reduces leukocyte degranulation [19,20]. AKT also stabilizes F-actin polymerization to enhance the chemotaxis of activated neutrophils [18,21,22]. Therefore, AKT may be a potential pharmacological target to treat neutrophilic inflammation. In addition to the well-known regulatory phosphorylation, AKT is inactivated through an intra-disulfide bond between Cys296 and Cys310 in the catalytic domain to cause misleading conformation along with dephosphorylation [23–26]. However, the mechanistic details of whether redox-controlled AKT activity contributes to neutrophilic inflammation remains to be explored.

In this study, we identified that 5,7-dimethoxy-1,4-phenanthrenequinone (CLLV-1) (Fig. 1a) is a AKT inhibitor via a redox reaction with the Cys310 residue of AKT to block its kinase activity. CLLV-1 has been shown to exhibit anti-cancer activity and anti-vascular cell migration effect [27,28]. However, the underlying mechanism and direct target of CLLV-1 are unknown. Here, we found that CLLV-1 has an anti-inflammatory potential to impede respiratory burst, degranulation, and chemotaxis in activated human neutrophils or neutrophil-like differentiated HL-60 (dHL-60) cells. Moreover, administration of CLLV-1 ameliorated the inflammatory lung injury in lipopolysaccharide (LPS)-induced ALI in mice. Our findings demonstrate that redox modification of AKT may be a novel pharmacological strategy for suppressing neutrophil-dominant lung disorders. We also suggest that CLLV-1 has the potential to be developed as an anti-inflammatory drug.

**2. Materials and methods****2.1. Reagents**

CLLV-1 was synthesized by Dr. Chia-Lin Lee, Dr. Fang-Rong Chang, and Dr. Yang-Chang Wu [28]. The CLLV-1 structure was determined by <sup>1</sup>H nuclear magnetic resonance (NMR) spectrum analysis (Fig. 6c). The purity of CLLV-1 was higher than 96% as determined by high-performance liquid chromatography. MK-2206 was purchased from Selleckchem (Houston, TX, USA). WKYMVM was purchased from Tocris Bioscience (Ellisville, MO, USA). FITC-labeled anti-CD11b, anti-Ly-6G, and anti-myeloperoxidase (MPO) antibodies were purchased from eBioscience (San Diego, CA, USA). The antibodies against p38 or p47<sup>phox</sup> and protein G beads were purchased from Santa Cruz Biotechnology (Santa Cruz, CA, USA). Anti-phospho-p47<sup>phox</sup> antibodies were purchased from Abcam (Cambridge, MA, USA). Anti-PIP3 antibodies were purchased from Echelon Biosciences (Salt Lake City, UT, USA). Nonradioactive AKT kinase assay kit, anti-Akt (pan), anti-phospho-Akt (Ser473), anti-phospho-Akt (Thr308), and other antibodies were purchased from Cell Signaling (Beverly, MA, USA). RPMI 1640, DMEM, L-glutamine, Antibiotic-Antimycotic, dihydrorhodamine 123 (DHR123), N-formyl-Met-Leu-Phe-Nle-Tyr-Lys (fMLFNYK), Alexa Fluor 594 Phalloidin, and Hoechst 33342 were purchased from Thermo Fisher Scientific (Waltham, MA, USA). Fetal bovine serum (FBS) was purchased from Biological Industries (Beth Haemek, Israel). Other reagents were purchased from Sigma-Aldrich (St. Louis, MO, USA).

**2.2. Neutrophil isolation and cell culture**

The procedure of neutrophil isolation was approved by the Institutional Review Board at Chang Gung Memorial Hospital. Neutrophils were isolated by dextran sedimentation and Ficoll-Hypaque centrifugation. Blood was obtained from healthy volunteers (20–35 years old), and written informed consent was obtained from every volunteer. The purified neutrophils contained >98% viable cells, determined by trypan blue exclusion assay [29].

bEnd.3 endothelial cells (ECs) were obtained from the Bioresource Collection and Research Centre (Hsinchu, Taiwan) and cultured in DMEM media supplemented with 10% FBS and 1× Antibiotic-Antimycotic. The human promyelocytic leukemic HL-60 cell line was purchased from ATCC and cultured in RPMI 1640 medium supplemented with 20% FBS, 2 mM L-glutamine, and 1× Antibiotic-Antimycotic. Both cell lines were grown in a humidified atmosphere (37 °C, 5% CO<sub>2</sub>). The HL-60 cells were differentiated to neutrophil-like cells (dHL-60 cells) by a 5-day treatment with 1.3% DMSO in the growth medium.

**2.3. Extracellular superoxide anion production**

Human neutrophils ( $6 \times 10^5$  cells/mL) or dHL-60 cells ( $1 \times 10^6$  cells/mL) were equilibrated with 0.5 mg/mL ferricytochrome c and 1 mM Ca<sup>2+</sup> at 37 °C for 5 min. The cells were then preincubated with DMSO, CLLV-1, or MK-2206 and stimulated with N-Formyl-Met-Leu-Phe (fMLF), sodium fluoride (NaF), or WKYMVM before being primed with cytochalasin B (CB; 1 or 2 μg/mL) for 3 min. The superoxide anion was determined using a spectrophotometer (Hitachi, Tokyo, Japan) at 550 nm.

**2.4. Intracellular ROS formation**

DHR123 (2 μM)-labeled human neutrophils or dHL-60 cells ( $1 \times 10^6$  cells/mL) were incubated at 37 °C for 10 min. Subsequently, the cells were pretreated with DMSO or CLLV-1 for 5 min and activated by fMLF (0.1 μM)/CB (1 μg/mL) for another 5 min. The intracellular ROS formation was determined using a flow cytometer (BD Bioscience).

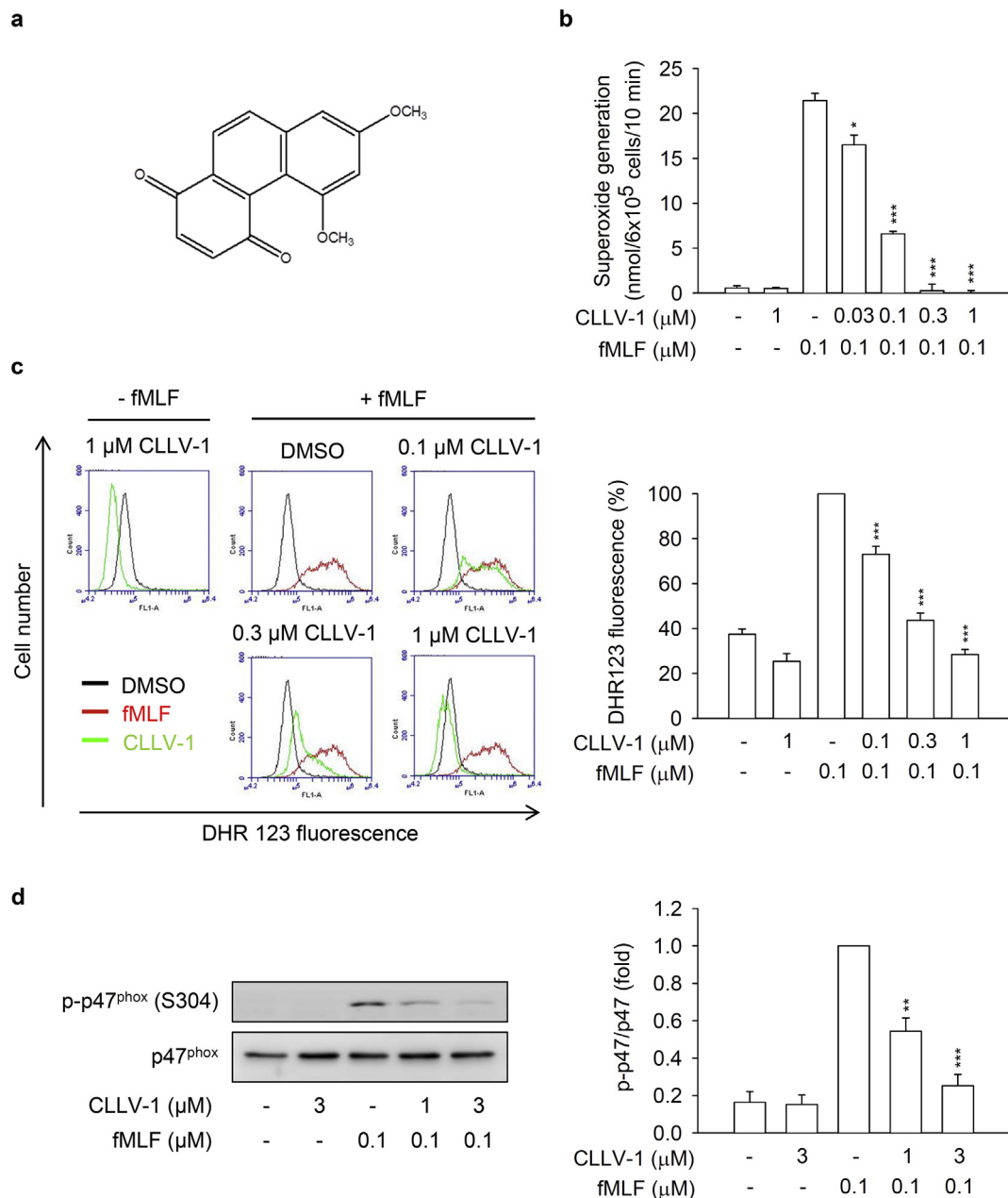


**Fig. 1.** CLLV-1 attenuates superoxide anion generation, ROS formation, and p47<sup>phox</sup> phosphorylation in fMLF-activated human neutrophils. (a) The chemical structure of CLLV-1. (B–C) Human neutrophils were preincubated with DMSO or CLLV-1 (0.03–3 μM) and then activated with or without fMLF (0.1 μM)/CB (1 μg/mL). (b) Superoxide anion generation was detected using cytochrome *c* reduction by a spectrophotometer at 550 nm. (c) The intracellular ROS was monitored by flow cytometry, using cell-permeable DHR123. (d) Phosphorylation of p47<sup>phox</sup> was analyzed by immunoblotting, using antibodies against the phosphorylated (S304) and total p47<sup>phox</sup>. All data are expressed as mean values ± SEM (*n* = 3); \**p* < .05, \*\**p* < .01, and \*\*\**p* < .001 compared with the DMSO + fMLF group (Student's *t*-test).

## 2.5. Elastase release

Human neutrophils ( $6 \times 10^5$  cells/mL) were equilibrated with an elastase substrate (MeO-Suc-Ala-Ala-Pro-Val-p-nitroanilide; 100 μM) at 37 °C for 5 min and then incubated with DMSO, CLLV-1, or MK-2206 for 5 min. The cells were then activated by fMLF, NaF, WKYMVm, interleukin-8 (IL-8), or leukotriene B<sub>4</sub> (LTB<sub>4</sub>) for a further 10 min. CB (0.5 or 2 μg/mL) was added 3 min before stimulation. Elastase release was determined by spectrophotometry at 405 nm.

## 2.6. CD11b expression

Neutrophils ( $5 \times 10^6$  cells/mL) were preincubated with DMSO or CLLV-1 for 5 min and activated by fMLF (0.1 μM)/CB (0.5 μg/mL) for

another 5 min. The cell pellets were then resuspended in 5% bovine serum albumin (BSA) containing FITC-labeled anti-CD11b antibodies (1 μg) at 4 °C for 90 min. The fluorescence intensity was measured by flow cytometry.

## 2.7. Western blotting

Human neutrophils were preincubated with DMSO or CLLV-1 at 37 °C for 5 min and then activated by fMLF, NaF, WKYMVm, IL-8, or LTB<sub>4</sub> before being primed with CB. The reaction was stopped using the sample buffer (62.5 mM pH 6.8 Tris-HCl, 4% SDS, 5% β-mercaptoethanol, 2.5 mM Na<sub>3</sub>VO<sub>4</sub>, 0.00125% bromophenol blue, 10 mM di-N-pentyl phthalate, and 8.75% glycerol) at 100 °C for 15 min. The cell lysates were separated by sodium dodecyl sulfate (SDS)-polyacrylamide gel



electrophoresis (PAGE), and assayed by immunoblotting with the corresponding antibodies, followed by incubation with horseradish peroxidase-conjugated secondary anti-rabbit or anti-mouse antibodies. The labeled proteins were measured using an enhanced chemiluminescence system (Amersham Biosciences, Piscataway, NJ, USA).

## 2.8. Phosphatidylinositol (3,4,5)-trisphosphate (PIP3) and F-actin expression

Neutrophils or dHL-60 cells ( $5 \times 10^6$  cells/mL) were preincubated with DMSO or CLLV-1 for 5 min and then activated by fMLF (0.1  $\mu$ M)/CB (1  $\mu$ g/mL). The reaction was stopped by 4% paraformaldehyde at 25 °C for 20 min and then permeabilized with 0.1% Triton-X-100. For F-actin staining, cells were incubated with Alexa Fluor 594 Phalloidin in Hank's balanced salt solution (HBSS) containing 2% BSA at 25 °C for 60 min. For PIP3 expression, cells were incubated with anti-PIP3 antibodies and FITC-labeled anti-mouse IgG antibodies in HBSS containing 2% BSA at 25 °C for 60 min, respectively. The fluorescence intensity was monitored using flow cytometry.

## 2.9. AKT kinase assay

The AKT activity was determined using the non-radioactive AKT kinase assay kit according to the manufacturer's protocol. In brief, dHL-60 cells were activated by fMLF (0.1  $\mu$ M)/CB (1  $\mu$ g/mL), and the active AKT in the cell lysate was immunoprecipitated with immobilized AKT primary antibodies. The precipitated AKT was treated with DMSO, CLLV-1, or MK-2206 at 30 °C for 15 min and then incubated with ATP and GSK-3 fusion protein as a kinase substrate at 30 °C for 30 min. The reaction was stopped by  $3 \times$  SDS sample buffer at 100 °C for 5 min. The phosphorylation of the GSK-3 fusion protein was determined by western blot.

## 2.10. Molecular docking

CLLV-1 was docked on AKT proteins by docking optimization (CDOCKER) and optimized with the CHARMM force field using Discovery Studio 4.1 (DS) (BIOVIA, San Diego, CA). The binding of CLLV-1 and AKT1 with the most favorable energy was estimated with -CDOCKER (−kcal/mol). The crystal structure of AKT1 was obtained from the Protein Data Bank (PDB; accession code 4ekl). The 3D structure of CLLV-1 was drawn using ChemDraw Ultra 9.0.

## 2.11. NMR spectrum analysis

CLLV-1 (1 mg) or synthetic AKT peptides (1 mg) were dissolved in 0.5 mL DMSO-*d*<sub>6</sub>. The mixtures of CLLV-1 (0.5 mg) and AKT peptides (1 mg) were vigorously mixed in 0.6 mL DMSO-*d*<sub>6</sub> and incubated at 25 °C for 1 h. The <sup>1</sup>H NMR spectra were acquired using a Bruker AVANCE-400 MHz FT-NMR spectrometer (Bruker BioSpin GmbH, Billerica, MA).

## 2.12. Mass spectrometer (MS) analysis

Synthetic AKT peptides were dissolved in PBS. The mixtures of AKT peptides (120  $\mu$ M) and CLLV-1 (60  $\mu$ M) were incubated at 25 °C for 2 h. The AKT peptides and their CLLV-1 adducts were detected using matrix-assisted laser desorption/ionization time of flight mass spectrometer (MALDI-TOF MS). The AKT peptides and their CLLV-1 adducts were mixed with  $\alpha$ -Cyano-4-hydroxycinnamic acid (CHCA) matrix (2 mg/mL in 80% acetonitrile containing 0.1% trichloroacetic acid) and loaded onto an MTP AnchorChip™ 600/384 TF (Bruker Daltonics GmbH, Bremen, Germany). After the crystallization of the peptides and the matrix, the samples were analyzed by an Ultraflex™ MALDI-TOF MS (Bruker Daltonics GmbH), controlled by the FlexControl software (v.2.2; Bruker Daltonics GmbH). Data processing was

performed and monoisotopic peptide mass was acquired using the FlexAnalysis 2.4 peak-picking software (Bruker Daltonics GmbH).

## 2.13. 4-acetamido-4'-maleimidylstilbene-2,2'-disulfonic acid (AMS) labeling assay

The redox states of the proteins were examined by conjugating free thiol with AMS [23]. The cells were lysed in the buffer (50 mM Tris, pH 7.4, 150 mM NaCl, 0.5% Triton-X-100, and  $1 \times$  protease inhibitor cocktail) and centrifuged at 12,000g for 10 min. The supernatants were incubated with 30 mM AMS at 4 °C for 24 h and then mixed with non-reducing sample buffer (62.5 mM pH 6.8 Tris-HCl, 4% SDS, 0.00125% bromophenol blue, and 8.75% glycerol) at 37 °C for 10 min. The redox states of the proteins were determined by immunoblotting.

## 2.14. Immunoprecipitation

Cells were lysed in the buffer (50 mM Tris, pH 7.4, 150 mM NaCl, 0.5% Triton X-100,  $1 \times$  protease inhibitor cocktail) and centrifuged at 12,000g for 10 min. The supernatants were incubated with AKT antibodies bound to protein G beads. The beads were washed with buffer and the precipitated proteins were assayed by immunoblotting.

## 2.15. Neutrophil adhesion and chemotactic migration assays

The bEnd.3 ECs were activated with LPS (2  $\mu$ g/mL) for 4 h. Hoechst 33342-labeled neutrophils were preincubated with DMSO or CLLV-1 for 5 min and activated by fMLF (0.1  $\mu$ M)/CB (1  $\mu$ g/mL) for another 5 min. Activated neutrophils were then co-cultured with LPS-pre-activated bEnd.3 ECs for 30 min. After gently washing, neutrophils adhering to bEnd.3 ECs were randomly counted in 4 fields by microscopy (IX81; Olympus, Center Valley, PA, USA) [29].

DMSO- or CLLV-1-pretreated neutrophils in the top microchemotaxis chamber (Merck Millipore, Darmstadt, Germany) were placed into the bottom well containing 0.1  $\mu$ M fMLF. After 90 min, the migrated neutrophils were counted.

## 2.16. LPS-induced ALI

ALI was induced by intra-tracheal spray of 2 mg/kg LPS (*Escherichia coli* 0111:B4) in seven to eight weeks old C57BL/6 male mice, according to the guidelines and approved by Institutional Animal Care and Use Committee of Chang Gung University, Taiwan. Mice were fasted overnight and then intraperitoneally injected with CLLV-1 (10 mg/kg), MK-2206 (10 mg/kg) or an equal volume of DMSO (50  $\mu$ l). After 1 h, tracheostomy was performed under anesthesia (30 mg/kg Zoletil 50 and 6 mg/kg xylazine). Mice were instilled with an intra-tracheal spray of 2 mg/kg LPS (dissolved in 40  $\mu$ l 0.9% saline) or 0.9% saline and kept in a warm chamber to keep body temperature. After 6 h, the lungs were fixed in 10% formalin for immunohistochemistry or frozen for MPO activity.

## 2.17. MPO activity

The lung tissues were immersed in 10 mM PBS, pH 6.0, with 0.5% hexadecyltrimethylammonium bromide and sonicated by a homogenizer. The MPO activity was determined using MPO substrate buffer (PBS, pH 6.0, 0.2 mg/mL o-dianisidine hydrochloride, and 0.001% hydrogen peroxide) and monitored the absorbance at 405 nm by a spectrophotometer. The serial concentration of human MPO was used as a standard curve to calculate the MPO activity. Total protein levels were measured by the Bradford protein assay (Bio-Rad, Hercules, CA, USA). The final MPO activity was normalized to the corresponding protein concentration (U/mg).

### 2.18. Immunohistochemistry (IHC)

Formalin-fixed paraffin-embedded tissue sections were used for IHC. All slides were stained with hematoxylin and eosin (H&E) for morphologic determination. The anti-MPO antibodies, anti-Ly6G antibodies, anti-pAKT (S473) antibodies, or the SuperPicture kit (Thermo Fisher Scientific) were used as the primary or secondary antibodies, following a previously published protocol by Pathology Core of Chang Gung University [30].

### 2.19. Statistical analysis

Data are presented as means  $\pm$  SEM. Statistical analysis was performed with SigmaPlot (Systat Software) using Student's *t*-test. *P* < .05 was considered statistically significant.

## 3. Results

### 3.1. CLLV-1 suppresses the inflammatory responses in fMLF-activated human neutrophils

To investigate the anti-inflammatory ability of CLLV-1, we first examined the effects of CLLV-1 on fMLF-induced respiratory burst, including superoxide anion production, ROS formation, and NADPH oxidase activation (p47<sup>phox</sup> phosphorylation) in human neutrophils. CLLV-1 dose-dependently inhibited superoxide anion generation and ROS formation with IC<sub>50</sub> values of  $0.058 \pm 0.006$  and  $0.106 \pm 0.022$   $\mu$ M, respectively (Fig. 1b and c). Importantly, it did not induce LDH release, suggesting that it did not cause membrane damage and cytotoxicity (Fig. S1a). We further evaluated how CLLV-1 inhibited the superoxide anion generation in fMLF-activated human neutrophils. In a cell-free xanthine/xanthine oxidase system, CLLV-1 (0.1–3  $\mu$ M) did not exhibit a superoxide anion-scavenging ability. Superoxide dismutase (SOD) was a positive control. Superoxide anion is produced by NADPH oxidase in human neutrophils [17]. The isolated neutrophil membrane and cytosol fractions were used to examine the inhibitory effect of CLLV-1 on NADPH oxidase: CLLV-1 (0.3 and 3  $\mu$ M) did not reduce superoxide anion production in SDS-reconstituted NADPH oxidase. Diphenyleneiodonium (DPI; 10  $\mu$ M), an NADPH oxidase inhibitor, was a positive control (Fig. S1b–c). The phosphorylation of p47<sup>phox</sup>, a component of NADPH oxidase, was repressed by CLLV-1 in fMLF-activated human neutrophils (Fig. 1d), suggesting that the anti-inflammatory effect of CLLV-1 on respiratory burst may be through modulating upstream signaling of NADPH oxidase in human neutrophils.

Next, the effects of CLLV-1 on human neutrophil degranulation and chemotaxis were determined. CLLV-1 repressed fMLF-induced elastase release with an IC<sub>50</sub> value of  $0.172 \pm 0.011$   $\mu$ M (Fig. 2a). In contrast, it failed to alter the activity of elastase in a cell-free assay (Fig. S1d), suggesting that it inhibited human neutrophil degranulation via the regulation of intracellular signaling pathways. In addition, integrin CD11b activation leads to neutrophils adhering to endothelial cells and subsequently induces neutrophil migration and infiltration. F-actin polymerization at the leading edge in polarized neutrophils governs the chemotaxis [22]. CLLV-1 decreased CD11b expression and F-actin assembly in fMLF-activated human neutrophils and suppressed fMLF-induced neutrophil adhesion to bEnd.3 ECs and migration (Fig. 2b–e and Fig. S2). Together, CLLV-1 exhibits an anti-inflammatory potential to alleviate neutrophilic inflammation, including respiratory burst, degranulation, and chemotaxis.

### 3.2. CLLV-1 ameliorates AKT activation in response to various stimuli in human neutrophils

This study aimed to identify the target protein of CLLV-1 in human neutrophils. The fMLF mainly binds to formyl peptide receptor 1 (FPR1) to activate neutrophils through multiple intracellular signaling

pathways such as AKT and mitogen-activated protein kinases (MAPKs) [31,32]. CLLV-1 (0.1–3  $\mu$ M) did not compete with the fluorescently labeled fMLF analog fNLFNYK for FPR1 binding (Fig. S1e), ruling out the effect of CLLV-1 on FPR1. Therefore, the activation of AKT, ERK, JNK, and p38 was examined in fMLF-activated human neutrophils. CLLV-1 inhibited the phosphorylation of AKT (Thr308 and Ser473), but not of ERK, JNK, or p38 (Fig. 3). Because CLLV-1 selectively restrained AKT activation, we wondered whether CLLV-1 suppressed AKT activation and inflammatory responses in different stimuli-activated human neutrophils, including NaF (direct G protein activator), WKYMVm (FPR2 agonist), IL-8, and LTB<sub>4</sub> [33]. Further, CLLV-1 significantly inhibited NaF- and WKYMVm-induced superoxide anion generation in human neutrophils. It also showed an inhibitory effect on elastase release in NaF-, WKYMVm-, IL-8-, and LTB<sub>4</sub>-activated human neutrophils (Fig. S3). Notably, it significantly suppressed the activation of AKT in human neutrophils activated by all tested stimuli (Fig. S4), suggesting that AKT may be the target of CLLV-1 in human neutrophils. Another potent AKT inhibitor, MK-2206 [34], also inhibited the superoxide anion generation and elastase release in fMLF-activated human neutrophils (Fig. S5), supporting that inhibition of AKT is a potential strategy to attenuate neutrophilic inflammation.

### 3.3. CLLV-1 inhibits the inflammatory responses and AKT activation in fMLF-activated dHL-60 cells

HL-60 cells were exposed to DMSO for 5 days to differentiate into neutrophil-like cells (dHL-60 cells). Usage of dHL-60 cells provided enough cells for several biochemical experiments instead of limited primary human neutrophils. The increased FPR1 expression and cellular morphology of dHL-60 were observed to represent the neutrophil-like status (Fig. S6). CLLV-1 diminished superoxide anion generation and intracellular ROS formation in fMLF-induced dHL-60 cells. It also repressed the p47<sup>phox</sup> phosphorylation and F-actin polymerization in fMLF-activated dHL-60 cells (Fig. S7), suggesting that dHL-60 cells provide a good inflammatory model and that CLLV-1 still restrains the respiratory burst and chemotaxis in fMLF-activated dHL-60 cells. Importantly, CLLV-1 also attenuated fMLF-induced activation of AKT in dHL-60 (Fig. 4f).

### 3.4. CLLV-1 directly alleviates AKT activity

We tested whether the CLLV-1-inhibited AKT activation is based on altering the upstream kinases of AKT, including phosphoinositide-dependent protein kinase 1 (PDK1), mammalian target of rapamycin C2 (mTORC2), and PI3K [35,36]. CLLV-1 (0.3–3  $\mu$ M) failed to affect the phosphorylation of PDK1 (S241), mTORC2 (S2481), and PI3K (Y199 of p85 subunit) in fMLF-activated dHL-60 cells and human neutrophils (Fig. 5a and Fig. S8). The level of PI3K-generated PIP3 was also not changed by CLLV-1 in fMLF-activated dHL-60 cells (Fig. 5b and Fig. S7c). Protein kinase A (PKA) has been shown to attenuate neutrophilic inflammation through inhibiting AKT activation [37,38]. However, CLLV-1 did not increase the level of cAMP. The PKA inhibitor, H89, did not reverse the CLLV-1-inhibited superoxide anion generation and elastase release in activated human neutrophils (Fig. S9).

We suggest that CLLV-1 may directly target AKT *per se* to repress inflammation in human neutrophils. To explore this hypothesis, the non-radioactive AKT kinase assay was performed *in vitro*. Clearly, our data showed that CLLV-1 (0.3–3  $\mu$ M) blocked the kinase activity of AKT *in vitro*. MK-2206 was used as a positive control to inhibit AKT activity (Fig. 5 and Fig. S5c). Therefore, CLLV-1 acts as a novel AKT inhibitor to restrict the enzymatic activity of AKT.

### 3.5. CLLV-1 covalently reacts with AKT Cys310

To determine how CLLV-1 blocked the AKT activity, the molecular docking of CLLV-1 with AKT was performed. Based on CDOCKER and

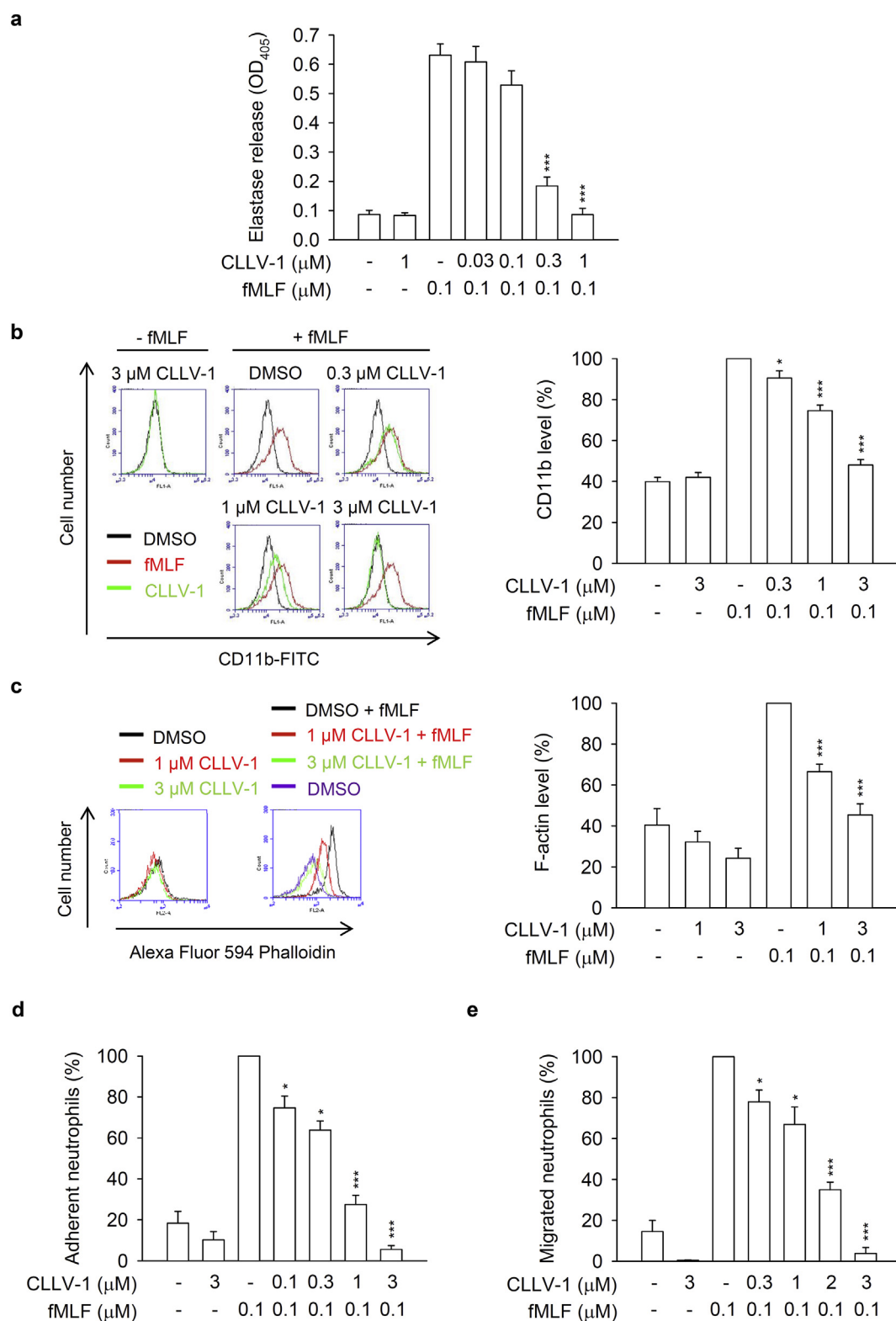


**Fig. 2.** CLLV-1 inhibits elastase release, CD11b/F-actin expression, and neutrophil adhesion/migration in fMLF-activated human neutrophils. (a-c) Human neutrophils were incubated with DMSO or CLLV-1 (0.3–3 μM) for 5 min before stimulation with or without fMLF (0.1 μM)/CB (0.5 or 1 μg/mL). (a) Elastase release was measured by a spectrophotometer at 405 nm, using elastase substrate. (b) The CD11b levels on cell surface were detected by flow cytometry, using FITC-labeled anti-CD11b antibodies. (c) The F-actin levels were assayed by flow cytometry, using Alexa Fluor 594 Phalloidin. (d) Hoechst 33342-labeled neutrophils were pretreated with DMSO or CLLV-1 (0.1–3 μM) for 5 min and stimulated with fMLF (0.1 μM)/CB (1 μg/mL). Sequentially, neutrophils were incubated with LPS-pretreated ECs for another 30 min. After gently washing, EC-associated neutrophils were counted under a microscope. (e) Neutrophils were preincubated with DMSO or CLLV-1 (0.3–3 μM) for 5 min in the top chamber. Migrated neutrophils in the bottom wells with or without fMLF were counted after 90 min. All data are expressed as mean values ± SEM ( $n = 3$ ); \* $p < .05$ , \*\* $p < .01$ , and \*\*\* $p < .001$  compared with the DMSO + fMLF group (Student's  $t$ -test).

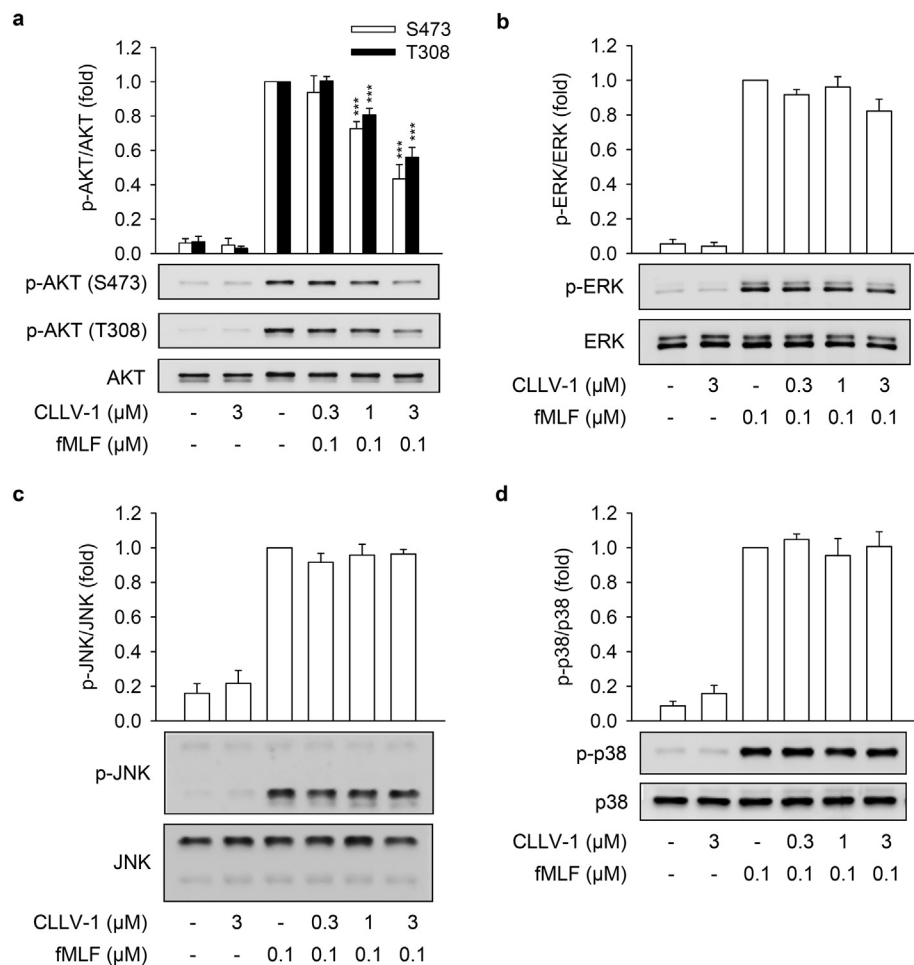


**Fig. 3.** CLLV-1 decreases the phosphorylation of AKT but not MAPKs in fMLF-activated human neutrophils. Human neutrophils were incubated with CLLV-1 (0.3–3 μM) for 5 min before stimulation with or without fMLF (0.1 μM)/CB (1 μg/mL). Phosphorylation of (a) AKT, (b) ERK, (c) JNK, or (d) p38 MAPK was analyzed by immunoblotting using antibodies against the phosphorylated form and the total of each protein. All data are expressed as mean values  $\pm$  SEM ( $n = 3$ ); \*\*\* $p < .001$  compared with the DMSO + fMLF group (Student's  $t$ -test).

the CHARMM force field, the CLLV-1-AKT binding modes were generated in receptor cavities with 10 poses. The binding of CLLV-1 and AKT with the most favorable energy was estimated with -CDOCKER (−474.532 kcal/mol). The *p*-benzoquinone, aromatic ring, or carboxyl group of CLLV-1 were proposed to interact with the R273, D274, L275, C310, G311, A317, L316, Y315, V320, or V330 residues of AKT (Fig. 6a–b), suggesting that CLLV-1 may preferably and specifically associate with this proposed “pocket” of AKT. Interestingly, the Cys310 residue of AKT was appeared in the predicted CLLV-1-binding site, and the redox modification of Cys310 in AKT is important for AKT enzymatic activity [23,39]. Hence, CLLV-1 may bind to the thiol group of Cys310 to interfere with the AKT activity. To address this hypothesis, the reaction between CLLV-1 and synthetic AKT peptides, AKT<sub>304–308</sub> (ATMKT), AKT<sub>309–313</sub> (FCGTP), AKT<sub>314–318</sub> (EYLAP), and AKT<sub>307–328</sub> (KTFCGTPEYLAPEVLEDNDYGR) were determined by NMR or MS (Fig. 6c–e): CLLV-1 covalently reacted with the AKT<sub>309–313</sub>, exhibiting a new singlet peak at  $\delta$  7.00, but did not react with the adjacent AKT<sub>304–308</sub> and AKT<sub>314–318</sub>, which lacked cysteine residues according to the <sup>1</sup>H NMR analysis (Fig. S10a). The AKT peptide-CLLV-1 adducts were also examined by MS (Fig. S10b): the molecular masses of AKT<sub>309–313</sub>, AKT<sub>307–328</sub>, and CLLV-1 were 524, 2389, and 268 Da, respectively. If CLLV-1 reacted with the AKT peptides, the proposed molecular masses of the adducts would be 792 Da (AKT<sub>309–313</sub>-CLLV-1) and 2657 Da (AKT<sub>307–328</sub>-CLLV-1). The corresponding signals were observed by MS, including AKT<sub>309–313</sub> ([M + H]<sup>+</sup>; 524.079), AKT<sub>307–328</sub> ([M + H]<sup>+</sup>; 2389.124), AKT<sub>309–313</sub>-CLLV-1 ([M<sub>CLL</sub> + H]<sup>+</sup>; 792.244), and AKT<sub>307–328</sub>-CLLV-1 ([M<sub>CLL</sub> + H]<sup>+</sup>; 2655.102). In addition, the sodium

adducts (plus 23 Da) were also found, AKT<sub>309–313</sub>-Na ([M + Na]<sup>+</sup>; 546.145), AKT<sub>307–328</sub>-Na ([M + Na]<sup>+</sup>; 2411.258), and AKT<sub>309–313</sub>-CLLV-1-Na ([M<sub>CLL</sub> + Na]<sup>+</sup>; 812.264). Similarly, the results of MS confirmed that CLLV-1 did not react with the adjacent peptides AKT<sub>304–308</sub> and AKT<sub>314–318</sub>, which do not contain Cys310. These results suggested that CLLV-1 covalently reacted with Cys310 in AKT via an electrophilic addition.

To confirm the effect of CLLV-1 on AKT redox status in cells, we used the alkylation agent, AMS, to label reduced form of protein along with increasing molecular weight [23]. The level of AMS-labeled AKT (reduced form) was increased in fMLF-activated dHL-60 cells. CLLV-1 (0.3–3 μM) dose-dependently decreased the levels of AMS-labeled AKT in fMLF-activated dHL-60 cells (Fig. 7a). It has been reported that oxidation of Cys310 residue in AKT diminished its enzymatic activity and increased the AKT-protein phosphatase 2A (PP2A) interaction along with inhibition of AKT phosphorylation [23,24]. CLLV-1 induced the AKT-PP2A interaction in fMLF-activated dHL-60 cells (Fig. 7b). These results suggest that CLLV-1 covalently targets Cys310 of AKT to alleviate AKT activity as well as phosphorylation.

### 3.6. CLLV-1 attenuates LPS-induced ALI in mice

LPS/endotoxin is a critical pathogen to trigger ALI [40,41]. However, the role of AKT as a potential drug target in ALI needs to be studied. To examine the anti-inflammatory potential of CLLV-1 *in vivo*, the protective effects of CLLV-1 on LPS-induced ALI was tested in mice. Intratracheal instillation of LPS showed an increase in pulmonary



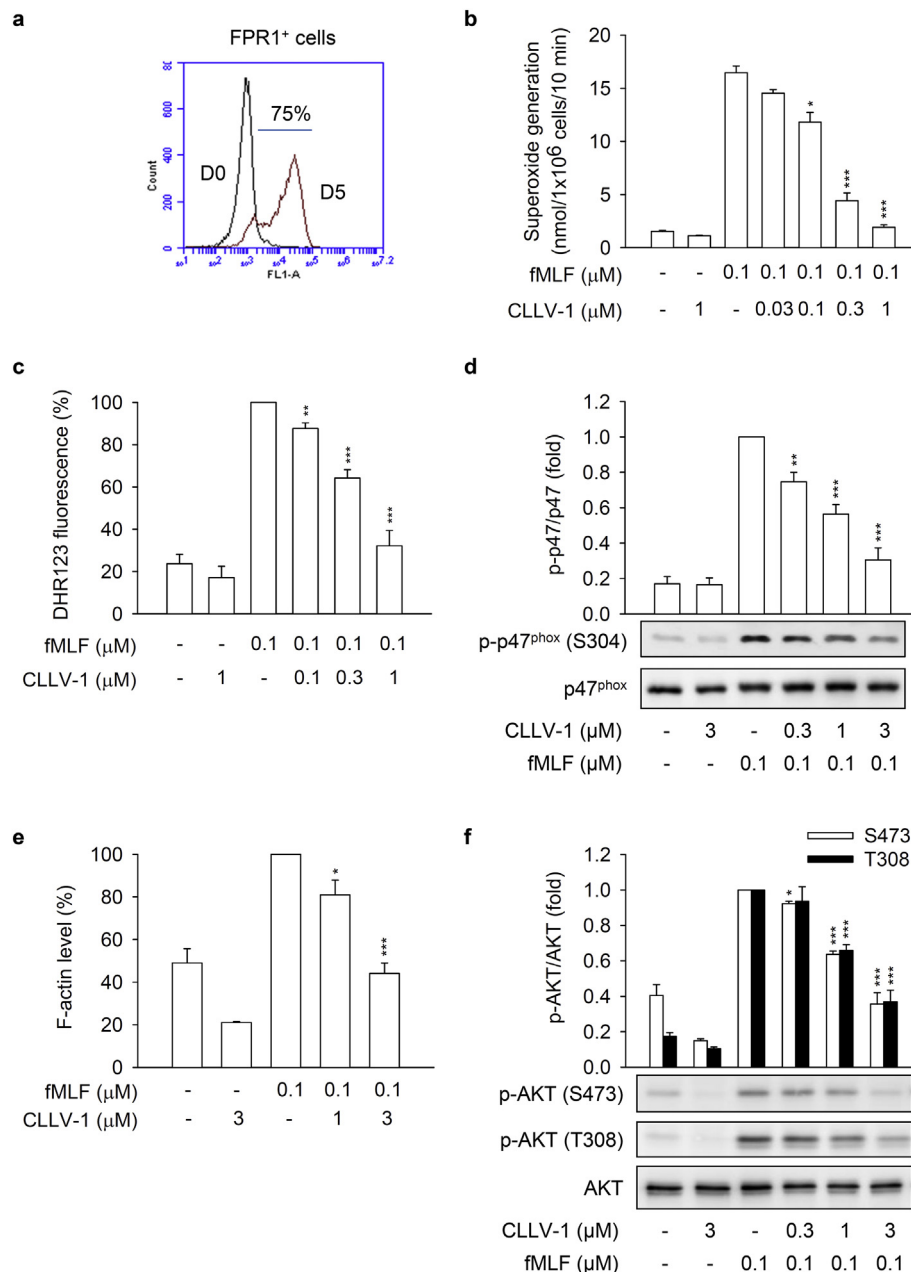


**Fig. 4.** CLLV-1 suppresses fMLF-induced inflammatory responses in differentiated HL-60 (dHL-60) cells. (a) The HL-60 cells were exposed to 1.3% DMSO for 5 days. The differentiation of HL-60 cells by DMSO was examined by flow cytometry, using anti-FPR1 antibodies. (b–f) The dHL-60 cells were preincubated with DMSO or CLLV-1 (0.03–1  $\mu$ M) and then activated with or without fMLF (0.1  $\mu$ M)/CB (1  $\mu$ g/mL). (b) Superoxide anion generation was detected by spectrophotometry at 550 nm, using cytochrome c reduction. (c) The intracellular ROS was monitored by flow cytometry, using cell-permeable DHR123. (d) Phosphorylation of p47<sup>phox</sup> was analyzed by immunoblotting, using antibodies against the phosphorylated (S304) and total p47<sup>phox</sup>. (e) F-actin levels were assayed by flow cytometry, using Alexa Fluor 594 Phalloidin. (f) Phosphorylation of AKT was analyzed by immunoblotting, using antibodies against the phosphorylated (S473 and T308) and total AKT. All data are expressed as mean values  $\pm$  SEM (n = 3); \* $p$  < .05, \*\* $p$  < .01, and \*\*\* $p$  < .001 compared with the DMSO + fMLF group (Student's *t*-test).

MPO, which was inhibited by intraperitoneal injection of CLLV-1 (10 mg/kg) or MK-2206 (10 mg/kg) (Fig. 8a). The total protein levels were measured to represent the severity of pulmonary edema. Both CLLV-1 and MK-2206 effectively attenuated the LPS-induced increase of protein levels in the lungs (Fig. 8b). The histopathological features of the lungs showed that LPS triggered inflammatory cell infiltration, inter-alveolar septal thickening, and interstitial edema. Moreover, LPS induced the infiltration of cells positive for Ly6G, a specific neutrophil marker, as well as AKT activation in the lungs. Noticeably, administration of CLLV-1 and MK-2206 ameliorated LPS-induced distortion of pulmonary architecture, Ly6G-positive infiltrated neutrophils, and AKT phosphorylation (Fig. 8c), suggesting the therapeutic potential of CLLV-1 in neutrophil-dominant lung diseases. Together, CLLV-1 and

MK-2206 successfully impeded the inflammatory ALI *in vivo*, supporting that pharmacologically targeting redox modification of AKT is a potential strategy for treating neutrophilic lung injury.

#### 4. Discussion

Neutrophils play a significant role in innate immunity; however, enhanced ROS generation and protease release by activated neutrophils can cause cell and tissue damage [5,42]. Neutrophilic inflammation has been found to play a central role in the pathogenesis of ALI/acute respiratory distress syndrome (ARDS). The AKT pathway is known to be involved in many neutrophil responses, including respiratory burst, degranulation, and chemotaxis [13–15,43]. However, the regulatory



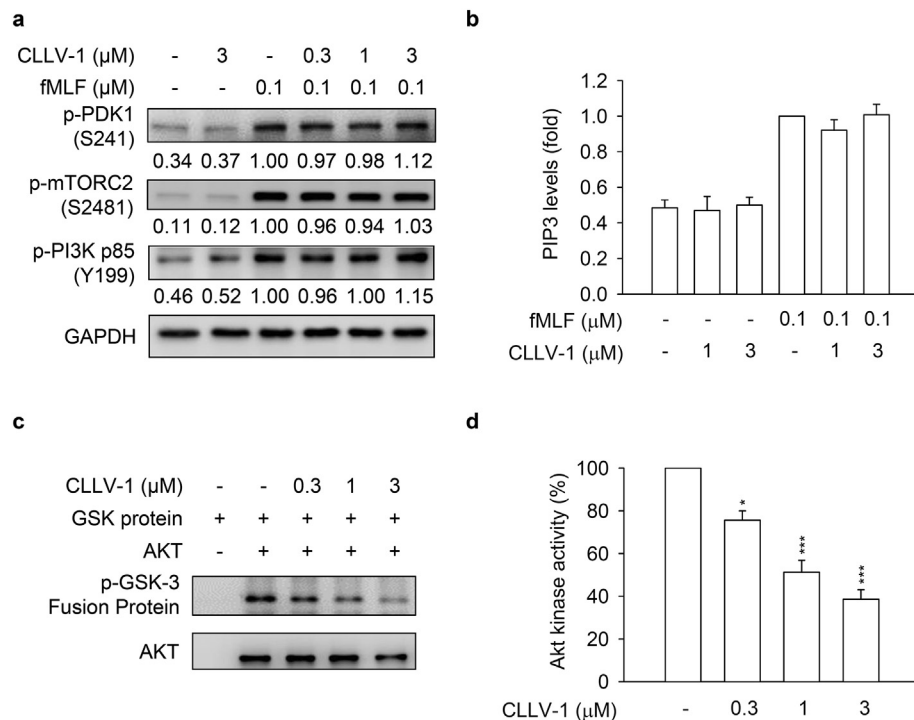


**Fig. 5.** CLLV-1 blocks AKT enzymatic activity but does not affect the AKT upstream kinases. (A-B) dHL-60 cells were preincubated with DMSO or CLLV-1 (0.03–1 μM) and then activated with or without fMLF (0.1 μM)/CB (1 μg/mL). (a) Phosphorylation of AKT upstream kinases, PDK1, mTORC2, and PI3K was determined by immunoblotting, using antibodies against the phosphorylated form and normalized to GAPDH. (b) PIP3 levels were assayed using anti-PIP3 antibodies by flow cytometry. (c) The active AKT proteins were immunoprecipitated using anti-phospho-AKT antibodies and treated with DMSO or CLLV-1 (0.3–3 μM) for 15 min at 30 °C. Subsequently, the GSK-3 fusion protein (AKT substrate) was added for another 30 min. The phospho-GSK-3 fusion protein was examined by immunoblotting. (d) The phosphorylation of the GSK-3 fusion protein was quantified and expressed as a percentage to represent AKT activity. All data are expressed as mean values ± SEM (n = 3); \*p < .05 and \*\*\*p < .001 compared with the DMSO + AKT group (Student's *t*-test).

mechanisms of AKT in human neutrophils are still elusive. Furthermore, the potential of AKT as a therapeutic target in ALI remains unknown. Herein, we show that a synthetic phenanthrenequinone compound, CLLV-1, inhibits inflammatory responses in human neutrophils or neutrophil-like dHL-60 cells triggered by various stimuli. CLLV-1 selectively blocked AKT activity through covalently targeting the Cys310 residue of AKT. Moreover, CLLV-1 attenuated the inflammatory responses in LPS-induced ALI in mice, indicating that it is a potential anti-inflammatory compound and providing an example of disruption of the redox modulation of AKT for treating neutrophil-dominant lung diseases.

AKT-mediated cellular signaling is significantly responsible for inflammatory responses in neutrophils [13,14]. With stimulation, AKT translocated to the leading edge in polarized neutrophils and induced p47<sup>phox</sup> phosphorylation and F-actin polymerization to trigger respiratory burst and chemotaxis in neutrophils, respectively [17,18,21]. It may be a preferentially remedial strategy to ameliorate the overwhelming neutrophilic inflammation via pharmacologically targeting of AKT. In the present study, we identified that CLLV-1 significantly abrogated AKT activation in response to various stimuli in human neutrophils (Fig. 3 and S4). As well, CLLV-1 dose-dependently restricted AKT-mediated p47<sup>phox</sup> phosphorylation and F-actin levels in activated human neutrophils and dHL-60 cells (Figs. 1, 2, and 4), confirming that CLLV-1-inhibited AKT activation is critical for halting inflammatory activation in human neutrophils.

AKT is composed of the pleckstrin homology (PH), catalytic kinase, and regulatory domains and its kinase activity is regulated through conformational dynamics. With stimulation, AKT is phosphorylated at Thr308 and Ser473 residues, leading to the PH domain becoming more distant from the kinase domain as “active” form. When AKT is dephosphorylated by PP2A, the catalytic domain would be interfered by more closed PH domain as “inactive” form [35,36]. Thus far, emerging evidence has supported the important role of redox modification of

AKT in conformational dynamics [25]. An intramolecular disulfide bond between Cys296 and Cys310 in the catalytic domain of AKT that prompts dephosphorylation by associating with PP2A has been identified; oxidized and dephosphorylated AKT is considered to have lost its kinase activity [23,24,39]. In the present study, we found that CLLV-1 covalently reacted with Cys310 of AKT *in vitro* and repressed the alkylation agent-labeled AKT levels (reduced form) in cells (Figs. 6 and 7), supporting that CLLV-1 brings about AKT oxidation. The AKT-PP2A interaction was also increased by CLLV-1 along with dephosphorylation of AKT (Fig. 7b) that was not modulated through AKT upstream kinases, including PDK1, mTORC2, and PI3K (Fig. 5a-b). Accordingly, CLLV-1-blocked AKT kinase activity may be dependent on redox modification of AKT.

CLLV-1 was proposed to interact with Cys310 of AKT by the molecular docking model (Fig. 6a-b). The adduct of AKT<sub>309–313</sub> peptides and CLLV-1 exhibited a new singlet peak at δ 7.00 in the <sup>1</sup>H NMR spectrum (Fig. 6c). The molecular masses of AKT peptide-CLLV-1 adducts (AKT peptide + CLLV-1 – 2H<sup>+</sup> Da) were also detected in MALDI-TOF MS, AKT<sub>309–313</sub>-CLLV-1-Na, and AKT<sub>307–328</sub>-CLLV-1 (Fig. 6d-e), suggesting that the reaction between AKT and CLLV-1 is an electrophilic addition. It has been reported that thiol-based association between electrophilic compounds and proteins possessed selectivity and specificity. The structural characteristic of proteins and stereochemical structures of electrophiles results in their targeting selectivity [44,45]. The redox modulations of ERK, JNK, or p38 have been characterized in response to intracellular ROS. The cysteines of ERK2 (Cys38 and Cys214), JNK2 (Cys41) and p38 (Cys162) are responsible for their activity and phosphorylation [25,46,47]. However, CLLV-1 only repressed AKT, but not ERK, JNK, or p38 activation in human neutrophils (Fig. 3), implying its specificity. Using molecular docking model, the most favorable CLLV-1-binding pocket of AKT was determined, including R273, D274, L275, C310, G311, A317, L316, Y315, V320, or V330 residues (Fig. 6a-b). Importantly, another critical Cys296 of catalytic region was not proposed

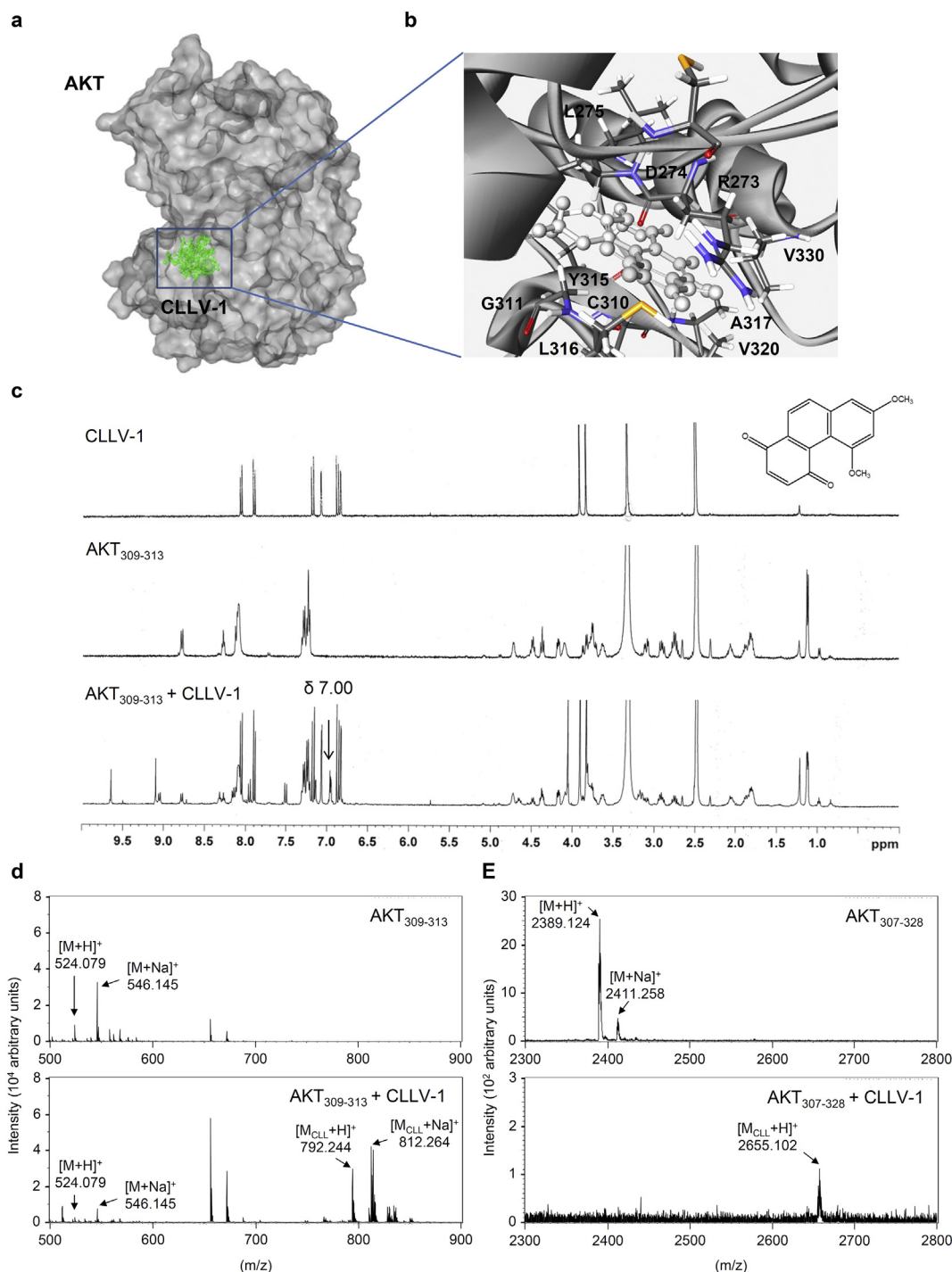


**Fig. 6.** CLLV-1 covalently reacts with the thiol group of an AKT cysteine *in vitro*. (a-b) Docking models of CLLV-1-targeted AKT. Surface presentation demonstrates the structure of AKT (gray). CLLV-1 moieties are colored green and rendered in stick representation (a). Close-up of CLLV-1 docking site (best energy mode) (b). The figures were prepared using Discovery Studio 4.1. The crystal structure of AKT was downloaded from PDB (accession code 4ekl). The chemical structure of CLLV-1 was drawn by ChemDraw Ultra 9.0. (c) <sup>1</sup>H NMR spectra of CLLV-1 (upper panel), synthetic AKT peptide (AKT<sub>309-313</sub>; FCGTP) (middle panel), and mixtures of CLLV-1 and AKT<sub>309-313</sub> (lower panel). (d-e) The synthetic AKT peptides AKT<sub>309-313</sub> and AKT<sub>307-328</sub> (KTFCTGPEYLAPVLEDNDYGR) were incubated in the presence or absence of CLLV-1. The molecular mass of the synthetic AKT peptides and their CLLV-1 adducts were detected using MALDI-TOF MS. M, molecular mass of AKT peptides; M<sub>CLL</sub>, molecular mass of adducts of AKT peptides and CLLV-1. (For interpretation of the references to colour in this figure legend, the reader is referred to the web version of this article.)

as CLLV-1-targeting site (data not shown), suggesting that CLLV-1 exhibits target-site selectivity in AKT.

Developed AKT inhibitors are classified as ATP-competitive and allosteric inhibitors [48,49]. However, the off-target effect of ATP-competitive inhibitors is still of concern because of the ATP-binding site being highly conserved among members of the AGC kinase family such as PKA and PKC [50]. A growing number of allosteric inhibitors

with higher efficacy and specificity, such as MK-2206, are being developed [34]. Recently, the development of structure-based covalent-allosteric AKT inhibitors has been mentioned because of their high potency and selectivity to stabilize AKT as inactive conformation [51,52]. The Cys296 and Cys310 residues in the catalytic domain of AKT were identified as allosteric sites for regulating AKT activity [49,53,54]. Therefore, the Cys296 and Cys310 residues of AKT are potential therapeutic

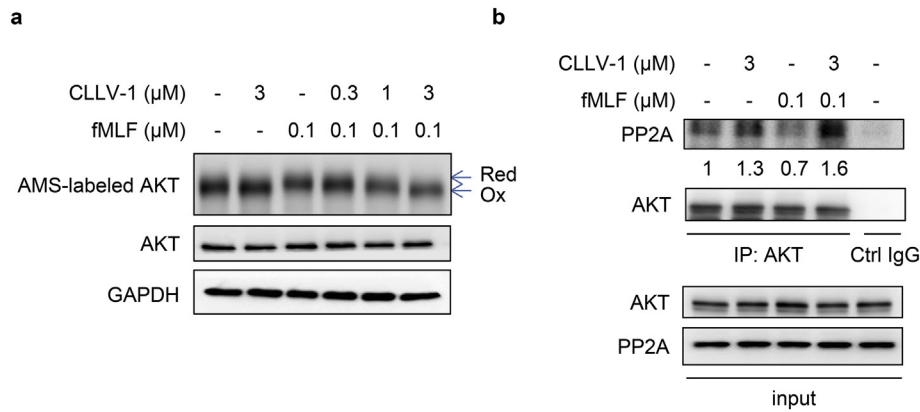


**Fig. 7.** CLLV-1 decreases the AMS-labeled reduced form of AKT and increases the AKT-PP2A interaction in fMLF-activated dHL-60 cells. dHL-60 cells were incubated with CLLV-1 (0.3–3 μM) for 5 min before stimulation with or without fMLF (0.1 μM)/CB (1 μg/mL). (a) The cell lysates were incubated with the thiol-alkylating agent AMS for 12 h on ice and analyzed by Western blotting under reducing (total lysate) or non-reducing conditions (AMS-labeled AKT). The AMS-labeled reduced form of AKT (Red) had a higher molecular weight than oxidized AKT (Oxi). (b) The cell lysates were immunoprecipitated with control (Ctrl) or AKT IgG. The precipitated substances were used for Western blotting of AKT and PP2A. (For interpretation of the references to colour in this figure legend, the reader is referred to the web version of this article.)

targets in AKT-associated disorders. In this study, CLLV-1 was found to be an allosteric inhibitor of AKT through covalently binding to Cys310 *in vitro* (Fig. 6). This is the first example of restraining neutrophilic inflammation by pharmacologically targeting the redox regulatory site of AKT. LPS-induced ALI is an important *in vivo* model to mimic clinical pulmonary destruction, such as pulmonary edema, alveolar-capillary

barrier loss or inflammatory cell infiltration [38,40]. The novel covalent allosteric AKT inhibitor, CLLV-1, showed its anti-inflammatory effects to ameliorate LPS-primed ALI in mice, including neutrophils infiltration, pulmonary protease release, inter-alveolar septal thickening, interstitial edema, and AKT activation (Fig. 8). It proves the therapeutic potential for curing neutrophilic lung damage, ALI/ARDS, via pharmacological

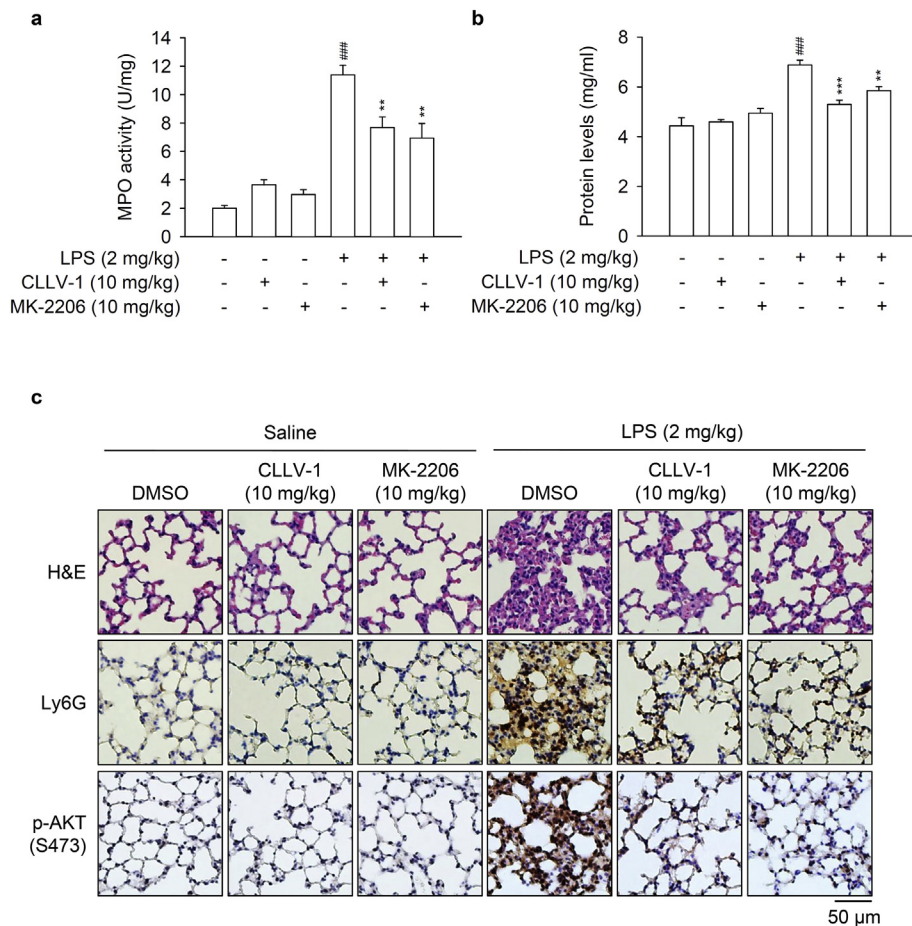


**Fig. 8.** CLLV-1 attenuates LPS-induced ALI in mice. C57BL/6 mice were intraperitoneally injected with CLLV-1 (10 mg/kg), MK-2206 (10 mg/kg), or an equal volume of DMSO for 1 h, and subsequently instilled 2 mg/kg LPS from *E. coli* 0111:B4 or 0.9% saline via tracheostomy. (a–b) Six hours later, lungs were collected and assayed for MPO activity (a) and protein levels (b). (c) Histological examination of lungs. The lung sections were stained with hematoxylin and eosin (H&E), anti-Ly6G antibodies, or anti-pAKT (S473) antibodies by IHC. All data are expressed as mean values ± SEM (n = 6); \*p < .01 and \*\*\*p < .001 compared with the LPS + DMSO group; ###p < .001 compared with the DMSO control (Student's t-test).



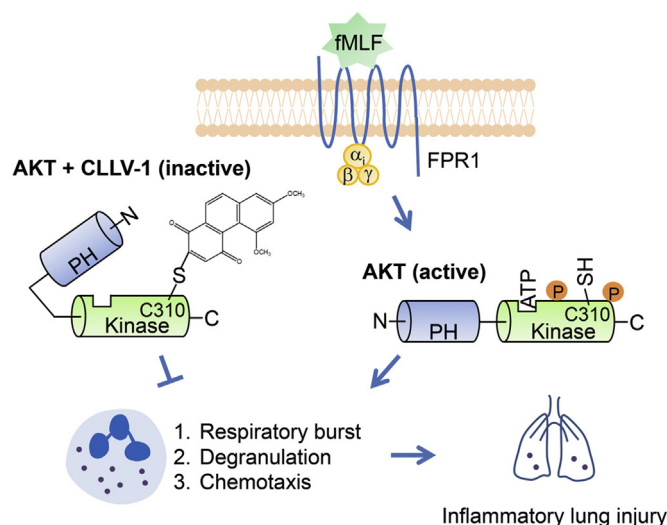


**Fig. 9.** Schematic model of CLLV-1-impeded neutrophilic inflammation. With stimulation, AKT is activated and phosphorylated, leading to the PH domain becoming more distant from the kinase domain. Active AKT is maintained in a reduced manner that contributes to overwhelming inflammatory responses in human neutrophils and neutrophil-dominant inflammatory disorders. Once CLLV-1 is administered, it covalently binds to Cys310 within the kinase domain of AKT, yielding an inactive and less reduced form of AKT. CLLV-1 can inhibit neutrophil activation, including respiratory burst, degranulation, and chemotaxis by modifying the redox state of AKT. Significantly, CLLV-1 ameliorates inflammatory ALI *in vivo*.

inhibition of AKT. Accordingly, anti-inflammatory drugs that target the redox modification of AKT could potentially be developed.

In summary, we demonstrate that AKT activation plays a critical role in neutrophilic lung injury. Targeting AKT Cys310 using drugs can regulate AKT enzymatic activity. Our findings also provide an important example of how a derivative of phenanthrenequinone, CLLV-1, restrains neutrophil-dominant inflammatory lung injury by inhibiting AKT activity in a redox-dependent manner (Fig. 9).

## Funding sources

This research was financial supported by the grants from the Ministry of Science Technology (MOST 106-2320-B-255-003-MY3 and MOST 104-2320-B-255-004-MY3), Taiwan; Ministry of Education (EMRPD1G0231 and EMRPD1H0381), Taiwan; Chang Gung Memorial Hospital (CMRPF1F0011~3, CMRPF1F0061~3, CMRPF1G0241~3, and BMRP450), Taiwan. The funders had no role in study design, data collection and analysis, decision to publish, or preparation of the manuscript.

## Declaration of interests

The authors declare that no competing interests exist.

## Author contributions

P.J.C. and I.L.K. designed and performed most experiments. C.L.L., F.R.C., Y.C.W., Y.L.L., C.C.W., Y.F.T., C.Y.L., and C.Y.P. helped to perform experiments and analyzed the data. C.L.L., H.C.H., F.R.C., and Y.C.W. synthesized and provided CLLV-1. P.J.C. and T.L.H. wrote and completed the manuscript. T.L.H. supervised the entire study.

## Appendix A. Supplementary data

Supplementary data to this article can be found online at <https://doi.org/10.1016/j.ebiom.2019.01.043>.

## References

- Jorch SK, Kubers P. An emerging role for neutrophil extracellular traps in noninfectious disease. *Nat Med* 2017;23(3):279–87.
- Leiding JW. Neutrophil evolution and their diseases in humans. *Front Immunol* 2017;8:1009.
- Nauseef WM, Borregaard N. Neutrophils at work. *Nat Immunol* 2014;15(7):602–11.
- Mortaz E, Alipour SD, Adcock IM, Mumby S, Koenderman L. Update on neutrophil function in severe inflammation. *Front Immunol* 2018;9:2171.
- Soehnlein O, Steffens S, Hidalgo A, Weber C. Neutrophils as protagonists and targets in chronic inflammation. *Nat Rev Immunol* 2017;17(4):248–61.
- Delano MJ, Ward PA. Sepsis-induced immune dysfunction: can immune therapies reduce mortality? *J Clin Invest* 2016;126(1):23–31.
- White MM, Geraghty P, Hayes E, Cox S, Leitch W, Alfawaz B, et al. Neutrophil membrane cholesterol content is a key factor in cystic fibrosis lung disease. *EBioMedicine* 2017;23:173–84.
- Rebets J, Sempke JW, Kapur R. The pathogenic involvement of neutrophils in acute respiratory distress syndrome and transfusion-related acute lung injury. *Transfus Med Hemother* 2018;45(5):290–8.
- Tsai YF, Yang SC, Hwang TL. Formyl peptide receptor modulators: a patent review and potential applications for inflammatory diseases (2012–2015). *Expert Opin Ther Pat* 2016:1–18.
- Yang SC, Hwang TL. The potential impacts of formyl peptide receptor 1 in inflammatory diseases. *Front Biosci (Elite Ed)* 2016;8:436–49.
- Liu J, Qian C, Cao X. Post-translational modification control of innate immunity. *Immunology* 2016;45(1):15–30.
- Weiss E, Kretschmer D. Formyl-peptide receptors in infection, inflammation, and cancer. *Trends Immunol* 2018;39(10):815–29.
- Zhang Y, Wang X, Yang H, Liu H, Lu Y, Han L, et al. Kinase AKT controls innate immune cell development and function. *Immunology* 2013;140(2):143–52.
- Manning BD, Tokar A. AKT/PKB signaling: navigating the network. *Cell* 2017;169(3):381–405.
- Chamcheu JC, Adhamsi VM, Esnault S, Sechi M, Siddiqui IA, Satyshur KA, et al. Dual inhibition of PI3K/Akt and mTOR by the dietary antioxidant, delphinidin, ameliorates psoriatic features in vitro and in an imiquimod-induced psoriasis-like disease in mice. *Antioxid Redox Signal* 2017;26(2):49–69.
- Hoyal CR, Gutierrez A, Young BM, Catz SD, Lin JH, Tschlis PN, et al. Modulation of p47PHOX activity by site-specific phosphorylation: Akt-dependent activation of the NADPH oxidase. *Proc Natl Acad Sci U S A* 2003;100(9):5130–5.
- El-Benna J, Dang PM, Gougerot-Pocidalo MA, Marie JC, Braut-Boucher F. p47phox, the phagocyte NADPH oxidase/NOX2 organizer: structure, phosphorylation and implication in diseases. *Exp Mol Med* 2009;41(4):217–25.
- Chen J, Tang H, Hay N, Xu J, Ye RD. Akt isoforms differentially regulate neutrophil functions. *Blood* 2010;115(21):4237–46.
- Nanamori M, Chen J, Du X, Ye RD. Regulation of leukocyte degranulation by cGMP-dependent protein kinase and phosphoinositide 3-kinase: potential roles in phosphorylation of target membrane SNARE complex proteins in rat mast cells. *J Immunol* 2007;178(1):416–27.
- Hoenderdos K, Lodge KM, Hirst RA, Chen C, Palazzo SG, Emerenciana A, et al. Hypoxia upregulates neutrophil degranulation and potential for tissue injury. *Thorax* 2016;71(11):1030–8.
- Kumar S, Xu J, Kumar RS, Lakshminathan S, Kapur R, Kofron M, et al. The small GTPase Rap1b negatively regulates neutrophil chemotaxis and transcellular diapedesis by inhibiting Akt activation. *J Exp Med* 2014;211(9):1741–58.
- Chodniewicz D, Zhelev DV. Novel pathways of F-actin polymerization in the human neutrophil. *Blood* 2003;102(6):2251–8.
- Ahmad F, Nidadavolu P, Durgados L, Ravindranath V. Critical cysteines in Akt1 regulate its activity and proteasomal degradation: implications for neurodegenerative diseases. *Free Radic Biol Med* 2014;74:118–28.
- Durgados L, Nidadavolu P, Valli RK, Saeed U, Mishra M, Seth P, et al. Redox modification of Akt mediated by the dopaminergic neurotoxin MPTP, in mouse midbrain, leads to down-regulation of pAkt. *FASEB J* 2012;26(4):1473–83.
- Corcoran A, Cotter TG. Redox regulation of protein kinases. *FEBS J* 2013;280(9):1944–65.
- Zeng T, Zhang CL, Zhao N, Guan MJ, Xiao M, Yang R, et al. Impairment of Akt activity by CYP2E1 mediated oxidative stress is involved in chronic ethanol-induced fatty liver. *Redox Biol* 2018;14:295–304.
- Lo HM, Hwang TL, Wu WB. A phenanthrene derivative, 5,7-dimethoxy-1,4-phenanthrenequinone, inhibits cell adhesion molecule expression and migration in vascular endothelial and smooth muscle cells. *Pharmacology* 2017;99(5–6):291–302.
- Lee CL, Lin YT, Chang FR, Chen GY, Backlund A, Yang JC, et al. Synthesis and biological evaluation of phenanthrenes as cytotoxic agents with pharmacophore modeling and ChemGPS-NP prediction as topo II inhibitors. *PLoS One* 2012;7(5):e37897.
- Chen PJ, Wang YL, Kuo LM, Lin CF, Chen CY, Tsai YF, et al. Honokiol suppresses TNF- $\alpha$ -induced neutrophil adhesion on cerebral endothelial cells by disrupting polyubiquitination and degradation of I $\kappa$ B $\alpha$ . *Sci Rep* 2016;6(6):26554.
- Yuan P, Temam S, El-Naggar A, Zhou X, Liu DD, Lee JJ, et al. Overexpression of podoplanin in oral cancer and its association with poor clinical outcome. *Cancer* 2006;107(3):563–9.
- Dorward DA, Lucas CD, Chapman GB, Haslett C, Dhaliwal K, Rossi AG. The role of formylated peptides and formyl peptide receptor 1 in governing neutrophil function during acute inflammation. *Am J Pathol* 2015;185(5):1172–84.
- Yang SC, Chen PJ, Chang SH, Weng YT, Chang FR, Chang KY, et al. Luteolin attenuates neutrophil oxidative stress and inflammatory arthritis by inhibiting Raf1 activity. *Biochem Pharmacol* 2018;154:384–96.

- [33] Futosi K, Fodor S, Mocsai A. Reprint of Neutrophil cell surface receptors and their intracellular signal transduction pathways. *Int Immunopharmacol* 2013;17(4):1185–97.
- [34] Hirai H, Sootome H, Nakatsuru Y, Miyama K, Taguchi S, Tsujioka K, et al. MK-2206, an allosteric Akt inhibitor, enhances antitumor efficacy by standard chemotherapeutic agents or molecular targeted drugs in vitro and in vivo. *Mol Cancer Ther* 2010;9(7):1956–67.
- [35] Weichhart T, Hengstschlager M, Linke M. Regulation of innate immune cell function by mTOR. *Nat Rev Immunol* 2015;15(10):599–614.
- [36] Brazil DP, Yang ZZ, Hemmings BA. Advances in protein kinase B signalling: AKTion on multiple fronts. *Trends Biochem Sci* 2004;29(5):233–42.
- [37] Sousa LP, Lopes F, Silva DM, Tavares LP, Vieira AT, Rezende BM, et al. PDE4 inhibition drives resolution of neutrophilic inflammation by inducing apoptosis in a PKA-PI3K/Akt-dependent and NF-kappaB-independent manner. *J Leukoc Biol* 2010;87(5):895–904.
- [38] Tsai YF, Chu TC, Chang WY, Wu YC, Chang FR, Yang SC, et al. 6-Hydroxy-5,7-dimethoxy-flavone suppresses the neutrophil respiratory burst via selective PDE4 inhibition to ameliorate acute lung injury. *Free Radic Biol Med* 2017;106:379–92.
- [39] Murata H, Ihara Y, Nakamura H, Yodoi J, Sumikawa K, Kondo T. Glutaredoxin exerts an antiapoptotic effect by regulating the redox state of Akt. *J Biol Chem* 2003;278(50):50226–33.
- [40] Yang SC, Chang SH, Hsieh PW, Huang YT, Ho CM, Tsai YF, et al. Dipeptide HCH6-1 inhibits neutrophil activation and protects against acute lung injury by blocking FPR1. *Free Radic Biol Med* 2017;106:254–69.
- [41] Yeh YC, Yang CP, Lee SS, Horng CT, Chen HY, Cho TH, et al. Acute lung injury induced by lipopolysaccharide is inhibited by wogonin in mice via reduction of Akt phosphorylation and RhoA activation. *J Pharm Pharmacol* 2016;68(2):257–63.
- [42] Nicolas-Avila JA, Adrover JM, Hidalgo A. Neutrophils in homeostasis, immunity, and cancer. *Immunity* 2017;46(1):15–28.
- [43] Kim K, Li J, Barazia A, Tseng A, Youn SW, Abbadessa G, et al. ARQ 092, an orally-available, selective AKT inhibitor, attenuates neutrophil-platelet interactions in sickle cell disease. *Haematologica* 2017;102(2):246–59.
- [44] Dennehy MK, Richards KA, Wernke GR, Shyr Y, Liebler DC. Cytosolic and nuclear protein targets of thiol-reactive electrophiles. *Chem Res Toxicol* 2006;19(1):20–9.
- [45] Mi L, Hood BL, Stewart NA, Xiao Z, Govind S, Wang X, et al. Identification of potential protein targets of isothiocyanates by proteomics. *Chem Res Toxicol* 2011;24(10):1735–43.
- [46] Galli S, Antico Arciuch VG, Poderoso C, Converso DP, Zhou Q, Bal de Kier Joffe E, et al. Tumor cell phenotype is sustained by selective MAPK oxidation in mitochondria. *PLoS One* 2008;3(6):e2379.
- [47] Luanpitpong S, Chanvorachote P, Nimmannit U, Leonard SS, Stehlik C, Wang L, et al. Mitochondrial superoxide mediates doxorubicin-induced keratinocyte apoptosis through oxidative modification of ERK and Bcl-2 ubiquitination. *Biochem Pharmacol* 2012;83(12):1643–54.
- [48] Keane NA, Glavey SV, Krawczyk J, O'Dwyer M. AKT as a therapeutic target in multiple myeloma. *Expert Opin Ther Targets* 2014;18(8):897–915.
- [49] Nitulescu GM, Margina D, Juzenas P, Peng Q, Olaru OT, Saloustros E, et al. Akt inhibitors in cancer treatment: the long journey from drug discovery to clinical use (Review). *Int J Oncol* 2016;48(3):869–85.
- [50] Jacinto E, Lorbberg A. TOR regulation of AGC kinases in yeast and mammals. *Biochem J* 2008;410(1):19–37.
- [51] Weisner J, Gontla R, van der Westhuizen L, Oeck S, Ketzler J, Janning P, et al. Covalent-allosteric kinase inhibitors. *Angew Chem Int Ed Engl* 2015;54(35):10313–6.
- [52] Nguyen T, Coover RA, Verghese J, Moran RG, Ellis KC. Phenylalanine-based inactivator of AKT kinase: design, synthesis, and biological evaluation. *ACS Med Chem Lett* 2014;5(5):462–7.
- [53] Lee JY, Lee YG, Lee J, Yang KJ, Kim AR, Kim JY, et al. Akt Cys-310-targeted inhibition by hydroxylated benzene derivatives is tightly linked to their immunosuppressive effects. *J Biol Chem* 2010;285(13):9932–48.
- [54] Shearn CT, Reigan P, Petersen DR. Inhibition of hydrogen peroxide signaling by 4-hydroxynonenal due to differential regulation of Akt1 and Akt2 contributes to decreases in cell survival and proliferation in hepatocellular carcinoma cells. *Free Radic Biol Med* 2012;53(1):1–11.



# NK Cell-Derived IFN- $\gamma$ Protects against Nontuberculous Mycobacterial Lung Infection

Hsin-Chih Lai,<sup>\*,†,‡,§,¶,||,##,\*</sup> Chih-Jung Chang,<sup>\*,†,‡,§,¶</sup> Chuan-Sheng Lin,<sup>\*,†,‡,§,¶</sup>  
Tsung-Ru Wu,<sup>\*</sup> Ya-Jing Hsu,<sup>\*</sup> Ting-Shu Wu,<sup>||,‡,‡</sup> Jang-Jih Lu,<sup>\*,||</sup> Jan Martel,<sup>‡,||</sup>  
David M. Ojcius,<sup>‡,||,§§</sup> Cheng-Lung Ku,<sup>||,‡,‡,¶</sup> John D. Young,<sup>‡,||,|||</sup> and Chia-Chen Lu<sup>##</sup>

In developed countries, pulmonary nontuberculous mycobacteria (NTM) infections are more prevalent than *Mycobacterium tuberculosis* infections. Given the differences in the pathogenesis of NTM and *M. tuberculosis* infections, separate studies are needed to investigate the pathological effects of NTM pathogens. Our previous study showed that anti-IFN- $\gamma$  autoantibodies are detected in NTM-infected patients. However, the role of NK cells and especially NK cell-derived IFN- $\gamma$  in this context has not been studied in detail. In the current study, we show that NK1.1 cell depletion increases bacterial load and mortality in a mouse model of pulmonary NTM infection. NK1.1 cell depletion exacerbates NTM-induced pathogenesis by reducing macrophage phagocytosis, dendritic cell development, cytokine production, and lung granuloma formation. Similar pathological phenomena are observed in IFN- $\gamma$ -deficient (IFN- $\gamma^{-/-}$ ) mice following NTM infection, and adoptive transfer of wild-type NK cells into IFN- $\gamma^{-/-}$  mice considerably reduces NTM pathogenesis. Injection of rIFN- $\gamma$  also prevents NTM-induced pathogenesis in IFN- $\gamma^{-/-}$  mice. We observed that NK cells represent the main producers of IFN- $\gamma$  in the lungs and production starts as soon as 1 d postinfection. Accordingly, injection of rIFN- $\gamma$  into IFN- $\gamma^{-/-}$  mice 1 d (but not 2 wk) postinfection significantly improves immunity against NTM infection. NK cells also stimulate mycobacterial killing and IL-12 production by macrophages. Our results therefore indicate that IFN- $\gamma$  production by NK cells plays an important role in activating and enhancing innate and adaptive immune responses at early stages of pulmonary NTM infection. *The Journal of Immunology*, 2018, 201: 000–000.

Nontuberculous mycobacteria (NTM) are ubiquitous environmental bacteria that cause severe diseases in humans (1, 2). In recent years, pulmonary NTM infections have been increasingly encountered in developed countries, even surpassing the prevalence of *Mycobacterium tuberculosis* infections (3, 4). Emergent NTM species, including *Mycobacterium kansasii* and *Mycobacterium abscessus*, have been implicated in pulmonary diseases in many countries (3, 5, 6). The pathogenesis and treatment of NTM infections and the host immune response against these pathogens differ from those associated with *M. tuberculosis* infections (7). Determining the factors that affect host immunity during NTM infections is therefore essential for the development of new strategies to prevent and treat these conditions.

*M. kansasii* has emerged as a prevalent NTM that causes severe pulmonary infections in both immunocompetent and

immunocompromised patients (8). *M. kansasii* causes diseases ranging from mild, self-limiting infections to a chronic, progressive disease resembling tuberculosis (9), producing symptoms that include acute suppurative, nonnecrotic tubercles, and caseous necrosis in the lungs (10). *M. kansasii* also infects other organs and may cause a systemic infection (11). Even though many studies have been performed to understand the pathogenesis of NTM infection, little is known about the pathogenesis of *M. kansasii*-related diseases. Although the symptoms caused by *M. kansasii* in the lungs are like those produced by *M. tuberculosis* (12), the host immune response against *M. kansasii* differs from that observed during *M. tuberculosis* infection (13, 14). Accordingly, previous studies have shown that CD4<sup>+</sup> lymphocytes protect against *M. tuberculosis* because CD4<sup>+</sup> knockout mice display reduced levels of pulmonary inflammation, adaptive Th1 cells,

\*Department of Medical Biotechnology and Laboratory Science, College of Medicine, Chang Gung University, Gueishan, Taoyuan 33302, Taiwan; <sup>†</sup>Graduate Institute of Biomedical Sciences, College of Medicine, Chang Gung University, Gueishan, Taoyuan 33302, Taiwan; <sup>‡</sup>Center for Molecular and Clinical Immunology, Chang Gung University, Gueishan, Taoyuan 33302, Taiwan; <sup>§</sup>Microbiota Research Center, Chang Gung University, Gueishan, Taoyuan 33302, Taiwan; <sup>¶</sup>Research Center for Emerging Viral Infections, Chang Gung University, Gueishan, Taoyuan 33302, Taiwan; <sup>||</sup>Chang Gung Immunology Consortium, Linkou Chang Gung Memorial Hospital, Gueishan, Taoyuan 33305, Taiwan; <sup>##</sup>Department of Laboratory Medicine, Linkou Chang Gung Memorial Hospital, Gueishan, Taoyuan 33305, Taiwan; <sup>§§</sup>Research Center for Chinese Herbal Medicine, College of Human Ecology, Chang Gung University of Science and Technology, Gueishan, Taoyuan 33303, Taiwan; <sup>¶¶</sup>Research Center for Food and Cosmetic Safety, College of Human Ecology, Chang Gung University of Science and Technology, Gueishan, Taoyuan 33303, Taiwan; <sup>|||</sup>Division of Infectious Diseases, Department of Internal Medicine, Linkou Chang Gung Memorial Hospital, Gueishan, Taoyuan 33305, Taiwan; <sup>§§</sup>Department of Biomedical Sciences, Arthur A. Dugoni School of Dentistry, University of the Pacific, San Francisco, CA 94103; <sup>¶¶</sup>Laboratory of Human Immunology and Infectious Diseases, Graduate Institute of Clinical Medical Sciences, Chang Gung University, Gueishan, Taoyuan 33302, Taiwan; <sup>|||</sup>Laboratory of Cellular Physiology and Immunology, Rockefeller University, New York, NY 10021; and <sup>##</sup>Department of Respiratory Therapy, Fu Jen Catholic University, Xinzhuang, New Taipei City 24205, Taiwan

ORCID: 0000-0003-1461-4495 (D.M.O.).

Received for publication January 31, 2018. Accepted for publication July 5, 2018.

This work was supported by Grants MOST105-2320-B-182-032-MY3, MOST106-2320-B-030-004, MOST106-2320-B-182-028-MY3, MOST107-2320-B-030-002, and MOST107-2321-B-182-002 from the Ministry of Science and Technology of Taiwan and by Grants CMRPDI0071-3, CORPD1F0011-3, CMRPDI0121-3, QZRPDI42, and BMRPA04 from Chang Gung Memorial Hospital and Chang Gung University.

Address correspondence and reprint requests to Dr. Chia-Chen Lu, Department of Respiratory Therapy, College of Medicine, Fu Jen Catholic University, 510 Zhong-Zheng Road, Xinzhuang, New Taipei City 24205, Taiwan. E-mail address: 082385@mail.fju.edu.tw

The online version of this article contains supplemental material.

Abbreviations used in this article: AAGM-1, anti-asialo-GM1 Ab; BALF, bronchoalveolar lavage fluid; DC, dendritic cell; MHCII, MHC class II; NK<sup>+</sup> mice, NK1.1 cell-depleted mice; NTM, nontuberculous mycobacteria; pNK, primary NK.

Copyright © 2018 by The American Association of Immunologists, Inc. 0022-1767/18/\$35.00

granuloma formation, and lymphocyte infiltration in the lungs (13, 14). However, CD4<sup>+</sup> knockout mice do not show impaired *M. kansasii* clearance compared with wild-type mice (13), suggesting that other immune cells and processes are involved in the host immune response against *M. kansasii*.

Autosomal and X-linked mutations conferring susceptibility to disseminated NTM infection have been observed in human patients (4, 15, 16). These mutations affect the interaction between IL-12-producing mononuclear phagocytes and NKT cells that secrete IFN- $\gamma$ . Production of anti-IFN- $\gamma$  autoantibodies has also been found to confer susceptibility to disseminated NTM infection, whereas these autoantibodies are rarely detected in *M. tuberculosis* infection (17). Many cases of severe and disseminated NTM infection in which tuberculosis symptoms are absent also frequently occur in immunocompetent individuals of all ages (18), suggesting the existence of distinct but partially overlapping roles for IFN- $\gamma$ -related immunity in the control of infection caused by *M. tuberculosis* and NTM (17, 19). Although the effects of NK cells and IFN- $\gamma$  in the immune response against *Mycobacterium avium* infection have been studied in the past (20–22), the role of IFN- $\gamma$  and NK cells in response to *M. kansasii* at early stages of NTM infection remains unclear.

NK cells represent 10–20% of the total lymphocyte population, and these cells play a pivotal role in the effector arm of the host innate immune system (23). NK cells defend the host against cancer, viruses, and bacteria (24–26). NK cells also show diverse functional activities, including “natural” (immediate) cytotoxicity and the capacity to produce cytokines (e.g., IFN- $\gamma$  and TNFs) and chemokines (e.g., MIP-1 $\alpha$  and MIP-1 $\beta$ ), which generate and sustain a proinflammatory environment (27). NK cells display activating and inhibitory surface receptors that recognize various molecular determinants on the surface of infected cells (28). Integration of these activating and inhibitory signals determines the nature and intensity of NK cell activities. Interactions between NK cells and dendritic cells (DCs) influence activation of both cells and lead to confinement and killing of *M. tuberculosis*, subsequently affecting the adaptive immune response (29). In addition to interacting with DCs, NK cells regulate the activity of T cells and participate directly in the adaptive immune response (30). Even though many studies have examined the role of NK cells in defense against *M. tuberculosis* and viral infections (31–35), the role and activities of NK cells against NTM lung infection have not been studied in detail.

Our previous study showed that NK cells can directly kill *M. tuberculosis* and *M. kansasii* by releasing the cytolytic proteins perforin and granzysin (36). We also reported that anti-IFN- $\gamma$  autoantibodies associated with specific MHC haplotypes play a crucial role in patients with mycobacterial infection (37). In the current study, we characterized the role of NK cells and IFN- $\gamma$  during early stages of *M. kansasii* infection in the lungs. In this context, NK cells act as the main producer of IFN- $\gamma$ , which activates innate and adaptive immune responses leading to eradication of mycobacteria and survival of the host. Our results provide important insights regarding the role of NK cells and IFN- $\gamma$  in early defense against NTM infection.

## Materials and Methods

### Mice

All experimental procedures were approved by the Institutional Animal Care and Use Committee of Chang Gung University. The experiments were performed in accordance with the guidelines. Eight- to ten-week-old, specific pathogen-free, C57BL/6 or IFN- $\gamma$ -deficient female mice were purchased from The Jackson Laboratory (Bar Harbor, ME). All mice were fed ad libitum with chow and water. Animals were housed in a specific

pathogen-free facility and were treated in accordance with guidelines from the National Institutes of Health (Bethesda, MD).

### Experimental infection

Lung infection was performed as described before (13). Briefly, mice were anesthetized with isoflurane (Halocarbon 1216400210) and infected intratracheally with 50  $\mu$ l of saline containing  $1 \times 10^6$  CFUs of *M. kansasii* or saline alone as negative control. At the indicated time points, eight mice per group were killed, and the lungs were removed aseptically and homogenized in 1 ml of PBS.

### NK cell depletion

C57BL/6 and IFN- $\gamma$ -deficient mice were treated every 5 d i.p. with 100  $\mu$ g of rabbit AAGM1 Ab (Wako Chemicals USA, Richmond, VA) or rabbit isotype IgG as negative control. Two weeks after the initiation of AAGM1 treatment, mice were infected intratracheally with *M. kansasii* or bacteria-free saline. Ab treatment continued for the duration of the experiment. Noninfected mice that had received AAGM1 or saline were included for each experimental time point. Flow cytometry analysis of lung, spleen, and liver cells was used to monitor the efficacy of NK1.1<sup>+</sup> cell depletion. Following depletion, NK cells represented <0.5% of lymphocytes in the three organs examined. Alternatively, mice were treated with anti-NK1.1 Ab (clone PK136; BD Biosciences, San Jose, CA), which produced similar results (data not shown).

### Culture of mycobacteria

*M. kansasii* type strain (ATCC 12478) was obtained from the American Type Culture Collection (Manassas, VA). Bacteria were grown at 37°C on Middlebrook 7H11 agar or in 7H9 broth (Difco Laboratories, Franklin Lakes, NJ) supplemented with 0.5% glycerol and 10% oleic acid-bovine albumin-dextrose-catalase (Becton Dickinson, Franklin Lakes, NJ). Bacteria were transferred into 7H9 broth media (Difco Laboratories) containing 10% glycerol, adjusted to an OD of 0.8 (absorbance was measured at a wavelength of 600 nm using a spectrophotometer) and stored at –80°C.

### Mycobacterial killing assay

Lungs were perfused with saline, and the right lung was excised. Special care was taken to exclude hilar tissues or proximal bronchi. The right lung was minced, suspended in 1 ml of PBS, and homogenized. CFUs were determined by preparation of serial bacterial dilutions in 7H9 broth, followed by plating onto Middlebrook 7H11 agar plates. Bacterial colonies were counted after incubation at 37°C for 14–18 d.

### Histological analysis

Lungs were fixed in buffered formalin and embedded in paraffin. Thin sections (4 mm) were prepared and stained with H&E. Stained sections were examined under an optical light microscope (Olympus, Tokyo, Japan). To quantify the surface of granulomas, histological images were analyzed using the ImageJ software (National Institutes of Health). The threshold was set to discriminate between granuloma and alveolae, and the percentage of granulomatous area was calculated using the Analyze Particle command. Two randomly selected fields from each 10–15 section were analyzed. Cryosections were stained as previously described (38). Briefly, sections were stained with PE-conjugated anti-CD11b mAb (red) and FITC-conjugated anti-CD3 mAb (green). Sections were analyzed using an LSM 510 Zeiss Confocal Laser Scanning Microscope (ZEISS, Jena, Germany).

### Lung single-cell preparation

Lung single cells were prepared as described by Ichinohe et al. (39) with minor modifications. Briefly, the right lung was perfused with 2 ml of sterile PBS (pH 7.4) and minced to ~1 mm pieces. Lung tissues were incubated in 10 ml of RPMI 1640 liquid culture medium (Life Technologies, Carlsbad, CA) containing HEPES (2.5 mM; Life Technologies) and EDTA (1.3 mM; Invitrogen) at 37°C for 30 min, followed by incubation in RPMI 1640 medium containing HEPES (2.5 mM), 5% FBS (Life Technologies), and collagenase (1 mg/ml; Sigma-Aldrich) at 37°C for 1 h. Single-cell suspension was collected after RBC lysis and mesh filtration.

### Flow cytometry analysis

Abs used for flow cytometry analysis were as follows: CD3-FITC (145-2C11), NK1.1-PE (PK136), CD11c-PE (HL3), F4/80-PE (BM9), Ly6G-PE (1A8), CD19-PE (1D3), CD4-PE (GK1.5),  $\gamma\delta$  TCR-FITC (GL3), CD80-FITC

(16-10A1), CD86-allophycocyanin, IL-6-allophycocyanin (MP5-20F3), IL-10-allophycocyanin, IL-12-allophycocyanin (p40/p70), TNF- $\alpha$ -allophycocyanin, IFN- $\gamma$ -allophycocyanin, IL-17A-Alexa Fluor 647 (TC11-18H10), NKp46-Alexa Fluor 647 (29A1.4), and CD69-allophycocyanin (H1.2F3) (BD Pharmingen). Perforin-allophycocyanin (eBioOMAK-D) and NKG2D-allophycocyanin (CX5) were purchased from eBioscience (San Diego, CA). IL-1 $\beta$ -allophycocyanin and IL-23-allophycocyanin were purchased from R&D Systems (Minneapolis, MN). Rabbit IgG-FITC was purchased from Beckman Coulter (Brea, CA). For surface staining, the single-cell suspension was directly stained with surface Ab, washed once with cold PBS containing 2% FBS, and resuspended in cold PBS. For surface and intracellular staining, cells were incubated in RPMI 1640 liquid medium containing PMA (25 ng/ml; Sigma-Aldrich) and ionomycin (1  $\mu$ g/ml; Sigma-Aldrich) for 1 h, followed by addition of BD GolgiPlug (BD Biosciences) for 3 h at 37°C under 5% CO<sub>2</sub>. Stimulated cells were stained with surface Ab and fixed and permeabilized using a Cytotfix/Cytoperm kit (BD Biosciences) according to the manufacturer's instructions, followed by intracellular staining. Stained cells were detected using BD FACSCalibur (BD Biosciences), and data were analyzed using the Kaluza software (Beckman Coulter).

### Cell isolation and purification

C57BL/6 lungs were harvested, and single-cell suspensions were prepared in PBS containing 10% FBS. NK cells were negatively selected from lung single-cell suspensions using the EasySep NK Cell Depletion Kit (Stemcell Technologies, Grenoble, France). The negatively selected NK cells were subjected to flow cytometry cell sorting to increase cell purity (NK1.1<sup>+</sup> CD3<sup>-</sup>). Cell purity was determined to be >95%. Lung macrophages were collected from lung single-cell suspensions. Briefly, lung single cells were resuspended in regular RPMI 1640 medium containing 100 U/ml penicillin, 100  $\mu$ g/ml streptomycin, 10% FBS, and 2 mM L-glutamine. Single cells were seeded in 24-well plates (1.5  $\times$  10<sup>6</sup> cells per well), and lung macrophages could adhere for 2 h at 37°C under 5% CO<sub>2</sub>, followed by removal of the medium and washing three times with culture medium to remove nonadherent cells. TCR  $\gamma\delta$  T cells were purified using a two-step procedure using MACS beads (Miltenyi Biotec, Bergisch Gladbach, Germany). Briefly, B cells and macrophages were depleted using biotin-conjugated anti-B220 and anti-CD11b mAbs and streptavidin microbeads. TCR  $\gamma\delta$  T cells were positively selected using PE-conjugated anti-TCR  $\gamma\delta$  mAb (BD Biosciences) and anti-PE microbeads with autoMACS (Miltenyi Biotec).

### Cytokine measurements

IFN- $\gamma$ , IL-12, and IL-17A were measured from lung homogenates using commercial ELISA kits (R&D Systems) according to the instructions from the manufacturer. For multiplex cytokine assays, lung homogenates from mice were evaluated for cytokine and chemokine levels using multiplex bead-based immunoassay kits (Bio-Plex Cytokine Assay; Bio-Rad, Hercules, CA) according to the manufacturer's instructions.

### Adoptive transfer of NK cells

NK cells were isolated from the spleen of C57BL/6 mice, and 1  $\times$  10<sup>6</sup> NK cells in 30  $\mu$ l of sterile PBS were transferred i.v. to NK1.1 cell-depleted mice (NK<sup>-</sup> mice), IFN- $\gamma$ -deficient mice, or naive control recipients. Recipient mice were intratracheally instilled with 1  $\times$  10<sup>6</sup> CFUs of *M. kansasii* 24 h after NK cell adoptive transfer or i.p. administration of rIFN- $\gamma$  (5  $\mu$ g in 100  $\mu$ l of 0.9% saline).

### Statistical analysis

Data are shown as mean  $\pm$  SD for parametric analysis. Differences between two groups were assessed using parametric unpaired two-tailed Student *t* test. Data sets involving more than two groups were assessed using one-way ANOVA. Animal survival rates were evaluated using Kaplan-Meier survival analysis with the log-rank test. The *p* values <0.05 were considered statistically significant.

## Results

### NK1.1 cells prevent mycobacteria dissemination and prolong survival in mice

To examine whether NK cells protect the host against NTM lung infection, we treated C57BL/6 mice i.p. with anti-asialo-GM1 Ab (AAGM-1) to deplete NK1.1 cells. NK1.1 cell depletion efficacy was verified using flow cytometry analysis of bronchoalveolar lavage fluid (BALF; Fig. 1A). NK1.1<sup>+</sup> CD3<sup>-</sup> NK cells represented 3.41% of BALF cells in control IgG-treated mice, whereas the cells decreased to 0.94% in AAGM-1-treated mice (Fig. 1A, week 2).

After 4 wk of AAGM-1 Ab treatment, NK1.1<sup>+</sup> CD3<sup>-</sup> cells represented only 0.78% of BALF cells (Fig. 1A, week 4). In contrast, NK1.1<sup>+</sup> CD3<sup>+</sup> NKT cells were not affected by AAGM-1 Ab treatment (Fig. 1A).

Mice were infected intratracheally with *M. kansasii* at a dose of 1  $\times$  10<sup>6</sup> CFUs using established procedures (13), and survival was monitored (Fig. 1B, *n* = 10/group). All control mice and NK<sup>-</sup> mice that were not infected with *M. kansasii* were alive at 10 wk (Fig. 1B). In contrast, only 50% of control mice were still alive 10 wk after *M. kansasii* infection, whereas all infected NK<sup>-</sup> mice were dead within 8 wk (Fig. 1B).

As early as 1 d after *M. kansasii* infection, mycobacterial load increased in the lungs of NK<sup>-</sup> mice compared with control mice, but the difference was not statistically significant (Fig. 1C, left panel, day 1). Although bacterial load remained relatively constant for 4 wk in the lungs of NK<sup>-</sup> mice, bacteria levels decreased in a time-dependent manner in the lungs of control mice (Fig. 1C). Notably, 2 wk postinfection, dissemination of *M. kansasii* bacteria to the spleen and liver occurred in NK<sup>-</sup> mice, whereas bacterial dissemination did not occur in control mice (Fig. 1C). Examination of NK<sup>-</sup> mice 4 wk postinfection revealed signs of splenomegaly, with the spleen of these mice being 10–20% larger than that of control mice (Supplemental Fig. 1A). These results suggest that NK1.1 cells protect the host against NTM lung infection.

### NK<sup>-</sup> mice show defective early innate immune responses against mycobacteria

We examined the effects of NK1.1 cell depletion on immune cells and cytokines found in lung tissues of *M. kansasii*-infected mice. Flow cytometry analysis of BALF from NK<sup>-</sup> mice revealed reduced levels of DCs (CD11c<sup>+</sup>), TCR  $\gamma\delta$  T cells (CD3<sup>+</sup>, TCR  $\gamma\delta$ <sup>+</sup>), and B cells (CD19<sup>+</sup>) as early as 1 d after mycobacteria infection, whereas the level of neutrophils increased (Ly6G<sup>+</sup>) (Fig. 2A, day 1, NK<sup>-</sup> mice versus control). No significant difference was noted for macrophages (F4/80<sup>+</sup>) or NKT cells (NK1.1<sup>+</sup> CD3<sup>+</sup>) in control and NK<sup>-</sup> mice (Supplemental Fig. 1B). Similar trends were observed at weeks 2 and 4 postinfection, with minor variations (Fig. 2A, Supplemental Fig. 1B; for instance, CD4<sup>+</sup> T lymphocytes were reduced in NK<sup>-</sup> mice at weeks 2 and 4, but no reduction of B cells was observed at week 2).

Robust immunity against mycobacteria depends on efficient cytokine production upon interactions between bacteria and innate immune cells (40–42). One day postinfection, the level of many cytokines and chemokines, including IL-1 $\beta$ , IL-6, IL-10, IL-12, IL-17A, IL-23, TNF- $\alpha$ , macrophage-derived chemokine, MIP-3 $\alpha$ , keratinocyte chemoattractant (also known as IL-8), and IFN- $\gamma$ , was reduced in the lungs of NK<sup>-</sup> mice (Fig. 2B, Supplemental Fig. 1C, NK<sup>-</sup> mice versus control). In contrast, chemokines and cytokines such as RANTES, MIP-1 $\alpha$ , MCP-1, LIX, MIP-2, and G-CSF increased in the lungs of NK<sup>-</sup> mice (Supplemental Fig. 1C), consistent with the observation that many neutrophils had infiltrated lung tissues in NK<sup>-</sup> mice (Fig. 2A, Ly6G<sup>+</sup>). Other cytokines such as GM-CSF and IL-1 $\alpha$  showed no variation between control and NK<sup>-</sup> mice on day 1 (Supplemental Fig. 1C). Similar results were obtained at weeks 2 and 4; however, RANTES showed a large reduction in NK<sup>-</sup> mice, whereas MIP-1 $\alpha$ , MCP-1, keratinocyte chemoattractant, and G-CSF increased in NK<sup>-</sup> mice (Fig. 2B, Supplemental Fig. 1C, NK<sup>-</sup> mice versus control).

To further confirm that altered cytokine response occurred in mycobacteria-infected NK<sup>-</sup> mice, we performed flow cytometry analysis to examine the level of macrophages and DCs producing specific cytokines. One day postinfection, the levels of DCs (Fig. 2C) and macrophages (Fig. 2D) producing various cytokines (i.e., IL-1 $\beta$ , IL-6, IL-10, IL-12, IL-23, and TNF- $\alpha$ ) were reduced



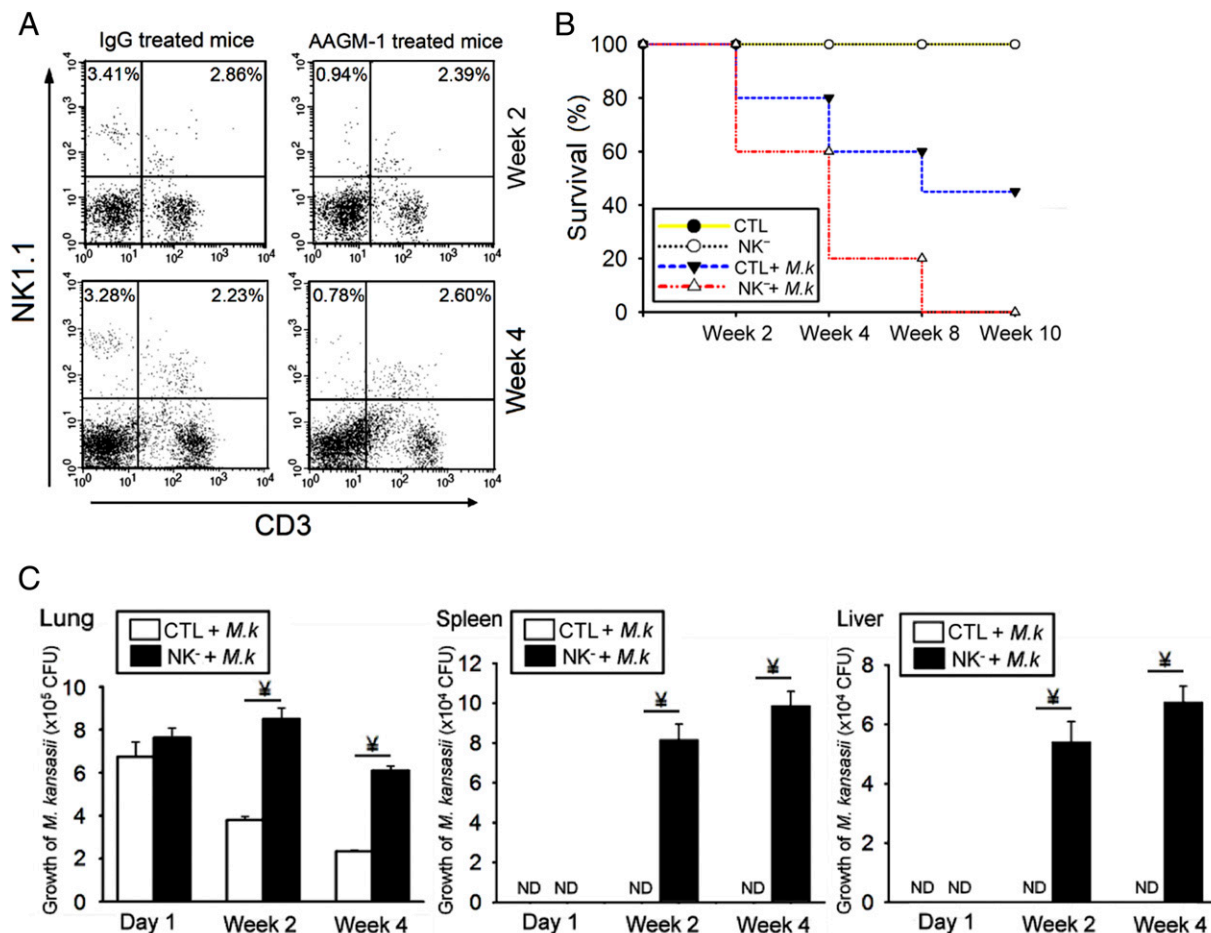


**FIGURE 1.** NK cells restrict mycobacterial lung infection and improve survival in mice. NK cells were depleted by i.p. injections of AAGM1 Ab (100  $\mu$ g) every 5 d in C57BL/6 mice. Isotype IgG (100  $\mu$ g) was used as negative control. **(A)** NK cell level in BALF was monitored by flow cytometry at the time indicated after injection. **(B)** After injection of AAGM1 or IgG for 4 wk, mice were infected intratracheally with *M.k* ( $1 \times 10^6$  CFUs) or a bacteria-free saline as negative control, and survival was monitored. **(C)** Bacterial growth was measured in the lungs, spleen, and liver at the time indicated postinfection. In **(B)**, the animal survival rate was evaluated using Kaplan–Meier survival analysis with the log-rank test ( $n = 10$  mice per group). In **(C)**, the data represent mean  $\pm$  SD from three independent experiments ( $n = 10$ ) using the unpaired Student *t* test.  $^*p < 0.001$ . CTL, control IgG-treated mice (containing NK cells); *M.k*, *M. kansasii*; ND, not detected.

in NK<sup>-</sup> mice compared with control mice. Similar trends were observed at weeks 2 and 4 (Fig. 2C, 2D). Thus, NK<sup>-</sup> mice display an altered profile of innate immune cells and cytokine production as early as 1 d after mycobacteria infection.

#### Impaired adaptive T cell response in NK<sup>-</sup> mice

After engulfment of mycobacteria, activated macrophages produce IL-12, which induces the secretion of IFN- $\gamma$  and other cytokines, eventually leading to differentiation of naive T cells toward the Th1 adaptive immunity pathway (43, 44). During lymphocyte activation, costimulation by APCs is crucial for the development of an effective immune response (45). In addition to the altered cytokine production noted above, we observed a decreased production of mycobacteria-induced costimulatory molecules (i.e., MHC class II [MHCII], CD80, CD40, and CD86) on DCs and macrophages isolated from the lungs of NK<sup>-</sup> mice 4 wk postinfection (Fig. 2C, 2D).

Given that reduced levels of costimulatory molecules on DCs and macrophages may lead to attenuated adaptive T cell response following mycobacteria infection, we examined the population of CD4<sup>+</sup> T cells using flow cytometry. As shown in Supplemental Fig. 2A, CD4<sup>+</sup> T cells were significantly reduced in BALF of NK<sup>-</sup> mice 2 and 4 wk postinfection. Consistent with these results, CD4<sup>+</sup> T cells producing IFN- $\gamma$  and IL-17A were also reduced 2 and 4 wk postinfection (Supplemental Fig. 2B). We also monitored TCR  $\gamma\delta$

T cells, which have been identified as a major producer of IL-17A within mycobacteria-induced lung granulomas (38). As shown in Supplemental Fig. 2C, TCR  $\gamma\delta$  T cells producing IFN- $\gamma$  and IL-17A were also considerably reduced 2 wk postinfection in NK<sup>-</sup> mice compared with control mice. These results suggest that NK1.1 cell deficiency affects adaptive T cell response during mycobacteria infection.

#### Impaired granuloma formation in lungs of NK<sup>-</sup> mice

Granuloma formation in the lungs plays an important role in limiting mycobacteria dissemination and tissue damage (46). Previous studies of *M. tuberculosis* infection showed that granuloma formation requires integration of many innate and adaptive immune activities controlled by NK cells (47). We therefore examined whether NK cell deficiency may impair lung granuloma formation following *M. kansasii* infection. Two weeks after mycobacteria infection, the granuloma structure was affected, and granuloma surface area was reduced in the lungs of NK<sup>-</sup> mice compared with the control mice (Fig. 3A, 3B). Granuloma surface area gradually increased with time in control mice; however, granulomas did not progress in NK<sup>-</sup> mice (Fig. 3B, week 4 versus week 2). By contrast, no significant pathological differences were observed in the lungs of control and NK<sup>-</sup> mice in the absence of mycobacterial infection (Supplemental Fig. 3).

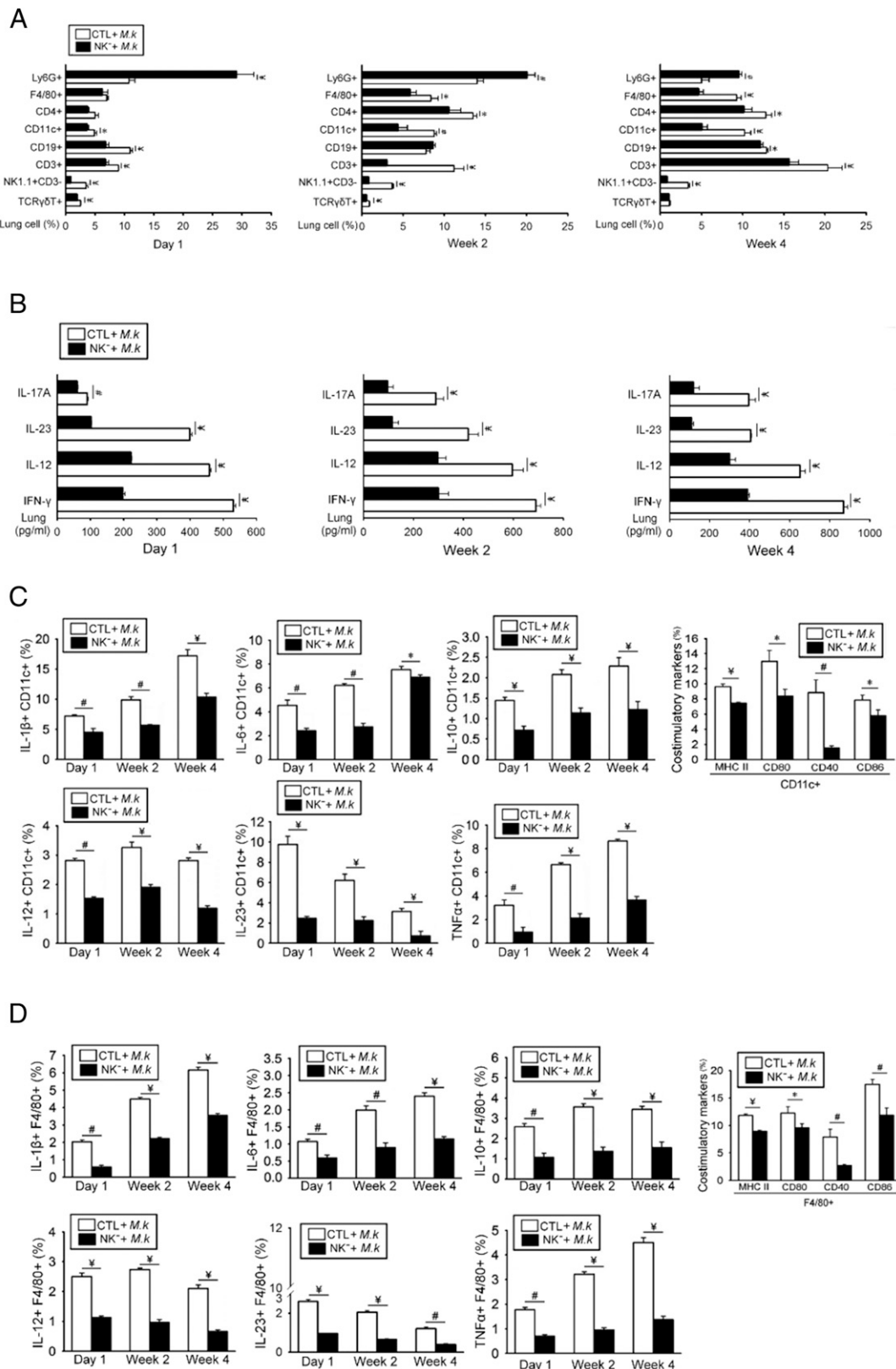


**FIGURE 2.** NK<sup>-</sup> mice show defective innate immune response against mycobacteria. **(A)** Immune cell markers and **(B)** cytokines were analyzed in CTL and NK<sup>-</sup> mice at the time indicated postinfection. Immune cells and cytokines were examined using flow cytometry and ELISA, respectively. Levels of **(C)** CD11c<sup>+</sup> DCs and **(D)** F4/80<sup>+</sup> macrophages harboring the indicated cytokines or costimulatory markers were analyzed using flow cytometry 1 d, 2 wk, or 4 wk postinfection. The data represent mean  $\pm$  SD from three independent experiments ( $n = 10$ ) using the unpaired Student  $t$  test. \* $p < 0.05$ , # $p < 0.01$ , ¥ $p < 0.001$ . CTL, control IgG-treated mice; M.k, *M. kansasii*.

Lung granuloma structure was examined following staining with fluorescent Abs that react against CD3<sup>+</sup> T cells or CD11b<sup>+</sup> DCs. A compact granuloma structure showing abundant CD3<sup>+</sup> T cells

and CD11b<sup>+</sup> DCs was observed in control mice 2 and 4 wk postinfection (Fig. 3C). In contrast, granulomas failed to form properly in mycobacteria-infected NK<sup>-</sup> mice (Fig. 3C). These



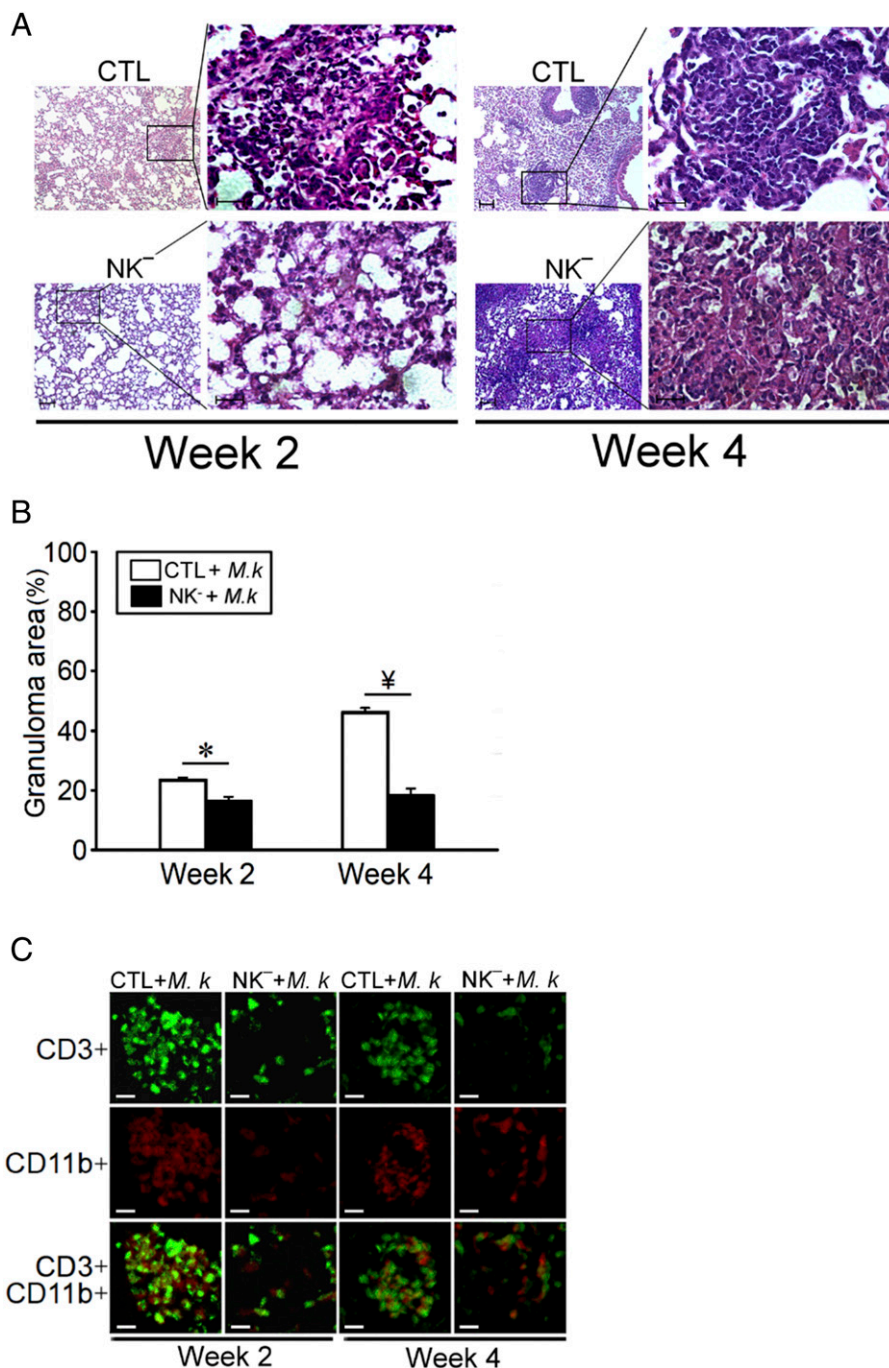


**FIGURE 3.** NK<sup>-</sup> mice show impaired lung granuloma formation. **(A)** Histopathology analysis of H&E-stained lung tissue sections from CTL and NK<sup>-</sup> mice was performed at the time indicated postinfection with *M.k*. Scale bars: low magnification, 100  $\mu$ m; inset, 25  $\mu$ m. **(B)** Lung granuloma area in tissue sections was determined using ImageJ at the time indicated postinfection. **(C)** Immunofluorescence staining of frozen lung sections was performed 2 and 4 wk postinfection. Anti-CD3 (green) and anti-CD11b (red) Abs were used and sections were observed under confocal laser scanning microscopy at an original magnification of  $\times 200$ . Scale bar, 25  $\mu$ m. Two different fields of the same sample from at least three tissue sections per group were analyzed. Representative slides are shown. In **(B)**, the data represent mean  $\pm$  SD from three independent experiments ( $n = 10$ ) using the unpaired Student *t* test. \* $p < 0.05$ ,  $\nless p < 0.001$ . CTL, control IgG-treated mice; *M.k*, *M. kansasii*.

results suggest that NK1.1 cells are required for lung granuloma formation in response to NTM infection.

#### *Interactions between NK cells and macrophages are required for the anti-NTM immune response*

We examined the possibility that the aberrant antimycobacterial response observed in NK<sup>-</sup> mice may be related to IFN- $\gamma$  production, as NK cells have been shown to produce this cytokine (48). In noninfected control mice, CD4<sup>+</sup> T cells, TCR  $\gamma\delta$  T cells, and NK cells producing IFN- $\gamma$  represented 0.58, 0.09, and 0.27% of BALF cells, respectively (Fig. 4A, 4B). One day postinfection with *M. kansasii*, the levels of CD4<sup>+</sup> T cells, TCR  $\gamma\delta$  T cells, and NK cells producing IFN- $\gamma$  increased to 2.03, 0.34, and 25.15%, respectively (Fig. 4A, 4B), indicating that NK cells represent the main producer of IFN- $\gamma$  in this context.

We reasoned that lung NK cells may work in concert with macrophages to enhance mycobacterial killing. To address this possibility, we isolated primary NK (pNK) cells and alveolar macrophages from lung tissues and measured the effects of pNK cells on mycobacterial killing by macrophages. As shown in Fig. 4C, macrophages significantly reduced the levels of live mycobacteria in vitro and pNK cells further enhanced the killing activity of macrophages. Moreover, pNK cells alone could kill mycobacteria (Fig. 4C).

We then measured the effect of pNK cells on production of IL-12 by macrophages. As shown in Fig. 4D, unstimulated macrophages produced  $\sim 3.5$  pg/ml IL-12. Incubation of macrophages with mycobacteria significantly enhanced IL-12 production to 45 pg/ml (Fig. 4D). Incubation of macrophages, mycobacteria, and pNK cells further enhanced IL-12 production (Fig. 4D; 70 pg/ml).

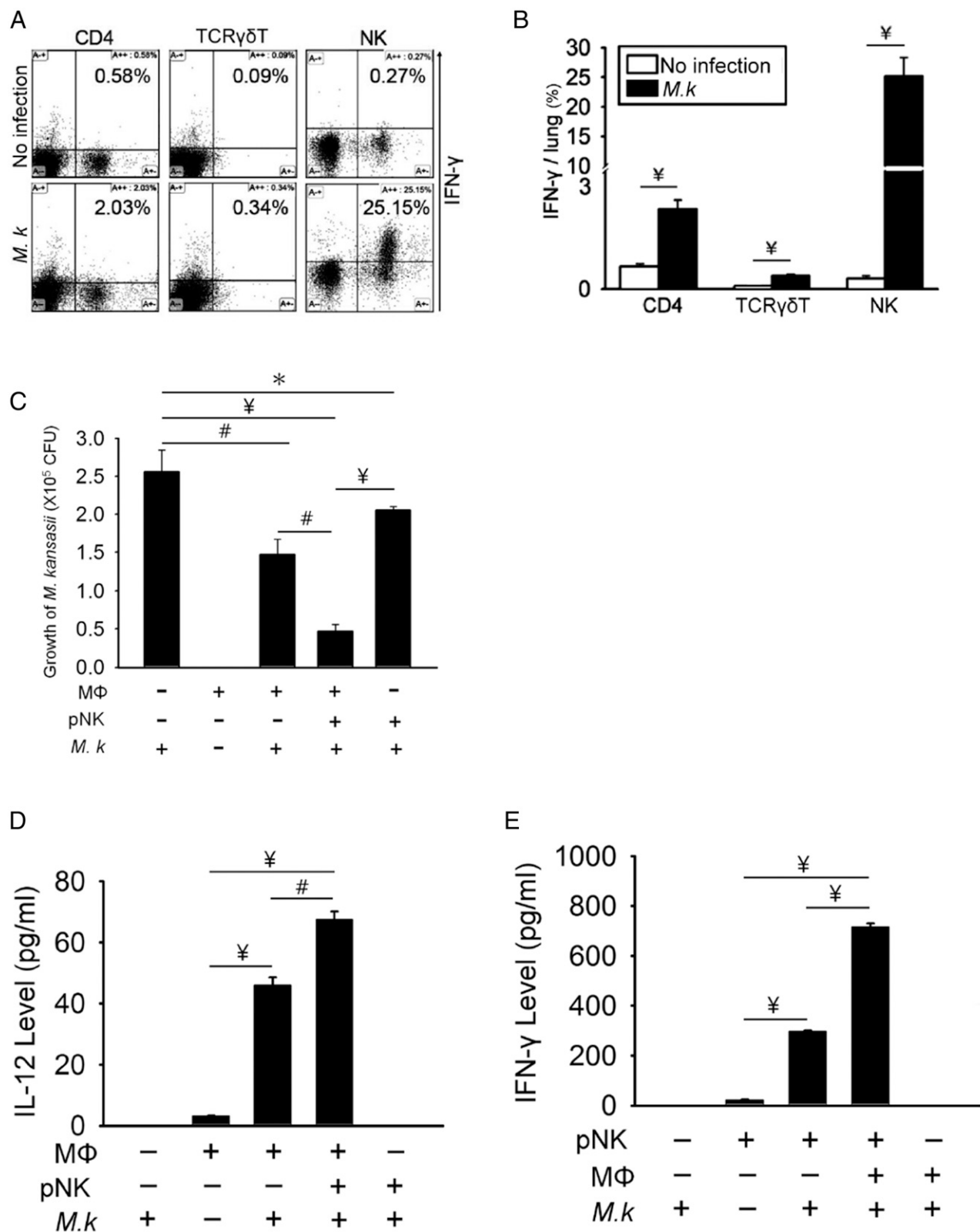


**FIGURE 4.** NK cells produce high levels of IFN- $\gamma$  and interact with macrophages following mycobacterial infection. **(A)** Percentage of IFN- $\gamma$  production by lymphocytes 1 d postinfection. IFN- $\gamma$  production by CD4 T cells, TCR  $\gamma\delta$ T cells, and NK cells was measured in BALF using flow cytometry. **(B)** Quantitative analysis of flow cytometry data shown in (A). **(C)** Mycobacterial killing by macrophages incubated with pNK cells. Macrophages ( $1 \times 10^5$  cells per well) were incubated with pNK cells ( $1 \times 10^5$  cells per well) and/or *M. k* ( $1 \times 10^4$  CFUs) at a multiplicity of infection (MOI) of 0.1 for 24 h. An effector/target ratio of 10:1 was used. **(D)** Production of IL-12 by macrophages. Conditions were similar to (C). **(E)** Effects of macrophages and *M. k* on IFN- $\gamma$  production by pNK cells. Conditions were similar to (C). In (B), data represent mean  $\pm$  SD from three independent experiments ( $n = 10$ ) using the unpaired Student  $t$  test. In (C)–(E), data represent mean  $\pm$  SD from three independent experiments ( $n = 6$ ) using one-way ANOVA analysis. \* $p < 0.05$ , # $p < 0.01$ , ¥ $p < 0.001$ . MΦ, macrophage; *M. k*, *M. kansasii*.

These results indicate that pNK cells and mycobacteria induce bacterial killing by macrophages.

To determine whether pNK cells may reciprocally interact with macrophages in response to NTM infection, we measured the effect of macrophages on pNK cell activity. Although incubation of macrophages with mycobacteria produced little or no IFN- $\gamma$ , pNK cells alone produced  $\sim 22$  pg/ml IFN- $\gamma$  (Fig. 4E). When pNK cells were mixed with mycobacteria, 300 pg/ml IFN- $\gamma$  was produced (Fig. 4E). In contrast, incubation of pNK cells with mycobacteria and macrophages increased IFN- $\gamma$  production to

750 pg/ml (Fig. 4E), indicating that IFN- $\gamma$  production by pNK cells is enhanced by infected macrophages.

#### NK cells and IFN- $\gamma$ reduce NTM-induced pathogenesis in NK $^{-}$ mice and IFN- $\gamma$ knockout mice

We examined the effects of adoptive NK cell transfer and IFN- $\gamma$  on bacterial load and macrophage phagocytosis activity during the early infection stage. One day after *M. kansasii* infection, adoptive transfer of NK cells significantly reduced bacterial load in lung tissues of NK $^{-}$  mice (Fig. 5A, NK $^{-}$  mice + NK versus NK $^{-}$  mice).

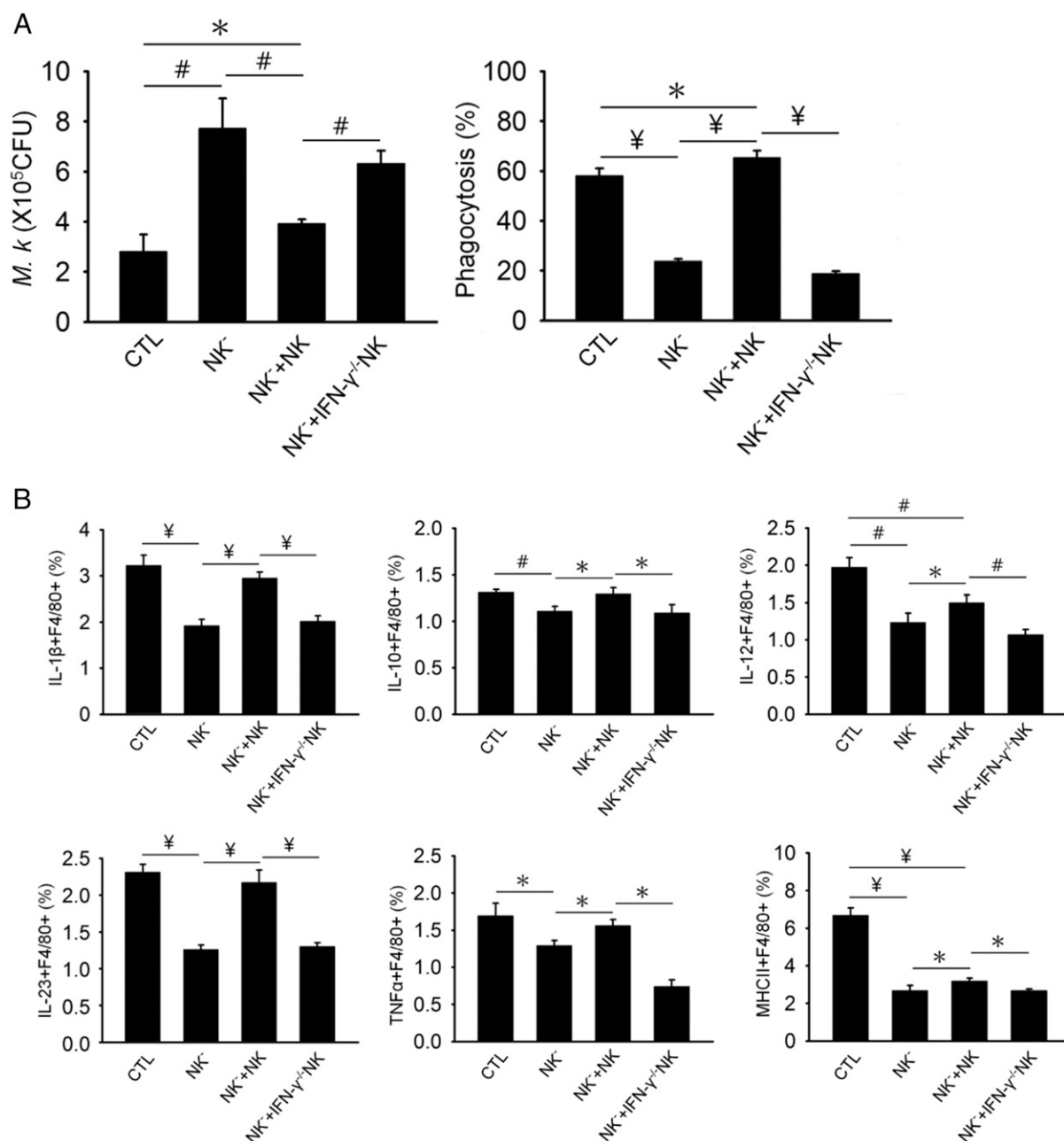


**FIGURE 5.** Adoptive transfer of NK cells improves immune response against mycobacteria in NK $^{-}$  mice. **(A)** One day after mycobacteria infection, bacterial load and macrophage phagocytosis activity were analyzed. **(B)** Levels of macrophages (F4/80 $^{+}$ ) producing the cytokines indicated or MHCII were measured using flow cytometry. CTL mice and NK $^{-}$  mice were treated with adoptive transfer of NK cells derived from untreated mice or IFN- $\gamma$  $^{-/-}$  mice. Mice were infected intratracheally with  $1 \times 10^6$  CFUs of *M.k.* Adoptive transfer of NK cells ( $1 \times 10^6$  cells) or IFN- $\gamma$ -deficient (IFN- $\gamma$  $^{-/-}$ ) NK cells ( $1 \times 10^6$  cells) into NK $^{-}$  mice was performed to evaluate the role of IFN- $\gamma$  from NK cells during the antimycobacteria immune response. rIFN- $\gamma$  (5  $\mu$ g) was used for injection. The data represent mean  $\pm$  SD from two independent experiments ( $n = 6$ ) and were analyzed using one-way ANOVA analysis. \* $p < 0.05$ , # $p < 0.01$ , ¥ $p < 0.001$ . CTL, control IgG-treated mice; IFN- $\gamma$  $^{-/-}$  NK, NK cells isolated from IFN- $\gamma$  $^{-/-}$  mice; *M.k.*, *M. kansasii*.

Adoptive transfer of NK cells also increased macrophage phagocytosis activity in NK<sup>-</sup> mice (Fig. 5A, right panel). By contrast, no significant improvement of bacterial load or macrophage phagocytosis was observed in mice that had received an adoptive transfer of NK cells derived from IFN- $\gamma$ <sup>-/-</sup> mice (Fig. 5A, NK<sup>-</sup> mice + IFN- $\gamma$ <sup>-/-</sup> NK versus NK<sup>-</sup> mice). These results further support the concept that NK cells enhance macrophage killing activity and mycobacteria eradication at the early stage of mycobacterial infection. Consistent with these observations, the level of macrophages producing IL-1 $\beta$ , IL-10, IL-12, IL-23, TNF- $\alpha$ , and MHCII was also enhanced following adoptive transfer of NK cells compared with NK<sup>-</sup> mice, whereas no effects were produced by

transfer of NK cells from IFN- $\gamma$ -deficient mice (Fig. 5B). In addition, a similar trend in the production of IL-17A and IFN- $\gamma$  by TCR  $\gamma\delta$  T cells was observed following adoptive transfer of NK cells and IFN- $\gamma$ -deficient NK cells into NK<sup>-</sup> mice (Supplemental Fig. 4A).

We examined the effects of IFN- $\gamma$  in this context using IFN- $\gamma$ <sup>-/-</sup> mice and rIFN- $\gamma$  (49). One day after mycobacterial infection, adoptive transfer of NK cells or injection of rIFN- $\gamma$  into IFN- $\gamma$ <sup>-/-</sup> mice reduced lung bacterial load and enhanced macrophage phagocytosis activity (Fig. 6A). In addition, levels of macrophages producing IL-1 $\beta$ , IL-10, IL-12, IL-23, TNF- $\alpha$ , or MHCII were also enhanced following adoptive

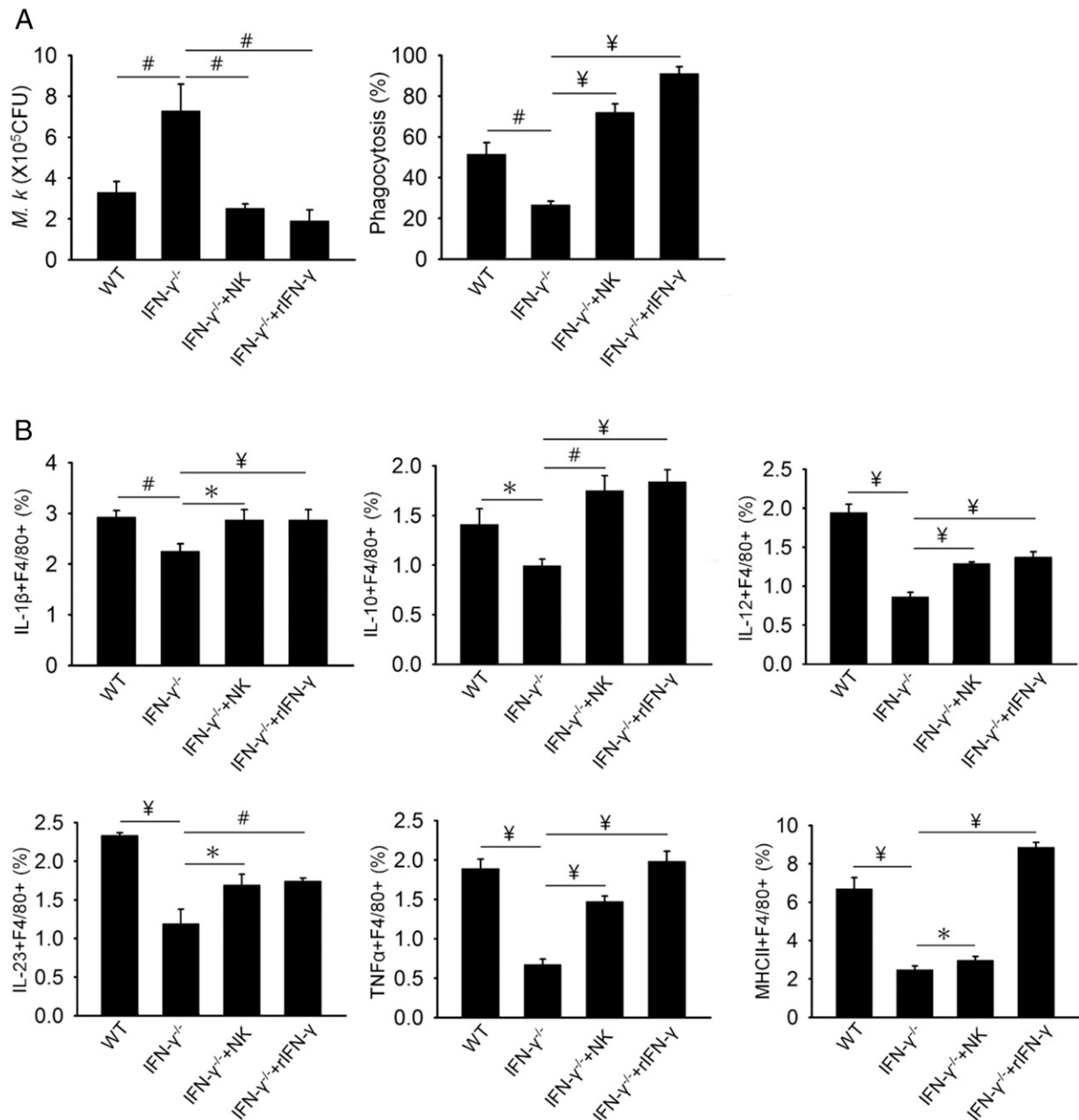


**FIGURE 6.** Adoptive transfer of NK cells and IFN- $\gamma$  treatment at the early stage of infection improves antimycobacterial activity in IFN- $\gamma$  knockout mice. **(A)** One day after mycobacteria infection, lung bacterial load and macrophage phagocytosis activity were measured. **(B)** Production of cytokines and MHCII in F4/80<sup>+</sup> macrophages were measured using flow cytometry. WT mice and IFN- $\gamma$ <sup>-/-</sup> mice received adoptive transfer of NK cells ( $1 \times 10^6$  cells) or injection of rIFN- $\gamma$  (5  $\mu$ g), 1 d after mycobacteria infection. Mice were infected intratracheally with  $1 \times 10^6$  CFUs of *M.k.* Data represent mean  $\pm$  SD from two independent experiments ( $n = 6$ ) and were analyzed using one-way ANOVA analysis. \* $p < 0.05$ , # $p < 0.01$ , and ¥ $p < 0.001$ . IFN- $\gamma$ <sup>-/-</sup>, IFN- $\gamma$ -deficient mice; *M.k.*, *M. kansasii*; NK, NK cells isolated from WT mice; WT, wild-type.



transfer of NK cells or rIFN- $\gamma$  treatment in IFN- $\gamma^{-/-}$  mice (Fig. 6B). Furthermore, production of IL-17A and IFN- $\gamma$  from IFN- $\gamma$ -deficient TCR  $\gamma\delta$  T cells was also significantly enhanced following adoptive transfer of NK cells or rIFN- $\gamma$  treatment in IFN- $\gamma^{-/-}$  mice (Supplemental Fig. 4B). These results indicate that NK cells and IFN- $\gamma$  play an important role at the early stage of the immune response against mycobacteria.

#### Early IFN- $\gamma$ treatment protects against mycobacteria infection

We investigated whether the timing of IFN- $\gamma$  treatment may affect protection against mycobacteria infection. Two weeks after infecting NK $^{-}$  mice with *M. kansasii*, bacterial load in lung tissues significantly increased in contrast to control mice (Fig. 7A). This phenomenon was still evident 4 wk postinfection (Fig. 7A). By contrast, daily injection of rIFN- $\gamma$  into NK $^{-}$  mice, starting on day 1 postinfection, significantly reduced lung bacterial load, as assessed 2 or 4 wk postinfection (Fig. 7A, NK $^{-}$  mice + rIFN- $\gamma$  Day 1). By contrast, daily injection of rIFN- $\gamma$ , starting 2 wk postinfection, failed to reduce bacterial load (Fig. 7A, NK $^{-}$  mice + rIFN- $\gamma$  Week 2). Similarly, early rIFN- $\gamma$  treatment restored macrophage phagocytosis activity in NK $^{-}$  mice, whereas late treatment was ineffective (Fig. 7A, right panel).

We also examined the effects of IFN- $\gamma$  treatment timing on lung granuloma formation following *M. kansasii* infection. Although control mice produced compact and well-formed lung granulomas following mycobacterial infection, NK $^{-}$  mice produced loosely formed granulomas and showed signs of necrotic inflammation in lung tissues (Fig. 7B, 7C). Notably, rIFN- $\gamma$  treatment at the early stage of infection, starting on day 1 postinfection, improved the structure of granulomas and increased their surface area (Fig. 7B, 7C, NK $^{-}$  mice + rIFN- $\gamma$  Day 1). In contrast, rIFN- $\gamma$  treatment at a later stage of infection, starting 2 wk postinfection, failed to improve the structure or area of granulomas (Fig. 7B, 7C, NK $^{-}$  mice + rIFN- $\gamma$  Week 2). Taken together, these results indicate that early IFN- $\gamma$  production following NTM infection plays a crucial role in the host immune response.

## Discussion

Previous studies of the immune response of the host against mycobacteria have focused on the effects of *M. tuberculosis* in tuberculosis. Clearance of *M. tuberculosis* by lung alveolar macrophages and DCs is usually poor. In response to TLR signaling, activated DCs and macrophages secrete IL-12 and IL-18 to activate lymphocytes. During the early immune response, mediators such as IFN- $\gamma$  and TNF- $\alpha$  further activate macrophages and promote bacterial clearance. IFN- $\gamma$  induces the production of many other proinflammatory cytokines, chemokines, and defensins, which help to recruit innate immune cells to the site of infection. However, because of factors related to host immunity and mycobacteria virulence, several *M. tuberculosis* strains are not completely eradicated by macrophages and even survive and proliferate within these cells (50). This phenomenon leads to the establishment of acquired T cell immunity and formation of granulomas, which confine bacteria and aim to prevent systemic dissemination.

In contrast, the immune response against NTM lung infection differs from that produced by *M. tuberculosis* (8). Previous studies showed that anti-IFN- $\gamma$  autoantibodies are detected in patients that suffer from disseminated NTM infection in Taiwan, Thailand, and Southeast Asia, thus highlighting the importance of optimal IFN- $\gamma$  production and activity against NTM infection (17, 37). For reasons that remain unclear, few cases of *M. tuberculosis* infection were identified among the autoimmune patients harboring anti-IFN- $\gamma$  autoantibodies (37). Thus, the role and underlying

molecular mechanism of IFN- $\gamma$  in defense against *M. tuberculosis* and NTM pathogens warrant further studies. Using an animal model of NTM lung infection, we report in this study that early production of IFN- $\gamma$  plays an important role to eradicate NTM from the lungs.

Although CD4 $^{+}$  T cells may secrete IFN- $\gamma$  during mycobacterial infection, emerging evidence indicates that NK cells and other T cell subsets, including TCR  $\gamma\delta$  T and CD8 $^{+}$  T cells, play a critical role in this process (51). NK cells have been shown to represent a major source of early IFN- $\gamma$  production in pleural fluid lymphocytes challenged with *M. tuberculosis*, and direct interaction between NK cells and APCs is important for subsequent activation of proinflammatory pathways (52, 53). During this process, robust innate immune activation involving NK cell activation and IFN- $\gamma$  secretion may be essential for efficient mycobacterial clearance, especially at the early infection stage (54). Furthermore, secretion of IFN- $\gamma$  and TNF- $\alpha$  from NK cells was strongly enhanced by IL-12 upon challenge with *Mycobacterium bovis* bacillus Calmette-Guérin (55). These results suggest that early IFN- $\gamma$  production from NK cells is required to eradicate *M. tuberculosis* during lung infection.

In the current study, we describe the role of NK cells and IFN- $\gamma$  produced by these cells in the immune response against *M. kansasii* infection. We show that NK cells act as the main producer of IFN- $\gamma$  in lung tissues at the early stage of mycobacterial infection. As early as 1 d after mycobacterial infection, NK cells produce significant amounts of IFN- $\gamma$ , which subsequently activates macrophages and DCs and enhances the antimycobacterial effects of these cells. Reciprocally, activated macrophages and DCs also produce IL-12 to stimulate NK cell activity. Some mycobacteria may survive these killing processes, and granulomas form in the lungs to prevent bacterial dissemination to distant organs. We observed that NK1.1 cell depletion reduces IFN- $\gamma$  production in lung tissues as early as 1 d after mycobacteria infection, a phenomenon associated with reduced mycobacteria killing by macrophages and NK cells. In addition, reduced Ag presentation to CD4 $^{+}$  T cells and aberrant granuloma formation was observed in NK $^{-}$  mice. These results indicate that environmental and host genetic factors that interfere with early IFN- $\gamma$  production by NK cells may prevent efficient interactions among NK cells, DCs, and macrophages and lead to severe mycobacteria infection.

It is interesting to note that adoptive transfer of NK cells or rIFN- $\gamma$  treatment fails to prevent mycobacteria-induced pathogenesis at a late stage of infection (2 wk) in IFN- $\gamma$ -deficient mice, whereas the same treatments are effective at the early stage of infection (day 1). These results highlight the important role of NK cells and IFN- $\gamma$  in activating innate and adaptive immunity immediately after NTM infection. Upon NK cell depletion, the immune response of the host seems to be significantly reduced. After a long period of infection in immunocompromised patients, mycobacteria may have resisted the early immune response observed in the lungs and spread to other organs of the body. Our results suggest that adoptive transfer of NK cells or rIFN- $\gamma$  treatment may not be efficient to confine and eradicate NTM pathogens from the lungs at a late stage of infection. In contrast, early interventions that stimulate the immune response may be effective for the prevention and control of NTM infections.

The effects of NK cells and IFN- $\gamma$  may not be specific to *M. kansasii* infection. A previous study on the environmental opportunistic NTM pathogen *Mycobacterium massiliense* indicates that infection by this bacterium causes a granulomatous inflammatory reaction that involves activation of macrophages, DCs, and NK cells induced by IFN- $\gamma$ , IL-12, and IL-17 in soft tissues (56). Furthermore, NK cell depletion leads to a disseminated lethal lung infection by *Bordetella pertussis*, and this response is associated



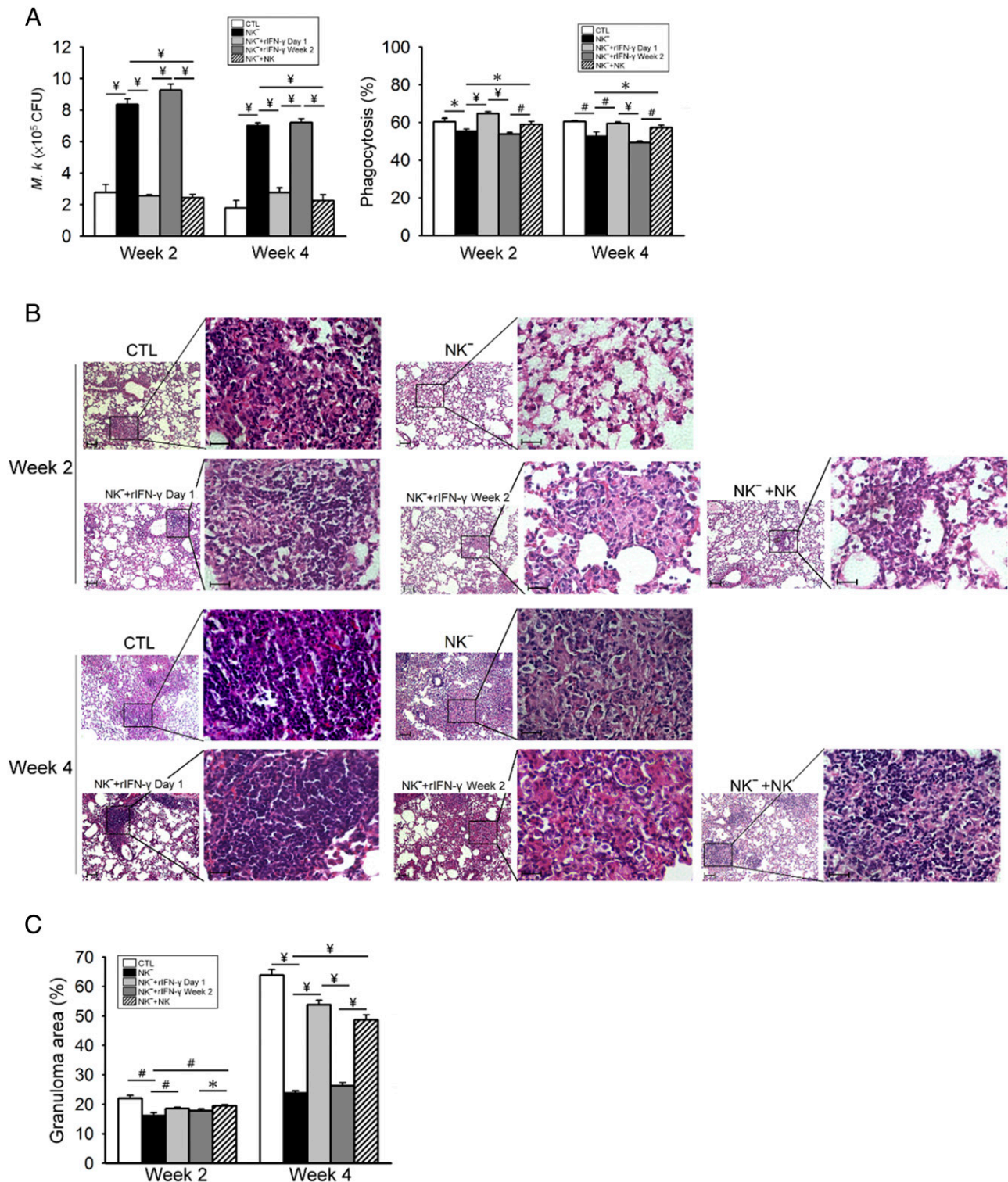


**FIGURE 7.** Early in vivo IFN- $\gamma$  treatment protects NK<sup>-</sup> mice against mycobacteria pathogenesis. CTL and NK<sup>-</sup> mice were intratracheally infected with  $1 \times 10^6$  CFUs of *M. kansasii*. NK<sup>-</sup> mice were injected with rIFN- $\gamma$  (5  $\mu$ g), starting either 1 d or 2 wk postinfection. **(A)** Two and four weeks postinfection, lung bacterial load and macrophage phagocytosis activity were monitored. **(B)** Histological examination of lung tissues was performed and **(C)** granuloma surface area was measured. Scale bars, low magnification, 100  $\mu$ m; inset, 25  $\mu$ m. In **(A)** and **(C)**, data represent mean  $\pm$  SD from three independent experiments ( $n = 10$ ) and were analyzed using one-way ANOVA analysis. \* $p < 0.05$ , # $p < 0.01$ , ¥ $p < 0.001$ . CTL, control IgG-treated mice; *M.k.*, *M. kansasii*.

with reduced Ag-specific Th1 response and enhancement of Th2 response (57). In this previous study, following respiratory challenge with *B. pertussis*, NK cells were also the primary producers of IFN- $\gamma$  in the lungs, and NK cells' IFN- $\gamma$  production was mediated by *B. pertussis*-induced IL-12 or IL-23 production from DCs.

Consistent with the results obtained in the current study, NK cells confer resistance to *B. pertussis* infection by activating IL-12-mediated production of IFN- $\gamma$ , which enhances the antibacterial activity of macrophages and promotes the differentiation of Th1 cells.

The important roles of NK cells and IFN- $\gamma$  have also been studied in response to respiratory infection with the bacterium *Francisella tularensis*, in which NK cells are the early responders responsible for IFN- $\gamma$  secretion. *F. tularensis* is a Gram-negative intracellular bacterium that may induce lethal pneumonic tularemia after inhalation (58). Significant increase in the number of cells secreting IFN- $\gamma$  was observed 72 h after intranasal infection, and CD11b<sup>+</sup> DX5<sup>+</sup> NK cells were primarily responsible for such production. In addition, NK cell depletion decreases the percentage of IFN- $\gamma$ -secreting cells, indicating that NK cells produce IFN- $\gamma$  and protect the host against intracellular pathogens (58). Besides lung infection, IFN- $\gamma$  and hepatic NK cells are also involved in *F. tularensis*-induced hepatic granuloma formation and in the subsequent pathological changes occurring in the liver (59).

The important role of NK cells and IFN- $\gamma$  derived from these cells was also highlighted by a study that assessed the functions of DCs in a murine model of *Chlamydia muridarum* infection (60). NK cell-depleted mice showed exacerbated infection and pathogenesis, reduced levels of IL-12 and IL-10, and reduced ability to direct primary and established Ag-specific Th1 CD4<sup>+</sup> T cell responses in respiratory tract infection caused by *C. muridarum*. Consistent with the results reported in this study, adoptive transfer of DCs from control mice, but not from NK cell-depleted mice, improves type 1 protective immunity in recipients postinfection (60). Furthermore, in this infection model, NK cells strongly enhance IL-12 production by DCs in an NK-DC coculture system, and this phenomenon is abolished by neutralizing IFN- $\gamma$  activity (60).

In addition to bacterial infection, NK cells were also reported to represent the major population of cells producing IFN- $\gamma$  during early infection in the lungs of neutropenic mice with invasive aspergillosis (61). Depletion of NK cells reduces lung IFN- $\gamma$  levels and increases lung fungal load, and these phenomena appear to be independent of T and B cell subsets. Depletion of NK cells and the absence of IFN- $\gamma$  result in a similar increased susceptibility to aspergillosis infection, but NK cell depletion in IFN- $\gamma$ -deficient hosts does not further increase the severity of the infection (61). NK cell-derived IFN- $\gamma$  enhances macrophage antimicrobial effects in vitro and results in greater expression of IFN- $\gamma$ -inducible chemokines in the lungs. Finally, transfer of activated NK cells from wild-type mice, but not IFN- $\gamma$ -deficient hosts, results in greater pathogen clearance from the lungs in both IFN- $\gamma$ -deficient and wild-type recipients. Taken together, these data indicate that NK cells are also responsible for the early production of IFN- $\gamma$  in the lungs in response to bacterial and fungal pathogens.

In addition to immunity against bacteria and fungus, NK cells and IFN- $\gamma$  are also involved in early virus infection. Interaction between monocytes and NK cells and production of IFN- $\gamma$  and TNF- $\alpha$  during the innate immune response are also shown to be important for host innate immunity (62). Within a day or so after mouse CMV infection, NK cells are activated to produce IFN- $\gamma$  and attack pathogen-infected cells (63). A similar observation on the role of NK cells was also reported following i.p. infection with *Toxoplasma gondii* cysts, in which NK cell-derived IFN- $\gamma$  was required for local differentiation of monocytes into inflammatory macrophages and DCs (64). In this context, the newly generated DC population may serve as the major source of IL-12 at the site of infection.

Taken together, these observations indicate that NK cell-derived IFN- $\gamma$  is important to regulate immune cell activities and the differentiation of monocytes into the immune cells required for initiating the response to intracellular bacterial, viral, and parasite infections. Our results highlight the important role of NK cells and

IFN- $\gamma$  in early defense against NTM lung infection in vivo. Further studies are needed to develop new strategies to modulate NK cell activity to enhance the efficacy of anti-NTM treatments against lung infections.

## Disclosures

The authors have no financial conflicts of interest.

## References

- Falkinham, J. O., III 2013. Ecology of nontuberculous mycobacteria—where do human infections come from? *Semin. Respir. Crit. Care Med.* 34: 95–102.
- Thomson, R., C. Tolson, R. Carter, C. Coulter, F. Huygens, and M. Hargreaves. 2013. Isolation of nontuberculous mycobacteria (NTM) from household water and shower aerosols in patients with pulmonary disease caused by NTM. *J. Clin. Microbiol.* 51: 3006–3011.
- Saleeb, P., and K. N. Olivier. 2010. Pulmonary nontuberculous mycobacterial disease: new insights into risk factors for susceptibility, epidemiology, and approaches to management in immunocompetent and immunocompromised patients. *Curr. Infect. Dis. Rep.* 12: 198–203.
- Wu, U. I., and S. M. Holland. 2015. Host susceptibility to non-tuberculous mycobacterial infections. *Lancet Infect. Dis.* 15: 968–980.
- Kendall, B. A., and K. L. Winthrop. 2013. Update on the epidemiology of pulmonary nontuberculous mycobacterial infections. *Semin. Respir. Crit. Care Med.* 34: 87–94.
- Lai, C. C., L. N. Lee, L. W. Ding, C. J. Yu, P. R. Hsueh, and P. C. Yang. 2006. Emergence of disseminated infections due to nontuberculous mycobacteria in non-HIV-infected patients, including immunocompetent and immunocompromised patients in a university hospital in Taiwan. *J. Infect.* 53: 77–84.
- Aksamit, T. R., J. V. Phillely, and D. E. Griffith. 2014. Nontuberculous mycobacterial (NTM) lung disease: the top ten essentials. *Respir. Med.* 108: 417–425.
- Wu, T. S., H. S. Leu, C. H. Chiu, M. H. Lee, P. C. Chiang, T. L. Wu, J. H. Chia, L. H. Su, A. J. Kuo, and H. C. Lai. 2009. Clinical manifestations, antibiotic susceptibility and molecular analysis of *Mycobacterium kansasii* isolates from a university hospital in Taiwan. *J. Antimicrob. Chemother.* 64: 511–514.
- Piersimoni, C., and C. Scarparo. 2008. Pulmonary infections associated with non-tuberculous mycobacteria in immunocompetent patients. *Lancet Infect. Dis.* 8: 323–334.
- Griffith, D. E., T. Aksamit, B. A. Brown-Elliott, A. Catanzaro, C. Daley, F. Gordin, S. M. Holland, R. Horsburgh, G. Huit, M. F. Iademaro, et al.; Infectious Disease Society of America. 2007. An official ATS/IDSA statement: diagnosis, treatment, and prevention of nontuberculous mycobacterial diseases. [Published erratum appears in 2007 *Am. J. Respir. Crit. Care Med.* 175: 744–745.] *Am. J. Respir. Crit. Care Med.* 175: 367–416.
- Alcaide, F., I. Richter, C. Bernasconi, B. Springer, C. Hagenau, R. Schulze-Röbbecke, E. Tortoli, R. Martín, E. C. Böttger, and A. Telenti. 1997. Heterogeneity and clonality among isolates of *Mycobacterium kansasii*: implications for epidemiological and pathogenicity studies. *J. Clin. Microbiol.* 35: 1959–1964.
- Shitrit, D., R. Priess, N. Peled, G. Bishara, D. Shlomi, and M. R. Kramer. 2007. Differentiation of *Mycobacterium kansasii* infection from *Mycobacterium tuberculosis* infection: comparison of clinical features, radiological appearance, and outcome. *Eur. J. Clin. Microbiol. Infect. Dis.* 26: 679–684.
- Wieland, C. W., S. Florquin, J. M. Pater, S. Weijer, and T. van der Poll. 2006. CD4<sup>+</sup> cells play a limited role in murine lung infection with *Mycobacterium kansasii*. *Am. J. Respir. Cell Mol. Biol.* 34: 167–173.
- Feng, C. G., M. Kaviratne, A. G. Rothfuchs, A. Cheever, S. Hieny, H. A. Young, T. A. Wynn, and A. Sher. 2006. NK cell-derived IFN- $\gamma$  differentially regulates innate resistance and neutrophil response in T cell-deficient hosts infected with *Mycobacterium tuberculosis*. *J. Immunol.* 177: 7086–7093.
- Ottenhoff, T. H., F. A. Verreck, E. G. Lichtenauer-Kaligis, M. A. Hoeve, O. Sanal, and J. T. van Dissel. 2002. Genetics, cytokines and human infectious disease: lessons from weakly pathogenic mycobacteria and salmonellae. [Published erratum appears in 2002 *Nat. Genet.* 32: 331.] *Nat. Genet.* 32: 97–105.
- Bogunovic, D., M. Byun, L. A. Durfee, A. Abhyankar, O. Sanal, D. Mansouri, S. Salem, I. Radovanovic, A. V. Grant, P. Adimi, et al. 2012. Mycobacterial disease and impaired IFN- $\gamma$  immunity in humans with inherited ISG15 deficiency. *Science* 337: 1684–1688.
- Browne, S. K., P. D. Burbelo, P. Chetchotisakd, Y. Suputtamongkol, S. Kiertiburanakul, P. A. Shaw, J. L. Kirk, K. Jutivorakool, R. Zaman, L. Ding, et al. 2012. Adult-onset immunodeficiency in Thailand and Taiwan. *N. Engl. J. Med.* 367: 725–734.
- Schlager, N. W. 2007. Tuberculosis and nontuberculous mycobacterial infections in older adults. *Clin. Chest Med.* 28: 773–781, vi.
- Shima, K., T. Sakagami, Y. Tanabe, N. Aoki, H. Moro, T. Koya, H. Kagamu, T. Hasegawa, E. Suzuki, and I. Narita. 2014. Novel assay to detect increased level of neutralizing anti-interferon gamma autoantibodies in non-tuberculous mycobacterial patients. *J. Infect. Chemother.* 20: 52–56.
- Flórido, M., R. Appelberg, I. M. Orme, and A. M. Cooper. 1997. Evidence for a reduced chemokine response in the lungs of beige mice infected with *Mycobacterium avium*. *Immunology* 90: 600–606.
- Flórido, M., J. E. Pearl, A. Solache, M. Borges, L. Haynes, A. M. Cooper, and R. Appelberg. 2005. Gamma interferon-induced T-cell loss in virulent *Mycobacterium avium* infection. *Infect. Immun.* 73: 3577–3586.



22. Resende, M., M. S. Cardoso, A. R. Ribeiro, M. Flório, M. Borges, A. G. Castro, N. L. Alves, A. M. Cooper, and R. Appelberg. 2017. Innate IFN- $\gamma$ -producing cells developing in the absence of IL-2 receptor common  $\gamma$ -chain. *J. Immunol.* 199: 1429–1439.
23. Freud, A. G., and M. A. Caligiuri. 2006. Human natural killer cell development. *Immunol. Rev.* 214: 56–72.
24. Smyth, M. J., Y. Hayakawa, K. Takeda, and H. Yagita. 2002. New aspects of natural-killer-cell surveillance and therapy of cancer. *Nat. Rev. Cancer* 2: 850–861.
25. Vivier, E., E. Tomasello, M. Baratin, T. Walzer, and S. Ugolini. 2008. Functions of natural killer cells. *Nat. Immunol.* 9: 503–510.
26. Björkström, N. K., H. G. Ljunggren, and J. Michaëlsson. 2016. Emerging insights into natural killer cells in human peripheral tissues. *Nat. Rev. Immunol.* 16: 310–320.
27. Huntington, N. D., C. A. Voshenrich, and J. P. Di Santo. 2007. Developmental pathways that generate natural-killer-cell diversity in mice and humans. *Nat. Rev. Immunol.* 7: 703–714.
28. Lodoen, M. B., and L. L. Lanier. 2005. Viral modulation of NK cell immunity. *Nat. Rev. Microbiol.* 3: 59–69.
29. Schierloh, P., M. Alemán, N. Yokobori, L. Alves, N. Roldán, E. Abbate, M. del C Sasiain, and S. de la Barrera. 2005. NK cell activity in tuberculosis is associated with impaired CD11a and ICAM-1 expression: a regulatory role of monocytes in NK activation. *Immunology* 116: 541–552.
30. Raulet, D. H. 2004. Interplay of natural killer cells and their receptors with the adaptive immune response. *Nat. Immunol.* 5: 996–1002.
31. Guerra, C., K. Johal, D. Morris, S. Moreno, O. Alvarado, D. Gray, M. Tanzil, D. Pearce, and V. Venketaraman. 2012. Control of *Mycobacterium tuberculosis* growth by activated natural killer cells. *Clin. Exp. Immunol.* 168: 142–152.
32. Vankayalapati, R., B. Wize, S. E. Weis, H. Safi, D. L. Lakey, O. Mandelboim, B. Samten, A. Porgador, and P. F. Barnes. 2002. The NKp46 receptor contributes to NK cell lysis of mononuclear phagocytes infected with an intracellular bacterium. *J. Immunol.* 168: 3451–3457.
33. Dhiman, R., M. Indramohan, P. F. Barnes, R. C. Nayak, P. Paidipally, L. V. Rao, and R. Vankayalapati. 2009. IL-22 produced by human NK cells inhibits growth of *Mycobacterium tuberculosis* by enhancing phagolysosomal fusion. *J. Immunol.* 183: 6639–6645.
34. Zhang, R., X. Zheng, B. Li, H. Wei, and Z. Tian. 2006. Human NK cells positively regulate gamma delta T cells in response to *Mycobacterium tuberculosis*. *J. Immunol.* 176: 2610–2616.
35. Portevin, D., L. E. Via, S. Eum, and D. Young. 2012. Natural killer cells are recruited during pulmonary tuberculosis and their ex vivo responses to mycobacteria vary between healthy human donors in association with KIR haplotype. *Cell. Microbiol.* 14: 1734–1744.
36. Lu, C. C., T. S. Wu, Y. J. Hsu, C. J. Chang, C. S. Lin, J. H. Chia, T. L. Wu, T. T. Huang, J. Martel, D. M. Ojcius, et al. 2014. NK cells kill mycobacteria directly by releasing perforin and granulysin. *J. Leukoc. Biol.* 96: 1119–1129.
37. Lin, C. H., C. Y. Chi, H. P. Shih, J. Y. Ding, C. C. Lo, S. Y. Wang, C. Y. Kuo, C. F. Yeh, K. H. Tu, S. H. Liu, et al. 2016. Identification of a major epitope by anti-interferon- $\gamma$  autoantibodies in patients with mycobacterial disease. *Nat. Med.* 22: 994–1001.
38. Okamoto Yoshida, Y., M. Umemura, A. Yahagi, R. L. O'Brien, K. Ikuta, K. Kishihara, H. Hara, S. Nakae, Y. Iwakura, and G. Matsuzaki. 2010. Essential role of IL-17A in the formation of a mycobacterial infection-induced granuloma in the lung. *J. Immunol.* 184: 4414–4422.
39. Ichinohe, T., I. K. Pang, Y. Kumamoto, D. R. Peaper, J. H. Ho, T. S. Murray, and A. Iwasaki. 2011. Microbiota regulates immune defense against respiratory tract influenza A virus infection. *Proc. Natl. Acad. Sci. USA* 108: 5354–5359.
40. Khader, S. A., S. Partida-Sanchez, G. Bell, D. M. Jelley-Gibbs, S. Swain, J. E. Pearl, N. Ghilardi, F. J. Desautave, F. E. Lund, and A. M. Cooper. 2006. Interleukin 12p40 is required for dendritic cell migration and T cell priming after *Mycobacterium tuberculosis* infection. *J. Exp. Med.* 203: 1805–1815.
41. Ladel, C. H., C. Blum, A. Dreher, K. Reifenberg, M. Kopf, and S. H. Kaufmann. 1997. Lethal tuberculosis in interleukin-6-deficient mutant mice. *Infect. Immun.* 65: 4843–4849.
42. Cooper, A. M., and S. A. Khader. 2008. The role of cytokines in the initiation, expansion, and control of cellular immunity to tuberculosis. *Immunol. Rev.* 226: 191–204.
43. Flynn, J. L., and J. Chan. 2001. Immunology of tuberculosis. *Annu. Rev. Immunol.* 19: 93–129.
44. Trinchieri, G. 2003. Interleukin-12 and the regulation of innate resistance and adaptive immunity. *Nat. Rev. Immunol.* 3: 133–146.
45. Khan, N., U. Gowthaman, S. Pahari, and J. N. Agrewala. 2012. Manipulation of costimulatory molecules by intracellular pathogens: veni, vidi, vici!! *PLoS Pathog.* 8: e1002676.
46. Saunders, B. M., and A. M. Cooper. 2000. Restraining mycobacteria: role of granulomas in mycobacterial infections. *Immunol. Cell Biol.* 78: 334–341.
47. van Crevel, R., T. H. Ottenhoff, and J. W. van der Meer. 2002. Innate immunity to *Mycobacterium tuberculosis*. *Clin. Microbiol. Rev.* 15: 294–309.
48. Junqueira-Kipnis, A. P., A. Kipnis, A. Jamieson, M. G. Juarrero, A. Diefenbach, D. H. Raulet, J. Turner, and I. M. Orme. 2003. NK cells respond to pulmonary infection with *Mycobacterium tuberculosis*, but play a minimal role in protection. *J. Immunol.* 171: 6039–6045.
49. Reljic, R. 2007. IFN-gamma therapy of tuberculosis and related infections. *J. Interferon Cytokine Res.* 27: 353–364.
50. Lin, P. L., and J. L. Flynn. 2010. Understanding latent tuberculosis: a moving target. *J. Immunol.* 185: 15–22.
51. Abebe, F. 2012. Is interferon-gamma the right marker for bacille Calmette-Guérin-induced immune protection? The missing link in our understanding of tuberculosis immunology. *Clin. Exp. Immunol.* 169: 213–219.
52. Schierloh, P., N. Yokobori, M. Alemán, V. Landoni, R. M. Musella, J. Castagnino, M. Baldini, E. Abbate, S. S. de la Barrera, and M. C. Sasiain. 2007. *Mycobacterium tuberculosis*-induced gamma interferon production by natural killer cells requires cross talk with antigen-presenting cells involving Toll-like receptors 2 and 4 and the mannose receptor in tuberculous pleurisy. *Infect. Immun.* 75: 5325–5337.
53. Pokkali, S., S. D. Das, and A. Selvaraj. 2009. Differential upregulation of chemokine receptors on CD56 NK cells and their transmigration to the site of infection in tuberculous pleurisy. *FEMS Immunol. Med. Microbiol.* 55: 352–360.
54. Korbel, D. S., B. E. Schneider, and U. E. Schaible. 2008. Innate immunity in tuberculosis: myths and truths. *Microbes Infect.* 10: 995–1004.
55. Marcenaro, E., B. Ferranti, M. Falco, L. Moretta, and A. Moretta. 2008. Human NK cells directly recognize *Mycobacterium bovis* via TLR2 and acquire the ability to kill monocyte-derived DC. *Int. Immunol.* 20: 1155–1167.
56. Martins de Sousa, E., F. Bonfim de Bortoli, E. P. Amaral, A. C. Batista, T. Liberman Kipnis, A. Marques Cardoso, A. Kipnis, and A. P. Junqueira-Kipnis. 2010. Acute immune response to *Mycobacterium massiliense* in C57BL/6 and BALB/c mice. *Infect. Immun.* 78: 1571–1581.
57. Byrne, P., P. McGuirk, S. Todryk, and K. H. Mills. 2004. Depletion of NK cells results in disseminating lethal infection with *Bordetella pertussis* associated with a reduction of antigen-specific Th1 and enhancement of Th2, but not Tr1 cells. *Eur. J. Immunol.* 34: 2579–2588.
58. López, M. C., N. S. Duckett, S. D. Baron, and D. W. Metzger. 2004. Early activation of NK cells after lung infection with the intracellular bacterium, *Francisella tularensis* LVS. *Cell. Immunol.* 232: 75–85.
59. Bokhari, S. M., K. J. Kim, D. M. Pinson, J. Slusser, H. W. Yeh, and M. J. Parmely. 2008. NK cells and gamma interferon coordinate the formation and function of hepatic granulomas in mice infected with the *Francisella tularensis* live vaccine strain. *Infect. Immun.* 76: 1379–1389.
60. Jiao, L., X. Gao, A. G. Joyee, L. Zhao, H. Qiu, M. Yang, Y. Fan, S. Wang, and X. Yang. 2011. NK cells promote type 1 T cell immunity through modulating the function of dendritic cells during intracellular bacterial infection. *J. Immunol.* 187: 401–411.
61. Park, S. J., M. A. Hughes, M. Burdick, R. M. Strieter, and B. Mehrad. 2009. Early NK cell-derived IFN- $\gamma$  is essential to host defense in neutropenic invasive aspergillosis. *J. Immunol.* 182: 4306–4312.
62. Kloss, M., P. Decker, K. M. Baltz, T. Baessler, G. Jung, H. G. Rammensee, A. Steinle, M. Krusch, and H. R. Salih. 2008. Interaction of monocytes with NK cells upon Toll-like receptor-induced expression of the NKG2D ligand MICA. *J. Immunol.* 181: 6711–6719.
63. Biron, C. A., K. B. Nguyen, G. C. Pien, L. P. Cousens, and T. P. Salazar-Mather. 1999. Natural killer cells in antiviral defense: function and regulation by innate cytokines. *Annu. Rev. Immunol.* 17: 189–220.
64. Goldszmid, R. S., P. Caspar, A. Rivollier, S. White, A. Dzutsev, S. Hieny, B. Kelsall, G. Trinchieri, and A. Sher. 2012. NK cell-derived interferon- $\gamma$  orchestrates cellular dynamics and the differentiation of monocytes into dendritic cells at the site of infection. *Immunity* 36: 1047–1059.



# Circulating microRNA-22-3p Predicts the Malignant Progression of Precancerous Gastric Lesions from Intestinal Metaplasia to Early Adenocarcinoma

Tsung-Hsing Chen<sup>1,2</sup> · Cheng-Tang Chiu<sup>1</sup> · Chieh Lee<sup>3</sup> · Yin-Yi Chu<sup>1</sup> · Hao-Tsai Cheng<sup>1</sup> · Jun-Te Hsu<sup>4</sup> · Ren-Chin Wu<sup>5</sup> · Ta-Sen Yeh<sup>4</sup> · Kwang-Huei Lin<sup>6,7,8</sup>

Received: 30 October 2017 / Accepted: 26 April 2018  
© Springer Science+Business Media, LLC, part of Springer Nature 2018

## Abstract

**Background** Gastric cancer has a poor outcome and identifying useful biomarkers from peripheral blood or tissue could allow its early detection, or potentially precancerous changes, thus improving the curative rates. MicroRNAs (miRNAs) have been shown to offer great potential in cancer diagnosis and prediction.

**Aim** Here, we investigated the role of plasma miRNAs in the natural course of gastric cancer, from intestinal metaplasia to early cancer. The findings were used to understand whether patients at a high risk of malignancy could be given appropriate interventions in the early disease process, such as using endoscopic submucosal dissection to treat gastric dysplasia or early gastric cancer.

**Methods** Participants were divided into healthy control, intestinal metaplasia (IM), and dysplasia/early cancer (pT1a/b) groups. Microarray was used to select potential markers in tissue.

**Results** Quantitative real-time polymerase chain reaction data showed circulating miRNA-22-3p had significantly different expression in patients with precancerous lesions or gastric adenocarcinoma. The areas under the curve of incomplete IM versus healthy control, low-grade/high-grade dysplasia, early gastric cancer, and GED were 0.8080, 0.8040, 0.8494, and 0.8095, respectively (all *P* values < 0.05).

**Conclusions** Circulating miRNA-22-3p could be a potential biomarker for gastric precancerous dysplasia and early cancer detection.

**Keywords** Gastric epithelial dysplasia · miRNAs · Endoscopic submucosal dissection · Liquid biopsy · Intestinal metaplasia · Dysplasia

## Introduction

Gastric cancer (GC) is a leading cause of cancer death worldwide, with a poor 5-year survival rate in its advanced stage [1, 2]. However, the high mortality rate can be mitigated by detecting precancerous lesions and GC in their early stages.

Esophagogastroduodenoscopy screening for GC is an invasive and costly procedure that often fails to detect precancerous lesions and GC in their early stages, even when image enhancement endoscopy (IEE) is used. IEE means using dye, optical, and/or electronic methods to provide easier assessment of lesion's morphology, mucosal microstructure and microvasculature features for adequate and accurate GED diagnosis. Here, we used the Olympus NBI system and linked color imaging technology (LASEREO system; Fujifilm, Tokyo, Japan) [3, 4]. Furthermore, molecular typing of precancerous gastric changes has not been developed satisfactorily. For this reason, molecular typing is not considered as a part of the strategy to prevent gastrointestinal cancer [5].

Although the pepsinogen I/II ratio, and carcinoembryonic antigen and carbohydrate antigen (CA) 19-9 levels have been used as noninvasive markers for GC screening and prognostic grading, the results have been disappointing [6, 7].

**Electronic supplementary material** The online version of this article (<https://doi.org/10.1007/s10620-018-5106-4>) contains supplementary material, which is available to authorized users.

✉ Ta-Sen Yeh  
tsy471027@cgmh.org.tw

✉ Kwang-Huei Lin  
khlin@mail.cgu.edu.tw

Extended author information available on the last page of the article



The positivity rates for carcinoembryonic antigen, CA 19-9, and CA 72-4 were 20.9, 34.6, and 28.1%, respectively. The sensitivity of serum pepsinogen testing was 77%, and the specificity was 73%. Hence, more useful biomarkers and noninvasive screening tools are required.

Several studies have reported that miRNAs play an important role in carcinogenesis, acting as either oncogenes or tumor suppressors. The expression patterns of miRNAs are believed to regulate tumor development and may clearly differentiate normal versus cancerous tissues [8]. Recent findings have revealed that circulating miRNAs may comprise a new class of biomarkers for GC [9–13]. A few studies have focused on miRNAs in early GC or precancerous lesions (including intestinal metaplasia (IM)) using tissue samples, but none has used plasma samples, especially in patients with IM, which is regarded as a “breaking point” [14–16].

IM is classified as complete or incomplete. Multivariate analysis revealed that incomplete IM has the highest risk of developing into GC (hazard ratio: 11.3, 95% confidence interval: 3.8–33.9) [14–17]. Despite the lack of clearly defined surveillance guidelines or a widely accepted surveillance program for gastric IM, early detection of GC may be accomplished by an annual surveillance program to improve the survival rates. Furthermore, endoscopic submucosal dissection (ESD) preserves the stomach and provides good quality of life for patients with early cancer (EC) or precursor lesions [18, 19].

In the light of this knowledge, the present study was designed to evaluate the expression of miRNAs from IM to EC and select potential plasma biomarkers for detecting precancerous dysplasia and early GC, so-called gastric epithelial dysplasia (GED).

## Materials and Methods

### Subjects

Tissue samples were collected from 55 patients [10 women and 45 men (Table 1)], and plasma samples were collected from another 75 patients, pathologically proven [21 women and 54 men (Table 2)] from 2014 to 2016 at the Chang Gung Memorial Hospital. The tissue samples were divided into four subgroups: IM, low-grade dysplasia (LGD), high-grade dysplasia (HGD), and early cancer (EC). In our study, we used incomplete IM to compare with other stages because of its' highest risk of developing into GC. We excluded diffuse-type gastric cancer owing to its' different pathway and with a poor 5-year survival rate [20–22]. Endoscopic biopsies were done from the abnormal lesion (T) and its adjacent normal area (N) located > 5 cm distal to the tumor site under the guidance of IEE from the same patient. EC specimens were obtained by

**Table 1** Tissue sample characteristics

Parameters	Cohort (n = 55)	Mean induction fold $\pm$ SE
<i>Gender</i>		
Female	10	0.7442 $\pm$ 0.08726
Male	45	1.057 $\pm$ 0.1069
<i>Age</i>		
$\leq 60$	17	1.164 $\pm$ 0.1779
> 60	38	0.9264 $\pm$ 0.1027
<i>Pathological stage</i>		
Intestinal metaplasia	23	1.254 $\pm$ 0.1788
Low-grade dysplasia	9	0.7373 $\pm$ 0.1134
High-grade dysplasia	6	1.065 $\pm$ 0.2941
Early cancer (pT1a/b)	17	0.7722 $\pm$ 0.07182

Induction fold: abnormal/normal; normalized with U6 of miR-22-3p

**Table 2** Plasma sample characteristics

Parameters	Cohort (n = 75)	Mean $\Delta C_t \pm$ SE
<i>Gender</i>		
Female	21	34.22 $\pm$ 0.3369
Male	54	34.72 $\pm$ 0.2135
<i>Age</i>		
$\leq 60$	29	35.07 $\pm$ 0.2395
> 60	46	34.27 $\pm$ 0.2449
<i>Pathological stage</i>		
Intestinal metaplasia	38	35.25 $\pm$ 0.2272
Low-grade dysplasia	10	33.78 $\pm$ 0.5426
High-grade dysplasia	7	34.21 $\pm$ 0.4124
Early cancer (pT1a/b)	20	33.84 $\pm$ 0.3243

$\Delta C_t$  values for miRNA-22-3p were normalized with cel-miRNA39 spike-in

ESD and immediately stored in RNeasy (Qiagen, Hilden, Germany) until use. All specimens were inspected by two pathologists at two separated specimens and regions, except for definite carcinoma, to avoid inter-observer errors. All tissue samples used in this study were fresh.

Blood samples (without tissue samples) were collected from 26 healthy volunteers (H), from the health checkup center and used as the control group. These volunteers were confirmed to be healthy by negative results of a routine blood test, chest X-ray, endoscopy inspection (white light endoscopy), ultrasonography, cancer screening pilot study, and computed tomography/positron emission tomography scan. The study was approved by the Institutional Review Board (IRB No. 103-2095C) of the Chang Gung Memorial Hospital, and all participants gave their informed consent. All methods were performed in accordance with relevant guidelines and regulations.

## Identification of Potential Markers

We identified potential markers from tissue microarray and plasma quantitative real-time polymerase chain reaction (qRT-PCR) and then confirmed these results by the qRT-PCR in tissue and plasma.

## Microarray Analysis

Thirteen independent pairs (T and N) of specimens from the study group were used to screen for miRNA expression in precancerous gastric stages: three pairs of intestinal metaplasia, four pairs of LGD, three pairs of HGD, and three pairs of EC. The Agilent (Santa Clara, CA, USA) Human miRNA Microarray V21.0 was used. This microarray contains probes for 2549 unique human miRNAs. The microarray was generated using known miRNA sequence information compiled in the Sanger miRBASE database v21.0. About 100 ng of total RNA was labeled with Cy3 and hybridized to the Agilent miRNA Microarray and then analyzed with an Agilent SureScan microarray scanner. Data were extracted from the scanned images using Agilent Feature Extract software v.10.5.1.1. Data were required to pass stringent quality control parameters established by Agilent that included tests for excessive background fluorescence, excessive variation among probe sequence replicates on the array, and measures of the total gene signal on the array to assess low signal [23].

## Pathologic Definition of IM

IM was classified into complete and incomplete subtypes according to histological features. Complete IM is characterized by the presence of both goblet and absorptive cells with a brush border. Incomplete IM lacks absorptive cells and is characterized by columnar cells with variably sized mucus vacuoles.

## Pathologic Definition of Dysplasia

Dysplasia and carcinoma were diagnosed according to the WHO Classification of Tumors of the Digestive System [24]. Dysplasia was defined as intraepithelial neoplastic proliferation with cytologic and architectural atypia, but without evidence of invasive growth. Carcinoma was diagnosed when there was convincing evidence of stromal invasion.

## Analysis of Tissue and Plasma miRNAs by qRT-PCR

Total RNA was extracted from fresh tissue using the TRIzol reagent kit (Life Technologies Inc., Carlsbad, CA, USA) and then converted to cDNA using reverse transcriptase (Life Technologies). SYBR Green mix (Applied Biosystems) was used for the qRT-PCR. Primer sequences used in the

qRT-PCR are shown in Supplemental Table 1. U6 was used as the internal control, as described previously [25].

Plasma miRNA was purified using the miRCURY RNA Isolation Kit (Exiqon, Woburn, MA, USA). Before the purified samples were mixed with isopropanol, we added sDNA of cel-miRNA-39 as a spike-in control. The samples were eluted with 20  $\mu$ L of nuclease-free water (Life Technologies). The purified plasma miRNA was converted to cDNA in 10  $\mu$ L of reaction mixture containing miRNA-specific stem-loop RT primers, dNTPs, reverse transcriptase (Life Technologies), and 20 ng miRNA. The qRT-PCR conditions were the same for plasma and tissue samples. The ABI Prism 7500 Fast Real-Time PCR system (Life Technologies) was used for the qRT-PCR. For tissue analysis, fold changes in gene expression of T relative to N specimens were calculated with the  $2^{-\Delta\Delta C_t}$  method and transformed to log 2, whereby  $\Delta\Delta C_t = \Delta C_t \text{ abnormal} - \Delta C_t \text{ adjacent normal}$  [25, 26]. For plasma analysis, after normalization to the spike-in control, we calculated  $39 - \Delta C_t$  to compare the values between patients and healthy volunteers [27].

## Statistical Analyses

The *t* test and one-way analysis of variance (ANOVA) were used to pairwise compare plasma miRNA-22-3p expression in each stage. The Shapiro–Wilk test with  $P=0.05$  was used to test the normality of samples. The receiver operating characteristic curve and area under the curve were used to assess the potential of using the plasma expression of miRNA-22-3p as a diagnostic tool for GED. Descriptive data analyses were done using Prism 5 (GraphPad Software, San Diego, CA, USA). Statistical analyses, including receiver operating characteristic and signal detection theory, were conducted using SAS 9.4 (SAS Institute, Cary, NC, USA).

## Results

To identify the miRNAs involved in precancerous changes, 13 pairs of tissues representing IM, LGD, HGD, and EC were examined with microarray for miRNA expression profiling. Using tissue analysis, miRNA-22-3p and miRNA-22-5p were found to have significantly different expression ( $P<0.05$ ) in all stages except EC (Fig. 1). To verify miRNA-22 expression, 55 pairs of tissue samples (Table 1) were used for qRT-PCR. The results indicated that miRNA-22-3p was downregulated 69% in abnormal lesions compared with normal tissue. Meanwhile, miRNA-22-3p had a higher expression level than miRNA-22-5p and significantly different expression between stages (Fig. 2). Based on these findings, we selected miRNA-22-3p as a potential marker for further study.



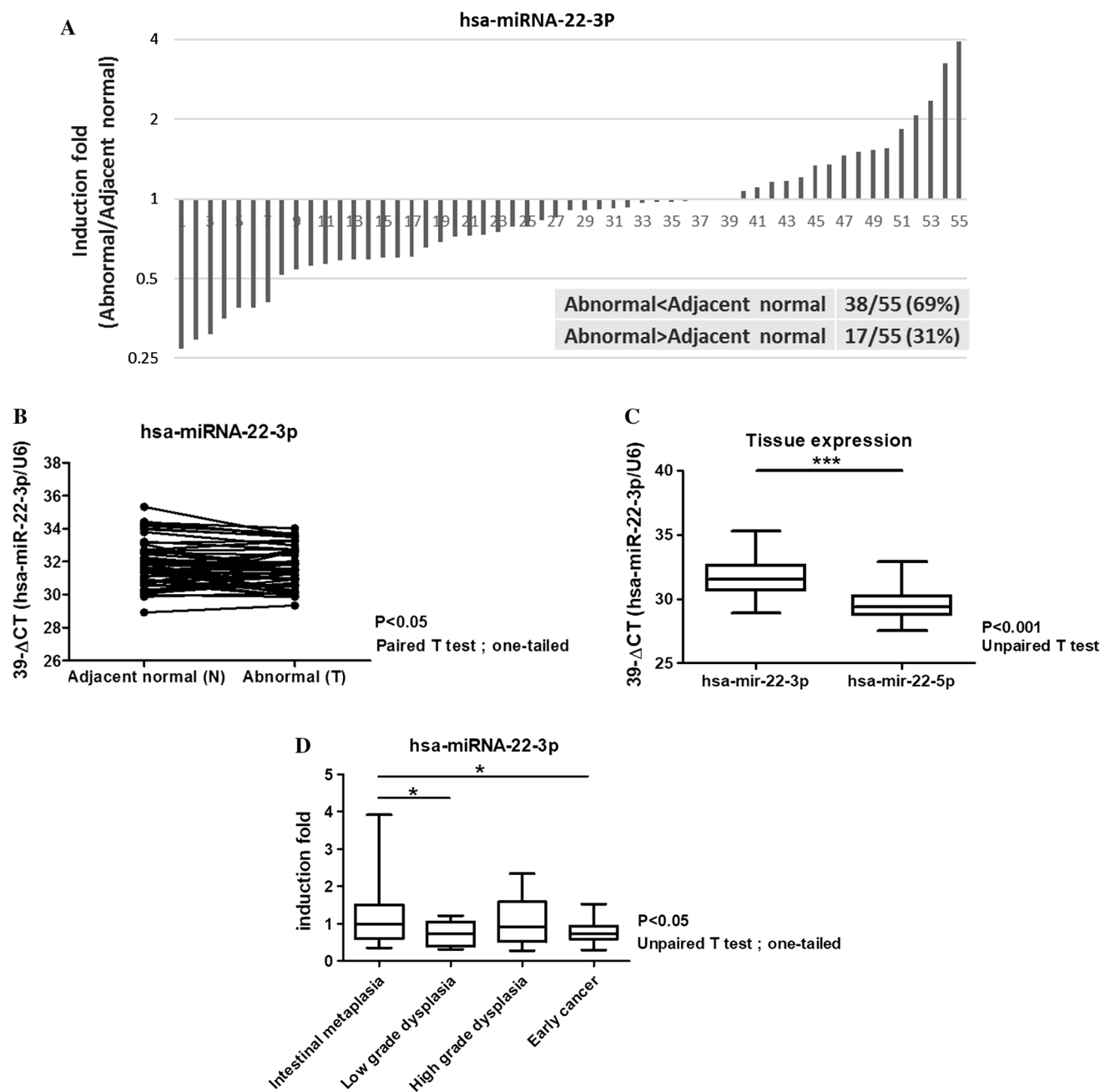


**Fig. 2** Fifty-five pairs of tissue samples were used for the quantitative real-time polymerase chain reaction to verify miRNA-22 expression. **a** miRNA-22-3p was downregulated in 69% of patients who had pre-cancerous gastric lesions, and upregulated in 31% of patients. **b** The expression of miRNA-22-3p in abnormal lesions was significantly

lower than in normal tissue. **c** miRNA-22-3p expression was higher than that of miRNA-22-5p in tissue. This indicates that miRNA-22-3p might be a more important indicator than miRNA-22-5p. **d** miRNA-22-3p had significantly different expression in each stage of cancer

(colonic-type intestinal metaplasia) or the small intestinal mucosa [5]. The incomplete type has a higher GC risk than the complete type. However, most patients are asymptomatic and the prevalence varies across regions [16]. Thus, in plasma analysis, we only enrolled incomplete IM samples.

GED is widely accepted as a precursor to gastric adenocarcinomas [28]. Some papers point out that the rate of

upgraded diagnosis in biopsy-proven LGD is high, and en bloc resection is recommended [29]. This is the reason why we combined patients with precursor and T1a/b cancer for analysis. In this study, the relative expression levels of circulating miRNA-22-3p gradually decreased from incomplete IM to GC, which was consistent with a previous study [30]. These results indicate that miRNA-22-3p



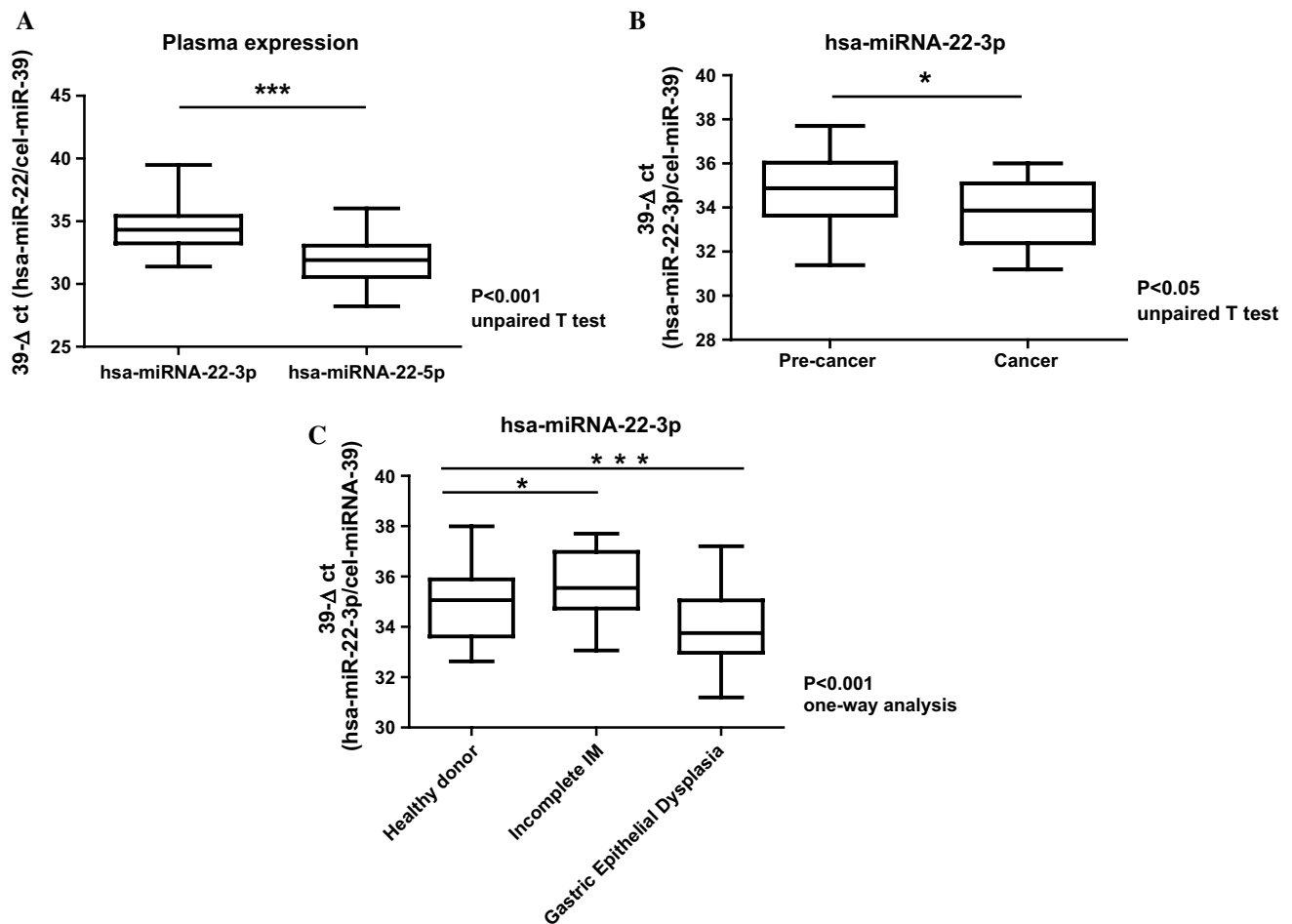


**Fig. 3** The expression of miRNA-22-3p in plasma using the quantitative real-time polymerase chain reaction. The data show that: **a** miRNA-22-3p expression is higher than that of miRNA-22-5p; **b**

miRNA-22-3p expression is higher in pre-cancer than in cancer; and **c** miRNA-22-3p has significantly different expression in each stage

could be used as a predictive marker for precancerous gastric lesions and early GC (Table 3).

MiRNA-22 inhibits tumor growth and metastasis in GC by directly targeting MMP14/Snail and metadherin [31, 32]. In addition, miRNA-22 acts as a suppressor in other cancers [33–35].

Theoretically, the expression of miRNA-22-3p in healthy control tissues should be distinguishable from incomplete

IM. However, our data do not support this assumption. This inconsistency might be due to inspection error because we do not routinely use IEE or high-definition endoscopy in our health checkup center, and the quality of endoscopists is variable. To overcome this limitation, a consistent method/ marker such as miRNA that is unaffected by the observer is needed. In this study, miRNA-22-3p and miRNA-22-5p have no significantly different expression in EC stage. The reason

**Table 3** Summary of cutoff points for different phases of diagnosis

Sages	AUC	95% CI	Sensitivity	Specificity	Cutoff point	Intercept	3p-D-CT	P value
H versus incomplete IM	0.8080	0.7187–0.9220	0.8182	0.2857	34.5657	−26.2594	0.7323	≤0.05
Incomplete IM versus HGD/LGD	0.8040	0.6591–0.9488	0.6250	0.9620	33.7700	28.5819	−0.8304	≤0.05
Incomplete IM versus LG+HG+EC (GED)	0.8095	0.6966–0.9221	0.8649	0.3810	35.3791	30.9006	−0.8707	≤0.05
Incomplete IM versus EC	0.8494	0.6866–0.9406	0.9170	0.6540	34.6600	36.4355	−1.0829	≤0.05

GED gastric epithelial dysplasia, H healthy control, IM intestinal metaplasia, LGD low-grade dysplasia, HGD high-grade dysplasia, EC early cancer, CI confidence interval

is not clear currently, and further study is needed. There are some other limitations to our study. First, there is no suitable model to prove that miRNA22 can inhibit the progression of IM to EC. Second, the number of dysplasia patients is too small to draw firm conclusions. Finally, it is difficult to select truly normal gastric mucosa tissue. A large-scale study using circulating miRNA-22-3p for gastric pre-cancer detection should be conducted in the future.

## Conclusions

Based on our results, we suggest the use of circulating miRNA-22-3p as a biomarker to improve theranostics of GC. For patients with incomplete IM combined with a significant change of the circulating miRNA-22-3p level, intensive esophagogastroduodenoscopy (best combined with IEE) follow-up is strongly advised. As a result, preventive and personalized medicine could be achieved using liquid biopsy, i.e., blood-based biomarkers.

**Author's contribution** THC, CTC, YYC, HTC, JTH, RCW, TSY, and KHL contributed to study concept and design. THC and CL involved in acquisition, analysis, and interpretation of data. THC drafted the manuscript. CL performed statistical analysis.

**Funding** This work was supported by a grant from Chang Gung Memorial Hospital, Taoyuan, Taiwan (CMRPG3D1392).

## Compliance with ethical standards

**Conflict of interest** The authors declare no conflicting financial interests.

## References

- Brenner H, Rothenbacher D, Arndt V. Epidemiology of stomach cancer. *Methods Mol Biol*. 2009;472:467–477.
- Karpeh M, Kelsen D, Tepper J. Cancer of the stomach. In: DeVita V, Hellman S, Rosenberg S, eds. *Cancer Principles & Practice of Oncology*. Philadelphia: Lippincott, Williams & Wilkins; 2001:1092–1126.
- Sugano K. Detection and management of early gastric cancer. *Curr Treat Options Gastroenterol*. 2015;13:398–408.
- Kanzaki H, Takenaka R, Kawahara Y, et al. Linked color imaging (LCI), a novel image-enhanced endoscopy technology, emphasizes the color of early gastric cancer. *Endosc Int Open*. 2017;5:E1005–E1013.
- Rugge M, Pennelli G, Pillozzi E, et al. Gastritis: the histology report. *Dig Liver Dis*. 2011;43:S373–S384.
- Leung WK, Wu MS, Kakugawa Y, et al. Screening for gastric cancer in Asia: current evidence and practice. *Lancet Oncol*. 2008;9:279–287.
- Marrelli D, Roviello F, De Stefano A, et al. Prognostic significance of CEA, CA 19-9 and CA 72-4 preoperative serum levels in gastric carcinoma. *Oncology*. 1999;57:55e62.
- Esquela-Kerscher A, Slack FJ. Oncomirs—microRNAs with a role in cancer. *Nat Rev Cancer*. 2006;6:259–269.
- Calin GA, Croce CM. MicroRNA signatures in human cancers. *Nat Rev Cancer*. 2006;6:857–866.
- Kosaka N, Iguchi H, Ochiya T. Circulating microRNA in body fluid: a new potential biomarker for cancer diagnosis and prognosis. *Cancer Sci*. 2010;101:2087–2092.
- Mitchell PS, Parkin RK, Kroh EM, et al. Circulating microRNAs as stable blood-based markers for cancer detection. *Proc Natl Acad Sci USA*. 2008;105:10513–10518.
- Tsujiura M, Ichikawa D, Komatsu S, et al. Circulating microRNAs in plasma of patients with gastric cancers. *Br J Cancer*. 2010;102:1174–1179.
- Tsai MM, Wang CS, Tsai CY, et al. Circulating microRNA-196a/b are novel biomarkers associated with metastatic gastric cancer. *Eur J Cancer*. 2016;64:137e148.
- Correa P. Human gastric carcinogenesis: a multistep and multifactorial process—first American Cancer Society award lecture on cancer epidemiology and prevention. *Cancer Res*. 1992;52:6735–6740.
- Busuttill RA, Boussioutas A. Intestinal metaplasia: a premalignant lesion involved in gastric carcinogenesis. *J Gastroenterol Hepatol*. 2009;24:193–201.
- Correa P, Piazzuelo MB, Wilson KT. Pathology of gastric intestinal metaplasia: clinical implications. *Am J Gastroenterol*. 2010;105:493–498.
- González CA, Pardo ML, Liso JM, et al. Gastric cancer occurrence in preneoplastic lesions: a long-term follow-up in a high-risk area in Spain. *Int J Cancer*. 2010;127:2654–2660.
- Oka S, Tanaka S, Kaneko I, et al. Advantage of endoscopic submucosal dissection compared with EMR for early gastric cancer. *Gastrointest Endosc*. 2006;64:877–883.
- Gotoda T. Endoscopic submucosal dissection of early gastric cancer. *Curr Opin Gastroenterol*. 2006;22:561–569.
- Salvon-Harman JC, Cady B, Nikulasson S, Khettry U, Stone MD, Lavin P. Shifting proportions of gastric adenocarcinomas. *Archives of surgery (Chicago, Ill: 1960)*. 1994;129:381–388. (discussion 388–389).
- Park JC, Lee YC, Kim JH, et al. Clinicopathological aspects and prognostic value with respect to age: an analysis of 3,362 consecutive gastric cancer patients. *J Surg Oncol*. 2009;99:395–401.
- Petrelli F, Berenato R, Turati L, et al. Prognostic value of diffuse versus intestinal histotype in patients with gastric cancer: a systematic review and meta-analysis. *J Gastrointest Oncol*. 2017;8:148–163.
- Slattery ML, Herrick JS, Pellatt DF, et al. MicroRNA profiles in colorectal carcinomas, adenomas and normal colonic mucosa: variations in miRNA expression and disease progression. *Carcinogenesis*. 2016;37:245–261.
- Bosman FT, Carneiro F, Hruban RH, Theise ND, eds. *WHO Classification of Tumours of the Digestive System*. 4th ed. Lyon: IARC Press; 2010.
- Lin YH, Wu MH, Liao CJ, et al. Repression of microRNA-130b by thyroid hormone enhances cell motility. *J Hepatol*. 2015;62:1328–1340.
- Livak KJ, Schmittgen TD. Analysis of relative gene expression data using real-time quantitative PCR and the 2<sup>-</sup>ΔΔCt method. *Methods*. 2001;25:402–408.
- Turchinovich A, Weiz L, Langheinz A, Burwinkel B. Characterization of extracellular circulating microRNA. *Nucleic Acids Res*. 2011;39:7223–7233.
- Correa P. Clinical implications of recent developments in gastric cancer pathology and epidemiology. *Semin Oncol*. 1985;12:2–10.
- Kim J-W, Jang JY. Optimal management of biopsy-proven low-grade gastric dysplasia. *World J Gastrointest Endosc*. 2015;7:396–402.

30. Wang W, Li F, Zhang Y, et al. Reduced expression of miR-22 in gastric cancer is related to clinicopathologic characteristics or patient prognosis. *Diagn Pathol.* 2013;8:102.
31. Zuo QF, Cao LY, Yu T, et al. MicroRNA-22 inhibits tumor growth and metastasis in gastric cancer by directly targeting MMP14 and Snail. *Cell Death Dis.* 2015;6:e2000.
32. Tang Y, Liu X, Su B, et al. microRNA-22 acts as a metastasis suppressor by targeting metadherin in gastric cancer. *Mol Med Rep.* 2015;11:454–460.
33. Wang G, Shen N, Cheng L, et al. Downregulation of miR-22 acts as an unfavorable prognostic biomarker in osteosarcoma. *Tumor Biol.* 2015;36:7891–7895.
34. Li B, Song Y, Liu TJ, et al. miRNA-22 suppresses colon cancer cell migration and invasion by inhibiting the expression of T-cell lymphoma invasion and metastasis 1 and matrix metalloproteinases 2 and 9. *Oncol Rep.* 2013;29:1932–1938.
35. You Y, Tan JX, Dai HS, et al. MiRNA-22 inhibits onco-gene galectin-1 in hepatocellular carcinoma. *Oncotarget.* 2016;7:57099–57116.

## Affiliations

**Tsung-Hsing Chen<sup>1,2</sup> · Cheng-Tang Chiu<sup>1</sup> · Chieh Lee<sup>3</sup> · Yin-Yi Chu<sup>1</sup> · Hao-Tsai Cheng<sup>1</sup> · Jun-Te Hsu<sup>4</sup> · Ren-Chin Wu<sup>5</sup> · Ta-Sen Yeh<sup>4</sup> · Kwang-Huei Lin<sup>6,7,8</sup>**

<sup>1</sup> Department of Gastroenterology and Hepatology, Linkou Chang Gung Memorial Hospital, Chang Gung University College of Medicine, Taoyuan, Taiwan

<sup>2</sup> Graduate Institute of Clinical Medical Sciences, Chang Gung University, Taoyuan, Taiwan

<sup>3</sup> Department of Industrial Engineering and Management, Yuan Ze University College of Engineering, Chung-Li City, Taiwan

<sup>4</sup> Department of Surgery, Linkou Chang Gung Memorial Hospital, Chang Gung University College of Medicine, 259 Wen-hwa 1 Road, Taoyuan, Taiwan

<sup>5</sup> Department of Pathology, Linkou Chang Gung Memorial Hospital, Chang Gung University College of Medicine, Taoyuan, Taiwan

<sup>6</sup> Graduate Institute of Biomedical Sciences, School of Medicine, Chang Gung University, Taoyuan, Taiwan

<sup>7</sup> Liver Research Center, Linkou Chang Gung Memorial Hospital, Taoyuan, Taiwan

<sup>8</sup> Research Center for Chinese Herbal Medicine, College of Human Ecology, Chang Gung University of Science and Technology, Taoyuan, Taiwan



## Research paper

# Inhalable multi-compartmental phospholipid enveloped lipid core nanocomposites for localized mTOR inhibitor/herbal combined therapy of lung carcinoma



Dalia M. Kabary<sup>a,b,c</sup>, Maged W. Helmy<sup>a,d</sup>, Elsayeda-Zeinab A. Abdelfattah<sup>e</sup>, Jia-You Fang<sup>f,g,h,\*</sup>, Kadria A. Elkhodairy<sup>a,b</sup>, Ahmed O. Elzoghby<sup>a,b,i,\*</sup>

<sup>a</sup> Cancer Nanotechnology Research Laboratory (CNRL), Faculty of Pharmacy, Alexandria University, Alexandria 21521, Egypt

<sup>b</sup> Department of Industrial Pharmacy, Faculty of Pharmacy, Alexandria University, Alexandria 21521, Egypt

<sup>c</sup> Department of Pharmaceutics, Faculty of Pharmacy and Drug Manufacturing, Pharos University in Alexandria, Alexandria, Egypt

<sup>d</sup> Department of Pharmacology and Toxicology, Faculty of Pharmacy, Damanshour University, Behira, Egypt

<sup>e</sup> Medical Research Institute (MRI), Alexandria University, Alexandria 21527, Egypt

<sup>f</sup> Pharmaceutics Laboratory, Graduate Institute of Natural Products, Chang Gung University, Taoyuan 333, Taiwan

<sup>g</sup> Research Center for Industry of Human Ecology and Research Center for Chinese Herbal Medicine, Chang Gung University of Science and Technology, Kweishan, Taoyuan 333, Taiwan

<sup>h</sup> Department of Anesthesiology, Chang Gung Memorial Hospital, Kweishan, Taoyuan 333, Taiwan

<sup>i</sup> Division of Engineering in Medicine, Department of Medicine, Brigham and Women's Hospital, Harvard Medical School, Boston, MA 02115, USA

## ARTICLE INFO

## Keywords:

Inhalable nanocomposites

Rapamycin

Berberine

Multi-compartmental nanoparticles

Hyaluronate targeting

Lactoferrin targeting

Lung cancer

## ABSTRACT

Pulmonary delivery of drug nanocarriers can overcome the shortcomings of systemic cancer therapy via the enhanced permeability and retention (EPR) based-nanomedicine. Herein, inhalable multi-compartmental nanocomposites with the capability for both localized and modulated release of the hydrophobic mTOR inhibitor, rapamycin (RAP) and the hydrophilic herbal drug, berberine (BER) have been developed for lung cancer therapy. Two types of multi-compartmental nanocarriers were fabricated by enveloping BER hydrophobic ion pair-lipid nanocore within a shell of RAP-phospholipid complex bilayer to reduce the delivery gap between the two drugs. To further enhance their tumor targeting, the nanocarriers were layer-by-layer coated by cationic lactoferrin and anionic hyaluronate resulting in enhanced internalization and cytotoxicity against lung cancer cells. The inhalable nanocomposites fabricated by spray-drying of multi-compartmental nanocarriers exhibited favorable aerosolization efficiency (MMAD of 3.28  $\mu\text{m}$  and FPF of 55.5%). The powerful anti-cancer efficacy of inhalable nanocomposites in lung cancer bearing mice compared to the inhaled free drugs was revealed by remarkable decrease in lung weight, and reduction in both number and diameters of lung adenomatous foci and angiogenic markers compared to positive control. Overall, localized delivery of RAP and BER to tumor cells via inhalable multi-compartmental nanocomposites holds great promise in management of lung cancer.

## 1. Introduction

Lung cancer is one of the most malignant types of cancer with mortality of 23% of total cancer-related mortality worldwide [1]. Systemic chemotherapy of lung cancer is usually unsuccessful because only a small fraction of the administered chemotherapeutic drug can reach tumor cells. Moreover, most chemotherapeutic drugs are non-selective

resulting in severe toxicity [2]. Systemic administration of drug-loaded nanocarriers has been extensively investigated for lung cancer therapy based on the concept of passive targeting [3–5]. However, several limitations have been emerged against the efficacy of enhanced permeation and retention (EPR) effect in human [6]. Thus, the efficiency of i.v. administered nanocarriers for lung cancer therapy has become doubtful.

**Abbreviations:** BER, berberine; DSC, differential scanning calorimeter; EE, entrapment efficacy; EPR, enhanced permeability and retention; FPF, fine particle fraction; FTIR, Fourier Transform Infrared Spectroscopy; h, hour; HA, hyaluronic acid; HIP, hydrophobic ion pair; HPLC, high performance liquid chromatography; LbL, layer-by-layer; LF, lactoferrin; MMAD, mass median aerodynamic diameter; NPs, nanoparticles; PC, phospholipid complex; RAP, rapamycin; SEM, scanning electron microscopy; SLNs, solid lipid nanoparticles; SLS, sodium lauryl sulfate; TEM, transmission electron microscopy; VEGF, vascular endothelial growth factor

\* Corresponding authors at: Division of Engineering in Medicine, Department of Medicine, Brigham and Women's Hospital, Harvard Medical School, Boston, MA 02115, USA (A. Elzoghby). Pharmaceutics Laboratory, Graduate Institute of Natural Products, Chang Gung University, Kweishan, Taoyuan 333, Taiwan (J.-Y. Fang).

E-mail addresses: [fajy@mail.cgu.edu.tw](mailto:fajy@mail.cgu.edu.tw) (J.-Y. Fang), [aelzoghby@bwh.harvard.edu](mailto:aelzoghby@bwh.harvard.edu) (A.O. Elzoghby).

<https://doi.org/10.1016/j.ejpb.2018.06.027>

Received 16 April 2018; Received in revised form 24 June 2018; Accepted 25 June 2018

Available online 28 June 2018

0939-6411/ © 2018 Elsevier B.V. All rights reserved.



Pulmonary delivery could potentially represent an interesting alternative to conventional systemic lung cancer therapy [7,8]. Inhalation treatment locally delivers the chemotherapeutic agent to tumor tissues thereby enhancing its efficacy and lowers its systemic side effects. Inhalable nanoparticles can successfully overcome the mucociliary clearance and escape macrophages. However, the mass median aerodynamic diameter (MMAD) of nano-sized particles is not suitable for inhalation thus; a large fraction of inhaled dose will be exhaled. The particles having 2–3  $\mu\text{m}$  diameter are found to be the most effective for deep lung deposition [9]. Therefore, nanocomposite particles consisting of drug-loaded nanoparticles microencapsulated within inert excipients combine the merits of both deep deposition of the microcarriers and effective cellular internalization and clearance bypass of nanocarriers. After lung deposition, the carrier dissolves and hence nanocomposites are disintegrated into the drug-loaded nanoparticles at alveolar surface followed by their uptake into lung cancer cells [10]. Dry powder inhalers (DPIs) have been widely used for pulmonary drug delivery because of their excellent stability, passive breath activation, and efficient-dose delivery [11]. However, many of the DPI products currently commercialized for treatment of various lung or systemic diseases show relatively poor efficiencies with FPF lower than 30% [12].

A critical disadvantage of cancer monotherapy lies in the high susceptibility of tumor cells for development of drug resistance [13,14]. Therefore, combined cancer therapy using a new generation of multi-compartmental nanocarriers has been an outstanding approach not only to delay the onset of resistance but also to provide a synergistic or additive anti-tumoral effect as well as their great capacity for modulating drug release [15]. Various techniques have been utilized in the fabrication of multi-compartmental nanocarriers for dual drug delivery. Sengupta et al. developed PLGA core-lipid shell nanoparticles for sequential drug delivery. Combretastatin was released quickly from the shell over 12 h while doxorubicin conjugated to PLGA core showed a slow release over 15 days [16]. Similarly, envelopment of mesoporous silica nanoparticles (MSNs) within a PEGylated lipid bilayer has enabled sequential delivery of axitinib and celastrol from the shell and core, respectively [17].

Recently, rapamycin (RAP), a hydrophobic immunosuppressive compound, has become a potential anti-cancer drug by acting as an inhibitor of mammalian target of rapamycin (mTOR) which was reported to play an important role in progression of lung cancer [18]. On the other hand, BER, a water soluble isoquinoline alkaloid, exerted an inhibitory effect on the invasion and motility of the highly metastatic A549 lung cancer cells [19]. More interestingly, it was previously reported that co-administration of RAP and BER had a synergistic anti-cancer effect, where BER maintained the cytotoxic effect of RAP on HCC cells at a lower RAP concentration and hence can minimize its immunosuppressive effect [20]. Moreover, BER was found to sensitize HCC cells to the anti-cancer effect of RAP through mTOR inhibition via downregulation of CD147 [21]. Therefore, we hypothesize that combined delivery of RAP and BER, which greatly differ in physicochemical properties, to lung cancer cells via nanocarriers would be an interesting and challenging approach.

In this study, we designed inhalable multi-compartmental lipid nanocomposites for localized combined delivery of BER and RAP to lung cancer cells. The water soluble BER and poorly soluble RAP were co-encapsulated into solid lipid nanoparticles (SLNs). However, the fast release of BER and extremely slow release of RAP from SLNs could reduce the benefits of synergistic combination. Therefore, to reduce the delivery gap between both drugs, multi-compartmental nanocarriers were fabricated. The cationic drug, BER, was incorporated as a hydrophobic ion pair (HIP) with the anionic surfactant SLS, in the lipid core of SLNs to enhance its miscibility with the lipid matrix and hence sustain its release. On the contrary, RAP was pre-formulated as phospholipid complex (PC) to help improve its solubility and relatively enhance its release from the nanocarriers. The RAP-PC complex bilayer was then used to envelop BER/SLS HIP-loaded lipid core to elaborate a

multi-compartmental nanocarrier. Furthermore, to enhance the tumor targeting of nanocarriers, a layer-by-layer assembly of the cationic protein lactoferrin and the anionic polysaccharide hyaluronate was used to coat the nanocarriers by targeting the CD44 receptors over-expressed by lung cancer cells. Finally, to enable deep lung deposition, the developed nanocarriers were microencapsulated into different carriers via spray-drying technology, thus elaborating inhalable nanocomposites. The developed delivery system was thoroughly investigated *in vitro* and *in vivo* to prove the anti-tumor superiority of the inhalable combined drug nano-delivery compared to the free drug combination.

## 2. Materials and methods

### 2.1. Materials

Berberine chloride hydrate (BER), coumarin-6, haematoxylin solution, eosin solution, Canada balsam, mannitol, maltodextrin, inulin, PVP K30, l-leucine, Dulbecco's modified eagle medium (DMEM), and 3-(4,5-dimethylthiazol-2-yl)-2,5-diphenyltetrazolium bromide (MTT) were purchased from Sigma-Aldrich (St. Louis, USA). Rapamycin (RAP) was purchased from Jianshi Yuantong Bioengineering Co., Ltd. (China). Hyaluronic acid (HA) was purchased from Baoding Faithful Industry Co., Ltd. (China). Lactoferrin (LF) was kindly donated by Westland Milk Products (Hokitika, New Zealand). Phosphatidylcholine (Lipoid S75) was kindly provided by Lipoid GmbH (Ludwigshafen, Germany). Glyceryl monostearate (GMS) was a gift from Gattefosse (Lyon, France). Poly(ethylene glycol) 400, sodium lauryl sulfate (SLS), ethanol, and methanol were purchased from ADWIC Pharmaceutical Chemicals Co. (Cairo, Egypt). Polyoxyethylene sorbitan monooleate (Tween 80) was purchased from Riedel-de Haën (Germany). Methanol and Acetonitrile HPLC grade was purchased from JT Baker (Phillipsburg, NJ, USA).

### 2.2. Preparation of BER/SLS HIP

For preparation of BER/SLS HIP [22], the aqueous solution of SLS was slowly added (at a rate of 2 ml/min) to 25 mg BER dissolved in distilled water under gentle magnetic stirring (at 100 rpm) till the appearance of strong turbidity indicating the complex formation which was then left for 30 min under magnetic stirring. The solution was then centrifuged for 45 min at 17,000 rpm (model 3K-30, Sigma laboratory, Germany) and the sediment complex was lyophilized using LyoQuest lyophilizer (Telstar, Spain) to obtain dry powders. Before freeze-drying, the sample was frozen at  $-80^{\circ}\text{C}$  for 8 h. Lyophilization was then carried out at a temperature of  $-50^{\circ}\text{C}$  and a pressure of 0.5 mbar for 24 h.

### 2.3. Preparation of BER/SLS-RAP-dual loaded SLNs (F1)

Dual drug-loaded SLNs were prepared by the hot homogenization method [23]. First, 10 mg of RAP and BER/SLS complex (eq. to 10 mg BER) were added to the melted lipid phase containing 100 mg GMS. The lipid phase was then mixed with aqueous phase (50 ml distilled water containing 100 mg Tween 80) and heated to  $70^{\circ}\text{C}$  using shaking water bath (Maxturdy 30, DAIHAN Scientific, South Korea). Keeping the same temperature, the aqueous phase was added to the oily phase under constant agitation, at 12,000 rpm for 5 min in an Ultra Turrax T-25 homogenizer (Ika Labortechnik, Germany). This emulsion was cooled to the room temperature to form the NPs.

### 2.4. Preparation of multi-compartmental SLNs

Two types of multi-compartmental nanocarriers were developed where the SLN core was enveloped within RAP/phospholipid (RAP/PC) complex bilayer. In the first one (F2), RAP was totally incorporated within the phospholipid bilayer encapsulating BER/SLS-SLNs. In the second nanocarrier (F3), RAP was divided between the two

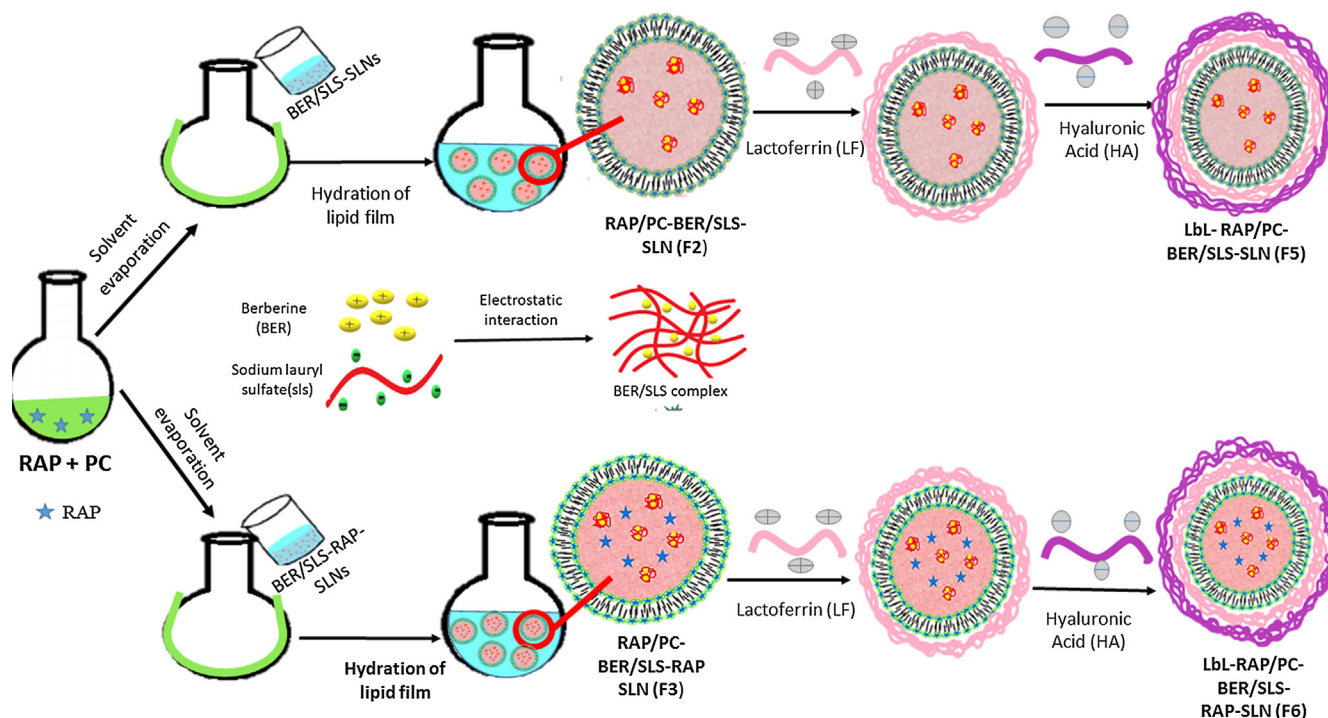


Fig. 1. Schematic diagram illustrating the preparation steps of multi-compartmental nanocarriers; LbL-RAP/PC-BER/SLS-SLNs (F5) and LbL-RAP/PC-BER/SLS-RAP-SLNs (F6).

compartments; one half was still entrapped into the SLN core and the other half was complexed with the phospholipid bilayer enveloping BER/SLS-SLNs. The preparation steps of both multi-compartmental nanocarrier approaches was illustrated in Fig. 1.

**For preparation of RAP/PC complex bilayer enveloping BER/SLS-loaded SLNs (F2),** RAP/PC complex was first prepared using 1:2 RAP/Lipoid S75 molar ratio by film hydration method [24]. Preparation and physicochemical characterization of the RAP/PC complex including entrapment efficiency, surface charge analysis, solid state characterization and in vitro drug release was detailed in Supplementary section. The thin film of RAP/PC complex eq. to 10 mg RAP was then hydrated for 1 h using the dispersion of previously-prepared BER/SLS-SLNs containing 10 mg BER.

**For preparation of RAP/PC complex bilayer enveloping RAP-BER/SLS-loaded SLNs (F3),** The thin film of RAP/PC complex eq. to only 5 mg RAP was then hydrated for 1 h using the dispersion of previously-prepared RAP-BER/SLS-SLNs containing 5 mg of RAP and BER/SLS eq. to 10 mg BER.

## 2.5. Preparation of tumor-targeted HA/LF-LbL-coated SLNs (F4-F6)

To prepare HA/LF-LbL-coated SLNs, certain volume of the negatively charged SLNs (F1-F3) (containing 2 mg RAP and 2 mg BER) was titrated with a cationic LF solution (10 mg/ml) at different volume ratios. The mixture was then incubated for 30 min under mild stirring, after which an anionic HA solution (0.5 mg/ml) was added dropwise to the positively charged LF-coated SLNs under gentle stirring for further 30 min. Thus, HA/LF-LbL-coated BER/SLS-RAP-SLNs (F4), HA/LF-LbL-coated RAP/PC-BER/SLS-loaded SLNs (F5), and HA/LF-LbL-coated RAP/PC-BER/SLS-RAP-loaded SLNs (F6) were developed.

## 2.6. Physicochemical characterization of NPs

The methodologies for assessment of drug loading, nanoparticle size, surface charge, morphology and drug release, were described previously [25–27] and detailed in the Supplementary section.

## 2.7. In vitro cytotoxicity and uptake

By MTT assay, the in vitro cytotoxicity of free drugs solution, RAP/PC-BER/SLS-RAP SLNs (F3) and LbL-RAP/PC-BER/SLS-RAP-SLNs (F6) were evaluated against A549 lung cancer cells. To investigate the internalization of the NPs into cells, NPs were loaded with coumarin-6 according to a previously described method [28]. Cellular uptake of free coumarin-6 compared to coumarin-loaded PC-SLNs and HA/LF-LbL-PC-SLNs was investigated using confocal microscopy (Detailed in Supplementary section).

## 2.8. Preparation of inhalable nanocomposites

Dual drug-loaded NPs were microencapsulated within different carrier matrices via spray-drying technique. The feed suspension was prepared by adding 30 ml of LbL-RAP-BER/SLS-SLNs (F4) or LbL-RAP/PC-BER/SLS-RAP-SLNs (F6) to 10 ml aqueous solutions of different carbohydrate carriers in 1:3 or 1:5 NP:carrier weight ratio under magnetic stirring. The composition of inhalable spray-dried nanocomposites is illustrated in Table 2. Spray-drying was performed using a Büchi Mini spray-dryer (Büchi B-290, Flawil, Switzerland) with the following settings: inlet temperature 100 °C, pump flow rate 10%, aspiration 100% and atomizing air flow rate (320 l/h). These settings resulted in an outlet temperature of 55 °C. The nanocomposites were collected with a high-performance cyclone and stored in sealed amber glass vials in a desiccator at room temperature [29].

## 2.9. Physicochemical characterization of nanocomposites

Yield, aqueous redispersibility, morphology and solid-state characteristics of nanocomposites were examined according to the methodology presented in Supplementary Section.

## 2.10. In-vitro pulmonary drug deposition (Aerodynamic properties)

Analysis of deposition profile of spray-dried nanocomposites was

**Table 1**Composition and physicochemical properties of single-compartment SLNs and multi-compartmental RAP/PC-SLNs. Data are expressed as mean  $\pm$  SD (n = 3).<sup>a</sup>

		RAP/Core (mg)	RAP/shell (mg)	Particle size (nm)	PDI	Zeta potential (mV)	RAP EE (%w/w)	BER EE (%w/w)
F1	RAP-BER/SLS-SLN	10	–	174.5 $\pm$ 5.5	0.260 $\pm$ 0.03	–21.1 $\pm$ 3.6	98.81 $\pm$ 0.21	88.12 $\pm$ 3.4
F2	RAP/PC-BER/SLS-SLNs	0	10	204.3 $\pm$ 5.3	0.275 $\pm$ 0.04	–33.0 $\pm$ 4.2	88.00 $\pm$ 2.60	89.65 $\pm$ 2.8
F3	RAP/PC-BER/SLS-RAP-SLNs	5	5	189.9 $\pm$ 7.1	0.265 $\pm$ 0.05	–24.5 $\pm$ 3.4	92.68 $\pm$ 0.85	88.48 $\pm$ 2.7
F4	LbL-RAP-BER/SLS-SLNs	10	–	219.5 $\pm$ 6.8	0.255 $\pm$ 0.03	–22.1 $\pm$ 3.9	98.82 $\pm$ 0.51	79.12 $\pm$ 6.1
F5	LbL-RAP/PC-BER/SLS-SLNs	0	10	239.6 $\pm$ 7.3	0.19 $\pm$ 0.014	–21.5 $\pm$ 2.9	88.22 $\pm$ 3.10	83.05 $\pm$ 5.6
F6	LbL-RAP/PC-BER/SLS-RAP-SLNs	5	5	224.2 $\pm$ 6.5	0.218 $\pm$ 0.06	–26.3 $\pm$ 3.1	92.61 $\pm$ 0.35	85.32 $\pm$ 2.8

<sup>a</sup> All nanocarriers were prepared using 20 mg GMS and BER/SLS HIP eq. to 10 mg BER. RAP/PC complex was prepared using 1:2 RAP/Lipoid S75 molar ratio by film hydration method.

performed using the eight stages Andersen Cascade Impactor (ACI; Copley Scientific Ltd., Nottingham, UK). ACI was operated at air flow rate of 28.5 l/min, with 4 kPa pressure drop. Budelizer (European Egyptian Pharm. Ind. Co., Alexandria, Egypt), a single-dose inhaler device, was connected to the ACI and filled with a hard gelatin capsule (size 2). Powder was actuated and withdrawn from capsules by the 28.5 l/min flow rate to be deposited in the device, throat, and each stage of ACI collection plates. Each actuation was set in 4 s and 2 aerosolization experiments were performed. HPLC mobile phase (10 ml) was used to wash the powders from the device and stages to be analyzed by HPLC. Aerodynamic parameters were automatically calculated using Copley Inhaler Testing Data Analysis Software (CITDAS) (Supplementary Section).

## 2.11. In vivo studies

### 2.11.1. Animals

For determination of the treatment efficiency of drug-loaded nanocomposites, male Albino mice (15–20 g) were used following the animal care and use protocol of Alexandria University (Supplementary Section).

### 2.11.2. Induction of tumor

Lung carcinoma was chemically-induced in 12–16 weeks male Albino mice by receiving I.P. injection of urethane (1.5 g/kg), dissolved in 0.9% NaCl, followed by a poster dose after 8th week [30].

### 2.11.3. Treatment protocol

The mice were indiscriminately divided into 4 groups (seven mice each); Group 1 mice were administered inhalable spray-dried nanocomposites (N12) prepared using HA/LF-LbL-RAP/PC-BER/SLS-RAP-SLNs (F6) eq. to 1.5 mg/kg of RAP and 1.5 mg/kg of BER using dry powder insufflator twice per week for three weeks using dry powder insufflator (DP-4M, Penn Century Inc. PA, USA). Group 2 mice were administered inhalable spray-dried physical mixture of free RAP/BER combination and mannitol:maltodextrin:leucine mixture at the same concentrations in nanocomposites by insufflation. Group 3; positive control (untreated chemically induced lung carcinoma bearing mice). Group 4; negative control (healthy mice). The method of pulmonary administration of the formulations is detailed in Supplementary section.

### 2.11.4. In vivo anti-tumor efficacy

#### i. Lung and body weight

The mice body weight was measured periodically during the treatment. All the surviving mice were sacrificed after 21 days. The extracted lungs were isolated, weighed, morphologically examined and separated into two parts; one was for biological evaluation of tumor biomarkers after freezing at  $-80^{\circ}\text{C}$  and the other was for histopathological and immunohistochemical examination after fixation with 4% paraformaldehyde solution.

#### ii. Tumor growth biomarkers

The level of tumor growth biomarkers was determined by ELISA (Supplementary section).

#### iii. Histopathological and immunohistochemical analysis

Histopathological changes, number of foci, their diameters and the proliferation extent indicated by Ki-67 protein were evaluated for the lung tumor samples (Supplementary section).

## 2.12. Statistics

Details of data analysis are in the Supplementary section.

## 3. Results and discussion

### 3.1. Single-compartment dual drug-loaded SLNs

Dual drug-loaded lipid nanoparticles (BER/SLS-RAP-SLNs, F1) were fabricated by hot homogenization method. The nanoparticles demonstrated a uniform size of 174.5 nm with a negatively charged surface ( $-21.1$  mV) reflecting high colloidal stability (Table 1). To facilitate the entrapment of the water-soluble drug BER into the lipid core of the nanoparticles, hydrophobic ion paired complex (HIP) was formed between the cationic quaternary ammonium group of BER and the anionic sulfate group of sodium lauryl sulfate (SLS) imparting higher lipophilicity. As a result, BER could be effectively incorporated in the lipid core with efficiency of 88.12%. However, a relatively fast release of BER was demonstrated with 59.36% of drug was released after 24 h (Fig. 2A). On the other hand, the highly hydrophobic drug RAP was most efficiently entrapped within the lipid core of BER/SLS-RAP-SLNs (F1) with 98.81% efficiency based on strong hydrophobic interaction (Table 1). However, this high drug affinity for the lipid core hindered its release into aqueous release medium with only 5.8% of RAP was released from the nanoparticles after 24 h (Fig. 2B). Thus, there would be high risk of sub-therapeutic activity of RAP at tumor sites which may also contribute to development of drug resistance. Moreover, the wide gap between the release rate of both drugs may cause loss of the benefit of the sensitizing action of BER for cancer cells to the anti-cancer effect of RAP. Therefore, multi-compartmental nanocarriers composed of RAP/PC complex bilayer enveloping the lipid nanoparticle core were required to enhance the release of RAP and hence reduce the release gap between the two drugs thus enabling much higher benefit from synergistic combined therapy.

### 3.2. Multi-compartmental dual drug-loaded nanocarriers

#### 3.2.1. Formation of RAP/PC complex

Developing drugs as phospholipid complexes was proved to be a potential approach to improve solubility, drug release and permeation [31,32]. In our study, RAP was successfully complexed with phospholipid by thin film hydration. High entrapment efficiency of RAP



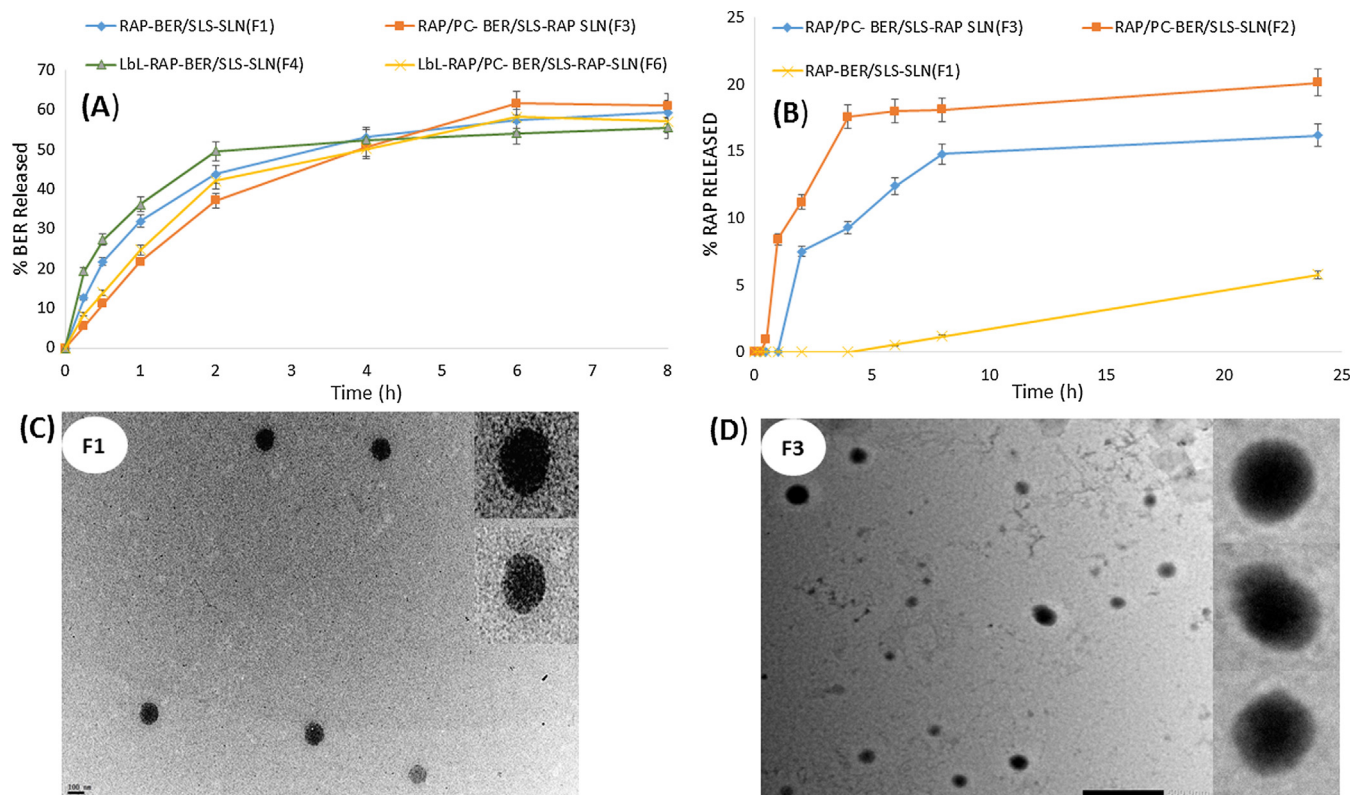


**Fig. 2.** In-vitro release of BER (A) and RAP (B) from different nanocarriers in 100 ml of purified water containing 0.2% w/v Tween as release medium at 37 °C, 100 rpm using dialysis bag method. Data are expressed as mean  $\pm$  SD (n = 3). TEM micrographs of single compartment, F1 (C) and multi-compartment, F3 (D) nanocarriers.

(84.34%) within the phospholipid bilayer was obtained based on hydrogen bonding between the hydroxyl group of RAP and phosphate group of phospholipid [33]. The surface of the RAP/PC complex bilayer was negatively charged with a zeta-potential of  $-37.8$  mV which could be explained by the presence of residual free fatty acids or phosphatidic acid in phospholipids [25]. The successful RAP-PC complex formation was confirmed via FTIR and DSC analysis (Figs. S1 and S2). More importantly, complexation of RAP with phospholipids was found to enhance its release profile compared to free drug (Fig. S3) (Details in Supplementary material).

### 3.2.2. Design of multi-compartmental nanocarriers

As a next step, the prepared RAP/PC complex thin film was hydrated by the previously prepared BER/SLS-SLNs. Thus, multi-compartmental nanoparticles were developed where the phospholipid bilayer shell was designed to encapsulate the whole RAP amount (10 mg) and promote a faster release of RAP enveloping inner core of BER/SLS-SLNs (F2). In a second approach, 50% of RAP amount was encapsulated within the phospholipid complex bilayer enveloping the lipid core (SLNs) containing the other 50% of RAP amount along with BER/SLS (F3). Fig. 1 illustrates the preparation steps of both multi-compartmental nanocarriers. The phospholipid bilayers were assembled on the surface of SLNs probably via hydrophilic interactions between the hydrophilic fraction of the surfactants at the water/lipid interface of SLNs and the polar head group of phospholipids [24,32].

By virtue of its HIP with SLS, BER was efficiently encapsulated within the lipid core of both types of nanocarriers (89.65 and 88.48% for F2 and F3, respectively) (Table 1). RAP was also highly encapsulated (88.00 and 92.68% within F2 and F3, respectively), due to strong hydrophobic interaction between the drug and both lipid core and phospholipid bilayer. After coating of SLNs (F1, 174.5 nm) with RAP/PC complex bilayer, the size was increased to 204.3 and 189.9 nm for F2 and F3, respectively maintaining a monomodal distribution thus

confirming entrapment of SLNs within the drug-phospholipid complex bilayer. The additional thickness of approximately 15–20 nm obtained for F3 was consistent with the previously reported thickness of lipid bilayers [34,35]. The lipid bilayer thickness is a critical parameter where much thin bilayer usually results in formation of non-uniform coating while much thicker bilayer can inhibit the drug release [36].

In agreement with our findings, increasing the amount of lipid used for coating MSNs led to increased thickness of the lipid bilayer formed. The authors found that the ideal thickness of the lipid bilayer to obtain uniform coating of MSNs surface and avoid the drug burst effect was 13–15 nm whereas thicker bilayer (30–33 nm) resulted in reduced drug loading [36]. The TEM image confirmed the formation of core-shell structure of the multi-compartmental nanocarriers (F3) exhibiting a size of about 150–160 nm with a phospholipid envelope around the SLNs compared to the single compartment nanocarriers (F1) (Fig. 2C and D).

The developed multi-compartmental nanocarriers (F2 and F3) could provide biphasic release of RAP where about 17.55 and 9.3% of RAP was released during the initial 4 h from both nanocarriers (F2 and F3), respectively (Fig. 2B). Comparatively, there was no drug released from the single compartment nanocarriers (F1) during 4 h. This faster release of RAP provided by the outer phospholipid envelope was attributed to complexation with phospholipid because of the lipid dynamics in the membrane, changing its binding sites very rapidly. This phase was followed by a phase of slow release of RAP provided by the drug fraction embedded within the lipid core where about 20.1 and 16.2% was released from F2 and F3 nanocarriers after 24 h, respectively (Fig. 2B). This biphasic pattern of RAP release would be expected to be useful at the tumor sites where the initially faster-released fraction can immediately inhibit mTOR pathway resulting in a rapid action. The slowly released fraction may be beneficial for prolonged mTOR inhibition. On the other hand, encapsulation of BER/SLS-SLNs within an envelope of RAP/PC bilayer has reduced the initial burst release of BER,



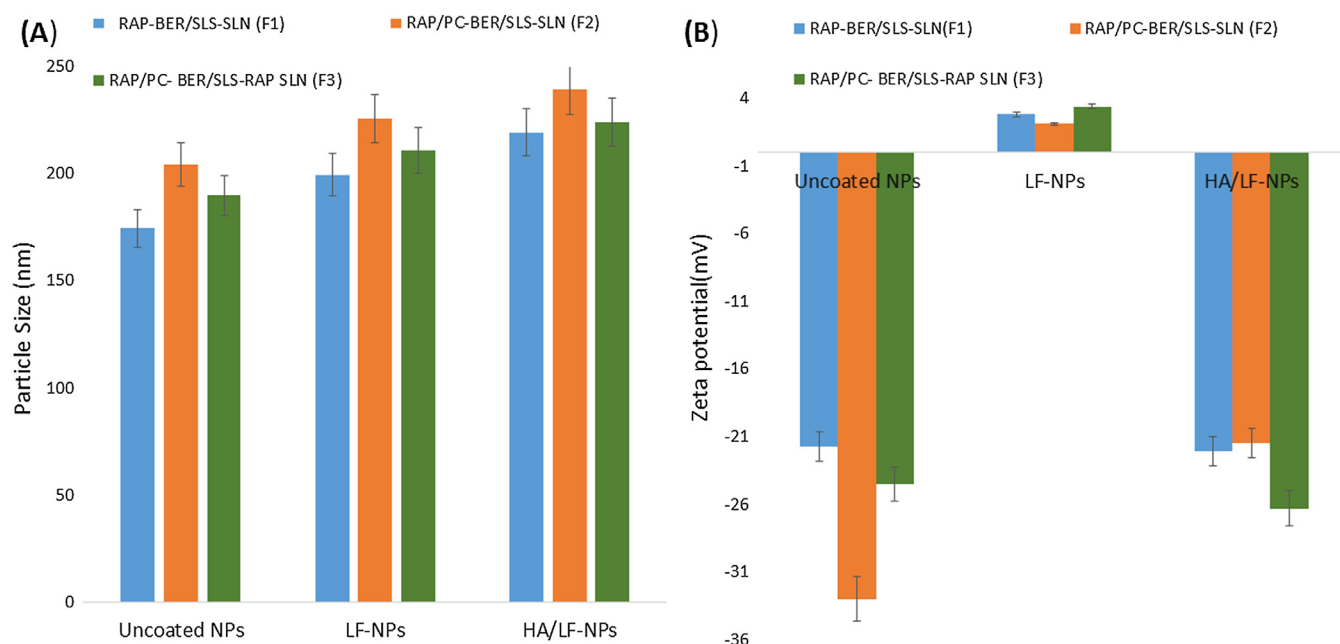


Fig. 3. Changes in particle size (A) and zeta potential (B) upon LbL deposition of LF and HA onto the surface of RAP-BER/SLS-SLNs (F1), RAP/PC-BER/SLS-SLNs (F2) and RAP/PC-BER/SLS-RAP SLNs (F3). Data are expressed as mean  $\pm$  SD (n = 3).

which has to diffuse through an additional barrier of phospholipid bilayer. After 2 h, about 37.14% of BER was released from the multi-compartmental nanocarrier (F3) compared to 42% from BER/SLS-SLNs (F1) (Fig. 2A).

### 3.2.3. Development of tumor-targeted multi-compartmental nanocarriers

To enhance the tumor targeting of our single and multi-compartmental nanocarriers, we exploited the layer-by-layer electrostatic assembly technique to coat the nanocarriers with tumor-targeting biopolymers. Two layers of cationic LF and anionic HA were deposited onto the surface of nanocarriers adopting a non-washing self-assembly procedure without the need to any anchoring moieties and tedious purification procedures [26,37,38]. In our preliminary study, different concentrations of LF and HA were investigated to optimize the required amounts of both polymers. The particle size was increased with increasing the volume added of LF solution. Accordingly, after addition of 4 ml LF solution (1 mg/ml), the size of F1 nanocarriers was increased by about  $30 \pm 5.3$  nm with reversal of zeta-potential from  $-21.1 \pm 3.6$  to  $+2.8 \pm 0.4$  mV (Fig. 3A and B). Subsequently, addition of 10 ml HA solution (0.5 mg/ml) caused about 10–15 nm increase in size with inversion of zeta-potential to  $-22.1 \pm 3.9$  mV. Overall, after coating with LF and HA, the size of nanocarriers was increased from 189.9 nm (F3) to 224.2 nm (F6) and from 204.3 nm (F2) to 239.6 nm (F5). The zeta potential values were  $-21.5$  and  $-26.3$  mV for F5 and F6, respectively. In our recent study, the LbL coating with LF/HA onto the outer surface of SLNs was found to significantly contribute to the high stability of our nanocarriers [39]. The presence of outer negatively charged HA layer enhanced the serum stability of the NPs by preventing the adsorption of negatively charged serum proteins. Moreover, after storage for 3 months, the coated NPs maintained their size compared to the uncoated ones thus reflecting their high colloidal stability.

It worth mention, that there was no significant effect on RAP release was observed after coating by LF and HA (F6) compared to uncoated formula (F3). Moreover, the phospholipid bilayer has overcome the initial burst release of BER encountered during the LbL-assembly process. During this process, it is possible that some of the incorporated drug (especially hydrophilic drugs) partitioned between the core and shell, facilitating its release to the external aqueous medium. This phenomenon resulted in 49.6% initial release of BER after 2 h from

single compartment LbL-SLNs (F4) compared to 42.0% from multi-compartment LbL-SLNs (F6) (Fig. 3A). Thus, the PC bilayer enveloping SLNs not only modulated the release of RAP, but also helped overcome the limitation of LbL-assembly. Although both multi-compartmental nanocarriers (F2 and F3) could enable biphasic release of RAP and reduced the initial release of BER, F3 nanocarriers (RAP was divided in both core and shell) was found to be superior to F2 nanocarriers (RAP was confined to the shell) based on its smaller size and higher stability. After 48 h, aggregation of the multi-compartmental nanocarrier (F2) was observed compared to the higher colloidal stability of F3 nanocarrier. This aggregation may be caused by the excess amount of phospholipid bilayer beyond that required for complete coating of the nanocarrier surface. Therefore, the multi-compartmental nanocarrier (F3) was selected for subsequent investigations including in vitro cytotoxicity and in vivo studies.

### 3.2.4. In vitro cytotoxicity and cellular uptake

The viability of A549 lung cancer cells was evaluated using MTT assay after treatment with the non-targeted and targeted multi-compartmental nanocarriers; RAP/PC-BER/SLS-RAP SLNs (F3) and HA/LF-LbL-RAP/PC-BER/SLS-RAP-SLNs (F6) at different concentrations (1–50  $\mu$ g/ml) at 24 and 48 h. Blank LbL-SLNs had almost no cytotoxicity and A549 cell number remained constant. Remarkably, dual free RAP/BER combination, and both nanocarrier dispersions (F3 and F6) exhibited remarkable decrease in cell viability in dose/time-dependent manner (Fig. 4). The non-targeted and tumor-targeted nanocarriers (F3 and F6) could reduce the  $IC_{50}$  by 1.13- and 1.98- folds, respectively compared to free drug combination. The higher cytotoxicity of F6 compared to F3 nanocarriers was attributed to the presence of the outer HA/LF LbL coating which target the CD44 or LDL receptors over-expressed by human lung cancer cells [40].

The superior cytotoxic activity of the nanocarriers was further confirmed by a qualitative cellular uptake study using confocal microscopy (Fig. 5). After 4 and 24 h incubation with free coumarin, no remarkable fluorescence was detected inside A549 cells. However, the fluorescence intensity of coumarin-loaded NPs was significantly higher and enhanced with increasing the incubation time. Moreover, the higher fluorescence intensity of cells incubated with F6 compared to F3 nanocarriers is attributable to the HA-targeted binding to CD44

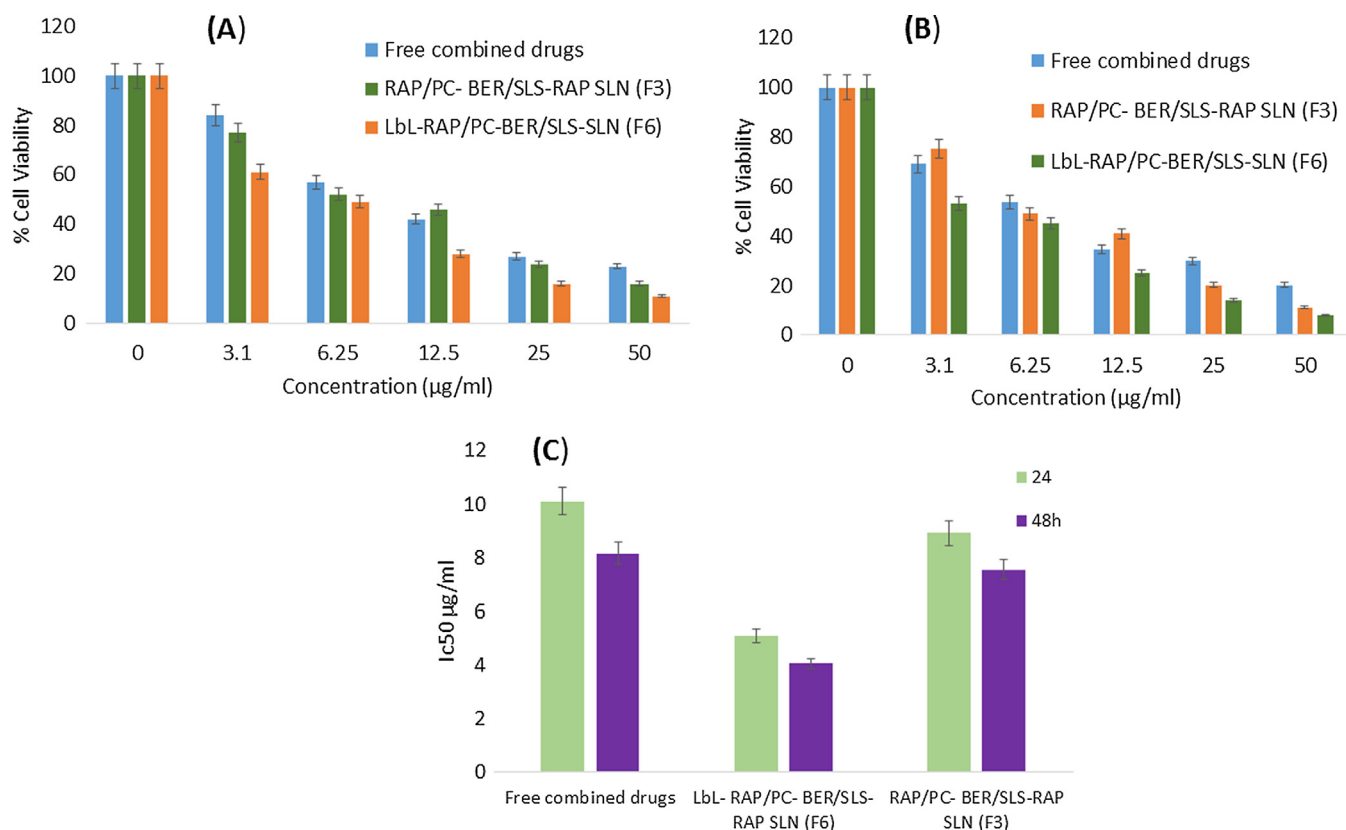


**Fig. 4.** Cytotoxicity analysis of free BER/RAP co-solvent compared to the prepared non-targeted (F3) and targeted (F6) multi-compartment nanocarriers against A549 lung cancer cells expressed as % cell viability after 24 h (A) and 48 h (B) incubation and IC<sub>50</sub> (µg/ml) values (C). Each value represents the mean  $\pm$  SD (n = 6).

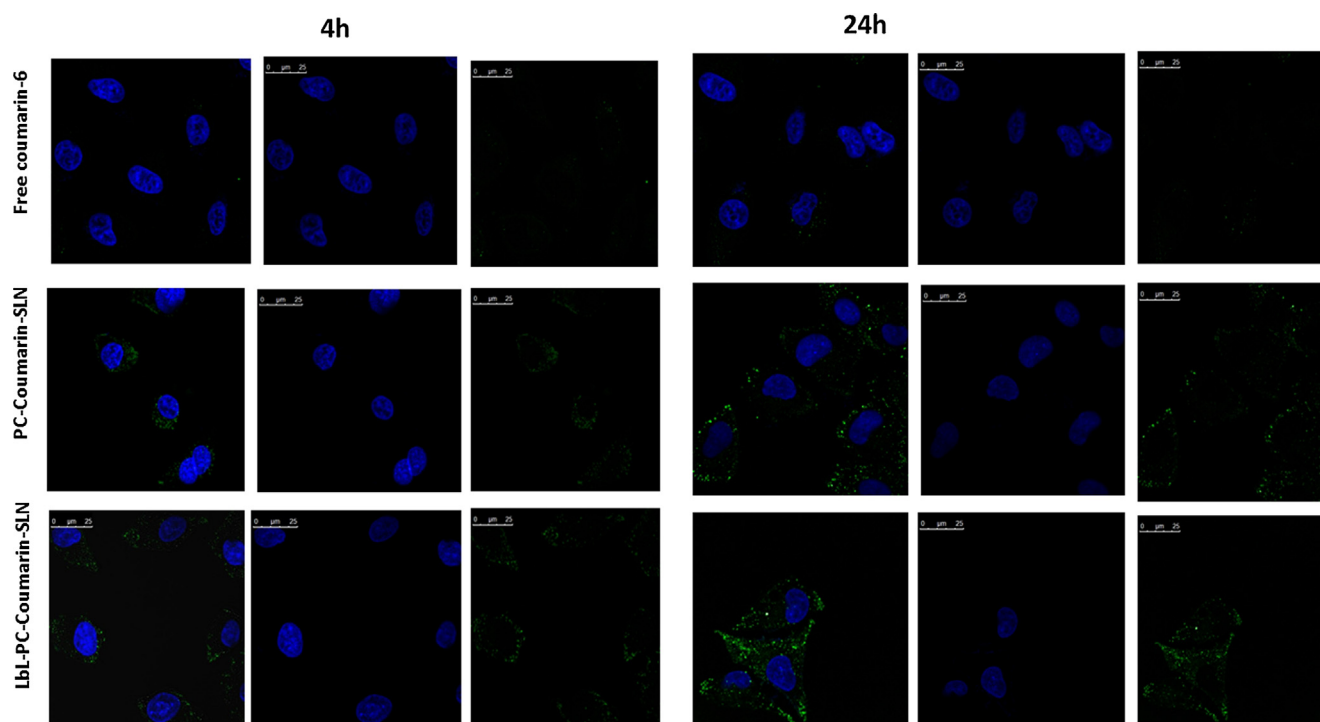


**Fig. 5.** Confocal microscopy images showing cellular uptake of free coumarin-6, coumarin-loaded non-targeted and targeted multi-compartment nanocarriers (PC-SLNs and LbL-PC-SLNs) within A549 lung cancer cells after incubation for 4 and 24 h. Cell nuclei were stained with DAPI and the cytoplasmic green fluorescence resulted from Coumarin-6.

receptors overexpressed by lung cancer cells resulting in higher cellular internalization [41]. The presence of PC complex bilayer in both nanocarriers also helps increase their membrane permeability thus contributing to the enhanced internalization and cytotoxicity of both nanocarriers [34].

### 3.3. Fabrication of inhalable nanocomposites

Nanocarriers (with a size range around 200–250 nm) are too small to be delivered to deep lung tissues. For deep lung deposition, the particles must be in an aerodynamic size range of 1–5  $\mu\text{m}$  [8,42]. Spray-drying is one of the most extensively used techniques for preparation of microparticles for pulmonary drug delivery because it commonly produces particles in the 1–3  $\mu\text{m}$  size range [43]. However, the high temperatures and shear forces used during spray-drying may lead to aggregation of lipid particles. Lipids with melting point higher than 70 °C can be successfully spray-dried [44]. In our study, the SLNs were microencapsulated into carriers elaborating inhalable nanocomposites with deep lung deposition. The lower hygroscopicity of mannitol relative to the other sugar carriers leads to formation of powder particles with lower adhesion and better drug release. However, mannitol has high tendency for recrystallization shortly after spray-drying because of its relatively low Tg value which may significantly affect the aerosolization efficiency and stability as well as dispersibility of nanocomposites [8,45]. Therefore, in the current study, mannitol was combined with other carriers, which help prevent its crystallization, to prepare inhalable fine powder of SLNs as illustrated in Tables 2 and 3.

#### 3.3.1. Spray-drying yield, drug content and redispersibility

Spray-dried nanocomposites have shown high drug content in the range of 60.2–79.2%. Spray-drying of the SLNs (F4) with mannitol resulted in nanocomposites of high yield (63.1%) and good redispersibility (RI = 1.16) (N1). However, spray-drying of SLNs with trehalose results in sticky non-recoverable powder (N2). Maltodextrin is known to aid in the powder formation by increasing both solid concentration and density [46]. Therefore, spray-drying of SLNs with maltodextrin alone (N3) resulted in nanocomposites with the highest yield (74.9%). However, using maltodextrin solely as carrier resulted in coarse particles with poor redispersibility (RI = 1.53). The mannitol-polymer combinations; mannitol-maltodextrin (N4) and mannitol-PVP (N5) were very difficult to spray-dry without additional excipients resulting in very hygroscopic, non-recoverable powder with low yield and relatively poor redispersibility (Table 2). Although spray-dried powders using PVP-maltodextrin mixture (N6) without leucine presented high yield (59.7%), poor reconstitution and irreversible aggregation between particles was revealed [47].

As depicted in Table 2, addition of leucine to the mannitol-maltodextrin (N4) mixture improved the yield of nanocomposites from 20.8 to 55.5%. Moreover, addition of leucine assisted encapsulation of

the highly hygroscopic non-recoverable mannitol-PVP particles (N5) into collectable powders (N7). Co-spray drying of powder with leucine was reported to improve the drying yield and reduce powder agglomeration resulting in enhanced aerosolization efficiency. By virtue of its hydrophilic and hydrophobic regions, leucine tends to migrate to the droplet surface during spray-drying which reduces the surface tension at the water-air interface thus allowing greater permeation of heat into the atomized liquid, which in turn produces drier powder particles with improved flowability [48]. Meanwhile, the leucine shell interferes with water evaporation, leading to the formation of particles with corrugated surface, reduced cohesion and better dispersion. Besides improvement of spray-drying yield, addition of leucine was found to enhance the redispersibility of nanocomposites to be almost 1.0 for PVP:maltodextrin:leucine (N9) and mannitol:maltodextrin:leucine (N10) mixture carriers.

#### 3.3.2. Solid state characterization

Mannitol was reported to be rapidly crystallized after spray-drying due to its small Tg value [47]. After 8 months storage, the DSC thermogram of spray-dried mannitol-maltodextrin-leucine nanocomposites (N10) showed the characteristic sharp mannitol crystalline peak at 169 °C but with lower intensity than that of pure mannitol, indicating that addition of maltodextrin has reduced the recrystallization of mannitol (Fig. 6A). Similarly, Shiga et al. has reported that addition of maltodextrin to mannitol resulted in retention of alcohol dehydrogenase activity during spray-drying due to inhibition of mannitol crystallization and increasing the solid content [49]. On the other hand, PVP-maltodextrin-leucine nanocomposites (N9) have shown less crystallinity because larger molecular weight ingredients with higher Tg values are less susceptible to recrystallization. The addition of high molecular weight components leads to increased viscosity, resulting in a reduction of the mobility of amorphous systems [50].

#### 3.3.3. Morphological analysis

SEM images of spray-dried nanocomposites (N9, N11 and N12, Table 3) showed microparticles in the size range of 1.31–3.59  $\mu\text{m}$  with spherical shape and wrinkled surface (Fig. 6B). The surface roughness resulting from a collapsed leucine shell, could enhance the aerosolization performance of the spray-dried powders [51,52]. Higher roughness lead to reduction of the particle-particle contact area and cohesiveness resulting in better aerosolization efficiency [53]. Interestingly, N12 nanocomposites; comprising RAP/PC complex shell coating of SLNs (F6) show interparticulate bridges with smoother surface than N11 nanocomposites; comprising SLNs lacking PC shell (F4). A possible explanation of the surface smoothening was the enrichment of phospholipids at the particle surface. Spray-dried PVP-maltodextrin-leucine nanocomposites (N9) have shown spherical particles with less interparticulate bridges than the other two nanocomposite formulations.

**Table 2**

Composition, yield and aqueous re-dispersibility of the spray-dried nanocomposites prepared using different carriers. Data are expressed as mean  $\pm$  SD (n = 3).

	Mannitol (% w/w)	Maltodextrin (%w/w)	PVP (%w/w)	Trehalose (%w/w)	Inulin (%w/w)	Leucine (%w/w)	Yield (%w/w)	RI Sf/Si
N1	100	–	–	–	–	–	63.1 $\pm$ 7.5	1.16 $\pm$ 0.05
N2	–	–	–	100	–	–	NA	–
N3	–	100	–	–	–	–	74.9 $\pm$ 6.8	1.53 $\pm$ 0.07
N4	40	60	–	–	–	–	20.8 $\pm$ 1.9	1.33 $\pm$ 0.03
N5	50	–	50	–	–	–	NA	–
N6	–	60	40	–	–	–	59.7 $\pm$ 4.9	1.36 $\pm$ 0.06
N7	40	–	40	–	–	20	27.8 $\pm$ 3.5	1.14 $\pm$ 0.04
N8	40	–	–	–	40	20	20.5 $\pm$ 2.3	1.17 $\pm$ 0.03
N9	–	40	40	–	–	20	51.7 $\pm$ 6.2	1.16 $\pm$ 0.06
N10	50	25	–	–	–	25	55.5 $\pm$ 4.1	1.1 $\pm$ 0.04

\*All nanocomposites were prepared by 1:5 SLNs/carrier weight ratio using LbL-RAP-BER/SLS-SLNs (F4). NA: A sticky non-redispersible mass rather than free flowing powder could be obtained.

**Table 3**

Aerodynamic properties and drug content of spray-dried LbL-BER/SLS-RAP-SLNs nanocomposites prepared with different carriers. All data are expressed as mean  $\pm$  SD (n = 3).

	Carrier composition (w/w)	Drug content (%w/w)	FPF (%w/w)	MMAD ( $\mu$ m)	ED (%w/w)	GSD
N1	Mannitol	67.62 $\pm$ 1.8	13.6 $\pm$ 3.08	6.8 $\pm$ 0.73	74.80 $\pm$ 5.61	1.27 $\pm$ 0.19
N7	Mannitol:PVP:leucine (2:2:1)	60.20 $\pm$ 1.3	16.8 $\pm$ 5.21	6.48 $\pm$ 0.64	83.32 $\pm$ 2.91	1.66 $\pm$ 0.23
N9	PVP:maltodextrin:leucine (2:2:1)	63.27 $\pm$ 2.5	50.47 $\pm$ 5.6	3.57 $\pm$ 0.19	87.51 $\pm$ 1.07	2.48 $\pm$ 0.28
N10	Mannitol:maltodextrin:leucine (2:2:1)	64.58 $\pm$ 3.3	65.6 $\pm$ 2.88	2.17 $\pm$ 0.23	94.38 $\pm$ 0.31	1.36 $\pm$ 0.15
N11	Mannitol:maltodextrin:leucine (2:2:1)	79.20 $\pm$ 4.2	62.9 $\pm$ 3.18	2.23 $\pm$ 0.28	93.12 $\pm$ 0.54	2.86 $\pm$ 0.35
N12	Mannitol:maltodextrin:leucine (2:2:1)	76.50 $\pm$ 2.7	55.5 $\pm$ 4.56	3.28 $\pm$ 0.34	87.9 $\pm$ 3.68	2.1 $\pm$ 0.41

\*The nanocomposites (N1, N7, N9, N10) were prepared by spray-drying of LbL-RAP-BER/SLS-SLNs (F4) using 1:5 SLNs:carrier weight ratio. The nanocomposites (N11) were prepared by spray-drying of LbL-RAP-BER/SLS-SLNs (F4) using 1:3 (SLNs: carrier) ratio weight to increase the drug loading. The nanocomposites (N12) were prepared by spray-drying of the multi-compartmental nanocarrier LbL-RAP/PC-BER/SLS-RAP-SLNs (F6) using 1:3 (SLNs:carrier) weight ratio.

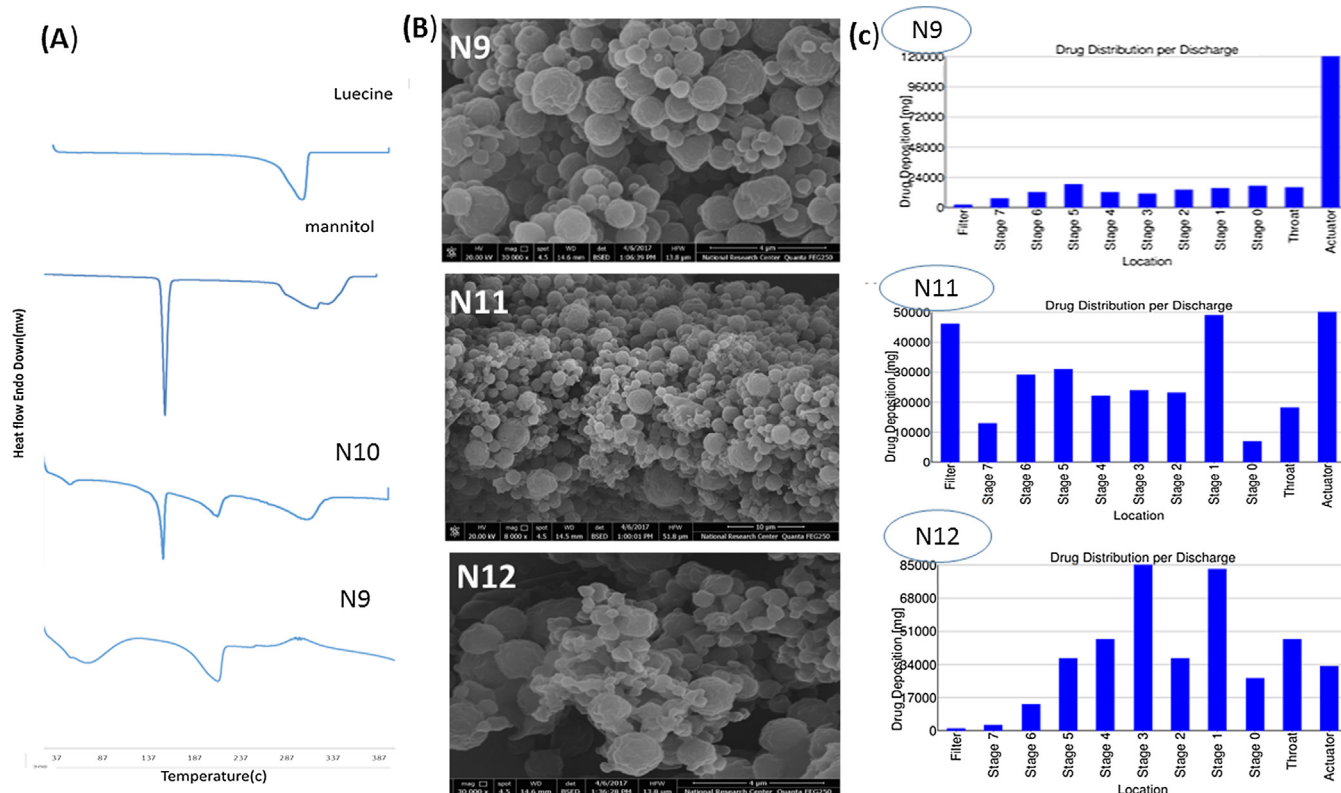


**Fig. 6.** DSC thermograms of spray-dried nanocomposites after storage in a desiccator at room temperature for 8 months (A), SEM micrographs of spray-dried nanocomposites prepared with different carriers; F4 SLNs/PVP-maltodextrin-leucine (N9); F4 SLNs/mannitol-maltodextrin-leucine (N11); and F6 PC-SLNs/mannitol-maltodextrin-leucine (N12) (B). The aerodynamic distribution of different spray-dried nanocomposites in different stages of Andersen cascade impactor obtained by CITDAS version 3.10 data processing software (C). Data are expressed as mean  $\pm$  SD (n = 3).

### 3.3.4. In-vitro pulmonary deposition

The aerodynamic properties of different DPI nanocomposites with high yield and good RI (N1, N7, N9, and N10) were evaluated using Andersen cascade impactor. The amounts of drug deposited on various stages varied for different samples are demonstrated in (Fig. 6C). The MMAD of the aerosol particles greatly affects their fate where particles with The particles having MMAD of 2–3  $\mu$ m are most suitable for deep lung deposition [7]. In our study, though they have shown high yield and good RI, solid lipid nanocomposites prepared using only mannitol (N1) have shown relatively high MMAD of 6.8  $\mu$ m and hence low FPF of 13.6% (Table 3). Similarly, nanocomposites prepared using PVP:maltodextrin:leucine (N7) showed high MMAD and low FPF and hence is likely to show poor lung deposition. In agreement with our results, the inhalable alendronate-loaded lipid nanocomposites prepared by spray-drying with mannitol demonstrated poor deposition revealed by MMAD of 6.7  $\mu$ m and FPF of 9.03% [54]. On the other hand, the lipid nanocomposite powders prepared using a mixture of

mannitol:maltodextrin:leucine (N10–N12) have shown good aerodynamic properties with MMAD < 3.5  $\mu$ m and FPF > 50% (Table 3). Both PVP:maltodextrin:leucine (N9) and mannitol:maltodextrin:leucine (N10) nanocomposites exhibited aerodynamic properties suitable for deep lung deposition [47]. However, the lower aerodynamic diameter of N10 nanocomposites significantly increased their respirable fraction.

In an attempt to increase the drug loading, N11 nanocomposites were prepared using the same carrier composition (mannitol:maltodextrin:leucine) of N10 nanocomposites but using less amount of carrier (1:3 SLNs:carrier weight ratio). The N11 nanocomposites has demonstrated FPF of 62.9% with no significant difference from that of N10 nanocomposites but with higher drug loading. Presence of RAP/PC envelope onto the surface of NPs in N12 nanocomposites was found to reduce the FPF of nanocomposites from 62.9% (N11) to 55.5% (N12) (Table 3). The relatively lower aerodynamic properties after coating with PC could be attributed to the increased viscosity as well as the less corrugated surface provided by the phospholipid envelope as



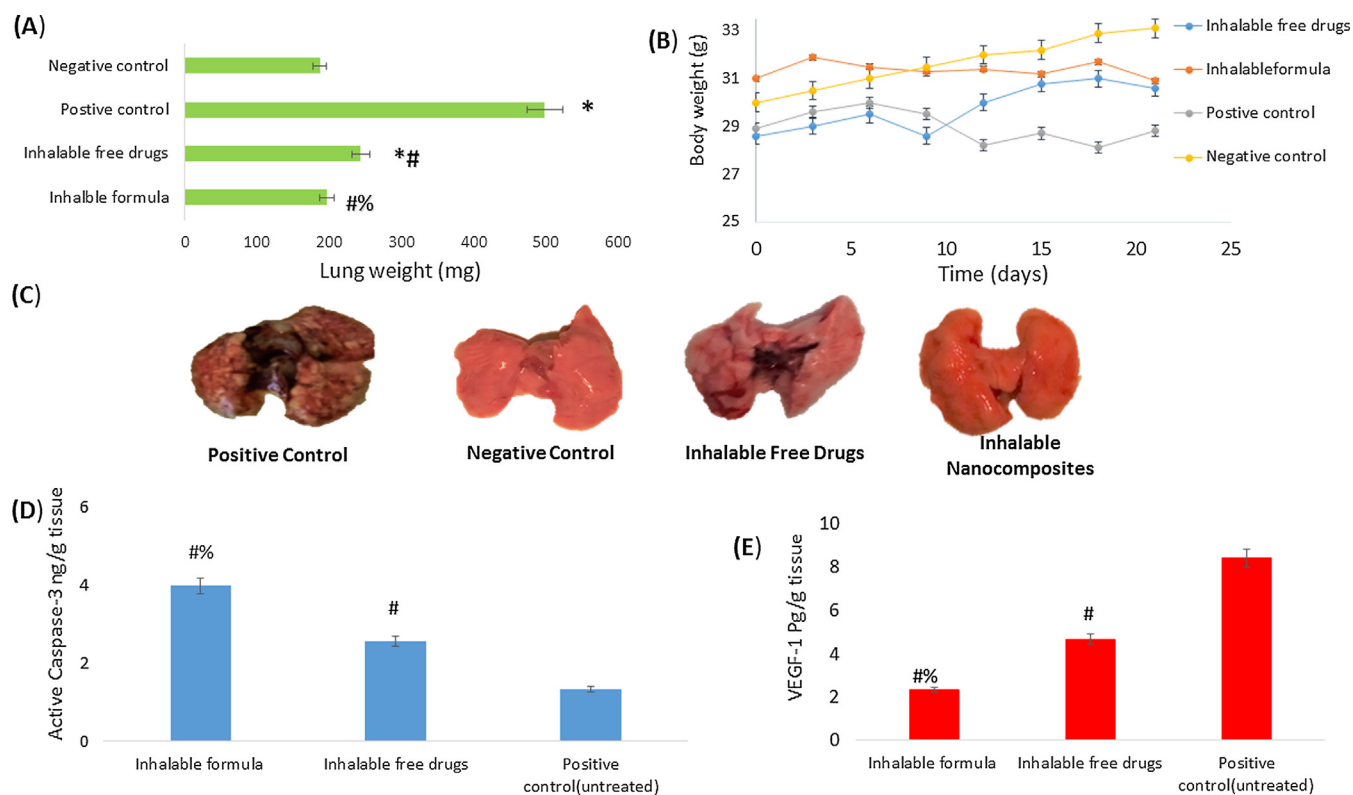


**Fig. 7.** In vivo anti-tumor efficacy of insuflated inhalable nanocomposites (N12) compared to inhaled free drugs powder after 21 day treatment expressed as; lung weight for different mice groups (A), change of total body weight of mice with time (B), representative images of lungs excised from different mice groups (C), and the level of tumor markers including apoptotic Caspase-3 (D) and angiogenic VEGF-1 (E) in mice compared to untreated positive control. \*  $P < 0.05$  vs negative control, #  $P < 0.05$  vs positive control, %  $P < 0.05$  vs Free BER/RAP mixture ( $n = 7$ ).

demonstrated by SEM.

Based on the previous data, **N12** nanocomposites were chosen for subsequent in-vivo tests as it shows suitable aerodynamic properties for deep lung deposition. Moreover, the **N12** nanocomposites would be anticipated to exhibit high anti-tumor efficacy due to the multi-compartmental nanocarrier structure with presence of RAP in both core and shell of NPs as previously discussed. By mimicking the lung surfactant function, incorporation of phospholipids in the inhalable nanocomposites also contributes to enhance their effect by decreasing the surface tension at alveolar surface and reducing friction in the lung tissue [55].

### 3.4. In vivo anti-tumor efficacy

#### 3.4.1. Lung weight and morphology

Mice treated with inhaled nanocomposites had significantly lower average lung weights compared to the positive control group (196.2 vs 498 mg), whereas mice treated with inhaled free BER/RAP powder has shown lung weight of 243.4 mg (Fig. 7A). No clear body weight loss was observed in the mice group treated with inhaled nanocomposites (**N12**) or inhaled free RAP/BER powder confirming their low systemic toxicity (Fig. 7B). The photographs of lungs excised from the negative control mice exhibited normal physiological features. On the other hand, lungs of the untreated positive control group were occupied by tumor nodules (Fig. 7C). In contrast, tumor growth was significantly inhibited to different degrees in terms of lung weight and number of foci in the treated groups. Thus, tumor growth was notably inhibited to different degrees in the groups treated with inhaled nanocomposites and inhaled free drugs combination.

#### 3.4.2. Tumor growth biomarkers

The effect of the inhaled nanocomposites (**N12**) on the apoptotic and anti-angiogenic effects of RAP and BER was evaluated and

compared to inhaled free drugs (Fig. 7D and E). RAP was reported to have anti-angiogenic activity caused by reduction of vascular endothelial growth factor (VEGF) level [56]. BER also can inhibit tumor progression through the inhibition of various pro-inflammatory and angiogenic factors [57]. In addition, BER can induce mitochondria-mediated apoptosis and increased the expression of caspase-3 [58]. In this study, the spray-dried lipid nanocomposites demonstrated the highest significant tumor growth inhibitory effect ( $P < 0.05$ ) with a 3.6-fold reduction of VEGF level and 2.99-fold elevation in caspase-3 level in lung tumors relative to the positive control group. Comparatively, the group treated with inhaled free combined drugs has shown merely 1.80-fold reduction of VEGF level and 1.93-fold elevation of caspase-3 relative to the positive control ( $P < 0.05$ ).

#### 3.4.3. Histopathological and immunohistochemical analysis

In H&E stained slides, lung sections of negative control demonstrated normal alveoli with a single layer epithelial lining. On the other hand, positive control group has shown several preneoplastic to neoplastic lesions ranging from epithelial hyperplasia to adenoma (blue arrow). In addition, there was evidence of hemorrhage (white arrow) and inflammatory cells infiltration (black arrow), whereas the lung tissues treated with inhaled nanocomposites were approximately recovered as normal ones (Fig. 8A). The mice group treated with inhaled free RAP/BER powder has shown more tumor lesions than group treated with inhaled nanocomposites. This study was further augmented by determination of both number and diameter of lung adenomatous foci (Fig. 8B). The inhaled nanocomposites treated group showed the best alleviation of both indices with 92.85% reduction in the average number of microscopic metastatic lung foci with highly reduced diameter (0.42 vs 5.53 mm) compared to positive control group ( $P < 0.05$ ). While, inhaled free drug powder treated group has shown 73.80% reduction in the average number of lung foci with

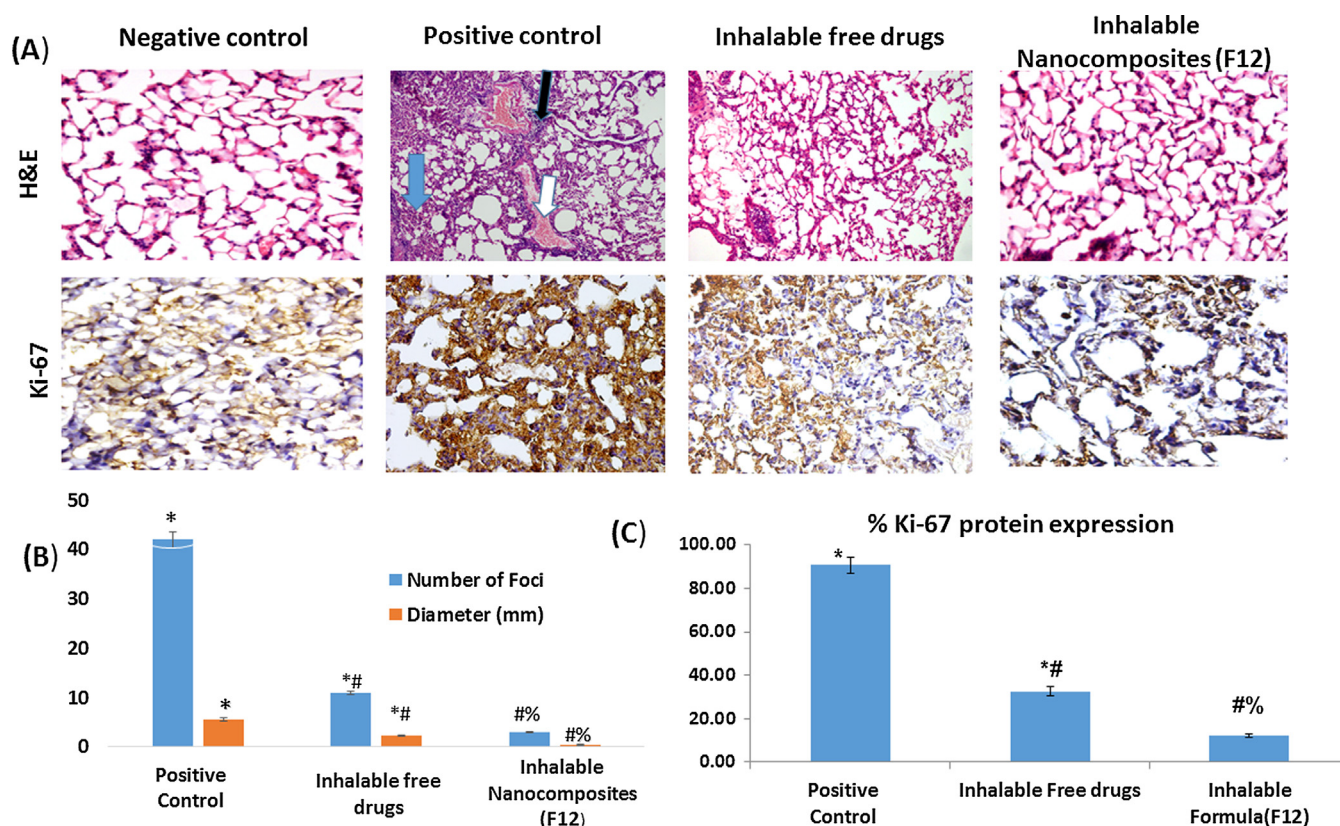


**Fig. 8.** Histopathological H&E and immunohistochemical Ki67 analysis of lung sections of mice treated with insufflated inhalable nanocomposites (N12) compared to inhaled free drugs powder for 21 days (A), the number and diameter of lung adenomatous foci (B), and the % expression of Ki-67 protein in corresponding groups (C). \*  $P < 0.05$  vs negative control, #  $P < 0.05$  vs positive control, % $P < 0.05$  vs Free BER/RAP mixture ( $n = 7$ ).

reduced diameter (2.25 vs 5.53 mm). Ki-67 protein is a prognostic marker which is directly associated with cell division [59]. Compared to positive control, both treatments with inhaled free RAP/BER combination and inhaled nanocomposites inhibited cell proliferation as confirmed by reduced Ki-67 staining. The % expression of Ki67 protein measured in groups treated with inhaled free drugs and inhaled nanocomposites were  $32.47 \pm 2.16$  and  $12.15 \pm 0.96\%$ , respectively compared to  $90.79 \pm 3.67\%$  for positive control (Fig. 8C). Thus, both histopathological and immunohistochemical analysis confirmed the superiority of inhalable nanocomposites.

In this study, despite the relatively complex nature of the developed nanocarriers, we believe they are urgently required to fulfill the unmet needs for efficient localized combined cancer therapy. The **complexity of nano-systems stems from the various challenges** we tried to address including: (1) The difficulty of co-loading of RAP & BER within the same carrier due to the big difference in their physicochemical properties, (2) The inefficient encapsulation and fast release of hydrophilic BER from SLNs, (3) The high lipophilicity and hence slow release rate of RAP from SLNs, (4) This big gap in the release rate of both drugs from SLNs could reduce the benefits of synergistic combination, (5) The low drug loading in the inhalable multi-component delivery system, (6) The low FPF and hence insufficient lung deposition of inhalable lipid nanocarriers, and (7) The non-selective delivery of anti-cancer drugs, even after lung deposition, to both cancerous and normal lung cells. Therefore, different approaches have been coordinated together elaborating these complex multi-compartmental nanocomposites **to overcome the abovementioned shortcomings**. First, hydrophobic ion pairing approach was used to enhance the miscibility the cationic drug, BER with the lipid matrix through its interaction with the anionic SLS and hence sustain its release from SLNs. Second, the lipophilic drug RAP was pre-formulated as phospholipid complex (PC) to help improve its solubility and relatively enhance its release from the nanocarriers.

Thus, we could reduce the delivery gap between both drugs. Then, the RAP-PC complex bilayer was then used to envelop BER/SLS HIP-loaded lipid core to elaborate a multi-compartmental nanocarrier. Furthermore, to overcome the problem of non-selectivity and enhance the tumor targeting of nanocarriers, a layer-by-layer assembly of the cationic lactoferrin and the anionic hyaluronate was used to coat the nanocarriers. Finally, to enable deep lung deposition, the developed nanocarriers were microencapsulated into different carriers via spray-drying technology, thus elaborating inhalable dry powder nanocomposites.

#### 4. Conclusion

Inhalable multi-compartmental lipid nanocomposites were developed for localized delivery of RAP and BER to lung cancer. Envelopment of lipid nanoparticles loaded with BER/SLS HIP within an outer bilayer of RAP-phospholipid complex resulted in core-shell multi-compartmental nanocarriers with biphasic RAP release together with reduced initial burst release of BER. The multi-compartmental nanocarriers have shown superior cytotoxicity and internalization against A549 cells compared to single compartment. Using spray-drying technology, the optimized multi-compartmental nanocarriers were microencapsulated using mannitol-maltodextrin-leucine mixture with 1:3 w/w ratio resulting in inhalable nanocomposites with small MMAD and high FPF suitable for deep lung deposition. In vivo studies displayed the higher anti-tumor activity of inhalable nanocomposites over the inhaled free drugs in lung cancer bearing mice.

#### Acknowledgment

This work was supported by the research grant (No. 5731) of Science and Technology Development Fund (STDF), Ministry of

Scientific Research, Egypt. The authors also acknowledge Westland Milk Products (Hokitika, New Zealand) for kind donation of lactoferrin.

## Declaration of interest

The authors declare no conflicts of interest.

## Appendix A. Supplementary material

Supplementary data associated with this article can be found, in the online version, at <https://doi.org/10.1016/j.ejpb.2018.06.027>.

## References

- [1] J. Ahmad, S. Akhter, M. Rizwanullah, S. Amin, M. Rahman, M.Z. Ahmad, M.A. Rizvi, M.A. Kamal, F.J. Ahmad, Nanotechnology-based inhalation treatments for lung cancer: state of the art, *Nanotechnol. Sci. Appl.* 8 (2015) 55.
- [2] C.-L. Tseng, S.Y.-H. Wu, W.-H. Wang, C.-L. Peng, F.-H. Lin, C.-C. Lin, T.-H. Young, M.-J. Shieh, Targeting efficiency and biodistribution of biotinylated-EGF-conjugated gelatin nanoparticles administered via aerosol delivery in nude mice with lung cancer, *Biomaterials* 29 (2008) 3014–3022.
- [3] A. Elzoghby, Polymeric nanocarriers as robust platforms for cancer therapy, *Curr. Pharm. Des.* 23 (35) (2017) 5211–5212.
- [4] S. Sabra, M. Abdelmoneem, M. Abdelwakil, M.M. Taha, D. Anwar, R. Mohamed, S. Khattab, A. Bekhit, K. Elkhodairy, M. Freag, Self-assembled nanocarriers based on amphiphilic natural polymers for anti-cancer drug delivery applications, *Curr. Pharm. Des.* 23 (35) (2017) 5213–5229.
- [5] A. Elzoghby, M. Freag, H. Mamdouh, K. Elkhodairy, Zein-based nanocarriers as potential natural alternatives for drug and gene delivery: focus on cancer therapy, *Curr. Pharm. Des.* 23 (35) (2017) 5261–5271.
- [6] F. Danhier, To exploit the tumor microenvironment: since the EPR effect fails in the clinic, what is the future of nanomedicine? *J. Control. Release* 244 (2016) 108–121.
- [7] K. Tomoda, T. Ohkoshi, T. Nakajima, K. Makino, Preparation and properties of inhalable nanocomposite particles: effects of the size, weight ratio of the primary nanoparticles in nanocomposite particles and temperature at a spray-dryer inlet upon properties of nanocomposite particles, *Colloids Surf. B Biointerfaces* 64 (2008) 70–76.
- [8] H.M. Abdelaziz, M. Gaber, M.M. Abd-Elwakil, M.T. Mabrouk, M.M. Elgohary, N.M. Kamel, D.M. Kabary, M.S. Freag, M.W. Samaha, S.M. Mortada, K.A. Elkhodairy, J.Y. Fang, A.O. Elzoghby, Inhalable particulate drug delivery systems for lung cancer therapy: nanoparticles, microparticles, nanocomposites and nanoaggregates, *J. Control. Release* 269 (2017) 374–392.
- [9] N. Labiris, M. Dolovich, Pulmonary drug delivery. Part II: the role of inhalant delivery devices and drug formulations in therapeutic effectiveness of aerosolized medications, *Brit. J. Clin. Pharmacol.* 56 (2003) 600–612.
- [10] S. Azarmi, X. Tao, H. Chen, Z. Wang, W.H. Finlay, R. Löbenberg, W.H. Roa, Formulation and cytotoxicity of doxorubicin nanoparticles carried by dry powder aerosol particles, *Int. J. Pharm.* 319 (2006) 155–161.
- [11] K. Berkenfeld, A. Lamprecht, J.T. McConville, Devices for dry powder drug delivery to the lung, *AAPS PharmSciTech* 16 (2015) 479–490.
- [12] J.E.N. Dolatabadi, Y. Omid, Solid lipid-based nanocarriers as efficient targeted drug and gene delivery systems, *TrAC Trends Anal. Chem.* 77 (2016) 100–108.
- [13] A.O. Elzoghby, S.A. El-Lakany, M.W. Helmy, M.M. Abu-Serie, N.A. Elgindy, Shell-crosslinked zein nanocapsules for oral codelivery of exemestane and resveratrol in breast cancer therapy, *Nanomedicine* 12 (2017) 2785–2805.
- [14] P. Parhi, C. Mohanty, S.K. Sahoo, Nanotechnology-based combinational drug delivery: an emerging approach for cancer therapy, *Drug Disc. Today* 17 (2012) 1044–1052.
- [15] S.W. El-Far, M.W. Helmy, S.N. Khattab, A.A. Bekhit, A.A. Hussein, A.O. Elzoghby, Phytosomal bilayer-enveloped casein micelles for codelivery of monascus yellow pigments and resveratrol to breast cancer, *Nanomedicine* 13 (5) (2018) 481–499.
- [16] S. Sengupta, D. Eavarone, I. Capila, G. Zhao, N. Watson, T. Kiziltepe, R. Sasisekharan, Temporal targeting of tumour cells and neovasculature with a nanoscale delivery system, *Nature* 436 (2005) 568–572.
- [17] J.Y. Choi, T. Ramasamy, S.Y. Kim, J. Kim, S.K. Ku, Y.S. Youn, J.R. Kim, J.H. Jeong, H.G. Choi, C.S. Yong, J.O. Kim, PEGylated lipid bilayer-supported mesoporous silica nanoparticle composite for synergistic co-delivery of axitinib and celestrol in multi-targeted cancer therapy, *Acta Biomater.* 39 (2016) 94–105.
- [18] S.K. Pal, R.A. Figlin, K.L. Reckamp, The role of targeting mammalian target of rapamycin in lung cancer, *Clin. Lung Cancer* 9 (2008) 340–345.
- [19] S.K. Katiyar, S.M. Meeran, N. Katiyar, S. Akhtar, p53 cooperates berberine-induced growth inhibition and apoptosis of non-small cell human lung cancer cells in vitro and tumor xenograft growth in vivo, *Mol. Carcinogen.* 48 (2009) 24–37.
- [20] R. Yu, Z.-Q. Zhang, B. Wang, H.-X. Jiang, L. Cheng, L.-M. Shen, Berberine-induced apoptotic and autophagic death of HepG2 cells requires AMPK activation, *Cancer Cell Int.* 14 (2014) 49.
- [21] N. Guo, A. Yan, X. Gao, Y. Chen, X. He, Z. Hu, M. Mi, X. Tang, X. Gou, Berberine sensitizes rapamycin-mediated human hepatoma cell death in vitro, *Mol. Med. Rep.* 10 (2014) 3132–3138.
- [22] S. Sun, N. Liang, Y. Kawashima, D. Xia, F. Cui, Hydrophobic ion pairing of an insulin-sodium deoxycholate complex for oral delivery of insulin, *Int. J. Nanomed.* 6 (2011) 3049.
- [23] W. Mehnert, K. Mäder, Solid lipid nanoparticles: production, characterization and applications, *Adv. Drug Deliv. Rev.* 47 (2001) 165–196.
- [24] L.P. Mendes, M.P.N. Gaeti, P.H.M. De Ávila, M. de Sousa Vieira, B. dos Santos Rodrigues, R.I. de Ávila Marcelino, L.C.R. Dos Santos, M.C. Valadares, E.M. Lima, Multicompartmental nanoparticles for co-encapsulation and multimodal drug delivery to tumor cells and neovasculature, *Pharm. Res.* 31 (2014) 1106–1119.
- [25] A.O. Elzoghby, S.K. Mostafa, M.W. Helmy, M.A. ElDemellawy, S.A. Sheweita, Superiority of aromatase inhibitor and cyclooxygenase-2 inhibitor combined delivery: hyaluronate-targeted versus PEGylated protamine nanocapsules for breast cancer therapy, *Int. J. Pharm.* 529 (2017) 178–192.
- [26] T. Ramasamy, T.H. Tran, J.Y. Choi, H.J. Cho, J.H. Kim, C.S. Yong, H.-G. Choi, J.O. Kim, Layer-by-layer coated lipid-polymer hybrid nanoparticles designed for use in anticancer drug delivery, *Carbohydr. Polym.* 102 (2014) 653–661.
- [27] S.N. Khattab, S.E.A. Naim, M. El-Sayed, A.A. El Bardan, A.O. Elzoghby, A.A. Bekhit, A. El-Faham, Design and synthesis of new s-triazine polymers and their application as nanoparticulate drug delivery systems, *New J. Chem.* 40 (2016) 9565–9578.
- [28] I. Rivolta, A. Panariti, B. Lettieri, S. Sesana, P. Gasco, M. Gasco, M. Masserini, G. Misericocchi, Cellular uptake of coumarin-6 as a model drug loaded in solid lipid nanoparticles, *J. Physiol. Pharmacol.* 62 (2011) 45.
- [29] A.O. Elzoghby, B.Z. Vranic, W.M. Samy, N.A. Elgindy, Swellable floating tablet based on spray-dried casein nanoparticles: near-infrared spectral characterization and floating matrix evaluation, *Int. J. Pharm.* 491 (2015) 113–122.
- [30] K.E. Gurley, R.D. Moser, C.J. Kemp, Induction of lung tumors in mice with ur-ethane, *Cold Spring Harbor Protoc.* 2015 (2015) (pdb. prot077446).
- [31] A. Semalty, M. Semalty, D. Singh, M. Rawat, Development and characterization of aspirin-phospholipid complex for improved drug delivery, *Int. J. Pharm. Sci. Nanotechnol.* 3 (2010) 940–947.
- [32] M.S. Freag, W.M. Saleh, O.Y. Abdallah, Self-assembled phospholipid-based phytosomal nanocarriers as promising platforms for improving oral bioavailability of the anticancer celestrol, *Int. J. Pharm.* 535 (1–2) (2017) 18–26.
- [33] A. Semalty, M. Semalty, B.S. Rawat, D. Singh, M. Rawat, Pharmacosomes: the lipid-based new drug delivery system, *Expert Opin. Drug Deliv.* 6 (2009) 599–612.
- [34] A.O. Elzoghby, S.K. Mostafa, M.W. Helmy, M.A. ElDemellawy, S.A. Sheweita, Multi-reservoir phospholipid shell encapsulating protamine nanocapsules for co-delivery of letrozole and celecoxib in breast cancer therapy, *Pharm. Res.* 34 (2017) 1956–1969.
- [35] J. Khan, A. Alexander, S. Saraf, S. Saraf, Recent advances and future prospects of phyto-phospholipid complexation technique for improving pharmacokinetic profile of plant actives, *J. Contr. Release* 168 (2013) 50–60.
- [36] J. Lin, Q. Cai, Y. Tang, Y. Xu, Q. Wang, T. Li, H. Xu, S. Wang, K. Fan, Z. Liu, PEGylated Lipid bilayer coated mesoporous silica nanoparticles for co-delivery of paclitaxel and curcumin: design, characterization and its cytotoxic effect, *Int. J. Pharm.* 536 (1) (2017) 272–282.
- [37] A. Elzoghby, Editorial (Thematic Issue: Nanocarriers Based on Natural Polymers as Platforms for Drug and Gene Delivery Applications), *Curr. Pharm. Des.* 22 (2016) 3303–3304.
- [38] M.S. Freag, W.M. Saleh, O.Y. Abdallah, Laminated chitosan-based composite sponges for transmucosal delivery of novel protamine-decorated tripterine phytosomes: ex-vivo mucopenetration and in-vivo pharmacokinetic assessments, *Carbohydr. Polym.* 188 (2018) 108–120.
- [39] D.M. Kabary, M.W. Helmy, K.A. Elkhodairy, J.-Y. Fang, A.O. Elzoghby, Hyaluronate/lactoferrin layer-by-layer-coated lipid nanocarriers for targeted co-delivery of rapamycin and berberine to lung carcinoma, *Colloids Surf. B Biointerfaces* 169 (2018) 183–194.
- [40] M.S. Freag, Hyaluronate-lipid nano-hybrids: fruitful harmony in cancer targeting, *Curr. Pharm. Des.* 23 (2017) 5283–5291.
- [41] M. Alamgeer, D.N. Watkins, I. Banakh, B. Kumar, D.J. Gough, B. Markman, V. Ganju, A phase IIa study of HA-irinotecan, formulation of hyaluronic acid and irinotecan targeting CD44 in extensive-stage small cell lung cancer, *Invest. New Drugs* 36 (2018) 288–298.
- [42] M. Vidgren, A. Kärkkäinen, P. Karjalainen, P. Paronen, J. Nuutinen, Effect of powder inhaler design on drug deposition in the respiratory tract, *Int. J. Pharm.* 42 (1988) 211–216.
- [43] M.I. Ré, Microencapsulation by spray drying, *Dry. Technol.* 16 (1998) 1195–1236.
- [44] Z. Bakhtyari, J. Barar, A. Aghanejad, A.A. Saei, E. Nemati, J. Ezzati Nazhad Dolatabadi, Y. Omid, Microparticles containing erlotinib-loaded solid lipid nanoparticles for treatment of non-small cell lung cancer, *Drug Dev. Ind. Pharm.* (2017) 1–10.
- [45] J.G. Weers, T.E. Tarara, A.R. Clark, Design of fine particles for pulmonary drug delivery, *Expert Opin. Drug Deliv.* 4 (2007) 297–313.
- [46] R.G. Costa, K. Andreola, R. de Andrade Mattietto, L.J.G. de Faria, O.P. Taranto, Effect of operating conditions on the yield and quality of açai (Euterpe oleracea Mart.) powder produced in spouted bed, *LWT-Food Sci. Technol.* 64 (2015) 1196–1203.
- [47] T. Sou, M.P. McIntosh, L.M. Kaminskas, R.J. Prankerd, D.A. Morton, Designing a multicomponent spray-dried formulation platform for pulmonary delivery of biomacromolecules: the effect of polymers on the formation of an amorphous matrix for glassy state stabilization of biomacromolecules, *Dry. Technol.* 31 (2013) 1451–1458.
- [48] J. Gliński, G. Chavepeyer, J.-K. Platten, Surface properties of aqueous solutions of L-leucine, *Biophys. Chem.* 84 (2000) 99–103.
- [49] H. Shiga, H. Joreau, T.L. Neoh, T. Furuta, H. Yoshii, Encapsulation of alcohol dehydrogenase in mannitol by spray drying, *Pharmaceutics* 6 (2014) 185–194.
- [50] T. Sou, R.T. Forbes, J. Gray, R.J. Prankerd, L.M. Kaminskas, M.P. McIntosh, D.A. Morton, Designing a multi-component spray-dried formulation platform for



- pulmonary delivery of biopharmaceuticals: the use of polyol, disaccharide, polysaccharide and synthetic polymer to modify solid-state properties for glassy stabilisation, *Powder Technol.* 287 (2016) 248–255.
- [51] S. Schüle, W. Frieß, K. Bechtold-Peters, P. Garidel, Conformational analysis of protein secondary structure during spray-drying of antibody/mannitol formulations, *Eur. J. Pharm. Biopharm.* 65 (2007) 1–9.
- [52] P.S. Pourshahab, K. Gilani, E. Moazeni, H. Eslahi, M.R. Fazeli, H. Jamalifar, Preparation and characterization of spray dried inhalable powders containing chitosan nanoparticles for pulmonary delivery of isoniazid, *J. Microencapsul.* 28 (2011) 605–613.
- [53] N. Shetty, L. Zeng, S. Mangal, H. Nie, M.R. Rowles, R. Guo, Y. Han, J.H. Park, Q.T. Zhou, Effects of moisture-induced crystallization on the aerosol performance of spray dried amorphous ciprofloxacin powder formulations, *Pharm. Res.* 35 (2018) 7.
- [54] J. Ezzati Nazhad Dolatabadi, H. Hamishehkar, H. Valizadeh, Development of dry powder inhaler formulation loaded with alendronate solid lipid nanoparticles: solid-state characterization and aerosol dispersion performance, *Drug Develop. Ind. Pharm.* 41 (2015) 1431–1437.
- [55] L. De Backer, K. Braeckmans, M.C. Stuart, J. Demeester, S.C. De Smedt, K. Raemdonck, Bio-inspired pulmonary surfactant-modified nanogels: a promising siRNA delivery system, *J. Control. Release* 206 (2015) 177–186.
- [56] M. Guba, P. von Breitenbuch, M. Steinbauer, G. Koehl, S. Flegel, M. Hornung, C.J. Bruns, C. Zuelke, S. Farkas, M. Anthuber, Rapamycin inhibits primary and metastatic tumor growth by antiangiogenesis: involvement of vascular endothelial growth factor, *Nat. Med.* 8 (2002) 128–135.
- [57] T. Hamsa, G. Kuttan, Antiangiogenic activity of berberine is mediated through the downregulation of hypoxia-inducible factor-1, VEGF, and proinflammatory mediators, *Drug Chem. Toxicol.* 35 (2012) 57–70.
- [58] L. Xu, X. Zheng, Y. Wang, Q. Fan, M. Zhang, R. Li, J. Ye, X. Wu, W. Zhao, Y. Zhang, Berberine protects acute liver failure in mice through inhibiting inflammation and mitochondria-dependent apoptosis, *Eur. J. Pharmacol.* 819 (2018) 161–168.
- [59] S.A. Sabra, A.O. Elzoghby, S.A. Sheweita, M. Haroun, M.W. Helmy, M.A. Eldemellawy, Y. Xia, D. Goodale, A.L. Allan, S. Rohani, Self-assembled amphiphilic zein-lactoferrin micelles for tumor targeted co-delivery of rapamycin and wogonin to breast cancer, *Eur. J. Pharm. Biopharm.* 128 (2018) 156–169.





# Hyaluronate/lactoferrin layer-by-layer-coated lipid nanocarriers for targeted co-delivery of rapamycin and berberine to lung carcinoma

Dalia M. Kabary<sup>a,b,c</sup>, Maged W. Helmy<sup>a,d</sup>, Kadria A. Elkhodairy<sup>a,b</sup>, Jia-You Fang<sup>e,f,g</sup>, Ahmed O. Elzoghby<sup>a,b,h,\*</sup>

<sup>a</sup> Cancer Nanotechnology Research Laboratory (CNRL), Faculty of Pharmacy, Alexandria University, Alexandria, 21521, Egypt

<sup>b</sup> Department of Industrial Pharmacy, Faculty of Pharmacy, Alexandria University, Alexandria, 21521, Egypt

<sup>c</sup> Department of Pharmaceutics, Faculty of Pharmacy and Drug Manufacturing, Pharos University in Alexandria, Egypt

<sup>d</sup> Department of Pharmacology and Toxicology, Faculty of Pharmacy, Damanhour University, Behira, Egypt

<sup>e</sup> Pharmaceutics Laboratory, Graduate Institute of Natural Products, Chang Gung University, Taoyuan, 333, Taiwan

<sup>f</sup> Research Center for Industry of Human Ecology and Research Center for Chinese Herbal Medicine, Chang Gung University of Science and Technology, Kweishan, Taoyuan, 333, Taiwan

<sup>g</sup> Department of Anesthesiology, Chang Gung Memorial Hospital, Kweishan, Taoyuan, 333, Taiwan

<sup>h</sup> Division of Engineering in Medicine, Brigham and Women's Hospital, Harvard Medical School, Boston, MA, 02115, USA

## ARTICLE INFO

### Article history:

Received 13 February 2018

Received in revised form 2 May 2018

Accepted 3 May 2018

### Keywords:

Layer-by-layer nanoparticles  
Hyaluronate targeting  
Lactoferrin targeting  
Rapamycin  
Berberine  
Hydrophobic ion pair  
Lung cancer

## ABSTRACT

The self-tumor targeting polymers, lactoferrin (LF) and hyaluronic acid (HA) were utilized to develop layer-by-layer (LbL) lipid nanoparticles (NPs) for dual delivery of berberine (BER) and rapamycin (RAP) to lung cancer. To control its release from the NPs, BER was hydrophobically ion paired with SLS prior to incorporation into NPs. Spherical HA/LF-LbL-RAP-BER/SLS-NPs 250.5 nm in diameter, with a surface charge of  $-18.5$  mV were successfully elaborated. The NPs exhibited sequential release pattern with faster release of BER followed by controlled release of RAP which enables sensitization of lung tumor cells to the anti-cancer action of RAP. LbL coating of the NPs was found to enhance the drug cytotoxicity against A549 lung cancer cells as augmented by remarkable increase in their cellular internalization through CD44 receptors overexpressed by tumor cells. *In vivo* studies in lung cancer bearing mice have revealed the superior therapeutic activity of LbL-RAP-BER/SLS-NPs over the free drugs as demonstrated by 88.09% reduction in the average number of microscopic lung foci and 3.1-fold reduction of the angiogenic factor VEGF level compared to positive control. Overall, the developed HA/LF-LbL-coated lipid NPs could be potential carriers for targeted co-delivery of BER and RAP to lung cancer cells.

© 2018 Elsevier B.V. All rights reserved.

## 1. Introduction

Lung cancer is one of the major causes of cancer-associated mortality with about 23% of total cancer related mortality [1]. The nanoparticles (NPs) have the ability to encapsulate therapeutics and release them in a controlled manner to specifically target cells, facilitate intracellular uptake and improve the solubility of poorly soluble drugs [2,3]. Although lipid NPs are characterized by their ability to carry both hydrophilic and lipophilic drugs with a high drug payload, their use is associated with burst or premature drug

release *in vivo*, mainly because the particles tend to crystallize and expel the drug from their cores. In addition, lipid NPs may be rapidly removed from circulation via the reticulo-endothelial system (RES) [4]. Therefore, to use lipid NPs for efficient tumor-targeted drug delivery, it will be necessary to overcome their limitations by enabling controlled drug release and surface modification.

Among surface modification approaches, layer-by-layer (LbL) self-assembly proves its flexibility and simplicity, as it is usually carried out in aqueous medium and does not entail drastic conditions. LbL assembly technique relies on electrostatic deposition of oppositely charged polyelectrolytes on the nanocarrier surface [5]. The LbL construction, mainly using hydrophilic polymers including proteins and polysaccharides, can delay RES clearance, prolong blood circulation and facilitate enhanced permeation and retention (EPR)-based passive diffusion of nanocarriers in interstitial tumors [6]. Additionally, the fact that the layering material is, itself, a targeting moiety could enhance the targeting ability of

\* Corresponding author at: Division of Engineering in Medicine, Department of Medicine, Brigham and Women's Hospital, Harvard Medical School, Boston, MA, 02115, USA.

E-mail addresses: [aelzoghby@bwh.harvard.edu](mailto:aelzoghby@bwh.harvard.edu), [ahmed.elzoghby@alexu.edu.eg](mailto:ahmed.elzoghby@alexu.edu.eg) (A.O. Elzoghby).

these structures. Recently, protein–polysaccharide LbL assembled nanocarriers have drawn great interest for tumor-targeted drug delivery by virtue of their biocompatibility, minimal opsonization and easy functionalization [7]. Lactoferrin (LF) is a cationic protein with essential role in iron transportation, in addition to its anti-viral, anti-inflammatory, and anti-cancer activity. It was found that bovine LF tends to inhibit esophagus and lung carcinogenesis at very low doses [8]. Moreover, LF can bind to transferrin receptor (TfR) and LDL receptors overexpressed on various cancer cells including breast, colon, nasopharyngeal and lung [9]. On the other hand, hyaluronic acid (HA) is one of the most commonly used anionic polysaccharides in targeted anti-cancer drug delivery via its inherent ability to bind with CD44 receptors overexpressed on tumor cells including lung cancer cells [10,11].

Rapamycin (RAP), a macrolide lactone with antifungal and immunosuppressant actions, was found to inhibit the mTOR pathway that regulates a number of cellular signals and mitogenic growth factors leading to impaired cancer cell metabolism [12]. However, the extremely lipophilic nature (partition coefficient 3.58) of RAP and hence poor aqueous solubility (2.6 µg/ml) and low oral bioavailability (about 17%) handicaps its parenteral administration and requires use of high amounts of solvents such as DMSO, PEG 400 and ethanol that may cause kidney injury and liver damage [12]. Additionally, RAP is unstable in electrolyte solutions and shown to be sensitive to both acids and bases, resulting in ring fragmentation and degradation. Moreover, its serious nephrotoxicity and hyperglycemic effect limit its clinical application [13].

On the other hand, berberine (BER), a quaternary isoquinoline alkaloid present in many medicinal herbs, displayed antimicrobial, anti-inflammatory and anti-cancer properties [14]. BER could inhibit the growth and invasion ability of H460 and A549 lung cancer cells at a relatively low IC<sub>50</sub> through a cell cycle arrest at the G0/G1 phase [15]. However, the clinical application of this compound has encountered several challenges, particularly in vivo, largely due to its low gastro-intestinal absorption, and rapid metabolism by CYP 450-dependent processes [16]. Thus, a potential solution to overcome the obstacles hindering the use of both drugs, RAP and BER, is to utilize nanoparticulate formulations for their tumor-targeted delivery.

While the inhibition of mTOR pathway by RAP and its analogs constitutes an outstanding anti-cancer target, RAP-induced immunosuppression represents a challenge facing its clinical application in cancer therapy [17]. On another avenue, BER was found to inhibit the proliferation of hepatocellular carcinoma cells (HCC) mediated by blocking the mTOR pathway via AMPK activation [18]. Accordingly, co-treatment of HepG2 cells with BER and RAP showed synergistic cytotoxicity where BER could maintain the cytotoxic action of RAP at a lower concentration. Thus, BER may reduce the RAP-associated immunosuppression by allowing its use in a lower dose [17]. Therefore, we hypothesize that a nanocarrier for combined delivery of both RAP and BER would benefit from: (a) the powerful anti-cancer action of RAP, (b) the synergistic mTOR inhibiting activity of BER, and (c) the broad anti-cancer activity of BER mediated via multiple mechanisms other than mTOR blocking.

Therefore, in this study, we propose for the first time up to our knowledge, HA/LF-LbL-coated lipid NPs for combined delivery of RAP and BER to lung cancer. **First**, to enable parenteral delivery of BER and RAP, both drugs were co-encapsulated into the lipid core by oil-in-water emulsification to elaborate lipid NPs. **Second**, to enhance its loading and overcome its relatively fast release, BER was pre-formulated as hydrophobic ion pair (HIP) with sodium lauryl sulfate or sodium deoxycholate. **Finally**, to reduce RES clearance of the NPs and enable active tumor-targeting, the RAP-BER/SLS-loaded lipid core NPs were coated with oppositely charged layers of cationic lactoferrin (LF) and anionic hyaluronic acid (HA) via LbL assembly to enhance their internalization into lung cancer cells via

binding to LDL or CD44 receptors overexpressed by human lung cancer cells. The developed delivery system was thoroughly investigated *in vitro* and *in vivo* to prove the anti-tumor superiority of the combined drug nano-delivery compared with the free drug combination.

## 2. Materials and methods

### 2.1. Materials

Berberine chloride hydrate (BER), sodium deoxycholate (SDC), Fetal bovine serum (FBS), Triton X100, coumarin-6, 3-(4,5-dimethylthiazol-2-yl)-2,5-diphenyltetrazolium bromide (MTT), urethane (ethyl carbamate), Dulbecco's modified eagle medium (DMEM), trypsin-EDTA, Canada balsam, Haematoxylin solution, and Eosin solution (H&E) were purchased from Sigma-Aldrich (St. Louis, USA). Rapamycin (RAP), purity 98% was purchased from Jianshi Yuantong Bioengineering Co., Ltd. (China). Hyaluronic acid (HA) was purchased from Baoding Faithful Industry Co., Ltd. (China). Lactoferrin (Lf) was kindly donated by Westland Milk Products (Hokitika, New Zealand). Phosphatidylcholine (Lipoid S75) was kindly provided by Lipoid (Ludwigshafen, Germany). Glyceryl monostearate (GMS) was a gift from Gattefosse (Lyon, France). Poly(ethylene glycol) 400, sodium lauryl sulfate (SLS), ethanol, and methanol were purchased from ADWIC (Cairo, Egypt). Polyoxyethylene sorbitan monooleate (Tween 80) was obtained from (Riedel de H#XPS##x00E4;en, Germany). Acetonitrile and Methanol HPLC grade were purchased from JT Baker (NJ, USA).

### 2.2. Preparation of BER-hydrophobic ion pair (BER-HIP)

The BER-HIP complex was prepared by the ionic interaction of BER and SLS or SDC under aqueous conditions. Briefly, 25 mg BER was dissolved in distilled water. The aqueous solution of SLS or SDC as ion pairing agents was added dropwise to BER solution under gentle magnetic stirring till the appearance of strong turbidity indicating the complex formation which was then left for 30 min under gentle magnetic stirring [19]. The HIP complex was formed spontaneously upon mixing of both aqueous solutions in 1:1 molar ratio. The solutions were then centrifuged for 45 min at 17000 rpm (3K-30 centrifuge, Sigma laboratory, Germany) and the sediment complex was lyophilized at –80 °C with LyoQuest lyophilizer (Telstar, Spain) to obtain dry powders. The concentration of non-complexed BER was determined in the supernatant by HPLC analysis and detailed in Supplementary Material. The solubility and partition coefficient of BER and BER-HIP complexes were determined as previously reported [20] and detailed in Supplementary Material.

### 2.3. Preparation of dual RAP/BER-loaded lipid NPs

BER-loaded NPs were prepared by the hot homogenization method [21]. First, oily phase (100 mg GMS) was heated to 70 °C at shaking water bath (Maxturdy 30, DAIHAN Scientific, South Korea). 10 mg of BER or equivalent amount of BER-HIP complex was added to the melted lipid phase. Keeping the temperature at 70 °C, 50 ml aqueous phase containing 100 mg Tween 80 was added into the oily phase under agitation at 12000 rpm for 5 min using Ultra Turrax T-25 homogenizer (Ika Labortechnik, Germany). This emulsion was cooled to the room temperature upon magnetic stirring for 30 min. For preparation of dual drug (RAP/BER)-loaded NPs, 10 mg of RAP along with BER-HIP eq. to 10 mg were added to the melted lipid phase and completed in the same method mentioned above.

#### 2.4. Preparation of HA/LF-LbL-coated dual RAP/BER-loaded NPs

To prepare the LbL-coated BER/RAP-NPs, 12.5 ml of the negatively charged BER/RAP-NPs containing 5 mg RAP and 5 mg BER were titrated with different volume ratios of a cationic LF aqueous solution (10 mg/ml) under gentle stirring. The mixture was then incubated for further 30 min under mild stirring. Anionic HA aqueous solution (0.5 mg/ml) was then added dropwise under gentle stirring to the positively charged LF-coated NPs, thus forming LbL-BER/RAP-NPs.

#### 2.5. Physicochemical characterization of NPs

The methodologies for assessing drug loading, nanoparticle size, surface charge, drug release, morphology, stability, redispersibility, hemolytic and serum stability were performed as described previously [22–24] and detailed in the Supplementary Material.

#### 2.6. Chemical stability of RAP

Chemical stability of RAP in PBS (10 mM, pH 7.4) was investigated to study effect of nano-encapsulation on RAP stability. Free RAP and nano-formulated RAP (RAP-NPs) at a fixed concentration (40 µg/ml) were incubated in PBS (10 mM, pH 7.4) at a total volume of 10 ml solution in a shaking water bath (100 rpm, 37 °C). Samples were protected from light to avoid any other factors that may induce RAP degradation. A mixture of ethanol (final concentration; 4% v/v), PEG 400 (final concentration; 5% v/v) and Tween 80 (final concentration; 5% v/v) was used to aid dissolving free RAP in PBS. At predetermined time points, 0.2 ml of solutions (either nano-formulated or free RAP) was withdrawn and added to 0.4 ml ethanol then subjected to HPLC analysis.

#### 2.7. In vitro cytotoxicity and uptake studies

The in vitro cytotoxicity of free RAP, free BER, free RAP/BER solution and RAP/BER-dual loaded NPs against A549 lung cancer cells was evaluated by MTT assay [25]. The internalization of nanocarriers into lung cancer cells was studied by confocal microscopy using coumarin-6 as a fluorescent probe (Methodology details of cytotoxicity and uptake tests are illustrated in Supplementary Material).

#### 2.8. In vivo studies

##### 2.8.1. Animals

According to an institutionally approved animal protocol, 5–6 weeks old male Albino mice (15–20 g) were maintained in a maximum isolation environment. (Details of animal protocol are illustrated in Supplementary Material).

##### 2.8.2. Induction of tumor

Tumors were induced by a single i.p. injection of 1 g/kg urethane dissolved in 0.9% NaCl, followed by a booster dose of 0.5 g/kg urethane after 15 days [26]. These mice were under observation for 12–14 weeks as expected time of induction of lung cancer.

##### 2.8.3. In vivo anti-tumor efficacy

The animal studies were performed using 12–16 weeks male Albino mice with chemically-induced lung carcinoma. The mice were randomly divided into 4 groups (six mice in each group) including (a) positive control (untreated lung carcinoma bearing mice), (b) free combined BER/RAP in a co-solvent solution (4% ethanol, 5% PEG 400 and 5% Tween 80), (c) HA/LF-LbL-RAP-BER/SLS-NPs treated group and (d) negative control (healthy mice receiving saline). Lung cancer bearing mice were injected via the tail vein with the drug-loaded NPs or free drugs eq. to 1.5 mg/kg RAP and

1.5 mg/kg BER three times per week for two weeks. All the surviving animals were sacrificed after 21 days. The excised lungs were isolated, weighed, morphologically examined.

#### 2.8.4. Quantification of angiogenic and apoptotic markers

The tumor growth biomarkers were determined quantitatively using ELISA. The experimental method is detailed in the Supplementary Material.

#### 2.8.5. Histopathological and immunohistochemical analysis

The tumor samples were examined for histopathological changes as well as tumor proliferation extent [27]. The experimental method is detailed in the Supplementary Material.

#### 2.9. Statistical analyses

Data analysis is detailed in the **Supplementary Material**.

### 3. Results and discussion

#### 3.1. Fabrication and characterization of BER-HIP complexes

Controlled release of water soluble drugs from nanoparticles is a great challenge. A number of approaches have been exploited to develop nanocarriers for prolonged release of water soluble drugs such as chemical crosslinking and hydrophobic ion pairing (HIP) [28]. Therefore, in this study, an attempt was carried out to retard the release of the water soluble drug, BER hydrochloride from lipid nanocarriers by formation of HIP complex [29]. Therefore, the quaternary ammonium group of BER was exploited for the formation of HIP complex with the negatively charged carboxyl group of SDC or sulfate group of SLS at 1:1 molar ratio.

The complexation efficiency of BER reached almost 100% in BER/SLS complex compared to only  $33.62 \pm 3.5\%$  in BER/SDC complex. The formed HIP complexes have acquired negative charge of  $-19.9 \pm 1.2$  and  $-27.1 \pm 2.3$  mV for BER/SLS and BER/SDC complexes, respectively. BER hydrochloride is a water soluble drug, with aqueous solubility of 0.71 mg/ml, while the aqueous solubilities of the BER/SLS and BER/SDC HIP complexes were significantly reduced to 0.007 and 0.170 mg/ml, respectively (Table S1). Furthermore, BER hydrochloride exhibited a very low partition coefficient ( $\log P = -1.54 \pm 0.013$ ), suggesting that the drug is hydrophilic in nature which is in agreement with previous literature [16]. The anionic HIP agents significantly increased the partitioning of BER into the more lipophilic 1-octanol phase. In this regard, SLS was better than SDC where the Log P value for BER/SDC and BER/SLS HIP complexes was found to be  $0.278 \pm 0.009$  and  $1.313 \pm 0.011$ , respectively (Table S1, Fig. S1). BER/SDC forms less hydrophobic complex may be because it forms a weaker ionic complex compared to BER/SLS. The rigid steroidal skeleton of SDC may induce steric hindrance against access of the negatively charged carboxylate group of SDC to the positively charged quaternary ammonium group in BER which may weaken the ion-pair formation.

#### 3.2. Characterization of BER- and BER/HIP-loaded NPs

In this study, BER-loaded lipid based nano-system was developed by hot homogenization method (Fig. 1). First, the NPs were prepared using glyceryl monostearate (GMS) and Tween 80, for efficient incorporation and persistent release of BER. The mean particle size of BER-loaded NPs was  $170.1 \pm 4.4$  nm, which is a little higher than blank NPs ( $164.3 \pm 3.6$  nm) which might confirm the entrapment of free BER into NPs (Table 1). On the other hand, the zeta potential of BER-loaded NPs was  $-21.7 \pm 0.45$  mV indicating a good colloidal stability. BER was successfully encapsulated into NPs with EE of  $78.3 \pm 3.5\%$  w/w.

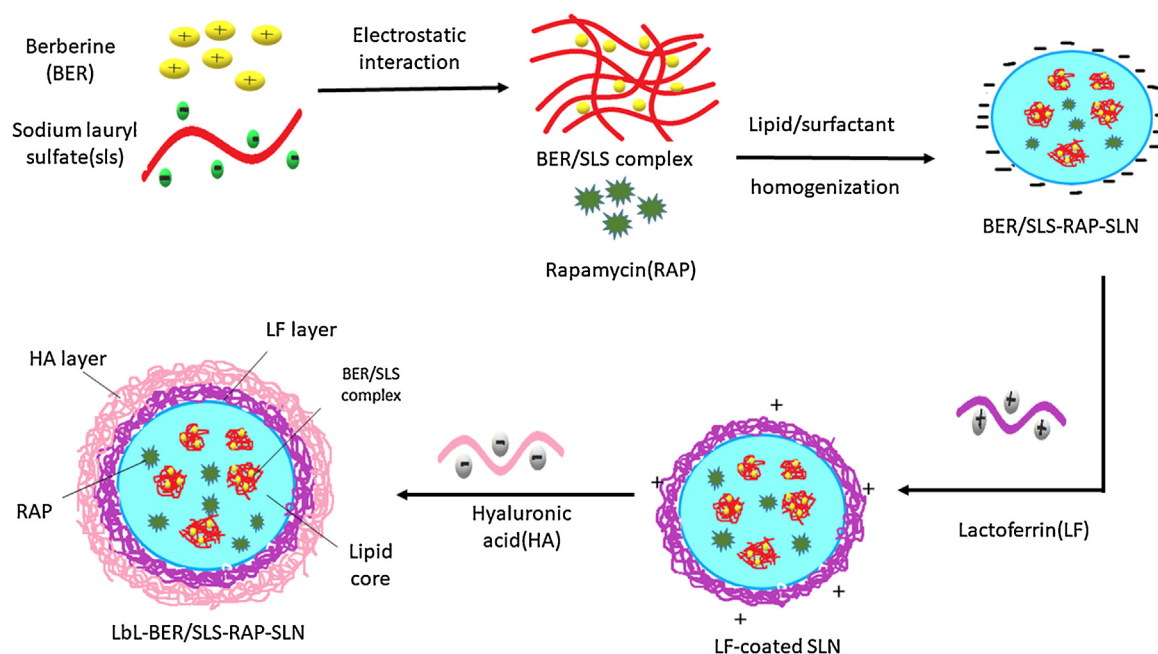


Fig. 1. Diagram illustrating the preparation steps of LbL-RAP-BER/SLS-NPs (F9).

**Table 1**  
Composition and physiochemical characteristics of blank, BER-NPs & BER-RAP-NPs.

	Formula	Particle Size (nm)	PDI	Zeta potential (mV)	EE (%)	DL (%)
F1	Blank NPs	164.3 ± 3.6	0.29 ± 0.025	−22.4 ± 0.54	–	–
F2	Blank LbL-NPs	210.2 ± 6.8	0.265 ± 0.02	−18.7 ± 0.7	–	–
F3	BER-NPs	170.1 ± 4.4	0.24 ± 0.01	−21.7 ± 0.45	78.3 ± 3.5	6.922 ± 0.06
F4	BER/SDC-NPs	175.6 ± 6.1	0.369 ± 0.05	−19.5 ± 0.65	84.3 ± 2.6	7.79 ± 0.22
F5	BER/SLS-NPs	168.9 ± 5.1	0.308 ± 0.05	−26.8 ± 0.41	93.5 ± 3.1	8.59 ± 0.4
F6	LbL-BER/SLS-NPs	233.0 ± 6.4	0.20 ± 0.011	−19.7 ± 0.32	89.1 ± 2.7	6.23 ± 0.23
F7	RAP-NPs	174.2 ± 5.1	0.21 ± 0.016	−17.8 ± 0.55	98.75 ± 0.54	9.18 ± 0.2
F8	RAP-BER/SLS-NPs	215.0 ± 7.8	0.25 ± 0.021	−17.4 ± 0.45	BER 93.1 ± 3.5 RAP 98.55 ± 0.4	BER 8.31 ± 0.5 RAP 8.98 ± 0.3
F9	LbL-RAP-BER/SLS-NPs	250.5 ± 7.5	0.255 ± 0.024	−18.5 ± 0.52	BER 88.2 ± 4.3 RAP 98.6 ± 0.32	BER 6.2 ± 0.42 RAP 8.9 ± 0.44

One of the major advantages of HIP complex is to increase the lipophilicity of the hydrophilic molecules. Incorporation of BER/HIP into the lipid NPs was found to increase the drug EE from 78.3 to 84.3% and 93.5% in BER/SDC-NPs and BER/SLS-NPs, respectively (Table 1). The increased EE of BER in into the lipid matrix of NPs could be explained by the enhanced lipophilic characteristics of the drug via ion pairing as illustrated by the solubility and partition coefficient results [30]. These results are in accordance with the increased EE of cationic doxorubicin into lipid NPs from 85.5 to 99.5% upon HIP complexation with dextran sulfate [23].

### 3.3. Characterization of HA/LF-LbL-coated RAP-BER/SLS-NPs

Layer-by-layer self-assembly on preformed NPs was reported as an outstanding approach to provide targeting potential to tumor cells as well as to control drug release by minimizing its initial burst release [31]. Proteins and polysaccharides have drawn much interest for drug delivery because of their natural origin and unique targeting properties [32–34]. In our study, the overall negative charge present on the surface of lipid NPs was exploited for deposition of the cationic protein, LF followed by a layer of the anionic polysaccharide, HA (Fig. 1). To ensure uniform coating of NPs, the amount of polyelectrolytes required to reverse the charge of NPs in each coating step was optimized by simple titration procedure.

By increasing the added volume of LF solution (10 mg/ml) to colloidal solution of the NPs during the assembly process, the size of NPs was increased from 164.3 to 240.1 nm along with a reduction of the negative surface charge from approximately −22.4 to −6.6 mV (Fig. 2A & B). Further increasing of LF volume led to an inflection point (neutralization) after which the zeta-potential was reversed to positive charge (+1.8 mV). However, the NP size was decreased to 195.0 nm. The cationic LF formed an island around the NPs surface that initially grew in size with the successive addition of polymer together with inversion of surface charge, finally resulting in the formation of a stable and much stiffer NP of a smaller size. Upon further addition of LF solution (8 ml), no significant change of surface charge from +1.8 to +2.1 mV was observed that might have indicated that the surface was completely coated with LF [35]. Therefore, 6 ml LF solution (10 mg/ml) was selected as the optimum volume of LF required for coating of 12.5 ml NPs solution resulting in a uniform PS of  $195.30 \pm 2$  nm and surface charge of +1.8 mV. When a second outer anionic layer of HA solution (5 ml; 0.5 mg/ml) was directly assembled on the positively charged LF-coated lipid NPs, an inversion of the zeta potential from +1.8 to −7.3 mV was obtained with a small size decrease from 195.30 to 185.61 nm. Upon addition of 10 ml HA solution, the surface charge was increased to −18.7 mV reflecting higher colloidal stability with only a small increase in particle size (about 15 nm) to reach 210.2 nm (Table 1, Fig. 2C & D). This behavior is explained by the ability of the HA chains



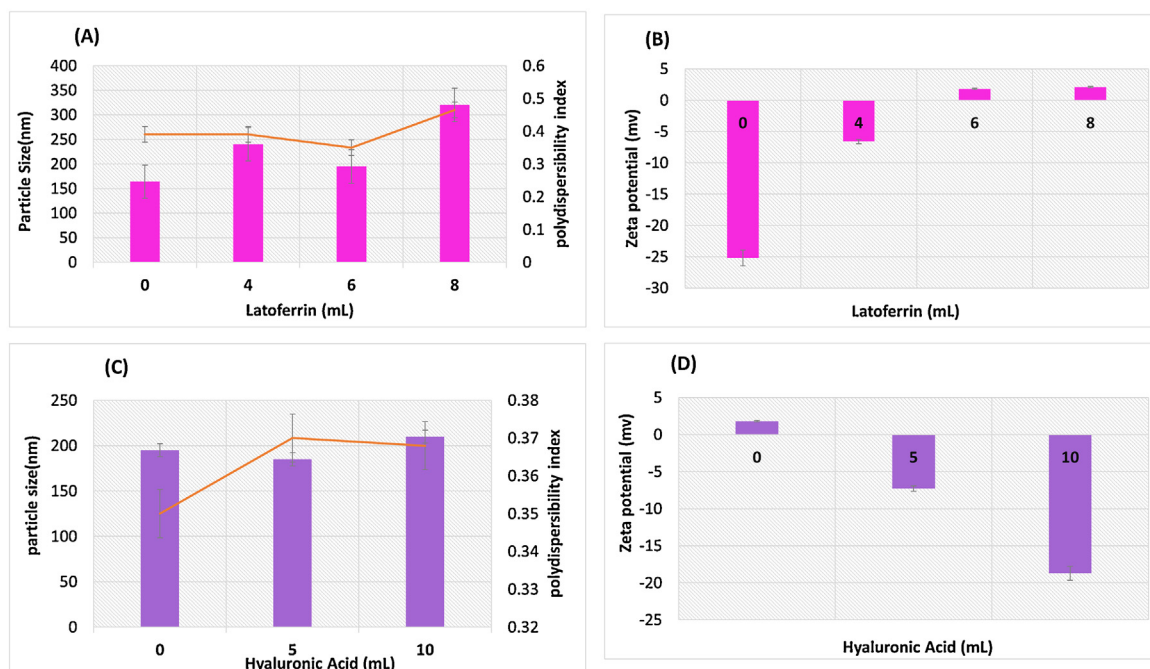


**Fig. 2.** Characterization of NPs during layer-by-layer build-up. Effect of the subsequent deposition of lactoferrin (LF) and hyaluronic acid (HA) on the hydrodynamic size and polydispersity index (A) and (C), corresponding zeta-potential (B) and (D). Data are expressed as mean  $\pm$  SD (n = 3).

to easily diffuse into the previously adsorbed LF layer by virtue of strong electrostatic interactions [23]. Overall, the HA/LF bi-layer deposition increased the thickness of our lipid NPs by  $\sim 46$  nm (from  $\sim 164.3$  nm prior to deposition to  $\sim 210.2$  nm (Table 1). Similarly, coating of lipid NPs with LbL assembly of chitosan and HA resulted in a size increase of 74 nm with a surface charge of  $-12$  mV [23]. Finally, incorporation of both drugs; RAP along with BER/SLS HIP within the lipid NPs resulted in a significant size increase from 210.2 for blank NPs (F2) to 250.5 nm for LbL-RAP-BER/SLS-NPs (F9) with a final surface charge of  $-18.5$  mV. The NPs demonstrated a high loading of both drugs (6.2 and 8.9% for BER and RAP, respectively).

### 3.4. Morphological analysis

TEM imaging of the NPs revealed spherical-shaped NPs with the particle size was consistent with DLS data (Fig. 3A). Overall, the average size of uncoated NPs and LbL-NPs measured by TEM was  $\sim 160$ – $170$  and  $200$ – $210$  nm, compared to 215.0 and 250.5 nm, respectively obtained by DLS. The smaller size obtained by TEM could be explained by the shrinkage occurred during dehydration step prior to microscopical examination [36]. The addition of LF/HA bilayer resulted in the formation of a compact core-shell structure (Fig. 3B). Because of the longitudinal attachment of the polymer chains, there was no clear distinction between the two polymer layers.

### 3.5. Solid state characterization

The DSC thermogram of pure BER and RAP exhibited sharp melting endothermic peaks at  $\sim 191^\circ\text{C}$  for BER and  $186.41$  and  $197.56^\circ\text{C}$  for RAP reflecting their crystallinity (Fig. S2A). After formation of HIP with either SLS and SDC, the BER peak disappeared with the appearance of very small new endothermic peaks at  $202.37$  and  $174^\circ\text{C}$  for BER/SLS and BER/SDC, respectively thus indicating complex formation. Absence of endothermic peaks of RAP in the thermograms of NPs reveals the drug amorphization after insertion into the particles. This phenomenon is thought to promote drug solubility in the lipid melt and hence enables maximum entrap-

ment efficiency [37]. The thermograms of the NPs showed sharp endothermic peak at  $165^\circ\text{C}$  corresponding to melting of mannitol used as a cryoprotectant during lyophilization.

The FTIR spectrum of BER showed its characteristic band at  $1597\text{ cm}^{-1}$  assigned to  $\text{C}=\text{C}$  and  $\text{C}=\text{N}$  stretching vibrations [38]. All the major absorption peaks of BER, including those at  $1507$ ,  $1385$ ,  $1362$ ,  $1340$ ,  $1271$  and  $1232\text{ cm}^{-1}$  were attenuated in the spectra of BER/SLS and BER/SDC HIP complexes (Fig. S2B) [39]. Spectrum of pure SLS depicted bands at  $1216$  and  $1080\text{ cm}^{-1}$  signifying  $\text{S}=\text{O}$  (stretching) vibrational modes of sulfonic group. In the BER/SLS complex spectrum, the first peak was shifted to the low field from  $1216$  to  $1208\text{ cm}^{-1}$ , while the peak at  $1080\text{ cm}^{-1}$  was diminished may be attributed to ionic interactions between amino group of BER and sulfate groups of SLS, resulting in complex formation. Similar results were observed in the spectrum of BER/SDC complex and detailed in Supplementary Results Section. FTIR spectrum of RAP exhibited its characteristic peaks at  $3408\text{ cm}^{-1}$  originating from  $\text{O}-\text{H}$  stretching vibrations,  $2874$  and  $2928\text{ cm}^{-1}$  attributable to  $\text{C}-\text{H}$  stretching vibrations, while the peak at  $1715\text{ cm}^{-1}$  is corresponding to  $\text{C}=\text{O}$  carbonyl stretching. The disappearance or slight shifting of the major peaks of both drugs in the IR spectrum of NPs reflects their successful encapsulation.

### 3.6. In vitro drug release

In contrast to the fast diffusion of BER from free drug solution (100% drug released within 4 h), a biphasic release pattern of BER from NPs (F3) was observed with high initial burst release (nearly 70% of drug released within 2–4 h) followed by controlled drug release up to 8 h. The adsorbed drug on the surface of NPs may account for the fast initial drug release, while the drug entrapped into the lipid core may be responsible for the sustained release pattern [40]. Since, BER has water solubility of  $\sim 1\text{ mg/ml}$  and  $\log P$  of  $-1.54$ , it could not be completely incorporated in the lipid matrix with high portion of drug could partition to the aqueous phase. On the other hand, the NPs prepared using BER-HIP showed a more sustained drug release pattern (Fig. 3C). Complexation of BER with SDC could not significantly decrease the initial burst release of drug from

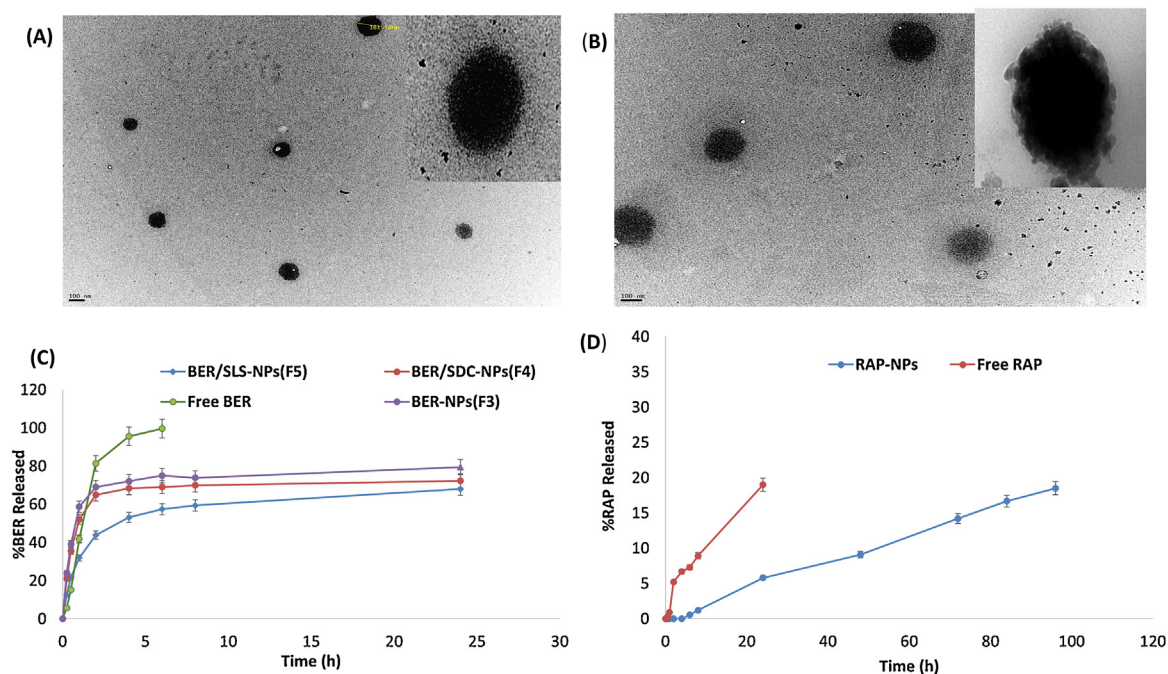


**Fig. 3.** TEM images of RAP-BER/SLS NPs (F8) and LbL-RAP-BER/SLS NPs (F9) (A, B), *in vitro* release of BER (C), RAP (D) from dual drug-loaded NPs and free drug solutions using 100 ml of purified water as release medium containing 0.2% w/v Tween at 37 °C, 100 rpm using dialysis bag method. Data are expressed as mean  $\pm$  SD (n = 3).

NPs (F4) compared to BER-NPs (F3). After 2 h, 64.9 and 69.65% of BER was released from BER/SDC- and BER-loaded NPs, respectively. However, HIP complexation of BER with SLS (F5) could significantly decrease the initial burst release of drug from NPs from 69.65 to 43.8% after 2 h. After 24 h, the accumulated drug release reached 68.4% from BER/SLS-NPs (F5) compared to 79.45% without HIP complexation (F3). These results confirmed the influential role of HIP complexation to prolong the drug release time. The HIP increased drug hydrophobicity and hence enhanced its incorporation in the lipid matrix of NPs thus providing slow drug release. The dissociation process of free BER from its ionic complex with the negatively charged SLS was possibly another important factor. Similarly, HIP complexation of the hydrophilic peptide leuprolide with sodium stearate, not only increased the EE of leuprolide within lipid NPs but also reduced its release rate from 43.9 to 8.3% in the first 2 h [41].

The *in vitro* release behavior of RAP from NPs was studied for 5 days in water containing 0.2% w/v Tween 80. PBS could not be used in this study because RAP is unstable in PBS [42]. The release of RAP from the NPs was very slow with only 5.8% released during the first 24 h compared to 19.0% released from free drug solution after 24 h (Fig. 3D). The amount of the drug released from the NPs continued to increase and reached 18.5% after 5 days. The very slow release of RAP from NPs can be explained by its extremely lipophilic nature (aqueous solubility = 2.6  $\mu$ g/ml at 25 °C and partition coefficient = 3.58). Thus, it was highly incorporated within the lipid core of NPs with very low tendency to partition to the aqueous release medium. The lack of immediate release of RAP is potentially useful to prevent drug loss before reaching the tumor site thus avoiding unwanted systemic side effects of the drug whereas the relatively faster release of BER could be exploited to sensitize cancer cells to the action of RAP.

### 3.7. Colloidal stability and lyophilized powder redispersibility

After 3-month storage at 4 °C, there was no significant increase in the particle size of LbL-NPs (F9) compared to the remarkable

size increase of the uncoated NPs (F8) (Fig. 4A). The high tendency of lipid NPs to aggregate upon storage may result from reduction in surfactant coating on the hydrophobic NP surface [43]. It was recently reported that LbL coating technique could improve the poor colloidal stability and pharmacokinetic pattern of the NPs [44].

Although freeze-drying is commonly used to enhance the stability of NPs by converting their colloidal suspension into powder form, some stresses could destabilize NPs during freeze-drying [45]. Therefore, the prepared NPs were lyophilized using mannitol (5% w/v) as a cryoprotectant. Under the mechanical freezing stress of ice crystals, there was a large increase of about 145 nm in the size of the uncoated NPs with redispersibility index (RI) of 1.66 indicating their aggregation. In comparison, there was only about 50 nm increase in the size of LbL-NPs (RI = 1.19) (Table S2). Polymeric NPs are more resistant to freezing stresses than lipid NPs by virtue of their higher mechanical resistance [45]. Takeuchi et al. found that coating the surface of liposomes by modified PVA layer could enhance their stability during lyophilization [46]. Therefore, it can be concluded that coating the surface of our lipid NPs with biopolymers such as LF and HA has improved their stability during freeze-drying and prevented their aggregation.

### 3.8. Serum stability and hemocompatibility

For parenteral administration, the NPs should be stable to avoid possible interaction with serum proteins. There was a significant increase in the particle size of the bare NPs from 170.2 to 290.3 nm once added to 10% FBS. The size of the uncoated NPs continued to increase in the first 2 h reaching 380.5 nm. After 4 h, the size started to decrease with a significant PS reduction was noticed after 6 h reaching 199.1 nm (Fig. 4B). The initial increase in size of the uncoated lipid NPs can be correlated to adsorption of serum proteins on the surface of NPs forming protein corona [47]. The osmotic effect of serum proteins is another way by which serum may impact NPs causing water to escape from the aqueous core resulting in shrinkage of the NPs [12,48].

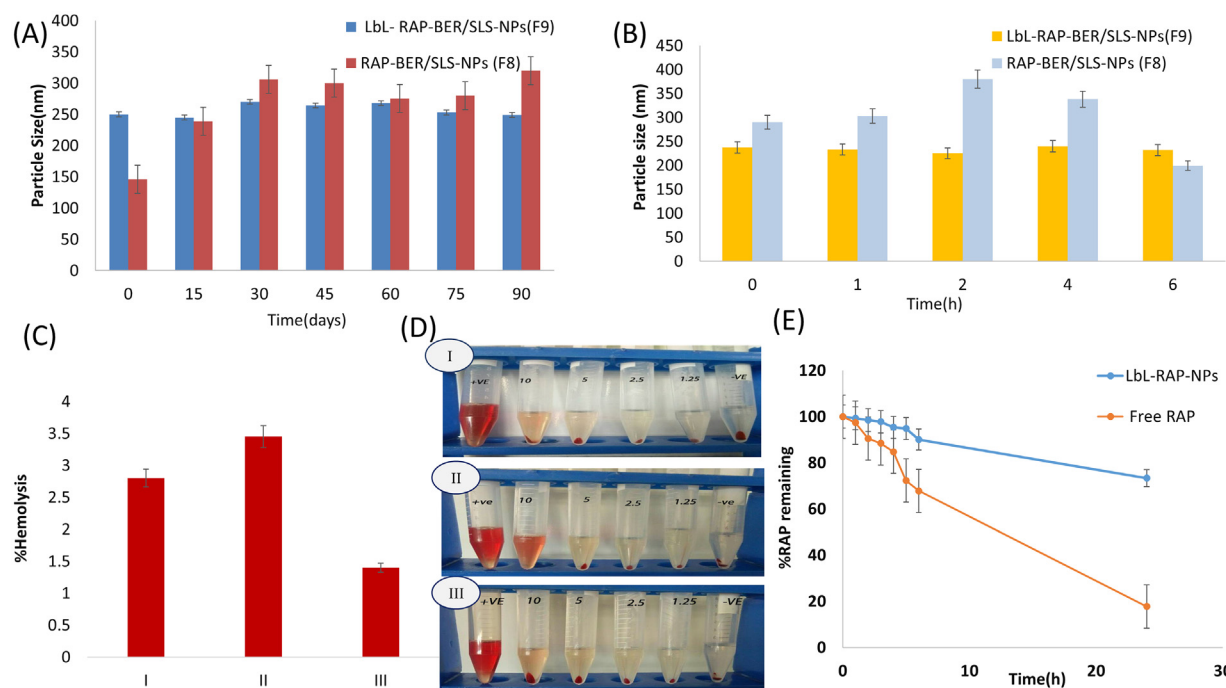


**Fig. 4.** Physical stability of RAP-BER/SLS NPs (F8) and LbL-RAP-BER/SLS NPs (F9) showing the change in particle size with time (A), Particle size of RAP-BER/SLS NPs (F8) and LbL-RAP-BER/SLS NPs (F9) after incubation in 10% fetal bovine serum (FBS) for 6 h at 37 °C (B), Hemolytic potential of different dual drug loaded NP showing % hemolysis (C), hemocompatibility images (D) of the uncoated NPs (D I), LF-NPs (D II) and HA-LF-NPs (D III) after 1 h of incubation at 37 °C and chemical stability of free RAP and encapsulated RAP-NPs in phosphate-buffered saline (PBS; 10 mM, pH 7.4) (E). Data are expressed as mean  $\pm$  SD (n = 3).

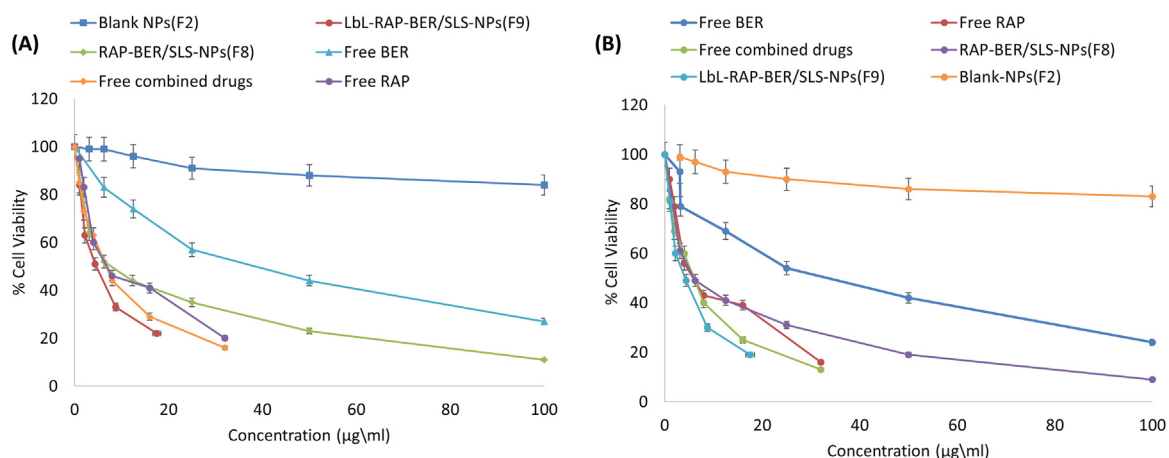


**Fig. 5.** Cytotoxicity analysis of free BER, free RAP and free BER/RAP co-solvent compared to the prepared nano-formulations RAP-BER/SLS-NPs (F8), targeted LbL-RAP-BER/SLS-NPs (F9) and Blank-NPs (F2) on A549 lung cancer cell line after 24 (A) and 48 h (B). Each value represents the mean  $\pm$  SD (n = 6).

Lipid NPs are hydrophobic carriers exposed to opsonization by serum proteins and quick clearance by macrophages of RES. Therefore, coating of lipid NPs with hydrophilic biocompatible polymers was thought to improve their systemic use and prolong its circulation [49]. In our study, there was no significant change in the PS of LbL-coated NPs after incubation in FBS for 6 h. LbL modification of NPs with highly negatively charged polyelectrolytes such as HA as the outer layer could greatly enhance the serum stability of NPs since it hinders the adsorption of anionic serum protein molecules. This could also result in decreased opsonization and hence reduce their RES clearance and enhance their accumulation in solid tumors [31].

Using 1.25 mg/ml NP concentration, un-coated and LF-coated NPs showed 2.8 and 3.45% hemolysis, respectively. On the other hand, HA/LF-LbL-coated NPs demonstrated only 1.4% hemolysis

(Fig. 4C & D). Even at higher NP concentration (2.5 mg/ml), HA/LF-LbL-NPs showed only 3.78% hemolysis compared to  $4.99 \pm 0.41\%$  and  $5.13 \pm 0.36\%$  hemolysis for un-coated and LF-coated NPs, respectively. Thus, HA/LF-LbL-coated NPs were found to be more hemocompatible that may be mediated by the negatively charged functional groups of HA. HA coating of liposomes was previously reported to enhance their biocompatibility and confirmed their safety for i.v. delivery of imatinib mesylate [50].

### 3.9. Chemical stability of RAP

According to previous report, RAP undergoes hydrolytic degradation in 0.01 M PBS at pH 7.4 particularly at  $37 \pm 0.5$  °C [42]. Also, RAP was found to be strongly accelerated at higher buffer concentration [51]. To study the protecting effect of our NPs on the



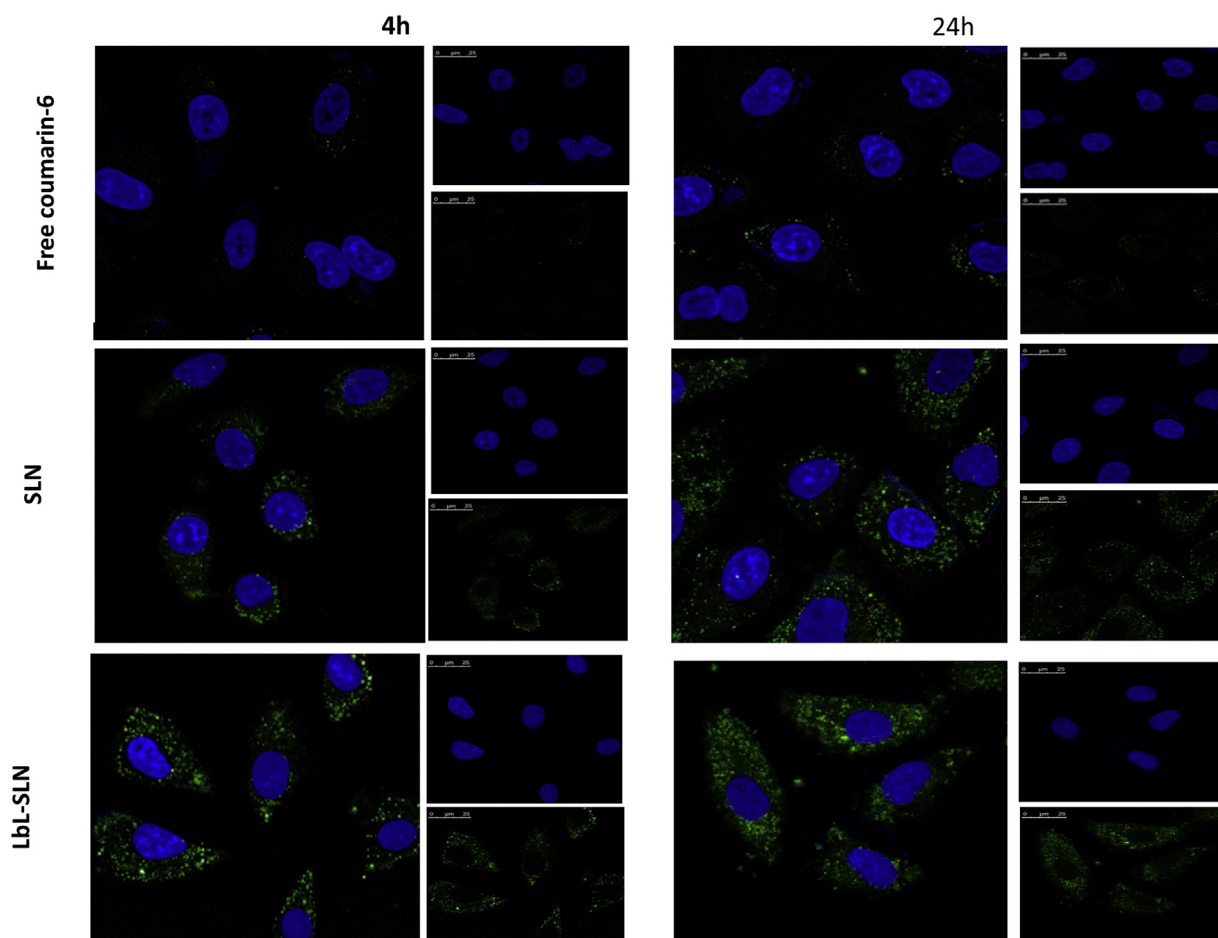


**Fig. 6.** Confocal images showing cellular uptake of free Coumarin-6, uncoated NPs and LbL-NPs (Coumarin-6 was incorporated in the place of the drugs as a fluorescent marker) within A549 lung cancer cells after incubation for 4 and 24 h (C). Cell nuclei were stained with DAPI and the cytoplasmic green fluorescence resulted from Coumarin-6. (For interpretation of the references to colour in this figure legend, the reader is referred to the web version of this article.)

stability of RAP, free RAP and RAP-loaded HA/LF-LbL-coated NPs were incubated in PBS (0.01 M, pH 7.4) followed by determination of its concentration by HPLC at predetermined time intervals. As shown in Fig. 4E & S3, free RAP was rapidly degraded in PBS (only 17.8% of RAP remained intact after 24 h of incubation). In contrast, RAP loaded in the NPs showed more stability in PBS under the same conditions with about 73.34% of RAP remained intact after 24 h of incubation. Thus, formulation of RAP into LbL-coated lipid NPs protected the encapsulated drug against hydrolysis and increased its stability in PBS. This could be attributed to the high entrapment efficiency of RAP in the lipid NPs (nearly 100%) by virtue of its highly lipophilic nature and its extremely slow release pattern as demonstrated by the drug release results.

### 3.10. In-vitro cytotoxicity

Dual free RAP/BER combination and the dual drug-loaded uncoated and LbL-NPs (F9) exhibited remarkable decrease in the viability of A549 non-small lung cancer cells at 24 and 48 h in a dose/time-dependent manner (Fig. 5A & B). The observed cytotoxic activity of non-targeted NPs(F8) ( $IC_{50}$ , 7.8  $\mu$ g/ml) was less than dual free drug combination ( $IC_{50}$ , 6.1  $\mu$ g/ml) after 24 h incubation period (Fig. S4). This behavior may be explained by the relatively faster release of the free combined drugs relative to their slow release from NPs. However, the HA/LF-LbL-NPs showed the highest cytotoxic potential ( $IC_{50}$ , 4.59  $\mu$ g/ml) after 24 h. The enhanced cytotoxicity demonstrated by LbL-NPs might be due to presence of

HA as the outer layer on the surface of LbL-NPs which could facilitate the active cellular uptake mediated by HA-CD44 interaction which resulted in increased intracellular drug concentration [52]. These results confirm the essential tumor-targeting effect of the polymer layers coating the particles. It was evident that blank NPs (F2) did not show any significant cytotoxicity indicating their safety and biocompatibility to tumor cells (cell viability was not less than 80%).

### 3.11. Cellular uptake

A qualitative cellular uptake study of uncoated and HA/LF-LbL-coated lipid NPs was performed by using confocal microscopy (Fig. 6). Fluorescent NPs were prepared using coumarin-6 instead of drugs. After 4 h incubation with fluorescent uncoated NPs, no remarkable fluorescence was detected inside A549 cells. However, the fluorescence intensity was enhanced with the incubation time so that obvious fluorescence was observed after 24 h incubation. Based on their structural similarity with the plasma membrane, the lipid components of our NPs may bind with cell membranes and enhance their internalization into cancer cells [53].

It was previously reported that LbL self-assembly on preformed NPs is an outstanding approach to provide targeting potential to tumor cells. Therefore, in this study, the cellular uptake of NPs was highly enhanced by coating with LF and HA as demonstrated by much stronger green fluorescence signals inside the cells compared to uncoated coumarin-6 loaded NPs (Fig. 6). Thus, decorating



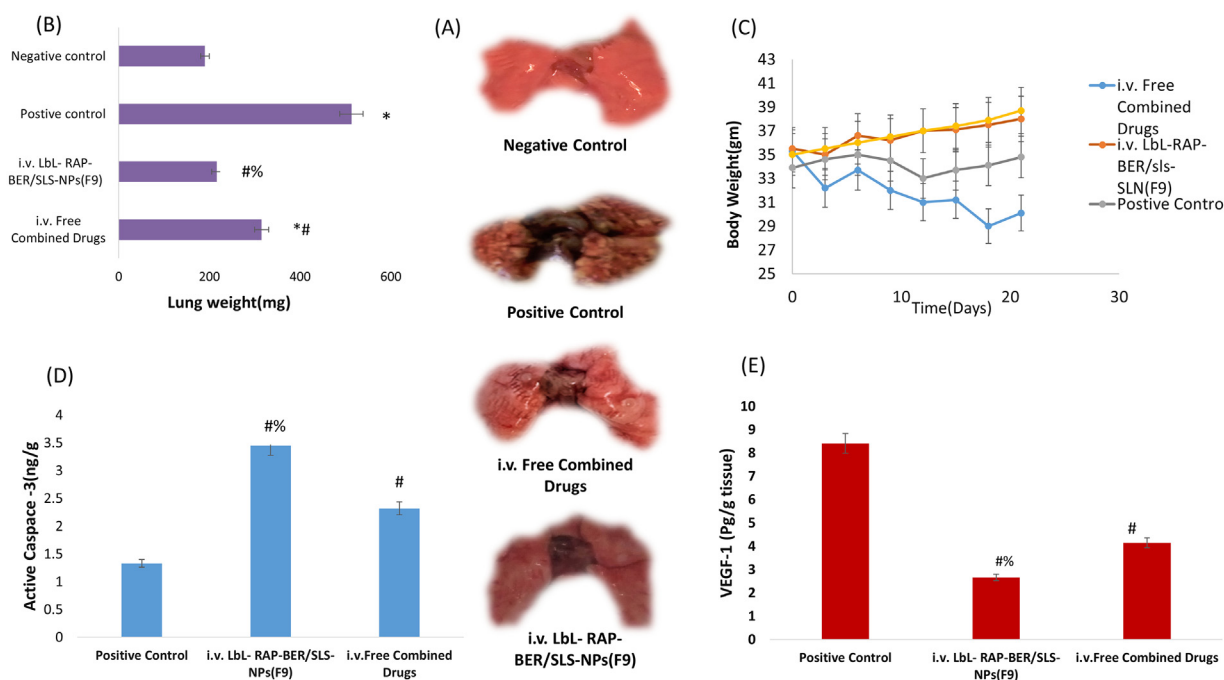


**Fig. 7.** Representative images of lungs for different groups after 21-day treatment (A), Lung weight for different groups after 21 day treatment (B), Change of total body weight of mice with time (C), In-vivo anti-tumor efficacy showing the level of the tumor markers including Caspase-3 (D) and VEGF-1 (E) in mice bearing lung cancer treated for 3 weeks with free combined drugs and LbL-RAP-BER/SLS NPs (F9) by intravenous injection compared to untreated positive control. \*  $P < 0.05$  vs negative control, #  $P < 0.05$  vs positive control, %  $P < 0.05$  vs Free BER/RAP mixture. Each value represents the mean  $\pm$  SD ( $n = 6$ ).

the surface of NPs with outer layer of HA may be responsible for efficient internalization into lung cancer cells via CD44 receptor-mediated endocytosis [10–12]. This also confirms the key role played by LbL assembled polymers in tumor targeting process.

### 3.12. In vivo anti-tumor efficacy

#### 3.12.1. Lung weight and morphology

Combined cancer therapy using nanocarriers could be a promising strategy for enhanced efficacy of anti-cancer therapy [54,55]. Macroscopic lung features were investigated after lung cancer induction. As shown in Fig. 7A & B, lungs excised from the negative control mice exhibited normal physiological features whereas the lungs of the positive control mice (untreated group) were almost completely occupied by tumors. In contrast, tumor growth was significantly inhibited to different degrees in terms of lung weight and number of foci in the groups treated with i.v. HA/LF-LbL-coated lipid NPs and i.v. free drugs combination. Particularly, the best anti-tumor effects were observed for mice treated with i.v. NPs. The latter resembled those of negative controls after 21 days of treatment showing significantly lower average lung weights compared to the positive control group (216 mg versus 513.6 mg). Whereas mice treated with BER/RAP free solution has showed lung weight of 315 mg. Also, mice treated with BER/RAP free solution has showed reduction in the total body weight with time (Fig. 7C). RAP was reported to cause a decrease in food intake, and fat mass loss resulting in weight loss [56]. It worth mention that the drug-NPs treated group has not shown body weight reduction indicating there was no or low systemic toxicity of the nano-formulations.

#### 3.12.2. Tumor growth biomarkers

The effect of nano-encapsulation on the apoptotic and anti-angiogenic effects of RAP and BER was evaluated (Fig. 7D & E). RAP induces cell cycle arrest and ultimately apoptosis through inhibition of mTOR. Additionally, RAP was reported to provoke anti-angiogenic effect by reducing the production of vascular

endothelial growth factor (VEGF) [57]. BER is an effective anti-angiogenic agent and can inhibit tumor progression through the inhibition of various pro-inflammatory and angiogenic factors [58]. In our study, i.v. administered HA/LF-LbL-RAP-BER/SLS-NPs (F9) demonstrated the best significant apoptotic and anti-angiogenic effects ( $P < 0.05$ ) with a 2.59-fold elevation in caspase-3 level and 3.16-fold reduction of VEGF level in lung tumors relative to the positive control group. In comparison, only 1.74-fold elevation of caspase-3 and 2.02-fold reduction of VEGF level was obtained in mice treated with i.v. free drug combination relative to the positive control ( $P < 0.05$ ).

#### 3.12.3. Histopathological & immunohistochemical study

As shown in Fig. 8, H&E staining of lung sections showed normal alveoli with a single layer epithelial lining in negative control. However, positive control group (urethane-treated group) has showed several preneoplastic to neoplastic lesions ranging from epithelial hyperplasia to adenoma (blue arrow). In addition, there was evidence of hemorrhage (white arrow) and inflammatory cells infiltration (black arrow). The lung tissues of tumor-bearing mice treated with i.v. free combined RAP/BER solution exhibited more tumor lesions than group treated with i.v. LbL-RAP-BER/SLS-NPs (F9), which is consistent with the macroscopic observation. Moreover, the superiority of i.v. drugs loaded NPs was further confirmed by a significant 88.09% reduction in the average number of microscopic metastatic lung foci with highly reduced diameter (0.91 mm vs 5.53 mm) compared to untreated control group ( $P < 0.05$ ) (Fig. 9A). On the other hand, the group treated with i.v. free drug combination revealed 64.28% reduction in the average number of microscopic metastatic lung foci with a diameter of 3.04 mm.

The expression of Ki-67 protein is directly correlated with cell proliferation [59]. Therefore, the in vivo Ki-67 levels in lung cancer bearing mice treated with free RAP/BER or LbL-RAP-BER/SLS-NPs (F9) were further evaluated by immunohistochemistry (Fig. 9B). Compared to positive control, both treatment inhibited cell proliferation evidenced by reduced Ki-67 staining. The expression of

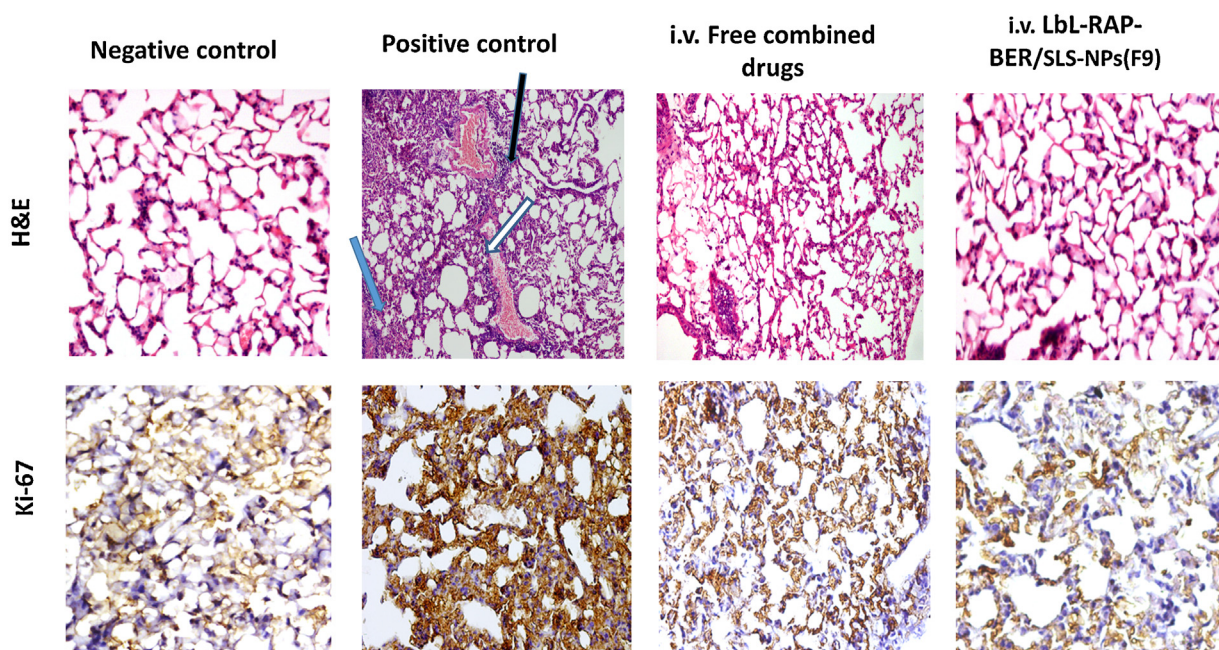


**Fig. 8.** Histopathological and immunohistochemical analysis of lung sections of mice treated with free RAP/BER combination and LbL- RAP-BER/SLS NPs (F9) compared to negative control and positive control groups (A).

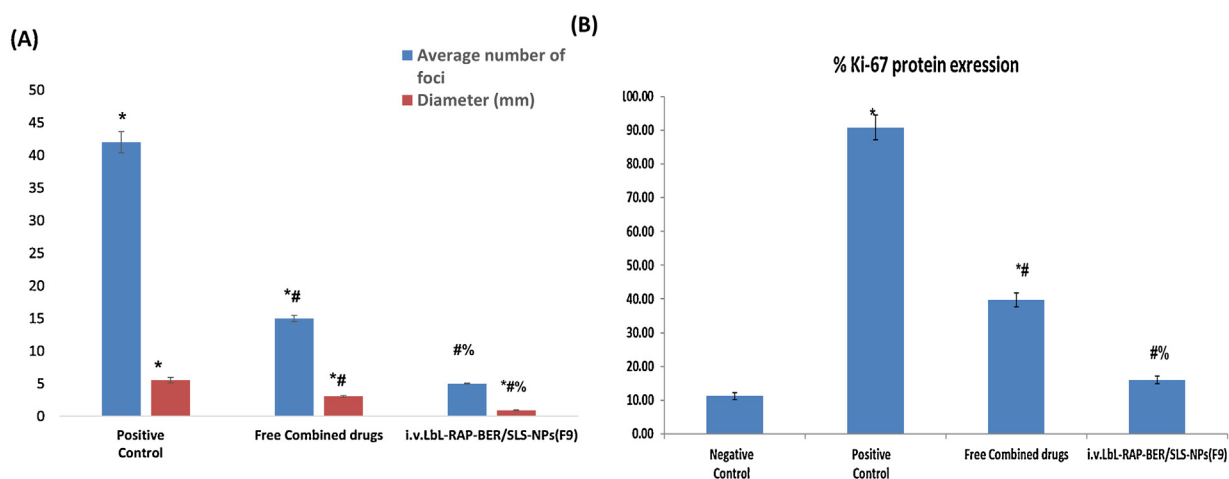


**Fig. 9.** Number of lung adenomatous foci and their diameter (A) in mice bearing lung cancer treated for 3 weeks for different groups, % expression of protein Ki-67 proliferation in corresponding groups (C). \*  $P < 0.05$  vs negative control, #  $P < 0.05$  vs positive control, %  $P < 0.05$  vs Free BER/ETP mixture. Each value represents the mean  $\pm$  SD ( $n = 6$ ).

Ki67 protein measured in groups treated with free drugs solution and NPs were  $39.74 \pm 2.08$  and  $15.98 \pm 1.09\%$ , respectively compared to  $90.79 \pm 3.67\%$  for positive control.

Generally, the enhanced *in vivo* anti-tumor efficacy of our nano-delivery system is mainly attributed to the improved accumulation of drugs in lung cancer cells by active targeting through binding to CD44 receptors. This was also supported by the results of *in-vitro* cytotoxicity study, where HA/LF-LbL-NPs showed higher cytotoxic potential than that of both non-targeted NPs and the free drug combination after 24 h. Moreover, the synergistic BER/RAP therapy had also contributed to the improved efficacy as demonstrated by the higher cytotoxicity of drug combination compared to each drug alone.

#### 4. Conclusion

Lipid NPs were successfully fabricated for the dual delivery of RAP and BER to lung cancer. BER/SLS ion pair complex could signifi-

cantly increase the hydrophobicity of the drug which was observed by reduction in aqueous solubility and its Log P value. Thus, it could be incorporated in the hydrophobic core of the NPs with 93.5 EE and also reduce the initial burst release. The LbL-NPs was formulated via layer-by-layer assembly of LF and HA on BER/SLS-RAP-NPs with particle size 250.5 nm. LbL nanoarchitecture build-up was monitored by means of a change in the hydrodynamic size and zeta-potential surface charge. The LbL -NPs were relatively stable. LbL Coating has enhanced the cellular uptake of lipid NPs and the cellular cytotoxicity of drugs due to CD44 receptor targeting. The *in vivo* studies carried on mice bearing urethane induced lung cancer has showed the superior anticancer activity of LbL-BER/RAP-NPs over the free drugs solution.

#### Declaration of interest

The authors declare that they have no conflicts of interests.

## Acknowledgement

This work was supported by the research grant (No. 5731) of Science and Technology Development Fund (STDF), Ministry of Scientific Research, Egypt. The authors acknowledge Westland Milk Products (Hokitika, New Zealand) for kind donation of lactoferrin.

## Appendix A. Supplementary data

Supplementary data associated with this article can be found, in the online version, at <https://doi.org/10.1016/j.colsurfb.2018.05.008>.

## References

- [1] C.S.D. Cruz, L.T. Tanoue, R.A. Matthay, Lung cancer: epidemiology, etiology, and prevention, *Clin. Chest Med.* 32 (2011) 605–644.
- [2] X. Xu, W. Ho, X. Zhang, N. Bertrand, O. Farokhzad, Cancer nanomedicine: from targeted delivery to combination therapy, *Trends Mol. Med.* 21 (2015) 223–232.
- [3] H.M. Abdelaziz, M. Gaber, M.M. Abd-Elwakil, M.T. Mabrouk, M.M. Elgohary, N.M. Kamel, D.M. Kabary, M.S. Freag, M.W. Samaha, S.M. Mortada, Inhalable particulate drug delivery systems for lung cancer therapy: nanoparticles, microparticles, nanocomposites and nanoaggregates, *J. Controlled Release* 10 (269) (2017) 374–392.
- [4] A.K. Kushwaha, P.R. Vuddanda, P. Karunanidhi, S.K. Singh, S. Singh, Development and Evaluation of Solid Lipid Nanoparticles of Raloxifene Hydrochloride for Enhanced Bioavailability, *BioMed research international*, 2013 (2013).
- [5] M.M. de Villiers, D.P. Otto, S.J. Strydom, Y.M. Lvov, Introduction to nanocoatings produced by layer-by-layer (LbL) self-assembly, *Adv. Drug Deliv. Rev.* 63 (2011) 701–715.
- [6] S. Sabra, M. Abdelmoneem, M. Abdelwakil, M.M. Taha, D. Anwar, R. Mohamed, S. Khattab, A. Bekhit, K. Elkhodairy, M. Freag, Self-assembled nanocarriers based on amphiphilic natural polymers for anti-cancer drug delivery applications, *Curr. Pharm. Des.* 23 (35) (2017) 5213–5229.
- [7] A.O. Elzoghby, M.M. Abd-Elwakil, K. Abd-El Salam, M.T. Elsayed, Y. Hashem, O. Mohamed, Natural polymeric nanoparticles for brain-targeting: implications on drug and gene delivery, *Curr. Pharm. Des.* 22 (2016) 3305–3323.
- [8] Y.-T. Tung, H.-L. Chen, C.-C. Yen, P.-Y. Lee, H.-C. Tsai, M.-F. Lin, C.-M. Chen, Bovine lactoferrin inhibits lung cancer growth through suppression of both inflammation and expression of vascular endothelial growth factor, *J. Dairy Sci.* 96 (2013) 2095–2106.
- [9] A.O. Elzoghby, M.M. Elgohary, N.M. Kamel, Implications of protein- and Peptide-based nanoparticles as potential vehicles for anticancer drugs, *Adv. Protein Chem. Struct. Biol.* 98 (2015) 169–221.
- [10] E.L.-H. Leung, R.R. Fiscus, J.W. Tung, V.P.-C. Tin, L.C. Cheng, A.D.-L. Sihoe, L.M. Fink, Y. Ma, M.P. Wong, Non-small cell lung cancer cells expressing CD44 are enriched for stem cell-like properties, *PLoS One* 5 (2010) e14062.
- [11] K.Y. Choi, G. Saravanakumar, J.H. Park, K. Park, Hyaluronic acid-based nanocarriers for intracellular targeting: interfacial interactions with proteins in cancer, *Colloids Surf. B: Biointerfaces* 99 (2012) 82–94.
- [12] M.S. Freag, Y.S. Elnaggar, D.A. Abdelmonsif, O.Y. Abdallah, Layer-by-layer-coated lyotropic liquid crystalline nanoparticles for active tumor targeting of rapamycin, *Nanomedicine* 11 (2016) 2975–2996.
- [13] H.-P. Marti, F.J. Frey, Nephrotoxicity of rapamycin: an emerging problem in clinical medicine, *Nephrol. Dial. Transplant.* 20 (2005) 13–15.
- [14] E.M. Galvez, M. Perez, P. Domingo, D. Nuñez, V. Cebolla, M. Matt, J. Pardo, Pharmacological/Biological Effects of Berberine, *Natural Products*, Springer, 2013, pp. 1301–1329.
- [15] J.H. Sung, J.B. Kim, S.H. Park, S.Y. Park, J.K. Lee, H.-S. Lee, N. Chung, Berberine decreases cell growth but increases the side population fraction of H460 lung cancer cells, *J. Korean Soc. Appl. Biol. Chem.* 55 (2012) 491–495.
- [16] S.K. Battu, M.A. Repka, S. Maddineni, A.G. Chittiboyina, M.A. Avery, S. Majumdar, Physicochemical characterization of berberine chloride: a perspective in the development of a solution dosage form for oral delivery, *AAPS PharmSciTech* 11 (2010) 1466–1475.
- [17] N. Guo, A. Yan, X. Gao, Y. Chen, X. He, Z. Hu, M. Mi, X. Tang, X. Gou, Berberine sensitizes rapamycin-mediated human hepatoma cell death in vitro, *Mol. Med. Rep.* 10 (2014) 3132–3138.
- [18] R. Yu, Z.-Q. Zhang, B. Wang, H.-X. Jiang, L. Cheng, L.-M. Shen, Berberine-induced apoptotic and autophagic death of HepG2 cells requires AMPK activation, *Cancer Cell Int.* 14 (2014) 49.
- [19] S. Sun, N. Liang, Y. Kawashima, D. Xia, F. Cui, Hydrophobic ion pairing of an insulin-sodium deoxycholate complex for oral delivery of insulin, *Int. J. Nanomed.* 6 (2011) 3049.
- [20] S.K. Battu, M.A. Repka, S. Maddineni, A.G. Chittiboyina, M.A. Avery, S. Majumdar, Physicochemical characterization of berberine chloride: a perspective in the development of a solution dosage form for oral delivery, *AAPS PharmSciTech* 11 (2010) 1466–1475.
- [21] W. Mehnert, K. Mader, Solid lipid nanoparticles: production, characterization and applications, *Adv. Drug Deliv. Rev.* 47 (2001) 165–196.
- [22] A.O. Elzoghby, S.K. Mostafa, M.W. Helmy, M.A. ElDemellawy, S.A. Sheweita, Superiority of aromatase inhibitor and cyclooxygenase-2 inhibitor combined delivery: hyaluronate-targeted versus PEGylated protamine nanocapsules for breast cancer therapy, *Int. J. Pharm.* 529 (2017) 178–192.
- [23] T. Ramasamy, T.H. Tran, J.Y. Choi, H.J. Cho, J.H. Kim, C.S. Yong, H.-G. Choi, J.O. Kim, Layer-by-layer coated lipid-polymer hybrid nanoparticles designed for use in anticancer drug delivery, *Carbohydr. Polym.* 102 (2014) 653–661.
- [24] S.W. El-Far, M.W. Helmy, S.N. Khattab, A.A. Bekhit, A.A. Hussein, A.O. Elzoghby, Phytosomal bilayer-enveloped casein micelles for codelivery of monascus yellow pigments and resveratrol to breast cancer, *Nanomedicine* (2018).
- [25] S.-J. Wang, Z.-J. Huo, K. Liu, N. Yu, Y. Ma, Y.-H. Qin, X.-C. Li, J.-M. Yu, Z.-Q. Wang, Ligand-conjugated pH-sensitive polymeric micelles for the targeted delivery of gefitinib in lung cancers, *RSC Adv.* 5 (2015) 73184–73193.
- [26] R.D. Gurley, C.J. Moser, Induction of lung tumors in mice with urethane, *Cold Spring Harbor Protocols* 2015 (2015) (pdb. prot077446).
- [27] P. Wang, L. Zhang, H. Peng, Y. Li, J. Xiong, Z. Xu, The formulation and delivery of curcumin with solid lipid nanoparticles for the treatment of on non-small cell lung cancer both in vitro and in vivo, *Mater. Sci. Eng. C* 33 (2013) 4802–4808.
- [28] A.O. Elzoghby, B.Z. Vranic, W.M. Samy, N.A. Elgindy, Swellable floating tablet based on spray-dried casein nanoparticles: near-infrared spectral characterization and floating matrix evaluation, *Int. J. Pharm.* 491 (2015) 113–122.
- [29] B. Devrim, A. Bozkir, Design and evaluation of hydrophobic ion-pairing complexation of lysozyme with sodium dodecyl sulfate for improved encapsulation of hydrophilic peptides/proteins by lipid-polymer hybrid nanoparticles, *J. Nanomed. Nanotechnol.* 6 (2015) 1.
- [30] M. Schafer-Korting, W. Mehnert, H.C. Korting, Lipid nanoparticles for improved topical application of drugs for skin diseases, *Adv. Drug Deliv. Rev.* 59 (2007) 427–443.
- [31] S. Pulakkat, S.A. Balaji, A. Rangarajan, A.M. Raichur, Surface engineered protein nanoparticles with hyaluronic acid based multilayers for targeted delivery of anticancer agents, *ACS Appl. Mater. Interfaces* 8 (2016) 23437–23449.
- [32] A. Elzoghby, M. Freag, H. Mamdouh, K. Elkhodairy, Zein-based nanocarriers as potential natural alternatives for drug and gene delivery: focus on cancer therapy, *Curr. Pharm. Des.* (2017).
- [33] A.O. Elzoghby, A.L. Hemasa, M.S. Freag, Hybrid protein-inorganic nanoparticles: from tumor-targeted drug delivery to cancer imaging, *J. Controlled Release* 243 (2016) 303–322.
- [34] M. Gaber, W. Medhat, M. Hany, N. Saher, J.-Y. Fang, A. Elzoghby, Protein-lipid nanohybrids as emerging platforms for drug and gene delivery: challenges and outcomes, *J. Controlled Release* (2017).
- [35] R.C. Haidar, M. Hamdy, Protein release kinetics for core-shell hybrid nanoparticles based on the layer-by-layer assembly of alginate and chitosan on liposomes, *Biomaterials* 29 (2008) 1207–1215.
- [36] S.N. Khattab, S.E.A. Naim, M. El-Sayed, A.A. El Barden, A.O. Elzoghby, A.A. Bekhit, A. El-Faham, Design and synthesis of new s-triazine polymers and their application as nanoparticulate drug delivery systems, *New J. Chem.* 40 (2016) 9565–9578.
- [37] M. Battaglia, M. Trotta, M.E. Gallarate, G.P. Carlotti, A. Zara, Solid lipid nanoparticles formed by solvent-in-water emulsion-diffusion technique: development and influence on insulin stability, *J. Microencapsul.* 24 (2007) 672–684.
- [38] M. Baranska, H. Schulz, Determination of alkaloids through infrared and Raman spectroscopy, *Alkaloids: Chem. Biol.* 67 (2009) 217–255.
- [39] C. Jian-Bo, Z. Qun, S. Su-Qin, B. Perston, P. Courtney, Rapid Quality Control of the Traditional Remedy Chinese Goldthread by FT-IR Spectrometry, *AND CHINESE*, 14.
- [40] A.K. Kushwaha, P.R. Vuddanda, P. Karunanidhi, S.K. Singh, S. Singh, Development and evaluation of solid lipid nanoparticles of raloxifene hydrochloride for enhanced bioavailability, *BioMed Res. Int.* 2013 (2013) 9.
- [41] H. Yuan, S.-P. Jiang, Y.-Z. Du, J. Miao, X.-G. Zhang, F.-Q. Hu, Strategic approaches for improving entrapment of hydrophilic peptide drugs by lipid nanoparticles, *Colloids Surf. B: Biointerfaces* 70 (2009) 248–253.
- [42] M. Rouf, E. Bilensoy, I. Vural, A. Hincal, Determination of stability of rapamycin following exposure to different conditions, *Eur. J. Pharm. Sci.* 32 (2007) S46.
- [43] Y. Yang, A. Corona, M.A. Henson, Experimental investigation and population balance equation modeling of solid lipid nanoparticle aggregation dynamics, *J. Colloid Interface Sci.* 374 (2012) 297–307.
- [44] H.B. Ruttala, T. Ramasamy, B.S. Shin, H.-G. Choi, C.S. Yong, J.O. Kim, Layer-by-layer assembly of hierarchical nanoarchitectures to enhance the systemic performance of nanoparticle albumin-bound paclitaxel, *Int. J. Pharm.* 519 (2017) 11–21.
- [45] N. Elgindy, K. Elkhodairy, A. Molokhia, A. Elzoghby, Lyophilization monophase solution technique for preparation of amorphous lyutamide dispersions, *Drug Dev. Ind. Pharm.* 37 (2011) 754–764.
- [46] H. Takeuchi, H. Yamamoto, T. Toyoda, H. Toyoboku, T. Hino, Y. Kawashima, Physical stability of size controlled small unilamellar liposomes coated with a modified polyvinyl alcohol, *Int. J. Pharm.* 164 (1998) 103–111.
- [47] S. Zanganeh, R. Spitler, M. Erfanzadeh, A.M. Alkilany, M. Mahmoudi, Protein corona: opportunities and challenges, *Int. J. Biochem. Cell Biol.* 75 (2016) 143–147.
- [48] J. Wolfram, K. Suri, Y. Yang, J. Shen, C. Celia, M. Fresta, Y. Zhao, H. Shen, M. Ferrari, Shrinkage of pegylated and non-pegylated liposomes in serum, *Colloids Surf. B: Biointerfaces* 114 (2014) 294–300.



- [49] M. Üner, G. Yener, Importance of solid lipid nanoparticles (SLN) in various administration routes and future perspectives, *Int. J. Nanomed.* 2 (2007) 289.
- [50] L.M. Negi, M. Jaggi, V. Joshi, K. Ronodip, S. Talegaonkar, Hyaluronan coated liposomes as the intravenous platform for delivery of imatinib mesylate in MDR colon cancer, *Int. J. Biol. Macromol.* 73 (2015) 222–235.
- [51] Y.V. Il'ichev, L. Alquier, C.A. Maryanoff, Degradation of rapamycin and its ring-opened isomer: role of base catalysis, *Arkivoc* 12 (2007) 110–131.
- [52] Y. Zhao, T. Zhang, S. Duan, N.M. Davies, M.L. Forrest, CD44-tropic polymeric nanocarrier for breast cancer targeted rapamycin chemotherapy, *Nanomed.: Nanotechnol. Biol. Med.* 10 (2014) 1221–1230.
- [53] I. Rivolta, A. Panariti, B. Lettiero, S. Sesana, P. Gasco, M. Gasco, M. Masserini, G. Miserocchi, Cellular uptake of coumarin-6 as a model drug loaded in solid lipid nanoparticles, *J. Physiol. Pharmacol.* 62 (2011) 45.
- [54] A.O. Elzoghby, S.K. Mostafa, M.W. Helmy, M.A. ElDemellawy, S.A. Sheweita, Multi-reservoir phospholipid shell encapsulating protamine nanocapsules for co-delivery of letrozole and celecoxib in breast cancer therapy, *Pharm. Res.* 34 (2017) 1956–1969.
- [55] A.O. Elzoghby, S.A. El-Lakany, M.W. Helmy, M.M. Abu-Serie, N.A. Elgindy, Shell-crosslinked zein nanocapsules for oral codelivery of exemestane and resveratrol in breast cancer therapy, *Nanomedicine* 12 (2017) 2785–2805.
- [56] N. Deblon, L. Bourgoïn, C. Veyrat-Durebex, M. Peyrou, M. Vinciguerra, A. Caillon, C. Maeder, M. Fournier, X. Montet, F. Rohner-Jeanrenaud, Chronic mTOR inhibition by rapamycin induces muscle insulin resistance despite weight loss in rats, *Br. J. Pharmacol.* 165 (2012) 2325–2340.
- [57] M. Guba, P. von Breitenbuch, M. Steinbauer, G. Koehl, S. Flegel, M. Hornung, C.J. Bruns, C. Zuelke, S. Farkas, M. Anthuber, Rapamycin inhibits primary and metastatic tumor growth by antiangiogenesis: involvement of vascular endothelial growth factor, *Nat. Med.* 8 (2002) 128–135.
- [58] T. Hamsa, G. Kuttan, Antiangiogenic activity of berberine is mediated through the downregulation of hypoxia-inducible factor-1, VEGF, and proinflammatory mediators, *Drug Chem. Toxicol.* 35 (2012) 57–70.
- [59] T. Scholzen, J. Gerdes, The Ki-67 protein: from the known and the unknown, *J. Cell. Physiol.* 182 (2000) 311–322.





## Research Paper

Carbon monoxide releasing molecule-2 attenuates *Pseudomonas aeruginosa*-induced ROS-dependent ICAM-1 expression in human pulmonary alveolar epithelial cellsChiang-Wen Lee<sup>a,b,c,1</sup>, Cheng-Hsun Wu<sup>d,1</sup>, Yao-Chang Chiang<sup>a,e</sup>, Yuh-Lien Chen<sup>f</sup>, Kuo-Ting Chang<sup>g</sup>, Chu-Chun Chuang<sup>h</sup>, I-Ta Lee<sup>i,j,\*</sup><sup>a</sup> Division of Basic Medical Sciences, Department of Nursing and Chronic Diseases and Health Promotion Research Center, Chang Gung University of Science and Technology, Chiayi, Taiwan, ROC<sup>b</sup> Research Center for Industry of Human Ecology and Research Center for Chinese Herbal Medicine, Chang Gung University of Science and Technology, Taoyuan, Taiwan, ROC<sup>c</sup> Department of Rehabilitation, Chang Gung Memorial Hospital, Chia-Yi, Taiwan, ROC<sup>d</sup> School of Medicine, College of Medicine, China Medical University, Taichung, Taiwan, ROC<sup>e</sup> Center for Drug Abuse and Addiction, China Medical University Hospital, China Medical University, Taichung, Taiwan, ROC<sup>f</sup> Department of Anatomy and Cell Biology, College of Medicine, National Taiwan University, Taipei, Taiwan, ROC<sup>g</sup> Translational Medicine Center, Taoyuan General Hospital, Ministry of Health and Welfare, Taoyuan, Taiwan, ROC<sup>h</sup> Department of Physical Therapy, China Medical University, Taichung, Taiwan, ROC<sup>i</sup> Department of Medical Research, Taichung Veterans General Hospital, Taichung, Taiwan, ROC<sup>j</sup> Department of Nursing, College of Nursing, Hungkuang University, Taichung, Taiwan, ROC

## ARTICLE INFO

## Keywords:

Carbon monoxide  
Lung inflammation  
Intercellular adhesion molecule-1  
*Pseudomonas aeruginosa*  
NADPH oxidase

## ABSTRACT

*Pseudomonas aeruginosa* (*P. aeruginosa*) infection in the lung is common in patients with cystic fibrosis (CF). Intercellular adhesion molecule-1 (ICAM-1) is known to play a key role in lung inflammation. Acute inflammation and its timely resolution are important to ensure bacterial clearance and limit tissue damage. Carbon monoxide (CO) has been shown to exert anti-inflammatory effects in various tissues and organ systems. Here, we explored the protective effects and mechanisms of carbon monoxide releasing molecule-2 (CORM-2) on *P. aeruginosa*-induced inflammatory responses in human pulmonary alveolar epithelial cells (HPAECs). We showed that *P. aeruginosa* induced prostaglandin E<sub>2</sub> (PGE<sub>2</sub>)/interleukin-6 (IL-6)/ICAM-1 expression and monocyte adherence to HPAECs. Moreover, *P. aeruginosa*-induced inflammatory responses were inhibited by transfection with siRNA of Toll-like receptor 4 (TLR4), PKCα, p47<sup>phox</sup>, JNK2, p42, p50, or p65. *P. aeruginosa* also induced PKCα, JNK, ERK1/2, and NF-κB activation. We further demonstrated that *P. aeruginosa* increased intracellular ROS generation via NADPH oxidase activation. On the other hand, *P. aeruginosa*-induced inflammation was inhibited by pretreatment with CORM-2. Preincubation with CORM-2 had no effects on TLR4 mRNA levels in response to *P. aeruginosa*. However, CORM-2 inhibits *P. aeruginosa*-induced inflammation by decreasing intracellular ROS generation. *P. aeruginosa*-induced PKCα, JNK, ERK1/2, and NF-κB activation was inhibited by CORM-2. Finally, we showed that *P. aeruginosa* induced levels of the biomarkers of inflammation in respiratory diseases, which were inhibited by pretreatment with CORM-2. Taken together, these data suggest that CORM-2 inhibits *P. aeruginosa*-induced PGE<sub>2</sub>/IL-6/ICAM-1 expression and lung inflammatory responses by reducing the ROS generation and the inflammatory pathways.

## 1. Introduction

*Pseudomonas aeruginosa* (*P. aeruginosa*) is one of the most important pathogens of nosocomial infection, which can often cause bacterial infection in immunocompromised patients. The number of cases of

respiratory infection caused by *P. aeruginosa* has increased year by year. *P. aeruginosa* can cause pneumonia, endocarditis, brain abscess, sepsis, necrotizing fasciitis, and so on. The route of infection can be through droplets, wounds, medical treatment pipelines, and even drinking contaminated water. The treatment of *P. aeruginosa* infections is

\* Corresponding author at: Department of Medical Research, Taichung Veterans General Hospital, 1650 Taiwan Boulevard Sect. 4, Taichung 40705, Taiwan, ROC.

E-mail address: [iti700128@gmail.com](mailto:iti700128@gmail.com) (I.-T. Lee).<sup>1</sup> These authors contributed equally to this work.

dominated by antibiotics while avoiding complications. However, the mortality rate of infection is still not low. Recently, Guillemot et al. proved that cytosolic phospholipase A<sub>2</sub>α (cPLA<sub>2</sub>α) promotes mouse mortality regulated by *P. aeruginosa* pulmonary infection through interleukin-6 (IL-6) [1]. Previous studies have shown that prostaglandin E<sub>2</sub> (PGE<sub>2</sub>) is a critical regulator in inflammatory responses during chronic and acute infections [2]. Moreover, PGE<sub>2</sub> can mediate the maturation, migration, activation, and cytokine secretion of immune cells [2]. During bacterial pathogenesis, both Gram-positive and Gram-negative bacteria can enhance PGE<sub>2</sub> release to mediate the immune responses [3]. Intercellular adhesion molecule-1 (ICAM-1) is an inducible surface glycoprotein, which can regulate adhesion-dependent cell-to-cell interactions [4]. Many studies indicated that IL-6 can induce ICAM-1 expression in various cell types [4,5].

Carbon monoxide (CO) is currently known to be generated in cells or tissues as a byproduct of heme oxygenase (HO) after heme catalytic activity [6]. Even though CO is toxic to humans at high concentrations, many studies have documented that low-doses exogenous CO (approximately 250–500 ppm) have protective function against various human diseases [7,8]. Previous studies have confirmed that low concentrations of CO or CO-releasing molecules (CORMs) can eliminate microorganisms [9], regulate cell death [10], and resist inflammation [10]. However, the lipid-soluble tricarbonyldichlororuthenium (II) dimer (CORM-2) is the most characterized CO-RMs [11]. In this study, we hypothesized that CORM-2 may be effective as an anti-inflammatory modulator and a therapeutic agent for pulmonary inflammation.

Increased oxidative stress often causes cell damage and leads to inflammation [12]. Oxidative stress may occur due to increased generation and/or reduced ROS destruction. It is known that NADPH oxidase is the critical enzyme for the generation of ROS under various pathological conditions [12]. Several lines of evidence have demonstrated that ROS contributes to ICAM-1 expression in various cell types [12,13]. On the other hand, PKCα [13,14], MAPKs [13,15], AP-1 [13,16], or NF-κB [13,15,16] has also been shown to be involved in ICAM-1 up-regulation and monocyte adhesion in various cell types. Previous study indicated that CORM-2 can mitigate inflammation via the inhibition of ROS/NF-κB and Erk1/2/AP-1 activation [17]. In addition, Chi et al. proved that CORM-2 decreases TNF-α-induced inflammatory protein expression by inhibiting PKCα-dependent NADPH oxidase/ROS and NF-κB [18].

Thus, in the present study we intend to establish whether the inhibition of ROS generation and inflammatory signaling pathways activation by CORM-2 may indeed result in the inhibition of *P. aeruginosa*-induced inflammation in human pulmonary alveolar epithelial cells (HPAEPiCs) and mice. We report here for the first time that in HPAEPiCs, CORM-2 inhibits *P. aeruginosa*-induced PGE<sub>2</sub>/IL-6/ICAM-1 expression and inflammatory responses by decreasing the NADPH oxidase/ROS generation and the activation of the PKCα/NADPH oxidase/ROS/JNK/NF-κB and PKCα/NADPH oxidase/ROS/ERK1/2 pathways.

## 2. Materials and methods

### 2.1. Materials

We purchased anti-ICAM-1, anti-GAPDH, anti-TLR2, and anti-TLR4 antibodies from Santa Cruz (Santa Cruz, CA). Anti-phospho-p65, anti-phospho-PKCα, anti-phospho-JNK, anti-phospho-p38 MAPK, and anti-phospho-ERK1/2 antibodies were purchased from Cell Signaling (Danver, MA). U0126, Gö6976, SC-51322, SP600125, PD98059, and SB203580 were purchased from Enzo Life Sciences (Farmingdale, NY). Bicinchoninic acid (BCA) protein assay kit was purchased from Pierce (Rockford, IL). CORM-2, hemoglobin (Hb), lipopolysaccharides (LPS), N-acetyl-L-cysteine (NAC), MitoTEMPO, enzymes, and other chemicals were purchased from Sigma (St. Louis, MO). Helenalin (HLN) and apocynin (APO) were purchased from Cayman (Ann Arbor, MI, U.S.A.).

### 2.2. Cell culture

We obtained HPAEPiCs (type II alveolar epithelial cells) from the ScienCell Research Laboratory (San Diego, CA). The cultured condition and procedure were described as previous published reference [19]. HPAEPiCs were used between passages 3 and 8. We used the XTT assay kit to examine the cytotoxicity of each inhibitor at the incubation time.

### 2.3. Preparation of *P. aeruginosa*

*P. aeruginosa* (RP73 clinical strain; a gift from Dr J. C. Shu, Department of Medical Biotechnology and Laboratory Science, Chang Gung University, Tao-Yuan, Taiwan) was cultured in BHI (brain heart infusion) broth (Sigma). However, the procedure of bacteria preparation can refer to our previous study [20]. In each experiment, approximately  $2 \times 10^7$  bacteria, representing a bacteria/epithelial cell ratio of 20:1, were added in 1 ml of RPMI 1640 medium (Gibco) to each well.

### 2.4. Transient transfection with siRNAs

Scrambled, ICAM-1, IL-6, p47<sup>phox</sup>, JNK2, p42, p38, p65, p50, TLR2, and TLR4 human siRNAs were purchased from Sigma (St. Louis, MO). We transiently transfected siRNA (100 nM) using a Lipofectamine® 2000 Reagent according to the manufacturer's instructions.

### 2.5. Real-time PCR

We used TRIzol reagent to extract total RNA. We then reverse-transcribed mRNA into cDNA and analysed by real-time PCR using SYBR Green PCR reagents (Applied Biosystems, Branchburg, NJ) and primers specific for human GAPDH, ICAM-1, TLR2, and TLR4 and mouse GAPDH and ICAM-1 mRNAs. Finally, ICAM-1, TLR2, and TLR4 mRNA levels were determined by normalizing to that of GAPDH expression.

### 2.6. Measurement of intracellular ROS accumulation

We used CellROX Green Reagent (Molecular Probes, Eugene, OR) to measure oxidative stress in HPAEPiCs. The fluorescence for CellROX Green Reagent staining was detected at 485/520 nm. HPAEPiCs were washed with warm HBSS and incubated in HBSS containing 5 μM CellROX Green Reagent at 37 °C for 30 min. Subsequently, HBSS containing CellROX Green Reagent was removed and replaced with fresh medium. HPAEPiCs were then incubated with *P. aeruginosa* for the indicated times. Finally, HPAEPiCs were washed twice with PBS and detached with trypsin/EDTA, and the fluorescence intensity of the cells was analysed using a FACScan flow cytometer (BD Biosciences, San Jose, CA) at 485 nm excitation and 520 nm emission.

### 2.7. Measurement of IL-6 generation

HPAEPiCs were cultured in 12-well culture plates. After reaching confluence, HPAEPiCs were incubated with *P. aeruginosa* for the indicated times. The media were gathered and IL-6 levels were assayed by using an IL-6 ELISA kit (BioSource International, Camarillo, CA).

### 2.8. Measurement of PGE<sub>2</sub> generation

HPAEPiCs were cultured in 12-well culture plates. After reaching confluence, HPAEPiCs were incubated with *P. aeruginosa* for the indicated times. The media were gathered and PGE<sub>2</sub> levels were assayed by using a PGE<sub>2</sub> ELISA kit (Enzo Life Sciences, Farmingdale, NY).

## 2.9. Measurement of phospho-JNK, phospho-ERK1/2, and phospho-NF- $\kappa$ B levels

HPAEpiCs were cultured in 6-well culture plates. After reaching confluence, HPAEpiCs were treated with *P. aeruginosa* for the indicated times. The levels of phospho-JNK, phospho-ERK1/2, and phospho-NF- $\kappa$ B were assayed by using the ELISA kits of phospho-JNK, phospho-ERK1/2, and phospho-NF- $\kappa$ B (Enzo Life Sciences, Farmingdale, NY), respectively.

## 2.10. Western blot

We cultured HPAEpiCs in 6-well culture plates. After reaching confluence, HPAEpiCs were treated with *P. aeruginosa* for the indicated times. Western blot condition and procedure can refer to previous published Ref. [19]. Finally, membranes were incubated with the anti-ICAM-1 antibody for one day, and then incubated with the anti-rabbit horseradish peroxidase antibody for 60 min. We used ECL reagents to detect immunoreactive bands.

## 2.11. Measurement of ICAM-1 luciferase promoter activity

The human ICAM-1 (pIC-339) firefly luciferase was kindly offered by Dr. P. T. van der Saag (Hubrecht Laboratory, Utrecht, The Netherlands). ICAM-1 luciferase promoter assay procedure can refer to previous published reference [19]. Firefly luciferase activities were finally normalized to  $\beta$ -gal activity.

## 2.12. Determination of NADPH oxidase activity by chemiluminescence assay

After incubation, HPAEpiCs were scraped and centrifuged at 400g for 10 min at 4 °C. The cell pellet was resuspended and the procedure and condition of chemiluminescence assay can refer to previous published reference [21].

## 2.13. Cell viability

Cell viability was measured by using the MTT assay. HPAEpiCs ( $2.5 \times 10^5$  cells/well in 24-well plates) were incubated with various concentrations of CORM-2, and then treated with an MTT solution (5 mg/ml) for 120 min. The procedure and condition of MTT assay can refer to previous published Ref. [22].

## 2.14. Adhesion assay

HPAEpiCs ( $2 \times 10^6$  cells/ml) were grown to confluence in 6-well plates and incubated with *P. aeruginosa*, and then adhesion assays were performed. Moreover, the procedure and condition of adhesion assay can refer to previous published reference [21]. Experiments were performed in triplicate and repeated at least three times.

## 2.15. Isolation of cell fractions

HPAEpiCs were harvested, sonicated for 5 s at output 1.5 with a sonicator (Misonix, Farmingdale, NY), and centrifuged at 8000 revolution/min for 15 min at 4 °C. The pellet was collected as the nuclear fraction. The supernatant was centrifuged at 14,000 revolution/min at 4 °C for 60 min to yield the pellet (membrane fraction) and the supernatant (cytosolic fraction).

## 2.16. Animal care and experimental procedures

Male ICR mice aged 6–8 weeks were purchased from the National Laboratory Animal Centre (Taipei, Taiwan) and were handled according to the NIH Guides for the Care and Use of Laboratory Animals.

ICR mice were exposed to *P. aeruginosa* by i.p. injection of 100  $\mu$ l bacterial suspension ( $2 \times 10^7$  CFU/mouse). Control mice were administered BHI. ICR mice were given i.p. (intraperitoneally) NAC, APO, Gö6976, SP600125, U0126, SB203580, HLN, or CORM-2 for 2 h before *P. aeruginosa* ( $2 \times 10^7$  CFU/mouse) treatment. The animals were killed after 48 h. Plasma MPO and serum CRP, IL-6, IL-8, IL-1 $\beta$ , and TNF- $\alpha$  were measured.

## 2.17. Statistical analysis of data

We estimated the data using the GraphPad Prism program (GraphPad, San Diego, CA). Quantitative data were expressed as the mean  $\pm$  S.E.M. and analysed by one-way ANOVA followed with Tukey's post-hoc test. We defined  $P < 0.05$  as a significant difference.

## 3. Results

### 3.1. *P. aeruginosa* induces PGE<sub>2</sub>/IL-6/ICAM-1-dependent monocyte adhesion

Many studies have pointed out that *P. aeruginosa* can induce PGE<sub>2</sub> production [23,24]. In this study, we explored whether *P. aeruginosa* could induce PGE<sub>2</sub> release in HPAEpiCs. As shown in Fig. 1A, *P. aeruginosa* time-dependently induced PGE<sub>2</sub> production. When IL-6 binds to its soluble receptor sIL-6R $\alpha$ , it can affect the transition from acute to chronic inflammation by regulating the properties of leukocyte infiltrate [25]. We previously proved that PGE<sub>2</sub> could induce IL-6 release in human tracheal smooth muscle cells (HTSMCs) [26]. In this study, we clearly pointed out that *P. aeruginosa* induced IL-6 release, which was reduced by pretreatment with the inhibitor of PGE<sub>2</sub> (SC-51322) (Fig. 1B). ICAM-1 is known to play an important role in lung inflammation [12]. Moreover, in this study, we proved that *P. aeruginosa* ( $2 \times 10^7$  CFU/ml and  $1 \times 10^7$  CFU/ml) induced ICAM-1 protein expression, mRNA levels, and promoter activity in HPAEpiCs (Fig. 1C and D). Wung et al. previously proved that TNF- $\alpha$  and IL-6 can induce ICAM-1 expression via a NF- $\kappa$ B signaling [27]. Indeed, we also observed that *P. aeruginosa*-induced ICAM-1 mRNA levels and monocyte adhesion were inhibited by transfection with IL-6 siRNA (Fig. 1E and F). CO can exert the anti-inflammatory effects in various cell types [28]. We examined the effects of CORM-2 on the cell viability of HPAEpiCs. As shown in Fig. 1G, we found that various concentrations of CORM-2 (1, 10, 50, and 100  $\mu$ M) had no effects on the cell viability of HPAEpiCs. Pretreatment with CORM-2 (50  $\mu$ M) could cut down *P. aeruginosa*-induced ICAM-1 protein and mRNA levels and monocyte adhesion (Fig. 1H and I). Taken together, we assume that *P. aeruginosa* induces monocyte adhesion via a PGE<sub>2</sub>/IL-6/ICAM-1-dependent pathway.

### 3.2. CORM-2 has no effects on TLR-2 and TLR4 expression in HPAEpiCs

TLR4 is the most widely studied TLR, which can identify LPS (the compounds of the outer surface of Gram-negative bacteria) [29]. In this study, we proved that *P. aeruginosa*-induced PGE<sub>2</sub> and IL-6 levels were curbed by transfection with TLR4 siRNA, but not TLR2 siRNA in these cells (Fig. 2A). Furthermore, *P. aeruginosa*-induced ICAM-1 expression was also inhibited by TLR4 siRNA transfection (Fig. 2B, upper panel). *P. aeruginosa* and LPS increased TLR4 protein levels directly (Fig. 2B, lower panel). Finally, we examined whether CORM-2 could inhibit ICAM-1 expression via the inhibition of TLRs expression. As shown in Fig. 2C, CORM-2 had no effects on *P. aeruginosa*- or LPS-induced TLR4 mRNA levels.

### 3.3. *P. aeruginosa* induces ICAM-1 expression via PKC $\alpha$ in HPAEpiCs

Previous studies have demonstrated that PKC $\alpha$  can regulate ICAM-1 expression and monocyte adhesion [13]. Indeed, we found that *P. aeruginosa*-induced IL-6 and PGE<sub>2</sub> release and ICAM-1 promoter activity

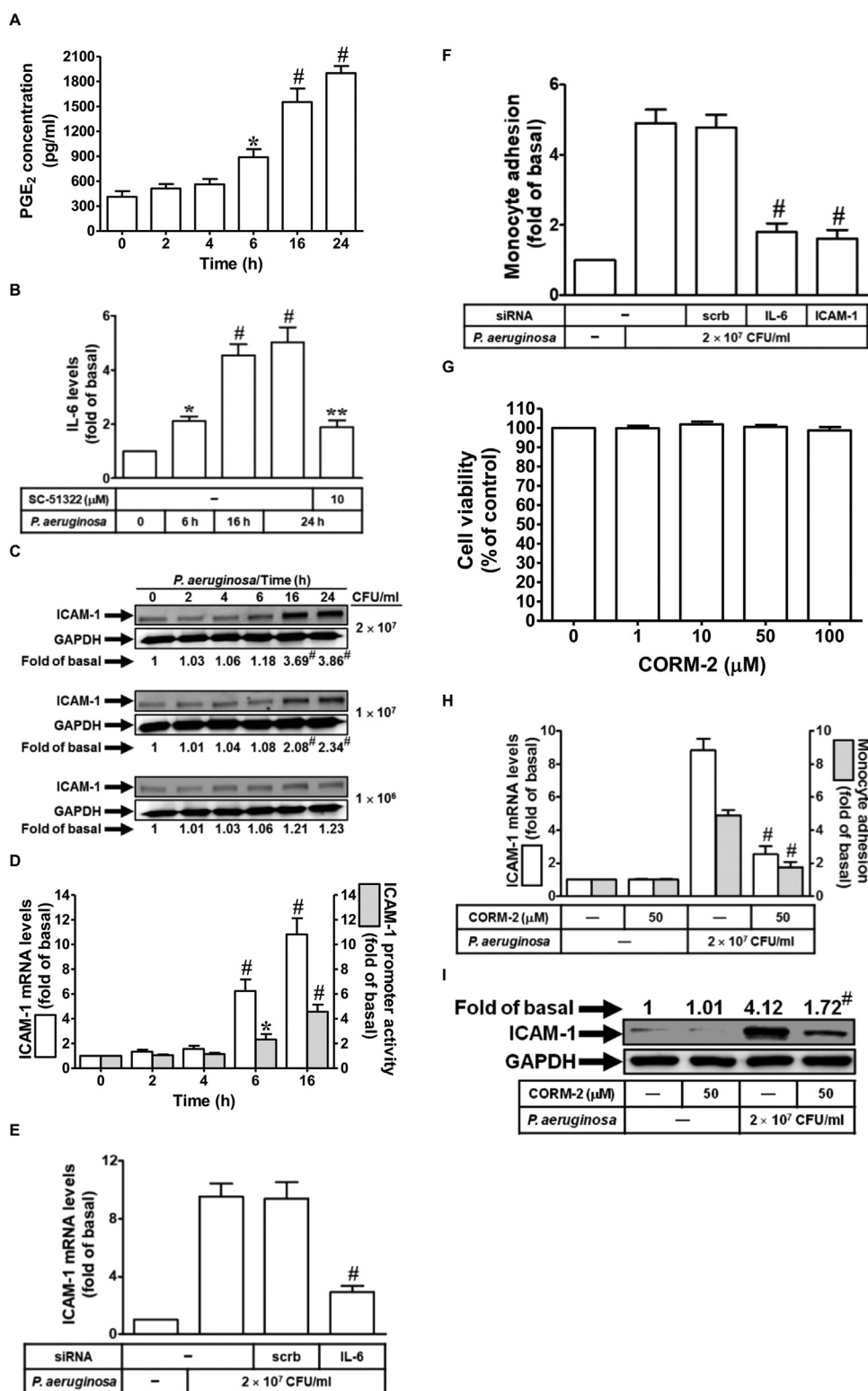


**Fig. 1.** *P. aeruginosa* induces PGE<sub>2</sub>/IL-6/ICAM-1-dependent monocyte adhesion. (A) Cells were treated with *P. aeruginosa* for the indicated times. The PGE<sub>2</sub> production was measured. (B) Cells were treated with *P. aeruginosa* for the indicated times or pretreated with SC-51322 for 1 h, and then treated with *P. aeruginosa* ( $2 \times 10^7$  CFU/ml) for 24 h. The IL-6 production was measured. Cells were treated with *P. aeruginosa* for the indicated times. The ICAM-1 protein expression was determined by Western blot (C). The ICAM-1 mRNA levels and promoter activity were determined by real-time PCR and promoter assay, respectively (D). (E) Cells were transfected with siRNA of scrambled or IL-6, and then treated with *P. aeruginosa* ( $2 \times 10^7$  CFU/ml) for 16 h. The ICAM-1 mRNA levels were determined by real-time PCR. (F) Cells were transfected with siRNA of scrambled, IL-6, or ICAM-1, and then treated with *P. aeruginosa* ( $2 \times 10^7$  CFU/ml) for 24 h. The monocyte adhesion was measurement by adhesion assay. (G) Cells were incubated with CORM-2 for the indicated times, and then the cell viability was determined. (H) Cells were pretreated with CORM-2 (50  $\mu$ M) for 2 h, and then treated with *P. aeruginosa* ( $2 \times 10^7$  CFU/ml) for 16 h (for ICAM-1 mRNA levels) or 24 h (for monocyte adhesion). The ICAM-1 mRNA levels were determined by real-time PCR. The monocyte adhesion was measurement by adhesion assay. (I) Cells were pretreated with CORM-2 (50  $\mu$ M) for 2 h, and then treated with *P. aeruginosa* ( $2 \times 10^7$  CFU/ml) for 24 h. The ICAM-1 protein expression was determined by Western blot. Data are expressed as mean  $\pm$  S.E.M. of three independent experiments. \* $P < 0.05$ ; # $P < 0.01$ , as compared with the basal level (A, B, C, D). \*\* $P < 0.01$ , as compared with the cells exposed to *P. aeruginosa* alone (B). # $P < 0.01$ , as compared with the cells exposed to *P. aeruginosa* + scrambled siRNA (E, F). # $P < 0.01$ , as compared with the cells exposed to *P. aeruginosa* alone (H, I).

and mRNA levels were inhibited by the siRNA of PKC $\alpha$  (Fig. 3A and B). On the other hand, *P. aeruginosa*-induced ICAM-1 protein expression was reduced by the inhibitor of PKC $\alpha$  (Gö6976) (Fig. 3C). We further demonstrated that *P. aeruginosa* could time-dependently induce PKC $\alpha$  phosphorylation in HPAEpiCs (Fig. 3D). Finally, we examined whether CORM-2 could affect *P. aeruginosa*-induced PKC $\alpha$  activation in HPAEpiCs. As shown in Fig. 3E, we showed that *P. aeruginosa* time-dependently induced PKC $\alpha$  activation, which was reduced by CORM-2. Taken

together, these data suggest that CORM-2 inhibits *P. aeruginosa*-induced ICAM-1 expression via the reduction of PKC $\alpha$  activation in HPAEpiCs.

### 3.4. *P. aeruginosa* induces ICAM-1 expression via NADPH oxidase/ROS in HPAEpiCs

Several lines of evidence have demonstrated that ROS contributes to ICAM-1 expression in various cell types [12,13]. It is known that



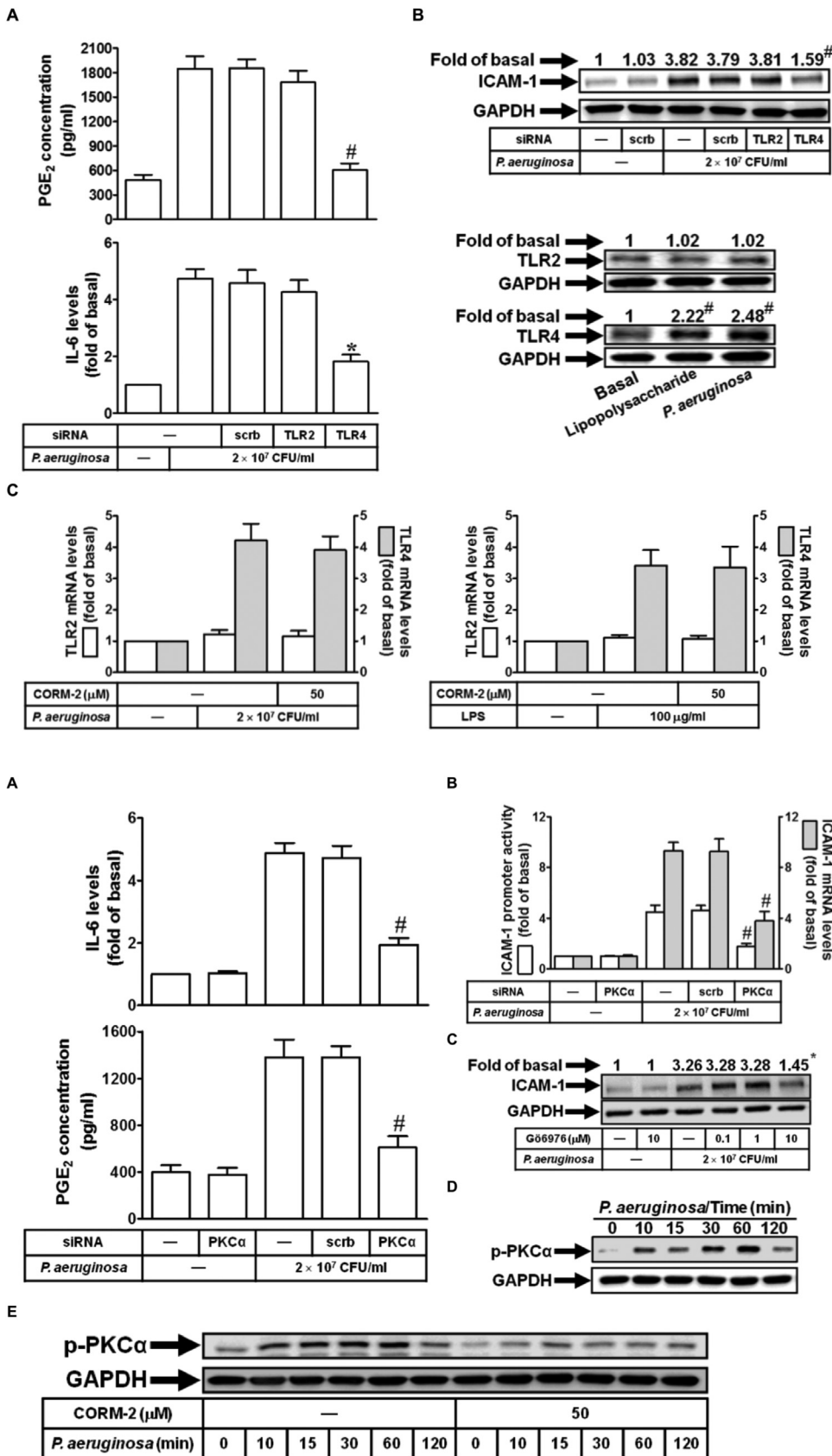
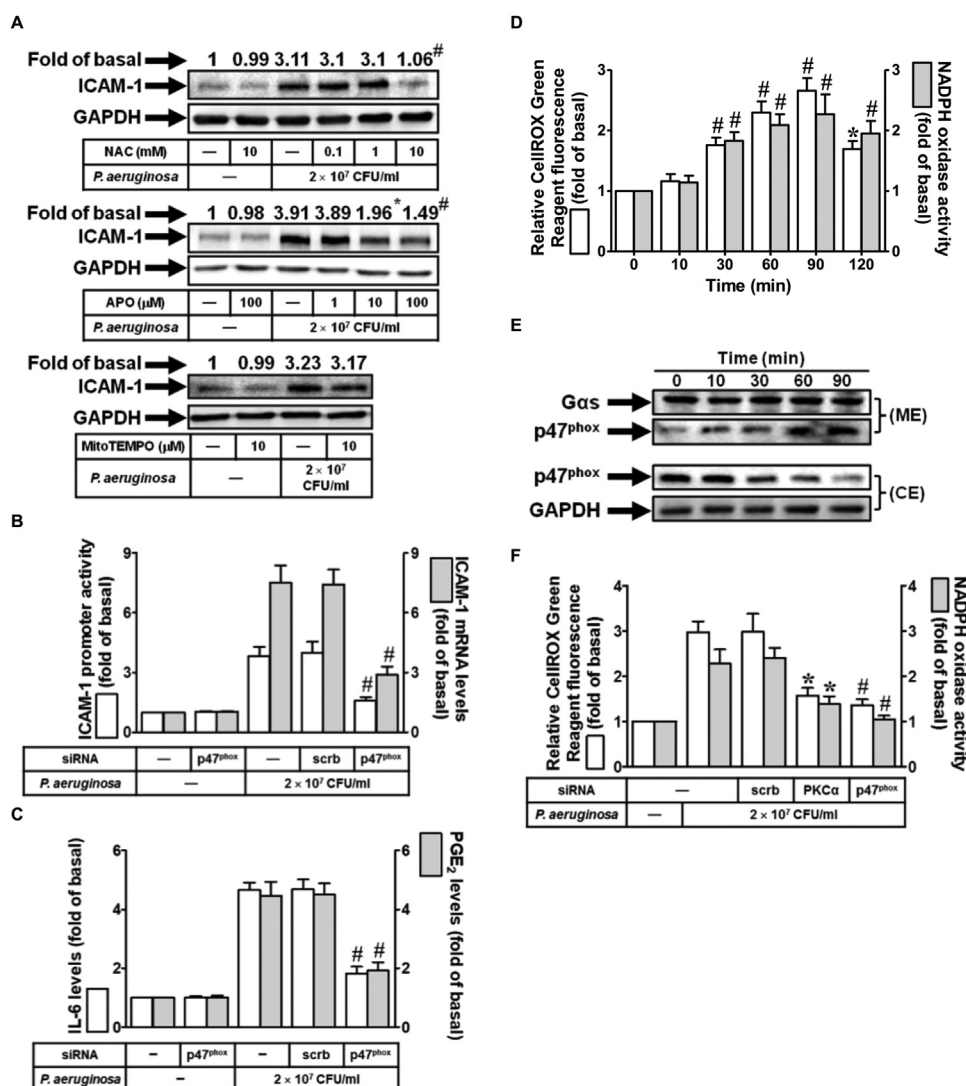


**Fig. 2.** CORM-2 has no effects on TLR-2 and TLR4 expression in HPAEpiCs. (A) Cells were transfected with siRNA of scrambled, TLR4, or TLR2, and then treated with *P. aeruginosa* ( $2 \times 10^7$  CFU/ml) for 24 h. The levels of PGE<sub>2</sub> and IL-6 were measured. (B) Cells were transfected with siRNA of scrambled, TLR4, or TLR2, and then treated with *P. aeruginosa* ( $2 \times 10^7$  CFU/ml) for 24 h. The ICAM-1 expression was determined by Western blot. Cells were treated with LPS (100 μg/ml) or *P. aeruginosa* ( $2 \times 10^7$  CFU/ml) for 24 h. The TLR2 and TLR4 expression was determined by Western blot. (C) Cells were treated with LPS (100 μg/ml) or *P. aeruginosa* ( $2 \times 10^7$  CFU/ml) in the presence or absence of CORM-2 (50 μM). The TLR2 and TLR4 mRNA levels were determined by real-time PCR. Data are expressed as mean  $\pm$  S.E.M. of three independent experiments. #*P* < 0.01, as compared with the cells exposed to *P. aeruginosa* + scrambled siRNA [A, B (upper panel)]. #*P* < 0.01, as compared with the basal level [B (lower panel)].

**Fig. 3.** *P. aeruginosa* induces ICAM-1 expression via PKCα in HPAEpiCs. (A) Cells were transfected with siRNA of scrambled or PKCα, and then treated with *P. aeruginosa* ( $2 \times 10^7$  CFU/ml) for 24 h. The levels of PGE<sub>2</sub> and IL-6 were measured. (B) Cells were transfected with siRNA of scrambled or PKCα, and then treated with *P. aeruginosa* ( $2 \times 10^7$  CFU/ml) for 16 h. The ICAM-1 mRNA levels and promoter activity were determined by real-time PCR and promoter assay, respectively. (C) Cells were pretreated with Gö6976 for 1 h, and then treated with *P. aeruginosa* for 24 h. The ICAM-1 expression was determined by Western blot. (D) Cells were treated with *P. aeruginosa* for the indicated times. The expression of phospho-PKCα was determined by Western blot. (E) Cells were pretreated without or with CORM-2 for 2 h, and then treated with *P. aeruginosa* ( $2 \times 10^7$  CFU/ml) for the indicated times. The expression of phospho-PKCα was determined by Western blot. Data are expressed as mean  $\pm$  S.E.M. of three independent experiments. #*P* < 0.01, as compared with the cells exposed to *P. aeruginosa* + scrambled siRNA (A, B). \**P* < 0.05, as compared with the cells exposed to *P. aeruginosa* alone (C).



NADPH oxidase is the critical enzyme for the generation of ROS under various pathological conditions [12]. Thus, the role of NADPH oxidase in ROS generation associated with ICAM-1 expression in response to *P. aeruginosa* was examined. Pretreatment of HPAEpiCs with the inhibitor of ROS (NAC) or NADPH oxidase (APO) significantly abrogated *P. aeruginosa*-induced ICAM-1 protein levels (Fig. 4A). The generation of ROS from mitochondria is important because it often causes oxidative damage [30]. However, in our study, we proved that pretreatment with the mitochondria-targeted antioxidant (MitoTEMPO) had no effects on *P. aeruginosa*-induced ICAM-1 expression (Fig. 4A). The NADPH oxidase components contain membrane-bound heterodimer (NOX and p22<sup>phox</sup>) and 4 cytosolic proteins including p47<sup>phox</sup>, p67<sup>phox</sup>, p40<sup>phox</sup>, and Rac1/2 [12]. We further proved that transfection with p47<sup>phox</sup> siRNA markedly inhibited *P. aeruginosa*-induced ICAM-1 promoter activity and mRNA levels (Fig. 4B). In addition, we also showed that IL-6 and PGE<sub>2</sub> release induced by *P. aeruginosa* was reduced by the p47<sup>phox</sup> siRNA (Fig. 4C). As shown in Fig. 4D, *P. aeruginosa* time-dependently enhanced intracellular ROS generation and NADPH oxidase activity in these cells. It has been demonstrated that p47<sup>phox</sup> organizes the translocation of other cytosolic factors, hence its designation as “organizer subunit” [12]. Moreover, we demonstrated that *P. aeruginosa* induced p47<sup>phox</sup> translocation from the cytosol to the membrane (Fig. 4E). Intracellular ROS generation has been shown to be mediated via PKCα [31]. Finally, we investigated whether PKCα could regulate *P. aeruginosa*-induced NADPH oxidase activation and intracellular ROS

generation. As shown in Fig. 4F, PKCα siRNA transfection markedly inhibited NADPH oxidase activation and intracellular ROS generation in response to *P. aeruginosa*. These results suggest that *P. aeruginosa*-induced ICAM-1 expression is mediated through NADPH oxidase/ROS generation in HPAEpiCs.

### 3.5. *P. aeruginosa* induces ICAM-1 expression via JNK and ERK1/2 in HPAEpiCs

MAPKs can integrate signals from numerous receptors and translate these signals into cellular functions. They are essential for metabolism, migration, generation of pro-inflammatory mediators, survival, and differentiation [32]. In this study, we proved that *P. aeruginosa*-induced ICAM-1 protein levels were inhibited by the inhibitor of JNK (SP600125) or MEK1/2 (PD98059), but not the inhibitor of p38 MAPK (SB203580) (Fig. 5A). In addition, transfection with JNK2 or p42 siRNA also markedly decreased *P. aeruginosa*-induced monocyte adhesion and ICAM-1 mRNA levels in these cells (Fig. 5B). We further proved that *P. aeruginosa* could induce p38 MAPK, JNK, and ERK1/2 activation in a time-dependent manner (Fig. 5C). MAPKs activation has been shown to be regulated through various signaling pathways [13]. Indeed, we proved that pretreatment with Gö6976, NAC, or APO inhibited *P. aeruginosa*-induced JNK and ERK1/2 phosphorylation (Fig. 5D). These data suggest that *P. aeruginosa* induces ERK1/2 and JNK activation via the PKCα/NADPH oxidase/ROS pathway. We investigated whether CORM-

**Fig. 4.** *P. aeruginosa* induces ICAM-1 expression via NADPH oxidase/ROS in HPAEpiCs. (A) Cells were pretreated with NAC, APO, or MitoTEMPO for 2 h, and then treated with *P. aeruginosa* for 24 h. The ICAM-1 expression was determined by Western blot. (B) Cells were transfected with siRNA of scrambled or p47<sup>phox</sup>, and then treated with *P. aeruginosa* ( $2 \times 10^7$  CFU/ml) for 16 h. The ICAM-1 mRNA levels and promoter activity were determined by real-time PCR and promoter assay, respectively. (C) Cells were transfected with siRNA of scrambled or p47<sup>phox</sup>, and then treated with *P. aeruginosa* ( $2 \times 10^7$  CFU/ml) for 24 h. The levels of PGE<sub>2</sub> and IL-6 were measured. (D) Cells were treated with *P. aeruginosa* for the indicated times. The intracellular ROS generation and NADPH oxidase activity were measured. (E) Cells were treated with *P. aeruginosa* for the indicated times. The cytosol and membrane extracts were prepared and subjected to Western blot using an anti-p47<sup>phox</sup> antibody. (F) Cells were transfected with siRNA of scrambled, PKCα, or p47<sup>phox</sup>, and then treated with *P. aeruginosa* ( $2 \times 10^7$  CFU/ml) for 90 min. The intracellular ROS generation and NADPH oxidase activity were measured. Data are expressed as mean  $\pm$  S.E.M. of three independent experiments. \**P* < 0.05; #*P* < 0.01, as compared with the cells exposed to *P. aeruginosa* alone (A). \**P* < 0.05; #*P* < 0.01, as compared with the cells exposed to *P. aeruginosa* + scrambled siRNA (B, C, F). \**P* < 0.05; #*P* < 0.01, as compared with the basal level (D).

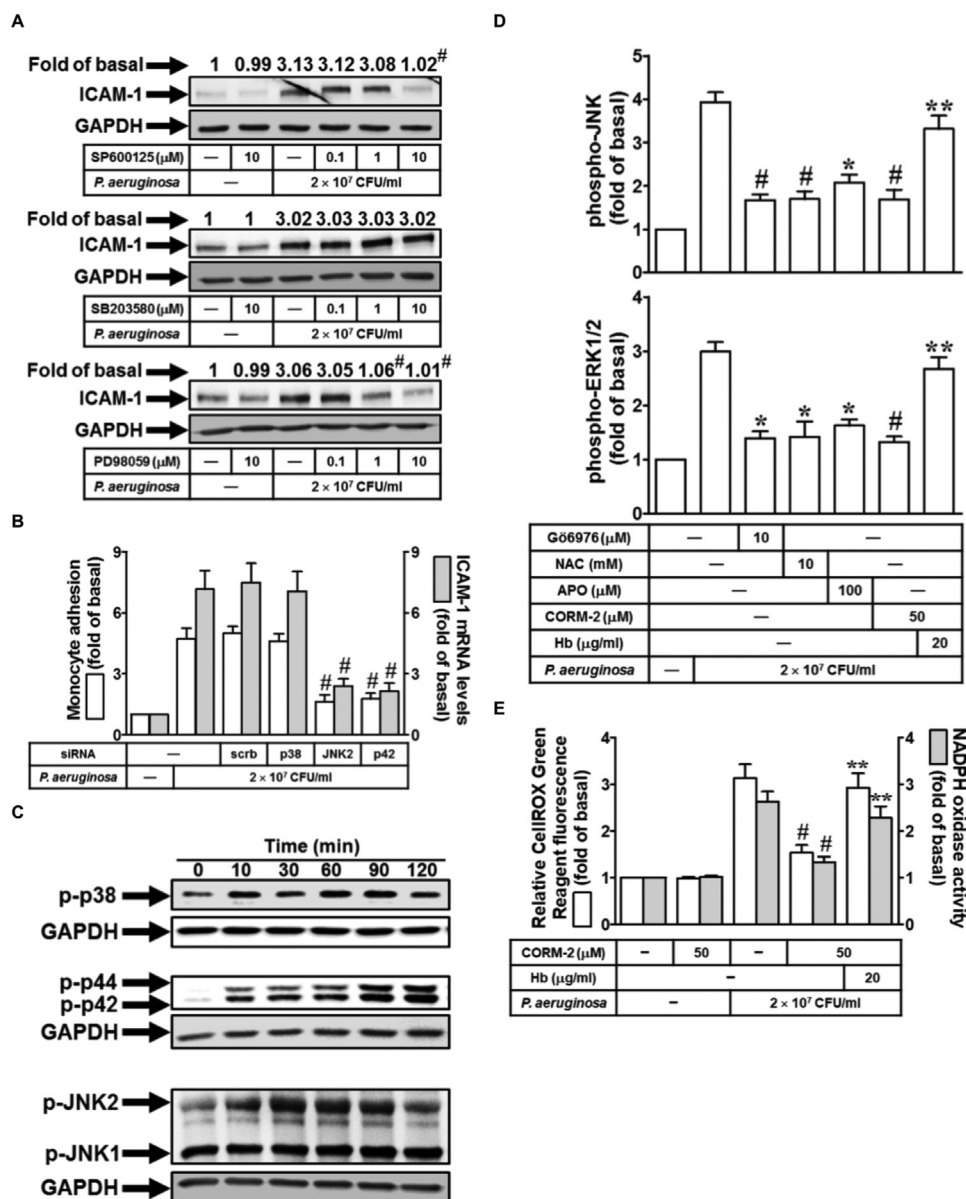


**Fig. 5.** *P. aeruginosa* induces ICAM-1 expression via JNK and ERK1/2 in HPAEpiCs. (A) Cells were pretreated with SP600125, SB203580, or PD98059 for 1 h, and then treated with *P. aeruginosa* for 24 h. The ICAM-1 expression was determined by Western blot. (B) Cells were transfected with siRNA of scrambled, p38, JNK2, or p42, and then treated with *P. aeruginosa* (2 × 10<sup>7</sup> CFU/ml) for 24 h (for monocyte adhesion) or 16 h (for ICAM-1 mRNA levels). The ICAM-1 mRNA levels were determined by real-time PCR. The monocyte adhesion was measurement by adhesion assay. (C) Cells were treated with *P. aeruginosa* for the indicated times. The expression of phospho-p38 MAPK, phospho-JNK, or phospho-ERK1/2 was determined by Western blot. (D) Cells were pretreated with G66976, NAC, APO, or CORM-2 in the presence or absence of Hb (20 μg/ml) for 2 h, and then treated with *P. aeruginosa* for 90 min. The levels of phospho-JNK and phospho-ERK1/2 were measured by the ELISA kits. (E) Cells were pretreatment with CORM-2 for 2 h in the presence or absence of Hb (20 μg/ml), and then treated with *P. aeruginosa* for 90 min. The intracellular ROS generation and NADPH oxidase activity were measured. Data are expressed as mean ± S.E.M. of three independent experiments. \**P* < 0.05; #*P* < 0.01, as compared with the cells exposed to *P. aeruginosa* alone (A, D, E). #*P* < 0.01, as compared with the cells exposed to *P. aeruginosa* + scrambled siRNA (B). \*\**P* < 0.05, as compared with the cells exposed to *P. aeruginosa* + CORM-2 (D, E).

2 could inhibit inflammatory responses induced by *P. aeruginosa* via the reduction of ERK1/2 and JNK activation in HPAEpiCs. As shown in Fig. 5D, preincubation with CORM-2 significantly inhibited *P. aeruginosa*-induced ERK1/2 and JNK activation, which was reversed by the addition of CO scavenger, hemoglobin (Hb). Finally, we showed that CORM-2 could decrease *P. aeruginosa*-enhanced intracellular ROS generation and NADPH oxidase activity (Fig. 5E). Taken together, we think that CORM-2 can inhibit inflammation induced by *P. aeruginosa* via the reduction of JNK and ERK1/2 activation and NADPH oxidase/ROS generation in HPAEpiCs.

### 3.6. CORM-2 inhibits *P. aeruginosa*-induced ICAM-1 expression via the reduction of NF-κB activation

NF-κB has been shown to regulate ICAM-1 expression in various cell types [33,34]. Indeed, we proved that *P. aeruginosa*-induced ICAM-1 protein and mRNA levels and monocyte adhesion were inhibited by the inhibitor of NF-κB (HLN) or siRNA of p65 or p50 (Fig. 6A and B). AP-1 is often activated during bacterial and viruses infections [35]. Similar to NF-κB, AP-1 has many transcriptional regulator binding sites for inflammatory regulators, and AP-1 can also bind promoters of

inflammatory mediators independent of NF-κB during inflammation [36]. However, we proved that pretreatment with the inhibitor of AP-1 (Tanshinone IIA) had no effects on *P. aeruginosa*-induced ICAM-1 protein levels (Fig. 6A). Transfection with c-Jun siRNA also did not inhibit *P. aeruginosa*-induced ICAM-1 mRNA levels and monocyte adhesion (Fig. 6B). We further proved that transfection with p65 siRNA markedly decreased *P. aeruginosa*-induced IL-6 and PGE<sub>2</sub> release in these cells (Fig. 6C). NF-κB activation has been shown to be regulated through various signaling pathways [13]. Indeed, we proved that pretreatment with G66976, NAC, APO, or SP600125, but not PD98059, inhibited *P. aeruginosa*-induced NF-κB phosphorylation (Fig. 6D). These data suggest that *P. aeruginosa* induces NF-κB activation via the PKCα/NADPH oxidase/ROS/JNK pathway. We investigated whether CORM-2 could inhibit inflammatory responses induced by *P. aeruginosa* via the reduction of NF-κB activation in HPAEpiCs. As shown in Fig. 6D, preincubation with CORM-2 significantly inhibited *P. aeruginosa*-induced NF-κB activation. Finally, we showed that CORM-2 also reduced NF-κB promoter activity enhanced by *P. aeruginosa* (Fig. 6E). Thus, we suggest that CORM-2 can inhibit inflammation induced by *P. aeruginosa* via the reduction of NF-κB activation in HPAEpiCs.

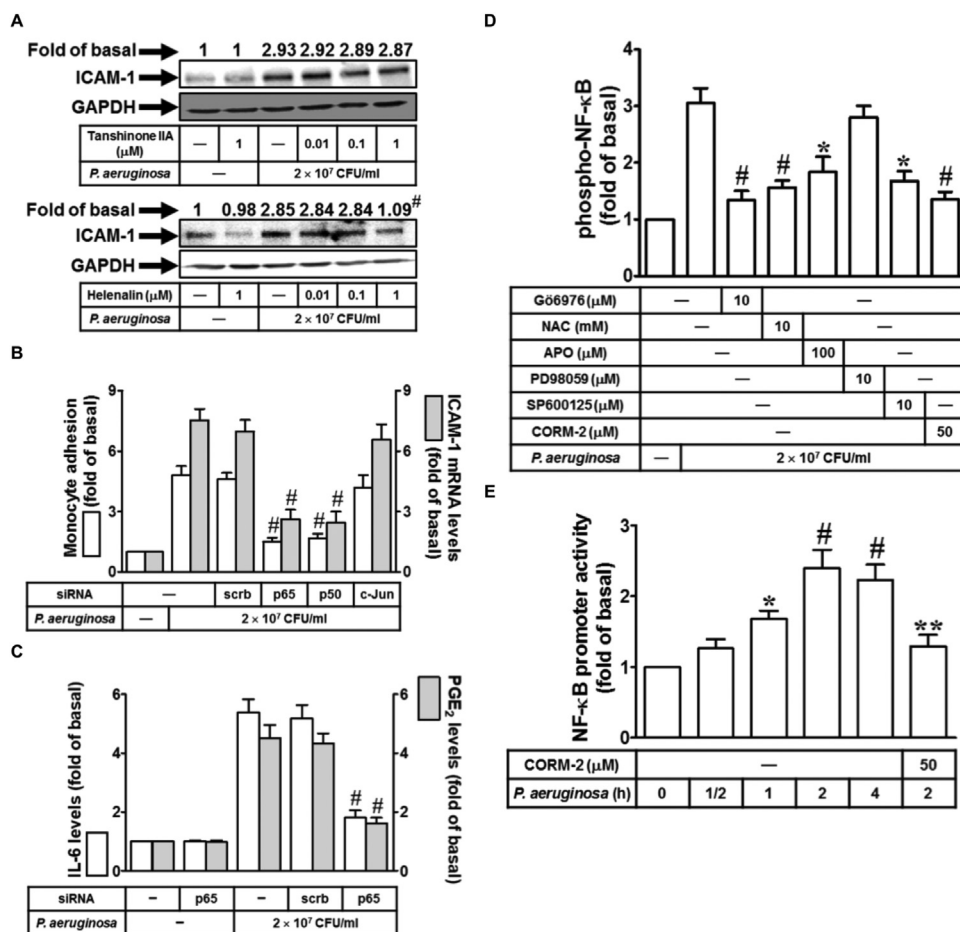


**Fig. 6.** CORM-2 inhibits *P. aeruginosa*-induced ICAM-1 expression via the reduction of NF-κB activation. (A) Cells were pretreated with Tanshinone IIA or HLN for 1 h, and then treated with *P. aeruginosa* for 24 h. The ICAM-1 expression was determined by Western blot. (B) Cells were transfected with siRNA of scrambled, p50, c-Jun, or p65, and then treated with *P. aeruginosa* (2 × 10<sup>7</sup> CFU/ml) for 24 h (for monocyte adhesion) or 16 h (for ICAM-1 mRNA levels). The ICAM-1 mRNA levels were determined by real-time PCR. The monocyte adhesion was measured by adhesion assay. (C) Cells were transfected with siRNA of scrambled or p65, and then treated with *P. aeruginosa* (2 × 10<sup>7</sup> CFU/ml) for 24 h. The levels of PGE<sub>2</sub> and IL-6 were measured. (D) Cells were pretreated with Gö6976, NAC, APO, PD98059, SP600125, or CORM-2 for 2 h, and then treated with *P. aeruginosa* for 2 h. The levels of phospho-NF-κB were measured by the NF-κB ELISA kit. (E) Cells were treated with *P. aeruginosa* for the indicated times or pretreated with CORM-2 for 2 h, and then incubated with *P. aeruginosa* for 2 h. The NF-κB promoter activity was determined by promoter assay. Data are expressed as mean ± S.E.M. of three independent experiments. \**P* < 0.05; #*P* < 0.01, as compared with the cells exposed to *P. aeruginosa* alone (A, D). #*P* < 0.01, as compared with the cells exposed to *P. aeruginosa* + scrambled siRNA (B, C). \**P* < 0.05; #*P* < 0.01, as compared with the basal level (E). \*\**P* < 0.05, as compared with the cells exposed to *P. aeruginosa* alone (E).

### 3.7. CORM-2 inhibits *P. aeruginosa*-induced ICAM-1 expression and lung inflammation in mice

In an in vivo study, mice were treated with *P. aeruginosa* (2 × 10<sup>7</sup> CFU/mouse), and then killed after 48 h. Preparation of lung tissues was analysed by Western blot to determine the levels of ICAM-1 protein. As shown in Fig. 7A, we found that *P. aeruginosa* induced ICAM-1 protein levels in the lung tissues. In addition, we observed that *P. aeruginosa* markedly caused lung tissue damage (Fig. 7B). Mice were given i.p. one dose of Gö6976, NAC, APO, U0126, SB203580, HLN, or SP600125 for 2 h before *P. aeruginosa* (2 × 10<sup>7</sup> CFU/mouse) treatment, and then killed after 48 h. Preparation of lung tissues was analysed by real-time PCR to determine the levels of ICAM-1 mRNA. We showed that *P. aeruginosa* induced ICAM-1 mRNA levels, which were reduced by Gö6976, NAC, APO, U0126, HLN, or SP600125, but not SB203580 (Fig. 7C). On the other hand, CORM-2 (8 mg/kg) could markedly inhibit *P. aeruginosa*-induced ICAM-1 mRNA levels (Fig. 7D). C-reactive protein (CRP) is the most extensively studied inflammatory biomarker in respiratory diseases. Myeloperoxidase (MPO) plays a crucial role in inflammation. Many studies have proved IL-8 as a key regulator in neutrophil-mediated acute inflammation [37]. Here, we proved that *P. aeruginosa* enhanced the levels of plasma MPO and serum CRP, IL-6, IL-8, IL-1β, and TNF-α, which were inhibited by CORM-2 (8 mg/kg) (Fig. 7E).

## 4. Discussion

*P. aeruginosa*-induced pneumonia is a serious and common infectious disease, and it often appears in the form of nosocomial infections. It often occurs in the immunocompromised patients, especially

elderly patients. Treatment of *P. aeruginosa*-induced pneumonia is difficult, with a mortality rate of up to 50%. Early diagnosis and effective antibiotic treatment are particularly important. Long-term exposure to low concentrations of CO can cause dizziness, vomiting, difficulty breathing, and muscle weakness. Even though CO is toxic to humans at high concentrations, many studies have documented that low-doses exogenous CO (approximately 250–500 ppm) have protective function against various human diseases [7,8]. In this study, we suggest that CO derived from CORM-2 can possibly be used as a therapeutic for lung inflammation. Here, we proved for the first time that in HPAEpiCs, *P. aeruginosa* induced PGE<sub>2</sub>/IL-6/ICAM-1-dependent monocyte adhesion, and then promoted the inflammatory responses. Moreover, CORM-2 could inhibit *P. aeruginosa*-induced PGE<sub>2</sub>/IL-6/ICAM-1 expression and inflammatory responses by decreasing the NADPH oxidase/ROS generation and the activation of the PKCα/NADPH oxidase/ROS/JNK/NF-κB and PKCα/NADPH oxidase/ROS/ERK1/2 pathways.

Recently, as CO has been proven to have anti-bacterial [9], anti-oxidant [10], and anti-inflammatory [10] effects, more and more researchers have begun to study the cytoprotective mechanisms of CO. Because it is still difficult to deliver the accurate doses of CO to the selected molecular target by directly inhaling the gas, CORMs are considered as a promising alternative technology. Many previous studies have demonstrated the therapeutic potential of CORMs [9,28]. Desmard et al. indicated that the water-soluble CORM-3 treatment could efficiently inhibit *P. aeruginosa*-induced infection [38]. CORM-2 is a CO-releasing agent. Due to its chemical structure, it has superior and more effective drug traits than gaseous CO [28]. Lian et al. proved that CORM-2 could inhibit IL-β-induced NADPH oxidase activation and ROS generation [17]. IL-6 is a pro-inflammatory cytokine and the elevation of IL-6 levels is often associated with various chronic diseases and



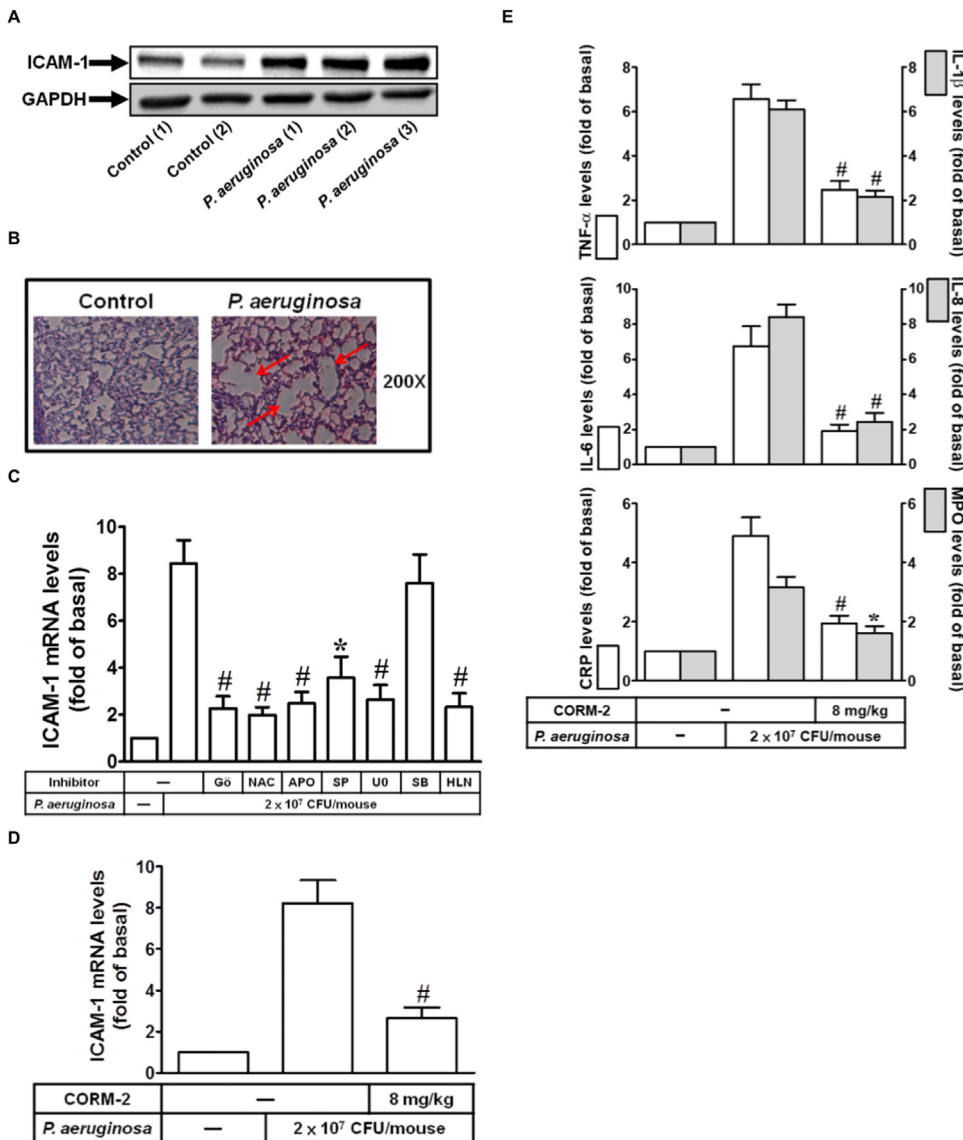


**Fig. 7.** CORM-2 inhibits *P. aeruginosa*-induced ICAM-1 expression and lung inflammation in mice. (A) Mice were treated with *P. aeruginosa* ( $2 \times 10^7$  CFU/mouse), and then killed after 48 h. Preparation of lung tissues was analysed by Western blot to determine the levels of ICAM-1 protein. (B) Mice were treated with *P. aeruginosa* ( $2 \times 10^7$  CFU/mouse), and then killed after 48 h. The morphology of lung tissues was observed by H&E stain. The arrows indicate the damaged alveoli. (C) Mice were given i.p. one dose of G66976, NAC, APO, U0126, SP600125, SB203580, or HLN for 2 h before *P. aeruginosa* ( $2 \times 10^7$  CFU/mouse) treatment, and then killed after 48 h. Preparation of lung tissues was analysed by real-time PCR to determine the levels of ICAM-1 mRNA. (D) Mice were given i.p. one dose of CORM-2 before *P. aeruginosa* ( $2 \times 10^7$  CFU/mouse) treatment, and then killed after 48 h. Preparation of lung tissues was analysed by real-time PCR to determine the levels of ICAM-1 mRNA. (E) Mice were pretreated with CORM-2, and then treated with *P. aeruginosa* ( $2 \times 10^7$  CFU/mouse) for 48 h. Levels of CRP, MPO, IL-8, IL-1 $\beta$ , IL-6, and TNF- $\alpha$  were measured. Data are expressed as mean  $\pm$  S.E.M. of three independent experiments. \* $P < 0.05$ ; # $P < 0.01$ , as compared with the mice exposed to *P. aeruginosa* alone.

inflammation. Previous studies have demonstrated that IL-6 can mediate cell migration in many cell types [39]. On the other hand, previous studies have also found a positive correlation between the PGE<sub>2</sub> up-regulation and the release of IL-6 [26]. ICAM-1 (also known as CD54) can regulate adhesion-dependent cell-to-cell interactions and promote inflammatory responses [4]. Many studies indicated that IL-6 can induce ICAM-1 expression in various cell types [4,5]. In HPAEpiCs, we proved that *P. aeruginosa* mediated monocyte adhesion through a PGE<sub>2</sub>/IL-6/ICAM-1 pathway. Moreover, we demonstrated that CORM-2 markedly inhibited *P. aeruginosa*-regulated inflammatory proteins up-regulation and monocyte adhesion in HPAEpiCs or mice.

TLRs are the very important receptors in the mammalian immune system. Their main function is to detect the invasion of foreign pathogens. Once the invasion of a pathogen is detected, the TLRs activate the signal transmission and induce innate immunity, which affects the subsequent adaptive immunity [29]. TLR4 is the most widely studied TLR, which can identify LPS (the compounds of the outer surface of Gram-negative bacteria) [29]. Indeed, we proved that *P. aeruginosa* induced ICAM-1 up-regulation and monocyte adhesion via TLR4, but not TLR2 in HPAEpiCs. However, CORM-2 had no effects on *P. aeruginosa*-enhanced TLR4 mRNA levels, suggesting that CORM-2 could not reduce *P. aeruginosa*-induced inflammation via the inhibition of TLR4 expression in these cells. PKC $\alpha$  is a serine/threonine kinase. Previous

studies proved that PKC $\alpha$  can regulate various cellular functions, such as cell migration, inflammation, differentiation, apoptosis, and proliferation [40]. In fact, in our study, we demonstrated that PKC $\alpha$  could activate the expression of downstream inflammatory proteins through TLR4 in HPAEpiCs. The current study rarely observes the correlation between CORM-2 and PKC $\alpha$  in various cell types. However, we proved that CORM-2 pretreatment significantly reduced PKC $\alpha$  phosphorylation in response to *P. aeruginosa*. The above data proved that CORM-2 could down-regulate *P. aeruginosa*-induced ICAM-1 expression through the inhibition of PKC $\alpha$  activation in HPAEpiCs. It also provides a very good research topic for the subsequent study on the correlation between CORM-2 and PKCs.

Increased oxidative stress often causes cell damage and leads to inflammation [12]. Oxidative stress may occur due to increased generation and/or reduced ROS destruction. It is known that NADPH oxidase is the critical enzyme for the generation of ROS under various pathological conditions [12]. Several lines of evidence have demonstrated that ROS contributes to ICAM-1 expression in various cell types [12,13]. However, as we expected, in HPAEpiCs, *P. aeruginosa* significantly induced NADPH oxidase activation and intracellular ROS generation. These responses induced by *P. aeruginosa* could further promote PGE<sub>2</sub>/IL-6/ICAM-1 up-regulation. The generation of ROS from mitochondria is important because it often causes oxidative damage

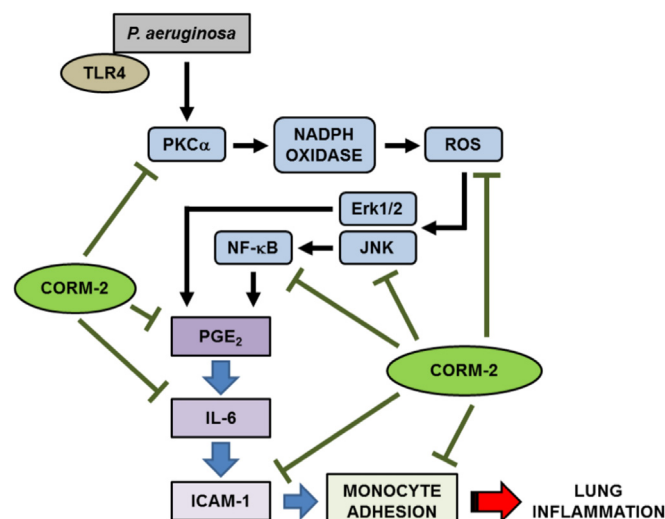


**Fig. 8.** Schematic diagram illustrating the proposed signaling pathway involved in the inhibitory effects of CORM-2 on *P. aeruginosa*-induced PGE<sub>2</sub>/IL-6/ICAM-1-dependent monocyte adhesion. In HPAEpiCs, CORM-2 inhibits *P. aeruginosa*-induced PGE<sub>2</sub>/IL-6/ICAM-1 expression and inflammatory responses by decreasing the NADPH oxidase/ROS generation and the activation of the PKCα/NADPH oxidase/ROS/JNK/NF-κB and PKCα/NADPH oxidase/ROS/ERK1/2 pathways.

[30]. It is worth mentioning that pretreatment with the mitochondria-targeted antioxidant (MitoTEMPO) had no effects on *P. aeruginosa*-induced ICAM-1 expression in HPAEpiCs. Thus, in this study, *P. aeruginosa*-induced ROS generation was mediated via the activation of NADPH oxidase, but not mitochondria. Intracellular ROS generation has been shown to be mediated via various signaling pathways, such as c-Src, PKCs, and PI3K/Akt [12]. This is confirmed by our observation that pretreatment with the PKCα inhibitor could reduce *P. aeruginosa*-induced ROS generation. CORM-2 and CO gases have been shown to have antioxidant properties [18]. On the other hand, Nagao et al. proved that CO-bound hemoglobin-vesicles (CO-HbV), a nanotechnology-based CO donor, could inhibit Nox4-generated ROS generation, and then reduce bleomycin-induced pulmonary fibrosis [41]. Taguchi et al. also indicated that HbV possess great potential for retaining CO, which has the cytoprotective effects, such as anti-inflammation and antioxidant [42]. Although the delivery principles and structural of CORM-2 and CO-HbV are different, at least we can prove that CO really has the cytoprotective effects. In this study, we showed that CORM-2 pretreatment markedly reduced *P. aeruginosa*-induced ROS generation and NADPH oxidase activation in HPAEpiCs. The above description allows us to suggest that CORM-2 can decrease *P. aeruginosa*-induced inflammation via the inhibition of the PKCα/NADPH oxidase/ROS pathway in HPAEpiCs. The above results also allow us to prove once again that CO has antioxidant properties.

MAPKs pathways have been shown to be involved in the regulation of some intracellular phenomena, including inflammation, apoptosis, cell migration, and metastasis [12,13]. Various types of bacteria often trigger inflammation through the activation of MAPKs pathways. This is confirmed by our observation that pretreatment with the inhibitor of JNK or MEK1/2 significantly reduced *P. aeruginosa*-induced ICAM-1 expression and monocyte adhesion. It is worth noting that *P. aeruginosa*-induced ICAM-1 expression was not reduced by the p38 MAPK inhibitor in these cells. On the other hand, MAPKs activation has been shown to be regulated through various signaling pathways [13]. In this study, although p38 MAPK could be activated by *P. aeruginosa*, it was not involved in regulating ICAM-1 up-regulation in HPAEpiCs. MAPKs activation has been shown to be regulated through various signaling pathways [13]. This is also confirmed by our observation that pretreatment with the inhibitor of PKCα, ROS, or NADPH oxidase

significantly inhibited *P. aeruginosa*-induced JNK and ERK1/2 activation. Finally, we proved that CORM-2 could perform its anti-inflammatory effect by inhibiting the activation of JNK and ERK1/2 in response to *P. aeruginosa* in HPAEpiCs.

NF-κB is an extremely important molecule in the process of inflammation. When cells receive extracellular stimulation, NF-κB is activated and translocated from the cytosol to the nucleus, which can further cause inflammation. NF-κB has been shown to regulate ICAM-1 expression in various cell types [33,34]. In addition, AP-1 is often activated during bacterial and viruses infections [35]. However, in this study, we proved that *P. aeruginosa* induced ICAM-1 expression and monocyte adhesion via NF-κB, but not AP-1 in HPAEpiCs. In general, NF-κB activation also has been shown to be regulated through various signaling pathways, such as PKCs, PI3K/Akt, and MAPKs [13]. In HPAEpiCs, we showed that *P. aeruginosa* induced NF-κB activation via the PKCα/NADPH oxidase/ROS/JNK pathway. It is worth mentioning that ERK1/2 did not play a key role in mediating *P. aeruginosa*-induced NF-κB activation in these cells. We also demonstrated that CORM-2 could decrease *P. aeruginosa*-induced NF-κB activation, and then inhibit PGE<sub>2</sub>/IL-6/ICAM-1 expression.

In the last part of the study, we used the animal model to examine the protective role of CORM-2 in *P. aeruginosa*-treated mice. At first, we monitored changes in some inflammatory markers in mice infected with *P. aeruginosa*. CRP is the most extensively studied inflammatory biomarker in respiratory diseases. MPO plays a crucial role in inflammation. Many studies have proved IL-8 as a key regulator in neutrophil-mediated acute inflammation [37]. In our study, we observed that *P. aeruginosa* enhanced the levels of plasma MPO and serum CRP, IL-6, IL-8, IL-1β, and TNF-α, which were inhibited by CORM-2. On the other hand, we also demonstrated that CORM-2 could significantly decrease *P. aeruginosa*-enhanced ICAM-1 expression in the lung tissues of mice.

In summary, as depicted in Fig. 8, our results demonstrate that in HAECS, CORM-2 inhibits *P. aeruginosa*-induced PGE<sub>2</sub>/IL-6/ICAM-1 expression and inflammatory responses by decreasing the NADPH oxidase/ROS generation and the activation of the PKCα/NADPH oxidase/ROS/JNK/NF-κB and PKCα/NADPH oxidase/ROS/ERK1/2 pathways. Altogether, the results of this study provide molecular mechanisms for antibacterial effects of CORM-2. In the future, we look forward to applying CORM-2 to clinical treatment.

## Acknowledgment

This work was supported by the Chang Gung Medical Research Program Foundation, grant numbers CMRPF6E0081, CMRPF6E0082, and CMRPF6E0083; the China Medical University, grant numbers CMU106-S-14 and CMU105-S-46.

## Conflict of interest

The authors declare no conflict of interest.

## References

- [1] L. Guillemot, M. Medina, E. Pernet, D. Leduc, M. Chignard, L. Touqui, Y. Wu, Cytosolic phospholipase A<sub>2</sub> enhances mouse mortality induced by *Pseudomonas aeruginosa* pulmonary infection via interleukin 6, *Biochimie* 107 (2014) 95–104.
- [2] T. Nagamatsu, D.J. Schust, The immunomodulatory roles of macrophages at the maternal-fetal interface, *Reprod. Sci.* 17 (2010) 209–218.
- [3] M. Agard, S. Asakrah, L.A. Morici, PGE<sub>2</sub> suppression of innate immunity during mucosal bacterial infection, *Front. Cell. Infect. Microbiol.* 3 (2013) 45.
- [4] Y.M. Lin, Z.L. Chang, Y.Y. Liao, M.C. Chou, C.H. Tang, IL-6 promotes ICAM-1 expression and cell motility in human osteosarcoma, *Cancer Lett.* 328 (2013) 135–143.
- [5] M. Marino, F. Scuderi, C. Provenzano, J. Scheller, S. Rose-John, E. Bartocioni, IL-6 regulates MCP-1, ICAM-1 and IL-6 expression in human myoblasts, *J. Neuroimmunol.* 196 (2008) 41–48.
- [6] J.C. Onyiah, R.E.M. Schaefer, S.P. Colgan, A central role for heme oxygenase-1 in the control of intestinal epithelial chemokine expression, *J. Innate Immun.* (2018) 1–11.

- [7] M. Zhao, M. Yang, W. Que, L. Zhong, M. Fujino, X.K. Li, Myeloid heme oxygenase-1: a new therapeutic target in anti-inflammation, *Front. Biosci. (Landmark Ed.)* 23 (2018) 2001–2015.
- [8] D.M. Culnan, B. Craft-Coffman, G.H. Bitz, K.D. Capek, Y. Tu, W.C. Lineaweaver, M.J. Kuhlmann-Capek, Carbon monoxide and cyanide poisoning in the burned pregnant patient: an indication for hyperbaric oxygen therapy, *Ann. Plast. Surg.* 80 (2018) S106–S112.
- [9] M. Desmard, R. Foresti, D. Morin, M. Dagouassat, A. Berdeaux, E. Denamur, S.H. Crook, B.E. Mann, D. Scapens, P. Montravers, J. Boczkowski, R. Motterlini, Differential antibacterial activity against *Pseudomonas aeruginosa* by carbon monoxide-releasing molecules, *Antioxid. Redox Signal.* 16 (2012) 153–163.
- [10] S.W. Ryter, A.M. Choi, Therapeutic applications of carbon monoxide in lung disease, *Curr. Opin. Pharmacol.* 6 (2006) 257–262.
- [11] L. Shao, Y.Y. Gu, C.H. Jiang, C.Y. Liu, L.P. Lv, J.N. Liu, Y. Zou, Carbon monoxide releasing molecule-2 suppresses proliferation, migration, invasion, and promotes apoptosis in non-small cell lung cancer Calu-3 cells, *Eur. Rev. Med. Pharmacol. Sci.* 22 (2018) 1948–1957.
- [12] I.T. Lee, C.M. Yang, Role of NADPH oxidase/ROS in pro-inflammatory mediators-induced airway and pulmonary diseases, *Biochem. Pharmacol.* 84 (2012) 581–590.
- [13] I.T. Lee, C.M. Yang, Inflammatory signalings involved in airway and pulmonary diseases, *Mediat. Inflamm.* 2013 (2013) 791231.
- [14] V.L. Bodiga, S.P. Inapurapu, P.K. Vemuri, M.R. Kudle, S. Bodiga, Intracellular zinc status influences cisplatin-induced endothelial permeability through modulation of PKC $\alpha$ , NF- $\kappa$ B and ICAM-1 expression, *Eur. J. Pharmacol.* 791 (2016) 355–368.
- [15] C.J. Liou, W.C. Huang, Casticin inhibits interleukin-1 $\beta$ -induced ICAM-1 and MUC5AC expression by blocking NF- $\kappa$ B, PI3K-Akt, and MAPK signaling in human lung epithelial cells, *Oncotarget* 8 (2017) 101175–101188.
- [16] L. Xia, H. Xie, Y. Yu, H. Zhou, T. Wang, J. Yan, The effects of NF- $\kappa$ B and c-Jun/AP-1 on the expression of prothrombotic and proinflammatory molecules induced by anti- $\beta_2$ GPI in mouse, *PLoS One* 11 (2016) e0147958.
- [17] S. Lian, Y. Xia, T.T. Ung, P.N. Khoi, H.J. Yoon, N.H. Kim, K.K. Kim, Y.D. Jung, Carbon monoxide releasing molecule-2 ameliorates IL-1 $\beta$ -induced IL-8 in human gastric cancer cells, *Toxicology* 361–362 (2016) 24–38.
- [18] P.L. Chi, C.J. Liu, I.T. Lee, Y.W. Chen, L.D. Hsiao, C.M. Yang, HO-1 induction by CO-RM2 attenuates TNF- $\alpha$ -induced cytosolic phospholipase A $_2$  expression via inhibition of PKC $\alpha$ -dependent NADPH oxidase/ROS and NF- $\kappa$ B, *Mediat. Inflamm.* 2014 (2014) 279171.
- [19] R.L. Cho, C.C. Yang, I.T. Lee, C.C. Lin, P.L. Chi, L.D. Hsiao, C.M. Yang, Lipopolysaccharide induces ICAM-1 expression via a c-Src/NADPH oxidase/ROS-dependent NF- $\kappa$ B pathway in human pulmonary alveolar epithelial cells, *Am. J. Physiol. Lung Cell. Mol. Physiol.* 310 (2016) L639–L657.
- [20] I.T. Lee, C.W. Lee, W.H. Tung, S.W. Wang, C.C. Lin, J.C. Shu, C.M. Yang, Cooperation of TLR2 with MyD88, PI3K, and Rac1 in lipoteichoic acid-induced cPLA $_2$ /COX-2-dependent airway inflammatory responses, *Am. J. Pathol.* 176 (2010) 1671–1684.
- [21] I.T. Lee, S.F. Luo, C.W. Lee, S.W. Wang, C.C. Lin, C.C. Chang, Y.L. Chen, L.Y. Chau, C.M. Yang, Overexpression of HO-1 protects against TNF- $\alpha$ -mediated airway inflammation by down-regulation of TNFR1-dependent oxidative stress, *Am. J. Pathol.* 175 (2009) 519–532.
- [22] I.T. Lee, C.C. Lin, C.Y. Lee, P.W. Hsieh, C.M. Yang, Protective effects of (-)-epigallocatechin-3-gallate against TNF- $\alpha$ -induced lung inflammation via ROS-dependent ICAM-1 inhibition, *J. Nutr. Biochem.* 24 (2013) 124–136.
- [23] Y.Z. Wu, M. Abolhassani, M. Ollero, F. Dif, N. Uozumi, M. Lagranderie, T. Shimizu, M. Chignard, L. Touqui, Cytosolic phospholipase A $_2\alpha$  mediates *Pseudomonas aeruginosa* LPS-induced airway constriction of CFTR-/- mice, *Respir. Res.* 11 (2010) 49.
- [24] B.P. Hurlley, W. Pirzai, K.L. Mumy, K. Gronert, B.A. McCormick, Selective eicosanoid-generating capacity of cytoplasmic phospholipase A $_2$  in *Pseudomonas aeruginosa*-infected epithelial cells, *Am. J. Physiol. Lung Cell. Mol. Physiol.* 300 (2011) L286–L294.
- [25] A.J. Ammit, L.M. Moir, B.G. Oliver, J.M. Hughes, H. Alkhouri, Q. Ge, J.K. Burgess, J.L. Black, M. Roth, Effect of IL-6 trans-signaling on the pro-remodeling phenotype of airway smooth muscle, *Am. J. Physiol. Lung Cell. Mol. Physiol.* 292 (2007) L199–L206.
- [26] C.C. Lin, I.T. Lee, Y.L. Yang, C.W. Lee, Y.R. Kou, C.M. Yang, Induction of COX-2/PGE $_2$ /IL-6 is crucial for cigarette smoke extract-induced airway inflammation: role of TLR4-dependent NADPH oxidase activation, *Free Radic. Biol. Med.* 48 (2010) 240–254.
- [27] B.S. Wung, C.W. Ni, D.L. Wang, ICAM-1 induction by TNF $\alpha$  and IL-6 is mediated by distinct pathways via Rac in endothelial cells, *J. Biomed. Sci.* 12 (2005) 91–101.
- [28] K. Ling, F. Men, W.C. Wang, Y.Q. Zhou, H.W. Zhang, D.W. Ye, Carbon monoxide and its controlled release: therapeutic application, detection, and development of carbon monoxide releasing molecules (CORMs), *J. Med. Chem.* 61 (2018) 2611–2635.
- [29] T.M. Vallance, M.T. Zeuner, H.F. Williams, D. Widera, S. Vaiyapuri, Toll-like receptor 4 signalling and its impact on platelet function, thrombosis, and haemostasis, *Mediat. Inflamm.* 2017 (2017) 9605894.
- [30] M.P. Murphy, How mitochondria produce reactive oxygen species, *Biochem. J.* 417 (2009) 1–13.
- [31] C.C. Lin, C.C. Yang, C.Y. Wang, H.C. Tseng, C.S. Pan, L.D. Hsiao, C.M. Yang, NADPH oxidase/ROS-dependent VCAM-1 induction on TNF- $\alpha$ -challenged human cardiac fibroblasts enhances monocyte adhesion, *Front. Pharmacol.* 6 (2016) 310.
- [32] C.M. Yang, I.T. Lee, R.C. Hsu, P.L. Chi, L.D. Hsiao, NADPH oxidase/ROS-dependent PYK2 activation is involved in TNF- $\alpha$ -induced matrix metalloproteinase-9 expression in rat heart-derived H9c2 cells, *Toxicol. Appl. Pharmacol.* 272 (2013) 431–442.
- [33] S. Zhu, X. Xu, K. Liu, Q. Gu, F. Wei, H. Jin, Peptide GC31 inhibits chemokines and ICAM-1 expression in corneal fibroblasts exposed to LPS or poly(I: c) by blocking the NF- $\kappa$ B and MAPK pathways, *Exp. Eye Res.* 164 (2017) 109–117.
- [34] X. Chen, M. Xiu, J. Xing, S. Yu, D. Min, F. Guo, Lanthanum chloride inhibits LPS mediated expressions of pro-inflammatory cytokines and adhesion molecules in HUVECs: involvement of NF- $\kappa$ B-Jmjd3 signaling, *Cell. Physiol. Biochem.* 42 (2017) 1713–1724.
- [35] J.H. Seo, J.W. Lim, H. Kim, K.H. Kim, *Helicobacter pylori* in a Korean isolate activates mitogen-activated protein kinases, AP-1, and NF- $\kappa$ B and induces chemokine expression in gastric epithelial AGS cells, *Lab. Investig.* 84 (2004) 49–62.
- [36] N.H. Cho, S.Y. Seong, M.S. Choi, I.S. Kim, Expression of chemokine genes in human dermal microvascular endothelial cell lines infected with *Orientia tsutsugamushi*, *Infect. Immun.* 69 (2001) 1265–1272.
- [37] N. Mukaida, Pathophysiological roles of interleukin-8/CXCL8 in pulmonary diseases, *Am. J. Physiol. Lung Cell. Mol. Physiol.* 284 (2003) L566–L577.
- [38] M. Desmard, K.S. Davidge, O. Bouvet, D. Morin, D. Roux, R. Foresti, J.D. Ricard, E. Denamur, R.K. Poole, P. Montravers, R. Motterlini, J. Boczkowski, A carbon monoxide-releasing molecule (CORM-3) exerts bactericidal activity against *Pseudomonas aeruginosa* and improves survival in an animal model of bacteraemia, *FASEB J.* 23 (2009) 1023–1031.
- [39] M. Jovanović, L. Vičová, Interleukin-6 stimulates cell migration, invasion and integrin expression in HTR-8/SVneo cell line, *Placenta* 30 (2009) 320–328.
- [40] S. Nakashima, Protein kinase C  $\alpha$  (PKC  $\alpha$ ): regulation and biological function, *J. Biochem.* 132 (2002) 669–675.
- [41] S. Nagao, K. Taguchi, H. Sakai, R. Tanaka, H. Horinouchi, H. Watanabe, K. Kobayashi, M. Otagiri, T. Maruyama, Carbon monoxide-bound hemoglobin-vesicles for the treatment of bleomycin-induced pulmonary fibrosis, *Biomaterials* 35 (2014) 6553–6562.
- [42] K. Taguchi, K. Yamasaki, H. Sakai, T. Maruyama, M. Otagiri, The use of hemoglobin vesicles for delivering medicinal gas for the treatment of intractable disorders, *J. Pharm. Sci.* 106 (2017) 2392–2400.

It is illegal to post this copyrighted PDF on any website.

# Impact of Drug Adherence on Oppositional Defiant Disorder and Conduct Disorder Among Patients With Attention-Deficit/Hyperactivity Disorder

Liang-Jen Wang, MD, MPH<sup>a</sup>; Sheng-Yu Lee, MD, MS<sup>b,c</sup>; Miao-Chun Chou, MD<sup>a</sup>; Kang-Chung Yang, PhD<sup>d</sup>; Tung-Liang Lee, PhD<sup>e</sup>; and Yu-Chiau Shyu, PhD<sup>d,f,g,\*</sup>

## ABSTRACT

**Objective:** Attention-deficit/hyperactivity disorder (ADHD) may be a predecessor of oppositional defiant disorder (ODD) and conduct disorder (CD), and medication is an effective treatment option for ADHD. This study aims to examine whether adherence to medication treatment is associated with developing ODD and CD among youths with ADHD.

**Methods:** A total of 33,835 youths (4 years ≤ age of diagnosis ≤ 18 years) with ADHD (ICD-9-CM code 314.X) undergoing medication treatment for at least 90 days were selected from Taiwan's National Health Insurance Research Database during the period of January 2000 through December 2009. Patients' medical records were monitored through December 31, 2011, or until they had a diagnosis of ODD or CD. We categorized participants as compliant or noncompliant on the basis of a medication possession ratio (MPR) of 50%.

**Results:** The patients with better drug adherence (MPR ≥ 50%) exhibited a significantly decreased probability of developing ODD (53% reduction,  $P < .001$ ) or CD (58% reduction,  $P < .001$ ) when compared to the patients with poor drug adherence (MPR < 50%). The results in our sensitivity analyses showed that good drug adherence consistently exerted protective effects on ODD or CD, irrespective of patients' characteristics. Moreover, the patients with the best drug adherence (MPR ≥ 75%) had the lowest risks of developing ODD or CD.

**Conclusion:** Among patients with ADHD undergoing drug therapy, a better drug adherence is associated with a lower likelihood of their developing ODD or CD in later life.

*J Clin Psychiatry* 2018;79(5):17m11784

**To cite:** Wang LJ, Lee SY, Chou MC, et al. Impact of drug adherence on oppositional defiant disorder and conduct disorder among patients with attention-deficit/hyperactivity disorder. *J Clin Psychiatry*. 2018;79(5):17m11784.

**To share:** <https://doi.org/10.4088/JCP.17m11784>

© Copyright 2018 Physicians Postgraduate Press, Inc.

<sup>a</sup>Department of Child and Adolescent Psychiatry, Kaohsiung Chang Gung Memorial Hospital and Chang Gung University College of Medicine, Kaohsiung, Taiwan

<sup>b</sup>Department of Psychiatry, Kaohsiung Veterans General Hospital, Kaohsiung, Taiwan

<sup>c</sup>Department of Psychiatry, College of Medicine, Graduate Institute of Medicine, School of Medicine, Kaohsiung Medical University, Kaohsiung, Taiwan

<sup>d</sup>Community Medicine Research Center, Keelung Chang Gung Memorial Hospital, Keelung, Taiwan

<sup>e</sup>Department of Microbiology, Soochow University, Taipei, Taiwan

<sup>f</sup>Institute of Molecular Biology, Academia Sinica, Taipei, Taiwan

<sup>g</sup>Department of Nursing and Department of Nutrition and Health Sciences, Research Center for Food and Cosmetic Safety, and Research Center for Chinese Herbal Medicine, College of Human Ecology, Chang Gung University of Science and Technology, Taoyuan, Taiwan

\*Corresponding author: Yu-Chiau Shyu, PhD, Community Medicine Research Center, Chang Gung Memorial Hospital, Keelung, Taiwan (yuchiaushyu@gmail.com).

Attention-deficit/hyperactivity disorder (ADHD) is a neuropsychiatric disorder that affects about 5%–10% of all children and adolescents.<sup>1</sup> Patients with ADHD commonly develop comorbid disruptive behavior disorders such as oppositional defiant disorder (ODD) and conduct disorder (CD).<sup>2,3</sup> ODD is characterized by a frequent and persistent pattern of disobedient, negativistic, and defiant behavior toward authority figures and is commonly accompanied by irritable mood.<sup>4,5</sup> CD is characterized by an enduring pattern of aggression, bullying, stealing, and violations of social rules and the rights of others.<sup>6–8</sup> The symptoms of ADHD typically occur in early childhood and, in some cases, are regarded as a predecessor of ODD or CD.<sup>9–14</sup> These comorbidities aggravate severe functional impairment and psychosocial problems and increase the difficulty of treatment.<sup>15,16</sup> Therefore, adequate intervention strategies for preventing individuals with ADHD from developing a comorbidity of ODD or CD are important.<sup>17</sup>

Medication is an effective treatment option for ADHD, with stimulants and nonstimulants being the 2 main approved categories for the disorder.<sup>18,19</sup> In addition to its effect on ADHD core symptoms, medication treatment is beneficial for improving emotional dysregulation, which is a collective feature of ODD and CD.<sup>20</sup> However, medication adherence is approximately 50% in the general pediatric population,<sup>21</sup> which implies that achieving compliance with pediatric medication therapy is challenging.<sup>22</sup> Poor drug adherence is also a common problem among pharmacologically treated children with ADHD in the clinical setting.<sup>23</sup> One review article<sup>24</sup> showed that the rates of medication nonadherence range between 15% and 87% in patients with ADHD during a follow-up period of up to 9 years. More recent studies have demonstrated similar findings. A study conducted in Korea<sup>25</sup> indicated that 20%–57% of the patients showed adherence to stimulant treatment after 36 months. In a Turkish ADHD cohort, the persistence rate of drug therapy over a 12-month period was only 30.2%.<sup>26</sup> Moreover, a study in the United Kingdom<sup>27</sup> demonstrated that only 57% of children with ADHD received medication treatment longer than 6 months after initial prescription.



- Medication is an effective treatment option for ADHD; however, whether drug compliance impacts the risk of developing oppositional defiant disorder and conduct disorder has yet to be definitively determined.
- This nationwide, population-based study found that ADHD patients with better drug adherence exhibited a decreased probability of developing oppositional defiant disorder or conduct disorder when compared with those with poor drug adherence.

Relative to the discontinuation rate, the medication possession ratio (MPR) is a generally acknowledged index for measuring drug adherence and is less likely influenced by the variety of treatment discontinuation definitions.<sup>28,29</sup> A systematic review indicates that the MPR is less than 0.7 among children with ADHD who are prescribed medications, for all age groups and medication classes, during a 12-month period.<sup>30</sup> Evidence has demonstrated that patients with ADHD undergoing drug therapy have persistently favorable clinical outcomes,<sup>31</sup> including a higher probability of achieving symptom remission,<sup>32</sup> and reduced risks of developing substance use disorders<sup>33</sup> or depressive disorders.<sup>34</sup> However, whether drug compliance influences the risk of developing ODD or CD among individuals with ADHD has yet to be definitively determined. To fill this research gap, this study aimed to analyze the probability of diagnoses with ODD or CD after medications prescribed for treating ADHD by comparing the patients with better drug adherence to those with poor drug adherence.

## METHODS

### Data Source

The protocol for this study conformed to the Helsinki Declaration and was approved by the Institutional Review Board (IRB) of Chang Gung Memorial Hospital. Patient records and information were anonymized and deidentified prior to analysis, and the need for written informed consent was waived by the IRB.

The database used in this study was that of ambulatory claims from the National Health Insurance Research Database of Taiwan (NHIRD-TW). Implemented in 1995, Taiwan's National Health Insurance (NHI) program is a compulsory universal health insurance program, and the NHI Bureau is the sole payer of health care services. The electronic claim forms include such information as the patient's sex, the medical institution visited, diagnostic codes, the date of any prescriptions given, the drugs prescribed, and any claimed medical expenses. The reliability of diagnostic codes in the NHIRD has been proved by a previous study.<sup>35</sup>

### Study Population

Figure 1 depicts the procedure employed to choose this study's population. The target population in this study includes patients with ADHD who received medication treatment for

at least 90 days. An ADHD diagnosis was defined as at least 2 NHI claim records with any diagnosis codes per visit and the presence of the *International Classification of Diseases, Ninth Revision, Clinical Modification (ICD-9-CM)* code of 314.X. ADHD subtypes included the inattentive type (314.00) and the predominantly hyperactive/impulsive or combined type (314.01, ADHD H/C type). This study considered all patients who were born before January 1, 2000, and were newly diagnosed with ADHD (4 years ≤ age of diagnosis ≤ 18 years) during the period of January 1, 2000, through December 31, 2011, in the entire NHIRD-TW (N = 70,810) database. To ensure the subjects had a follow-up time of 2 years or longer, we excluded patients who were diagnosed with ADHD after December 31, 2009 (n = 5,031). Patients' NHIRD-TW medical records were monitored through December 31, 2011. Subsequently, we excluded patients with no prescription of ADHD drugs (n = 18,148), those who had drug prescriptions prior to their ADHD diagnosis (n = 1,171), and those whose drug therapy lasted fewer than 90 days (n = 12,625).

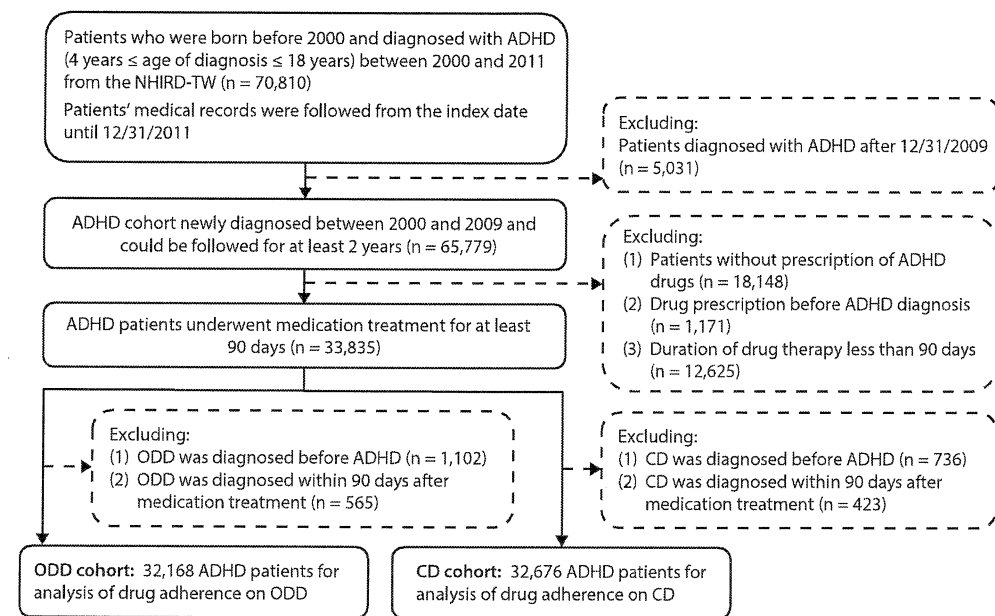
Hence, there were 33,835 patients treated with medication for at least 90 days. We also excluded patients who had an ODD diagnosis prior to their ADHD diagnosis (n = 1,102) and whose ODD diagnosis was made within 90 days after medication treatment (n = 565). Finally, our ODD cohort for examining the impact of drug adherence on subsequent diagnosis of ODD consisted of 32,168 patients. We also excluded patients who had a CD diagnosis prior to their ADHD diagnosis (n = 736) and those whose CD diagnosis was made within 90 days after medication treatment (n = 423). Eventually, the CD cohort consisted of 32,676 patients for further analyses.

### Definition of Drug Therapy and Adherence

ADHD medications were identified by using the Anatomic Therapeutic Chemical classification system.<sup>36</sup> Methylphenidate and atomoxetine are 2 medications approved by the NHI Bureau for the treatment of ADHD in Taiwan. Because atomoxetine is generally considered as a second-line pharmacotherapy for ADHD, duration and doses of methylphenidate and atomoxetine in use were composited as a whole. Drug adherence was defined using the MPR, which represents the ratio of total number of defined daily doses (DDD) the patients received to the total number of days of follow-up.<sup>28,29</sup> For example, if the amount of ADHD medication a patient received was for 6 months (183 DDD) during a 1-year period, the patient would be considered 50% compliant. If the calculated MPR for a patient was > 100%, the MPR was considered 100%. The total days of follow-up were defined as the time interval between the index date and the end point (ie, discontinuation of the patient's treatment with medication or December 31, 2011). Discontinuation of drug therapy was defined as when patients stop taking their medication for 180 days or longer.<sup>30</sup> We categorized participants into compliant patients and noncompliant patients based on an MPR of 50%. We further examined the results by adjusting

**It is illegal to post this copyrighted PDF on any website.**

**Figure 1. Flowchart of the Selection of Study Subjects**



Abbreviations: ADHD = attention-deficit/hyperactivity disorder, CD = conduct disorder, NHIRD-TW = National Health Insurance Research Database of Taiwan, ODD = oppositional defiant disorder.

the cutoff point upward (75%) and downward (25%) for the sensitivity analyses.

### Definition of Outcome and Covariates

The study's outcome was defined as diagnosis of ODD (ICD-9-CM code 313.81) or CD (ICD-9-CM code 312.X) that followed an ADHD diagnosis and a medication prescription of at least 90 days. For the purposes of this study, the index date occurred when the ADHD medication was prescribed for the first time. Patients' NHIRD-TW medical records were monitored through December 31, 2011, or until they had a diagnosis of ODD or CD.

Other variables that were considered as covariates of developing ODD or CD were age at ADHD diagnosis, age when first medication was prescribed, sex, ADHD subtypes, and the time interval between ADHD diagnosis and the first medication prescription. We categorized patients' ages into the following 3 groups: (1) subjects younger than 6 years (preschoolers), (2) subjects between the ages of 6 and 12 years (school-age), and (3) subjects older than 12 years (adolescents). Time intervals between ADHD diagnosis and the first medication prescription were categorized into the following 3 groups: (1) < 90 days, (2) 90–365 days, and (3) > 365 days.

### Statistical Analysis

The Statistical Package for the Social Sciences (SPSS) Version 16.0 (SPSS Inc, Chicago, Illinois) was used to carry out all statistical analyses in this study. A 2-tailed value of  $P < .05$  indicated statistical significance. A  $\chi^2$  test or  $t$  test was used to compare the characteristics between noncompliant patients (MPR < 50%) and compliant patients (MPR ≥ 50%).

Univariate logistic regression was used to examine the potential effect of each independent variable on the risk of developing ODD or CD among patients with ADHD. Moreover, multiple logistic regression models were applied to determine the impact of drug adherence on the diagnosis of ODD or CD, controlling for the effects of patients' demographic characteristics. In the logistic regression models, diagnosis of ODD or CD was set as a dependent variable (outcome), and drug adherence (MPR ≥ 50% vs MPR < 50%) was treated as an independent variable. The adjusted odds ratio (aOR) and 95% confidence interval (95% CI) were calculated.

Furthermore, we conducted a series of sensitivity analyses across various subgroups to test the robustness of our findings. First, we examined the effects of different thresholds of drug compliance (MPR at 25%, 50%, and 75%) on the risks of ODD and CD. Second, we stratified patients by their age, sex, ADHD subtype and the interval between ADHD diagnosis and first medication prescription. Third, we used the multiple logistic regression models to identify the effects of drug adherence (MPR ≥ 50% vs MPR < 50%) on the risk of developing ODD or CD in each stratification.

### RESULTS

Table 1 lists the characteristics of the ODD cohort and the CD cohort. For the ODD cohort, 4.1% of patients had an ODD diagnosis during the follow-up period. The mean MPR was 41.1% in the ODD cohort. On the basis of the MPR scores, 67.6% and 32.4% of patients were categorized into a noncompliant group (MPR < 50%) and compliant group (MPR ≥ 50%), respectively. For the CD cohort, 4.0%

Table 1. Characteristics of Patients With Poor Drug Adherence (MPR &lt; 50%) and Better Drug Adherence (MPR ≥ 50%) in the ODD and CD Cohorts

Characteristic	ODD Cohort <sup>a</sup>				CD Cohort <sup>a</sup>			
	Total (n=32,168)	MPR < 50% (n=21,760)	MPR ≥ 50% (n=10,408)	Statistic*	Total (n=32,676)	MPR < 50% (n=21,958)	MPR ≥ 50% (n=10,718)	Statistic*
Age at ADHD diagnosis, y	9.13 ± 2.87	8.79 ± 2.74	9.85 ± 2.99	30.726	9.15 ± 2.86	8.79 ± 2.73	9.88 ± 2.97	31.821
< 6 y	3,653 (11.4)	2,773 (12.7)	880 (8.5)		3,637 (11.1)	2,764 (12.6)	873 (8.1)	
6–12 y	22,609 (70.3)	15,805 (72.6)	6,804 (65.4)	678.301	23,000 (70.4)	15,984 (72.8)	7,016 (65.5)	723.168
> 12 y	5,906 (18.4)	3,182 (14.6)	2,724 (26.2)		6,039 (18.5)	3,210 (14.6)	2,829 (26.4)	
Sex				31.011				33.359
Female	5,576 (17.3)	3,595 (16.5)	1,981 (19.0)		5,701 (17.4)	3,645 (16.6)	2,056 (19.2)	
Male	26,592 (82.7)	18,165 (83.5)	8,427 (81.0)		26,975 (82.6)	18,313 (83.4)	8,662 (80.8)	
ADHD subtypes				28.992				33.370
Inattentive type (314.00)	15,304 (47.6)	10,578 (48.6)	4,726 (45.4)		15,337 (46.9)	10,551 (48.1)	4,786 (44.7)	
H/C type (314.01)	16,864 (52.4)	11,182 (51.4)	5,682 (54.6)		17,339 (53.1)	11,407 (51.9)	5,932 (55.3)	
Age at first prescription, y	9.75 ± 2.75	9.36 ± 2.64	10.57 ± 2.80	36.844	9.77 ± 2.74	9.37 ± 2.63	10.59 ± 2.77	38.023
< 6 y	1,285 (4.0)	1,059 (4.9)	226 (2.2)		1,266 (3.9)	1,049 (4.8)	217 (2.0)	
6–12 y	23,651 (73.5)	16,842 (77.4)	6,809 (65.4)	936.690	24,049 (73.6)	17,025 (77.5)	7,024 (65.5)	977.593
> 12 y	7,232 (22.5)	3,859 (17.7)	3,373 (32.4)		7,361 (22.5)	3,884 (17.7)	3,477 (32.4)	
Interval between ADHD diagnosis and medication, mo	7.59 ± 17.17	7.03 ± 15.58	8.76 ± 20.02	7.733	7.50 ± 17.08	6.96 ± 15.53	8.61 ± 19.82	7.555
< 3 mo	23,622 (73.4)	15,867 (72.9)	7,755 (74.5)		24,125 (73.8)	16,099 (73.3)	8,026 (74.9)	
3–12 mo	2,969 (9.2)	2,177 (10.0)	792 (7.6)	48.807	2,966 (9.1)	2,154 (9.8)	812 (7.6)	43.856
> 12 mo	5,577 (17.3)	3,716 (17.1)	1,861 (17.9)		5,585 (17.1)	3,705 (16.9)	1,880 (17.5)	
Diagnosed with ODD	1,329 (4.1)	1,093 (5.0)	236 (2.3)	134.966	...	...	...	...
Age at diagnosis, y	12.21 ± 2.45	12.43 ± 2.40	11.21 ± 2.48	7.033	...	...	...	...
Diagnosed with CD	...	...	...	...	1,308 (4.0)	1,087 (5.0)	221 (2.1)	156.372
Age at diagnosis, y	...	...	...	...	12.78 ± 3.04	12.96 ± 3.01	11.88 ± 3.02	4.844

<sup>a</sup>Data are expressed by n (%) or mean ± SD; statistical values were obtained using Pearson  $\chi^2$  or t using an independent t test.

\* $P < .001$ .

Abbreviations: ADHD = attention-deficit/hyperactivity disorder, CD = conduct disorder, H/C type = hyperactive/impulsive or combined type, MPR = medication possession ratio, ODD = oppositional defiant disorder. Symbol: ... = not applicable.

Table 2. Logistic Regression Models for the Factors Associated With Diagnosis of ODD or CD Among Patients With ADHD

Variable	ODD Cohort				CD Cohort			
	OR (95% CI)	P Value	aOR (95% CI)	P Value	OR (95% CI)	P Value	aOR (95% CI)	P Value
Age at ADHD diagnosis								
< 6 y	1		1		1		1	
6–12 y	0.78 (0.67–0.92)	.002	0.82 (0.69–0.97)	.019	0.83 (0.71–0.98)	.031	0.80 (0.67–0.96)	.018
> 12 y	0.40 (0.32–0.50)	<.001	0.49 (0.37–0.63)	<.001	0.72 (0.58–0.88)	.001	0.77 (0.61–0.96)	.023
Sex								
Female	1		1		1		1	
Male	1.75 (1.47–2.08)	<.001	1.68 (1.41–2.01)	<.001	1.38 (1.17–1.62)	<.001	1.35 (1.15–1.59)	<.001
ADHD subtypes								
Inattentive type (314.00)	1		1		1		1	
H/C type (314.01)	1.02 (0.91–1.14)	.767	1.00 (0.90–1.12)	.982	0.92 (0.83–1.03)	.156	0.92 (0.82–1.03)	.131
Interval between ADHD diagnosis and medication								
< 3 mo	1		1		1		1	
3–12 mo	1.31 (1.10–1.57)	.002	1.17 (0.98–1.40)	.092	1.05 (0.87–1.27)	.614	0.97 (0.80–1.17)	.723
> 12 mo	1.16 (1.01–1.34)	.041	0.99 (0.84–1.16)	.871	0.90 (0.77–1.05)	.167	0.81 (0.68–0.96)	.015
Drug adherence								
MPR < 50%	1		1		1		1	
MPR ≥ 50%	0.44 (0.38–0.51)	<.001	0.47 (0.41–0.55)	<.001	0.40 (0.35–0.47)	<.001	0.42 (0.36–0.48)	<.001

Abbreviations: ADHD = attention-deficit/hyperactivity disorder, aOR = adjusted odds ratio, CD = conduct disorder, CI = confidence interval, H/C type = hyperactive/impulsive or combined type, MPR = medication possession ratio, ODD = oppositional defiant disorder, OR = odds ratio.

of patients had a CD diagnosis during the follow-up period, and the mean MPR was 41.5% (67.2% were noncompliant and 32.8% were compliant).

In comparison with the noncompliant patients in the ODD cohort (Table 1), the compliant patients were older (mean age at ADHD diagnosis: 9.85 ± 2.99 years), contained a higher proportion of female subjects (19.0%) and ADHD H/C type (54.6%), were prescribed an ADHD medication at an older age (10.57 ± 2.80 years), had a longer interval

between ADHD diagnosis and first prescription (8.76 ± 20.02 months), and were less likely to have a diagnosis of ODD (2.3%). For the CD cohort, the comparisons between the noncompliant patients and the compliant patients exhibited similar trends as those in the ODD cohort.

Table 2 shows the results of the logistic regression models, which demonstrate the factors associated with risks of developing ODD or CD. We found that the risks of ODD and CD among compliant patients were 53% (aOR = 0.47; 95%

# It is illegal to post this copyrighted PDF on any website.

**Table 3. Sensitivity Analyses of the Impact of Drug Adherence on the Diagnosis of ODD or CD Among Patients With ADHD<sup>a</sup>**

Variable	ODD Cohort		CD Cohort	
	aOR (95% CI)	P Value	aOR (95% CI)	P Value
Drug adherence threshold				
MPR <25%	1		1	
MPR 25%–49%	0.36 (0.31–0.41)	<.001	0.38 (0.33–0.43)	<.001
MPR 50%–74%	0.37 (0.32–0.44)	<.001	0.32 (0.27–0.38)	<.001
MPR ≥75%	0.19 (0.14–0.25)	<.001	0.20 (0.15–0.26)	<.001
Age at ADHD diagnosis <sup>b</sup>				
<6 y	0.48 (0.32–0.72)	<.001	0.50 (0.32–0.79)	.003
6–12 y	0.49 (0.41–0.58)	<.001	0.47 (0.40–0.56)	<.001
>12 y	0.40 (0.27–0.58)	<.001	0.25 (0.17–0.35)	<.001
Sex <sup>b</sup>				
Female	0.41 (0.26–0.62)	<.001	0.29 (0.19–0.44)	<.001
Male	0.48 (0.42–0.56)	<.001	0.44 (0.38–0.51)	<.001
ADHD subtypes <sup>b</sup>				
Inattentive type (314.00)	0.44 (0.35–0.55)	<.001	0.42 (0.34–0.53)	<.001
H/C type (314.01)	0.50 (0.42–0.61)	<.001	0.41 (0.34–0.50)	<.001
Interval between ADHD diagnosis and medication <sup>b</sup>				
<3 mo	0.48 (0.41–0.57)	<.001	0.39 (0.33–0.46)	<.001
3–12 mo	0.43 (0.27–0.69)	.001	0.52 (0.32–0.84)	.008
>12 mo	0.46 (0.33–0.63)	<.001	0.51 (0.36–0.71)	<.001

<sup>a</sup>Adjusted for all variables in Table 2.

<sup>b</sup>The effect of better drug adherence (MPR ≥ 50%) vs poor adherence (MPR < 50%) in each stratification.

Abbreviations: ADHD = attention-deficit/hyperactivity disorder, aOR = adjusted odds ratio, CD = conduct disorder, CI = confidence interval, H/C type = hyperactive/impulsive or combined type, MPR = medication possession ratio, ODD = oppositional defiant disorder.

CI, 0.41–0.55) and 58% (aOR = 0.42; 95% CI, 0.36–0.48) lower, respectively, than those of their noncompliant counterparts. In addition, female sex and ADHD diagnosis at an older age were associated with a lower risk of developing ODD. Furthermore, the following subjects had a lower risk of developing CD: female subjects, those with ADHD diagnosed at an older age, and those with an interval between ADHD diagnosis and first prescription of > 365 days.

Table 3 shows the sensitivity analyses for drug adherence on the risk of developing ODD or CD. We found that drug compliance exhibited dose-response effects of developing ODD or CD. The risks of ODD and CD among patients who had the best drug compliance (MPR ≥ 75%) were 81% (aOR = 0.19; 95% CI, 0.14–0.25) and 80% (aOR = 0.20; 95% CI, 0.15–0.26) lower than those among patients who had the worst drug compliance (MPR < 25%), respectively. Moreover, drug adherence (MPR ≥ 50% vs MPR < 50%) consistently exerted protective effects on ODD or CD in each stratification.

## DISCUSSION

The main finding in this study is that, among patients with ADHD undergoing drug therapy, better drug adherence is associated with a lower likelihood of later developing ODD or CD. Some possible explanations may be related to this phenomenon. First, improving drug adherence may be beneficial for preventing the occurrence of ODD or CD in patients with ADHD. The pathophysiology of ODD or CD has been associated with neurobiological factors and negative environmental events.<sup>13,14</sup> Medication is an effective treatment option for ADHD,<sup>18,19</sup> and persistence of drug therapy for ADHD is linked to better

outcomes.<sup>31</sup> Regular medication treatment for ADHD may improve patients' academic performance, family function, and peer relationships and reduce the likelihood of difficult life events.<sup>37</sup> Therefore, patients with better drug compliance may benefit more from medication treatment and have reduced risks of ODD or CD. Second, many factors potentially contribute to both drug compliance and diagnosis of ODD or CD, including treatment responses, adverse effects to treatment, patients' temperaments or personality traits, family function, parenting skills, and socioeconomic status.<sup>38</sup> Therefore, the correlation of good drug compliance and reduced rates of ODD or CD should be controlled for the above factors. Nonetheless, such factors have not been identified in the claims data.

We found the mean MPR was approximately 40% in our study population, which is generally compatible with previous international studies.<sup>23,24,30</sup> This finding implies that medication nonadherence (eg, drug holiday or temporary discontinuation and irregular use of medication) is common in realistic settings for treating ADHD. However, the current study recruited only patients with ADHD undergoing drug therapy for longer than 90 days. In addition, individuals in our cohort were observed within a wide age range of 4 to 18 years, but not within a fixed time period. Moreover, we found that patients' characteristics were significantly associated with MPR (Table 1). Previous studies<sup>23,24</sup> have also suggested that various factors potentially influence drug compliance in patients with ADHD, including patients' age, ethnicity, family structure, and neuropsychiatric comorbidities and drug formulations in use. It is noteworthy that most of the previous studies used premature discontinuation, not MPR, as an indicator of nonadherence to medication. Therefore, we should be cautious of comparing the drug adherence and its associated factors in the current study with those reported in previous investigations.

The diagnostic rates of ODD and CD were only 4.1% and 4.0%, respectively, in our study population. These comorbid rates were much lower than those reported in systematic review articles.<sup>5–7</sup> The low comorbid rates in our cohort may be partly attributed to the case-recruitment procedure. In this study, patients whose ODD or CD diagnosis was made before ADHD diagnosis or occurred within 90 days of first prescription were considered as having no relationship with medication treatment. Hence, we excluded a large number of patients who had comorbidity of ODD (n = 1,667) or CD (n = 1,159), and this led to a low comorbid rate. A 3-year panel study in Taiwan<sup>39</sup> revealed that the prevalence rates of ODD and CD among general adolescent population were 1.3%–2.8% and 2.5%–2.9%, respectively. By contrast, the estimated lifetime prevalence of ODD and CD in the US general population is 10.2% and 9.5%.<sup>40,41</sup> It is likely that disruptive behavior disorders are less prevalent

You are prohibited from making this PDF publicly available.



in Taiwan compared to Western countries. However, we previously found that around 11% of youths with ADHD in the same nationwide dataset had comorbid ODD or CD,<sup>34,42</sup> but the rate is still lower than the reports using structural interviews in Taiwan (69% of ADHD comorbid with ODD and 33% of ADHD comorbid with CD).<sup>43,44</sup> On the other hand, the prevalence rates of ODD and CD in youths with ADHD are around 60% and 15% in the United States, respectively.<sup>5–7</sup> Therefore, the findings in our study indicate that ODD and CD may be still underdiagnosed among the ADHD population in Taiwan, and we suggest that clinicians increase their awareness of ODD and CD in clinical settings.

Some methodological issues warrant concern. First, the target population in this study was patients with ADHD who received medication treatment. In real-world nonrandomized conditions, patients with ADHD who receive drug therapy may actually experience greater symptom severity and functional impairments than patients who have never been exposed to medication.<sup>38</sup> These manifestations were not easily identified from the claims data. Therefore, we did not recruit patients who never received drug therapy for comparison. Future longitudinal study with assessment of severity of ADHD (eg, symptom counts, severity ratings, or scores of functional impairments) would help to elucidate the role of severity of ADHD in development of ODD or CD. Second, the follow-up period was not analyzed for the purpose of examining adherence. The main reason for this is that patients who underwent longer medication treatment before ODD or CD diagnosis naturally had a lower hazard ratio of ODD or CD occurrence than those who underwent shorter treatments. Therefore, we used a logistic regression model, not a Cox regression model, to avoid the survival bias in the study analyses.<sup>45</sup> Third, because drug switching could be complex in real-world clinical settings, duration and doses of medications for treating ADHD were composited. We were unable to determine whether stimulants (eg, methylphenidate) or

nonstimulants (eg, atomoxetine) exerted differential effects on subsequent ODD or CD.

This study has a number of limitations. First, we used reimbursement data, so the diagnoses of ADHD, ODD, and CD were not validated using structural diagnostic instruments and instead were identified solely on the basis of ICD codes, which could have been improperly classified. Hence, some patients may already have had a tendency toward ODD or CD at the initial visit with clinicians, but the clinicians missed the diagnosis. Second, several predictors (eg, patients' emotional regulation, family function, socioeconomic status, and frequency of outpatient visits or psychosocial intervention) have been associated with the risk of developing ODD or CD among youths with ADHD.<sup>13,14</sup> But the claims data retrieved for this study did not include this information or other potential mediating factors. Third, ODD and CD could be a continuity and may appear in patients with ADHD in sequence. However, the interrelationship between ODD and CD was not analyzed in this study. Finally, significant differences were found regarding various demographic characteristics within the compliant and the noncompliant groups. We did not apply a propensity score matching strategy; instead, we used stratification analyses to clarify the influence of drug adherence on patients with ADHD.

In conclusion, this study finds that among patients with ADHD receiving medication treatment, those with better drug adherence had a decreased risk of developing ODD or CD in comparison with their counterparts with worse drug adherence. This indicates that improving drug adherence may be beneficial for preventing the occurrence of ODD or CD in patients with ADHD. However, further investigation of the causal relationships between ADHD diagnoses in childhood, persistence of medication treatment, and the onset of ODD or CD would benefit from a longitudinal study containing comprehensive assessments of potential confounding factors.

**Submitted:** July 4, 2017; accepted January 8, 2018.

**Published online:** August 28, 2018.

**Potential conflicts of interest:** The authors declare no conflicts of interest.

**Funding/support:** This study was supported by the Chang Gung Memorial Hospital Research Project (CMRPG8D0581, CMRPG2G0312, CMRPG2G0082, CLRP2G0081, and CLRP2G2H0041).

**Role of the sponsor:** The funder did not participate in the study design, data analysis, or manuscript preparation. All aforementioned works were administered by the authors of this manuscript.

**Disclaimer:** The interpretation and conclusions contained herein do not represent those of the National Health Insurance Administration, Ministry of Health and Welfare, or National Health Research Institutes (Taiwan).

**Additional information:** This study is based in part on data from the National Health Insurance Research Database of Taiwan (NHIRD-TW) provided by the National Health Insurance Administration, Ministry of Health and Welfare and managed by National Health Research Institutes (Taiwan) (registered number NHIRD-102-088). Data are available from the NHIRD published by Taiwan

National Health Insurance Bureau. Due to legal restrictions imposed by the Government of Taiwan in relation to the Personal Information Protection Act, data cannot be made publicly available. Requests for data can be sent as a formal proposal to the NHIRD (<http://nhird.nhri.org.tw>).

## REFERENCES

1. Thomas R, Sanders S, Doust J, et al. Prevalence of attention-deficit/hyperactivity disorder: a systematic review and meta-analysis. *Pediatrics*. 2015;135(4):e994–e1001.
2. Spencer TJ, Biederman J, Mick E. Attention-deficit/hyperactivity disorder: diagnosis, lifespan, comorbidities, and neurobiology. *J Psychiatr Psychol*. 2007;32(6):631–642.
3. Inci SB, Ipci M, Akyol Ardic U, et al. Psychiatric comorbidity and demographic characteristics of 1,000 children and adolescents with ADHD in Turkey [published online ahead of print August 31, 2016]. *J Atten Disord*.
4. Noordermeer SD, Luman M, Oosterlaan J. A systematic review and meta-analysis of neuroimaging in oppositional defiant disorder (ODD) and conduct disorder (CD) taking attention-deficit hyperactivity disorder (ADHD) into account. *Neuropsychol Rev*. 2016;26(1):44–72.
5. Connor DF, Steeber J, McBurnett K. A review of attention-deficit/hyperactivity disorder complicated by symptoms of oppositional defiant disorder or conduct disorder. *J Dev Behav Pediatr*. 2010;31(5):427–440.
6. Loeber R, Burke JD, Lahey BB, et al. Oppositional defiant and conduct disorder: a review of the past 10 years, part I. *J Am Acad Child Adolesc Psychiatry*. 2000;39(12):1468–1484.
7. Burke JD, Loeber R, Birmaher B. Oppositional defiant disorder and conduct disorder: a review of the past 10 years, part II. *J Am Acad Child Adolesc Psychiatry*. 2002;41(11):1275–1293.
8. Matthys W, Vanderschuren LJ, Schutter DJ. The neurobiology of oppositional defiant disorder and conduct disorder: altered functioning in three mental domains. *Dev Psychopathol*. 2013;25(1):193–207.
9. Biederman J, Petty CR, Dolan C, et al. The long-term longitudinal course of oppositional defiant disorder and conduct disorder in ADHD boys: findings from a controlled 10-year prospective longitudinal follow-up

# It is illegal to post this copyrighted PDF on any website.

- study. *Psychol Med*. 2008;38(7):1027–1036.
10. Gau SS, Ni HC, Shang CY, et al. Psychiatric comorbidity among children and adolescents with and without persistent attention-deficit hyperactivity disorder. *Aust N Z J Psychiatry*. 2010;44(2):135–143.
11. Qian Y, Chang W, He X, et al. Emotional dysregulation of ADHD in childhood predicts poor early-adulthood outcomes: a prospective follow up study. *Res Dev Disabil*. 2016;59:428–436.
12. Husby SM, Wichstrøm L. Interrelationships and continuities in symptoms of oppositional defiant and conduct disorders from age 4 to 10 in the community. *J Abnorm Child Psychol*. 2017;45(5):947–958.
13. Steinberg EA, Drabick DA. A developmental psychopathology perspective on ADHD and comorbid conditions: the role of emotion regulation. *Child Psychiatry Hum Dev*. 2015;46(6):951–966.
14. Moroney E, Tung I, Brammer WA, et al. Externalizing outcomes of youth with and without ADHD: time-varying prediction by parental ADHD and mediated effects. *J Abnorm Child Psychol*. 2017;45(3):457–470.
15. Taurines R, Schmitt J, Renner T, et al. Developmental comorbidity in attention-deficit/hyperactivity disorder. *Atten Defic Hyperact Disord*. 2010;2(4):267–289.
16. Liu CY, Huang WL, Kao WC, et al. Influence of disruptive behavior disorders on academic performance and school functions of youths with attention-deficit/hyperactivity disorder. *Child Psychiatry Hum Dev*. 2017;48(6):870–880.
17. Connor DF, Carlson GA, Chang KD, et al; Stanford/Howard/AACAP Workgroup on Juvenile Impulsivity and Aggression. Juvenile maladaptive aggression: a review of prevention, treatment, and service configuration and a proposed research agenda. *J Clin Psychiatry*. 2006;67(5):808–820.
18. Cortese S, Holtmann M, Banaschewski T, et al; European ADHD Guidelines Group. Practitioner review: current best practice in the management of adverse events during treatment with ADHD medications in children and adolescents. *J Child Psychol Psychiatry*. 2013;54(3):227–246.
19. Rabito-Alcón MF, Correias-Laufer J. Treatment guidelines for attention deficit and hyperactivity disorder: a critical review. *Actas Esp Psiquiatr*. 2014;42(6):315–324.
20. Kutlu A, Akyol Ardıc U, Ercan ES. Effect of methylphenidate on emotional dysregulation in children with attention-deficit/hyperactivity disorder + oppositional defiant disorder/ conduct disorder. *J Clin Psychopharmacol*. 2017;37(2):220–225.
21. Matsui DM. Drug compliance in pediatrics: clinical and research issues. *Pediatr Clin North Am*. 1997;44(1):1–14.
22. Wilmick S, Lucas DO, Hartman AL, et al. How do you improve compliance? *Pediatrics*. 2005;115(6):e718–e724.
23. Adler LD, Nierenberg AA. Review of medication adherence in children and adults with ADHD. *Postgrad Med*. 2010;122(1):184–191.
24. Ahmed R, Aslani P. Attention-deficit/hyperactivity disorder: an update on medication adherence and persistence in children, adolescents and adults. *Expert Rev Pharmacoecon Outcomes Res*. 2013;13(6):791–815.
25. Hong M, Lee WH, Moon DS, et al. A 36 month naturalistic retrospective study of clinic-treated youth with attention-deficit/hyperactivity disorder. *J Child Adolesc Psychopharmacol*. 2014;24(6):341–346.
26. Ayaz M, Ayaz AB, Soylu N, et al. Medication persistence in Turkish children and adolescents with attention-deficit/hyperactivity disorder. *J Child Adolesc Psychopharmacol*. 2014;24(6):442–447.
27. Raman SR, Marshall SW, Gaynes BN, et al. An observational study of pharmacological treatment in primary care of children with ADHD in the United Kingdom. *Psychiatr Serv*. 2015;66(6):617–624.
28. Lin KJ, Schneeweiss S. Considerations for the analysis of longitudinal electronic health records linked to claims data to study the effectiveness and safety of drugs. *Clin Pharmacol Ther*. 2016;100(2):147–159.
29. Sanchez RJ, Crismon ML, Barner JC, et al. Assessment of adherence measures with different stimulants among children and adolescents. *Pharmacotherapy*. 2005;25(7):909–917.
30. Gajria K, Lu M, Sikirica V, et al. Adherence, persistence, and medication discontinuation in patients with attention-deficit/hyperactivity disorder—a systematic literature review. *Neuropsychiatr Dis Treat*. 2014;10:1543–1569.
31. Wu SH, Wang K, Chen Y, et al. Exploratory analysis of early treatment discontinuation and clinical outcomes of patients with attention-deficit/hyperactivity disorder. *Asia-Pac Psychiatry*. 2017;9(1):e12231.
32. Treuer T, Feng Q, Desai D, et al. Predictors of pharmacological treatment outcomes with atomoxetine or methylphenidate in patients with attention-deficit/hyperactivity disorder from China, Egypt, Lebanon, Russian Federation, Taiwan, and United Arab Emirates. *Int J Clin Pract*. 2014;68(9):1152–1160.
33. Groenman AP, Oosterlaan J, Rommelse NN, et al. Stimulant treatment for attention-deficit hyperactivity disorder and risk of developing substance use disorder. *Br J Psychiatry*. 2013;203(2):112–119.
34. Lee MJ, Yang KC, Shyu YC, et al. Attention-deficit hyperactivity disorder, its treatment with medication and the probability of developing a depressive disorder: a nationwide population-based study in Taiwan. *J Affect Disord*. 2016;189:110–117.
35. Wu CS, Lai MS, Gau SS, et al. Concordance between patient self-reports and claims data on clinical diagnoses, medication use, and health system utilization in Taiwan. *PLoS One*. 2014;9(12):e112257.
36. World Health Organization. Guidelines for ATC Classification and DDD Assignment. Oslo, Norway (2018). [https://www.whocc.no/atc\\_ddd\\_index/](https://www.whocc.no/atc_ddd_index/)
37. Waxmonsky J. Assessment and treatment of attention deficit hyperactivity disorder in children with comorbid psychiatric illness. *Curr Opin Pediatr*. 2003;15(5):476–482.
38. Atzori P, Usala T, Carucci S, et al. Predictive factors for persistent use and compliance of immediate-release methylphenidate: a 36-month naturalistic study. *J Child Adolesc Psychopharmacol*. 2009;19(6):673–681.
39. Gau SS, Chong MY, Chen TH, et al. A 3-year panel study of mental disorders among adolescents in Taiwan. *Am J Psychiatry*. 2005;162(7):1344–1350.
40. Nock MK, Kazdin AE, Hiripi E, et al. Prevalence, subtypes, and correlates of DSM-IV conduct disorder in the National Comorbidity Survey Replication. *Psychol Med*. 2006;36(5):699–710.
41. Nock MK, Kazdin AE, Hiripi E, et al. Lifetime prevalence, correlates, and persistence of oppositional defiant disorder: results from the National Comorbidity Survey Replication. *J Child Psychol Psychiatry*. 2007;48(7):703–713.
42. Shyu YC, Yuan SS, Lee SY, et al. Attention-deficit/hyperactivity disorder, methylphenidate use and the risk of developing schizophrenia spectrum disorders: a nationwide population-based study in Taiwan. *Schizophr Res*. 2015;168(1–2):161–167.
43. Yang LK, Shang CY, Gau SS. Psychiatric comorbidities in adolescents with attention-deficit hyperactivity disorder and their siblings. *Can J Psychiatry*. 2011;56(5):281–292.
44. Gau SS, Lin YJ, Cheng AT, et al. Psychopathology and symptom remission at adolescence among children with attention-deficit-hyperactivity disorder. *Aust N Z J Psychiatry*. 2010;44(4):323–332.
45. Zhou Z, Rahme E, Abrahamowicz M, et al. Survival bias associated with time-to-treatment initiation in drug effectiveness evaluation: a comparison of methods. *Am J Epidemiol*. 2005;162(10):1016–1023.

**Editor's Note:** We encourage authors to submit papers for consideration as a part of our Focus on Childhood and Adolescent Mental Health section. Please contact Karen D. Wagner, MD, PhD, at [kwagner@psychiatrist.com](mailto:kwagner@psychiatrist.com).

You are prohibited from making this PDF publicly available.



Article

# Bone Regeneration Using Adipose-Derived Stem Cells in Injectable Thermo-Gelling Hydrogel Scaffold Containing Platelet-Rich Plasma and Biphasic Calcium Phosphate

Han Tsung Liao <sup>1,2,3</sup> , Ming-Jin Tsai <sup>2</sup>, Manuri Brahmayya <sup>1</sup> and Jyh-Ping Chen <sup>1,2,4,5,\*</sup>

<sup>1</sup> Department of Plastic and Reconstructive Surgery and Craniofacial Research Center, Chang Gung Memorial Hospital, Chang Gung University School of Medicine, Kwei-San, Taoyuan 33305, Taiwan; lia01211@gmail.com (H.T.L.); brahma.orgchem@gmail.com (M.B.)

<sup>2</sup> Department of Chemical and Materials Engineering, Chang Gung University, Kwei-San, Taoyuan 33302, Taiwan; duo8704024@hotmail.com

<sup>3</sup> College of Medicine, Chang Gung University, Kwei-San, Taoyuan 33302, Taiwan

<sup>4</sup> Research Center for Food and Cosmetic Safety, Research Center for Chinese Herbal Medicine, College of Human Ecology, Chang Gung University of Science and Technology, Taoyuan 33302, Taiwan

<sup>5</sup> Department of Materials Engineering, Ming Chi University of Technology, Tai-Shan, New Taipei City 24301, Taiwan

\* Correspondence: jpchen@mail.cgu.edu.tw; Tel.: +886-3-211-8800 (ext. 5298)

Received: 27 July 2018; Accepted: 24 August 2018; Published: 27 August 2018



**Abstract:** For bone regeneration, a biocompatible thermo-gelling hydrogel, hyaluronic acid-g-chitosan-g-poly(N-isopropylacrylamide) (HA-CPN) was used as a three-dimensional organic gel matrix for entrapping rabbit adipose-derived stem cells (rASCs). Biphasic calcium phosphate (BCP) ceramic microparticles were embedded within the gel matrix as a mineralized bone matrix, which was further fortified with platelet-rich plasma (PRP) with osteo-inductive properties. In vitro culture of rASCs in HA-CPN and HA-CPN/PRP/BCP was compared for cell proliferation and osteogenic differentiation. Overall, HA-CPN/PRP/BCP was a better injectable cell carrier for osteogenesis of rASCs with increased cell proliferation rate and alkaline phosphatase activity, enhanced calcium deposition and mineralization of extracellular matrix, and up-regulated expression of genetic markers of osteogenesis. By implanting HA-CPN/PRP/BCP/rASCs constructs in rabbit critical size calvarial bone defects, new bone formation at the defect site was successfully demonstrated from computed tomography, and histological and immunohistochemical analysis. Taken together, by combining PRP and BCP as the osteo-inductive and osteo-conductive factor with HA-CPN, we successfully demonstrated the thermo-gelling composite hydrogel scaffold could promote the osteogenesis of rASCs for bone tissue engineering applications.

**Keywords:** scaffold; hydrogel; thermo-gelling; biphasic calcium phosphate; platelet-rich plasma; adipose-derived stem cells

## 1. Introduction

Autogenous bone graft and bone substitutes are current approaches for bone defect repair after trauma, tumor ablation or infection [1]. Nevertheless, these approaches all have drawbacks such as an unpredictable absorption rate, donor site morbidity, foreign body reaction, possible infection and unpredictable bone regeneration [2]. For the healing of bone defects, a tissue engineering approach combining stem cells with osteogenic property with a suitable scaffolding material can

be suggested. Therefore, bone tissue engineering (BTE) is now a popular research topic for bone defect repair/regeneration, which consists of three main factors, i.e., cells, scaffolds and growth factors [3]. The revelation of such an idea is that stem cells could be osteo-induced into the osteoblast lineage by the action of growth factors that function as signaling molecules within the bone-mimetic three-dimensional (3D) scaffold for bone tissue formation [4].

Bio-ceramics such as calcium phosphates are attractive for BTE applications due to their biocompatibility, bioactivity, degradability and osteo-conductivity [5]. In addition, an added advantage of using calcium phosphates is their structural and chemical similarity to the mineral phase of native bone [6]. The most widely investigated calcium phosphates that are used for bone regeneration and repairs are hydroxyapatite (HAP),  $\beta$ -tricalcium phosphate ( $\beta$ -TCP), and their mixture biphasic calcium phosphate (BCP). As an ideal bone substitute, BCP is the preferred ceramic material, due to its controllable degradability, high bio-resorption rate and favorable biological properties [7]. Indeed, evolution of the concept of using macroporous BCP, which contained HAP and  $\beta$ -TCP mixed in various ratios, for bone regeneration has been reported nearly 30 years ago [8,9]. The usefulness of BCP stemmed from the preferential dissolution of  $\beta$ -TCP compared to HAP, which allowed the manipulation of the biodegradation rate of BCP with different HAP/ $\beta$ -TCP ratios [10]. Although calcium phosphates are known to enhance osteoblast proliferation and differentiation, these ceramic materials are brittle and difficult to mold in order to fill irregular bone defects [11,12]. Besides, the dispersion of calcium phosphate particles during implantation may be difficult in both ectopic and bony sites [13].

Hydrogels are soft materials with 3D cross-linked network formed from hydrophilic homopolymers or copolymers. Other than using their 3D networks for cell entrapment, hydrogels can absorb a large amount of water and allow for diffusion of nutrients and metabolites from the cells. As a scaffolding material for tissue engineering applications, hydrogels could fulfill the requirement to temporarily provide an extracellular matrix (ECM) environment for the cells during the early stage of tissue regeneration [14]. This will be followed by replacement of the hydrogel matrices by a natural ECM secreted by the cells as the tissue formation process proceeds [15].

By responding to environmental stimuli for sol-to-gel transition, such as change in temperature, pH, light or ionic strength, a physical in situ forming hydrogel is one of the most popular injectable scaffolds for BTE [16]. Using the in situ forming hydrogel, an injectable scaffold could be molded to fit a bone defect of irregular shape, shorten the operation time, lessen the post-operative discomfort and fasten post-surgical recovery. In view of the popularity of minimally invasive surgery, cell delivery in such an injectable hydrogel scaffold by endoscope could be suggested as a feasible clinical application of BTE [17]. Being a particular kind of injectable in situ forming hydrogel responsive to temperature change, a thermo-gelling hydrogel shows sol-to-gel phase transition upon heating up to a temperature above its critical transition temperature [18,19]. Poly(N-isopropyl acrylamide) (PNIPAM) is a typical thermo-gelling polymeric hydrogel commercially available in the market. However, non-biodegradability, low biocompatibility and the toxicity of degradation products limit its biomedical applications [20,21]. Therefore, PNIPAM has been modified with many natural polymers, including chitosan, collagen, or hyaluronic acid, to form PNIPAM-based copolymers with better biodegradability, increased cell attachment and improved cell proliferation, without changing the sol-to-gel phase transition characteristics [22–25].

Chitosan is a linear polysaccharide derived from chitin and composed of glucosamine and N-acetyl glucosamine linked by  $\beta(1\rightarrow4)$  covalent bonds. In recent years, biomaterials based on chitosan have been applied in BTE, which was demonstrated to be osteo-inductive, and promote cell proliferation and mineral-rich matrix deposition when used for osteoblast culture [26]. Interestingly, previous studies have reported that chitosan-modified calcium phosphates could enhance the mechanical strength of the inorganic phase when used as a scaffold for BTE applications [27,28]. Hyaluronic acid (HA) is a non-sulfated glycosaminoglycan formed from repeating disaccharide units of N-acetyl-D-glucosamine and D-glucuronate with  $\beta(1\rightarrow4)$  and  $\beta(1\rightarrow3)$  bonds. HA was shown to



have strong effects on cell–cell interactions and migration [29]. As a scaffold for BTE, HA-based materials were proved to be suitable for bone regeneration in many studies [30,31].

Considering the advantages of those natural biomaterials for BTE, we have successfully prepared a thermo-gelling hydrogel copolymer, hyaluronic acid-g-chitosan-g-poly(N-isopropylacrylamide) (HA-CPN) and demonstrated its potentials as a BTE scaffold using bone marrow-derived stem cells from *in vitro* and *in vivo* ectopic bone formation studies [32]. Follow up studies by incorporation of osteo-conductive BCP microparticles into a HA-CPN scaffold further proved HA-CPN/BCP to be a suitable injectable composite hydrogel scaffold for human fetal osteoblast culture with improved osteoblastic differentiation and ECM mineralization, which formed ectopic bone tissue from nude mice subcutaneous implantation experiments [33]. Nonetheless, osteoblasts are not a good cell source for BTE. Adult stem cells are better sources due to their ability of self-renewal and multi-potent differentiation. Among them, adipose-derived stem cells (ASCs) seemed to be a preferred cell source for clinical application as harvesting adipose tissue is easy and safe using local anesthesia. Furthermore, higher amount of ASCs within fat tissue could be harvested compared to harvesting bone marrow-derived stem cells from the bone marrow aspirate and the harvesting procedure is associated with less donor site morbidity [34].

As stated before, growth factor is also one of the key components for BTE. Therefore, scaffolds for enhanced bone regeneration should be endowed with growth factors retaining and releasing properties to mediate accelerated bone regeneration. Indeed, allografts and xenografts are combined with growth factors as the osteo-inductive substances for natural bone-like performance [35]. Consider that a complete bone healing cascade depends on a wide range of growth factors, it could be suggested that incorporation of a spectrum of necessary growth factors would be a more rational approach compared with solely relying on a specific growth factor for BTE [36].

Platelets in the blood play an important role during the early stage of wound healing by taking part in blood clot formation and creating the right microenvironment to guide and control the healing cascade [37]. For more efficient bone repair by external use of platelets, enriching platelets in the plasma by removing red blood cells represents a feasible approach. This enriched blood plasma, platelet-rich plasma (PRP), is a promising alternative approach to enhance bone formation as it is a rich source of growth factors originating from  $\alpha$ -granules in PRP, which contain various growth factors, such as platelet-derived growth factor, transforming growth factor- $\beta$ , epidermal growth factor, insulin growth factor and vascular endothelial growth factor [38,39]. Abundant examples in the literature have addressed the positive effects of PRP on bone regeneration by combining with different biomaterials and various cell sources [40]. Improvement of osteogenesis of ASCs by PRP was also confirmed in a previous study by us [41]. Therefore, we hypothesize the incorporation of PRP and BCP as the osteo-inductive and osteo-conductive factor in the thermo-gelling hydrogel HA-CPN would influence the osteogenesis of ASCs.

To test this hypothesis, we evaluate the biological response of rabbit adipose-derived stem cells (rASCs) in HA-CPN and HA-CPN/PRP/BCP scaffolds in this study. The injectable scaffolds were first compared for rASCs differentiation into the osteogenic phenotype *in vitro*, followed by evaluation of HA-CPN/PRP/BCP composite scaffolds seeded with rASCs for regeneration of critical-size rabbit cranial defects *in vivo*.

## 2. Results and Discussion

### 2.1. Cell Proliferation

As an autogenous blood fraction without transmissible infectious agents, PRP is endowed with preferred properties for clinical use such as a high platelet concentration and being free from hypersensitivity reactions [42]. The platelet concentration in our prepared PRP was determined to contain  $3.2 \pm 0.4 \times 10^9$  platelet/mL, which is ~10 times that in the blood collected for preparing PRP.

It should be noted that a platelet concentration higher than  $1 \times 10^9$  platelet/mL was reported to be suitable for the clinical application of PRP [38].

As shown in Figure 1, rASCs proliferated steadily in HA-CPN and HA-CPN/PRP/BCP from day 7 to day 28 as revealed from the continued increase of the optical density (OD<sub>490</sub>) value using the 3-(4,5-dimethylthiazol-2-yl)-5-(3-carboxymethoxyphenyl)-2-(4-sulfophenyl)-2H-tetrazolium (MTS) cell proliferation assay kit, which is directly correlated with the number of viable cells. At the same seeding density, there were more viable cells in HA-CPN/PRP/BCP than in HA-CPN with significant difference found throughout the culture period ( $p < 0.05$ ), which indicates HA-CPN/PRP/BCP provided a better environment for rASCs proliferation than HA-CPN. This result is consistent with a previous report showing HA/gelatin/PRP hydrogel loaded in BCP scaffolds could enhance proliferation rate of MC3T3-E1 pre-osteoblast cells [43]. We also reported that incorporation of BCP into HA-CPN could significantly raise the cell proliferation rate of human fetal osteoblastic cells due to the beneficial effects of BCP [44]. Furthermore, enhancement of proliferation rate of ASCs by PRP was reported by us [45] and confirmed by other groups [46,47]. The use of rASCs in HA-CPN/PRP/BCP is expected to play a crucial role in the treatment of bone defect as recent studies on BTE clearly demonstrated the strong commitment of ASCs towards the osteogenic phenotype under appropriate induction conditions [48].

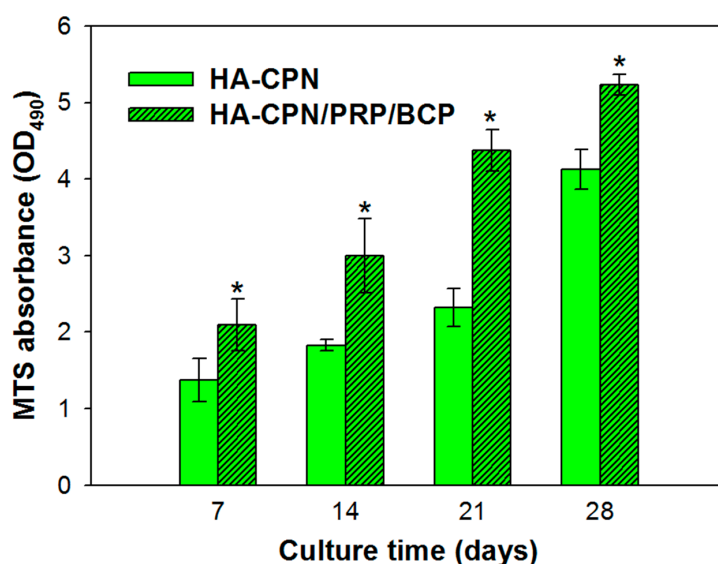


**Figure 1.** Proliferation of rabbit adipose-derived stem cells (rASCs) in hyaluronic acid-g-chitosan-g-poly (N-isopropylacrylamide) (HA-CPN) and HA-CPN/platelet-rich plasma (PRP)/biphasic calcium phosphate (BCP) thermo-gelling hydrogel scaffolds. \*  $p < 0.05$  compared with HA-CPN.

## 2.2. Live/Dead Staining

After using MTS assays to confirm the increase of viable cell number in different hydrogels, the Live/Dead fluorescence cell staining assay was used to qualitatively confirm the viability of rASCs with green color representing live cells and red color identifying any possible dead cells. As shown in Figure 2, the Live/Dead staining result revealed high viability of rASCs in both HA-CPN and HA-CPN/PRP/BCP with negligible dead cells found from the confocal image, which underlines the biocompatibility of all hydrogel scaffolds. The number of viable cells (green fluorescence) also gradually increased from day 14 to day 28 for both groups. Nonetheless, more cells were found in HA-CPN/PRP/BCP than in HA-CPN, which is consistent with the MTS results shown in Figure 1. In addition, rASCs started to show a cuboidal morphology of osteoblasts in HA-CPN/PRP/BCP on day 14, indicating accelerated differentiation of cells toward the osteogenic lineage [49]. Taken together, the biocompatibility of HA-CPN/PRP/BCP towards rASCs could be confirmed.

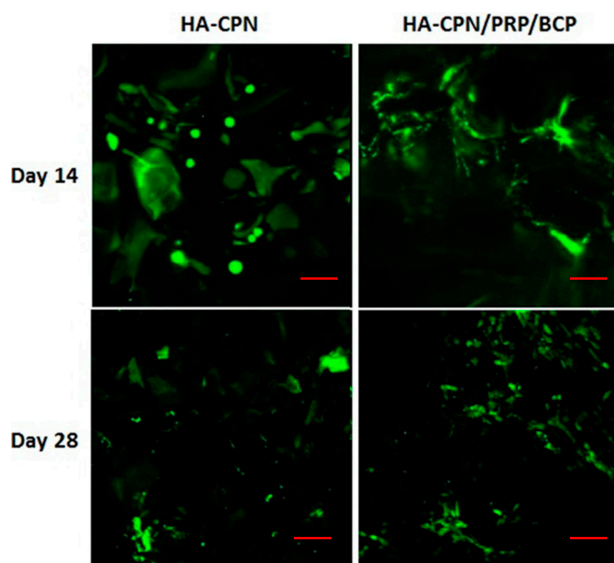


**Figure 2.** The viability of rASCs in HA-CPN and HA-CPN/PRP/BCP thermo-gelling hydrogel scaffolds by Live/Dead cell viability assays. Bar = 100  $\mu$ m.

### 2.3. Alkaline Phosphatase (ALP) Activities

Initiation of bone mineralization could be noticed by recognizing the alkaline phosphatase (ALP) marker, which as a marker for early osteoblastic differentiation and commitment of stem cells towards the osteoblast phenotype [50]. As nucleation starts with the deposition of calcium with inorganic phosphates and leads to local calcification, hydrolysis of phosphate esters leads to elevated mineralization of ECM and stimulates osteogenic differentiation [51]. Thus, ALP could be considered as a worthy measurement tool to determine the extent of osteo-differentiation of stem cells. Figure 3 indicates continued ALP production throughout the 28-day culture period for both groups; nonetheless, the ALP activity of rASCs in HA-CPN/PRP/BCP was significantly higher than in HA-CPN at all time points. Therefore, combinatory effects from PRP and BCP accelerated rASCs differentiation toward the osteoblast lineage, with ASCs in HA-CPN/PRP/BCP exhibiting enhanced ALP activity. Comparing the trend of ALP expression at various time points in different thermo-gelling hydrogel scaffolds, HA-CPN/PRP/BCP clearly showed dominance in rASCs differentiation [52].

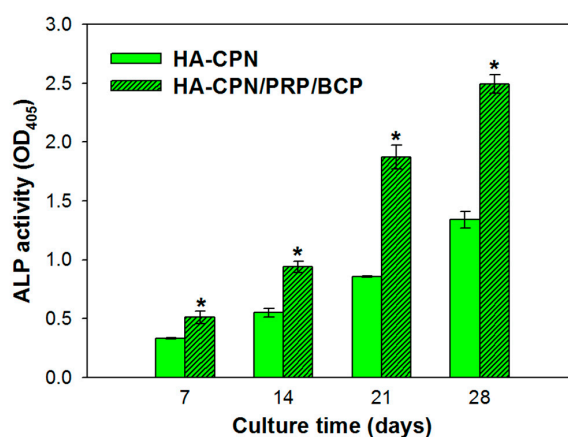


**Figure 3.** The time-dependent changes of alkaline phosphatase (ALP) activities of rASCs in HA-CPN and HA-CPN/PRP/BCP thermo-gelling hydrogel scaffolds. \*  $p < 0.05$  compared with HA-CPN.

#### 2.4. Von Kossa, Alizarin Red and ALP Stains

For qualitative evaluation of the mineralization of ASCs in HA-CPN and HA-CPN/PRP/BCP, the cryosection slices of cell/scaffold constructs were subject to von Kossa, Alizarin red (AR) and ALP stains. The mineralized nodules were revealed by staining with von Kossa staining reagents while calcium deposition on matured ECM was determined by AR stain. As shown in Figure 4, both von Kossa and Alizarin red stains revealed time-dependent mineralization of rASCs in HA-CPN hydrogel matrix. Nonetheless, the staining intensity was dramatically enhanced in HA-CPN/PRP/BCP. The concentration of mineralized ECM stained dark brown to black from von Kossa stain increased with culture time and appeared early for rASCs in HA-CPN/PRP/BCP than in HA-CPN, indicating more mineralized nodules formation with rapid development of osteoblast phenotype to form a mineralized matrix, which could be ascribed to the osteogenic natures of incorporated PRP/BCP in HA-CPN. More prominent AR staining was also evident in HA-CPN/PRP/BCP, in which nodules stained in red color originating from calcium ions in mineralized ECM secreted by osteo-differentiated rASCs increased with culture time. Since the capacity to deposit minerals is a marker for mature osteoblasts, it could be concluded that rASCs encapsulated in HA-CPN/PRP/BCP develop into an osteoblast phenotype faster than in HA-CPN, with accelerated mineralization stage to deposit mineralized ECM [53].

Considering ALP staining results in Figure 4, positive ALP stains (violet color) for rASCs in HA-CPN/PRP/BCP evidence the increase of intracellular ALP activity with culture time, particularly for cell constructs cultured longer than 2 weeks. On the other hand, minimum ALP staining intensity was observed for HA-CPN. HA-CPN showed light violet color while thick violet color dots with brownish red shadows were observed in HA-CPN/PRP/BCP on day 7. For rASCs in HA-CPN/PRP/BCP, violet and reddish brown violet ALP stains were observed on day 14 and day 21, respectively. The staining intensity turned much stronger and was a dark purple color on day 28, indicating continued elevation of ALP activity in HA-CPN/PRP/BCP. Taken together, the enhanced ALP staining intensity for rASCs in HA-CPN/PRP/BCP strongly endorse elevated ALP activity of rASCs in the presence of PRP and BCP, especially for cell constructs cultured longer than 14 days, which is consistent with the trend observed by biochemical assays (Figure 3).

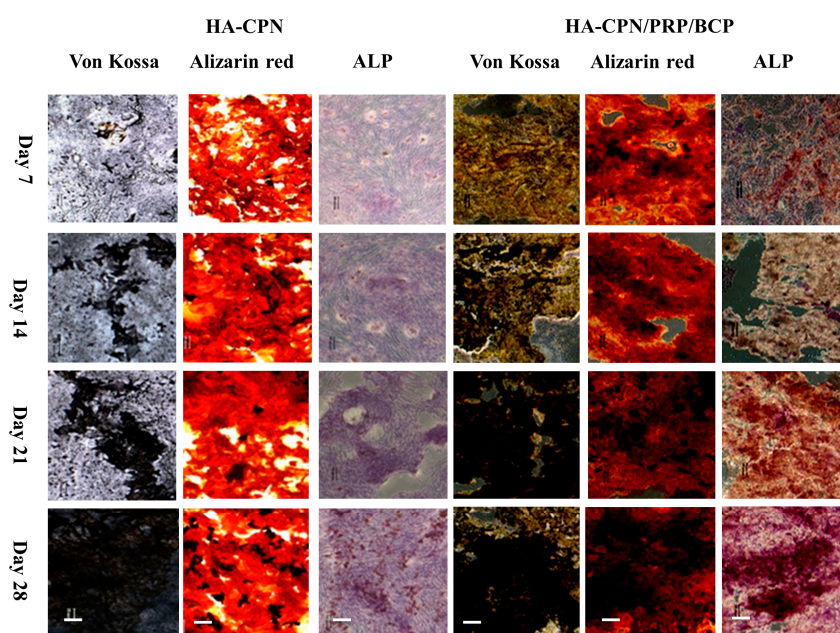


**Figure 4.** The von Kossa, Alizarin red and alkaline phosphatase (ALP) staining of cryosection slices of rASCs in HA-CPN and HA-CPN/PRP/BCP thermo-gelling hydrogel scaffolds. Bar = 100 µm.



## 2.5. Calcium Content

A quantitative determination of calcium content was used to cross confirm the calcium-based mineralization of rASCs (Figure 5). By extracting Alizarin red S (ARS) that binds to  $\text{Ca}^{2+}$  on cell surface with 10% cetylpyridinium chloride, quantitative evaluation of rASCs mineralization could be achieved by determining  $\text{OD}_{540}$  and augment the qualitative AR staining results shown in Figure 4. Since stem cells start depositing calcium during their later cell proliferation phase, the extent of calcium deposition depends strongly on the duration of the cell culture period [54]. As shown in Figure 5, the calcium content represented by  $\text{OD}_{540}$  increased rapidly with time from day 7 to day 28 in both hydrogel scaffolds. Nonetheless, the HA-CPN/PRP/BCP group showed significantly higher calcium content than the HA-CPN group throughout the 28-day culture period, which is in agreement with the qualitative AR staining images shown in Figure 4 and in line with ALP activity increase shown in Figure 3.

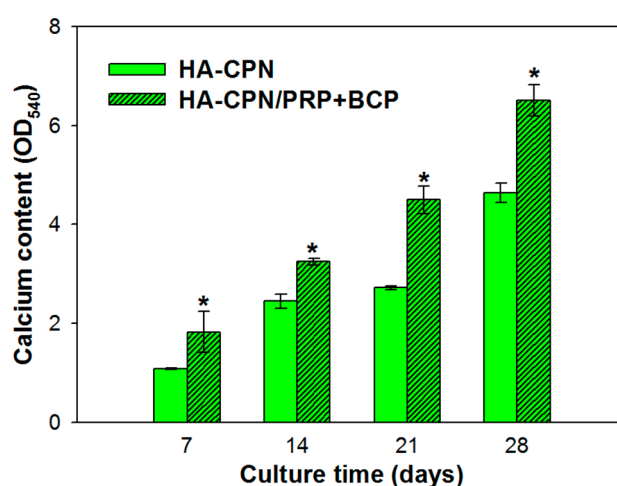


**Figure 5.** The calcium content of rASCs cultured in HA-CPN and HA-CPN/PRP/BCP thermo-gelling hydrogel scaffolds. \*  $p < 0.05$  compared with HA-CPN.

## 2.6. Scanning Electron Microscopy/Energy Dispersive X-Ray (SEM/EDX) Analysis

To examine cell morphology and mineralization, scanning electron microscopy/energy dispersive X-ray (SEM/EDX) analysis of cell/scaffold constructs at day 14 and 28 was attempted and the results are reported in Figure 6. Although cell morphology variance may arise due to rASCs being entrapped in the hydrogel matrix rather than adhered to a substrate surface, a morphological change could still be observed when rASCs were cultured in HA-CPN/PRP/BCP, which showed better cell spreading than in HA-CPN. This implies better osteogenesis of rASCs since stem cells will flatten and spread when undergoing osteogenesis [55]. In addition, the presence of mineralized nodules on the cell surface is higher for rASCs in HA-CPN/PRP/BCP compared to HA-CPN, which underlines the importance of the combinatory cues from PRP and BCP in HA-CPN/PRP/BCP for effective mineralization of rASCs [52]. It is well recognized that mineral formation during stem cell culture implied cellular osteoblastic differentiation [56]. As deposition of calcium phosphate leads to mineralization, the mineralization of inorganic phosphates on cell surface could be deemed as prime evidence for osteo-differentiation of rASCs [57]. Thus, the white mineral deposition from SEM observation could qualitatively identify mineralization, which could be further analyzed quantitatively through elemental analysis by EDX analysis. The EDX spectra associated with each SEM image was shown in Figure 6, from which the atomic percentages of elements in minerals deposited by rASCs were determined for quantitative comparison. As shown in Figure 6, the extent of mineralization increased from day 14 to day 28 and higher percentages of Ca and P were found for HA-CPN/PRP/BCP than HA-CPN. Specifically, the Ca/P atomic percentage was 6.64%/4.52% for HA-CPN/PRP/BCP at

day 14 and 7.46%/5.55% at day 28. In comparison, the Ca/P atomic percentage was only 1.01%/0.72% at day 14 and 3.85%/2.74% at day 28 for HA-CPN. Comparing HA-CPN/PRP/BCP with HA-CPN, the Ca and P atomic percentage increase was 6.6-fold and 6.3-fold on day 14 and 1.9-fold and 2.0-fold on day 28, indicating early and accelerated mineralization of rASCs in HA-CPN/PRP/BCP. Furthermore, the Ca/P ratios in HA-CPN and HA-CPN/PRP/BCP were between 1.4 and 1.5 and close to that of bone, whose mineral primarily consists of Ca and P with a Ca/P ratio from 1.4–1.7 [58]. Therefore, the atomic percentage values of Ca and P from EDX thus further demonstrate the potential application of HA-CPN/PRP/BCP for bone regeneration.

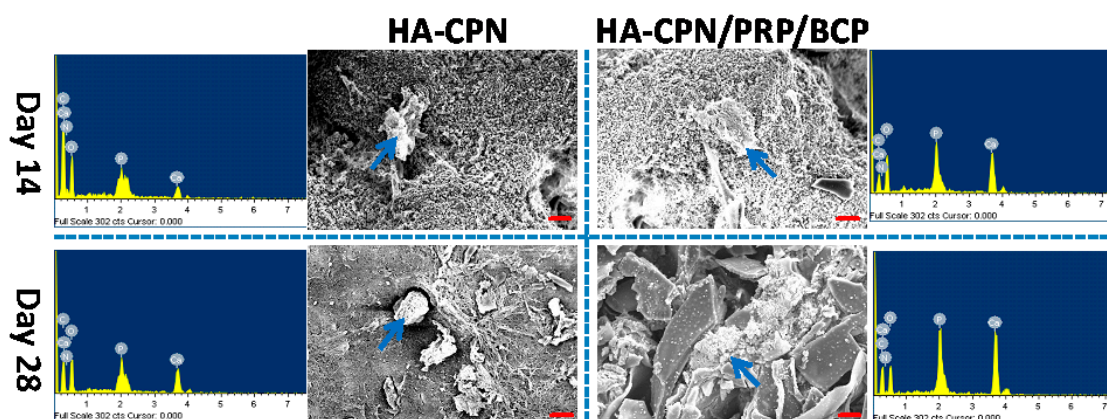


**Figure 6.** Scanning electron microscopy (SEM) micrographs and energy dispersive X-ray (EDX) measurements for detecting mineralization of rASCs in HA-CPN and HA-CPN/PRP/BCP thermo-gelling hydrogel scaffolds. The arrow in each SEM image indicates the place subject to EDX analysis with the spectrum shown besides the SEM image. Bar = 20 μm.

## 2.7. Gene Expression by Quantitative Real-Time Polymerase Chain Reaction (qRT-PCR)

The analysis of osteogenic gene expression could endorse the successful differentiation of rASCs into the osteoblast lineage. Thus, we further compared the relative mRNA expressions of major osteogenic differentiation marker genes (ALP, collagen type 1 (COL I), and osteocalcin (OCN)) of rASCs cultured in HA-CPN and HA-CPN/PRP/BCP (Figure 7). Being expressed at the early to middle stages of osteo-differentiation, ALP and COL were up-regulated during the first 2 weeks of cell culture without further increase of mRNA expression after day 21 [59]. On the other hand, the late expression of OCN could be confirmed from the continued increase of mRNA expression up to 28 days [60]. The scaffold-dependent analysis on gene expression further endorses the effect of PRP/BCP in controlling the expression of various osteogenic markers. Indeed, HA-CPN/PRP/BCP showed a significant enhancement of ALP and COL I gene expression over HA-CPN starting from day 7, which is consistent with their time-dependent gene expression sequence during osteogenic differentiation. On the other hand, being a late marker for osteogenesis, OCN would be up-regulated at a later stage of cell culture. Therefore, a significant difference of OCN mRNA expression was only noted between HA-CPN and HA-CPN/PRP/BCP after 14 days. Overall, we can infer that response of rASCs to BCP as well as PRP in HA-CPN leads to the difference in gene expression levels and control the time sequence of up-regulation of osteogenic genes. Considering the accelerated development of osteogenic phenotype of rASCs in HA-CPN/PRP/BCP *in vitro*, we proceeded with *in vivo* experiments to test the *in vivo* bone regeneration potential of HA-CPN/PRP/BCP/rASCs.

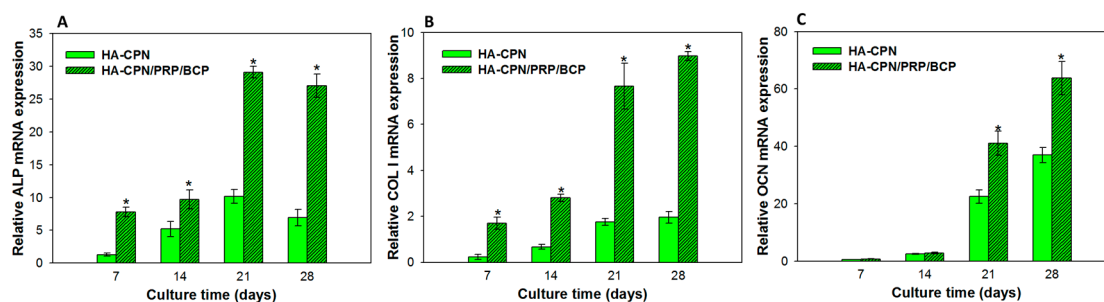


**Figure 7.** Osteogenic gene expression levels of rASCs after cultured in HA-CPN or HA-CPN/PRP/BCP thermo-gelling hydrogel scaffolds. Alkaline phosphatase (ALP) (A), collagen type 1 (COL I) (B) and osteocalcin (OCN) (C) gene expression was quantified using quantitative real-time PCR. \*  $p < 0.05$  compared with HA-CPN.

## 2.8. In Vivo Studies

After investigating in vitro osteogenesis, the critical size cranial bone defect model created in rabbits was used to test the in vivo bone regeneration potential of allogenic rASCs in HA-CPN/PRP/BCP. The HA-CPN/PRP/BCP/rASCs construct was cultured in vitro for 21 days prior to implantation. Since the 16-week animal experiment period did not lead to infection or inflammation symptoms around the implant sites and all rabbits stayed alive, we could confirm the in vivo biocompatibility of HA-CPN/PRP/BCP. One and 16 weeks post-implantation, the animals underwent computed tomography (CT) examination to evaluate new bone formation (Figure 8A). The 3D reconstructed CT images at week 1 showed some bone formation starting from one end and penetrated towards the center of the defect zone, without bridging the defect. After 16 weeks, the image density was elevated obviously with bone formation throughout the scaffold. The new bone was compact and bridged between the two ends of the circular defect and the defect was mostly covered with neo-bone formation based on the CT image density. For the control implanted with HA-CPN, negligible bone formation was found from CT images after 16 weeks. After sacrificing all animals at week 16, the specimen was harvested and bone formation was examined through histological evaluation, including hematoxylin and eosin (H&E), Masson's trichrome and immunohistochemical (IHC) staining of OCN, to cross-confirm the high-density area found in the CT image, was bone tissue (Figure 8B). From the H&E stain, osteoblasts in the bone matrix were observed together with osteoid formation, indicating bone growth in the defect region. Residual scaffold materials (labelled as S) could be observed 16 weeks after in vivo implantation. Masson's trichrome stain further clearly revealed bone formation as collagen in the osteoid was stained blue in sections of implanted HA-CPN/PRP/BCP/ASCs constructs as differentiated from rASCs deposited bone matrix (osteoid) and were embedded in the newly synthesized ECM. Osteoid is the organic portion of the bone matrix that is secreted by osteoblasts during new bone formation [61]. It contained several specific proteins with COL I being the predominant one and the rest being ground substance. Therefore, the development of new bone tissue may be verified from mineralized osteoid and adjacent bone cells. From IHC staining, the major ground substance in osteoid, OCN, could be identified in tissue sections, confirming that differentiated rASCs displayed an osteoblast phenotype. Taken together, the histological and IHC staining results support active osteogenesis from implanted rASCs and the observation that injected cell mass in the HA-CPN/PRP/BCP scaffold has formed new bone tissue.

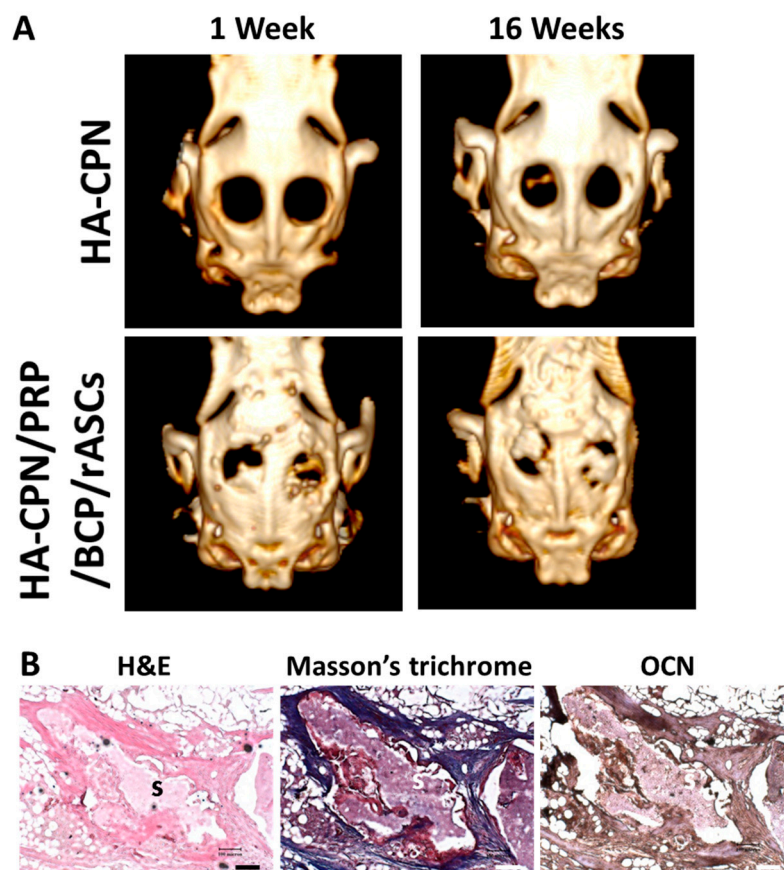


**Figure 8.** (A) The computed tomography (CT) scanning images of rabbit calvarial defects filled with HA/CPN and HA-CPN/PRP/BCP/rASCs 1 and 16 weeks post-implantation. (B) Hematoxylin and eosin (H&E), Masson's trichrome and immunohistochemical staining of OCN of implanted HA-CPN/PRP/BCP/rASCs in rabbit calvarial defects 16 weeks post-implantation. Bar = 100  $\mu$ m. S indicates remaining scaffold material.

### 3. Materials and Methods

#### 3.1. Materials

N-isopropylacrylamide (NIPAM) and 2,2-azoisobutyronitrile were acquired from Sigma-Aldrich (St Louis, MO, USA) and were recrystallized prior to use from methanol and hexane, respectively. Chitosan (molecular weight =  $1.5 \times 10^5$  Da) and 2-morpholinoethane sulfonic acid (MES) was purchased from Sigma-Aldrich (St Louis, MO, USA). N-Hydroxysuccinimide (NHS) and 1-ethyl-3-(3-dimethylaminopropyl) carbodiimide (EDC) were OBTAINED from Acros Organics, Thermo Fisher Scientific (Geel, Belgium). Hyaluronic acid (HA) (molecular weight =  $1.3 \times 10^6$  Da) was obtained from Bloomage Freda Biopharm Co. (Jinan, China). Dulbecco's modified Eagle medium (DMEM, Gibco, Thermo Fisher Scientific, Waltham, MA, USA) and fetal bovine serums (FBS, HyClone, Thermo Fisher Scientific, Waltham, MA, USA) were prearranged for cell culture. Biphasic calcium phosphate (BCP) microparticles (0.5–1 mm particle size) contained 60% (*w/w*) of beta-tricalcium phosphate ( $\beta$ -TCP) and 40% (*w/w*) hydroxyapatite (HAP) were provided by Berkeley Advanced Biomaterials, Inc. (San Leandro, CA, USA). CellTiter AQueous One Solution Reagent for cell proliferation assay was supplied by Promega Life Sciences (Madison, WI, USA).



### 3.2. Synthesis of Hyaluronic Acid-g-Chitosan-G-Poly(N-Isopropylacrylamide) (HA-CPN)

The HA-CPN copolymer was prepared as reported previously [23]. Briefly, carboxylic acid terminated PNIPAM (PNIPAM-COOH) was readily prepared in benzene by free radical polymerization between NIPAM with mercaptoacetic acid as a chain-terminating agent and 2,2-azoisobutyronitrile as an initiator. Chitosan-g-poly(N-isopropylacrylamide) (CPN) was prepared from 0.5 g of chitosan and 5 g of PNIPAM-COOH in 50 mL MES buffer (pH 5.0) using EDC and NHS as crosslinking agents. After reacting for 12 h at 25 °C and 180 rpm, temperature of the solution was raised to 50 °C for complete recovery of the copolymer by thermal precipitation. For the synthesis of HA-CPN copolymer, CPN prepared above was mixed with HA (0.25 g) in 100 mL of 0.1 M MES buffer (pH 5) and the grafting reaction was carried out at 25 °C and 180 rpm for 12 h in the presence of EDC and NHS. After completing the reaction, impurities and residual HA were removed by the thermal precipitation at 50 °C. The final HA-CPN copolymer used for forming the thermo-gelling hydrogel scaffold was purified by dialysis at 4 °C for 4 days and freeze-dried for storage at room temperature in a desiccator.

### 3.3. Preparation of Platelet-Rich Plasma (PRP)

The preparation of PRP from rabbits by double centrifugation followed the procedures described in our previous report [45]. The procedures were approved by the Institutional Animal Care and Use Committee of Chang Gung University (IACUC Approval No.: CGU13-063, 30 September 2013). In short, ~30 mL of whole blood was withdrawn from ear vessels of rabbits into a tube that contained a citrate phosphate dextrose solution as an anticoagulant. The whole blood was centrifuged at  $400 \times g$  for 10 min to separate the platelet layer from the plasma and red blood cells. The lower red blood cell layer was discarded while the middle platelet layer and the upper plasma layer were collected and further centrifuged at  $800 \times g$  for 10 min. The PRP was collected as the precipitated platelet layer with part of the plasma layer. The platelet number in whole blood and PRP were determined by a hematology analyzer (CELL-DYN Emerald, Abbott, Abbott Park, IL, USA) to check the quality of PRP obtained by this method.

### 3.4. Isolation of Rabbit Adipose-Derived Stem Cells (rASCs)

The animal experiments were approved by the Institutional Animal Care and Use Committee of Chang Gung University (IACUC Approval No.: CGU13-140, 18 March 2014) and confirmed to the standards of the Association for Assessment and Accreditation of Laboratory Animal Care. Rabbit adipose-derived stem cells (rASCs) were harvested and isolated according to our former report [51]. Briefly, fat tissue was harvested from a rabbit's inguinal area and diced into small pieces. The diced fat tissue was washed extensively with phosphate buffered saline (PBS), and digested with 0.05% collagenase in a 37 °C water bath shaker at 165 rpm for 30 min. The enzyme activity was neutralized by adding an equal volume of DMEM/10% FBS, and centrifuged at  $250 \times g$  for 10 min to obtain a high density cell pellet. After removing the supernatant, the cell pellet was re-suspended in 160 mM  $\text{NH}_4\text{Cl}$  and incubated at room temperature for 10 min to lyse the contaminated red blood cells. The cell pellet was collected again by the same centrifugation step, filtered through a 100  $\mu\text{m}$  nylon mesh to remove cellular debris, placed in culture dishes and incubated overnight with DMEM at 37 °C in a 5%  $\text{CO}_2$  incubator for attachment of rASCs to dish surface. Following incubation, the culture dishes were washed extensively with PBS to remove residual no-adherent red blood cells to obtain rASCs-enriched cell population.

### 3.5. In Vitro Culture of rASCs in HA-CPN and HA-CPN/Platelet-Rich Plasma/Biphasic Calcium Phosphate (HA-CPN/PRP/BCP)

For the culture of rASCs in the thermo-gelling hydrogel, 10% (w/v) HA-CPN or 10% (w/v) HA-CPN/10% (v/v) PRP/3% (w/v) BCP solution were prepared in DMEM at 4 °C. Suspension of rASCs was mixed at room temperature with 0.4 mL of HA-CPN or HA-CPN/PRP/BCP solution.

The mixture was carefully transferred to a 24-well cell culture plate and incubated at 37 °C for 1 h at a cell seeding density of  $1 \times 10^5$  cells/well. One milliliter of cell culture medium (90% DMEM, 10% FBS, 50  $\mu\text{mol/L}$  L-ascorbic acid phosphate, 100 nmol/L dexamethasone, 10 mmol/L glycerol 2-phosphate and 1% (v/v) antibiotic–antimycotic) was added to each well and cell culture was carried out at 37 °C in a humidified 5% CO<sub>2</sub> incubator with medium change on every 2 to 3 days.

### 3.6. Cell Proliferation

To determine the proliferation of ASCs, the viable cell number was determined by the 3-(4,5-dimethylthiazol-2-yl)-5-(3-carboxymethoxyphenyl)-2-(4-sulfophenyl)-2H tetrazolium (MTS) assay using the CellTiter AQueous One Solution Reagent. After cooling to 4 °C to reverse the cell/hydrogel constructs to a solution state, 200  $\mu\text{L}$  of cold DMEM was added to obtain cell suspension. The MTS assay were performed by adding 20  $\mu\text{L}$  of MTS solution to 200  $\mu\text{L}$  of cell suspension, followed by incubating at room temperature for 3 h in the absence of light. Colorimetric measurement of the formazan product was performed by measuring the optical density value at 490 nm (OD<sub>490</sub>) using an ELISA plate reader (BioTek Synergy HT, Winooski, VT, USA) [24].

### 3.7. Live/Dead Assay

The qualitative assessment on the cell viability of rASCs was evaluated using the Live/Dead Viability/Cytotoxicity kit (Molecular Probes, Thermo Fisher Scientific, Waltham, MA, USA). Once cultured for 21 days, the medium was removed from each well and samples were washed three times with PBS. A Live/Dead staining solution contained 2  $\mu\text{M}$  calcein AM (excitation 494 nm, emission 517 nm) and 5  $\mu\text{M}$  ethidium homodimer-1 (EthD-1) (excitation 528 nm, emission 617 nm) was prepared in DMEM, with calcein AM detecting live cell and EthD-1 for dead cell identification. The samples were incubated with the staining solution at 37 °C for 30 min and stained cells were imaged under a Zeiss LSM 510 Meta confocal laser scanning microscope (Carl Zeiss Microscopy GmbH, Jena, Germany).

### 3.8. ALP Activity

To analyze the intracellular ALP activity, 800  $\mu\text{L}$  cold cell lysis solution containing 0.1% Triton X-100 and 5 mM MgCl<sub>2</sub> was added to each well after PBS washing. After incubating at 4 °C for 10 min to lysis cells, the solution was centrifuged at  $13,000 \times g$  for 10 min and the supernatant was examined for ALP activity using *p*-nitrophenyl phosphate as a substrate for the enzymatic hydrolysis reaction. Briefly, 50  $\mu\text{L}$  supernatant was reacted with 50  $\mu\text{L}$  *p*-nitrophenyl phosphate (5 mM) for 60 min at 37 °C before adding 50  $\mu\text{L}$  0.2 N NaOH as a stop solution to denature ALP. The ALP activity was determined from the optical density value of the solution at 405 nm (OD<sub>405</sub>) using an enzyme-linked immunosorbent assay (ELISA) reader.

### 3.9. Alizarin Red, Von Kossa and ALP Stains

After detaching the cell-loaded hydrogel from each well, the sample was embedded in an optimal cutting temperature (OCT) compound. The sample in the cryomold was first placed at −20 °C until the OCT compound becomes translucent, followed by transferring to −80 °C overnight. After removing from the cryomold, the frozen block was mounted on a chuck in a cryostat and slices (5 to 10  $\mu\text{m}$ ) were collected. The samples were fixed at 37 °C in 4% formaldehyde for 3 h and washed with PBS before subject to different stains. For ALP stain, the sample was stained with ALP substrate solution containing fast blue RR (2 mg/mL) and 1-naphthyl phosphate sodium salt (2 mg/mL) in distilled de-ionized (DDI) water for 30 min at 37 °C. To detect mineralized nodules, Alizarin red stain was used by incubating samples in 2% Alizarin red S (ARS) solution in DDI water for 1 h at 37 °C. For von Kossa stain, samples were pre-treated with silver nitrate solution (5% in DDI water) for 20 min before placed in a UV box for UV light exposure for 2 h. The sample was finally soaked in sodium thiosulfate (5%) for 5 min to remove excess silver nitrate.

### 3.10. Calcium Content

Alizarin red S (ARS) was used to quantify the calcium ion ( $\text{Ca}^{2+}$ ) content in mineralized ECM of osteo-differentiated rASCs. The cell-seeded hydrogel scaffold was removed from wells of the culture plate and washed 3 times with PBS at 37 °C. After fixing with 4% glutaraldehyde solution (in 0.01 M phosphate buffer) for 3 h at 37 °C, 1 mL of ARS solution (2 g ARS in 100 mL DDI water) was added and incubated for 1 h at room temperature. After several washes with DDI water to remove excess dye, the sample was incubated with 1 mL of 10% cetylpyridinium chloride solution to elute the ARS- $\text{Ca}^{2+}$  chelating complex. The solution was transferred to an ELISA reader (Synergy HT, BioTek, Winooski, Vermont, VT, USA) and the solution absorbance was determined at 540 nm ( $\text{OD}_{540}$ ).

### 3.11. Scanning Electron Microscopy/Energy Dispersive X-Ray (SEM/EDX) Analysis

The samples were firstly rinsed with 37 °C PBS and then fixed in 4% glutaraldehyde (in 0.1 M phosphate buffer) at 37 °C. After subsequently fixation for another 3 h, the samples were washed 3 times in PBS buffer at 37 °C for 10 min each and then post-fixed in 1%  $\text{OsO}_4$  (in 0.1 M phosphate buffer) at 37 °C for 2.5 h. Later, samples were washed 3 times with DDI water and dehydrated in stepwise increasing concentrations of ethanol from 50% to 100%. Lastly, the specimens were dried in a critical point dryer, sputter coated with gold, and examined under an S-3000N scanning electron microscope (Hitachi, Tokyo, Japan). The extent of cell mineralization was determined from the atomic percentage of elements using an energy dispersive X-ray (EDX) micro-analyzer (Horiba EX-250, Tokyo, Japan).

### 3.12. Expression of Osteogenic Genes by qRT-PCR

The expression of osteogenic differentiation marker genes was studied using qRT-PCR following standard protocols for RNA isolation and cDNA preparation. Total RNA of each specimen was isolated with TRIzol reagent (Invitrogen, Carlsbad, CA, USA) and dissolved in RNase-free water. The amount of RNA was determined by measuring the OD value at 260 nm ( $\text{OD}_{260}$ ) with a NanoDrop microvolume spectrophotometer (Thermo Fisher Scientific, Waltham, MA, USA). RNA quality was verified by measurement of  $\text{OD}_{260}/\text{OD}_{280}$ . The cDNA was prepared from 2 µg of total RNA with Revert Aid First Strand cDNA Synthesis Kit in a final volume of 20 µL. The relative mRNA expression of ALP, OCN and COL I osteogenic marker genes was used for study of osteogenesis by designing the primer sequence using the Oligo 6.0 Primer Analysis Software Molecular Biology Insights, Inc. (Colorado Springs, CO, USA). For a single PCR reaction amounting to 20 µL, 0.2 µL of cDNA was used. To make the visualization of PCR products possible in real time, a SYBR Green I Supermix (Yeastern Biotech Co., Taipei, Taiwan) was used. A three temperature cycling, consisting of a denaturation step at 95 °C for 30 s, a annealing step at 57.6 °C for 30 s and an extension step at 72 °C for 30 s, was carried out in an iCycler iQ5 real-time detection system (Bio-Rad Laboratories Inc., Hercules, CA, USA). The specificity of each PCR reaction was assessed by performing melting curve analysis after each reaction. Glyceraldehyde-3-phosphate dehydrogenase (GAPDH) acted as a housekeeping control. Results were quantified for osteogenic marker genes using the  $2^{-\Delta\Delta C_t}$  relative quantification method. The expression of each gene was evaluated in triplicate.

### 3.13. In Vivo Experiment

The critical size calvarial bone defect model in rabbits was used to evaluate bone formation by implanting HA-CPN/PRP/BCP/ASCs in rabbit skull. Animal protocols were approved by the Institutional Animal Care and Use Committee of Chang Gung University (IACUC Approval No.: CGU13-035). New Zealand white male rabbits weighing 3–4 kg were utilized for the experimental studies. Animals were anesthetized with xylazine (7 mg/kg) and ketamine (140 mg/kg) and the scalp was sterilized with 75% alcohol solution. Animals were kept in single rooms and fed with standard animal feeds. For an assessment of bone regeneration, two 10 mm diameter circular

defects were made at the calvarial bone of the rabbit. Five hundred microliter of HA-CPN/PRP/BCP solution containing  $5 \times 10^6$  rASCs was cultured in vitro for 3 weeks before injecting into each defect. The control group was injected with 500  $\mu$ L of HA-CPN. Bone formation was examined by computed tomography (CT) examination using a CT scanner (Somatom Sensation 16, Siemens Healthcare GmbH, Erlangen, Germany) 16 weeks post-operation. The CT image acquisition, processing, and manipulation procedures followed standard protocols at a medical facility. The animals were sacrificed 16-week post-implantation with overdosed pentobarbital to retrieve the implants for histological analysis. The samples were fixed in 10% formaldehyde and dehydrated by embedding in paraffin. After sectioning into 5  $\mu$ m slice sections, hematoxylin and eosin (H & E), Masson's trichrome and IHC staining of OCN were carried out following standard protocols [62]. The images were recorded under an inverted optical microscope (Olympus IX-71, Tokyo, Japan).

### 3.14. Statistical Analysis

All data are reported as mean  $\pm$  standard deviation. Tukey's post hoc test was used to determine the difference between two groups with  $p < 0.05$  being considered statistically significant.

## 4. Conclusions

Thermo-gelling HA-CPN/PRP/BCP hydrogel scaffold is found to be a suitable injectable cell carrier for rASCs. In vitro culture of rASCs in HA-CPN/PRP/BCP exhibited better cell proliferation and enhanced osteogenic differentiation. From gene expression, tissue section staining, SEM/EDX and calcium content analysis, PRP/BCP boosts osteoblastic differentiation and ECM mineralization of rASCs in a HA-CPN gel matrix. Using allogenic rASCs in composite HA-CPN/PRP/BCP scaffold to repair critical size calvarial defects in rabbits, the CT analysis confirmed successful bone formation using the cell/hydrogel construct. The phenotypic markers for osteogenesis in the neo-bone tissue could be further identified from histology and IHC staining. Overall, the HA-CPN hydrogel scaffold fortified with PRP/BCP as osteo-inductive/osteo-conductive factors was shown to provide synergistic cues to promote the osteogenesis of rASCs in vitro and in vivo. This composite biomaterial could potentially be useful for development of an injectable cell carrier to assist bone regeneration in a non-load bearing defect site.

**Author Contributions:** H.T.L. and J.-P.C. conceived and designed the experiments; H.T.L. and M.-J.T. performed the experiments; H.T.L., M.-J.T. and J.-P.C. analyzed the data; H.-T.L., M.B. and J.-P.C. wrote the paper.

**Acknowledgments:** This work was supported by grants from Chang Gung Memorial Hospital (CRRPD2G0012, CRRPG3G0012, CMRPGBH0011 and BMRP 249) and the Ministry of Science and Technology (MOST105-2314-B-182-009).

**Conflicts of Interest:** The authors declare no conflict of interest.

## Abbreviations

HA	Hyaluronic acid
PNIPAM	Poly(N-isopropylacrylamide)
HA-CPN	Hyaluronic acid-g-chitosan-g-PNIPAM
CPN	Chitosan-g-poly(N-isopropylacrylamide)
LCST	Lower critical solution temperature
PBS	Phosphate buffered saline
HAP	Hydroxyapatite
FBS	Fetal bovine serum
DMEM	Dulbecco's modified Eagle medium
ASCs	Adipose-derived stem cells
rASCs	Rabbit adipose-derived stem cells
ECM	Extracellular matrix



H&E	Hematoxylin and eosin
PRP	Platelet-rich plasma
SEM	Scanning electron microscopy
BCP	Biphasic calcium phosphate
$\beta$ -TCP	$\beta$ -Tricalcium phosphate
BTE	Bone tissue engineering
AR	Alizarin red
ARS	Alizarin red S
3D	Three-dimensional
IHC	Immunohistochemical
CT	Computed tomography
OD	Optical density
SEM/EDX	Scanning electron microscopy/energy dispersive X-ray
ALP	Alkaline phosphatase
NHS	N-Hydroxysuccinimide
EDC	1-Ethyl-3-(3-dimethylaminopropyl) carbodiimide
DDI	Distilled de-ionized
MES	2-Morpholinoethane sulfonic acid
OCT	Optimal cutting temperature
qRT-PCR	Quantitative real-time polymerase chain reaction

## References

1. Sheikh, Z.; Sima, C.; Glogauer, M. Bone replacement materials and techniques used for achieving vertical alveolar bone augmentation. *Materials* **2015**, *8*, 2953. [[CrossRef](#)]
2. Rogers, G.F.; Greene, A.K. Autogenous bone graft: Basic science and clinical implications. *J. Craniofac. Surg.* **2012**, *23*, 323–327. [[CrossRef](#)] [[PubMed](#)]
3. Rose, F.R.; Oreffo, R.O. Bone tissue engineering: Hope vs hype. *Biochem. Biophys. Res. Commun.* **2002**, *292*, 1–7. [[CrossRef](#)] [[PubMed](#)]
4. Salgado, A.J.; Coutinho, O.P.; Reis, R.L. Bone tissue engineering: State of the art and future trends. *Macromol. Biosci.* **2004**, *4*, 743–765. [[CrossRef](#)] [[PubMed](#)]
5. LeGeros, R.Z. Calcium phosphate-based osteoinductive materials. *Chem. Rev.* **2008**, *108*, 4742–4753. [[CrossRef](#)] [[PubMed](#)]
6. Rizzi, S.C.; Heath, D.J.; Coombes, A.G.; Bock, N.; Textor, M.; Downes, S. Biodegradable polymer/hydroxyapatite composites: Surface analysis and initial attachment of human osteoblasts. *J. Biomed. Mater. Res.* **2001**, *55*, 475–486. [[CrossRef](#)]
7. Fellah, B.H.; Gauthier, O.; Weiss, P.; Chappard, D.; Layrolle, P. Osteogenicity of biphasic calcium phosphate ceramics and bone autograft in a goat model. *Biomaterials* **2008**, *29*, 1177–1188. [[CrossRef](#)] [[PubMed](#)]
8. Daculsi, G.; LeGeros, R.; Nery, E.; Lynch, K.; Kerebel, B. Transformation of biphasic calcium phosphate ceramics in vivo: Ultrastructural and physicochemical characterization. *J. Biomed. Mater. Res. A* **1989**, *23*, 883–894. [[CrossRef](#)] [[PubMed](#)]
9. Daculsi, G.; LeGeros, R.; Mitre, D. Crystal dissolution of biological and ceramic apatites. *Calcif. Tissue Int.* **1989**, *45*, 95–103. [[CrossRef](#)] [[PubMed](#)]
10. LeGeros, R. Calcium phosphate materials in restorative dentistry: A review. *Adv. Dent. Res.* **1988**, *2*, 164–180. [[CrossRef](#)] [[PubMed](#)]
11. Marra, K.G.; Szem, J.W.; Kumta, P.N.; DiMilla, P.A.; Weiss, L.E. In vitro analysis of biodegradable polymer blend/hydroxyapatite composites for bone tissue engineering. *J. Biomed. Mater. Res.* **1999**, *47*, 324–335. [[CrossRef](#)]
12. Chen, J.-P.; Chang, Y.-S. Preparation and characterization of composite nanofibers of polycaprolactone and nanohydroxyapatite for osteogenic differentiation of mesenchymal stem cells. *Colloids Surf. B Biointerfaces* **2011**, *86*, 169–175. [[CrossRef](#)] [[PubMed](#)]
13. Baroth, S.; Bourges, X.; Goyenvalle, E.; Aguado, E.; Daculsi, G. Injectable biphasic calcium phosphate bioceramic: The hydros concept. *Biomed. Mater. Eng.* **2009**, *19*, 71–76. [[PubMed](#)]

14. Slaughter, B.V.; Khurshid, S.S.; Fisher, O.Z.; Khademhosseini, A.; Peppas, N.A. Hydrogels in regenerative medicine. *Adv. Mater.* **2009**, *21*, 3307–3329. [[CrossRef](#)] [[PubMed](#)]
15. Akalp, U.; Bryant, S.J.; Vernerey, F.J. Tuning tissue growth with scaffold degradation in enzyme-sensitive hydrogels: A mathematical model. *Soft Matter* **2016**, *12*, 7505–7520. [[CrossRef](#)] [[PubMed](#)]
16. Tozzi, G.; De Mori, A.; Oliveira, A.; Roldo, M. Composite hydrogels for bone regeneration. *Materials* **2016**, *9*, 267. [[CrossRef](#)] [[PubMed](#)]
17. Kretlow, J.D.; Klouda, L.; Mikos, A.G. Injectable matrices and scaffolds for drug delivery in tissue engineering. *Adv. Drug Deliv. Rev.* **2007**, *59*, 263–273. [[CrossRef](#)] [[PubMed](#)]
18. Huayang, S.A.; Lu, J.; Zibiao, L. Biodegradable polyester thermogelling system as emerging materials for therapeutic applications. *Macromol. Mater. Eng.* **2018**, *303*, 1700656.
19. Liow, S.S.; Dou, Q.; Kai, D.; Karim, A.A.; Zhang, K.; Xu, F.; Loh, X.J. Thermogels: In situ gelling biomaterial. *ACS Biomater. Sci. Eng.* **2016**, *2*, 295–316. [[CrossRef](#)]
20. Vihola, H.; Laukkanen, A.; Valtola, L.; Tenhu, H.; Hirvonen, J. Cytotoxicity of thermosensitive polymers poly(N-isopropylacrylamide), poly(N-vinylcaprolactam) and amphiphilically modified poly(N-vinylcaprolactam). *Biomaterials* **2005**, *26*, 3055–3064. [[CrossRef](#)] [[PubMed](#)]
21. Cooperstein, M.A.; Canavan, H.E. Assessment of cytotoxicity of (N-isopropyl acrylamide) and poly(N-isopropyl acrylamide)-coated surfaces. *Biointerphases* **2013**, *8*, 19. [[CrossRef](#)] [[PubMed](#)]
22. Cho, J.H.; Kim, S.H.; Park, K.D.; Jung, M.C.; Yang, W.I.; Han, S.W.; Noh, J.Y.; Lee, J.W. Chondrogenic differentiation of human mesenchymal stem cells using a thermosensitive poly(N-isopropylacrylamide) and water-soluble chitosan copolymer. *Biomaterials* **2004**, *25*, 5743–5751. [[CrossRef](#)] [[PubMed](#)]
23. Chen, J.-P.; Cheng, T.-H. Preparation and evaluation of thermo-reversible copolymer hydrogels containing chitosan and hyaluronic acid as injectable cell carriers. *Polymer* **2009**, *50*, 107–116. [[CrossRef](#)]
24. Chen, J.P.; Cheng, T.H. Thermo-responsive chitosan-graft-poly(N-isopropylacrylamide) injectable hydrogel for cultivation of chondrocytes and meniscus cells. *Macromol. Biosci.* **2006**, *6*, 1026–1039. [[CrossRef](#)] [[PubMed](#)]
25. Chen, C.H.; Kuo, C.Y.; Chen, S.H.; Mao, S.H.; Chang, C.Y.; Shalumon, K.T.; Chen, J.P. Thermosensitive injectable hydrogel for simultaneous intraperitoneal delivery of doxorubicin and prevention of peritoneal adhesion. *Int. J. Mol. Sci.* **2018**, *19*, 1373. [[CrossRef](#)] [[PubMed](#)]
26. Levengood, S.L.; Zhang, M. Chitosan-based scaffolds for bone tissue engineering. *J. Mater. Chem. B* **2014**, *2*, 3161–3184. [[CrossRef](#)] [[PubMed](#)]
27. Liu, H.; Li, H.; Cheng, W.; Yang, Y.; Zhu, M.; Zhou, C. Novel injectable calcium phosphate/chitosan composites for bone substitute materials. *Acta Biomater.* **2006**, *2*, 557–565. [[CrossRef](#)] [[PubMed](#)]
28. Sendemir-Urkmez, A.; Jamison, R.D. The addition of biphasic calcium phosphate to porous chitosan scaffolds enhances bone tissue development in vitro. *J. Biomed. Mater. Res. Part A* **2007**, *81*, 624–633. [[CrossRef](#)] [[PubMed](#)]
29. Tan, H.; Gong, Y.; Lao, L.; Mao, Z.; Gao, C. Gelatin/chitosan/hyaluronan ternary complex scaffold containing basic fibroblast growth factor for cartilage tissue engineering. *J. Mater. Sci. Mater. Med.* **2007**, *18*, 1961–1968. [[CrossRef](#)] [[PubMed](#)]
30. Solchaga, L.A.; Dennis, J.E.; Goldberg, V.M.; Caplan, A.I. Hyaluronic acid-based polymers as cell carriers for tissue-engineered repair of bone and cartilage. *J. Orthop. Res.* **1999**, *17*, 205–213. [[CrossRef](#)] [[PubMed](#)]
31. Chung, C.; Burdick, J.A. Influence of three-dimensional hyaluronic acid microenvironments on mesenchymal stem cell chondrogenesis. *Tissue Eng. Part A* **2009**, *15*, 243–254. [[CrossRef](#)] [[PubMed](#)]
32. Liao, H.T.; Chen, C.T.; Chen, J.P. Osteogenic differentiation and ectopic bone formation of canine bone marrow-derived mesenchymal stem cells in injectable thermo-responsive polymer hydrogel. *Tissue Eng. Part C Methods* **2011**, *17*, 1139–1149. [[CrossRef](#)] [[PubMed](#)]
33. Chen, J.-P.; Tsai, M.-J.; Liao, H.-T. Incorporation of biphasic calcium phosphate microparticles in injectable thermoresponsive hydrogel modulates bone cell proliferation and differentiation. *Colloids Surf. B Biointerfaces* **2013**, *110*, 120–129. [[CrossRef](#)] [[PubMed](#)]
34. Gimble, J.; Guilak, F. Adipose-derived adult stem cells: Isolation, characterization, and differentiation potential. *Cytotherapy* **2003**, *5*, 362–369. [[CrossRef](#)] [[PubMed](#)]
35. Plachokova, A.S.; van den Dolder, J.; Stoelinga, P.J.; Jansen, J.A. Early effect of platelet-rich plasma on bone healing in combination with an osteoconductive material in rat cranial defects. *Clin. Oral Implant. Res.* **2007**, *18*, 244–251. [[CrossRef](#)] [[PubMed](#)]

36. Su, J.; Xu, H.; Sun, J.; Gong, X.; Zhao, H. Dual delivery of bmp-2 and bfgf from a new nano-composite scaffold, loaded with vascular stents for large-size mandibular defect regeneration. *Int. J. Mol. Sci.* **2013**, *14*, 12714. [[CrossRef](#)] [[PubMed](#)]
37. Lacci, K.M.; Dardik, A. Platelet-rich plasma: Support for its use in wound healing. *Yale J. Biol. Med.* **2010**, *83*, 1–9. [[PubMed](#)]
38. Marx, R.E. Platelet-rich plasma: Evidence to support its use. *J. Oral Maxillofac. Surg.* **2004**, *62*, 489–496. [[CrossRef](#)] [[PubMed](#)]
39. Liao, H.-T.; Marra, K.G.; Rubin, J.P. Application of platelet-rich plasma and platelet-rich fibrin in fat grafting: Basic science and literature review. *Tissue Eng. Part B Rev.* **2014**, *20*, 267–276. [[CrossRef](#)] [[PubMed](#)]
40. Feng, L.; Chang, W.; Tian, B.; Zeng, W.; Zhou, D. Bone regeneration combining platelet rich plasma with engineered bone tissue. *J. Biomater. Tissue Eng.* **2017**, *7*, 841–847. [[CrossRef](#)]
41. Liao, H.-T.; Chen, J.-P.; Lee, M.-Y. Bone tissue engineering with adipose-derived stem cells in bioactive composites of laser-sintered porous polycaprolactone scaffolds and platelet-rich plasma. *Materials* **2013**, *6*, 4911–4929. [[CrossRef](#)] [[PubMed](#)]
42. Griffin, X.L.; Smith, C.M.; Costa, M.L. The clinical use of platelet-rich plasma in the promotion of bone healing: A systematic review. *Injury* **2009**, *40*, 158–162. [[CrossRef](#)] [[PubMed](#)]
43. Son, S.R.; Sarkar, S.K.; Nguyen-Thuy, B.L.; Padalhin, A.R.; Kim, B.R.; Jung, H.I.; Lee, B.T. Platelet-rich plasma encapsulation in hyaluronic acid/gelatin-bcp hydrogel for growth factor delivery in bcp sponge scaffold for bone regeneration. *J. Biomater. Appl.* **2015**, *29*, 988–1002. [[CrossRef](#)] [[PubMed](#)]
44. Juan, S.; Yubao, L.; Yi, Z.; Qin, Z.; Lin, C.; Li, Z.; Mei, G.; Shibo, G. Characterization and cytocompatibility of biphasic calcium phosphate/polyamide 6 scaffolds for bone regeneration. *J. Biomed. Mater. Res. B Appl. Biomater.* **2010**, *95B*, 330–338.
45. Liao, H.T.; James, I.B.; Marra, K.G.; Rubin, J.P. The effects of platelet-rich plasma on cell proliferation and adipogenic potential of adipose-derived stem cells. *Tissue Eng. Part A* **2015**, *21*, 2714–2722. [[CrossRef](#)] [[PubMed](#)]
46. Gersch, R.P.; Glahn, J.; Tecce, M.G.; Wilson, A.J.; Percec, I. Platelet rich plasma augments adipose-derived stem cell growth and differentiation. *Aesthet. Surg. J.* **2017**, *37*, 723–729. [[CrossRef](#)] [[PubMed](#)]
47. Lai, F.; Kakudo, N.; Morimoto, N.; Taketani, S.; Hara, T.; Ogawa, T.; Kusumoto, K. Platelet-rich plasma enhances the proliferation of human adipose stem cells through multiple signaling pathways. *Stem Cell Res. Ther.* **2018**, *9*, 107. [[CrossRef](#)] [[PubMed](#)]
48. Paduano, F.; Marrelli, M.; Amantea, M.; Rengo, C.; Rengo, S.; Goldberg, M.; Spagnuolo, G.; Tatullo, M. Adipose tissue as a strategic source of mesenchymal stem cells in bone regeneration: A topical review on the most promising craniomaxillofacial applications. *Int. J. Mol. Sci.* **2017**, *18*, 2140. [[CrossRef](#)] [[PubMed](#)]
49. Ravichandran, R.; Venugopal, J.R.; Sundarrajan, S.; Mukherjee, S.; Ramakrishna, S. Precipitation of nanohydroxyapatite on plla/pblg/collagen nanofibrous structures for the differentiation of adipose derived stem cells to osteogenic lineage. *Biomaterials* **2012**, *33*, 846–855. [[CrossRef](#)] [[PubMed](#)]
50. Anderson, H.C.; Sipe, J.B.; Hessle, L.; Dhanyamraju, R.; Atti, E.; Camacho, N.P.; Millan, J.L.; Dhanyamraju, R. Impaired calcification around matrix vesicles of growth plate and bone in alkaline phosphatase-deficient mice. *Am. J. Pathol.* **2004**, *164*, 841–847. [[CrossRef](#)]
51. Park, K.W.; Yun, Y.P.; Kim, S.E.; Song, H.R. The effect of alendronate loaded biphasic calcium phosphate scaffolds on bone regeneration in a rat tibial defect model. *Int. J. Mol. Sci.* **2015**, *16*, 26738–26753. [[CrossRef](#)] [[PubMed](#)]
52. Liao, H.-T.; Shalumon, K.T.; Chang, K.-H.; Sheu, C.; Chen, J.-P. Investigation of synergistic effects of inductive and conductive factors in gelatin-based cryogels for bone tissue engineering. *J. Mater. Chem. B* **2016**, *4*, 1827–1841. [[CrossRef](#)]
53. Shalumon, K.; Kuo, C.-Y.; Wong, C.-B.; Chien, Y.-M.; Chen, H.-A.; Chen, J.-P. Gelatin/nanohydroxyapatite cryogel embedded poly(lactic-co-glycolic acid)/nanohydroxyapatite microsphere hybrid scaffolds for simultaneous bone regeneration and load-bearing. *Polymers* **2018**, *10*, 620. [[CrossRef](#)]
54. Ngiam, M.; Liao, S.; Patil, A.J.; Cheng, Z.; Chan, C.K.; Ramakrishna, S. The fabrication of nano-hydroxyapatite on PLGA and PLGA/collagen nanofibrous composite scaffolds and their effects in osteoblastic behavior for bone tissue engineering. *Bone* **2009**, *45*, 4–16. [[CrossRef](#)] [[PubMed](#)]
55. McBeath, R.; Pirone, D.M.; Nelson, C.M.; Bhadriraju, K.; Chen, C.S. Cell shape, cytoskeletal tension, and rhoa regulate stem cell lineage commitment. *Dev. Cell* **2004**, *6*, 483–495. [[CrossRef](#)]

56. Zur Nieden, N.I.; Kempka, G.; Ahr, H.J. In vitro differentiation of embryonic stem cells into mineralized osteoblasts. *Differentiation* **2003**, *71*, 18–27. [[CrossRef](#)] [[PubMed](#)]
57. Heinemann, S.; Heinemann, C.; Bernhardt, R.; Reinstorf, A.; Nies, B.; Meyer, M.; Worch, H.; Hanke, T. Bioactive silica-collagen composite xerogels modified by calcium phosphate phases with adjustable mechanical properties for bone replacement. *Acta Biomater.* **2009**, *5*, 1979–1990. [[CrossRef](#)] [[PubMed](#)]
58. Fernandez, J.M.; Molinuevo, M.S.; Cortizo, M.S.; Cortizo, A.M. Development of an osteoconductive pcl-pdipf-hydroxyapatite composite scaffold for bone tissue engineering. *J. Tissue Eng. Regen. Med.* **2011**, *5*, e126–e135. [[CrossRef](#)] [[PubMed](#)]
59. Robert, A.W.; Angulski, A.B.B.; Spangenberg, L.; Shigunov, P.; Pereira, I.T.; Bettes, P.S.L.; Naya, H.; Correa, A.; Dallagiovanna, B.; Stimamiglio, M.A. Gene expression analysis of human adipose tissue-derived stem cells during the initial steps of in vitro osteogenesis. *Sci. Rep.* **2018**, *8*, 4739. [[CrossRef](#)] [[PubMed](#)]
60. Liu, H.; Wei, L.K.; Jian, X.F.; Huang, J.; Zou, H.; Zhang, S.Z.; Yuan, G.H. Isolation, culture and induced differentiation of rabbit mesenchymal stem cells into osteoblasts. *Exp. Ther. Med.* **2018**, *15*, 3715–3724. [[CrossRef](#)] [[PubMed](#)]
61. Yu, X.; Botchwey, E.A.; Levine, E.M.; Pollack, S.R.; Laurencin, C.T. Bioreactor-based bone tissue engineering: The influence of dynamic flow on osteoblast phenotypic expression and matrix mineralization. *Proc. Natl. Acad. Sci. USA* **2004**, *101*, 11203–11208. [[CrossRef](#)] [[PubMed](#)]
62. Lai, G.J.; Shalumon, K.T.; Chen, J.P. Response of human mesenchymal stem cells to intrafibrillar nanohydroxyapatite content and extrafibrillar nanohydroxyapatite in biomimetic chitosan/silk fibroin/nanohydroxyapatite nanofibrous membrane scaffolds. *Int. J. Nanomed.* **2015**, *10*, 567–584.



© 2018 by the authors. Licensee MDPI, Basel, Switzerland. This article is an open access article distributed under the terms and conditions of the Creative Commons Attribution (CC BY) license (<http://creativecommons.org/licenses/by/4.0/>).



# Spilanthol inhibits TNF- $\alpha$ -induced ICAM-1 expression and pro-inflammatory responses by inducing heme oxygenase-1 expression and suppressing pJNK in HaCaT keratinocytes

CHUN-HSUN HUANG<sup>1,2\*</sup>, LI-CHUN CHANG<sup>3\*</sup>, SINDY HU<sup>1,2,4</sup>, CHIEN-YU HSIAO<sup>2,3</sup> and SHU-JU WU<sup>2,3</sup>

<sup>1</sup>Department of Cosmetic Science, Research Center for Food and Cosmetic Safety, and Research Center for Chinese Herbal Medicine, College of Human Ecology, Chang Gung University of Science and Technology;

<sup>2</sup>Department of Dermatology, Aesthetic Medical Center, Chang Gung Memorial Hospital; <sup>3</sup>Department of Nutrition and Health Sciences, Research Center for Food and Cosmetic Safety, and Research Center for Chinese Herbal Medicine, College of Human Ecology, Chang Gung University of Science and Technology; <sup>4</sup>College of Medicine, Chang Gung University, Taoyuan 33303, Taiwan R.O.C.

Received January 20, 2018; Accepted May 31, 2018

DOI: 10.3892/mmr.2018.9245

**Abstract.** Spilanthol has been reported to possess antioxidant, anti-inflammatory, antimicrobial and antinociceptive properties. At present, the literature has reported the beneficial role of spilanthol on tumor necrosis factor- $\alpha$  (TNF- $\alpha$ )-stimulated HaCaT cells. The present study investigated the effects of spilanthol on the expression of TNF- $\alpha$ -induced intercellular adhesion molecule 1 (ICAM-1) and cyclooxygenase (COX)-2 in the human keratinocyte cell line HaCaT. Cells were pretreated with various concentrations of spilanthol (10-150  $\mu$ M) followed by TNF- $\alpha$  to induce inflammation. Pretreatment with spilanthol decreased TNF- $\alpha$ -induced COX-2 expression by western blotting and suppressed the expression of pro-inflammatory mediators, including interleukin (IL)-6, IL-8 and monocyte chemoattractant protein 1 using ELISA. Spilanthol also decreased the expression of TNF- $\alpha$ -induced ICAM-1 protein and mRNA assay by western blotting and RT-qPCR, respectively, in addition to the monocyte adhesiveness of HaCaT cells. Furthermore, spilanthol significantly suppressed the phosphorylation of c-Jun N-terminal kinase (JNK), while pretreatment with spilanthol enhanced heme oxygenase (HO)-1 protein expression by western blotting. These results demonstrated that spilanthol may exert its

anti-inflammatory activity by suppressing the TNF- $\alpha$ -induced expression of ICAM-1, COX-2 and pro-inflammatory mediators by enhancing that of HO-1, and inhibiting the activation of the phosphorylated JNK signaling pathway. It is hypothesized that spilanthol may be a natural anti-inflammatory drug to attenuate skin inflammatory disease.

## Introduction

Epidermal defense against the intrusion of harmful substances from the environment, including chemicals and radiation, acts as an important barrier to prevent skin injury (1,2). Keratinocytes are the principal cells of the epidermis. In addition to their barrier-serving role, these cells are involved in immune responses within the skin; however, unperturbed keratinocytes exhibit deficient or absent production of inflammatory mediators (2). Under environmental or chemical stimuli (for example, UV irradiation or ambient air pollution), activated keratinocytes express numerous inflammation-associated cytokines including TNF- $\alpha$ , interleukin (IL)-1 $\beta$ , IL-8, and inducible nitric oxide synthase (iNOS), which may result in the abnormal expression and dysregulated action of inflammatory mediators (3,4). Activated keratinocytes may induce strong infiltration of inflammatory cells in the epidermis, which is associated with the underlying pathogenesis of inflammatory skin diseases, including psoriasis, atopic dermatitis (AD) and allergic contact dermatitis (5).

Increased expression of intercellular adhesion molecule-1 (ICAM-1) may induce leukocyte and keratinocyte interaction and is considered an important initiator in numerous types of inflammatory skin diseases (6). It has been reported that tumor necrosis factor- $\alpha$  (TNF- $\alpha$ )-induced ICAM-1 expression is a principal mediator of increased lymphocyte infiltration into inflamed areas in the skin. In addition, keratinocytes are activated by TNF- $\alpha$ , eliciting an inflammatory response with the release of proinflammatory cytokines and chemokines, including interleukin (IL)-1 $\beta$ , IL-6, IL-8 and monocyte chemoattractant protein-1 (MCP-1), in addition to

---

*Correspondence to:* Dr Shu-Ju Wu, Department of Nutrition and Health Sciences, Research Center for Food and Cosmetic Safety, and Research Center for Chinese Herbal Medicine, College of Human Ecology, Chang Gung University of Science and Technology, 261 Wenhua 1st Road, Taoyuan 33303, Taiwan R.O.C.  
E-mail: sjwu@mail.cgu.edu.tw

\*Contributed equally

**Key words:** spilanthol, intercellular adhesion molecule 1, heme oxygenase-1, keratinocyte, phosphorylated-Jun N-terminal kinase, tumor necrosis factor- $\alpha$

ICAM-1 (7-9). Additionally, TNF- $\alpha$ -induced expression of inflammatory mediators within keratinocytes simultaneously activates inflammatory signaling pathways, nuclear factor- $\kappa$ B (NF- $\kappa$ B) and mitogen-activated protein kinases (MAPKs), resulting in aggravated inflammation (10).

Phosphorylation of inhibitor of NF- $\kappa$ B due to inflammatory stimuli induces the translocation of the transcription factor NF- $\kappa$ B to the nucleus and activates the transcription of proinflammatory genes (11,12). Extracellular signal-regulated kinase (ERK), c-Jun-N-terminal kinase (JNK), and p38 MAPK are members of the MAPK family (12). Activation of MAPKs has also been associated with the production of inflammatory mediators and the regulation of numerous inflammation-associated genes (9,12). The role of inflammation is to protect against harmful stimuli; however, long-term and excessive inflammation may cause severe tissue damage, which may lead to the development of inflammation-associated diseases, including diabetes, cancer and AD (13). Therefore, inhibiting the activation of the NF- $\kappa$ B and MAPK signaling pathways may be important for controlling and ameliorating the development of various skin diseases. On the contrary, heme oxygenase-1 (HO-1) has been reported to possess anti-inflammatory activity and is regulated by cytokine and chemokine interactions in AD; HO-1 has been suggested to alleviate inflammation (14,15).

To develop therapeutic drugs for the treatment of dermatitis, an initial step may include the identification of effective anti-inflammatory agents to abrogate and suppress inflammatory mediators in keratinocytes. Spilanthol [(2E, 6Z, 8E)-N-isobutylamide-2,6,8-decatrienamide] is a bioactive compound detected in *Acmella oleracea* (*Spilanthus acmella*) and other *Acmella* species, including *A. brachyglossa* and *A. ciliata* (16). *A. acmella* exerts a variety of biological properties, including antipyretic (17,18), anti-inflammatory (19-21), analgesic (22-24) and antimicrobial activities (22-26). Spilanthol inhibits lipopolysaccharide-induced inflammatory responses in murine RAW 264.7 macrophages via inactivation of the NF- $\kappa$ B signaling pathway (19). Leaf extracts of *S. acmella* have exhibited immunomodulatory activity, which may be beneficial for the treatment of rheumatism (27); spilanthol enhances immune activities in influenza and respiratory infections (28). In addition, spilanthol is absorbed by human skin (29); however, whether the compound is able to modulate inflammatory responses is unclear, and the associated mechanism underlying the effects of spilanthol within keratinocytes requires further investigation.

The present study investigated the biological activities and modulatory effects of spilanthol on TNF- $\alpha$ -induced HaCaT cells. Spilanthol was observed to inhibit TNF- $\alpha$ -induced ICAM-1 expression, which may be associated with protection against injuries induced by cytokines, including IL-6, IL-8, MCP-1 and ICAM-1 in the present study. In addition, the anti-inflammatory effects of spilanthol may be mediated by enhancing HO-1 expression and inhibiting the pJNK signaling pathway in HaCaT cells.

## Materials and methods

**Materials and antibodies.** Spilanthol (ChromaDex, Inc., Irvine, CA, USA; Fig. 1A) was prepared as a 100 mM stock solution in

dimethyl sulfoxide (DMSO) with a final DMSO concentration of  $\leq 0.1\%$  in the culture medium. ELISA kits were purchased from R&D Systems, Inc. (Minneapolis, MN, USA). Primary antibodies against  $\beta$ -actin, cyclooxygenase-2 (COX-2), HO-1 and ICAM-1 were obtained from Santa Cruz Biotechnology, Inc. (Dallas, TX, USA), and JNK, ERK, p38, phosphorylated (p)-JNK, p-ERK, and p-p38 antibodies were purchased from EMD Millipore (Billerica, MA, USA). Calcein-AM was purchased from Sigma-Aldrich (Merck KGaA, Darmstadt, Germany). RNA was isolated using TRIzol reagent obtained from Thermo Fisher Scientific, Inc. (Waltham, MA, USA).

**Cell line and treatment.** HaCaT cells (human keratinocyte cell line) were purchased from the Bioresource Collection and Research Center (Hsinchu, Taiwan). Cells were cultured in Dulbecco's modified Eagle's medium (DMEM; Thermo Fisher Scientific, Inc.) supplemented with 10% fetal bovine serum (Biological Industries, Ltd., Beit-Haemek, Israel), antibiotics (1% penicillin and streptomycin) and 2 mM glutamine; cells were incubated in a humidified incubator containing 5% CO<sub>2</sub> at 37°C. THP-1 cells (a human monocytic cell line) were purchased from the Bioresource Collection and Research Center and incubated in RPMI-1640 medium (Gibco; Thermo Fisher Scientific, Inc.) with 10% fetal bovine serum and 2 mM L-glutamine added.

**Cell viability assay.** An MTT assay (Sigma-Aldrich; Merck KGaA) was performed to assess cell viability. HaCaT cells ( $10^6$  cells/well) were seeded onto 96-well plates and incubated with spilanthol at concentrations between 3 and 200  $\mu$ M for 1 h and then TNF- $\alpha$  (10 ng/ml) was added and the cells co-cultured for 24 h in a humidified incubator containing 5% CO<sub>2</sub> at 37°C. MTT solution (5 mg/ml) was added to each well for 2 h at 37°C. Following removal of the MTT solution, DMSO (0.5 ml) was added to dissolve the blue formazan crystals. Using a microplate reader (Gene5, Synergy HT; BioTek Instruments, Inc., Winooski, VT, USA), the absorbance was measured at 570 nm. A subsequent analysis was conducted with 0-150  $\mu$ M spilanthol. Cells without TNF- $\alpha$  and spilanthol treatment served as negative control and cells treated with TNF- $\alpha$  as a positive control.

**ELISA for the analysis of proinflammatory cytokines, chemokines and ICAM-1 production.** HaCaT cells ( $10^6$  cells/ml) were pretreated with spilanthol (10-150  $\mu$ M) for 1 h in a humidified incubator containing 5% CO<sub>2</sub> at 37°C, and TNF- $\alpha$  (10 ng/ml) was added, followed by incubation in a humidified incubator containing 5% CO<sub>2</sub> at 37°C for 24 h. Supernatants were centrifuged (19,000  $\times$  g at 4°C for 5 min) and collected for assaying the expression levels of IL-8, IL-6, MCP-1 and ICAM-1. The present study employed specific ELISA kits (cat. nos. DY208, DY206, DY279 and DY720, respectively; R&D Systems, Inc.) and the optical density was spectrophotometrically measured at 450 nm with a microplate reader (Multiskan FC; Thermo Fisher Scientific, Inc.).

**Preparation of total proteins.** HaCaT cells ( $10^6$  cells/ml) were seeded onto 6-well plates and pretreated with spilanthol (10, 30, 100 and 150  $\mu$ M) for 1 h in a humidified incubator containing 5% CO<sub>2</sub> at 37°C, and then stimulated with TNF- $\alpha$  (10 ng/ml)

for 24 h in a humidified incubator containing 5% CO<sub>2</sub> at 37°C to evaluate total proteins or for 30 min to detect phosphorylated proteins. Cell lysates were collected after centrifuged at 19,000 x g for 15 min duration 4°C, and the proteins were extracted in 300 µl protein lysis buffer [50 mM Tris-HCl (pH 8), 1 mM EDTA, 0.5% NP40, 150 mM NaCl and 0.1% SDS] containing a protease inhibitor cocktail and phosphatase inhibitors (Sigma-Aldrich; Merck KGaA). Proteins were extracted and a bicinchoninic acid protein assay kit (Pierce; Thermo Fisher Scientific, Inc.) was used for quantification.

**Western blot analysis.** Equal amounts of protein (20–30 µg) were obtained from HaCaT cells as mentioned above and underwent separation via 10% SDS-PAGE. The proteins were transferred to polyvinylidene fluoride membranes (EMD Millipore). Subsequently, the membranes were blocked with 5% BSA and incubated overnight with primary antibodies at 4°C, including COX-2 (1:500; cat. no. sc-1746; Santa Cruz Biotechnology, Inc.); HO-1 (1:500; cat. no. sc-10789; Santa Cruz Biotechnology, Inc.); ERK1/2 (1:2,000; cat. no. ABS44; Millipore), p38 (1:500; cat. no. ABS29; EMD Millipore), JNK1/2 (1:1,000; cat. no. 06-748 EMD Millipore), phosphorylated-ERK 1/2 (1:1,000; cat. no. P27361; EMD Millipore), phosphorylated-p38 (1:1,000; cat. no. 09-272; EMD Millipore), and phosphorylated-JNK1 (1:500; cat. no. 07-175; EMD Millipore); ICAM-1 (1:1,000; cat. no. GTX100450; Sigma-Aldrich; Merck KGaA) and β-actin (1:500; cat. no. MAB1501; Sigma-Aldrich; Merck KGaA).

The membrane was washed with TBS with Tween-20 [TBST; 150 mM NaCl, 10 mM Tris (pH 8.0) and 0.1% Tween-20], and incubated with horseradish peroxidase-conjugated secondary antibodies for 1 h at room temperature. The bound antibodies, including goat anti-rabbit IgG-HRP (1:10,000; cat. no. A2315; Santa Cruz Biotechnology, Inc.) and goat anti-mouse IgG (1:10,000; cat. no. A90-116P; Bethyl Laboratories, Inc., Montgomery, TX, USA) on the membranes were washed with TBST and incubated in Luminol/Enhancer Solution (EMD Millipore) according to the manufacturer's protocols for detection of the bands; quantification of protein expression was conducted using the BioSpectrum 600 automated system (UVP, LLC, Phoenix, AZ, USA) and its included software.

**RNA isolation and reverse transcription-quantitative polymerase chain reaction (RT-qPCR) analysis of gene expression.** ICAM-1 mRNA expression levels were determined by RT-qPCR, with β-actin as the internal control. TRIzol solution (Thermo Fisher Scientific, Inc.) was used to extract total RNA, and reverse transcribed to acquire cDNA using a cDNA synthesis kit (Thermo Fisher Scientific, Inc.). qPCR using SYBR Green Master Mix (Bio-Rad Laboratories, Inc., Hercules, CA, USA) was performed using a spectrofluorometric thermal cycler (iCycler; Bio-Rad Laboratories, Inc.) to quantitative the expression of specific genes. The cycling conditions were as follows: Samples preincubated at 95°C for 10 min. Next, the PCR was performed as 40 cycles of 95°C for 15 sec and 60°C for 1 min, followed by analysis using TaqMan real-time quantitative PCR (Applied Biosystems; Thermo Fisher Scientific, Inc.). The specific primers used were as follows: ICAM-1, forward 5'-AGACGCAGAGGACCTTAA-3' and reverse 5'-CACACTTCACAGTTACTTGG-3'; β-actin,

forward 5'-AAGACCTCTATGCCAACACAGT-3' and reverse 5'-AGCCAGAGCAGTAATCTCCTTC-3' (30). The specific genes were determined by comparing the average of gene cycle quantification (Cq), measured for each experiment and repeated three times, as described previously (31). The comparison Cq method was used for the specific genes determined by relative cDNA expressions ( $2^{-\Delta\Delta Cq}$ ).  $2^{-\Delta\Delta Cq}$  was the discrepancy between specific gene and housekeeping genes β-actin for each sample.

**Cell-cell adhesion assay.** To perform the cell-cell adhesion assay, HaCaT cells (10<sup>6</sup> cells/ml) were pretreated with spilanthol (10, 30, 100 and 150 µM) for 1 h in a humidified incubator containing 5% CO<sub>2</sub> at 37°C and subsequently incubated with TNF-α (10 ng/ml) for 24 h in a humidified incubator containing 5% CO<sub>2</sub> at 37°C. The control groups was treated with TNF-α alone. THP-1 cells (10<sup>6</sup> cells/ml) labeled with calcein-AM were co-cultured with HaCaT cells for 1 h in DMEM medium in a humidified incubator containing 5% CO<sub>2</sub> at 37°C. Cells were washed with PBS and the extent of adhesion of THP-1 cells to HaCaT cells was observed under a fluorescence microscope (3 per view; magnification, x200; Olympus Corporation, Tokyo, Japan) with excitation and emission wavelengths of 490 and 515 nm, respectively. All experiments were repeated three times.

**Statistical analysis.** Data are presented as the mean ± standard deviation of at least three independent experiments. Data were analyzed with one-way analysis of variance and Dunnett's post hoc test using SPSS statistical software package version 19.0 (IBM Corp., Armonk, NY, USA). P<0.05 was considered to indicate a statistically significant difference.

## Results

**Inhibition of proinflammatory cytokine and chemokine production by pretreatment with spilanthol in TNF-α-treated HaCaT cells.** An MTT assay was used to evaluate the cytotoxicity of HaCaT cells against spilanthol. The present study reported that spilanthol did not significantly affect cell viability at concentrations ≤200 µM (Fig. 1B). Therefore, the present study conducted a subsequent analysis with 0–150 µM spilanthol. Spilanthol at 3 µM did not significantly affect cell viability and it had no effects in pretesting and was thus excluded from subsequent experimentation. Furthermore, the inhibitory effects of spilanthol on TNF-α-induced proinflammatory cytokine and chemokine production were investigated. HaCaT cells were pretreated with various concentrations of spilanthol and stimulated with TNF-α for 24 h. Pretreatment with spilanthol was associated with significantly decreased expression levels of IL-6, IL-8 and MCP-1 in TNF-α-stimulated HaCaT cells compared with TNF-α alone (Fig. 1C–E). Spilanthol concentrations ≥10 µM significantly inhibited IL-6 and MCP-1 expression levels; however, concentrations ≥30 µM significantly inhibited IL-8 production. The results of the present study suggested that spilanthol can inhibit proinflammatory cytokine (IL-6) and chemokines (IL-8 and MCP-1) expression levels, thus preventing inflammation.

**Effects of spilanthol on TNF-α-induced ICAM-1 protein and mRNA expression.** In the present study, the effects of spilanthol



on ICAM-1 expression in TNF- $\alpha$ -induced HaCaT cells were investigated. Spilanthol significantly reduced ICAM-1 protein expression levels compared with treatment with TNF- $\alpha$  alone, as determined by ELISA and western blotting (Fig. 2A and B). In addition, the mRNA expression levels of ICAM-1 were significantly decreased (Fig. 2C) compared with treatment with TNF- $\alpha$  alone, as determined by RT-qPCR. Collectively, these results suggested that spilanthol significantly suppressed ICAM-1 in TNF- $\alpha$ -induced HaCaT cells.

*Spilanthol inhibits monocyte adhesion to TNF- $\alpha$ -activated HaCaT cells.* A recent study reported that increased monocyte adhesion to human keratinocytes may be associated with increased ICAM-1 expression (31). In the present study, it was demonstrated that spilanthol significantly decreased ICAM-1 expression levels in inflammatory HaCaT cells (Fig. 2). Thus, the present study investigated whether spilanthol may suppress TNF- $\alpha$ -induced monocyte adhesion. The results revealed that THP-1 cells adhered to TNF- $\alpha$ -stimulated HaCaT cells; however, the extent of monocyte adhesion significantly decreased in a dose-dependent manner in response to treatment with spilanthol, compared with in HaCaT cells treated with TNF- $\alpha$  alone (Fig. 3). Fluorescence density is highest in Fig. 3A-b indicating that TNF- $\alpha$  induced THP-1 adhesion to HaCaT cells compared with negative control (Fig. 3A-a). SP-treatment decreased THP-1 adhesion to HaCaT cells compared with positive control (Fig. 3A-b).

*Spilanthol induces HO-1 expression and inactivates the pJNK signaling pathway to inhibit COX-2 protein expression in TNF- $\alpha$ -induced HaCaT cells.* To improve understanding as to how spilanthol reduces inflammations, the expression levels of inflammation-associated proteins were analyzed. A recent study suggested that the induction of HO-1 inhibits inflammation in HaCaT cells (32). It was observed that spilanthol concentrations  $\geq 100 \mu\text{M}$  significantly increased the expression levels of HO-1 expression in HaCaT cells compared with TNF- $\alpha$  alone ( $P < 0.01$ ; Fig. 4A). A previous study reported that COX-2 expression is associated with inflammation in human keratinocytes (33). Thus, the present study investigated the effects of spilanthol on TNF- $\alpha$ -activated HaCaT cells, and it was indicated that pretreatment with  $\geq 30 \mu\text{M}$  spilanthol significantly suppressed COX-2 protein expression compared with TNF- $\alpha$ -stimulated control cells (Fig. 4B). The activation of the MAPK signaling pathway is closely associated with the expression of proinflammatory mediators in keratinocytes (34); whether spilanthol affects the MAPK signaling pathway in TNF- $\alpha$ -activated HaCaT cells was analyzed in the present study. Treatment with  $\geq 30 \mu\text{M}$  spilanthol significantly decreased the phosphorylation of JNK compared with in TNF- $\alpha$ -activated HaCaT control cells (Fig. 4C). These results suggested that spilanthol may induce the expression of HO-1 expression via inactivation of pJNK to potentially inhibit the expression of COX-2 in TNF- $\alpha$ -activated HaCaT cells; however, spilanthol did not suppress the phosphorylation of ERK and P38 MAPK (data not shown).

## Discussion

Epidermal keratinocytes are subjected to exposure to harmful factors, including ultraviolet light, which may

induce keratinocyte activation and the release of inflammatory mediators (1). ICAM-1 is expressed on activated keratinocytes to attract more inflammatory cells to infiltrate the inflamed skin (2-4). Numerous reports have described the importance of ICAM-1 expression in keratinocytes in skin inflammation-associated diseases (4,5), which has led to a focus on the regulation of this particular adhesion molecule in drug development for the treatment of dermatitis. The present study reported that pretreatment with spilanthol significantly suppressed ICAM-1 protein and mRNA expression, as detected by ELISA and western blotting, and RT-PCR analyses, respectively. In addition, treatment with spilanthol reduced the extent of adhesion between HaCaT and THP-1 cells; this may have been mediated by reductions in the secretion and expression of ICAM-1 by HaCaT cells. Inflammatory keratinocytes could have released proteins into culture medium and excess ICAM-1 cleaved to soluble ICAM, and moved into the supernatant. Thus, ELISA could detect specific protein (soluble ICAM) in the supernatant. Soluble ICAM-1 is a molecule meriting exploration in the future. Additionally, the present study reported that spilanthol affected the extent of monocyte adhesion to keratinocytes, suggesting that spilanthol may attenuate the inflammatory response via the inhibition of ICAM-1 expression in TNF- $\alpha$ -induced keratinocytes.

Spilanthol possesses antioxidant and antinociceptive properties and is of particular importance as a potential anti-inflammatory agent (16), which is mediated via the inactivation of NF- $\kappa\text{B}$ ; spilanthol negatively regulates the production of proinflammatory mediators, including IL-1 $\beta$ , IL-6, TNF- $\alpha$  and COX-2 (19). Flavonoid extracts from *S. acmella* inhibit the secretion of IL-1 $\beta$  and TNF- $\alpha$ , reducing infection-associated inflammation, and suppress COX-2 expression, reducing fever (16,19). These findings suggest that *S. acmella* extracts have analgesic and antipyretic effects (17,18). In addition, spilanthol exerts anti-inflammatory effects in *in vitro* and *in vivo* models (16-19); however, the associated anti-inflammatory mechanisms in keratinocytes require further investigation. In the present study, spilanthol was observed to significantly suppress the expression of pro-inflammatory cytokines, including IL-6, IL-8 and MCP-1 production. Additionally, spilanthol effectively suppressed COX-2 protein expression in keratinocytes, indicating that spilanthol may inhibit inflammatory responses and prevent the inflammatory loop within TNF- $\alpha$ -induced keratinocytes.

Of note, HO-1 expression has been reported to exert an anti-inflammatory response in keratinocytes, and attenuates AD-like lesions via its protective effects against inflammatory skin diseases (7,9,15). HO-1 expression is regulated by inflammation-associated cytokines and chemokines associated with the development of AD (15). The present study observed that spilanthol induced HO-1 protein expression, and decreased cytokine and chemokine expression levels, indicating that HO-1 expression may be associated with the underlying anti-inflammatory mechanism of spilanthol within keratinocytes.

Furthermore, previous studies demonstrated that flavonoid and immunosuppressive drugs (rapamycin and mycophenolic acid) modulated the expression of ICAM-1, which is regulated by NF- $\kappa\text{B}$  activation within TNF- $\alpha$ -induced HaCaT cells (7,9,10). The modulatory activity of spilanthol on the signaling of NF- $\kappa\text{B}$



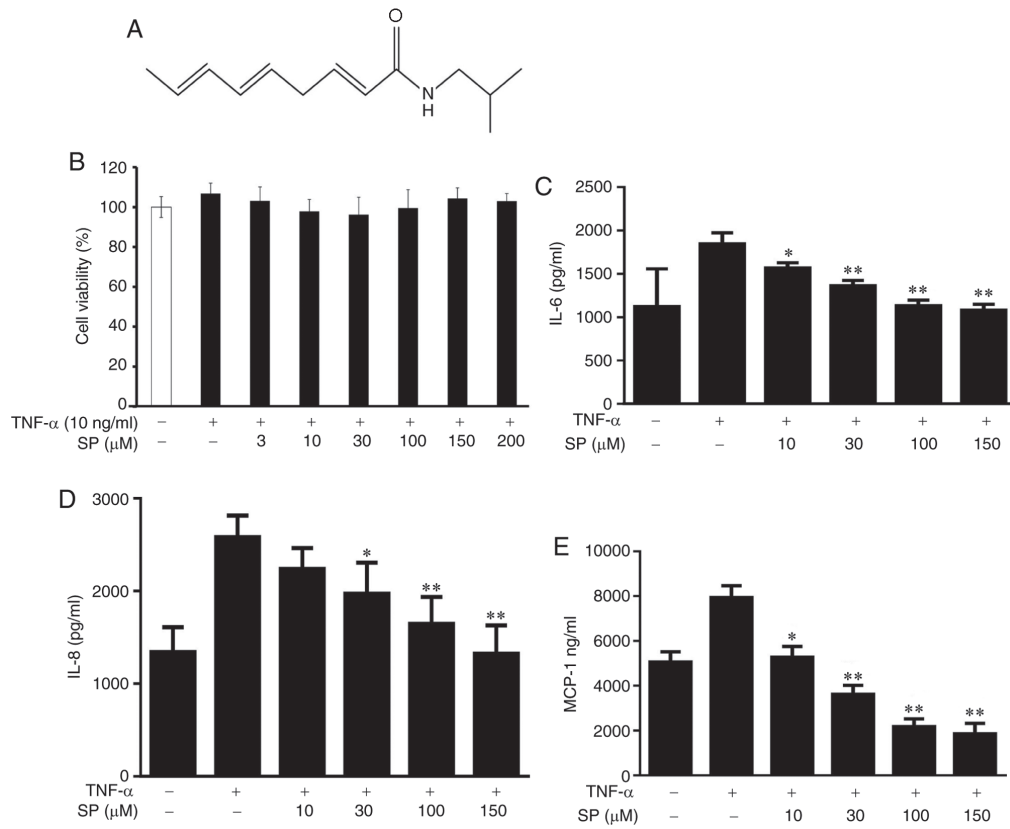


Figure 1. SP inhibition of proinflammatory cytokine and chemokine production in TNF- $\alpha$ -stimulated HaCaT cells. (A) Structure of SP. (B) Cytotoxicity of SP-treated HaCaT cells. SP inhibited TNF- $\alpha$ -induced cytokine and chemokine expression: (C) IL-6, (D) IL-8 and (E) MCP-1. HaCaT cells ( $10^6$  cells/well) were pretreated with the indicated concentrations of SP (3-150  $\mu$ M) for 1 h and subsequently stimulated with TNF- $\alpha$  (10 ng/ml) for 24 h. Data are presented as the mean  $\pm$  standard deviation. \* $P < 0.05$ , \*\* $P < 0.01$  vs. TNF- $\alpha$ -treated group. IL, interleukin; MCP-1, monocyte chemoattractant protein-1; SP, spilanthol; TNF- $\alpha$ , tumor necrosis factor- $\alpha$ .

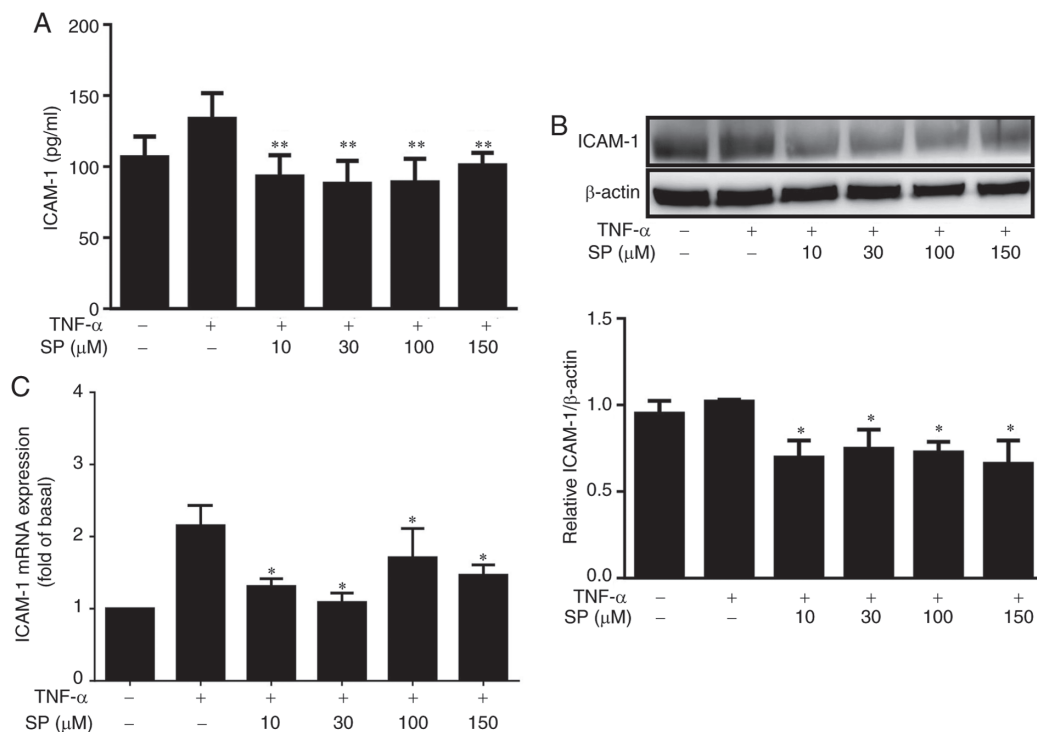


Figure 2. SP effects on ICAM-1 production and expression in TNF- $\alpha$ -induced HaCaT cells. (A) SP inhibited ICAM-1 expression levels as determined by (A) ELISA and (B) western blotting. HaCaT cells ( $10^6$  cells/ml) were pretreated with 10-150  $\mu$ M SP for 1 h and subsequently stimulated with TNF- $\alpha$  (10 ng/ml) for 24 h. (C) SP suppressed ICAM-1 gene expression. HaCaT cells ( $10^6$  cells/ml) were pretreated with the indicated doses of SP for 1 h and subsequently exposed to TNF- $\alpha$  (10 ng/ml) for 1 h. Data are presented as the mean  $\pm$  standard deviation. \* $P < 0.05$ , \*\* $P < 0.01$  vs. TNF- $\alpha$ -treated group. ICAM-1, intercellular adhesion molecule 1; SP, spilanthol; TNF- $\alpha$ , tumor necrosis factor- $\alpha$ .

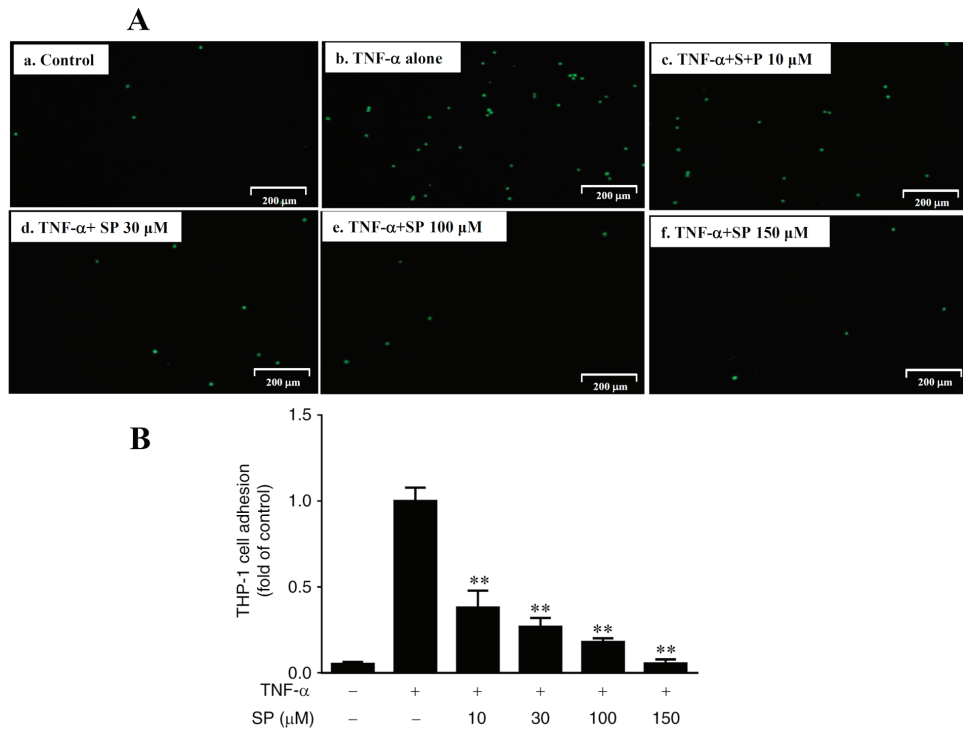


Figure 3. SP suppresses the monocyte adhesive ability of TNF- $\alpha$ -activated HaCaT cells. Effects of SP on monocyte adhesiveness in TNF- $\alpha$ -induced HaCaT cells were investigated; THP-1 cells were incubated with: (A-a) Untreated HaCaT cells; (A-b) TNF- $\alpha$ -treated HaCaT cells; (A-c) HaCaT cells treated with 10  $\mu$ M SP; (A-d) HaCaT cells treated with 30  $\mu$ M SP; (A-e) HaCaT cells treated with 100  $\mu$ M SP; and (A-f) HaCaT cells treated with 150  $\mu$ M SP, respectively. Scale bar=200  $\mu$ m. (B) A fluorescence plate reader was used to quantify calcein-AM fluorescence. Data are presented as the mean  $\pm$  standard deviation. \*\*P<0.01 vs. TNF- $\alpha$ -treated group. SP, spilanthol; TNF- $\alpha$ , tumor necrosis factor- $\alpha$ .

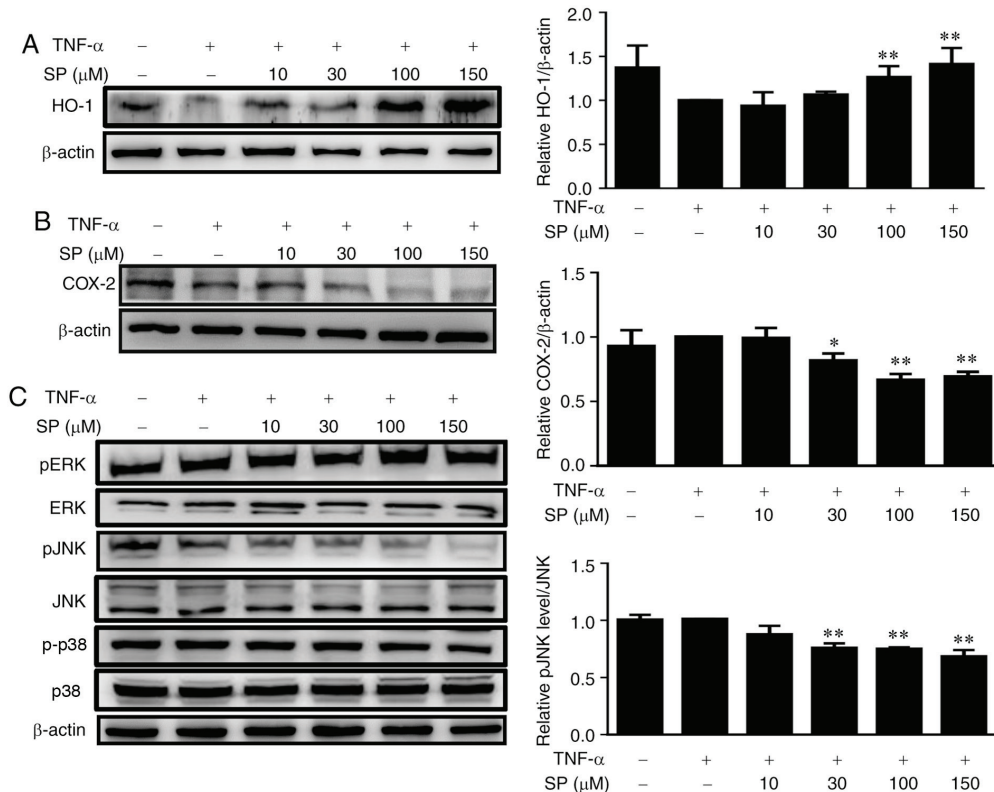


Figure 4. SP induces HO-1 expression and inactivates the pJNK signaling pathway to inhibit COX-2 protein expression in TNF- $\alpha$ -induced HaCaT cells. (A) SP induced HO-1 expression. (B) SP inhibited COX-2 protein expression. (C) SP inactivated the pJNK signaling pathway. HaCaT cells ( $10^6$  cells/ml) were incubated in the absence or presence of 10-150  $\mu$ M SP for 1 h and subsequently exposed to TNF- $\alpha$  (10 ng/ml) for 24 h (total proteins) or 30 min (phosphorylated proteins), followed by western blot analysis. Data are presented as the mean  $\pm$  standard deviation. \*P<0.05, \*\*P<0.01 vs. TNF- $\alpha$ -treated group. COX-2, cyclooxygenase-2; ERK, extracellular signal-regulated kinase; HO-1, heme oxygenase-1; JNK, c-Jun N-terminal kinase; p, phosphorylated; SP, spilanthol; TNF- $\alpha$ , tumor necrosis factor- $\alpha$ .

activation was evaluated in TNF- $\alpha$ -induced HaCaT cells, and no effect on the NF- $\kappa$ B signaling pathway detected (data not show). Collectively, these results indicated that spilanthol may inhibit the upregulation of proinflammatory cytokines induced by TNF- $\alpha$ , and suppress ICAM-1 expression via spilanthol-induced HO-1 expression in keratinocytes.

The p38/MAPK, ERK and JNK signaling pathways are important in the mediation of cellular inflammation, and these MAPK signal transduction pathways may be induced by TNF- $\alpha$  (2,12). Furthermore, MAPK signaling has been associated with the expression of pro-inflammatory mediators and skin inflammation (9). In particular, JNK signaling serves a critical role in inflammatory responses; TNF- $\alpha$  may induce the phosphorylation of JNK (35). The present study indicated that TNF- $\alpha$  induced the activation of JNK signaling via phosphorylation; however, pretreatment with spilanthol reduced the extent of this activation. The findings of the present study suggested that the TNF- $\alpha$ -induced inflammatory response may be mediated by JNK signaling in HaCaT cells and that spilanthol may ameliorate the inflammatory response by inhibiting JNK phosphorylation. In addition, the JNK-MAPK signaling pathway is also involved in ultraviolet B-induced keratinocyte inflammation (36). Therefore, the JNK-MAPK signaling pathway may be considered as a therapeutic target in treatment of conditions associated with inflammation. Collectively, these data suggested that spilanthol attenuated the production of IL-6, IL-8 and MCP-1 induced by TNF- $\alpha$ , in addition to JNK activation, in HaCaT cells.

In conclusion, to the best of our knowledge, the present study is the first to report that spilanthol may exert an inhibitory effect on the production of inflammation-associated mediators, including IL-6, IL-8, MCP-1, ICAM-1 and COX-2, and may decrease the extent of monocyte adhesion to TNF- $\alpha$ -induced HaCaT cells. In addition, the anti-inflammatory activity of spilanthol may be associated with enhanced HO-1 expression levels and the inhibition of pJNK-MAPK signaling. The present study proposed that spilanthol may possess therapeutic potential for the treatment of inflammatory skin diseases.

## Acknowledgements

The authors would like to thank the Graduate Institute of Health Industry Technology of Chang Gung University of Science and Technology and Dr Wen-Chung Huang for their support in using bioinformatics tools.

## Funding

The present study was supported by grants from the Chang Gung Memorial Hospital (grant nos. CMRPF1F0122 and CMRPF1G0041) and the Ministry of Science and Technology in Taiwan (grant no. MOST 105-2320-B-255-004), and in part by a grant from the Chang Gung University of Science and Technology (grant no. EZRPF3FG0061).

## Availability of data and materials

The datasets used and/or analyzed during the current study are available from the corresponding author upon reasonable request.

## Authors' contributions

CHH, LC and SW designed and performed the experiments. SH and CYH performed analysis and interpretation of data. SW drafted the manuscript.

## Ethics approval and consent to participate

Not applicable.

## Patient consent for publication

Not applicable.

## Competing interests

The authors declare that they have no competing interests.

## References

- Coman G, Blickenstaff NR and Maibach HI: Skin and the environment. *Rev Environ Health* 29: 143, 2014.
- Subhan F, Kang HY, Lim Y, Ikram M, Baek SY, Jin S, Jeong YH, Kwak JY and Yoon S: Fish scale collagen peptides protect against CoCl<sub>2</sub>/TNF- $\alpha$ -induced cytotoxicity and inflammation via inhibition of ROS, MAPK, and NF- $\kappa$ B pathways in HaCaT cells. *Oxid Med Cell Longev* 2017: 9703609, 2017.
- Dustin ML, Singer KH, Tuck DT and Springer TA: Adhesion of T lymphoblasts to epidermal keratinocytes is regulated by interferon gamma and is mediated by intercellular adhesion molecule 1 (ICAM-1). *J Exp Med* 167: 1323-1340, 1988.
- Youn GS, Kwon DJ, Ju SM, Choi SY and Park J: Curcumin ameliorates TNF- $\alpha$ -induced ICAM-1 expression and subsequent THP-1 adhesiveness via the induction of heme oxygenase-1 in the HaCaT cells. *BMB Rep* 46: 410-415, 2013.
- Albanesi C, Scarponi C, Giustizieri ML and Girolomoni G: Keratinocytes in inflammatory skin diseases. *Curr Drug Targets Inflamm Allergy* 4: 329-334, 2005.
- Middleton MH and Norris DA: Cytokine-induced ICAM-1 expression in human keratinocytes is highly variable in keratinocyte strains from different donors. *J Invest Dermatol* 104: 489-496, 1995.
- Kim H, Youn GS, An SY, Kwon HY, Choi SY and Park J: 2,3-Dimethoxy-2'-hydroxychalcone ameliorates TNF- $\alpha$ -induced ICAM-1 expression and subsequent monocyte adhesiveness via NF- $\kappa$ B inhibition and HO-1 induction in HaCaT cells. *BMB Rep* 49: 57-62, 2016.
- Nedoszytko B, Sokołowska-Wojdyło M, Ruckemann-Dziurdzińska K, Roszkiewicz J and Nowicki RJ: Chemokines and cytokines network in the pathogenesis of the inflammatory skin diseases: Atopic dermatitis, psoriasis and skin mastocytosis. *Postepy Dermatol Alergol* 31: 84-91, 2014.
- Kim MY, Lim YY, Kim HM, Park YM, Kang H and Kim BJ: Synergistic inhibition of tumor necrosis factor- $\alpha$ -stimulated pro-inflammatory cytokine expression in HaCaT cells by a combination of rapamycin and mycophenolic acid. *Ann Dermatol* 27: 32-39, 2015.
- Banno T, Gazel A and Blumenberg M: Effects of tumor necrosis factor- $\alpha$  (TNF  $\alpha$ ) in epidermal keratinocytes revealed using global transcriptional profiling. *J Biol Chem* 279: 32633-32642, 2004.
- Karin M and Greten FR: NF- $\kappa$ B: Linking inflammation and immunity to cancer development and progression. *Nat Rev Immunol* 5: 749-759, 2005.
- Chang CF, Liao KC and Chen CH: 2-phenyl-naphthalene derivatives inhibit lipopolysaccharide-induced pro-inflammatory mediators by downregulating of MAPK/NF- $\kappa$ B pathways in RAW 264.7 macrophage cells. *PLoS One* 12: e0168945, 2017.
- Wang JK, Xiong GM, Luo B, Choo CC, Yuan S, Tan NS and Choong C: Surface modification of PVDF using non-mammalian sources of collagen for enhancement of endothelial cell functionality. *J Mater Sci Mater Med* 27: 45, 2016.

14. Listopad J, Asadullah K, Sievers C, Ritter T, Meisel C, Sabat R and Döcke WD: Heme oxygenase-1 inhibits T cell-dependent skin inflammation and differentiation and function of antigen-presenting cells. *Exp Dermatol* 16: 661-670, 2007.
15. Kirino M, Kirino Y, Takeno M, Nagashima Y, Takahashi K, Kobayashi M, Murakami S, Hirasawa T, Ueda A, Aihara M, *et al*: Heme oxygenase 1 attenuates the development of atopic dermatitis-like lesions in mice: Implications for human disease. *J Allergy Clin Immunol* 122: 290-297, 297.e1-e8, 2008.
16. Barbosa AF, de Carvalho MG, Smith RE and Sabaa-Srur AUO: Spilanthol: Occurrence, extraction, chemistry and biological activities. *Rev bras Farmacogn* 26: 128-133, 2016.
17. Elumalai A, Pendem N, Eswaraiah MC and Naresh V: An updated annual review on antipyretic medicinal plants. *Int J Univers Pharm Life Sci* 2: 207-215, 2012.
18. Chakraborty A, Devi RKB, Rita S, Sharatchandra KH and Singh THI: Preliminary studies on antiinflammatory and analgesic activities of *Spilanthus acmella* in experimental animal models. *Indian J Pharmacol* 36: 148-150, 2004.
19. Wu LC, Fan NC, Lin MH, Chu IR, Huang SJ, Hu CY and Han SY: Anti-inflammatory effect of spilanthol from *Spilanthus acmella* on murine macrophage by down-regulating LPS-induced inflammatory mediators. *J Agric Food Chem* 56: 2341-2349, 2008.
20. Hernández I, Márquez L, Martínez I, Dieguez R, Delporte C, Prieto S, Molina-Torres J and Garrido G: Anti-inflammatory effects of ethanolic extract and alkamides-derived from *Heliopsis longipes* roots. *J Ethnopharmacol* 124: 649-652, 2009.
21. Nair JJ, Aremu AO and Van SJ: Anti-inflammatory effects of *Leucosidea sericea* (Rosaceae) and identification of the active constituents. *S Afr J Bot* 80: 75-76, 2012.
22. Ratnasooriya WD and Pieris KPP: Attenuation of persistent pain and hyperalgesia by *Spilanthus acmella* flowers in rats. *Pharm Biol* 43: 614-619, 2005.
23. Déciga-Campos M, Rios MY and Aguilar-Guadarrama AB: Antinociceptive effect of *Heliopsis longipes* extract and affinin in mice. *Planta Med* 76: 665-670, 2010.
24. Arora S, Vijay S and Kumar D: Phytochemical and antimicrobial studies on the leaves of *Spilanthus acmella*. *J Chem Pharm Res* 3: 145-150, 2011.
25. Rosas-Piñón Y, Mejía A, Díaz-Ruiz G, Aguilar MI, Sánchez-Nieto S and Rivero-Cruz JF: Ethnobotanical survey and antibacterial activity of plants used in the Altiplane region of Mexico for the treatment of oral cavity infections. *J Ethnopharmacol* 141: 860-865, 2012.
26. Prachayasittikul S, Suphamong S, Worachartcheewan A, Lawung R, Ruchirawat S and Prachayasittikul V: Bioactive metabolites from *Spilanthus acmella* Murr. *Molecules* 14: 850-867, 2009.
27. Savadi R, Yadav R and Yadav N: Study on immunomodulatory activity of ethanolic extract *Spilanthus acmella* Murr. Leaves. *Indian J Nat Prod Resour* 1: 204-207, 2010.
28. Saritha KV and Naidu CV: Direct shoot regeneration from leaf explants of *Spilanthus acmella*. *Biol Plant* 52: pp334-338, 2008.
29. Boonen J, Baert B, Roche N, Burvenich C and De Spiegeleer B: Transdermal behaviour of the N-alkylamide spilanthol (affinin) from *Spilanthus acmella* (Compositae) extracts. *J Ethnopharmacol* 127: 77-84, 2010.
30. Huang WC, Wu SJ, Tu RS, Lai YR and Liou CJ: Phloretin inhibits interleukin-1 $\beta$ -induced COX-2 and ICAM-1 expression through inhibition of MAPK, Akt, and NF- $\kappa$ B signaling in human lung epithelial cells. *Food Funct* 6: 1960-1967, 2015.
31. Huang WC, Fang LW and Liou CJ: Phloretin attenuates allergic airway inflammation and oxidative stress in asthmatic mice. *Front Immunol* 8: 134, 2017.
32. Kundu J, Chae IG and Chun KS: Fraxetin induces heme oxygenase-1 expression by activation of Akt/Nrf2 or AMP-activated protein kinase  $\alpha$ /Nrf2 pathway in HaCaT cells. *J Cancer Prev* 21: 135-143, 2016.
33. Cho JW, Park K, Kweon GR, Jang BC, Baek WK, Suh MH, Kim CW, Lee KS and Suh SI: Curcumin inhibits the expression of COX-2 in UVB-irradiated human keratinocytes (HaCaT) by inhibiting activation of AP-1: p38 MAP kinase and JNK as potential upstream targets. *Exp Mol Med* 37: 186-192, 2005.
34. Seo WY, Youn GS, Choi SY and Park J: Butein, a tetrahydroxychalcone, suppresses pro-inflammatory responses in HaCaT keratinocytes. *BMB Rep* 48: 495-500, 2015.
35. Roy PK, Rashid F, Bragg J and Ibdah JA: Role of the JNK signal transduction pathway in inflammatory bowel disease. *World J Gastroenterol* 14: 200-202, 2008.
36. Zhai Y, Dang Y, Gao W, Zhang Y, Xu P, Gu J and Ye X: P38 and JNK signal pathways are involved in the regulation of phlorizin against UVB-induced skin damage. *Exp Dermatol* 24: 275-279, 2015.





Article

# Mechanism of Lakoochin A Inducing Apoptosis of A375.S2 Melanoma Cells through Mitochondrial ROS and MAPKs Pathway

Kuo-Ti Peng <sup>1,2</sup>, Yao-Chang Chiang <sup>3</sup> , Horng-Huey Ko <sup>4</sup>, Pei-Ling Chi <sup>5,6</sup>, Chia-Lan Tsai <sup>7</sup>, Ming-I Ko <sup>3</sup>, Ming-Hsueh Lee <sup>8,9</sup>, Lee-Fen Hsu <sup>8,9,\*</sup> and Chiang-Wen Lee <sup>3,10,11,\*</sup>

<sup>1</sup> Department of Orthopaedic Surgery, Chang Gung Memorial Hospital, Puzi City, Chiayi County 61363, Taiwan; mr3497@adm.cgmh.org.tw

<sup>2</sup> College of Medicine, Chang Gung University, Guishan Dist., Taoyuan City 33303, Taiwan

<sup>3</sup> Department of Nursing, Division of Basic Medical Sciences, and Chronic Diseases and Health Promotion Research Center, Chang Gung University of Science and Technology, Puzi City, Chiayi County 61363, Taiwan; yaochang.chiang@gmail.com (Y.-C.C.); s041055@mail.cgust.edu.tw (M.-I.K.)

<sup>4</sup> Department of Fragrance and Cosmetic Science, College of Pharmacy, Kaohsiung Medical University, Kaohsiung 80708, Taiwan; hhko@kmu.edu.tw

<sup>5</sup> Department of Medical Education and Research, Kaohsiung Veterans General Hospital, Zuoying Dist., Kaohsiung City 81362, Taiwan; chi542738@gmail.com

<sup>6</sup> Department of Pathology and Laboratory Medicine, Kaohsiung Veterans General Hospital, Zuoying Dist., Kaohsiung City 81362, Taiwan

<sup>7</sup> Department of Nursing, Division of Basic Medical Sciences, Chang Gung University of Science and Technology, Guishan Dist., Taoyuan City 33303, Taiwan; cltsai@mail.cgust.edu.tw

<sup>8</sup> Division of Neurosurgery, Department of Surgery, Chang Gung Memorial Hospital, Puzi City, Chiayi County 61363, Taiwan; ma2072@gmail.com

<sup>9</sup> Department of Respiratory Care, Chang Gung University of Science and Technology, Puzi City, Chiayi County 61363, Taiwan

<sup>10</sup> Research Center for Industry of Human Ecology and Research Center for Chinese Herbal Medicine, Chang Gung University of Science and Technology, Guishan Dist., Taoyuan City 33303, Taiwan

<sup>11</sup> Department of Rehabilitation, Chang Gung Memorial Hospital, Chang Gung Memorial Hospital, Puzi City, Chiayi County 61363, Taiwan

\* Correspondence: lfhsu@mail.cgust.edu.tw (L.-F.H.); cwlee@mail.cgust.edu.tw (C.-W.L.); Tel.: +886-5-8800 (ext. 2237) (L.-F.H.); +886-5-8800 (ext. 2388) (C.-W.L.); Fax: +886-5-3628232 (C.-W.L.)

Received: 13 August 2018; Accepted: 4 September 2018; Published: 6 September 2018



**Abstract:** Malignant melanoma is developed from pigment-containing cells, melanocytes, and primarily found on the skin. Malignant melanoma still has a high mortality rate, which may imply a lack of therapeutic agents. Lakoochin A, a compound isolated from *Artocarpus lakoocha* and *Artocarpus xanthocarpus*, has an inhibitory function of tyrosinase activity and melanin production, but the anti-cancer effects are still unclear. In the current study, the therapeutic effects of lakoochin A with their apoptosis functions and possible mechanisms were investigated on A375.S2 melanoma cells. Several methods were applied, including 3-(4,5-Dimethylthiazol-2-yl)-2,5-diphenyltetrazolium bromide (MTT), flow cytometry, and immunoblotting. Results suggest that lakoochin A attenuated the growth of A375.S2 melanoma cells through an apoptosis mechanism. Lakoochin A first increase the production of cellular and mitochondrial reactive oxygen species (ROSs); mitochondrial ROSs then promote mitogen-activated protein kinases (MAPKs) pathway activation and raise downstream apoptosis-related protein and caspase expression. This is the first study to demonstrate that lakoochin A, through ROS-MAPK, apoptosis-related proteins, caspases cascades, can induce melanoma cell apoptosis and may be a potential candidate compound for treating malignant melanoma.

**Keywords:** lakoochin A; mitochondria; melanoma cells; MAPKs; pro-oxidation; apoptosis

## 1. Introduction

Melanoma is a common form of skin cancer, especially among Caucasians [1]. The malignant form of melanoma, called malignant melanoma, still has a poor prognosis. Several methods, including surgical excision, chemotherapy, radiotherapy, and immunotherapy, have been applied to treat malignant melanoma. However, these treatment methods do not effectively reduce the adverse effects or increase the long-term survival rate [2,3]. For this reason, investigating novel agents or methods to increase the efficacy and prognosis of malignant melanoma treatment are of clinical importance.

Lakoochin A is a stilbene derivative identified from *Artocarpus lakoocha* [4] and *Artocarpus xanthocarpus* [5]. Evidence suggests that *Artocarpus* species have inhibitory activities against tyrosinase [5,6], pancreatic lipase [7], antibacterial (such as *Mycobacterium tuberculosis*), and antiviral activity (such as herpes simplex virus and human immunodeficiency virus) [8,9]. Furthermore, studies have also suggested that extractions from *Artocarpus* sp. show anti-cancer properties for melanoma [10], hepatocellular carcinoma [11], gastric carcinoma [12], and colorectal carcinoma [13]. The functions of lakoochin A have been reported to inhibit  $\alpha$ -glucosidase activity [14], melanin biosynthesis [5], antimycobacterial activity against *Mycobacterium tuberculosis*, and cytotoxicity against breast cancer and nasopharyngeal carcinoma cell lines [4]. However, the details of lakoochin A on its anti-cancer function and related mechanisms are still unclear and require further investigation.

The roles of reactive oxygen species (ROS) have been associated with anti-cancer function for some flavonoids from *Artocarpus* sp. [10,15,16]. It is well known that reactive oxygen species (ROS) are a double-edged sword in terms of physiological and pathological organism functions [17–19]. For example, in physiological conditions, ROSs play important roles in phagocytosis, cell signaling, and homeostasis. Subsequently, reactive species could be eliminated by the scavenging system of normal cells [20,21]. However, under oxidative stress conditions, ROSs accumulate in higher concentrations and oxidize cellular lipids, proteins, and DNA. Finally, these ROSs cause aggravation and exacerbation of several clinical diseases and phenomena, such as inflammation, neurodegeneration, aging, cancer, and cardiovascular disease [21–25]. Additionally, some anti-cancer agents, isolated from traditional Chinese herbal medicine, such as paclitaxel [26], resveratrol [27], and curcumin [28], can increase ROS production to inhibit cancer growth, activate the mitogen-activated protein kinase (MAPK) pathway, and increase expression of apoptosis-related proteins. In this study, the role that lakoochin A plays in A375.S2 melanoma cell proliferation and apoptosis were investigated. The underlying mechanisms were also evaluated, including the ROSs, MAPK pathways, and their downstream signaling.

## 2. Results

### 2.1. Lakoochin A Inhibits Proliferation and Viability of A375.S2 Melanoma Cells

Cell proliferation was assayed by using the Sulforhodamine B (SRB) assay. Results showed that treatment with lakoochin A (2.5–20  $\mu$ M, dissolved in dimethyl sulfoxide (DMSO)) on A375.S2 melanoma cells for 24 h could inhibit cell proliferation in a concentration-dependent manner and with a half maximal inhibitory concentration (IC<sub>50</sub>) value of 4.956  $\mu$ M (Figure 1B). The MTT assay suggested that lakoochin A treatment for 24 or 48 h reduced the cell viability in a concentration-dependent manner (0–20  $\mu$ M, Figure 1C). Additionally, as shown in Figure 1D, lakoochin A did not significantly change the cell viability of human skin fibroblasts and keratinocytes, until high doses (100  $\mu$ M) were administered.

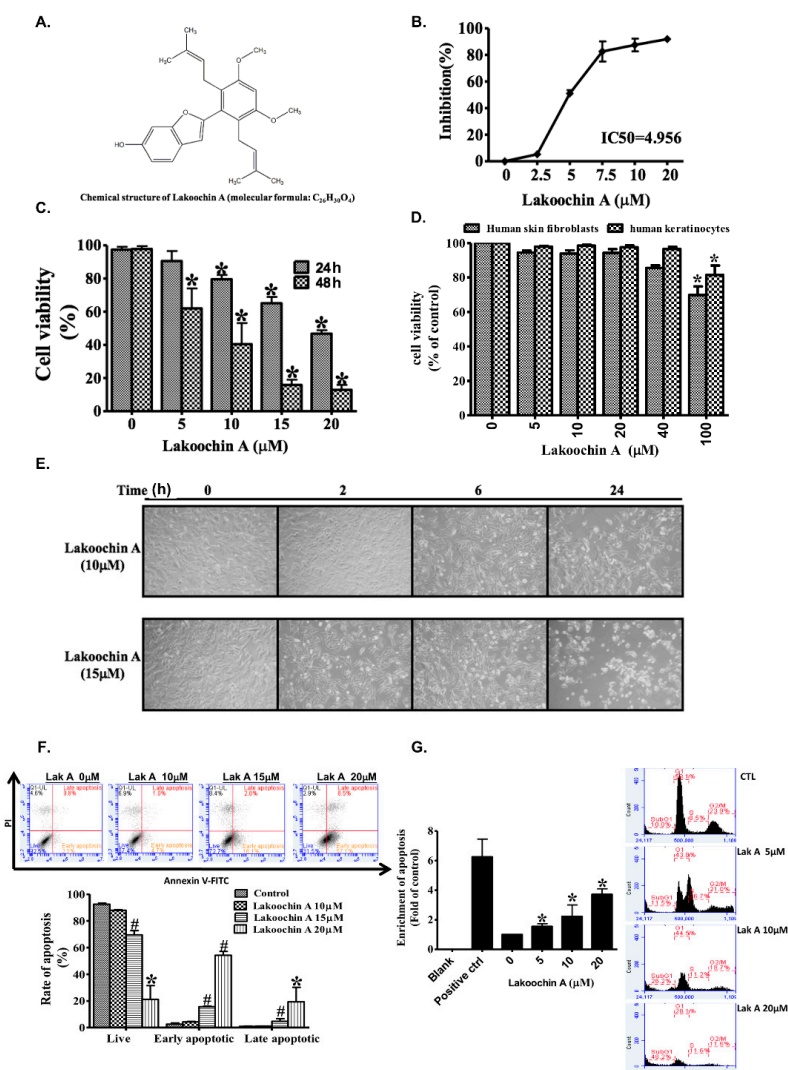


**Figure 1.** (A) The chemical structure of lakoochin A. (B) The inhibitory effect of lakoochin A on A375.S2 cell proliferation, as determined by the SRB assay at 24 h. (C) Dose and time effects of lakoochin A on A375.S2 cell viability, as determined by the 3-(4,5-Dimethylthiazol-2-yl)-2,5-diphenyltetrazolium bromide (MTT) assay at 24 and 48 h. (D) The effects of lakoochin A on human skin fibroblast and keratinocytes as determined by the MTT assay at 24 h. The cell apoptosis effects of lakoochin A on A375.S2 cells, as (E) presented by the morphology and (F) determined by flow cytometry with AnnexinV-Fluorescein isothiocyanate (FITC) and propidium iodide staining at 24 h. The right lower quadrant indicates early apoptosis. (G) Effects of lakoochin A on cell apoptosis (left panel) and sub-G1 cell cycle arrest (right panel) were determined by DNA fragmentation assay and flow cytometry, with propidium iodide staining on A375.S2 cells at 24 h, respectively. Results (B–G) expressed as mean  $\pm$  S.E.M. from three individual experiments. \*  $p < 0.05$  and #  $p < 0.01$  compared to the control group.

## 2.2. Lakoochin A Promotes Apoptosis and Cell Cycle Arrest in A375.S2 Melanoma Cells

Staining was used to test whether lakoochin A has an apoptosis function on A375.S2 cells, cell morphology and flow cytometry with AnnexinV-FITC and propidium iodide. As shown in Figure 1E, lakoochin A (10 and 15  $\mu M$ ) promoted apoptosis in a concentration- and time-dependent manner on A375.S2 cells. As shown in Figure 1F, the percentage of early apoptosis of cells after lakoochin A treatment for 24 h was 2.1% (0  $\mu M$ ), 4.7% (10  $\mu M$ ), 16.1% (15  $\mu M$ ), and 57.1% (20  $\mu M$ ). Treatment also led to a concentration-dependent increase in DNA fragmentation (Figure 1G, left panel). Furthermore, treatment with lakoochin A resulted in an increase in the percentage of cells being arrested in the sub-G1 phase (Figure 1G, right panel). The percentage of sub-G1 phase was observed

as 10.0% (0  $\mu$ M), 11.5% (5  $\mu$ M), 26.2% (10  $\mu$ M), and 48.2% (20  $\mu$ M) in cells after lakoochin A treatment for 24 h.

### 2.3. Lakoochin A Increases Apoptosis of A375.S2 Cells through the Mitochondrial Pathway

The 5,5',6,6'-Tetrachloro-1,1',3,3'-tetraethylbenzimidazolylcarbocyanineiodide (JC-1) assay showed that the treatment of A375.S2 cells with lakoochin A (2.5–20  $\mu$ M) for 24 h decreased mitochondrial membrane potential in a concentration- and time-dependent manner (Figure 2A,B). This result indicates that lakoochin A raised apoptosis in A375.S2 cells, affecting the mitochondrial functions.

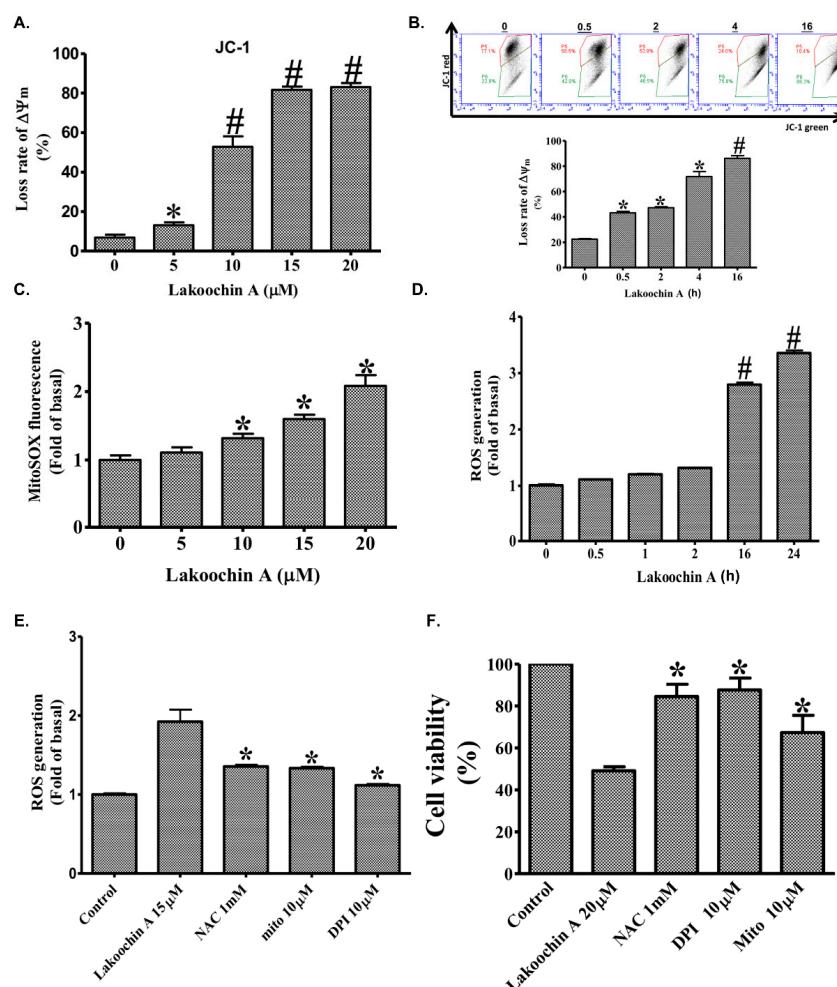


**Figure 2.** (A) The dose effect of lakoochin A at 24 h on the mitochondrial membrane potential ( $\Delta\Psi_m$ ) of A375.S2 cells, as determined by flow cytometry staining with JC-1. (B) The time effects of lakoochin A on the  $\Delta\Psi_m$  of A375.S2 cells pre-labeled with 5,5',6,6'-Tetrachloro-1,1',3,3'-tetraethylbenzimidazolylcarbocyanineiodide (JC-1) (10  $\mu$ g/mL) for the indicated times (0.5–16 h). (C) Effect of lakoochin A on mitochondrial reactive oxygen species (ROS) production (determined by flow cytometry after staining with MitoSOX Red indicator) in A375.S2 cells. (D) Effect of lakoochin A on cellular ROS production (determined by flow cytometry after staining with H2DCFDA reagent). (E) The cellular ROS production of several antioxidants and lakoochin A, determined by flow cytometry staining with H2DCFDA reagent. The A375.S2 cells were pretreated for 1 h with mitochondria-targeted antioxidant (MitoTEMPOL), antioxidant (NAC), or nicotinamide adenine dinucleotide phosphate (NADPH) oxidase inhibitor (DPI) and then treated with lakoochin A for 4 h. (F) Effect of MitoTEMPOL, NAC, and DPI on lakoochin A-induced A375.S2 cell apoptosis (determined by MTT assay). The data were collected from at least three individual experiments and expressed as mean  $\pm$  S.E.M. \*  $p < 0.05$ , #  $p < 0.01$  compared to the control group.



#### 2.4. Lakoochin A Induces Cellular and Mitochondrial ROS Production in A375.S2 Cells

Figure 2C shows the dose-dependent manner of lakoochin A-induced mitochondrial ROS production (determined by MitoSOX). According to the results of the whole cell ROS generation (determined by H2DCFDA), lakoochin A (10  $\mu$ M) induced cellular ROS production in a time-dependent manner in A375.S2 cells (Figure 2D). Furthermore, several inhibitors were used to identify the source of ROS production in cells. As shown in Figure 2E, lakoochin A (15  $\mu$ M)-induced cellular ROS production (determined using the H2DCFDA assay) could be attenuated by a general antioxidant (NAC, 2 mM), a mitochondria-targeted antioxidant (MitoTEMPOL, 10  $\mu$ M), and a NADPH oxidase inhibitor (DPI, 2 mM). Similarly, lakoochin A (20  $\mu$ M) caused a decrease in the viability of A375.S2 cells which could be reversed by NAC, MitoTEMPOL, and DPI. This indicates that lakoochin A-induced cell death is required for ROS production.

#### 2.5. Lakoochin A Induces Mitochondrial ROS Generation to Activate the MAPK Pathway in A375.S2 Cells

To characterize the effects of lakoochin A on MAPK pathways, Western blotting was conducted in A375.S2 (Figure 3A). As shown, lakoochin A (10  $\mu$ M) induced phosphorylation of p38, extracellular signal-regulated kinases (ERK, p44/p42), and c-Jun N-terminal kinases (JNK), in a time-dependent manner, in A375.S2 cells (from 0 to 6 h). On the other hand, these phosphorylation effects could be suppressed by pre-treating specific inhibitors (SB-202190, U-0126, and SP600125, respectively) and MitoTEMPOL (mitochondria-targeted antioxidant, 10  $\mu$ M) for 1 h. Furthermore, lakoochin A (20  $\mu$ M) caused decreases in the viability of A375.S2 cells which could be reversed by MAPKs inhibitors, namely SB-202190, U-0126, and SP600125. The results indicate that lakoochin A-induced MAPK pathways activation can be generated by mitochondrial ROSs in A375.S2 melanoma cells.

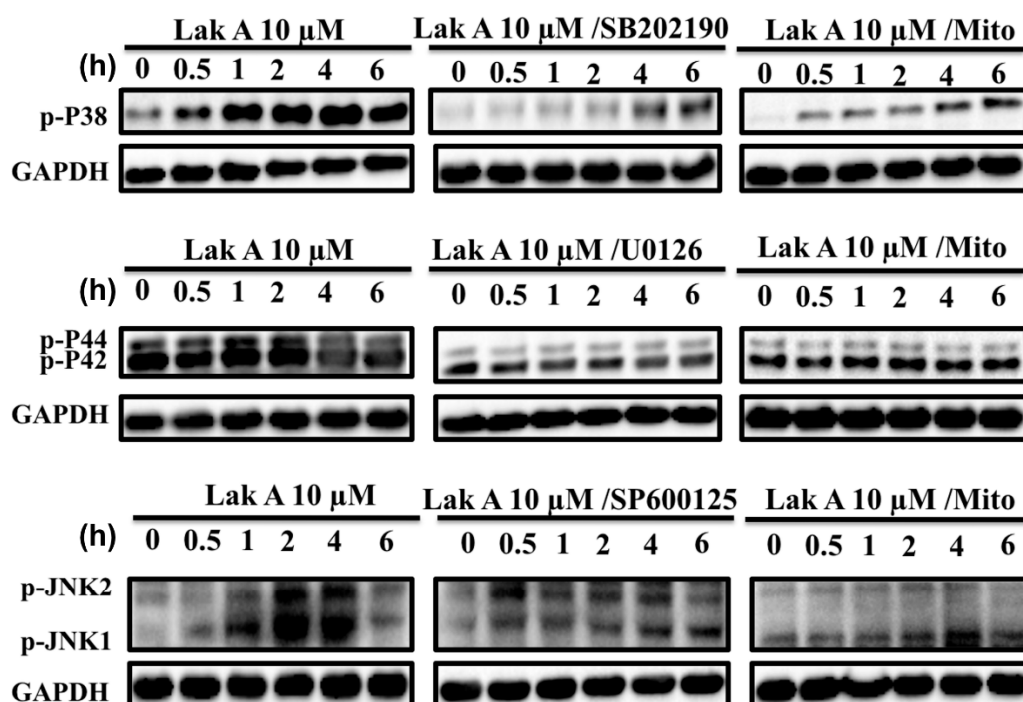
#### 2.6. Lakoochin A Induces Apoptosis-Related Protein Expression in A375.S2 Cells via Mitochondrial ROS Generation

According to the Western blotting results, lakoochin A (10  $\mu$ M) can increase the apoptosis-related protein expression, such as Puma, Bax, Bad, Bid, Apaf-1, and cytochrome c, in a time-dependent manner (from 0 to 24 h) (Figure 4A). Furthermore, the mitochondria-targeted antioxidant (MitoTEMPOL with 1 or 10  $\mu$ M) was pre-treated to confirm the role of mitochondrial ROSs. As shown in Figure 4B, 10  $\mu$ M lakoochin A-induced expression of Puma, Bax, Bad, Bid, Apaf-1, and cytochrome c can be suppressed by treatment with MitoTEMPOL in A375.S2. These results suggest that lakoochin A promotes apoptosis-related protein expression in A375.S2 cells dependent on mitochondrial ROS production.

#### 2.7. Lakoochin A Induces the Activation of Caspase-3, Caspase-7, and Caspase-9 in A375.S2 Cells

Caspases play a critical role in cell inflammation and death [29]. Caspase-3, caspase-7, and caspase-9 in particular, play important roles during apoptosis [30]. Hence, the effects of lakoochin A on caspase-7, caspase-3, and caspase-9 were conducted. As shown in Figure 5A, treatment of the A375.S2 cells with lakoochin A (10  $\mu$ M) increased the expression of caspase-7, caspase-3, and caspase-9 in a time-dependent manner (from 0 to 24 h). Additionally, the activation of caspase-7, caspase-3, and caspase-9 in A375.S2 cells can be significantly suppressed by pre-treating with 1 and 10  $\mu$ M caspase inhibitor Z-VAD-FMK (Figure 5B). Like the caspase immunoblotting results, the decrease effect of lakoochin A (20  $\mu$ M) on cell viability of A375.S2 cells can also be blocked by the caspase inhibitor carbobenzoxy-valyl-alanyl-aspartyl-[O-methyl]-fluoromethylketone (Z-VAD-FMK). This result suggests that lakoochin A induced apoptosis of A375.S2 cells, which mediated caspase pathways.

A.



B.

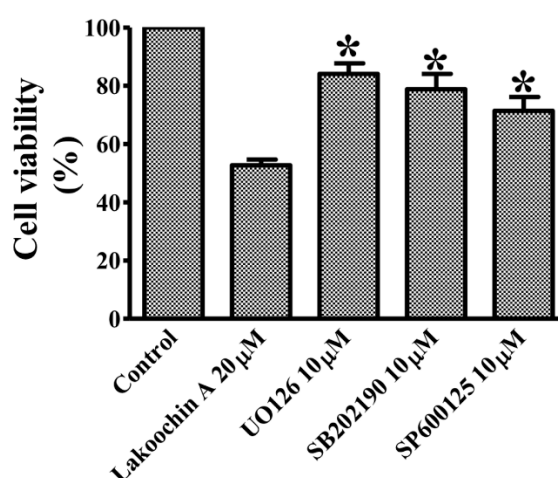


**Figure 3.** (A) Effects of different time course of lakoochin A, with or without being pre-treated for 1 h with a p38 inhibitor (SB202190), MEK1/ERK inhibitor (U0126), JNK inhibitor (SP600125), and mitochondria-targeted antioxidant (MitoTEMPOL), on expressions of the phosphorylation status of p38, ERK (p44/p42), and JNK in A375.S2 cells. Glyceraldehyde 3-phosphate dehydrogenase (GAPDH) was used as a loading control. Blots were representative of three independent experiments. (B) Effect of U0126, SP600125, and MitoTEMPOL on lakoochin A-induced A375.S2 cell apoptosis (determined by MTT assay). The data were collected from at least three individual experiments and expressed as mean  $\pm$  S.E.M. \*  $p < 0.05$  as compared to the control group.

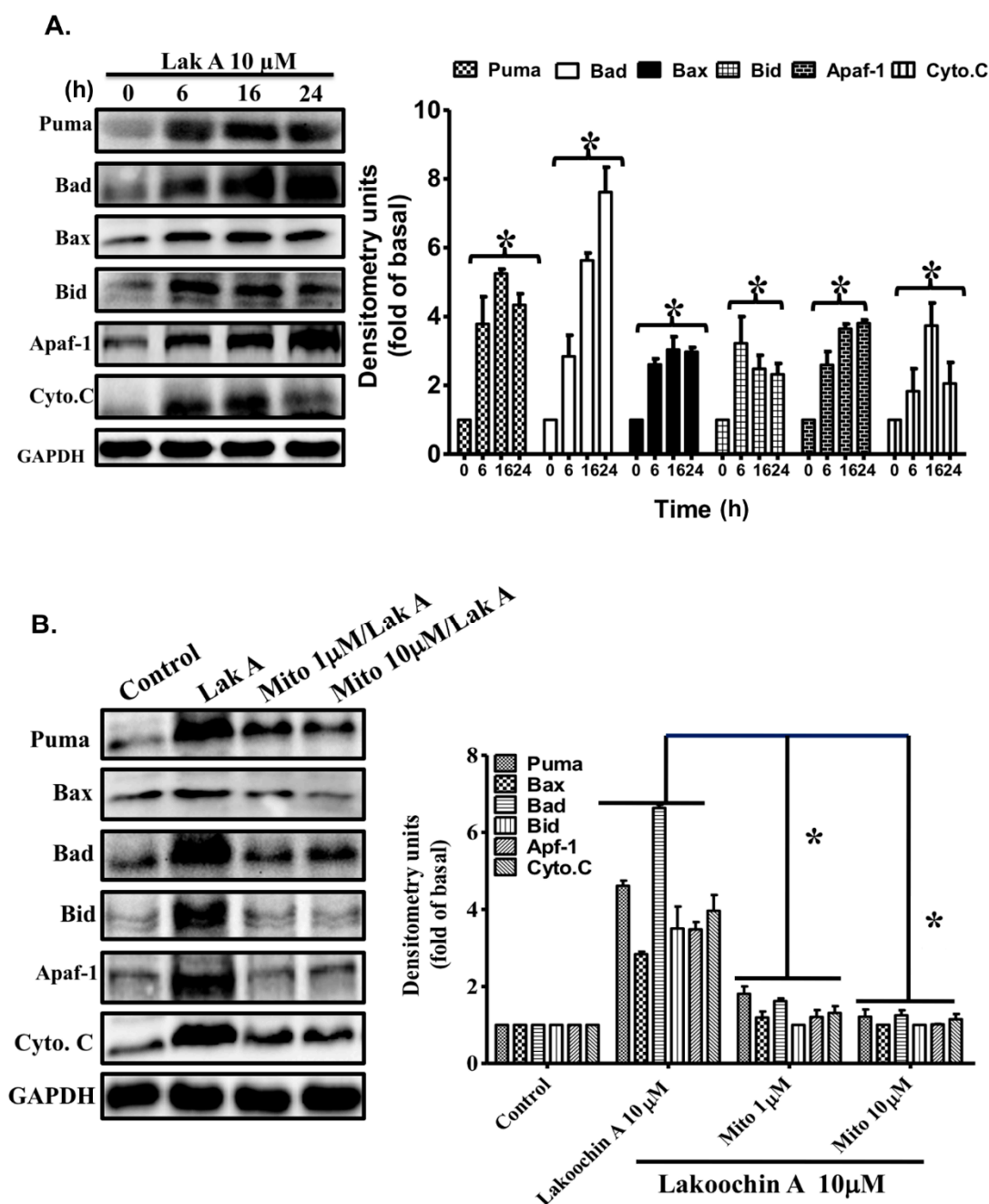


**Figure 4.** (A) Effects of lakoochin A on the expression levels of apoptosis-related proteins Puma, Bax, Bad, Bid, Apaf-1, and cytochrome c in A375.S2 cells, over various time periods (0–24 h) (B) The cells were pre-treated with 1 and 10  $\mu$ M MitoTEMPOL for 1 h followed by treatment of lakoochin A for 16 h. Expression of apoptosis-related proteins was determined by Western blotting. GAPDH was used for a loading control. The intensity of the bands was quantified by densitometry, and the data were collected from three individual experiments and expressed as mean  $\pm$  S.E.M. \*  $p < 0.05$ , compared to the control group.

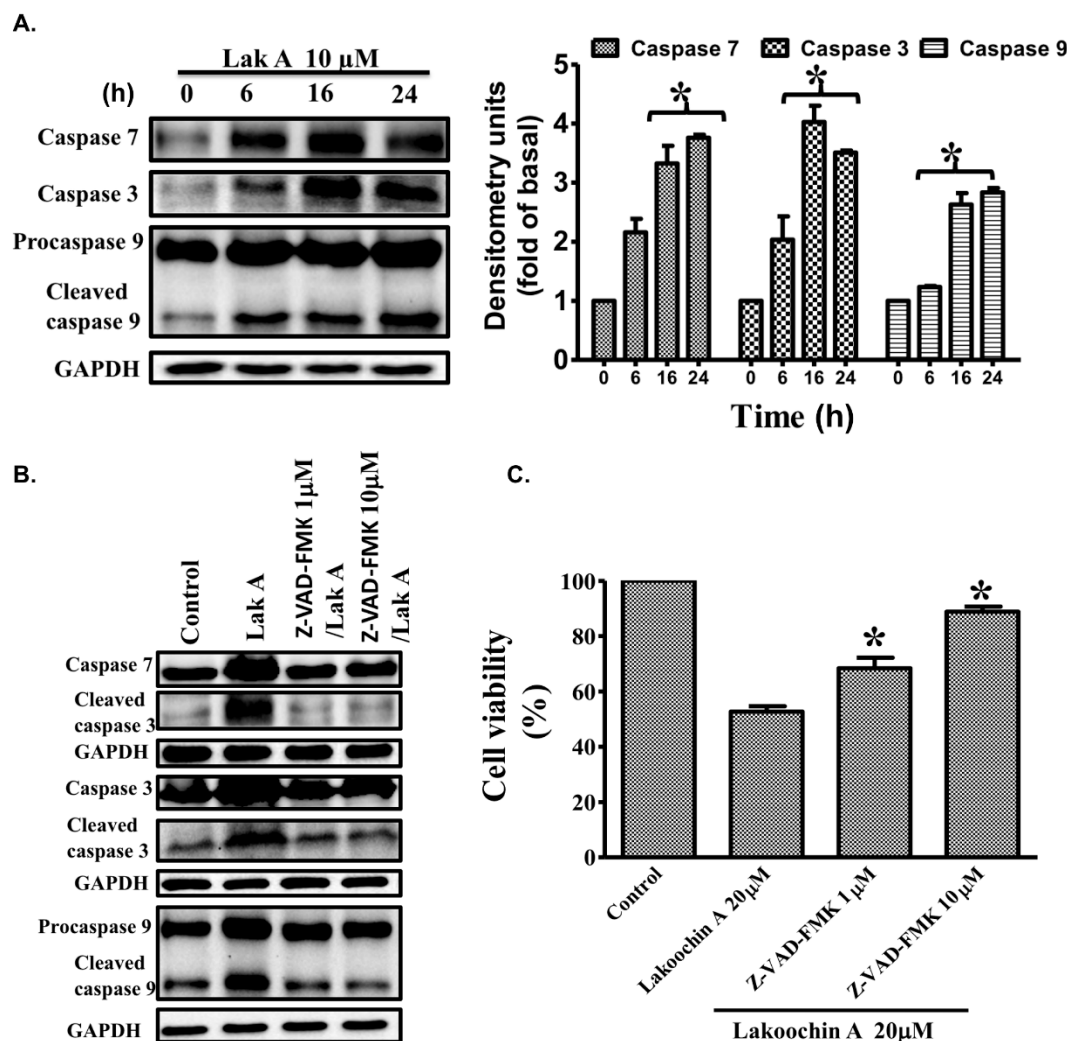


**Figure 5.** (A) Effects of lakoochin A (10  $\mu$ M) on the expression status of caspase-7, caspase-3, and caspase-9 in A375.S2 cells in a serial time-period (0–24 h). (B) Effects of caspase inhibitor carbobenzoxy-valyl-alanyl-aspartyl-[O-methyl]-fluoromethylketone (Z-VAD-FMK) on lakoochin A-induced increases in caspase-3, -7, and -9. Cells were pre-treated for 1 h with Z-VAD-FMK (1 or 10  $\mu$ M) followed by treatment with lakoochin A for 16 h. The levels of caspase-3, -7, and -9 were evaluated by immunoblotting. (C) Effect of Z-VAD-FMK (1 or 10  $\mu$ M) on lakoochin A-induced A375.S2 cell apoptosis (determined by MTT assay). The data were collected from at least three individual experiments and expressed as mean  $\pm$  S.E.M. \*  $p < 0.05$ , as compared to the control group.

### 3. Discussion

In the current study, we first demonstrate that lakoochin A has anti-melanoma cancer cell activity linked to ROS generation and MAPK pathways. Lakoochin A treatment in A375.S2 cells results in apoptosis via an increase in ROS formation, while pre-treatment of NAC, DPI, and MitoTEMPOL appear to reduce ROS generation from cellular and mitochondria. In addition, the expressions of phosphorylation type of p38, ERK (p44/p42), and JNK can be suppressed by SB-202190, U-0126, SP600125, and MitoTEMPOL respectively, indicating that MAPK pathways are down-stream pathways of ROSs. Furthermore, inhibiting mitochondrial ROS formation also reduces expressions of various apoptosis-related proteins induced by lakoochin A. This may imply that lakoochin A-induced apoptosis to A375.S2 cell requests the ROS production of mitochondria. In an attempt to characterize the possible cytotoxic mechanisms of lakoochin A, we analyzed the levels of apoptosis-related proteins, and caspase expression. Results suggest that lakoochin A promotes an



increase of apoptosis-related protein via mitochondrial ROS formation. Moreover, caspase-3, -7 and -9 activities and expressions, that were increased by lakoochin A, can be suppressed with treatment of MitoTEMPOL, a mitochondria-targeted antioxidant.

Malignant melanoma, a kind of transformation and uncontrolled growth of melanocytes, is an aggressive and most malignant form of skin cancer [2]. Although several medicines have been developed to treat malignant melanoma the incidence rates of malignant melanoma are still increasing, especially in the Caucasian population [1]. Malignant melanoma causes a higher mortality rate. Svedman et al. [31] suggests that, among patients with melanoma stage IV, there is only a 9–28%, five-year survival rate. These findings may imply that there is still a lack of therapeutic agents. In clinical practice, melanoma may be initially observed anywhere on the skin, as pigmented or non-pigmented papules, plaques, or nodules, particularly in sun-exposed areas. Malignant melanocytes rapidly metastasize to lymph nodes and pass to other visceral organs [3]. Several methods, such as surgery, radiotherapy, chemotherapy, immunotherapy, and biological agents, have been applied to treat melanoma [32]. Unfortunately, there is still no method for increasing long-term survival rate for malignant melanoma patients. Therefore, the task of identifying novel compounds with potential therapeutic effects for treating melanoma is urgent.

Recently, various bioactive compounds derived from natural sources have been demonstrated as candidates for anti-cancer medicines. Evidence suggests that compounds from *Artocarpus* species have cytotoxic functions for treating cancer. Lakoochin A (Figure 1A) contains stilbene derivatives isolated from *Artocarpus lakoocha* [4] and *Artocarpus xanthocarpus* [5]. Previous studies suggest lakoochin A has functions on the inhibition of  $\alpha$ -glucosidase activity [14], melanin biosynthesis [5], antimycobacterial activity and cytotoxicity for breast cancer, and nasopharyngeal carcinoma cell lines [4]. This study is the first to demonstrate that lakoochin A has anti-melanoma effects.

It is well known that cell apoptosis may be a result of exposure with an increase in oxidative stress. ROSs produced from cells may have two main sources, namely NADPH oxidase and mitochondria. This mechanism involves anti-cancer growth. For example, Beberok et al. [33] suggested that lomefloxacin, a kind of fluoroquinolone, can induce ROSs and reduce topoisomerase II to cause apoptosis of COLO829 melanoma cells. Similar mechanisms were also found in the current study. Lakoochin A can increase cellular and mitochondrial ROS formation in A375.S2 cells and be suppressed by pre-treating with NAC (cellular antioxidant), DPI (NADPH oxidase inhibitor), and MitoTEMPOL (mitochondria antioxidant). However, the major source of ROSs, generated by lakoochin A, requires further investigation. Various signal transduction pathways can be activated upon oxidative stress formation in cells. It has been demonstrated that the MAPK signaling pathway plays an important regulation role in human diseases, including cancer growth and metastasis [34,35]. ERK1/2 (p44/p42), JNK, and p38 are the three main components in human cells. They have different functions: ERK1/2 mainly mediates in cell proliferation, survival, migration, and invasion, while JNK and p38 are involved in cell apoptosis [36,37]. Previous studies suggest that resveratrol, a kind of stilbene [38], presents antitumor activity with respect to melanoma cells associated with the suppression of telomerase [39] and attenuates the Akt/PKB activity [40], via the p53 pathway. The activation of caspase-9 and caspase-3, works to upregulate Bcl-2-associated X protein and B-cell lymphoma 2 expressions [41], and the activation of ERK1/2, but not p38 or JNK [42]. Our results show that lakoochin A can activate caspase-9, -7 and -3, as well as the phosphorylation of ERK1/2 (p44/p42), p38, and JNK. They seem to present differently with resveratrol, which implies that the stilbene-induced apoptosis of cancer cells may occur via multiple pathways. Furthermore, the phosphorylation of MAPK signaling can be suppressed by pre-treating cells with specific MAPK inhibitors (SB-202190, U-0126, and SP600125) and by a mitochondria-targeted antioxidant (MitoTEMPOL). These findings strongly suggest that the lakoochin A-induced activation of MAPK signaling in A375.S2 melanoma cells, occurs via the mediation of mitochondrial ROS production. These results are consistent with previous studies where mitochondrial ROS generation promoted MAPK activation and led to apoptosis [15,43].

Two distinct pathways, the death receptor and mitochondrial (death receptor-independent) pathways, can bring about apoptosis [44,45]. Cellular stress responses may lead pro-apoptotic proteins of the Bcl-2 family (Puma, Bax, Bad, and Bid) to translocate from cytosol into mitochondria through the mitochondrial pathway [46,47]. This results in a rise in the mitochondrial permeability and activation of caspases, via releases of cytochrome c from the mitochondria [48,49]. Cytochrome c coordinates with Apaf-1 and procaspase-9 to form the apoptosome [50], which regulates the caspase 9 homo- and heterodimer [51], and subsequently activates caspase-9 and caspase-3/7, causing apoptosis [52]. This was also observed in the current study. Lakoochin A increased the expression of the pro-apoptotic Bcl-2 family (Puma, Bax, Bad, and Bid), Apaf-1, and cytochrome c, which can be attenuated by pre-treatment with MitoTEMPOL in A375.S2 melanoma cells. Additionally, lakoochin A can decrease the mitochondrial membrane potential and increase the activity of caspase-9, -7 and -3. This indicates that lakoochin A induces apoptosis for melanoma cells via the mitochondrial pathway.

In conclusion, our study is the first to demonstrate that lakoochin A causes cytotoxicity for A375.S2 melanoma cells. It regulates mitochondrial ROS production, increases pro-apoptotic proteins of the Bcl-2 family (Puma, Bax, Bad, Bid) expression, MAPK (p38/ERK/JNK) signaling activation, and the activation of caspases. Therefore, lakoochin A may be considered as a potential agent for treating malignant melanoma.

#### 4. Materials and Methods

##### 4.1. Materials

A human melanoma cell line (A375.S2) was provided by Feng-Lin Yen (Kaohsiung Medical University). Dulbecco's Modified Eagle Medium/Nutrient Mixture F-12 (DMEM/F-12) was obtained from GIBCO (Grand Island, NY, USA) and supplemented with 10% fetal bovine serum (FBS) (Hazelton Research Products, Denver, PA, USA). Antibodies for Western blotting (phospho-p38, phospho-ERK, and phospho-JNK) were obtained from Cell Signaling Technology (Danvers, MA, USA). Puma, Bax, Bad, Bid, Apaf-1, cytochrome C, caspase-3, caspase-7, and caspase-9 were obtained from Santa Cruz Biotechnology (Santa Cruz, CA, USA). The GAPDH antibody was obtained from Biogenesis (Bournemouth, UK). N-acetylcysteine (NAC), apocynin (APO), U-0126, SB-202190, and SP600125 were procured from Biomol (Plymouth Meeting, PA, USA). MitoSOX Red mitochondrial superoxide indicator was purchased from Molecular Probes (Eugene, OR, USA). Lakoochin A was provided by co-author Horng-Huey Ko (Kaohsiung Medical University), and isolated from the methanolic extract of *A. xanthocarpus* as described previously in [5,6]. Its purity was determined (>97%) using high-performance liquid chromatography (HPLC) analysis. The lakoochin A was powdered and stored in a black bottle at  $-20^{\circ}\text{C}$ , and dissolved in DMSO before the experiments were performed. Each control group was treated equivalent to DMSO volume of their tested groups.

##### 4.2. Cell Culture

A human melanoma cell line (A375.S2) was grown in culture utilizing Dulbecco's Modified Eagle Medium/Nutrient Mixture F-12 (DMEM/F-12, Gibco, Grand Island, NY, USA) supplemented with 10% FBS (Hazelton Research Products, Denver, PA, USA). Cells were maintained at  $37^{\circ}\text{C}$  in a humidified atmosphere of 5%  $\text{CO}_2$ /95% air.

##### 4.3. Cell Proliferation Assay

Cell proliferation was performed by the sulforhodamine B (SRB) assay in accordance with a previous study [15]. Briefly, A375.S2 cells were treated with lakoochin A (isolated from methanolic extract of *Artocarpus xanthocarpus* as described in a previous study [5]) for 24 h and subsequently fixed in 10% trichloroacetic acid (TCA). The cells were then stained with SRB (Sigma-Aldrich, St. Louis, MO, USA) and washed with acetic acid (1%). Cell-bound SRB dye was dissolved with Tris-base (10 mM), and the absorbance was measured with a spectrometer at a wavelength of 515 nm.

#### 4.4. Cell Viability Assay

The cell viability of A375.S2 was determined using the 3-(4,5-dimethylthiazol-2-yl)-2,5-diphenyltetrazolium bromide (MTT) assay (Sigma-Aldrich). First, cells were plated onto 96-well plates and incubated overnight before testing. The next morning, different concentrations of lakoochin A cells were added for 24 or 48 h. After MTT solution incubation at 37 °C for 1 h, the plates were read at 550 nm.

#### 4.5. Cell Apoptosis Measurement

The cell apoptosis was measured by flow cytometry with the Annexin V-FITC/propidium iodide assay kit (Thermo Fisher Scientific, Waltham, MA, USA) and DNA fragmentation assay. Different concentrations of lakoochin A (10, 15, and 20 µM) were added to A375.S2 cells for 24 h, and these cells were then stained with Annexin V-FITC and propidium iodide, according to the manual, and subjected to flow cytometry (Accuri C6, BD Biosciences, San Jose, CA, USA).

#### 4.6. Cell Cycle Analysis

Following treatment with varying concentrations of lakoochin A (5, 10, and 20 µM) for 24 h, A375.S2 cells were stained with RNAase and propidium iodide, then subjected to an Accuri C6 Flow Cytometer (BD Biosciences, San Jose, CA, USA). In the DNA fragmentation assay, A375.S2 cells were treated with different concentrations of lakoochin A (5, 10, and 20 µM) for 24 h, and the degree of DNA fragmentation was measured using the Cell Death Detection ELISA kit (Roche Diagnostics, Basel, Switzerland) and read by the ELISA reader.

#### 4.7. Assessment of Mitochondrial Membrane Potential

A375.S2 cells were seeded onto 96-well plates (dose) or 12-well plates (time) and then incubated overnight. Cells were then treated with lakoochin A at varying concentrations for 24 h or 10 µM with different time intervals. Cells were stained with 5,5',6,6'-Tetrachloro-1,1',3,3'-tetraethylbenzimidazolylcarbocyanineiodide (JC-1; Sigma-Aldrich). The cells were incubated at 37 °C for 30 min and analyzed using a flow cytometer at 590 nm and 520 nm (for red and green fluorescence, respectively). The ratio of fluorescence (590/520 nm) reflected the change in mitochondrial membrane potential.

#### 4.8. Determination of Cellular and Mitochondrial ROS Production

Cellular ROS production was measured using the 2',7'-dichlorodihydrofluorescein diacetate (H2DCFDA) assay. A375.S2 cells were seeded onto 12-well plates and incubated overnight. Cells were treated with different concentrations of lakoochin A, with or without inhibitors for different amounts of time, and then stained with H2DCFDA Reagent (Thermo Fisher Scientific, USA). The fluorescence intensity of the cells was assessed using flow cytometry (excitation wavelength, 488 nm; emission wavelength, 530 nm). Furthermore, MitoSOX™, a Red Mitochondrial Superoxide Indicator assay was used for evaluating the production of the mitochondrial ROSs. In accordance with the treatment schedule described above, after lakoochin A treatment, cells were stained with MitoSOX Red mitochondrial superoxide indicator (Molecular Probes, Eugene, OR, USA) and measured via flow cytometry (excitation wavelength, 488 nm; emission wavelength, 585 nm). The inhibitors, N-acetylcysteine (NAC) and diphenylene iodonium (DPI), were purchased from Biomol (Plymouth Meeting, PA, USA); MitoTEMPOL was purchased from Cayman Chemical (Ann Arbor, MI, USA).

#### 4.9. Immunoblotting Analysis for MAPKs, Apoptosis-Related Proteins, and Caspases

A375.S2 cells were seeded onto 12-well plates and incubated overnight. Cells were treated with 10 µM lakoochin A (with or without inhibitors) for different amounts of time. Following treatment, the cells were lysed in a lysis buffer and subjected to protein extraction. Afterward, equal amounts

of the protein were separated by SDS-polyacrylamide gel electrophoresis (10–12.5% polyacrylamide) and transferred onto nitrocellulose membranes. Samples were incubated overnight with different primary antibodies to measure the levels of the targets (phospho-p38, phospho-ERK, and phospho-JNK (Cell Signaling Technology, Danvers, MA, USA), Puma, Bax, Bad, Bid, Apaf-1, cytochrome C, caspase-3, caspase-7, and caspase-9 (Santa Cruz Biotechnology, Santa Cruz, CA, USA), and GAPDH (Biogenesis, Bournemouth, UK)). Next, secondary antibodies conjugated with horseradish peroxidase were added, and immunoreactivity was assessed using the enhanced chemiluminescence (ECL) detection system. The signals were detected on a ChemiDoc™ XRS+ image system (Bio-Rad Laboratories, Hercules, CA, USA). The inhibitors, U-0126, SB-202190 and SP600125, were purchased from Biomol (Plymouth Meeting, PA, USA). The immunoblotting data were collected from at least three replicates with a similar pattern. The value was calculated from those figures, then a closer figure pattern was selected to present the statistical values.

#### 4.10. Statistical Analysis

All data were analyzed using GraphPad Prism software (v4, GraphPad, San Diego, CA, USA). Results were expressed as mean  $\pm$  SEM. Continuous data were analyzed by one-way or two-way ANOVA followed by post-hoc Tukey's multiple comparison (multiple groups). A *p* value < 0.05 was considered significant.

**Author Contributions:** K.-T.P., L.-F.H. and C.-W.L. performed the experiments and wrote the manuscript. Y.-C.C., H.-H.K., P.-L.C., C.-L.T., M.-I.K. and M.-H.L. supervised the Western blotting, compound isolation and flow, and oversaw analysis of the results. K.-T.P., Y.-C.C. and C.-W.L. helped with writing the manuscript. K.-T.P. and L.-F.H. designed the experimental protocols, supervised all experiments, interpreted the results, and contributed to writing the paper. All authors have read and approved the final manuscript.

**Funding:** This work was supported by the Chang Gung Medical Research Program Foundation (grants CMRPF6E0031, CMRPF6E0032, CMRPF6E0033, and CMRPF6G0021).

**Acknowledgments:** We thank Feng-Lin Yen (Kaohsiung Medical University) for providing the human melanoma cell line (A375.S2) for this study.

**Conflicts of Interest:** The authors declare no conflict of interest.

#### Abbreviations

Apaf-1	apoptotic protease activating factor 1
Bad	Bcl-2-associated death promoter
Bax	BH3-interacting domain death agonist (Bid), BCL2-associated X protein
DPI	diphenylene iodonium
ERK	extracellular regulated protein kinase
JNK	c-Jun N-terminal kinase
MAPK	mitogen-activated protein kinases
NAC	N-acetylcysteine
ROS	reactive oxygen species
Puma	p53 upregulated modulator of apoptosis

#### References

1. McCourt, C.; Dolan, O.; Gormley, G. Malignant melanoma: A pictorial review. *Ulster Med. J.* **2014**, *83*, 103–110. [[PubMed](#)]
2. Miller, A.J.; Mihm, M.C., Jr. Melanoma. *N. Engl. J. Med.* **2006**, *355*, 51–65. [[CrossRef](#)] [[PubMed](#)]
3. Eggermont, A.M.; Spatz, A.; Robert, C. Cutaneous melanoma. *Lancet* **2014**, *383*, 816–827. [[CrossRef](#)]
4. Puntumchai, A.; Kittakoop, P.; Rajviroongit, S.; Vimuttipong, S.; Likhitwitayawuid, K.; Thebtaranonth, Y. Lakoochins A and B, new antimycobacterial stilbene derivatives from *Artocarpus lakoocha*. *J. Nat. Prod.* **2004**, *67*, 485–486. [[CrossRef](#)] [[PubMed](#)]



5. Jin, Y.J.; Lin, C.C.; Lu, T.M.; Li, J.H.; Chen, I.S.; Kuo, Y.H.; Ko, H.H. Chemical constituents derived from *Artocarpus xanthocarpus* as inhibitors of melanin biosynthesis. *Phytochemistry* **2015**, *117*, 424–435. [[CrossRef](#)] [[PubMed](#)]
6. Nguyen, M.T.T.; Le, T.H.; Nguyen, H.X.; Dang, P.H.; Do, T.N.V.; Abe, M.; Takagi, R.; Nguyen, N.T. Artocarmins G–M, Prenylated 4-Chromenones from the Stems of *Artocarpus rigida* and Their Tyrosinase Inhibitory Activities. *J. Nat. Prod.* **2017**, *80*, 3172–3178. [[CrossRef](#)] [[PubMed](#)]
7. Zhao, T.; Yan, G.R.; Pan, S.L.; Wang, H.Y.; Hou, A.J. New isoprenylated 2-arylbenzofurans and pancreatic lipase inhibitory constituents from *Artocarpus nitidus*. *Chem. Biodivers.* **2009**, *6*, 2209–2216. [[CrossRef](#)] [[PubMed](#)]
8. Sritularak, B.; Tantrakarnsakul, K.; Lipipun, V.; Likhitwitayawuid, K. Flavonoids with anti-HSV activity from the root bark of *Artocarpus lakoocha*. *Nat. Prod. Commun.* **2013**, *8*, 1079–1080. [[PubMed](#)]
9. Jagtap, U.B.; Bapat, V.A. *Artocarpus*: A review of its traditional uses, phytochemistry and pharmacology. *J. Ethnopharmacol.* **2010**, *129*, 142–166. [[CrossRef](#)] [[PubMed](#)]
10. Arung, E.T.; Yoshikawa, K.; Shimizu, K.; Kondo, R. Isoprenoid-substituted flavonoids from wood of *Artocarpus heterophyllus* on B16 melanoma cells: Cytotoxicity and structural criteria. *Fitoterapia* **2010**, *81*, 120–123. [[CrossRef](#)] [[PubMed](#)]
11. Tzeng, C.W.; Tzeng, W.S.; Lin, L.T.; Lee, C.W.; Yen, M.H.; Yen, F.L.; Lin, C.C. *Artocarpus communis* Induces Autophagic Instead of Apoptotic Cell Death in Human Hepatocellular Carcinoma Cells. *Am. J. Chin. Med.* **2015**, *43*, 559–579. [[CrossRef](#)] [[PubMed](#)]
12. Ma, J.P.; Qiao, X.; Pan, S.; Shen, H.; Zhu, G.F.; Hou, A.J. New isoprenylated flavonoids and cytotoxic constituents from *Artocarpus tonkinensis*. *J. Asian Nat. Prod. Res.* **2010**, *12*, 586–592. [[CrossRef](#)] [[PubMed](#)]
13. Soo, H.C.; Chung, F.F.; Lim, K.H.; Yap, V.A.; Bradshaw, T.D.; Hii, L.W.; Tan, S.H.; See, S.J.; Tan, Y.F.; Leong, C.O.; et al. Cudraflavone C Induces Tumor-Specific Apoptosis in Colorectal Cancer Cells through Inhibition of the Phosphoinositide 3-Kinase (PI3K)-AKT Pathway. *PLoS ONE* **2017**, *12*, e0170551. [[CrossRef](#)] [[PubMed](#)]
14. Nuntawong, P.; Kongkatitham, V.; Likhitwitayawuid, K.; Mekboonsonglarp, W.; Sukrong, S.; Tanasupawat, S.; Sritularak, B. New 2-arylbenzofurans from the root bark of *Artocarpus gomezianus* and their alpha-glucosidase inhibitory activity. *Nat. Prod. Res.* **2017**. [[CrossRef](#)] [[PubMed](#)]
15. Lee, C.W.; Yen, F.L.; Ko, H.H.; Li, S.Y.; Chiang, Y.C.; Lee, M.H.; Tsai, M.H.; Hsu, L.F. Cudraflavone C Induces Apoptosis of A375.S2 Melanoma Cells through Mitochondrial ROS Production and MAPK Activation. *Int. J. Mol. Sci.* **2017**, *18*, 1508. [[CrossRef](#)] [[PubMed](#)]
16. Tsai, M.H.; Liu, J.F.; Chiang, Y.C.; Hu, S.C.; Hsu, L.F.; Lin, Y.C.; Lin, Z.C.; Lee, H.C.; Chen, M.C.; Huang, C.L.; et al. Artocarpin, an isoprenyl flavonoid, induces p53-dependent or independent apoptosis via ROS-mediated MAPKs and Akt activation in non-small cell lung cancer cells. *Oncotarget* **2017**, *8*, 28342–28358. [[CrossRef](#)] [[PubMed](#)]
17. Brandes, R.P.; Weissmann, N.; Schroder, K. Nox family NADPH oxidases: Molecular mechanisms of activation. *Free Radic. Biol. Med.* **2014**, *76*, 208–226. [[CrossRef](#)] [[PubMed](#)]
18. Day, B.J. Antioxidant therapeutics: Pandora’s box. *Free Radic. Biol. Med.* **2014**, *66*, 58–64. [[CrossRef](#)] [[PubMed](#)]
19. Singh, S.; Bocker, C.; Koppaka, V.; Chen, Y.; Jackson, B.C.; Matsumoto, A.; Thompson, D.C.; Vasiliou, V. Aldehyde dehydrogenases in cellular responses to oxidative/electrophilic stress. *Free Radic. Biol. Med.* **2013**, *56*, 89–101. [[CrossRef](#)] [[PubMed](#)]
20. Devasagayam, T.P.; Tilak, J.C.; Boloor, K.K.; Sane, K.S.; Ghaskadbi, S.S.; Lele, R.D. Free radicals and antioxidants in human health: Current status and future prospects. *J. Assoc. Physicians India* **2004**, *52*, 794–804. [[PubMed](#)]
21. Trachootham, D.; Alexandre, J.; Huang, P. Targeting cancer cells by ROS-mediated mechanisms: A radical therapeutic approach? *Nat. Rev. Drug Discov.* **2009**, *8*, 579–591. [[CrossRef](#)] [[PubMed](#)]
22. Farmer, E.E.; Mueller, M.J. ROS-mediated lipid peroxidation and RES-activated signaling. *Annu. Rev. Plant Biol.* **2013**, *64*, 429–450. [[CrossRef](#)] [[PubMed](#)]
23. Radak, Z.; Zhao, Z.; Goto, S.; Koltai, E. Age-associated neurodegeneration and oxidative damage to lipids, proteins and DNA. *Mol. Aspects Med.* **2011**, *32*, 305–315. [[CrossRef](#)] [[PubMed](#)]
24. Zhang, W.; Xiao, S.; Ahn, D.U. Protein oxidation: Basic principles and implications for meat quality. *Crit. Rev. Food Sci. Nutr.* **2013**, *53*, 1191–1201. [[CrossRef](#)] [[PubMed](#)]

25. Schieber, M.; Chandel, N.S. ROS function in redox signaling and oxidative stress. *Curr. Biol.* **2014**, *24*, R453–R462. [[CrossRef](#)] [[PubMed](#)]
26. Alexandre, J.; Hu, Y.; Lu, W.; Pelicano, H.; Huang, P. Novel action of paclitaxel against cancer cells: Bystander effect mediated by reactive oxygen species. *Cancer Res.* **2007**, *67*, 3512–3517. [[CrossRef](#)] [[PubMed](#)]
27. Colin, D.J.; Limagne, E.; Ragot, K.; Lizard, G.; Ghiringhelli, F.; Solary, E.; Chauffert, B.; Latruffe, N.; Delmas, D. The role of reactive oxygen species and subsequent DNA-damage response in the emergence of resistance towards resveratrol in colon cancer models. *Cell Death Dis.* **2014**, *5*, e1533. [[CrossRef](#)] [[PubMed](#)]
28. Han, X.; Xu, B.; Beevers, C.S.; Odaka, Y.; Chen, L.; Liu, L.; Luo, Y.; Zhou, H.; Chen, W.; Shen, T.; et al. Curcumin inhibits protein phosphatases 2A and 5, leading to activation of mitogen-activated protein kinases and death in tumor cells. *Carcinogenesis* **2012**, *33*, 868–875. [[CrossRef](#)] [[PubMed](#)]
29. McIlwain, D.R.; Berger, T.; Mak, T.W. Caspase functions in cell death and disease. *Cold Spring Harb. Perspect. Biol.* **2015**, *7*, a026716. [[CrossRef](#)] [[PubMed](#)]
30. Brentnall, M.; Rodriguez-Menocal, L.; De Guevara, R.L.; Cepero, E.; Boise, L.H. Caspase-9, caspase-3 and caspase-7 have distinct roles during intrinsic apoptosis. *BMC Cell Biol.* **2013**, *14*, 32. [[CrossRef](#)] [[PubMed](#)]
31. Svedman, F.C.; Pillas, D.; Taylor, A.; Kaur, M.; Linder, R.; Hansson, J. Stage-specific survival and recurrence in patients with cutaneous malignant melanoma in Europe—A systematic review of the literature. *Clin. Epidemiol.* **2016**, *8*, 109–122. [[CrossRef](#)] [[PubMed](#)]
32. Harries, M.; Malvey, J.; Lebbe, C.; Heron, L.; Amelio, J.; Szabo, Z.; Schadendorf, D. Treatment patterns of advanced malignant melanoma (stage III-IV)—A review of current standards in Europe. *Eur. J. Cancer* **2016**, *60*, 179–189. [[CrossRef](#)] [[PubMed](#)]
33. Beberok, A.; Wrzesniok, D.; Szlachta, M.; Rok, J.; Rzepka, Z.; Respondek, M.; Buszman, E. Lomefloxacin Induces Oxidative Stress and Apoptosis in COLO829 Melanoma Cells. *Int. J. Mol. Sci.* **2017**, *18*, 2194. [[CrossRef](#)] [[PubMed](#)]
34. Kim, E.K.; Choi, E.J. Pathological roles of MAPK signaling pathways in human diseases. *Biochim. Biophys. Acta* **2010**, *1802*, 396–405. [[CrossRef](#)] [[PubMed](#)]
35. McCubrey, J.A.; Steelman, L.S.; Chappell, W.H.; Abrams, S.L.; Wong, E.W.; Chang, F.; Lehmann, B.; Terrian, D.M.; Milella, M.; Tafuri, A.; et al. Roles of the Raf/MEK/ERK pathway in cell growth, malignant transformation and drug resistance. *Biochim. Biophys. Acta* **2007**, *1773*, 1263–1284. [[CrossRef](#)] [[PubMed](#)]
36. Chang, L.; Karin, M. Mammalian MAP kinase signalling cascades. *Nature* **2001**, *410*, 37–40. [[CrossRef](#)] [[PubMed](#)]
37. Boutros, T.; Chevet, E.; Metrakos, P. Mitogen-activated protein (MAP) kinase/MAP kinase phosphatase regulation: Roles in cell growth, death, and cancer. *Pharmacol. Rev.* **2008**, *60*, 261–310. [[CrossRef](#)] [[PubMed](#)]
38. Bertelli, A.A.; Ferrara, F.; Diana, G.; Fulgenzi, A.; Corsi, M.; Ponti, W.; Ferrero, M.E.; Bertelli, A. Resveratrol, a natural stilbene in grapes and wine, enhances intraphagocytosis in human promonocytes: A co-factor in antiinflammatory and anticancer chemopreventive activity. *Int. J. Tissue React.* **1999**, *21*, 93–104. [[PubMed](#)]
39. Platella, C.; Guida, S.; Bonmassar, L.; Aquino, A.; Bonmassar, E.; Ravagnan, G.; Montesarchio, D.; Roviello, G.N.; Musumeci, D.; Fuggetta, M.P. Antitumour activity of resveratrol on human melanoma cells: A possible mechanism related to its interaction with malignant cell telomerase. *Biochim. Biophys. Acta* **2017**, *1861*, 2843–2851. [[CrossRef](#)] [[PubMed](#)]
40. Bhattacharya, S.; Darjatmoko, S.R.; Polans, A.S. Resveratrol modulates the malignant properties of cutaneous melanoma through changes in the activation and attenuation of the antiapoptotic protooncogenic protein Akt/PKB. *Melanoma Res.* **2011**, *21*, 180–187. [[CrossRef](#)] [[PubMed](#)]
41. Wu, Z.; Liu, B.; E, C.; Liu, J.; Zhang, Q.; Liu, J.; Chen, N.; Chen, R.; Zhu, R. Resveratrol inhibits the proliferation of human melanoma cells by inducing G1/S cell cycle arrest and apoptosis. *Mol. Med. Rep.* **2015**, *11*, 400–404. [[CrossRef](#)] [[PubMed](#)]
42. Niles, R.M.; McFarland, M.; Weimer, M.B.; Redkar, A.; Fu, Y.M.; Meadows, G.G. Resveratrol is a potent inducer of apoptosis in human melanoma cells. *Cancer Lett.* **2003**, *190*, 157–163. [[CrossRef](#)]
43. Huang, C.Y.; Chen, J.Y.; Kuo, C.H.; Pai, P.Y.; Ho, T.J.; Chen, T.S.; Tsai, F.J.; Padma, V.V.; Kuo, W.W.; Huang, C.Y. Mitochondrial ROS-induced ERK1/2 Activation and HSF2-mediated AT1 R Upregulation Are Required for Doxorubicin-induced Cardiotoxicity. *J. Cell. Physiol.* **2018**, *233*, 463–475. [[CrossRef](#)] [[PubMed](#)]
44. Hengartner, M.O. The biochemistry of apoptosis. *Nature* **2000**, *407*, 770–776. [[CrossRef](#)] [[PubMed](#)]
45. Gupta, S. Molecular signaling in death receptor and mitochondrial pathways of apoptosis (Review). *Int. J. Oncol.* **2003**, *22*, 15–20. [[CrossRef](#)] [[PubMed](#)]

46. Martinou, J.C.; Youle, R.J. Mitochondria in apoptosis: Bcl-2 family members and mitochondrial dynamics. *Dev. Cell* **2011**, *21*, 92–101. [[CrossRef](#)] [[PubMed](#)]
47. Shamas-Din, A.; Kale, J.; Leber, B.; Andrews, D.W. Mechanisms of action of Bcl-2 family proteins. *Cold Spring Harb. Perspect. Biol.* **2013**, *5*, a008714. [[CrossRef](#)] [[PubMed](#)]
48. Czabotar, P.E.; Lessene, G.; Strasser, A.; Adams, J.M. Control of apoptosis by the BCL-2 protein family: Implications for physiology and therapy. *Nat. Rev. Mol. Cell Biol.* **2014**, *15*, 49–63. [[CrossRef](#)] [[PubMed](#)]
49. Desagher, S.; Martinou, J.C. Mitochondria as the central control point of apoptosis. *Trends Cell Biol.* **2000**, *10*, 369–377. [[CrossRef](#)]
50. Zhou, M.; Li, Y.; Hu, Q.; Bai, X.C.; Huang, W.; Yan, C.; Scheres, S.H.; Shi, Y. Atomic structure of the apoptosome: Mechanism of cytochrome c- and dATP-mediated activation of Apaf-1. *Genes Dev.* **2015**, *29*, 2349–2361. [[CrossRef](#)] [[PubMed](#)]
51. Wu, C.C.; Lee, S.; Malladi, S.; Chen, M.D.; Mastrandrea, N.J.; Zhang, Z.; Bratton, S.B. The Apaf-1 apoptosome induces formation of caspase-9 homo- and heterodimers with distinct activities. *Nat. Commun.* **2016**, *7*, 13565. [[CrossRef](#)] [[PubMed](#)]
52. Schafer, Z.T.; Kornbluth, S. The apoptosome: Physiological, developmental, and pathological modes of regulation. *Dev. Cell* **2006**, *10*, 549–561. [[CrossRef](#)] [[PubMed](#)]



© 2018 by the authors. Licensee MDPI, Basel, Switzerland. This article is an open access article distributed under the terms and conditions of the Creative Commons Attribution (CC BY) license (<http://creativecommons.org/licenses/by/4.0/>).

## Article

# New Anti-Inflammatory Aporphine and Lignan Derivatives from the Root Wood of *Hernandia nymphaeifolia*

Chuan-Yen Wei <sup>1,†</sup>, Shih-Wei Wang <sup>2,†</sup>, Jin-Wang Ye <sup>3</sup>, Tsong-Long Hwang <sup>4,5,6</sup> , Ming-Jen Cheng <sup>7</sup>, Ping-Jyun Sung <sup>8</sup> , Tsung-Hsien Chang <sup>9</sup>  and Jih-Jung Chen <sup>10,11,\*</sup>

- <sup>1</sup> Department of General Surgery, Taitung MacKay Memorial Hospital, Taitung City 950, Taiwan; lpshop@gmail.com
  - <sup>2</sup> Department of Medicine, Mackay Medical College, New Taipei City 252, Taiwan; shihwei@mmc.edu.tw
  - <sup>3</sup> Graduate Institute of Pharmaceutical Technology, Tajen University, Pingtung 907, Taiwan; jjc8506674@gmail.com
  - <sup>4</sup> Graduate Institute of Natural Products, School of Traditional Chinese Medicine, College of Medicine, Chang Gung University, Taoyuan 333, Taiwan; htl@mail.cgu.edu.tw
  - <sup>5</sup> Research Center for Chinese Herbal Medicine, Research Center for Food and Cosmetic Safety, Graduate Institute of Health Industry Technology, College of Human Ecology, Chang Gung University of Science and Technology, Taoyuan 333, Taiwan
  - <sup>6</sup> Department of Anesthesiology, Chang Gung Memorial Hospital, Taoyuan 333, Taiwan
  - <sup>7</sup> Bioresource Collection and Research Center (BCRC), Food Industry Research and Development Institute (FIRDI), Hsinchu 300, Taiwan; cmj@firdi.org.tw
  - <sup>8</sup> National Museum of Marine Biology and Aquarium, Pingtung 944, Taiwan; pjsung@nmmba.gov.tw
  - <sup>9</sup> Department of Medical Education and Research, Kaohsiung Veterans General Hospital, Kaohsiung 813, Taiwan; changth@vghks.gov.tw
  - <sup>10</sup> Faculty of Pharmacy, School of Pharmaceutical Sciences, National Yang-Ming University, Taipei 112, Taiwan
  - <sup>11</sup> Department of Medical Research, China Medical University Hospital, China Medical University, Taichung 404, Taiwan
- \* Correspondence: chenjj@ym.edu.tw; Tel.: +886-2-2826-7195  
† Authors have contributed equally in this manuscript.

Received: 15 August 2018; Accepted: 1 September 2018; Published: 7 September 2018



**Abstract:** A new aporphine, 3-hydroxyhernandonine (**1**) and a new lignin, 4'-O-demethyl-7-O-methyldehydropodophyllotoxin (**2**), have been isolated from the root wood of *Hernandia nymphaeifolia*, together with thirteen known compounds (**3–15**). The structures of these compounds were determined through mass spectrometry (MS) and spectroscopic analyses. The known isolate, 2-O-methyl-7-oxolaetine (**3**), was first isolated from natural sources. Among the isolated compounds, 3-hydroxyhernandonine (**1**), 4'-O-demethyl-7-O-methyldehydropodophyllotoxin (**2**), hernandonine (**4**), oxohernangerine (**5**), and oxohernagine (**6**) displayed inhibition (IC<sub>50</sub> values ≤5.72 µg/mL) of superoxide anion production by human neutrophils in response to formyl-L-methionyl-L-leucyl-L-phenylalanine/cytochalasin B (fMLP/CB). In addition, 3-hydroxyhernandonine (**1**), 4'-O-demethyl-7-O-methyldehydropodophyllotoxin (**2**), oxohernangerine (**5**), and oxohernagine (**6**) suppressed fMLP/CB-induced elastase release with IC<sub>50</sub> values ≤5.40 µg/mL.

**Keywords:** *Hernandia nymphaeifolia*; Hernandiaceae; root wood; structure elucidation; aporphine; lignan; anti-inflammatory activity



## 1. Introduction

*Hernandia nymphaeifolia* (Presl) Kubitzki (Hernandiaceae) is an evergreen tree that is distributed in the tropical island shores of the Indian and western Pacific Oceans [1]. Its seed is used as a cathartic [2]. Various aporphines [3–7], isoquinolones [4,5], lignans [4,7,8], benzyloquinoline [5], steroids [7], and their derivatives were isolated from this species in past studies. Many of these isolates display cytotoxic [4,5,8], vasorelaxing [6], antioxidant [6], and antiplatelet aggregation [7] activities.

The extensive or inappropriate activation of neutrophils leads to many inflammatory disorders such as chronic obstructive pulmonary disease (COPD), ischemia-reperfusion injury, asthma, rheumatoid arthritis, and metabolic diseases [9,10]. In response to various stimuli, activated neutrophils secrete a series of cytotoxins, such as granule proteases, bioactive lipids, and superoxide anion ( $O_2^{\bullet-}$ ), a precursor of other reactive oxygen species (ROS) [10–12]. The inhibition of the abnormal activation of neutrophils by medicines has been recommended as a way to improve inflammatory diseases. In our researches on the anti-inflammatory constituents of Formosan plants, numerous species have been screened for anti-inflammatory activity, and *H. nymphaeifolia* has been found to be an active species. A new aporphine, 3-hydroxyhernandonine (1), a new lignin, 4'-O-demethyl-7-O-methyldehydropodophyllotoxin (2), and thirteen known compounds (3–15) have been isolated and determined from the root wood of *Hernandia nymphaeifolia*, and their structures are described in Figure 1.

This article describes the structural elucidation of new compounds 1 and 2 and the inhibitory effects of all isolates on elastase release and superoxide generation by human neutrophils.

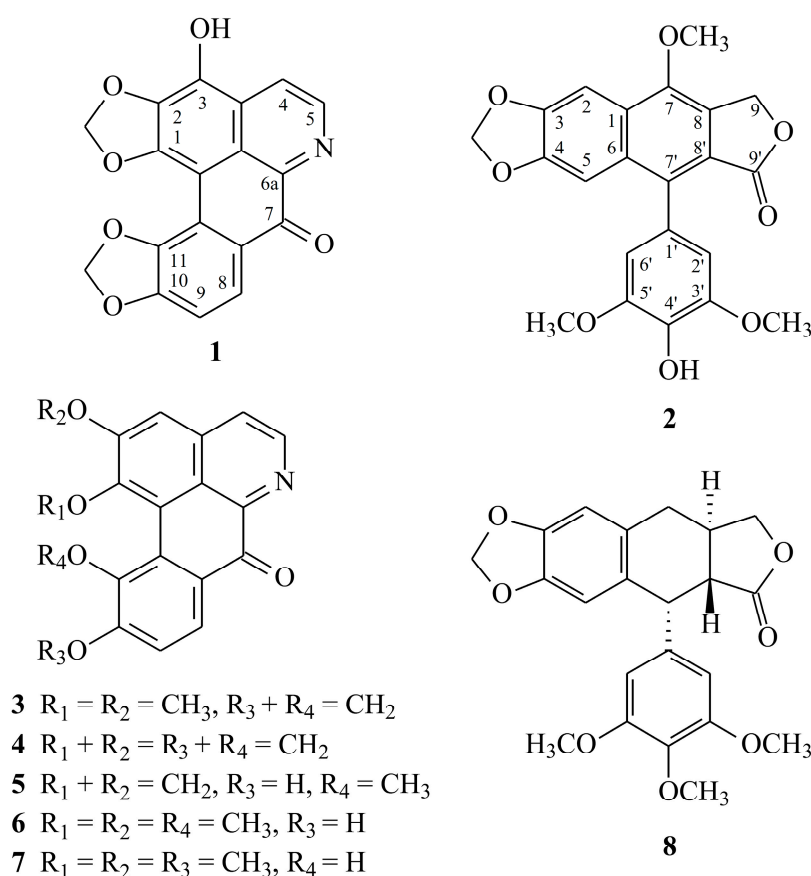
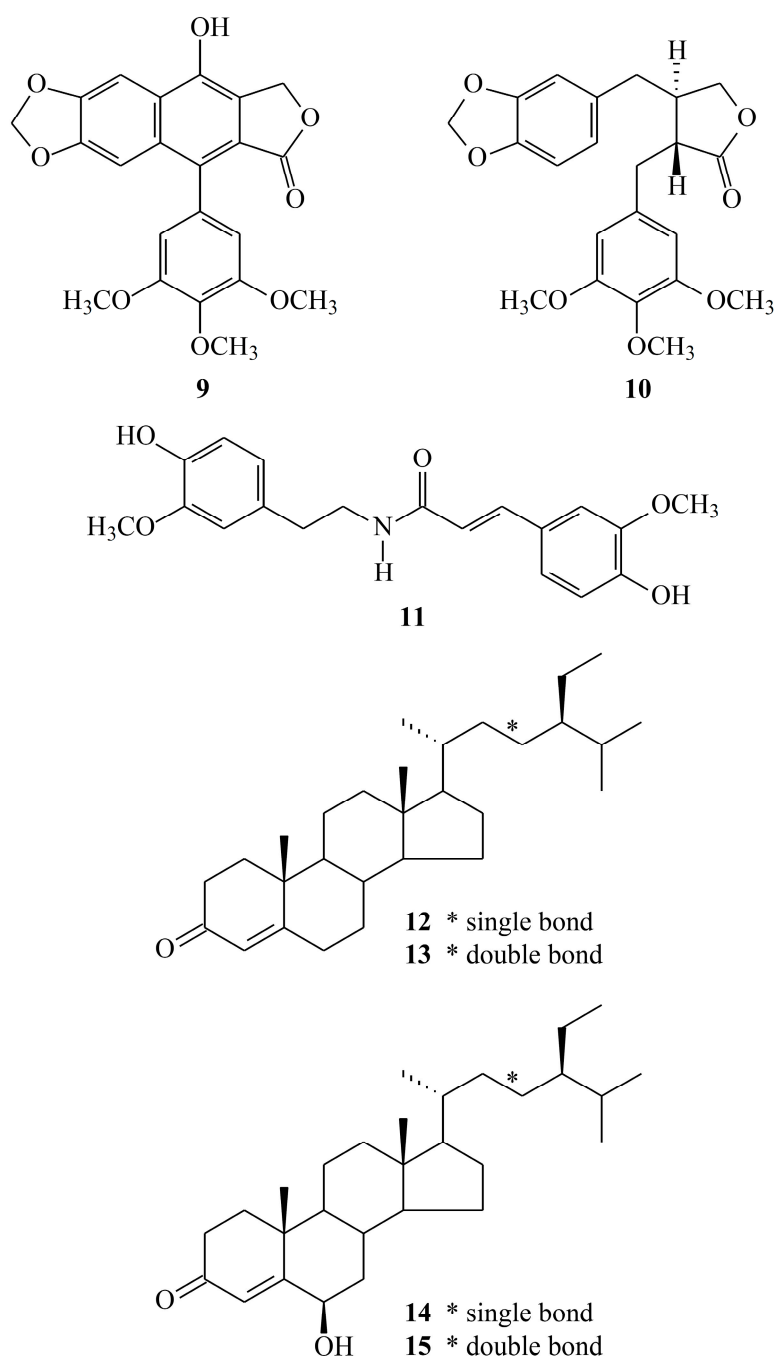


Figure 1. Cont.



**Figure 1.** The chemical structures of compounds 1–15 isolated from *H. nymphaeifolia*.

## 2. Results and Discussion

### 2.1. Isolation and Structural Elucidation

Chromatographic purification of the  $\text{CH}_2\text{Cl}_2$ -soluble fraction of a MeOH extract of root wood of *H. nymphaeifolia* through a silica gel column, medium pressure liquid chromatography (MPLC), and preparative thin-layer chromatography (TLC) yielded two new (1 and 2) and thirteen known compounds (3–15) (Figure 1).

The aporphine, 3-hydroxyhernandonine (1), was obtained as yellow needles. The electrospray ionization mass spectrometry (ESI-MS) (Figure S1) afford the quasi-molecular ion  $[\text{M} + \text{Na}]^+$  at  $m/z$  358, implying a molecular formula of  $\text{C}_{18}\text{H}_9\text{NO}_6\text{Na}$ , which was confirmed by the high-resolution

(HR)-ESI-MS ( $m/z$  358.0325  $[M + Na]^+$ , calcd 358.0328) ( $-0.84$  ppm) (Figure S2) and by the  $^{13}C$ -,  $^1H$ -, and distortionless enhancement by polarization transfer (DEPT) NMR data. IR absorptions for OH ( $3439\text{ cm}^{-1}$ ) and conjugated carbonyl ( $1646\text{ cm}^{-1}$ ) functions were observed. The  $^1H$ -NMR spectrum (Figure S3) of **1** showed the presence of a hydroxy group at  $\delta_H$  6.52 (1H, s,  $D_2O$  exchangeable, OH-3), two methylenedioxy groups at  $\delta_H$  6.20 (2H, s,  $OCH_2O$ -10,11) and 6.28 (2H, s,  $OCH_2O$ -1,2), and two pairs of AB-doublets at  $\delta_H$  7.08 (1H, d,  $J = 8.5$  Hz, H-9), 8.10 (1H, d,  $J = 5.0$  Hz, H-4), 8.28 (1H, d,  $J = 8.5$  Hz, H-8), and 8.88 (1H, d,  $J = 5.0$  Hz, H-5). The  $^1H$ - and  $^{13}C$ -NMR (Figure S4) data of **1** were similar to those of hernandonine [13,14], except that the 3-hydroxy group [ $\delta_H$  6.52 (1H, s,  $D_2O$  exchangeable)] of **1** replaced H-3 of hernandonine [13,14]. This was supported by HMBC correlations between OH-3 ( $\delta_H$  6.52) and C-2 ( $\delta_C$  139.2), as well as between C-3 ( $\delta_C$  148.4), and C-3a ( $\delta_C$  123.9). The full assignment of  $^1H$ - and  $^{13}C$ -NMR resonances was supported by DEPT,  $^1H$ - $^1H$  COSY (Figure S5), NOESY (Figure 2 and Figure S6), HMBC (Figure 2 and Figure S7), and HSQC (Figure S8) spectral analyses. Based on the above data, the structure of **1** was revealed as 3-hydroxyhernandonine.

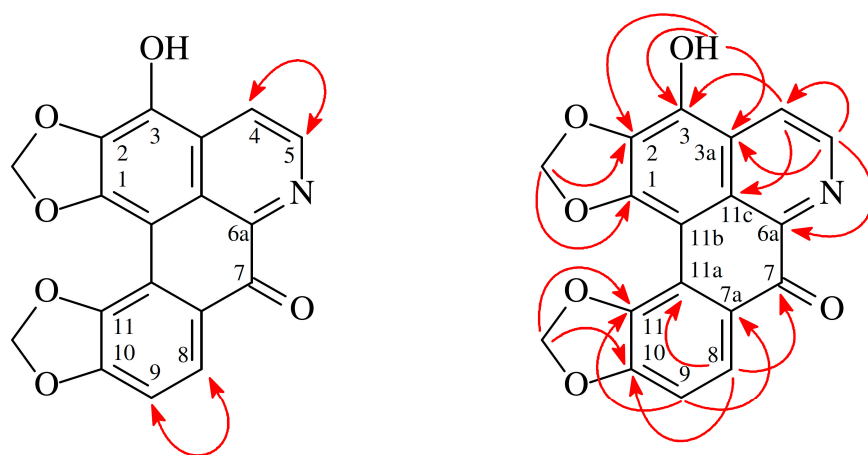


Figure 2. Key NOESY (↔) and HMBC (↔) correlations of **1**.

4'-O-Demethyl-7-O-methyldehydropodophyllotoxin (**2**) was isolated as colorless needles. The ESI-MS (Figure S9) display the sodium adduct ion  $[M + Na]^+$  at  $m/z$  433, hinting a molecular formula of  $C_{22}H_{18}O_8$ , which was supported by the HR-ESI-MS ( $m/z$  433.0898  $[M + Na]^+$ , calcd 433.0899) ( $-0.23$  ppm) (Figure S10). The IR spectrum showed the presence of OH ( $3452\text{ cm}^{-1}$ ) and  $\gamma$ -lactone carbonyl ( $1764\text{ cm}^{-1}$ ) groups. The  $^1H$ -NMR spectrum (Figure S11) of **2** showed the presence of three methoxy groups at  $\delta_H$  3.88 (6H, s, OMe-3' and OMe-5') and 4.09 (3H, s, OMe-7), a hydroxyl group at  $\delta_H$  5.65 (1H, br s,  $D_2O$  exchangeable, OH-4'), a methylenedioxy group at  $\delta_H$  6.09 (2H, s,  $OCH_2O$ ), a  $\gamma$ -lactone methylene proton at 5.52 (2H, s, H-9), and four aromatic protons at  $\delta_H$  6.57 (2H, s, H-2' and H-6'), 7.07 (1H, s, H-5), and 7.57 (1H, s, H-2). The  $^1H$ - and  $^{13}C$ -NMR (Figure S12) data of **2** were similar to those of 4'-O-demethyldehydropodophyllotoxin [15], except that the 7-methoxy groups [ $\delta_H$  4.09 (3H, s);  $\delta_C$  59.9 (OMe-7)] of **2** replaced the 7-OH group of 4'-O-demethyldehydropodophyllotoxin [15]. This was supported by NOESY correlations between OMe-7 ( $\delta_H$  4.09) and H-2 ( $\delta_H$  7.57) and by HMBC correlations between OMe-7 ( $\delta_H$  4.09) and C-7 ( $\delta_C$  148.5). According to the above evidence, the structure of **2** was elucidated as 4'-O-demethyl-7-O-methyldehydropodophyllotoxin. This was further affirmed by the  $^1H$ - $^1H$ -COSY (Figure S13), NOESY (Figure 3 and Figure S14), DEPT, HMBC (Figure 3 and Figure S15), and HSQC (Figure S16) experiments.





fMLP-induced superoxide anion generation; (g) 3-hydroxyhernandonine (1) was the most effective among the isolates, with an  $IC_{50}$  value of  $3.93 \pm 0.48 \mu\text{g/mL}$  against fMLP-induced elastase release.

**Table 1.** Inhibitory effects of compounds 1–15 from the root wood of *H. nymphaeifolia* on superoxide radical anion generation and elastase release by human neutrophils in response to fMet-Leu-Phe/cytochalasin B <sup>a</sup>.

Compounds	Superoxide anion	Elastase
	$IC_{50} [\mu\text{g/mL}]^b$ or $(\text{Inh } \%)^c$	
3-Hydroxyhernandonine (1)	$4.09 \pm 0.44^{***}$	$3.93 \pm 0.48^{***}$
4'-O-Demethyl-7-O-methyldehydro-podophyllotoxin (2)	$5.72 \pm 0.42^{***}$	$5.40 \pm 0.40^{***}$
2-O-Methyl-7-oxolaetine (3)	$7.37 \pm 0.46^{***}$	$6.82 \pm 0.09^{***}$
Hernandonine (4)	$4.41 \pm 0.76^{***}$	$(45.76 \pm 6.92)^{***}$
Oxohernangerine (5)	$2.65 \pm 0.97^{***}$	$4.82 \pm 0.39^{***}$
Oxohernagine (6)	$2.86 \pm 0.85^{***}$	$4.87 \pm 0.27^{***}$
7-Oxonorisocorydine (7)	$6.62 \pm 0.28^{***}$	$6.58 \pm 0.08^{***}$
(-)-Deoxypodophyllotoxin (8)	$(38.95 \pm 4.83)^{**}$	$(33.76 \pm 3.82)$
Dehydropodophyllotoxin (9)	$(43.91 \pm 3.86)^{***}$	$9.53 \pm 0.84^{***}$
(-)-Yatein (10)	$(42.36 \pm 3.41)^*$	$(36.74 \pm 3.05)^{**}$
<i>N-trans</i> -Feruloylmethoxytyramine (11)	$6.26 \pm 0.65^{***}$	$7.03 \pm 0.21^{***}$
Mixture of $\beta$ -sitostenone (12) and stigmasta-4,22-dien-3-one (13)	$(24.71 \pm 2.67)$	$(29.15 \pm 2.89)$
Mixture of $6\beta$ -hydroxystigmast-4-en-3-one (14) and $6\beta$ -hydroxystigmasta-4,22-dien-3-one (15)	$(16.74 \pm 2.66)^{**}$	$7.91 \pm 1.20^{**}$
Diphenyleneiodonium <sup>d</sup>	$0.55 \pm 0.22^{***}$	–
Phenylmethylsulfonyl fluoride <sup>d</sup>	–	$34.5 \pm 5.3^{***}$

<sup>a</sup> Results are displayed as averages  $\pm$  SEM ( $n = 4$ ). <sup>b</sup> Concentration necessary for 50% inhibition ( $IC_{50}$ ). If  $IC_{50}$  value of tested compound was  $<10 \mu\text{g/mL}$ , it was presented as  $IC_{50} [\mu\text{g/mL}]$ . <sup>c</sup> Percentage of inhibition (Inh %) at  $10 \mu\text{g/mL}$ . If  $IC_{50}$  value of tested compound was  $\geq 10 \mu\text{g/mL}$ , it was displayed as (Inh %) at  $10 \mu\text{g/mL}$ . <sup>d</sup> Diphenyleneiodonium and phenylmethylsulfonyl were employed as positive controls for superoxide anion ( $O_2^{\bullet-}$ ) production and elastase release, respectively. \*  $p < 0.05$  compared with the control. \*\*  $p < 0.01$  compared with the control. \*\*\*  $p < 0.001$  compared with the control.

### 3. Experimental Section

#### 3.1. General Procedures

Melting points were determined on a Yanaco micromelting point apparatus and were uncorrected. Ultraviolet (UV) spectra were measured on a Jasco UV-240 spectrophotometer. Optical rotations were acquired using a Jasco DIP-370 polarimeter (Japan Spectroscopic Corporation, Tokyo, Japan) in  $\text{CHCl}_3$ . Infrared (IR) spectra (KBr or neat) were recorded on a Perkin Elmer 2000 FT-IR spectrometer (Perkin Elmer Corporation, Norwalk, CT, USA). Nuclear magnetic resonance (NMR) spectra, including correlation spectroscopy (COSY), nuclear overhauser effect spectrometry (NOESY), heteronuclear multiple-bond correlation (HMBC) experiments, and heteronuclear single-quantum coherence (HSQC), were obtained using a Varian Inova 500 spectrometer (Varian Inc., Palo Alto, CA, USA) operating at 500 MHz ( $^1\text{H}$ ) and 125 MHz ( $^{13}\text{C}$ ), respectively, with chemical shifts given in ppm ( $\delta$ ) and applying tetramethylsilane (TMS) as an internal standard. Electrospray ionization (ESI) and high-resolution electrospray ionization (HRESI)-mass spectra were recorded on a VG Platform Electrospray ESI/MS mass spectrometer (Fison, Villeurbanne, France) or a Bruker APEX II (Bruker, Bremen, Germany). Silica gel (70–230, 230–400 mesh, Merck) was used for column chromatography (CC). Silica gel 60 F-254 (Merck, Darmstadt, Germany) was employed for thin-layer chromatography (TLC) and preparative thin-layer chromatography (PTLC).

### 3.2. Plant Material

The root wood of *Hernandadia nymphaeifolia* (Presl) Kubitzki (Hernandiaceae) was collected from Mudan Township, Pingtung County, Taiwan, in August 2008 and identified by Prof. I.-S. Chen. A voucher specimen (Chen 5521) was deposited in the Herbarium of School of Pharmacy, Kaohsiung Medical University, Kaohsiung, Taiwan.

### 3.3. Extraction and Isolation

The dried root wood (5.1 kg) of *H. nymphaeifolia* was sliced and extracted three times with MeOH (40 L each) for three days. The extract was concentrated under reduced pressure at 35 °C, and the residue (386 g) was partitioned between CH<sub>2</sub>Cl<sub>2</sub> and H<sub>2</sub>O (1:1) to provide the CH<sub>2</sub>Cl<sub>2</sub>-soluble fraction (fraction A; 87 g). Fraction A (87 g) was purified by CC (3.9 kg of SiO<sub>2</sub>, 70–230 mesh; CH<sub>2</sub>Cl<sub>2</sub>/MeOH gradient) to produce 12 fractions: A1–A12. Fraction A3 (7.5 g) was subjected to CC (340 g of SiO<sub>2</sub>, 230–400 mesh; CH<sub>2</sub>Cl<sub>2</sub>/acetone 30:1–0:1, 900 mL fractions) to give 11 subfractions: A3-1–A3-11. Fraction A3-4 (340 mg) was purified by MPLC (silica column, CH<sub>2</sub>Cl<sub>2</sub>/acetone 8:1–0:1) to produce eight subfractions (each 250 mL, A3-4-1–A3-4-8). Fraction A3-4-4 (46 mg) was purified by preparative TLC (silica gel, CHCl<sub>3</sub>/MeOH, 10:1) to obtain a mixture of  $\beta$ -sitostenone (**12**) and stigmasta-4,22-dien-3-one (**13**) (8.5 mg). Fraction A5 (6.9 g) was subjected to CC (365 g of SiO<sub>2</sub>, 230–400 mesh; CH<sub>2</sub>Cl<sub>2</sub>/MeOH 15:1–0:1, 950 mL fractions) to form ten subfractions: A5-1–A5-10. Fraction A5-3 (625 mg) was purified by CC (28 g of SiO<sub>2</sub>, 230–400 mesh, CHCl<sub>3</sub>/acetone (7:1–0:1), 250 mL fractions) to give nine subfractions: A5-3-1–A5-3-9. Fraction A5-3-5 (88 mg) was further purified by preparative TLC (SiO<sub>2</sub>; CH<sub>2</sub>Cl<sub>2</sub>/acetone 8:1) to yield a mixture of 6 $\beta$ -hydroxystigmast-4-en-3-one (**14**) and 6 $\beta$ -hydroxystigmasta-4,22-dien-3-one (**15**) (3.7 mg). Fraction A7 (7.3 g) was subjected to CC (330 g of SiO<sub>2</sub>, 230–400 mesh; CHCl<sub>3</sub>/MeOH 10:1–0:1, 800 mL fractions) to give nine subfractions: A7-1–A7-9. A part (142 mg) of fraction A7-2 was further purified by preparative TLC (SiO<sub>2</sub>; CH<sub>2</sub>Cl<sub>2</sub>/MeOH 15:1) to form (–)-deoxypodophyllotoxin (**8**) (7.2 mg). A part (133 mg) of fraction A7-3 was further purified by preparative TLC (SiO<sub>2</sub>; CHCl<sub>3</sub>/MeOH 12:1) to yield (–)-yatein (**10**) (5.1 mg). A part (136 mg) of fraction A7-4 was further purified by preparative TLC (SiO<sub>2</sub>; CHCl<sub>3</sub>/MeOH 9:1) to obtain 2-O-methyl-7-oxolaetine (**3**) (5.3 mg). A part (118 mg) of fraction A7-6 was further purified by preparative TLC (SiO<sub>2</sub>; CH<sub>2</sub>Cl<sub>2</sub>/MeOH 5:1) to produce 7-oxonorisocorydine (**7**) (6.5 mg). Fraction A7-7 (650 mg) was purified by MPLC (silica column, CH<sub>2</sub>Cl<sub>2</sub>/MeOH 9:1–0:1) to form seven subfractions (each 170 mL, A7-7-1–A7-7-7). A part (112 mg) of fraction A7-7-4 was further purified by preparative TLC (SiO<sub>2</sub>; CHCl<sub>3</sub>/acetone 5:1) to form 4'-O-demethyl-7-O-methyldehydropodophyllotoxin (**2**) (5.5 mg). A part (125 mg) of fraction A7-7-5 was purified by preparative TLC (SiO<sub>2</sub>; CH<sub>2</sub>Cl<sub>2</sub>/acetone 4:1) to obtain dehydropodophyllotoxin (**9**) (6.9 mg). A part (122 mg) of fraction A7-8 was purified by preparative TLC (SiO<sub>2</sub>; CH<sub>2</sub>Cl<sub>2</sub>/EtOAc 2:1) to yield *N-trans*-feruloylmethoxytyramine (**11**) (4.9 mg). Fraction A8 (7.2 g) was subjected to CC (325 g of SiO<sub>2</sub>, 230–400 mesh; CH<sub>2</sub>Cl<sub>2</sub>/MeOH 8:1–0:1, 850 mL fractions) to give ten subfractions: A8-1–A8-10. Fraction A8-2 (530 mg) was purified by MPLC (silica column, CHCl<sub>3</sub>/MeOH 7:1–0:1) to form six subfractions (each 180 mL, A8-2-1–A8-2-6). Fraction A8-2-4 (83 mg) was further purified by preparative TLC (SiO<sub>2</sub>; CH<sub>2</sub>Cl<sub>2</sub>/acetone 6:1) to obtain hernandonine (**4**) (8.2 mg). Fraction A8-5 (135 mg) was further purified by preparative TLC (SiO<sub>2</sub>; CH<sub>2</sub>Cl<sub>2</sub>/MeOH 4:1) to obtain oxohernagine (**6**) (7.1 mg). Fraction A8-6 (135 mg) was further purified by preparative TLC (SiO<sub>2</sub>; CHCl<sub>3</sub>/MeOH 3:1) to yield oxohernangerine (**5**) (6.5 mg). Fraction A9 (6.4 g) was subjected to CC (290 g of SiO<sub>2</sub>, 230–400 mesh; CHCl<sub>3</sub>/MeOH 6:1–0:1, 1 L fractions) to obtain eight subfractions: A9-1–A9-8. A part (142 mg) of fraction A9-3 was purified by preparative TLC (SiO<sub>2</sub>; CHCl<sub>3</sub>/MeOH 5:1) to obtain 3-hydroxyhernandonine (**1**) (4.5 mg). A part (105 mg) of fraction A9-5 was purified by preparative TLC (SiO<sub>2</sub>; CH<sub>2</sub>Cl<sub>2</sub>/MeOH 4:1) to obtain oxohernangerine (**5**) (5.9 mg).

*3-Hydroxyhernandonine* (**1**): yellow needles; m.p. 268–270 °C (MeOH); UV (MeOH):  $\lambda_{\max}$  (log  $\epsilon$ ) = 220 (3.90), 268 (3.79), 284 (3.78), 343 (3.46), 362 (3.47) nm; IR (KBr):  $\nu_{\max}$  = 3315 (OH), 1652 (C=O), 1060, 969 (OCH<sub>2</sub>O) cm<sup>−1</sup>; <sup>1</sup>H-NMR (CDCl<sub>3</sub>, 500 MHz):  $\delta$  6.20 (2H, s, OCH<sub>2</sub>O-10,11), 6.28 (2H, s, OCH<sub>2</sub>O-1,2),

6.52 (1H, s, D<sub>2</sub>O exchangeable, OH-3), 7.08 (1H, d,  $J = 8.5$  Hz, H-9), 8.10 (1H, d,  $J = 5.0$  Hz, H-4), 8.28 (1H, d,  $J = 8.5$  Hz, H-8), 8.88 (1H, d,  $J = 5.0$  Hz, H-5); <sup>13</sup>C-NMR (CDCl<sub>3</sub>, 125 MHz):  $\delta$  101.3 (OCH<sub>2</sub>O-1,2), 101.7 (OCH<sub>2</sub>O-10,11), 108.6 (C-9), 114.9 (C-11b), 118.7 (C-8), 119.1 (C-4), 122.3 (C-11a), 122.9 (C-11c), 123.9 (C-3a), 127.6 (C-7a), 139.2 (C-2), 145.2 (C-5), 145.8 (C-11), 148.4 (C-3), 149.6 (C-1), 150.4 (C-10), 157.3 (C-6a), 182.5 (C-7); ESI-MS:  $m/z = 358$  [M + Na]<sup>+</sup>; HR-ESI-MS:  $m/z = 358.0325$  [M + Na]<sup>+</sup> (calcd for C<sub>18</sub>H<sub>9</sub>NO<sub>6</sub>Na, 358.0328).

*4'-O-Demethyl-7-O-methyldehydropodophyllotoxin (2)*: colorless needles; m.p. 273–275 °C (MeOH); UV (MeOH):  $\lambda_{\max}$  (log  $\epsilon$ ) = 223 (4.47), 262 (4.58), 321 (3.98), 355 (3.69) nm; IR (KBr):  $\nu_{\max} = 3452$  (OH), 1764 (C=O) cm<sup>-1</sup>; <sup>1</sup>H-NMR (CDCl<sub>3</sub>, 500 MHz):  $\delta$  3.88 (6H, s, OMe-3' and OMe-5'), 4.09 (3H, s, OMe-7), 5.52 (2H, s, H-9), 5.65 (1H, br s, D<sub>2</sub>O exchangeable, OH-4'), 6.09 (2H, s, OCH<sub>2</sub>O), 6.57 (2H, s, H-2' and H-6'), 7.07 (1H, s, H-5), 7.57 (1H, s, H-2); <sup>13</sup>C-NMR (CDCl<sub>3</sub>, 125 MHz):  $\delta$  56.0 (OMe-3'), 56.0 (OMe-5'), 59.9 (OMe-7), 66.4 (C-9), 98.4 (C-2), 101.8 (OCH<sub>2</sub>O), 103.9 (C-5), 107.7 (C-2'), 107.7 (C-6'), 119.5 (C-8'), 125.8 (C-8), 127.8 (C-6), 130.4 (C-1), 132.2 (C-1'), 133.6 (C-4'), 137.7 (C-7'), 148.5 (C-7), 148.9 (C-4), 148.9 (C-3'), 148.9 (C-5'), 150.0 (C-3), 169.3 (C-9'); ESI-MS:  $m/z = 433$  [M + Na]<sup>+</sup>; HR-ESI-MS:  $m/z = 433.0898$  [M + Na]<sup>+</sup> (calcd for C<sub>22</sub>H<sub>18</sub>O<sub>8</sub>Na, 433.0899).

*2-O-Methyl-7-oxolaetene (3)*: yellow needles; m.p. > 300 °C (MeOH); UV (MeOH):  $\lambda_{\max}$  (log  $\epsilon$ ) = 221 (4.49), 266 (4.33), 362 (4.00), 427 (3.95) nm; IR (KBr):  $\nu_{\max} = 1652$  (C=O) cm<sup>-1</sup>; <sup>1</sup>H-NMR (CDCl<sub>3</sub>, 400 MHz):  $\delta$  3.93 (3H, s, OMe-1), 6.21 (2H, s, OCH<sub>2</sub>O-10,11), 7.08 (1H, d,  $J = 8.4$  Hz, H-9), 7.21 (1H, s, H-3), 7.77 (1H, d,  $J = 5.2$  Hz, H-4), 8.24 (1H, d,  $J = 8.4$  Hz, H-8), 8.86 (1H, d,  $J = 5.2$  Hz, H-5); ESI-MS:  $m/z = 358$  [M + Na]<sup>+</sup>; HR-ESI-MS:  $m/z = 358.0692$  [M + Na]<sup>+</sup> (calcd for C<sub>19</sub>H<sub>13</sub>O<sub>5</sub>Na, 358.0691).

*Hernandonine (4)*: yellow needles; m.p. > 350 °C (CH<sub>2</sub>Cl<sub>2</sub>-MeOH); UV (MeOH):  $\lambda_{\max}$  (log  $\epsilon$ ) = 222 (4.50), 265 (4.34), 295 (sh, 3.90), 312 (sh, 3.63), 364 (4.02), 428 (3.97) nm; IR (KBr):  $\nu_{\max} = 1651$  (C=O), 1062, 971 (OCH<sub>2</sub>O) cm<sup>-1</sup>; <sup>1</sup>H-NMR (CDCl<sub>3</sub>, 500 MHz):  $\delta$  6.20 (2H, s, OCH<sub>2</sub>O-10,11), 6.28 (2H, s, OCH<sub>2</sub>O-1,2), 7.08 (1H, d,  $J = 8.5$  Hz, H-9), 7.21 (1H, s, H-3), 7.74 (1H, d,  $J = 5.0$  Hz, H-4), 8.29 (1H, d,  $J = 8.5$  Hz, H-8), 8.85 (1H, d,  $J = 5.0$  Hz, H-5); ESI-MS:  $m/z = 342$  [M + Na]<sup>+</sup>.

*Oxohernangerine (5)*: yellow prisms; m.p. 257–258 °C (MeOH); UV (MeOH):  $\lambda_{\max}$  (log  $\epsilon$ ) = 211 (4.55), 252 (4.46), 268 (sh, 4.42), 316 (3.87), 362 (4.04), 408 (4.02), 477 (3.55) nm; IR (KBr):  $\nu_{\max} = 3415$  (OH), 1642 (C=O) cm<sup>-1</sup>; <sup>1</sup>H-NMR (CDCl<sub>3</sub>, 400 MHz):  $\delta$  3.68 (3H, s, OMe-11), 6.32 (2H, s, OCH<sub>2</sub>O-1,2), 7.24 (1H, d,  $J = 8.4$  Hz, H-9), 7.27 (1H, s, H-3), 7.76 (1H, d,  $J = 5.2$  Hz, H-4), 8.37 (1H, d,  $J = 8.4$  Hz, H-8), 8.86 (1H, d,  $J = 5.2$  Hz, H-5); ESI-MS:  $m/z = 344$  [M + Na]<sup>+</sup>.

*Oxohernagine (6)*: yellow prisms; m.p. 253–255 °C (MeOH); UV (MeOH):  $\lambda_{\max}$  (log  $\epsilon$ ) = 213 (4.51), 274 (4.41), 361 (3.95), 403 (3.92) nm; IR (KBr):  $\nu_{\max} = 3424$  (OH), 1650 (C=O) cm<sup>-1</sup>; <sup>1</sup>H-NMR (CDCl<sub>3</sub>, 400 MHz):  $\delta$  3.54 (3H, s, OMe-1), 3.76 (3H, s, OMe-11), 4.11 (3H, s, OMe-2), 7.21 (1H, s, H-3), 7.22 (1H, d,  $J = 8.4$  Hz, H-9), 7.77 (1H, d,  $J = 5.2$  Hz, H-4), 8.31 (1H, d,  $J = 8.4$  Hz, H-8), 8.86 (1H, d,  $J = 5.2$  Hz, H-5); ESI-MS:  $m/z = 360$  [M + Na]<sup>+</sup>.

*7-Oxonorisocorydine (7)*: yellow needles; m.p. 250–252 °C (EtOAc); UV (MeOH):  $\lambda_{\max}$  (log  $\epsilon$ ) = 212 (4.49), 273 (4.40), 362 (3.94), 403 (3.90) nm; IR (KBr):  $\nu_{\max} = 3385$  (OH), 1653 (C=O) cm<sup>-1</sup>; <sup>1</sup>H-NMR (CDCl<sub>3</sub>, 400 MHz):  $\delta$  3.53 (3H, s, OMe-1), 4.03 (3H, s, OMe-10), 4.08 (3H, s, OMe-2), 7.14 (1H, d,  $J = 8.4$  Hz, H-9), 7.23 (1H, s, H-3), 7.77 (1H, d,  $J = 5.2$  Hz, H-4), 8.28 (1H, d,  $J = 8.4$  Hz, H-8), 8.86 (1H, d,  $J = 5.2$  Hz, H-5); ESI-MS:  $m/z = 360$  [M + Na]<sup>+</sup>.

*(-)-Deoxypodophyllotoxin (8)*: colorless needles; m.p. 168–170 °C (MeOH); UV (MeOH):  $\lambda_{\max}$  (log  $\epsilon$ ) = 212 (4.62), 291 (3.68) nm; IR (KBr):  $\nu_{\max} = 1765$  (C=O), 1581, 1502, 1474 (aromatic ring C=C stretch), 1032, 941 (OCH<sub>2</sub>O) cm<sup>-1</sup>; <sup>1</sup>H-NMR (CDCl<sub>3</sub>, 500 MHz):  $\delta$  2.73 (3H, m, H-7, H-8, and H-8'), 3.07 (1H, m, H-7), 3.75 (6H, s, OMe-3' and OMe-5'), 3.80 (3H, s, OMe-4'), 3.92 (1H, m, H-9), 4.46 (1H, m, H-9), 4.60 (1H, d,  $J = 3.5$  Hz, H-7'), 5.93, 5.95 (each 1H, each d,  $J = 1.5$  Hz, OCH<sub>2</sub>O), 6.34 (2H, s, H-2' and H-6'), 6.52 (1H, s, H-5), 6.67 (1H, s, H-2); ESI-MS:  $m/z = 421$  [M + Na]<sup>+</sup>.

*Dehydriopodophyllotoxin (9)*: colorless needles; m.p. 264–266 °C (CH<sub>2</sub>Cl<sub>2</sub>-MeOH); UV (MeOH):  $\lambda_{\max}$  (log  $\epsilon$ ) = 262 (4.57), 311 (3.95), 321 (3.97) nm; IR (KBr):  $\nu_{\max}$  = 3421 (OH), 1762 (C=O) cm<sup>-1</sup>; <sup>1</sup>H-NMR (CDCl<sub>3</sub>, 500 MHz):  $\delta$  3.83 (6H, s, OMe-3', and OMe-5'), 3.95 (3H, s, OMe-4'), 5.37 (2H, br s, H-9), 5.68 (1H, br s, D<sub>2</sub>O exchangeable, OH-7), 6.10 (2H, s, OCH<sub>2</sub>O), 6.52 (2H, s, H-2', and H-6'), 7.09 (1H, s, H-5), 7.49 (1H, s, H-2); ESI-MS:  $m/z$  = 433 [M + Na]<sup>+</sup>.

(-)-*Yatein (10)*: yellowish solid (MeOH); UV (MeOH):  $\lambda_{\max}$  (log  $\epsilon$ ) = 212 (4.35), 230 (sh, 3.93), 287 (3.47) nm; IR (KBr):  $\nu_{\max}$  = 1764 (C=O), 1591, 1502, 1488 (aromatic ring C=C stretch), 1037, 925 (OCH<sub>2</sub>O) cm<sup>-1</sup>; <sup>1</sup>H-NMR (CDCl<sub>3</sub>, 400 MHz):  $\delta$  2.49 (1H, m, H-8), 2.53 (1H, m, H-7 $\alpha$ ), 2.58 (1H, m, H-8'), 2.62 (1H, dd,  $J$  = 13.2, 6.4 Hz, H-7 $\beta$ ), 2.89 (1H, dd,  $J$  = 14.0, 6.2 Hz, H-7' $\alpha$ ), 2.93 (1H, dd,  $J$  = 14.0, 5.2 Hz, H-7' $\beta$ ), 3.82 (6H, s, OMe-3', and OMe-5'), 3.83 (3H, s, OMe-4'), 3.88 (1H, dd,  $J$  = 9.2, 7.6 Hz, H-9 $\beta$ ), 4.18 (1H, dd,  $J$  = 9.2, 7.2 Hz, H-9 $\alpha$ ), 5.93, 5.94 (each 1H, each d,  $J$  = 1.2 Hz, OCH<sub>2</sub>O), 6.36 (2H, s, H-2', and H-6'), 6.46 (1H, d,  $J$  = 1.6 Hz, H-2), 6.47 (1H, dd,  $J$  = 7.6, 1.6 Hz, H-6), 6.69 (1H, d,  $J$  = 7.6 Hz, H-5); ESI-MS:  $m/z$  = 423 [M + Na]<sup>+</sup>.

*N-trans-Feruloylmethoxytyramine (11)*: white needles; m.p. 112–114 °C (CHCl<sub>3</sub>-MeOH); UV (MeOH):  $\lambda_{\max}$  (log  $\epsilon$ ) = 221 (3.61), 290 (2.86), 319 (3.34) nm; IR (KBr):  $\nu_{\max}$  = 3362 (OH), 1652 (C=O) cm<sup>-1</sup>; <sup>1</sup>H-NMR (CDCl<sub>3</sub>, 400 MHz):  $\delta$  2.82 (2H, t,  $J$  = 6.8 Hz, H-11), 3.62 (2H, q,  $J$  = 6.8 Hz, H-10), 3.88 (3H, s, OMe-14), 3.92 (3H, s, OMe-3), 5.52 (1H, br t,  $J$  = 6.8 Hz, D<sub>2</sub>O exchangeable, NH), 5.53 (1H, s, D<sub>2</sub>O exchangeable, OH), 5.79 (1H, s, D<sub>2</sub>O exchangeable, OH), 6.16 (1H, d,  $J$  = 15.6 Hz, H-8), 6.71 (1H, dd,  $J$  = 8.0, 1.6 Hz, H-17), 6.73 (1H, d,  $J$  = 1.6 Hz, H-13), 6.87 (1H, d,  $J$  = 8. Hz, H-16), 6.90 (1H, d,  $J$  = 8.4 Hz, H-5), 6.97 (1H, d,  $J$  = 1.6 Hz, H-2), 7.04 (1H, dd,  $J$  = 8.4, 1.6 Hz, H-5), 7.53 (1H, d,  $J$  = 15.6 Hz, H-7); ESI-MS:  $m/z$  = 366 [M + Na]<sup>+</sup>.

*Mixture of  $\beta$ -Sitostenone (12) and stigmasta-4,22-dien-3-one (13)*: colorless needles; m.p. 88–90 °C (MeOH);  $[\alpha]_D^{25}$  = +85.8° ( $c$  0.18, CHCl<sub>3</sub>); UV (MeOH):  $\lambda_{\max}$  (log  $\epsilon$ ) = 242 (4.21); IR (KBr):  $\nu_{\max}$  = 1685 (C=O) cm<sup>-1</sup>; <sup>1</sup>H-NMR (CDCl<sub>3</sub>, 400 MHz) of **12**:  $\delta$  0.70 (3H, s, H-18), 0.81 (3H, d,  $J$  = 6.8 Hz, H-27), 0.83 (3H, d,  $J$  = 6.8 Hz, H-26), 0.86 (3H, t,  $J$  = 7.2 Hz, H-29), 0.92 (3H, d,  $J$  = 6.4 Hz, H-21), 1.18 (3H, s, H-19), 5.71 (1H, s, H-4); <sup>1</sup>H-NMR (CDCl<sub>3</sub>, 400 MHz) of **13**:  $\delta$  0.72 (3H, s, H-18), 0.79 (3H, d,  $J$  = 6.8 Hz, H-27), 0.82 (3H, t,  $J$  = 7.2 Hz, H-29), 0.83 (3H, d,  $J$  = 6.8 Hz, H-26), 1.02 (3H, d,  $J$  = 6.8 Hz, H-21), 1.18 (3H, s, H-19), 5.02 (1H, dd,  $J$  = 15.2, 8.8 Hz, H-23), 5.14 (1H, dd,  $J$  = 15.2, 8.8 Hz, H-22), 5.71 (1H, s, H-4); ESI-MS of **12**:  $m/z$  = 435 [M + Na]<sup>+</sup>; ESI-MS of **13**:  $m/z$  = 433 [M + Na]<sup>+</sup>.

*Mixture of 6 $\beta$ -Hydroxystigmasta-4-en-3-one (14) and 6 $\beta$ -hydroxystigmasta-4,22-dien-3-one (15)*: colorless needles; m.p. 208–209 °C (CH<sub>2</sub>Cl<sub>2</sub>-MeOH);  $[\alpha]_D^{25}$  = +29.7° ( $c$  0.17, CHCl<sub>3</sub>); UV (MeOH):  $\lambda_{\max}$  (log  $\epsilon$ ) = 235 (4.11) nm; IR (KBr):  $\nu_{\max}$  = 3412 (OH), 1679 (C=O) cm<sup>-1</sup>; <sup>1</sup>H-NMR (CDCl<sub>3</sub>, 400 MHz) of **14**:  $\delta$  0.74 (3H, s, H-18), 0.81 (3H, d,  $J$  = 6.8 Hz, H-27), 0.84 (3H, d,  $J$  = 7.2 Hz, H-26), 0.87 (3H, t,  $J$  = 7.2 Hz, H-29), 0.92 (3H, d,  $J$  = 6.4 Hz, H-21), 1.38 (3H, s, H-19), 4.35 (1H, br s, H-6), 5.82 (1H, s, H-4); <sup>1</sup>H-NMR (CDCl<sub>3</sub>, 500 MHz) of **15**:  $\delta$  0.76 (3H, s, H-18), 0.80 (3H, d,  $J$  = 6.8 Hz, H-27), 0.81 (3H, d,  $J$  = 6.8 Hz, H-26), 0.85 (3H, t,  $J$  = 7.2 Hz, H-29), 1.02 (3H, d,  $J$  = 6.8 Hz, H-21), 1.38 (3H, s, H-19), 4.35 (1H, br s, H-6), 5.03 (1H, dd,  $J$  = 15.2, 8.6 Hz, H-23), 5.15 (1H, dd,  $J$  = 15.2, 8.6 Hz, H-22), 5.82 (1H, s, H-4); ESI-MS of **14**:  $m/z$  = 451 [M + Na]<sup>+</sup>; ESI-MS of **15**:  $m/z$  = 449 [M + Na]<sup>+</sup>.

### 3.4. Biological Assay

The effect of the isolates on the neutrophil proinflammatory response was assessed by detecting the inhibition of elastase release and O<sub>2</sub><sup>•-</sup> generation in fMLP/CB-activated neutrophils in a concentration-dependent manner.

#### 3.4.1. Mensuration of Human Neutrophils

Human neutrophils from the venous blood of adult, healthy volunteers (20–27 years old) were isolated by a standard pattern of dextran sedimentation before centrifugation in a Ficoll Hypaque gradient and hypotonic lysis of the erythrocytes [27]. The purified neutrophils had >98% viable cells,



as detected by the trypan blue exclusion method [28], were resuspended in a calcium ( $\text{Ca}^{2+}$ )-free HBSS buffer at pH 7.4 and were kept at 4 °C prior to use.

#### 3.4.2. Mensuration of Superoxide Anion ( $\text{O}_2^{\bullet-}$ ) Generation

The assay for the measurement of  $\text{O}_2^{\bullet-}$  generation was based on the superoxide dismutase (SOD)-inhibitable reduction of ferricytochrome *c* [29,30]. In short, after supplementation with 1 mM  $\text{Ca}^{2+}$  and 0.5 mg/mL ferricytochrome *c*, neutrophils ( $6 \times 10^5/\text{mL}$ ) were equilibrated at 37 °C for 2 min and incubated with varied concentrations (10–0.01  $\mu\text{g}/\text{mL}$ ) of either DMSO (as a control) or tested compounds **1–15** (purity  $\geq 98\%$ ) for 5 min. Cells were incubated with cytochalasin B (1  $\mu\text{g}/\text{mL}$ ) for 3 min before they were activated with 100 nM formyl-L-methionyl-L-leucyl-L-phenylalanine for 10 min. Changes in absorbance with the reduction of ferricytochrome *c* at 550 nm were constantly detected in a double-beam, six-cell positioner spectrophotometer with continuous stirring (Hitachi U-3010, Tokyo, Japan). Calculations were founded on differences in the reactions with and without SOD (100 U/mL) divided by the extinction coefficient for the reduction of ferricytochrome *c* ( $\epsilon = 21.1/\text{mM}/10 \text{ mm}$ ).

#### 3.4.3. Mensuration of Elastase Release

The degranulation of azurophilic granules was measured by determining elastase release as reported previously [30,31]. Assays were carried out by applying MeO-Suc-Ala-Ala-Pro-Val-*p*-nitroanilide as the elastase substrate. In brief, after supplementation with MeO-Suc-Ala-Ala-Pro-Val-*p*-nitroanilide (100  $\mu\text{M}$ ), neutrophils ( $6 \times 10^5/\text{mL}$ ) were equilibrated at 37 °C for 2 min and incubated with tested compounds for 5 min. Cells were treated with fMLP (100 nM)/CB (0.5  $\mu\text{g}/\text{mL}$ ), and the changes in absorbance at 405 nm were detected constantly in order to measure elastase release. The results were displayed as the percent of elastase release in the fMLP/CB-activated, drug-free control system.

#### 3.4.4. Statistical Analysis

Results are represented as mean  $\pm$  SEM, and comparisons were done by applying student's *t*-test. A probability of 0.05 or less was deemed significant. The software SigmaPlot was employed for the statistical analysis.

### 4. Conclusions

Fifteen compounds, including a new aporphine, 3-hydroxyhernandonine (**1**), and a new lignin, 4'-*O*-demethyl-7-*O*-methyldehydropodophyllotoxin (**2**), were isolated from the resinous wood of the root wood of *H. nymphaeifolia*. The structures of these isolates were elucidated according to spectroscopic data. Granule proteases (e.g., cathepsin G, elastase) and reactive oxygen species (ROS) [e.g., hydrogen peroxide, superoxide anion ( $\text{O}_2^{\bullet-}$ )] generated by human neutrophils gave rise to the pathogenesis of inflammatory diseases. The effects of the isolated compounds on proinflammatory responses were assessed by inhibiting fMLP/CB-induced elastase release and  $\text{O}_2^{\bullet-}$  generation by neutrophils. The results of anti-inflammatory assays reveal that compounds **1–7** and **11** can obviously inhibit fMLP-induced elastase release and/or  $\text{O}_2^{\bullet-}$  generation. Oxohernangerine (**5**) and 3-hydroxyhernandonine (**1**) were the most effective among the isolated compounds, with  $\text{IC}_{50}$  values of  $2.65 \pm 0.97$  and  $3.93 \pm 0.48 \mu\text{g}/\text{mL}$ , respectively, against fMLP-induced  $\text{O}_2^{\bullet-}$  generation and elastase release. Our research indicates *H. nymphaeifolia* and its isolated compounds (especially **1–7** and **11**) are worth further study and may be expectantly developed as candidates for the prevention or treatment of diverse inflammatory diseases.

**Supplementary Materials:** Supplementary materials are available online, Figures S1–S8: MS, 1D, and 2D-NMR spectra for 3-hydroxyhernandonine (**1**), Figures S9–S16: MS, 1D, and 2D-NMR spectra for 4'-*O*-demethyl-7-*O*-methyldehydropodophyllotoxin (**2**).

**Author Contributions:** C.-Y.W. and J.-J.C. performed the isolation and structure elucidation of the constituents and manuscript writing. C.-Y.W., S.-W.W., J.-W.Y., T.-L.H., M.-J.C., P.-J.S., T.-H.C., and J.-J.C. conducted the bioassay and analyzed the data. J.-J.C. planned, designed, and organized all of the research of this study and the preparation of the manuscript. All authors read and approved the final version of the manuscript.

**Acknowledgments:** This research was supported by grants from the Ministry of Science and Technology, Taiwan (No. MOST 106-2320-B-010-033-MY3 and MOST 105-2320-B-010-040), awarded to J.-J. Chen. This work was also supported by the grants from Chang Gung Memorial Hospital (CMRPD1B0281~3, CMRPF1D0442~3, CMRPF1F0011~3, CMRPF1F0061~3 and BMRP450). We are grateful to Ih-Sheng Chen for unselfishly providing us with plant material (root wood of *H. nymphaeifolia*).

**Conflicts of Interest:** The authors declare no conflict of interest.

## References

- Yang, Y.P.; Lu, S.Y. Hernandiaceae. In *Flora of Taiwan*, 2nd ed.; Editorial Committee of the Flora of Taiwan: Taipei, Taiwan, 1996; Volume 2, pp. 500–503. ISBN 957-9019-52-5.
- Kan, W.S. *Manual of Medicinal Plants in Taiwan*; National Research Institute of Chinese Medicine: Taipei, Taiwan, 1970; pp. 178–179.
- Chen, J.J.; Tsai, I.L.; Ishikawa, T.; Wang, C.J.; Chen, I.S. Alkaloids from trunk bark of *Hernandia nymphaeifolia*. *Phytochemistry* **1996**, *42*, 1479–1484. [[CrossRef](#)]
- Chen, J.J.; Ishikawa, T.; Duh, C.Y.; Tsai, I.L.; Chen, I.S. New dimeric aporphine alkaloids and cytotoxic constituents of *Hernandia nymphaeifolia*. *Planta Med.* **1996**, *62*, 528–533. [[CrossRef](#)] [[PubMed](#)]
- Chen, I.S.; Chen, J.J.; Duh, C.Y.; Tsai, I.L.; Chang, C.T. New aporphine alkaloids and cytotoxic constituents of *Hernandia nymphaeifolia*. *Planta Med.* **1997**, *63*, 154–157. [[CrossRef](#)] [[PubMed](#)]
- Chen, J.J.; Chang, Y.L.; Teng, C.M.; Chen, I.S. Vasorelaxing and antioxidant constituents from *Hernandia nymphaeifolia*. *Planta Med.* **2001**, *67*, 593–598. [[CrossRef](#)] [[PubMed](#)]
- Chen, J.J.; Chang, Y.L.; Teng, C.M.; Chen, I.S. Anti-platelet aggregation alkaloids and lignans from *Hernandia nymphaeifolia*. *Planta Med.* **2000**, *66*, 251–256. [[CrossRef](#)] [[PubMed](#)]
- Chen, I.S.; Chen, J.J.; Duh, C.Y.; Tsai, I.L. New cytotoxic lignans from Formosan *Hernandia nymphaeifolia*. *Phytochemistry* **1997**, *45*, 991–996. [[CrossRef](#)]
- Ennis, M. Neutrophils in asthma pathophysiology. *Curr. Allergy Asthma Rep.* **2003**, *3*, 159–165. [[CrossRef](#)] [[PubMed](#)]
- Borregaard, N. The human neutrophil. Function and dysfunction. *Eur. J. Haematol.* **1998**, *41*, 401–413. [[CrossRef](#)]
- Witko-Sarsat, V.; Rieu, P.; Descamps-Latscha, B.; Lesavre, P.; Halbwachs-Mecarelli, L. Neutrophils: Molecules, functions and pathophysiological aspects. *Lab. Invest.* **2000**, *80*, 617–653. [[CrossRef](#)]
- Roos, D.; van Bruggen, R.; Meischl, C. Oxidative killing of microbes by neutrophils. *Microbes Infect.* **2003**, *5*, 1307–1315. [[CrossRef](#)] [[PubMed](#)]
- Furukawa, H.; Ueda, F.; Ito, M.; Ishii, H.; Hagiwara, J. Alkaloids of *Hernandia ovigera*. IV. Constituents of *Hernandia ovigera* collected in the Bonin Islands. *Yakugaku Zasshi* **1972**, *92*, 150–154. [[CrossRef](#)] [[PubMed](#)]
- Yang, T.H.; Liu, S.C.; Lin, T.S.; Yang, L.M. Studies on the constituents of the root-bark of *Hernandia ovigera* L. III. *J. Chin. Chem. Soc.* **1976**, *23*, 29–34. [[CrossRef](#)]
- Atta-ur-Rahman; Ashraf, M.; Choudhary, M.I.; Habib-ur-Rehman; Kazmi, M.H. Antifungal aryltetralin lignans from leaves of *Podophyllum hexandrum*. *Phytochemistry* **1995**, *40*, 427–431. [[CrossRef](#)]
- Orito, K.; Uchiito, S.; Satoh, Y.; Tatsuzawa, T.; Harada, R.; Tokuda, M. Aryl radical cyclizations of 1-(2'-bromobenzyl) isoquinolines with AIBN-Bu<sub>3</sub>SnH: Formation of aporphines and indolo[2,1-*a*]isoquinolines. *Org. Lett.* **2000**, *2*, 307–310. [[CrossRef](#)] [[PubMed](#)]
- Chen, J.J.; Tsai, I.L.; Chen, I.S. New oxoaporphine alkaloids from *Hernandia nymphaeifolia*. *J. Nat. Prod.* **1996**, *59*, 156–158. [[CrossRef](#)]
- Kametani, T.; Nitadori, R.; Terasawa, H.; Takahashi, K.; Ihara, M.; Fukumoto, K. Studies on the syntheses of heterocyclic compounds—DCXCIII: A total synthesis of atheroline by photolysis. *Tetrahedron* **1977**, *33*, 1069–1071. [[CrossRef](#)]
- Yamaguchi, H.; Arimoto, M.; Yamamoto, K.; Numata, A. Studies on the constituents of the seeds of *Hernandia ovigera* L. *Yakugaku Zasshi* **1979**, *99*, 674–677. [[CrossRef](#)] [[PubMed](#)]

20. Tanoguchi, M.; Arimoto, M.; Saika, H.; Yamaguchi, H. Studies on the constituents of the seeds of *Hernandia ovigera* L. VI. Isolation and structural determination of three lignans. *Chem. Pharm. Bull.* **1987**, *35*, 4162–4168. [[CrossRef](#)]
21. Ito, C.; Matsui, T.; Wu, T.S.; Furukawa, H. Isolation of 6,7-demethyl-enedesoxypodophyllotoxin from *Hernandia ovigera*. *Chem. Pharm. Bull.* **1992**, *40*, 1318–1321. [[CrossRef](#)]
22. Chen, C.Y.; Wang, Y.D.; Wang, H.M. Chemical constituents from the roots of *Synsepalum dulcificum*. *Chem. Nat. Compd.* **2010**, *46*, 46–448. [[CrossRef](#)]
23. Chen, C.Y.; Chang, F.R.; Wu, Y.C. The constituents from the stems of *Annona cherimola*. *J. Chin. Chem. Soc.* **1997**, *44*, 313–319. [[CrossRef](#)]
24. Sun, X.B.; Zhao, P.H.; Xu, Y.J.; Sun, L.M.; Cao, M.A.; Yuan, C.S. Chemical constituents from the roots of *Polygonum bistorta*. *Chem. Nat. Compd.* **2007**, *43*, 563–566. [[CrossRef](#)]
25. Ayyad, S.N. A new cytotoxic stigmastane steroid from *Pistia stratiotes*. *Pharmazie* **2002**, *57*, 212–214. [[PubMed](#)]
26. Chen, C.H.; Hwang, T.L.; Chen, L.C.; Chang, T.H.; Wei, C.S.; Chen, J.J. Isoflavones and anti-inflammatory constituents from the fruits of *Psoralea corylifolia*. *Phytochemistry* **2017**, *143*, 186–193. [[CrossRef](#)] [[PubMed](#)]
27. Boyum, A. Isolation of mononuclear cells and granulocytes from human blood. Isolation of monuclear cells by one centrifugation, and of granulocytes by combining centrifugation and sedimentation at 1 g. *Scand. J. Clin. Lab. Investig.* **1968**, *97*, 77–89.
28. Jauregui, H.O.; Hayner, N.T.; Driscoll, J.L.; Williams-Holland, R.; Lipsky, M.H.; Galletti, P.M. Trypan blue dye uptake and lactate dehydrogenase in adult rat hepatocytes-freshly isolated cells, cell suspensions, and primary monolayer cultures. *In Vitro* **1981**, *17*, 1100–1110. [[CrossRef](#)] [[PubMed](#)]
29. Babior, B.M.; Kipnes, R.S.; Curnutte, J.T. Biological defense mechanisms. The production by leukocytes of superoxide, a potential bactericidal agent. *J. Clin. Investig.* **1973**, *52*, 741–744. [[CrossRef](#)] [[PubMed](#)]
30. Hwang, T.L.; Leu, Y.L.; Kao, S.H.; Tang, M.C.; Chang, H.L. Viscolin, a new chalcone from *Viscum coloratum*, inhibits human neutrophil superoxide anion and elastase release via a cAMP-dependent pathway. *Free Radic. Biol. Med.* **2006**, *41*, 1433–1441. [[CrossRef](#)] [[PubMed](#)]
31. Chen, J.J.; Ting, C.W.; Wu, Y.C.; Hwang, T.L.; Cheng, M.J.; Sung, P.J.; Wang, T.C.; Chen, J.F. New labdane-type diterpenoids and anti-inflammatory constituents from *Hedychium coronarium*. *Int. J. Mol. Sci.* **2013**, *14*, 13063–13077. [[CrossRef](#)] [[PubMed](#)]

**Sample Availability:** Samples of the compounds are available from the authors.



© 2018 by the authors. Licensee MDPI, Basel, Switzerland. This article is an open access article distributed under the terms and conditions of the Creative Commons Attribution (CC BY) license (<http://creativecommons.org/licenses/by/4.0/>).



# Targeting sialic acid residues on lung cancer cells by inhalable boronic acid-decorated albumin nanocomposites for combined chemo/herbal therapy

Mayada M. Elgohary<sup>a,b</sup>, Maged W. Helmy<sup>a,c</sup>, Elsayeda-Zeinab A. Abdelfattah<sup>d</sup>, Doaa M. Ragab<sup>b</sup>, Sana M. Mortada<sup>a,b</sup>, Jia-You Fang<sup>e,f,g,\*\*</sup>, Ahmed O. Elzoghby<sup>a,b,h,i,\*</sup>

<sup>a</sup> Cancer Nanotechnology Research Laboratory (CNRL), Faculty of Pharmacy, Alexandria University, Alexandria 21521, Egypt

<sup>b</sup> Department of Industrial Pharmacy, Faculty of Pharmacy, Alexandria University, Alexandria 21521, Egypt

<sup>c</sup> Department of Pharmacology and Toxicology, Faculty of Pharmacy, Damanhour University, Damanhour, Egypt

<sup>d</sup> Medical Research Institute (MRI), Alexandria University, Alexandria 21527, Egypt

<sup>e</sup> Pharmaceutics Laboratory, Graduate Institute of Natural Products, Chang Gung University, Taoyuan 333, Taiwan

<sup>f</sup> Research Center for Industry of Human Ecology and Research Center for Chinese Herbal Medicine, Chang Gung University of Science and Technology, Kweishan, Taoyuan 333, Taiwan

<sup>g</sup> Department of Anesthesiology, Chang Gung Memorial Hospital, Kweishan, Taoyuan 333, Taiwan

<sup>h</sup> Division of Engineering in Medicine, Department of Medicine, Brigham and Women's Hospital, Harvard Medical School, Boston, MA 02115, USA

<sup>i</sup> Harvard-MIT Division of Health Sciences and Technology, Cambridge, MA 02139, USA

## ARTICLE INFO

### Keywords:

Albumin nanoparticles  
Inhalable nanocomposites  
Drug-phospholipid complex  
Phenylboronic targeting  
Pulmonary drug delivery  
Lung cancer

## ABSTRACT

Etoposide (ETP), as a potential treatment for lung cancer, has limited application due to its poor solubility, and systemic side effects. In the current study, we propose inhalable boronate-targeted HSA nanocomposites for combined delivery of ETP and the herbal drug, berberine (BER) for localized therapy of lung cancer. First, ETP was pre-formulated as phospholipid complex (EPC) to enhance drug solubility and facilitate its encapsulation within the hydrophilic albumin nanoparticles (NPs). Second, EPC and BER were then co-loaded with high efficiency into HSA NPs as a synergistic therapy for lung cancer. The NPs displayed suitable size around 200 nm and sequential drug release pattern. Moreover, conjugation of aminophenylboronic acid (APBA) to HSA NPs resulted in enhanced cytotoxicity and internalization into A549 lung cancer cells, compared to non-targeted NPs or free drugs via binding to sialic acid residues over-expressed by cancer cells. Using mannitol as a spray-drying carrier, the developed inhalable nanocomposites demonstrated deep pulmonary deposition, confirmed by small MMAD (2.112  $\mu\text{m}$ ) and high FPF (77.86%). In vivo investigations in lung cancer animal models revealed the superior anti-tumor efficacy of the inhalable nanocomposites. Overall, the inhalable APBA-HSA nanocomposites offered an alternative strategy for systemic delivery of ETP and BER in lung cancer therapy.

## 1. Introduction

Lung cancer is considered to be the most serious type of cancer, as it presents the highest percentage of cancer-related death worldwide. Conventional chemotherapy and radiation are widely used as a protocol of treatment. However, those strategies suffer from non-specificity to cancer cells and serious side effects which limit their application. Therefore, considerable research is being directed towards the development of a novel regimen to overcome these limitations [1].

As a promising alternative to systemic therapy, inhalational chemotherapeutics provide a localized therapy for lung tumors with the

benefit of avoiding the side effects of intravenous administration and delivery of high drugs doses [2]. Nanoparticles (NPs) encapsulating anti-cancer drugs possess the advantages of high cellular penetration, avoiding uptake by macrophages, increased drug loading and sustained release behavior [3–5]. However, the small particle size of NPs leads to their quick exhalation thus limiting their application for pulmonary administration [6]. On another avenue, development of inhalable microparticles encapsulating cytotoxic compounds ensures efficient lung deposition [7]. This signifies the rationale of developing nanoparticles-in-microparticles (nanocomposites), as they possess the advantages of both microparticles, to enable effective aerosolization and deep lung

\* Correspondence to: Ahmed O. Elzoghby, Division of Engineering in Medicine, Department of Medicine, Brigham and Women's Hospital, Harvard Medical School, Boston, MA 02115, USA.

\*\* Correspondence to: Jia-You Fang, Graduate Institute of Natural Products, Chang Gung University, Taoyuan 333, Taiwan.

E-mail addresses: [fajy@mail.cgu.edu.tw](mailto:fajy@mail.cgu.edu.tw) (J.-Y. Fang), [aelzoghby@bwh.harvard.edu](mailto:aelzoghby@bwh.harvard.edu), [ahmed\\_elzoghby@alexu.edu.eg](mailto:ahmed_elzoghby@alexu.edu.eg) (A.O. Elzoghby).

<https://doi.org/10.1016/j.jconrel.2018.07.014>

Received 22 March 2018; Received in revised form 6 July 2018; Accepted 9 July 2018

0168-3659/© 2018 Elsevier B.V. All rights reserved.



deposition, and nanoparticles in targeting the tumor cells [8].

Etoposide (ETP) is a potent inhibitor of topoisomerase II used for treatment for non-small cell lung cancer (NSCLC) [9]. However, the dose-dependent side effects of ETP treatment include reduced count of white blood cells and platelets, and secondary leukemia [10]. Additionally, resistance to ETP could occur due to up-regulation or mutation of topoisomerase II molecule and the rapid repair of DNA breaks [11]. Cellular extrusion of ETP mediated by transport systems could lead to cross-resistance against other cytostatic agents, as observed for MDR-1-mediated multidrug resistance [12]. Clinical studies revealed that combinatorial cancer treatment significantly reduces individual drug-related toxic effect and evade multi-drug resistance (MDR) via different pathways [13]. In the present study, ETP was combined with the natural isoquinoline alkaloid berberine (BER) as a unique drug combination for effective treatment of lung cancer. BER was previously reported to modulate the MDR through inhibition of P-gp and/or MRP efflux activity in A549 lung cancer cells [14]. Moreover, BER was found to inhibit DNA topoisomerases and protein kinase C, sensitize cancer cells to drugs by increasing their ROS levels and reversal of MDR, thus elevates the cytotoxic effect of combined anticancer drugs [14, 15].

Among promising nanocarriers, human serum albumin (HSA) has attracted great attention in the preparation of NPs due to its biocompatibility, biodegradability, non-immunogenicity, and stability. Moreover, HSA can be chemically modified through its amine and carboxylate moieties for active targeting to cancer cells, beside its targeting abilities through transcytosis pathway by binding to gp60 and SPARC proteins [16, 17]. Unfortunately, hydrophobic anti-cancer drugs are not easily incorporated in hydrophilic albumin NPs except using high energy and shearing technology such as high pressure homogenization (HPH) in case of nab-paclitaxel (Abraxane®) approved by FDA for treatment of advanced and metastatic NSCLC [18]. Therefore, novel pre-formulation approaches may be required to enhance the solubility of hydrophobic drugs and hence facilitate their loading into albumin NPs.

Among those solubility enhancing approaches, complexes between drugs and native phospholipids like soybean phosphatidylcholines, are formed based on hydrogen bonding between the polar parts in both phospholipids and drug [19–21]. The water-insoluble cytotoxic drug, teniposide was pre-formulated as phospholipid complex prior to incorporation into albumin NPs [22]. In addition to the poor water solubility, another challenge lies in non-selective biodistribution of chemotherapeutics leading to systemic toxicity. Therefore, active-targeted nanocarriers were designed to enhance drug accumulation into tumor cells [23, 24]. The presence of over-expressed sialic acid on cancer cell surface is implicated in metastasis, progression, and resistance to chemotherapy [25]. Those sialic acid residues provide a potential binding site for boronic acid group-modified nanocarriers leading to enhanced intra-tumoral transport of nanocarriers through sialic acid recognition [26].

In comparison to the previously reported ETP-albumin NPs prepared by high pressure homogenization (HPH), the desolvation approach does not produce an increase in temperature that may affect the stability of incorporated drugs or induce changes in the protein structure with disruption of some disulfide bonds, thus varying the availability of hydrophobic groups [27, 28]. Moreover, NPs prepared by HPH suffer from low stability and high probability of dis-assembly in the systemic circulation [29]. Concerning injectable APBA-targeted NPs, normal cells may express traces of sialic acid residues for cellular/extracellular interaction which makes the NPs not entirely selective to cancer cells [30]. In addition, higher i.v. doses should be administered compared to those delivered locally via inhalation, thus raising the systemic toxicity and increasing the drug costs. Although nebulized NPs have been widely used for pulmonary administration, they suffer from suspension instability and strong particle-particle interactions, leading to non-adequate nebulization and exhalation of low-inertia NPs [31]. Inhalable NPs powder could solve the stability issue but still suffers

from non-suitability for deep lung delivery [6]. Our inhalable nanocomposites offered optimum size for deep lung deposition compared to previously reported inhalable ETP delivery systems [2, 9]. In addition, the NPs would be recovered from microparticles only after reaching deep lung tissues and selectively target cancerous cells offering maximal antitumor efficacy.

So far, the current study is the first to develop inhalable dry powder composed of spray-dried APBA targeted-albumin nanocomposites for combined delivery of ETP and BER to lung cancer. First, to facilitate its incorporation into the hydrophilic HSA matrix without solubilizer, the hydrophobic chemotherapeutic drug, ETP was pre-formulated as phospholipid complex (EPC) by direct lyophilization. Second, for enhancing ETP anti-tumor efficacy, and reducing its therapeutic dose thus minimizing its toxicity and prevent the development of resistance, the water-soluble herbal drug, BER was directly co-encapsulated with EPC into HSA NPs via desolvation method using different crosslinkers. Third, maximal targeting efficacy was hypothesized by sialic acid targeting via anchoring phenylboronic acid to the surface of HSA NPs. Finally, to reduce systemic toxicity, inhalable dry powder nanocomposites were developed via co-spray drying of dual-drug-loaded HSA NPs with inert carriers to prepare micro-sized powders suitable for deep lung deposition. The developed delivery system was thoroughly investigated in vitro and in vivo to prove the anti-tumor superiority of the combined drug nano-delivery compared with the free drug combination.

## 2. Materials and methods

### 2.1. Materials

Human serum albumin (HSA), Berberine chloride hydrate (BER), 3-Aminophenyl boronic acid (APBA), tertiary Butyl Alcohol (TBA), N-(3-Dimethylaminopropyl)-N'-ethylcarbodiimide hydrochloride (EDC), N-Hydroxysuccinamide (NHS), sodium hydroxide (NaOH), glutaraldehyde solution (GA, 25%), zinc nitrate hexahydrate (Zn (NO<sub>3</sub>)<sub>2</sub>·6H<sub>2</sub>O), Sodium Chloride (NaCl), mannitol, maltodextrin, trehalose, L-leucine, 3-(4,5-dimethylthiazolyl-2)-2,5-diphenyltetrazolium bromide (MTT), Fluorescein isothiocyanate (FITC), urethane (ethyl carbamate), Haematoxylin solution, Eosin solution (H&E) and Canada balsam were purchased from Sigma-Aldrich (St. Louis, USA). Etoposide (ETP) and genipin (GNP) were purchased from Xian Natural Field Bio-Technique Co., Ltd. (Xian, China). Fat-free soybean phospholipids with 70% phosphatidylcholine (Lipoid S75) were kindly provided by Lipoid GmbH (Ludwigshafen, Germany). Poly (ethylene glycol) 400 (PEG-400) was supplied by Pharonia Pharmaceuticals (Alexandria, Egypt). Absolute ethanol and methanol were purchased from ADWIC, El-Nasr Pharmaceutical Chemicals Co. (Cairo, Egypt). Methanol and acetonitrile HPLC grade were purchased from JT Baker (Phillipsburg, NJ, USA).

### 2.2. Preparation and characterization of EPC

ETP-PC complex (EPC) was prepared by direct freeze-drying method [32]. Different molar ratios (1:1, 1:2 and 1:4) of ETP and phospholipid (Lipoid S75) were dissolved in tertiary butyl alcohol (TBA, 10 ml). The mixture was maintained at room temperature on a magnetic stirrer until complex formation. The complex was frozen at −80 °C for 4 h then lyophilized for 24 h using mannitol as a cryoprotectant (LyoQuest-55 freeze-dryer, Telstar, Spain). The prepared EPC was evaluated for their physicochemical, and solid state characteristics [33] (Detailed in the Supporting Information). To confirm the enhanced solubility of EPC, the dissolution profiles of EPC prepared with different molar ratios of phospholipid were compared to free ETP. The optimized EPC powder (P1 and P4), equivalent to 5 mg ETP, was added to 50 ml PBS (pH 7.4) and shaken at 100 rpm and 37 °C (Shaking water bath, Maxturdy 30, daihan scientific Co. Ltd., Shanghai, China). Fixed volume samples were

withdrawn at different time intervals, replaced with fresh medium for compensation and analyzed using HPLC.

### 2.3. Preparation of ETP/BER-loaded HSA NPs

EPC or EPC/BER-loaded HSA NPs were prepared via desolvation method [34, 35]. Briefly, HSA (200 mg) was dissolved in NaCl (2.0 ml, 10 mM) solution containing BER/EPC (20 and 30 mg, respectively) incubated for 1 h at room temperature. The solution pH was adjusted to 8.0 by 0.1 N NaOH. Drop-wise addition of absolute ethanol (8 ml) upon stirring (500 rpm) at a rate of 1 ml/min leads to NPs formation. Different crosslinker types were used to harden the NPs upon overnight stirring at room temperature. Purification of the produced NPs was performed by differential centrifugation (3–30 KS, Sigma Laborzentrifugen GmbH, Germany) at 16,500 rpm, 30 min, and 4 °C. The obtained NPs were re-suspended in distilled water using an ultrasonic bath (Daihan scientific Co. Ltd., Shanghai, China).

### 2.4. Preparation of APBA-targeted HSA NPs

APBA-targeted HSA NPs were prepared using APBA-HSA by the same procedures mentioned above. APBA was conjugated to HSA via EDC/NHS reaction to form amide bond Method [36]. The conjugation was confirmed by MALDI-TOF analysis, tryptophan fluorescence quenching, Alizarin Red S (ARS) test, FTIR, and DSC.

#### 2.4.1. MALDI-TOF MS analysis

The conjugation of APBA to HSA was confirmed by MALDI-TOF MS analysis using Bruker Daltonics ultraflex TOF/TOF instrument (Bremen, Germany). The matrix system used was DHB (20 mg/ml) dissolved in TFA (0.1%) and acetonitrile mixture (70/30 v/v). Spectra were obtained in positive ion mode using an accelerating voltage of 25 kV and data analysis was performed using flexAnalysis software.

#### 2.4.2. Tryptophan fluorescence spectra

Protein intrinsic fluorescence was obtained by tryptophan excitation at 295 nm and emission spectra were collected from 320 to 420 nm with 5 nm excitation and emission slits, using LS 55 fluorescence spectrometer (Perkin Elmer, USA). Each sample (10 mg) was dissolved in 50 mM PBS pH 7.2 and the absorbance of the samples was adjusted to 0.05 at 280 nm. Emission spectra of PBS were subtracted from those containing the samples and the conjugate emission spectra were normalized to native HSA.

#### 2.4.3. Alizarin red test

An aqueous stock solution of  $4 \times 10^{-4}$  M ARS in phosphate buffer (pH 7.4) was prepared. 1.5 ml APBA-HSA (10 mg/ml) was added to 2.0 ml of ARS stock solution for 30 min. The change in color and absorbance was observed by UV/VIS spectroscopy.

### 2.5. Physicochemical characterization of HSA NPs

Particle size, surface charge, in vitro drug release and morphology of the prepared NPs were evaluated [4, 37] and detailed in the Supplementary section.

### 2.6. In vitro cytotoxicity and cellular uptake

By MTT assay, the in vitro cytotoxicity of free drugs solution, non-targeted and APBA-targeted ETP/BER-dual loaded HSA NPs were evaluated against A549 lung cancer cells. For localization of the NPs in cells, NPs were labeled with FITC according to a previously described method [38]. The FITC-labeled HSA NPs were purified from unreacted FITC by dialysis (12–14 kDa MWCO VISKING dialysis tubing, SERVA, Germany) for 48 h. Cellular uptake of free FITC, FITC-HSA NPs, and FITC-APBA-HSA NPs was investigated using confocal microscopy [39] (Supplementary section).

### 2.7. Preparation of inhalable spray-dried HSA nanocomposites

Drug-loaded HSA NPs were microencapsulated within different carrier matrices via spray-drying technique. The sedimented HSA NPs were re-dispersed in an aqueous solution containing the selected carrier combination and spray-dried using a laboratory scale B-290 Büchi spray-dryer (Flawil, Switzerland), equipped with a high-performance cyclone, two component nozzles, and co-current flow. For optimization of the process, the inlet air temperature (110 °C), the pump flow rate (10%), the aspirator (100%) and the atomizing air flow rate (320 l/h) were adjusted. Experimental variables including total solid concentration, carrier type, and HSA NPs/carrier ratio have been investigated.

### 2.8. Characterizations of the spray-dried nanocomposites

Yield, aqueous redispersibility, morphology, particle size, density, calculated aerodynamic properties, solid state characteristics, drug release and long-term stability were examined according to the methodology presented in Supplementary Section.

### 2.9. In vitro aerosol deposition of nanocomposites

Analysis of deposition profile of spray-dried HSA nanocomposites was performed using the eight stages Andersen Cascade Impactor (ACI; Copley Scientific Ltd., Nottingham, UK). ACI was operated at air flow rate of 28.5 l/min, with 4 kPa pressure drop. Budelizer (European Egyptian Pharm. Ind. Co., Alexandria, Egypt), a single-dose inhaler device, was connected to the ACI and filled with a hard gelatin capsule (size 2). Powder was actuated and withdrawn from capsules by the 28.5 l/min flow rate to be deposited in the device, throat, and each stage of ACI collection plates. Each actuation was set in 4 s and 2 aerosolization experiments were performed. HPLC mobile phase (10 ml) was used to wash the powders from the device and stages to be analyzed by HPLC. Aerodynamic parameters (FPF, MMAD, and GSD) were automatically calculated using Copley Inhaler Testing Data Analysis Software (CITDAS) (Supplementary Section).

### 2.10. In vivo study

#### 2.10.1. Animals

For determination of the deposition and treatment efficiency of HSA nanocomposites, male Albino mice (15–20 g) were used following the animal care and use protocol of Alexandria University (Supplementary section).

#### 2.10.2. In vivo lung deposition study

In order to investigate the in vivo lung deposition profile, the dry powder insufflator (DP-4 M, Penn Century Inc. PA, USA) was used for administration of the tested powders. Mice were anesthetized with intra-peritoneal (I.P.) injection of ketamine (12.5 mg/kg) and xylazine (1.5 mg/kg) and restrained in a supine position. FITC-APBA-HSA nanocomposite powder and free FITC were quickly administered via intratracheal route. After sacrifice of mice at different time points (4, 24, 48, and 72 h) post-administration, lungs were collected and washed by PBS. The tissue sections of lungs were imaged using fluorescence microscopy (Olympus BX41, Japan; excitation and emission  $\lambda_{\text{max}}$  at 495 and 520 nm, respectively). The concentration of the fluorescent nanocomposites relative to the fluorescence intensity in lung sections was analyzed by Image J software (Systat, San Jose, CA, USA).

#### 2.10.3. Induction of lung cancer

Lung carcinoma was chemically-induced in 12–16 weeks male Albino mice weighing 15–20 g by receiving I.P. injection of urethane (1.5 g/kg), dissolved in 0.9% NaCl, followed by a poster dose after 8th week [40].

**Table 1**  
Physicochemical properties of different ETP-phospholipid complex (EPC).<sup>a</sup>

	ETP/lipid molar ratio	Mannitol (% w/v)	Lyophilization yield (%)	EE (%)	DL (%)	Particle size (nm)	PDI	Zeta potential (mV)
P1	1:1	0.5	76.2 ± 4.20	100.0 ± 0.08	21.8 ± 0.09	121.0 ± 2.70	0.208 ± 0.08	−27.9 ± 0.51
P2	1:2	0.5	82.2 ± 3.90	81.4 ± 2.35	15.0 ± 0.14	139.0 ± 5.20	0.593 ± 0.10	−42.0 ± 2.63
P3	1:4	0.5	82.4 ± 3.30	91.2 ± 3.60	11.4 ± 0.19	251.0 ± 8.06	0.420 ± 0.10	−43.2 ± 1.98
P4	1:1	1.0	95.0 ± 2.98	95.3 ± 3.10	12.6 ± 0.10	140.0 ± 3.79	0.200 ± 0.07	−27.0 ± 1.13

<sup>a</sup> All EPCs were prepared using 20 mg ETP.

#### 2.10.4. Treatment protocol

The mice were indiscriminately divided into 6 groups (seven mice each): Group 1 mice were administered inhalable spray-dried EPC/BER-loaded APBA-HSA mannitol nanocomposites (S4) eq. to 3 mg/kg of ETP (60 µg/mouse) using dry powder insufflator three times per week for two weeks. Group 2 mice were administered inhalable spray-dried physical mixture of free ETP/BER combination and mannitol at the same concentrations in nanocomposites by insufflation. Group 3 mice were injected in the tail vein with EPC/BER-loaded APBA-HSA NPs (T5) eq. to 3 mg/kg of ETP 3 times for two weeks. Group 4 mice were injected in the tail vein with combined free ETP/BER solution at the same concentrations in the NPs. Group 5; positive control (untreated chemically induced lung carcinoma bearing mice). Group 6; negative control (healthy mice).

For pulmonary administration, mice were placed in a supine position, to expose the trachea, after I.P. administration of ketamine (12.5 mg/kg) and xylazine (1.5 mg/kg) for anesthesia. Intratracheal administration was applied according to the method reported by Duret et al. [41]. For the formulations administered via the dry powder insufflations (DPI) method, an otoscope (Heine Mini 3000, Germany) was used to visualize tracheal openings. Pumping 0.2 ml of air contained in a syringe connected to the insufflator powder chamber was performed. Then, the powder chamber was weighed before and after powder filling and administration to detect the real quantity of sample released and aerosolized into the lungs.

#### 2.10.5. In vivo anti-tumor efficacy

**2.10.5.1. Lung and body weight.** The mice body weight was measured periodically during the treatment. All the surviving mice were sacrificed after 21 days. The extracted lungs were isolated, weighed, morphologically examined and separated into two parts; one was for biological evaluation of tumor biomarkers after freezing at −80 °C and the other was for histopathological and immunohistochemical examination after fixation with 4% paraformaldehyde solution.

**2.10.5.2. Tumor growth biomarkers.** ELISA was used for the determination of the tumor growth biomarkers (Supplementary section).

**2.10.5.3. Histopathological and immunohistochemical analysis.** Histopathological changes, number of foci, their diameters and the proliferation extent indicated by Ki-67 protein were evaluated for the lung tumor samples (Supplementary section).

#### 2.11. Statistics

Statistical analysis was done using GraphPad (Prism Version 5, CA, USA). Quantitative data were described using mean ± SD. For normally distributed quantitative data, comparisons among the different groups were done using analysis of variance (ANOVA; F test) with multiple comparisons between deposition data using a Tukey Kramer HSD test. Values for  $P < .05$  were considered statistically significant.

### 3. Results and discussion

#### 3.1. Preparation and characterization of EPC

As an approach to overcome its poor solubility, ETP-phospholipid complex (EPC) was formed via freeze-drying to obviate the heat used in solvent evaporation technique. For the preparation of EPC, dissolving and mixing the phospholipid and ETP together in a co-solvent was a prerequisite to prevent drug precipitation [32]. TBA was chosen as an organic co-solvent for lyophilization due to its high vapor pressure (41.25 mmHg at 25 °C), and high melting point (24 °C) [42]. In our preliminary trials, EPC was successfully prepared with 1:1, 1:2 and 1:4 molar ratios of ETP and phospholipid (Table 1). In contrast to 1:1 EPC (P1), the EPC prepared at the ratio of 1:2 and 1:4 (P2, P3) were very sticky and not easily reconstituted in water. This could be due to the excess unbound phospholipids that formed extra layers surrounding the complex as indicated by their high  $\zeta$  potential values (−42.0 and −43.2 mV; respectively) (Fig. S1). Additionally, their PS and PDI were higher than P1, suggesting their non-homogeneity. Moreover, no difference was observed in their dissolution rate compared to P1 (Data not shown). Therefore, P2 and P3 were not recommended for formulation of aqueous HSA NPs.

Dissolution testing of the EPC in PBS (pH 7.4) showed improved drug dissolution via complexation with phospholipid (Fig. 1A). The enhanced dissolution of the drug complex can be explained by two factors. First, complexation of ETP with Lipoid S75 based on hydrogen bonding improved its hydrophilicity. Second, the reduced crystallinity of EPC contributed to the enhancement of ETP solubility (as indicated from DSC and XRD results). The presence of higher amount of mannitol obviously enhanced the dissolution rate of ETP. About 79.5% of ETP was dissolved after 2 h from 1:1 EPC (P4) prepared using 1% w/v mannitol compared to only 54.4% ETP dissolved from 1:1 EPC (P1) lyophilized using 0.5% w/v mannitol. The higher amount of mannitol, as a hydrophilic freeze-drying carrier, can increase the wettability and improve the dispersibility of ETP thus enhancing its dissolution profile [43]. The 1:1 EPC prepared using 1% mannitol (P4) exhibited a smaller particle size of 140 nm,  $\zeta$  potential value of −27.0 mV and acceptable drug loading of 12.6% with enhanced dissolution and good powder flowability. Therefore; it was selected to be incorporated in HSA NPs (Fig. S2).

The FTIR spectrum of native ETP showed a broad characteristic band of phenolic –OH at 3412 cm<sup>−1</sup>, an intense stretched band of ether in the 1660–1610 cm<sup>−1</sup> region and C=O stretch band of ester bond at 1763 cm<sup>−1</sup> (Fig. 1B) [44]. For Lipoid S75, peaks at the range from 1200 to 960 cm<sup>−1</sup> were assigned to the phosphate group also shown in the physical mixture. The additive effect of both ETP and Lipoid S75 (3268.2 cm<sup>−1</sup> of ETP-OH and 1762.21 cm<sup>−1</sup> of the carbonyl in the acyl chains, respectively) was observed in the spectra of both physical mixture and EPC (P4). These findings suggested some weak physical interactions such as hydrogen bonding between the hydroxyl group of ETP and the phosphate group of phospholipid during complex formation [32].

The DSC thermogram of ETP showed a sharp endothermic melting peak at 275.13 °C (Fig. 1C). In the physical mixture thermogram, the peak of mannitol was still detectable at 166.076 °C but peaks'

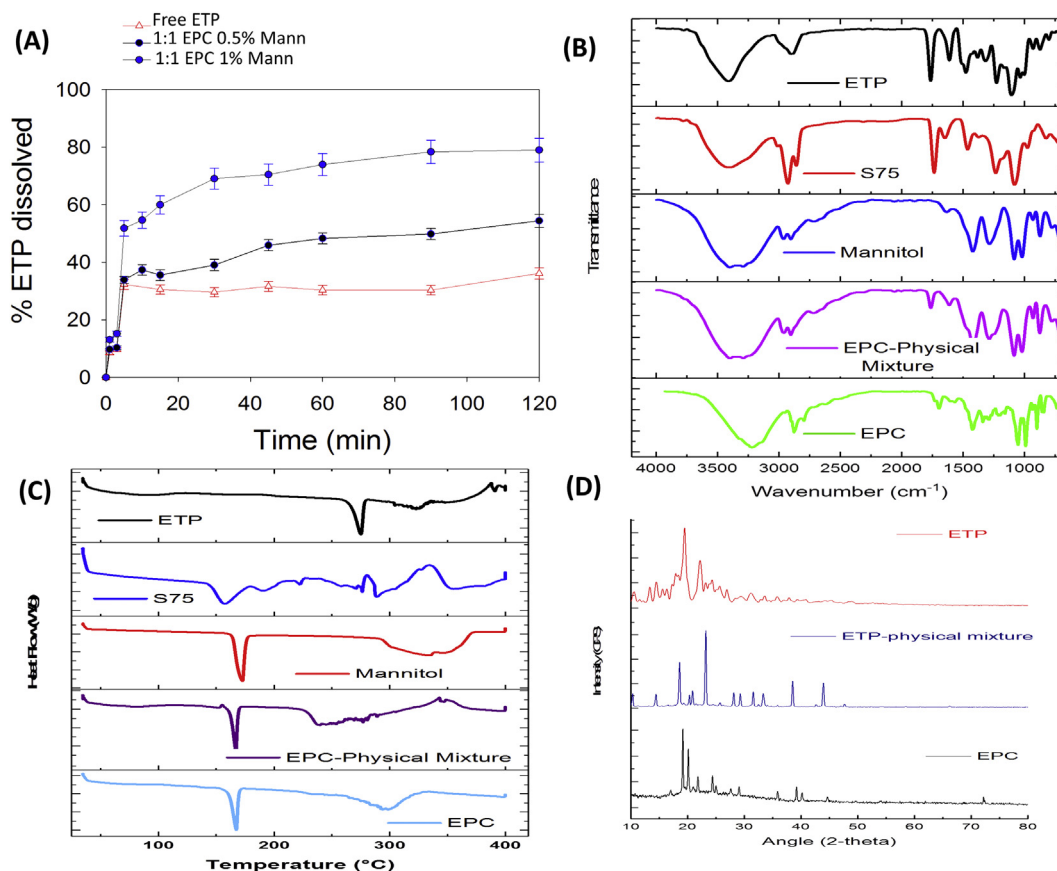


**Fig. 1.** Physicochemical properties of EPC; In vitro dissolution rate of ETP from the prepared EPC in PBS pH 7.4 at 37 °C (A), FTIR spectra of ETP, Lipid S75, mannitol, EPC and their physical mixture (B), their corresponding Differential scanning calorimetry (DSC) thermograms (C), their Powder X-ray diffractogram (D).

broadening was observed in the range of 230–330 °C may be attributed to the partial interaction between ETP and lipid. On the contrary, EPC thermogram showed the disappearance of the genuine peaks of ETP and lipid with a broad endothermal peak appearing at 297.77 °C. This could be explained by complex formation between ETP and lipid via hydrogen bonds and/or van der Waals forces [45]. As shown in XRD Fig. 1D, the crystalline state of ETP was confirmed by sharp peaks at  $2\theta = 17.86^\circ$ ,  $19.41^\circ$ , and  $22.17^\circ$ . While the diffraction pattern of the physical mixture showed no modification of ETP crystallinity, XRD of EPC showed a relatively lower intensity peak of ETP; indicating reduction of its crystallinity upon formation of EPC.

### 3.2. Formulation and characterization HSA NPs

#### 3.2.1. Particle size, DL, and EE

**3.2.1.1. EPC-loaded HSA NPs.** After pre-formulation of ETP as phospholipid complex (EPC, P4), it could be easily incorporated in HSA NPs via desolvation method. Desolvation process is well-controlled (pH, ethanol addition time, albumin concentration), robust process indicated by the little variability in PS, ZP, DL, and EE of drugs [46]. In our study, the NPs were obtained by the drop-wise addition of ethanol to continuously stirred aqueous solution of albumin containing EPC leading to the appearance of turbidity. EPC-loaded HSA NPs were then hardened using different crosslinkers (GA, GNP, and GA/Zn<sup>2+</sup>). The fabricated NPs (T1–T3) showed a size range of 136–190 nm with a highly negatively charged surface (−21.0 to −22.4 mV) indicating their high colloidal stability (Table 2). GA-crosslinked NPs (T1) were with 182.2 nm diameter and 70% EE of ETP. In comparison, HSA NPs crosslinked with GNP (T2) showed a smaller particle size (136 nm) but with a significantly lower EE (49.43%). In another strategy, the NPs were crosslinked with GA and further stabilized through Zn<sup>2+</sup>

coordinating bond. Zinc nitrate, as a bivalent metal ion, was reported to stabilize proteins to obtain preferable release behavior [47]. Consequently, HSA NPs (T3) with suitable PS of 190 nm were obtained but with a much lower drug EE (16%) may be due to the drug loss during the double centrifugation step. From all those results, GA-crosslinked NPs (T1) was selected as the optimized NPs due to their suitable size and high EE and DL.

**3.2.1.2. EPC/BER co-loaded HSA NPs.** To enhance the anti-tumor efficacy of ETP, the herbal drug BER was successfully co-loaded with EPC into HSA NPs using GA as a crosslinker. The EPC/BER co-loaded HSA NPs (T4) demonstrated a preferable PS of 173 nm and  $\zeta$  potential of −24 mV with a high EE of both drugs (81.7 and 90.8% for BER and ETP, respectively). HSA offers a high capacity carrier for reversible binding to both drugs BER & ETP. BER is likely bound to the lipophilic cavity in HSA sub-domain IIA by the hydrophobic interaction in addition to the electrostatic force between the positively charged BER and the negatively charged HSA (at pH > pI = 4.9). Moreover, the amphiphilic property of phospholipid component of EPC not only facilitates its aqueous dispersion but also enables the hydrophobic binding to albumin binding domains.

To develop tumor-targeted NPs, APBA was coupled to HSA via simple carbodiimide reaction. The APBA-HSA conjugate was then used in the preparation of NPs incorporating BER/EPC (T5). The increase in particle size to 219 nm ensured the conjugation of the APBA onto the surface of HSA NPs. Conjugation of APBA on HSA was also confirmed by MALDI-TOF analysis revealing that the molecular mass of HSA and APBA-HSA were 68.83 and 71.04 kDa (*m/z*) respectively, thus suggesting that 16 molecules of APBA were conjugated to 1 HSA molecule (Fig. 2A). Conjugation of APBA to HSA was found to reduce the intrinsic tryptophan emission fluorescence intensity (Fig. 2B). This might be



**Table 2**

Composition and physicochemical properties of EPC-loaded &amp; EPC/BER co-loaded HSA NPs.

	Cross-linker <sup>a,b</sup>	EE (%w/w)		DL (%w/w)		Particle size (nm)	PDI	Zeta potential (mV)
		BER	ETP	BER	ETP			
T1	GA (8%, 117 $\mu$ l)	–	70.00 $\pm$ 1.02	–	4.94 $\pm$ 0.13	182.2 $\pm$ 7.10	0.305 $\pm$ 0.09	–22.4 $\pm$ 0.89
T2	GNP (0.035 M)	–	49.43 $\pm$ 2.03	–	3.49 $\pm$ 0.22	136.0 $\pm$ 3.98	0.100 $\pm$ 0.02	–21.0 $\pm$ 1.16
T3	GA(8%, 117 $\mu$ l)/(0.025 M Zn)	–	16.00 $\pm$ 0.95	–	1.13 $\pm$ 0.10	190.0 $\pm$ 4.62	0.165 $\pm$ 0.02	–21.3 $\pm$ 1.03
T4	GA (8%, 117 $\mu$ l)	81.7 $\pm$ 2.64	90.80 $\pm$ 3.07	6.8 $\pm$ 0.21	5.85 $\pm$ 0.11	173.0 $\pm$ 2.50	0.132 $\pm$ 0.04	–24.0 $\pm$ 0.54
T5	GA (8%, 117 $\mu$ l)	60.5 $\pm$ 2.41	90.93 $\pm$ 2.87	5.2 $\pm$ 0.19	5.86 $\pm$ 0.10	219.0 $\pm$ 4.90	0.217 $\pm$ 0.08	–26.0 $\pm$ 1.42

<sup>a</sup> All NPs were prepared with 200 mg HSA, 40 mg BER and 30 mg EPC except T5 was prepared by 200 mg APBA-HSA instead of HSA.

<sup>b</sup> T3 NPs were crosslinked with 117  $\mu$ l GA overnight and then separated by centrifugation. Then, the redispersed NPs were further stabilized by addition of 0.025 M zinc nitrate at ambient temperature under stirring for further 2 h then re-centrifuged to remove excess ions.

referred to the partial effect of APBA on the native packing of HSA without observation of denaturation (blue or red shift in the maximum  $\lambda_{em}$ ) [48]. By the fact of the high affinity of boronic acid to Alizarin Red S dye (ARS), a change in the color of APBA-HSA conjugate from pink to slightly yellow accompanied with UV/VIS spectrum shift from 510 to 488 nm was recorded upon addition of ARS (Fig. S3 and S4) [49].

### 3.2.2. Morphological analysis

TEM micrographs revealed spherical shape and smooth surface non-targeted (T4) and APBA-HSA NPs (T5) with diameters of 148.3 and 201.21 nm, respectively which was quite smaller as compared with the results obtained from DLS technique (173 and 219 nm) (Fig. 3A and B). The hydrodynamic diameter of hydrated particles was measured by the laser scattering approach which was affected by the solvent phase [50]. In contrast, TEM measures the diameter of particles in the dried state. The conjugation of APBA onto the surface of HSA was also confirmed by the size increase of APBA-HSA NPs compared to the non-targeted HSA ones.

### 3.2.3. In vitro drug release

A sustained release behavior of ETP was observed from single-loaded EPC-HSA NPs (T1–T3), formulated with different crosslinkers over 3 days (Fig. 3C). GA was the most effective crosslinker with about 30.01 and 65.73% of ETP was released after 24 and 72 h, respectively without initial burst effect. First, ETP molecules were dissociated from EPC and distributed within the NPs, followed by the release of free ETP molecules from the NPs. Therefore, EPC acted as an additional physical

barrier to drug release [51]. In contrast, Wang et al. observed the biphasic release of ETP from BSA nanosuspensions prepared by high pressure homogenization with 2 h initial fast release of 25% followed by completely released drug after 24 h [52]. In another investigation, about 60% of ETP was released from PLGA NPs after 24 h and 100% was released after 72 h [53]. In the combined GA crosslinked BER/EPC HSA NPs (T4), a similar controlled release pattern of ETP up to 72 h was observed (Fig. 3D). On the other hand, a biphasic release of BER from HSA NPs (T4) was observed characterized by initial burst release of 41.9% during the first 3–4 h, followed by a second phase of slow release (45.3% of drug released after 72 h) (Fig. 3D). Notably, surface modification of HSA NPs by APBA (T5) did not much affect the release behavior of both drugs with the conservation of the sustained release pattern after APBA targeting.

Differences in the release pattern of the two drugs could be correlated to the differences in the physicochemical characteristics of the water-soluble BER (Log P  $\sim$  –1.5) and the relatively hydrophobic ETP. The faster release of BER can sensitize tumor cells to ETP action by activation of ROS, besides its cytotoxic activity via topoisomerase inhibition thus retarding MDR. The delayed release of ETP could prevent premature drug release into circulation and maintain the synergistic efficacy at lower concentration and toxicity. A similar sequential release pattern was reported by Narayanan et al. where the faster release of epigallocatechin gallate from the shell of PLGA/casein core-shell NPs could sensitize tumor cells to the anti-cancer effect of the slowly released paclitaxel from its core [54].

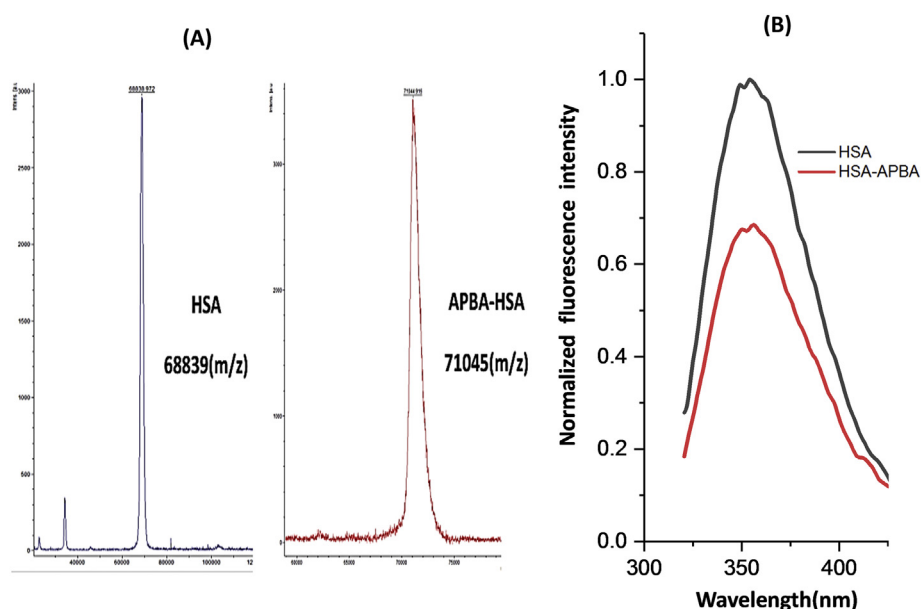


**Fig. 2.** Characterization of APBA-HSA conjugate; MALDI-TOF analysis of HSA and APBA-HSA (A). Intrinsic tryptophan emission fluorescence spectra of HSA and APBA-HSA were collected from 320 to 420 nm ( $\lambda_{ex}$  = 295) (B).

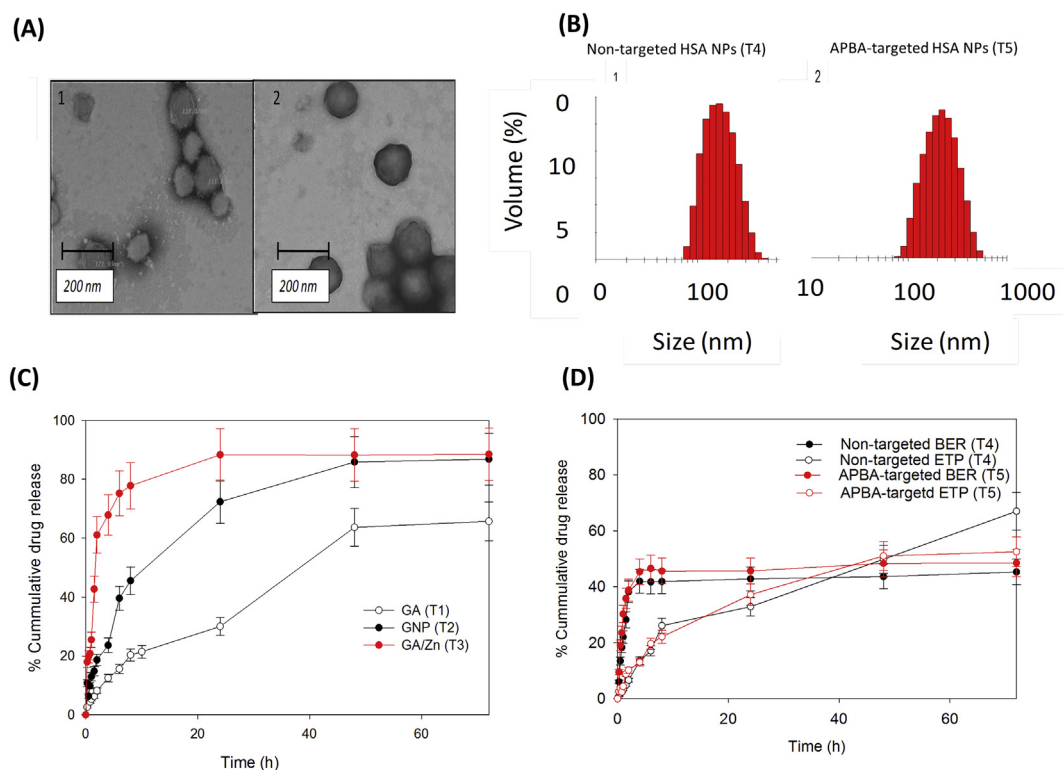


**Fig. 3.** Physicochemical properties of the prepared HSA NPs; TEM photographs (A) showing the morphology of HSA NPs (A1) non-targeted HSA NPs and (A2) APBA-targeted HSA NPs and their particle size distribution histograms (B). Release profiles of EPC from single-loaded EPC-HSA NPs, formulated with the different crosslinkers (C) and from the combined BER/ETP formulation (D) in PBS pH 7.4 at 37 °C.

### 3.3. *In vitro* cytotoxicity

Time- and concentration-dependency of the cytotoxic activity of ETP and BER, in both free and nano-encapsulated form, against A549 human lung cancer cells at 24 and 48 h was demonstrated (Fig. 4A and

B). The  $IC_{50}$  of non-targeted and APBA-targeted HSA NPs was 1.2- and 2-fold, respectively lower than free combined BER/ETP solution after 24 h (Fig. 4C). Compared to the NPs, the weak therapeutic activity of the free drugs could be correlated to the absence of controlled release characteristics and lack of targeting moieties, thus the cellular

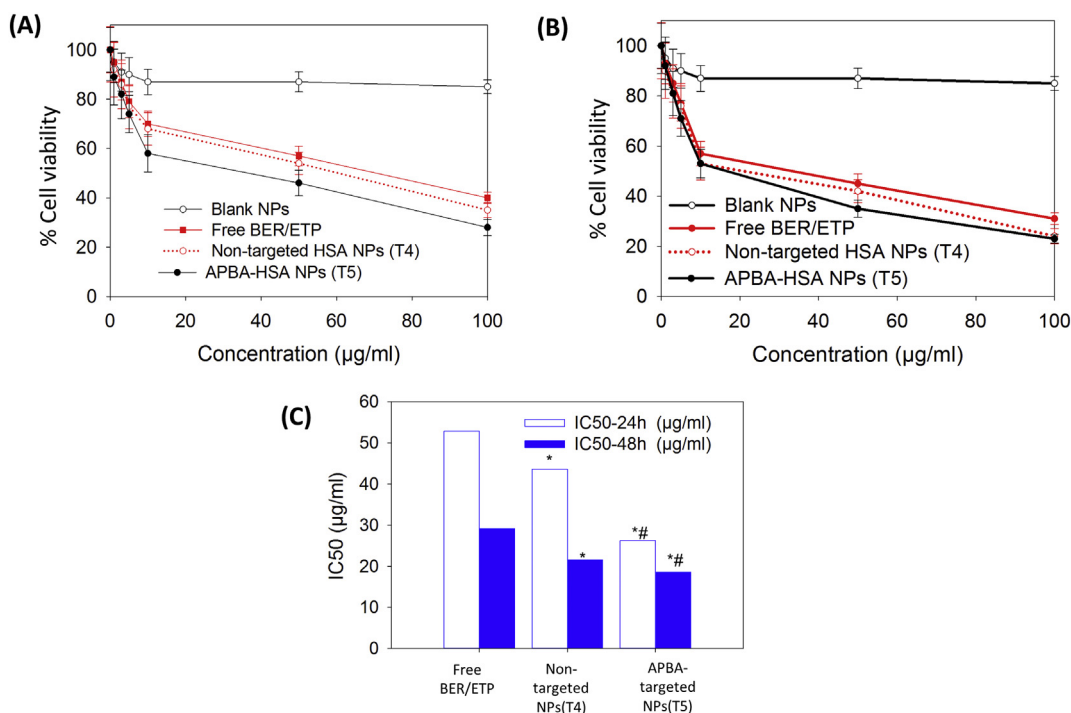


**Fig. 4.** Cytotoxicity analysis of free drugs and different BER/ETP HSA NPs on A549 human non-small cell lung cancer cell line at the concentration of 1–100 μg/ml after 24 h (A) and 48 h (B).  $IC_{50}$  (μg/ml) values of different BER/ETP-NCs HSA NPs (C). \* $P < .05$  vs free ETP-BER, # $P < .05$  vs non-targeted HSA NPs.

internalization was only mediated by diffusion [55]. In contrast, the enhancement of the BER/ETP combination potency in NPs might be related to their efficient cellular internalization in tumor cells and the sustained drug release that preserves the drug level within cells. First, the intrinsic ability of HSA to bind with gp60 and SPARC on tumor cells contributed to the high cellular uptake [16]. Compared to non-targeted NPs, the inhibitory effect was increased by 1.6 times after anchoring APBA on the NPs surface. This amplified cytotoxicity of APBA-HSA NPs was attributed to sialic acid-dependent endocytosis by APBA, resulting in enhanced accumulation in tumor cells [26]. Moreover, complexation of ETP with phospholipid, the main constituent of the cell membrane, might enhance ETP permeability into the cells with increased cytotoxicity. A similar enhanced cytotoxic effect of camptothecin–phospholipid complex self-assembled NPs was reported [56].

After 48 h incubation with cells, the free combined ETP/BER solution showed more cytotoxic effect which ensured the time dependency of BER/ETP synergistic combination. The delayed release of ETP from NPs over 48 h enhanced its cytotoxic effect. The two formulations diminished the cell viability by the increased treatment time (Fig. 4B). These results were in agreement with a previously reported combination of ETP/quercetin loaded in PLGA NPs [11]. Safety of HSA NPs was confirmed by 85% viability of A549 human lung cancer cells after 48 h.

### 3.4. Qualitative analysis of cellular uptake

Confocal microscopy (CLSM) was used for tracking the cellular uptake of FITC-labeled HSA and APBA-HSA NPs into A549 lung cancer cells after incubation for 4 and 24 h. After 4 h, the DAPI stained nuclei (blue fluorescence) were surrounded by the green fluorescence of FITC-HSA and FITC-APBA-HSA NPs, indicating that sufficient quantity of the NPs could be internalized into the cytoplasm (Fig. 5). To exclude the role of albumin in cellular uptake by SPARC and gp60 and any interference by FITC (fluorescent probe), APBA-targeted NPs were compared to the non-targeted NPs and free FITC. Free FITC showed faded green fluorescence due to its relatively slow diffusion mechanism [39]. FITC-APBA-HSA NPs exhibited enhanced cellular uptake than FITC-HSA NPs, confirming the role of sialic acid-mediated endocytosis by APBA. Results showed that the cellular uptake was increased gradually in a time-dependent manner. After 24 h, the green fluorescence became denser

and well dispersed in the whole area of cytoplasm. Compared to the non-targeted NPs and free FITC, APBA-targeted NPs revealed elevated cellular internalization, which was indicated by intense green fluorescence. Thus, APBA-HSA NPs would offer a pathway to BER and EPC to enter and accumulate into the cells. This could explain the high cytotoxicity and low  $IC_{50}$  values when compared to free drugs.

### 3.5. Development and characteristics of inhalable APBA-HSA nanocomposites

Development of inhalable formulations provides a rational strategy for treatment of NSCLC. Localized pulmonary drug delivery could be utilized for decreasing the non-specific distribution of cytotoxic drugs, increasing its localization at the tumor site, and hence increasing the efficiency of treatment [1]. In the current study, dry powders embedding APBA-HSA NPs co-loaded with EPC and BER were developed via spray-drying as a speedy and single-step technique to form a dry powder of NPs embedded into microparticles (nanocomposites).

**Yield and redispersibility:** Carbohydrates are the most popular inhalation carriers, due to their ability to guard against drying. Upon inhalation, they dissolved rapidly releasing the incorporated NPs and preventing the phagocytic opsonization [57]. For albumin NPs, mannitol is more preferable than lactose, in order to avoid lactose interaction with albumin via Maillard reaction [58]. To target cancer cells, the nanocomposites have to recover their original nanosize after dissolving in the alveolar aqueous medium. Initial examination of mannitol as a pulmonary carrier at a fixed NPs/carrier ratio (1:5 w/w), with different total solid concentrations resulted in spray-dried nanocomposite powders with a yield range of 63.78–78.11% and good aqueous redispersibility ( $RI = 1.19$ – $1.22$ ) (Table 3, Fig. S5). Upon using the least aqueous volume for spray-drying to prevent the release of the water-soluble drug BER, a total solid concentration of 10.8% w/v was obtained. To further increase drug loading, mannitol was used at a lower NPs/carrier ratio (1:3 w/w), resulting in nanocomposites (F4) with the highest yield of 78.4% and superior aqueous redispersibility ( $RI = 1.01$ ). Screening of different carbohydrate carriers suggested that mannitol is best recommended for our designed nanocomposites. Trehalose produced lower yield due to the cohesive nature of particles leading to powder adhesion to the spray-dryer wall while maltodextrin

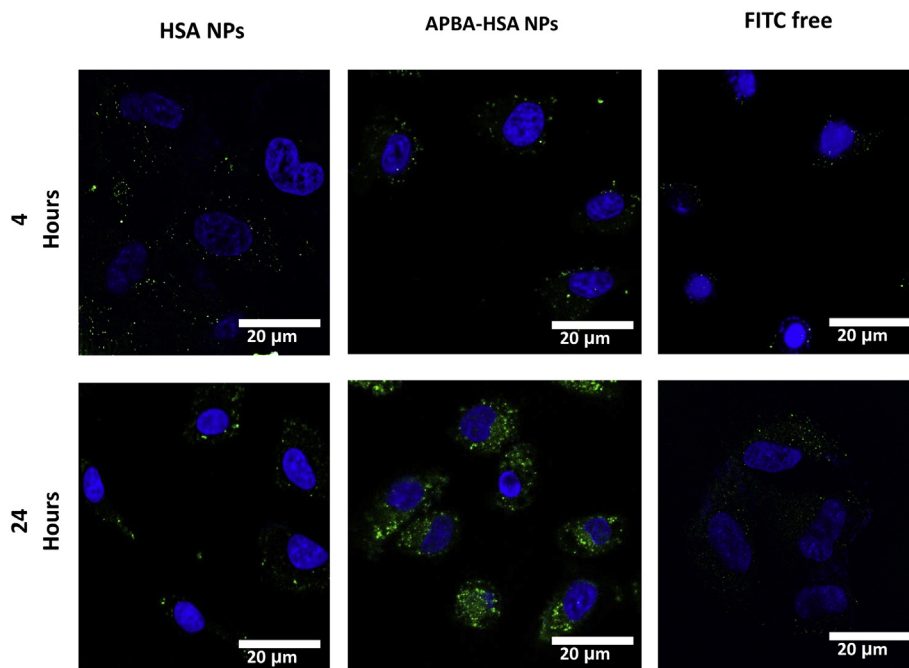


Fig. 5. Cellular uptake of non-targeted HSA NPs and APBA-HSA NPs with A549 cells after incubation for 4 h and 24 h.

**Table 3**

Composition, yield and aqueous re-dispersibility index of different prepared spray-dried nanocomposite formulations using different carriers.

	Carrier <sup>a</sup>	Aqueous solution volume (ml)	Formula/carrier ratio (w/w)	Solid Conc. (w/v %)	Yield (%)	RI
F1	Mannitol	10.00	1:5	27.00	63.78	1.22
F2	Mannitol	25.00	1:5	10.80	78.00	1.18
F3	Mannitol	50.00	1:5	5.40	78.11	1.19
F4	Mannitol	25.00	1:3	7.20	78.40	1.01
F5	Maltodextrin	25.00	1:3	7.20	71.10	1.25
F6	Trehalose	25.00	1:3	7.20	60.00	1.20
F7	Leucine/Mannitol	25.00	1:1:2	7.20	70.40	1.50

<sup>a</sup> RI was calculated as the ratio between the recovered PS of NPs from spray dried powder and the fresh NPs preparation.

gave lower yield and higher aqueous redispersibility, compared to mannitol.

Amino acids have been used, combined with polysaccharides, to reduce the adsorption of moisture and enhance the surface activity [59]. A carrier composed of leucine/mannitol in a ratio of 1:1:2 w/w (F7) was used to form nanocomposite powder with 70.4% yield and 1.5 RI. This relatively high RI value could be referred to the hydrophobic nature of leucine, which acted as a water repellent and reduced the sugars moisture uptake when re-suspended in aqueous medium [60]. Based on the investigation results of the effect of leucine addition to mannitol as a spray-drying carrier, F4 and F7 were selected.

**SEM:** The surface structure of spray-dried nanocomposites prepared using the two selected inhalation carriers: 1:3 w/w NPs/mannitol (F4) and 1:1:2 w/w NPs/leucine/mannitol (F7) was compared (Fig. 6). Addition of mannitol (F4) was found to produce spherical particles, with rough surfaces (Fig. 6A). The spherical wrinkled structure could be attributed to the

high vapor pressure, during spray-drying process, that leads to collapsing of the surface layer of particles [61]. On the other hand, the addition of leucine to mannitol (F7) produced hollow, collapsed doughnut-shaped particles (Fig. 6B). By virtue of leucine hydrophobicity and surface activity, it had a good propensity to be collected on the surface of the droplet; lessening their particle cohesiveness. The hydrodynamic impacts and the depletion of structural stability upon drying of the droplets lead to the formation of doughnut-like particles [62]. During fast solvent evaporation, the pressure obtained from the internal slow evaporation and gas expansion make the outer coat thinner, thus solvent diffused faster. Due to the impermeability of leucine, rupture of the particles occurred and the hollow structure was formed [63]. Compared to spherical particles, the high specific surface area of doughnut-shaped particles made it less desirable for nanoparticles encapsulation [64]. Producing rough surface particles contributes to the enhancement of the quality of dry powders for inhalation due to the reduced particles contact area and; thus decreases the particles adhesion [65]. Image analysis was performed, in order to compare the degree of surface roughness for the two selected formulations (F4 and F7). The 3D and 2D surface plots indicate that F7 has a relatively less corrugated surface as described by the green area in Fig. 6Bc and 6Cb.

**Particle diameter:** For efficient lung deposition, particles should have a volume median diameter value in the range of 1–5  $\mu\text{m}$ . The size analysis data showed  $D_{0.5}$  values of 2.5 and 2.82  $\mu\text{m}$  for F4 and F7, respectively (Table 4); confirming their adequacy for pulmonary deposition. The slightly higher geometric diameter ( $D_{0.5}$ ) for F7 may be due to the presence of leucine on the droplet surface during spray-drying that form the collapsed doughnut shape particles. For both F4 and F7, the particle size volume distribution was narrow and monomodal. Addition of leucine has reduced the value of span index from 1.58 (F7) to 1.98 (F4) indicating a better powder homogeneity [6]. Better inhalation performance in terms of higher pulmonary deposition was reported for formulations with lower span index [66].

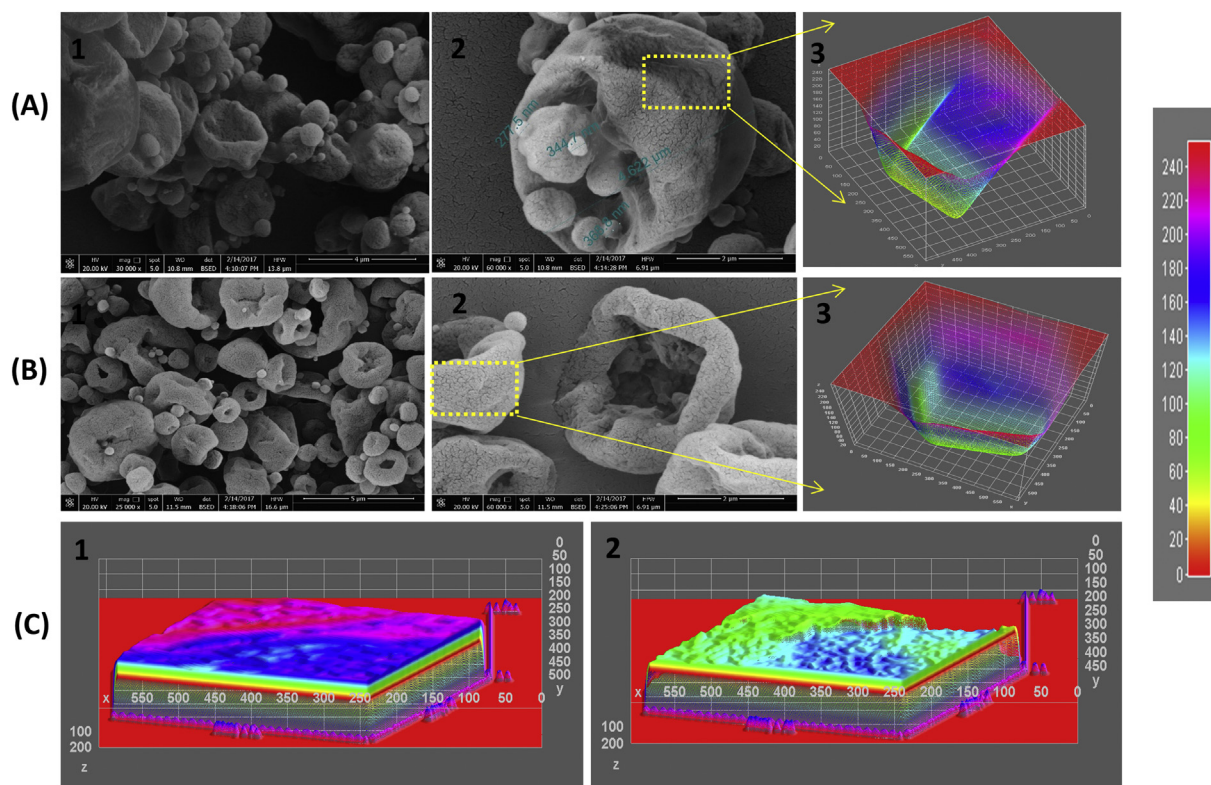


**Fig. 6.** Scanning electron micrographs of spray dried powder APBA-targeted HSA nanocomposites using mannitol as a carrier [(1:3), (A)] and APBA-targeted HSA nanocomposites using leucine and mannitol as a carrier [(1:1:2), (B)]. SEM Images Aa, Ba and Ab, Bb were captured at 30,000 $\times$  magnification and 60,000 $\times$  magnification, 2D plot (Ac, Bc) and 3D plot for mannitol carrier (Ca) and leucine and mannitol (Cb).



**Table 4**

Aerodynamic properties of spray-dried APBA-targeted HSA nanocomposites using mannitol (1:3 w/w) (F4) and leucine/mannitol (1:1:2 w/w) (F7) as pulmonary carriers.

	D <sub>0.5</sub> (μm)	Span index	FPF (%)	ED (%)	MMAD (μm)	GSD
F4	2.50	1.99	77.86	80.45	2.12	2.13
F7	2.82	1.58	92.48	88.21	1.24	2.00

### 3.6. In vitro aerosol deposition

The effect of particle characteristics and carrier types on the in-vitro deposition of spray-dried HSA nanocomposites had been evaluated using ACI at a flow rate of 28.4 l/min (Fig. 7A). Results showed a high emitted dose percentage (ED = 80.45%) of the drugs from aerosolized powders containing mannitol (F4). The total amount of drugs deposited in stages 3–7 of ACI was considered as the FPF and was estimated to be 77.86%, with MMAD of 2.112 μm and GSD of 2.128 (Table 4). The surface properties of the particles related to mannitol carrier might be the reason for these high aerosolization parameters [67]. Leucine addition resulted in better aerosolization properties; indicated by the higher FPF value of 92.48% and ED of 88.21% with lower MMAD of 1.238 μm and GSD of 2.003 (Table 4). The enhanced aerosolization of nanocomposites prepared with leucine/mannitol combination (F7) could be referred to decreased moisture uptake due to the water-repellent action of leucine which might render the particles less cohesive [62]. In addition, leucine enhanced the dispersibility of the particles by shell formation and decreasing the surface free energy [68]. Additionally, the doughnut-shaped particles reduced inter-particulate contact surface areas, ensuring better particle dispersions [65].

Comparing with previously reported inhalable ETP delivery systems, inhalable freeze-dried ETP liposomes using various cryoprotectants at 1:10 ratio demonstrated particle diameter of 5.5 to 7.5 μm and FPF of about 50% [9]. Moreover, inhalable freeze-dried ETP-loaded PLGA microspheres, using 0.2% mannitol as a cryoprotectant, showed an average diameter of 11.9 μm indicating poor lung deposition [2]. On the contrary, our both nanocomposites powders (F4 and F7) exhibited appropriate characteristics for pulmonary drug delivery to lung cancer with acceptable diameter range (1–5 μm) and GSD range (1.3–3.0) for respirable particles.

Although nanocomposites prepared using leucine/mannitol (F7) showed better aerodynamic properties, it demonstrated high RI with

less effective dissolution of the complex carrier matrix which hindered the complete recovery of NPs to its original size (PS of the recovered NPs was 328.5 nm with high PDI). On the other hand, nanocomposites prepared using mannitol (F4) could recover the entrapped NPs with no change in their PS, with a rough surface and smaller calculated  $d_{aer}$ . Based on these results, the spray-dried APBA-HSA nanocomposites prepared using mannitol (F4) was selected as the optimized formulation for further in vivo investigations.

### 3.7. Drug release & long term stability

The effect of the spray-drying process on the release behavior of drugs was investigated in 37 °C in pH 7.4 PBS (Fig. 7B). Initially, about 40% of BER was burst released from spray-dried HSA nanocomposites (F4) during the first 6 h and then reached a plateau with about 46.7% of BER was released after 72 h. On the other hand, ETP showed sustained release with no initial burst effect with about 55.7% of the drug was released in 72 h, compared to 51.4% ETP released from HSA NPs (T5) before spray-drying. This confirms that the spray-dried nanocomposites maintained the sequential controlled release pattern of BER and ETP. After 4 months storage in a desiccator at room temperature, the spray-dried HSA nanocomposite powders appeared to maintain their original characteristics with no observed aggregation or clumps. After reconstitution in distilled water, a very slight increase in particle size to 225.2 nm with PDI of 0.173 was observed compared to the initial size of 219 nm. Interestingly, the spray-dried nanocomposites demonstrated a size of 234.8 nm with PDI of 0.205 and zeta potential of −23.6 mV after 1 year of storage thus confirming the long term stability of spray-dried HSA nanocomposites. The solid state characterization confirmed the absence of any drug-carrier interactions (discussed in details in the Supplementary section).

### 3.8. In vivo lung deposition and retention study

Cascade impactors do not adequately simulate the real in vivo conditions and give no idea about the retaining efficiency of the particles after pulmonary administration. So, in vivo testing should be performed to confirm particle retention in lung tissues [69]. The fluorescent microscopic images of mice lung sections at different time intervals following powder insufflation of spray-dried FITC-labeled APBA-HSA nanocomposite powder and free FITC powder are shown in Fig. 8A. Maximum fluorescence intensity was observed after 4 h of pulmonary administration of FITC-labeled nanocomposites, indicating

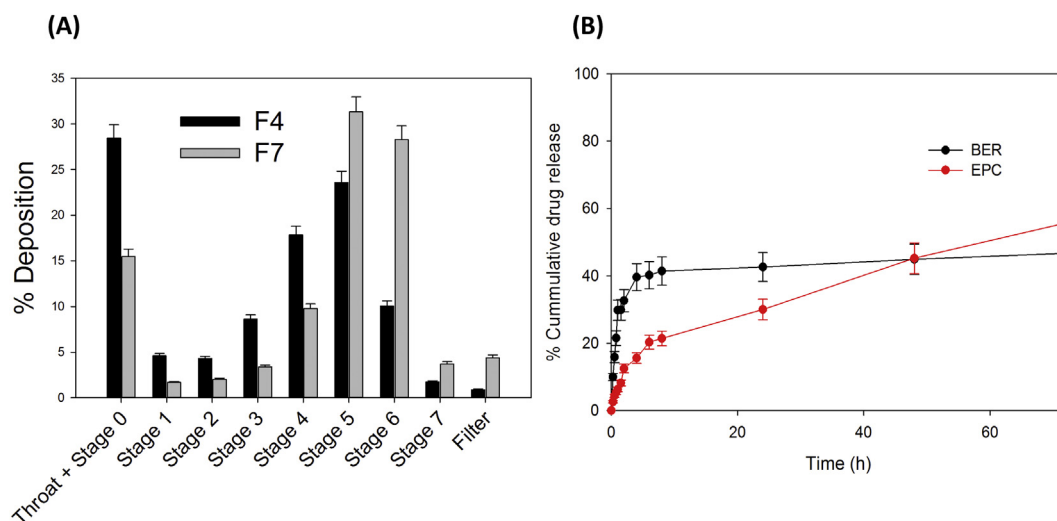


**Fig. 7.** In vitro aerosol deposition profiles of spray dried APBA-targeted HSA nanocomposites (A) using mannitol as a carrier [(1:3), F4] and APBA-targeted HSA nanocomposites using leucine and mannitol as a carrier [(1:1:2), F7] using Andersen Cascade Impactor (ACI). Experiments were performed at air flow rate 28.5 l/min. The release profile of spray dried albumin nanoparticles loaded BER/EPC using mannitol as a carrier with (1:3) weight ratio in PBS pH 7.4 at 37 °C (B).

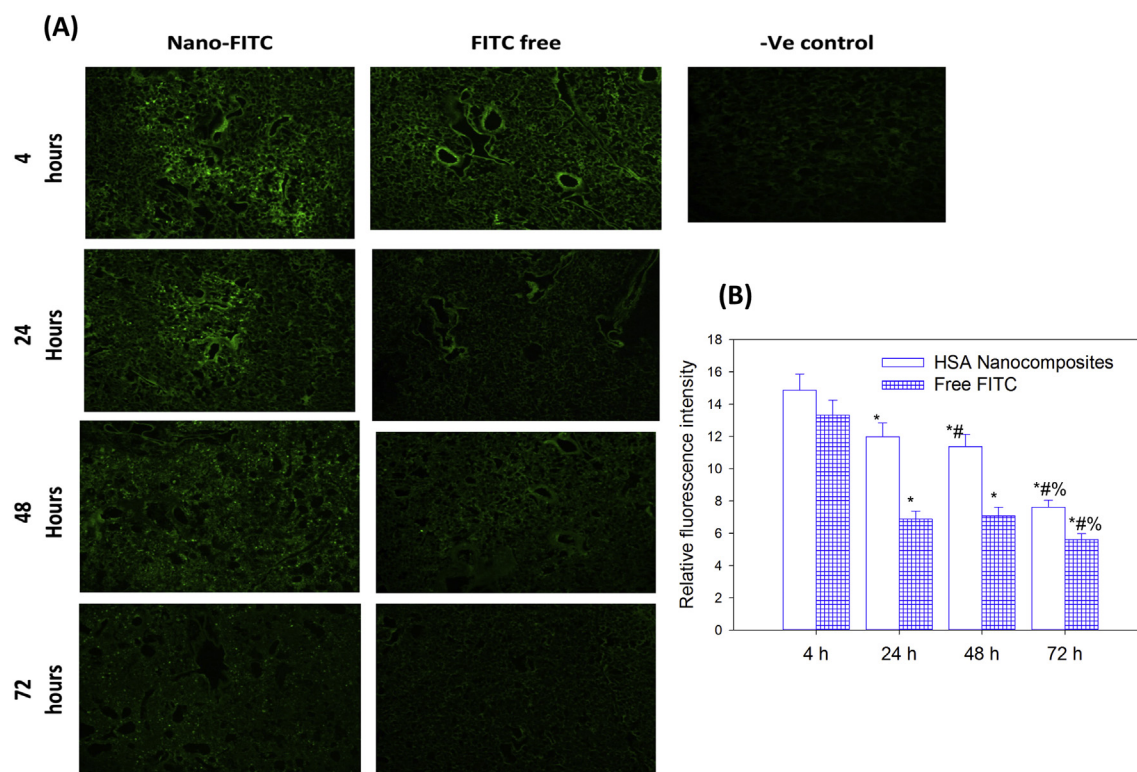


**Fig. 8.** Fluorescent images of cross-section of lung at 4, 24, 48, 72 h after intratracheal administration of APBA-targeted HSA nanocomposites powder labeled by FITC dye (original magnification, 10) versus free FITC dye (A), and their relative fluorescence intensity vs time (B). \* $P < .05$  vs 4 h, #  $P < .05$  vs 24 h, % $P < .05$  vs 48 h.

their quickly distribution and deposition into the lungs (Fig. 8A and B). Free FITC powder exhibited lower inhalation efficiency when compared to nanocomposite powder reflecting the in vivo lung deposition superiority of the nanocomposites. Autofluorescence of the native lung tissues (the control group) was neglected (autocorrected). By time, the fluorescence intensity and particles number in lung sections were declined in both FITC-APBA-HSA nanocomposites and free FITC powder, suggesting their biodegradation and clearance from lung tissues. Although the fluorescence was faded after 72 h but nanocomposites were still detectable with higher intensity than free FITC (Fig. 8B). These results ensured the appropriate aerodynamic parameters of spray-dried nanocomposite powder for in vivo pulmonary delivery of ETP and BER to the deep lung tissues and being well-retained over 3 days, confirming the efficiency of treatment.

### 3.9. In vivo anti-tumor efficacy

#### 3.9.1. Safety and therapeutic activity evaluation by determination of body and lung weight

The wet lung weight was determined by weighing the isolated lungs after removal of the trachea and other extraneous tissue to eliminate any interference (Fig. 9A and B). Untreated positive control mice displayed the highest lung weight compared to the different treatment groups, indicating lung damage due to tumor growth, excluding any formulation inflammatory effect. There was no significant difference in the weight of lungs between the insufflated HSA nanocomposites (F4) and normal negative control group ( $p < .05$ ), with 2.8-fold reduction in lung weight ( $p < .05$ ) compared to the positive control group. This confirmed the nanocomposite ability of suppressing the tumor growth in lungs. Mice treated with inhalable free drugs powder and I.V. HSA NPs (T5) showed 1.89- and 2.03-fold reduction in lung weight ( $p < .05$ ) compared to the positive control group. Notably, cancerous lesions in huge number were observed in positive control extracted lungs, whereas native control lungs showed normal physiological

features. Compared to the positive control and I.V. HSA NPs, inhalable nanocomposites powder displayed superior treatment strategy with visibly much reduced tumor tissues number (Fig. 9B).

Mice body weight was monitored during the treatment (Fig. 9C). There was approximately no change in the body weights of mice treated with the inhalable nanocomposites powder at the end of 21 days, confirming the safety of the inhalable formulations. Group treated with inhalable free drugs powder showed 31.5% reduction of body weight during the treatment while the positive control group exhibited only 13.2% reduction, indicating the possible absorption of drugs into systemic circulation. In comparison with the inhalable nanocomposites, I.V. HSA NPs administered with the same dose showed more reduction in the body weight, suggesting the superiority of the inhalable nanocomposite powder formulation.

#### 3.9.2. Effect of different treatments on lung homogenate VEGF and caspase

Relatively to the positive control group, the inhalable nanocomposite powder treatment group showed a 3.64-fold reduction in the VEGF expression level, compared to only 1.87- fold reduction in I.V. HSA NPs group ( $P < .05$ ) confirming a potential reduction effect on tumor angiogenesis by the inhalation route of administration over the I.V. route. Inhalable free drugs powder could only exhibit a 1.6-fold reduction of VEGF level which ensured their inadequacy in inhibition of tumor growth (Fig. 9D).

As shown in Fig. 9E, all treated groups exhibited a higher apoptotic effect compared to untreated positive control group. An enhancement in apoptosis activation ( $p < .05$ ) was observed in mice treated with inhalable nanocomposites powder (16.8 ng/g tissue) over the inhalable free drugs powder treated group (13.08 ng/g tissue) and the positive group (1.66 ng/g tissue). In addition, injectable HSA NPs treatment succeeded to significantly ( $p < .05$ ) exhibited higher Casp-3 levels compared to I.V. free drugs and control group (Fig. 9E).

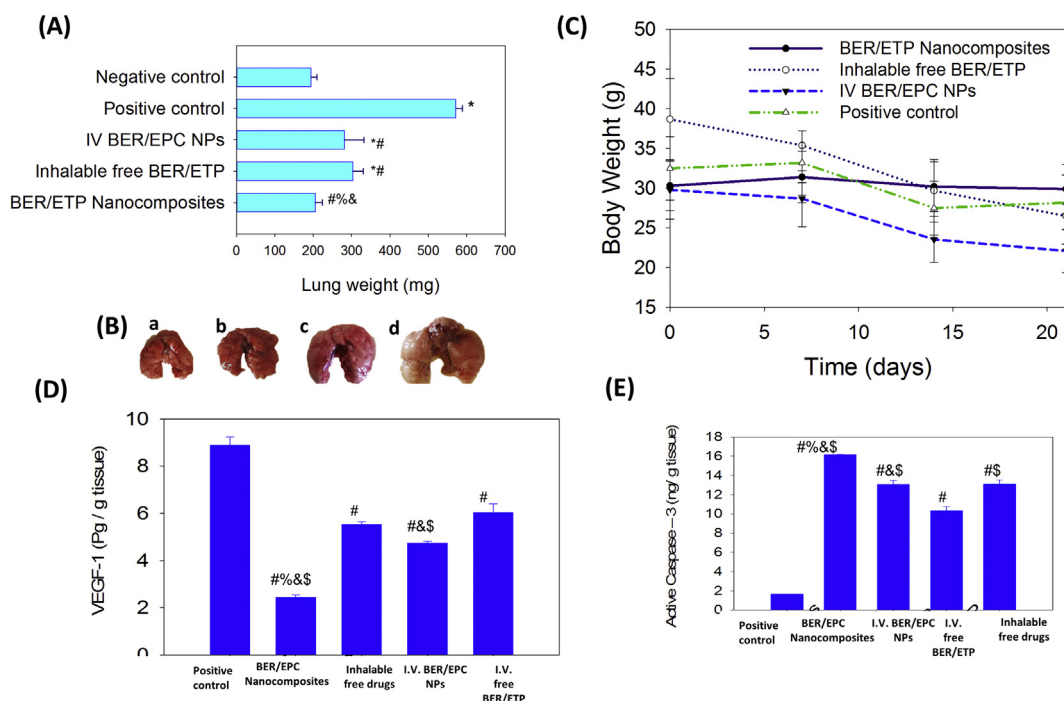


**Fig. 9.** Lung weights of the different groups post 3 weeks treatment (I.V./inhalation) compared to untreated positive control (A), Excised lungs from different treatment groups (B); negative control (Ba), inhalable APBA-targeted HSA nanocomposites (Bb) I.V. APBA-targeted HSA NPs (Bc) and positive control (Bd). Body weights measurements of mice at indicated time-points along the treatment duration with different treatments (I.V./inhalation) compared to untreated positive control (C), and the level of the tumor markers including Caspase-3 (D), and VEGF (E) in urethane induced lung cancer bearing mice treated with different treatments compared to untreated positive control. \* $P < .05$  vs negative control, # $P < .05$  vs positive control, & $P < .05$  vs inhalable free drugs, % $P < .05$  vs I.V. APBA-targeted HSA NPs, \$ $P < .05$  vs I.V. free drugs.

### 3.9.3. Histopathological and immunohistochemical analysis

As shown in Fig. 10A, normal epithelial single-layered alveolar tissue was observed in the negative control group, while the positive control group showed epithelial hyperplasia to adenoma (blue arrow), hemorrhage (white arrow) and inflammatory cells infiltration (black arrow) as signs of pre-cancerous and cancerous tissues upon histopathological examination. Compared to I.V. HSA NPs, the inhalable nanocomposites-treated group revealed superlative enhancement in the histopathological neoplastic insult with reduced signs of cancerous transformation. Additionally, inhalable nanocomposites and I.V. NPs treated groups exhibited a significant 12.25- and 2.58-fold reduction in the number of metastatic lung foci, respectively with highly reduced diameter (0.62 and 2.85 mm, respectively), compared to untreated control group ( $P < .05$ ), confirming the efficacy of the inhalation route of administration in treatment of the lung cancer (Fig. 10B).

Additionally, immunohistochemical examination of the proliferation marker Ki-67 confirmed the superiority of inhalable nanocomposites, over other tested routes of administration (I.V.) and the control group, indicated by the reduction in brown staining density (Fig. 10A). Significant reduction in Ki-67-expression was detected in inhalable nanocomposites-treated mice (16.8%) than I.V. NPs and untreated control group (52.6, and 92.94%, respectively) ( $P < .05$ ) (Fig. 10C).

From all these results, it was confirmed that dry nanocomposite powder inhalational therapy was superior in anti-tumor efficacy, anti-angiogenic, apoptotic and anti-proliferative activity than the I.V. NPs and both inhalable and injectable free drugs. The substantial improvement in suppressing tumor growth is likely due to the local, concentrated and deep lung deposition treatment achieved with inhalable nanocomposites that maintained targeted effective drug levels over long periods to kill tumor cells.

## 4. Conclusion

To the best of our knowledge, there is no inhalable ETP delivery system for local delivery to the deep lungs was evaluated in lung cancer bearing mice. In the present study, we proposed inhalable APBA-targeted HSA nanocomposites for combined delivery of BER and ETP to urethane-induced lung cancer bearing mice. First, ETP was incorporated within albumin nanoparticles via its pre-formulation as phospholipid complex (EPC). Second, BER and EPC were successfully co-encapsulated into albumin nanoparticles with high drug loading and suitable size. The tumor-targeting effect of APBA could enhance the internalization of the nanocarriers and hence their cytotoxicity against lung cancer cells. Finally, the APBA-HSA nanoparticles were spray-dried into inhalable nanocomposites for deep lung deposition. The spray-dried nanocomposites prepared using mannitol carrier displayed favorable aerosolization performance with small MMAD (2.11  $\mu$ m) and high FPF (77.86%) as well as high aqueous redispersibility. The superior anti-tumor efficacy of the inhalable nanocomposites was revealed by reduction of lung weights and growth biomarkers in lung cancer bearing mice and augmented by histopathological and immunohistochemical analysis. The inhalable dose of ETP administered to mice was much lower than that used in other studies via systemic routes. Overall, the developed inhalable dry powder APBA-targeted HSA nanocomposites co-loaded with ETP and BER could present a promising alternative to systemic therapy of lung cancer. However, further studies should be performed in the future on large animal models that may have significantly different characteristics and profiles from small animals (particles deposition, internalization, and risk/cost-benefit ratio). Long-term efficacy and safety including inflammation and immunogenicity could be evaluated specifically in repeated-cycles treatment.



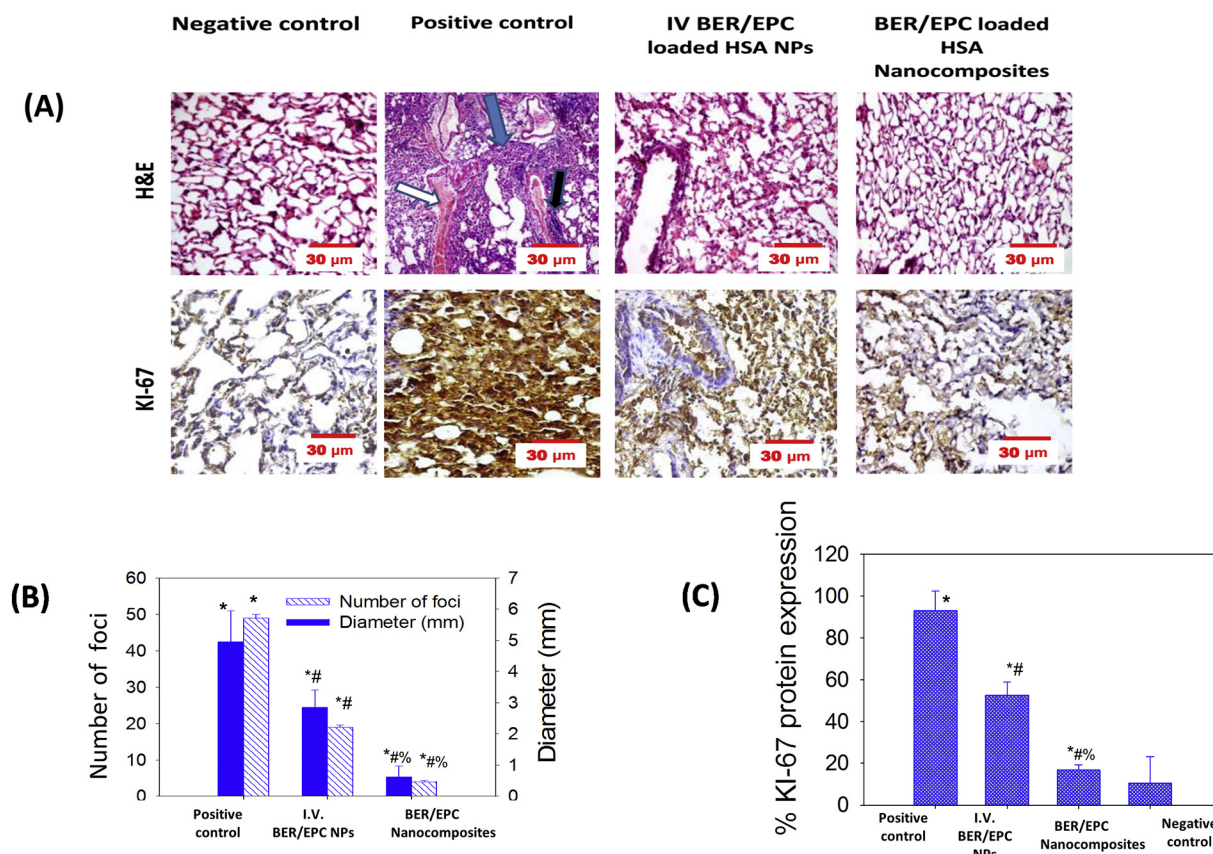


**Fig. 10.** Histopathological and Immunohistochemical analysis of lung sections of I.V. APBA-targeted HSA NPs and inhalable APBA-targeted HSA nanocomposites treatment groups compared to untreated positive control and healthy negative control groups; H&E and Ki-67 expression (A), Number of foci and their diameter related to H&E sections (B) and % expression of proliferating protein Ki-67 related to Ki-67 sections (C). \* $P < .05$  vs negative control, # $P < .05$  vs positive control, % $P < .05$  vs I.V. APBA-targeted HSA NPs.

## Acknowledgement

This work was supported by the research grant (No. 5731) of Science and Technology Development Fund (STDF), Ministry of Scientific Research, Egypt.

## Appendix A. Supplementary data

Supplementary data to this article can be found online at <https://doi.org/10.1016/j.jconrel.2018.07.014>.

## References

- H.M. Abdelaziz, M. Gaber, M.M. Abd-Elwakil, M.T. Mabrouk, M.M. Elgohary, N.M. Kamel, D.M. Kabary, M.S. Freag, M.W. Samaha, S.M. Mortada, K.A. Elkhodairy, J.Y. Fang, A.O. Elzoghby, Inhalable particulate drug delivery systems for lung cancer therapy: nanoparticles, microparticles, nanocomposites and nanoaggregates, *J. Control. Release* 269 (2017) 374–392.
- R. Feng, Z. Zhang, Z. Li, G. Huang, Preparation and in vitro evaluation of etoposide-loaded PLGA microspheres for pulmonary drug delivery, *Drug Deliv.* 21 (2014) 185–192.
- S. Sabra, M. Abdelmoneem, M. Abdelwakil, M. Mabrouk, D. Anwar, R. Mohamed, S. Khattab, A. Bekhit, K. Elkhodairy, M. Freag, A.O. Elzoghby, Self-assembled nanocarriers based on amphiphilic natural polymers for anti-cancer drug delivery applications, *Curr. Pharm. Des.* 23 (2017) 5213–5229.
- S.N. Khattab, S.E. Abdel Naim, M. El-Sayed, A.A. El Bardan, A.O. Elzoghby, A.A. Bekhit, A. El-Faham, Design and synthesis of new s-triazine polymers and their application as nanoparticulate drug delivery systems, *New J. Chem.* 40 (2016) 9565–9578.
- A.O. Elzoghby, Editorial: polymeric nanocarriers as robust platforms for cancer therapy, *Curr. Pharm. Des.* 23 (2017) 5211–5212.
- T. Peng, S. Lin, B. Niu, X. Wang, Y. Huang, X. Zhang, G. Li, X. Pan, C. Wu, Influence of physical properties of carrier on the performance of dry powder inhalers, *Acta Pharm. Sin. B* 6 (2016) 308–318.
- C.L. Tseng, S.Y. Wu, W.H. Wang, C.L. Peng, F.H. Lin, C.C. Lin, T.H. Young,

M.J. Shieh, Targeting efficiency and biodistribution of biotinylated-EGF-conjugated gelatin nanoparticles administered via aerosol delivery in nude mice with lung cancer, *Biomaterials* 29 (2008) 3014–3022.

- Y. Abbas, H.M. Azzazy, S. Tammam, A. Lamprecht, M.E. Ali, A. Schmidt, S. Sollazzo, S. Mathur, Development of an inhalable, stimuli-responsive particulate system for delivery to deep lung tissue, *Colloids Surf. B: Biointerfaces* 146 (2016) 19–30.
- J. Parmar, D.J. Singh, A.A. Lohade, D.D. Hegde, P.S. Soni, A. Samad, M.D. Menon, Inhalational system for etoposide liposomes: formulation development and in vitro deposition, *Indian J. Pharm. Sci.* 73 (2011) 656–662.
- Z. Heger, H. Polanska, S. Krizkova, J. Balvan, M. Raudenska, S. Dostalova, A. Moullick, M. Masarik, V. Adam, Co-delivery of VP-16 and Bcl-2-targeted antisense on PEG-grafted mWCNTs for synergistic in vitro anti-cancer effects in non-small and small cell lung cancer, *Colloids Surf. B: Biointerfaces* 150 (2017) 131–140.
- S. Pimple, A.S. Manjappa, M. Ukawala, R.S. Murthy, PLGA nanoparticles loaded with etoposide and quercetin dihydrate individually: in vitro cell line study to ensure advantage of combination therapy, *Cancer Nanotechnol.* 3 (2012) 25–36.
- U. Schroeder, Hydrolytically activated etoposide prodrugs inhibit MDR-1 function and eradicate established MDR-1 multidrug-resistant T-cell leukemia, *Blood* 102 (2003) 246–253.
- L. Gianni, E. Munzone, G. Capri, F. Fulfaro, E. Tarenzi, F. Villani, C. Spreafico, A. Laffranchi, A. Caraceni, C. Martini, Paclitaxel by 3-hour infusion in combination with bolus doxorubicin in women with untreated metastatic breast cancer: high antitumor efficacy and cardiac effects in a dose-finding and sequence-finding study, *J. Clin. Oncol.* 13 (1995) 2688–2699.
- C. He, R. Rong, J. Liu, J. Wan, K. Zhou, J.X. Kang, Effects of Coptis extract combined with chemotherapeutic agents on ROS production, multidrug resistance, and cell growth in A549 human lung cancer cells, *Chin. Med.* 7 (2012) 11.
- B.S. Anisha, D. Sankar, A. Mohandas, K.P. Chennazhi, S.V. Nair, R. Jayakumar, Chitosan–hyaluronan/nano chondroitin sulfate ternary composite sponges for medical use, *Carbohydr. Polym.* 92 (2013) 1470–1476.
- A.O. Elzoghby, M.M. Elgohary, N.M. Kamel, Implications of protein- and peptide-based nanoparticles as potential vehicles for anticancer drugs, *Adv. Protein Chem. Struct. Biol.* 98 (2015) 169–221.
- A. Elzoghby, Editorial (thematic issue: nanocarriers based on natural polymers as platforms for drug and gene delivery applications), *Curr. Pharm. Des.* 22 (2016) 3303–3304.
- M. Socinski, Update on taxanes in the first-line treatment of advanced non-small-cell lung cancer, *Curr. Oncol.* 21 (2014) e691–e703.



- [19] K.R. Vinod, S. Sandhya, J. Chandrashekar, R. Swetha, T. Rajeshwar, B. David, S. Anbuazaghan, Review on genesis and characterization of phytosomes, *ILPSRR* 4 (2010) 69–75.
- [20] A.O.M. Elzoghby, S. Khamees, M.W. Helmy, M.A. ElDemellawy, S.A. Sheweita, Superiority of aromatase inhibitor and cyclooxygenase-2 inhibitor combined delivery: hyaluronate-targeted versus PEGylated protamine nanocapsules for breast cancer therapy, *Int. J. Pharm.* 529 (2017) 178–192.
- [21] S.W. El-Far, M.W. Helmy, S.N. Khattab, A.A. Bekhit, A.A. Hussein, A.O. Elzoghby, Phytosomal bilayer-enveloped casein micelles for codelivery of monascus yellow pigments and resveratrol to breast cancer, *Nanomedicine (London)* 13 (2018) 481–499.
- [22] X. He, N. Xiang, J. Zhang, J. Zhou, Y. Fu, T. Gong, Z. Zhang, Encapsulation of teniposide into albumin nanoparticles with greatly lowered toxicity and enhanced antitumor activity, *Int. J. Pharm.* 487 (2015) 250–259.
- [23] D.M. Kabary, M.W. Helmy, K.A. Elkhodairy, J.Y. Fang, A.O. Elzoghby, Hyaluronate/lactoferrin layer-by-layer-coated lipid nanocarriers for targeted co-delivery of rapamycin and berberine to lung carcinoma, *Colloids Surf. B: Biointerfaces* 169 (2018) 183–194.
- [24] S.A. Sabra, A.O. Elzoghby, S.A. Sheweita, M. Haroun, M.W. Helmy, M.A. ElDemellawy, Y. Xia, D. Goodale, A.L. Allan, S. Rohani, Self-assembled amphiphilic zein-lactoferrin micelles for tumor targeted co-delivery of rapamycin and wogonin to breast cancer, *Eur. J. Pharm. Biopharm.* 128 (2018) 156–169.
- [25] J.Y. Lee, S.J. Chung, H.J. Cho, D.D. Kim, Phenylboronic acid-decorated chondroitin sulfate A-based theranostic nanoparticles for enhanced tumor targeting and penetration, *Adv. Funct. Mater.* 25 (2015) 3705–3717.
- [26] X. Wang, H. Tang, C. Wang, J. Zhang, W. Wu, X. Jiang, Phenylboronic acid-mediated tumor targeting of chitosan nanoparticles, *Theranostics* 6 (2016) 1378–1392.
- [27] H. Jasmina, O. Džana, E. Alisa, V. Edina, R. Ognjenka, Preparation of nanoemulsions by high-energy and lowenergy emulsification methods, in: A. Badnjevic (Ed.), *CMBEBIH 2017*, Springer Nature Singapore Pte Ltd., 2017, pp. 317–322.
- [28] F. Donsi, B. Senatore, Q. Huang, G. Ferrari, Development of novel pea protein-based nanoemulsions for delivery of nutraceuticals, *J. Agric. Food Chem.* 58 (2010) 10653–10660.
- [29] Y. Wei, Y. Wang, D. Xia, S. Guo, F. Wang, X. Zhang, Y. Gan, Thermosensitive liposomal codelivery of HSA-paclitaxel and HSA-Ellagic acid complexes for enhanced drug perfusion and efficacy against pancreatic cancer, *ACS Appl. Mater. Interfaces* 9 (2017) 25138–25151.
- [30] A. Varki, R. Schauer, Sialic acids, In: A. Varki, R.D. Cummings, J.D. Esko, H.H. Freeze, P. Stanley, C.R. Bertozzi, G.W. Hart, M.E. Etzler Editors. *Essentials of Glycobiology* 2nd Ed. Cold Spring Harbor (NY): Cold Spring Harbor Laboratory Press, (2009) (Chapter 14).
- [31] J.C. Sung, B.L. Pulliam, D.A. Edwards, Nanoparticles for drug delivery to the lungs, *Trends Biotechnol.* 25 (2007) 563–570.
- [32] M.S. Freag, Y.S. Elnaggar, O.Y. Abdallah, Lyophilized phytosomal nanocarriers as platforms for enhanced diosmin delivery: optimization and ex vivo permeation, *Int. J. Nanomedicine* 8 (2013) 2385–2397.
- [33] A.O. Elzoghby, S.A. El-Lakany, M.W. Helmy, M.M. Abu-Serie, N.A. Elgindy, Shell-crosslinked Zein nanocapsules for oral codelivery of exemestane and resveratrol in breast cancer therapy, *Nanomedicine (London)* 12 (2017) 2785–2805.
- [34] S. Dreis, F. Rothweiler, M. Michaelis Jr., J. Cinatl, J. Kreuter, K. Langer, Preparation, characterisation and maintenance of drug efficacy of doxorubicin-loaded human serum albumin (HSA) nanoparticles, *Int. J. Pharm.* 14 (2007) 341 (207).
- [35] A. Jahanban-Esfahlan, S. Dastmalchi, S. Davaran, A simple improved desolvation method for the rapid preparation of albumin nanoparticles, *Int. J. Biol. Macromol.* 91 (2016) 703–709.
- [36] J. Liu, B. Zhang, Z. Luo, X. Ding, J. Li, L. Dai, J. Zhou, X. Zhao, J. Ye, K. Cai, Enzyme responsive mesoporous silica nanoparticles for targeted tumor therapy in vitro and in vivo, *Nanoscale* 7 (2015) 3614–3626.
- [37] A.O.M. Elzoghby, S. Khamees, M.W. Helmy, M.A. ElDemellawy, S.A. Sheweita, Multi-reservoir phospholipid shell encapsulating protamine nanocapsules for co-delivery of letrozole and celecoxib in breast cancer therapy, *Pharm. Res.* 34 (2017) 1956–1969.
- [38] N. Alam, R.D. Dubey, A. Kumar, M. Koul, N. Sharma, P.R. Sharma, B.K. Chandan, S.K. Singh, G. Singh, P.N. Gupta, Reduced toxicological manifestations of cisplatin following encapsulation in folate grafted albumin nanoparticles, *Life Sci.* 142 (2015) 76–85.
- [39] R.D. Dubey, N. Alam, A. Saneja, V. Khare, A. Kumar, S. Vaidh, G. Mahajan, P.R. Sharma, S.K. Singh, D.M. Mondhe, P.N. Gupta, Development and evaluation of folate functionalized albumin nanoparticles for targeted delivery of gemcitabine, *Int. J. Pharm.* 492 (2015) 80–91.
- [40] M.A. Hamzawy, A.M. Abo-Youssef, H.F. Salem, S.M. Ali, An additional risk of lung cancer from recurrent exposure to ethyl carbamate (EC) in BALB/C mice, *J. Cancer Sci. Therap.* (2015) (2015) 7–11.
- [41] C. Duret, N. Wauthoz, R. Merlos, J. Goole, C. Maris, I. Roland, T. Sebti, F. Vanderbist, K. Amighi, In vitro and in vivo evaluation of a dry powder endotracheal insufflator device for use in dose-dependent preclinical studies in mice, *Eur. J. Pharm. Biopharm.* 81 (2012) 627–634.
- [42] D.L. Teagarden, D.S. Baker, Practical aspects of lyophilization using non-aqueous co-solvent systems, *Eur. J. Pharm. Sci.* 15 (2002) 115–133.
- [43] A. Das, A.K. Nayak, B. Mohanty, S. Panda, Solubility and dissolution enhancement of etoricoxib by solid dispersion technique using sugar carriers, *ISRN Pharm.* 2011 (2011) 819765.
- [44] W.Y. Qian, D.M. Sun, R.R. Zhu, X.L. Du, H. Liu, S.L. Wang, pH-sensitive strontium carbonate nanoparticles as new anticancer vehicles for controlled etoposide release, *Int. J. Nanomedicine* 7 (2012) 5781–5792.
- [45] H. Chen, S. Shi, M. Zhao, L. Zhang, H. He, X. Tang, A lyophilized etoposide sub-micron emulsion with a high drug loading for intravenous injection: preparation, evaluation, and pharmacokinetics in rats, *Drug Dev. Ind. Pharm.* 36 (2010) 1444–1453.
- [46] H. Kouchakzadeh, M.S. Safavi, S.A. Shojaosadati, Efficient delivery of therapeutic agents by using targeted albumin nanoparticles, *Adv. Protein Chem. Struct. Biol.* 98 (2015) 121–143.
- [47] C. Li, L. Xing, S. Che, Coordination bonding based pH-responsive albumin nanoparticles for anticancer drug delivery, *Dalton Trans.* 41 (2012) 3714–3719.
- [48] A.I. Ledesma-Osuna, G. Ramos-Clamont, L. Vazquez-Moreno, Biorecognition of chemically modified bovine serum albumin with lactose prepared under different conditions, *J. Agric. Food Chem.* 57 (2009) 9734–9739.
- [49] S.N. Narla, P. Pinnamaneni, H. Nie, Y. Li, X.L. Sun, BSA-boronic acid conjugate as lectin mimetics, *Biochem. Biophys. Res. Commun.* 443 (2014) 562–567.
- [50] W. She, K. Luo, C. Zhang, G. Wang, Y. Geng, L. Li, B. He, Z. Gu, The potential of self-assembled, pH-responsive nanoparticles of mPEGylated peptide dendron-doxorubicin conjugates for cancer therapy, *Biomaterials* 34 (2013) 1613–1623.
- [51] J. Xie, Y. Li, L. Song, Z. Pan, S. Ye, Z. Hou, Design of a novel curcumin-soybean phosphatidylcholine complex-based targeted drug delivery systems, *Drug Deliv.* 24 (2017) 707–719.
- [52] Z. Wang, Z. Li, D. Zhang, L. Miao, G. Huang, Development of etoposide-loaded bovine serum albumin nanosuspensions for parenteral delivery, *Drug Deliv.* 22 (2014) 79–85.
- [53] K.S. Yadav, K.K. Sawant, Formulation optimization of etoposide loaded PLGA nanoparticles by double factorial design and their evaluation, *Curr. Drug Deliv.* 7 (2010) 51–64.
- [54] S. Narayanan, M. Pavithran, A. Viswanath, D. Narayanan, C.C. Mohan, K. Manzoor, D. Menon, Sequentially releasing dual-drug-loaded PLGA-casein core/shell nanomedicine: design, synthesis, biocompatibility and pharmacokinetics, *Acta Biomater.* 10 (2014) 2112–2124.
- [55] Y.C. Kuo, Y.C. Chen, Targeting delivery of etoposide to inhibit the growth of human glioblastoma multiforme using lactoferrin- and folic acid-grafted poly(lactide-co-glycolide) nanoparticles, *Int. J. Pharm.* 479 (2015) 138–149.
- [56] Z. Fan, G. Liu, Y. Li, J. Ma, J. Lin, F. Guo, Z. Hou, L. Xie, Self-assembly of the active lactone form of a camptothecin-phospholipid complex for sustained nuclear drug delivery, *RSC Adv.* 6 (2016) 82949–82960.
- [57] H. Zhang, C.P. Hollis, Q. Zhang, T. Li, Preparation and antitumor study of camptothecin nanocrystals, *Int. J. Pharm.* 415 (2011) 293–300.
- [58] C. Sinsuebpol, J. Chatchawalsaisin, P. Kulvanich, Preparation and in vivo absorption evaluation of spray dried powders containing salmon calcitonin loaded chitosan nanoparticles for pulmonary delivery, *Drug Des. Devel. Ther.* 7 (2013) 861–873.
- [59] T. Rattanaputamat, T. Srichana, Budesonide dry powder for inhalation: effects of leucine and mannitol on the efficiency of delivery, *Drug Deliv.* 21 (2014) 397–405.
- [60] Y. Wang, K. Kho, W.S. Cheow, K.A. Hadinoto, Comparison between spray drying and spray freeze drying for dry powder inhaler formulation of drug-loaded lipid-polymer hybrid nanoparticles, *Int. J. Pharm.* 424 (2012) 98–106.
- [61] R. Osman, K.T. Al Jamal, P.L. Kan, G. Awad, N. Mortada, A.E. El-Shamy, O. Alpar, Inhalable DNase I microparticles engineered with biologically active excipients, *Pulm. Pharmacol. Ther.* 26 (2013) 700–709.
- [62] S.H. Lee, D. Heng, W.K. Ng, H.K. Chan, R.B. Tan, Nano spray drying: a novel method for preparing protein nanoparticles for protein therapy, *Int. J. Pharm.* 403 (2011) 192–200.
- [63] K. Kanogwan, T. Srichana, Nano spray-dried pyrazinamide-l-leucine dry powders, physical properties and feasibility used as dry powder aerosols, *Pharm. Dev. Technol.* 21 (2016) 68–75.
- [64] B.D. Nandiyanto, K. Okuyama, Progress in developing spraydrying methods for the production of controlled morphology particles: from the nanometer to sub-micrometer size ranges, *Int. J. Antimicrob. Agents* 22 (2011) 1–19.
- [65] N.Y. Chew, P. Tang, H.K. Chan, J.A. Raper, How much particle surface corrugation is sufficient to improve aerosol performance of powders? *Pharm. Res.* 22 (2005) 148–152.
- [66] N.Y. Chew, H.K. Chan, Effect of powder polydispersity on aerosol generation, *J. Pharm. Pharm. Sci.* 5 (2002) 162–168.
- [67] N.Y. Chew, H.K. Chan, Use of solid corrugated particles to enhance powder aerosol performance, *Pharm. Res.* 18 (2001) 1570–1577.
- [68] K. Kho, K. Hadinoto, Optimizing aerosolization efficiency of dry-powder aggregates of thermally-sensitive polymeric nanoparticles produced by spray-freeze-drying, *Powder Technol.* 214 (2011) 169–176.
- [69] K. Nahar, N. Gupta, R. Gauvin, S. Absar, B. Patel, V. Gupta, A. Khademhosseini, F. Ahsan, In vitro, in vivo and ex vivo models for studying particle deposition and drug absorption of inhaled pharmaceuticals, *Eur. J. Pharm. Sci.* 49 (2013) 805–818.



## UV filter entrapment in mesoporous silica hydrogel for skin protection against UVA with minimization of percutaneous absorption

Yu-Chih Lin<sup>a</sup>, Chwan-Fwu Lin<sup>b,c</sup>, Ahmed Alalaiwe<sup>d</sup>, Pei-Wen Wang<sup>e</sup>, Yi-Ping Fang<sup>f,g,\*</sup>, Jia-You Fang<sup>c,h,i,j,\*\*</sup>

<sup>a</sup> Department of Environmental Engineering and Health, Yuanpei University, Hsinchu, Taiwan

<sup>b</sup> Department of Cosmetic Science, Chang Gung University of Science and Technology, Kweishan, Taoyuan, Taiwan

<sup>c</sup> Research Center for Industry of Human Ecology and Research Center for Chinese Herbal Medicine, Chang Gung University of Science and Technology, Taoyuan, Taiwan

<sup>d</sup> Department of Pharmaceutics, College of Pharmacy, Prince Sattam Bin Abdulaziz University, Al Kharj, Saudi Arabia

<sup>e</sup> Department of Medical Research, China Medical University Hospital, China Medical University, Taichung, Taiwan

<sup>f</sup> School of Pharmacy, College of Pharmacy, Kaohsiung Medical University, Kaohsiung, Taiwan

<sup>g</sup> Department of Medical Research, Kaohsiung Medical University Hospital, Kaohsiung, Taiwan

<sup>h</sup> Pharmaceutics Laboratory, Graduate Institute of Natural Products, Chang Gung University, Taoyuan, Taiwan

<sup>i</sup> Chinese Herbal Medicine Research Team, Healthy Aging Research Center, Chang Gung University, Taoyuan, Taiwan

<sup>j</sup> Department of Anesthesiology, Chang Gung Memorial Hospital at Linkou, Taoyuan, Taiwan

### ARTICLE INFO

#### Keywords:

UV filter

Avobenzone

Mesoporous silica

UVA

Skin

Percutaneous absorption

### ABSTRACT

The UVA absorbers such as avobenzone are widely used for sunlight protection; however, they show a significant skin penetration. The aim of the present study was to formulate UVA absorbers into mesoporous silicas (MSs) for enhanced UVA protection with reduced percutaneous absorption. Two MSs prepared with different structure-directing agents (Pluronic P123 as single MS and combined Pluronic P123-Pluronic F68 as hybrid MS) were synthesized in this study. The hybrid MS exhibited higher specific surface area (853 m<sup>2</sup>/g) than the single MS (764 m<sup>2</sup>/g). The particle sizes of single MS and hybrid MS were about 1 and 1.5 μm, respectively. The adsorbed avobenzone had greatly decreased crystallinity compared with free avobenzone. The *in vitro* photoprotection determined by UVA/UVB ratio showed that the MS-loaded avobenzone in hydrogel endowed a synergistic effect on UVA protection compared to the free avobenzone. The skin absorption test using Franz diffusion cell indicated that the skin permeation of avobenzone and oxybenzone from MSs in semisolid preparations was one-third to one-half of those from free control. This effect was observed by using both pig skin and UVA-damaged nude mouse skin as the penetration barriers. Topical application of hybrid MS on nude mouse skin before UVA irradiation had prevented the increased transepidermal water loss (TEWL), furrow formation, keratinocyte apoptosis, and neutrophil infiltration. Our findings conclude that MSs containing avobenzone or oxybenzone effectively ameliorated UVA-induced skin disruption and reduced the possible toxicity elicited by percutaneous penetration.

### 1. Introduction

Ultraviolet (UV) radiation of UVA (320–400 nm) and UVB (290–320 nm) can reach the earth's surface and injure the skin; UVA and UVB contribute about 95% and 5% of the damage, respectively (Karran and Brem, 2016). The sunburn risk by UVB has long been recognized by scientists. Increasing concern about the deleterious effect of UVA is revealed in the more recent investigations (Gies et al., 2018).

UVB exposure is stronger in the summer, while UVA always remains constant during the whole year. The photoaging induced by UVA generates the oxidative stress which activates cytokines, matrix metalloproteinases (MMPs), DNA mutation, and the enzymes for degrading elastin and collagen. The resulting photoaged skin contributes to wrinkling, fragility, and even the growth of cutaneous carcinomas (Wang et al., 2008). The development of potent UVA filters for skin protection is the main advance for topical sunscreens. UV filters consist

\* Correspondence to: Y.-P. Fang, School of Pharmacy, College of Pharmacy, Kaohsiung Medical University, 100 Shih-Chuan 1st Road, Kaohsiung 807, Taiwan.

\*\* Correspondence to: J.-Y. Fang, Pharmaceutics Laboratory, Graduate Institute of Natural Products, Chang Gung University, 259 Wen-Hwa 1st Road, Kweishan, Taoyuan 333, Taiwan.

E-mail addresses: [ypfang@kmu.edu.tw](mailto:ypfang@kmu.edu.tw) (Y.-P. Fang), [fajy@mail.cgu.edu.tw](mailto:fajy@mail.cgu.edu.tw) (J.-Y. Fang).

<https://doi.org/10.1016/j.ejps.2018.07.013>

Received 15 March 2018; Received in revised form 12 June 2018; Accepted 4 July 2018

Available online 04 July 2018

0928-0987/ © 2018 Published by Elsevier B.V.

of organic or inorganic molecules which can reflect, scatter, or absorb solar irradiation. An ideal sunscreen should exhibit retarded percutaneous absorption and systemic penetration as it displays the effect on cutaneous surface. Nevertheless, the fact is that some of the UV filters penetrate into and across skin, leading to the phototoxicity, allergy, dermatitis, and systemic adverse effects (Lee et al., 2012). The presence of sunscreens in a large amount of cosmetics and the daily application of the products has resulted in the high risk of over absorption. Adjusting the formulations of sunscreen may decrease the percutaneous absorption and enhance the UVA protection capability.

Due to their physicochemical stability, uniform porosity, great surface area, and biocompatibility, mesoporous silicas (MSs) are widely employed as drug delivery carriers, biosensors, catalysts, and adsorbents (Hao et al., 2017; Daneluti et al., 2018). It is feasible to load the molecules inside the pores with high encapsulation efficiency, controlled delivery, and increased drug stability (He and Shi, 2011). It is reported that MSs can reflect the light (Yamada et al., 2006), which is an implication of UV filters. The combination of UV filters is useful to promote solar protection for avoiding skin damage. An approach that can synergize the UV filter ability and reduce the skin absorption responsible for toxicity would be advantageous. MSs may efficiently entrap the UV filters to protect the labile molecules against decomposition and diminish the skin absorption. The present study aimed to immobilize the UVA filters in MSs to evaluate the percutaneous permeation and photoprotection effectiveness on skin.

The UV filter agents used herein were mainly avobenzone. Besides avobenzone, oxybenzone was also loaded in MSs for testing skin absorption. Both compounds are reported to be detectable in plasma and urine for the suspected eczema, melanoma, and breast cancer induced by the organic sunscreens (Afonso et al., 2014; DiNardo and Downs, 2018). The facility of UV filters depends upon the particular type of vehicles used. We respectively used Pluronic P123 and Pluronic P123-Pluronic F68 as the single and hybrid composite structure-directing agents, respectively, to fabricate MSs for the comparison of avobenzone/oxybenzone permeation and UVA-filtering activity. It is important to formulate the sunscreens or their complexations in a cosmetically acceptable dosage form (Latha et al., 2013). We incorporated the avobenzone/oxybenzone-MS systems into hydrogels and creams to obtain the suitable formulations for topical application. The skin absorption of avobenzone and oxybenzone was estimated by *in vitro* Franz diffusion assembly by using pig skin and UVA-irradiated nude mouse skin as the permeation barriers. The evidence of skin protection by the topical filter-MS complexes was determined by cutaneous blood flow, transepidermal water loss (TEWL), and immunohistochemistry (IHC) after UVA exposure on the dorsal region of the mouse.

## 2. Materials and methods

### 2.1. Preparation of MSs

MSs were prepared by employing Pluronic P123 (single MS) or Pluronic P123-Pluronic F68 (hybrid MS) as the structure-directing agent and tetraethyl orthosilicate (TEOS) as the silica source. Pluronic P123 (4 g) or the hybrid of Pluronic P123 (3 g) and Pluronic F68 (1 g) was dissolved in 160 ml of 2 M HCl at 30 °C by 1-h stirring. Subsequently TEOS was added into the solution with stirring at 30 °C for 24 h. The solution was transferred to an autoclave for heating at 90 °C. After 24 h, the resulting precursor was filtered, washed with water, and air-dried at 100 °C for 5 h. The resultant solid was then placed in a furnace at 550 °C for 5 h to remove the template. The final product was obtained after cooling down the temperature to 25 °C.

### 2.2. The loading of avobenzone/oxybenzone into MSs

Avobenzone or oxybenzone (20 mg) was dissolved in absolute ethanol (30 ml). Then the MSs (90 mg) was incorporated in the solution

with stirring for 24 h to maximize the avobenzone/oxybenzone loading efficiency. The organic solvent was evaporated at 90 °C for 9 h. The final product was obtained by further drying in a vacuum overnight. The entrapment percentage of avobenzone/oxybenzone was determined by utilizing the ultracentrifugation method to separate the incorporated compound from the free form. The MSs in water was centrifuged at 48,000  $\times g$  and 4 °C for 40 min. The free avobenzone/oxybenzone in the supernatant and the encapsulated filter in the precipitate were analyzed by high-performance liquid chromatography (HPLC) to measure the entrapment efficiency.

### 2.3. Nitrogen adsorption analysis

The specific surface area and pore size distribution of MSs was estimated from the adsorption of N<sub>2</sub> adsorption-desorption isotherm by a porosimetry system (ASAP 2000, Micromeritics, Norcross, GA, USA). The surface area was calculated by the Brunauer-Emmett-Teller (BET) process. The pore diameter and pore volume were calculated on the adsorption branch of the isotherm based on the Barrett-Joyner-Halenda (BJH) method.

### 2.4. Electron microscopy

High resolution transmission electron microscopy (HRTEM, JEM 2100, Jeol, Tokyo, Japan) and high resolution scanning electron microscopy (HRSEM, Nova NanoSEM 230, Thermo Fisher, Waltham, MA, USA) were used to visualize the morphology of MSs. The instrument was operated at 300 kV. The powder of MSs was dispersed on a copper grid coated with the perforated carbon film before detection.

### 2.5. X-ray diffraction (XRD)

The powder XRD pattern of MSs was collected by a diffractometer (Kappa Apex II, Bruker, Billerica, MA, USA). Cu K $\alpha$  radiation was used with a scan speed of 0.01°/min.

### 2.6. Differential scanning calorimetry (DSC)

The transition point of avobenzone in free form and MS form was measured using a Q2000 calorimeter (TA Instruments, New Castle, DE, USA). The samples were weighed and sealed in the calorimeter. The heating curve was recorded from 40 to 150 °C at a scan rate of 10 °C/min under nitrogen.

### 2.7. Preparation of topically applied semisolid vehicles

The Carbopol 940 (C940) hydrogel was prepared by dispersing C940 (0.6%, w/w) and triethanolamine (2%) in water by stirring for 4 h. The MSs containing avobenzone or oxybenzone were added into the hydrogel for further mixing. The avobenzone/oxybenzone concentration in the final product was 0.67%. The carboxymethyl cellulose (CMC) hydrogel was prepared by adding CMC (6%) into water for 4-h stirring. The avobenzone/oxybenzone-entrapped MSs was incorporated into CMC hydrogel with a final avobenzone/oxybenzone concentration of 0.67%. The hydrophilic cream containing 0.67% avobenzone/oxybenzone was prepared according to the common process used in compounding practice. The cream was composed of white petrolatum (20%), stearyl alcohol (18%), sodium dodecyl sulfate (0.45%), and water to produce a total amount of 100%.

### 2.8. *In vitro* UVA protection analysis

The ratio of UVA absorbance to mean UVB absorbance was utilized as the UVA protection parameter for avobenzone by using SPF 290S analyzer (Optometrics, Littleton, MA, USA). This approach was carried out according to the technique proposed by Diffey (1994). The sample

(1.86 mg/cm<sup>2</sup>) was uniformly applied on polymethylmethacrylate plate and irradiated with UVA (320–400 nm) and UVB (290–320 nm). The UVA/UVB absorbance ratio was calculated based on the equation reported previously (Moyal, 2008).

## 2.9. Animals

The pathogen-free, one-week-old pig was supplied by the Animal Technology Institute Taiwan (Miaoli, Taiwan). The eight-week-old female nude mouse was provided by the National Laboratory Animal Center (Taipei, Taiwan). The animal experiment was done in strict accordance with the recommendations in the Guidelines for the Care and Use of Laboratory Animals of Chang Gung University. The protocol was approved by the Institutional Animal Care and Use Committee of Chang Gung University. The protocol of epicutaneous sensitization for inducing photoaged skin was the same as in our previous study (Hung et al., 2015a, 2015b).

## 2.10. Skin permeation of avobenzone/oxybenzone

Franz diffusion cell was employed to measure avobenzone/oxybenzone penetration into and across the skin. The pig skin or photoaged nude mouse skin was mounted between the donor and receptor with the stratum corneum (SC) facing up toward the donor. The receptor medium (5.5 ml) was 30% ethanol in pH 7.4 buffer. The donor vehicle (0.5 g) was avobenzone/oxybenzone in 20% propylene glycol (PG) or semisolid preparations. The effective permeation area of the Franz cell was 0.785 cm<sup>2</sup>. The stirring rate of the stir bar and the receptor medium were kept at 600 rpm and 37 °C, respectively. At the determined intervals, a 300-μl receptor medium was withdrawn to analyze avobenzone/oxybenzone penetration across skin. The fresh buffer was added to the receptor for maintaining a constant volume. The skin was removed at 24 h post-administration. We then washed and weighed the skin, and placed it in MagNA Lyser (Roche, Indianapolis, IN, USA) for homogenization. The homogenate was centrifuged at 10,000 × g for 10 min. The avobenzone/oxybenzone amount in the receptor and skin reservoir was quantified by HPLC as described previously (Hung et al., 2014).

## 2.11. In vivo UVA protection of avobenzone

The Bio-Sun illuminator (Vilber Lourmat, Marne-la-Vallée, France) was used to irradiate UVA (365 nm). Avobenzone in the form of free compound, single MS, or hybrid MS was incorporated into C940 hydrogel for topical application on the dorsal region. The hydrogel (0.4 g) was spread onto the skin with an area of 24 cm<sup>2</sup>. Subsequently UVA was irradiated to the animals. The distance between the nude mouse dorsal skin and the lamp was about 10 cm. The spectral irradiance for UVA was 10 J/cm<sup>2</sup>. The dorsal area was exposed with UVA every other day for 5 d. After the course of UVA irradiation for 3 times, the mouse skin was evaluated by skin blood flow (LAB Laser Doppler Flowmetry, Moor, Devon, UK) and TEWL (TM 300, Courage and Khazaka, Köln, Germany). The macroscopic appearance of skin surface was observed using a handheld digital magnifier (Mini Scope-V, M&T Optics, Taipei, Taiwan).

## 2.12. Histological analysis

The skin specimen was immersed in a 10% buffered formaldehyde using ethanol, embedded in paraffin wax, and sliced at a thickness of 3 μm for hematoxylin and eosin (H&E) staining. The unstained slices were prepared for IHC. After dewaxing and rehydration, the paraffin-embedded sections were subjected to heat-induced epitope retrieval according to the manufacturer's instructions, followed by blocking with diluted normal serum. The sections were incubated with anti-mouse TUNEL antibody, anti-mouse Ki67 antibody, or anti-mouse Ly6G

**Table 1**  
Structural parameters of mesoporous silicas.

Formulation	BET surface area (m <sup>2</sup> /g)	Pore diameter (Å)	Pore volume (cm <sup>3</sup> /g)
Single	764.25 ± 6.61	54.62 ± 8.10	0.82 ± 0.10
Hybrid	852.54 ± 33.14	47.33 ± 0.05	0.71 ± 0.01

Each value represents the mean ± SD (n = 3).

BET, specific surface area measured by Brunauer-Emmett-Teller method.

antibody for 1 h at room temperature; washed with saline containing 0.5% Tween 20, and subsequently incubated at ambient temperature with biotinylated donkey anti-goat IgG for 20 min. Photographs were obtained using a Leica DMi8 microscopy (München, Germany).

## 2.13. Statistical analysis

The data are presented as mean and standard deviation (S.D.) of the mean. The difference in the data of different treatment groups was assayed using Kruskal-Wallis test. The post hoc test for checking individual differences was Dunn's test. Significance was indicated as  $p < 0.05$ .

## 3. Results

### 3.1. Physicochemical characterization of MSs

We had prepared MSs based on the catalyzation reaction of TEOS in the presence of Pluronic P123 (single MS) or Pluronic P123-Pluronic F68 (hybrid MS). Table 1 summarizes the textural properties of MSs. The specific surface area, pore diameter, and pore volume derived from N<sub>2</sub> adsorption estimation were 764 m<sup>2</sup>/g, 55 Å, and 0.82 cm<sup>3</sup>/g, respectively. These data supported the mesoporous architecture of the MSs, indicating a high potential for loading sufficient avobenzone amount. In comparison to single MS, the addition of Pluronic F68 (hybrid MS) led to a catalyst with higher BET surface area and narrower pores ( $p < 0.05$ ). The hybrid formulation had a surface area of 853 m<sup>2</sup>/g and an average pore diameter of 47 Å, while the pore volume was about 0.71 cm<sup>3</sup>/g. The two MSs had a pore size of approximately 50 Å, which was similar to the reference of SBA-15 (Castanheiro et al., 2017).

The typical HRTEM and HRSEM images of MSs are illustrated in Fig. 1. As shown in Fig. 1A, the rod-like MSs with mesopores are clearly observed. The MSs were formed by a cluster of numerous silica particles. Fig. 1B is the higher magnification of HRTEM. The mesopores of single MS are uniformly aligned along the long axes, exhibiting a typical mesoporous structure. In the case of hybrid MS, the regular mesopores packed in hexagonal symmetry were revealed, as is typical with SBA-15-like structure. The HRSEM images of single MS and hybrid MS exhibit the morphology of long and short kidney-shaped rods with a particle size of about 1 and 1.5 μm, respectively (Fig. 1C). The MSs could be controlled at a micrometer level.

Fig. 2A displays the XRD pattern of MSs. Both formulations showed one prominent peak and two weak peaks in the 2θ region of 0.5° to 2°, confirming the hexagonal array with a high degree of structural order, the same as SBA-15 (Carrero et al., 2017). The addition of Pluronic F68 in the structure-directing agents (hybrid) exhibited broader and less intense peaks than the single MS, suggesting less crystallinity. The DSC thermograms of avobenzone, MSs, and avobenzone-loaded MSs are depicted in Fig. 2B. The raw avobenzone was a highly crystalline compound showing a strong endothermic peak at 79 °C. MSs displayed a broad peak in the range of 80–100 °C, indicating a slight phase change. This broad peak shifted to the lower temperature by using the hybrid structure-directing reagents. This is an indication of crystallinity reduction, confirming the result of XRD. The avobenzone-containing MSs showed no significant peak at 79 °C, indicating that most of the



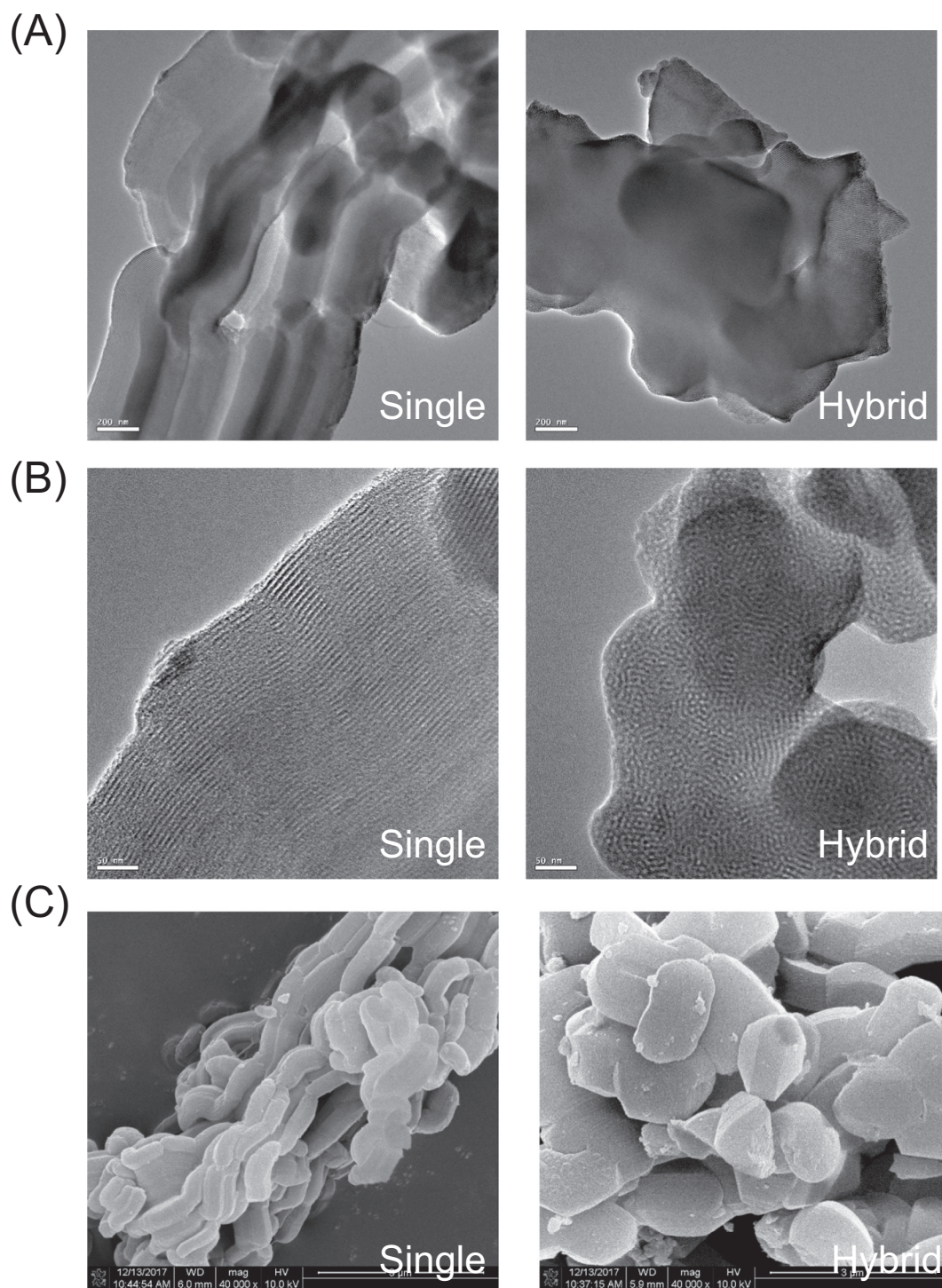


**Fig. 1.** The morphology of single MS and hybrid MS visualized by electron microscopy: (A) the HRTEM images with a lower magnification, (B) the HRTEM images with a higher magnification, and (C) the HRSEM images.

avobenzone molecules were adsorbed in the MSs with less crystallinity. The left shift of the broad peak demonstrated the greater crystallinity reduction of avobenzone-loaded MSs than raw MSs. We also determined the avobenzone encapsulation percentage in MSs by using the ultracentrifugation method. HPLC was employed as the analytical tool to detect the encapsulated avobenzone in MSs. The result revealed that the respective entrapment percentages of avobenzone in single MS and hybrid MS were 76.3% and 87.7%, respectively.

The *in vitro* UVA/UVB ratio is a screening approach representing a fast and reasonable tool to determine the UVA protection ability. We

sought to evaluate the degree of UVA protection by MSs, as shown in Fig. 2C. The raw avobenzone in 20% PG was prepared and tested along as the control. The free control achieved a UVA/UVB ratio of 0.56. The single MS and hybrid MS in 20% PG without avobenzone also showed the capability of defense against UVA with ratios of 0.49 and 0.44, respectively. A synergistic effect on UVA protection occurred when avobenzone was adsorbed by the MSs. The MSs were incorporated in hydrogels and cream for their applicability on topical administration. The prepared semisols were used for the UVA prevention test and avobenzone absorption study. It could be seen that the synergistic UVA

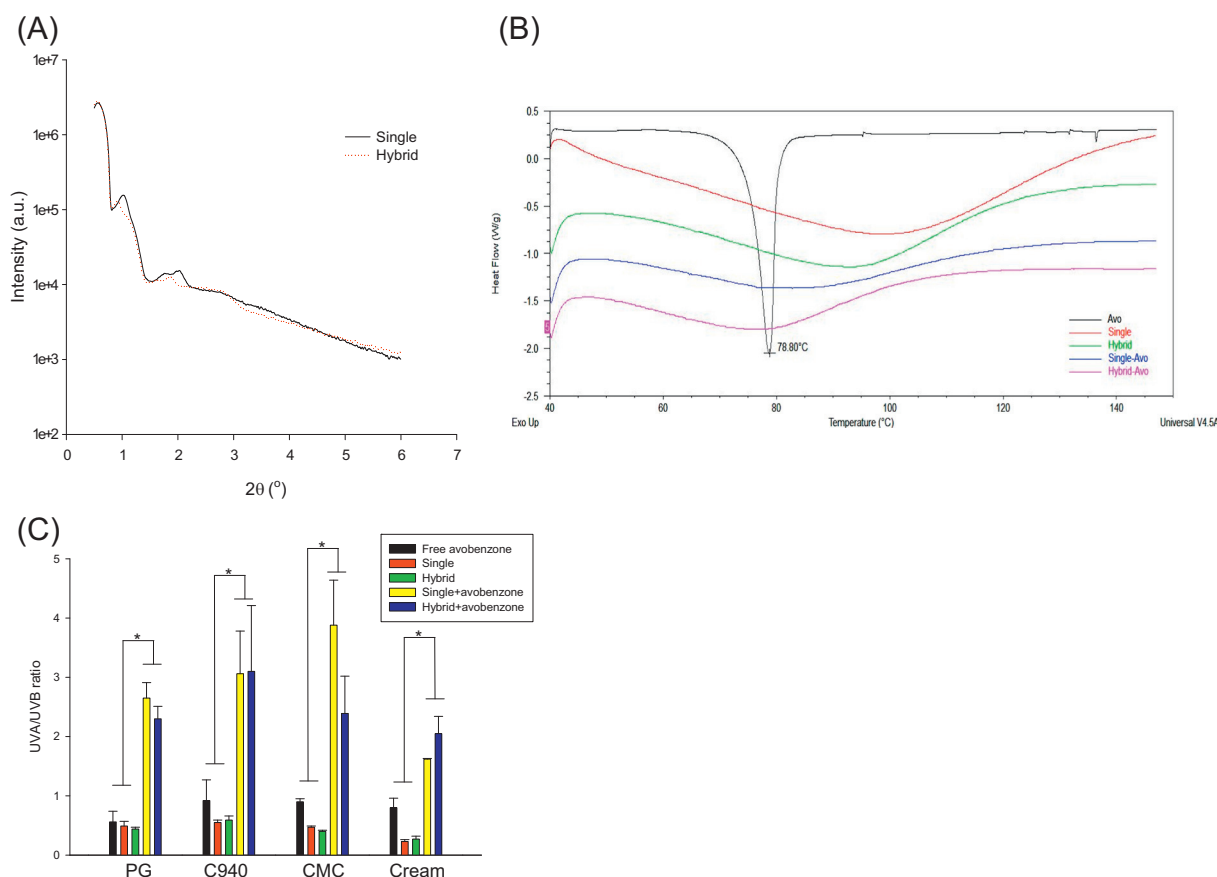


**Fig. 2.** Comparison of physicochemical properties of single MS and hybrid MS: (A) low angle XRD patterns, (B) thermograms of DSC, and (C) UVA/UVB ratio of spectrophotometry. Each value represents the mean  $\pm$  S.D. ( $n = 3$ ).

protection remained valid when the avobenzone-loaded MSs were dispersed in the semisolids. The UVA absorption spectrum of MSs was affected by the vehicles. The hydrogels (C940 and CMC) had a higher UVA/UVB ratio than the cream. The spectrophotometry data indicated a comparable UVA protection between single MS and hybrid MS ( $p > 0.05$ ).

### 3.2. Skin permeation of avobenzone/oxybenzone

The target of this experiment was to assess the possibility of MS inclusion for lessening percutaneous absorption of UV filter agents. We employed Franz diffusion cell to evaluate the skin absorption. The avobenzone/oxybenzone amount in the skin reservoir and across the skin was determined. The accumulation within the skin indicates the skin deposition, whereas the permeated amount across the skin anticipates the transdermal transport to the deeper skin strata and systemic circulation. Pig skin is a good model barrier for skin permeation study because of its similarity to human skin. Fig. 3A illustrates avobenzone deposition in pig skin after a 24-h application of various vehicles. The corresponding free avobenzone was examined as the control. The inclusion of MSs in 20% PG solution did not result in the decrease of avobenzone deposition when compared to free control ( $p > 0.05$ ). On the other hand, the skin deposition of avobenzone was significantly inhibited ( $p < 0.05$ ) by MSs in the presence of semisolid formulations. It can be seen that the MS-immobilized avobenzone absorption from semisolids was one-third to one-half that of the free control. This result suggests that entrapment of avobenzone in the MSs is a feasible strategy to reduce avobenzone uptake by the skin. There was no significant difference ( $p > 0.05$ ) among the free avobenzone depositions from different vehicles. In the cases of C940 gel and cream, the hybrid MS demonstrated lower avobenzone deposition compared to

single MS ( $p < 0.05$ ).

No avobenzone molecules were detectable in the Franz cell receptor after 24-h delivery. The percutaneous absorption of another UV filter, oxybenzone, was additionally measured because of its easier penetration across skin than avobenzone (Hung et al., 2014). As shown in Fig. 3B, oxybenzone deposition is not significantly decreased ( $p > 0.05$ ) by MS inclusion in PG solution, although a lower mean value was achieved. The same as avobenzone, the skin deposition of oxybenzone from semisolids was found to be lower in the MS form than in the free form ( $p < 0.05$ ) except for hybrid MS in CMC hydrogel. Comparing MS-immobilized oxybenzone deposition from different semisolids, C940 hydrogel was the vehicle showing the lowest absorption ( $p < 0.05$ ). After topical application of hybrid MS in C940 formulation, oxybenzone deposition decreased by a factor of 3 compared to the free form. Fig. 3C shows the time course of the permeated amount of oxybenzone transported per unit area across pig skin. The permeated oxybenzone amount was lesser in the MSs than in the free form, with the hybrid MS exhibiting the greatest reduction ( $p < 0.05$ ). The semisolid preparations resulted in decreased oxybenzone diffusion compared to the PG solution.

It is conceivable that the UV filters are frequently applied on the photoaged skin; thus, it is important to know the absorption level of the filter agents permeating into/across diseased skin. To understand whether there was a risk of over absorption, we exposed the nude mouse to UVA before the skin permeation experiment. As shown in Fig. 3D, oxybenzone has a tendency to permeate the UVA-irradiated skin with much greater deposition ( $p < 0.05$ ) compared to the intact pig skin. The single MS-immobilized oxybenzone permeated the barrier-compromised skin at a deposition 2 times less than the free control in PG. The deposition was not significantly different ( $p > 0.05$ ) between the hybrid MS and free form in PG. Upon topical application of

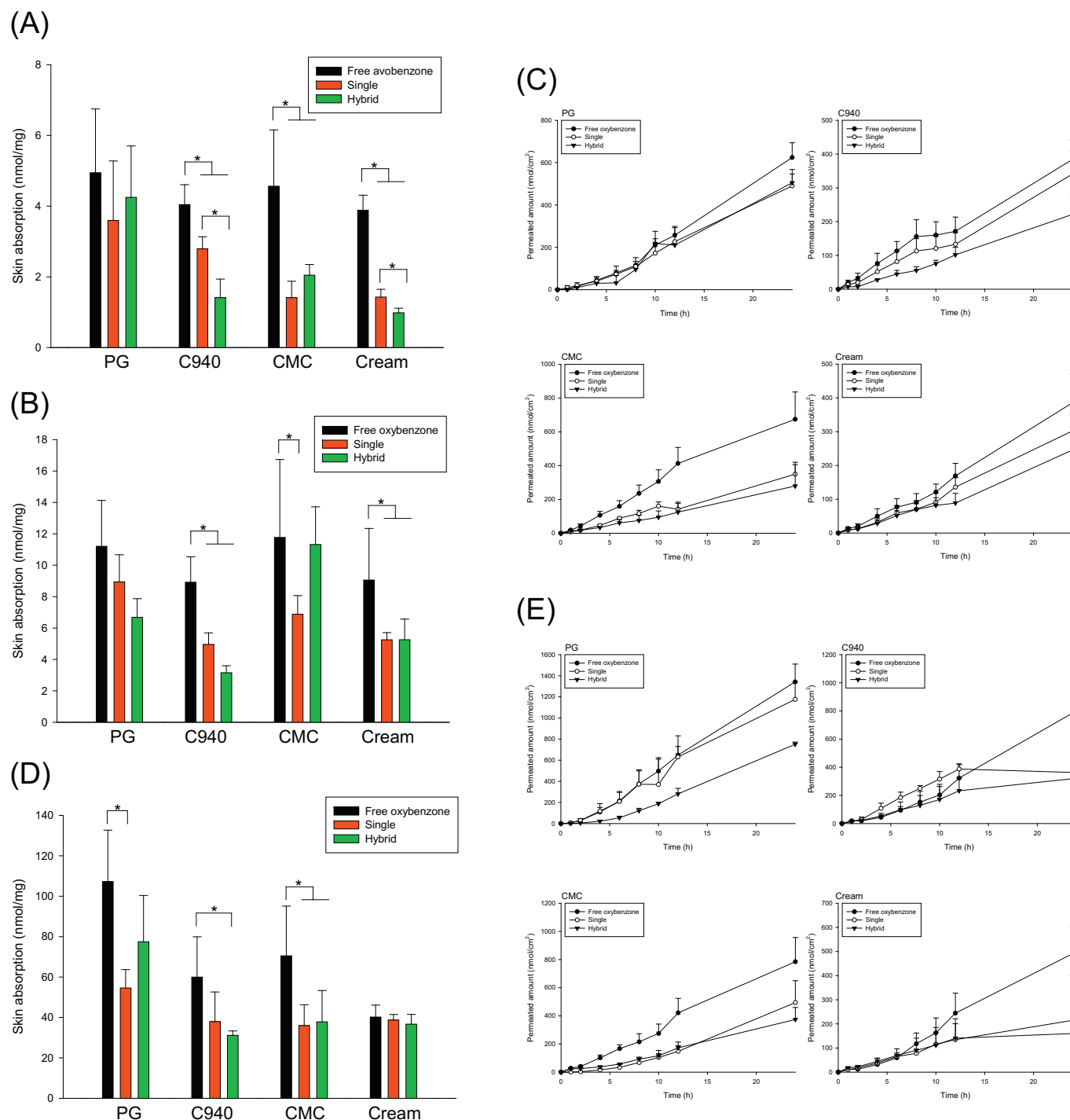


**Fig. 3.** Skin deposition and permeated amount in receptor compartment after topical treatment of avobenzone or oxybenzone on pig and UVA-irradiated nude mouse skins: (A) pig skin deposition of free and MS-immobilized avobenzone from different semisolid preparations, (B) pig skin deposition of free and MS-immobilized oxybenzone from different semisolid preparations, (C) permeated amount-time curves of oxybenzone penetration across pig skin from different semisolid preparations, (D) UVA-irradiated nude mouse skin deposition of free and MS-immobilized oxybenzone from different semisolid preparations, and (E) permeated amount-time curves of oxybenzone penetration across UVA-irradiated nude mouse skin from different semisolid preparations. Each value represents the mean  $\pm$  S.D. ( $n = 4$ ).

C940 and CMC hydrogels, oxybenzone deposition in UVA-irradiated skin was generally reduced to one-half by MS inclusion compared to the control group. In the case of cream, no significant difference ( $p > 0.05$ ) was observed regardless of the oxybenzone type in MSs and free form. The permeated amount-time profiles of oxybenzone delivery across the disrupted skin are given in Fig. 3E. Entrapment into MSs suppressed oxybenzone penetration better than the free oxybenzone.

The hybrid MS produced lower penetration than single MS and free control in the case of PG vehicle. The oxybenzone penetration across UVA-exposed skin was not further decreased by the hybrid MS relative to single MS ( $p > 0.05$ ) when incorporated into the semisolids.



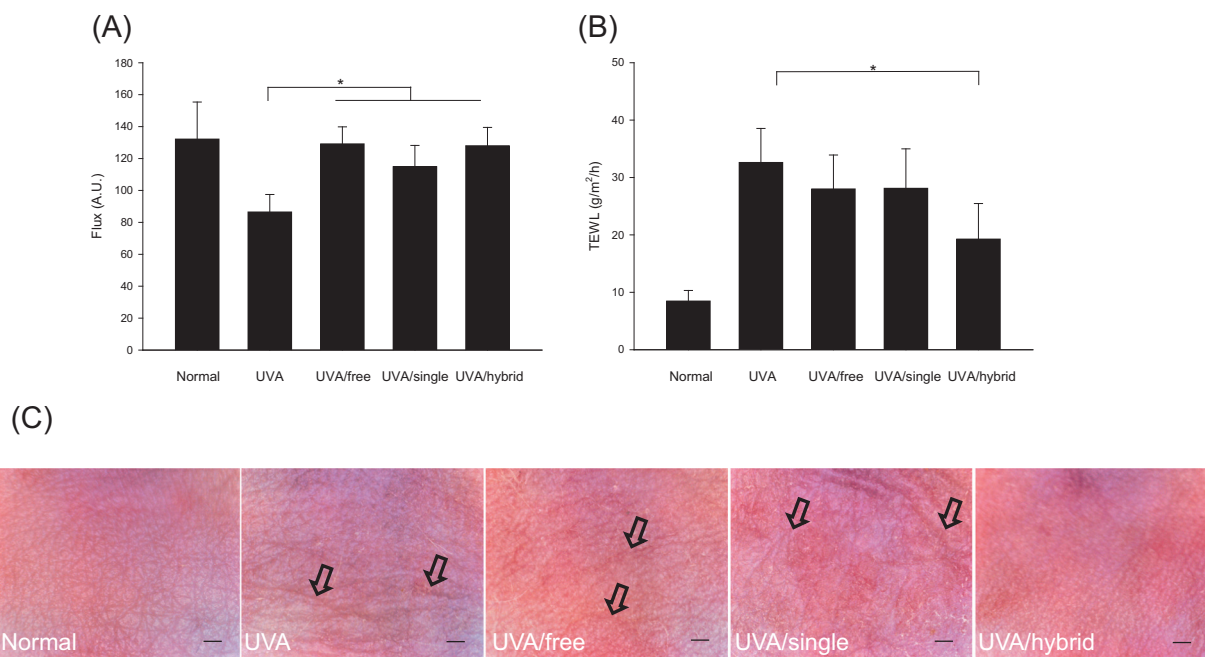


**Fig. 4.** In vivo examination of UVA protection capability of free and MS-immobilized avobenzone in C940 hydrogel: (A) skin blood flux determined by laser Doppler flowmetry, (B) skin barrier function determined by TEWL, and (C) skin surface appearance visualized by handheld digital magnifier. Each value represents the mean  $\pm$  S.D. ( $n = 8$ ).

### 3.3. In vivo UVA protection of avobenzone

We examined whether avobenzone loaded in the MSs increased the photoprotective activity in the nude mouse which was like the real-use condition. The physiological and histological profiles of UVA-irradiated skin were assessed with and without avobenzone treatment. We used laser Doppler flowmetry to recognize the change of cutaneous blood flow to UVA stimuli, as shown in Fig. 4A. UVA inhibited the blood flux of nude mouse skin from 132 to 86 A.U. ( $p < 0.05$ ). The blood flux could be reserved to the baseline by the UVA prevention of avobenzone. The blood flow of avobenzone application in the presence and absence of MSs did not reach a statistical significance ( $p > 0.05$ ). The barrier integrity of UVA-irradiated skin was measured by TEWL, as summarized in Fig. 4B. TEWL significantly increased from 8 to 33 g/m²/h ( $p < 0.05$ ) by UVA exposure. The treatment of free avobenzone and avobenzone-loaded single MS did not improve the disrupted barrier prompted by UVA. The topical application of hybrid MS on UVA skin can prevent barrier damage by reducing TEWL to 19 g/m²/h. A handheld digital magnifier offered visualization of the change by UVA exposure on the mouse skin surface. Fig. 4C exhibits the en face view of the skin with and without photoaging. The morphology of the skin surface without any treatment (normal skin) was found to be intact with no damage. The mouse treated with UVA revealed deep and extensive wrinkling (arrows in the image) with sagging in the dorsal region. Clinical signs of dryness and slight peeling were also detected. The deep furrow (arrows in the image) was still observed by the treatment of free and single MS-loaded avobenzone. The UVA-irradiated mouse treated by hybrid MS had no visible wrinkles in the back, demonstrating superior protection against photodamage.

Fig. 5 shows the qualitative evaluation of skin histopathology with the treatment of UVA with and without UV filter management. As compared to the untreated healthy skin, UVA exposure results in a pronounced structural alteration in the H&E-stained specimen (Fig. 5A). A thinning of the SC and epidermis with the loss of keratinocyte nuclei was evident, indicating cellular apoptosis and epidermal degeneration by UVA. The SC thinning confirmed the deficiency of barrier integrity as measured by the enhanced TEWL. Epidermal

hyperplasia was evident when applying the sunscreen formulation before UVA irradiation, suggesting a proliferative activity of the epidermis. The epidermal layer with avobenzone treatment was thicker than the normal skin. There was a significant increase in SC thickness in the UVA-irradiated mouse pretreated with all avobenzone-containing groups. The thickening of SC and epidermis seemed to be milder in the mouse that received hybrid MS than that receiving free avobenzone and single MS. The UV-induced internucleosomal DNA fragmentation is a hallmark of apoptosis, which can be identified by TUNEL IHC assay. Irradiation of the skin with UVA was found to elevate the number of TUNEL-positive nuclei in both epidermis and dermis (Fig. 5B). The images illustrated that avobenzone treatment prior to UVA substantially reduced the apoptotic DNA fragmentation. The number of TUNEL-positive keratinocytes in the epidermis for the MS-treated group was lower than the free avobenzone-treated mouse.

The phenomenon of epidermal proliferation was visualized by Ki67 staining (Fig. 5C). Exposure of UVA resulted in the scarce Ki67-expressing cells in the epidermis as compared to the healthy skin, confirming the cell death observed in the H&E staining. The number of Ki67-stained cells was further increased after the treatment of avobenzone. The consequence of the increased proliferation was the epidermal hyperplasia. The distribution of the infiltrated neutrophils in the skin was determined using Ly6G IHC (Fig. 5D). Neutrophils are important in the regulation of immune and inflammatory responses of UVA radiation. No neutrophilic migration was detected in the normal skin. Extensive neutrophil infiltration was present in the dermis after UVA treatment. The application of avobenzone reduced the neutrophilia, with the MSs displaying better attenuation. There was still a focal neutrophil accumulation in the dermis of free avobenzone group.

## 4. Discussion

The harmful potential of UVA on skin has come into the highlight, with the priority of UVA protection emerging. The solar care products should provide a broad spectrum protection against aging, erythema, and photocarcinogenesis. It is our aim to design the MS-based formulations loaded with avobenzone/oxybenzone for examining the UVA



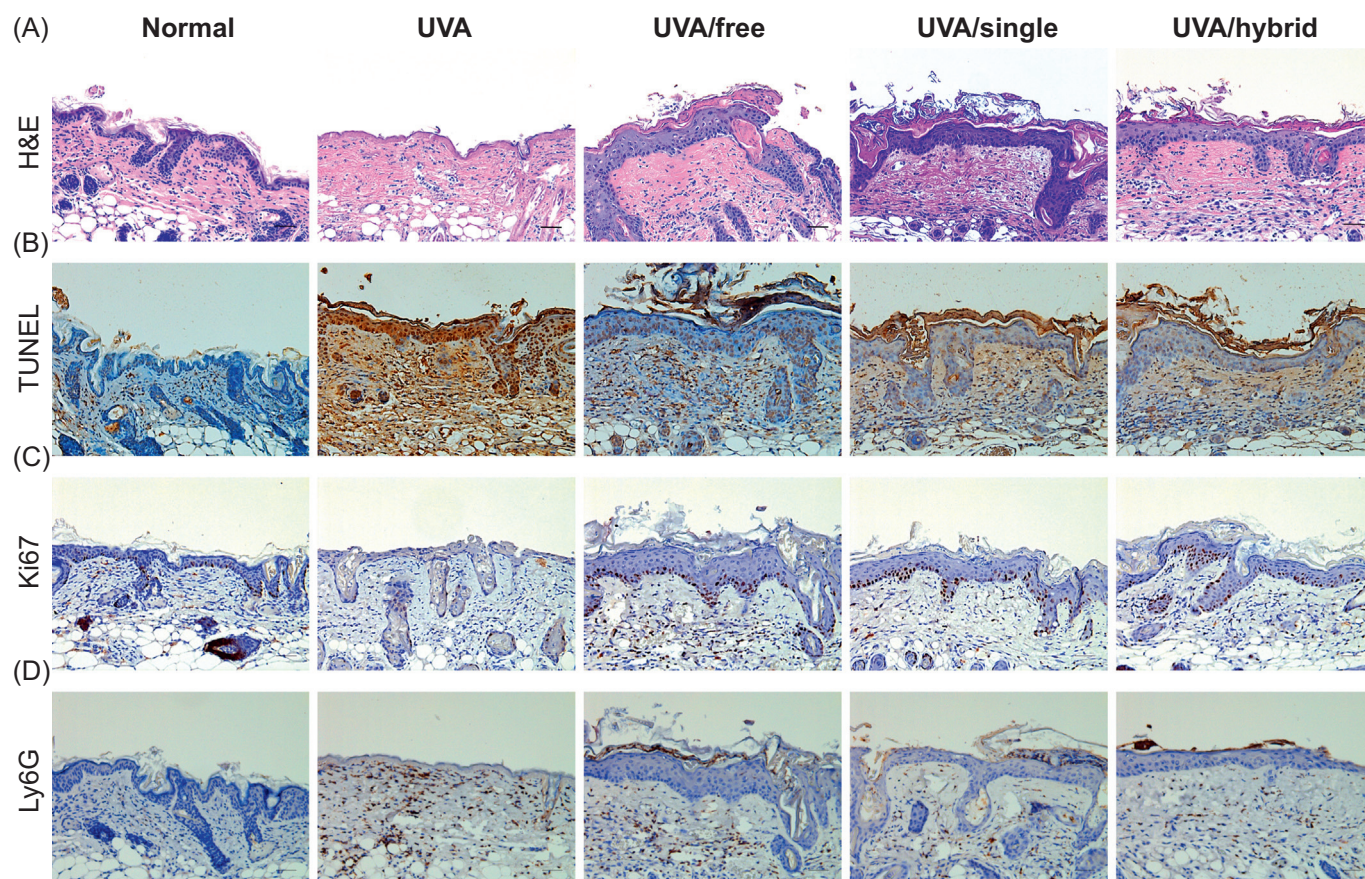


**Fig. 5.** The nude mouse skin histology with and without UVA irradiation treated by free and MS-immobilized avobenzone in C940 hydrogel: (A) H&E staining, (B) TUNEL antibody staining, (C) Ki67 antibody staining, and (D) Ly6G antibody staining. The scale bar in the images is 50 nm.

protection capability and percutaneous absorption. The experimental results demonstrated that MSs entrapped with avobenzone show a synergistic UVA protection ability. The incorporation of avobenzone/oxybenzone into MSs had decreased skin penetration, thus preserving the UVA filter effect and reducing the risk of possible toxicity. The morphology and pore of MSs with SBA-15 type of structure could be altered by changing the structure-directing agents. Utilizing the hybrid structure-directing reagents yielded higher surface area and narrower pores as compared to the single agents.

The MSs with a high surface volume of 0.5–1 cm<sup>3</sup>/g can facilitate a large loading of drugs (Eltohamy et al., 2016). The surface volume of our MSs fell within this range. The solvent evaporation was used as the method for avobenzone loading in MSs. The loading process is continuous along with the evaporation, leading to the high adsorption on the surface and in the mesopores of MSs (Geng et al., 2016). The superior avobenzone entrapment efficiency of > 75% in MSs was attributed to the ordered mesopores. The complexation of avobenzone with MSs was attested by the DSC. The less crystallinity of hybrid MS, as measured by XRD and DSC, demonstrated the stronger interaction with avobenzone compared to the single MS, indicating higher avobenzone entrapment in hybrid MS than in single MS. Avobenzone is a UVA absorber used worldwide. However, the low stability and photoisomerization to inert compounds have limited its application (González et al., 2008). Our result showed that raw MSs gave partial protection against UVA in a manner comparable to avobenzone; this is possible since the mesoporous structure may physically reflect or scatter the light (Yamada et al., 2006; Li et al., 2014). This result demonstrated the potential of MSs as a raw material for filters, although the UV protection ability of MSs alone can only be categorized as mild in this study. A synergistic effect on the UVA protection ability of MSs

and avobenzone was detected due to the high specific surface area of MSs for loading the avobenzone molecules and the additional light scattering elicited by the mesoporous texture. The high entrapment of avobenzone in MSs (> 75%) indicates that avobenzone was not just mixed with MSs but also adsorbed in MSs. The synergistic impact of the photoprotection can be attributed to light scattering in the mesopores that enhanced the opportunity for absorption by avobenzone adsorbed in the pores, leading to promoted UV absorption (Li et al., 2014, 2015). Avobenzone and MSs used in this study may show different mechanisms of UV protection for producing the synergistic effect. Cream is the most common vehicle for sunscreen preparation (Scalia et al., 2007); nevertheless, in our case, the UVA protection was lower for MSs in cream type than those in hydrogels. The less relevant efficacy of avobenzone-loaded MSs in cream could be related to the encapsulation of MSs in the oil droplets of cream, forming a protective barrier to absorb or reflect UVA radiation. There is increasing evidence that the sunscreens do not completely protect the skin against oxidative stress (Souza and Maia Campos, 2017). It is of great interest that we had improved the UVA protection by the development of MSs containing a low concentration of avobenzone (0.67%).

When administering UV filter to the skin, the absorption of the filter agent into/across skin should be minimized to prevent the unwanted effects to the body. Most of the studies examining UV filter permeation employed the artificial membrane as the transport barrier; the artificial membrane produces quite different permeation profiles as compared to the real skin model (Wang et al., 2014). Besides avobenzone, oxybenzone was used as the model filter agent in the skin permeation experiment since this molecule easily penetrates across the skin. The retardation of oxybenzone penetration into circulation is important when designing the sunscreen formulations. According to the experimental

data, oxybenzone, but not avobenzone, could penetrate across the skin into the receptor compartment perhaps due to the higher lipophilicity of avobenzone ( $\log P = 4.56$ ) than oxybenzone ( $\log P = 3.79$ ) for a preferable retention of avobenzone in skin reservoir. Oxybenzone is commonly used as the UVA absorber at the dose of  $> 0.5\%$  in personal care products. Oxybenzone has a small molecular size of 228 g/mol for a facile penetration across the skin. Previous clinical studies (Gustavsson et al., 2002; Gonzalez et al., 2006) reported that a large amount of topically applied oxybenzone was absorbed into the circulation and excreted via the urine. Another study (DiNardo and Downs, 2018) demonstrated that 97% of the volunteers receiving topically applied oxybenzone found this filter in their urine. The systemic absorption of oxybenzone can cause endocrine disrupting dysfunction (Søeborg et al., 2007). It is also reported that oxybenzone located in skin can induce allergic dermatitis and skin irritation (Heurung et al., 2014).

The avobenzone/oxybenzone inclusion in MSs demonstrated the desirable potential of lessening percutaneous absorption into and through pig skin and UVA-irradiated mouse skin. The inclusion of filter agents in the MS pores contributed to an obstacle of release, resulting in less absorption into skin. As the MS particles were larger than  $1\ \mu\text{m}$ , the penetration across the formidable SC layer could be prevented. The vehicle in which the MS-immobilized filters incorporated is crucial to decide the absorption level (Sapino et al., 2015). It is mentioned that the UVA absorbers exhibited lower permeation in the semisolids than solution; this could be due to the viscosity and cross-linkage structure of the semisolid forms retarding avobenzone/oxybenzone release. Rating the percutaneous absorption of topically applied actives relevant to environmental exposure is essential for the assessment of efficacy and toxicity. Most of the investigations for determining filter absorption are established for intact skin. We had generated barrier-deficient skin by UVA exposure as the model to estimate the skin absorption. UVA can weaken the barrier function of skin by disorganizing intercellular SC lipids and by keratinocyte apoptosis (Hung et al., 2015a, 2015b). The structural deficiency of the skin allowed the enhancement of oxybenzone absorption in our study. MSs were still effective in reducing oxybenzone delivery into/across the barrier-disrupted skin. Thus the systemic absorption through the skin can be expected to be restricted.

Reactive oxygen species (ROS) accumulation and impaired antioxidant defense system by UVA have caused photoaging, necrosis, and cutaneous cancer (Hseu et al., 2015). The signs of UVA-induced photoaging include wrinkling, sagging, and laxity (Battie et al., 2014). A similar appearance was observed in the UVA-irradiated nude mouse skin in the present study. As reported in our data, the UVA protection efficacy of avobenzone was enhanced upon immobilization in the MSs. The administration of MSs led to photoprotection against apoptotic cell death and neutrophil infiltration. TEWL is an indicator of the function of skin barrier, especially SC integrity (Boireau-Adamezyk et al., 2014). UVA had largely elevated TEWL, resulting in the increased oxybenzone absorption as reported in this study. This elevation could be inhibited by applying avobenzone-containing hybrid MS. The H&E staining also demonstrated that the hybrid MS reversed the SC loss evoked by UVA. Although the free avobenzone and single MS also increased the SC thickness of UVA-irradiated skin, recovery of barrier function, as measured by TEWL, was not detected.

The H&E images show the cell death and epidermal thinning in the UVA-irradiated skin and the hyperplasia in the avobenzone-treated UVA skin. The response of skin to UVA is considered to be dependent on the quantity of radiation. It is possible that UVA creates skinfold thickening in low or moderate energy (Tsukahara et al., 2005; de la Coba et al., 2009). On the other hand, high intensity UVA can cause quite a different impact on skin compared to the lower irradiation dose. The apoptosis and coagulative necrosis could be formed in the skin with high UVA intensity irradiation (Hung et al., 2012). This severe photoaging is believed to be irreversible (Reeve et al., 2005). The UVA used in this study led to a complete keratinocyte apoptosis without the

possibility of recovery. The hyperproliferation in the UVA skin treated by avobenzone implied cutaneous healing, suggesting that avobenzone could absorb the UVA radiation to reduce the UVA intensity reaching the skin tissue. The proliferative activity in the epidermis results in the thickening of epidermal layer. Ki67 as the marker of regenerative hyperplasia attested to the basal keratinocyte proliferation in the avobenzone-treated UVA skin. This effect was quite different to the UVA-irradiated skin without avobenzone. A sharp decrease in Ki67-expressing keratinocytes by UVA exposure was also demonstrated in the previous study (Armento et al., 2015).

UVA raises the level of ROS in skin by the photosensitized process, contributing to the DNA damage, caspase stimulation, and the subsequent apoptosis (Kulms and Schwarz, 2000). UVA generates more ROS causing plasma membrane damage 10-fold greater than UVB (Damiani et al., 2006). The dermal fibroblasts are more sensitive to UVA-activated oxidative stress than keratinocytes (Battie et al., 2014). The TUNEL assay showed cell death in both the epidermis and dermis of UVA skin. The UVA-induced apoptosis might produce the loss of skin blood supply as evidenced by the decreased blood flux. Photoaging is associated with lessened vasodilation of cutaneous microcirculation because of the endothelial dysfunction (Tew et al., 2010). The apoptosis was attenuated by the MSs, suggesting the DNA repair process and tissue regeneration.

The overexposure of solar radiation causes cutaneous inflammation characterized by neutrophil influx in the dermis (Lee et al., 2008). UVA induces immunosuppression associated with ROS release in neutrophils. Our result demonstrated a significant neutrophil infiltration after UVA application. The elastase and MMPs derived from the activated neutrophils would degrade collagen and elastic network to form wrinkles and cause elasticity loss (Naylor et al., 2011). The experimental result suggested the possibility of using MSs capable of restraining UVA-stimulated neutrophil infiltration and wrinkle formation. This effect was especially significant for the hybrid MS. This hybrid formulation generally revealed superior UVA protection than the single MS based on the *in vivo* animal study, including TEWL, wrinkling, and neutrophil migration. Since the *in vitro* UVA/UVB ratio was comparable for both formulations, the lower avobenzone absorption of hybrid MS compared to single MS from C940 hydrogel could be the reason for greater UVA protection *in vivo*. The hybrid MS retained more avobenzone molecules outside the skin, exhibiting a stronger UVA absorption. Another possibility was the higher specific surface area of hybrid MS than single MS for rendering more mesopores to scatter the UVA light, although this influence was not detected in the *in vitro* UVA prevention test. Further study is needed to elucidate the detailed mechanisms.

Although the filter incorporation in nanoparticles was shown to increase the filter efficiency, the nanotoxicity induced by the nanoparticles may cause cytotoxicity, genotoxicity, and photocarcinogenicity in some cases (Heng et al., 2011; Tran and Salmon, 2011). The development of the carriers at a micrometer level is able to diminish the possibility of causing toxicity. The MSs fabricated in this study can fit this criterion. The greasy feature of cream or ointment as the vehicle of sunscreens has decreased consumer compliance and exacerbated acne and rosacea (Latha et al., 2013). C940 hydrogel solves these problems besides the employment as the vehicle of avobenzone MSs showing good *in vivo* UVA protection.

## 5. Conclusions

The predominant concerns arising from the topical application of UV filter agents are the potential of sunlight protection and whether the filters may penetrate the skin to elicit adverse effects. In the present study, MSs were prepared to entrap avobenzone or oxybenzone in order to achieve ideal sunscreen formulations. Avobenzone were adsorbed inside the mesopores of MSs and found to reduce crystallization. The results reported in this study indicate that avobenzone loading in MSs



allowed a synergistic photoprotection due to the light scattering efficiency of MSs. The MSs in various semisolid preparations generally reduced the retention of avobenzone/oxybenzone in skin reservoir and the penetration across skin, where their action would be undesirable. The hybrid MS exhibited lower filter absorption as compared to the single MS. Our finding demonstrated that UVA damaged nude mouse skin, resulting in the keratinocyte death in the epidermis and neutrophil infiltration in the dermis. These injuries could be minimized by avobenzone preparations, especially the formulation of hybrid MS. The hybrid MS in C940 hydrogel also reversed the increased TEWL raised by UVA exposure. The experimental results of this work suggest that MSs are an attractive avobenzone/oxybenzone carrier for the protection of UVA photodamage to the skin. Further studies are warranted to conduct the clinical test for examining the UVA protection capability and safety of the MSs.

## Acknowledgement

The authors are grateful to the financial support by Chang Gung Memorial Hospital (CMRPD1F0231-3).

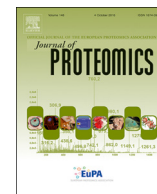
## References

- Afonso, S., Horita, K., Sousa E Silva, J.P., Almeida, I.F., Amaral, M.H., Lobão, P.A., Costa, P.C., Miranda, M.S., da Silva, J.C.G.E., Lobo, J.M.S., 2014. Photodegradation of avobenzone: stabilization effect of antioxidants. *J. Photochem. Photobiol. B* 140, 36–40.
- Armento, A.J., Oldach, J., Stolper, G., Li, M., Bachelor, M.A., Hayden, P.J., 2015. Evaluation of cutaneous damage and repair following acute solar ultraviolet radiation exposure: experiments with an in vitro reconstructed human skin model and excised human skin. *Appl. In Vitro Toxicol.* 1, 109–117.
- Battie, C., Jitsukawa, S., Bernerd, F., Del Bino, S., Marionnet, C., Verschoore, M., 2014. New insights in photoaging, UVA induced damage and skin types. *Exp. Dermatol.* 23 (Suppl. 1), 7–12.
- Boireau-Adamezyk, E., Baillet-Guffroy, A., Stamatas, G.N., 2014. Age-dependent changes in stratum corneum barrier function. *Skin Res. Technol.* 20, 409–415.
- Carrero, A., Vizcaino, A.J., Calles, J.A., Garcia-Moreno, L., 2017. Hydrogen production through glycerol steam reforming using Co catalysts supported on SBA-15 doped with Zr, Ce and La. *J. Energ. Chem.* 26, 42–48.
- Castanheiro, J.E., Fonseca, I.M., Ramos, A.M., Vital, J., 2017. Tungstophosphoric acid immobilized in SBA-15 as an efficient heterogeneous acid catalyst for the conversion of terpenes and free fatty acids. *Microporous Mesoporous Mater.* 249, 16–24.
- Damiani, E., Rosati, L., Castagna, R., Carloni, P., Greci, L., 2006. Changes in ultraviolet absorbance and hence in protective efficacy against lipid peroxidation of organic sunscreens after UVA irradiation. *J. Photochem. Photobiol. B* 82, 204–213.
- Daneluti, A.L.M., Neto, F.M., Velasco, M.V.R., Baby, A.R., Matos, J.D.R., 2018. Evaluation and characterization of the encapsulation/entrapping process of octyl methoxycinnamate in ordered mesoporous silica type SBA-15. *J. Therm. Anal. Calorim.* 131, 789–798.
- de la Coba, F., Aguilera, J., de Gálvez, M.V., Álvarez, M., Gallego, E., Figueroa, F.L., Herrera, E., 2009. Prevention of the ultraviolet effects on clinical and histopathological changes, as well as the heat shock protein-70 expression in mouse skin by topical application of algal UV-absorbing compounds. *J. Dermatol. Sci.* 55, 161–169.
- Diffey, B.L., 1994. A method for broadspectrum classification of sunscreens. *Int. J. Cosmet. Sci.* 16, 47–52.
- DiNardo, J.C., Downs, C.A., 2018. Dermatological and environmental toxicological impact of the sunscreen ingredient oxybenzone/benzophenone-3. *J. Cosmet. Dermatol.* 17, 15–19.
- Eltohamy, M., Seo, J.W., Hwang, J.Y., Jang, W.C., Kim, H.W., Shin, U.S., 2016. Ionic and thermo-switchable polymer-masked mesoporous silica drug-nanocarrier: high drug loading capacity at 10°C and fast drug release completion at 40°C. *Colloids Surf. B* 144, 229–237.
- Geng, H., Zhao, Y., Liu, J., Cui, Y., Wang, Y., Zhao, Q., Wang, S., 2016. Hollow mesoporous silica as a high drug loading carrier for regulation insoluble drug release. *Int. J. Pharm.* 510, 184–194.
- Gies, P., van Deventer, E., Green, A.C., Sinclair, C., Tinker, R., 2018. Review of the global solar UV index 2015 workshop report. *Health Phys.* 114, 84–90.
- Gonzalez, H., Farbrot, A., Larkö, O., Wennberg, A.M., 2006. Percutaneous absorption of the sunscreen benzophenone-3 after repeated whole-body applications, with and without ultraviolet irradiation. *Br. J. Dermatol.* 154, 337–340.
- González, S., Fernández-Lorente, M., Gilaberte-Calzada, Y., 2008. The latest on skin photoprotection. *Clin. Dermatol.* 26, 614–626.
- Gustavsson, G.H., Farbrot, A., Larkö, O., 2002. Percutaneous absorption of benzophenone-3, a common component of topical sunscreens. *Clin. Exp. Dermatol.* 27, 691–694.
- Hao, N., Li, L., Tang, F., 2017. Roles of particle size, shape and surface chemistry of mesoporous silica nanomaterials on biological systems. *Int. Mater. Rev.* 62, 57–77.
- He, Q., Shi, J., 2011. Mesoporous silica nanoparticle based nano drug delivery systems: synthesis, controlled drug release and delivery, pharmacokinetics and biocompatibility. *J. Mater. Chem.* 21, 5845.
- Heng, B.C., Zhao, X., Tan, E.C., Khamis, N., Assodani, A., Xiong, S., Ruedl, C., Ng, K.W., Loo, J.S., 2011. Evaluation of the cytotoxic and inflammatory potential of differentially shaped zinc oxide nanoparticles. *Arch. Toxicol.* 85, 1517–1528.
- Heurung, A.R., Raju, S.I., Warshaw, E.M., 2014. Adverse reactions to sunscreen agents: epidemiology, responsible irritants and allergens, clinical characteristics, and management. *Dermatitis* 25, 289–326.
- Hseu, Y.C., Lo, H.W., Korivi, M., Tsai, Y.C., Tang, M.J., Yang, H.L., 2015. Dermato-protective properties of ergothioneine through induction of Nrf/ARE-mediated anti-oxidant genes in UVA-irradiated human keratinocytes. *Free Radic. Biol. Med.* 86, 102–117.
- Hung, C.F., Fang, C.L., Al-Suwayeh, S.A., Yang, S.Y., Fang, J.Y., 2012. Evaluation of drug and sunscreen permeation via skin irradiated with UVA and UVB: comparisons of normal skin and chronologically aged skin. *J. Dermatol. Sci.* 68, 135–148.
- Hung, C.F., Chen, W.Y., Aljuffali, I.A., Shih, H.C., Fang, J.Y., 2014. The risk of hydroquinone and sunscreen over-absorption via photodamaged skin is not greater in senescent skin as compared to young skin: nude mouse as an animal model. *Int. J. Pharm.* 471, 135–145.
- Hung, C.F., Chen, W.Y., Aljuffali, I.A., Lin, Y.K., Shih, H.C., Fang, J.Y., 2015a. Skin aging modulates percutaneous drug absorption: the impact of ultraviolet irradiation and ovariectomy. *Age* 37, 21.
- Hung, C.F., Chen, W.Y., Hsu, C.Y., Aljuffali, I.A., Shih, H.C., Fang, J.Y., 2015b. Cutaneous penetration of soft nanoparticles via photodamaged skin: lipid-based and polymer-based nanocarriers for drug delivery. *Eur. J. Pharm. Biopharm.* 94, 94–105.
- Karran, P., Brem, R., 2016. Protein oxidation, UVA and human DNA repair. *DNA Repair* 44, 178–185.
- Kulms, D., Schwarz, T., 2000. Molecular mechanisms of UV-induced apoptosis. *Photodermatol. Photoimmunol. Photomed.* 16, 195–201.
- Latha, M.S., Martis, J., Shobha, V., Shinde, R.S., Bangera, S., Krishnakutty, B., Bellary, S., Varughese, S., Rao, P., Kumar, B.R.N., 2013. Sunscreening agents: a review. *J. Clin. Aesthet. Dermatol.* 6, 16–26.
- Lee, P.L., van Weelden, H., Bruijnzel, P.L.B., 2008. Neutrophil infiltration in normal human skin after exposure to different ultraviolet radiation sources. *Photochem. Photobiol.* 84, 1528–1534.
- Lee, W.R., Shen, S.C., Al-Suwayeh, S.A., Li, Y.C., Fang, J.Y., 2012. Erbium:YAG laser resurfacing increases skin permeability and the risk of excessive absorption of antibiotics and sunscreens: the influence of skin recovery on drug absorption. *Toxicol. Lett.* 211, 150–158.
- Li, C.C., Chen, Y.T., Lin, Y.T., Sie, S.F., Chen-Yang, Y.W., 2014. Mesoporous silica aerogel as a drug carrier for the enhancement of the sunscreen ability of benzophenone-3. *Colloids Surf. B* 115, 191–196.
- Li, C.C., Lin, Y.T., Chen, Y.T., Sie, S.F., Chen-Yang, Y.W., 2015. Improvement in UV protection retention capability and reduction in skin penetration of benzophenone-3 with mesoporous silica as drug carrier by encapsulation. *J. Photochem. Photobiol. B* 148, 277–283.
- Moyal, D., 2008. How to measure UVA protection afforded by sunscreen products. *Expert. Rev. Dermatol.* 3, 307–313.
- Naylor, E.C., Watson, R.E.B., Sherratt, M.J., 2011. Molecular aspects of skin ageing. *Maturitas* 69, 249–256.
- Reeve, V.E., Widyarini, S., Domanski, D., Chew, E., Barnes, K., 2005. Protection against photoaging in the hairless mouse by the isoflavone equol. *Photochem. Photobiol.* 81, 1548–1553.
- Sapino, S., Ugazio, E., Gastaldi, L., Miletto, I., Berlier, G., Zonari, D., Oliaro-Bosso, S., 2015. Mesoporous silica as topical nanocarriers for quercetin: characterization and in vitro studies. *Eur. J. Pharm. Biopharm.* 89, 116–125.
- Scalia, S., Tursilli, R., Iannuccelli, V., 2007. Complexation of the sunscreen agent, 4-methylbenzylidene camphor with cyclodextrins: effect on photostability and human stratum corneum penetration. *J. Pharm. Biomed. Anal.* 44, 29–34.
- Søeborg, T., Basse, L.H., Halling-Sørensen, B., 2007. Risk assessment of topically applied products. *Toxicology* 236, 140–148.
- Souza, C., Maia Campos, P.M.B.G., 2017. Development and photoprotective effect of a sunscreen containing the antioxidants *Spirulina* and dimethylmethoxy chromanol on sun-induced skin damage. *Eur. J. Pharm. Sci.* 104, 52–64.
- Tew, G.A., Klonizakis, M., Saxton, J.M., 2010. Effects of ageing and fitness on skin-microvessel vasodilator function in humans. *Eur. J. Appl. Physiol.* 109, 173–181.
- Tran, D.T., Salmon, R., 2011. Potential photocarcinogenic effects of nanoparticle sunscreens. *Australas. J. Dermatol.* 52, 1–6.
- Tsukahara, K., Moriwaki, S., Hotta, M., Fujimura, T., Sugiyama-Nakagiri, Y., Sugawara, S., Kitahara, T., Takema, Y., 2005. The effect of sunscreen on skin elastase activity induced by ultraviolet-A irradiation. *Biol. Pharm. Bull.* 28, 2302–2307.
- Wang, S.Q., Stanfield, J.W., Osterwalder, U., 2008. In vitro assessments of UVA protection by popular sunscreens available in the United States. *J. Am. Acad. Dermatol.* 59, 934–942.
- Wang, T., Miller, D., Burczynski, F., Gu, X., 2014. Evaluation of percutaneous permeation of repellent DEET and sunscreen oxybenzone from emulsion-based formulations in artificial membrane and human skin. *Acta Pharm. Sin. B* 4, 43–51.
- Yamada, Y., Nakamura, T., Ishi, M., Yano, K., 2006. Reversible control of light reflection of a colloidal crystal film fabricated from monodisperse mesoporous silica spheres. *Langmuir* 22, 2444–2446.



Contents lists available at ScienceDirect

Journal of Proteomics

journal homepage: [www.elsevier.com/locate/jprot](http://www.elsevier.com/locate/jprot)

# Proteomic characterization of six Taiwanese snake venoms: Identification of species-specific proteins and development of a SISCAPA-MRM assay for cobra venom factors

Chien-Chun Liu<sup>a,1</sup>, Chih-Chuan Lin<sup>b,1</sup>, Yung-Chin Hsiao<sup>c,d</sup>, Po-Jung Wang<sup>b</sup>, Jau-Song Yu<sup>a,c,d,e,\*</sup>

<sup>a</sup> Graduate Institute of Biomedical Sciences, College of Medicine, Chang Gung University, Taoyuan 333, Taiwan

<sup>b</sup> Department of Emergency Medicine, Chang Gung Memorial Hospital at Linkou, Taoyuan 333, Taiwan

<sup>c</sup> Molecular Medicine Research Center, Chang Gung University, Taoyuan 333, Taiwan

<sup>d</sup> Liver Research Center, Chang Gung Memorial Hospital at Linkou, Taoyuan 333, Taiwan

<sup>e</sup> Research Center for Food and Cosmetic Safety, Research Center for Chinese Herbal Medicine, College of Human Ecology, Chang Gung University of Science and Technology, Taoyuan 333, Taiwan

## ARTICLE INFO

### Keywords:

Venom proteome  
Taiwanese venomous snakes  
Cobra venom factor  
SISCAPA-MRM

## ABSTRACT

*Deinagkistrodon acutus*, *Trimeresurus stejnegeri*, *Protobothrops mucrosquamatus*, *Daboia russelii siamensis*, *Bungarus multicinctus* and *Naja atra* are the six medically important venomous snake species in Taiwan. In this study, we characterized and compared their venom protein profiles using proteomic approaches. The major snake venom proteins were identified by GeLC-MS/MS and the total venom proteome was characterized by in-solution digestion coupled with LC-MS/MS. A total of 27–52 proteins, categorized into 23 protein families, were identified in each snake's venom. The major venom components found in *Viperidae* species (*D. acutus*, *T. stejnegeri*, *P. mucrosquamatus* and *D. russelii*) were C-type lectin, snake venom serine proteinase, venom metalloproteinase and phospholipase A<sub>2</sub>, whereas three-finger toxin and phospholipase A<sub>2</sub> were the major components detected in the venom of *Elapidae* snakes (*B. multicinctus* and *N. atra*). This study also provided the first demonstration of some low-abundance proteins in these six snake venoms, including 5'-nucleotidase, glutaminyl-peptide cyclotransferase and phosphodiesterase, among others. Furthermore, we found that cobra venom factor (CVF) is a cobra-specific protein. We produced anti-peptide antibodies against CVF and used it to develop a highly sensitive SISCAPA-MRM assay for quantifying CVF. The limit of detection and lower limit of quantification were 3.2 and 9.6 attomoles, respectively. This assay was used to precisely quantify CVF in 1 µg crude venom proteins from three *Naja* species and king cobra. The amount of CVF varied from 0.9 to 54.36 femtomoles (equivalent to 0.16–10.03 mg/g of venom protein).

**Biological significance:** There are six medically significant venomous snakes in Taiwan. The venoms of the four *Viperidae* species (*Deinagkistrodon acutus*, *Trimeresurus stejnegeri*, *Protobothrops mucrosquamatus* and *Daboia russelii siamensis*) cause local tissue swelling; this symptom is also seen in *N. atra* envenomation in humans, potentially complicating the differential diagnosis of envenomation by *N. atra* and *Viperidae* species. Thus, characterization of the venom proteomes of the six Taiwanese snakes, including the relative abundance of the major components and species-specific protein(s) in each venom type, could be useful for future venom research, including the development of new assay(s) for detecting snake species-specific venom protein(s) and new type(s) of anti-venom.

## 1. Introduction

Bites and stings by venomous animals cause significant human morbidity and mortality in all parts of the world [1]. Because of their potential mortality, venomous snake bites require immediate medical attention [2]. Snake envenomation is a life-threatening situation in

many regions of the world, particularly in tropical and sub-tropical countries, as well as some poor rural communities [3–5]. According to the epidemiological study of snakebite, at least 1,800,000–2,700,000 envenoming cases and 81,410–137,880 associated deaths occur globally each year [6]. Populations in South Asia, Southeast Asia, and Africa are most at risk for venomous snakebites [6, 7].

\* Corresponding author.

E-mail address: [yusong@mail.cgu.edu.tw](mailto:yusong@mail.cgu.edu.tw) (J.-S. Yu).

<sup>1</sup> Contribute equally to this work.

<https://doi.org/10.1016/j.jprot.2018.06.003>

Received 10 April 2018; Received in revised form 28 May 2018; Accepted 13 June 2018  
1874-3919/ © 2018 Elsevier B.V. All rights reserved.



Taiwan is located in the South Pacific region, which provides habitats for more than 40 snake species [8] and where snakebites caused by six venomous snakes need immediate medical attention [9]. Among these six species, four—*Deinagkistrodon acutus*, *Trimeresurus stejnegeri*, *Protobothrops mucrosquamatus* and *Daboia russelii siamensis*—belong to the *Viperidae* family, whereas the other two—*Bungarus multicinctus* and *Naja atra*—belong to the *Elapidae* family. Approximately 1000 envenoming cases occur between May and November each year in Taiwan [10]. Owing to patients' awareness and the availability of antivenoms, mortality due to snakebites in Taiwan is less than 1%. However, precise identification of the snake species and timely treatment with appropriate antivenom are required to improve the outcome of snakebite patients.

In clinical practice, early and correct diagnosis of the culprit snake for a given snakebite is crucial for treatment and patient prognosis. For example, antivenom treatment is unable to prevent acute renal failure if administered more than 3–6 h after envenomation by *D. russelii* [11–13]. *N. atra* snakebites are associated with rapid, extensive tissue necrosis in the bitten limb [14, 15]. If treatment is delayed or the incorrect antivenom is administered, cobra-envenomed patients require multiple surgical debridement of tissue necrosis and skin grafts [16]. In addition, bites by non-venomous snake species often occur, forcing physicians to rely largely on the patient's description of the snakebite, potentially resulting in a misdiagnosis [17, 18]. Developing a rapid and reliable global diagnostic platform has become an emerging issue in snakebite cases. Comprehensive characterization of the protein composition of venoms of closely related snake species could provide a solid basis for further development of effective diagnostic assays and antivenoms for snakebite patients.

Multiple reaction monitoring mass spectrometry (MRM-MS), an MS scanning mode performed on triple quadrupole mass spectrometers, is a robust technology for analysis of chemical compounds in various fields [19, 20]. When coupled with stable isotope-labeled (SIS) peptide standards, MRM-MS enables precise and specific quantification of target proteins using specific transitions from proteotypic peptides, which represent the proteins in stoichiometric analyses [21–23].

Stable isotope standards and capture by anti-peptide antibodies (SISCAPA) is a method that uses anti-peptide antibodies to enrich target peptides from biological or clinical bodily fluid samples prior to MS analysis [24]. The combination of SISCAPA and MRM-MS can generate a more sensitive assay in which the limit of quantification can be as low as nanograms of protein per milligram [25].

To date, only a few studies have analyzed the protein profiles of venoms from some Taiwanese venomous snakes [26–28]. However, only one previous study, which used multidimensional chromatographic methods, has reported an analysis of differences in venom protein patterns of all six Taiwanese snakes [28]. Notably, the identities of venom proteins in the six Taiwanese venomous snakes have not been fully investigated and the proteome profiles of these venoms have not been comprehensively established and compared. In this study, we applied proteomic technologies (GeLC-MS/MS and in-solution digestion coupled with LC-MS/MS) to profile all venom proteins from the six Taiwanese venomous snakes and characterize their major protein components. We compared the identified proteins to establish which proteins are present in common among all six venoms, as well as proteins that are specific to only one type of venom. Finally, we selected one cobra-specific protein, cobra venom factor (CVF), as a target to develop a sensitive SISCAPA-MRM assay.

## 2. Materials and methods

### 2.1. Snake venoms

Six venoms from six species of snakes, *Deinagkistrodon acutus*, *Trimeresurus stejnegeri*, *Protobothrops mucrosquamatus*, *Daboia russelii siamensis*, *Bungarus multicinctus* and *Naja atra* were analyzed. Venom

was collected from adult snakes at various locations in Taiwan, then freeze-dried and stored at  $-20^{\circ}\text{C}$  before use. We obtained the lyophilized venom from Center of Disease and Control, Ministry of Health and Welfare, Taiwan. The venoms of other three Southeast Asia *Naja* species, *Ophiophagus hannah*, *Naja kaouthia* and *Naja siamensis*, were purchased from Latoxan (Valence, France).

### 2.2. Proteomic analysis of snake venom

#### 2.2.1. In-gel tryptic digestion of snake venoms

In preparation for venom proteome analyses, 100  $\mu\text{g}$  of lyophilized venom proteins was redissolved in PBS and applied to 12–18% linear gradient gel for SDS-PAGE. After staining by Coomassie Brilliant Blue, the protein bands were excised from the gel and subjected to in-gel tryptic digestion as described by Lin et al. [29]. Briefly, the gel pieces were destained three times with 40% acetonitrile containing 50 mM ammonium bicarbonate for 15 min each, reduced by incubating with 10 mM dithiothreitol (DTT) at  $60^{\circ}\text{C}$  for 30 min, and then alkylated by incubating with 55 mM iodoacetamide (IAM) at room temperature in the dark for 30 min. After washing out excess reagents, DTT and IAM, with 40% acetonitrile containing 50 mM ammonium bicarbonate, proteins in the processed gel pieces were digested with freshly prepared trypsin solution (20  $\mu\text{g}/\text{ml}$  of trypsin (Promega, Madison, WI) in 50 mM ammonium bicarbonate) at  $37^{\circ}\text{C}$  for 16 h, then extracted with 100% acetonitrile containing 1% formic acid. Finally, the extracted tryptic peptides were concentrated and dried by SpeedVac.

#### 2.2.2. In-solution digestion of snake venoms

Each lyophilized venom containing 10  $\mu\text{g}$  protein was dissolved in 100  $\mu\text{l}$  of 25 mM ammonium bicarbonate and subjected to in-solution tryptic digestion as described by Chen et al. [21]. Briefly, each venom sample was reduced by incubating with 5 mM DTT for 30 min at  $60^{\circ}\text{C}$ , and alkylated by incubating with 5 mM IAM for 30 min at room temperature in the dark. Before addition of trypsin, it was incubated with 5 mM DTT for 30 min at  $60^{\circ}\text{C}$  again to neutralize excess IAM. Finally, the samples were incubated with 1  $\mu\text{g}/\mu\text{l}$  trypsin (at a 1:25 enzyme:substrate ratio) at  $37^{\circ}\text{C}$  for 16 h. The tryptic peptides were then lyophilized and stored at  $-80^{\circ}\text{C}$  for subsequent processing.

#### 2.2.3. LC-MS/MS analysis

Each peptide sample was reconstituted with 0.1% formic acid, and then analyzed on a nanoLC-LTQ-Orbitrap hybrid mass spectrometer (Thermo Fisher, San Jose, CA, USA), as described previously [30]. Briefly, the sample loaded across a trap column (Zorbax 300SB-C18,  $0.3 \times 5 \text{ mm}$ ; Agilent Technologies, Wilmington, DE) at a flow rate of 0.2  $\mu\text{l}/\text{min}$  in solution A (0.1% formic acid in  $\text{H}_2\text{O}$ ), and separated on a resolving 10-cm analytical C18 column (inner diameter, 75  $\mu\text{m}$ ) using a 15- $\mu\text{m}$  tip (New Objective, Woburn, MA). The peptides were eluted using a linear gradient of 0–10% solution B (0.1% formic acid in acetonitrile) for 3 min, 10–30% solution B for 35 min, 30–35% solution B for 4 min, 35–50% solution B for 1 min, 50–95% solution B for 1 min, and 95% solution B for 8 min with a flow rate of 0.25  $\mu\text{l}/\text{min}$  across the analytical column. The resolution of the Orbitrap is set at 30000. The ion signal of  $(\text{Si}(\text{CH}_3)_2\text{O})_6\text{H}^+$  at 445.120025 ( $m/z$ ) was used as a lock mass for internal calibration. A procedure that alternated between one MS scan followed by ten MS/MS scans for the ten most abundant precursor ions in the MS scan was applied. The  $m/z$  values selected for MS/MS were dynamically excluded for 180 s. For MS scan, the  $m/z$  value of scan range was from 400 to 2000 Da. For MS/MS scan, over  $1 \times 10^4$  ions were accumulated in the ion trap for generating MS/MS spectra. Both MS and MS/MS spectra were acquired using one scan with maximum fill-times of 1000 and 100 ms for MS and MS/MS analysis, respectively.

#### 2.2.4. Database searching and bioinformatics analysis

MS raw data files were analyzed by Proteome Discoverer Software

(version 1.4.1.14; Thermo Fisher, San Jose, CA, USA), and searched against other lobe-finned fish and tetrapod clade taxonomy in the Swiss-Prot database (released March 16, 2016; 548,457 entries) using MASCOT. The enzyme specificity parameter was set to “trypsin” and one missed cleavage was allowed. Carbamidomethylation of cysteine was set as a static modification and oxidation of methionine, acetyl (protein N-term) and Gln- > pyro-Glu (N-term Q) was set as dynamic modification. The tolerance of MS is 10 ppm and MS/MS is 0.5 Da. The criteria used for protein identification are set as below: the peptide confidence is high; lowest peptide length is 5 amino acids; minimal number of peptide per protein is 2.

### 2.3. Production and purification of anti-CVF antibody

The anti-CVF antibody was produced in rabbits using the D16 peptide (DDNEDGFIADSDIISR), corresponding to the amino acid residues 723–748 of cobra venom factor in venom of *Naja atra*, as the antigen. This peptide was synthesized by Kelowna International Scientific Inc. A cysteine residue was added to the N-terminus to facilitate coupling of the peptide to bovine serum albumin by the procedure described by Reichlin [31], with glutaraldehyde as the cross-linker. The methods used for production and affinity purification of the anti-peptide antibody were described previously [32, 33]. Briefly, the peptide was coupled to bovine serum albumin and used as the antigen to antibodies raised in rabbits as described above. The antiserum (10 ml) was then affinity-purified by the D16 peptide-coupled Sepharose 4B column (1 cm × 5 cm). The bound antibodies were eluted from the column with 20 ml of 100 mM triethylamine at pH 11.5, and the eluted fractions (1 ml per tube) were collected in tubes containing 0.1 ml of 1 M Tris/HCl, pH 8.0. The purified antibodies were concentrated to approximately 1 ml, dialyzed against PBS containing 50% (v/v) glycerol and 0.04% Na<sub>2</sub>S<sub>2</sub>O<sub>3</sub>, and then stored at –20 °C. This purified antibody can specifically recognize the venom of *Naja atra* (see the Results section).

### 2.4. Western blot analysis

Whole venom from each snake (containing 5 µg protein) was separated by SDS-PAGE, transferred onto PVDF membranes (Millipore, Billerica, MA, USA), and probed with anti-CVF antibody. Proteins of interest on the PVDF membranes were detected by incubating for 1 h with the appropriate alkaline phosphatase-conjugated secondary antibodies (Santa Cruz Biotechnology, Dallas, Texas, USA) and visualized using the CDP-Star Western Blot Chemiluminescence Reagent (PerkinElmer, Boston, MA, USA).

### 2.5. Enzyme-linked immunosorbent assay (ELISA)

Whole venom from each snake (containing 100 ng protein) was diluted in 100 µl phosphate-buffered saline (PBS) and coated onto 96-well polystyrene microplates (Corning, New York, USA) by incubating at 4 °C overnight. The plates were washed six times with 300 µl of TTBS buffer (20 mM Tris-HCl (pH 7.4), 0.5 M NaCl, 0.05% and 0.1% Tween-20) and blocked with 200 µl of 1% ovalbumin in PBS at room temperature for 2 h. After washing wells with TTBS six times, anti-CVF antibody (1 mg/ml) was serially diluted from 1:2000 to 1:128000 and added to each well, then plate was incubated at room temperature for 2 h. After washing six times with TTBS, the alkaline phosphatase-conjugated secondary antibody (Santa Cruz Biotechnology, Dallas, Texas, USA) was added to each well and the plate was incubated at room temperature for 1 h. After washing six times with TTBS, the substrate, 4-methyl umbelliferyl phosphate (100 µM, 100 µl/well; Molecular Probes), was added to each well. Finally, fluorescence value was measured by a SpectraMax M5 microplate reader (Molecular Devices, Sunnyvale, CA) at excitation and emission wavelengths of 355 and 460 nm.

### 2.6. Stable isotope standards and capture by anti-peptide antibodies coupled with multiple reaction monitoring (SISCAPA-MRM) analysis

#### 2.6.1. Synthetic peptides and stable isotope standard (SIS) peptides

The synthetic D16 peptide, DDNEDGFIADSDIISR, was obtained from Kelowna International Scientific Inc. (Taipei, Taiwan) without any modification. The purity of synthetic peptide was higher than 85% as measured by HPLC. The SIS peptide, DDNEDGFIADSDIIS[<sup>13</sup>C<sub>6</sub>,<sup>15</sup>N<sub>4</sub>]R was purchased from New England Peptide Inc. (Gardner, MA). The amino acid sequence of this SIS peptide is the same with the synthetic peptide, but the C-terminal Arg residue was replaced with [<sup>13</sup>C<sub>6</sub>,<sup>15</sup>N<sub>4</sub>]Arg.

#### 2.6.2. Preparation of trypsin-digested human plasma

A bulk preparation of plasma, which was provided from volunteers, was used as a background matrix for the experiments. To begin with, 20 µl of pooled human plasma was diluted with Tris-HCl (final concentration, 50 mM, pH 8.5), denatured in 5% deoxycholate (DOC) at 100 °C for 5 min, reduced with 5 mM Tris(2-carboxyethyl)phosphine (TCEP) at 65 °C for 30 min, and then alkylated by 10 mM iodoacetamide (IAM) at 37 °C in dark for 30 min. More Tris-HCl buffer (pH 8.5) was added to the samples to decrease the concentration of DOC below 1%. Subsequently, sequencing-grade modified trypsin (Promega, Madison, WI) was added (enzyme-to-substrate ratio: 1 to 50), and the reaction mixture was incubated at 37 °C overnight. After that, trifluoroacetic acid (TFA) and formic acid (FA) were added to samples, as final concentrations of TFA and FA are 0.1% and 0.4%, to precipitate DOC. The samples were then centrifuged at 15,500g for 10 min at 4 °C, and the supernatants were collected. The process was repeated once, and the resulting supernatants were combined. Finally, the digested plasma samples were desalted using Waters Oasis 30-mg HLB 96-well plate (Waters, Milford, Massachusetts, USA), according to the manufacturer's protocols, lyophilized and stored at –20 °C until use.

#### 2.6.3. Immunoaffinity enrichment of target peptide

We adopted the method described by Whiteaker et al. [34] to establish the enrichment procedure, which consisted of following steps with some modifications. These experiments were performed in 96-well plates using the KingFisher magnetic particle processor (Thermo Scientific, San Jose, CA, USA). The plasma digests derived from 20 µl of original plasma (approximately 1.2 mg total proteins) were added to each sample well, and 100 fmol of synthetic light peptide and varied amounts of SIS peptide were then spiked into the sample wells. For analysis, the KingFisher magnetic particle processor was used for automatically handling the transfer of magnetic beads in different plates (plates 1 to 7) with the magnetic head. The wells of plate 1 contained 10 µl of protein G magnetic beads (GE Healthcare, Chicago, Illinois, USA) in 190 µl of PBS with 0.03% 3-[(3-cholamidopropyl)dimethylammonio]-1-propanesulfonate (CHAPS). The magnetic beads were washed for 5 min in plate 1 and subsequently transferred to plate 2 containing 10 µg anti-CVF antibodies and incubated for 1 h to form antibody-bead complexes. The antibody-bead complexes were then transferred to plate 3, where the wells contained plasma digests spiked with peptides. After incubation for 2 h, the antibody-bead-peptide complexes were transferred to plates 4, 5 and 6 for wash in PBS 3 times, and then to plate 7 for eluting the bound peptides for 5 min in 100 µl of 5% acetic acid and 70% ACN. Eluted peptides were lyophilized and stored at –20 °C until analysis.

#### 2.6.4. LC-MRM-MS analysis and data acquisition

The nanoACQUITY UPLC System was used for LC – MRM-MS analysis. Samples were injected into the trap column (nanoACQUITY UPLC C18, 180 µm × 20 mm, 5-µm particle size; Waters) at flow rate of 15 µl/min in solution A (0.1% formic acid in H<sub>2</sub>O), and separated on a resolving analytical column (ACQUITY UPLC BEH130 C18, 75 µm × 150 mm, 1.7-µm particle size; Waters) at a flow rate of

400 nl/min with a 13-min linear gradient from 3 to 50% solution B (0.1% formic acid in acetonitrile), followed by a 1-min linear gradient from 50 to 95% solution B. The analytical column was then reconditioned by holding solvent B at 97% for 5 min prior to ramping back down to 3% solvent B over 1 min and re-equilibrating for 10 min with 3% solvent B. A blank was analyzed between all samples to prevent sample carryover on the HPLC column. An AB/MDS Sciex 5500 QTRAP with a nano-electrospray ionization source controlled by Analyst 1.5.1 software (AB Sciex) was used for all LC-MRM-MS analyses. Acquisition methods used the following parameters: ion spray voltage, 1900–2000 V; curtain gas setting, 20 psi (UHP nitrogen); interface heater temperature, 150 °C; and MS operating pressure,  $3.5 \times 10^{-5}$  Torr; Q1 and Q3 were set to unit resolution (0.6–0.8 Da full width at half height). MRM acquisition methods were constructed using three MRM ion-pairs per peptide with fragment-ion-specific tuned collision energy (CE) voltage and retention time constraint. A default collision cell exit potential of 35 V was used for all MRM ion pairs.

### 2.6.5. Data analysis for MRM

The LC-MRM-MS data analysis and protein quantification was performed as previously described [35]. Briefly, the amino acid sequence and retention time for synthetic D16 peptides were determined by LC-MS/MS analysis. Response curve was generated for the CVF protein using the heavy SIS peptide. All MRM data were processed using the Skyline (MacCoss Lab Software) [36]. The mass list of transitions for measuring CVF-derived D16 peptide sequences was preloaded, and the peak areas of the selected target peptides were extracted for calculation. All the retention times and transition profiles for the endogenous and exogenously spiked heavy peptides were manually checked to ensure that they were internally consistent. The endogenous peptide-specific peaks were identified by comparison with the exogenously added  $^{13}\text{C}/^{15}\text{N}$ -labeled peptides, which were 10 Da heavier for Arg-containing peptides. The concentration of each  $^{13}\text{C}/^{15}\text{N}$ -labeled peptide was known, allowing the CVF protein concentration in each sample to be determined from the observed peak area ratios. The limit of detection (LOD) was determined using the MRM statistical software package, QuaSAR; this software uses the “blank and low concentration sample” method, in which the mean of the blank samples and the standard deviations of the blank and low-concentration samples are estimated [37]. The lower limit of quantification (LLOQ) was calculated as the LOD value multiplied by 3 [38].

## 3. Results and discussion

### 3.1. Characterization of the venom proteomes of six Taiwanese snakes

Gradient sodium dodecyl sulfate-polyacrylamide gel electrophoresis (SDS-PAGE) coupled with Coomassie Blue staining was used to generate a general overview of protein components in the six snake venoms, allowing us to identify compositional differences among these venoms (Fig. 1). This analysis revealed that major proteins with molecular weights of 10–55 kDa were presented in venoms of *D. acutus*, *T. stejnegeri*, and *P. mucrosquamatus*. On the other hand, the dominant protein components of *D. russelii*, *B. multicinctus*, and *N. atra* were smaller than 15 kDa. Images of protein-stained gradient gels showed clear differences in snake venom protein patterns between *Viperidae* and *Elapidae* families. More than half of the protein components of *Elapidae* family snake venoms were approximately 10 kDa; however, major proteins of venoms from snakes of the *Viperidae* family were evenly distributed from 10 to 55 kDa.

To identify the major protein components in each venom, we performed in-gel digestion of each band coupled with LC-MS/MS analysis. This analysis showed that the major protein components in the six snake venoms belonged to 4–6 of the following 11 protein families (Table 1): C-type lectin, cysteine-rich secretory protein, L-amino-acid oxidase, nerve growth factor, snake venom serine protease,

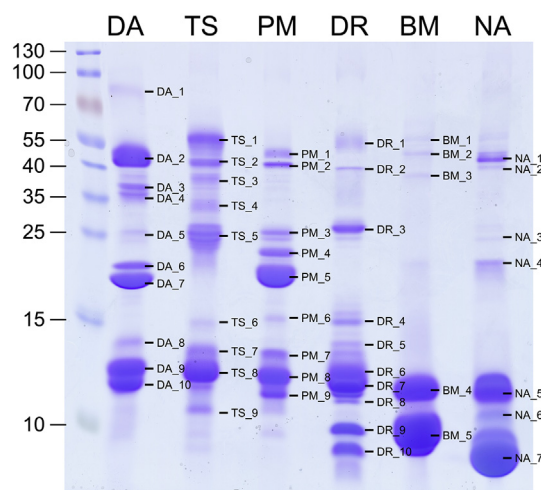


**Fig. 1.** SDS-PAGE analysis of the venom protein profiles of six Taiwanese snakes. Whole venom proteins (50 µg) from each snake species were resolved on a linear gradient (12–18%) SDS gel and visualized by Coomassie Brilliant Blue staining. DA, *D. acutus*; TS, *T. stejnegeri*; PM, *P. mucrosquamatus*; DR, *D. russelii siamensis*; BM, *B. multicinctus*; NA, *N. atra*. (For interpretation of the references to colour in this figure legend, the reader is referred to the web version of this article.)

phospholipase A<sub>2</sub>, three-finger toxin, acetylcholinesterase, venom complement C3 (CVF), venom metalloproteinase, and venom Kunitz-type inhibitor. The proteins identified in the venom from each snake are detailed in Supplemental Tables S1–S6.

Most of the identified proteins among *D. acutus* (DA), *T. stejnegeri* (TS), *P. mucrosquamatus* (PM) and *D. russelii* (DR) venoms belong to protein families commonly identified in *Viperidae* snake venoms (Table 1). For example, C-type lectin (bands DA<sub>9</sub>, DA<sub>10</sub>, TS<sub>6</sub>, PM<sub>7</sub>, PM<sub>9</sub>, DR<sub>4</sub> and DR<sub>8</sub>), snake venom serine protease (bands DA<sub>3</sub>, DA<sub>4</sub>, DA<sub>5</sub>, TS<sub>3</sub>, TS<sub>4</sub>, PM<sub>3</sub>, PM<sub>4</sub> and DR<sub>3</sub>), and venom metalloproteinase (bands DA<sub>2</sub>, DA<sub>6</sub>, DA<sub>7</sub>, TS<sub>2</sub>, TS<sub>5</sub>, PM<sub>2</sub>, PM<sub>5</sub>, DR<sub>1</sub> and DR<sub>2</sub>) were present in all four *Viperidae* snake venoms. For venoms of *Elapidae* snakes, the most abundant proteins in *B. multicinctus* (BM) and *N. atra* (NA) (bands BM<sub>5</sub> and NA<sub>7</sub>) belonged to the three-finger toxin protein family. Apart from these proteins, which could be used to categorize snakes according to family, some proteins were specifically detected in only one species. For example, the venom Kunitz-type inhibitor (bands DR<sub>9</sub> and DR<sub>10</sub>) and CVF (band NA<sub>2</sub>) were identified exclusively in the *D. russelii* and *N. atra* venom proteomes, respectively. Additionally, a specific protein family, phospholipase A<sub>2</sub>, was pre-dominant in all Taiwanese snake venoms (bands DA<sub>8</sub>, TS<sub>7</sub>, TS<sub>8</sub>, TS<sub>9</sub>, PM<sub>8</sub>, DR<sub>6</sub>, DR<sub>7</sub>, BM<sub>4</sub> and NA<sub>5</sub>). Accordingly, in the case of snake envenoming in Taiwan, detection of phospholipase A<sub>2</sub> in blood samples could be a feasible strategy for determining whether the victim was bitten by a venomous or non-venomous snake. One research group in Australia has been attempting to measure phospholipase A<sub>2</sub> activity to diagnose snake envenoming [39].

To provide a more comprehensive characterization of the venom proteomes of these six Taiwanese snakes, we digested the crude venom of each snake with trypsin, and analyzed the resulting tryptic peptides by LC-MS/MS. This analysis enables the identification of numerous low-abundance proteins in the venom proteome. The proteins identified in each type of venom are detailed in Supplemental Tables S7–S12, and the number of proteins in distinct protein families in the venoms of the six Taiwanese snakes is summarized in Table 2.

As shown in Table 2, 34 proteins were identified in *D. acutus* venom (see also Supplemental Table S7). These proteins could be classified into 11 protein families. Notably, this is the first study to characterize the venom proteome of *D. acutus*, and 5 protein families, glutaminyl peptide cyclotransferase, nerve growth factor, ohanin,

**Table 1**

Summary of the major protein components identified in the venoms of six Taiwanese snakes using SDS-PAGE coupled with LC-MS/MS analysis.

Protein family	<i>D. acutus</i>	<i>T. stejnegeri</i>	<i>P. mucrosquamatus</i>	<i>D. russelli siamensis</i>	<i>B. multicinctus</i>	<i>N. atra</i>
	(DA)	(TS)	(PM)	(DR)	(BM)	(NA)
	Band <sup>a</sup>	Bands	Bands	Bands	Bands	Bands
C-type lectin	DA_9, DA_10	TS_6	PM_7, PM_9	DR_4, DR_8	–	–
Cysteine-rich secretory protein	–	–	PM_6	–	–	NA_4
L-amino-acid oxidase	–	TS_1	PM_1	–	BM_2	–
Nerve growth factor	–	–	–	DR_5	–	NA_6
Snake venom serine protease	DA_3, DA_4, DA_5	TS_3, TS_4	PM_3, PM_4	DR_3	–	–
Phospholipase A <sub>2</sub>	DA_8	TS_7, TS_8, TS_9	PM_8	DR_6, DR_7	BM_4	NA_5
Three-finger toxin	–	–	–	–	BM_5	NA_7
Acetylcholinesterase	–	–	–	–	BM_1	–
Venom complement C3	–	–	–	–	–	NA_2, NA_3
Venom Kunitz-type inhibitor	–	–	–	DR_9, DR_10	–	–
Venom metalloproteinase	DA_2, DA_6, DA_7	TS_2, TS_5	PM_2, PM_5	DR_1, DR_2	–	NA_1

<sup>a</sup> Bands: indicate the major sites of the protein family in the stained SDS-PAGE gel shown in Fig. 2.

phosphodiesterase, and phospholipase B, identified in *D. acutus* venom proteome did not be annotated in previous transcriptomic analysis of *D. acutus* venomous gland [40, 41].

A total of 52 and 45 proteins were identified in *T. stejnegeri* and *P. mucrosquamatus* venoms, respectively (Supplemental Tables S8 and S9), and both showed similar venom protein profiles. The proteins in *T. stejnegeri* venom could be categorized into 13 protein families, and the identified proteins from *P. mucrosquamatus* venom could be classified into 12 protein families (Table 2). Compared with previous venomomics studies of these two snakes [26], proteins belonging to the following families were identified for the first time in the present study: 5'-nucleotidase, glutaminyl-peptide cyclotransferase, phosphodiesterase, glycosyl hydrolase, phospholipase B, protein disulfide-isomerase, and vascular endothelial growth factor.

For *D. russelli* venom, 27 proteins were identified (Supplemental Table S10); these could be classified into 12 protein families (Table 2). Overall, the identified proteins were similar to those found in previous venomomics research on *D. russelli* from Myanmar [42]. In the current study, however, we additionally identified proteins in six protein

families: 5'-nucleotidase, glutaminyl-peptide cyclotransferase, glycosyl hydrolase, nerve growth factor, phosphodiesterase, and venom Kunitz-type inhibitor. Among these protein families, venom Kunitz-type inhibitor may be the most significant; it has been reported to inhibit activated protein C, trypsin, coagulation factor FXIa and plasmin in vitro and promote coagulation in mice when factor V activator RVV-V gamma (a snake venom serine protease type *D. russelli* protein) is co-injected with inhibitor [43]. Its function is related to potentially fatal thrombotic complications—the clinical symptoms of *D. russelli* envenomation [44]—indicating that venom Kunitz-type inhibitor proteins are important components of Taiwanese *D. russelli* venom.

For snakes of the *Elapidae* family, we identified 27 and 30 proteins in *B. multicinctus* and *N. atra* venom, respectively (Supplemental Table S11 and S12). Proteins identified from *B. multicinctus* venom could be categorized into 11 protein families, and venom proteins from *N. atra* could be classified into 12 protein families (Table 2). The venom Kunitz-type inhibitor proteins identified in *B. multicinctus* venom come from  $\beta$ -bungarotoxin, a protein with two chains; the A chain is homologous to phospholipase A<sub>2</sub>, and the B chain is homologous to venom

**Table 2**

Overview of LC-MS/MS-identified proteins of different protein families in the venoms of six Taiwanese snakes.

Protein family	Number of identified proteins					
	<i>D. acutus</i>	<i>T. stejnegeri</i>	<i>P. mucrosquamatus</i>	<i>D. russelli siamensis</i>	<i>B. multicinctus</i>	<i>N. atra</i>
5'-nucleotidase	1	2	2	1	–	1
Acetylcholinesterase	–	–	–	–	1	1
C-type lectin	10	9	7	4	–	–
Cysteine-rich secretory protein	1	2	1	–	1	2
Globin	–	–	–	–	1	–
Glutaminyl-peptide cyclotransferase	1	1	1	1	–	–
Glycosyl hydrolase	–	1	–	1	–	–
L-amino-acid oxidase	–	2	2	–	1	1
Natriuretic peptide	–	–	–	–	1	–
Nerve growth factor	1	1	1	1	1	2
Ohanin/Vespryn	1	–	–	–	1	1
Snake venom serine protease	2	12	9	2	–	1
Phosphodiesterase	1	1	1	1	–	1
Phospholipase A <sub>2</sub>	3	8	5	7	4	1
Phospholipase B	1	1	1	1	–	–
Protein disulfide isomerase	–	1	–	–	–	–
Three-finger toxin (Long chain)	–	–	–	–	7	1
Three-finger toxin (Non-conventional)	–	–	–	–	3	2
Three-finger toxin (Short chain)	–	–	–	–	1	10
Vascular endothelial growth factor	–	–	1	2	–	–
Venom complement C3	–	–	–	–	–	3
Venom Kunitz-type inhibitor	–	–	–	3	4	–
Venom metalloproteinase	12	11	14	3	1	3
Total	34	52	45	27	27	30



Kunitz-type inhibitor. However, the B chain does not have protease inhibitor activity, but can function as a  $K^+$  channel blocker, even though it belongs to the venom Kunitz-type inhibitor protein family [45]. In addition, CVF, which has been claimed to be present in the venom of *Naja kaouthia* [46], was identified in *N. atra* venom as well.

### 3.2. Comparison of the venom proteomes of six Taiwanese snakes

As expected, the venom proteomes of snakes from the same family shared a number of highly similar proteins from major protein families owing to their close evolutionary and phylogenetic relationships. Based on venom toxin proteins identified by LC-MS/MS analysis from both in-gel-digested samples of SDS-gel-fractionated bands and in-solution-digested samples of the whole venom, the major protein components of Taiwanese snakes from the *Viperidae* family (*D. acutus*, *T. stejnegeri*, *P. mucrosquamatus*, and *D. russelii*) belong to C-type lectin, snake venom serine protease, phospholipase  $A_2$ , and venom metalloproteinase families, whereas two protein families—phospholipase  $A_2$  and three-finger toxin—appear to be dominant in the venom of *Elapidae* snakes (*B. multicinctus* and *N. atra*) in Taiwan. However, the information obtained from our analytical strategy cannot provide the information regarding relative abundance of proteins identified.

In particular, our data revealed that phospholipase  $A_2$  family members are not only the dominant components of venom of *Viperidae* snakes, but are also the second-most important protein family in the venom of *Elapidae* snakes. These enzymes are widely present in the animal kingdom, and at least 15 groups have been described [47]. The venom of snakes from *Colubridae*, *Viperidae*, and *Elapidae* families represent abundant sources of phospholipase  $A_2$  [48]. However, different venom phospholipase  $A_2$  family members have been reported to possess distinct toxic effects, including neurotoxic, myotoxic, hemolytic, edematogenic, hyperalgesic, pro-inflammatory, hypotensive, anticoagulant and cytotoxic, despite their similar three-dimensional structures [49]. For the purpose of improving the clinical management of snakebites in Taiwan, phospholipase  $A_2$  may be a suitable marker for distinguishing patients bitten by venomous snakes from those bitten by non-venomous snakes.

Proteins of the three-finger toxin family are the most abundant components in the venom proteome of *Elapidae* snakes [27, 50–52]. This family is subdivided into a number of subfamilies, including neurotoxin, cytotoxin and cardiotoxin, each with its own specific activity and function. According to our LC-MS/MS analysis and database search results shown in the present study,  $\alpha$ -bungarotoxin and  $\kappa$ -bungarotoxin, classified into the neurotoxin subfamily, are only present in the venom of *B. multicinctus*. These proteins bind with high affinity to muscular and neuronal nicotinic acetylcholine receptors and prevent acetylcholine from binding to the receptor, thereby impairing neuromuscular and neuronal transmission [53, 54]. By contrast, cytotoxin was the dominant protein component in the venom of *N. atra*. Proteins belonging to this subfamily bind to cell membranes, exerting lytic activity and depolarizing cardiomyocytes [55]. The functions of these two subfamilies are known to correlate with clinical symptoms; victims bitten by *B. multicinctus* exhibit rapid respiratory failure caused by respiratory muscle paralysis, and those bitten by *N. atra* suffer serious local damage, including wound necrosis, bleeding, and swelling.

LC-MS/MS analyses of in-gel digested (Table 1) and in-solution digested (Table 2) samples showed that CVF protein was present only in *N. atra* venom. Detailed structural and functional investigations of CVF from the monocled cobra, *N. kaouthia*, have been reported previously [56, 57]. CVF is composed of three chains:  $\alpha$ ,  $\beta$  and  $\gamma$  (Fig. 2A). Because of its structural homology to the complement protein C3, CVF continuously activates the complement system, resulting in depletion of complement activity [58]. The complement system represents part of the immune system and plays important roles in both innate and adaptive immunity; it is also involved in the pathogenesis of many diseases. Thus, CVF has become an important research tool for studying

both the biological functions of complement and its role in the pathogenesis of complement-related diseases [59]. In addition to *N. kaouthia* and *N. atra* [27], several MS-based studies have revealed the presence of CVF in the venom of *Naja naja* [60], *Naja haje legionis* [50], *Naja sumatrana* [61] and *Ophiophagus hannah* [62]. To confirm that CVF is present in the venom of *N. atra* but not in venoms of the other five venomous Taiwanese snakes, we produced an in-house anti-CVF antibody in rabbits using the D16 peptide (DDNEDGFIADSDIISR), corresponding to amino acids 723–748 of the CVF  $\gamma$ -chain, as the antigen (Fig. 2A). This peptide sequence is apparently unique to CVF, as no similar sequences could be found by BLAST search of protein databases (UniProt Knowledgebase, UniProtKB). The affinity-purified anti-CVF antibody was first used to probe the six Taiwanese snake venoms by direct enzyme-linked immunosorbent assay (ELISA). As expected, a significant ELISA signal was detected in the venom of *N. atra*, but not in venoms of the other five snake species (Fig. 2B). Consistent with ELISA data, Western blot analyses showed that this antibody clearly recognized a major protein band at ~28 kDa in *N. atra* venom (Fig. 2C, upper panel). In this Western blot, an additional weak signal band detected at ~10 kDa in *B. multicinctus* venom was verified as a background signal attributable to the secondary antibody used (Fig. 2C, lower panel).

### 3.3. Development of SISCAPA-MRM assay for quantification of CVF in human plasma background

MRM-MS is a powerful tool for monitoring protein-derived peptides obtained by proteolytic treatment and has been widely used to quantify target proteins in complex biological samples [21, 63–65]. Combining MRM-MS with the SISCAPA protocol (SISCAPA-MRM) could yield an assay that would further improve the specificity and sensitivity of target protein quantification. Taking advantage of the availability of an in-house-generated antibody against a CVF peptide antigen, we sought to develop a SISCAPA-MRM assay for CVF that could be useful for quantification of this protein in whole venom or, potentially, in snake-venom patients. To this end, we first synthesized light and heavy CVF-derived D16 peptides and chose three fragment ions derived from the D16 peptide that had the highest intensities in positive ion mode MS/MS analyses. The optimized MRM parameters used to detect light and heavy D16 peptides in QTRAP 5500 are shown in Tables S13 and S14, respectively.

To examine the performance of the SISCAPA-MRM assay, we constructed a concentration-response curve for D16 peptide. Serially diluted samples of heavy SIS peptide covering four orders of magnitude (0.024 to 100 femtomoles) were prepared and spiked into 20  $\mu$ l samples of plasma digests containing an equal amount of the light peptide (100 fmol) as test samples. D16 peptides were then enriched by adding anti-CVF antibody to each sample, and samples were analyzed by MRM-MS. Fig. S1 shows the extracted ion chromatograms of three selected fragment ions (2y7, 2y8 and 2y9) of the light and heavy SIS peptides. All data were combined and the signals of these three fragment ions were used to construct concentration-response curves (Fig. 3A and B). As is evident from these response curves, the observed heavy peptide/light peptide (H/L) peak area ratios were linearly correlated with the actual spiked-in H/L ratios, and the  $R^2$  values for the three fragment ions were all greater than 0.99 (Table 3). The measured coefficient of variation (CV) values for each analyzed heavy peptide quantity, except for 0.0244 fmol, were less than 20% (Fig. 3C). The limit of detection (LOD) and lower limit of quantification (LLOQ) of the SISCAPA-MRM assay varied according to the fragment ion (Table 3); LOD values ranged from 3.2 to 10.73 amol, whereas the values of LLOQ ranged from 9.6 to 32.19 amol. The 2y9 fragment ion of this CVF-derived peptide had the lowest LOD and LLOQ, and thus was used as the quantifier ion. This work represents the first immune-MRM assay developed to date for quantification of snake venom components.

A number of previous studies have identified CVF in the venom of

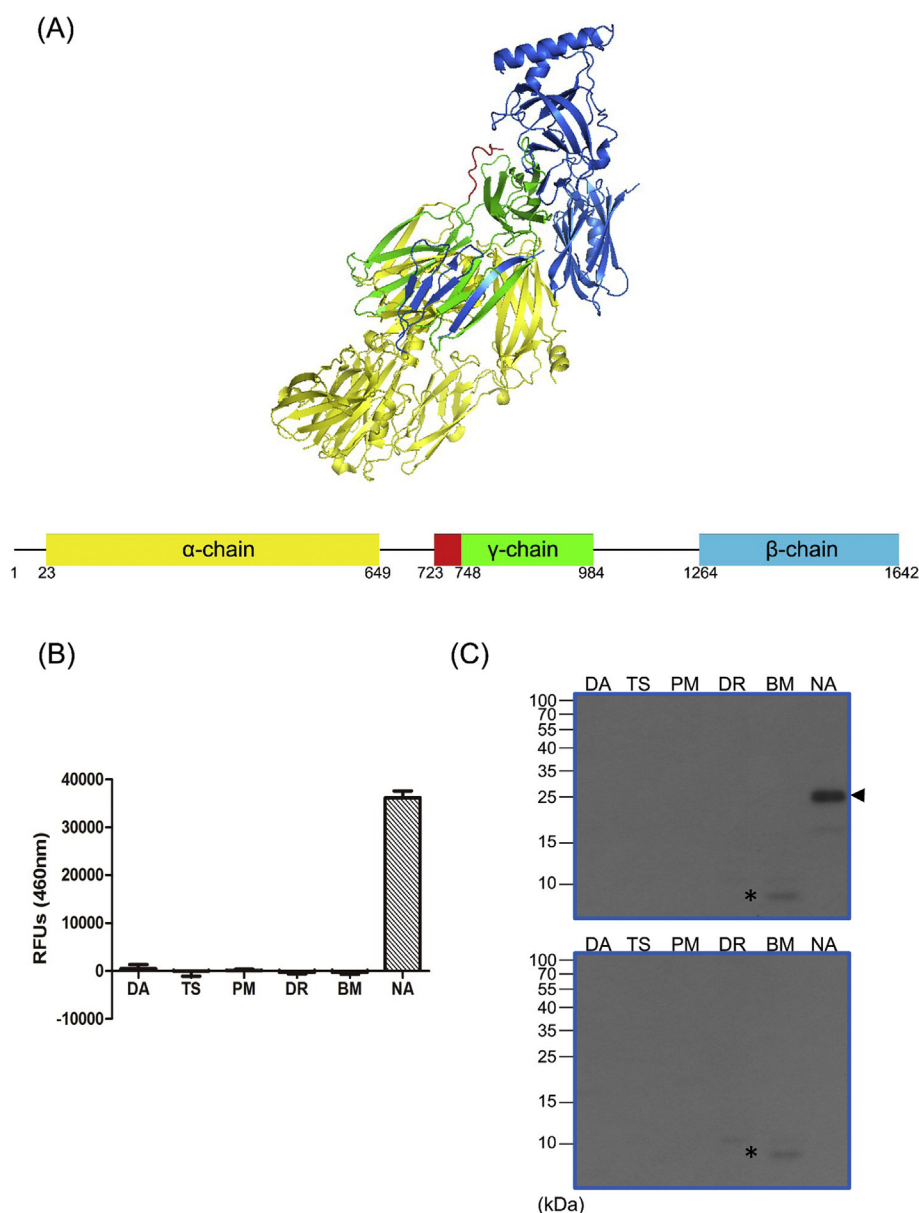


**Fig. 2.** Immunoassay-based detection of CVF in venom of *N. atra*. (A) Three-dimensional structure of CVF (PDB code: Q91132). The peptide segment used as the antigen for generating the in-house anti-CVF antibody is denoted in red. (B) An ELISA plate was coated with whole venom proteins (100 ng) from each snake, washed, and then CVF was detected using the anti-CVF antibody. (C) Whole venom proteins (5  $\mu$ g) from each snake were resolved on SDS gels, transferred to PVDF membranes, and then probed with the anti-CVF antibody (upper panel) or with the secondary antibody only (lower panel). The CVF signal is indicated by an arrowhead; background signals recognized by the secondary antibody alone (control) are denoted by asterisks. (For interpretation of the references to colour in this figure legend, the reader is referred to the web version of this article.)

*Naja* species, but none has assessed the proportion of CVF among total venom proteins. Therefore, we used the newly developed SISCAPA-MRM assay to quantify CVF in the venom of four cobras belonging to the *Naja* genus: *N. atra*, *N. kaouthia*, *N. siamensis* and *O. hannah* (king cobra). A fixed amount of venom protein (1  $\mu$ g) was subjected to the analysis described above. As expected, the CVF peptide (DDNEDGFIA-DSDIISR) was detected in all venoms at amounts ranging from 0.9 to 54.36 fmol (Table 4). Extracted ion chromatograms of selected fragment ions of heavy SIS peptide and the corresponding unlabeled peptide from the endogenous CVF protein in the venom of four cobras are shown in Fig. S2. The CVF level was determined to be 7.03, 10.03 and 8.38 mg per gram of venom protein in the venom of *N. atra*, *N. kaouthia* and *N. siamensis*, respectively, but only 0.16 mg per gram in king cobra (Fig. 3D). Thus, our newly developed SISCAPA-MRM assay was able to precisely quantify CVF protein, and showed that CVF constitutes nearly 1% of total venom protein in *Naja* species and 0.1% in king cobra.

#### 4. Conclusions

In this study, we applied MS-based approaches to characterize and

compare the venom proteomes of six Taiwanese venomous snakes that collectively are responsible for almost 100% of clinically significant incidents in Taiwan. Our data revealed that in the venom of *Viperidae* snakes, C-type lectin, venom metalloproteinase and snake venom serine proteinase are identified in the dominant protein bands resolved by SDS-gels, whereas proteins of the three-finger toxin family are specific venom components of *Elapidae* species. Moreover, we identified additional protein components in these six venoms that have not been previously reported, including 5'-nucleotidase, acetylcholinesterase, glutaminyl-peptide cyclotransferase, glycosyl hydrolase, phosphodiesterase and phospholipase B. This information should contribute to a deeper understanding of the biology and pathophysiology of these Taiwanese snakes and aid in predicting clinical symptoms, which will improve snakebite management.

The SISCAPA-MRM assay developed here is a highly sensitive assay that is capable of quantifying proteins at the sub-femtomole level. Notably, this study is the first to report the development of a SISCAPA-MRM assay for snake venom proteins. Using the SISCAPA-MRM assay, we quantified the *N. atra*-specific protein CVF, and precisely quantified its levels in the venom of three *Naja* species and that of king cobra.

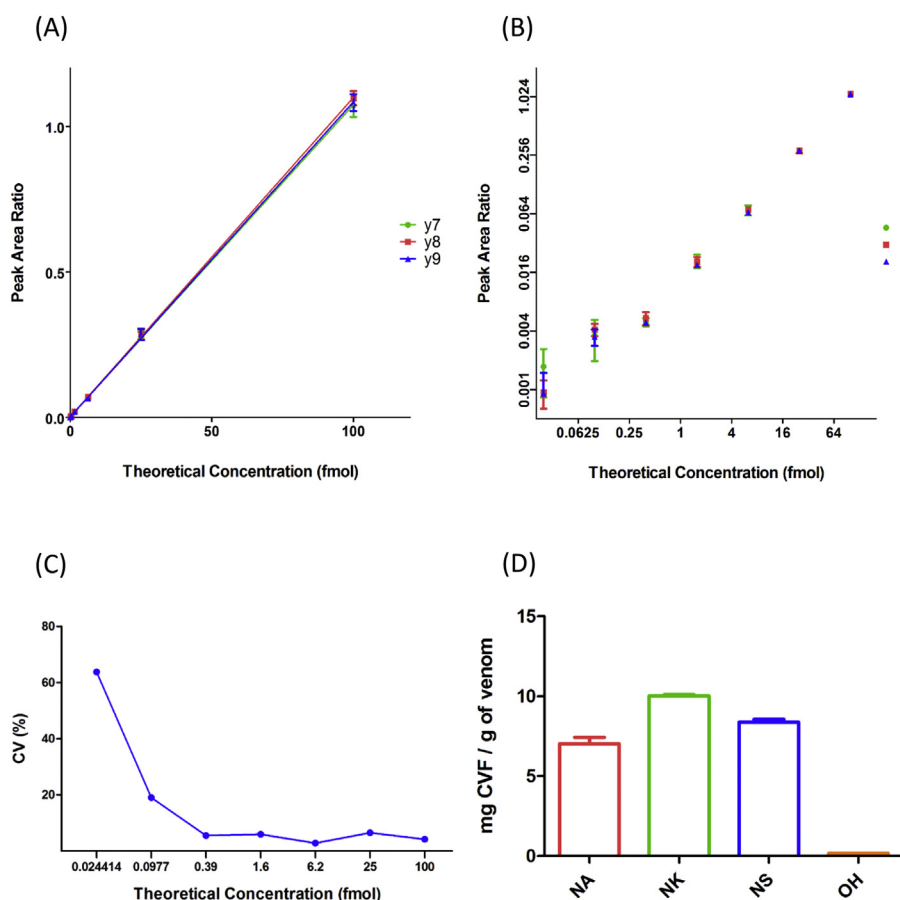


**Fig. 3.** Concentration-response curves of the SISCAPA-MRM assay for the CVF-derived peptide in a human plasma matrix. Concentration-responses curves shown in linear (A) and log (B) scale. The dynamic range was from 24.4 amol to 100 fmol, with 4-fold serial dilutions. (C) CV% of each data point in triplicate experiments. (D) The absolute concentration (mg/g) of CVF protein in four cobra venoms, quantified using our SISCAPA-MRM assay. NK, *N. kaouthia*; NS, *N. siamensis*; OH, *O. Hannah*.

**Table 3**

LOD and LLOQ of CVF peptides in the SISCAPA-MRM assay, determined from concentration-response curves.

Protein	Peptide	Transition.id	slope		y-intercept			R <sup>2</sup>	LOD <sup>a</sup>	LLOQ <sup>b</sup>	
									(amol)	(amol)	
Cobra venom factor (CVF)	DDNEDGFIADSDIISR	2/9y <sup>*</sup>	0.011489	±	0.000358	0.000976	±	0.000022	0.9989	3.20	9.60
	DDNEDGFIADSDIISR	2/8y	0.011279	±	0.000243	0.000300	±	0.000015	0.9988	3.98	11.93
	DDNEDGFIADSDIISR	2/7y	0.011072	±	0.000366	0.001116	±	0.000022	0.9981	10.73	32.19

<sup>\*</sup> Represents the Quantifier ion.

<sup>a</sup> LOD: Display the limit of detection of this transition ion.

<sup>b</sup> LLOQ: Represent the lower limit of quantification of this transition ion.

**Table 4**

Quantification of CVF protein in four Southeast Asia snake venoms.

Snake venom	DDNEDGFIADSDIISR			CVF protein		
	Mean ± SD <sup>a</sup> (fmol)			Mean ± SD <sup>a</sup> (ng)		
<i>N. atra</i>	38.113	±	3.718	7.033	±	0.686
<i>N. kaouthia</i>	54.360	±	0.765	10.030	±	0.141
<i>N. siamensis</i>	45.413	±	1.701	8.380	±	0.314
<i>O. hannah</i>	0.908	±	0.044	0.168	±	0.008

<sup>a</sup> Mean ± SD: shows the average value (Mean) and standard deviation (SD) calculated from triplicate results.

Given that CVF has emerged as an important research tool for studying the biological functions of complement and the pathogenesis of complement-related diseases, the MS-based quantitative assay described here should facilitate future CVF-related basic and clinical studies.

#### Author contributions

C.C.Liu, C.C.Lin and J.S.Y. designed the study; C.C.Liu, P.J.W. and Y.C.H. conducted the experiments and analyzed data; C.C.Lin contributed reagents and materials; C.C.Liu, C.C.Lin and J.S.Y. interpreted the results and wrote the manuscript.

#### Conflict of interest

The authors declare no competing financial interests.

Supplementary data to this article can be found online at <https://doi.org/10.1016/j.jprote.2018.06.003>.

#### Acknowledgments

This work was financially supported by the “Molecular Medicine Research Center, Chang Gung University” from The Featured Areas

Research Center Program within the framework of the Higher Education Sprout Project by the Ministry of Education (MOE) in Taiwan (grant EMRPD1H0171), by the Ministry of Science and Technology, Taiwan (grants MOST 106-2632-B-182-002 and 106-2320-B-182-029-MY3 to JSY), and by Chang Gung Memorial Hospital, Taiwan (grants CMRPG3F0241-243 to C.C.Lin, CMRPD1B0531, CIRPD3B0013, CRRPD1F0051-52, CMRPD190364, CLRPD190018 and BMRP208 to JSY). The funders had no role in study design, data collection and analysis, decision to publish, or preparation of the manuscript. We wish to acknowledge Center for Research, Diagnostics and Vaccine Development of Centers for Disease Control, Ministry of Health and Welfare, Taiwan, for their excellent assistance providing six snake venoms presented in this investigation.

## References




- [1] D.A. Warrell, Venomous bites, stings, and poisoning, *Infect. Dis. Clin. N. Am.* 26 (2) (2012) 207–223.
- [2] J. White, Venomous animals: clinical toxicology, *EXS* 100 (2010) 233–291.
- [3] J.P. Chippaux, Snake-bites: appraisal of the global situation, *Bull. World Health Organ.* 76 (5) (1998) 515–524.
- [4] S. Swaroop, B. Grab, Snakebite mortality in the world, *Bull. World Health Organ.* 10 (1) (1954) 35–76.
- [5] R.A. Harrison, A. Hargreaves, S.C. Wagstaff, B. Faragher, D.G. Laloo, Snake envenoming: a disease of poverty, *PLoS Negl. Trop. Dis.* 3 (12) (2009) e569.
- [6] J.M. Gutierrez, J.J. Calvete, A.G. Habib, R.A. Harrison, D.J. Williams, D.A. Warrell, Snakebite envenoming, *Nat Rev Dis Primers* 3 (2017) 17063.
- [7] A. Kasturiratne, A.R. Wickremasinghe, N. de Silva, N.K. Gunawardena, A. Pathmeswaran, R. Premaratna, L. Savioli, D.G. Laloo, H.J. de Silva, The global burden of snakebite: a literature analysis and modelling based on regional estimates of envenoming and deaths, *PLoS Med.* 5 (11) (2008) e218.
- [8] M.Y. Liao, R.J. Huang, Toxoids and antivenoms of venomous snakes in Taiwan, *J. Toxicol.-Toxin Rev.* 16 (3) (1997) 163–175.
- [9] D.Z. Hung, Taiwan's venomous snakebite: epidemiological, evolution and geographic differences, *Trans. R. Soc. Trop. Med. Hyg.* 98 (2) (2004) 96–101.
- [10] K.P. Chang, C.S. Lai, S.D. Lin, Management of poisonous snake bites in southern Taiwan, *Kaohsiung J. Med. Sci.* 23 (10) (2007) 511–518.
- [11] C. Mitrakul, U. Juzzi, W. Pongrujijorn, Antivenom therapy in Russell's viper bite, *Am. J. Clin. Pathol.* 95 (3) (1991) 412–417.
- [12] A. Beamud Gomez, A. Cabo Valle, M. Martinez Verduch, F. Estornell Moragues, V. Sabater Marco, F. Garcia Ibarra, Renal function: implications in the normal and abnormal development of the urinary tract; role of echography, *Actas Urol. Esp.* 10 (2) (1986) 137–140.
- [13] D.A. Warrell, Snake venoms in science and clinical medicine. 1. Russell's viper: biology, venom and treatment of bites, *Trans. R. Soc. Trop. Med. Hyg.* 83 (6) (1989) 732–740.
- [14] S.A. Kularatne, B.D. Budagoda, I.B. Gawarammana, W.K. Kularatne, Epidemiology, clinical profile and management issues of cobra (*Naja naja*) bites in Sri Lanka: first authenticated case series, *Trans. R. Soc. Trop. Med. Hyg.* 103 (9) (2009) 924–930.
- [15] H.A. Reid, Cobra-Bites, *Br. Med. J.* 2 (5408) (1964) 540–545.
- [16] D.Z. Hung, M.Y. Liao, S.Y. Lin-Shiau, The clinical significance of venom detection in patients of cobra snakebite, *Toxicon* 41 (4) (2003) 409–415.
- [17] E. Alirol, S.K. Sharma, H.S. Bawaskar, U. Kuch, F. Chappuis, Snake bite in South Asia: a review, *PLoS Negl. Trop. Dis.* 4 (1) (2010) e603.
- [18] J.B. Harris, M.A. Faiz, M.R. Rahman, M.M. Jalil, M.F. Ahsan, R.D. Theakston, D.A. Warrell, U. Kuch, Snake bite in Chittagong division, Bangladesh 104 (5) (2010) 320–327.
- [19] S. Dresen, N. Ferreiros, H. Gnann, R. Zimmermann, W. Weinmann, Detection and identification of 700 drugs by multi-target screening with a 3200 Q TRAP LC-MS/MS system and library searching, *Anal. Bioanal. Chem.* 396 (7) (2010) 2425–2434.
- [20] R. Wei, G. Li, A.B. Seymour, High-throughput and multiplexed LC/MS/MS/MS method for targeted metabolomics, *Anal. Chem.* 82 (13) (2010) 5527–5533.
- [21] Y.T. Chen, H.W. Chen, D. Domanski, D.S. Smith, K.H. Liang, C.C. Wu, C.L. Chen, T. Chung, M.C. Chen, Y.S. Chang, C.E. Parker, C.H. Borchers, J.S. Yu, Multiplexed quantification of 63 proteins in human urine by multiple reaction monitoring-based mass spectrometry for discovery of potential bladder cancer biomarkers, *J. Proteome* 75 (12) (2012) 3529–3545.
- [22] J.R. Barr, V.L. Maggio, D.G. Patterson Jr., G.R. Cooper, L.O. Henderson, W.E. Turner, S.J. Smith, W.H. Hannon, L.L. Needham, E.J. Sampson, Isotope dilution-mass spectrometric quantification of specific proteins: model application with apolipoprotein A-I, *Clin. Chem.* 42 (10) (1996) 1676–1682.
- [23] V. Lange, P. Picotti, B. Dorn, R. Aebersold, Selected reaction monitoring for quantitative proteomics: a tutorial, *Mol. Syst. Biol.* 4 (2008) 222.
- [24] N.L. Anderson, N.G. Anderson, L.R. Haines, D.B. Hardie, R.W. Olafson, T.W. Pearson, Mass spectrometric quantitation of peptides and proteins using stable isotope standards and capture by anti-peptide antibodies (SISCAPA), *J. Proteome Res.* 3 (2) (2004) 235–244.
- [25] J.R. Whiteaker, L. Zhao, L. Anderson, A.G. Paulovich, An automated and multiplexed method for high throughput peptide immunoaffinity enrichment and multiple reaction monitoring mass spectrometry-based quantification of protein biomarkers, *Mol. Cell. Proteomics* 9 (1) (2010) 184–196.
- [26] M. Villalta, D. Pla, S.L. Yang, L. Sanz, A. Segura, M. Vargas, P.Y. Chen, M. Herrera, R. Estrada, Y.F. Cheng, C.D. Lee, M. Cerdas, J.R. Chiang, Y. Angulo, G. Leon, J.J. Calvete, J.M. Gutierrez, Snake venomomics and antivenomics of *Protobothrops mucrosquamatus* and *Viridovipera stejnegeri* from Taiwan: keys to understand the variable immune response in horses, *J. Proteome* 75 (18) (2012) 5628–5645.
- [27] H.W. Huang, B.S. Liu, K.Y. Chien, L.C. Chiang, S.Y. Huang, W.C. Sung, W.G. Wu, Cobra venom proteome and glycome determined from individual snakes of *Naja atra* reveal medically important dynamic range and systematic geographic variation, *J. Proteome* 128 (2015) 92–104.
- [28] J. Nawarak, S. Sinchaikul, C.Y. Wu, M.Y. Liao, S. Phutrakul, S.T. Chen, Proteomics of snake venoms from Elapidae and Viperidae families by multidimensional chromatographic methods, *Electrophoresis* 24 (16) (2003) 2838–2854.
- [29] S.J. Lin, K.P. Chang, C.W. Hsu, L.M. Chi, K.Y. Chien, Y. Liang, M.H. Tsai, Y.T. Lin, J.S. Yu, Low-molecular-mass secretome profiling identifies C-C motif chemokine 5 as a potential plasma biomarker and therapeutic target for nasopharyngeal carcinoma, *J. Proteome* 94 (2013) 186–201.
- [30] C.C. Wu, C.W. Hsu, C.D. Chen, C.J. Yu, K.P. Chang, D.I. Tai, H.P. Liu, W.H. Su, Y.S. Chang, J.S. Yu, Candidate serological biomarkers for cancer identified from the secretomes of 23 cancer cell lines and the human protein atlas, *Mol. Cell. Proteomics* 9 (6) (2010) 1100–1117.
- [31] M. Reichlin, Use of glutaraldehyde as a coupling agent for proteins and peptides, *Methods Enzymol.* 70 (A) (1980) 159–165.
- [32] J.S. Yu, S.D. Yang, Okadaic acid, a serine/threonine phosphatase inhibitor, induces tyrosine dephosphorylation/inactivation of protein kinase FA/GSK-3 alpha in A431 cells, *J. Biol. Chem.* 269 (20) (1994) 14341–14344.
- [33] J.S. Yu, S.D. Yang, Tyrosine dephosphorylation and concurrent inactivation of protein kinase FA/GSK-3 alpha by genistein in A431 cells, *J. Cell. Biochem.* 56 (1) (1994) 131–141.
- [34] J.R. Whiteaker, L. Zhao, C. Lin, P. Yan, P. Wang, A.G. Paulovich, Sequential multiplexed analyte quantification using peptide immunoaffinity enrichment coupled to mass spectrometry, *Mol. Cell. Proteomics* 11 (6) (2012) M111–015347.
- [35] H. Chen, Y.C. Hsiao, S.F. Chiang, C.C. Wu, Y.T. Lin, H. Liu, H. Zhao, J.S. Chen, Y.S. Chang, J.S. Yu, Quantitative analysis of wild-type and V600E mutant BRAF proteins in colorectal carcinoma using immunoenrichment and targeted mass spectrometry, *Anal. Chim. Acta* 933 (2016) 144–155.
- [36] B. Maclean, D.M. Tomazela, N. Shulman, M. Chambers, G.L. Finney, B. Frewen, R. Kern, D.L. Tabb, D.C. Liebler, M.J. Maccoss, Skyline: an open source document editor for creating and analyzing targeted proteomics experiments, *Bioinformatics* 26 (7) (2010) 966–968.
- [37] L. Lazerini-Ospri, P. Stano, P. Luisi, R. Marangoni, Characterization of the emergent properties of a synthetic quasi-cellular system, *BMC Bioinformatics* 13 (Suppl. 4) (2012) S9.
- [38] T.A. Addona, S.E. Abbatiello, B. Schilling, S.J. Skates, D.R. Mani, D.M. Bunk, C.H. Spiegelman, L.J. Zimmerman, A.J. Ham, H. Keshishian, S.C. Hall, S. Allen, R.K. Blackman, C.H. Borchers, C. Buck, H.L. Cardasis, M.P. Cusack, N.G. Dodder, B.W. Gibson, J.A. Held, T. Hiltke, A. Jackson, E.B. Johansen, C.R. Kinsinger, J. Li, M. Mesri, T.A. Neubert, R.K. Niles, T.C. Pulsipher, D. Ransohoff, H. Rodriguez, P.A. Rudnick, D. Smith, D.L. Tabb, T.J. Tegeler, A.M. Variyath, L.J. Vega-Montoto, A. Wahlander, S. Waldemarson, M. Wang, J.R. Whiteaker, L. Zhao, N.L. Anderson, S.J. Fisher, D.C. Liebler, A.G. Paulovich, F.E. Regnier, P. Tempst, S.A. Carr, Multi-site assessment of the precision and reproducibility of multiple reaction monitoring-based measurements of proteins in plasma, *Nat. Biotechnol.* 27 (7) (2009) 633–641.
- [39] K. Maduware, M.A. O'Leary, G.K. Isbister, Diagnosis of snake envenomation using a simple phospholipase A2 assay, *Sci. Rep.* 4 (2014) 4827.
- [40] B. Zhang, Q. Liu, W. Yin, X. Zhang, Y. Huang, Y. Luo, P. Qiu, X. Su, J. Yu, S. Hu, G. Yan, Transcriptome analysis of *Deinagkistrodon acutus* venomous gland focusing on cellular structure and functional aspects using expressed sequence tags, *BMC Genomics* 7 (2006) 152.
- [41] L. Qinghua, Z. Xiaowei, Y. Wei, L. Chenji, H. Yijun, Q. Pengxin, S. Xingwen, H. Songnian, Y. Guangmei, A catalog for transcripts in the venom gland of the *Agkistrodon acutus*: identification of the toxins potentially involved in coagulopathy, *Biochem. Biophys. Res. Commun.* 341 (2) (2006) 522–531.
- [42] M. Risch, D. Georgieva, M. von Bergen, N. Jehmlich, N. Genov, R.K. Arni, C. Betzel, Snake venomomics of the Siamese Russell's viper (*Daboia russellii siamensis*) – relation to pharmacological activities, *J. Proteome* 72 (2) (2009) 256–269.
- [43] A.C. Cheng, H.L. Wu, G.Y. Shi, I.H. Tsai, A novel heparin-dependent inhibitor of activated protein C that potentiates consumptive coagulopathy in Russell's viper envenomation, *J. Biol. Chem.* 287 (19) (2012) 15739–15748.
- [44] D.Z. Hung, M.L. Wu, J.F. Deng, S.Y. Lin-Shiau, Russell's viper snakebite in Taiwan: differences from other Asian countries, *Toxicon* 40 (9) (2002) 1291–1298.
- [45] P.F. Wu, S.N. Wu, C.C. Chang, L.S. Chang, Cloning and functional expression of B chains of beta-bungarotoxins from *Bungarus multicinctus* (Taiwan banded krait), *Biochem. J.* 334 (Pt 1) (1998) 87–92.
- [46] C.W. Vogel, H.J. Muller-Eberhard, Cobra venom factor: improved method for purification and biochemical characterization, *J. Immunol. Methods* 73 (1) (1984) 203–220.
- [47] R.H. Schaloske, E.A. Dennis, The phospholipase A2 superfamily and its group numbering system, *Biochim. Biophys. Acta* 1761 (11) (2006) 1246–1259.
- [48] B.G. Fry, W. Wuster, Assembling an arsenal: origin and evolution of the snake venom proteome inferred from phylogenetic analysis of toxin sequences, *Mol. Biol. Evol.* 21 (5) (2004) 870–883.
- [49] J.M. Gutierrez, B. Lomonte, Phospholipases A2: unveiling the secrets of a functionally versatile group of snake venom toxins, *Toxicon* 62 (2013) 27–39.
- [50] I. Malihi, M.R. Ahmad Rusmili, T.Y. Tee, R. Saile, N. Ghalim, I. Othman, Proteomic analysis of Moroccan cobra *Naja haje* venom using tandem mass spectrometry, *J. Proteome* 96 (2014) 240–252.



- [51] K.Y. Tan, C.H. Tan, S.Y. Fung, N.H. Tan, Venomics, lethality and neutralization of *Naja kaouthia* (monocled cobra) venoms from three different geographical regions of Southeast Asia, *J. Proteome* 120 (2015) 105–125.
- [52] M.R. Rusmili, T.T. Yee, M.R. Mustafa, W.C. Hodgson, I. Othman, Proteomic characterization and comparison of Malaysian *Bungarus candidus* and *Bungarus fasciatus* venoms, *J. Proteome* 110 (2014) 129–144.
- [53] L. Chang, S. Lin, H. Huang, M. Hsiao, Genetic organization of alpha-bungarotoxins from *Bungarus multicinctus* (Taiwan banded krait): evidence showing that the production of alpha-bungarotoxin isotoxins is not derived from edited mRNAs, *Nucleic Acids Res.* 27 (20) (1999) 3970–3975.
- [54] V.A. Chiappinelli, W.R. Weaver, K.E. Mclane, B.M. Conti-Fine, J.J. Fiordalisi, G.A. Grant, Binding of native kappa-neurotoxins and site-directed mutants to nicotinic acetylcholine receptors, *Toxicon* 34 (11–12) (1996) 1243–1256.
- [55] S.H. Chiou, R.L. Raynor, B. Zheng, T.C. Chambers, J.F. Kuo, Cobra venom cardiotoxin (cytotoxin) isoforms and neurotoxin: comparative potency of protein kinase C inhibition and cancer cell cytotoxicity and modes of enzyme inhibition, *Biochemistry* 32 (8) (1993) 2062–2067.
- [56] V. Krishnan, K. Ponnuraj, Y. Xu, K. Macon, J.E. Volanakis, S.V. Narayana, The crystal structure of cobra venom factor, a cofactor for C3- and C5-convertase CVFBb, *Structure* 17 (4) (2009) 611–619.
- [57] C.W. Vogel, D.C. Fritzinger, Cobra venom factor: structure, function, and humanization for therapeutic complement depletion, *Toxicon* 56 (7) (2010) 1198–1222.
- [58] C.W. Van den Berg, P.C. Aerts, H. Van Dijk, In vivo anti-complementary activities of the cobra venom factors from *Naja naja* and *Naja haje*, *J. Immunol. Methods* 136 (2) (1991) 287–294.
- [59] C.W. Vogel, P.W. Finnegan, D.C. Fritzinger, Humanized cobra venom factor: structure, activity, and therapeutic efficacy in preclinical disease models, *Mol. Immunol.* 61 (2) (2014) 191–203.
- [60] S. Li, J. Wang, X. Zhang, Y. Ren, N. Wang, K. Zhao, X. Chen, C. Zhao, X. Li, J. Shao, J. Yin, M.B. West, N. Xu, S. Liu, Proteomic characterization of two snake venoms: *Naja naja atra* and *Agkistrodon halys*, *Biochem. J.* 384 (Pt 1) (2004) 119–127.
- [61] M.K. Yap, S.Y. Fung, K.Y. Tan, N.H. Tan, Proteomic characterization of venom of the medically important southeast Asian *Naja sumatrana* (Equatorial spitting cobra), *Acta Trop.* 133 (2014) 15–25.
- [62] D. Petras, P. Heiss, R.D. Sussmuth, J.J. Calvete, Venom proteomics of Indonesian king cobra, *Ophiophagus hannah*: Integrating Top-Down and Bottom-Up Approaches, *J. Proteome Res.* 14 (6) (2015) 2539–2556.
- [63] P. Picotti, R. Aebersold, Selected reaction monitoring-based proteomics: workflows, potential, pitfalls and future directions, *Nat. Methods* 9 (6) (2012) 555–566.
- [64] C.E. Parker, D. Domanski, A.J. Percy, A.G. Chambers, A.G. Camenzind, D.S. Smith, C.H. Borchers, Mass spectrometry in high-throughput clinical biomarker assays: multiple reaction monitoring, *Top. Curr. Chem.* 336 (2014) 117–137.
- [65] E.S. Boja, H. Rodriguez, Mass spectrometry-based targeted quantitative proteomics: achieving sensitive and reproducible detection of proteins, *Proteomics* 12 (8) (2012) 1093–1110.

Review

# Natural Product Chemistry of Gorgonian Corals of Genus *Junceella*—Part III

Hsu-Ming Chung <sup>1,†</sup>, Yi-Chen Wang <sup>2,†</sup>, Chung-Chih Tseng <sup>3,4</sup> , Nan-Fu Chen <sup>5,6</sup>,  
Zhi-Hong Wen <sup>3</sup>, Lee-Shing Fang <sup>7,8</sup>, Tsong-Long Hwang <sup>9,10,11,12,\*</sup> ,  
Yang-Chang Wu <sup>13,14,15,16,\*</sup> and Ping-Jyun Sung <sup>3,13,16,17,18,\*</sup> 

- <sup>1</sup> Department of Applied Chemistry, National Pingtung University, Pingtung 900, Taiwan; shiuanmin@mail.nptu.edu.tw
- <sup>2</sup> Division of Cardiology, Department of Internal Medicine, Kaohsiung Armed Forces General Hospital, Kaohsiung 802, Taiwan; cvyc.wang@gmail.com
- <sup>3</sup> Department of Marine Biotechnology and Resources, National Sun Yat-sen University, Kaohsiung 804, Taiwan; caviton@gmail.com (C.-C.T.); wzh@mail.nsysu.edu.tw (Z.-H.W.)
- <sup>4</sup> Division of Dentistry, Zuoying Branch of Kaohsiung Armed Forces General Hospital, Kaohsiung 813, Taiwan
- <sup>5</sup> Division of Neurosurgery, Department of Surgery, Kaohsiung Armed Forces General Hospital, Kaohsiung 802, Taiwan; chen06688@gmail.com
- <sup>6</sup> Department of Neurological Surgery, Tri-Service General Hospital, National Defense Medical Center, Taipei 114, Taiwan
- <sup>7</sup> Center for Environmental Toxin and Emerging-Contaminant Research, Cheng Shiu University, Kaohsiung 833, Taiwan; lsfang@csu.edu.tw
- <sup>8</sup> Super Micro Mass Research and Technology Center, Cheng Shiu University, Kaohsiung 833, Taiwan
- <sup>9</sup> Graduate Institute of Natural Products, College of Medicine, Chang Gung University, Taoyuan 333, Taiwan
- <sup>10</sup> Chinese Herbal Medicine Research Team, Healthy Aging Research Center, Chang Gung University, Taoyuan 333, Taiwan
- <sup>11</sup> Research Center for Chinese Herbal Medicine, Research Center for Food and Cosmetic Safety, Graduate Institute of Healthy Industry Technology, College of Human Ecology, Chang Gung University of Science and Technology, Taoyuan 333, Taiwan
- <sup>12</sup> Department of Anaesthesiology, Chang Gung Memorial Hospital, Taoyuan 333, Taiwan
- <sup>13</sup> Graduate Institute of Natural Products, Kaohsiung Medical University, Kaohsiung 807, Taiwan
- <sup>14</sup> Research Center for Natural Products and Drug Development, Kaohsiung Medical University, Kaohsiung 807, Taiwan
- <sup>15</sup> Department of Medical Research, Kaohsiung Medical University Hospital, Kaohsiung 807, Taiwan
- <sup>16</sup> Chinese Medicine Research and Development Center, China Medical University Hospital, Taichung 404, Taiwan
- <sup>17</sup> National Museum of Marine Biology and Aquarium, Pingtung 944, Taiwan
- <sup>18</sup> Graduate Institute of Marine Biology, National Dong Hwa University, Pingtung 944, Taiwan
- \* Correspondence: htl@mail.cgu.edu.tw (T.-L.H.); yachwu@kmu.edu.tw (Y.-C.W.); pjsung@nmmba.gov.tw (P.-J.S.); Tel.: +886-3-211-8800 (ext. 5523) (T.-L.H.); +886-7-312-1101 (ext. 5347) (Y.-C.W.); +886-8-882-5037 (P.-J.S.); Fax: +886-3-211-8506 (T.-L.H.); +886-7-311-4773 (Y.-C.W.); +886-8-882-5087 (P.-J.S.)
- † These authors contributed equally to this work.

Received: 28 August 2018; Accepted: 15 September 2018; Published: 17 September 2018



**Abstract:** The structures, names, bioactivities, and references of 82 natural products, including 48 new metabolites, purified from the gorgonian corals belonging to the genus *Junceella* are described in this review. All compounds mentioned in this review were obtained from *Junceella fragilis*, *Junceella gemmacea*, *Junceella juncea*, and *Junceella* sp., collected from tropical Indo-Pacific Ocean. Some of these compounds exhibited potential biomedical activities.

**Keywords:** *Junceella*; gorgonian; briarane; biomedical activity

## 1. Introduction

Following previous review articles focused on marine-origin natural products, this review covers the literature from October 2011 to August 2018, and describes 82 natural products (including 48 new metabolites) from gorgonian corals belonging to the genus *Junceella* (family Ellisellidae) [1–4]. Extending from previous reviews in 2004 and 2011 [5,6], this review provides structures, names, bioactivities, and references for all compounds including briarane- and norcembrane-type diterpenoids, sterol, and nucleosides. Many of these compounds exhibited interesting bioactivities in vitro, which might indicate a potential for use in biomedical applications. This survey of natural products from *Junceella* is presented taxonomically according to species.

## 2. Junceella

### 2.1. Junceella Fragilis

Eight 8-hydroxybriaranes, including four new compounds, frajunolides P–S (1–4), and four known metabolites, umbraculolide A (5) [7,8], juncenolide C (6) [9], junceellonoid A (7) [10], and juncin R (8) [11], were isolated from *J. fragilis*, collected from the waters of Taiwan [12] (Figure 1). The structures of briaranes 1–4 were established by spectroscopic methods, and determination of the absolute configuration of 1 was completed by X-ray diffraction analysis [12]. At a concentration of 10 µg/mL, briaranes 1 and 2 were found to exert inhibitory activities on elastase release (inhibition rate = 35.6% and 34.1%, respectively) and superoxide anion production (inhibition rate = 32.5 and 28.7%, respectively) by human neutrophils [12].

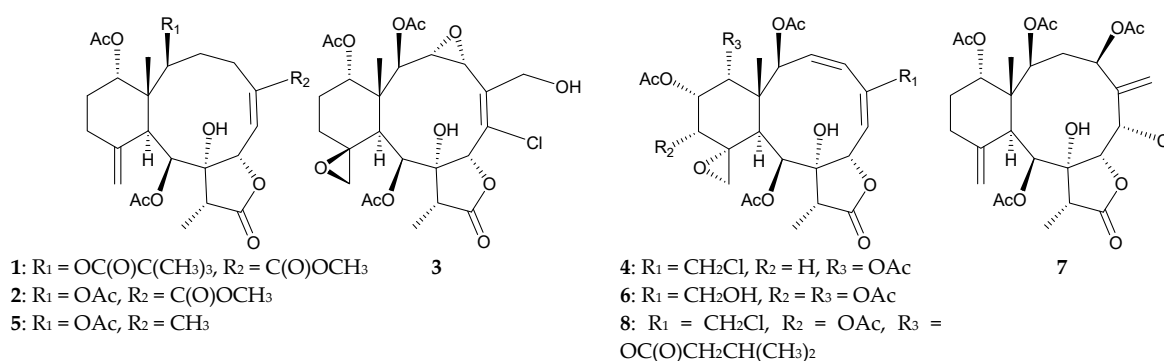


**Figure 1.** Structures of frajunolides P–S (1–4), umbraculolide A (5), juncenolide C (6), junceellonoid A (7), and juncin R (8).

In 2014, *J. fragilis*, collected from the South China Sea, was found to contain 12 new briaranes, fragilisins A–L (9–20) [13], along with seven known analogues, junceellolides A (21) and B (22) [14], junceol A (23) [15], junceellonoid D (24) [16,17], fragilide C (25) [18], and frajunolides A (26) [19] and E (27) [20] (Figure 2) [13]. The structures of briaranes 9–20 were determined by spectroscopic methods. Briaranes 17–20 were the first iodine-containing briaranes to be isolated. The absolute configuration of briarane 9 was confirmed by single-crystal X-ray diffraction data [13]. Briaranes 13, 14, 18, 21, and 24 showed potent antifouling activities against the settlement of barnacle *Balanus amphitrite* larvae, with EC<sub>50</sub> values of 14.0, 12.6, 11.9, 5.6, and 10.0 µM, respectively [13].

In addition, a new norditerpenoid, fragilolide A (28), 16 new briaranes, fragilolides B–Q (29–44), along with two known briaranes, frajunolides H (45) [20] and N (46) [21], and three known norcembranoids, scabrolide D (47) [22], sinuleptolide (48) [23], and 5-*epi*-sinuleptolide (49) [24–26], were obtained from *J. fragilis*, collected from the inner coral reef around in Hainan Island of China [27] (Figure 3). The structures of metabolites 28–44 were determined by spectroscopic methods, including calculated electronic circular dichroism (ECD) data. The structures, including the absolute configurations of briaranes 37 and 46, were further established by single-crystal X-ray diffraction

analysis using Flack parameter in this study [27]. Compound **28** featured an unprecedented 4,13- and 7,11-fused tetracyclic norcembranoid [27].

Briarane **45** exhibited cytotoxicity toward Hep G2 (human hepatocellular carcinoma), Huh7 (human hepatocellular carcinoma), SMMC-7721 (human papillomavirus-related endocervical adenocarcinoma), A2780 (human ovarian carcinoma), BGC-823 (human gastric adenocarcinoma), HGC-27 (human gastric carcinoma), MGC-803 (human gastric carcinoma), NCI-H1650 (human bronchoalveolar carcinoma), and PA-1 (human ovarian mixed germ cell tumor) cells with IC<sub>50</sub> values 0.89, 16.52, 0.61, 1.18, 2.10, 0.61, 1.97, 6.47, and 0.42  $\mu$ M, respectively. Briaranes **31**, **34**, **36**, **39**, **43**, and **46** exerted selective inhibitory effects toward hepatitis B and antigen (HBeAg) in a dose of 10  $\mu$ M, whereas no activity was observed against the expression of hepatitis B surface antigen (HBsAg) [27].

Moreover, the norcembranoids **28** and **47–49** were assayed for their potential inhibitory effects against nitric oxide (NO) production induced by lipopolysaccharides (LPS) (large molecules consisting of lipids and polysaccharide composed of O-antigen joined by chemical bonds), in RAW264.7 cells, and these four compounds exhibited the inhibitory activities with 27.8%, 43.5%, 56.0%, and 57.9% inhibition, respectively, at a dose of 100  $\mu$ M [27]. In order to explore the mechanism of these NO inhibitors, the expression of the antioxidant response element (ARE) mediated luciferase and NF- $\kappa$ B was evaluated. Norcembranoids **48** and **49** showed the effects against NF- $\kappa$ B by the inhibitory rates of 25.1% and 28.6% in a dose of 50  $\mu$ M, respectively. Significant induction of luciferase was observed as the dose of 50  $\mu$ M for **48** and **49** with 3.8 and 5.6 folds more than that of blank control [27]. The antioxidant capacity of **28** and **47–49** were evaluated by the modified 2,2'-azino-bis-(3-ethylbenzothiazoline-6-sulfonic acid) radical cation decolorization assay [27].

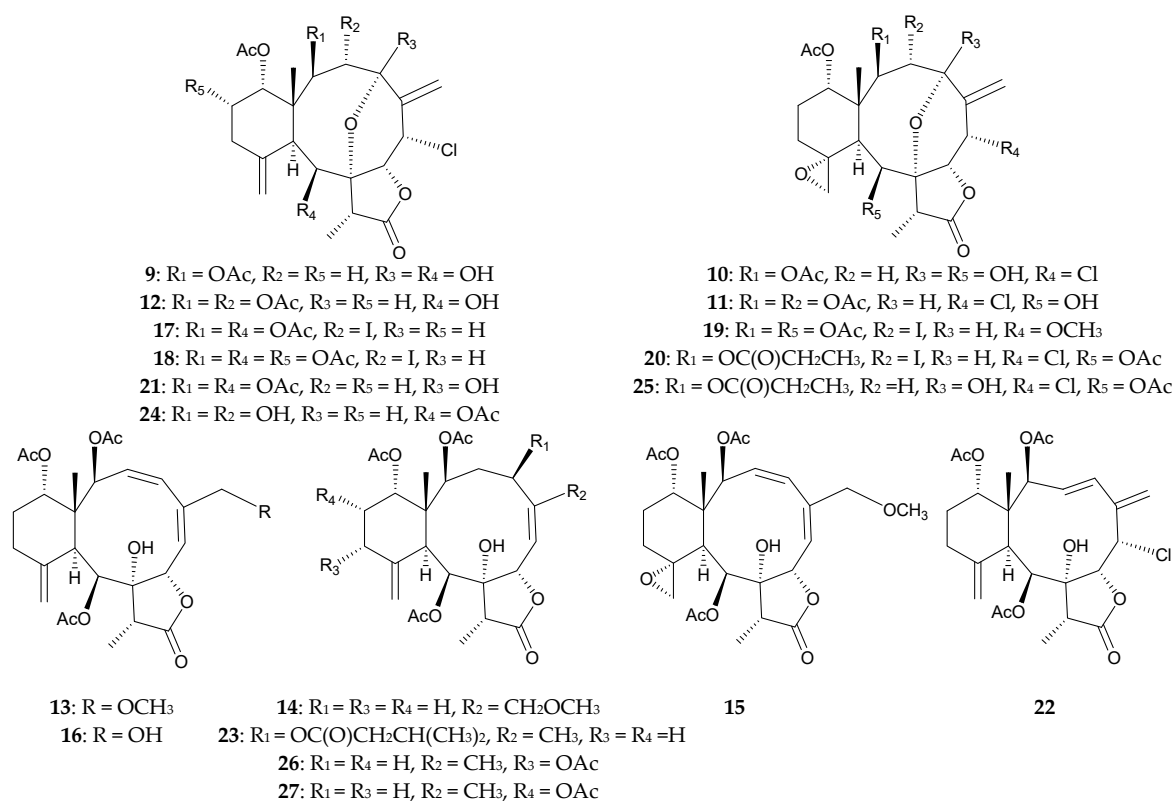


**Figure 2.** Structures of fragilisins A–L (**9–20**), juncellolides A (**21**) and B (**22**), juncel A (**23**), juncellonoid D (**24**), fragilide C (**25**), and frajunolides A (**26**) and E (**27**).



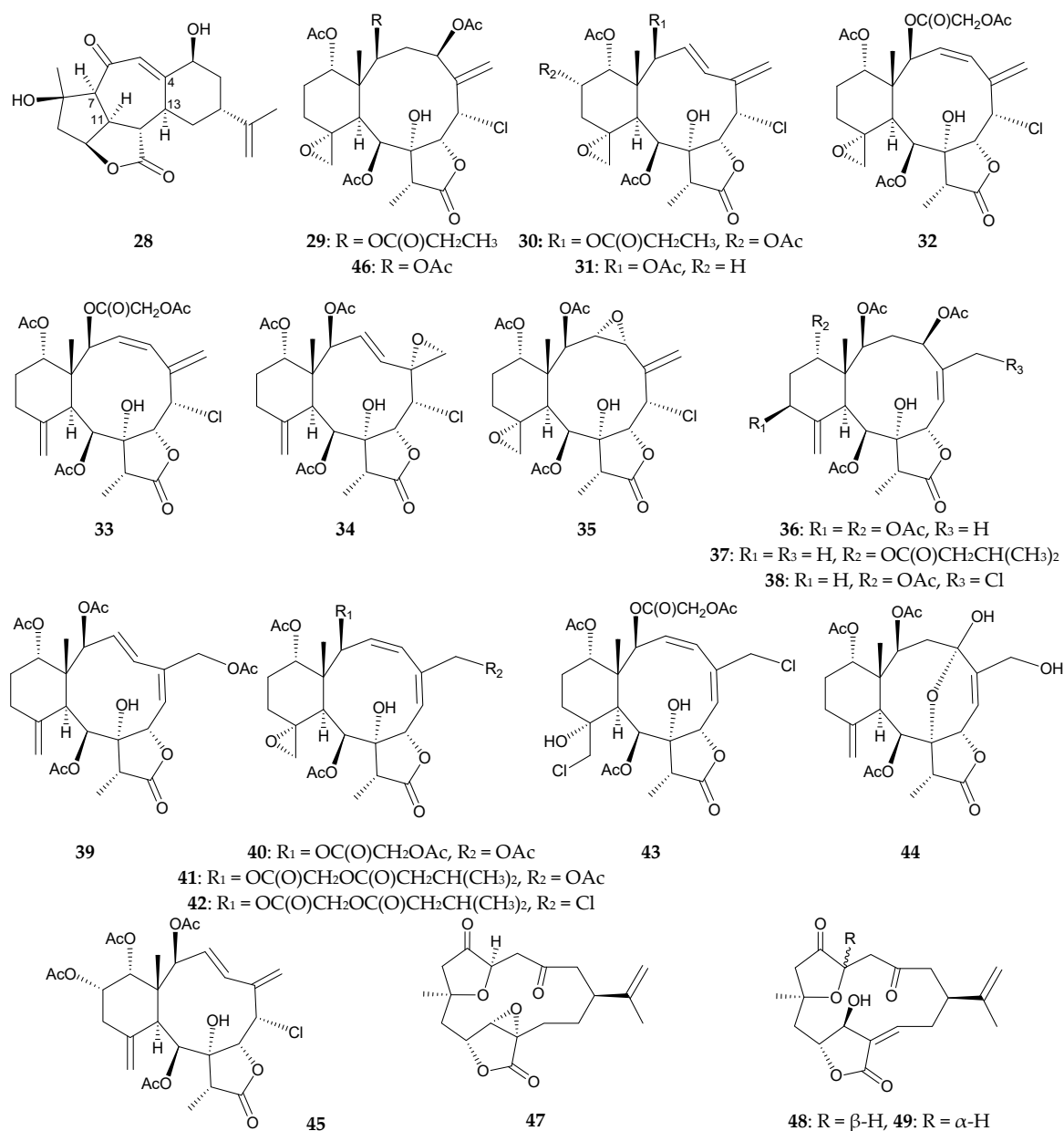


**Figure 3.** Structures of fragilolides A–Q (28–44), frajunolides H (45) and N (46), scabrolide D (47), sinuleptolide (48), and 5-*epi*-sinuleptolide (49).

In 2017, Cheng et al. reported the occurrence of four pairs of chlorinated briarane derivatives, including five new metabolites, 3-deacetylpraelolide (50), 13- $\alpha$ -acetoxy-3-deacetylpraelolide (51), 13- $\alpha$ -acetoxy-2-deacetylpraelolide (52), 13- $\alpha$ -acetoxy-3-deacetyljunceellin (53), 13- $\alpha$ -acetoxy-2-deacetyljunceellin (54), along with three known metabolites, fragilide J (55) [28], 3-deacetyljunceellin (56), and 2-deacetyljunceellin (57) [29], from *J. fragilis*, collected off the inner coral reef in Hainan Island, China (Figure 4), although briaranes 56 and 57 were obtained as a pair of inseparable mixture [30].

The structures of briaranes 50–54 were elucidated by spectroscopic methods in association with chemical conversion. The absolute configurations of briaranes 50 and 55 were further determined by acetylation of these two compounds to yield the same crystal product and analyses of X-ray crystal data of this compound by *Flack* parameter further confirmed the absolute configurations of briaranes 50 and 55 [30], although briaranes 56 and 57 existed in an inseparable mixture in CHCl<sub>3</sub> at room temperature. Lowering the temperature to 4 °C resulted in the generation of a crystal, while the

X-ray diffraction analysis using *Flack* parameter determined the crystal product to be in accordance with briarane **56**. Each pair of the isomers (**50/55**, **51/52**, **53/54**, and **56/57**) featured by dynamical interconversion through as acetyl migration in 1,2-diol, which was postulated to be generated under the formation of cyclic orthoacetate intermediated. In the mixture of briaranes **56** and **57**, increasing temperature gradients resulted in the variation of **56/57** ratio, while the ratio of **56/57** varied from 1:1 to 2:3 at 50 °C [30]. The mixtures of **50/55**, **51/52**, **53/54**, and **56/57** were tested for their inhibitory effects against NO production induced by LPS in RAW264.7 cells and these four components displayed inhibitory activities against NO production with the inhibition rates of 39.4%, 46.4%, 42.7%, and 36.3%, respectively, at a concentration of 50  $\mu$ M [30].



**50:** R<sub>1</sub> = OAc, R<sub>2</sub> = OH, R<sub>3</sub> = H, **55:** R<sub>1</sub> = OH, R<sub>2</sub> = OAc, R<sub>3</sub> = H      **53:** R<sub>1</sub> = R<sub>3</sub> = OAc, R<sub>2</sub> = OH, **54:** R<sub>1</sub> = OH, R<sub>2</sub> = R<sub>3</sub> = OAc  
**51:** R<sub>1</sub> = R<sub>3</sub> = OAc, R<sub>2</sub> = OH, **52:** R<sub>1</sub> = OH, R<sub>2</sub> = R<sub>3</sub> = OAc      **56:** R<sub>1</sub> = OAc, R<sub>2</sub> = OH, R<sub>3</sub> = H, **57:** R<sub>1</sub> = OH, R<sub>2</sub> = OAc, R<sub>3</sub> = H

**Figure 4.** Structures of 3-deacetylpraelolide (**50**), 13- $\alpha$ -acetoxy-3-deacetylpraelolide (**51**), 13- $\alpha$ -acetoxy-2-deacetylpraelolide (**52**), 13- $\alpha$ -acetoxy-3-deacetyljunceellin (**53**), 13- $\alpha$ -acetoxy-2-deacetyljunceellin (**54**), fragilide J (**55**), 3-deacetyljunceellin (**56**), and 2-deacetyljunceellin (**57**).

Two new briaranes, fragilides K (**58**) and L (**59**), along with five known chlorinated briaranes, gemmacolides V (**60**) and X (**61**) [31], praelolide (**62**) [7,14,16,32–37], and juncins P (**63**) [35] and ZI (**64**) [11], were obtained from a Formosan *J. fragilis* [38] (Figure 5).

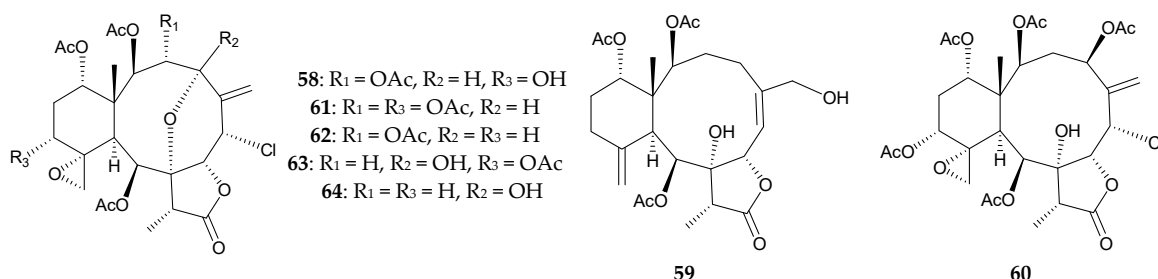


**Figure 5.** Structures of fragilides K (**58**) and L (**59**), gemmacolides V (**60**) and X (**61**), praelolide (**62**), juncins P (**63**) and ZI (**64**).

Based on spectroscopic methods, the structures of briaranes **58** and **59** were elucidated and the cyclohexane rings in **58** and **59** were found to exist in chair and twist boat conformation, respectively. At a concentration of 10  $\mu$ M, briaranes **59**, **61**, and **64** showed anti-inflammatory activity against the expression of pro-inflammatory protein inducible nitric oxide synthase (iNOS) to 49.13%, 36.22%, and 43.33%, respectively, and briaranes **60** and **61** elicited reduction of the pro-inflammatory protein cyclooxygenase-2 (COX-2) to 47.49% and 43.64%, respectively [38].

## 2.2. *Junceella Gemmacea*

Four new briaranes, junceollolides M–P (**65–68**), along with seven known briaranes, junceollolides A–D (**21,22,69,70**) [14] (the structures of briaranes **21** and **22**, please see Figure 2), junceellin A (= junceellin) (**71**) [7,14,16,34–37,39,40], praelolide (**62**) [7,14,16,32–37], and juncin ZI (**64**) [11] (the structures of briaranes **62** and **64**, please see Figure 5) were isolated from *J. gemmacea*, collected from the South China Sea [41] (Figure 6). The structures, including the absolute configurations,

of new briaranes **65–68** were deduced on the basis of spectroscopic analyses, particularly with ECD experiments.

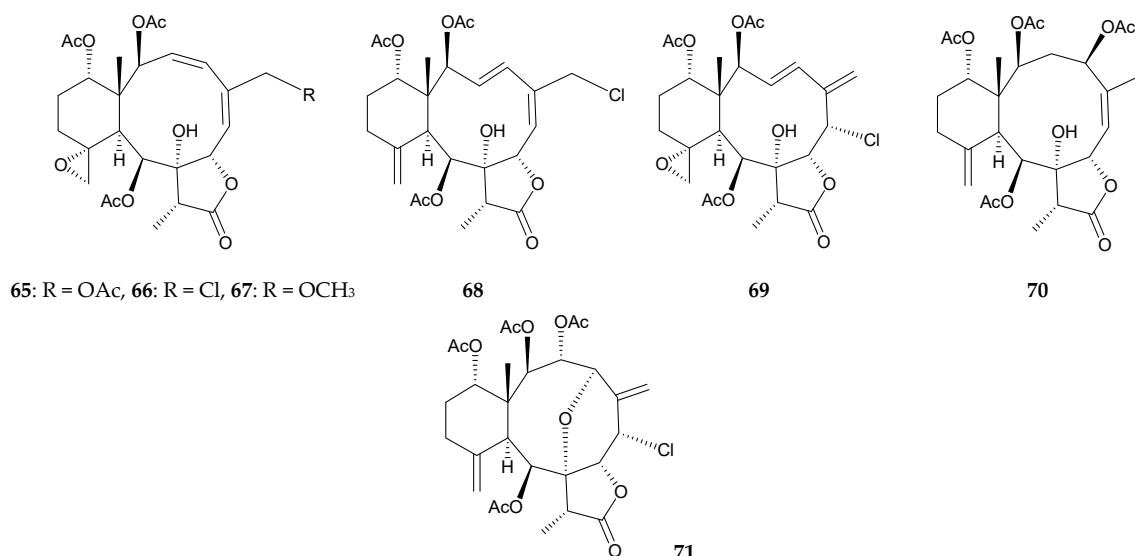


**Figure 6.** Structures of juncecellolides M–P (**65–68**), juncecellolides C (**69**) and D (**70**), and juncecellin A (**71**).

### 2.3. *Juncea Juncea*

Five 8-hydroxybriaranes, including a new briarane, (1*S*\*,2*S*\*,8*S*\*,9*S*\*,10*S*\*,11*R*\*,12*R*\*,14*S*\*,17*R*\*)-11,20-epoxy-14-(3-methylbutanoyl)-2,9,12-triacetoxy-8-hydroxybriar-5(16)-en-18,7-olide (**72**) along with four known metabolites, gemmacolides A (**73**) and B (**74**) [42,43], and juncins H (**75**) [44] and K (**76**) [45], were isolated from *J. juncea* collected from Tuticorin coast of the Indian Ocean (Figure 7) [46]. The structure of briarane **72** was established by spectroscopic data and **72** was found to exhibit activities against the fungi *Aspergillus niger*, *Candida albicans*, and *Penicillium notatum*. Briaranes **73** and **74** displayed activities against the bacteria *Bacillus pumilis* and *Escherichia coli*. While the briaranes **75** and **76** showed activities against *B. subtilis*, *B. pumilis*, *Proteus vulgaris*, and *E. coli* [46].

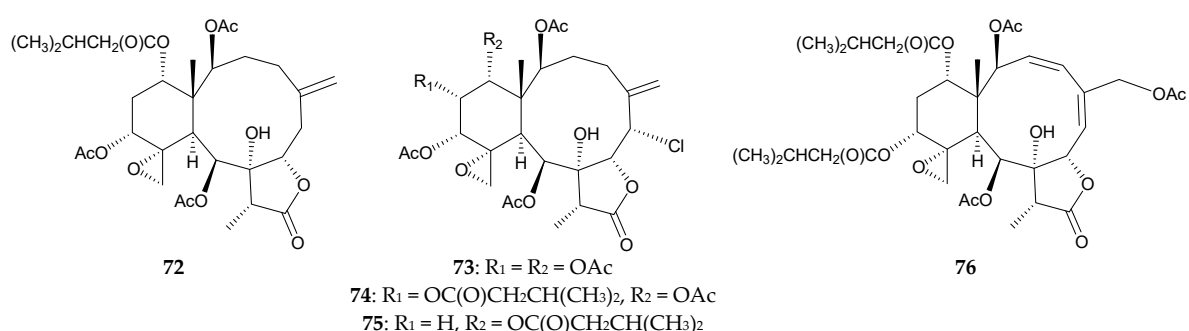


**Figure 7.** Structures of (1*S*\*,2*S*\*,8*S*\*,9*S*\*,10*S*\*,11*R*\*,12*R*\*,14*S*\*,17*R*\*)-11,20-epoxy-14-(3-methylbutanoyl)-2,9,12-triacetoxy-8-hydroxybriar-5(16)-en-18,7-olide (**72**), gemmacolides A (**73**) and B (**74**), and juncins H (**75**) and K (**76**).

Furthermore, Chang et al. isolated three new briaranes, juncenlides M–O (**77–79**), from *J. juncea*, collected in the waters of Taiwan [47] (Figure 8). Structures of new briaranes **77–79** were established by spectroscopic methods. Briaranes **78** and **79** showed inhibitory activities against the release of elastase and **79** also exhibited inhibitory activity against the generation of superoxide anion [47].

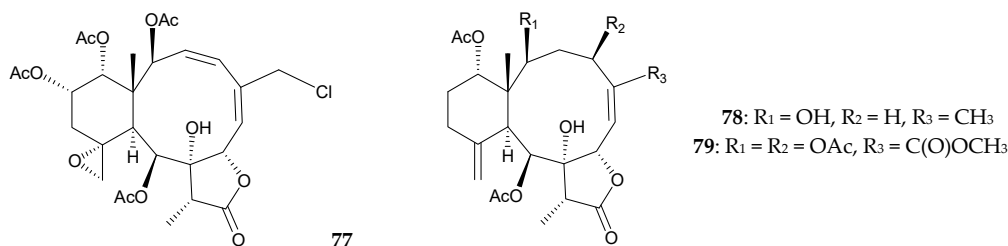


Figure 8. Structures of juncenolides M–O (77–79).

#### 2.4. *Junceella* sp.

Three known briaranes, juncellolide A (**21**) [14], praelolide (**62**) [7,14,16,32–37], and juncellin A (**71**) [7,14,16,34–37,39,40], (the structures of briaranes **21**, **62**, and **71**, please see Figure 2, Figure 5, and Figure 6, respectively), and a known sterol, 5 $\alpha$ ,8 $\alpha$ -epidioxy-24( $\xi$ )-methylcholesta-6,22-dien-3 $\beta$ -ol (**80**) [48] (Figure 9), were obtained from the ethanol extract of a gorgonian coral identified as *Junceella* sp., collected off the Vietnam Thu Island in May 2010 [49]. However, by assuming that enantiomeric series for sterols, the configuration at C-24 in **80** should be assigned as *S*\*-form on the basis of the  $^{13}\text{C}$  NMR chemical shift of C-24 and C-28 [50]. Furthermore, two nucleosides, deoxyadenosine (**81**) and deoxythymidine (**82**) [51,52], were obtained from aqueous solution of this specimen. Structures of all isolates were established using spectroscopic data (Figure 9) [49].

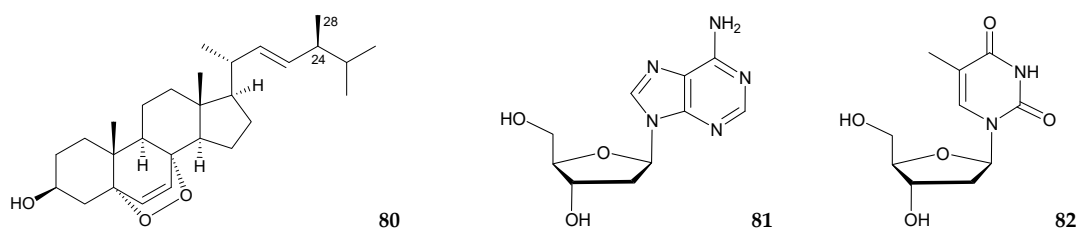


Figure 9. Structures of 5 $\alpha$ ,8 $\alpha$ -epidioxy-24( $\xi$ )-methylcholesta-6,22-dien-3 $\beta$ -ol (**80**), deoxyadenosine (**81**), and deoxythymidine (**82**).

In the cytotoxic activity test, briaranes **71** and sterol **80** exhibited weak cytotoxicity toward the THP-1 (human acute monocytic leukemia) tumor cells with  $\text{IC}_{50}$  values 55.4 and 130  $\mu\text{M}$ , respectively. Sterol **80** also possessed weak clonogenic activity with  $\text{INCC}_{50}$  53.3  $\mu\text{M}$  toward THP-1. Moreover, sterol **80** produced an inhibition zone 12 mm in diameter against *Bacillus subtilis*. Briarane **62** inhibited weakly *Candida albicans*. Briaranes **21** and **71** and sterol **80** inhibited weakly *Vibrio parahaemolyticus* [49].

### 3. Conclusions

The natural products obtained from gorgonian corals belonging to the genus *Junceella* complied in this review indicated that the terpenoid derivatives, particularly briarane-type diterpenoids, are the major components of the natural products isolated. Of the 82 metabolites, 75 compounds (91.5%) are briarane-type diterpenoids. Of the briaranes, 50 compounds are halogenated ( $50/75 = 66.7\%$ ). Briarane-type natural products are a large family of natural products that are only isolated from marine organisms and the compounds of this type were suggested originally synthesized from the 3,8-cyclization of cembranoids by the host corals and not by their zooxanthellae [37,53,54]. Briarane-type diterpenoids continue to attract attention owing to their complex structures and potential biomedical activities.

Studies on the novel substances for biomedical use from the marine invertebrates originally distributed in the Indo-Pacific Ocean will play an important role in natural product research [55]. Marine natural products currently under clinical trials are limited. Based on the potential medical use and complex structures, it is very difficult to obtain enough material for further studies by



chemical methods. How to make the best use of aquaculture technology to enhance in captivity mass production of raw materials needed for extraction of biomedical use marine natural compounds is very important in the future [56].

**Author Contributions:** H.-M.C. and Y.-C.W. contributed in terms of writing the manuscript. T.-L., Y.-C.W., and P.-J.S. conceived and designed the format of the manuscript. All the authors contributed in terms of critical reading and discussion of the manuscript.

**Funding:** This research was supported by grants from the National Museum of Marine Biology and Aquarium; the National Dong Hwa University; and the Ministry of Science and Technology (Grant Nos. MOST 104-2320-B-291-001-MY3, 106-2320-B-291-001-MY3, and 107-2320-B-291-001-MY3), Taiwan, awarded to, Ping-Jyun Sung.

**Conflicts of Interest:** The authors declare no conflicts of interest.

## References

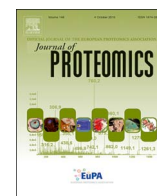
1. Bayer, F.M. Key to the genera of Octocorallia exclusive of Pennatulacea (Coelenterata: Anthozoa), with diagnoses of new taxa. *Proc. Biol. Soc. Wash.* **1981**, *94*, 902–947.
2. Bayer, F.M.; Grasshoff, M. The genus group taxa of the family Ellisellidae, with clarification of the genera established by J. E. Gray (Cnidaria: Octocorallia). *Senckenberg. Biol.* **1994**, *74*, 21–45.
3. Chen, C.-C.; Chang, K.-H. Gorgonacea (Coelenterata: Anthozoa: Octocorallia) of Southern Taiwan. *Bull. Inst. Zool. Acad. Sin.* **1991**, *30*, 149–181.
4. Fabricius, K.; Alderslade, P. *Soft Corals and Sea Fans—A Comprehensive Guide to the Tropical Shallow-Water Genera of the Central-West Pacific, the Indian Ocean and the Red Sea*, 1st ed.; Australian Institute of Marine Science: Queensland, Australia, 2001; pp. 62, 230–231.
5. Sung, P.-J.; Gwo, H.-H.; Fan, T.-Y.; Li, J.-J.; Dong, J.; Han, C.-C.; Wu, S.-L.; Fang, L.-S. Natural product chemistry of gorgonian corals of the genus *Junceella*. *Biochem. Syst. Ecol.* **2004**, *32*, 185–196. [[CrossRef](#)]
6. Wu, Y.-C.; Su, J.-H.; Chou, T.-T.; Cheng, Y.-P.; Weng, C.-F.; Lee, C.-H.; Fang, L.-S.; Wang, W.-H.; Li, J.-J.; Lu, M.-C.; et al. Natural product chemistry of gorgonian corals of genus *Junceella*. *Mar. Drugs* **2011**, *9*, 2773–2792. [[CrossRef](#)] [[PubMed](#)]
7. Subrahmanyam, C.; Kulatheeswaran, R.; Ward, R.S. Briarane diterpenes from the Indian Ocean gorgonian *Gorgonella umbraculum*. *J. Nat. Prod.* **1998**, *61*, 1120–1122. [[CrossRef](#)] [[PubMed](#)]
8. Subrahmanyam, C.; Ratnakumar, S.; Ward, R.S. Umbraculolides B–D, further briarane diterpenes from the gorgonian *Gorgonella umbraculum*. *Tetrahedron* **2000**, *56*, 4585–4588. [[CrossRef](#)]
9. Shen, Y.-C.; Lin, Y.-C.; Ko, C.-L.; Wang, L.-T. New briaranes from the Taiwanese gorgonian *Junceella juncea*. *J. Nat. Prod.* **2003**, *66*, 302–305. [[CrossRef](#)] [[PubMed](#)]
10. Zhang, W.; Guo, Y.-W.; Mollo, E.; Cimino, G. Junceallonoids A and B, two new briarane diterpenoids from the Chinese gorgonian *Junceella fragilis* Ridley. *Helv. Chim. Acta* **2004**, *87*, 2341–2345. [[CrossRef](#)]
11. Qi, S.-H.; Zhang, S.; Qian, P.-Y.; Xiao, Z.-H.; Li, M.-Y. Ten new antifouling briarane diterpenoids from the South China Sea gorgonian *Junceella juncea*. *Tetrahedron* **2006**, *62*, 9123–9130. [[CrossRef](#)]
12. Liaw, C.-C.; Lin, Y.-C.; Lin, Y.-S.; Chen, C.-H.; Hwang, T.-L.; Shen, Y.-C. Four new briarane diterpenoids from Taiwanese gorgonian *Junceella fragilis*. *Mar. Drugs* **2013**, *11*, 2042–2053. [[CrossRef](#)] [[PubMed](#)]
13. Lei, H.; Sun, J.-F.; Han, Z.; Zhou, X.-F.; Yang, B.; Liu, Y. Fragilisinins A–L, new briarane-type diterpenoids from gorgonian *Junceella fragilis*. *RSC Adv.* **2014**, *4*, 5261–5271. [[CrossRef](#)]
14. Shin, J.; Park, M.; Fenical, W. The junceallolides, new anti-inflammatory diterpenoids of the briarane class from the Chinese gorgonian *Junceella fragilis*. *Tetrahedron* **1989**, *45*, 1633–1638. [[CrossRef](#)]
15. Sung, P.-J.; Pai, C.-H.; Su, Y.-D.; Hwang, T.-L.; Kuo, F.-W.; Fan, T.-Y.; Li, J.-J. New 8-hydroxybriarane diterpenoids from the gorgonians *Junceella juncea* and *Junceella fragilis* (Ellisellidae). *Tetrahedron* **2008**, *64*, 4224–4232. [[CrossRef](#)]
16. Qi, S.-H.; Zhang, S.; Wen, Y.-M.; Xiao, Z.-H.; Li, Q.-X. New briaranes from the South China Sea gorgonian *Junceella fragilis*. *Helv. Chim. Acta* **2005**, *88*, 2349–2354. [[CrossRef](#)]
17. Sung, P.-J.; Wang, S.-H.; Chiang, M.-Y.; Su, Y.-D.; Chang, Y.-C.; Hu, W.-P.; Tai, C.-Y.; Liu, C.-Y. Discovery of new chlorinated briaranes from *Junceella fragilis*. *Bull. Chem. Soc. Jpn.* **2009**, *82*, 1426–1432. [[CrossRef](#)]
18. Sung, P.-J.; Lin, M.-R.; Su, Y.-D.; Chiang, M.-Y.; Hu, W.-P.; Su, J.-H.; Cheng, M.-C.; Hwang, T.-L.; Sheu, J.-H. New briaranes from the octocorals *Briareum excavatum* (Briareidae) and *Junceella fragilis* (Ellisellidae). *Tetrahedron* **2008**, *64*, 2596–2604. [[CrossRef](#)]

19. Shen, Y.-C.; Chen, Y.-H.; Hwang, T.-L.; Guh, J.-H.; Khalil, A.T. Four new briarane diterpenoids from the gorgonian coral *Junceella fragilis*. *Helv. Chim. Acta* **2007**, *90*, 1391–1398. [[CrossRef](#)]
20. Liaw, C.-C.; Shen, Y.-C.; Lin, Y.-S.; Hwang, T.-L.; Kuo, Y.-H.; Khalil, A.T. Frajunolides E–K, briarane diterpenes from *Junceella fragilis*. *J. Nat. Prod.* **2008**, *71*, 1551–1556. [[CrossRef](#)] [[PubMed](#)]
21. Liaw, C.-C.; Kuo, Y.-H.; Lin, Y.-S.; Hwang, T.-L.; Shen, Y.-C. Frajunolides L–O, four new 8-hydroxybriarane diterpenoids from the gorgonian *Junceella fragilis*. *Mar. Drugs* **2011**, *9*, 1477–1486. [[CrossRef](#)] [[PubMed](#)]
22. Sheu, J.-H.; Ahmed, A.F.; Shiue, R.-T.; Dai, C.-F.; Kuo, Y.-H. Scabrolides A–D, four new norditerpenoids isolated from the soft coral *Sinularia scabra*. *J. Nat. Prod.* **2002**, *65*, 1904–1908. [[CrossRef](#)] [[PubMed](#)]
23. Shoji, N.; Umeyama, A.; Arihara, S. A novel norditerpenoid from the Okinawan soft coral *Sinularia* sp. *J. Nat. Prod.* **1993**, *56*, 1651–1653. [[CrossRef](#)]
24. Bowden, B.F.; Coll, J.C.; Mitchell, S.J.; Mulder, J.; Stokie, G.J. Studies of Australian soft corals. IX A novel nor-diterpene from the soft coral *Sinularia leptoclados*. *Aust. J. Chem.* **1978**, *31*, 2049–2056. [[CrossRef](#)]
25. Turner, K.E.; Bowden, B.F.; Stokie, G.J. (4R\*,8S\*,11R\*,13S\*,14R\*)-8,11-Epoxy-14-hydroxy-11-methyl-4-(1-methylvinyl)-6,9-dioxocyclotetradec-1-ene-1,13-carbolactone. *Acta Cryst.* **1979**, *B35*, 1283–1284. [[CrossRef](#)]
26. Sato, A.; Fenical, W.; Zheng, Q.-T.; Clardy, J. Norcembrane diterpenoids from Pacific soft-corals of the genus *Sinularia* (Alcyonacea: Octocorallia). *Tetrahedron* **1985**, *41*, 4303–4308. [[CrossRef](#)]
27. Cheng, W.; Ji, M.; Li, X.; Ren, J.; Yin, F.; van Ofwegen, L.; Yu, S.; Chen, X.; Lin, W. Fragilolides A–Q, norditerpenoid and briarane diterpenoids from the gorgonian coral *Junceella fragilis*. *Tetrahedron* **2017**, *73*, 2518–2528. [[CrossRef](#)]
28. Wang, S.-H.; Chang, Y.-C.; Chiang, M.-Y.; Chen, Y.-H.; Hwang, T.-L.; Weng, C.-F.; Sung, P.-J. Chlorinated briarane diterpenoids from the sea whip gorgonian corals *Junceella fragilis* and *Ellisella robusta* (Ellisellidae). *Chem. Pharm. Bull.* **2010**, *58*, 928–933. [[CrossRef](#)] [[PubMed](#)]
29. Kubota, N.K.; Kobayashi, Y.; Iwamoto, H.; Fukazawa, Y.; Uchio, Y. Two new halogenated briarane diterpenes from the Papuan gorgonian coral *Junceella fragilis*. *Bull. Chem. Soc. Jpn.* **2006**, *79*, 634–636. [[CrossRef](#)]
30. Cheng, W.; Li, X.; Yin, F.; van Ofwegen, L.; Lin, W. Halogenated briarane diterpenes with acetyl migration from the gorgonian coral *Junceella fragilis*. *Chem. Biodivers.* **2017**, *14*, e1700053. [[CrossRef](#)] [[PubMed](#)]
31. Li, C.; La, M.-P.; Tang, H.; Pan, W.-H.; Sun, P.; Krohn, K.; Yi, Y.-H.; Li, L.; Zhang, W. Bioactive briarane diterpenoids from the South China Sea gorgonian *Dichotella gemmacea*. *Bioorg. Med. Chem. Lett.* **2012**, *22*, 4368–4372. [[CrossRef](#)] [[PubMed](#)]
32. Luo, Y.; Long, K.; Fang, Z. Studies of the chemical constituents of the Chinese gorgonia (III). Isolation and identification of a new polyacetoxo chlorine-containing diterpene lactone (praelolide). *Acta Sci. Nat. Univ. Sunyatseni* **1983**, *1*, 83–92.
33. Dai, J.; Wan, Z.; Rao, Z.; Liang, D.; Fang, Z.; Luo, Y.; Long, K. Molecular structure and absolute configuration of the diterpene lactone, praelolide. *Sci. Sin. B* **1985**, *28*, 1132–1142. [[PubMed](#)]
34. Sung, P.-J.; Fan, T.-Y.; Fang, L.-S.; Wu, S.-L.; Li, J.-J.; Chen, M.-C.; Cheng, Y.-M.; Wang, G.-H. Briarane derivatives from the gorgonian coral *Junceella fragilis*. *Chem. Pharm. Bull.* **2003**, *51*, 1429–1431. [[CrossRef](#)] [[PubMed](#)]
35. Qi, S.-H.; Zhang, S.; Huang, H.; Xiao, Z.-H.; Huang, J.-S.; Li, Q.-X. New briaranes from the South China Sea gorgonian *Junceella juncea*. *J. Nat. Prod.* **2004**, *67*, 1907–1910. [[CrossRef](#)] [[PubMed](#)]
36. García, M.; Rodríguez, J.; Jiménez, C. Absolute structures of new briarane diterpenoids from *Junceella fragilis*. *J. Nat. Prod.* **1999**, *62*, 257–260. [[CrossRef](#)] [[PubMed](#)]
37. Sung, P.-J.; Fan, T.-Y.; Chen, M.-C.; Fang, L.-S.; Lin, M.-R.; Chang, P.-C. Junceellin and praelolide, two briaranes from the gorgonian corals *Junceella fragilis* and *Junceella juncea* (Ellisellidae). *Biochem. Syst. Ecol.* **2004**, *32*, 111–113. [[CrossRef](#)]
38. Zheng, L.-G.; Chang, Y.-C.; Hu, C.-C.; Wen, Z.-H.; Wu, Y.-C.; Sung, P.-J. Fragilides K and L, new briaranes from the gorgonian coral *Junceella fragilis*. *Molecules* **2018**, *23*, 1510. [[CrossRef](#)] [[PubMed](#)]
39. Lin, Y.; Long, K. Studies of the chemical constituents of the Chinese gorgonia (IV)-*Junceella*, a new chlorine-containing diterpenoid from *Junceella squamata*. *Acta Sci. Nat. Univ. Sunyatseni* **1983**, *2*, 46–51.
40. Yao, J.; Qian, J.; Fan, H.; Shin, K.; Huang, S.; Lin, Y.; Long, K. The structure of crystal and molecule of junceellin. *Acta Sci. Nat. Univ. Sunyatseni* **1984**, *1*, 83–87.
41. Zhou, W.; Li, J.; E, H.-C.; Liu, B.-S.; Tang, H.; Gerwick, W.H.; Hua, H.-M.; Zhang, W. Briarane diterpenes from the South China Sea gorgonian coral, *Junceella gemmacea*. *Mar. Drugs* **2014**, *12*, 589–600. [[CrossRef](#)] [[PubMed](#)]

42. He, H.-Y.; Faulkner, D.J. New chlorinated diterpenes from the gorgonian *Junceella gemmacea*. *Tetrahedron* **1991**, *47*, 3271–3280. [[CrossRef](#)]
43. Hamann, M.T.; Harrison, K.N.; Carroll, A.R.; Scheuer, P.J. Briarane diterpenes from Micronesian gorgonians. *Heterocycles* **1996**, *42*, 325–331.
44. Anjaneyulu, A.S.R.; Rao, N.S.K. Juncins G and H: New briarane diterpenoids of the Indian Ocean gorgonian *Junceella juncea* Pallas. *J. Chem. Soc. Perkin Trans.* **1997**, *1*, 959–962. [[CrossRef](#)]
45. Anjaneyulu, A.S.R.; Rao, V.L.; Sastry, V.G.; Venugopal, M.J.R.V.; Schmitz, F.J. Juncins I–M, five new briarane diterpenoids from the Indian Ocean gorgonian *Junceella juncea* Pallas. *J. Nat. Prod.* **2003**, *66*, 507–510. [[CrossRef](#)] [[PubMed](#)]
46. Murthy, Y.L.N.; Rajack, D.M.A.; Reddy, G.D. A new antifungal briarane diterpenoid from the gorgonian *Junceella juncea* Pallas. *Bioorg. Med. Chem. Lett.* **2011**, *21*, 7522–7525. [[CrossRef](#)] [[PubMed](#)]
47. Chang, J.-Y.; Liaw, C.-C.; Fazary, A.E.; Hwang, T.-L.; Shen, Y.-C. New briarane diterpenoids from the gorgonian coral *Junceella juncea*. *Mar. Drugs* **2012**, *10*, 1321–1330. [[CrossRef](#)] [[PubMed](#)]
48. Gauvin, A.; Smadja, J.; Aknin, M.; Faure, R.; Gaydou, E.-M. Isolation of bioactive 5 $\alpha$ ,8 $\alpha$ -epidioxy sterols from the marine sponge *Luffariella cf. variabilis*. *Can. J. Chem.* **2000**, *78*, 986–992. [[CrossRef](#)]
49. Kapustina, I.I.; Kalinovskii, A.I.; Dmitrenok, P.S.; Kuz'mich, A.S.; Nedashkovskaya, O.I.; Grebnev, B.B. Diterpenoids and other metabolites from the Vietnamese gorgonians *Lophogorgia* sp. and *Junceella* sp. *Chem. Nat. Comp.* **2014**, *50*, 1140–1142. [[CrossRef](#)]
50. Wright, J.L.C.; McInnes, A.G.; Shimizu, S.; Smith, D.G.; Walter, J.A.; Idler, D.; Khalil, W. Identification of C-24 alkyl epimers of marine sterols by <sup>13</sup>C nuclear magnetic resonances spectroscopy. *Can. J. Chem.* **1978**, *56*, 1898–1903.
51. Orji, C.C.; Kelly, J.; Ashburn, D.A.; Silks, L.A., III. First synthesis of  $\beta$ -2'-deoxy[9-<sup>15</sup>N]adenosine. *J. Chem. Soc. Perkin Trans.* **1996**, *1*, 595–597. [[CrossRef](#)]
52. Moyroud, E.; Biala, E.; Strazewski, P. Synthesis and enzymatic digestion of an RNA nonamer in both enantiomeric forms. *Tetrahedron* **2000**, *56*, 1475–1484. [[CrossRef](#)]
53. Su, Y.-D.; Su, J.-H.; Hwang, T.-L.; Wen, Z.-H.; Sheu, J.-H.; Wu, Y.-C.; Sung, P.-J. Briarane diterpenoids isolated from octocorals between 2014 and 2016. *Mar. Drugs* **2017**, *15*, 44. [[CrossRef](#)] [[PubMed](#)]
54. Kokke, W.C.M.C.; Epstein, S.; Look, S.A.; Rau, G.H.; Fenical, W.; Djerassi, C. On the origin of terpenes in symbiotic associations between marine invertebrates and algae (zooxanthellae). *J. Biol. Chem.* **1984**, *259*, 8168–8173. [[PubMed](#)]
55. Putra, M.Y.; Wibowo, J.T.; Murniasih, T. A review of chemistry and biological activities of the Indonesian octocorallia. *J. Appl. Pharm. Sci.* **2017**, *7*, 219–227.
56. Yan, H.-Y. Harvesting drugs from the seas and how Taiwan could contribute to this effort. *Changhua J. Med.* **2004**, *9*, 1–6.



© 2018 by the authors. Licensee MDPI, Basel, Switzerland. This article is an open access article distributed under the terms and conditions of the Creative Commons Attribution (CC BY) license (<http://creativecommons.org/licenses/by/4.0/>).



# Integrated omics profiling identifies hypoxia-regulated genes in HCT116 colon cancer cells

Jeng-Ting Chen<sup>a,d</sup>, Chien-Chun Liu<sup>a</sup>, Jau-Song Yu<sup>a,c,f,g</sup>, Hung-Hsuan Li<sup>a,b</sup>, Ming-Chih Lai<sup>a,b,e,\*</sup>

<sup>a</sup> Graduate Institute of Biomedical Sciences, Chang Gung University, Taoyuan 33302, Taiwan

<sup>b</sup> Department of Biomedical Sciences, Chang Gung University, Taoyuan 33302, Taiwan

<sup>c</sup> Liver Research Center, Chang Gung Memorial Hospital, Linkou, Taoyuan 33305, Taiwan

<sup>d</sup> Department of Surgery, Department of Medical Research and Development, Chang Gung Memorial Hospital, Linkou, Taoyuan 33305, Taiwan

<sup>e</sup> Department of Obstetrics and Gynecology, Chang Gung Memorial Hospital, Linkou, Taoyuan 33305, Taiwan

<sup>f</sup> Molecular Medicine Research Center, Chang Gung University, Taoyuan 33302, Taiwan

<sup>g</sup> Research Center for Food and Cosmetic Safety, Research Center for Chinese Herbal Medicine, College of Human Ecology, Chang Gung University of Science and Technology, Taoyuan 33302, Taiwan



## ARTICLE INFO

### Keywords:

Colorectal cancer

Hypoxia

Proteome

Secretome

Transcriptome

Translatome

## ABSTRACT

Hypoxia is associated with poor prognosis in most solid tumors due to its multiple effects on therapy resistance, angiogenesis, apoptotic resistance, and tumor invasion/metastasis. Here we used a comprehensive omics profiling to investigate hypoxia-regulated gene expression in HCT116 colon cancer cells. Quantitative analyses of proteome and secretome were performed in HCT116 cells cultured under hypoxic or normoxic conditions. A total of 5700 proteins were quantified in proteome analysis and 722 proteins were quantified in secretome analysis. Both datasets were combined with the transcriptome and translatome datasets for further analysis. Verification of candidate proteins/genes in this integrated omics analysis was performed using immunoblotting and quantitative real-time RT-PCR analyses. We also performed polysome profiling to assess changes in translational efficiency of hypoxia-induced genes. Notably, several genes were differently regulated at the transcriptional and translational levels in HCT116 cells during hypoxia. Bioinformatics analysis suggested that hypoxia regulates translation of genes involved in extracellular matrix organization, extracellular exosomes, and protein processing in endoplasmic reticulum. Aberrations in these metabolic pathways appear to be correlated with an increased risk of tumor invasion/metastasis.

**Biological significance:** This study integrates transcriptome/translatome and proteome/secretome to analyze gene expression changes in human colon cancer cells under hypoxic conditions. Candidate proteins/genes in this integrated omics analysis were further validated by immunoblotting, quantitative real-time RT-PCR, and polysome profiling. The datasets would be useful to uncover the molecular mechanisms of hypoxia-induced gene regulation in colorectal cancer.

## 1. Introduction

Cancer starts from a single cell that acquires genetic mutations to promote uncontrolled cell division. Once the tumor reaches a size of 1–2 mm in diameter, diffusion of oxygen provided by nearby blood vessels is insufficient to maintain cancer cell growth and metabolic homeostasis, a phenomenon called tumor hypoxia [1,2]. It has been reported that hypoxia plays a critical role in cancer development and progression, such as glycolysis, angiogenesis, genomic instability, apoptotic resistance, and tumor invasion/metastasis [3,4]. Recent studies have established a direct link between hypoxia and the organization of the extracellular matrix (ECM) which plays an important role in

tumor invasion/metastasis [5]. In addition, hypoxia has been implicated in conferring resistance to anti-cancer radiotherapy and chemotherapy [6–8].

In order to sustain survival and cell growth under hypoxic conditions, cancer cells have to adapt to low oxygen stress by altering their gene expression and metabolism [9,10]. Since hypoxia has profound effects on cancer development and progression, it is very important to understand gene expression changes under hypoxic conditions. Most of the transcriptional changes are thought to be controlled by hypoxia inducible factors (HIFs) during hypoxia. In response to hypoxia, cells rapidly increase the protein level of HIF-1, a heterodimeric transcription factor consisting of an oxygen-sensitive HIF-1 $\alpha$  subunit and a

\* Corresponding author at: 259 Wen-Hwa 1st Rd, Kwei-Shan, Taoyuan 33302, Taiwan.  
E-mail address: [mclai@mail.cgu.edu.tw](mailto:mclai@mail.cgu.edu.tw) (M.-C. Lai).

<https://doi.org/10.1016/j.jprot.2018.02.031>

Received 21 December 2017; Received in revised form 23 February 2018; Accepted 27 February 2018

Available online 07 March 2018

1874-3919/© 2018 Elsevier B.V. All rights reserved.



constitutively expressed HIF-1 $\beta$  subunit [11,12]. HIF-1 plays a key role during hypoxia by regulating the transcription of > 100 target genes, which contain hypoxia response elements (HREs) in their promoter regions. Overexpression of HIF-1 is frequently observed in different types of cancer, and this has made it an attractive therapeutic target for cancer treatment [13]. In addition to HIF-1, other transcription factors have also been regarded as contributors in the transcriptional response to hypoxia [14].

Compared to transcription, translational control permits more rapid changes at the protein level. General translation is repressed by hypoxia to conserve ATP for cell survival. It is thought that mammalian target of rapamycin (mTOR) and the endoplasmic reticulum resident kinase (PERK) play a key role in translational repression during hypoxia [15–17]. Global translation is largely inhibited during hypoxia; however, selected mRNAs required for cellular adaption to hypoxia remain to be translated. Hypoxia-induced translational activation requires alternative mechanisms, such as internal ribosome entry site (IRES) or upstream open reading frame (uORF) in the 5' untranslated region (UTR) of mRNAs [18–21]. Moreover, a subset of RNA-binding proteins (RBPs) or microRNAs (miRNAs) have been shown to control translation in the 3' UTR of mRNAs during hypoxia [22]. Recently, an alternative cap-dependent translation that depends on a complex composed of the cap-binding protein eIF4E2, the RNA-binding protein RBM4, and the oxygen-regulated HIF-2 $\alpha$  was shown to express a subset of hypoxia-induced genes [23]. It is proposed that hypoxia causes a switch from eIF4E to eIF4E2-dependent translation initiation [24]. They also provide evidence that translational efficiency, rather than mRNA levels, is the most important determinant of protein output under hypoxic conditions. However, the molecular details of hypoxia-induced translational regulation are still not well characterized.

Because hypoxia does not affect translation of mRNAs to the same extent [25], the expression of mRNAs can't completely reflect the amount of protein [26]. Transcriptome analysis of the cellular response to hypoxia has been extensively studied [27–29]. In contrast, proteomic studies of hypoxia-regulated proteins in cancer cells are relatively limited [30–32]. It has recently become possible to investigate changes of protein expression profile of cultured cells using quantitative proteome analysis. A lot of mass spectrometry (MS)-based quantitative proteomic methods are commonly used today. Among them, stable isotope labeling with amino acids in cell culture (SILAC) is a simple and accurate method for relative quantitation of protein abundance [33–35].

We previously used microarray analysis of total RNA and polysome-associated mRNAs to identify hypoxia-regulated genes at the transcriptional and translational levels in HCT116 colon cancer cells [17]. Here, we further performed quantitative proteome analysis using SILAC-labeled HCT116 cells in conjunction with liquid chromatography tandem-mass spectrometry (LC-MS/MS) to investigate changes in protein expression profile during hypoxia. Secretome is generally used to refer to a subset of proteome in which all of the secreted proteins released from a cell, tissue, or organism are analyzed. Cancer cell secretome has received increasing interest for the discovery of diagnosis/prognosis cancer biomarkers, and it can be a good source of information on cancer biology [36,37]. To elucidate how gene expression could be regulated during hypoxia, we performed integrated omics analysis of transcriptome/translatome and proteome/secretome in hypoxic HCT116 cells compared to normoxic controls. Functional annotation clustering analysis of hypoxia-regulated proteins indicates that hypoxia induces glucose metabolism but represses translational elongation and cell cycle progression. Furthermore, translation of genes involved in ECM organization is regulated by hypoxia. This suggests that hypoxia is correlated with an increased risk of tumor invasion/metastasis.

## 2. Material and methods

### 2.1. Cell culture and hypoxic treatment

HCT116 cells were grown in DMEM medium supplemented with 10% fetal bovine serum at 37 °C in 5% CO<sub>2</sub> incubator. For hypoxic (1% O<sub>2</sub>) treatment, cells were transferred to a specially designed hypoxia chamber (NexBiOxy Inc., Hsinchu, Taiwan) which was flushed with 95% N<sub>2</sub> and 5% CO<sub>2</sub> at 37 °C.

### 2.2. SILAC labeling

HCT116 cells were grown in lysine, arginine depleted DMEM (Biological industries, CT, USA) supplemented with 10% heat-inactivated dialyzed fetal bovine serum (Biological industries) at 37 °C in 5% CO<sub>2</sub> incubator. Before use, media was re-supplemented with either normal 100 mg/l [<sup>12</sup>C<sub>6</sub>]lysine/[<sup>12</sup>C<sub>6</sub>]arginine or 100 mg/l [<sup>13</sup>C<sub>6</sub>]lysine/[<sup>13</sup>C<sub>6</sub>]arginine (Invitrogen, Carlsbad, CA USA) and additional 100 mg/l proline. Cells were grown for at least 6 doublings to allow full incorporation of labeled amino acids.

### 2.3. Conditioned media

The conditioned media from HCT116 cells were collected as previous described [38]. In brief, cells were grown in the 15-cm culture dishes. The cells were washed with serum-free media and incubated in serum-free media for 24 h. The serum-free media were then harvested and removed the intact cells followed by centrifugation in Amicon Ultra-15 tubes (molecular mass cutoff, 3 kDa; Millipore, Billerica, MA) to concentrate and desalt the supernatants. The resulting supernatants were used as conditioned media. The protein concentrations of the conditioned media were determined using the Pierce BCA Protein Assay Kit (Thermo Fisher Scientific).

### 2.4. Dimethyl labeling

The sample (25  $\mu$ g of proteolytic peptides in 100  $\mu$ l of 0.1 M TEAB buffer, pH 8) was mixed with 7.5  $\mu$ l of 2 M sodium cyanoborohydride. Four microliter of 4% (w/w) <sup>12</sup>CH<sub>2</sub>-formaldehyde (light) or <sup>13</sup>CD<sub>2</sub>-formaldehyde (heavy) solution was added to the mixture, and incubated for 1 h at 37 °C [39,40]. After incubation, 4  $\mu$ l of 1 M ammonium bicarbonate was added to the mixture to quench the reaction. This procedure converts primary amines to dimethylamines in proteolytic peptides (N-terminus and the side chain of lysine residues). The mass shifts per labeling site were +28 Da or +34 Da for light labeling or heavy labeling samples, respectively.

### 2.5. Preparation and digestion of cell samples

To monitor isotopic amino acid incorporation and conversion, trypsin digests were prepared from whole cell lysates and conditioned medium samples for LC-MS/MS analysis. Cell culture media were removed, and then washed twice with ice-cold PBS and lysed in lysis buffer (0.1% SDS, 20 mM HEPES, 1 mM Na<sub>3</sub>VO<sub>4</sub> and 2.5 mM Na<sub>4</sub>P<sub>2</sub>O<sub>7</sub>, 1 mM EDTA, 1 mM glycerophosphate, 1 mM benzamidine and 1 mM phenylmethylsulfonyl fluoride) on ice. The cell lysates were collected and sonicated on ice with a probe sonicator (model W-380, Heat Systems-Ultrasonics) for 3  $\times$  10 s at 50% power output followed by centrifugation at 11,000  $\times$  g for 20 min at 4 °C. The supernatant was used as the cell extracts and subjected to protein concentration determination by the Pierce BCA Protein Assay Kit. Five hundred and fifty micrograms of the SILAC samples was used for proteome analysis. The sample was subjected to reduction and alkylation by 10 mM DTT at 56 °C for 1 h and 30 mM iodoacetamide at RT for 30 min in the dark and quenched by 10 mM DTT, followed by in-solution digestion with freshly prepared sequencing-grade trypsin (20 ng/ $\mu$ l in 25 mM NH<sub>4</sub>HCO<sub>3</sub>;

Promega, Madison, WI) (protein: trypsin = 50:1) at 37 °C for 16 h. The reaction was stopped by adding formic acid (FA) to a final concentration of 0.05%. Micro-columns (packed with LiChrospher® 100 RP-18) were regenerated using the following steps: 100% acetonitrile (ACN)/0.1% FA, 80% ACN/0.1% FA, 50% ACN/0.1% FA, and 0.1% FA. The samples were acidified with 0.1% FA and desalted using a micro-column by a brief centrifugation at  $840 \times g$  for 2 min at RT. The peptides bound to the resins were sequentially eluted by 25% ACN/0.1% FA, 50% ACN/0.1% FA, and 80% ACN/0.1% FA. The eluted fractions were combined and re-concentrated in a vacuum centrifuge. Dried fractions were dissolved in 0.1% FA for LC-MS/MS analysis.

## 2.6. On-line strong ion exchange/reverse phase liquid chromatography-tandem mass spectrometry

For proteome analysis, peptides prepared from in-solution digestion were separated and analyzed via the online two-dimensional (2D) LC-MS/MS technique using a strong cation exchange (SCX) and reverse-phase 18 (RP18) nanoscale liquid chromatography system coupled with a LTQ-Orbitrap mass spectrometer (Thermo Fisher Scientific). Briefly, equal mixtures of SILAC peptides were injected into an in-house packed SCX column (Luna SCX, 5  $\mu$ m,  $0.5 \times 150$  mm; Phenomenex, CA, USA) and fractionated into 66 fractions using a 66 h (for secretome, sample was fractionated into 22 fractions using a 22 h analysis) continuous ammonium chloride gradient in the presence of 30% ACN and 0.1% FA. Each effluent of SCX fraction (1  $\mu$ l/min) was continuously mixed with a stream of 0.1% FA/H<sub>2</sub>O (50  $\mu$ l/min), and peptides were trapped on a RP column (Source 15 RPC,  $0.5 \times 5$  mm; GE Healthcare, PA, USA) and separated using coupled BEH C18 chromatography (1.7  $\mu$ m,  $0.1 \times 120$  mm; Waters, MA, USA) with an acetonitrile gradient in 0.1% FA. MS analysis was performed on a Dionex UltiMate 3000 nano LC system.

## 2.7. MS data processing

Mass spectra were acquired in the positive ion mode applying a data-dependent automatic switch between survey scan and tandem mass spectra (MS/MS) acquisition. Proteome samples were analyzed with a top 5 method; acquiring one Orbitrap survey scan in the mass range of  $m/z$  300–2000 followed by MS/MS of the five most intense ions in the LTQ. The target value in the LTQ-Orbitrap was 1,000,000 for survey scan at a resolution of 60,000 at  $m/z$  400 using lock masses for recalibration to improve the mass accuracy of precursor ions. Fragmentation in the LTQ was performed by collision-induced dissociation with a target value of 5000 ions. Ion selection threshold was 500 counts. Selected sequenced ions were dynamically excluded for 90 s.

## 2.8. Database search and protein quantification pipeline

The proteome MS datasets were analyzed with the software Proteome Discoverer (version: 1.4.0.288; Thermo Fisher Scientific, San Jose, CA, USA) with Mascot (version 2.2; Matrix Science, London, UK). To perform the database search against respective Swiss-Prot protein database (version: sprot\_2014.fasta, number of sequences after taxonomy: 20266) for these raw data files. The search parameters used were as follows: trypsin as enzyme specificity; maximum missed cleavage sites: 2; cysteine carbamidomethylation as a fixed modification; protein N-terminal acetylation, Gln  $\rightarrow$  pyro Glu (N-term Q), methionine oxidation, 13C(6) (K) and 13C(6) (R) as variable modifications. The processing of secretome MS datasets were analyzed with similar setting but Dimethyl:2H(4)13C(2) (K), Dimethyl:2H(4)13C(2) (N-term), Dimethyl (K) and Dimethyl (N-term) as variable modifications. Peptide charge:  $1^+$  to  $3^+$ ; peptide tolerance: 10 ppm; MS/MS tolerance: 0.6 Da; identify sets peptide FDR (false discovery rates): 0.01; protein FDR: 0.01; min. peptide length: 7; Minimal number of peptides: 1, Count only

rank 1 peptides: True, Count Peptide only in top scored proteins: True.

## 2.9. Immunoblot analysis

Proteins were transferred onto a PVDF Transfer Membrane (Millipore). The membranes were blocked with 3% skim milk in TBST buffer (100 mM Tris-HCl (pH 7.6), 150 mM NaCl, and 0.05% Tween 20) at RT for 1 h. Protein blots were incubated with primary antibodies in blocking buffer at RT for 2 h, followed by incubation with HRP-conjugated secondary antibodies at RT for 2 h. After washing with TBST buffer, signals were detected using Immobilon Western Chemiluminescent HRP Substrate (Millipore) and images from autoradiograms were captured with the ChemiDoc™ Touch Imaging System (Bio-Rad). For re-probing, the membranes were stripped with 2% SDS, 100 mM  $\beta$ -mercaptoethanol and 62.5 mM Tris at 56 °C for 45 min with occasional agitation. After washing with TBST buffer, the membranes were re-probed with another antibody.

## 2.10. Quantitative real-time RT-PCR

Extracted RNA was reverse-transcribed into cDNA using the High-Capacity cDNA Reverse Transcription Kits (Thermo Fisher Scientific) according to manufacturer's instructions. The resulting cDNA was subjected to quantitative real-time PCR analysis using gene-specific primers. Quantitative real-time PCR was performed using StepOne™ Real-Time PCR Systems according to suppliers' recommendations (Thermo Fisher Scientific). The levels of mRNAs were detected with Fast SYBR® Green Master Mix (Thermo Fisher Scientific). Quantitative analysis was performed by the measurement of CT values during the exponential phase of amplification. Relative quantitation values were calculated using the  $2^{-\Delta\Delta CT}$  method [41].

## 2.11. Sucrose gradient sedimentation and polysome profiling

Cells were collected in cold PBS containing 100  $\mu$ g/ml cycloheximide. All subsequent steps were performed at 4 °C. Cell pellets were resuspended in RSB-150 (10 mM Tris-HCl (pH 7.4), 3 mM MgCl<sub>2</sub>, and 150 mM NaCl) containing 100  $\mu$ g/ml cycloheximide, 40  $\mu$ g/ml digitonin (Calbiochem), 20 U/ml RNasin (Promega), and  $1 \times$  protease inhibitor cocktail (Thermo Fisher Scientific). After incubation on ice for 5 min, cells were disrupted by passage through a 26-gauge needle five times. Cytoplasmic extracts were collected by centrifugation at  $3000 \times g$  for 2 min, and clarified by further centrifugation at  $11,000 \times g$  for 15 min. The samples were loaded on a linear 15–40% sucrose gradient and centrifuged at  $178,000 \times g$  for 3 h in a Beckman SW41 rotor. After centrifugation, total RNA was extracted from each fraction using phenol/chloroform extraction in the presence of 1% SDS and 0.25 M NaCl, followed by ethanol precipitation. For polysome profile analysis, the gradients were monitored at 254 nm using an ISCO fractionation system (Lincoln, NE).

## 2.12. DAVID gene ontology (GO) and STRING network analyses

To detect significant GO biological processes from the omics analyses, the DAVID functional annotation clustering tool was used by choosing the “GOTERM\_BP\_FAT”, “GOTERM\_CC\_FAT”, or “GOTERM\_MF\_FAT” option or KEGG\_PATHWAY [42]. The UNIPROT\_ACCESSION names corresponding to interesting proteins were searched against the DAVID Bioinformatics Resources 6.7. The initial group membership and final group membership were set at 2, while results filter by P-value < 0.01. Pathway analyses of protein candidates obtained from up/down-regulated proteins were performed using DAVID, as well as by Kyoto Encyclopedia of Genes and Genomes (KEGG). The statistical significance of the identified networks was based on P-values, which are defined as the probability that a given number of proteins from the input list will match a certain number of gene nodes in the

pathway network. In addition, the gene symbols corresponding to proteins of interest were searched against the STRING database version 11.0 for protein-protein correlations [43]. STRING defines a metric called “confidence score” to define interaction confidence; it fetched all correlations that had a confidence score  $\geq 0.4$  (medium confidence).

### 2.13. Data availability

All uncropped versions of immunoblots are provided in Supplementary figures (raw data). Most of the raw data for the figures and tables presented in this paper are also provided in Supplementary Datasets. The mass spectrometry proteomics data have been deposited to the ProteomeXchange Consortium (<http://proteomecentral.proteomexchange.org>) via the PRIDE partner repository [44] with the dataset identifier (PXD009009).

## 3. Results

### 3.1. Quantitative proteome and secretome analysis in HCT116 cells during hypoxia

In order to maintain cell survival under hypoxic stress, cancer cells have to alter their gene expression and/or protein synthesis. Here, we performed SILAC-based quantitative proteome analysis to monitor protein expression changes in HCT116 colon cancer cells during hypoxia. Strategy to investigate proteomic changes in response to hypoxia was shown in Fig. 1A. HCT116 cells were grown on medium containing [ $^{12}\text{C}_6$ ]Arg/[ $^{12}\text{C}_6$ ]Lys (Light a.a.) and [ $^{13}\text{C}_6$ ]Arg/[ $^{13}\text{C}_6$ ]Lys (Heavy a.a.), respectively. Proline was added to SILAC media to prevent the metabolic conversion of Arg to Pro [45]. The light a.a.-labeled cells were incubated under normoxic (21%  $\text{O}_2$ ) conditions and the heavy a.a.-labeled cells were subjected to hypoxia treatment (1%  $\text{O}_2$  for 24 h). Protein extracts from both sets of SILAC-labeled cells were mixed in a mass ratio of 1:1. The SILAC-labeled, Hypoxia/Ctrl.-treated samples were simultaneously analyzed by conventional proteome analysis (biological replicates,  $n = 2$ ; 33  $\mu\text{g}$  protein/66 fractions/experiment). This data was further confirmed by a reciprocal experiment in which the light a.a.-labeled cells were treated with hypoxia and the heavy a.a.-labeled cells were incubated under normoxic conditions. Immunoblot analysis showed that HIF-1 $\alpha$  protein, a hallmark of hypoxia, was dramatically induced by hypoxia in the SILAC-labeled cells (Fig. 1B). HIF-1 has been shown to activate the transcription of vascular endothelial growth factor (VEGF) during hypoxia [46]. However, the expression of VEGF protein was only slightly increased in hypoxic HCT116 cells as compared to normoxic controls (Fig. 1B). The expression of tubulin and actin proteins remained almost unchanged under hypoxic conditions and thus served as loading controls.

Cancer cells can secrete various soluble factors such as epidermal growth factor (EGF) and VEGF that can promote cell proliferation and angiogenesis. They also secrete cell-derived proteases that alter the adjacent stroma toward a permissive and supportive environment for cancer progression [5,38]. A comprehensive analysis of the hypoxic cancer cell secretome may provide a valuable source for biomarker discovery and putative therapeutic targets for cancer treatment [36,47]. Metabolic labeling (SILAC) was applied not only for proteome analysis, but also for secretome analysis in several reports [48,49]. The main reason for using SILAC with 10% FBS is to encounter culture conditions that are similar to those of transcriptome and translational datasets. However, most secretome studies were performed under serum-free conditions for 24 h [48], and chemical labeling (dimethyl labeling) is a cheaper and more convenient method for quantitative secretome analysis. Although this research design is not perfect, we still integrate all omics data to find the interesting regulations for further validation. To perform quantitative secretome analysis, HCT116 cells were incubated under hypoxic or normoxic conditions for 24 h. The conditioned media were harvested and further purified into secreted

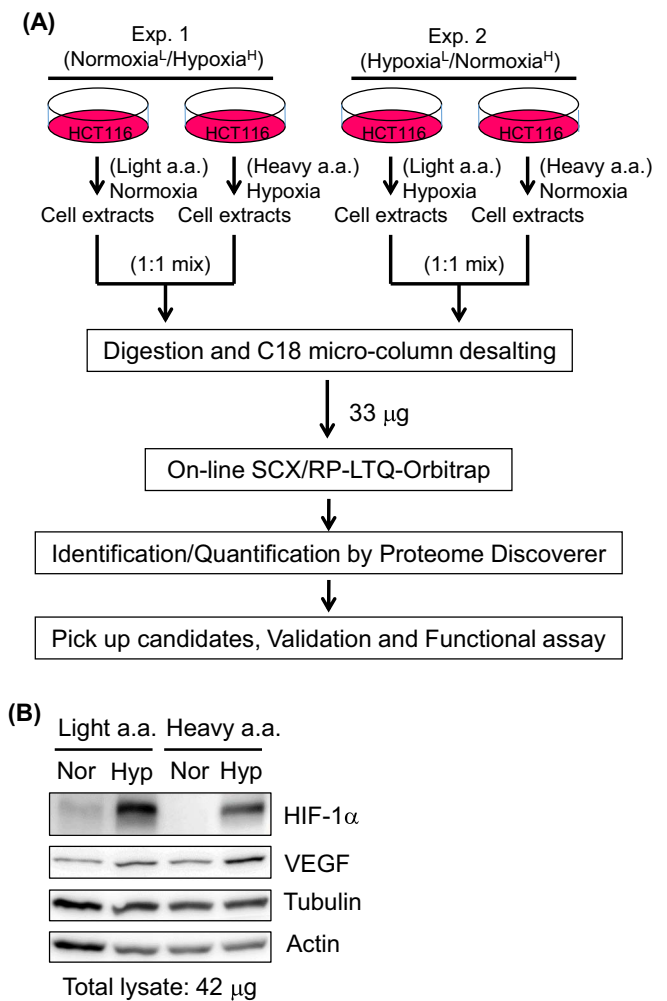


**Fig. 1.** Strategy to investigate proteomic changes in HCT116 cells during hypoxia. (A) HCT116 cells were grown on medium containing [ $^{12}\text{C}_6$ ]Arg/[ $^{12}\text{C}_6$ ]Lys (Light a.a.) or [ $^{13}\text{C}_6$ ]Arg/[ $^{13}\text{C}_6$ ]Lys (Heavy a.a.), respectively. Both culture media were added proline to prevent amino acid conversion. SILAC-labeled cells were subjected to 24 h of normoxic (21%  $\text{O}_2$ ) or hypoxic (1%  $\text{O}_2$ ) treatment. Extracts from both sets of SILAC-labeled cells were mixed in a mass ratio of 1:1, digested by trypsin, and then subjected to proteomic analysis (on-line SCX/RP-LTQ-Orbitrap). Proteome Discoverer software was used for mass spectrometric data analysis. (B) Total extracts (42  $\mu\text{g}$ ) from SILAC-labeled HCT116 cells treated with hypoxia or normoxia for 24 h were resolved by 10% SDS-PAGE and subjected to immunoblotting with the indicated antibodies.

proteins (including ECM and exosomal proteins). As shown in Fig. 2A, the conditioned medium collected from normoxic HCT116 cells was digested by trypsin and labeled with heavy isotope of dimethyl compound, while the conditioned medium collected from hypoxic HCT116 cells was digested by trypsin and labeled with light isotope of dimethyl compound [39,40]. Both dimethyl-labeled protein samples were mixed at a 1:1 mass ratio, and then subjected to proteomic analysis. This data was further confirmed by a reciprocal experiment in which secreted proteins of hypoxic cells were labeled with heavy isotope of dimethyl compound. The dimethyl-labeled, Hypoxia/Ctrl.-treated samples were simultaneously analyzed by conventional proteome analysis (biological replicates,  $n = 2$ ; 12.5  $\mu\text{g}$  protein/22 fractions/experiment). Immunoblot analysis showed that HIF-1 $\alpha$  was dramatically increased in hypoxic cell lysates (Fig. 2B). VEGF was also strikingly increased in conditioned medium from hypoxic HCT116 cells as compared to normoxic cells. This indicates that secreted proteins, such as VEGF, should be assessed by secretome rather than proteome analysis. Our experiments also showed that 24 h of hypoxia treatment has no significant effect on cell viability and cell death of HCT116 cells (Fig. 2C).

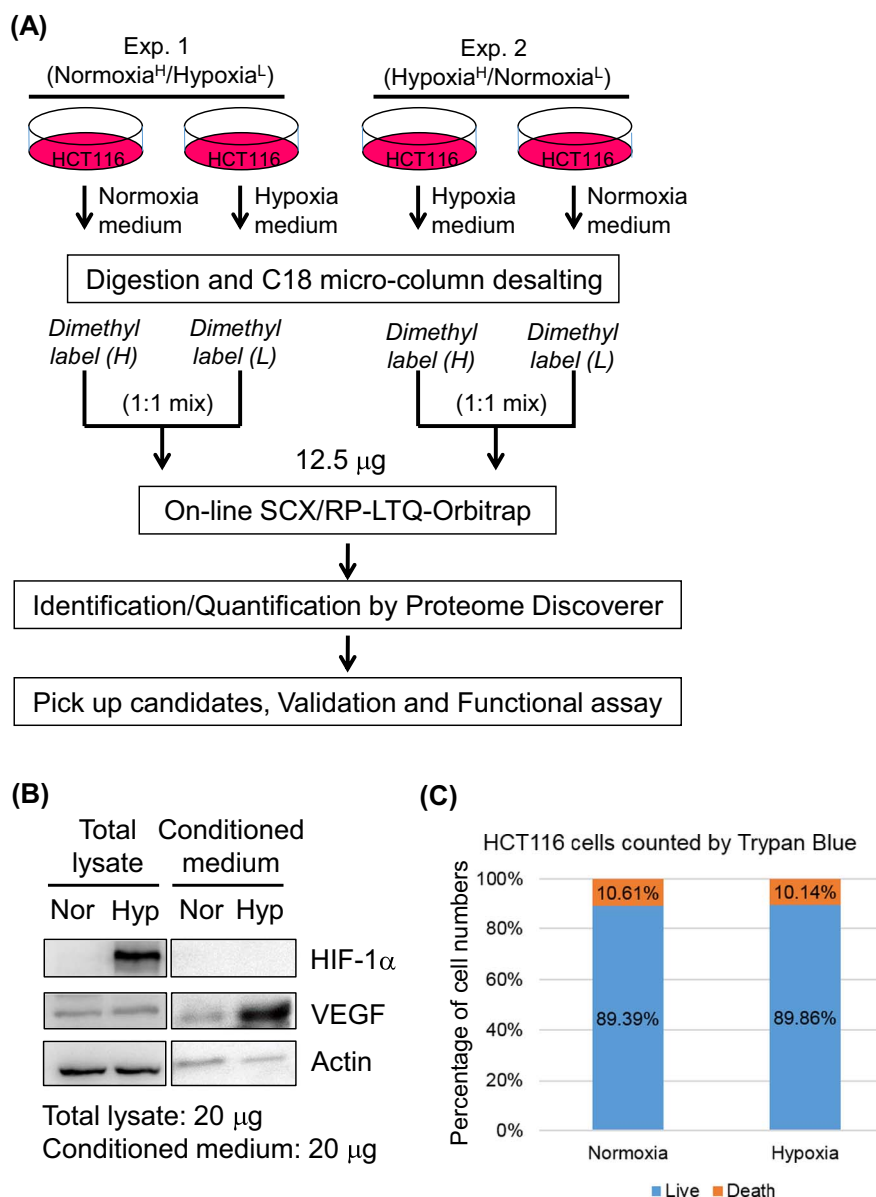


**Fig. 2.** Strategy to investigate secretomic changes in HCT116 cells during hypoxia. (A) The conditioned medium collected from normoxic or hypoxic HCT116 cells was digested with trypsin and labeled with heavy or light isotope of dimethyl compound, respectively. Both dimethyl-labeled protein samples were mixed in a mass ratio of 1:1, and then subjected to proteomic analysis (on-line SCX/RP-LTQ-Orbitrap). Proteome Discoverer software was used for mass spectrometric data analysis. (B) Total extracts (20  $\mu$ g) and conditioned medium proteins (20  $\mu$ g) from HCT116 cells treated with normoxia or hypoxia for 24 h were subjected to 10% SDS-PAGE followed by immunoblotting with the indicated antibodies. (C) To compare cell viability and cell death, HCT116 cells cultured in serum-free medium were treated with normoxia or hypoxia for 24 h. Cell viability is calculated as the number of viable cells divided by the total number of cells within the grids on the hemocytometer. If cells take up trypan blue, they are considered as cell death.

### 3.2. Improvement of the performance of quantitative proteome and secretome analysis

To compare the relative levels of intracellular (proteome) and extracellular (secretome) proteins in hypoxic and normoxic HCT116 cells, we used the Proteome Discoverer software to process the quantitative mass spectrometric data. Data of biological reduplicates were combined and processed using unified statistical criteria (Supplementary Fig. S1A). The level of HIF-1 $\alpha$  (HIF1A) protein is controlled by ubiquitin-mediated degradation under normoxic conditions [50]. As expected, HIF1A was obviously increased in hypoxia-treated HCT116 cells (mean  $\log_2$  (ratio) = 2.13, equivalent to 4.378-fold change from Exp. 1). However, protein products of house-keeping genes such as nucleolin (NCL) (mean  $\log_2$  (ratio) = -0.015, equivalent to 0.989-fold change) and actin (ACTG1) (mean  $\log_2$  (ratio) = 0.069, equivalent to 1.049-fold change) did not significantly change after hypoxic treatment. The MS-based quantification results are consistent with those observed from immunoblot analysis (Fig. 1B). In addition to the quantification of paired light/heavy peptides, it is necessary to identify proteins with unpaired peptides (i.e., light or heavy peptide observed alone in the mass spectra) which have dramatic changes from these experiments.

The results from the analysis of SILAC-labeled HCT116 cells showed that 28 and 29 proteins with unpaired peptides are only identified in the hypoxic or normoxic cells, respectively (Supplementary Table S1). The results from the analysis of secretome showed that 3 and 3 proteins with unpaired peptides are only identified in the hypoxic or normoxic cells, respectively (Supplementary Table S2). Although many interesting targets have been unraveled in these datasets described above, we narrowed down the target list from the quantitative proteome/secretome analysis. For quantitative proteome analysis, replicated experiments can improve the quantification coverage and accuracy. The false quantification rate (FQR) is a measurement to evaluate the accuracy of quantification results [51]. However, it is important to test whether combining multiple replicates and precision control criterion can improve the accuracy of quantitative results. The data with at least two ratio counts in reciprocal experiments were combined for evaluation. By this way, the FQR of unique protein quantification was estimated from 4.78% to 2.88% for the 5902 quantified proteins from proteome dataset and from 33.3% to 28.76% for the 772 quantified proteins from secretome dataset (Supplementary Table S3), respectively. When the relative standard deviation (RSD) filter < 0.5 was applied, their FQR were decreased to 2.21% for the 5700 quantified



**Table 1**

Numbers of unique proteins were identified and quantified in SILAC-labeled HCT116 cells after hypoxic treatment.

Hypoxia/ctrl.	Identification	Quantification	Up-regulated protein ( $> \text{mean} + 2\text{SD}$ )	Down-regulated protein ( $< \text{mean} - 2\text{SD}$ )
Proteome Exp. 1	6738	6397	122	149
Proteome Exp. 2	6628	6282	193	85
Sum of protein	7137	6777	163 ( $> 1.671$ )	124 ( $< 0.609$ )
Replicated protein	6229	<b>5700<sup>a</sup></b>	<b>127<sup>a</sup> (<math>&gt; 1.473</math>)</b>	<b>108<sup>a</sup> (<math>&lt; 0.688</math>)</b>

All proteins were identified with at least two unique peptides (peptides FDR  $< 1\%$ , protein FDR  $< 1\%$ ) and quantified with at least two H/L ratio counts from each experiments. The “a” indicates protein with high confidence which were selected with at least two ratio counts from the reduplicate experiments (RSD  $< 0.5$ ) and differently regulated parts (ratio more than  $\text{mean} + 2 \times \text{SD}$  or smaller than  $\text{mean} - 2 \times \text{SD}$ ). FQR = 2.21%.

Bold indicates the final results of “proteome dataset”.

**Table 2**

Numbers of unique proteins were identified and quantified from secretome of HCT116 cells after hypoxic treatment.

Hypoxia/ctrl.	Identification	Quantification	Up-regulated protein ( $> \text{mean} + 1\text{SD}$ )	Down-regulated protein ( $< \text{mean} - 1\text{SD}$ )	Up-regulated protein ( $> \text{mean} + 2\text{SD}$ )	Down-regulated protein ( $< \text{mean} - 2\text{SD}$ )
Secretome Exp. 1	984	924	120	124	39	10
Secretome Exp. 2	946	887	117	127	33	9
Sum of protein	1102	1039	141 ( $> 1.802$ )	155 ( $< 0.613$ )	41 ( $> 3.088$ )	14 ( $< 0.358$ )
Replicated protein	828	<b>722<sup>a</sup></b>	<b>88 (<math>&gt; 1.679</math>)</b>	<b>104 (<math>&lt; 0.628</math>)</b>	<b>28<sup>a</sup> (<math>&gt; 2.746</math>)</b>	<b>11<sup>a</sup> (<math>&gt; 0.384</math>)</b>

All proteins were identified with at least two unique peptides (peptides FDR  $< 1\%$ , protein FDR  $< 1\%$ ) and quantified with at least two H/L ratio counts from each experiments. The “a” indicates protein with high confidence which were selected with at least two ratio counts from the reduplicate experiments (RSD  $< 0.5$ ) and differently regulated parts (ratio more than  $\text{mean} + 2 \times \text{SD}$  or smaller than  $\text{mean} - 2 \times \text{SD}$ ). FQR = 25.48%.

Bold indicates the final results of “secretome dataset”.

proteins from proteome dataset and 25.48% for the 722 quantified proteins from secretome dataset (Supplementary Table S3), respectively. The scattered quantified results of potential experimental errors were effectively removed by replicates and precision control criterion that significantly improved the final quantitative accuracy (Tables 1 and 2). Compared to proteome, the difficulty in replicated measurements of secretome is derived from their low abundance and high complexity. The quantified proteins from proteome dataset have high reproducibility than those from secretome dataset of the replicate experiments (87.09% of quantified proteins from proteome dataset existed in both two experiments but only 74.3% of quantified proteins from secretome dataset were observed) (Supplementary Figs. S1B and S1C). Therefore, an alternative approach to improve the data accuracy while retaining a large number of quantified results is required. To quantify protein levels with high confidence, ambiguous targets which contain single ratio count or ratio of relative standard deviation (RSD)  $\geq 0.5$  were removed. By this way, we have quantified the levels of 5700 proteins from proteome dataset (Supplementary Dataset 1) and 722 proteins from secretome dataset (Supplementary Dataset 2) with high confidence (Supplementary Figs. S1D and S1E). In this study, summary statistics (Mean, Standard deviation, etc.) for proteome analysis have been shown in Supplementary Datasets 1 and 2. The methods for data preprocessing were described in previous reports [52,53]. Briefly, data were normalized by raw median, and transformed to log2 format. Accuracy of quantitation depends on the abundance and signal-to-noise ratio of the peptide pair, and missing values were filtered out. Finally, we selected targets based on their ratios which are more than  $\text{mean} \pm 2\text{SD}$  in proteome (protein ratio  $> 1.473$  or  $< 0.688$ ) and  $\text{mean} \pm 1\text{SD}$  in secretome (protein ratio  $> 1.679$  or  $< 0.628$ ) as described previously [53].

### 3.3. Selection of hypoxia-regulated proteins at the translational level

To elucidate hypoxia-induced gene expression and regulation in HCT116 cells, we have monitored the changes of omics profiling: transcriptome, translome, proteome, and secretome. We first integrated transcriptome/translome and proteome/secretome datasets to search for hypoxia-regulated genes. This integrated analysis yielded

1189 genes with their corresponding transcription/translation/protein levels (Supplementary Dataset 3). The following criteria were used to select candidates with hypoxia-induced translational regulation for further verification: (i) The candidates are significantly up-regulated at the translation level in hypoxic HCT116 cells; (ii) The candidates have secretory properties (Extracellular space, Secreted and Signal peptide) which were defined by UniProt database (<http://www.uniprot.org/>) or exosome database (<http://www.exocarta.org/>); (iii) The candidates have important biological functions such as key regulatory enzymes or transcription factors. By this way, 30 significantly up-regulated candidates at the level of translation but not transcription (Table 3) and 27 significantly up-regulated candidates at both transcriptional and translational levels (Table 4) were identified with high confidence in hypoxic HCT116 cells. On the other hand, 19 significantly down-regulated candidates at the level of translation but not transcription (Supplementary Table S4) and 12 significantly down-regulated candidates at both the transcriptional and translational levels (Supplementary Table S5) are shown. Half of the 30 translationally up-regulated proteins have rare reports of hypoxia ( $\leq 5$  references). LMAN2 and PROS1 were identified as novel hypoxia-regulated proteins at the translational level (Table 3). IGFBP6, LOXL2, COL12A1, COL6A1, IGFBP2 and HYOU1 had also been identified as hypoxia-induced proteins in U373MG glioma [54]. AREG and DNMT1 have already been described as important oncogenes in human cancers [55,56]. Jagged1 has been described as a Notch ligand that has a positive effect on tumor angiogenesis [57]. CD44 and ALCAM have been shown to be associated with cancer metastasis [58,59]. Therefore, the hypoxia-induced proteins may have the potential to provide new biomarkers for diagnosis and prognosis prediction.

### 3.4. Validation of hypoxia-induced proteins in HCT116 cells

Supplementary Tables S6–S9 show list of the significantly up- or down-regulated proteins from proteome and secretome datasets of HCT116 cells during hypoxia. As shown in Supplementary Table S6, ANGPTL4 (29.92-fold change), PLOD2 (10.24-fold change), P4HA1 (5.51-fold change), BNIP3L (4.83-fold change), PDK1 (4.52-fold change), SLC2A1 (4.08-fold change), P4HA2 (3.48-fold change), and

**Table 3**

Thirty genes are significantly up-regulated at the translational level in hypoxic HCT116 cells.

Accession	Gene	Transcriptome Hypoxia/ctrl. Fold mean	Translatome Hypoxia/ctrl. Fold mean	Proteome Hypoxia/ctrl. Fold mean	Secretome Hypoxia/ctrl. Fold mean	Exosome protein	Extracellular space	Secreted	Signal peptide	PubMed (gene, hypoxia)
P24592	IGFBP6	1.47	2.27	Hypoxia only		X		X	X	7
Q9Y4K0	LOXL2	1.41	8.11		2.69	X	X	X	X	23
P13726	F3	1.41	5.11	2.39		X		X	X	20
P16070	CD44	1.37	8.97	1.10	1.80	X			X	185
Q99715	COL12A1	1.36	7.58	1.71	0.74	X	X	X	X	1
P15514	AREG	1.36	5.61	1.59		X			X	7
P31431	SDC4	1.29	4.33	2.61		X		X	X	6
Q9UBN6	TNFRSF10D	1.26	4.23	4.72		X			X	1
P07686	HEXB	1.20	9.38	0.96	2.76	X			X	1
Q96BD0	SLCO4A1	1.19	5.19	2.08		X				1
Q12907	LMAN2	1.19	3.54	0.96	3.34	X			X	0
Q02487	DSC2	1.17	5.18	1.14	2.75	X			X	2
P27797	CALR	1.16	9.03	1.09	1.92	X	X	X	X	1
P21399	ACO1	1.16	2.50	1.07	2.11	X				3
P23284	PPIB	1.09	4.98	1.09	2.96	X			X	1
P07225	PROS1	1.09	3.13	2.88	1.01	X		X	X	0
O43291	SPINT2	1.04	5.09	1.62		X			X	4
Q13740	ALCAM	1.00	8.32	1.01	3.99	X		X	X	5
P18065	IGFBP2	1.00	4.71		1.86	X		X	X	32
P05067	APP	0.98	13.28	1.71	2.51	X			X	149
O00180	KCNK1	0.98	3.77	1.52						1
P26358	DNMT1	0.98	3.54	0.73	2.45	X			X	29
O15427	SLC16A3	0.91	7.97	1.61		X				9
Q13162	PRDX4	0.89	5.74	0.99	1.76	X		X	X	4
Q8NBS9	TXNDC5	0.83	4.61	1.03	4.95	X			X	7
P78504	JAG1	0.81	8.55	1.96		X			X	23
Q9BRK5	SDF4	0.81	5.21	1.00	1.78	X			X	1
P12109	COL6A1	0.76	19.25	1.69	0.62	X	X	X	X	3
O00767	SCD	0.76	6.18	1.65						163
Q9Y4L1	HYOU1	0.70	12.73	1.04	1.88	X			X	11

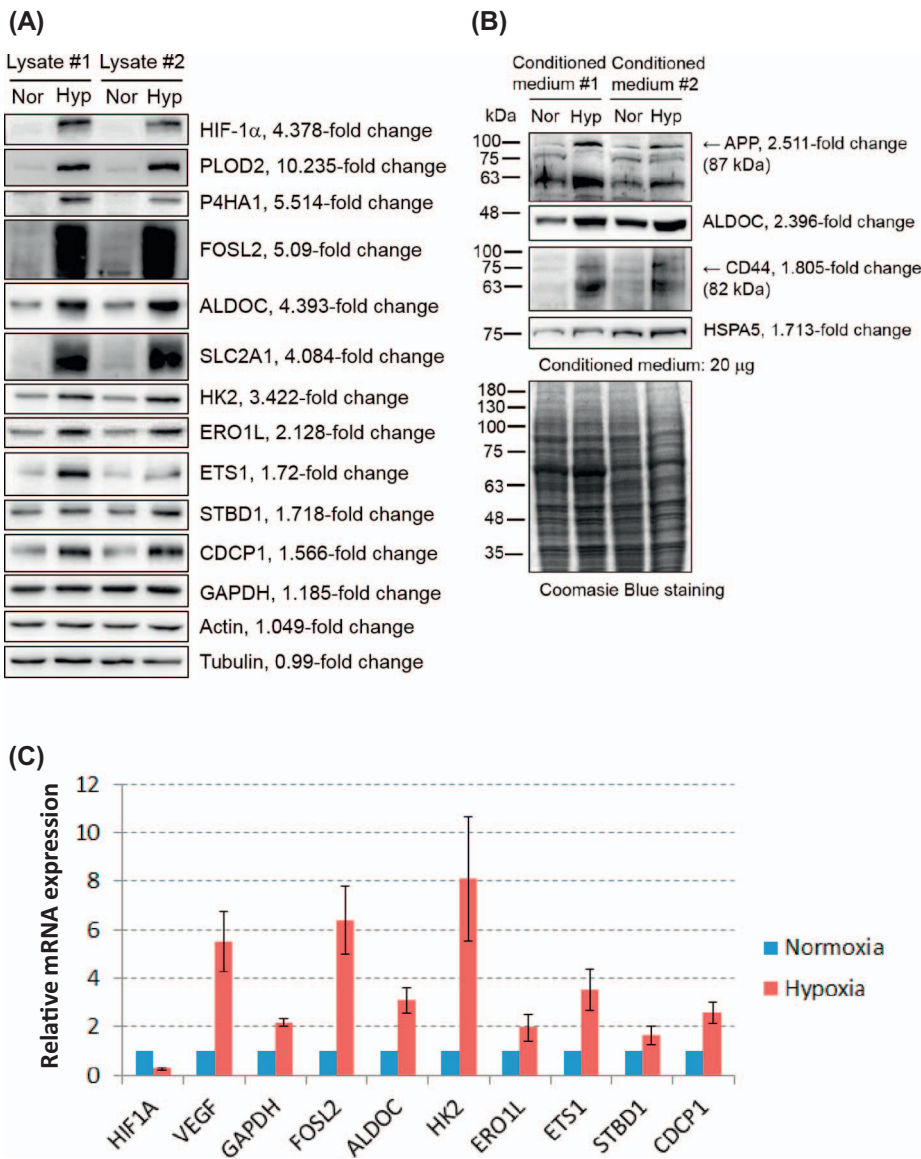
The significance of transcriptome and translatome are defined with ratios out of  $> 1.5$  or  $< 0.67$  fold. The significance of proteome/secretome are defined with ratios out of mean  $\pm 2$  SD/  $\pm 1$  SD.

**Table 4**

Twenty-seven genes are significantly up-regulated at both the transcriptional and translational levels in hypoxic HCT116 cells.

Accession	Gene	Transcriptome Hypoxia/ctrl. Fold mean	Translatome Hypoxia/ctrl. Fold mean	Proteome Hypoxia/ctrl. Fold mean	Secretome Hypoxia/ctrl. Fold mean	Exosome protein	Extracellular space	Secreted	Signal peptide	PubMed (gene, hypoxia)
P35318	ADM	10.29	5.99	Hypoxia only				X	X	123
P15408	FOSL2	6.55	2.37		5.09					6
P52789	HK2	5.78	3.22	3.42						192
P13674	P4HA1	5.74	8.23	5.51		X			X	12
O76061	STC2	5.47	3.25		3.53	X		X	X	10
O00469	PLOD2	4.37	7.43	10.23		X			X	14
P09972	ALDOC	4.35	2.05	4.39	2.40	X				5
P11166	SLC2A1	3.35	7.93	4.08		X				347
P14921	ETS1	2.88	2.24	1.72						54
Q02809	PLOD1	2.62	8.26	2.46	1.47	X			X	2
P19012	KRT15	2.38	1.59	1.91		X				0
Q8NFJ5	GPRC5A	2.35	7.35	2.21		X				1
O95210	STBD1	2.33	2.91	1.72						0
O60281	ZNF292	2.30	1.61	1.93						2
Q96HE7	ERO1L	2.29	8.57	2.13						16
O15460	P4HA2	2.10	7.13	3.48					X	7
Q9H5V8	CDCP1	2.00	4.83	1.57		X		X	X	8
P06744	GPI	1.96	2.03	2.34	1.38	X		X		78
P00558	PGK1	1.87	2.08	1.91	1.66	X				59
P19367	HK1	1.81	2.55	1.39	1.89	X				20
O94953	KDM4B	1.78	2.09	3.18						10
P13797	PLS3	1.72	2.07	1.58	1.43	X				0
Q9NQW6	ANLN	1.70	2.24	1.98		X			X	0
P11021	HSPA5	1.66	23.43	1.12	1.71	X			X	38
Q9Y4H2	IRS2	1.66	3.35	1.97		X			X	17
P48723	HSPA13	1.55	9.16		5.59	X			X	0
P50454	SERPINH1	1.54	6.46	1.25	1.78	X			X	7

The significance of transcriptome and translatome are defined with ratios out of  $> 1.5$  or  $< 0.67$  fold. The significance of proteome/secretome are defined with ratios out of mean  $\pm 2$  SD/  $\pm 1$  SD.



HK2 (3.42-fold change) are known as hypoxia-induced genes. To validate proteomic data (Supplementary Table S6), we performed immunoblot analysis to determine the relative amount of up-regulated candidates (PLOD2, P4HA1, FOSL2, ALDOC, SLC2A1, HK2, ERO1L, ETS1, STBD1, and CDCP1) in HCT116 cells during hypoxia compared to normoxia (Fig. 3A). The results of validation experiments are largely consistent with those observed from the quantitative proteome analysis. We also detected these hypoxia-induced proteins in HT-29 colon cancer cells, and similar results were obtained (Supplementary Fig. S2). This indicates that hypoxia regulates gene expression possibly through similar mechanisms in colon cancer cells. From secretome analysis (Supplementary Table S8), STC2 (3.53-fold change), LOXL2 (2.69-fold change), and IGFBP2 (1.86-fold change) were significantly increased in HCT116 cells during hypoxia. APP (0.98-fold change of transcriptome, 13.28-fold change of translome, 1.71-fold change of proteome, 2.51-fold change of secretome) and CD44 (1.37-fold change of transcriptome, 8.97-fold change of translome, 1.10-fold change of proteome, 1.81-fold change of secretome) were increased at the levels of translation and secretion. ALDOC (4.35-fold change of transcriptome, 2.05-fold change of translome, 4.39-fold change of proteome, 2.40-fold change of secretome) and HSPA5 (1.66-fold change of transcriptome, 23.43-fold change of translome, 1.12-fold change of

proteome, 1.71-fold change of secretome) were increased from transcription to protein translation and secretion. We also performed immunoblot analysis to verify several up-regulated candidates (APP, ALDOC, CD44, and HSPA5) from secretome (Supplementary Table S8). The results of validation experiments are largely consistent with those observed from secretome analysis (Fig. 3B). Furthermore, we also performed quantitative real-time RT-PCR to detect the mRNA level of these candidate genes. The majority of hypoxia-induced genes showed increased mRNA expression in hypoxic HCT116 cells compared to normoxic cells (Fig. 3C). Nevertheless, the mRNA level of HIF1A was markedly decreased (0.27-fold change) but not increased in HCT116 cells during hypoxia. The molecular mechanism of its down-regulation at the mRNA level remains unknown. Glycolytic enzyme GAPDH often serves as a housekeeping gene in many studies. It has been reported that GAPDH is up-regulated by HIF-1 in different cell lines [60,61]. Although we also observed that the mRNA level of GAPDH was up-regulated (2.18-fold change) in HCT116 cells during hypoxia (Fig. 3C), its protein level was not significantly increased in proteome dataset (GAPDH, 1.19-fold change) and immunoblot analysis (Fig. 3A). We further demonstrated that translation of GAPDH mRNA is more sensitive to hypoxia-induced translational repression than other mRNAs.

**Fig. 3.** Validation of the proteome and transcriptome data. HCT116 cells were treated with normoxia or hypoxia for 24 h. (A) Total extracts from HCT116 cells were resolved by 10% SDS-PAGE and subjected to immunoblotting with the indicated antibodies. Induction of HIF-1 $\alpha$  protein is a hallmark of hypoxia. The expression levels of GAPDH,  $\beta$ -actin, and  $\alpha$ -tubulin proteins which remained almost constant between normoxia and hypoxia served as loading controls. (B) Conditioned medium proteins (20  $\mu$ g) from HCT116 cells treated with hypoxia or normoxia for 24 h were analyzed as described above. (C) RNA extraction from HCT116 cells was analyzed by quantitative real-time RT-PCR using gene-specific primers. Bar graphs show relative mRNA levels normalized to  $\beta$ -actin mRNA from at least three independent experiments.

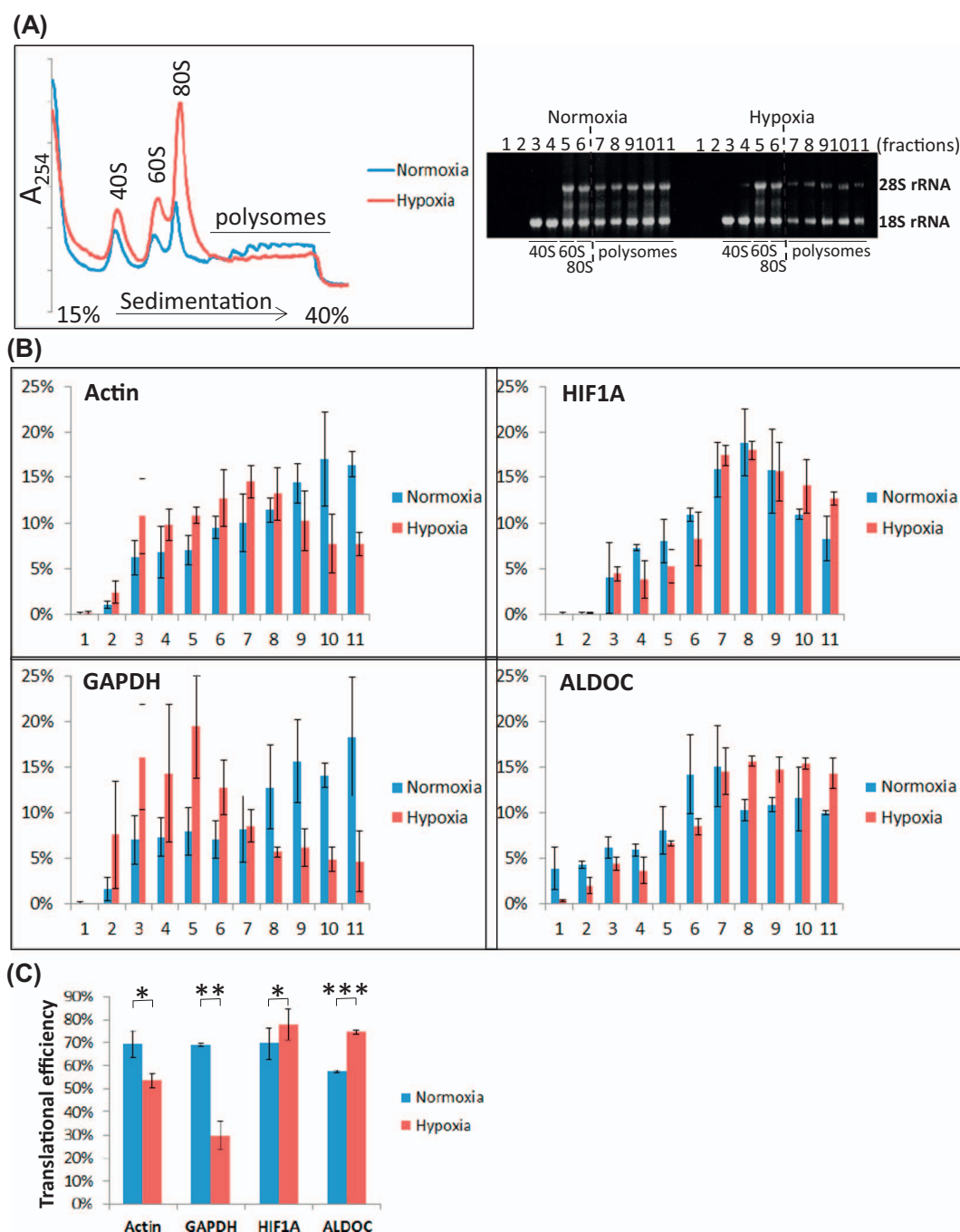


**Fig. 4.** Validation of the translome data using polysome profile analysis. HCT116 cells were treated with normoxia or hypoxia for 24 h. Cytoplasmic extracts were loaded on a 15–40% linear sucrose density gradient, and followed by ultracentrifugation. (A) Polysome profiles of HCT116 cells were monitored at 254 nm using an ISCO fractionation system (left). RNA extracted from sucrose gradient fractionation was resolved on a 1% formaldehyde/agarose gel. 28S and 18S rRNAs were visualized by ethidium bromide staining (right). The distribution of ribosomes, including 40S and 60S ribosomal subunits, 80S monosome, and polysomes, are indicated. (B) The distribution of mRNAs (%) in each fraction was analyzed by quantitative real-time RT-PCR. Bar graphs show mean  $\pm$  standard deviation from at least three independent experiments. (C) Translational efficiency of  $\beta$ -actin, GAPDH, HIF1A, and ALDOC mRNAs was calculated and shown as a percentage (%) in HCT116 cells under normoxic and hypoxic conditions. Bar graphs show mean  $\pm$  standard deviation from at least three independent experiments (\* $P$  < 0.05, \*\* $P$  < 0.01, \*\*\* $P$  < 0.001).

### 3.5. GAPDH mRNAs are susceptible to hypoxia-induced translational repression in HCT116 cells

Several lines of evidence indicate that translation of general mRNAs is repressed by hypoxia in many different types of cells [15–17]. However, selected hypoxia-responsive genes can escape from translational repression under such a condition. We also performed sucrose gradient sedimentation and polysome profile analysis to evaluate the translational status of HCT116 cells in response to hypoxia. As

expected, hypoxia causes a decrease in polysomes and a corresponding increase in translation initiation complexes, including 40S, 60S ribosomal subunits and 80S monosome (Fig. 4A, left panel). After sucrose gradient centrifugation, the mRNA/ribosome complexes were separated into 11 fractions (Fig. 4A, right panel). Denaturing agarose gel electrophoresis of rRNAs also showed a shift from polysomes (fractions 7–11) into 40S (fractions 3–4), 60S (fraction 5) ribosomal subunits and 80S monosome (fraction 6). This indicates that general translation is inhibited by hypoxia in HCT116 cells. We further analyzed translational



efficiency of several genes by polysome profiling and quantitative real-time RT-PCR (Fig. 4B). The polysomal association of  $\beta$ -actin and GAPDH mRNAs was decreased in HCT116 cells exposed to hypoxia. Notably, translation of GAPDH mRNA is more susceptible to hypoxia-induced translational repression than  $\beta$ -actin mRNA. In contrast, the polysomal distribution of HIF1A and ALDOC mRNAs were increased in HCT116 cells during hypoxia (Fig. 4B). This indicates that HIF1A and ALDOC mRNAs remain efficiently translated during hypoxia. The distribution of an mRNA within the polysomal fractions is reflective of its translational efficiency. After calculation, translational efficiency of GAPDH mRNA changes from 69% to 30% in HCT116 cells exposed to hypoxia (Fig. 4C). HIF1A and ALDOC mRNAs show an increase in translational efficiency during hypoxia compared to normoxia (Fig. 4C), suggesting that selected genes can escape from translational repression and remain efficiently translated in HCT116 cells during hypoxia. Therefore, only transcriptome is not sufficient to interpret gene expression under hypoxic conditions. We need to integrate multiple types of omics data, including transcriptome, translome, proteome, and secretome.

### 3.6. Bioinformatics analysis of the hypoxia-regulated proteins in HCT116 cells

To figure out hypoxia-induced gene expression and regulation, the DAVID functional annotation clustering was used to analyze the 420 hypoxia-regulated proteins (210 up-regulated proteins and 210 down-regulated proteins) from the combined proteome and secretome datasets in the context of the Gene Ontology (GO) [42]. As shown in Fig. 5, “translational elongation” was selectively enriched in biological process (Fig. 5A,  $P$ -value =  $7.02E-09$ ), and “cytosol” was selectively enriched in cellular component (Fig. 5B,  $P$ -value =  $2.69E-12$ ), and “RNA binding” was selectively enriched in molecular function (Fig. 5C,  $P$ -value =  $1.73E-10$ ). If we only analyzed the 210 up-regulated proteins from the combined proteome and secretome datasets, “glucose metabolic process” was selectively enriched in biological process (Supplementary Fig. S3A,  $P$ -value =  $1.44E-09$ ), and “iron ion binding” was selectively enriched in molecular function (Supplementary Fig. S3B,  $P$ -value =  $9.73E-06$ ). If we only analyzed the 210 down-regulated proteins from the combined proteome and secretome datasets, “translational elongation” was selectively enriched in biological process (Supplementary Fig. S4A,  $P$ -value =  $4.20E-11$ ), and “cytosolic ribosome” was selectively enriched in cellular component (Supplementary Fig. S4B,  $P$ -value =  $1.60E-11$ ), and “RNA binding” was selectively enriched in molecular function (Supplementary Fig. S4C,  $P$ -value =  $3.12E-10$ ). Collectively, the results of bioinformatics analysis indicate that hypoxia induces glucose metabolic process to generate energy for cells but represses translational elongation.

For KEGG pathway analysis, the 210 up-regulated proteins from the combined proteome and secretome datasets were analyzed. The results showed that the “Glycolysis/Gluconeogenesis” pathway ( $P$ -value =  $3.48E-06$ , Fold Enrichment = 9.43,  $FDR$  =  $3.79E-03$ ) was selectively enriched, including ALDOA, ALDOC, ENO2, GPI, HK1, HK2, LDHA, and PGK1 (Supplementary Fig. S5A). The 210 down-regulated proteins from the combined proteome and secretome datasets were also analyzed. The results showed that the “Ribosome” pathway ( $P$ -value =  $2.31E-10$ , Fold Enrichment = 10.77,  $FDR$  =  $2.37E-07$ ) was selectively enriched, including RPL10, RPL13, RPL13A, RPL18, RPL18A, RPL35, RPSA, RPS2, RPS3, RPS8, RPS9, RPS16, RPS18, and RPS20 (Supplementary Fig. S5B). The “Cell cycle” pathway ( $P$ -value =  $1.64E-06$ , Fold Enrichment = 6.42,  $FDR$  =  $1.69E-03$ ) was also selectively enriched, including MCM4, PLK1, BUB3, TTK, CDK4, CDC25B, CDC20, CDKN1A, MCM2, PKMYT1, BUB1B, and PRKDC (Supplementary Fig. S5C). In addition to functional annotation described above, 49 proteins from hypoxia-induced translational regulation (30 significantly up-regulated candidates and 19 significantly down-regulated candidates) were further mapped to protein-protein

correlation networks using the STRING database [43]. This analysis revealed that 30 proteins (25 candidates with 5 interactors) in different correlations from distinct protein complexes were involved in “extracellular matrix organization (CD44, COL6A1, COL12A1, and SDC4)” ( $FDR$  =  $1.74E-03$ ), “extracellular exosome (APP, CALR, CHD2, COL6A1, HYOU1, NEDD4L, PROS1 and SDF4)” ( $FDR$  =  $2.91E-09$ ), and “protein processing in endoplasmic reticulum (CALR, DNAJB1, HSP90B1, HYOU1, LMAN2, TXNDC5)” ( $FDR$  =  $2.91E-09$ ) (Supplementary Fig. S5D).

## 4. Discussion

Given that hypoxia may alter transcription, translation, and protein stability, we present comprehensive transcriptome/translatome/proteome/secretome analyses to study changes in gene expression that occur in HCT116 cells during hypoxia. Quantitative mass spectrometry analysis of the hypoxic proteome and secretome was performed using SILAC or Dimethyl labeling approach. It is necessary to establish that in existing cancer cells hypoxia permanently, rather than transiently, alters the expression of proteins involved in energy metabolism, angiogenesis, and tumor invasion/metastasis. Hypoxia induced intra- and inter-cellular proteins (ECM context) which are important for tumor heterogeneity and invasion/metastasis. The integrated omics analysis of omics profiling may provide the possibility of developing new methods of anti-cancer therapy [62]. In contrast to the genetic and epigenetic changes that induce host cell transformation to initiate tumor development, those that promote the malignant progression of cancer remain poorly understood. Emerging evidence suggests that the hypoxic tumor microenvironment could remodel the chromatin-associated proteome (chromatome) to induce epigenetic changes and alter gene expression in cancer cells [63]. Mammalian gene expression patterns change profoundly in response to hypoxia. These changes in gene expression are strongly influenced by post-transcriptional mechanisms mediated by RNA-binding proteins (RBPs) and microRNAs (miRNAs). RBPs are also involved in the processes of subcellular localization, translation initiation, mRNA stability, and RNA degradation. Among the putative factors for hypoxia-induced translational regulation are heterogeneous nuclear ribonucleoproteins (hnRNPs), which control the fate of cytosolic mRNAs. Several miRNAs have been functionally implicated in hypoxic cells. For example, biogenesis of miR-210 and miR-215 were induced in pancreatic cancer (PC) cells and glioma-initiating cells [64,65], respectively. The miR-210 expression in PC cells is induced by hypoxia through the HIF-1-dependent pathway, and the GTPase-activating protein GIT2 may be potential miR-210 target in PC cells [64]. Although we found that hypoxia can induce GIT2 expression at the mRNA level (1.8-fold change of transcriptome), there is no significant difference at the protein level (1.0-fold change of proteome) between normoxic and hypoxic HCT116 cells (Supplementary Table S4). This is a hint on how to explain why the protein level of GIT2 is not correlated with its transcription, implicating that post-transcriptional and translational controls have a major impact on gene expression and regulation during hypoxia.

Protein translation typically begins with the recruitment of the 43S ribosomal complex to the 5' cap of mRNAs by a cap-binding complex eIF4F (eIF4E-eIF4G1-eIF4A). However, a subset of mRNAs may be translated in a cap-independent manner during hypoxia. It was recently reported that mRNAs containing N<sup>6</sup>-methyladenosine (m<sup>6</sup>A) in their 5' UTR can be translated in a cap-independent manner under stress conditions [66]. More recently, it was proposed that an alternative cap-dependent translation that depends on eIF4F<sup>H</sup> (eIF4E2-eIF4G3-eIF4A) complex mediates translation of selected mRNAs during hypoxia [24]. This study also showed that hypoxic cells depend on a switch in translation, rather than mRNA levels, to alter protein expression pattern. Among the reported candidates [24], P4HA1 (5.7-fold change of transcriptome, 8.2-fold change of translome, 5.5-fold change of proteome), PLOD2 (4.4-fold change of transcriptome, 7.4-fold change of

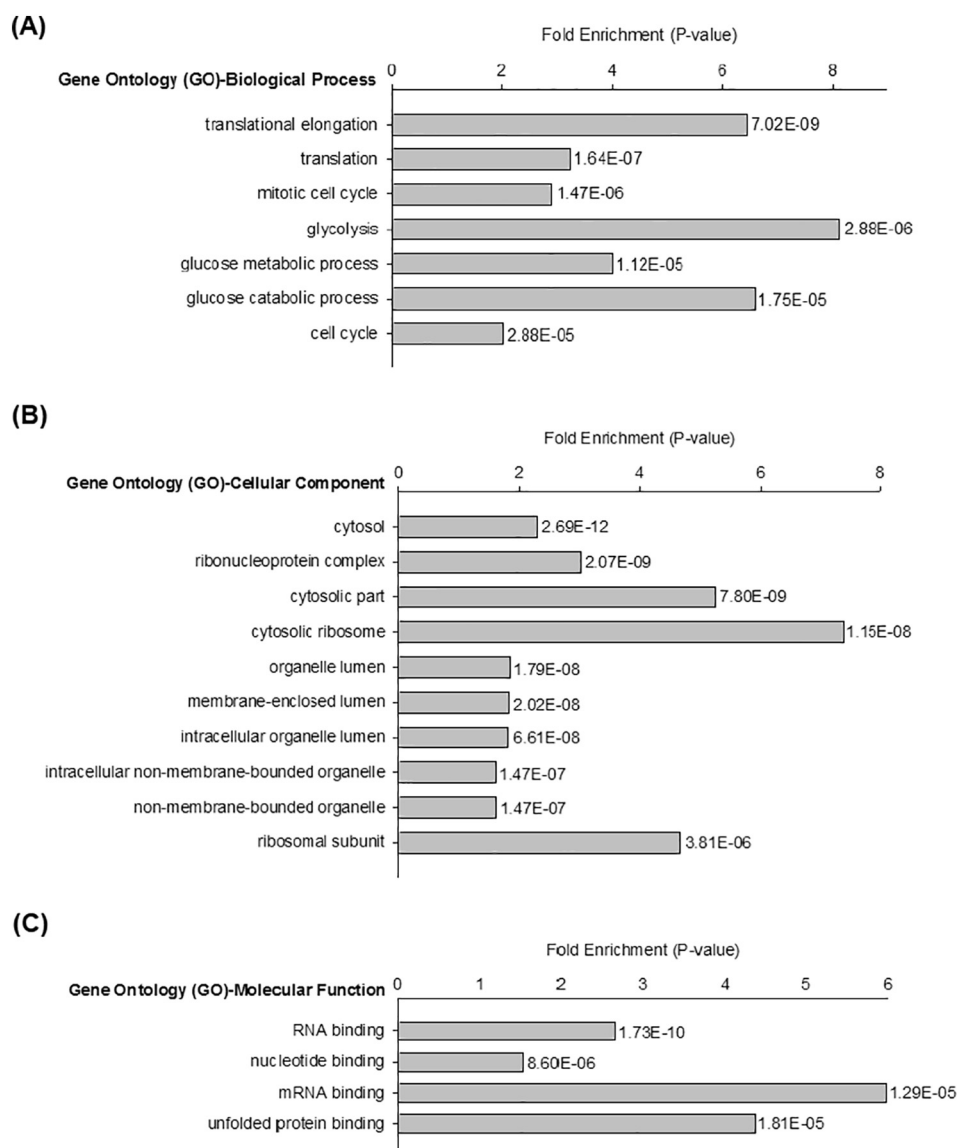


**Fig. 5.** Functional annotation clustering of hypoxia-regulated proteins in HCT116 cells during hypoxia. The 420 hypoxia-regulated proteins in HCT116 cells were analyzed by Gene Ontology (GO) enrichment analysis (Top 10 and FDR < 0.05). (A) The “translational elongation” was selectively enriched in biological process (P-value = 7.02E–09). (B) The “cytosol” (P-value = 2.69E–12) were selectively enriched in cellular component. (C) The “RNA binding” (P-value = 1.73E–10) was selectively enriched in molecular function.

translatome, 10.2-fold change of proteome), and SLC2A1 (3.4-fold change of transcriptome, 7.9-fold change of translatome, 4.1-fold change of proteome) were also identified as candidate genes in our translatome dataset.

Here, we identified 30 candidates whose translation is up-regulated by hypoxia (Table 3). Among these candidates, lectin mannose binding 2 (LMAN2) (1.2-fold change of transcriptome, 3.5-fold change of translatome, 1-fold change of proteome, 3.3-fold change of secretome) and protein S (PROS1) (1.1-fold change of transcriptome, 3.1-fold change of translatome, 2.9-fold change of proteome, 1-fold change of secretome) are two novel hypoxia-induced proteins at the translational level. Although PROS1 has been identified as a secreted protein in androgen-independent prostate cancer cells, no secretion was detected in the secretomes of normal and androgen-dependent cell lines [67]. We herein show that hypoxia increases the intracellular level of PROS1 protein through translational regulation, with no detectable changes in the secretome. LMAN2 functions as an intracellular lectin in the early secretory pathway, and it was identified in the gastric cancer secretome [68]. PROS1 is a ligand of the proto-oncogenic receptor protein tyrosine kinases TAMs (TYRO3, AXL, and MER). PROS1 had been reported as a

mediator of cell proliferation, survival, and migration in oral squamous cell carcinoma (OSCC) [69]. Moreover, the 27 significantly up-regulated candidates at both the transcriptional and translational levels in hypoxic HCT116 cells contain several novel hypoxia-induced proteins, including KRT15, ANLN, PLS3, and adrenomedullin (ADM) (Table 4). KRT15 had been identified as one of the up-regulated genes in a subset of urothelial cell carcinomas [70]. ANLN is required for cytokinesis and has been reported as a prognostic biomarker of CRC [71]. Microarray analyses suggested a major role of ANLN in cell migration and several cancer-related signaling pathways. The actin-bundling protein PLS3 can be used as a circulating tumor cells (CTC) marker for metastatic CRC cells [72]. In particular, ADM is a potent hypotensive and vasodilator agent. ADM is only identified in the hypoxic cells, and it has been shown to promote angiogenesis and increase the tolerance of cells to oxidative stress and hypoxic injury [73].

Tumor invasion/metastasis is a complex process involving the reciprocal interplay between cancer cells and host stroma at both primary and secondary sites, and is strongly influenced by microenvironmental factors such as hypoxia. Tumor-secreted proteins may play a crucial role in tumor invasion/metastasis and have therapeutic potential. The

obtained results will improve our understanding of the complex events in the cancer microenvironment by providing reliable information about changes from genes to proteins in cancer cells under hypoxic conditions. Quantitative analysis of the relative abundance of expressed proteins is an essential issue in comprehensive proteomics for verification. Further functional studies based on our results can provide important clues with regard to cancer biology such as tumor invasion/metastasis or angiogenesis and the development of biomarkers and therapeutic targets for human cancers.

## 5. Conclusions

Here, we use a combined omics approach to investigate gene expression and regulation in HCT116 cells during hypoxia. Quantitative mass spectrometry (MS) analyses of hypoxic and normoxic proteome/secretome were performed in human colon cancer cells for the first time. A total of 1189 MS-identified proteins were compared to transcriptome and translational datasets, and we found that 49 proteins were regulated during hypoxia at the translational level, including 30 up-regulated and 19 down-regulated genes. Notably, secretory proteins IGFBP6 and LOXL2 which have been suggested as hypoxia biomarkers were up-regulated in hypoxic HCT116 cells. This approach provides a more comprehensive view of gene expression and regulation during hypoxia in cancer cells. Identified hypoxia-regulated genes may provide a novel therapeutic target for cancer treatment and biomarkers for diagnosis/prognosis. We also found that hypoxia induces translation of many genes involved in extracellular matrix organization, extracellular exosome, and protein processing in endoplasmic reticulum in colon cancer cells. These findings support the idea that hypoxia is correlated with an increased risk of tumor invasion/metastasis.

## Conflicts of interest

The authors declare no conflicts of interest.

## Acknowledgement

This work was financially supported by grants from Ministry of Science and Technology, Taiwan (MOST104-2320-B-182-037) and Chang Gung Memorial Hospital, Linkou, Taiwan (CMRPD3E0013, CIRPD3B0013 and CLRPD190017).

## Appendix A. Supplementary data

Supplementary data to this article can be found online at <https://doi.org/10.1016/j.jprote.2018.02.031>.


## References

- [1] R.G. Bristow, R.P. Hill, Hypoxia and metabolism. Hypoxia, DNA repair and genetic instability, *Nat. Rev. Cancer* 8 (2008) 180–192.
- [2] M. Hockel, P. Vaupel, Tumor hypoxia: definitions and current clinical, biologic, and molecular aspects, *J. Natl. Cancer Inst.* 93 (2001) 266–276.
- [3] J.A. Bertout, S.A. Patel, M.C. Simon, The impact of O<sub>2</sub> availability on human cancer, *Nat. Rev. Cancer* 8 (2008) 967–975.
- [4] K. Ruan, G. Song, G. Ouyang, Role of hypoxia in the hallmarks of human cancer, *J. Cell. Biochem.* 107 (2009) 1053–1062.
- [5] D.M. Gilkes, G.L. Semenza, D. Wirtz, Hypoxia and the extracellular matrix: drivers of tumour metastasis, *Nat. Rev. Cancer* 14 (2014) 430–439.
- [6] M.W. Dewhirst, Y. Cao, B. Moeller, Cycling hypoxia and free radicals regulate angiogenesis and radiotherapy response, *Nat. Rev. Cancer* 8 (2008) 425–437.
- [7] J.M. Brown, Q.T. Le, Tumor hypoxia is important in radiotherapy, but how should we measure it? *Int. J. Radiat. Oncol. Biol. Phys.* 54 (2002) 1299–1301.
- [8] B.A. Teicher, Hypoxia and drug resistance, *Cancer Metastasis Rev.* 13 (1994) 139–168.
- [9] L. Liu, M.C. Simon, Regulation of transcription and translation by hypoxia, *Cancer Biol. Ther.* 3 (2004) 492–497.
- [10] N.C. Denko, Hypoxia, HIF1 and glucose metabolism in the solid tumour, *Nat. Rev. Cancer* 8 (2008) 705–713.
- [11] G.L. Wang, B.H. Jiang, E.A. Rue, G.L. Semenza, Hypoxia-inducible factor 1 is a basic-helix-loop-helix-PAS heterodimer regulated by cellular O<sub>2</sub> tension, *Proc. Natl. Acad. Sci. U. S. A.* 92 (1995) 5510–5514.
- [12] Q. Ke, M. Costa, Hypoxia-inducible factor-1 (HIF-1), *Mol. Pharmacol.* 70 (2006) 1469–1480.
- [13] G.L. Semenza, Targeting HIF-1 for cancer therapy, *Nat. Rev. Cancer* 3 (2003) 721–732.
- [14] E.P. Cummins, C.T. Taylor, Hypoxia-responsive transcription factors, *Pflugers Arch.* 450 (2005) 363–371.
- [15] T. van den Beucken, M.G. Magagnin, B. Jutten, R. Seigneure, P. Lambin, M. Koritzinsky, B.G. Wouters, Translational control is a major contributor to hypoxia induced gene expression, *Radiother. Oncol.* 99 (2011) 379–384.
- [16] B.G. Wouters, M. Koritzinsky, Hypoxia signalling through mTOR and the unfolded protein response in cancer, *Nat. Rev. Cancer* 8 (2008) 851–864.
- [17] M.C. Lai, C.M. Chang, H.S. Sun, Hypoxia induces autophagy through translational up-regulation of lysosomal proteins in human colon cancer cells, *PLoS One* 11 (2016) e0153627.
- [18] K.J. Lang, A. Kappel, G.J. Goodall, Hypoxia-inducible factor-1α mRNA contains an internal ribosome entry site that allows efficient translation during normoxia and hypoxia, *Mol. Biol. Cell* 13 (2002) 1792–1801.
- [19] I. Stein, A. Itin, P. Einat, R. Skaliter, Z. Grossman, E. Keshet, Translation of vascular endothelial growth factor mRNA by internal ribosome entry: implications for translation under hypoxia, *Mol. Cell. Biol.* 18 (1998) 3112–3119.
- [20] J.D. Blais, V. Filipenko, M. Bi, H.P. Harding, D. Ron, C. Koumenis, B.G. Wouters, J.C. Bell, Activating transcription factor 4 is translationally regulated by hypoxic stress, *Mol. Cell. Biol.* 24 (2004) 7469–7482.
- [21] K.M. Vattam, R.C. Wek, Reinitiation involving upstream ORFs regulates ATF4 mRNA translation in mammalian cells, *Proc. Natl. Acad. Sci. U. S. A.* 101 (2004) 11269–11274.
- [22] M. Gorospe, K. Tominaga, X. Wu, M. Fahling, M. Ivan, Post-transcriptional control of the hypoxic response by RNA-binding proteins and microRNAs, *Front. Mol. Neurosci.* 4 (2011) 7.
- [23] J. Uniacke, C.E. Holterman, G. Lachance, A. Franovic, M.D. Jacob, M.R. Fabian, J. Payette, M. Holcik, A. Pause, S. Lee, An oxygen-regulated switch in the protein synthesis machinery, *Nature* 486 (2012) 126–129.
- [24] J.J. Ho, M. Wang, T.E. Audas, D. Kwon, S.K. Carlsson, S. Timpano, S.L. Evangelou, S. Brothers, M.L. Gonzalgo, J.R. Krieger, S. Chen, J. Uniacke, S. Lee, Systemic reprogramming of translation efficiencies on oxygen stimulus, *Cell Rep.* 14 (2016) 1293–1300.
- [25] M. Koritzinsky, R. Seigneure, M.G. Magagnin, T. van den Beucken, P. Lambin, B.G. Wouters, The hypoxic proteome is influenced by gene-specific changes in mRNA translation, *Radiother. Oncol.* 76 (2005) 177–186.
- [26] J.D. Thomas, G.J. Johannes, Identification of mRNAs that continue to associate with polysomes during hypoxia, *RNA* 13 (2007) 1116–1131.
- [27] J.T. Chi, Z. Wang, D.S. Nuyten, E.H. Rodriguez, M.E. Schaner, A. Salim, Y. Wang, G.B. Kristensen, A. Helland, A.L. Borresen-Dale, A. Giaccia, M.T. Longaker, T. Hastie, G.P. Yang, M.J. van de Vijver, P.O. Brown, Gene expression programs in response to hypoxia: cell type specificity and prognostic significance in human cancers, *PLoS Med.* 3 (2006) e47.
- [28] X.D. Huang, Z.F. Wang, L.M. Dai, Z.Q. Li, Microarray analysis of the hypoxia-induced gene expression profile in malignant C6 glioma cells, *Asian Pac. J. Cancer Prev.* 13 (2012) 4793–4799.
- [29] J.J. Ord, E.H. Streeter, I.S. Roberts, D. Cranston, A.L. Harris, Comparison of hypoxia transcriptome in vitro with in vivo gene expression in human bladder cancer, *Br. J. Cancer* 93 (2005) 346–354.
- [30] M.C. Djidja, J. Chang, A. Hadjiropocis, F. Schlich, J. Sinclair, M. Mrsnik, E.M. Schoof, H.E. Barker, R. Lindling, C. Jorgensen, J.T. Erler, Identification of hypoxia-regulated proteins using MALDI-mass spectrometry imaging combined with quantitative proteomics, *J. Proteome Res.* 13 (2014) 2297–2313.
- [31] Y.H. Han, L. Xia, L.P. Song, Y. Zheng, W.L. Chen, L. Zhang, Y. Huang, G.Q. Chen, L.S. Wang, Comparative proteomic analysis of hypoxia-treated and untreated human leukemic U937 cells, *Proteomics* 6 (2006) 3262–3274.
- [32] L.H. Stockwin, J. Blonder, M.A. Bumke, D.A. Lucas, K.C. Chan, T.P. Conrads, H.J. Issaq, T.D. Veenstra, D.L. Newton, S.M. Rybak, Proteomic analysis of plasma membrane from hypoxia-adapted malignant melanoma, *J. Proteome Res.* 5 (2006) 2996–3007.
- [33] S.E. Ong, B. Blagoev, I. Kratchmarova, D.B. Kristensen, H. Steen, A. Pandey, M. Mann, Stable isotope labeling by amino acids in cell culture, SILAC, as a simple and accurate approach to expression proteomics, *Mol. Cell. Proteomics* 1 (2002) 376–386.
- [34] S.E. Ong, M. Mann, A practical recipe for stable isotope labeling by amino acids in cell culture (SILAC), *Nat. Protoc.* 1 (2006) 2650–2660.
- [35] H.C. Harsha, H. Molina, A. Pandey, Quantitative proteomics using stable isotope labeling with amino acids in cell culture, *Nat. Protoc.* 3 (2008) 505–516.
- [36] M.P. Pavlou, E.P. Diamandis, The cancer cell secretome: a good source for discovering biomarkers? *J. Proteome Res.* 73 (2010) 1896–1906.
- [37] Y.C. Hsiao, L.J. Chu, J.T. Chen, T.S. Yeh, J.S. Yu, Proteomic profiling of the cancer cell secretome: informing clinical research, *Expert Rev. Proteomics* (2017), <http://dx.doi.org/10.1080/14789450.2017.1353913>.
- [38] C.C. Wu, C.W. Hsu, C.D. Chen, C.J. Yu, K.P. Chang, D.I. Tai, H.P. Liu, W.H. Su, Y.S. Chang, J.S. Yu, Candidate serological biomarkers for cancer identified from the secretomes of 23 cancer cell lines and the human protein atlas, *Mol. Cell. Proteomics* 9 (2010) 1100–1117.
- [39] J.L. Hsu, S.Y. Huang, N.H. Chow, S.H. Chen, Stable-isotope dimethyl labeling for quantitative proteomics, *Anal. Chem.* 75 (2003) 6843–6852.
- [40] C.L. Chen, Y.F. Lai, P. Tang, K.Y. Chien, J.S. Yu, C.H. Tsai, H.W. Chen, C.C. Wu, T. Chung, C.W. Hsu, C.D. Chen, Y.S. Chang, P.L. Chang, Y.T. Chen, Comparative and targeted proteomic analyses of urinary microparticles from bladder cancer and

- hernia patients, *J. Proteome Res.* 11 (2012) 5611–5629.
- [41] K.J. Livak, T.D. Schmittgen, Analysis of relative gene expression data using real-time quantitative PCR and the  $2(-\Delta\Delta C_T)$  method, *Methods* 25 (2001) 402–408.
- [42] W. Huang da, B.T. Sherman, R.A. Lempicki, Systematic and integrative analysis of large gene lists using DAVID bioinformatics resources, *Nat. Protoc.* 4 (2009) 44–57.
- [43] D. Szklarczyk, A. Franceschini, M. Kuhn, M. Simonovic, A. Roth, P. Minguez, T. Doerks, M. Stark, J. Muller, P. Bork, L.J. Jensen, C. von Mering, The STRING database in 2011: functional interaction networks of proteins, globally integrated and scored, *Nucleic Acids Res.* 39 (2011) D561–568.
- [44] J.A. Vizcaino, A. Csordas, N. Del-Toro, J.A. Dianas, J. Griss, I. Lavidas, G. Mayer, Y. Perez-Riverol, F. Reisinger, T. Ternent, Q.W. Xu, R. Wang, H. Hermjakob, 2016 update of the PRIDE database and its related tools, *Nucleic Acids Res.* 44 (2016) 11033.
- [45] S.C. Bendall, C. Hughes, M.H. Stewart, B. Doble, M. Bhatia, G.A. Lajoie, Prevention of amino acid conversion in SILAC experiments with embryonic stem cells, *Mol. Cell. Proteomics* 7 (2008) 1587–1597.
- [46] J.A. Forsythe, B.H. Jiang, N.V. Iyer, F. Agani, S.W. Leung, R.D. Koos, G.L. Semenza, Activation of vascular endothelial growth factor gene transcription by hypoxia-inducible factor 1, *Mol. Cell. Biol.* 16 (1996) 4604–4613.
- [47] T.R. Cox, R.M. Rumney, E.M. Schoof, L. Perryman, A.M. Hoye, A. Agrawal, D. Bird, N.A. Latif, H. Forrest, H.R. Evans, I.D. Huggins, G. Lang, R. Linding, A. Gartland, J.T. Erler, The hypoxic cancer secretome induces pre-metastatic bone lesions through lysyl oxidase, *Nature* 522 (2015) 106–110.
- [48] Q. Lin, H.T. Tan, H.S. Lim, M.C. Chung, Sieving through the cancer secretome, *Biochim. Biophys. Acta* 1834 (2013) 2360–2371.
- [49] O. Mendez, J. Villanueva, Challenges and opportunities for cell line secretomes in cancer proteomics, *Proteomics Clin. Appl.* 9 (2015) 348–357.
- [50] L.E. Huang, J. Gu, M. Schau, H.F. Bunn, Regulation of hypoxia-inducible factor 1 $\alpha$  is mediated by an O<sub>2</sub>-dependent degradation domain via the ubiquitin-proteasome pathway, *Proc. Natl. Acad. Sci. U. S. A.* 95 (1998) 7987–7992.
- [51] C. Song, F. Wang, M. Ye, K. Cheng, R. Chen, J. Zhu, Y. Tan, H. Wang, D. Figeys, H. Zou, Improvement of the quantification accuracy and throughput for phosphoproteome analysis by a pseudo triplex stable isotope dimethyl labeling approach, *Anal. Chem.* 83 (2011) 7755–7762.
- [52] L. Valledor, J. Jorin, Back to the basics: maximizing the information obtained by quantitative two dimensional gel electrophoresis analyses by an appropriate experimental design and statistical analyses, *J. Proteome* 74 (2011) 1–18.
- [53] M. Mann, Functional and quantitative proteomics using SILAC, *Nat. Rev. Mol. Cell Biol.* 7 (2006) 952–958.
- [54] J.H. Yoon, J. Kim, K.L. Kim, D.H. Kim, S.J. Jung, H. Lee, J. Ghim, D. Kim, J.B. Park, S.H. Ryu, T.G. Lee, Proteomic analysis of hypoxia-induced U373MG glioma secretome reveals novel hypoxia-dependent migration factors, *Proteomics* 14 (2014) 1494–1502.
- [55] B. Busser, L. Sancey, E. Brambilla, J.L. Coll, A. Hurbini, The multiple roles of amphiregulin in human cancer, *Biochim. Biophys. Acta* 1816 (2011) 119–131.
- [56] R. Pathania, S. Ramachandran, S. Elangovan, R. Padia, P. Yang, S. Cinghu, R. Veeranan-Karmegam, P. Arjunan, J.P. Gnana-Prakasam, F. Sadanand, L. Pei, C.S. Chang, J.H. Choi, H. Shi, S. Manicassamy, P.D. Prasad, S. Sharma, V. Ganapathy, R. Jothi, M. Thangaraju, DNMT1 is essential for mammary and cancer stem cell maintenance and tumorigenesis, *Nat. Commun.* 6 (2015) 6910.
- [57] J. Dufraigne, Y. Funahashi, J. Kitajewski, Notch signaling regulates tumor angiogenesis by diverse mechanisms, *Oncogene* 27 (2008) 5132–5137.
- [58] J. Lesley, R. Hyman, N. English, J.B. Catterall, G.A. Turner, CD44 in inflammation and metastasis, *Glycoconj. J.* 14 (1997) 611–622.
- [59] S.R. Davies, C. Dent, G. Watkins, J.A. King, K. Mokbel, W.G. Jiang, Expression of the cell to cell adhesion molecule, ALCAM, in breast cancer patients and the potential link with skeletal metastasis, *Oncol. Rep.* 19 (2008) 555–561.
- [60] R. Yamaji, K. Fujita, S. Takahashi, H. Yoneda, K. Nagao, W. Masuda, M. Naito, T. Tsuruo, K. Miyatake, H. Inui, Y. Nakano, Hypoxia up-regulates glyceraldehyde-3-phosphate dehydrogenase in mouse brain capillary endothelial cells: involvement of Na<sup>+</sup>/Ca<sup>2+</sup> exchanger, *Biochim. Biophys. Acta* 1593 (2003) 269–276.
- [61] Y. Higashimura, Y. Nakajima, R. Yamaji, N. Harada, F. Shibasaki, Y. Nakano, H. Inui, Up-regulation of glyceraldehyde-3-phosphate dehydrogenase gene expression by HIF-1 activity depending on Sp1 in hypoxic breast cancer cells, *Arch. Biochem. Biophys.* 509 (2011) 1–8.
- [62] W.R. Wilson, M.P. Hay, Targeting hypoxia in cancer therapy, *Nat. Rev. Cancer* 11 (2011) 393–410.
- [63] B. Dutta, R. Yan, S.K. Lim, J.P. Tam, S.K. Sze, Quantitative profiling of chromatome dynamics reveals a novel role for HP1BP3 in hypoxia-induced oncogenesis, *Mol. Cell. Proteomics* 13 (2014) 3236–3249.
- [64] W.Y. Chen, W.J. Liu, Y.P. Zhao, L. Zhou, T.P. Zhang, G. Chen, H. Shu, Induction, modulation and potential targets of miR-210 in pancreatic cancer cells, *Hepatobiliary Pancreat. Dis. Int.* 11 (2012) 319–324.
- [65] J. Hu, T. Sun, H. Wang, Z. Chen, S. Wang, L. Yuan, T. Liu, H.R. Li, P. Wang, Y. Feng, Q. Wang, R.E. McLendon, A.H. Friedman, S.T. Keir, D.D. Bigner, J. Rathmell, X.D. Fu, Q.J. Li, H. Wang, X.F. Wang, MiR-215 is induced post-transcriptionally via HIF-drosha complex and mediates glioma-initiating cell adaptation to hypoxia by targeting KDM1B, *Cancer Cell* 29 (2016) 49–60.
- [66] K.D. Meyer, D.P. Patil, J. Zhou, A. Zinoviev, M.A. Skabkin, O. Elemento, T.V. Pestova, S.B. Qian, S.R. Jaffrey, 5' UTR m(6A) promotes cap-independent translation, *Cell* 163 (2015) 999–1010.
- [67] P. Saraon, N. Musrap, D. Cretu, G.S. Karagiannis, I. Batruch, C. Smith, A.P. Drabovich, D. Trudel, T. van der Kwast, C. Morrissey, K.A. Jarvi, E.P. Diamandis, Proteomic profiling of androgen-independent prostate cancer cell lines reveals a role for protein S during the development of high grade and castration-resistant prostate cancer, *J. Biol. Chem.* 287 (2012) 34019–34031.
- [68] A. Marimuthu, Y. Subbannayya, N.A. Sahasrabudhe, L. Balakrishnan, N. Syed, N.R. Sekhar, T.V. Katte, S.M. Pinto, S.M. Srikanth, P. Kumar, H. Pawar, M.K. Kashyap, J. Maharudraiah, H. Ashktorab, D.T. Smoot, G. Ramaswamy, R.V. Kumar, Y. Cheng, S.J. Meltzer, J.C. Roa, R. Chaerkady, T.S. Prasad, H.C. Harsha, A. Chatterjee, A. Pandey, SILAC-based quantitative proteomic analysis of gastric cancer secretome, *Proteomics Clin. Appl.* 7 (2013) 355–366.
- [69] G. Abboud-Jarrous, S. Priya, A. Maimon, S. Fischman, M. Cohen-Elisha, R. Czerninski, T. Burstyn-Cohen, Protein S drives oral squamous cell carcinoma tumorigenicity through regulation of AXL, *Oncotarget* 8 (2017) 13986–14002.
- [70] G. Tai, P. Ranjzad, F. Marriage, S. Rehman, H. Denley, J. Dixon, K. Mitchell, P.J. Day, A.S. Woolf, Cytokeratin 15 marks basal epithelia in developing ureters and is upregulated in a subset of urothelial cell carcinomas, *PLoS One* 8 (2013) e81167.
- [71] G. Wang, W. Shen, L. Cui, W. Chen, X. Hu, J. Fu, Overexpression of Anillin (ANLN) is correlated with colorectal cancer progression and poor prognosis, *Cancer Biomark.* 16 (2016) 459–465.
- [72] R. Kujawski, K. Przybyłowska-Sygut, M. Mik, M. Lewandowski, R. Trzcinski, M. Berut, L. Dziki, I. Majsterek, A. Dziki, Expression of the PLS3 gene in circulating cells in patients with colorectal cancer, *Pol. Przegl. Chir.* 87 (2015) 59–64.
- [73] G.N. Masoud, W. Li, HIF-1 $\alpha$  pathway: role, regulation and intervention for cancer therapy, *Acta Pharm. Sin. B* 5 (2015) 378–389.



# Correlation between attention-deficit/hyperactivity disorder, its pharmacotherapy and thyroid dysfunction: A nationwide population-based study in Taiwan

Po-Hao Chen<sup>1</sup> | Yu-Chiau Shyu<sup>2,3,4</sup> | Meng-Yun Tsai<sup>5</sup> | Sheng-Yu Lee<sup>6,7</sup> |  
Kang-Chung Yang<sup>2</sup> | Chun-Ju Yang<sup>8,2</sup> | Tung-Liang Lee<sup>9</sup> | Liang-Jen Wang<sup>10</sup> 

<sup>1</sup>Department of Psychiatry, Kaohsiung Chang Gung Memorial Hospital and Chang Gung University College of Medicine, Kaohsiung, Taiwan

<sup>2</sup>Community Medicine Research Center, Keelung Chang Gung Memorial Hospital, Keelung, Taiwan

<sup>3</sup>Institute of Molecular Biology, Academia Sinica, Taipei, Taiwan

<sup>4</sup>Department of Nursing, Department of Nutrition and Health Sciences, Research Center for Food and Cosmetic Safety, and Research Center for Chinese Herbal Medicine, College of Human Ecology, Chang Gung University of Science and Technology, Kaohsiung, Taiwan

<sup>5</sup>Department of Internal Medicine, Kaohsiung Chang Gung Memorial Hospital and Chang Gung University College of Medicine, Kaohsiung, Taiwan

<sup>6</sup>Department of Psychiatry, Kaohsiung Veterans General Hospital, Kaohsiung, Taiwan

<sup>7</sup>Department of Psychiatry, College of Medicine, Graduate Institute of Medicine, School of Medicine, Kaohsiung Medical University, Kaohsiung, Taiwan

<sup>8</sup>Institute of Biopharmaceutical Sciences, National Yang-Ming University, Taipei, Taiwan

<sup>9</sup>Department of Radiation Oncology, University of Texas MD Anderson Cancer Center, Houston, Texas

<sup>10</sup>Department of Child and Adolescent Psychiatry, Kaohsiung Chang Gung Memorial Hospital and Chang Gung University College of Medicine, Kaohsiung, Taiwan

**Correspondence:** Liang-Jen Wang, Department of Child and Adolescent Psychiatry, Kaohsiung Chang Gung Memorial Hospital, No.123, Ta-Pei Road, Kaohsiung City, Taiwan (wangliangjen@gmail.com).

## Funding information

This study was sponsored by the Chang Gung Memorial Hospital Research Projects (CMRPG8D0581, CMRPG2G0072, CLRPG2G0081 and CMRPG2F0452).

## Summary

**Objective:** The aim of this study was to examine the comorbid rates of thyroid dysfunction among patients with attention-deficit/hyperactivity disorder (ADHD) and the general population. We further examined whether pharmacotherapy affects ADHD patients' risk of developing thyroid dysfunction.

**Design and Measurement:** We recruited 75 247 newly diagnosed ADHD patient and 75 247 healthy controls between January 1999 and December 2011 from the National Health Insurance database in Taiwan. We compared hyperthyroidism, hypothyroidism and other common paediatric psychiatric diseases between ADHD patients and controls. We carried out logistic regression analysis to identify an independent factor for predicting thyroid dysfunction. Furthermore, we analysed the time sequence of the diagnosis and the risk of developing a thyroid disorder after receiving pharmacotherapy.

**Results:** Compared to the control group, the ADHD group had higher comorbidity rates of both hyperthyroidism (1.1% of ADHD vs 0.7% of controls, aOR: 1.72,  $P < 0.001$ ) and hypothyroidism (0.6% of ADHD vs 0.2% of controls, aOR: 2.23,  $P < 0.001$ ). Of the ADHD patients with comorbid thyroid dysfunction, about two-thirds and half of patients were diagnosed with ADHD prior to their diagnosis of hyperthyroidism and hypothyroidism, respectively. Furthermore, pharmacotherapy had

no significant influence on the risk of developing hyperthyroidism (aHR: 1.09,  $P = 0.363$ ) or hypothyroidism (aHR: 0.95,  $P = 0.719$ ) among ADHD patients.

**Conclusion:** Patients with ADHD had greater comorbid rates with thyroid dysfunction than the control subjects, but pharmacotherapy for treating ADHD did not affect thyroid dysfunction later in life. However, these findings should be further verified using a clinical cohort with comprehensive laboratory assessment in future.

#### KEYWORDS

ADHD, comorbidity, epidemiology, medication, thyroid dysfunction

## 1 | INTRODUCTION

Attention-deficit/hyperactivity disorder (ADHD) affects 5%-8% of children worldwide.<sup>1</sup> This disorder is characterized by difficulty sustaining attention, an inability to control impulses and an inability to present proper behaviours for specific situations. The aetiology of ADHD is still not completely understood. The endocrine system is associated with the neurological development and behaviour of children. Within the endocrine system, thyroid dysfunction (both hyperthyroidism and hypothyroidism) commonly exhibits behavioural and cognitive symptoms.<sup>2</sup> Molecular mechanisms underlie the various effects of the thyroid hormone on proliferation, differentiation, migration, synaptogenesis and myelination in the developing nervous system.<sup>3</sup>

In the past, studies have explored the relationship between thyroid function and ADHD, but the findings have varied.<sup>4-10</sup> Weiss et al<sup>4</sup> found that the prevalence of thyroid abnormalities is higher (5.4%) in children with ADHD than in the general population (<1%). Furthermore, Kuppli et al<sup>11</sup> indicated that serum levels of thyroxine (T4) were significantly lower in children with ADHD compared with those in healthy control subjects. One previous study reported that patients with X-linked IGSF1 deficiency syndrome, who were characterized by central hypothyroidism, demonstrated attention defects and lower energy.<sup>12</sup> However, many studies have found no association between thyroid dysfunction and ADHD and have disputed the suggestion that thyroid function should be routinely screened for in ADHD children.<sup>5-8</sup> Furthermore, Soldin et al<sup>13</sup> reported that neonatal thyroxine levels had no correlation with the subsequent risk of developing ADHD. However, Alvarez-Pedrerol et al<sup>14</sup> reported that high thyroid-stimulating hormone (TSH) concentrations are associated with a lower cognitive function, and high TSH and low free T4 are linked to ADHD symptoms in healthy preschoolers. Meanwhile, dysregulated thyroxine and TSH concentrations are also related to mood symptoms and the severity of children's behavioural symptoms.<sup>9,10,15</sup>

Over the past decade, studies have turned their focus on gestational thyroid hormones in infants. Thyroid dysfunction during pregnancy has been found to influence the neurodevelopment of neonates, especially before mid-gestation, at which point the thyroid gland of the foetus begins to mature, consequently causing behavioural and psychiatric disorders<sup>16</sup> or ADHD.<sup>17-20</sup> Maternal thyroid

dysfunction has been regarded as an independent risk factor that exposes children to the potential of developing ADHD,<sup>19,21,22</sup> while one study recognized maternal thyroid dysfunction as only being related to the development of inattention in female children.<sup>23</sup> Many polluting chemical substances can interfere with thyroid hormone (TH) metabolism, which may lead to abnormalities in the neurological development of a foetus or child.<sup>24</sup> However, maternal thyroxine supplement during pregnancy did not improve children's cognitive function.<sup>25</sup>

Pharmacotherapy is an effective treatment option for ADHD. Pharmacotherapy works by enhancing catecholamine function (dopamine or norepinephrine) in the brain. Whether pharmacotherapy affects the endocrine system has been the subject of considerable debate. Bereket et al<sup>26</sup> reported that during a 4-month stimulant treatment, they observed decreasing levels of serum T4 and free-T4 and increasing levels of TSH in children with ADHD, although the pre- and post-treated levels of T4, free-T4 and TSH were maintained within normal limits. ADHD medication influences the function of dopaminergic neurotransmitters at the hypothalamic level<sup>27</sup> and may also affect thyroid function.

Hyperthyroidism is a condition in which the thyroid gland is overactive and makes excessive amounts of thyroid hormone. In contrast, hypothyroidism refers to the thyroid gland not making enough thyroid hormone to keep the body functioning properly. However, no studies have used a large-scale database to investigate the relationship between hyperthyroidism or hypothyroidism and ADHD. Furthermore, it remains unclear whether ADHD treatment with medication influences thyroid function. Therefore, we conducted this nationwide population-based analysis to explain the co-occurrence rate of ADHD and thyroid dysfunction. We also examined whether pharmacotherapy may affect ADHD patients' risk of developing thyroid dysfunction.

## 2 | METHODS

### 2.1 | Data source

This study has been approved by the institutional review board of Chang Gung Memorial Hospital. We obtained data for this

study from the ambulatory claims database of the National Health Insurance Research Database of Taiwan (NHIRD-TW). First implemented in 1995, Taiwan's National Health Insurance (NHI) programme is a compulsory universal health insurance programme, and the Bureau of NHI is the single payer for healthcare services. The Bureau of NHI has contracted 93% of all health care providers in Taiwan, and at least 96% of insured people have used healthcare services once or more through those contracted hospitals and clinics since the programme's start. As of the end of 2008, 22.8 million people in Taiwan (more than 98% of the population) had been enrolled in the NHI programme. The contracted medical care institutions are required to electronically submit medical expense-related claim documents every month. The electronic claim forms include such information as the patient's gender, as well as the medical institution visited, diagnostic codes, the date of any prescriptions given, the drugs prescribed and any claimed medical expenses. The Bureau of NHI have medical experts regularly review the rationality of patients' diagnoses, prescribed drugs or disposal and to some extent also maintain the validity of the health insurance data. The reliability of diagnostic codes, medication use and health system utilization in the NHIRD has already been proven in a previous study.<sup>28,29</sup>

## 2.2 | Selection of ADHD patients

We studied all patients newly diagnosed with ADHD between January 1999 and December 2011 and whose records were found in the NHIRD-TW ( $N = 146\,063$ ). To reduce potential misdiagnosis, ADHD was defined as at least two NHI claims records with the International Classification of Diseases, 9th revision, Clinical Modifications (ICD-9-CM) code 314.X. The incidence of ADHD in this data set has been published previously, ADHD diagnosis rate among the study cohort increased from 0.11% in 2000 to 1.24% in 2011.<sup>30</sup> The prevalence in this study is similar to that of previous studies that have used the same research database.<sup>31,32</sup> The control group in this study was selected from another subset cohort of the NHIRD-TW, the Longitudinal Health Insurance Database 2000 (LHID2000). As all subjects in the LHID2000 were born before 31 December 1999, this database cannot be used to find a match for any ADHD patient born after 31 December 1999. Therefore, patients with ADHD born after 31 December 1999 were excluded ( $n = 70\,816$ ). After excluding these patients, our data set included 75 247 patients in the ADHD group. We defined the index date as the date when ADHD was first diagnosed, and the patients' medical records in the NHIRD-TW were followed through 31 December 2011.

## 2.3 | Selection of the control group

We selected the control group from another subset cohort of the NHIRD-TW, the LHID2000, which consists of the original claims data for one million beneficiaries randomly sampled from the 2000 Registry of Beneficiaries of the NHIRD-TW. The control subjects had

no ADHD diagnosis between 1 January 1996 and 3 December 2011. In this study, we used the propensity score matching technique to create a matching control with a ratio of 1:1 for the ADHD group. The propensity scores were determined using multivariate logistic regression analysis with gender and birth year as the confounding covariates.<sup>33,34</sup> We determined an index date for each matched control, which was established as the ADHD diagnosis date from its matching ADHD case. This study utilizes the aforementioned matched index dates to reduce potential temporal biases for subsequent survival analysis. The 75 247 controls were followed from this entry date until the end of the study period (31 December 2011).

## 2.4 | Comorbidities and outcomes

We further identified neurodevelopmental disorders commonly comorbid with ADHD, which are oppositional defiant disorder (ODD) (ICD-9-CM code 313.81), conduct disorder (ICD-9-CM code 312.X), autism spectrum disorder (ASD) (ICD-9-CM code 299.X) tic disorders (ICD-9-CM codes 307.2X), and intellectual disability (ICD-9-CM code 317 to 319). In our ADHD cohort, patients are mostly children and teenagers. They are mostly enrolled to the NHI after birth immediately and continued the insurance during the follow-up. Therefore, the death and emigration factors were not taken into account in the analysis.

Thyroid dysfunction was defined as having a diagnosis of thyrotoxicosis with or without a goitre (ICD-9-CM code 242.X), congenital hypothyroidism (ICD-9-CM code 243.X) or acquired hypothyroidism (ICD-9-CM code 244.X). Diagnoses of thyroid dysfunction and the date of diagnosis were identified based on insurance status and outpatient and hospitalization claims databases. We established a diagnosis of hyperthyroidism (ICD-9-CM code 242.X) and one of hypothyroidism (ICD-9-CM code 243.X or 244.X) as two different outcomes and analysed them separately.

## 2.5 | Definition of pharmacotherapy

Medications were acknowledged using the Anatomical Therapeutic Chemical classification system.<sup>35</sup> Methylphenidate (MPH) and atomoxetine (ATX) are two medications that have been approved by the NHI Bureau for treating ADHD in Taiwan. Patients treated with medication were defined as those who had any prescription record of MPH or ATX in an ambulatory care, pharmacy or hospital care claim. To explore the potential influence of pharmacotherapy on developing thyroid dysfunction in ADHD patients, we followed their medical records in the NHIRD-TW until 31 December 2011 or the development of a thyroid dysfunction. To prevent an immortal time bias,<sup>36</sup> we defined the index date as the date when ADHD medication was first prescribed in patients that received pharmacotherapy.

We also studied patients with hyperthyroidism and received treatment with carbimazole propylthiouracil or methimazole, and patients who were diagnosed with hypothyroidism and received treatment with levothyroxine.

## 2.6 | Statistical analysis

We used the Statistical Package for the Social Sciences (SPSS) version 16.0 (SPSS Inc., Chicago, IL, USA) to carry out all the statistical analyses in this study. We considered a two-tailed value of  $P < 0.05$  as statistically significant.

A chi-square ( $\chi^2$ ) test or *t*-test was adopted to compare characteristics between the ADHD group and the control group. Furthermore, we used a multivariate logistic regression model to examine the potential influence of ADHD on the comorbidity of thyroid dysfunction and controlled for the effects of age, gender and comorbidities. We treated a diagnosis of hyperthyroidism and one of hypothyroidism as two different outcomes and analysed them individually. We calculated the adjusted odds ratio (aOR) and 95% confidence interval (CI).

We then utilized the Cox regression model to estimate the potential influence of pharmacotherapy on the risk of developing thyroid dysfunction, controlling for the effects of age, gender and psychiatric comorbidities. The time function of the survival analysis was calculated as the number of days from the initial observation until 31 December 2011 (end of follow-up). To avoid the immortal time bias,<sup>36,37</sup> we set drug therapy as a time-dependent covariate in the Cox regression model and calculated both the adjusted hazard ratio (aHR) and the 95% confidence interval (CI).

We have further performed sensitivity analyses, in which the patients with hyperthyroidism were defined as ICD-code plus the drug prescription history. In the sensitivity analyses for hypothyroidism, hypothyroidism was defined as ICD-code plus the drug prescription history, and we excluded patients who had history of hyperthyroidism prior to the hypothyroidism diagnosis. We also used a multivariate logistic regression model to examine the association between ADHD and thyroid dysfunction, and we utilized the Cox regression model to estimate the potential influence of ADHD pharmacotherapy on the risk of developing thyroid dysfunction.

## 3 | RESULTS

Table 1 shows the characteristics of the ADHD group (mean age: 9.8 years, 79.4% male) and the control group (mean age: 10.2 years, 69.1% male). During the study period, 71.3% of ADHD patients received pharmacotherapy. Compared to the control group, the ADHD group had higher comorbidity rates of both hyperthyroidism (1.1% of ADHD vs 0.7% of controls) and hypothyroidism (0.6% of ADHD vs 0.2% of controls). The ages at which a patient was diagnosed with hyperthyroidism in the ADHD patient group were generally younger than those of the control group, while the ages when diagnosed with hypothyroidism did not differ significantly between the groups.

The multivariate logistic regression models, as shown in Table 2, demonstrate that ADHD patients were more likely to be diagnosed with hyperthyroidism (aOR, 1.72; 95% CI, 1.53-1.94) or

hypothyroidism (aOR, 2.23; 95% CI, 1.85-2.68) than the control subjects. Being female and an older recruitment age were collectively associated with the comorbidity of hyperthyroidism or hypothyroidism. Furthermore, subjects also diagnosed with a conduct disorder were associated with a greater risk of hyperthyroidism, while subjects diagnosed with an intellectual disability were associated with a greater risk of hypothyroidism.

Table 3 provides the time sequence of comorbid thyroid dysfunction diagnoses among ADHD patients. Of the ADHD patients who also had hyperthyroidism ( $n = 818$ ), 34.5% were diagnosed with hyperthyroidism prior to being diagnosed with ADHD, while 65.5% of patients were diagnosed with ADHD first. Of the ADHD patients who also had hypothyroidism ( $n = 439$ ), 50.1% were diagnosed with hypothyroidism prior to being diagnosed with ADHD, while 49.9% of patients received their ADHD diagnosis first.

We further examined the potential influence of pharmacotherapy on the risk of developing thyroid dysfunction (Table 4) in ADHD patients. Upon controlling for the effects of age, gender and psychiatric comorbidities, we found that pharmacotherapy did not significantly influence the risk of developing hyperthyroidism (aHR, 1.09; 95% CI, 0.90-1.32) or hypothyroidism (aHR, 0.95; 95% CI, 0.72-1.26). Among ADHD patients, being female and an older age at ADHD diagnosis were collectively associated with an increased risk of both hyperthyroidism and hypothyroidism. Having a conduct disorder was associated with a greater risk of hyperthyroidism diagnosis, while having an intellectual disability was associated with a greater risk of hypothyroidism diagnosis.

We found that approximately 19%-20% and 18%-22.5% of individuals diagnosed with hyperthyroidism/hypothyroidism received relevant drug therapy. The sensitivity analyses (outcomes defined as patients who had ICD-code of hyperthyroidism/hypothyroidism plus the drug prescription history) revealed similar results. Compared to the control group, the ADHD group had higher comorbidity rates of both hyperthyroidism (aOR: 3.29, 95% CI, 2.57-4.21) and hypothyroidism (aOR: 2.32, 95% CI, 1.55-3.46) (Table S1 found in the Supporting Information). Also, pharmacotherapy had no significant influence on the risk of developing hyperthyroidism (aHR: 1.12, 95% CI, 0.76-1.72) or hypothyroidism (aHR: 0.55, 95% CI, 0.24-1.28) among ADHD patients (Table S2 found in the Supporting Information).

## 4 | DISCUSSION

From our nationwide database, we found that ADHD patients were more likely to be comorbid with hyperthyroidism (1.72 fold) or with hypothyroidism (2.23 fold) than control subjects. These findings are consistent with those of Weiss et al<sup>4</sup> who reported that hypothyroidism is more frequent than hyperthyroidism in ADHD children. A greater incidence of abnormal thyroid function was noted within ADHD children.<sup>4,9-11</sup> Two previous studies have supported the relationship between lower free-T4 and inattention,<sup>4,10</sup> while two other studies indicated that free-T4 was only related to



**TABLE 1** Characteristics of patients with ADHD and control subjects in Taiwan from 2002 to 2011

Characteristics	ADHD (N = 75 247)	Controls (N = 75 247)	Statistics	P-value
Age at diagnosis or recruitment (y)	9.8 ± 4.0	10.2 ± 4.2	20.39	<0.001*
Gender				
Female	15 501 (20.6)	23 239 (30.9)	2081.39	<0.001*
Male	59 746 (79.4)	52 008 (69.1)		
Comorbidity				
Oppositional defiant disorder	4360 (5.8)	28 (0.0)	4405.16	<0.001*
Conduct disorder	4555 (6.1)	167 (0.2)	4209.71	<0.001*
Tic disorders	4905 (6.5)	609 (0.8)	3474.34	<0.001*
Autism spectrum disorder	6573 (8.7)	193 (0.3)	6299.23	<0.001*
Intellectual disability	10 724 (14.3)	699 (0.9)	9520.75	<0.001*
Received pharmacotherapy	53 674 (71.3)	74 (0.1)	83 148.31	<0.001*
Age at first prescription (y)	10.5 ± 3.6	12.0 ± 4.9	2.57	0.012*
Diagnosed hyperthyroidism	818 (1.1)	513 (0.7)	70.52	<0.001*
Age at diagnosis (y)	14.5 ± 5.2	15.5 ± 5.1	3.45	0.001*
Drug for treating hyperthyroidism <sup>a</sup>				
Carbimazole	48 (5.9)	35 (6.8)	0.491	0.483
Propylthiouracil	115 (14.1)	61 (11.9)	1.291	0.256
Methimazole	60 (7.3)	42 (8.1)	0.324	0.569
Any drug of above	159 (19.4)	100 (19.5)	0.001	0.980
Diagnosed hypothyroidism	439 (0.6)	182 (0.2)	106.80	<0.001*
Age at diagnosis (y)	10.8 ± 6.9	10.7 ± 6.5	0.18	0.857
Drug for treating hypothyroidism <sup>b</sup>				
Levothyroxine	78 (17.8)	41 (22.5)	1.882	0.170
Previous history of hyperthyroidism <sup>b</sup>	43 (9.8)	15 (8.2)	0.367	0.545

Data is expressed by n (%) or mean ± SD; Statistic values were expressed using Pearson's  $\chi^2$  or t using an independent t-test.

ADHD, attention-deficit hyperactivity disorder.

<sup>a</sup>Denominator is patients with diagnosis of hyperthyroidism.

<sup>b</sup>Denominator is patients with diagnosis of hypothyroidism.

\* $P < 0.05$ .

delinquent behaviour.<sup>9,11</sup> Still other studies showed no correlation between ADHD and thyroid dysfunction or TSH levels compared with the control group.<sup>5-8</sup> Hauser et al<sup>38</sup> divided affected individuals into two subgroups: inattention and hyperactivity/impulsivity. When diagnosed according to DSM-IV criteria, in which impulsivity is reassigned from the inattention to the hyperactivity category, the abnormal total T3 and total T4 only correlated to the hyperactivity/impulsivity subgroup. In Holtmann et al's<sup>15</sup> study of 114 children aged 4-17.7 years, those with a Child Behaviour Checklist Dysregulation Profile (CBCL-DP) greater than 2.5 SD were found to have a higher serum TSH, but no differences were found in serum free T3 and free T4 levels. In general, the incidence of thyroid dysfunction did not differ significantly between non-familial ADHD children and the general population, and therefore, routine thyroid hormone screening has not been suggested.<sup>5,7,8</sup>

Thyroid hormone concentration's effect on neonatal neurocognitive function has been proven in Simic's study.<sup>39</sup> The fundamental role of thyroid hormones on the development of monoaminergic and cholinergic neurotransmitter systems was noted in attention deficit

in an animal model,<sup>40</sup> but the results have not been replicated in human trials. A greater prevalence of comorbid ADHD in children with generalized resistance to thyroid hormone (GRTH) has been found in two previous studies.<sup>4,41</sup> Children with GRTH have an incidence rate of 5.4% of being comorbid with ADHD, compared with <1% in the general population.<sup>4</sup> However, children with GRTH are relatively rare, even within the ADHD population.<sup>6</sup> In Joustra's study of patients with IGSF1 deficiency syndrome that manifest central hypothyroidism, a mild defect in attentional control and reduced activities were recorded.<sup>12</sup> The two symptoms resemble the inattentive presentation of ADHD. Stein et al<sup>42</sup> compared ADHD patients with and those without resistance to thyroid hormone (RTH). Although their behavioural index was similar on the Conners Parent questionnaire, ADHD patients with RTH performed significantly worse in wide-ranging achievement tests, indicating a weaker perceptual-organization ability and school performance within this group.

In our study population, the prevalence of hyperthyroidism and hypothyroidism was 0.7%-1.1% and 0.2%-0.6%, respectively. In comparison with international data, a nationwide study revealed

**TABLE 2** Logistic regression models for the risk of diagnosis with thyroid dysfunction among youths in Taiwan

Variables	Hyperthyroidism			Hypothyroidism		
	n/N (%)	aOR (95% CI)	P-value	n/N (%)	aOR (95% CI)	P-value
Age at recruitment	-	1.13 (1.12-1.14)	<0.001*	-	1.07 (1.05-1.09)	<0.001*
Gender						
Female	518/38 740 (1.3)	1.97 (1.76-2.20)	<0.001*	244/38 740 (0.6)	2.05 (1.74-2.42)	<0.001*
Male	813/111 754 (0.7)	1		377/111 754 (0.3)	1	
ADHD						
With	818/75 247 (1.1)	1.72 (1.53-1.94)	<0.001*	439/75 247 (0.6)	2.23 (1.85-2.68)	<0.001*
Without	513/75 247 (0.7)	1		182/75 247 (0.2)	1	
ODD						
With	42/4388 (1.0)	0.94 (0.68-1.28)	0.677	19/4388(0.4)	0.85 (0.53-1.35)	0.481
Without	1289/146 106 (0.9)	1		602/146 106 (0.4)	1	
Conduct disorder						
With	73/4722 (1.5)	1.54 (1.21-1.97)	0.001*	27/4722 (0.6)	0.96 (0.65-1.42)	0.829
Without	1258/145 772 (0.9)	1		594/145 772 (0.4)	1	
Tic disorders						
With	51/5514 (0.9)	1.12 (0.84-1.49)	0.434	32/5514 (0.6)	1.27 (0.89-1.83)	0.191
Without	1280/144 980 (0.9)	1		589/144 980 (0.4)	1	
ASD						
With	58/6766 (0.9)	1.02 (0.78-1.35)	0.866	48/6766 (0.7)	1.15 (0.84-1.57)	0.398
Without	1273/143 728 (0.9)	1		573/143 728 (0.4)	1	
Intellectual disability						
With	111/11 423 (1.0)	0.97 (0.79-1.19)	0.786	128/11 423 (1.1)	2.38 (1.92-2.94)	<0.001*
Without	1220/139 071 (0.9)	1		493/139 071 (0.4)	1	

95% CI, 95% confidence interval; ADHD, attention-deficit hyperactivity disorder; aOR, adjusted odds ratios; ASD, autism spectrum disorder; n, number of diagnosed thyroid dysfunction; ODD, oppositional defiant disorder.

\* $P < 0.05$ .

that incidence of juvenile thyrotoxicosis ranged from 1.31 to 1.83/100 000 person-years during 1982-2012.<sup>43</sup> A review article indicated that congenital hypothyroidism occurs in one in 1500-3000 newborns.<sup>44</sup> And the prevalence of autoimmune hypothyroidism in childhood is an estimated 1%-2%.<sup>45</sup> The prevalence both hyperthyroidism and hypothyroidism in our cohort varied with the reported figures elsewhere for children of this age.<sup>46</sup> Some methodological issues might be related to the discrepancies. First, race/ethnicity differences had been observed in the prevalence of thyrotoxicosis.<sup>47</sup> Second, our rates of hyperthyroidism and hypothyroidism

represented prevalence rates, but some international studies reported incidence rates.<sup>43,44</sup> In addition, our study population was patients who had used medical service; therefore, the prevalence of hyperthyroidism/hypothyroidism could be higher than which investigated in communities.

Furthermore, we reviewed the timing of ADHD diagnosis and thyroid dysfunction in those subjects with comorbid diseases. Given that ADHD frequently predates the thyroid diagnosis, it may be attributed to that clinicians might routinely screen thyroid function for children with neuropsychiatric symptoms. This ascertainment bias may influence the results. Interestingly, in subjects comorbid with hyperthyroidism, two-thirds were diagnosed with ADHD prior to hyperthyroidism. However, in subjects comorbid with hypothyroidism, only half of the patients were diagnosed with ADHD prior to hypothyroidism. This result may be due to the diagnosis of ADHD being based on the observation of symptoms. ADHD children comorbid with hyperthyroidism were more likely to display labile mood and social misbehaviours,<sup>10</sup> thus increasing the burden of care on their parents and teachers; as a result, such caregivers may seek psychiatric help before a thyroid scan. In contrast, ADHD subjects comorbid with hypothyroidism were more likely to present inattention,

**TABLE 3** Time sequence of receiving diagnoses among patients who had a comorbidity of ADHD and thyroid dysfunction

Time sequence of receiving diagnoses	Hyperthyroidism (N = 818)	Hypothyroidism (N = 439)
	n (%)	n (%)
Thyroid dysfunction diagnosis prior to ADHD	282 (34.5)	220 (50.1)
ADHD diagnosis prior to thyroid dysfunction	536 (65.5)	219 (49.9)

**TABLE 4** Relationships of pharmacotherapy and diagnoses of thyroid dysfunction among patients with ADHD, controlling for sex, age and psychiatric comorbidities

Variables	Hyperthyroidism			Hypothyroidism		
	n/N (%)	aHR (95% CI)	P-value	n/N (%)	aHR (95% CI)	P-value
Pharmacotherapy						
With	611/53 674 (1.1)	1.09 (0.90-1.32)	0.363	311/53 674 (0.6)	0.95 (0.72-1.26)	0.719
Without	207/21 573 (1.0)	1		128/	21 573 (0.6)	1
Age at ADHD diagnosis	-	1.14 (1.12-1.16)	<0.001*	-	1.11 (1.08-1.15)	<0.001*
Gender						
Female	305/15 501 (2.0)	2.15 (1.79-2.57)	<0.001*	160/15 501 (1.0)	2.69 (2.05-3.53)	<0.001*
Male	513/59 746 (0.9)	1		279/59 746 (0.5)	1	
ODD						
With	42/4360 (1.0)	1.09 (0.76-1.57)	0.647	19/4360 (0.4)	1.03 (0.56-1.91)	0.918
Without	776/70 887 (1.1)	1		420/70 887 (0.6)	1	
Conduct disorder						
With	72/4555 (1.6)	1.53 (1.15-2.03)	0.003*	30/4905 (0.6)	1.10 (0.66-1.81)	0.721
Without	746/70 692 (1.1)	1		409/70 342 (0.6)	1	
Tic disorders						
With	47/4905 (1.0)	1.31 (0.94-1.82)	0.108	26/4555 (0.6)	1.59 (0.99-2.56)	0.054
Without	771/70 342 (1.1)	1		413/70 692 (0.6)	1	
ASD						
With	57/6573 (0.9)	1.05 (0.77-1.43)	0.776	47/6573 (0.7)	1.25 (0.82-1.91)	0.295
Without	761/68 674 (1.1)	1		392/68 674 (0.6)	1	
Intellectual disability						
With	99/10 724 (0.9)	0.80 (0.62-1.02)	0.073	119/10 724 (1.1)	1.65 (1.20-2.26)	0.002*
Without	719/64 523 (1.1)	1		320/64 523 (0.5)	1	

95% CI, 95% confidence interval; ADHD, attention-deficit hyperactivity disorder; aHR, adjusted hazards ratios; ASD, autism spectrum disorder; n, number of diagnosed thyroid dysfunction; ODD, oppositional defiant disorder.

\* $P < 0.05$ .

withdrawal and social isolation<sup>10</sup> and therefore may easily be neglected until a significant academic performance delay is noticed. Meanwhile, these patients are more likely to undergo physical examination before being transferred to a psychiatric department. It is noticeable that the children with ADHD were more likely to receive medical information and hospital contact, and frequent diagnosis of milder degrees of thyroid dysfunction. This sampling bias could inflate the comorbidity rate of ADHD and thyroid dysfunction, and it should be cautious to explain the study results.

In our study, we observed no significant difference of incidence in either hyperthyroidism or hypothyroidism between patients with and without pharmacotherapy. This finding agrees with that of Bereket et al<sup>26</sup> reporting that thyroid levels were within normal limits after 4 months of methylphenidate treatment in ADHD patients. We found no evidence that the use of methylphenidate in ADHD subjects would cause secondary thyroid dysfunction, although a more precise case-control study should be conducted in the future. Moreover, we found that approximate 19%-20% and 18%-22.5% of individuals diagnosed with hyperthyroidism/hypothyroidism

received relevant drug therapy. This finding indicated that only a proportion of patients with hyperthyroidism/hypothyroidism who exhibited certain clinical manifestations received drug therapy. But the sensitivity analyses (ICD-code plus drug prescription history) still revealed that drug therapy for treating thyroid dysfunction did not confound the association between ADHD, its pharmacotherapy and the risk of developing hyperthyroidism or hypothyroidism.

This study has a number of limitations that should be mentioned at this point. First of all, this study is based on reimbursement data from NHIRD-TW, and thus, the diagnosis of ADHD was identified according to ICD records, instead of being validated using structural diagnostic instruments. Therefore, the classification of ADHD may not be rigorous enough. Second, the database did not show the severity of the symptoms of affected individuals, and clinically severe patients are more likely to receive pharmacotherapy. Due to the baseline differences between the patients receiving pharmacotherapy and those who did not, the ability to declare a disconnect between ADHD medication and the development of thyroid dysfunction was limited. Third, the assessment of thyroid dysfunction

was made according to ICD records, so this study lacks laboratory data related to thyroid function. Therefore, we were unable to validate the diagnostic accuracy of hyperthyroidism and hypothyroidism using laboratory data. Fourth, several factors which may be relevant to a diagnosis of ADHD, such as socio-economic class, parental education and parental income, were undetectable in the claims data. The results of our study might have been confounded by these factors. Finally, despite applying a propensity score matching strategy, significant differences in raw data were still found among the ADHD group and control group. This matter was the result of the recruited number being so large, so the LHID 2000 cohort could not provide enough perfectly matched controls to the given criteria.

In conclusion, we propose that patients with ADHD had greater comorbid rates with hyperthyroidism or hypothyroidism than the control subjects. Nevertheless, receiving pharmacotherapy did not significantly influence the risk of developing thyroid dysfunction among ADHD patients. Clinicians should pay attention to identify potential thyroid dysfunction among ADHD patients, and caregivers and patients with ADHD can be reassured that pharmacotherapy will have no effect on their thyroid function later in life. However, the findings in this study should be further verified using a clinical cohort with comprehensive laboratory assessment in future.

## ACKNOWLEDGEMENT

Po-Hao Chen and Yu-Chiau Shyu are co-first authors and contributed equally to this manuscript. This study is based in part on data from the NHIRD-TW provided by the National Health Insurance Administration, Ministry of Health and Welfare and managed by the National Health Research Institutes (registration number: NHIRD-102-088). The interpretations and conclusions contained herein do not represent those of the National Health Insurance Administration, Ministry of Health and Welfare or National Health Research Institutes.

## CONFLICTS OF INTEREST

The authors declare that there are no competing interests.

## ORCID

Liang-Jen Wang  <http://orcid.org/0000-0002-5320-1151>

## REFERENCES

1. Thomas R, Sanders S, Doust J, Beller E, Glasziou P. Prevalence of attention-deficit/hyperactivity disorder: a systematic review and meta-analysis. *Pediatrics*. 2015;135:e994-e1001.
2. Segni M. Disorders of the thyroid gland in infancy, childhood and adolescence. In: De Groot LJ, Chrousos G, Dungan K, et al., eds. *Endotext*. South Dartmouth, MA: MDText.com, Inc; 2000.
3. Preau L, Fini JB, Morvan-Dubois G, Demeneix B. Thyroid hormone signaling during early neurogenesis and its significance as a vulnerable window for endocrine disruption. *Biochim Biophys Acta*. 2015;1849:112-121.
4. Weiss RE, Stein MA, Trommer B, Refetoff S. Attention-deficit hyperactivity disorder and thyroid function. *J Pediatr*. 1993;123:539-545.
5. Elia J, Gulotta C, Rose SR, Marin G, Rapoport JL. Thyroid function and attention-deficit hyperactivity disorder. *J Am Acad Child Adolesc Psychiatry*. 1994;33:169-172.
6. Spencer T, Biederman J, Wilens T, Guite J, Harding M. ADHD and thyroid abnormalities: a research note. *J Child Psychol Psychiatry*. 1995;36:879-885.
7. Valentine J, Rossi E, O'Leary P, Parry TS, Kurinczuk JJ, Sly P. Thyroid function in a population of children with attention deficit hyperactivity disorder. *J Paediatr Child Health*. 1997;33:117-120.
8. Toren P, Karasik A, Eldar S, et al. Thyroid function in attention deficit and hyperactivity disorder. *J Psychiatr Res*. 1997;31:359-363.
9. Cakaloz B, Akay AP, Bober E, Yulug B. Thyroid function and oppositional defiant disorder: more than a coincidence in prepubertal boys with attention-deficit hyperactivity disorder? *J Neuropsychol Clin Neurosci*. 2011;23(2):E9-E10.
10. Stein MA, Weiss RE. Thyroid function tests and neurocognitive functioning in children referred for attention deficit/hyperactivity disorder. *Psychoneuroendocrinology*. 2003;28:304-316.
11. Kuppi PP, Pattanayak RD, Sagar R, Mehta M, Vivekanandhan S. Thyroid and cortisol hormones in attention deficit hyperactivity disorder: a case-control study. *Asian J Psychiatr*. 2017;28:73-77.
12. Joustra SD, Andela CD, Oostdijk W, et al. Mild deficits in attentional control in patients with the IGSF1 deficiency syndrome. *Clin Endocrinol (Oxf)*. 2016;84:896-903.
13. Soldin OP, Nandedkar AK, Japal KM, et al. Newborn thyroxine levels and childhood ADHD. *Clin Biochem*. 2002;35:131-136.
14. Alvarez-Pedrerol M, Ribas-Fito N, Torrent M, Julvez J, Ferrer C, Sunyer J. TSH concentration within the normal range is associated with cognitive function and ADHD symptoms in healthy preschoolers. *Clin Endocrinol (Oxf)*. 2007;66:890-898.
15. Holtmann M, Duketis E, Goth K, Poustka L, Boelte S. Severe affective and behavioral dysregulation in youth is associated with increased serum TSH. *J Affect Disord*. 2010;121:184-188.
16. Fetene DM, Betts KS, Alati R. MECHANISMS IN ENDOCRINOLOGY: Maternal thyroid dysfunction during pregnancy and behavioural and psychiatric disorders of children: a systematic review. *Eur J Endocrinol*. 2017;177:R261-R273.
17. Vermiglio F, Lo Presti VP, Moleti M, et al. Attention deficit and hyperactivity disorders in the offspring of mothers exposed to mild-moderate iodine deficiency: a possible novel iodine deficiency disorder in developed countries. *J Clin Endocrinol Metab*. 2004;89:6054-6060.
18. Andersen SL, Laurberg P, Wu CS, Olsen J. Attention deficit hyperactivity disorder and autism spectrum disorder in children born to mothers with thyroid dysfunction: a Danish nationwide cohort study. *BJOG*. 2014;121:1365-1374.
19. Mathew JL, Mukherjee SB, Sukumar SP, Bhadada S. Maternal mild thyroid insufficiency and risk of attention deficit hyperactivity disorder: evidence-based medicine viewpoint. *Indian Pediatr*. 2015;52:797-800.
20. Oostenbroek MHW, Kersten RHJ, Tros B, Kunst AE, Vrijkotte TGM, Finken MJJ. Maternal hypothyroxinaemia in early pregnancy and problem behavior in 5-year-old offspring. *Psychoneuroendocrinology*. 2017;81:29-35.
21. Modesto T, Tiemeier H, Peeters RP, et al. Maternal mild thyroid hormone insufficiency in early pregnancy and attention-deficit/hyperactivity disorder symptoms in children. *JAMA Pediatr*. 2015;169:838-845.
22. Ghassabian A, Bongers-Schokking JJ, de Rijke YB, et al. Maternal thyroid autoimmunity during pregnancy and the risk of attention

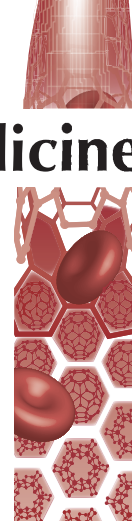


- deficit/hyperactivity problems in children: the Generation R Study. *Thyroid*. 2012;22:178-186.
23. Pakkila F, Mannisto T, Pouta A, et al. The impact of gestational thyroid hormone concentrations on ADHD symptoms of the child. *J Clin Endocrinol Metab*. 2014;99:E1-E8.
  24. Ozzola G. Pollution, the thyroid and neurodevelopment. *Clin Ter*. 2016;167:191-197.
  25. Hales C, Taylor PN, Channon S, et al. Controlled antenatal thyroid screening II: effect of treating maternal sub-optimal thyroid function on child cognition. *J Clin Endocrinol Metab*. 2018;103:1583-1591.
  26. Bereket A, Turan S, Karaman MG, Haklar G, Ozbay F, Yazgan MY. Height, weight, IGF-I, IGFBP-3 and thyroid functions in prepubertal children with attention deficit hyperactivity disorder: effect of methylphenidate treatment. *Horm Res*. 2005;63:159-164.
  27. Boesgaard S, Hagen C, Andersen AN, Eldrup E, Lange P. Effect of Fenoldopam, A Dopamin D-1 receptor agonist, On Thyroid Hormone Secretion. *Clin Endocrinol*. 1989;30:231-239.
  28. Wu CS, Lai MS, Gau SS, Wang SC, Tsai HJ. Concordance between patient self-reports and claims data on clinical diagnoses, medication use, and health system utilization in Taiwan. *PLoS One*. 2014;9:e112257.
  29. Yu ST, Chang HY, Lin MC, Lin YH. Agreement between self-reported and health insurance claims on utilization of health care: a population study. *J Clin Epidemiol*. 2009;62:1316-1322.
  30. Wang LJ, Lee SY, Yuan SS, et al. Prevalence rates of youths diagnosed with and medicated for ADHD in a nationwide survey in Taiwan from 2000 to 2011. *Epidemiol Psychiatr Sci*. 2017;26:624-634.
  31. Huang CL, Chu CC, Cheng TJ, Weng SF. Epidemiology of treated attention-deficit/hyperactivity disorder (ADHD) across the lifespan in Taiwan: a nationwide population-based longitudinal study. *PLoS One*. 2014;9:e95014.
  32. Huang CL, Weng SF, Ho CH. Gender ratios of administrative prevalence and incidence of attention-deficit/hyperactivity disorder (ADHD) across the lifespan: a nationwide population-based study in Taiwan. *Psychiatry Res*. 2016;244:382-387.
  33. Shyu YC, Yuan SS, Lee SY, et al. Attention-deficit/hyperactivity disorder, methylphenidate use and the risk of developing schizophrenia spectrum disorders: a nationwide population-based study in Taiwan. *Schizophr Res*. 2015;168:161-167.
  34. Lee MJ, Yang KC, Shyu YC, et al. Attention-deficit hyperactivity disorder, its treatment with medication and the probability of developing a depressive disorder: a nationwide population-based study in Taiwan. *J Affect Disord*. 2016;189:110-117.
  35. World Health Organization CCfDSM, ed. Guidelines for ATC Classification and DDD Assignment. Oslo, Norway; 2009.
  36. Suissa S. Immortal time bias in observational studies of drug effects. *Pharmacoepidemiol Drug Saf*. 2007;16:241-249.
  37. Suissa S. Immortal time bias in pharmaco-epidemiology. *Am J Epidemiol*. 2008;167:492-499.
  38. Hauser P, Soler R, Brucker-Davis F, Weintraub BD. Thyroid hormones correlate with symptoms of hyperactivity but not inattention in attention deficit hyperactivity disorder. *Psychoneuroendocrinology*. 1997;22:107-114.
  39. Simic N, Asztalos EV, Rovet J. Impact of neonatal thyroid hormone insufficiency and medical morbidity on infant neurodevelopment and attention following preterm birth. *Thyroid*. 2009;19:395-401.
  40. Jin ZZY, Zeng YW. Striatal neuronal loss or dysfunction and choline rise in children with attention-deficit hyperactivity disorder: a 1H-magnetic resonance spectroscopy study. *Neurosci Lett*. 2001;315:45-48.
  41. Hauser P, Zametkin AJ, Martinez P, et al. Attention deficit-hyperactivity disorder in people with generalized resistance to thyroid hormone. *N Engl J Med*. 1993;328:997-1001.
  42. Stein MA, Weiss RE, Refetoff S. Neurocognitive characteristics of individuals with resistance to thyroid hormone: comparisons with individuals with attention-deficit hyperactivity disorder. *J Dev Behav Pediatr*. 1995;16:406-411.
  43. Havgaard Kjaer R, Smedegard Andersen M, Hansen D. Increasing incidence of Juvenile Thyrotoxicosis in Denmark: a Nationwide Study, 1998-2012. *Horm Res Paediatr*. 2015;84:102-107.
  44. Wassner AJ, Brown RS. Congenital hypothyroidism: recent advances. *Curr Opin Endocrinol Diabetes Obes*. 2015;22:407-412.
  45. de Vries L, Bulvik S, Phillip M. Chronic autoimmune thyroiditis in children and adolescents: at presentation and during long-term follow-up. *Arch Dis Child*. 2009;94:33-37.
  46. Hanley P, Lord K, Bauer AJ. Thyroid disorders in children and adolescents: a review. *JAMA Pediatr*. 2016;170:1008-1019.
  47. McLeod DS, Cooper DS, Ladenson PW, Whiteman DC, Jordan SJ. Race/Ethnicity and the prevalence of thyrotoxicosis in young Americans. *Thyroid*. 2015;25:621-628.

## SUPPORTING INFORMATION

Additional supporting information may be found online in the Supporting Information section at the end of the article.

**How to cite this article:** Chen P-H, Shyu Y-C, Tsai M-Y, et al. Correlation between attention-deficit/hyperactivity disorder, its pharmacotherapy and thyroid dysfunction: A nationwide population-based study in Taiwan. *Clin Endocrinol (Oxf)*. 2018;89:496-504. <https://doi.org/10.1111/cen.13817>



# Decorating protein nanospheres with lactoferrin enhances oral COX-2 inhibitor/herbal therapy of hepatocellular carcinoma

Mona A Abdelmoneem<sup>1,2</sup>, Mazen Mahmoud<sup>3</sup>, Amira Zaky<sup>3</sup>, Maged W Helmy<sup>1,4</sup>, Marwa Sallam<sup>2</sup>, Jia-You Fang<sup>5,6,7</sup>, Kadria A Elkhodairy<sup>1,2</sup> & Ahmed O Elzoghby<sup>\*,1,2,8,9</sup>

<sup>1</sup>Cancer Nanotechnology Research Laboratory (CNRL), Faculty of Pharmacy, Alexandria University, Alexandria 21521, Egypt

<sup>2</sup>Department of Industrial Pharmacy, Faculty of Pharmacy, Alexandria University, Alexandria 21521, Egypt

<sup>3</sup>Department of Biochemistry, Faculty of Science, Alexandria University, Alexandria 21511, Egypt

<sup>4</sup>Department of Pharmacology & Toxicology, Faculty of Pharmacy, Damanhur University, Damanhur 22511, Egypt

<sup>5</sup>Pharmaceutics Laboratory, Graduate Institute of Natural Products, Chang Gung University, Taoyuan 333, Taiwan

<sup>6</sup>Research Center for Industry of Human Ecology & Research Center for Chinese Herbal Medicine, Chang Gung University of Science & Technology, Kweishan, Taoyuan 333, Taiwan

<sup>7</sup>Department of Anesthesiology, Chang Gung Memorial Hospital, Kweishan, Taoyuan 333, Taiwan

<sup>8</sup>Division of Engineering in Medicine, Brigham & Women's Hospital, Harvard Medical School, Boston, MA 02115, USA

<sup>9</sup>Harvard-MIT Division of Health Sciences and Technologies, Cambridge, MA 02139, USA

\*Author for correspondence: Tel.: +1 781 366 8703; [aelzoghby@bwh.harvard.edu](mailto:aelzoghby@bwh.harvard.edu)

**Aim:** Lactoferrin (LF)-targeted gliadin nanoparticles (GL-NPs) were developed for targeted oral therapy of hepatocellular carcinoma. **Materials & methods:** Celecoxib and diosmin were incorporated in the hydrophobic matrix of GL-NPs whose surface was decorated with LF by electrostatic interaction for binding to asialoglycoprotein receptors overexpressed by liver cancer cells. **Results:** Targeted GL-NPs showed enhanced cytotoxic activity and increased cellular uptake in liver tumor cells compared with nontargeted NPs. Moreover, they demonstrated superior *in vivo* antitumor effects including reduction in the expression levels of tumor biomarkers and induction of caspase-mediated apoptosis. *Ex vivo* imaging of isolated organs exhibited extensive accumulation of NPs in livers more than other organs. **Conclusion:** LF-targeted GL-NPs could be considered as an efficient nanoplatform for targeted oral drug delivery for liver cancer therapy.

First draft submitted: 19 April 2018; Accepted for publication: 10 July 2018; Published online: 22 October 2018

**Keywords:** COX-2 inhibitors • diosmin • gliadin nanoparticles • hepatocellular carcinoma • lactoferrin-targeting • oral delivery

Hepatocellular carcinoma (HCC) is one of the most malignant types of liver cancers [1]. Surgical resection is believed as the optimal treatment for HCC, but this is not always feasible as many patients are diagnosed in the late stage or underlying liver dysfunction. Moreover, traditional cytotoxic chemotherapy is not successful in improving the survival rate of liver cancer patients and is associated with significant toxicities due to the lack of tumor selectivity [2]. Nanoparticle (NP)-based drug carriers are employed to improve the therapeutic outcome of chemotherapeutic drugs through targeting the desired cells, which offers the potential for a successful HCC therapy [3–5].

Celecoxib (CXB), a nonsteroidal anti-inflammatory drug, selectively inhibits the COX-2 enzyme overexpressed in various cancer tissues. It was reported that COX-2 enzyme has an important contribution to hepatocarcinogenesis; thus, selective COX-2 inhibitors, for example, CXB showed antiproliferative and proapoptotic actions in HCC cells [6]. Moreover, selective COX-2 inhibitors (CXB) have been shown to act additionally through COX-2-independent mechanisms, indicating that CXB can be considered as efficient therapy of HCC by both COX-2-dependent and independent mechanisms [7]. On the other hand, diosmin (DSN) is a potent herbal drug with

chemopreventive action against hepatic cancer. It acts by downregulation of NF- $\kappa$ B and p38 MAP kinase in liver cancer cells resulting in reduced expression of COX-2 and iNOS liver [8]. Moreover, DSN causes apoptosis in human liver cancer cells through mitochondria-dependent apoptotic pathway [9]. Therefore, CXB and DSN are anticipated to have a synergistic anticancer action due to their common inhibitory effects on COX-2, NF- $\kappa$ B and TNF- $\alpha$  [8–11]. Furthermore, both drugs have common inhibitory effect on PI3K/AKT signaling pathway in cancer [12,13]. Accordingly, it would be beneficial to develop a novel drug-delivery system allowing combined delivery of both drugs.

Unfortunately, DSN has very low solubility in water and most organic solvents together with a pH-dependent solubility. Limited attempts were reported to enhance aqueous solubility and intestinal permeability of DSN. Freag *et al.* [14], reported that DSN nanosuspension remarkably improved DSN dissolution with about 100% of drug was dissolved within 5 min in comparison with only 51% of pure drug. In another study also, lyophilized phytosomal nanocarriers for DSN, with improved dissolution and permeation characteristics, were developed [15]. However, the literature still lacks studies that proved the enhanced *in vivo* antitumor activity of DSN via its targeted delivery. Also, CXB has poor solubility in water (3–7  $\mu$ g/ml at 37°C), which in turn causes poor oral bioavailability [16]. Moreover, the marketed oral formulations of DSN (Daflon<sup>®</sup>) and CXB (Celebrex<sup>®</sup>) offer uncontrolled delivery, lack specificity, often lead to poor patient compliance and result in systemic side effects following long treatment such as thromboembolism and cardiovascular risk for CXB. In addition, these drugs are also rapidly cleared from circulation, which can reduce their therapeutic concentration at tumor site. Therefore, novel tumor-targeted delivery systems are required to enhance tumor targeting and decrease toxicity of both drugs, thus improving their clinical utility.

Oral drug delivery is known as one of the easiest and most convenient routes for drug administration [17]. Despite the presence of marketed products for CXB and DSN in tablet form for oral administration, they have low oral bioavailability due to their poor solubility. Recently, hydrophobic and amphiphilic food proteins have demonstrated great potential for development of oral nanoparticulate drug-delivery systems. Soy protein isolate (SPI)-coated nanoemulsion was found to improve the intestinal permeation and hence the absorption of water-insoluble drugs, for example, fenofibrate [18]. The hydrophobic shell provided by SPI could help cellular internalization and escape the endolysosomes. The nanocarriers demonstrated enhanced intestinal penetration into the systemic circulation followed by distribution to different tissues. In our laboratory, nanocapsules fabricated from the hydrophobic protein, zein, were developed for oral delivery of exemestane and resveratrol. The nanocapsules displayed efficient solubilization and controlled release of drugs within their oily core as well as higher oral stability and resistance to digestion via hydrophobic protein shell could be enabled by glutaraldehyde cross-linking of zein [19,20]. However, all previous trials used nontargeted protein nanocarriers for oral drug-delivery which may result in undesired toxicity to normal tissues.

Gliadin (GL), a gluten protein, was exploited for oral drug delivery based on its biocompatibility, hydrophobic nature, bioadhesive properties and its resistance to enzymatic digestion [21]. GL was successfully used for preparation of mucoadhesive NPs that effectively protected the encapsulated drugs and controlled their release after oral administration [21–23]. On another avenue, recent studies revealed that the cationic ion-binding protein, lactoferrin (LF), could successfully internalized into hepatocytes via binding to low-density lipoprotein-related protein receptors and asialoglycoprotein receptors (ASGP-R) [24].

In this study, we propose LF-coated GL nanospheres coloaded with CXB and DSN (CXB/DSN/LF-GL-NPs) for oral-targeted therapy of HCC. First, to overcome its high hydrophobicity and improve its oral bioavailability, DSN was entrapped within the hydrophobic GL matrix via pH-modulated nanoprecipitation technique. Second, for improving their antitumor efficacy, both drugs, CXB and DSN were coencapsulated within GL nanospheres. Finally, the surface of GL was coated with LF through electrostatic interaction to enhance tumor selectivity and improve the internalization of GL nanospheres into HCC cells, via binding to lipoprotein-related protein receptor and ASGP-R overexpressed by HCC cells. The developed delivery system was thoroughly investigated *in vitro* and *in vivo* to prove the antitumor superiority of combined drug nanocarriers.

## Materials & methods

### Materials

DSN was purchased from Xi'an Natural Field Bio-Technique CO., Ltd (Shaanxi, China), while CXB was kindly supplied by Amriya Pharmaceutical Industries (Alexandria, Egypt). LF was donated by Westland Milk Products (Hokitika, NZ). Hydroxypropyl methylcellulose (HPMC) was purchased from Zhengzhou Sino Chemical Co.

Ltd. (Henan, China). GL, fetal bovine serum, 3-[4,5-dimethylthiazolyl-2]-2,5-diphenyltetrazolium bromide, rhodamine B isothiocyanate (RBITC), dimethyl sulfoxide (DMSO), EDTA, Triton X100, Hematoxylin solution, Eosin solution and Canada balsam were purchased from Sigma–Aldrich (MO, USA). 2-(4-Ethoxyphenyl)-6-[6-(4-methylpiperazin-1-yl)-1H-benzimidazol-2-yl]-1H-benzimidazole (Hoechst) was purchased from Thermo-Fisher (MA, USA). A mounting medium known to be composed of a mixture of distyrene (a polystyrene), a plasticiser (tricresyl phosphate), and xylene (DPX) mounting medium was obtained from Loba Chemie Pvt. Ltd. (Mumbai, India). Sodium lauryl sulfate and absolute ethanol were obtained from ADWIC Pharmaceutical Chemicals Co. (Cairo, Egypt). Methanol HPLC grade was purchased from JT Baker (NJ, USA). Human liver cancer cells HepG2 were supplied by the American Type Culture Collection.

### Preparation of drug-loaded GL-NPs

GL-NPs were prepared by the nanoprecipitation method using HPMC as stabilizer [25]. GL (100 mg) was dissolved in 70% v/v aqueous ethanolic solution (adjusted to pH 9.5 to ensure solubilization of DSN). Different quantities of DSN and/or CXB were dissolved in the GL hydroalcoholic solution. The drug/protein solution was then added into aqueous phase containing HPMC (adjusted to pH 2.0) under continuous stirring (200 rpm) at room temperature. The organic:aqueous phase ratio was 1:5 v/v. The resulting NPs were left under constant stirring till ethanol evaporation and then purified by two cycles of centrifugation (3–30 KS Sigma, Darmstadt, Germany) at 16,000 rpm for 30 min at 4°C. The aqueous redispersed NPs were then spray-dried using Büchi B-290 Mini spray-dryer (Flawil, Switzerland), with inlet temperature of 125°C, outlet temperature of 50°C, aspiration air of 90%, feed flow of 5 ml/min, spraying pressure of 5.0–5.8 mbar and air flow rate of 320 l/h.

### Preparation of LF-coated GL-NPs

GL-NPs were prepared the same as mentioned above. After centrifugation, the pH of GL-NPs aqueous suspension (~2 mg protein/ml) was adjusted to 7.8 using 0.1 N NaOH. Different concentrations of LF aqueous solution (0.05, 0.1, 0.2% w/v) was added dropwise to the GL-NPs suspensions under mild stirring for 30 min [26]. The resulting NPs suspension were then spray-dried as mentioned in the previous section.

### Physicochemical characterization of GL-NPs

The methodologies for assessing NP size, zeta potential [27], drug-encapsulation efficiency [28,29], drug release, morphology, solid-state characteristics including fourier transform infra-red spectroscopy (FTIR) spectra and differential scanning calorimetry (DSC) thermograms, and hemolytic stability [30,31] were performed as described and detailed in the Supplementary Materials.

### *In vitro* cytotoxicity & uptake study

The cytotoxicity of the free drugs, blank GL-NPs, dual-drug-loaded GL-NPs and LF-coated dual-drug-loaded GL-NPs on HepG2 liver cancer cells was assessed by the 3-(4,5-dimethylthiazolyl-2)-2,5-diphenyltetrazolium bromide assay [30] performed as described and detailed in the Supporting Information. Cellular uptake of RBITC-labeled GL-NPs, LF-GL-NPs and free RBITC into HepG2 liver cancer cells was evaluated using confocal microscopy as described previously and detailed in the Supplementary Materials [32].

### *In vivo* studies

#### *Animals*

The antitumor efficacy of targeted (LF-GL-NPs) and nontargeted (GL-NPs) was evaluated compared with free CXB, free DSN and CXB/DSN solution on tumor-bearing mice housed in stainless steel mesh cages following standard protocol mentioned in the Supplementary Materials.

#### *HCC induction in mice*

Induction of HCC in mice was achieved chemically by weekly intraperitoneal injection of diethyl nitrosamine (DEN) at a dose of 75 mg/kg for the first 3 weeks and followed by 100 mg/kg for another 3 weeks [33] as described and mentioned in the Supplementary Materials.



*In vivo antitumor efficacy*

Mice were randomly divided into seven groups (seven mice each). The mice groups included negative control, positive control (untreated HCC-bearing mice) and groups treated with: free CXB, free DSN, free combined CXB–DSN in cosolvent solution (DMSO:PEG400:Saline 1.5:3:5 v/v), nontargeted GL-NPs (CXB/DSN/GL-NPs, S8), LF-targeted GL-NPs (CXB/DSN/LF-GL-NPs, M4). The tumor-bearing mice were treated orally using oral gavage with the drugs either free solution (in DMSO:PEG400:Saline 1.5:3:5 v/v) or NPs equivalent to 7 mg/kg CXB and 7 mg/kg DSN three times weekly for 3 weeks with continuous monitoring to mice weights. All the surviving animals were sacrificed after 21 days of treatment. The excised livers were divided into two parts: one part was stored at -80°C for determination of tumor growth biomarkers and the second part was fixed with 10% formalin for histopathological studies.

*Reverse transcription polymerase chain reaction (RT-PCR) analysis of liver tissues*

RT-PCR was used to assess mRNA expression levels of COX-2, VEGF, TNF- $\alpha$  and NF- $\kappa$ B, semiquantitatively. The experimental method is detailed in the Supplementary Materials.

*ELISA of liver tissues*

The tumor growth biomarkers were determined quantitatively using ELISA. The experimental method is detailed in the Supplementary Materials[34].

*Measurement of serum hepatotoxicity markers*

The serum hepatotoxicity-indicating enzymes: ALT and AST levels were quantified via AU5400 biochemical analyzer (Beckman Coulter, IN, USA) [35].

*Histopathological & immunohistochemical analysis of liver tissues*

The liver samples were examined for histopathological changes as well as proliferation extent. The experimental method is detailed in the Supplementary Materials[36].

*Ex vivo imaging of isolated organs*

RBITC-conjugated LF-GL-NPs and free RBITC at concentration (6.75 mg/kg) have been administered orally to tumor-bearing mice. At predetermined postadministration time points, the mice were sacrificed and excised organs were imaged using *in vivo* photon imager [37,38].

*Statistical analysis*

Data analysis is detailed in the Supplementary Materials.

**Results & discussion****Preparation of single & dual drug-loaded GL nanospheres***DSN or CXB single-loaded GL-NPs*

In this study, GL was exploited as a carrier for oral drug delivery to HCC based on its hydrophobicity, resistance to the enzymatic digestion and mucoadhesive properties which are advantageous for oral administration.

GL nanospheres were prepared using nanoprecipitation technique where the organic phase containing GL and drugs codissolved in hydroalcoholic solution (pH 9.5) was added dropwise to antisolvent aqueous solution containing HPMC as a stabilizer under mild stirring (Figure 1). The diffusion of the organic solvent in the aqueous solution resulted in the precipitation of GL-NPs with size range of 163.6–281.8 nm in agreement with the previously obtained results [25]. At the final pH of GL-NPs suspension ( $4.5 < pI$  of GL; 6.5), the resultant NPs were positively charged (+12.2 to +4.3 mV, Table 1) [39]. The stability of bare protein NPs is often limited because of their sensitivity to environmental conditions, including pH, temperature and ionic strength. Although reported that the optimum colloidal stability of nanocarriers is usually observed with a surface charge higher than 30 mV [40], the stability of our nanospheres could be attributed to steric stabilization conferred by the HPMC. HPMC was reported to form a relatively thick layer around the particles hindering their aggregation, besides stabilization via hydrogen bonding to a lesser extent [41]. Moreover, the zeta potential values of our elaborated GL-NPs could be more favorable than very high zeta potential values as it is reported that the later might hinder GL-NPs formation due to electrostatic repulsion. Finally, the formed GL-NPs dispersion was spray-dried to convert the nanocarriers into redispersible powder of long-term stability. The effect of the drug/polymer ratio on the physicochemical

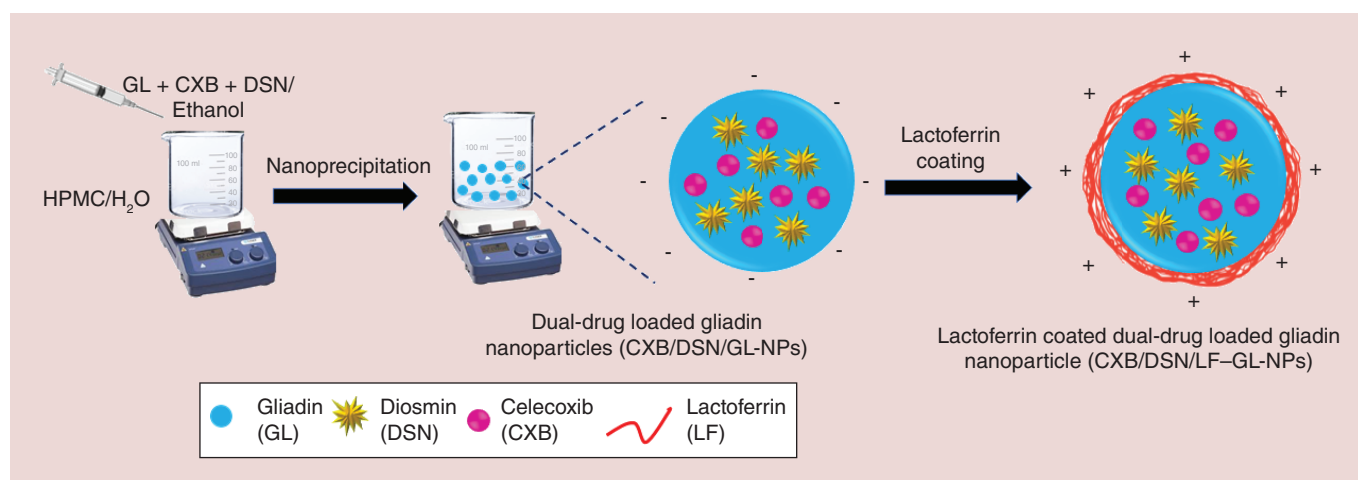


**Figure 1. Schematic diagram for lactoferrin-coated gliadin nanoparticles.**

GL-NPs: Gliadin nanoparticles; HPMC: Hydroxypropyl methylcellulose.

**Table 1. Composition and physicochemical characteristics of gliadin nanoparticles prepared at pH 4.5.**

Nanoparticles	Gliadin (mg)	Diosmin (mg)	Celecoxib (mg)	HPMC (% w/v)	Particle size (nm)	PDI	Zeta potential (mV)	Yield	%EE DSN	%EE CXB
S0	100	–	–	0.25	163.6 ± 0.46	0.135	+12.2 ± 0.36	65.5	–	–
S1	100	25	–	0.25	281.8 ± 0.66	0.557	+13.0 ± 0.35	75.2	88.2	–
S2	100	20	–	0.25	243.3 ± 0.11	0.183	+15.1 ± 0.34	73.2	85.5	–
S3	100	10	–	0.25	179.9 ± 0.68	0.265	+18.0 ± 0.23	67.8	92.0	–
S4	100	–	10	0.25	234.6 ± 0.13	0.380	+13.2 ± 0.52	60.0	–	73.9
S5	100	10	10	0.25	557.8 ± 0.65	0.392	+4.65 ± 0.47	53.0	N.A.	N.A.
S6	100	5	5	0.25	348.1 ± 0.48	0.253	+4.9 ± 0.61	60.5	84.5	82.7
S7	50	5	5	0.25	528.1 ± 0.72	0.327	+5.5 ± 0.52	69.18	93.0	79.24
S8	100	5	5	0.5	220.3 ± 0.71	0.252	+4.3 ± 0.36	71.1	95.5	88.0

N.A.: The formulation S5 showed large size with low stability and tends to aggregate quickly, which did not allow determination of EE.

CXB: Celecoxib; DSN: Diosmin; EE: Encapsulation efficiency; EPR: Enhanced Permeation and Retention Effect; HPMC: Hydroxypropyl methylcellulose; PDI: Polydispersity index.

properties of the resultant NPs was investigated. Accordingly, it was found that a drug/GL ratio of 1:10 resulted in formation of DSN/GL-NPs with acceptable particle size of  $179.9 \pm 0.68$  nm (S3), and the highest encapsulation efficiency (92.0%) for DSN. Also, CXB/GL-NPs (S4) were prepared using the same drug/GL ratio resulted in NPs with particle size of  $234.6 \pm 0.13$  and encapsulation efficiency of 73.9% for CXB.

In the dual CXB/DSN-loaded GL-NPs, increasing the drug/polymer ratio to 1:5 resulted in formation of GL-NPs with higher particle size of  $557.8 \pm 0.65$  and  $528.1 \pm 0.72$  nm for S5 and S7, respectively, compared with  $348.1 \pm 0.48$  nm for S6 (1:10 drug/polymer ratio). Therefore, the 1:10 drug/polymer ratio was selected as the optimized one. However, the size of formed nanospheres (S6) was still outside the size range suitable for enhanced permeation and retention effect (EPR) effect. For this reason, the amount of the stabilizer was modulated in order to further reduce the particle size of nanospheres. Increasing the HPMC concentration from 0.25 to 0.5% w/v, an NP dispersion of smaller particle size ( $220.3 \pm 0.71$ ) and good PDI (0.252) was obtained with good encapsulating efficiency for both drugs (S8; 88.0, 95.5% for CXB and DSN, respectively; Table 1). Therefore, GL-NPs (S8) prepared using 0.5% HPMC was selected for further investigation.

#### LF-coated (DSN/CXB/LF-GL-NPs; M3, M4, M5)

For active targeting of ASGP-R overexpressed on HCC cells, the cationic protein (pI 8.7), LF, was used for coating of DSN/CXB-GL-NPs. At pH 7.8 (above GL pI 6.5), the positively charged LF molecules can be electrostatically adsorbed on the surface of negatively charged GL-NPs [41,42]. Upon addition of 0.05% w/v LF, the zeta potential of GL-NPs was changed from -8.95 to -1.9 mV together with an increase in particle size from  $284.0 \pm 0.72$  to

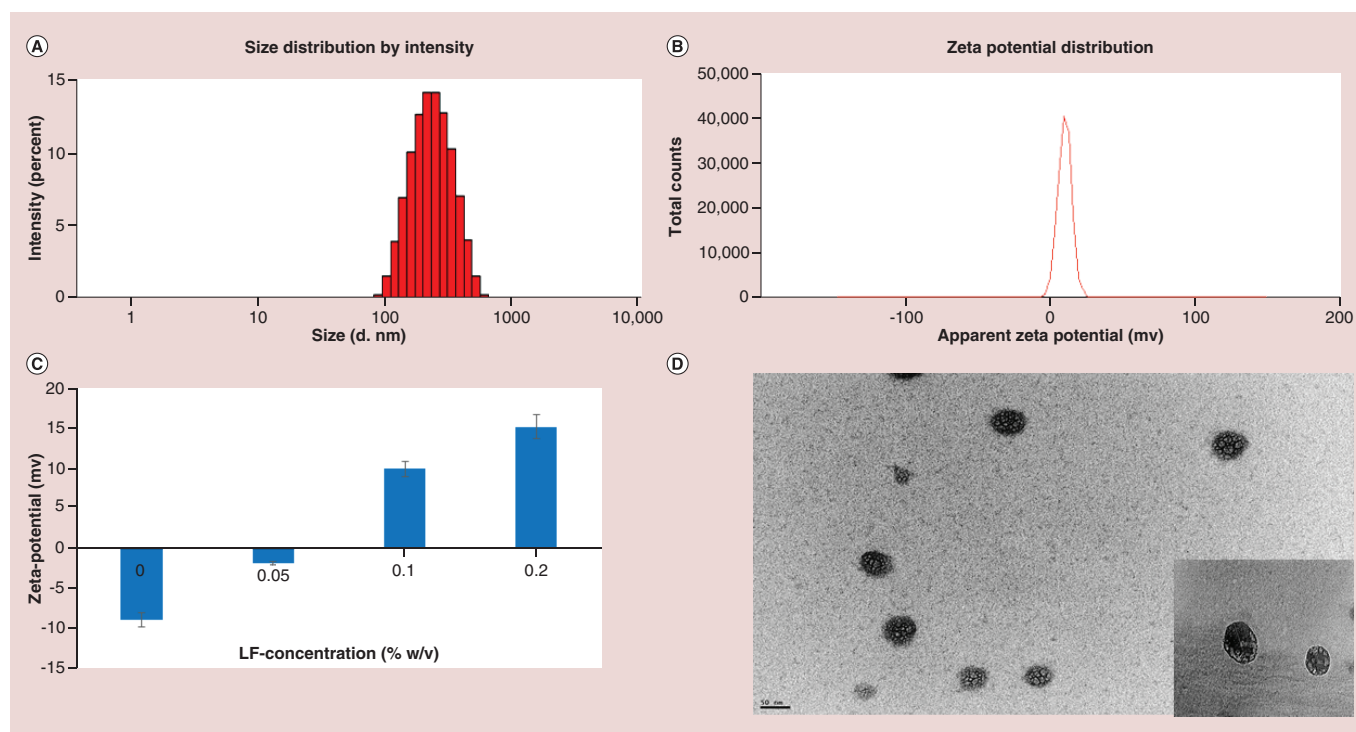


**Figure 2. Physicochemical characteristics of gliadin nanoparticle. (A)** Size distribution diagram of targeted celecoxib/diosmin/lactoferrin–gliadin nanoparticles (M4) measured by dynamic light scattering. **(B)** Zeta potential of targeted celecoxib/diosmin/lactoferrin–gliadin nanoparticles (M4). **(C)** Charge reversal of gliadin nanoparticles upon adding different lactoferrin concentration. **(D)** Transmission electron microscopy images showing morphology of targeted celecoxib/diosmin/lactoferrin–gliadin nanoparticles (M4). LF: Lactoferrin.

**Table 2. Composition and physicochemical characteristics of blank and drug-loaded gliadin nanoparticles prepared at pH 7.8.**

Nanoparticles	LF (% w/v)	HPMC (% w/v)	Particle size (nm)	Zeta potential (mV)	PDI	% yield	%EE DSN	%EE CXB
M1	–	0.25	271.1 ± 0.59	-9.33 ± 0.26	0.350	61.0	67.86	72.66
M2	–	0.2	284.0 ± 0.72	-8.95 ± 0.39	0.364	63.2	87.34	84.08
M3	0.05	0.2	509.0 ± 0.66	-1.9 ± 0.35	0.449	60.5	N.A.	N.A.
M4	0.1	0.2	241.0 ± 0.80	+9.86 ± 0.47	0.220	64.6	87.53	88.1
M5	0.2	0.25	315.0 ± 0.50	+15.1 ± 0.34	0.490	59.44	76.6	80.44

N.A.: The formulation M3 showed large size with low stability and tends to aggregate quickly, which did not allow determination of EE.  
CXB: Celecoxib; DSN: Diosmin; EE: Encapsulation efficiency; GL-NP: Gliadin nanoparticle; HPMC: Hydroxypropyl methylcellulose; LF: Lactoferrin; PDI: Polydispersity index.

509.0 ± 0.66 nm. Further increasing the concentration of added LF from 0.05 to 0.1% w/v, reversal of surface charge to +9.86 ± 0.47 mV was observed together with a decrease in particle size to 241.0 ± 0.80 nm (Figure 2A–C & Table 2). Further increasing in the amount of LF caused a large increase in particle size to 315.0 nm with no significant change of zeta potential (+15.1 ± 0.34 mV). The initial increase in particle size upon adding LF could be due to reduction in the value of surface charge resulting in colloidal instability (particle aggregation), since the amount of LF was not sufficient to provide complete coverage of the particle surface. The consequent reduction in particle size observed upon further increasing the amount of LF added, indicated firm electrostatic interaction between the negatively charged GL-NPs and cationic LF molecules, which was further confirmed by reversal of zeta potential to a higher positive value. Further increase in LF concentration beyond 0.1% w/v caused a significant increase in particle size which could be attributed to the formation of thick layer of LF on the surface of GL-NPs. In similar study, LF was used as a stabilizer in zein NPs preparation that intended for oral drug delivery [43].

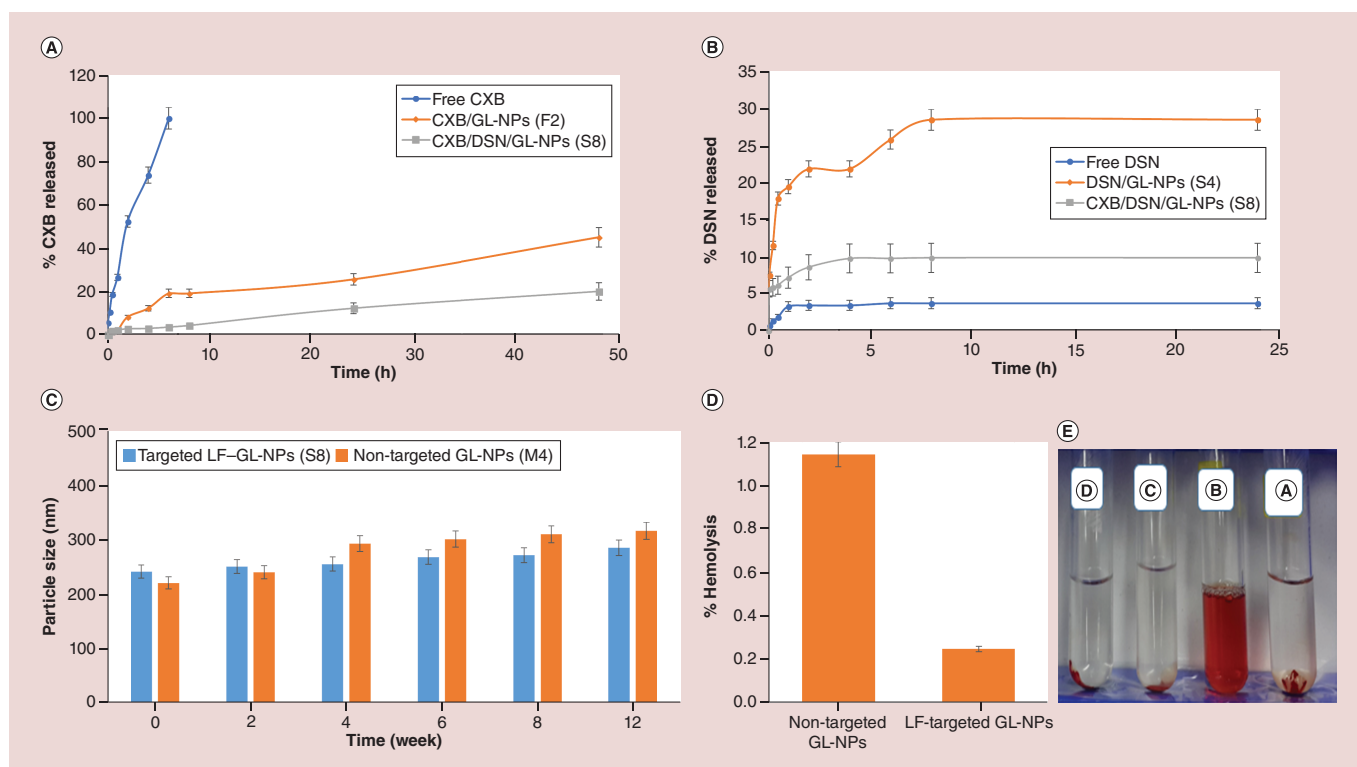


**Figure 3.** *In vitro* drug release, colloidal stability and hemocompatibility study of GL-NPs. *In vitro* release study of (A) CXB and (B) DSN from different formulations in medium simulating intestinal fluid at 100 rpm and 37°C using the dialysis bag method. (C) Physical stability of nontargeted CXB/DSN/GL-NPs (S8) and targeted CXB/DSN/LF-GL-NPs (M4) showing the change in particle size with time. Hemolytic potential of S8 and M4 showing % hemolysis (D) and hemocompatibility image (E) after 1 h of incubation with RBC at 37°C. The samples include: (A) negative control, (B) positive control, (C) nontargeted GL-NPs (S8), (D) LF-targeted GL-NPs (M4). CXB: Celecoxib; DSN: Diosmin; GL-NP: Gliadin nanoparticle; LF: Lactoferrin; RBC: Red blood cell.

Furthermore, it has been observed that LF is relatively resistant to proteolysis in the GI tract, so it could be used as promising targeted oral drug-delivery system [44].

### Morphological examination

TEM analysis of targeted DSN/CXB LF-GL-NPs showed that the particles were spherical and with relatively smooth surface with no aggregation observed (Figure 2D). The apparent size measured by TEM (around 80 nm) was less than that measured by DLS, which could be attributed to the dehydration-induced shrinkage of particles during preparation for TEM analysis [45].

### *In vitro* drug release

The *in vitro* release of drug was performed in a medium simulating GI fluid with 0.5% sodium lauryl sulfate to maintain sink conditions. A sustained release behavior of CXB from GL-NPs (S4) was observed with 45% of the drug was released over 48 h without initial burst effect. Thus, GL-NPs succeeded in sustaining CXB release by entrapping drug in hydrophobic matrix of GL-NPs, which is anticipated to avoid the premature drug release in circulation and decrease side effects. This in contrast to the free drug that showed almost 100% released within 6 h (Figure 3A). In Figure 3B, since free DSN has negligible solubility in water and most of organic solvents, it could not maintain its solubility in the dialysis bag and tends to precipitate quickly resulting in very slow release pattern [46]. In contrast, our GL-NPs succeeded in solubilizing DSN within its hydrophobic core while being compatible with the aqueous medium based on their nanosize and thus significantly improved its release profile. These results confirm our rationale of NP design, so that encapsulation of the highly insoluble drug DSN into GL-NPs could enable its administration, improve its solubility and consequently enhance its bioavailability. Overall, DSN showed slow release from DSN/GL-NPs with about 28.49% of drug was released after 24 h (Figure 3B). The slow release of



both drugs might be correlated to their hydrophobic nature of CXB and DSN that in turn increases their affinity for hydrophobic interaction with GL matrix [47]. Upon coencapsulation of DSN and CXB in the NPs, a reduction in the release rate of both drugs was observed where only 20.49 and 11.45% of CXB and DSN, respectively, were released after 48 h (Figure 3A & B). This may be attributed to the possible drug–drug hydrophobic interaction within NP core. However, the sustained drug release from our hydrophobic GL-NPs is considered advantageous property to reduce the premature drug leakage in the GI tract until reaching its site of action at tumor. Since the *in vitro* release medium is not simulating the real-tumor conditions where NPs would degrade by lysosomal enzymes in cancer cells, the encapsulated drugs would be released reaching the effective concentration of drugs and thus achieving the required therapeutic effect. Our results are in agreement with previous findings that showed sustained release of docetaxel from biodegradable hydrophobic Polylactic-*co*-glycolic acid (PLGA) NPs [48].

### *Solid-state characterization*

The DSC thermograms of free CXB and DSN displayed sharp melting endothermic peaks at 165 and 291°C, respectively, revealing their crystallinity (Supplementary Figure 1) [14,15,49]. On the other hand, the DSN and CXB endothermic peaks disappeared in the thermogram of GL-NPs suggesting their possible transformation into the amorphous form upon successful encapsulation within GL-NPs. A new broad peak appeared at around 190°C, which may indicate an interaction between CXB and GL within the nanomatrix.

In the FTIR spectrum of nontargeted CXB/DSN/GL-NPs (S8), the characteristic peaks of DSN at 3500 and 950 cm<sup>-1</sup> corresponding to OH stretching and C–H bonds, respectively, were detected (Supplementary Figure 2) [15]. Most of the characteristic peaks of CXB disappeared when it was loaded in GL-NPs, this could indicate the intermolecular interaction between CXB and GL [50]. Moreover; the characteristic CXB peaks corresponding to S = O symmetric and asymmetric stretching were shifted from 1162.03 to 1119 cm<sup>-1</sup> and from 1346.44 to 1373 cm<sup>-1</sup>, respectively. These shifts may be associated with interactions, for example, hydrogen bonds, hydrophobic forces and electrostatic interactions between the GL and CXB (More details in the Supplementary Information).

### *Physical stability*

After 3 months storage, spray-dried noncoated CXB/DSN/GL-NPs (S8) showed increase in particle size from 220.3 ± 0.42 to 315.6 ± 0.22 nm. However, the size of spray-dried coated CXB/DSN/LF–GL-NPs (M4) showed a minor increase in particle size from 241.0 ± 0.64 to 254.8 ± 0.34 nm (Figure 3C). This indicated that the postproduction coating of GL-NPs with LF maintained their physical stability [26]. The stability of LF–GL-NPs is probably due to surface coating of GL-NPs by LF providing both hydrophilic surface and charge-based stabilization [51]. In addition, the glycan chains of LF may add steric stabilization mechanism. These findings are in agreement with previous literature that reported the increased stability of GL-NPs after surface coating with hydrophilic polysaccharide (0.10 w/v % pectin). Below this concentration, aggregation was observed while above this concentration, a significant increase in particle size was noticed [26].

### *In vitro hemolysis test*

The hemolytic assay is widely used to evaluate the hemocompatibility of the nanoformulation by measuring the extent of damage to red blood cells via the release of hemoglobin. Upon incubation with RBCs for 1 h, nontargeted (S8) and LF-targeted (M4) GL-NPs demonstrated 1.14 and 0.25% hemolysis, respectively (Figure 3D & E). The low hemolytic potential was due to its proteinaceous composition proves the blood compatibility of GL-NPs, indicating their possible use for systemic administration [52]. Similarly, the hemocompatibility of apotransferrin and LF-NPs was previously noticed to be below 2% [53].

### *In vitro cytotoxicity*

Cell viability testing of free CXB, free DSN, free CXB/DSN combination, nontargeted, LF-targeted CXB/DSN/GL-NPs as well as blank GL-NPs was carried out using HepG2 liver cancer cells at 48 h (Figure 4). Blank NPs (S0) demonstrated very little toxicity to HepG2 cells (viability was >94% after 48 h). The IC<sub>50</sub> values of free CXB (IC<sub>50, CXB</sub>) and free DSN (IC<sub>50, DSN</sub>) against HepG2 cells at 48 h were 56.44 and 105.324 μM, respectively (Table 3). On the other hand, the combination of the two free drugs caused a reduction of the IC<sub>50</sub> values by 1.31- and 2.44-fold compared with that of CXB and DSN, respectively, which proves synergistic cytotoxicity (Table 3). The low improvement of *in vitro* cytotoxicity of drugs upon nanoencapsulation is mainly attributed to the significantly sustained drug release from NPs. Actually, this slow and gradual drug release pattern

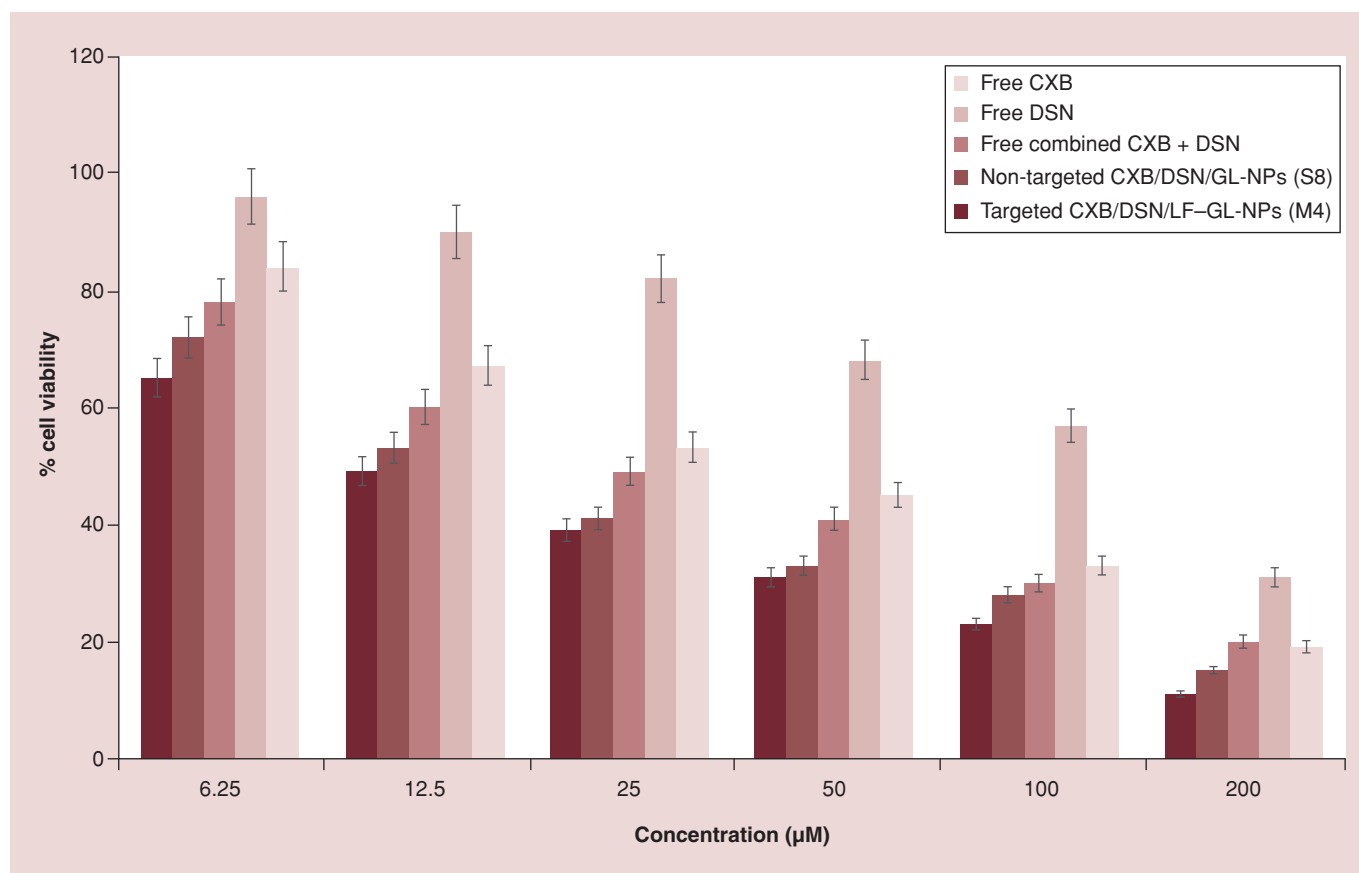


**Figure 4.** *In vitro* cytotoxicity analysis of free CXB, free DSN and free CXB/DSN cosolvent compared with the prepared nanoformulations S8 (nontargeted CXB/DSN/GL nanoparticles) and M4 (targeted CXB/DSN/LF–GL nanoparticles) on HepG2 liver cancer cell line at the concentration of 0–200  $\mu\text{M}$  after 48 h. CXB: Celecoxib; DSN: Diosmin; GL-NP: Gliadin nanoparticle; LF: Lactoferrin.

**Table 3.**  $\text{IC}_{50}$  values of free drugs compared with the prepared nanocarriers on HepG2 liver cancer cells at the concentration of 0–200  $\mu\text{M}$  after 48 h.

Formula	$\text{IC}_{50}$ value ( $\mu\text{M}$ )
Free CXB	56.4452
Free DSN	105.324
Free CXB + DSN	43.135
Nontargeted CXB/DSN/GL-NPs (S8)	36.2748
Targeted CXB/DSN/LF–GL-NPs (M4)	28.1347
Blank GL-NPs (S0)	0.04471

CXB: Celecoxib; DSN: Diosmin; GL-NP: Gliadin nanoparticle; LF: Lactoferrin.

upon degradation of the polymeric NPs inside the cells helps reduce the emergence of drug resistance [54]. Hence, NPs are taken up by the cell via endocytosis often bypass the ABC transporters responsible for efflux of drugs once released into the cytoplasm while free drugs enter cell by simple diffusion [55]. Therefore, the availability of high drug concentration as in free mix (CXB + DSN) will decrease  $\text{IC}_{50}$  but activate the efflux pump quickly resulted in drug resistance [56].

It seemed that coating of GL-NPs with LF enhanced the drug combination potency compared with the free combined drugs solution and the nontargeted GL-NPs. This was demonstrated by the reduction in  $\text{IC}_{50}$  of HepG2 cells treated with LF-targeted GL-NPs by 1.53- and 1.19-fold compared with free drug combination and nontargeted GL-NPs, respectively. These results clearly demonstrated the superior anticancer efficacy of LF-targeted GL-NPs and the efficient active targeting potential of LF. The higher internalization of LF-targeted NPs into liver cancer cells via

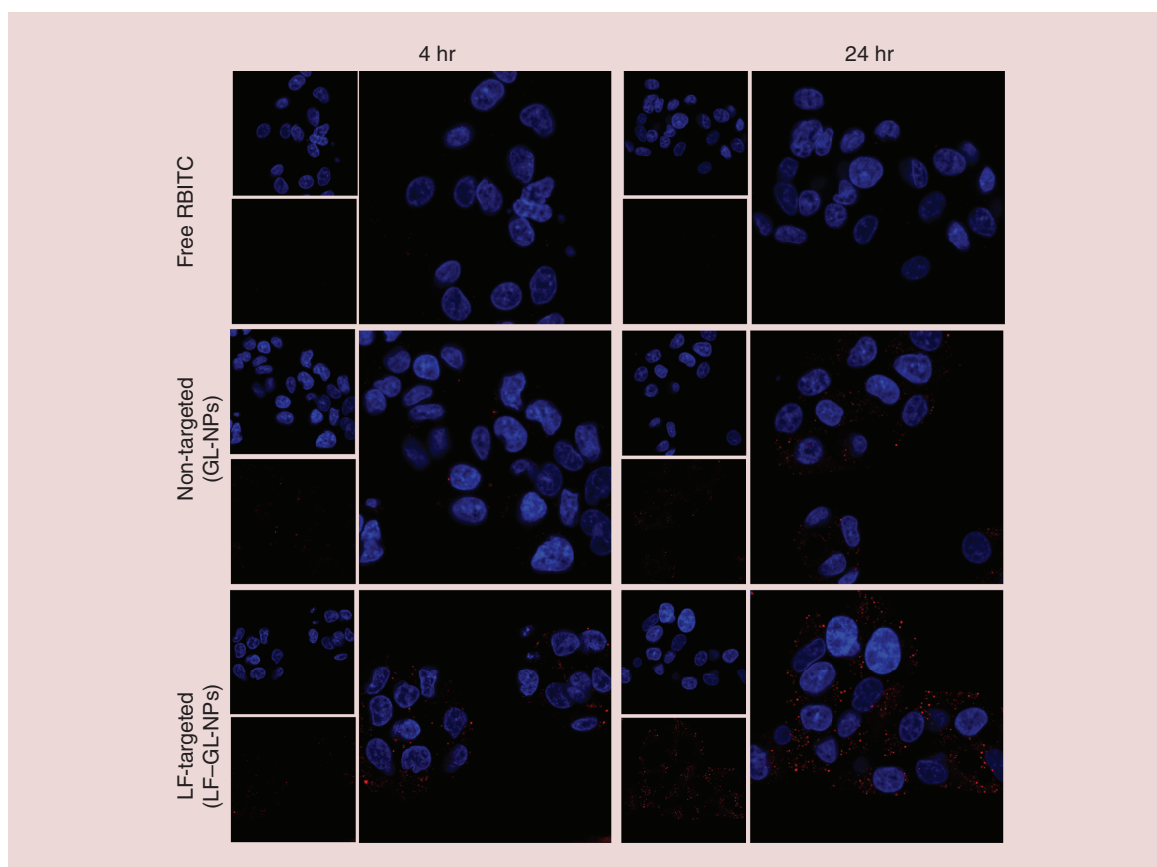


**Figure 5.** Confocal images showing cellular uptake of free RBITC, RBITC-nontargeted GL-NPs and RBITC-targeted LF-GL nanoparticles within HepG2 liver cancer cells after incubation for 4 and 24 h. GL-NP: Gliadin nanoparticle; LF: Lactoferrin; RBITC: Rhodamine B isothiocyanate.

asialoglycoprotein receptor-mediated endocytosis could be responsible for its enhanced cytotoxicity [57]. Our results are in agreement with the previously reported stronger antiproliferative effects of LF-modified, doxorubicin-loaded PEGylated liposomes on ASGP-R-expressing HCC cells compared with nonmodified liposomes [58].

#### *In vitro cellular uptake of NPs*

The cellular uptake of LF-targeted GL-NPs (S8), nontargeted GL-NPs and free RBITC into HepG2 liver cancer cells (overexpressing ASGP-R) upon 4 and 24 h incubation was evaluated by visualization of the fluorescent images obtained by confocal laser scanning microscopy. The fluorescent dye RBITC was conjugated via its thiocyanate group to the amino group of GL to develop fluorescently labeled GL-NPs (Figure 5). Confocal microscopy revealed bright red fluorescence signals in the cytoplasm of HepG2 cells, which was attributed to RBITC, indicating that RBITC-conjugated NPs successfully entered the cells. Intracellular fluorescence signal intensity in all groups were increased with increasing incubation time, indicating that the cellular uptake of RBITC-conjugated NPs was time-dependent. At the same incubation time, the uptake of LF-GL-NPs by HepG2 was noticeably higher than that of nontargeted GL-NPs, which would be related with the receptor-mediated endocytosis through LF moiety due to high surface expression of ASGP-R on HepG2 cells [58]. LF was reported to interact with high affinity to ASGP-R on HepG2 cells in a galactose-independent manner, indicating the suitability of LF is a good ligand to ASGP-R binding. In addition to, the positive surface charge promotes the cellular internalization of NPs that is possibly due to the negatively charged cell surface prefer to uptake the positively charged NPs via their electrostatic interaction [59].

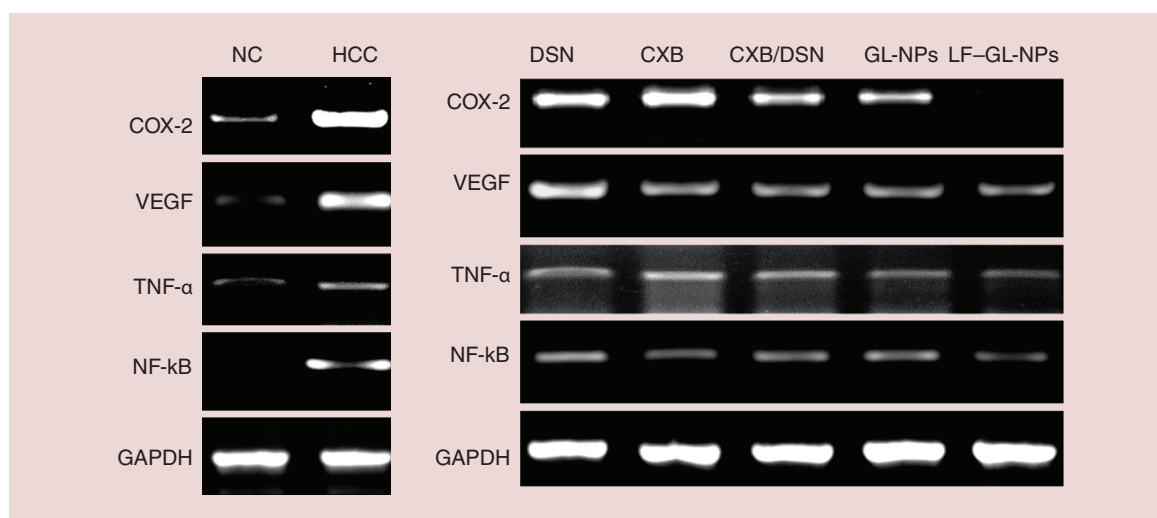


**Figure 6.** Expression profile for mRNA levels of COX-2, VEGF, TNF- $\alpha$  and NF- $\kappa$ B in groups treated with free CXB, free DSN, free combined CXB/DSN, nontargeted CXB/DSN/GL-NPs (S8), targeted CXB/DSN/GL-NPs (M4) individual tissues was measured by (RT-PCR) and normalized to GAPDH,  $n = 7$ .

CXB: Celecoxib; DSN: Diosmin; GL-NP: Gliadin nanoparticle; LF: Lactoferrin.

### *In vivo antitumor efficacy*

#### *Measurement of cell necrosis markers expression levels*

##### **NF- $\kappa$ B**

Activated NF- $\kappa$ B is reported to contribute an essential role in tumor angiogenesis by upregulating necessary genes including VEGF, iNOS, IL-6 and IL-8 [60]. In our study, we assessed the expression level of NF- $\kappa$ B by RT-PCR (Figure 6 to 7). The group treated with free combined drugs showed a significant ( $p < 0.01$ ) suppression of the expression level of NF- $\kappa$ B unlike the group treated with either CXB or DSN where no significant reduction in level of NF- $\kappa$ B was detected compared with the positive control. Both groups treated with either nontargeted (S8) or LF-targeted (M4) GL-NPs showed a significant inhibition ( $p < 0.001$ ) in NF- $\kappa$ B expression level compared with the positive control, although no significant difference was observed between both groups. CXB was reported to efficiently suppress nuclear translocation and activation of NF- $\kappa$ B in liver cancer cells [11]. In addition, some studies reported the role of DSN in suppressing NF- $\kappa$ B expression level in HCC-induced rats [8,61]. This could account for the superior performance of such drug combination assumed in our study.

##### **TNF- $\alpha$**

TNF- $\alpha$  is a multifunctional cytokine that plays a key role in regulating signaling pathways involved in tumorigenesis and inflammation [62]. CXB is reported to potently inhibit TNF- $\alpha$ -induced transcriptional activity [11,63]. DSN was also reported to show a remarkable decrease in the hepatic TNF- $\alpha$  levels [8,61]. In our study, we also assessed the expression level of TNF by RT-PCR (Figure 6 to 7). The mice treated with the nontargeted dual-drug-loaded GL-NPs (S8) showed no significant difference in the expression level of TNF- $\alpha$  compared with the group treated with the free combined drugs ( $p > 0.05$ ). On the other hand, the group receiving LF-targeted GL-NPs (M4) demonstrated a significant ( $p < 0.001$ ) decrease in the expression level of TNF- $\alpha$  compared with all the other treated groups ensuring their effective delivery to their desired site of action. There was no significant difference ( $p > 0.05$ ) between the TNF- $\alpha$  expression level measured in such group and that of the negative control.

#### *Measurement of COX-2 expression level*

COX-2 enzyme is implicated in stimulating angiogenesis by induction of VEGF and FGF-2 [64]. Moreover, COX-2 has found to be a key mediator involved in cancer-associated inflammation and progression. In our study, COX-2 expression level was determined by RT-PCR (Figure 6 to 7). The combined free drugs (CXB + DSN) exhibited significant reduction ( $p < 0.001$ ) in the level of COX-2 compared with positive control that could be related to a synergistic effect. The privilege of passively targeted CXB/DSN/GL-NPs (S8) was obvious by its significant inhibitory effect ( $p < 0.01$ ) on the expression level of COX-2 compared with the free combined drugs. The group



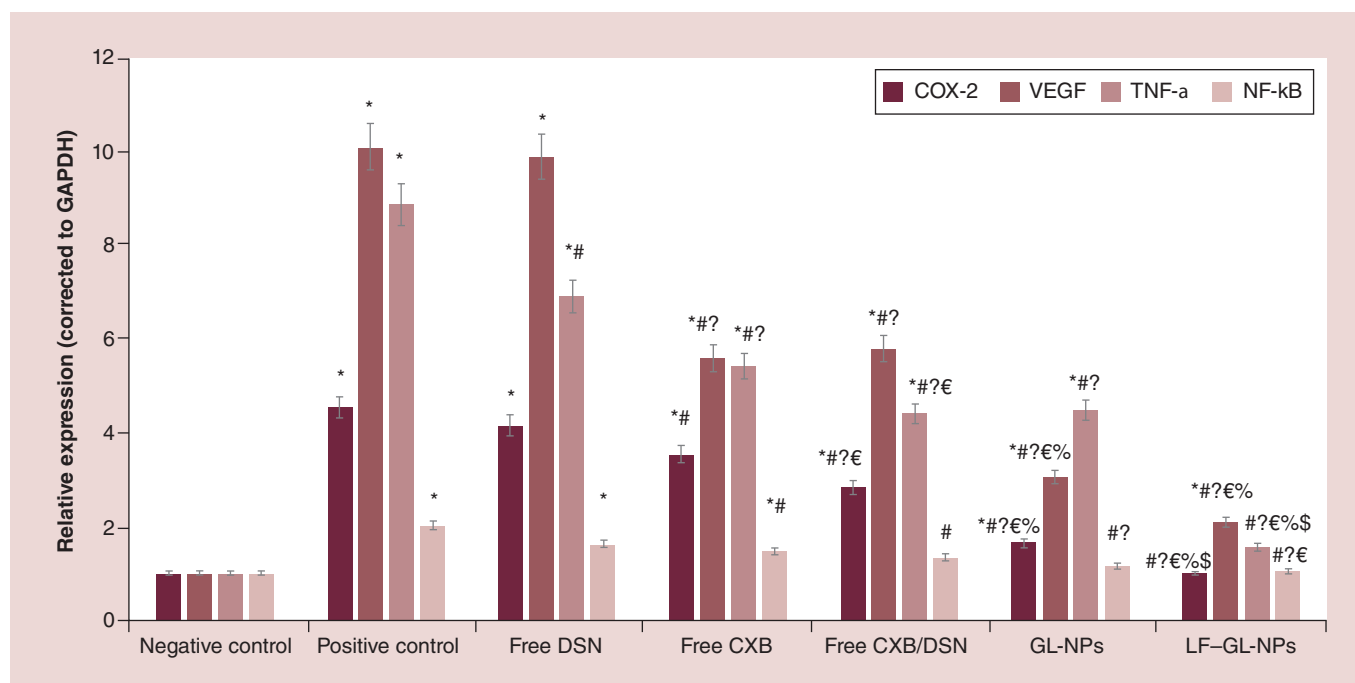


**Figure 7.** Quantitative expression of VEGF, TNF- $\alpha$ , COX-2 and NF- $\kappa$ B levels quantified by RT-PCR for the studied groups, normalized according to GAPDH,  $n = 7$ .

\* $p < 0.05$  vs negative control; # $p < 0.05$  vs positive control; ? $p < 0.05$  vs free DSN; € $p < 0.05$  vs free Celecoxib; % $p < 0.05$  vs free celecoxib/diosmin; \$ $p < 0.05$  vs nontargeted gliadin nanoparticles.

CXB: Celecoxib; DSN: Diosmin; GL-NP: Gliadin nanoparticle.

treated with LF-targeted NPs (M4) exerted demonstrated significantly 4.5- and 2.58-fold lower level of COX-2 expression than free combined drugs treated group ( $p < 0.001$ ) and nontargeted NPs treated group ( $p < 0.01$ ), respectively. Moreover, treatment with LF-targeted GL-NPs showed the ability to reduce the COX-2 expression level to the normal values with no significant difference from normal control ( $p > 0.05$ ). While CXB is known to inhibit COX-2 [7,65,66], DSN was also reported to downregulate both COX-2 and iNOS by reducing the expression of NF- $\kappa$ B and p38 MAP kinase in HCC-induced rats [8]. Accordingly, the combination of both drugs in a single nanoparticulate carrier augments their effect, which is further fortified by their active targeting to the tumor site.

#### Detection of antiangiogenic effect

VEGF is a secreted protein that strongly contributes in tumor-related angiogenesis [67]. Therefore, VEGF expression level was assessed at both the mRNA level and protein level by RT-PCR and ELISA, respectively (Figure 6–8A). The group treated with free combined drugs did not show a significant difference ( $p < 0.05$ ) in reduction VEGF expression compared with free CXB-treated group at both mRNA and protein level. CXB is reported to inhibit angiogenesis via downregulating the mRNA expression of *VEGF* gene, reduce tumor growth and promote apoptosis in HCC cells [68]. However, there were no data found about the effect of DSN on VEGF expression level, which explains why there was no significant difference between CXB-treated group and free combined treated group. Incorporation of both drugs in nontargeted GL-NPs (S8) resulted in a significant 1.9-fold reduction ( $p < 0.01$ ) in VEGF expression at both mRNA and protein levels compared with free combined treated group. Moreover, LF-targeted GL-NPs (M4) demonstrated a highly significant suppression in VEGF expression level ( $p < 0.001$ ) with 2.8-fold reduction in the VEGF mRNA expression level compared with free combined treated group with no significant difference from the normal control ( $p > 0.05$ ).

#### Measurement of apoptosis induction

Caspases 3 and 9 play a critical role in the programmed cell death and in particular caspase 3 is implicated in the terminal phase of apoptosis [69]. Previous reports indicated that CXB promotes apoptosis of HCC cells through activation of caspases 3 and 9 by COX-2 dependent and independent cell growth inhibition [7]. DSN also showed

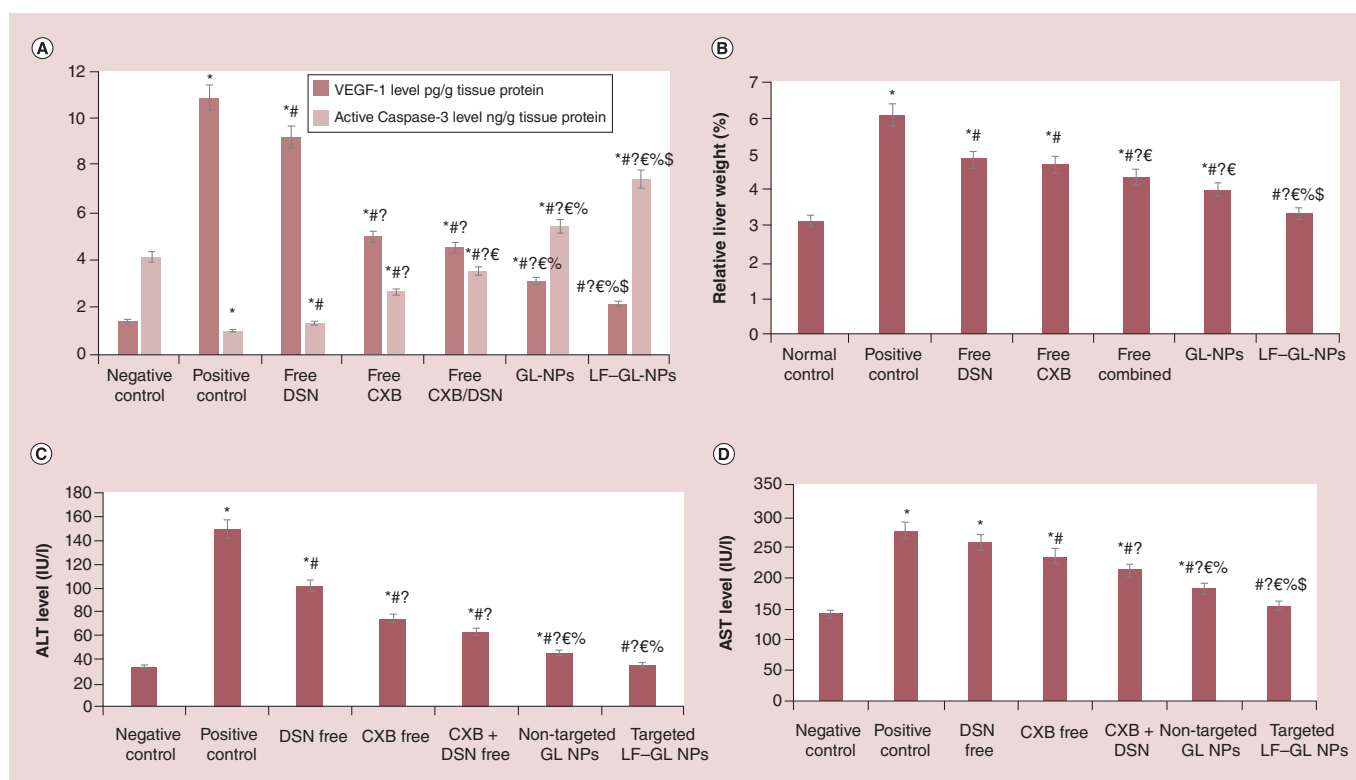


**Figure 8.** *In vivo* anti-tumor efficacy of GL-NPs. Comparison between the studied groups (free CXB, free DSN, free CXB/DSN cosolvent, nontargeted CXB/DSN/GL-NPs (S8) and targeted CXB/DSN/LF-GL-NPs (M4) treated groups in addition to the positive and negative control groups) according to (A) VEGF-1 level and active caspase-3 levels, (B) RLW%, (C) ALT level and (D) AST level,  $n = 7$ . \* $p < 0.05$  vs negative control, # $p < 0.05$  vs positive control, ? $p < 0.05$  vs free DSN, € $p < 0.05$  vs free CXB, % $p < 0.05$  vs free CXB/DSN, \$ $p < 0.05$  vs nontargeted GL-NPs.

CXB: Celecoxib; DSN: Diosmin; GL-NP: Gliadin nanoparticle; LF: Lactoferrin; RLW: Relative liver weight.

increased expression of caspases 3 and 9, thus confirming its apoptotic induction potential [70]. Therefore, in our study, apoptosis was assessed by measuring the expression level of caspase-3 by ELISA in HCC tumor tissue of mice (Figure 8A). Compared with the positive control, the group treated with free combined drugs showed 3.6-fold increase in the level of caspase 3. While the groups treated with nontargeted (S8) and LF-targeted GL-NPs (M4) showed 5.52- and 7.57-fold elevation in the level of caspase 3, respectively, compared with the positive control. This demonstrated the privilege of nanoencapsulation of both drugs, which is further fortified by active targeting.

#### Measurement of serum AST & ALT levels & relative liver weight %

In comparison with normal mice, the liver/body weight ratio (relative liver weight [RLW] %) in positive control mice has shown remarkable increase from  $3.12 \pm 0.2$  to  $6.08 \pm 0.2$  (Figure 8B). The serum levels of ALT and AST were highly increased in positive control mice group in comparison with negative control one, revealing the liver damage caused by DEN [35]. Compared with free combined drugs treated group, nontargeted dual-drug-loaded GL-NPs (S8) caused about 1.08-fold reduction in the liver/body weight ratio, 1.38- and 1.167-fold decrease in the expression levels of ALT and AST, respectively (Figure 8C & D). LF-targeted GL-NPs (M4)-treated group caused about 1.3-fold decrease in the liver/body weight ratio and 1.79- and 1.37-fold decrease in the expression levels of ALT and AST, respectively, compared with the group treated with the free combined drugs, which was comparable to negative control. These results confirmed the potential effect of LF-targeted dual-drug-loaded GL-NPs (M4) on alleviation of liver damage induced by DEN.

#### Histopathological study

The liver specimens from negative control mice showed normal liver parenchyma with granulated cytoplasm, central vein and small uniform nuclei (Figure 9A). The hepatic lobules were intact with polygonal cells around

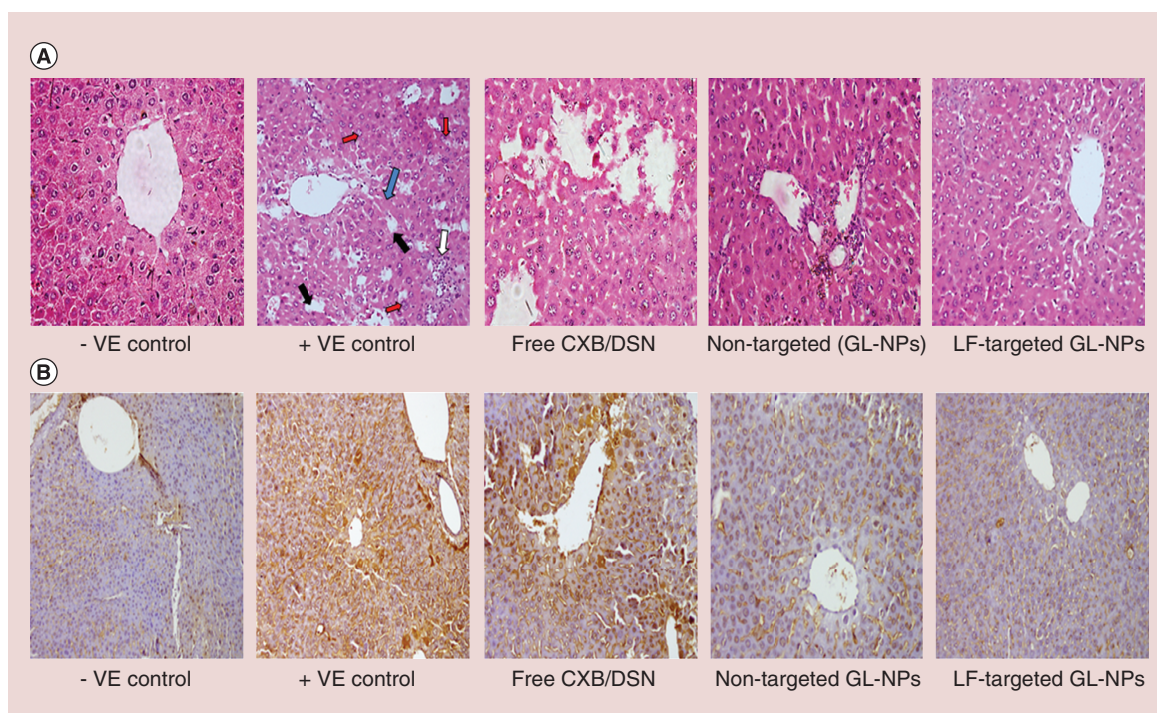


**Figure 9.** Hematoxylin & eosin staining of liver cancer tissues of negative control, positive control group, free drug combination, nontargeted celecoxib/diosmin/gliadin nanoparticles (S8) and targeted celecoxib/diosmin/lactoferrin-gliadin nanoparticles (M4) treated group. (A) Immunohistopathological staining of the proliferative marker Ki-67 in liver cancer tissues of positive control group and free CXB/DSN combination, nontargeted CXB/DSN/GL-NPs (S8) and targeted CXB/DSN/LF-GL-NPs (M4). CXB: Celecoxib; DSN: Diosmin; GL-NP: Gliadin nanoparticle; LF: Lactoferrin.

the central vein with one or rarely two spherical nuclei and abundant strongly eosinophilic cytoplasm. In contrast, mice of positive control treated with DEN (HCC induced) demonstrated abnormal irregular-shaped cytoplasm and enlarged nuclei (Figure 9A). Numerous binucleated hepatocytes were noticed with abundant vacuoles in the cytoplasm surrounding the nucleus [33]. Treatment of mice with nontargeted dual-drug-loaded GL-NPs has shown improvement in the hepatic architecture with less altered hepatocytes in comparison with the group treated with free combined drugs (Figure 9A). The cellular architecture of hepatic specimens from mice that treated with LF-targeted dual-drug-loaded GL-NPs were comparable with that of the negative control mice. The hepatocytes from such mice group showed a compact cytoplasm revealing the absence of hepatic toxicity.

#### *Immunohistochemical analysis of cell proliferation (Ki-67 antigen)*

Ki-67 is considered the most widely used proliferation-associated prognostic marker in HCC patients [71]. The antibody kit detects a specific antibody bounded to Ki-67 antigen in tissue sections. As can be seen in Figure 9B, Ki-67 was strongly stained in tumor specimens of the positive control and free drug-treated mice group compared with tumor specimens of LF-targeted (M4) and nontargeted dual-drug-loaded GL-NPs (S8). The reduced density of Ki-67-stained cells of the NPs-treated groups reflected the high efficiency of NPs in suppression of cancer cell proliferation thereby reducing the tumor growth. The % expression of the proliferation protein Ki-67 in liver cancer tissues, as quantified using digital image analysis technique, was summarized in Figure 10. The results showed a significant elevation of Ki-67 (96.10%) in the positive control group compared with mice treated with nontargeted dual-drug-loaded GL-NPs (26.70%) and to mice treated with LF-targeted dual-drug-loaded GL-NPs, which exhibited the lowest density of Ki-67 corresponding to 16.20%.

#### *Ex vivo imaging of isolated organs*

The *ex vivo* images of isolated organs demonstrated time-dependent accumulation of RBITC/LF-GL-NPs into the organs (Figure 11A). At 4 h after oral delivery of RBITC/LF-GL-NPs, the optical imaging signals increased

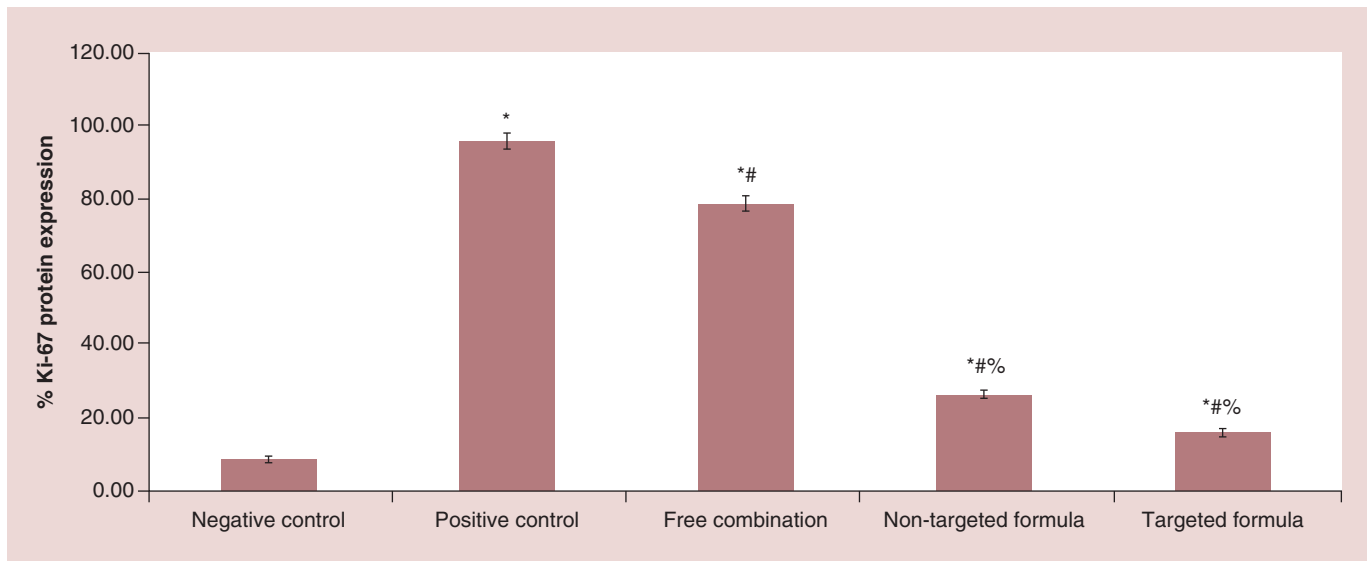


**Figure 10.** Percent Ki-67 proliferation marker in positive control group and liver cancer tissues of free celecoxib/diosmin combination, nontargeted celecoxib/diosmin/gliadin nanoparticles (S8) and targeted celecoxib/diosmin/lactoferrin-gliadin nanoparticles (M4) treated group (c), n = 7.

\*p < 0.05 vs negative control; #p < 0.05 vs positive control; %p < 0.05 vs free celecoxib/diosmin.

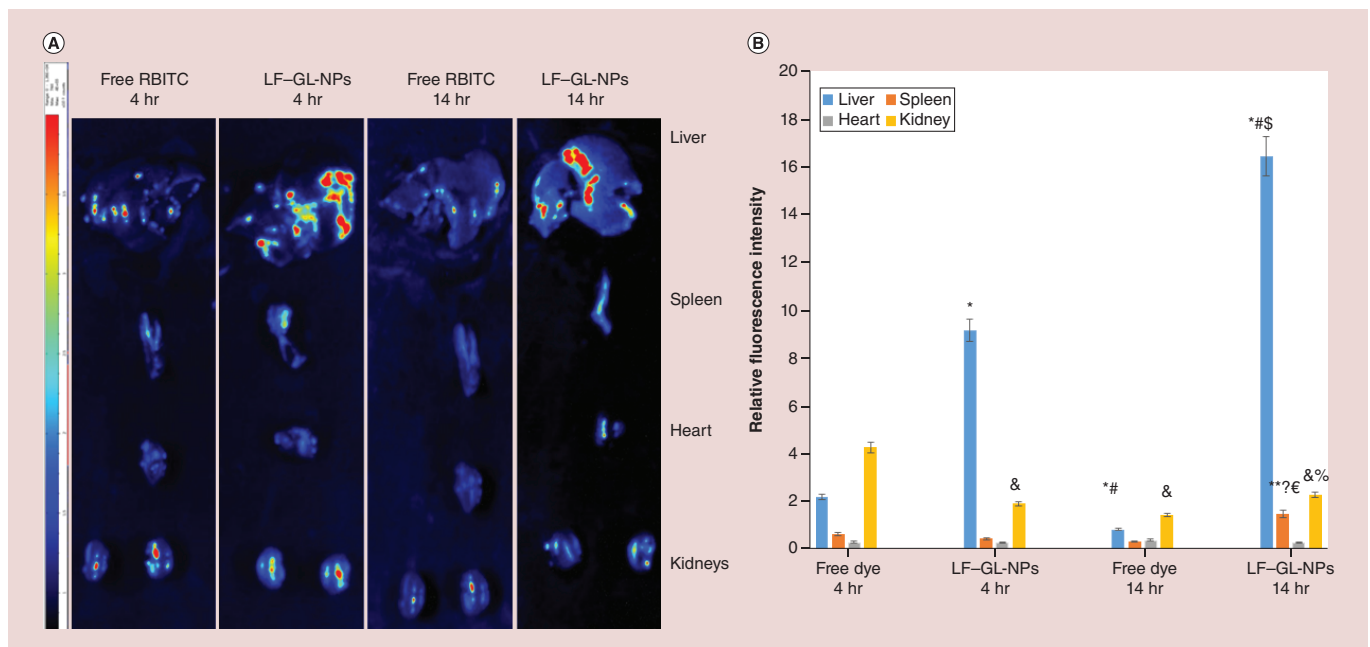


**Figure 11.** *Ex vivo* fluorescence imaging study. (A) *Ex vivo* fluorescence images of dissected livers, spleens, hearts and kidneys after 4 and 14 h postoral administration and (B) Quantitative estimation of fluorescence intensity acquired from different organs of mice after 4 and 14 h postinjection, n = 6.

\*p < 0.05 vs livers free dye 4 h; #p < 0.05 vs livers LF-GL-NPs 14 h; §p < 0.05 vs livers free dye 14 h; \*\*p < 0.05 vs spleens free dye 4 h; ?p < 0.05 vs spleens LF-GL-NPs 4 h; €p < 0.05 spleens free dye 14 h; & p < 0.05 kidneys free dye 4 h; % p < 0.05 kidneys LF-GL-NPs 4 h. LF-GL-NP: Lactoferrin-gliadin nanoparticle; RBITC: Rhodamine B isothiocyanate.

in the liver which was increased by twofold after 14 h compared with 4 h after oral administration (Figure 11B). Particularly, it was previously reported that LF has receptors found in the intestinal epithelium that can facilitate the absorption and transport of NPs across GI tract [54,72]. On the other hand, the optical imaging signal in mice



liver that orally received free dye faded after 14 h. These results ensuring the effective targetability of LF-targeted NPs to liver cancer cells.

The 'proof of concept' presented here substantiates the notion that the fabricated LF-coated GL-NPs offer potential targeted carriers with promising antitumor effects against HCC-bearing animals upon oral administration. Future work will extend to investigate the pathway of these NPs through GIT and tracking their uptake via LF receptors in intestinal epithelium. In addition, comparing the efficacy of NPs when administrated through tail vein versus oral administration. Also, pharmacokinetic study for dual-drug-loaded NPs will conducted upon administration via intravenous and oral routes. For theranostic approach, inorganic NPs such as quantum dots may be conjugated to the surface of NPs to enable tumor imaging and therapeutic goals.

## Conclusion

As an orally active nanocarrier, hydrophobic GL-NPs-encapsulating CXB and DSN were successfully prepared by nanoprecipitation technique followed by spray-drying. For active targeting to ASGP-R overexpressed by HepG2 cells, the surface of GL-NPs was coated with LF layer via electrostatic interactions. Both LF-targeted and nontargeted GL-NPs exhibited acceptable particle size and zeta potential, good entrapment efficiency and sustained release properties for both drugs. LF-targeted GL-NPs have shown higher cellular uptake and enhanced antitumor efficacy compared with nontargeted GL-NPs, which would be related to the receptor-mediated endocytosis into HepG2 cells through LF moiety. *In vivo* anticancer efficacy in HCC-bearing mice revealed the superiority of LF-targeted GL-NPs as manifested by the marked reduction in the evaluated tumor markers (TNF- $\alpha$ , NF- $\kappa$ B, COX-2, VEGF) as well as minimal histopathological and immunohistochemical alterations.

## Summary points

- We have developed hydrophobic gliadin nanoparticles (GL-NPs) prepared by nanoprecipitation technique followed by spray-drying for the targeted codelivery of celecoxib (CXB) and diosmin (DSN).
- To achieve active tumor-targeting, the surface of drug-loaded GL-NPs was coated with lactoferrin (LF) via electrostatic interactions for binding to asialoglycoprotein receptors overexpressed by human liver cancerous cells.
- The resultant LF-GL-NPs exhibited uniform spherical shape with high encapsulation efficiency for CXB and DSN and a sustained release property for both drugs.
- Solid-state characterization showed the disappearance of the characteristic endothermal peak of DSN indicating its conversion to amorphous state, while the CXB endothermal peak was shifted and broadened indicating an interaction between CXB and GL within the nanomatrix.
- *In vitro* cytotoxicity studies on HepG2 liver cancer cells revealed that the LF-targeted GL-NPs enhanced the combination potency compared with the free combined drugs solution and the nontargeted GL-NPs.
- Cellular uptake study revealed that at the same incubation time, the uptake of LF-GL-NPs within HepG2 liver cancer cells was noticeably higher than that of nontargeted GL-NPs, which would be related with the receptor-mediated endocytosis through LF moiety due to high surface expression of asialoglycoprotein receptors on HepG2 cells.
- Biological evaluations of the antitumor effects of the elaborated formulations revealed the superiority of the LF-GL-NPs as manifested from the marked reduction in the expression levels of TNF- $\alpha$ , NF- $\kappa$ B, COX, VEGF and induction of caspase-mediated apoptosis process.
- *Ex vivo* imaging of isolated organs showed that LF-GL-NPs exhibited a much higher accumulation in livers more than other organs after oral administration in hepatocellular carcinoma-induced mice.

## Supplementary data

To view the supplementary data that accompany this paper please visit the journal website at: [www.futuremedicine.com/doi/full/10.2217/nnm-2018-0134](http://www.futuremedicine.com/doi/full/10.2217/nnm-2018-0134)

## Financial & competing interests disclosure

The authors have no relevant affiliations or financial involvement with any organization or entity with a financial interest in or financial conflict with the subject matter or materials discussed in the manuscript. This includes employment, consultancies, honoraria, stock ownership or options, expert testimony, grants or patents received or pending or royalties.

No writing assistance was utilized in the production of this manuscript.

## References

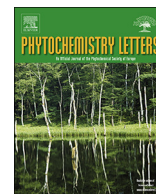
- 1 Flores A, Marrero JA. Emerging trends in hepatocellular carcinoma: focus on diagnosis and therapeutics. *Clin. Med. Insights: Oncol.* 8, 71–76 (2014).
- 2 Bruix J, Sherman M, Llovet JM *et al.* Clinical management of hepatocellular carcinoma. Conclusions of the Barcelona-2000 EASL conference. *J. Hepatol.* 35(3), 421–430 (2001).
- 3 Xie H, Xu X, Chen J *et al.* Rational design of multifunctional small-molecule prodrugs for simultaneous suppression of cancer cell growth and metastasis *in vitro* and *in vivo*. *Chem. Commun.* 52(32), 5601–5604 (2016).
- 4 Elzoghby A. Polymeric nanocarriers as robust platforms for cancer therapy. *Curr. Pharm. Des.* (2017).
- 5 Sabra S, Abdelmoneem M, Abdelwakil M *et al.* Self-assembled nanocarriers based on amphiphilic natural polymers for anti-cancer drug delivery applications. *Curr. Pharm. Des.* (2017).
- 6 Bae SH, Jung ES, Park YM *et al.* Expression of cyclooxygenase-2 (COX-2) in hepatocellular carcinoma and growth inhibition of hepatoma cell lines by a COX-2 inhibitor, NS-398. *Clin. Cancer Res.* 7(5), 1410–1418 (2001).
- 7 Cui W, Yu CH, Hu KQ. *In vitro* and *in vivo* effects and mechanisms of celecoxib-induced growth inhibition of human hepatocellular carcinoma cells. *Clin. Cancer Res.* 11(22), 8213–8221 (2005).
- 8 Tahir M, Rehman MU, Lateef A *et al.* Diosmin abrogates chemically induced hepatocarcinogenesis via alleviation of oxidative stress, hyperproliferative and inflammatory markers in murine model. *Toxicol. Lett.* 220(3), 205–218 (2013).
- 9 Dung TD, Lin CH, Binh TV *et al.* Diosmin induces cell apoptosis through protein phosphatase 2A activation in HA22T human hepatocellular carcinoma cells and blocks tumour growth in xenografted nude mice. *Food Chem.* 132(4), 2065–2073 (2012).
- 10 Dholakiya SL, Benzeroual KE. Protective effect of diosmin on LPS-induced apoptosis in PC12 cells and inhibition of TNF- $\alpha$  expression. *Toxicol. in Vitro* 25(5), 1039–1044 (2011).
- 11 Funakoshi-Tago M, Shimizu T, Tago K *et al.* Celecoxib potently inhibits TNF $\alpha$ -induced nuclear translocation and activation of NF- $\kappa$ B. *Biochem. Pharmacol.* 76(5), 662–671 (2008).
- 12 Sui W, Zhang Y, Wang Z *et al.* Antitumor effect of a selective COX-2 inhibitor, celecoxib, may be attributed to angiogenesis inhibition through modulating the PTEN/PI3K/Akt/HIF-1 pathway in an H22 murine hepatocarcinoma model. *Oncology Rep.* 31(5), 2252–2260 (2014).
- 13 Dung TD, Day CH, Binh TV *et al.* PP2A mediates diosmin p53 activation to block HA22T cell proliferation and tumor growth in xenografted nude mice through PI3K–Akt–MDM2 signaling suppression. *Food Chem Toxicol.* 50(5), 1802–1810 (2012).
- 14 Freag MS, Elnaggar YS, Abdallah OY. Development of novel polymer-stabilized diosmin nanosuspensions: *In vitro* appraisal and *ex vivo* permeation. *Int. J. Pharm.* 454(1), 462–471 (2013).
- 15 Freag MS, Elnaggar YS, Abdallah OY. Lyophilized phytosomal nanocarriers as platforms for enhanced diosmin delivery: optimization and *ex vivo* permeation. *Int. J. Nanomedicine* 8, 2385 (2013).
- 16 Paulson SK, Vaughn MB, Jessen SM *et al.* Pharmacokinetics of celecoxib after oral administration in dogs and humans: effect of food and site of absorption. *J. Pharmacol. Exp. Ther.* 297(2), 638–645 (2001).
- 17 Nakamura K, Nara E, Akiyama Y. Development of an oral sustained release drug delivery system utilizing pH-dependent swelling of carboxyvinyl polymer. *J. Control. Rel.* 111(3), 309–315 (2006).
- 18 He W, Tan Y, Tian Z, Chen L, Hu F, Wu W. Food protein-stabilized nanoemulsions as potential delivery systems for poorly water-soluble drugs: preparation, *in vitro* characterization, and pharmacokinetics in rats. *Int. J. Nanomed.* 6, 521 (2011).
- 19 Elzoghby AO, El-Lakany SA, Helmy MW, Abu-Serie MM, Elgindy NA. Shell-crosslinked zein nanocapsules for oral codelivery of exemestane and resveratrol in breast cancer therapy. *Nanomedicine* 12(24), 2785–2805 (2017).
- 20 Elzoghby A, Freag M, Mamdouh H, Elkhodairy K. Zein-based nanocarriers as potential natural alternatives for drug and gene delivery: focus on cancer therapy. *Curr. Pharm. Des.* 23(35), 5261–5271 (2017).
- 21 Arango M, Ponchel G, Orecchioni A, Renedo M, Duchene D, Irache J. Bioadhesive potential of gliadin nanoparticulate systems. *Eur. J. Pharm. Sci.* 11(4), 333–341 (2000).
- 22 Ezpeleta I, Irache JM, Stainmesse S *et al.* Gliadin nanoparticles for the controlled release of all-trans-retinoic acid. *Int. J. Pharm.* 131(2), 191–200 (1996).
- 23 Nehra V, Marietta EV, Murray JA. Celiac disease and its therapy: current approaches and new advances. In: *Wheat and Rice in Disease Prevention and Health*. Watson RR, Preedy VR, Zibadi S. (Eds). Academic Press, Elsevier Inc., MA, USA 143–155 (2014).
- 24 Sabra SA, Elzoghby AO, Sheweita SA *et al.* Self-assembled amphiphilic zein–lactoferrin micelles for tumor targeted co-delivery of rapamycin and wogonin to breast cancer. *Eur. J. Pharm. Biopharm.* 128, 156–169 (2018).
- 25 Joye IJ, Nelis VA, McClements DJ. Gliadin-based nanoparticles: fabrication and stability of food-grade colloidal delivery systems. *Food Hydrocolloids* 44, 86–93 (2015).
- 26 Joye IJ, Nelis VA, McClements DJ. Gliadin-based nanoparticles: Stabilization by post-production polysaccharide coating. *Food Hydrocolloids* 43, 236–242 (2015).

- 27 El-Far SW, Helmy MW, Khattab SN, Bekhit AA, Hussein AA, Elzoghby AO. Phytosomal bilayer-enveloped casein micelles for codelivery of monascus yellow pigments and resveratrol to breast cancer. *Nanomedicine (Lond)*. 13(5), 481–499 (2018).
- 28 Wang J, Wang H, Li J *et al.* iRGD-decorated polymeric nanoparticles for the efficient delivery of vandetanib to hepatocellular carcinoma: preparation and *in vitro* and *in vivo* evaluation. *ACS Appl. Mater. Interfaces*. 8(30), 19228–19237 (2016).
- 29 Khattab SN, Naim SEA, El-Sayed M *et al.* Design and synthesis of new s-triazine polymers and their application as nanoparticulate drug delivery systems. *New J. Chem.* 40(11), 9565–9578 (2016).
- 30 Yu Nie LJ, Ding H, Xie L *et al.* Cholesterol derivatives based charged liposomes for doxorubicin delivery: preparation, *in vitro* and *in vivo* characterization. *Theranostics* 2(11), 1092 (2012).
- 31 El-Far SW, Helmy MW, Khattab SN, Bekhit AA, Hussein AA, Elzoghby AO. Folate conjugated vs PEGylated phytosomal casein nanocarriers for codelivery of fungal-and herbal-derived anticancer drugs. *Nanomedicine* 13(12), 1463–1480 (2018).
- 32 Yang T, Sun D, Xu P *et al.* Stability of bovine serum albumin labelled by rhodamine B isothiocyanate. *Biomed. Res.* 28(9), (2017).
- 33 Nasr M, Nafee N, Saad H, Kazem A. Improved antitumor activity and reduced cardiotoxicity of epirubicin using hepatocyte-targeted nanoparticles combined with tocotrienols against hepatocellular carcinoma in mice. *Eur. J. Pharm. Biopharm.* 88(1), 216–225 (2014).
- 34 Kuppen P, Jonges L, Van De Velde C *et al.* Liver and tumour tissue concentrations of TNF-alpha in cancer patients treated with TNF-alpha and melphalan by isolated liver perfusion. *Br. J. Cancer* 75(10), 1497–1500 (1997).
- 35 Zhao X, Chen Q, Li Y, Tang H, Liu W, Yang X. Doxorubicin and curcumin co-delivery by lipid nanoparticles for enhanced treatment of diethylnitrosamine-induced hepatocellular carcinoma in mice. *Eur. J. Pharm. Biopharm.* 93, 27–36 (2015).
- 36 Kaczmarek E, Gorna A, Majewski P. Techniques of image analysis for quantitative immunohistochemistry. *Rocz Akad Med Bialymst.* 49(Suppl.1), 155–158 (2004).
- 37 Xu L, Xu S, Wang H *et al.* Enhancing the efficacy and safety of doxorubicin against hepatocellular carcinoma through a modular assembly approach: the combination of polymeric prodrug design, nanoparticle encapsulation, and cancer cell-specific drug targeting. *ACS Appl. Mater. Interfaces* 10(4), 3229–3240 (2018).
- 38 Khatun Z, Nurunnabi M, Reeck GR, Cho KJ, Lee YK. Oral delivery of taurocholic acid linked heparin–docetaxel conjugates for cancer therapy. *J. Control Release.* 170(1), 74–82 (2013).
- 39 Reis CP, Neufeld RJ, Ribeiro AJ, Veiga F. Nanoencapsulation I. Methods for preparation of drug-loaded polymeric nanoparticles. *Nanomedicine*. 2(1), 8–21 (2006).
- 40 Clogston JD, Patri AK. Zeta potential measurement. *Methods Mol. Biol.* 63–70 (2011).
- 41 Thorat AA, Dalvi SV. Liquid antisolvent precipitation and stabilization of nanoparticles of poorly water soluble drugs in aqueous suspensions: recent developments and future perspective. *Chem. Eng. J.* 181, 1–34 (2012).
- 42 Kabary DM, Helmy MW, Elkhodairy KA, Fang JY, Elzoghby AO. Hyaluronate/lactoferrin layer-by-layer-coated lipid nanocarriers for targeted co-delivery of rapamycin and berberine to lung carcinoma. *Colloids and Surfaces B: Biointerfaces* 169, 183–194 (2018).
- 43 Alqahtani MS, Islam MS, Podaralla S *et al.* Food protein based core–shell nanocarriers for oral drug delivery: Effect of shell composition on *in vitro* and *in vivo* functional performance of zein nanocarriers. *Mol. Pharm.* 14(3), 757–769 (2017).
- 44 Brines R, Brock J. The effect of trypsin and chymotrypsin on the *in vitro* antimicrobial and iron-binding properties of lactoferrin in human milk and bovine colostrum: unusual resistance of human apolactoferrin to proteolytic digestion. *Biochim. Biophys. Acta.* 759(3), 229–235 (1983).
- 45 Zhang HZ, Gao FP, Liu LR, Li XM, Zhou ZM, Zhang QQ. Pullulan acetate nanoparticles prepared by solvent diffusion method for epirubicin chemotherapy. *Colloids and Surf. B: Biointerfaces* 71(1), 19–26 (2009).
- 46 Anwer MK, Jamil S, Ansari MJ *et al.* Water soluble binary and ternary complexes of diosmin with  $\beta$ -cyclodextrin: Spectroscopic characterization, release studies and anti-oxidant activity. *J. Molec. Liquids* 199, 35–41 (2014).
- 47 Elzoghby AO, Mostafa SK, Helmy MW, Eldemellawy MA, Sheweita SA. Superiority of aromatase inhibitor and cyclooxygenase-2 inhibitor combined delivery: hyaluronate-targeted versus PEGylated protamine nanocapsules for breast cancer therapy. *Int. J. Pharm* 529(1–2), 178–192 (2017).
- 48 Ma Y, Zheng Y, Liu K *et al.* Nanoparticles of poly (lactide-co-glycolide)-da-tocopheryl polyethylene glycol 1000 succinate random copolymer for cancer treatment. *Nanoscale Res. Lett.* 5(7), 1161 (2010).
- 49 Elzoghby AO, Mostafa SK, Helmy MW, Eldemellawy MA, Sheweita SA. Multi-reservoir phospholipid shell encapsulating protamine nanocapsules for co-delivery of letrozole and celecoxib in breast cancer therapy. *Pharm. Res.* 34(9), 1956–1969 (2017).
- 50 Fouad EA, Yassin AEB, Alajami HN. Characterization of celecoxib-loaded solid lipid nanoparticles formulated with tristearin and softisan 100. *Trop. J. Pharm. Res.* 14(2), 205–210 (2015).
- 51 Kumari S, Ahsan SM, Kumar JM, Kondapi AK, Rao NM. Overcoming blood brain barrier with a dual purpose Temozolomide loaded Lactoferrin nanoparticles for combating glioma (SERP-17-12433). *Sci. Repo.* 7(1), 6602 (2017).
- 52 Elzoghby A. Editorial (Thematic Issue: Nanocarriers based on natural polymers as platforms for drug and gene delivery applications). *Curr. Pharm. Des.* 22(22), 3303–3304 (2016).

- 53 Golla K, Cherukuvada B, Ahmed F, Kondapi AK. Efficacy, safety and anticancer activity of protein nanoparticle-based delivery of doxorubicin through intravenous administration in rats. *PLoS ONE* 7(12), e51960 (2012).
- 54 Zhang ZH, Wang XP, Ayman WY, Munyendo WL, Lv HX, Zhou JP. Studies on lactoferrin nanoparticles of gambogic acid for oral delivery. *Drug Deliv.* 20(2), 86–93 (2013).
- 55 Yuan Y, Cai T, Xia X, Zhang R, Chiba P, Cai Y. Nanoparticle delivery of anticancer drugs overcomes multidrug resistance in breast cancer. *Drug Deliv.* 23(9), 3350–3357 (2016).
- 56 Spoelstra EC, Dekker H, Schuurhuis GJ, Broxterman HJ, Lankelma J. P-glycoprotein drug efflux pump involved in the mechanisms of intrinsic drug resistance in various colon cancer cell lines: evidence for a saturation of active daunorubicin transport. *Biochem. Pharma.* 41(3), 349–359 (1991).
- 57 Wei M, Xu Y, Zou Q *et al.* Hepatocellular carcinoma targeting effect of PEGylated liposomes modified with lactoferrin. *Eur. J. Pharm. Sci.* 46(3), 131–141 (2012).
- 58 Wei M, Guo X, Tu L *et al.* Lactoferrin-modified PEGylated liposomes loaded with doxorubicin for targeting delivery to hepatocellular carcinoma. *Int. J. Nanomed.* 10, 5123 (2015).
- 59 Yue ZG, Wei W, Lv PP *et al.* Surface charge affects cellular uptake and intracellular trafficking of chitosan-based nanoparticles. *Biomacromolecules* 12(7), 2440–2446 (2011).
- 60 Bharti AC, Aggarwal BB. Nuclear factor-kappa B and cancer: its role in prevention and therapy. *Biochem. Pharma.* 64(5–6), 883–888 (2002).
- 61 Tahir M, Rehman MU, Lateef A *et al.* Diosmin protects against ethanol-induced hepatic injury via alleviation of inflammation and regulation of TNF- $\alpha$  and NF- $\kappa$ B activation. *Alcohol* 47(2), 131–139 (2013).
- 62 Jang MK, Su Kim H, Chung YH. Clinical aspects of tumor necrosis factor- $\alpha$  signaling in hepatocellular carcinoma. *Curr. Pharm. Des.* 20(17), 2799–2808 (2014).
- 63 Márquez-Rosado L, Trejo-Solís MC, García-Cuellar CM, Villa-Treviño S. Celecoxib, a cyclooxygenase-2 inhibitor, prevents induction of liver preneoplastic lesions in rats. *J. Hepatol.* 43(4), 653–660 (2005).
- 64 Boosani CS, Mannam AP, Cosgrove D *et al.* Regulation of COX-2-mediated signaling by  $\alpha$ 3 Type IV noncollagenous domain in tumor angiogenesis. *Blood* 110(4), 1168–1177 (2007).
- 65 Grosch S, Tegeder I, Niederberger E, Bräutigam L, Geisslinger G. COX-2 independent induction of cell cycle arrest and apoptosis in colon cancer cells by the selective COX-2 inhibitor celecoxib. *FASEB J.* 15(14), 2742–2744 (2001).
- 66 Tegeder I, Pfeilschifter J, Geisslinger G. Cyclooxygenase-independent actions of cyclooxygenase inhibitors. *FASEB J.* 15(12), 2057–2072 (2001).
- 67 Carmeliet P. VEGF as a key mediator of angiogenesis in cancer. *Oncology* 69 (Suppl. 3), 4–10 (2005).
- 68 Liu Y, Liu A, Li H, Li C, Lin J. Celecoxib inhibits interleukin-6/Interleukin-6 receptor-induced JAK2/STAT3 phosphorylation in human hepatocellular carcinoma cells. *Cancer Prev. Res.* 4(8), 1296–1305 (2011).
- 69 Shi Y. Mechanisms of caspase activation and inhibition during apoptosis. *Mol. Cell* 9(3), 459–470 (2002).
- 70 Buddhan R, Manoharan S. Diosmin reduces cell viability of A431 skin cancer cells through apoptotic induction. *J. Cancer Res. Ther.* 13(3), 471 (2017).
- 71 King KL, Hwang JJ, Chau GY *et al.* Ki-67 expression as a prognostic marker in patients with hepatocellular carcinoma. *J. Gastroenterol. Hepatol.* 13(3), 273–279 (1998).
- 72 Wolf JS, Li G, Varadhachary A *et al.* Oral lactoferrin results in T cell-dependent tumor inhibition of head and neck squamous cell carcinoma *in vivo*. *Clin. Cancer Res.* 13(5), 1601–1610 (2007).







## Briaviolides O and P, new briaranes from a cultured octocoral *Briareum violaceum*

Jing-Hao Xu<sup>a,b</sup>, Yu-Chia Chang<sup>b,c</sup>, Guo-Qiang Li<sup>d,e</sup>, Zhi-Hong Wen<sup>f,\*</sup>, Yang-Chang Wu<sup>g,h,i,\*</sup>, Ping-Jyun Sung<sup>a,b,f,g,j,\*</sup>

<sup>a</sup> Graduate Institute of Marine Biology, National Dong Hwa University, Pingtung 94450, Taiwan

<sup>b</sup> National Museum of Marine Biology and Aquarium, Pingtung 94450, Taiwan

<sup>c</sup> Research Center for Chinese Herbal Medicine, Research Center for Food and Cosmetic Safety, Graduate Institute of Health Industry Technology, College of Human Ecology, Chang Gung University of Science and Technology, Taoyuan 33303, Taiwan

<sup>d</sup> Key Laboratory of Marine Drugs, Chinese Ministry of Education, School of Medicine and Pharmacy, Ocean University of China, Qingdao 266003, China

<sup>e</sup> Laboratory of Marine Drugs and Biological Products, National Laboratory for Marine Science and Technology, Qingdao 266235, China

<sup>f</sup> Department of Marine Biotechnology and Resources, National Sun Yat-sen University, Kaohsiung 80424, Taiwan

<sup>g</sup> Graduate Institute of Natural Products, Kaohsiung Medical University, Kaohsiung 80708, Taiwan

<sup>h</sup> Research Center for Natural Products and Drug Development, Kaohsiung Medical University, Kaohsiung 80708, Taiwan

<sup>i</sup> Department of Medical Research, Kaohsiung Medical University Hospital, Kaohsiung 80756, Taiwan

<sup>j</sup> Chinese Medicine Research and Development Center, China Medical University Hospital, Taichung 40447, Taiwan

### ARTICLE INFO

#### Keywords:

*Briareum violaceum*

Octocoral

Briarane

Briaviolide

Anti-inflammatory activity

iNOS

### ABSTRACT

Chemical investigation of the EtOAc-soluble fraction from the MeOH/DCM extract of a cultured octocoral *Briareum violaceum* afforded two new briarane diterpenoids, briaviolides O (1) and P (2). The structures of briaranes 1 and 2 were elucidated on the basis of spectroscopic analysis, and 1 was shown to inhibit the accumulation of pro-inflammatory iNOS protein in LPS-stimulated RAW264.7 macrophage cells.

### 1. Introduction

The octocoral *Briareum violaceum* (family Briareidae) (Samimi-Namin and van Ofwegen, 2016) is a rich source of diterpenoids with a briarane carbon skeleton that often have complex structures and bioactivities (Ito et al., 2007; Iwasaki et al., 2006; Liaw et al., 2014; Sheu et al., 1996; Xu et al., 2000, 2018). In studies of the chemical constituents of cultured *B. violaceum*, two new briaranes, briaviolides O (1) and P (2), were obtained (Fig. 1). We isolated these two compounds, determined their structures, and further studied their anti-inflammatory activities in terms of inhibition of inducible oxide synthase (iNOS) and cyclooxygenase-2 (COX-2) in an *in vitro* pro-inflammatory macrophage culture model.

### 2. Results and discussion

Briaviolide O (1) was obtained as an amorphous powder. HRESIMS

of compound 1 showed a pseudomolecular peak at  $m/z$  675.26248, which established the molecular formula  $C_{32}H_{44}O_{14}$  (calcd for  $C_{32}H_{44}O_{14} + Na$ , 675.26233), indicating eleven degrees of unsaturation. Absorption peaks at 3580, 1781 and 1738  $cm^{-1}$  in the IR spectrum of 1 indicated a structure containing hydroxy,  $\gamma$ -lactone and ester groups. Data from a DEPT experiment and  $^1H$  NMR study, together with analysis of the molecular formula, suggested the existence of one exchangeable proton, which required the presence of one hydroxy group. A trisubstituted olefin was identified from two carbon signals ( $\delta_C$  143.1 and 123.5; C and CH, respectively), and a tetrasubstituted epoxide containing a methyl substituent was confirmed from signals of two oxygenated quaternary carbons ( $\delta_C$  70.3 and 66.1; both C) and from the proton signal of a methyl ( $\delta_H$  1.78, 3H, s) in the  $^{13}C$  and  $^1H$  NMR spectra of 1 (Table 1), respectively. In addition, six carbonyl resonances ( $\delta_C$  172.4, 170.2, 170.1, 170.0, 170.0 and 168.0) further confirmed the existence of one  $\gamma$ -lactone and five other ester groups. On the other hand, the results of  $^1H$  NMR spectrum analysis indicated four acetate

\* Corresponding authors at: National Museum of Marine Biology and Aquarium, Pingtung 94450, Taiwan.

\*\* Corresponding author at: Department of Marine Biotechnology and Resources, National Sun Yat-sen University, Kaohsiung 80424, Taiwan.

E-mail addresses: [wzh@mail.nsysu.edu.tw](mailto:wzh@mail.nsysu.edu.tw) (Z.-H. Wen), [yachwu@kmu.edu.tw](mailto:yachwu@kmu.edu.tw) (Y.-C. Wu), [pjsung@nmmba.gov.tw](mailto:pjsung@nmmba.gov.tw) (P.-J. Sung).

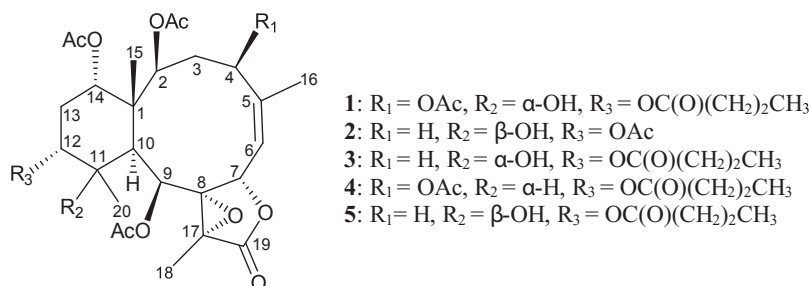


Fig. 1. The structures of briaranolides O (1), P (2), L (3), M (4) and K (5).

Table 1

<sup>1</sup>H and <sup>13</sup>C NMR data for briaranolides 1 and 2.

Position	1		2	
	δ <sub>H</sub> (J in Hz) <sup>a</sup>	δ <sub>C</sub> , Mult. <sup>b</sup>	δ <sub>H</sub> (J in Hz) <sup>a</sup>	δ <sub>C</sub> , Mult. <sup>b</sup>
1		47.5, C		46.5, C
2	5.10 d (8.0)	73.3, CH	5.17 d (7.2)	75.3, CH
3α/β	2.02 m; 2.96 dd (15.2, 12.4)	37.5, CH <sub>2</sub>	1.99 m; 2.62 ddd (15.2, 15.2, 9.6)	32.2, CH <sub>2</sub>
4/4'	5.03 dd (12.4, 5.2)	72.3, CH	2.53 br d (15.2); 1.97 m	28.6, CH <sub>2</sub>
5		143.1, C		146.2, C
6	5.38 d (8.8)	123.5, CH	5.29 br d (9.2)	117.4, CH
7	5.54 d (8.8)	73.8, CH	5.38 d (9.2)	75.1, CH
8		70.3, C		70.7, C
9	5.83 s	67.2, CH	5.74 d (2.0)	68.0, CH
10	2.30 s	45.4, CH	2.35 d (2.0)	44.9, CH
11		73.8, C		75.9, C
12	4.80 br s	74.0, CH	4.83 dd (2.8, 2.8)	75.3, CH
13/13'	2.26 m; 1.97 m	25.8, CH <sub>2</sub>	2.18 m; 2.01 m	24.2, CH <sub>2</sub>
14	4.70 br s	73.3, CH	4.72 dd (3.2, 3.2)	74.9, CH
15	1.24 s	14.4, CH <sub>3</sub>	1.28 s	14.8, CH <sub>3</sub>
16	2.16 s	25.4, CH <sub>3</sub>	2.05 s	27.0, CH <sub>3</sub>
17		66.1, C		64.6, C
18	1.78 s	10.3, CH <sub>3</sub>	1.70 s	10.2, CH <sub>3</sub>
19		170.2, C		171.3, C
20	1.24 s	23.2, CH <sub>3</sub>	1.31 s	30.0, CH <sub>3</sub>
2-OAc		170.0, C		170.3, C
	2.00 s	21.3, CH <sub>3</sub>	2.00 s	21.3, CH <sub>3</sub>
4-OAc		170.0, C		
	2.05 s	21.1, CH <sub>3</sub>		
9-OAc		168.0, C		169.4, C
	2.24 s	21.1, CH <sub>3</sub>	2.22 s	21.5, CH <sub>3</sub>
12-OAc				169.8, C
			2.06 s	21.2, CH <sub>3</sub>
14-OAc		170.1, C		170.4, C
	1.97 s	21.4, CH <sub>3</sub>	1.98 s	21.5, CH <sub>3</sub>
12- <i>n</i> -OC(O)Pr		172.4, C		
	2.33 t (7.2)	36.3, CH <sub>2</sub>		
	1.67 sext (7.2)	18.3, CH <sub>2</sub>		
	0.97 t (7.2)	13.7, CH <sub>3</sub>		
11-OH	n. o. <sup>c</sup>		2.12 s	

<sup>a</sup> Spectra recorded at 400 MHz in CDCl<sub>3</sub> at 25 °C.

<sup>b</sup> Spectra recorded at 100 MHz in CDCl<sub>3</sub> at 25 °C.

<sup>c</sup> n. o. = Not observed.

methyls (δ<sub>H</sub> 2.24, 2.05, 2.00 and 1.97; all 3H, s); the additional ester group was identified as an *n*-butyryloxy group, and <sup>1</sup>H–<sup>1</sup>H COSY correlations revealed seven contiguous protons [δ<sub>H</sub> 0.97 (3H, t), 1.67 (2H, sext) and 2.33 (2H, t); all *J* values 7.2 Hz] (Table 1). Based on correlations identified by HMBC analysis, the carbon signal (δ<sub>C</sub> 172.4, C) was found to be associated with the signals of the methylene protons (δ<sub>H</sub> 2.33 and 1.67) (Fig. 2), and was consequently assigned as the carbon atom of the *n*-butyrate carbonyl. From the aforementioned data, metabolite 1 was identified as a compound with four rings.

From the <sup>1</sup>H–<sup>1</sup>H COSY spectrum of 1, four different structural units, H-2/H<sub>2</sub>-3/H-4, H-6/H-7 and H-12/H<sub>2</sub>-13/H-14, were identified (Fig. 2),

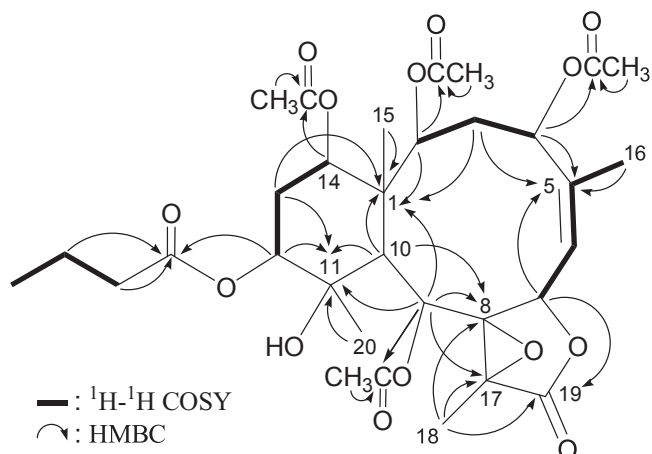


Fig. 2. The <sup>1</sup>H–<sup>1</sup>H COSY and selective HMBC (protons→quaternary carbons) correlations of 1.

which were assembled with the assistance of an HMBC experiment. The HMBC correlations between protons and quaternary carbons of 1 (Fig. 2), such as H-2, H<sub>2</sub>-3, H-9, H-10, H<sub>2</sub>-13, H<sub>3</sub>-15/C-1; H<sub>2</sub>-3, H-7, H<sub>3</sub>-16/C-5; H-9, H-10, H<sub>3</sub>-18/C-8; H-9, H-10, H-12, H<sub>2</sub>-13, H<sub>3</sub>-20/C-11; H-9, H<sub>3</sub>-18/C-17; and H-7, H<sub>3</sub>-18/C-19, permitted elucidation of the carbon skeleton of 1. The ring-junction C-15 methyl group was positioned at C-1 in light of the HMBC correlations between H<sub>3</sub>-15/C-1. At C-5, a vinyl methyl connected to this carbon was confirmed by HMBC correlations between H<sub>3</sub>-16/C-5, and further supported by allylic coupling between H-6 and H<sub>3</sub>-16 in the <sup>1</sup>H–<sup>1</sup>H COSY spectrum analysis of 1. At C-12, an *n*-butyrate ester was located according to connectivity between H-12 (δ<sub>H</sub> 4.80) and the carbonyl carbon of the *n*-butyrate (δ<sub>C</sub> 172.4). Furthermore, the other four acetoxy groups were located at C-2, C-4, C-9 and C-14 based on the HMBC correlations of the oxymethine protons at δ<sub>H</sub> 5.10 (H-2), 5.03 (H-4), 5.83 (H-9) and 4.70 (H-14) with the ester carbonyls at δ<sub>C</sub> 170.0, 170.0, 168.0 and 170.1, respectively. Thus, the remaining hydroxy group was positioned at C-11, an oxygenated quaternary carbon at δ<sub>C</sub> 73.8. The aforementioned data defined the molecular framework of 1.

The stereochemistry of 1 was established by a NOESY experiment, and further supported by MM2 force field analysis (Allinger, 1977), demonstrating that the most stable conformer of 1 was as shown in Fig. 3. In the NOESY spectrum of 1, H-10 was associated with H-2 and H-9, while no associations were seen with Me-15 and Me-20, which suggested that these protons were positioned on the α face, due to the fact that the C-15 and C-20 methyls were β-substituents at C-1 and C-11, respectively. H-12 showed a correlation with Me-20, and H-14 was correlated with Me-15; there were no correlations between H-10/H-12 and H-10/H-14, demonstrating that the *n*-butyryloxy group at C-12, hydroxy group at C-11 and acetoxy group at C-14 were α-oriented. One of the C-3 methylene protons (δ<sub>H</sub> 2.96) showed a correlation with H-7, but not with H-2, and this proton was designated β-oriented. A correlation between H-7 and H-3β, but not H-6, as well as a large coupling constant

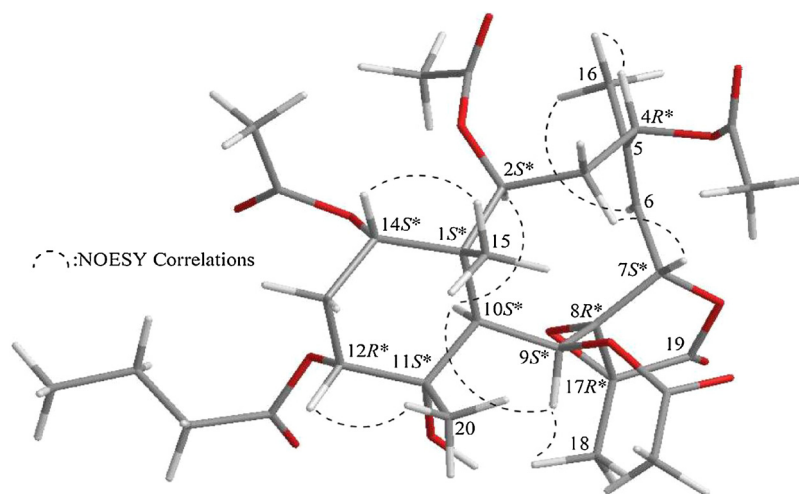


Fig. 3. Selected protons with key NOESY correlations of **1**.

between H-7 and H-6 ( $J = 8.8$  Hz), suggested that the dihedral angle between H-7 and H-6 was nearly  $180^\circ$ , and H-7 was  $\beta$ -oriented and the 8,17-epoxy group was  $\alpha$ -oriented according to modeling analysis. The *Z*-configuration of the C-5/6 double bond was confirmed based on the fact that the C-6 olefin proton ( $\delta_{\text{H}}$  5.38) was correlated with the C-16 vinyl methyl ( $\delta_{\text{H}}$  2.16). Furthermore, correlation of H-4 with H<sub>3</sub>-16 indicated that the acetoxy group at C-4 was  $\beta$ -oriented. Thus, on the basis of the above results, **1** was found to possess the configurations  $1S^*, 2S^*, 4R^*, 7S^*, 8R^*, 9S^*, 10S^*, 11S^*, 12R^*, 14S^*, 17R^*$ . It was found that the NMR signals of **1** were similar to those of known briarane analogues, briaviolides L (**3**) and M (**4**) (Fig. 1) (Xu et al., 2018), except that the signals corresponding to the acetoxy group at C-4 in **1** were replaced by signals for a proton in **3**; and the signals corresponding to the proton at C-11 in **4** were replaced by signals for a hydroxy group in **1** (Xu et al., 2018).

Briaviolide P (**2**) was found to have the molecular formula  $\text{C}_{28}\text{H}_{38}\text{O}_{12}$  based on the HRESIMS peak at  $m/z$  589.22546 (calcd for  $\text{C}_{28}\text{H}_{38}\text{O}_{12} + \text{Na}$ , 589.22555). Its absorption peaks in the IR spectrum showed an ester carbonyl, a  $\gamma$ -lactone and broad OH stretching at 1730, 1779 and  $3480\text{ cm}^{-1}$ , respectively. The  $^{13}\text{C}$  NMR spectrum indicated that one  $\gamma$ -lactone and four esters were present, as carbonyl resonances were observed at  $\delta_{\text{C}}$  171.3, 170.4, 170.3, 169.8 and 169.4, respectively (Table 1). The  $^1\text{H}$  NMR spectrum also indicated the presence of four acetate methyls ( $\delta_{\text{H}}$  2.22, 2.06, 2.00 and 1.98, each  $3\text{H} \times \text{s}$ ) (Table 1), and the NMR data were found to be similar to those of a known briarane analogue, briaviolide K (**5**) (Fig. 1) (Xu et al., 2018), with the exception that the 12-*n*-butyryloxy group in **5** was replaced by an acetoxy group in **2**. The locations of the functional groups were further confirmed by other  $^1\text{H}$ - $^1\text{H}$  COSY and HMBC correlations (Fig. 4), and hence briaviolide P (**2**) was assigned the structure of **2**, with the same stereochemistry as that of briaviolide K (**5**), because the stereogenic centers that **2** had in common with **5**, in addition to the  $^1\text{H}$  and  $^{13}\text{C}$  NMR chemical shifts and proton coupling constants, matched well, and were further supported by a NOESY experiment.

The relative stereochemistry of **2** was established based on the NOE interaction results from a NOESY experiment (Fig. 5). In the NOESY spectrum of **2**, H-10 was associated with H-2, H-9 and H<sub>3</sub>-20, while no association was seen with Me-15, which suggested that these protons were positioned on the  $\alpha$  face, due to the fact that the C-15 methyl and 11-hydroxy group were  $\beta$ -substituents at C-1 and C-11. H-12 showed correlations with H<sub>3</sub>-20 and C-13 methylene protons ( $\delta_{\text{H}}$  2.18 and 2.01), and H-14 was correlated with Me-15; there were no correlations between H-10/H-12 and H-10/H-14, demonstrating that the acetoxy groups at C-12 and C-14 were  $\alpha$ -oriented. As one of the methylene protons at C-4 ( $\delta_{\text{H}}$  2.53) was correlated with H-7, these two protons

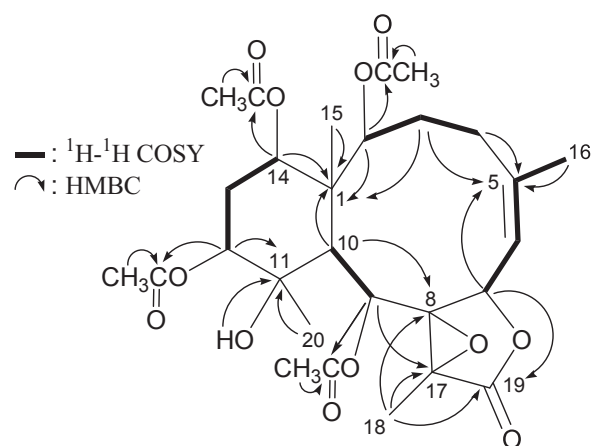


Fig. 4. The  $^1\text{H}$ - $^1\text{H}$  COSY and selective HMBC (protons  $\rightarrow$  quaternary carbons) correlations of **2**.

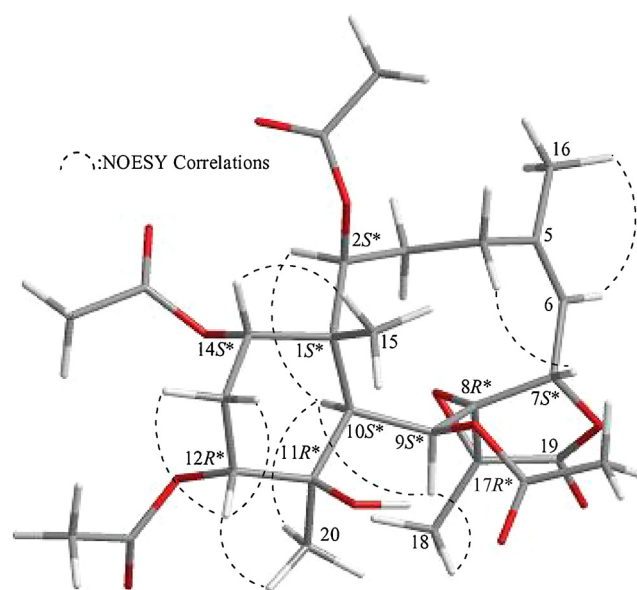


Fig. 5. Selected protons with key NOESY correlations of **2**.



**Table 2**Effects of briaranes **1** and **2** (10  $\mu$ M) on LPS-induced iNOS and COX-2 protein expressions in macrophages.

Compounds	iNOS Expression (% of LPS)	COX-2 Expression (% of LPS)
Control	5.31 $\pm$ 1.47	1.54 $\pm$ 0.27
LPS	100 $\pm$ 8.96	100 $\pm$ 3.91
<b>1</b>	10.53 $\pm$ 1.38	84.31 $\pm$ 2.14
<b>2</b>	78.72 $\pm$ 25.07 <sup>a</sup>	87.83 $\pm$ 3.36

<sup>a</sup> Compound **2** did not statistically significantly inhibit iNOS protein expression.

were  $\beta$ -oriented according to modeling analysis. The Z-configuration of the C-5/6 double bond was established based on the interaction between H-6 and H<sub>3</sub>-16. Furthermore, correlation between H-9 and H<sub>3</sub>-18 indicated that Me-18 should be positioned on the  $\beta$ -face in the  $\gamma$ -lactone ring. Thus, on the basis of the above results, **2** was found to possess the configuration 1S\*,2S\*,7S\*,8R\*,9S\*,10S\*,11R\*,12R\*,14S\*,17R\*.

In an *in vitro* anti-inflammatory activity assay, Western blot analysis was used to evaluate the upregulation of pro-inflammatory iNOS and COX-2 protein expressions in lipopolysaccharide (LPS)-stimulated RAW264.7 macrophage cells. At a concentration of 10  $\mu$ M, briarane **1** was found to significantly reduce the level of iNOS to 10.53% in comparison with control cells stimulated with LPS only (Table 2 and Fig. 6).

### 3. Experimental

#### 3.1. General

Melting points of the natural products were determined using Fargo apparatus and the values were uncorrected. Optical rotation values were measured using a Jasco P-1010 digital polarimeter. IR spectra were obtained with a Thermo Scientific Nicolet iS5 FT-IR spectrophotometer. NMR spectra were recorded on a 400 MHz Jeol ECZ 400S NMR spectrometer using the residual CHCl<sub>3</sub> signal ( $\delta_{\text{H}}$  7.26 ppm) and CDCl<sub>3</sub> ( $\delta_{\text{C}}$  77.1 ppm) as the internal standard for <sup>1</sup>H NMR and <sup>13</sup>C NMR, respectively; coupling constants (*J*) are presented in Hz. ESIMS and HRESIMS were recorded using a Bruker 7 T solariX FTMS system. Column chromatography was carried out with silica gel (230–400 mesh, Merck). TLC was performed on plates precoated with Kieselgel 60 F<sub>254</sub> (0.25-mm-thick, Merck), then sprayed with 10% H<sub>2</sub>SO<sub>4</sub> solution followed by heating to visualize the spots. Normal-phase HPLC (NP-HPLC) was performed using a system comprised of a Hitachi L-7100 pump and a Rheodyne 7725 injection port. A semi-preparative normal-

phase column (YMC-Pack SIL 250  $\times$  20 mm I.D.S-5, 5  $\mu$ M,) was used for NP-HPLC. Reverse-phase HPLC (RP-HPLC) was performed using a system equipped with a Hitachi L-2130 pump, a Hitachi L-2455 photodiode array detector, a Rheodyne 7725 injection port, and a 250 mm  $\times$  21.2 mm column (5  $\mu$ M, Luna RP-18e) or a 25 cm  $\times$  10 mm column (5  $\mu$ M, Ascentis C18 Cat#:581343-U, Sigma-Aldrich).

#### 3.2. Animal material

Specimens of the octocoral *B. violaceum* were collected from the waters off Taiwan and relocated to a 270-ton cultivation tank located in the National Museum of Marine Biology and Aquarium (NMMBA), Taiwan, in 2011; the material used for this study was cultured-type *B. violaceum* collected from the tank in December 2016. This organism was identified by comparison with previous descriptions. A voucher specimen was deposited in the NMMBA, Taiwan (NMMBA-CSC-002).

#### 3.3. Extraction and isolation

Sliced bodies of *B. violaceum* (wet and dry weights, 251 and 95.0 g, respectively) were extracted with a mixture of organic solvent (MeOH:CH<sub>2</sub>Cl<sub>2</sub> = 1:1; volume ratio). The resulting 9.79 g extract was partitioned between ethyl acetate (EtOAc) and H<sub>2</sub>O. The EtOAc layer (3.30 g) was separated on silica gel and eluted with a mixture of *n*-hexane/EtOAc (stepwise from 100:1 to 100% EtOAc; volume ratio) to yield fifteen subfractions A–O. Fraction M was separated by silica gel column chromatography and then eluted with a mixture of *n*-hexane/EtOAc (stepwise 5:1 to 100% EtOAc; volume ratio) to afford twelve subfractions M1–M12. Fraction M6 was purified by NP-HPLC using a mixture of *n*-hexane/acetone/CH<sub>2</sub>Cl<sub>2</sub> (8:4:1; volume ratio) to afford twenty-one subfractions M6A–M6U. Fraction M6H was purified by RP-HPLC using a mixture of MeOH/H<sub>2</sub>O (80:20 of volume ratio at a flow rate of 2.0 mL/min) to yield **2** (0.6 mg). Fraction M7 was purified by RP-HPLC using a mixture of MeOH/H<sub>2</sub>O (70:30 of volume ratio at a flow rate of 5.0 mL/min) to yield **1** (1.0 mg).

#### 3.4. Briaviolide O (**1**)

Amorphous powder; mp 90–92 °C, [ $\alpha$ ]<sub>D</sub><sup>25</sup> +62 (c 0.05, CHCl<sub>3</sub>), IR (neat)  $\nu_{\text{max}}$  3580, 1781, 1738 cm<sup>−1</sup>; <sup>1</sup>H and <sup>13</sup>C NMR data, see Table 1. ESIMS: *m/z* 675 [M+Na]<sup>+</sup>, HRESIMS: *m/z* 675.26248 (calcd for C<sub>32</sub>H<sub>44</sub>O<sub>14</sub> + Na, 675.26233).

#### 3.5. Briaviolide P (**2**)

Amorphous powder; mp 99–101 °C, [ $\alpha$ ]<sub>D</sub><sup>25</sup> +62 (c 0.05, CHCl<sub>3</sub>).

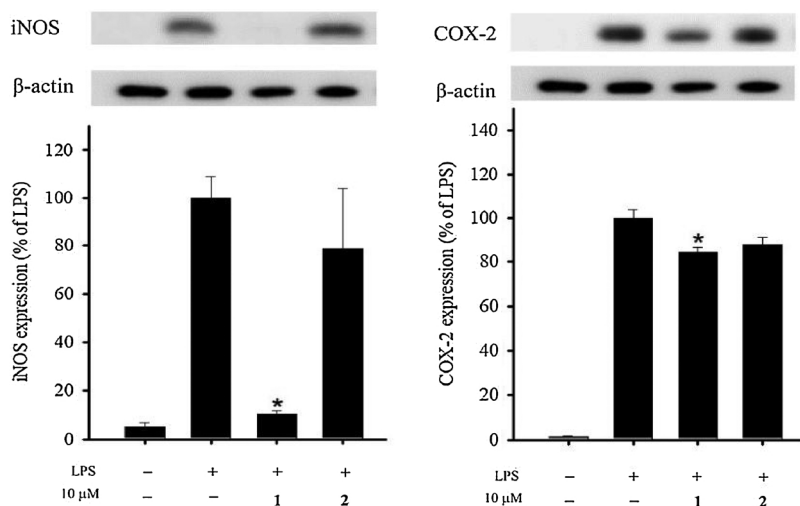


**Fig. 6.** Effects of compounds **1** and **2** on pro-inflammatory iNOS and COX-2 protein expressions in the LPS-stimulated murine macrophage cell line RAW264.7. (A) Relative density of the iNOS immunoblot; (B) relative density of the COX-2 immunoblot. The relative intensity of the LPS-stimulated group was taken to be 100%. Band intensities were quantified by densitometry and are indicated as the percentage change relative to that of the LPS-stimulated group. Briarane **1** significantly inhibited LPS-induced iNOS protein expression in macrophages. The experiments were repeated three times (\* *p* < 0.05, significantly different from the LPS-stimulated group).

2(D)) + 20 (*c* 0.03, CHCl<sub>3</sub>), IR (neat)  $\nu_{\max}$  3480, 1779, 1730 cm<sup>-1</sup>; <sup>1</sup>H and <sup>13</sup>C NMR data, see Table 2. ESIMS: *m/z* 589 [M + Na]<sup>+</sup>; HRESIMS: *m/z* 589.22546 (calcd for C<sub>28</sub>H<sub>38</sub>O<sub>12</sub> + Na, 589.22555).

### 3.6. In vitro anti-inflammatory assay

RAW264.7 (TIB-71) cells were purchased from the American Type Culture Collection (ATCC, No TIB-71) (Manassas, VA, USA). The *in vitro* anti-inflammatory activities of compounds **1** and **2** were measured by investigating their inhibition effects on LPS-induced pro-inflammatory iNOS and COX-2 protein expressions in the macrophage cell line using Western blot analysis (Huang et al., 2012; Jean et al., 2008, 2009). Briefly, an inflammation response in RAW264.7 cells was induced by incubating cells in medium containing only LPS (10 μM) without test compounds for 16 h. For the anti-inflammatory activity assays, compounds **1** and **2** were added to the cells 10 min before LPS treatment. After incubation, the cells were lysed and the protein lysates analyzed by Western blotting. The protein expression levels were determined based on the immunoreactivity of proteins to antibodies, and were calculated with respect to the average optical density of the corresponding LPS-stimulated cells. Moreover, the effects of compounds **1** and **2** on the viability of RAW264.7 cells were also evaluated by the trypan blue exclusion test (Jean et al., 2008, 2009). For statistical analysis, the data were analyzed by one-way analysis of variance (ANOVA), followed by the Student–Newman–Keuls *post hoc* test for multiple comparisons. A significant difference was defined as a *p*-value of < 0.05.

### Acknowledgments

This research was supported by grants from the National Museum of Marine Biology and Aquarium; the National Dong Hwa University; and the Ministry of Science and Technology (Grant Nos MOST 104-2320-B-291-001-MY3 and 106-2320-B-291-001-MY3), Taiwan, awarded to P.-J.S.

### Appendix A. Supplementary data

Supplementary material related to this article can be found, in the online version, at doi:<https://doi.org/10.1016/j.phytol.2018.07.016>.

### References

- Allinger, N.L., 1977. Conformational analysis. 130. MM2. A hydrocarbon force field utilizing V<sub>1</sub> and V<sub>2</sub> torsional terms. J. Am. Chem. Soc. 99, 8127–8134.
- Huang, S.-Y., Chen, N.-F., Chen, W.-F., Hung, H.-C., Lee, H.-P., Lin, Y.-Y., Wang, H.-M., Sung, P.-J., Sheu, J.-H., Wen, Z.-H., 2012. Sinularin from indigenous soft coral attenuates nociceptive responses and spinal neuroinflammation in carrageenan-induced inflammatory rat model. Mar. Drugs 10, 1899–1919.
- Ito, H., Iwasaki, J., Sato, Y., Aoyagi, M., Iguchi, K., Yamori, T., 2007. Marine diterpenoids with a briarane skeleton from the Okinawan soft coral *Pachyclavularia violacea*. Chem. Pharm. Bull. 55, 1671–1676.
- Iwasaki, J., Ito, H., Aoyagi, M., Sato, Y., Iguchi, K., 2006. Briarane-type diterpenoids from the Okinawan soft coral *Pachyclavularia violacea*. J. Nat. Prod. 69, 2–6.
- Jean, Y.-H., Chen, W.-F., Duh, C.-Y., Huang, S.-Y., Hsu, C.-H., Lin, C.-S., Sung, C.-S., Chen, I.-M., Wen, Z.-H., 2008. Inducible nitric oxide synthase and cyclooxygenase-2 participate in anti-inflammatory and analgesic effects of the natural marine compound lemnalol from Formosan soft coral *Lemnalia cervicorni*. Eur. J. Pharmacol. 578, 323–331.
- Jean, Y.-H., Chen, W.-F., Sung, C.-S., Duh, C.-Y., Huang, S.-Y., Lin, C.-S., Tai, M.-H., Tzeng, S.-F., Wen, Z.-H., 2009. Capnellene, a natural marine compound derived from soft coral, attenuates chronic constriction injury-induced neuropathic pain in rats. Br. J. Pharmacol. 158, 713–725.
- Liaw, C.-C., Cheng, Y.-B., Lin, Y.-S., Kuo, Y.-H., Hwang, T.-L., Shen, Y.-C., 2014. New briarane diterpenoids from Taiwanese soft coral *Briareum violacea*. Mar. Drugs 12, 4677–4692.
- Samimi-Namin, K., van Ofwegen, L.P., 2016. Overview of the genus *Briareum* (Cnidaria, Octocorallia, Briareidae) in the Indo-Pacific, with the description of a new species. ZooKeys 557, 1–44.
- Sheu, J.-H., Sung, P.-J., Huang, L.-H., Lee, S.-F., Wu, T., Chang, B.-Y., Duh, C.-Y., Fang, L.-S., Soong, K., Lee, T.-J., 1996. New cytotoxic briarane diterpenes from the Formosan gorgonian *Briareum* sp. J. Nat. Prod. 59, 935–938.
- Xu, L., Patrick, B.O., Roberge, M., Allen, T., van Ofwegen, L.P., Andersen, R.J., 2000. New diterpenoids from the octocoral *Pachyclavularia violacea* collected in Papua New Guinea. Tetrahedron 56, 9031–9037.
- Xu, J.-H., Lai, K.-H., Su, Y.-D., Chang, Y.-C., Peng, B.-R., Backlund, A., Wen, Z.-H., Sung, P.-J., 2018. Briaviolides K–N, new briarane-type diterpenoids from cultured octocoral *Briareum violaceum*. Mar. Drugs 16, 75.

# RESEARCH PAPER

## Haem oxygenase-1 up-regulation by rosiglitazone *via* ROS-dependent Nrf2-antioxidant response elements axis or PPAR $\gamma$ attenuates LPS-mediated lung inflammation

**Correspondence** Chuen-Mao Yang, PhD, Department of Physiology and Pharmacology, Chang Gung University, College of Medicine, 259 Wen-Hwa 1st Road, Kwei-San, Tao-Yuan, Taiwan. E-mail: chuenmao@mail.cgu.edu.tw; Chih-Chung Lin, MD, PhD, Department of Anesthetics, Chang Gung Memorial Hospital at Linkuo and Chang Gung University, Kwei-San, Tao-Yuan, Taiwan. E-mail: chihchung@adm.cgmh.org.tw

**Received** 6 March 2018; **Revised** 24 July 2018; **Accepted** 24 July 2018

Rou-Ling Cho<sup>1</sup>, Chien-Chung Yang<sup>1,2</sup>, Hui-Ching Tseng<sup>1</sup>, Li-Der Hsiao<sup>3</sup>, Chih-Chung Lin<sup>3</sup> and Chuen-Mao Yang<sup>1,3,4</sup> 

<sup>1</sup>Department of Physiology and Pharmacology and Health Ageing Research Center, College of Medicine, Chang Gung University, Tao-Yuan, Taiwan, <sup>2</sup>Department of Traditional Chinese Medicine, Chang Gung Memorial Hospital at Tao-Yuan, Tao-Yuan, Taiwan, <sup>3</sup>Department of Anesthetics, Chang Gung Memorial Hospital at Linkuo and Chang Gung University, Tao-Yuan, Taiwan, and <sup>4</sup>Research Center for Chinese Herbal Medicine and Research Center for Food and Cosmetic Safety, College of Human Ecology, Chang Gung University of Science and Technology, Tao-Yuan, Taiwan

### BACKGROUND AND PURPOSE

Haem oxygenase-1 (HO-1) is induced by thiazolidinediones including rosiglitazone and exerts anti-inflammatory effects in various models. However, the molecular mechanisms underlying rosiglitazone-induced HO-1 expression remain largely unknown in human pulmonary alveolar epithelial cells (HPAEPiCs).

### EXPERIMENTAL APPROACH

HO-1 expression was determined by real time-PCR, Western blotting and promoter reporter analyses. Signalling pathways were investigated using pharmacological inhibitors or specific siRNAs. Interactions between nuclear factor erythroid-2-related factor (Nrf2) and antioxidant response elements (ARE) binding site of the HO-1 promoter were investigated with chromatin immunoprecipitation assays.

### KEY RESULTS

Up-regulation of HO-1 in HPAEPiCs or in mice by rosiglitazone blunted ICAM-1 expression and monocyte adhesion to HPAEPiCs challenged with LPS. Rosiglitazone-induced HO-1 expression was significantly attenuated by NADPH oxidase (NOX) inhibitors (apocynin and diphenyleneiodonium) or ROS scavenger (N-acetyl cysteine). The involvement of NOX activity and ROS generation in rosiglitazone-induced HO-1 expression was confirmed by transfection with p47<sup>phox</sup> or NOX2 siRNA. Moreover, pretreatment with the inhibitors of c-Src (c-Srci II), proline-rich tyrosine kinase 2 (Pyk2) (PF431396), Akt (Akti VIII) or PPAR $\gamma$  (GW9662) and transfection with siRNA of c-Src, Pyk2, Akt or PPAR $\gamma$  abolished the rosiglitazone-induced HO-1 expression in HPAEPiCs. Subsequently, Nrf2 was activated by phosphorylation of c-Src, Pyk2 and Akt, which turned on transcription of HO-1 gene by binding to AREs binding site and enhancing ARE promoter activity.

### CONCLUSIONS AND IMPLICATIONS

Rosiglitazone induces HO-1 expression *via* either NOX/ROS/c-Src/Pyk2/Akt-dependent Nrf2 activation or PPAR $\gamma$  in HPAEPiCs and suppresses LPS-mediated inflammatory responses, suggesting that PPAR $\gamma$  agonists may be useful for protection against pulmonary inflammation.

## Abbreviations

AREs, antioxidant response elements; ChIP, chromatin immunoprecipitation; DHE, dihydroethidium; H<sub>2</sub>DCFDA, 2',7'-dichlorodihydrofluorescein diacetate; HO-1, haem oxygenase-1; HPAEpiCs, human pulmonary alveolar epithelial cells; ICAM-1, intercellular adhesion molecule; IF, immunofluorescence; IHC, immunohistochemistry; Keap1, Kelch like ECH associated protein 1; Nrf2, nuclear factor erythroid-2-related factor; Pyk2, proline-rich tyrosine kinase 2; TZDs, thiazolidinediones

## Introduction

**LPS** triggers acute lung inflammation during bacterial infections, through up-regulation of adhesion molecules, such as intercellular adhesion molecule (**ICAM-1**) and **VCAM-1**, leading to the recruitment of polymorphonuclear cells to inflammatory tissues and airway fluid (Liou *et al.*, 2016; Woodfin *et al.*, 2016). The up-regulation of adhesion molecules is involved in pathological changes in the lung. Thus, either ICAM-1 or VCAM-1 could serve as an inflammatory marker and have been used to evaluate the anti-inflammatory effects of **haem oxygenase 1 (HO-1)** in our studies. We also confirmed that LPS-induced ICAM-1 or VCAM-1 expression and monocytes (THP-1) adhesion might be used to evaluate the progression of lung inflammation (Cho *et al.*, 2016). Therefore, pursuing an effective medicine to target these critical components is important in the management of pulmonary inflammatory diseases.

Thiazolidinediones (TZD) have been shown to activate **PPAR $\gamma$**  and have potential value in treatment of animal models of inflammatory diseases. Their anti-inflammatory effects result from up-regulation of HO-1 which suppresses pulmonary artery cell proliferation and vascular remodelling (Kronke *et al.*, 2007; Li *et al.*, 2010) and decreases LPS-induced lung inflammatory responses (Liu *et al.*, 2005; Wang *et al.*, 2014). We recently also confirmed that suppression of LPS-mediated inflammation (VCAM-1 expression and cell adhesion) by HO-1, induced by **rosiglitazone**, was mediated through PKC $\alpha$ /AMPK $\alpha$ /p38 MAPK $\alpha$ /SIRT1-dependent deacetylation of Ac-PGC1 $\alpha$  and fragmentation of NCoR/PPAR $\gamma$  activation in human pulmonary alveolar epithelial cells (HPAEpiCs) (Cho *et al.*, 2018). These studies demonstrate that PPAR $\gamma$  agonists could exert anti-inflammatory effects through a PPAR $\gamma$ -dependent HO-1 up-regulation.

HO-1 induced by various stimuli and oxidative stresses protects against inflammatory responses (Rushworth *et al.*, 2005; Huang *et al.*, 2014). The ROS-dependent activation of signalling kinases (Polvani *et al.*, 2012) by PPAR agonists could regulate the expression of various genes (Gardner *et al.*, 2005). PPAR $\gamma$  ligands could also inhibit airway inflammation and hyperresponsiveness *via* a PPAR $\gamma$ -independent mechanism in mouse models challenged with allergen (Donovan *et al.*, 2012). In addition, the **NADPH oxidase (NOX)**ROS system could induce HO-1 expression through different signalling components. Indeed, c-**Src** is an upstream component of proline-rich tyrosine kinase 2 (**Pyk2**) phosphorylation stimulated by TZDs (Peng *et al.*, 2003; Dewar *et al.*, 2007), which is regulated by ROS (Ke *et al.*, 2014), leading to HO-1 expression in various cell types (Han *et al.*, 2009; Chi *et al.*, 2015; Yang *et al.*, 2015). Activated **Akt** triggers nuclear factor erythroid-2-related factor (Nrf2)/HO-1 expression which could protect against cellular injury and promote cell survival (Deng *et al.*, 2013; Xu *et al.*,

2015b). However, whether rosiglitazone-induced HO-1 expression mediated through NOX/ROS, c-Src, Pyk2, Akt and Nrf2 was still unknown in HPAEpiCs.

Nrf2 is involved in the HO-1 gene transcription through binding to antioxidant response elements (AREs) in the promoter region in response to ROS (Alam and Cook, 2007; Loboda *et al.*, 2016). On exposure to ROS, Nrf2 dissociates from kelch like ECH associated protein 1 (**Keap1**) and translocates into the nucleus, wherein Nrf2 oligomerizes with the protein Maf binding to the ARE sites of target genes and leading to gene transcription (Itoh *et al.*, 1999; Baird *et al.*, 2013; Foresti *et al.*, 2013). However, the detailed mechanisms of intracellular signalling pathways involved in the rosiglitazone-induced HO-1 expression in HPAEpiCs were not completely defined. Here, we have shown that the expression of HO-1 induced by rosiglitazone is mediated through not only PPAR $\gamma$ -dependent but also through a separate NOX/ROS/c-Src/Pyk2/Akt-dependent Nrf2 activation pathway and protects against the LPS-mediated inflammatory responses.

## Methods

### Animal care and experimental procedures

All animal care and experimental procedures complied with the guidelines of the Animal Care Committee of Chang Gung University (Approval Document No. CGU 16-046) and NIH Guides for the Care and Use of Laboratory Animals. Animal studies are reported in compliance with the ARRIVE guidelines (Kilkenny *et al.*, 2010; McGrath and Lilley, 2015).

Male ICR mice aged 6–8 weeks were purchased from the National Laboratory Animal Centre (Taipei, Taiwan). Mice were assigned randomly into three groups: sham [0.1 mL of DMSO-PBS (1:100) with 0.1% (W/V) BSA treated mice], LPS (LPS-treated mice) and Rosi + LPS (rosiglitazone plus LPS mice); five mice in each group/cage and kept in standard individually ventilated cages in an animal facility under standardized conditions (12 h light/dark cycle, 21–24°C, humidity of 50–60%) with food and water *ad libitum*. Mice treated with rosiglitazone (i.p.; 0.1 mg·kg<sup>-1</sup>) and 1 h later were anaesthetized with pentothal (i.p.; 50 mg·kg<sup>-1</sup>). Mice were placed individually on a board in a near vertical position and the tongues withdrawn with lined forceps. LPS (3 mg·kg<sup>-1</sup>; 45  $\mu$ L in 30g mouse) was placed posteriorly in the throat and aspirated into lungs for 16 h to provide a model of lung inflammation (Hsu *et al.*, 2014). At the end of the experimental period, mice were killed by an overdose of pentothal (i.p.; 100 mg·kg<sup>-1</sup>) for collection of lung tissues. These tissues were extracted for protein (right superior lobe + post caval lobe) and mRNA (right middle lobe + right inferior lobe) for ICAM-1, HO-1 or  $\beta$ -actin. Data collection and evaluation of



all *in vivo* and *in vitro* experiments were performed without knowledge of the treatment of the group.

### Immunohistochemical (IHC) staining

To examine the cellular expression and location of the ICAM-1 or HO-1 protein, immunohistochemical (IHC) staining was performed on the sections of the lung tissues (left lung), which were deparaffinized, rehydrated and washed with TTBS (composition; 50 mM Tris-HCl, 150 mM NaCl, 0.05% (w/v) Tween 20, pH7.4). Non-specific binding was blocked by preincubation with PBS containing 5 mg·mL<sup>-1</sup> of BSA for 1 h at room temperature. The sections were incubated with an anti-ICAM-1 or anti-HO-1 antibody (1:100 dilution) at 4°C for 16 h and then with anti-mouse or anti-rabbit HRP antibody at room temperature for 1 h. Bound antibodies were detected by incubation in 0.5 mg·mL<sup>-1</sup> of 3,3-diaminobenzidine/0.01% (v/v) hydrogen peroxide (H<sub>2</sub>O<sub>2</sub>) in 0.1 M Tris-HCl buffer, as chromogen (Vector Lab, Burlingame, CA, USA).

### Cell culture

HPAECs were purchased from the ScienCell Research Laboratories (San Diego, CA, USA). Cells were cultured in DMEM/F12 medium containing 10% (v/v) FBS and antibiotics (100 U·mL<sup>-1</sup> penicillin G, 100 µg·mL<sup>-1</sup> gentamicin and 250 ng·mL<sup>-1</sup> fungizone) at 37°C in a humidified 5% CO<sub>2</sub>. Experiments were performed with cells from passages 4 to 7. The growth medium was changed after 24 h and then every 3 days. The viability of HPAECs after treatment with 1% (v/v) DMSO or the pharmacological inhibitors alone was determined by a cell counting Kit-8 assay, which showed no significant differences (data not shown).

### Protein preparation and Western blot analysis

Cells were incubated with or without different concentrations of rosiglitazone at 37°C for the indicated time periods. When inhibitors used, they were added 1 h prior to the application of rosiglitazone. The collected cells were lysed with a lysis buffer. The mixed samples (15 µL) were subjected to 10% SDS-PAGE and transferred to nitrocellulose membrane. Membranes were washed with TTBS four times for 5 min each, incubated with anti-rabbit or anti-mouse HRP antibody (1:2000 dilution) for 1 h. The immunoreactive bands were detected by ECL reagents and captured by a UVP BioSpectrum 500 Imaging System (Upland, CA, USA). The values of Western blot were quantified by UN-SCAN-IT gel version 6.1 (Utah, USA) and normalized to GAPDH or total protein for five individual experiments. Changes after LPS are expressed as fold change, relative to the mean basal value.

### Real-time PCR analysis

Total RNA was extracted from HPAEC using TRIzol reagent. The mRNA was reverse-transcribed into cDNA and analysed by real-time PCR. Real-time PCR was performed with a StepOnePlus™ real-time PCR system (ThermoScientific-Applied Biosystems, Waltham, MA, USA) and Kapa Probe Fast qPCR Kit Master Mix (2X) Universal (KK4705; KAPA Biosystems, Wilmington, MA, USA). The expression of HO-1 and ICAM-1 was quantified by normalization to the GAPDH expression. Relative gene expression was determined by the  $\Delta\Delta C_t$  method, where  $C_t$  meant threshold cycle. All experiments were performed five times ( $n = 5$ ).

### Adhesion assay

HPAECs were plated on six-well culture plates with coverslips and pretreated with rosiglitazone for 1 h, and then incubated with or without ZnPP IX before incubation with LPS for 16 h at 37°C in a humidified 5% CO<sub>2</sub> atmosphere. THP-1 cells (human monocytic cell line, BCRC Cat# 60430, RRID: CVCL\_0006) were purchased from Bioresource Collection and Research Center (Hsinchu, Taiwan) and maintained in suspension in DMEM/F-12 containing 10% (v/v) FBS medium. Before labelling, THP-1 cells were washed and resuspended in warm PBS. BCECF-AM (10 µM) was added to THP-1 in warm PBS for 1 h at 37°C. After labelling, cells were washed thrice and resuspended in warm PBS and kept in the dark at room temperature and then the labelled THP-1 cells were added to HPAECs. The cultures were incubated in a CO<sub>2</sub> incubator for 1 h. Non-adherent cells were removed from the plate by gentle washing with warm PBS. The numbers of adherent THP-1 cells were determined by counting four fields per 200X high-power field well using a fluorescence microscope (Axiovert 200M, Zeiss, Jena, Germany). Experiments were performed in triplicate and repeated five times ( $n = 5$ ).

### Transient transfection with siRNAs in HPAECs

Human siRNAs of scrambled, SMARTpool RNA duplexes corresponding to p47<sup>phox</sup> (SASI\_Hs02\_00302212), NOX2 (SASI\_Hs01\_00086110), c-Src (SASI\_Hs01\_00112905), Pyk2 (SASI\_Hs01\_00032249), Akt (SASI\_Hs01\_00105954), Nrf2 (SASI\_Hs02\_00302212), Keap1 (SASI\_Hs01\_00080908) and Scrambled control siRNA were from Sigma-Aldrich (St. Louis, MO, USA). Briefly, siRNA (100 nM) was formulated with Lipofectamine 2000 transfection reagent according to the manufacturer's instruction.

### NADPH oxidase activity assay

After exposure to 30 µM rosiglitazone for the indicated time intervals, cells were gently scraped and centrifuged at 400× *g* for 10 min at 4°C. The cell pellet was resuspended with 35 µL of ice-cold PBS, and the cell suspension was kept on ice. To a final 200 µL volume of pre-warmed (37°C) PBS containing either NADPH (1 µM) or lucigenin (20 µM), 5 µL of cell suspension ( $2 \times 10^4$  cells) was added to initiate the reaction followed by immediate measurement of chemiluminescence in a luminometer (Synergy<sup>H1</sup> Hybrid Reader, BioTek, Winooski, VT, USA).

### Measurement of intracellular ROS accumulation

Cells were cultured in DMEM/F-12 for 24 h and then treated with rosiglitazone. When inhibitors were used, they were added 1 h prior to the application of rosiglitazone. After washing twice with warm PBS, the cells were stained with 2',7'-dichlorodihydrofluorescein diacetate (H<sub>2</sub>DCFDA) (10 µM) or DHE (5 µM) for 30 or 10 min. After staining, the cells were recovered with DMEM/F-12 containing 10% (v/v) FBS for 30 min in H<sub>2</sub>DCFDA group. For ELISA assay, the fluorescence for DCF and DHE staining was detected at 495/529 and 518/605 nm using a fluorescence microplate reader (Synergy<sup>H1</sup> Hybrid Reader, BioTek) and FACSCalibur equipped with CellQuest software (BD Biosciences, San Jose,

CA, USA). For immunofluorescence staining, the stained cells were washed three times with cold-PBS and then the fluorescence for DCF and DHE staining was detected at 495/529 and 518/605 nm, respectively, using a fluorescence microscope (Axiovert 200M, Zeiss).

### Transfection and promoter luciferase assay

ARE-luc reporter construct plasmids were transiently transfected at a concentration of  $0.8 \mu\text{g}\cdot\text{mL}^{-1}$ , and the control pGal encoding for  $\beta$ -galactosidase presented at  $0.2 \mu\text{g}\cdot\text{mL}^{-1}$  to normalize the transfection efficiency. ARE-luc luciferase activities were determined by using a luciferase assay system (Abcam, Cambridge, UK) according to the manufacturer's instructions. Detected firefly luciferase activities were standardized with  $\beta$ -galactosidase activity.

### Isolation of subcellular fractions

The cytosolic and nuclear fractions were isolated, as described previously (Cho *et al.*, 2016). The cells were harvested, sonicated for 10 s at output 1.5 with a sonicator (Misonix, Farmingdale, NY, USA) and centrifuged at  $5000\times g$  at  $4^\circ\text{C}$  for 15 min. The pellet was collected as the nuclear fraction and the supernatant collected as the cytosolic fraction.

### Chromatin immunoprecipitation (ChIP) assay

To detect the association of transcription factors with the human HO-1 promoter, the ChIP analysis was performed as previously described (Cho *et al.*, 2016). Briefly, HPAEpiCs were cross-linked with 1% (v/v) formaldehyde at  $37^\circ\text{C}$  for 30 min and stop this reaction with 0.125 M glycine, then washed three times with ice-cold PBS containing 1 mM PMSF, 1% (v/v) aprotinin and 1% (v/v) leupeptin. Soluble chromatin was prepared using a ChIP assay kit (Upstate) according to the instructions of the manufacturer and immunoprecipitated without (control) or with an anti-Nrf2 antibody and normal goat IgG. Following washing and elution, immunoprecipitates were heated overnight at  $65^\circ\text{C}$  to reverse cross-linking of DNA and protein. To avoid the possibility of amplification artefacts, PCR products for all SYBR Green primer pairs were verified to produce single products by agarose electrophoresis and high resolution melt curve. The relative mRNA levels were calculated using the comparative Ct method ( $\Delta\Delta\text{Ct}$ ). The DNA was extracted and resuspended in  $\text{H}_2\text{O}$  and subjected to PCR amplification with the ARE primers:

ARE (327 bp)

F: 5'-GCTGC CCAAA CCACT TCTGT-3'

R: 5'-GCCCT TTCAC CTCCC ACCTA-3'

### Data and statistical analysis

The data and statistical analysis comply with the recommendations on experimental design and analysis in pharmacology (Curtis *et al.*, 2018). Statistical analysis was performed only when  $n = 5$  independent samples were acquired. All data are expressed as means  $\pm$  SEM, from five individual experiments ( $n \geq 5$ ). Statistical analysis was performed by using GraphPad Prism Program 6.0 software (GraphPad, San Diego, CA). We used one-way ANOVA followed by Dunnett's *post hoc* test when comparing more than two groups of data and

one-way ANOVA with a non-parametric Kruskal–Wallis test, followed by Dunnett's *post hoc* test when comparing multiple independent groups. Post tests were run only if F achieved  $P < 0.05$  and there was no significant variance inhomogeneity.  $P < 0.05$  was considered to show statistical significance. Error bars are omitted when they fell within the dimensions of the symbols.

### Materials

Apocynin (APO), diphenyleneiodonium chloride (DPI) was from Biomol (Plymouth Meeting, PA, USA). Anti-GAPDH (mouse monoclonal antibody, Cat# MCA-1D4, AB\_2107599) antibody was from EnCor Biotechnology (Gainesville, FL, USA). Anti- $\beta$ -actin (C4) (mouse monoclonal antibody, Cat# sc-47778 HRP, RRID:AB\_2714189), anti-c-Src (SRC 2) (rabbit polyclonal antibody, Cat# sc-18, RRID:AB\_631324), anti-Akt1/2/3 (H-136) (rabbit monoclonal antibody, Cat# sc-8312, RRID:AB\_671714), anti-Nrf2 (C-20) (rabbit polyclonal antibody, Cat# sc-722, RRID:AB\_2108502), anti-Keap1 (H-190) (rabbit polyclonal antibody, Cat# sc-33569, RRID:AB\_2280949), anti-Lamin A (H-102) (rabbit polyclonal antibody, Cat# sc-20680, RRID:AB\_648148), anti-ICAM-1 (H-108) (rabbit polyclonal antibody, Cat# sc-7891, RRID:AB\_647486) antibodies were from Santa Cruz Biotechnology (Santa Cruz, CA, USA). Anti-HO-1 pAb (rabbit polyclonal antibody, Cat# ADI-SPA-895, RRID:AB\_10618757) was from Enzo Life Sciences (Farmingdale, NY, USA). Anti-NOX2/gp91<sup>phox</sup> [EP6991] (rabbit monoclonal antibody, Cat# ab129068, RRID:AB\_11144496), anti-Pyk2 [E354] (rabbit monoclonal antibody, Cat# ab32448, RRID:AB\_777568), anti-ICAM-1 [EP16608] (rabbit monoclonal antibody, Cat# ab179707) (animal experimentation used) and Anti-Nrf2 (phospho S40) [EP1809Y] (rabbit monoclonal antibody, Cat# ab76026, RRID:AB\_1524049) were from Abcam. Anti-p47<sup>phox</sup> (Phospho-Ser<sup>370</sup>) (rabbit polyclonal antibody, Cat# A1171, RRID:AB\_10696129) was from Assay Biotech (Sunnyvale, CA, USA). Anti-p47<sup>phox</sup> (D21F6) (rabbit monoclonal antibody, Cat# 4301S, RRID:AB\_2150286), anti-phospho-c-Src family (Tyr<sup>416</sup>) (rabbit polyclonal antibody, Cat# 2101, RRID:AB\_331697), anti-phospho-Pyk2 (Tyr<sup>402</sup>) (rabbit polyclonal antibody, Cat# 3291, RRID:AB\_2300530) and anti-phospho-Akt (Ser<sup>473</sup>) (rabbit polyclonal antibody, Cat# 9271, RRID:AB\_329825) were from Cell Signaling Technology (Danvers, MA, USA). Rosiglitazone, GW590735, **GW0742**, **ciglitazone**, **pioglitazone**, **troglitazone**, **GW9662** and **ZnPPiX** were from Cayman Chemical (Ann Arbor, MI, USA). PF431396, c-Src II and **Akt inhibitor VIII** were from Merck (Merck Millipore, Billerica, MA, USA). BCECF-AM, dihydroethidium (DHE) and CM-H<sub>2</sub>DCFDA were from Molecular Probes (Eugene, OR, USA). N-acetyl-L-cysteine (NAC), LPS (L2630) and other chemicals were from Sigma-Aldrich. SDS-PAGE supplies were from MDBio Inc (Taipei, Taiwan).

### Nomenclature of targets and ligands

Key protein targets and ligands in this article are hyperlinked to corresponding entries in <http://www.guidetopharmacology.org>, the common portal for data from the IUPHAR/BPS Guide to PHARMACOLOGY (Harding *et al.*, 2018), and are permanently archived in the Concise Guide to PHARMACOLOGY 2017/18 (Alexander *et al.*, 2017a,b,c)

## Results

### *Up-regulation of HO-1 inhibits inflammatory responses in mice challenged with LPS*

HO-1 has been shown to protect against the inflammatory responses induced by various insults including LPS (Liu *et al.*, 2005; Xu *et al.*, 2015a). Therefore, we confirmed these results in an *in vivo* study. We observed that LPS markedly induced ICAM-1 expression, which was attenuated by rosiglitazone through up-regulation of HO-1, determined by IHC staining

(Figure 1A). We also found that LPS significantly enhanced ICAM-1 mRNA and protein expression, which were attenuated by rosiglitazone *via* up-regulation of HO-1 (Figure 1B,C). These results suggested that up-regulation of HO-1 by rosiglitazone protects lung tissues against the expression of inflammatory proteins such as ICAM-1, following exposure to LPS.

### *PPARs stimulate expression of HO-1 protein*

Activation of PPARs by agonists could inhibit the proliferation of pulmonary artery cells and reduce pulmonary

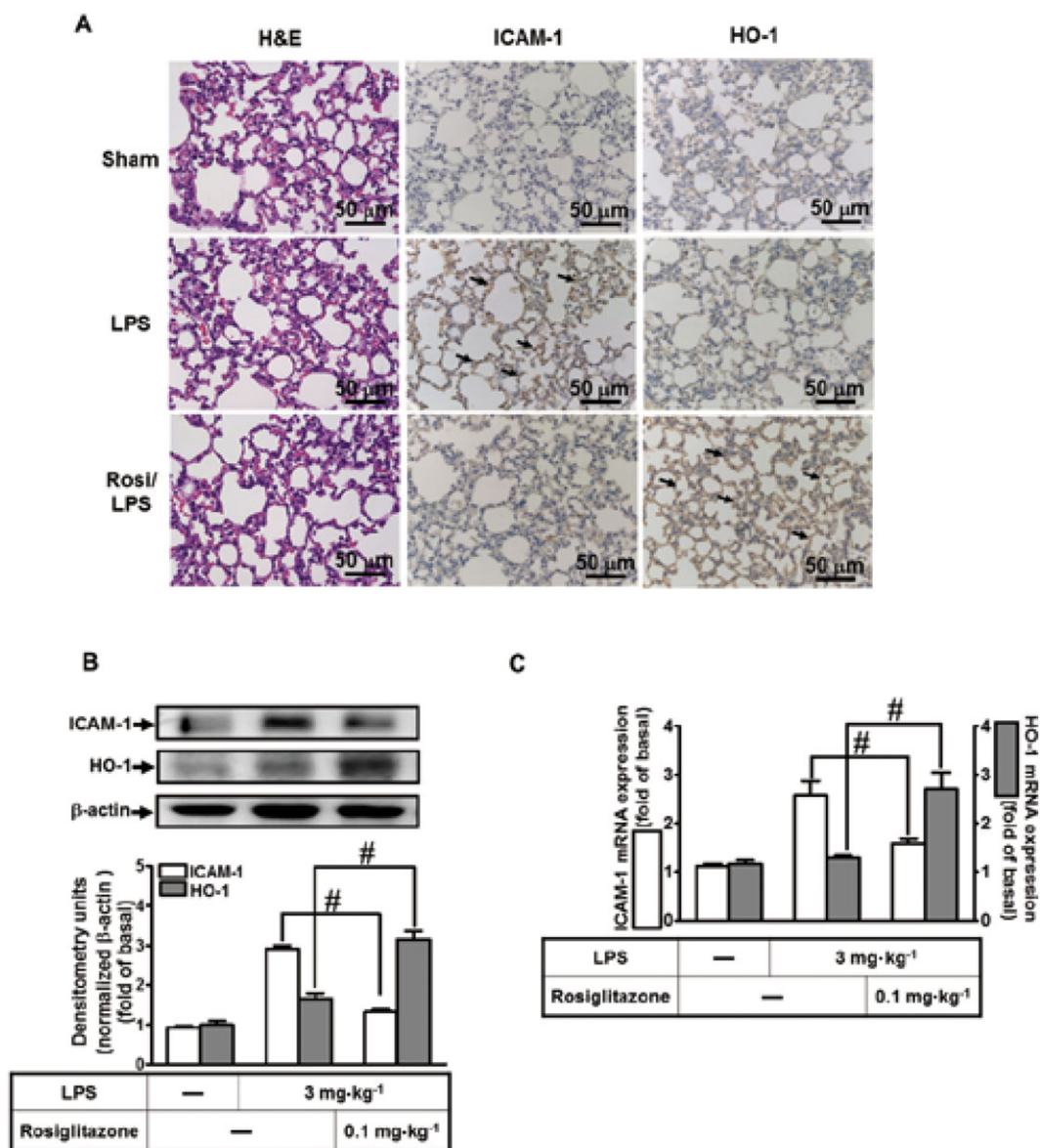


**Figure 1**

Rosiglitazone alleviates LPS-induced pulmonary inflammatory responses *in vivo*. (A) Mice were pre-treated with rosiglitazone (i.p., 0.1 mg·kg<sup>-1</sup>) or vehicle and 1 h later treated with or without LPS (intra-tracheally; 3 mg·kg<sup>-1</sup>) for 16 h. H&E and immunohistochemical staining for ICAM-1 and HO-1 in serial sections of the lung tissues from Sham [0.1 mL of DMSO-PBS (1:100) with 0.1% (W/V) BSA treated mice], LPS (LPS-treated mice) and Rosi + LPS (rosiglitazone plus LPS mice). The arrows indicate the ICAM-1 and HO-1 expression on pulmonary alveolar cells. All images are representative of five mice per group. (B, C) Lung tissues were homogenized to extract protein and mRNA. The protein and mRNA levels of ICAM-1 and HO-1 were determined by Western blot and real-time PCR. Data are expressed as mean ± SEM, from five independent experiments (*n* = 5). #*P* < 0.05, significantly different as indicated.



vascular remodelling by HO-1 up-regulation (Kronke *et al.*, 2007; Li *et al.*, 2010). To investigate whether **PPAR $\alpha$** , **PPAR $\delta$**  or PPAR $\gamma$  agonists could induce HO-1 expression in HPAEpiCs, the cells were treated with the agonist of PPAR $\alpha$  (GW590735), PPAR $\delta$  (GW0742) or PPAR $\gamma$  (rosiglitazone) for the indicated time intervals. These

agonists time-dependently induced HO-1 protein expression (Figure 2A). Other PPAR $\gamma$  agonists (ciglitazone, pioglitazone and troglitazone) over a range of concentrations (0.1 - 30  $\mu$ M) were used to induce HO-1 expression. At the highest concentration (30  $\mu$ M), these three agonists, but not rosiglitazone, induced cell death of HPAEpiCs. We

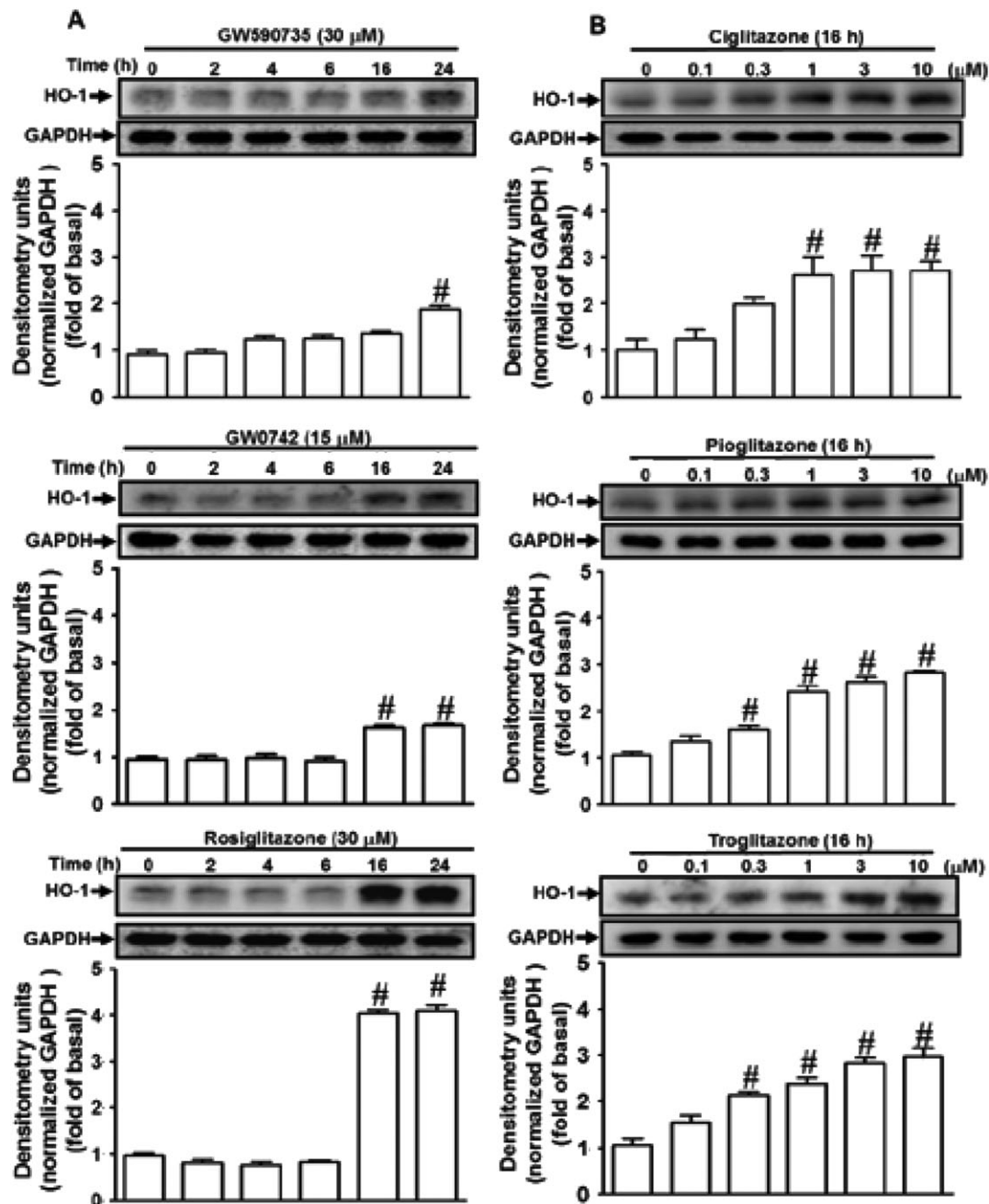


**Figure 2**

PPAR agonists induce HO-1 expression in HPAEpiCs. (A) The effects of PPAR $\alpha$ , PPAR $\delta$  and PPAR $\gamma$  agonists on HO-1 expression, the cells were treated with the agonist of PPAR $\alpha$  (GW590735), PPAR $\delta$  (GW0742) or PPAR $\gamma$  (rosiglitazone) for the indicated time intervals. (B) The effects of PPAR $\gamma$  agonists on HO-1 expression, the cells were treated with various concentrations of ciglitazone, pioglitazone or troglitazone for 16 h. The levels of HO-1 and GAPDH protein were determined by Western blot. Data are expressed as mean  $\pm$  SEM, from five independent experiments ( $n = 5$ ). <sup>#</sup> $P < 0.05$ , significantly different from vehicle (0 h) alone.



therefore chose lower concentrations of ciglitazone, pioglitazone and troglitazone to induce the expression of HO-1 (Figure 2B). As the level of HO-1 expression by rosiglitazone ( $3.6 \pm 0.1$  fold; Figure 3A) was greater than those after ciglitazone ( $2.7 \pm 0.2$  fold), pioglitazone ( $2.8 \pm 0.1$  fold) and troglitazone ( $3.0 \pm 0.3$  fold) over 16 h (all at  $10 \mu\text{M}$ ). Therefore, we chose rosiglitazone as an inducer for the following experiments in this study.

### *Rosiglitazone induces HO-1 expression*

The mechanisms underlying rosiglitazone-induced HO-1 gene expression were dissected in HPAEpiCs. We found that rosiglitazone time- and concentration-dependently induced HO-1 protein expression (Figure 3A). There was a significant increase within 10 h and reaching a maximal response within 24 h. Moreover, the levels of HO-1 mRNA were also enhanced by rosiglitazone (Figure 3B). We also evaluated the effect of HO-1 up-regulation induced by rosiglitazone on LPS-induced ICAM-1 expression. HPAEpiCs were pretreated with  $30 \mu\text{M}$  rosiglitazone for 1 h and then continuously incubated with or without  $1 \mu\text{M}$  ZnPPiX (a HO-1 activity inhibitor) for 1 h, and finally treated with  $20 \mu\text{g}\cdot\text{mL}^{-1}$  LPS for 16 h. As shown in Figure 3C,D the levels of HO-1 protein and mRNA were significantly increased in HPAEpiCs challenged with rosiglitazone, which accompanied with down-regulation of ICAM-1 expression induced by LPS and was reversed by treatment with ZnPPiX. In addition, treatment with ZnPPiX also blunted the reduction, induced by rosiglitazone, of the adhesion of THP-1 cells to HPAEpiCs challenged with LPS (Figure 3E), suggesting that HO-1 induction by rosiglitazone protects against monocyte adhesion to HPAEpiCs, challenged with LPS.

### *NOX-derived ROS generation is required for rosiglitazone-induced HO-1 expression*

HO-1 is induced by intracellular oxidative stress or imbalance between intracellular redox conditions (Loboda *et al.*, 2016). Activation of NOX is one of the sources of ROS which could act as second messengers leading to HO-1 expression (Seo *et al.*, 2011). To determine whether NOX activation and ROS generation were involved in the HO-1 expression, HPAEpiCs were pretreated with a scavenger of ROS (NAC), or inhibitors of  $\text{p47}^{\text{phox}}$  (APO) or NOX (DPI). As shown in Figure 4A,B, these treatments concentration-dependently attenuated the induction of HO-1 protein (Figure 4A) and mRNA (Figure 4B) by rosiglitazone. In NOX enzymes, NOX2 has been shown to distinctly recruit  $\text{p22}^{\text{phox}}$  (presence) and  $\text{p47}^{\text{phox}}$  (regulatory subunits) to produce superoxide ( $\text{O}_2^{\cdot-}$ ) in pulmonary alveolar epithelial cells (Tickner *et al.*, 2011). To confirm the roles of  $\text{p47}^{\text{phox}}$  and NOX2 in rosiglitazone-induced responses, the levels of  $\text{p47}^{\text{phox}}$  and NOX2 protein were knocked down by their respective siRNAs. As shown in Figure 4C, transfection with either  $\text{p47}^{\text{phox}}$  or NOX2 siRNA knocked down the level of  $\text{p47}^{\text{phox}}$  or NOX2 protein and attenuated the rosiglitazone-induced HO-1 expression in HPAEpiCs.

Phosphorylation of  $\text{p47}^{\text{phox}}$  is a key event in NOX activation and ROS generation (Lam *et al.*, 2010). We found that, in HPAEpiCs, rosiglitazone-stimulated  $\text{p47}^{\text{phox}}$  phosphorylation,

which was significantly inhibited by APO (Figure 5A). To further investigate whether rosiglitazone stimulates NOX activity leading to ROS generation, as shown in Figure 5B, rosiglitazone-stimulated NOX activity was blocked by pretreatment with APO ( $100 \mu\text{M}$ ) or DPI ( $3 \mu\text{M}$ ). Furthermore, to directly detect ROS generation in rosiglitazone-treated HPAEpiCs, the levels of intracellular  $\text{H}_2\text{O}_2$  and  $\text{O}_2^{\cdot-}$  were determined by  $\text{H}_2\text{DCFDA}$  and DHE respectively. Pretreatment with either APO or DPI inhibited the ROS generation induced by rosiglitazone (Figure 5C). These results were further supported by the data of DCF and DHE fluorescence images obtained by fluorescence microscopy (Figure 5D). These results suggested that rosiglitazone-induced HO-1 expression is mediated through NOX2-dependent ROS generation in HPAEpiCs.

### *Rosiglitazone-induced HO-1 expression is mediated via a NOX/ROS-dependent c-Src/Pyk2/Akt pathway*

NOX/ROS production activates downstream components such as c-Src and Pyk2 to modulate cellular functions (Peng *et al.*, 2003; Ke *et al.*, 2014). In addition, rosiglitazone also attenuated endothelial progenitor cell dysfunction and increased NO production via phosphorylation of Akt, which is one of downstream signalling components of the c-Src/Pyk2 pathway (Liang *et al.*, 2009; Deng *et al.*, 2013). Therefore, we investigated whether the rosiglitazone-induced HO-1 expression is mediated through activation of ROS-dependent c-Src, Pyk2 and Akt signalling components in HPAEpiCs. The inhibitors of c-Src (c-Srci II), Pyk2 (PF431396) and Akt (Akti VIII) were used for these purposes. Pretreatment with c-Srci II, PF431396 or Akti VIII significantly attenuated the rosiglitazone-induced HO-1 protein and mRNA expression in HPAEpiCs (Figure 6A,B). To confirm the involvement of c-Src, Pyk2 and Akt in rosiglitazone-mediated responses, as shown in Figure 6C, transfection with c-Src, Pyk2 or Akt siRNA down-regulated the level of c-Src, Pyk2 or Akt protein and then attenuated the rosiglitazone-induced HO-1 protein expression.

We further determined whether phosphorylation of c-Src, Pyk2 and Akt participated in rosiglitazone-induced HO-1 expression in HPAEpiCs, by Western blot, using an antibody specific for the phosphorylated form of c-Src, Pyk2 or Akt. Rosiglitazone-stimulated the phosphorylation of c-Src which was attenuated by the siRNA for  $\text{p47}^{\text{phox}}$  or NOX2 and APO, DPI or c-Srci II (Figure 7A,B). Similarly, pretreatment with c-Srci II inhibited rosiglitazone-stimulated phosphorylation of Pyk2, but not  $\text{p47}^{\text{phox}}$  (Figure 7B), suggesting that rosiglitazone-stimulated c-Src-dependent Pyk2 phosphorylation is mediated through NOX/ROS. Moreover, pretreatment with PF431396 attenuated rosiglitazone-stimulated Pyk2 phosphorylation, but not c-Src (Figure 7C), implying that Pyk2 was a downstream component of NOX/ROS/c-Src cascade. Further, rosiglitazone time-dependently stimulated Akt phosphorylation which was attenuated by pretreatment with either PF431396 or Akti VIII (Figure 7C,D). Akti VIII failed to inhibit the Pyk2 phosphorylation. Collectively, these data suggested that rosiglitazone-induced HO-1 expression is mediated through a NOX/ROS/c-Src/Pyk2/Akt cascade in HPAEpiCs.

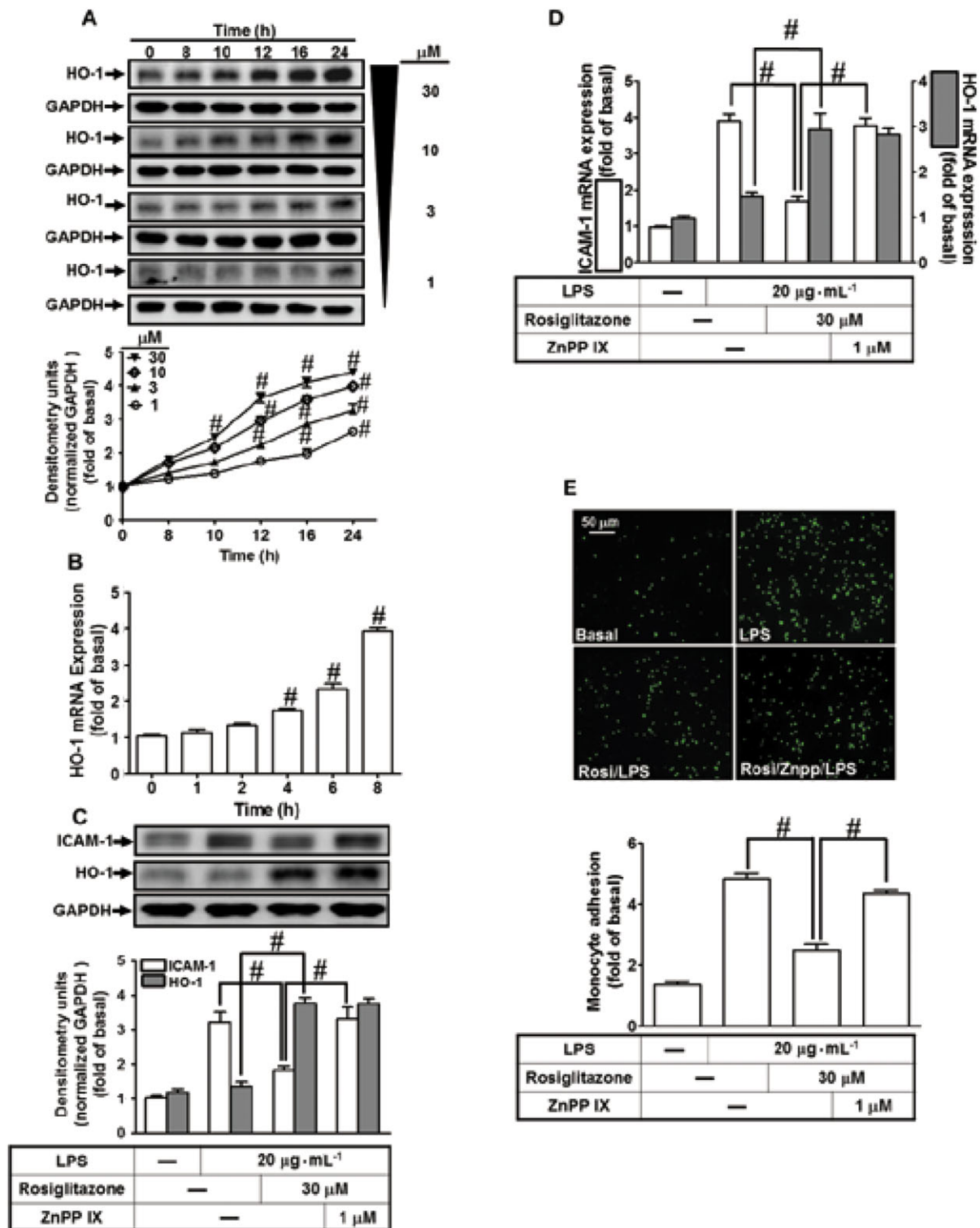


**Figure 3**

Overexpression of HO-1 inhibits LPS-mediated monocyte adhesion *in vitro*. (A) Cells were incubated with different concentrations of rosiglitazone (30, 10, 3 or 1  $\mu\text{M}$ ) for various time intervals. The levels of HO-1 and GAPDH expression were determined by Western blot. (B) Total RNA was isolated from HPAEpiCs treated with rosiglitazone (30  $\mu\text{M}$ ) for the indicated time intervals. The levels of HO-1 and GAPDH mRNA were determined by real-time PCR. (C–E) Cells were pretreated rosiglitazone for 1 h, then incubated with ZnPPiX for 1 h and finally stimulated with LPS for 16 h (protein and cell adhesion) or 4 h (mRNA). The levels of ICAM-1, HO-1 and GAPDH protein and mRNA were determined by Western blot and real-time PCR respectively. (E) The adhesion of THP-1 cells was measured. Data are expressed as mean  $\pm$  SEM, from five independent experiments ( $n = 5$ ).  $^{\#}P < 0.05$ , significantly different from vehicle alone (A, B); or significantly different as indicated (C–E).

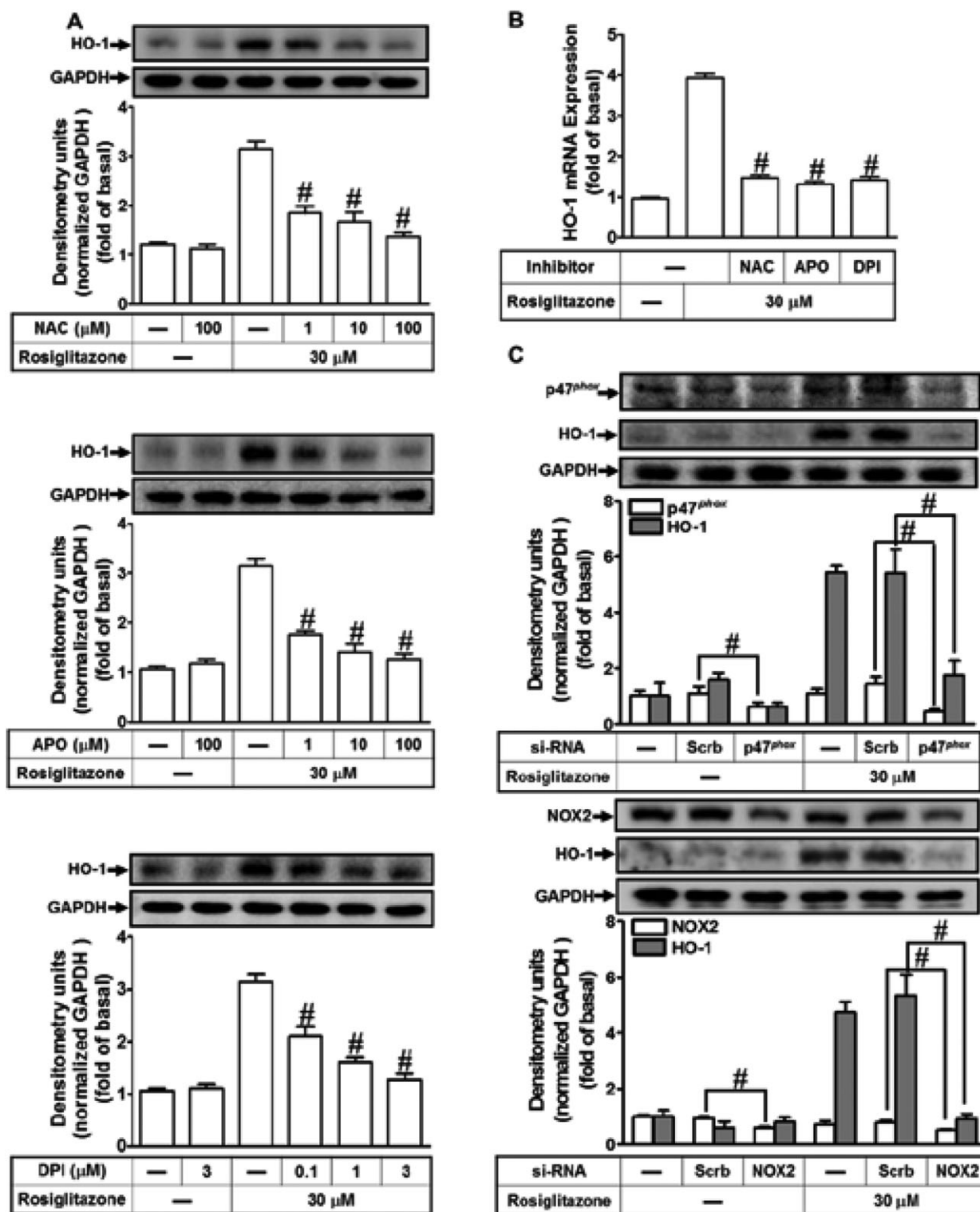


**Figure 4**

Activated NADPH oxidase and ROS generation are involved in rosiglitazone-increased HO-1 expression. (A) The cells were pretreated with various concentrations of NAC, APO or DPI for 1 h and then incubated with vehicle or rosiglitazone (30 μM) for 16 h. The levels of HO-1 and GAPDH protein were determined by Western blot. (B) The cells were pretreated with NAC (100 μM), APO (100 μM) and DPI (3 μM) for 1 h and then incubated with vehicle or rosiglitazone (30 μM) for 8 h. The levels of HO-1 and GAPDH mRNA were determined by real-time PCR. (C) HPAEpiCs were transfected with p47<sup>phox</sup> or NOX2 siRNA and then incubated with rosiglitazone for 16 h. The levels of HO-1, p47<sup>phox</sup>, NOX2 or GAPDH were determined by Western blot. Data are expressed as mean ± SEM, from five independent experiments ( $n = 5$ ),  $^{\#}P < 0.05$ , significantly different from rosiglitazone alone (A, B); or significantly different as indicated (C).





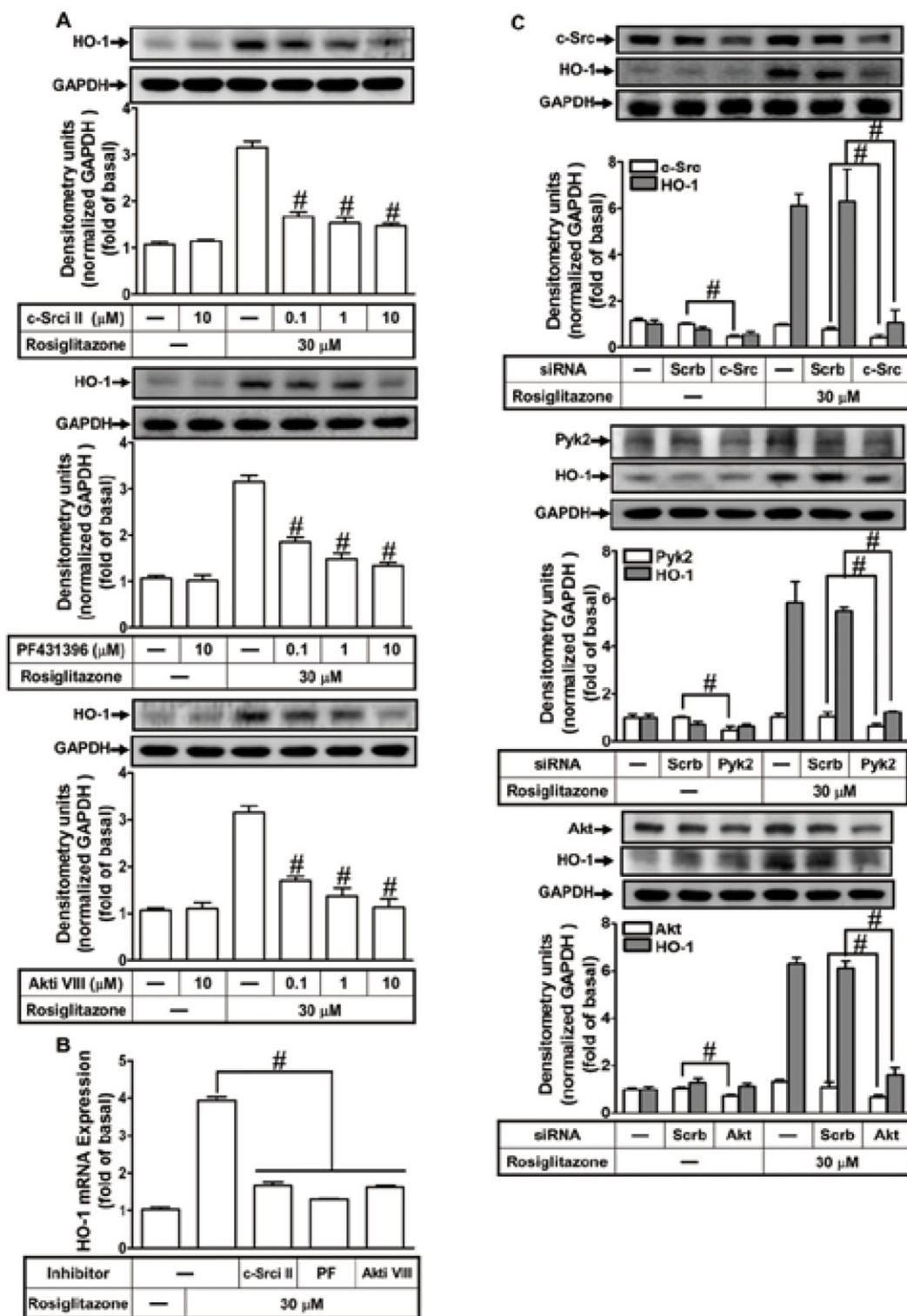


**Figure 6**

Activated c-Src, Pyk2 and Akt play crucial roles in rosiglitazone-induced HO-1 expression. (A) The cells were incubated with various concentrations of c-Src II, PF431396 or Akti VIII for 1 h and then stimulated by vehicle or rosiglitazone (30  $\mu$ M) for 16 h. The levels of HO-1 and GAPDH protein were determined by Western blot. (B) The cells were pretreated with c-Src II (10  $\mu$ M), PF431396 (10  $\mu$ M) or Akti VIII (10  $\mu$ M) for 1 h and then incubated with vehicle or rosiglitazone (30  $\mu$ M) for 8 h. The levels of HO-1 and GAPDH mRNA were determined by real-time PCR. (C) HPAEpiCs were transfected with c-Src, Pyk2 or Akt siRNA and then incubated with rosiglitazone for 16 h. The levels of HO-1, c-Src, Pyk2 and GAPDH protein were determined by Western blot. Data are expressed as mean  $\pm$  SEM, from five independent experiments ( $n = 5$ ). <sup>#</sup> $P < 0.05$ , significantly different from rosiglitazone alone (A, B); or significantly different as indicated (C).

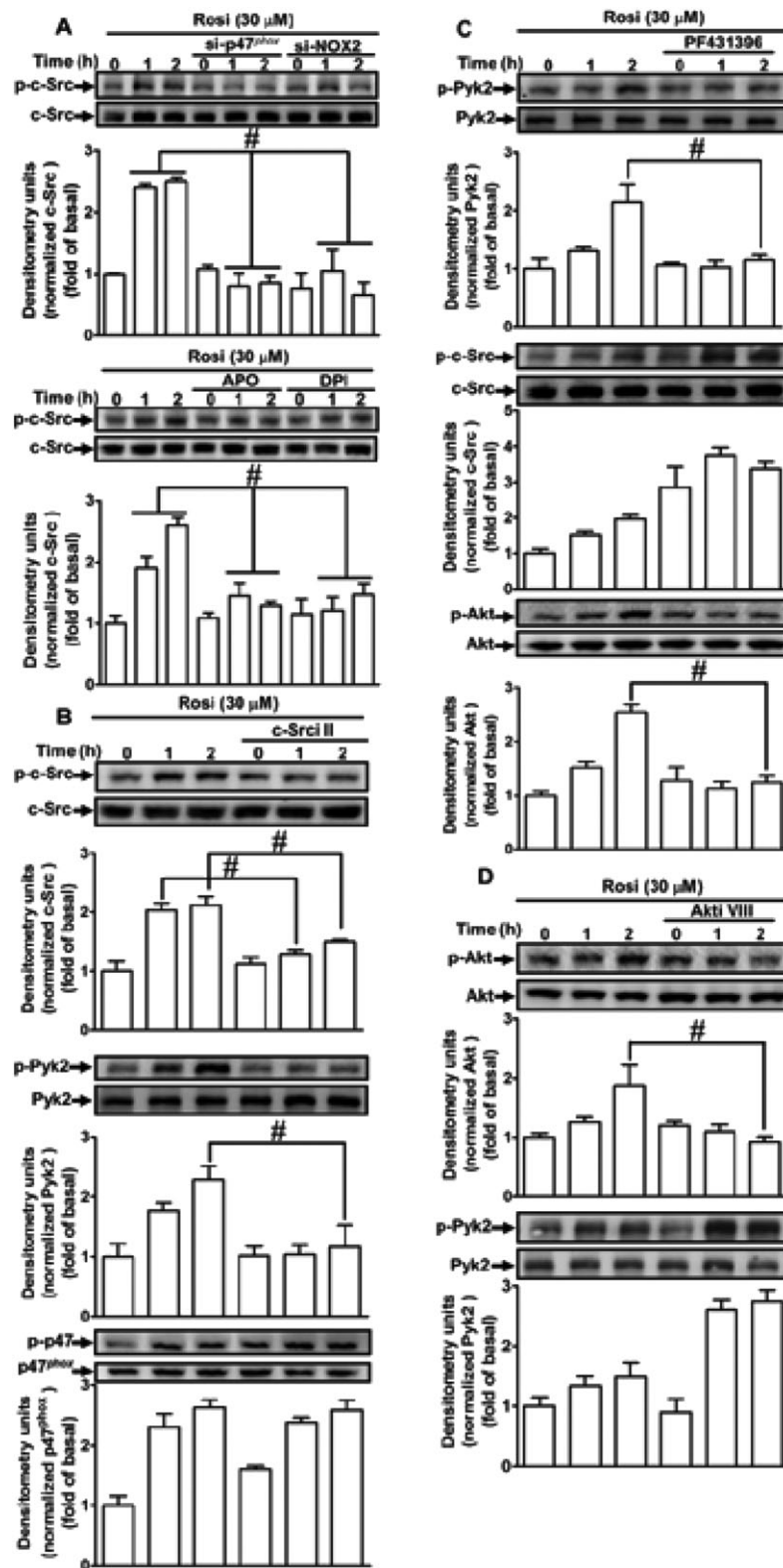


**Figure 7**

Rosiglitazone-induced HO-1 expression via NOX/ROS-dependent c-Src/Pyk2/Akt pathway. HPAEpiCs were (A) transfected with p47<sup>phox</sup> or NOX2 siRNA, and pretreated with APO or DPI, (B) c-SrcII, (C) PF431396 or (D) Akti VIII for 1 h, and then incubated with vehicle or rosiglitazone (30  $\mu$ M) for the indicated time intervals. Western blot was performed by using an anti-phospho-c-Src, anti-c-Src, anti-phospho-Pyk2, anti-Pyk2, anti-phospho-Akt or anti-Akt antibody. Data are expressed as mean  $\pm$  SEM, from five independent experiments ( $n = 5$ ). #  $P < 0.05$ , significantly different from rosiglitazone alone.

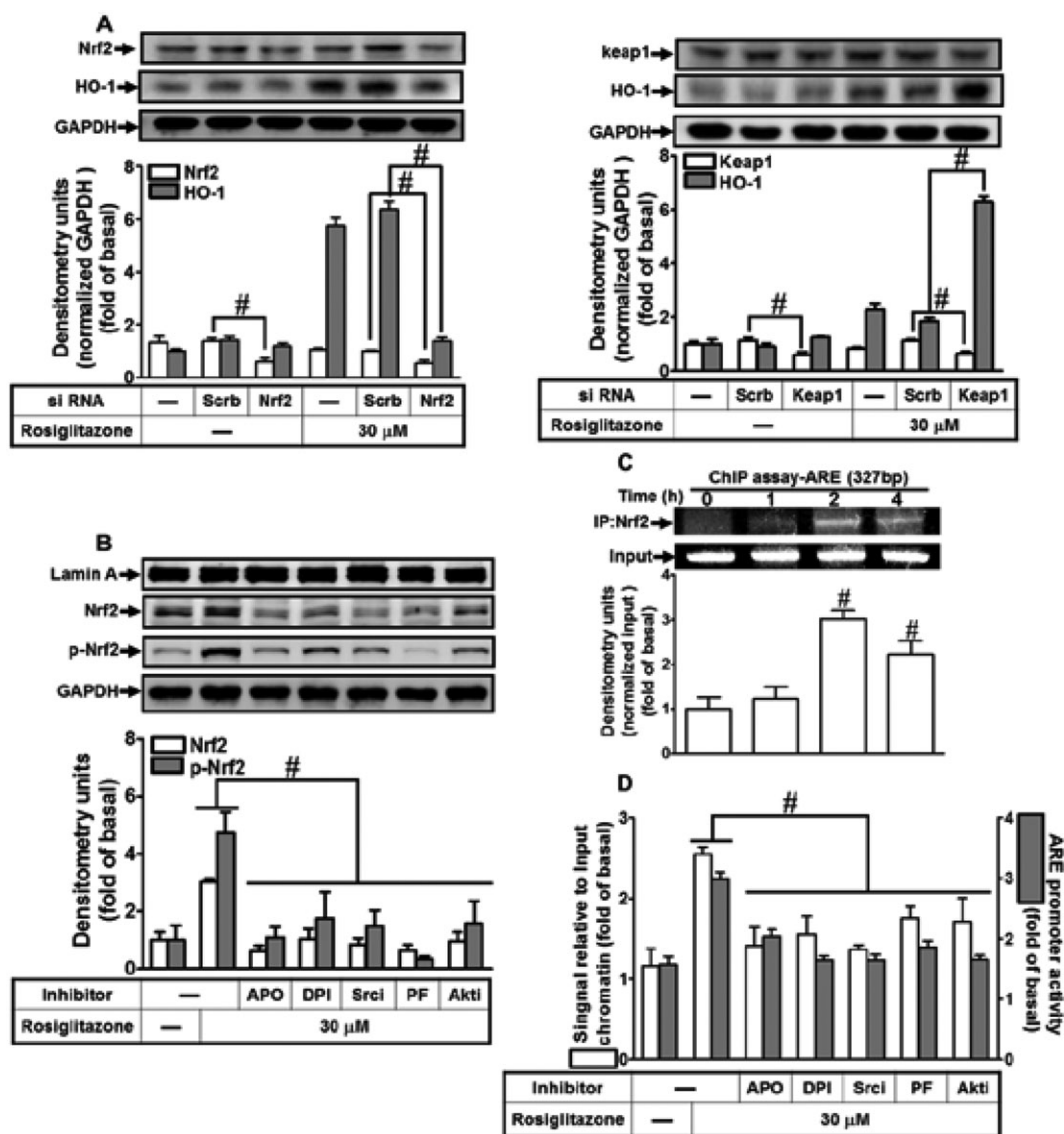


## Figure 8

The involvement of NOX/ROS/c-Src/Pyk2/Akt/Nrf2 cascade in the rosiglitazone-stimulated ARE promoter activity. (A) HPAEpiCs were transfected with Nrf2 or Keap1 siRNA and then incubated with rosiglitazone for 16 h. The levels of Nrf2, Keap1, HO-1 and GAPDH proteins were determined by Western blot. (B) Cells were pretreated with APO, DPI, c-Srci II, PF431396 or Akti VIII for 1 h and then stimulated with rosiglitazone for 2 h. The cytoplasmic and nuclear fractions were extracted and analysed by Western blot by using an anti-Nrf2, anti-phospho-Nrf2, anti-GAPDH or anti-Lamin A antibody. (C, D) Cells were treated with 30  $\mu$ M of rosiglitazone for the indicated time points or pretreated with APO, DPI, c-Srci II, PF431396 and Akti VIII for 1 h and then stimulated by rosiglitazone for 2 h. The levels of Nrf2 binding to ARE region of the HO-1 promoter were detected by a ChIP assay (C) or SYBR green real-time PCR (D, open bars). ARE-luc plasmids transfected HPAEpiCs were pretreated with APO, DPI, c-Srci II, PF431396 or Akti VIII for 1 h and then incubated with vehicle or rosiglitazone (30  $\mu$ M) for 2 h. ARE promoter luciferase activity was determined. Data are expressed as mean  $\pm$  SEM, from five independent experiments ( $n = 5$ ). # $P < 0.05$ , significantly different as indicated (A); significantly different from rosiglitazone alone (B, D); or significantly different from vehicle (0 h) alone (C).

against inflammatory responses (Chawla *et al.*, 2001). As shown in Figure 9A, pretreatment of HPAEpiCs with the PPAR $\gamma$  antagonist, GW9662, concentration-dependently inhibited the rosiglitazone-induced HO-1 protein and mRNA expression. These results were further confirmed by transfection with PPAR $\gamma$  siRNA, which markedly knocked down the level of PPAR $\gamma$  protein of either control or rosiglitazone treatment (control:  $44 \pm 7\%$ ; rosiglitazone:  $51 \pm 6\%$ , si-PPAR $\gamma$  vs. Scrb) and also reduced the rosiglitazone-induced HO-1

expression by  $33 \pm 4\%$  in HPAEpiCs (Figure 9B). Further, we observed that rosiglitazone time-dependently enhanced PPAR $\gamma$  promoter activity, which was inhibited by pretreatment with PPAR $\gamma$  antagonist GW9662 (Figure 9C). These results suggested the participation of PPAR $\gamma$  in the rosiglitazone-induced HO-1 expression in HPAEpiCs. Phosphorylation on Ser<sup>112</sup> residue of PPAR $\gamma$  has been shown to correlate to its binding affinity with PPAR $\gamma$  ligands and post-translational events (Burns and Vanden Heuvel, 2007; Rai

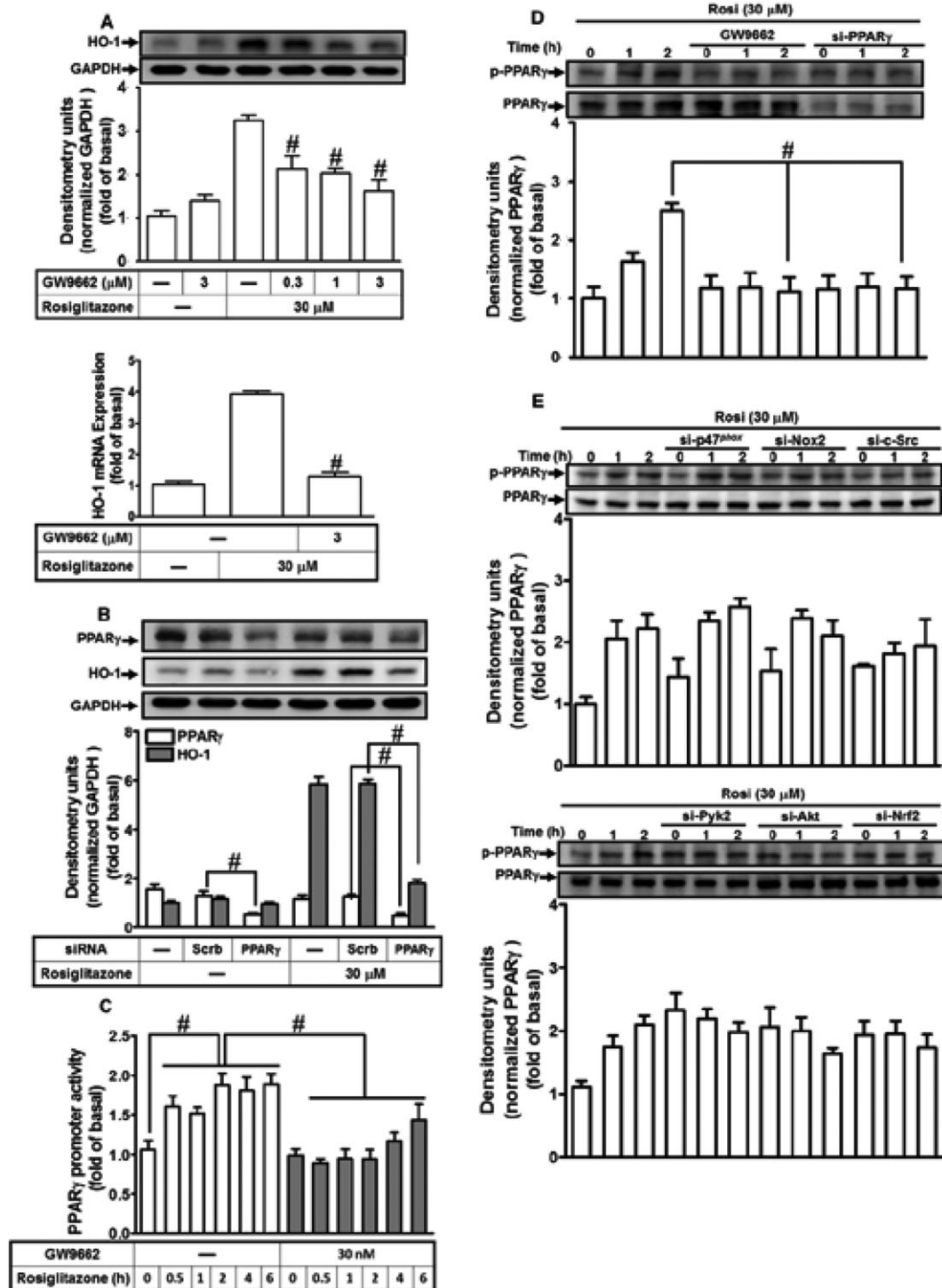


**Figure 9**

Rosiglitazone induces HO-1 expression through a PPAR $\gamma$ -dependent manner. (A) HPAEpiCs were pretreated with various concentrations of GW9662 for 1 h and then incubated with vehicle or rosiglitazone (30  $\mu$ M) for 16 h. The levels of HO-1 and GAPDH proteins were determined by Western blot. (B) Cells were transfected with PPAR $\gamma$  siRNA and then incubated with rosiglitazone for 16 h. The levels of PPAR $\gamma$ , HO-1 and GAPDH were detected by Western blot. (C) PPAR $\gamma$ -RE reporter construct-transfected cells were pretreated with GW9662 (30 nM) for 1 h and then incubated rosiglitazone (30  $\mu$ M) for 2 h. PPAR $\gamma$  RE promoter luciferase activity was determined in the cell lysates. (D, E) HPAEpiCs were pretreated with GW9662 and transfected with PPAR $\gamma$ , p47<sup>phox</sup>, NOX2, c-Src, Pyk2, Akt or Nrf2 siRNA, and then incubated with vehicle or rosiglitazone (30  $\mu$ M) for the indicated time intervals. Western blot was used to detect the phosphorylation of PPAR $\gamma$  and the levels of total PPAR $\gamma$ . Data are expressed as mean  $\pm$  SEM, from five independent experiments ( $n = 5$ ).  $^{\#}P < 0.05$ , significantly different from rosiglitazone alone (A, D); or significantly different as indicated (B–D).



*et al.*, 2014). Data in Figure 9D showed that both PPAR $\gamma$  antagonist (GW9662) and PPAR $\gamma$  siRNA markedly attenuated phosphorylation of PPAR $\gamma$  stimulated by rosiglitazone. Thus, whether rosiglitazone stimulated PPAR $\gamma$  phosphorylation *via* activation of NOX/ROS/c-Src/Pyk2/Akt/Nrf2 cascade was determined in HPAEpiCs. We found that transfection with p47<sup>phox</sup>, NOX2, c-Src, Pyk2, Akt or Nrf2 siRNA had no significant effect on PPAR $\gamma$  phosphorylation stimulated by rosiglitazone (Figure 9E). Further, we also differentiated whether rosiglitazone-induced HO-1 expression was mediated through a PPAR $\gamma$ -dependent c-Src/Pyk2/Akt cascade. We found that pretreatment with GW9662 or transfection with PPAR $\gamma$  siRNA failed to reduce the phosphorylation of c-Src, Pyk2 or Akt (Supporting Information Figure S1). These results suggested that rosiglitazone-induced HO-1 expression is mediated through either PPAR $\gamma$ -dependent or -independent manner in HPAEpiCs.

## Discussion

Accumulating evidence indicates that rosiglitazone exerts anti-inflammatory effects through up-regulation of HO-1 in the pulmonary system (Liu *et al.*, 2005; Kronke *et al.*, 2007; Li *et al.*, 2010; Xu *et al.*, 2015b), suggesting a possible therapeutic application for treatment of inflammatory diseases (Belvisi and Mitchell, 2009). In our previous study, we found that rosiglitazone suppressed LPS-induced nuclear translocation of phosphorylated NF- $\kappa$ B (p65) and expression of adhesion molecules through a PPAR $\gamma$ -dependent, up-regulation of HO-1 (Cho *et al.*, 2018). Here, we confirmed that rosiglitazone inhibited LPS-induced lung inflammation by inducing HO-1 independently of PPAR $\gamma$ . Further, application of pharmacological inhibitors and transfection with siRNAs inhibited rosiglitazone-induced HO-1 expression in HPAEpiCs. Our results demonstrated that HO-1 expression induced by rosiglitazone was mediated through activation of either a NOX/ROS/c-Src/Pyk2/Akt/Nrf2 pathway or a PPAR $\gamma$  cascade to suppress the inflammatory responses triggered by LPS (Figure 10).

PPAR subtypes are expressed in many tissues (Kota *et al.*, 2005), and regulate several cellular functions (Michalik *et al.*, 2006). PPAR agonists such as WY-14643 (PPAR $\alpha$ ), GW501516 (PPAR $\beta/\delta$ ) and rosiglitazone (PPAR $\gamma$ ) induce HO-1 expression to inhibit inflammatory responses (Kronke *et al.*, 2007; Sodhi *et al.*, 2014). Consistent with these findings, our results showed that agonists of these three subtypes of PPAR enhanced HO-1 expression in HPAEpiCs. Particularly, rosiglitazone possesses potential effects against acute lung injury and inflammation *via* HO-1 expression (Lin *et al.*, 2014; Lv *et al.*, 2016). Our results also confirmed that treatment of mice or HPAEpiCs with rosiglitazone significantly attenuated LPS-induced ICAM-1 expression and leukocyte adhesion, *via* up-regulation of HO-1.

ROS act as messengers in normal physiological functions or as inflammatory mediators, dependent on their concentration (Kamata and Hirata, 1999). NOX/ROS-dependent HO-1 expression is induced by different stimuli (Srisook *et al.*, 2006; Jamal Uddin *et al.*, 2016). Recently, an endogenous PPAR $\gamma$  ligand, **15d-PGJ<sub>2</sub>**, induced ROS generation which promoted Nrf2-dependent expression of HO-1 (Koyani *et al.*,

2016). Therefore, NOX-dependent ROS generation may be involved in HO-1 up-regulation induced by rosiglitazone in HPAEpiCs. This was confirmed by the results that rosiglitazone-induced HO-1 expression was inhibited by NAC, APO and DPI. Moreover, NOX inhibitors prevent p47<sup>phox</sup> phosphorylation or translocation to the membrane and thus inhibit NOX activation and ROS generation (Barbieri *et al.*, 2004). In line with these reports, our results demonstrated that pretreatment with APO or DPI attenuated rosiglitazone-induced NOX/ROS generation associated with HO-1 expression, suggesting that NOX/ROS play an important role in these responses.

NOX/ROS-dependent HO-1 expression has been shown to be mediated through the activation of c-Src and Pyk2 (Han *et al.*, 2009; Chi *et al.*, 2015) and PI3K/Akt (Deng *et al.*, 2013; Xu *et al.*, 2015b), which protects against oxidative injury. Our results confirmed that c-Src, Pyk2 and Akt are involved in HO-1 expression in HPAEpiCs, which may result from the phosphorylation of c-Src, Pyk2 and Akt stimulated by rosiglitazone. We also demonstrated that c-Src, Pyk2 and Akt are downstream targets of NOX/ROS, as rosiglitazone-stimulated phosphorylation of c-Src was attenuated by NOX inhibitors or siRNA. The relationship among c-Src, Pyk2 and Akt in rosiglitazone-mediated responses was further differentiated by using the corresponding inhibitors. Pretreatment with c-Src II inhibited the rosiglitazone-stimulated phosphorylation of c-Src and Pyk2, whereas PF43139 only attenuated phosphorylation of Pyk2, suggesting that Pyk2 is downstream of c-Src in rosiglitazone-mediated responses. We also observed that rosiglitazone-stimulated Akt phosphorylation was attenuated by PF431396 or Akti VIII, implying that Akt is downstream of c-Src/Pyk2. It is worth noting that phosphorylation of c-Src, Pyk2 and Akt was not changed by GW9662 or PPAR $\gamma$  siRNA. These results confirmed that rosiglitazone-induced HO-1 expression through a NOX/ROS-mediated c-Src/Pyk2/Akt phosphorylation is independent on PPAR $\gamma$  in HPAEpiCs.

Nrf2 controls the basal and inducible expression of an array of ARE-dependent genes to regulate the pathophysiological outcomes of oxidant exposure (Espinosa-Diez *et al.*, 2015). In our study, rosiglitazone mediated Nrf2 phosphorylation by promoting the degradation of Keap1 and nuclear accumulation of Nrf2 in HPAEpiCs. Phosphorylated Nrf2 translocation from the cytosol into the nucleus and binding to ARE were essential for HO-1 induction (Yang *et al.*, 2015). Indeed, ChIP assay suggested that rosiglitazone increases Nrf2 interactions with ARE binding sites on the HO-1 promoter. Silencing Nrf2 expression by its siRNA attenuated HO-1 expression, but down-regulated Keap1 expression increased HO-1 protein levels in rosiglitazone-stimulated HPAEpiCs. These results are consistent with the reports that expression of HO-1, in response to up-regulated Nrf2 in post-transcriptional sites, protects cells from apoptosis in an Nrf2-dependent manner (Foresti *et al.*, 2013). Moreover, the Akt/Nrf2 signalling pathway protects against toxicity (de Oliveira *et al.*, 2015). Here, we reported that blockade of the NOX/ROS/c-Src/Pyk2/Akt cascade by their respective inhibitors reduced rosiglitazone-stimulated phosphorylation/nuclear translocation of Nrf2, HO-1 promoter binding and ARE promoter activity in HPAEpiCs. These results suggested that Nrf2 is an acceptor of these protein kinases in rosiglitazone-mediated responses.

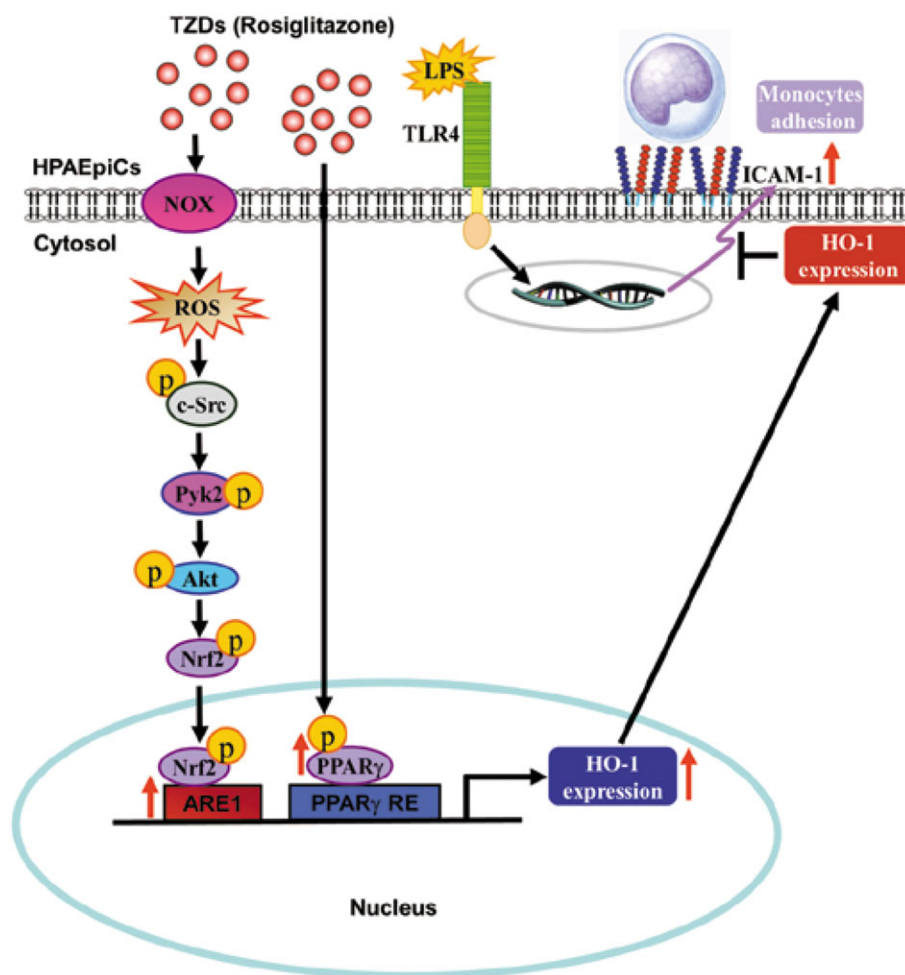


**Figure 10**

A schematic pathway for rosiglitazone induced HO-1 expression in HPAEpiCs. Rosiglitazone attenuated LPS-induced ICAM-1 expression and lung monocyte/leukocyte accumulation by up-regulating HO-1 expression *via* two manners: PPAR $\gamma$  dependence and PPAR $\gamma$  independence. Activated PPAR $\gamma$  directly bound to PPAR $\gamma$  responsive element of HO-1 promoter, which increased the expression of HO-1 gene. In the PPAR $\gamma$  independent pathway, rosiglitazone enhanced NADPH oxidase activity, which resulted in the accumulation of intracellular ROS. Imbalance of oxidative stress promoted the phosphorylation of c-Src/Pyk2/Akt and the activation of Nrf2. After nuclear translocation, Nrf2 binds to the ARE region of HO-1 promoter and increases the expression of the HO-1 gene.

On the other hand, PPAR $\gamma$  activation by rosiglitazone significantly increases HO-1 expression and attenuates airway inflammation and remodelling (Xu *et al.*, 2015a). In this study, blockade of PPAR $\gamma$  by its antagonist (GW9662) or siRNA, diminished rosiglitazone-mediated PPAR $\gamma$  phosphorylation and promoter activity in HPAEpiCs, suggesting the dependence of PPAR $\gamma$  on HO-1 expression. These results were consistent with the report indicating that PPAR $\gamma$  agonists block cigarette smoke extract-induced inflammatory responses through multiple PPAR $\gamma$ -mediated mechanisms (Lakshmi *et al.*, 2014). However, phosphorylation of PPAR $\gamma$  was independent on Nox/ROS/c-Src/Pyk2/Akt/Nrf2 cascade in rosiglitazone-stimulated HPAEpiCs. This was confirmed by transfection with respective siRNAs which had no significant effect on the rosiglitazone-stimulated phosphorylation of PPAR $\gamma$ . We also noted that both PPAR $\gamma$ -dependent and PPAR $\gamma$ -independent pathways are regulated by rosiglitazone. Our previous report indicated that

rosiglitazone activated PPAR $\gamma$  binding to PPRE on HO-1 promoter to induce HO-1 transcription (Cho *et al.*, 2018). Moreover, in the present study, we focused on the Nrf2 activity in HO-1 induction. The studies of promoter activity indicated that PPAR $\gamma$ -PPRE (–1740 to –1881 bp) and Nrf2-ARE (–4019 to –4082 bp) response elements exhibited a similar trend in the transcriptional regulation (Kronke *et al.*, 2007; Wang *et al.*, 2013). Our previous report also indicated that arachidonic acid increases HO-1 expression through the association of Nrf2 and PPAR $\gamma$  with ARE in rat astrocytes (Lin *et al.*, 2018). Rosiglitazone shared the similar mechanism to induce the cooperation of PPAR $\gamma$  and Nrf2 on HO-1 expression.

In summary, these findings suggest that rosiglitazone-induced HO-1 expression might play a protective role in lung inflammatory diseases, mediated *via* either NOX/ROS-dependent c-Src/Pyk2/Akt activation of Nrf2 which binds to ARE regions or PPAR $\gamma$ . Although several detailed

mechanisms should be elucidated in the future, these findings expand the application of PPAR $\gamma$  agonists as potential interventions for the prevention or treatment of pulmonary inflammatory diseases. Treatment with rosiglitazone at 2–4 weeks was associated with a modest improvement in pre-bronchodilator FEV<sub>1</sub> (forced expiratory volume in 1 s), peak expiratory flow and FEF<sub>25–75</sub> (forced expiratory flow between 25 and 75% of the forced vital capacity) of asthmatic reaction (Spears *et al.*, 2009; Richards *et al.*, 2010). Compared with rosiglitazone, administration of pioglitazone in mild asthma failed to improve any markers of airway inflammation, although it produced significant weight gains in asthmatic who were obese (Dixon *et al.*, 2015; Anderson *et al.*, 2016). Rosiglitazone has been reported to be associated with an increased risk of congestive heart failure, acute myocardial infarction and mortality in the patients during treatment for Type 2 diabetes. However, they are still of research value because of their anti-inflammatory activity in lung diseases (Home *et al.*, 2007; Azimova *et al.*, 2014).

## Acknowledgements

We thank Ms. Yu-Wen Chen for her technical assistance. This work was supported by the Ministry of Education, Taiwan, grant numbers: EMRPD1H032 and EMRPD1H055; the Ministry of Science and Technology, Taiwan, grant numbers: MOST104-2320-B-182A-003-MY3, MOST105-2320-B-182-005-MY3, MOST107-2320-B-182A-011 and MOST107-2320-B-182-020-MY2; Chang Gung Medical Research Foundation, Taiwan, grant numbers: CMRPD1F0022, 0CMRPD1F0023, CMRPD1F0551, CMRPD1F0552, CMRPG3E2232, CMRPG3F1532, CMRPG3F1533, CMRPG3H0061 and CMRPG5F0202.

## Author contributions

R.L.C., C.C.Y., H.C.T., L.D.H., C.C.L. and C.M.Y. conceived and designed the experiments. R.L.C., H.C.T., C.C.Y., L.D.H. and C.C.L. performed the experiments. R.L.C., C.C.Y., H.C.T., L.D.H., C.C.L. and C.M.Y. analysed the data and drafted relevant text. R.L.C., C.C.L. and C.M.Y. wrote the manuscript. All authors have read and approved the final version of this manuscript.

## Conflict of interest

The authors declare no conflicts of interest.

## Declaration of transparency and scientific rigour

This Declaration acknowledges that this paper adheres to the principles for transparent reporting and scientific rigour of preclinical research recommended by funding agencies, publishers and other organisations engaged with supporting research.

## References

- Alam J, Cook JL (2007). How many transcription factors does it take to turn on the heme oxygenase-1 gene? *Am J Respir Cell Mol Biol* 36: 166–174.
- Alexander SPH, Cidlowski JA, Kelly E, Marrion NV, Peters JA, Faccenda E *et al.* (2017a). The Concise Guide to PHARMACOLOGY 2017/18: Nuclear hormone receptors. *Br J Pharmacol* 174: S208–S224.
- Alexander SPH, Fabbro D, Kelly E, Marrion NV, Peters JA, Faccenda E *et al.* (2017b). The Concise Guide to PHARMACOLOGY 2017/18: Enzymes. *Br J Pharmacol* 174: S272–S359.
- Alexander SPH, Kelly E, Marrion NV, Peters JA, Faccenda E, Harding SD *et al.* (2017c). The Concise Guide to PHARMACOLOGY 2017/18: Other proteins. *Br J Pharmacol* 174: S1–S16.
- Anderson JR, Mortimer K, Pang L, Smith KM, Bailey H, Hodgson DB *et al.* (2016). Evaluation of the PPAR $\gamma$  agonist pioglitazone in mild asthma: a double-blind randomized controlled trial. *PLoS One* 11: e0160257.
- Azimova K, San Juan Z, Mukherjee D (2014). Cardiovascular safety profile of currently available diabetic drugs. *Ochsner J* 14: 616–632.
- Baird L, Lleres D, Swift S, Dinkova-Kostova AT (2013). Regulatory flexibility in the Nrf2-mediated stress response is conferred by conformational cycling of the Keap1-Nrf2 protein complex. *Proc Natl Acad Sci U S A* 110: 15259–15264.
- Barbieri SS, Cavalca V, Eligini S, Brambilla M, Caiani A, Tremoli E *et al.* (2004). Apocynin prevents cyclooxygenase 2 expression in human monocytes through NADPH oxidase and glutathione redox-dependent mechanisms. *Free Radic Biol Med* 37: 156–165.
- Belvisi MG, Mitchell JA (2009). Targeting PPAR receptors in the airway for the treatment of inflammatory lung disease. *Br J Pharmacol* 158: 994–1003.
- Burns KA, Vanden Heuvel JP (2007). Modulation of PPAR activity via phosphorylation. *Biochim Biophys Acta* 1771: 952–960.
- Chawla A, Barak Y, Nagy L, Liao D, Tontonoz P, Evans RM (2001). PPAR- $\gamma$  dependent and independent effects on macrophage-gene expression in lipid metabolism and inflammation. *Nat Med* 7: 48–52.
- Chi PL, Lin CC, Chen YW, Hsiao LD, Yang CM (2015). CO induces Nrf2-dependent heme oxygenase-1 transcription by cooperating with Sp1 and c-Jun in rat brain astrocytes. *Mol Neurobiol* 52: 277–292.
- Cho RL, Lin WN, Wang CY, Yang CC, Hsiao LD, Lin CC *et al.* (2018). Heme oxygenase-1 induction by rosiglitazone via PKC $\alpha$ /AMPK $\alpha$ /p38 MAPK $\alpha$ /SIRT1/PPAR $\gamma$  pathway suppresses lipopolysaccharide-mediated pulmonary inflammation. *Biochem Pharmacol* 148: 222–237.
- Cho RL, Yang CC, Lee IT, Lin CC, Chi PL, Hsiao LD *et al.* (2016). Lipopolysaccharide induces ICAM-1 expression via a c-Src/NADPH oxidase/ROS-dependent NF- $\kappa$ B pathway in human pulmonary alveolar epithelial cells. *Am J Physiol Lung Cell Mol Physiol* 310: L639–L657.
- Curtis MJ, Alexander S, Cirino G, Docherty JR, George CH, Gienbycz MA *et al.* (2018). Experimental design and analysis and their reporting II: updated and simplified guidance for authors and peer reviewers. *Brit J Pharmacol* 175: 987–993.
- de Oliveira MR, Ferreira GC, Schuck PF, Dal Bosco SM (2015). Role for the PI3K/Akt/Nrf2 signaling pathway in the protective effects of

- carnosic acid against methylglyoxal-induced neurotoxicity in SH-SY5Y neuroblastoma cells. *Chem Biol Interact* 242: 396–406.
- Deng X, Rui W, Zhang F, Ding W (2013). PM2.5 induces Nrf2-mediated defense mechanisms against oxidative stress by activating PIK3/AKT signaling pathway in human lung alveolar epithelial A549 cells. *Cell Biol Toxicol* 29: 143–157.
- Dewar BJ, Gardner OS, Chen CS, Earp HS, Samet JM, Graves LM (2007). Capacitative calcium entry contributes to the differential transactivation of the epidermal growth factor receptor in response to thiazolidinediones. *Mol Pharmacol* 72: 1146–1156.
- Dixon AE, Subramanian M, DeSarno M, Black K, Lane L, Holguin F (2015). A pilot randomized controlled trial of pioglitazone for the treatment of poorly controlled asthma in obesity. *Respir Res* 16: 143.
- Donovan C, Tan X, Bourke JE (2012). PPAR $\gamma$  ligands regulate noncontractile and contractile functions of airway smooth muscle: implications for asthma therapy. *PPAR Res* 2012: 809164.
- Espinosa-Diez C, Miguel V, Mennerich D, Kietzmann T, Sanchez-Perez P, Cadenas S *et al.* (2015). Antioxidant responses and cellular adjustments to oxidative stress. *Redox Biol* 6: 183–197.
- Foresti R, Bains SK, Pitchumony TS, de Castro Bras LE, Drago F, Dubois-Rande JL *et al.* (2013). Small molecule activators of the Nrf2-HO-1 antioxidant axis modulate heme metabolism and inflammation in BV2 microglia cells. *Pharmacol Res* 76: 132–148.
- Gardner OS, Dewar BJ, Graves LM (2005). Activation of mitogen-activated protein kinases by peroxisome proliferator-activated receptor ligands: an example of nongenomic signaling. *Mol Pharmacol* 68: 933–941.
- Han Z, Varadharaj S, Giedt RJ, Zweier JL, Szeto HH, Alevriadou BR (2009). Mitochondria-derived reactive oxygen species mediate heme oxygenase-1 expression in sheared endothelial cells. *J Pharmacol Exp Ther* 329: 94–101.
- Harding SD, Sharman JL, Faccenda E, Southan C, Pawson AJ, Ireland S *et al.* (2018). The IUPHAR/BPS Guide to PHARMACOLOGY in 2018: updates and expansion to encompass the new guide to IMMUNOPHARMACOLOGY. *Nucl Acids Res* 46: D1091–D1106.
- Home PD, Pocock SJ, Beck-Nielsen H, Gomis R, Hanefeld M, Jones NP *et al.* (2007). Rosiglitazone evaluated for cardiovascular outcomes—an interim analysis. *N Engl J Med* 357: 28–38.
- Hsu CK, Lee IT, Lin CC, Hsiao LD, Yang CM (2014). Nox2/ROS-dependent human antigen R translocation contributes to TNF- $\alpha$ -induced SOCS-3 expression in human tracheal smooth muscle cells. *Am J Physiol Lung Cell Mol Physiol* 306: L521–L533.
- Huang J, Shen XD, Yue S, Zhu J, Gao F, Zhai Y *et al.* (2014). Adoptive transfer of heme oxygenase-1 (HO-1)-modified macrophages rescues the nuclear factor erythroid 2-related factor (Nrf2) antiinflammatory phenotype in liver ischemia/reperfusion injury. *Mol Med* 20: 448–455.
- Itoh K, Wakabayashi N, Katoh Y, Ishii T, Igarashi K, Engel JD *et al.* (1999). Keap1 represses nuclear activation of antioxidant responsive elements by Nrf2 through binding to the amino-terminal Neh2 domain. *Genes Dev* 13: 76–86.
- Jamal Uddin M, Joe Y, Kim SK, Oh Jeong S, Ryter SW, Pae HO *et al.* (2016). IRG1 induced by heme oxygenase-1/carbon monoxide inhibits LPS-mediated sepsis and pro-inflammatory cytokine production. *Cell Mol Immunol* 13: 170–179.
- Kamata H, Hirata H (1999). Redox regulation of cellular signalling. *Cell Signal* 11: 1–14.
- Ke K, Sul OJ, Choi EK, Safdar AM, Kim ES, Choi HS (2014). Reactive oxygen species induce the association of SHP-1 with c-Src and the oxidation of both to enhance osteoclast survival. *Am J Physiol Endocrinol Metab* 307: E61–E70.
- Kilkenny C, Browne W, Cuthill IC, Emerson M, Altman DG, Group NCRGW (2010). Animal research: reporting in vivo experiments: the ARRIVE guidelines. *Br J Pharmacol* 160: 1577–1579.
- Kota BP, Huang TH, Roufogalis BD (2005). An overview on biological mechanisms of PPARs. *Pharmacol Res* 51: 85–94.
- Koyani CN, Kitz K, Rossmann C, Bernhart E, Huber E, Trummer C *et al.* (2016). Activation of the MAPK/Akt/Nrf2-Egr1/HO-1-GCLC axis protects MG-63 osteosarcoma cells against 15d-PGJ2-mediated cell death. *Biochem Pharmacol* 104: 29–41.
- Kronke G, Kadl A, Ikonomu E, Bluml S, Furnkranz A, Sarembok IJ *et al.* (2007). Expression of heme oxygenase-1 in human vascular cells is regulated by peroxisome proliferator-activated receptors. *Arterioscler Thromb Vasc Biol* 27: 1276–1282.
- Lakshmi SP, Reddy AT, Zhang Y, Sciruba FC, Mallampalli RK, Duncan SR *et al.* (2014). Down-regulated peroxisome proliferator-activated receptor  $\gamma$  (PPAR $\gamma$ ) in lung epithelial cells promotes a PPAR $\gamma$  agonist-reversible proinflammatory phenotype in chronic obstructive pulmonary disease (COPD). *J Biol Chem* 289: 6383–6393.
- Lam GY, Huang J, Brumell JH (2010). The many roles of NOX2 NADPH oxidase-derived ROS in immunity. *Semin Immunopathol* 32: 415–430.
- Li M, Li Z, Sun X, Yang L, Fang P, Liu Y *et al.* (2010). Heme oxygenase-1/p21WAF1 mediates peroxisome proliferator-activated receptor- $\gamma$  signaling inhibition of proliferation of rat pulmonary artery smooth muscle cells. *FEBS J* 277: 1543–1550.
- Liang C, Ren Y, Tan H, He Z, Jiang Q, Wu J *et al.* (2009). Rosiglitazone via upregulation of Akt/eNOS pathways attenuates dysfunction of endothelial progenitor cells, induced by advanced glycation end products. *Br J Pharmacol* 158: 1865–1873.
- Lin CC, Yang CC, Chen YW, Hsiao LD, Yang CM (2018). Arachidonic acid induces ARE/Nrf2-dependent heme oxygenase-1 transcription in rat brain astrocytes. *Mol Neurobiol* 55: 3328–3343.
- Lin CF, Young KC, Bai CH, Yu BC, Ma CT, Chien YC *et al.* (2014). Rosiglitazone regulates anti-inflammation and growth inhibition via PTEN. *Biomed Res Int* 2014: 787924.
- Liou CJ, Lai YR, Chen YL, Chang YH, Li ZY, Huang WC (2016). Matrine attenuates COX-2 and ICAM-1 expressions in human lung epithelial cells and prevents acute lung injury in LPS-induced mice. *Mediators Inflamm* 2016: 3630485.
- Liu D, Zeng BX, Zhang SH, Yao SL (2005). Rosiglitazone, an agonist of peroxisome proliferator-activated receptor  $\gamma$ , reduces pulmonary inflammatory response in a rat model of endotoxemia. *Inflamm Res* 54: 464–470.
- Loboda A, Damulewicz M, Pyza E, Jozkowicz A, Dulak J (2016). Role of Nrf2/HO-1 system in development, oxidative stress response and diseases: an evolutionarily conserved mechanism. *Cell Mol Life Sci* 73: 3221–3247.
- Lv H, Yu Z, Zheng Y, Wang L, Qin X, Cheng G *et al.* (2016). Isovitexin exerts anti-inflammatory and anti-oxidant activities on lipopolysaccharide-induced acute lung injury by inhibiting MAPK and NF- $\kappa$ B and activating HO-1/Nrf2 pathways. *Int J Biol Sci* 12: 72–86.
- McGrath JC, Lilley E (2015). Implementing guidelines on reporting research using animals (ARRIVE etc.): new requirements for publication in BJP. *Br J Pharmacol* 172: 3189–3193.



- Michalik L, Auwerx J, Berger JP, Chatterjee VK, Glass CK, Gonzalez FJ *et al.* (2006). International union of pharmacology. LXI. peroxisome proliferator-activated receptors. *Pharmacol Rev* 58: 726–741.
- Peng G, Huang J, Boyd M, Kleinberg ME (2003). Properties of phagocyte NADPH oxidase p47<sup>phox</sup> mutants with unmasked SH3 (Src homology 3) domains: full reconstitution of oxidase activity in a semi-recombinant cell-free system lacking arachidonic acid. *Biochem J* 373: 221–229.
- Polvani S, Tarocchi M, Galli A (2012). PPAR $\gamma$  and oxidative stress: Con( $\beta$ ) catenating NRF2 and FOXO. *PPAR Res* 2012: 641087.
- Rai A, Tripathi S, Kushwaha R, Singh P, Srivastava P, Sanyal S *et al.* (2014). CDK5-induced p-PPAR $\gamma$ <sup>(Ser 112)</sup> downregulates GFAP via PPRES in developing rat brain: effect of metal mixture and troglitazone in astrocytes. *Cell Death Dis* 5: e1033.
- Richards DB, Bareille P, Lindo EL, Quinn D, Farrow SN (2010). Treatment with a peroxisomal proliferator activated receptor  $\gamma$  agonist has a modest effect in the allergen challenge model in asthma: a randomised controlled trial. *Respir Med* 104: 668–674.
- Rushworth SA, Chen XL, Mackman N, Ogborne RM, O'Connell MA (2005). Lipopolysaccharide-induced heme oxygenase-1 expression in human monocytic cells is mediated via Nrf2 and protein kinase C. *J Immunol* 175: 4408–4415.
- Seo WY, Goh AR, Ju SM, Song HY, Kwon DJ, Jun JG *et al.* (2011). Celastrol induces expression of heme oxygenase-1 through ROS/Nrf2/ARE signaling in the HaCaT cells. *Biochem Biophys Res Commun* 407: 535–540.
- Sodhi K, Puri N, Kim DH, Hinds TD, Stechschulte LA, Favero G *et al.* (2014). PPAR  $\delta$  binding to heme oxygenase 1 promoter prevents angiotensin II-induced adipocyte dysfunction in Goldblatt hypertensive rats. *Int J Obes (Lond)* 38: 456–465.
- Spears M, Donnelly I, Jolly L, Brannigan M, Ito K, McSharry C *et al.* (2009). Bronchodilatory effect of the PPAR $\gamma$  agonist rosiglitazone in smokers with asthma. *Clin Pharmacol Ther* 86: 49–53.
- Srisook K, Han SS, Choi HS, Li MH, Ueda H, Kim C *et al.* (2006). CO from enhanced HO activity or from CORM-2 inhibits both O<sup>2-</sup> and NO production and downregulates HO-1 expression in LPS-stimulated macrophages. *Biochem Pharmacol* 71: 307–318.
- Tickner J, Fan LM, Du J, Meijles D, Li JM (2011). Nox2-derived ROS in PPAR $\gamma$  signaling and cell-cycle progression of lung alveolar epithelial cells. *Free Radic Biol Med* 51: 763–772.
- Wang G, Liu L, Zhang Y, Han D, Liu J, Xu J *et al.* (2014). Activation of PPAR $\gamma$  attenuates LPS-induced acute lung injury by inhibition of HMGB1-RAGE levels. *Eur J Pharmacol* 726: 27–32.
- Wang S, Hannafon BN, Zhou J, Ding WQ (2013). Clofibrate induces heme oxygenase 1 expression through a PPAR $\alpha$ -independent mechanism in human cancer cells. *Cell Physiol Biochem* 32: 1255–1264.
- Woodfin A, Beyrau M, Voisin MB, Ma B, Whiteford JR, Hordijk PL *et al.* (2016). ICAM-1-expressing neutrophils exhibit enhanced effector functions in murine models of endotoxemia. *Blood* 127: 898–907.
- Xu J, Zhu YT, Wang GZ, Han D, Wu YY, Zhang DX *et al.* (2015a). The PPAR $\gamma$  agonist, rosiglitazone, attenuates airway inflammation and remodeling via heme oxygenase-1 in murine model of asthma. *Acta Pharmacol Sin* 36: 171–178.
- Xu X, Li H, Hou X, Li D, He S, Wan C *et al.* (2015b). Punicalagin induces Nrf2/HO-1 expression via upregulation of PI3K/AKT pathway and inhibits LPS-induced oxidative stress in RAW264.7 macrophages. *Mediators Inflamm* 2015: 380218.
- Yang CM, Lin CC, Lee IT, Hsu CK, Tai YC, Hsieh HL *et al.* (2015). c-Src-dependent transactivation of EGFR mediates CORM-2-induced HO-1 expression in human tracheal smooth muscle cells. *J Cell Physiol* 230: 2351–2361.

## Supporting Information

Additional supporting information may be found online in the Supporting Information section at the end of the article.

<https://doi.org/10.1111/bph.14465>

**Figure S1** Rosiglitazone-induced c-Src/Pyk2/Akt pathway through the PPAR $\gamma$ -independent manner. HPAEpiCs were pretreated with GW9662 or transfected with PPAR $\gamma$  siRNA, and then incubated with vehicle or rosiglitazone (30  $\mu$ M) for the indicated time intervals. Western blot was performed by using an anti-phospho-c-Src, anti-c-Src, anti-phospho-Pyk2, anti-Pyk2, anti-phospho-Akt or anti-Akt antibody. Data are expressed as mean  $\pm$  SEM, from five independent experiments ( $n = 5$ ).  $^{\#}P < 0.05$ , as compared with the cells exposed to rosiglitazone alone.

Original Paper

# Fisetin Protects Against Hepatic Steatosis Through Regulation of the Sirt1/AMPK and Fatty Acid $\beta$ -Oxidation Signaling Pathway in High-Fat Diet-Induced Obese Mice

Chian-Jiun Liou<sup>a,b</sup>   Ciao-Han Wei<sup>c</sup>   Ya-Ling Chen<sup>b,d</sup>   Ching-Yi Cheng<sup>c,e,f</sup>  
Chia-Ling Wang<sup>c</sup>   Wen-Chung Huang<sup>b,c</sup>

<sup>a</sup>Department of Nursing, Research Center for Chinese Herbal Medicine, Chang Gung University of Science and Technology, Taoyuan, <sup>b</sup>Division of Allergy, Asthma, and Rheumatology, Department of Pediatrics, Chang Gung Memorial Hospital, Linkou, <sup>c</sup>Graduate Institute of Health Industry Technology, Research Center for Food and Cosmetic Safety, Research Center for Chinese Herbal Medicine, College of Human Ecology, Chang Gung University of Science and Technology, Taoyuan, <sup>d</sup>Department of Nutrition and Health Sciences, Chang Gung University of Science and Technology, Taoyuan, <sup>e</sup>Department of Ophthalmology, Chang Gung Memorial Hospital, Linkou, <sup>f</sup>Department of Traditional Chinese Medicine, Chang Gung Memorial Hospital, Keelung, Taiwan

## Key Words

AMPK • CPT-1 • Fisetin • FL83B • Lipolysis • Nonalcoholic fatty liver disease

## Abstract

**Background/Aims:** Fisetin is a naturally abundant flavonoid isolated from various fruits and vegetables that was recently identified to have potential biological functions in improving allergic airway inflammation, as well as anti-oxidative and anti-tumor properties. Fisetin has also been demonstrated to have anti-obesity properties in mice. However, the effect of fisetin on nonalcoholic fatty liver disease (NAFLD) is still elusive. Thus, the present study evaluated whether fisetin improves hepatic steatosis in high-fat diet (HFD)-induced obese mice and regulates lipid metabolism of FL83B hepatocytes *in vitro*. **Methods:** NAFLD was induced by HFD in male C57BL/6 mice. The mice were then injected intraperitoneally with fisetin for 10 weeks. In another experiment, FL83B cells were challenged with oleic acid to induce lipid accumulation and treated with various concentrations of fisetin. **Results:** NAFLD mice treated with fisetin had decreased body weight and epididymal adipose tissue weight compared to NAFLD mice. Fisetin treatment also reduced liver lipid droplet and hepatocyte steatosis, alleviated serum free fatty acid, and leptin concentrations, significantly decreased fatty acid synthase, and significantly increased phosphorylation of AMPK $\alpha$  and the production of sirt-1 and carnitine palmitoyltransferase I in the liver tissue. *In vitro*, fisetin decreased lipid

C.-J. Liou and C.-H. Wei contributed equally to this work.

Wen-Chung Huang, PhD

Graduate Institute of Health Industry Technology, Chang Gung University of Science and Technology  
No. 261, Wenhua 1st Rd., Guishan Dist., Taoyuan City 33303 (Taiwan)  
Tel. 886-3-2118999, Fax 886-3-2118293, E-Mail [wchuang@mail.cgu.edu.tw](mailto:wchuang@mail.cgu.edu.tw)

accumulation and increased lipolysis and  $\beta$ -oxidation in hepatocytes. **Conclusion:** This study suggests that fisetin is a potential novel treatment for alleviating hepatic lipid metabolism and improving NAFLD in mice via activation of the sirt1/AMPK and  $\beta$ -oxidation pathway.

© 2018 The Author(s)  
Published by S. Karger AG, Basel

## Introduction

Nonalcoholic fatty liver disease (NAFLD) is a common liver disease typically characterized by excessive lipid accumulation and metabolic disorder in hepatocytes [1]. The initial symptoms of NAFLD generally implicate the progress of simple fatty liver, which gradually develops into increasingly severe forms of liver disease, including nonalcoholic steatohepatitis, liver fibrosis, cirrhosis, and hepatocellular carcinoma [2]. Obesity would increase the risk of chronic diseases, including type 2 diabetes, hypertension, stroke, and cancer [3]. In addition, excess triglycerides (TGs) stored in hepatocytes may cause hepatic steatosis and interfere with the metabolic function of the liver [4]. Therefore, obesity could cause hepatic steatosis, which an important risk factor for the development of NAFLD.

Sterol regulatory element binding protein 1c (SREBP-1c) is an essential transcription factor in the regulation of lipid synthesis and maintenance of cellular homeostasis [5]. Previous studies have found that peroxisome proliferator-activated receptor (PPAR) and

CCAAT/enhancer-binding protein (C/EBP) are also important transcription factors for controlled lipid biosynthesis and can switch on fatty acid synthase (FAS) gene expression to synthesize fatty acid chains [6]. Therefore, the activation of lipid transcription factors would accelerate liver lipid accumulation and result in fatty liver disease.

AMPK is a heterotrimeric enzyme that is composed by AMPK $\alpha$  (a catalytic subunit), AMPK $\beta$  (a scaffolding subunit), and AMPK $\gamma$  (a regulatory subunit) [7]. Recent studies have found that AMPK regulates energy balance [8]. When the liver, muscle, and adipose tissue accumulate excessive energy, these tissues activate the AMPK pathway to regulate lipid and glucose metabolism [9]. AMPK activity could induce ACC phosphorylation and decrease ACC activity for suppressed lipid biosynthesis [10, 11]. Thus, phosphorylation of AMPK can not only maintain energy balance, but also inhibit the formation of TGs to reduce lipid accumulation in the liver. In addition, sirt1 plays a role in regulating AMPK activity to enhance AMPK phosphorylation in adipocyte and hepatocytes [12]. Sirt1-deficient mice lack AMPK activity, but SREBP-1c expression is promoted in mice with induced obesity and hepatic steatosis compared to wild-type HFD-induced obese mice [13]. Animal studies have found that metformin is an antidiabetic drug that can activate AMPK and reduce hepatic steatosis by increasing fatty acid  $\beta$ -oxidation and reducing SREBP-1c expression [14, 15]. Therefore, sirt1/AMPK pathway activity potentially inhibits lipid accumulation in hepatocytes and improves hepatic steatosis.

Interestingly, accelerating lipid decomposition is an important strategy for improving NAFLD [6]. In the liver, excessive lipid biosynthesis is mainly a phenomenon of excessive energy accumulation. Exercise or calorie restriction can increase lipolysis to consume liver TGs and eliminate liver steatosis [16, 17]. Many studies have suggested that some vegetable and fruit extracts could increase TG metabolism in NAFLD therapy [18-20]. Omega-3 fatty acids (DHA and EPA), medium-chain fatty acids, *Lactobacillus plantarum*, and mulberry anthocyanins also reduce TG levels in the liver [21-23]. Furthermore, hepatocytes activate adipose triglyceride lipase (ATGL) and hormone-sensitive lipase (HSL) to decompose TGs and form glycerol and free fatty acids in the citric cycle for energy production [24]. However, free fatty acids will stimulate liver macrophages and cause inflammatory responses, and activated macrophages release inflammatory mediators to induce insulin resistance in hepatocytes [25]. Notably, excess TGs in the liver are broken down, and released free fatty acids must be decomposed to produce energy via fatty acid  $\beta$ -oxidation and reduce the damage to liver and adipose tissue.

Fisetin is a flavonoid isolated from various fruits and vegetables [26] that can suppress inflammatory effects, with strong anti-oxidant and anti-tumor effects [27, 28]. Previous studies have found that fisetin can enhance the levels of adiponectin in 3T3-L1 adipocytes by enhancing sirt1 expression, and inhibit mTORC1 signaling to block differentiation of 3T3-L1 preadipocytes [29, 30]. Fisetin can also regulate fatty acid synthase (FAS), ATP citrate lyase, and glucose 6-phosphatase gene expression and enhance glucose transporter type 4 gene expression in hepatocytes compared to HFD-fed mice [30], but how fisetin regulates lipid accumulation in the liver and improves NAFLD is not clear. In the present study, we evaluated whether fisetin regulates lipid metabolism in FL83B hepatocytes *in vitro*. We also investigated whether fisetin modulates adipogenesis and lipolysis in steatotic hepatocytes, and improves NAFLD in HFD-induced obese mice.

## Materials and Methods

### *Animals and administration of fisetin*

Four-week-old male C57BL/6 mice were procured from the National Laboratory Animal Center, Taipei, Taiwan. All experimental animals were approved and supervised by the Laboratory Animal Care Committee of Chang Gung University of Science and Technology (IACUC approval numbers 2016-002 and 2017-007). The mice were housed in an air conditioned room at a constant temperature of  $23 \pm 2^\circ\text{C}$ , and maintained on a normal chow diet with clean water ad libitum for 1 week before being randomly divided into three groups of 12 (Fig. 1A): normal mice maintained with normal chow diet (11.4% fat), HFD-fed mice maintained with HFD (60% fat), and F20 mice maintained with HFD and administered 20 mg/kg fisetin (purity  $\geq 98\%$ , St. Louis, MO, USA) dissolved in DMSO. The HFD and normal mice administered DMSO as control by intraperitoneal injection twice a week for last 10 weeks. F20 groups were maintained on HFD for 4 weeks and then treated with 20 mg/kg fisetin by intraperitoneal injection twice a week for last 10 weeks. Food intake was defined as weight of consumed food (g)  $\times$  calorie of diet per day, and the diet intake of mouse was monitored per day and body weight recorded weekly [31]. We also calculated the food efficiency ratio as defined by weight gain (g)/food intake (g)  $\times$  100 [32].

### *Biochemical analysis*

After sacrificing the mice, serum was collected and assayed by a biochemistry analyzer (DRI-CHEM NX500, Fuji, Tokyo, Japan). We investigated the levels of total cholesterol (TC), high-density lipoprotein (HDL), and total TGs according to the manufacturer's instructions. Free fatty acid was measured using the free fatty acid quantitation kit (Sigma) and the manufacturer's protocol. Serum treated with the assay reagent and the levels of free fatty acids were determined by the absorbance at 570 nm using a microplate reader (Multiskan FC, Thermo, Waltham, MA, USA).

### *Histological analysis*

Liver and adipose tissue was fixed in 10% formalin and embedded with paraffin before staining with hematoxylin and eosin (HE) solution as previously described [33, 34]. Periodic acid-Schiff (PAS) stain using the periodic acid-Schiff staining system (Sigma) indicated glycogen accumulation in liver tissue as described previously [35]. All biopsy specimens were assayed using a light microscope (Olympus, Tokyo, Japan).

### *Immunohistochemistry (IHC)*

The liver was fixed and embedded with paraffin and the tissue sliced into 6- $\mu\text{m}$  sections. Each slide was incubated with CPT-1 or sirt1 antibody (1:50) overnight, washed, and incubated with HRP anti-rabbit secondary antibody. Finally, the slide was treated with DAB substrate and CPT-1 or sirt1 expression observed with a light microscope.



## Western blot analysis

Protein bands were separated on 8–10% SDS–PAGE gels and transferred to polyvinylidene difluoride (PVDF) membrane for probing with primary antibodies overnight. The membrane was washed and incubated with secondary antibodies and specific protein signals detected with Luminol/Enhancer solution (Millipore, Billerica, MA, USA) by the BioSpectrum 600 system (UVP, Upland, CA, USA). Primary antibodies included acetyl CoA carboxylase-1 (ACC-1), phosphorylated-ACC-1 (pACC-1), ATGL, HSL, phosphorylated HSL (pHSL), C/EBP $\alpha$ , C/EBP $\beta$ , PPAR- $\alpha$  and PPAR- $\gamma$  (Abcam, Cambridge, MA, USA), phosphorylated AMPK $\alpha$  (pAMPK $\alpha$ ), AMPK $\alpha$ , FAS, carnitine palmitoyltransferase 1 (CPT-1), CPT2, sirt1, SREBP-1c (Cell Signaling Technology, MA, USA), and  $\beta$ -actin (Sigma).

## Cell culture and induced fatty liver cells

Normal mouse liver cell line FL83B was purchased from the Bioresource Collection and Research Center (BCRC, Taiwan). Cells cultured in F12 medium (Invitrogen-Gibco™, Paisley, Scotland) contained 10% FBS at 37°C in a 5% CO<sub>2</sub> atmosphere. FL83B cells were incubated with 0.5 mM oleic acid to induce lipid accumulation in hepatocytes for 48 h, then treated with fisetin (0–100  $\mu$ M) for 24 h to analyze the experimental results.

## Cell viability assay

Fisetin was dissolved in DMSO and  $\leq 0.1\%$  DMSO was used in all cell experiments. FL83B cells were incubated with fisetin for 24 h and treated with MTT solution (Sigma) for 4 h. The culture plate was then treated with isopropanol and absorbance measured at 570 nm to evaluate cell viability using a spectrophotometer (Multiskan FC).

## Oil red O staining

FL83B cells were seeded in 6-well plate and incubated with 0.5 mM oleic acid for 48 h before being treated with fisetin (0–100  $\mu$ M) for 24 h. FL83B cells were fixed with formalin and oil droplets stained using oil red O solution (Sigma) as described previously [36]. The oil droplets in hepatocytes were observed using an inverted microscope (Olympus).

## Hepatic lipid accumulation and lipoperoxidation

FL83B cells were seeded in culture plates and incubated with 0.5 mM oleic acid for 48 h before being treated with fisetin (0–100  $\mu$ M) for 24 h. FL83B cells were fixed with formalin, and stained with BODIPY 581/591 C11 and BODIPY 493/503 (Invitrogen, Carlsbad, CA, USA) to investigate lipoperoxidation and lipid accumulation, respectively. Cell nuclei were stained with DAPI and all results observed with a fluorescence microscope (Olympus).

## Hepatic fatty acid uptake

FL83B cells were incubated with 0.5 mM oleic acid for 48 h and then treated with fisetin for 24 h before staining with BODIPY FL C12 fluorescent probe to evaluate fatty acid uptake by fluorescence microscopy (Olympus).

## Statistical analysis

Statistical analyses included one-way analysis of variance (ANOVA) and a Dunnett post hoc test. Results are expressed as mean  $\pm$  SEM. *P*-values < 0.05 were considered significant.

## Results

### Fisetin reduced HFD-induced obesity in mice

Visual observation revealed that HFD mice had greater body weight than normal mice. Interestingly, F20 mice had significantly reduced body weight compared to HFD mice in the last weeks of the experiment (Fig. 1B). We also found that F20 mice did not have altered food intake, but inhibited food efficiency ratio compared to HFD mice (Fig. 1C–D). The last week of the experiment, F20 mice had significantly reduced body weight compared to HFD

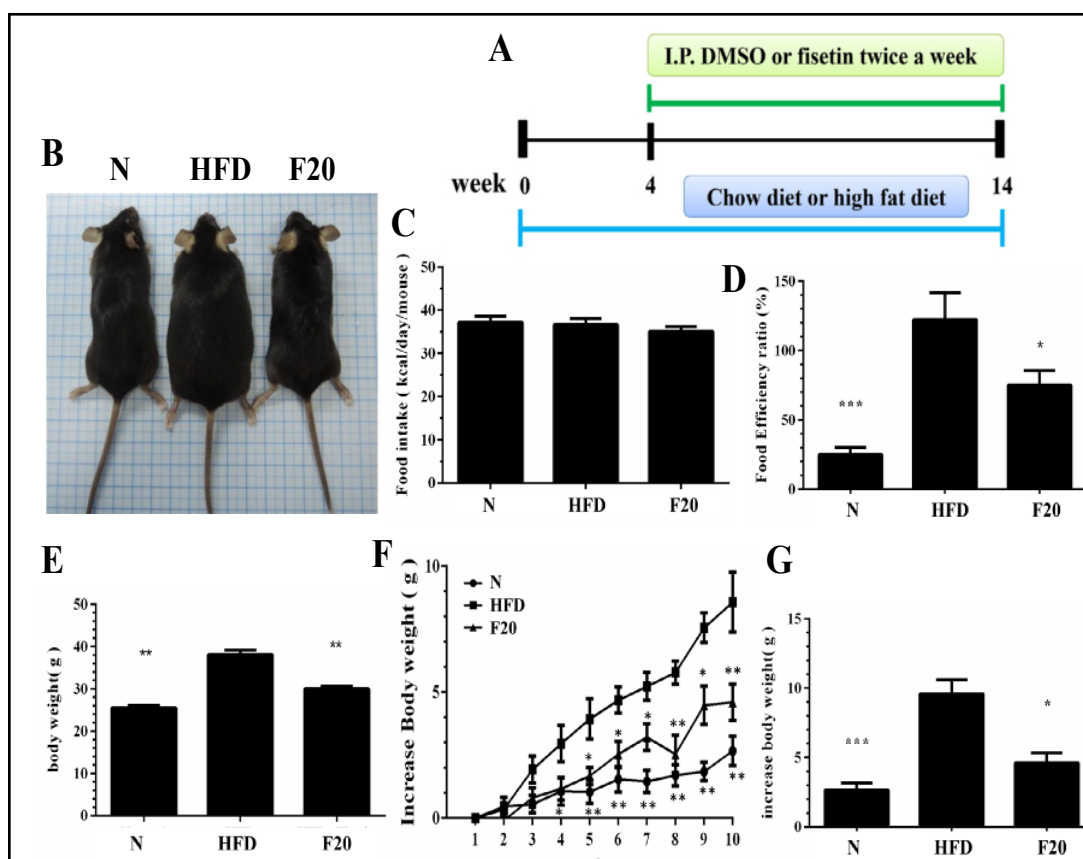


**Fig. 1.** Fisetin reduced body weight in HFD-induced obese mice. (A) Male mice were fed a HFD (containing 60% fat) for 14 weeks, and administered DMSO, 20 mg/kg fisetin (F20) by intraperitoneal injection (I.P.) twice a week from Week 4 to Week 14. (B) The appearance of the animal, (C) food intake, (D) food efficiency ratio, and (E) body weight. (F) Weight gain was measured when fisetin was administered by intraperitoneal injection for 10 weeks. (G) Weight gain was measured in the last week. Data are presented as mean  $\pm$  SEM; n = 12. \*P<0.05, \*\*P<0.01 compared to mice with HFD-induced obesity.

mice ( $34.5 \pm 1.41$  g vs.  $39.4 \pm 1.52$  g; Fig. 1E). As fisetin was given for 10 weeks, body weight in F20 mice was significantly decreased compared to HFD mice (Fig. 1F). Weight gain was measured in the last week, and F20 mice were significantly decreased weight gain compared to HFD mice (F20:  $4.62 \pm 1.25$  g vs. HFD:  $9.55 \pm 1.38$  g; Fig. 1G).

#### *Fisetin attenuated liver steatosis in obese mice*

Grossly, the livers of the normal group were dark brown/red, and the livers of the HFD group were yellowish and lacked luster. The F20 group had recovered the dark brown/red color of the liver (Fig. 2A). Interestingly, fisetin did not eliminate the liver weight and relative weight of liver/body weight compared to obese mice (Fig. 2B-C). However, histologically, many lipid droplets and fat vacuoles were observed in HFD mice, and fisetin significantly reduced the number of lipid droplets and fat vacuoles in F20 mice (Fig. 2D-E). Glycogen accumulation in hepatocytes was evaluated by PAS staining, which showed that the HFD group had significantly reduced glycogen accumulation. Fisetin elevated glycogen accumulation in F20 mice compared to HFD mice (Fig. 2F).

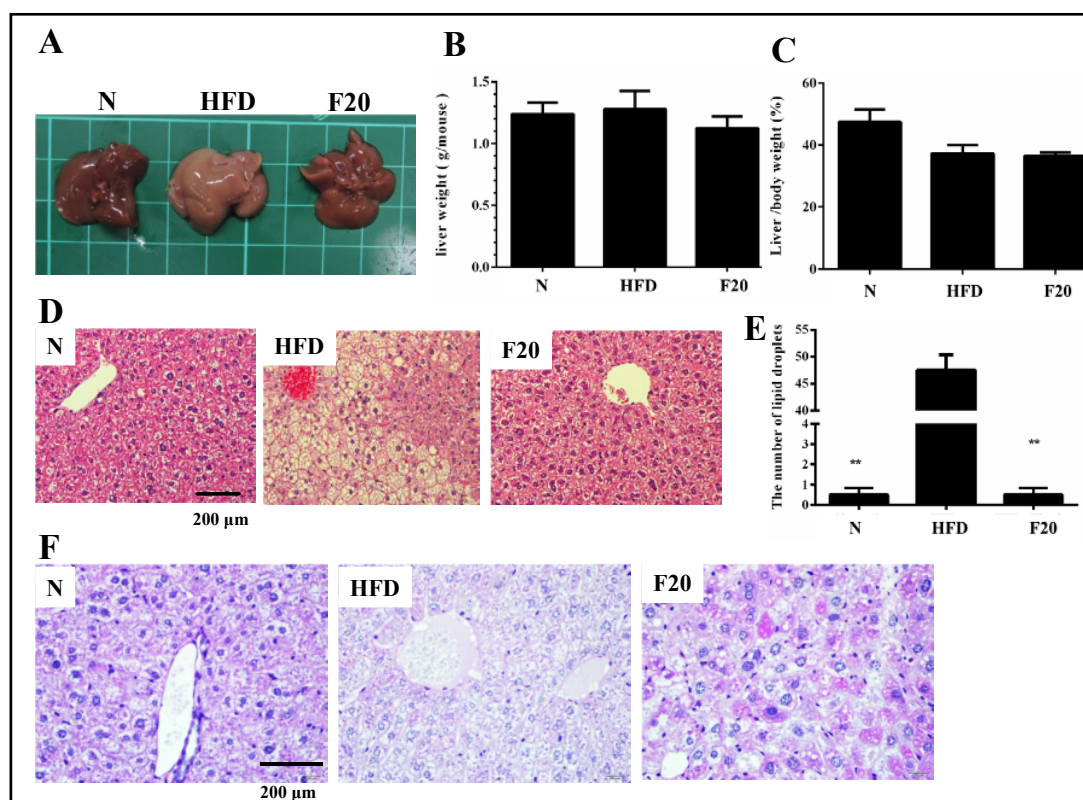
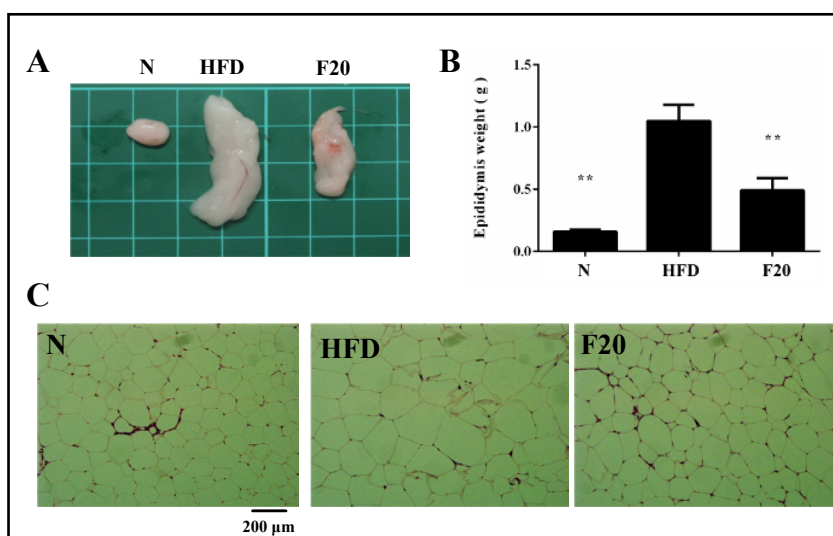


**Fig. 2.** Fisetin ameliorated hepatic steatosis in HFD-induced obese mice. (A) The appearance of the liver, (B) liver weight, and (C) relative weight of the liver. (D) HE staining of liver tissues (200× magnification). (E) Calculated number of lipid droplets in liver tissue (400× magnification). Data are presented as mean ± SEM; n = 12. \*\*P<0.01 compared to mice with HFD-induced obesity. (F) PAS stain demonstrating the glycogen distribution in the liver.

**Fig. 3.** Fisetin reduced the epididymal tissue weight in HFD-induced obese mice. (A) Appearance and (B) weight of epididymal adipose tissue. (C) HE staining of epididymal adipose tissue (200× magnification). Data are presented as mean ± SEM; n = 12. \*\*P<0.01 compared to mice with HFD-induced obesity.



#### *Fisetin attenuated the weight of adipose tissue in obese mice*

Fisetin significantly reduced the epididymal adipose tissue weight compared to HFD mice (Fig. 3A-B). Histological staining and analysis demonstrated that fisetin reduced adipocyte size compared to HFD mice (Fig. 3C).

*Effects of fisetin on serum lipid metabolism*

Serum analysis showed that fisetin did not significantly decrease TC, TG, and HDL levels in HFD mice (Fig. 4A-C). However, fisetin significantly decreased free fatty acid levels compared to the HFD group (Fig. 4D). Fisetin also significantly suppressed serum leptin levels compared to HFD mice (Fig. 4E).

*Fisetin regulated adipogenesis in liver tissue*

Western blot detecting specific liver proteins showed that fisetin significantly suppressed transcription factor expression associated with adipogenesis, including SREBP-1c, C/EBP $\alpha$ , C/EBP $\beta$ , and PPAR- $\gamma$ , compared to the HFD group. However, fisetin increased PPAR $\alpha$  expression and suppressed FAS expression compared to the HFD group (Fig. 5A).

*Fisetin regulated the AMPK/sirt1 pathway and lipolysis in liver tissue*

In liver tissue, fisetin significantly enhanced sirt1, pAMPK $\alpha$ , and pACC-1 expression compared to the HFD group (Fig. 5B). In lipolysis, fisetin could also promote ATGL and the phosphorylation of HSL expression compared to the HFD group (Fig. 5C). Fisetin increased CPT-1, but not CPT2, expression in the fatty acid  $\beta$ -oxidation pathway compared to the HFD group (Fig. 5C). Using IHC, we examined stained liver tissue slides to observe the distribution

**Fig. 4.** Effects of fisetin on serum biochemical analysis. (A) HDL, (B) TC, (C) TG, (D) free fatty acids, (E) leptin. Data are presented as mean  $\pm$  SEM; n = 12. \*P<0.05, \*\*P<0.01 compared to mice with HFD-induced obesity.

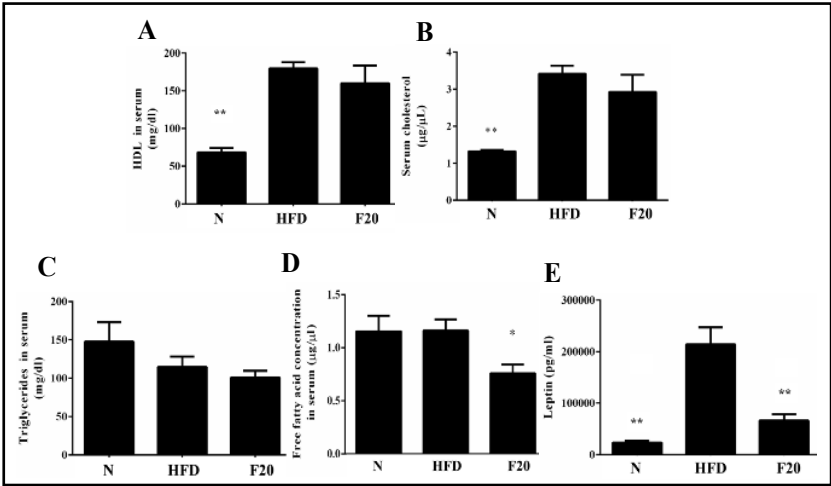


**Fig. 5.** Effects of fisetin on lipid metabolism in mouse liver tissue. (A) Transcription factors associated with adipogenesis and lipogenesis, (B) the sirt-1/AMPK pathway, and (C) lipolysis and  $\beta$ -oxidation were detected by Western blot. Three independent experiments were analyzed using  $\beta$ -actin as an internal control.

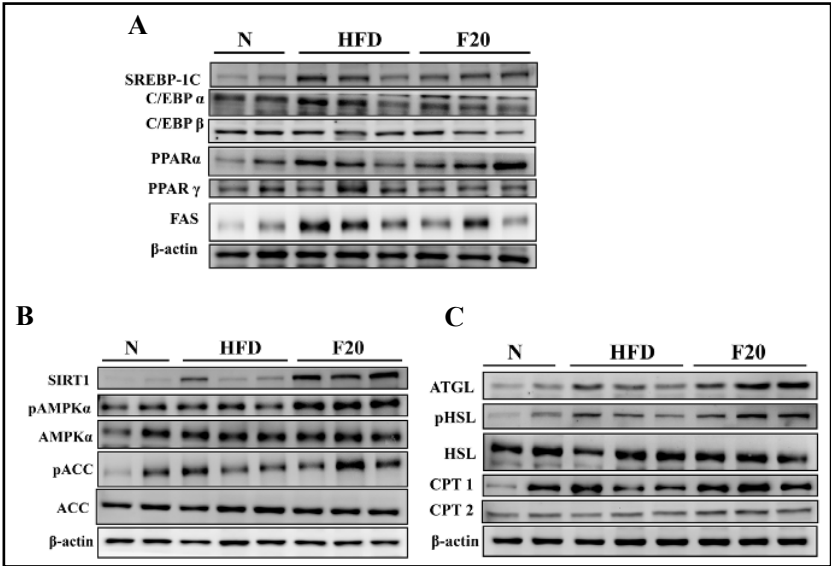




**Fig. 6.** Fisetin modulated sirt-1 and CPT-1 expression in the liver. (A) sirt1 and (B) CPT-1 expression was analyzed by immunohistochemistry and labeled as a brown color drop. Three independent experiments were analyzed.

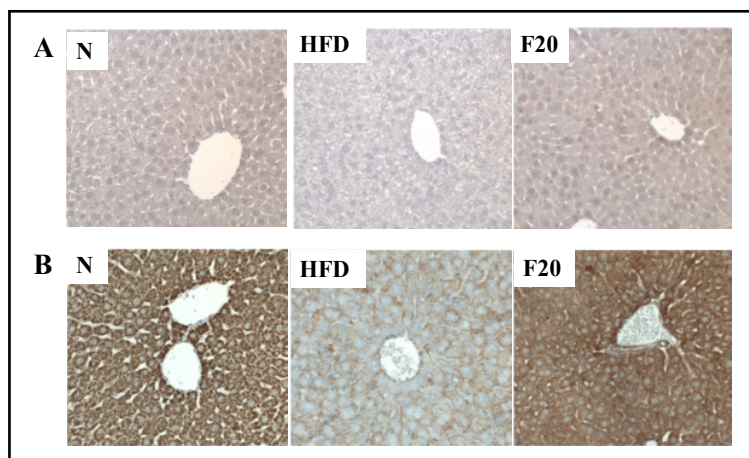
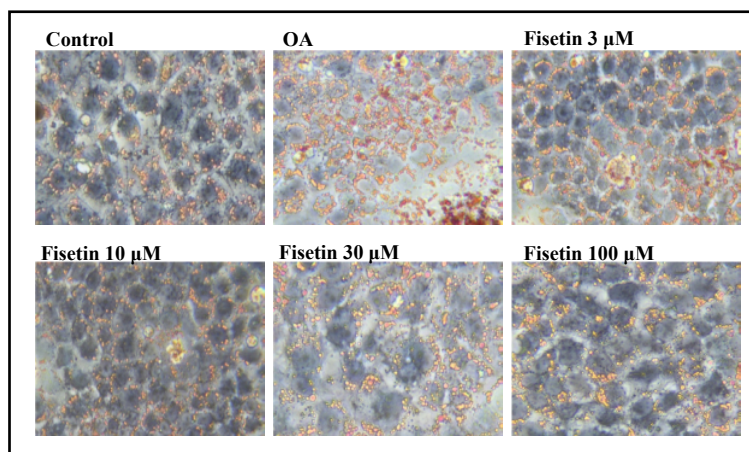


**Fig. 7.** Fisetin reduced lipid accumulation in FL83B cells. FL83B cells were treated with 0.5 mM oleic acid (OA) at 37°C for 48 h to induce lipid accumulation in hepatocytes, followed by fisetin (3–100  $\mu$ M) for 24 h. Oil Red O stain shows lipid accumulation. Three independent experiments were analyzed.



of sirt1 and CPT-1 protein, finding a large amount of sirt1 and CPT-1 in the normal group, but sirt1 and CPT-1 was significantly decreased in the liver tissue of HFD mice. Notably, fisetin significantly recovered sirt1 and CPT-1 expression in the liver tissue compared to the HFD group (Fig. 6).

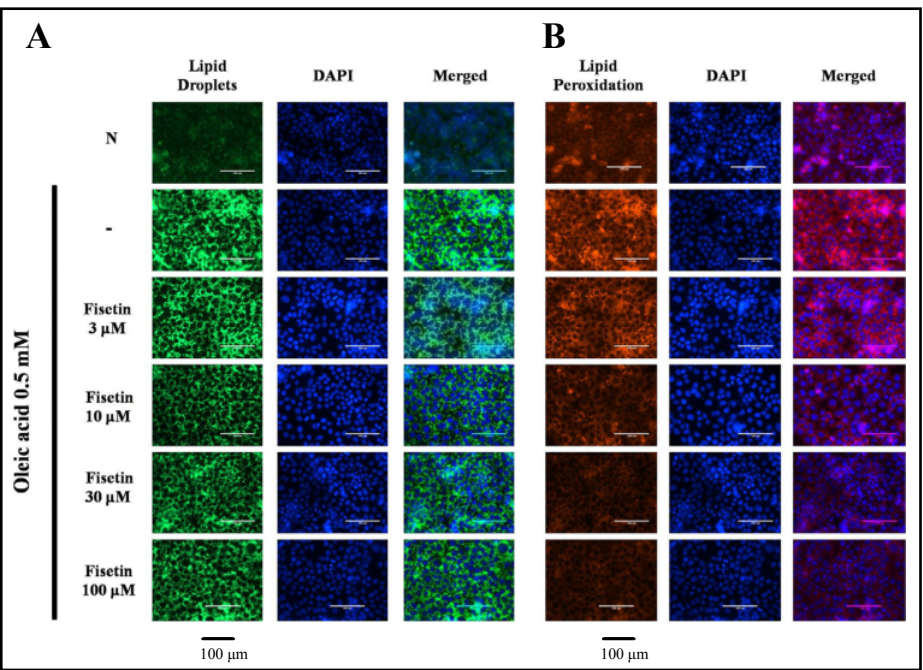
#### Cell viability of fisetin in FL83B cells

We investigated whether fisetin can modulate lipid metabolism in hepatocytes *in vitro*. First, we used the MTT assay to investigate the cytotoxicity of fisetin in FL83B hepatocytes. We found no cell cytotoxicity at fisetin concentrations  $\leq 100$   $\mu$ M (data not shown), and 3–100  $\mu$ M fisetin was assayed in all cell experiments.

#### Fisetin regulated lipid accumulation and lipoperoxidation in FL83B cells

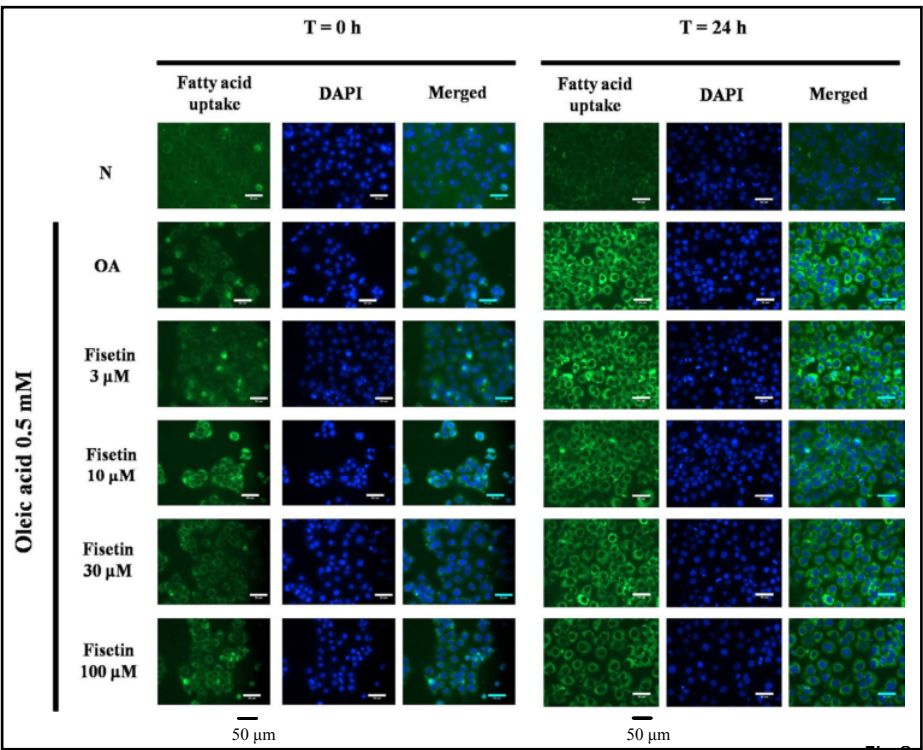
Fisetin alleviated lipid droplets induced by oleic acid treatment (Fig. 7). The fluorescent dye BODIPY 493/503 confirmed that fisetin treatment decreased lipid accumulation (Fig. 8A). Furthermore, BODIPY 581/591 C11 detected hepatic lipoperoxidation, and the immunofluorescent images demonstrated that fisetin significantly decreased lipoperoxidation compared to oleic acid-induced hepatocytes (Fig. 8B). Next, fatty acid uptake was detected using the BODIPY FL C12 fluorescent probe at 0 and 24 h. Oleic acid promoted fatty acid uptake in hepatocytes after 24 h. Fisetin clearly suppressed fatty acid uptake compared to the oleic acid group (Fig. 9).

**Fig. 8.** Fisetin reduced lipid accumulation in FL83B cells. FL83B cells were treated with 0.5 mM oleic acid (OA) at 37°C for 48 h to induce lipid accumulation in hepatocytes, followed by fisetin (3–100  $\mu$ M) for 24 h. The fluorescent dyes BODIPY 493/503 (green) and BODIPY



581/591 C11 (red) were used to detect hepatic lipid droplets and lipoperoxidation, respectively, under a fluorescent microscope. Three independent experiments were analyzed. Nuclei were stained with DAPI (blue).

**Fig. 9.** Fisetin reduced fatty acid uptake into FL83B cells. FL83B cells were treated with 0.5 mM oleic acid (OA) and fisetin (3–30  $\mu$ M) and observed by fluorescence microscopy. BODIPY FL C12 (green) was used to detect fatty acid uptake by hepatocytes at 0 and 24 h. Three independent experiments were analyzed.



Nuclei were stained with DAPI (blue).

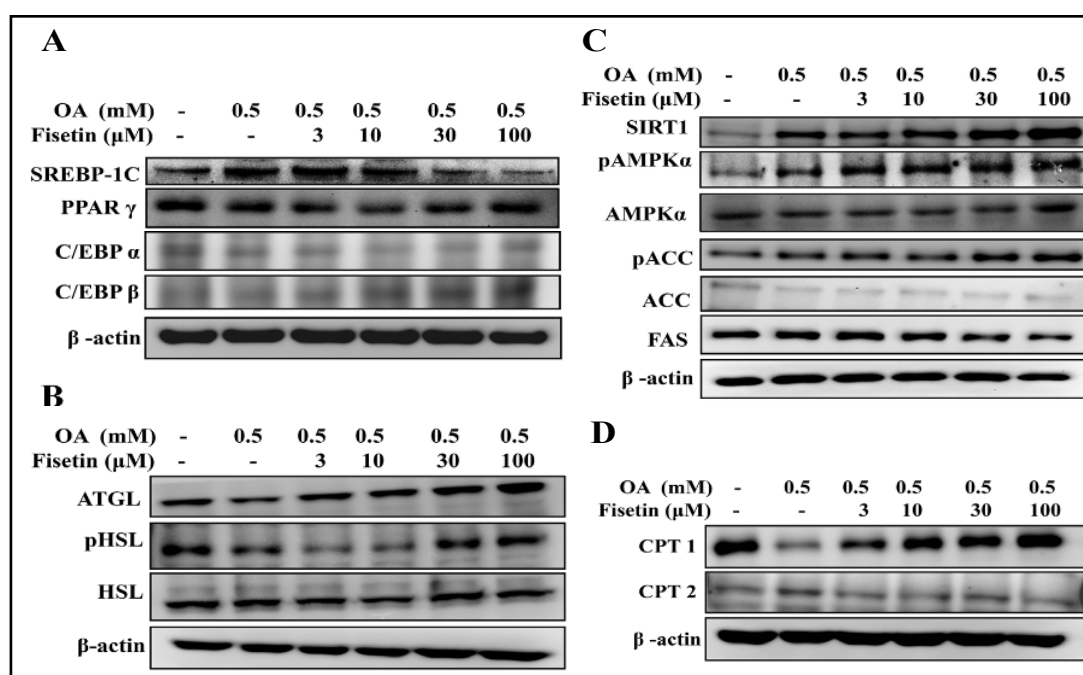


**Fig. 10.** Effects of fisetin on lipid metabolism in FL83B cells. FL83B cells were treated with 0.5 mM oleic acid (OA) for 48 h to induce lipid accumulation in hepatocytes, followed by fisetin (3–100  $\mu$ M) 24 h. (A) Transcription factors associated with adipogenesis and lipogenesis proteins, (B) lipolysis, (C) the AMPK/Sirt-1 pathway, and (D)  $\beta$ -oxidation were detected by Western blot. Three independent experiments were analyzed using  $\beta$ -actin as an internal control.

#### *Effect of fisetin on lipid metabolism in hepatocytes*

Western blot showed that fisetin reduced SREBP-1c, PPAR- $\gamma$ , and C/EBP $\alpha$  expression, but not C/EBP $\beta$  expression, compared to oleic acid (Fig. 10A). Fisetin also increased ATGL and pHSL expression in a concentration-dependent manner compared to oleic acid (Fig. 10B). Furthermore, fisetin significantly promoted sirt1, phosphorylation of AMPK, and phosphorylation of ACC, and decreased FAS production compared to oleic acid (Fig. 10C). Finally, fisetin increased CPT-1, but not CPT2, expression (Fig. 10D).

## Discussion

Obesity is an important factor in many serious chronic diseases, and studies have shown that obesity is a high risk group for hypertension, coronary atherosclerosis, type 2 diabetes, and cancer [1, 37]. Being overweight and obesity do not only increase adipocyte size and hyperplasia, but in these states the liver tissue accumulates excessive lipid droplets, causing hepatic steatosis, the early stage of NAFLD [3, 37]. Therefore, in the hepatic steatosis stage, treating and maintaining liver health and function, or attenuating the deterioration of liver steatosis, would create an opportunity to prevent and attenuate the development of NAFLD. In liver tissue, excessive lipid accumulation would interfere with the normal physiological function of hepatocytes, causing lipid and carbohydrate metabolism abnormalities, liver cell inflammation, peroxidation, and insulin resistance [1, 3]. These symptoms may not only cause diabetes, but can also promote chronic liver fibrosis and liver cancer [2]. A recent study pointed out that new therapy targets of hepatic steatosis mainly block lipid generation and accumulation in the liver, leading to the decomposition of fat oil droplets, enhancing the  $\beta$ -oxidation metabolism of fatty acids, and maintaining mitochondrial function [14, 38, 39].

In recent years, some plant compounds have been found to improve NAFLD [19, 40–42]. In obese mice, resveratrol can improve body weight and reduce hepatic steatosis by



enhancing sirt1 and AMPK activity [38]. Luteolin could attenuate NAFLD by blocking the expression of liver X receptor and SERBP-1c [43]. Quercetin has also been confirmed to alleviate oxidized LDL levels in the liver and decrease hepatic steatosis in HFD-induced obese mice [44]. In this current study, fisetin effectively alleviated body weight and epididymal adipose tissue weight. However, fisetin did not decrease the liver weight. Interestingly, fisetin could suppress lipid accumulation and fat vacuoles in the livers of HFD-fed mice. Fisetin also inhibited lipogenesis, regulated the sirt1/AMPK pathways, and enhanced  $\beta$ -oxidation to reduce the development of hepatic steatosis in HFD-induced obese mice. Therefore, fisetin has the potential to ameliorate obesity-induced NAFLD.

AMPK is an important enzyme in sensing and regulating cellular and whole-body energy balance, and sirt-1 has a regulatory effect on lipid metabolism by activating AMPK expression for the maintenance and regulation of energy metabolism [45]. Phosphorylation of Thr172 in AMPK $\alpha$  is required for kinase activity and enhanced more 100-fold activation [46]. AMPK $\alpha$  activation can inhibit lipid biosynthesis, accelerating the decomposition of lipid to reducing liver fat accumulation [10]. Sirt1 is an NAD-dependent deacetylase and has been reported to have many beneficial effects for controlled glucose homeostasis, lipid metabolism, and insulin resistance in the liver tissue of obese mice [12]. In our current experiment, we found that HFD obese mice treated with fisetin express increased level of sirt1 and pAMPK $\alpha$  in liver tissue, and FL83B hepatocyte experiments demonstrated that fisetin significantly promotes sirt1 and pAMPK $\alpha$  expression *in vitro*. Resveratrol, a sirt1 agonist, could significantly increase sirt1 and pAMPK expression in the liver tissue of NAFLD mice [38]. Resveratrol could reduce total cholesterol and triacylglycerol in serum and reduce liver adipogenesis through increased phosphorylation of ACC to regulate fatty acid synthesis [47]. Our results also demonstrate that fisetin could significantly increase ACC phosphorylation in HFD-induced obese mice and oleic acid-induced hepatocytes *in vitro*. Activated ACC could catalyze acetyl CoA to produce malonyl-CoA for elongated fatty acid chains [24]. Recent research found that phosphorylation of AMPK could stimulate phosphorylation of its substrate, which suppresses ACC phosphorylation [10]. Interestingly, dephosphorylation of ACC is activated and phosphorylation of ACC switched off [24]. Thus, we thought that fisetin could effectively increase sirt1 and pAMPK $\alpha$  expression to block the synthesis of fatty acid chains.

Hepatocytes took up excessive free fatty acids and switched transcription factors on for lipogenesis, causing lipid accumulation, and these free fatty acid would reduce AMPK activity and disturb the energy balance [6, 9]. Previous studies reported that AMPK phosphorylation can suppress the expression of lipogenesis-related transcription factors, including SREBP-1c, PPAR, and C/EBP [48]. In this study, the HFD mice had increased expression of SREBP-1c, C/EBP $\alpha$ , and PPAR- $\gamma$ , and fisetin significantly suppressed SREBP-1c, C/EBP $\alpha$  and PPAR- $\gamma$  expression in liver tissue. Similarly, fatty liver cells treated with fisetin exhibited attenuated SREBP-1c, PPAR- $\gamma$ , and C/EBP $\alpha$  expression *in vitro*. Previous studies confirmed that C/EBP $\alpha$  and C/EBP $\beta$  are able to assist adipocyte differentiation and increase lipid accumulation in adipocytes and hepatocytes [49]. However, our results demonstrated that fisetin does not significantly regulate C/EBP $\beta$  expression in cellular and animal models. The results confirm that fisetin has the ability to block lipid synthesis in hepatocytes, mainly by blocking the transcription factors SREBP-1c, C/EBP $\alpha$ , and PPAR- $\gamma$ .

ACC could switch on the synthesis of fatty acid chains and stimulate FAS expression [24]. Therefore, activated AMPK could reduce ACC activity to block FAS production for lipid synthesis. SREBP-1c could bind to the FAS gene promoter to give assist fatty acid chain synthesis in hepatocytes [49]. Obviously, HFD-induced obese mice, liver tissue could significantly FAS expression, and fisetin could reduce FAS production compared to obese mice. We found that fisetin can reduce FAS expression in oleic acid-induced fatty liver cells. Cell and animal experiments confirmed that fisetin has the ability to block FAS expression to reduce lipid synthesis in liver tissue, improving hepatic steatosis.

Another strategy for improving hepatic steatosis is to accelerate lipid metabolism in hepatocytes [50]. Many studies have suggested that a good lifestyle and regular exercise promote liver lipid metabolism and restore normal liver function [39, 51]. In addition,



appropriate diet could regulate the liver lipid metabolism and attenuate the development of NAFLD. Previous studies found that quercetin not only inhibits the differentiation of adipocytes and lipid synthesis, but also enhances the decomposition of lipids in obese mice [44]. Quercetin has also been shown to promote lipolysis in the livers of NAFLD mice.  $\alpha$ -Linolenic acid-rich flaxseed oil also increases lipolysis through enhanced ATGL expression, preventing alcoholic hepatic steatosis in mice [16]. Ginsenoside Rb2 also suppresses lipid accumulation in the liver by upregulating ATGL and phosphorylation of HSL in obese mice [52]. In the current study, fisetin markedly increased ATGL and pHSL production in the livers of obese mice and fatty hepatocytes *in vitro*, indicating a direct role for ATGL and HSL in lipolysis in the mouse liver. ATGL can hydrolyze TGs to form diglycerides and release a free fatty acid, and phosphorylation of HSL hydrolyzes diglycerides to form monoglycerides and releases a free fatty acid [53]. Consequently, fisetin is effective at reducing lipid accumulation, improving hepatic steatosis in obese mice.

Excess TGs, which are broken down into excess free fatty acids and released into the blood to interfere with metabolism, stimulate inflammatory responses in the liver and vasculature, deteriorating into insulin resistance, metabolic syndrome, and cardiovascular disease [54, 55]. Therefore, these free fatty acids need to be immediately converted into energy via  $\beta$ -oxidation or the formation of cholic acid through fecal exclusion to reduce the inflammatory response [56, 57]. In  $\beta$ -oxidation, CPT-1 functions to transfer the acyl group of a long-chain fatty acyl-CoA to form acyl carnitines [24]. Studies have shown that AMPK and sirt1 activation can enhance CPT-1 expression, promoting  $\beta$ -oxidation [58]. Resveratrol could increase AMPK activity to inhibit ACC activity, reducing fatty acid synthesis; resveratrol promotes lipolysis and increases  $\beta$ -oxidation, decreasing lipid accumulation in hepatocytes [59]. Celastrol also increases sirt1/AMPK expression, promoting  $\beta$ -oxidation for lipolysis and decreasing inflammatory and oxidative damage in the livers of NAFLD mice [13]. We used IHC to confirm CPT-1 expression in the liver and found that fisetin can significantly recover CPT-1 expression. Therefore, we thought that fisetin could accelerate the decomposition of fatty acids and reduce inflammatory damage. In addition, the decomposition of fatty acids will result in liver cell oxidative damage [25, 37]. Using BODIPY 581/591 C11 fluorescent dye, we found that fisetin ameliorates lipid peroxidation in oleic acid-induced fatty liver cells. Thus, fisetin could accelerate the decomposition of fatty acids and reduce lipid peroxidation causing cell damage.

We found that the caloric intake of both F20 and HFD mice did not differ from the normal mice. However, the F20 and HFD mice had greater food efficiency than the normal mice and the HFD contained more fat energy, which could significantly increase body weight and lead to the accumulation of excess oil droplets, interfering with carbohydrate metabolism for glycogen synthesis. Interestingly, fisetin could significantly decrease the epididymal adipose tissue and body weight. PAS stain demonstrated that fisetin could recover glycogen accumulation in hepatocytes compared to HFD-induced obese mice and has the potential to regulate lipid accumulation and glycogen synthesis to maintain liver metabolic function.

Adipose tissue secretes leptin, which binds to the leptin receptor of hypothalamic neurons to suppress appetite and reduce body weight [60]. Studies have shown that blood levels of leptin are higher in obesity, and reducing leptin levels would improve insulin resistance and metabolic syndrome [61]. Fisetin significantly reduced serum leptin levels, but appetite was not affected. Therefore, whether fisetin regulates insulin sensitivity needs to be studied further.

Our experimental results confirmed that fisetin can inhibit body weight and epididymal adipose tissue weight. Fisetin also significantly suppresses lipid accumulation in the liver tissue of obese mice through activation of the sirt1/AMPK pathway and enhances lipolysis and  $\beta$ -oxidation to ameliorate hepatic steatosis. We conclude that fisetin is an excellent anti-obesity flavonoid for blocking NAFLD development.

## Acknowledgements

This study was supported in part by grants from the Chang Gung Memorial Hospital (CMRPF1G0231, CMRPF1F0083, and CMRPF1C0201) and from the Ministry of Science and Technology in Taiwan (106-2320-B-255-008-MY3 and 106-2320-B-255-007-MY3).

Designed the experiments: WCH and CJL; Performed the experiments: CHW, YLC, CLW, and CYC; Analysis and interpretation of data: WCH, CHW, and YLC; Drafting the manuscript: WCH and CJL.

## Disclosure Statement

The authors have no conflicts of interest to declare.

## References

- 1 Reccia I, Kumar J, Akladios C, Virdis F, Pai M, Habib N, Spalding D: Non-alcoholic fatty liver disease: A sign of systemic disease. *Metabolism* 2017;72:94-108.
- 2 Kitade H, Chen G, Ni Y, Ota T: Nonalcoholic fatty liver disease and insulin resistance: new insights and potential new treatments. *Nutrients* 2017;9:E387.
- 3 Hazlehurst JM, Woods C, Marjot T, Cobbold JF, Tomlinson JW: Non-alcoholic fatty liver disease and diabetes. *Metabolism* 2016;65:1096-1108.
- 4 He XX, Wu XL, Chen RP, Chen C, Liu XG, Wu BJ, Huang ZM: Effectiveness of omega-3 polyunsaturated fatty acids in non-alcoholic fatty liver disease: a meta-analysis of randomized controlled trials. *PLoS One* 2016;11:e0162368.
- 5 Tian J, Goldstein JL, Brown MS: Insulin induction of SREBP-1c in rodent liver requires LXRA/C/EBPbeta complex. *Proc Natl Acad Sci U S A* 2016;113:8182-8187.
- 6 Wang Y, Viscarra J, Kim SJ, Sul HS: Transcriptional regulation of hepatic lipogenesis. *Nat Rev Mol Cell Biol* 2015;16:678-689.
- 7 Carling D: The AMP-activated protein kinase cascade--a unifying system for energy control. *Trends Biochem Sci* 2004;29:18-24.
- 8 Choi YJ, Lee KY, Jung SH, Kim HS, Shim G, Kim MG, Oh YK, Oh SH, Jun DW, Lee BH: Activation of AMPK by berberine induces hepatic lipid accumulation by upregulation of fatty acid translocase CD36 in mice. *Toxicol Appl Pharmacol* 2017;316:74-82.
- 9 Lage R, Dieguez C, Vidal-Puig A, Lopez M: AMPK: a metabolic gauge regulating whole-body energy homeostasis. *Trends Mol Med* 2008;14:539-549.
- 10 Lim CT, Kola B, Korbonits M: AMPK as a mediator of hormonal signalling. *J Mol Endocrinol* 2010;44:87-97.
- 11 Peng IC, Chen Z, Sun W, Li YS, Marin TL, Hsu PH, Su MI, Cui X, Pan S, Lytle CY, Johnson DA, Blaaser F, Chatila T, Shyy JY: Glucagon regulates ACC activity in adipocytes through the CAMKKbeta/AMPK pathway. *Am J Physiol Endocrinol Metab* 2012;302:E1560-1568.
- 12 Chen H, Liu X, Chen H, Cao J, Zhang L, Hu X, Wang J: Role of SIRT1 and AMPK in mesenchymal stem cells differentiation. *Ageing Res Rev* 2014;13:55-64.
- 13 Zhang Y, Geng C, Liu X, Li M, Gao M, Fang F, Chang Y: Celastrol ameliorates liver metabolic damage caused by a high-fat diet through Sirt1. *Mol Metab* 2017;6:138-147.
- 14 Li M, Sharma A, Yin C, Tan X, Xiao Y: Metformin ameliorates hepatic steatosis and improves the induction of autophagy in HFD induced obese mice. *Mol Med Rep* 2017;16:680-686.
- 15 Yang S, Lv Q, Luo T, Liu L, Gao R, Chen S, Ye P, Cheng Q, Li Q: Metformin inhibits expression and secretion of PEDF in adipocyte and hepatocyte via promoting AMPK phosphorylation. *Mediators Inflamm* 2013;2013:429207.
- 16 Miotto PM, Horbatuk M, Proudfoot R, Matravadia S, Bakovic M, Chabowski A, Holloway GP: alpha-Linolenic acid supplementation and exercise training reveal independent and additive responses on hepatic lipid accumulation in obese rats. *Am J Physiol Endocrinol Metab* 2017;312:E461-E470.

- 17 Rusli F, Boekschoten MV, Zubia AA, Lute C, Muller M, Steegenga WT: A weekly alternating diet between caloric restriction and medium fat protects the liver from fatty liver development in middle-aged C57BL/6J mice. *Mol Nutr Food Res* 2015;59:533-543.
- 18 Sabater AG, Ribot J, Priego T, Vazquez I, Frank S, Palou A, Buchwald-Werner S: Consumption of a mango fruit powder protects mice from high-fat induced insulin resistance and hepatic fat accumulation. *Cell Physiol Biochem* 2017;42:564-578.
- 19 Huang CZ, Tung YT, Hsia SM, Wu CH, Yen GC: The hepatoprotective effect of *Phyllanthus emblica* L. fruit on high fat diet-induced non-alcoholic fatty liver disease (NAFLD) in SD rats. *Food Funct* 2017;8:842-850.
- 20 Chen YJ, Wallig MA, Jeffery EH: Dietary broccoli lessens development of fatty liver and liver cancer in mice given diethylnitrosamine and fed a Western or control diet. *J Nutr* 2016;146:542-550.
- 21 Gupta V, Mah XJ, Garcia MC, Antonypillai C, van der Poorten D: Oily fish, coffee and walnuts: Dietary treatment for nonalcoholic fatty liver disease. *World J Gastroenterol* 2015;21:10621-10635.
- 22 Li C, Nie SP, Zhu KX, Ding Q, Xiong T, Xie MY: *Lactobacillus plantarum* NCU116 improves liver function, oxidative stress and lipid metabolism in rats with high fat diet induced non-alcoholic fatty liver disease. *Food Funct* 2014;5:3216-3223.
- 23 Valenti L, Riso P, Mazzocchi A, Porrini M, Fargion S, Agostoni C: Dietary anthocyanins as nutritional therapy for nonalcoholic fatty liver disease. *Oxid Med Cell Longev* 2013;2013:145421.
- 24 Ducharme NA, Bickel PE: Lipid droplets in lipogenesis and lipolysis. *Endocrinol* 2008;149:942-949.
- 25 Huang WC, Chang WT, Wu SJ, Xu PY, Ting NC, Liou CJ: Phloretin and phlorizin promote lipolysis and inhibit inflammation in mouse 3T3-L1 cells and in macrophage-adipocyte co-cultures. *Mol Nutr Food Res* 2013;57:1803-1813.
- 26 Sak K, Kasemaa K, Everaus H: Potentiation of luteolin cytotoxicity by flavonols fisetin and quercetin in human chronic lymphocytic leukemia cell lines. *Food Funct* 2016;7:3815-3824.
- 27 Pal HC, Pearlman RL, Afaq F: Fisetin and its role in chronic diseases. *Adv Exp Med Biol* 2016;928:213-244.
- 28 Seo SH, Jeong GS: Fisetin inhibits TNF-alpha-induced inflammatory action and hydrogen peroxide-induced oxidative damage in human keratinocyte HaCaT cells through PI3K/AKT/Nrf-2-mediated heme oxygenase-1 expression. *Int Immunopharmacol* 2015;29:246-253.
- 29 Kim SC, Kim YH, Son SW, Moon EY, Pyo S, Um SH: Fisetin induces Sirt1 expression while inhibiting early adipogenesis in 3T3-L1 cells. *Biochem Biophys Res Commun* 2015;467:638-644.
- 30 Watanabe M, Hisatake M, Fujimori K: Fisetin suppresses lipid accumulation in mouse adipocytic 3T3-L1 cells by repressing GLUT4-mediated glucose uptake through inhibition of mTOR-C/EBPalpha signaling. *J Agric Food Chem* 2015;63:4979-4987.
- 31 Kim DH, Do MS: BAFF knockout improves systemic inflammation via regulating adipose tissue distribution in high-fat diet-induced obesity. *Exp Mol Med* 2015;47:e129.
- 32 Melnyk RB, Boshes M: Efficiency of food utilization during body weight gain in dormice (*Glis glis*). *Physiol Behav* 1980;24:1017-1021.
- 33 Liou CJ, Huang YL, Huang WC, Yeh KW, Huang TY, Lin CF: Water extract of *Helminthostachys zeylanica* attenuates LPS-induced acute lung injury in mice by modulating NF-kappaB and MAPK pathways. *J Ethnopharmacol* 2017;199:30-38.
- 34 Liou CJ, Huang WC: Casticin inhibits interleukin-1β-induced ICAM-1 and MUC5AC expression by blocking NF-κB, PI3K-Akt, and MAPK signaling in human lung epithelial cells. *Oncotarget* 2017;8:101175-101188.
- 35 Huang WC, Fang LW, Liou CJ: Phloretin attenuates allergic airway inflammation and oxidative stress in asthmatic mice. *Front Immunol* 2017;8:134.
- 36 Liou CJ, Lai XY, Chen YL, Wang CL, Wei CH, Huang WC: Ginkgolide C Suppresses Adipogenesis in 3T3-L1 Adipocytes via the AMPK Signaling Pathway. *Evid Based Complement Alternat Med* 2015;2015:298635.
- 37 Heindel JJ, Newbold R, Schug TT: Endocrine disruptors and obesity. *Nat Rev Endocrinol* 2015;11:653-661.
- 38 Tian Y, Ma J, Wang W, Zhang L, Xu J, Wang K, Li D: Resveratrol supplement inhibited the NF-kappaB inflammation pathway through activating AMPKalpha-SIRT1 pathway in mice with fatty liver. *Mol Cell Biochem* 2016;422:75-84.
- 39 Romero-Gomez M, Zelber-Sagi S, Trenell M: Treatment of NAFLD with diet, physical activity and exercise. *J Hepatol* 2017; 67:829-846.
- 40 Feng X, Yu W, Li X, Zhou F, Zhang W, Shen Q, Li J, Zhang C, Shen P: Apigenin, a modulator of PPARgamma, attenuates HFD-induced NAFLD by regulating hepatocyte lipid metabolism and oxidative stress via Nrf2 activation. *Biochem Pharmacol* 2017;136:136-149.

- 41 Wu L, Yan M, Jiang J, He B, Hong W, Chen Z: Pure total flavonoids from citrus improve non-alcoholic fatty liver disease by regulating TLR/CCL signaling pathway: A preliminary high-throughput 'omics' study. *Biomed Pharmacother* 2017;93:316-326.
- 42 Gu M, Zhao P, Huang J, Zhao Y, Wang Y, Li Y, Fan S, Ma YM, Tong Q, Yang L, Ji G, Huang C: Silymarin ameliorates metabolic dysfunction associated with diet-induced obesity via activation of farnesyl X Receptor. *Front Pharmacol* 2016;7:345.
- 43 Yin Y, Gao L, Lin H, Wu Y, Han X, Zhu Y, Li J: Luteolin improves non-alcoholic fatty liver disease in db/db mice by inhibition of liver X receptor activation to down-regulate expression of sterol regulatory element binding protein 1c. *Biochem Biophys Res Commun* 2017;482:720-726.
- 44 Liu L, Gao C, Yao P, Gong Z: Quercetin alleviates high-fat diet-induced oxidized low-density lipoprotein accumulation in the liver: implication for autophagy regulation. *Biomed Res Int* 2015;2015:607531.
- 45 Wang Z, Pini M, Yao T, Zhou Z, Sun C, Fantuzzi G, Song Z: Homocysteine suppresses lipolysis in adipocytes by activating the AMPK pathway. *Am J Physiol Endocrinol Metab* 2011;301:E703-712.
- 46 Ross FA, Hawley SA, Auciello FR, Gowans GJ, Atrih A, Lamont DJ, Hardie DG: Mechanisms of paradoxical activation of AMPK by the kinase inhibitors SU6656 and sorafenib. *Cell Chem Biol* 2017; 24:813-824.
- 47 Ji G, Wang Y, Deng Y, Li X, Jiang Z: Resveratrol ameliorates hepatic steatosis and inflammation in methionine/choline-deficient diet-induced steatohepatitis through regulating autophagy. *Lipids Health Dis* 2015;14:134.
- 48 Gaidhu MP, Fediuc S, Anthony NM, So M, Mirpourian M, Perry RL, Ceddia RB: Prolonged AICAR-induced AMP-kinase activation promotes energy dissipation in white adipocytes: novel mechanisms integrating HSL and ATGL. *J Lipid Res* 2009;50:704-715.
- 49 Mota de Sa P, Richard AJ, Hang H, Stephens JM: Transcriptional regulation of adipogenesis. *Compr Physiol* 2017;7:635-674.
- 50 Fu A, Shi X, Zhang H, Fu B: Mitotherapy for fatty liver by intravenous administration of exogenous mitochondria in male mice. *Front Pharmacol* 2017;8:241.
- 51 Gibson PS, Lang S, Dhawan A, Fitzpatrick E, Blumfield ML, Truby H, Hart KH, Moore JB: Systematic review: Nutrition and physical activity in the management of paediatric non-alcoholic fatty liver disease. *Aliment Pharmacol Ther* 2014;40:1155-1170.
- 52 Huang Q, Wang T, Yang L, Wang HY: Ginsenoside Rb2 alleviates hepatic lipid accumulation by restoring autophagy via induction of Sirt1 and activation of AMPK. *Int J Mol Sci* 2017;18:E1063.
- 53 Frühbeck G, Méndez-Giménez L, Fernández-Formoso JA, Fernández S, Rodríguez A: Regulation of adipocyte lipolysis. *Nutr Res Rev* 2014;27:63-93.
- 54 Neuschwander-Tetri BA: Non-alcoholic fatty liver disease. *BMC Med* 2017;15:45.
- 55 Geeraerts X, Bolli E, Fendt SM, Van Ginderachter JA: Macrophage metabolism as therapeutic target for cancer, atherosclerosis, and obesity. *Front Immunol* 2017;8:289.
- 56 Ali AT, Hochfeld WE, Myburgh R, Pepper MS: Adipocyte and adipogenesis. *Eur J Cell Biol* 2013;92:229-236.
- 57 Lumeng CN, Saltiel AR: Inflammatory links between obesity and metabolic disease. *J Clin Invest* 2011;121:2111-2117.
- 58 Szkudelski T, Szkudelska K: Effects of AMPK activation on lipolysis in primary rat adipocytes: studies at different glucose concentrations. *Arch Physiol Biochem* 2017;123:43-49.
- 59 Elgebaly A, Radwan IA, AboElnas MM, Ibrahim HH, Eltoomy MF, Atta AA, Mesalam HA, Sayed AA, Othman AA: Resveratrol supplementation in patients with non-alcoholic fatty liver disease: systematic review and meta-analysis. *J Gastrointest Liver Dis* 2017;26:59-67.
- 60 Coppari R, Bjorbaek C: Leptin revisited: its mechanism of action and potential for treating diabetes. *Nat Rev Drug Discov* 2012;11:692-708.
- 61 Cui H, Lopez M, Rahmouni K: The cellular and molecular bases of leptin and ghrelin resistance in obesity. *Nat Rev Endocrinol* 2017;13:338-351.



ORIGINAL ARTICLE

# Spilanthol Inhibits COX-2 and ICAM-1 Expression via Suppression of NF- $\kappa$ B and MAPK Signaling in Interleukin-1 $\beta$ -Stimulated Human Lung Epithelial Cells

Wen-Chung Huang,<sup>1,2</sup> Ling-Yu Wu,<sup>3</sup> Sindy Hu,<sup>4,5</sup> and Shu-Ju Wu<sup>1,3,4,6</sup>

**Abstract**— Spilanthol a phytochemical derived from the *Spilanthes acmella* plant has antimicrobial, antioxidant, and anti-inflammatory properties. This study evaluated its effects on the expression of intercellular adhesion molecule 1 (ICAM-1) and inflammation-related mediators in IL-1 $\beta$ -stimulated human lung epithelial A549 cells. Human lung epithelial A549 cells were pretreated with various concentrations of spilanthol (3–100  $\mu$ M) followed by treatment with IL-1 $\beta$  to induce inflammation. The protein levels of pro-inflammatory cytokines, chemokines, and prostaglandin E2 (PGE2) were measured using ELISA. Cyclooxygenase-2 (COX-2), heme oxygenase (HO-1), nuclear transcription factor kappa-B (NF- $\kappa$ B), and mitogen-activated protein kinase (MAPK) were measured by immunoblotting. The mRNA expression levels of ICAM-1 and MUC5AC were determined by real-time polymerase chain reaction. Spilanthol decreased the expression of PGE<sub>2</sub>, COX-2, TNF- $\alpha$ , and MCP-1. It also decreased ICAM-1 expression and suppressed monocyte adhesion to IL-1 $\beta$ -stimulated A549 cells. Spilanthol also significantly inhibited the phosphorylation of MAPK and I- $\kappa$ B. These results suggest that spilanthol exerts anti-inflammatory effects by inhibiting the expression of the pro-inflammatory cytokines, COX-2, and ICAM-1 by inhibiting the NF- $\kappa$ B and MAPK signaling pathways.

**KEY WORDS:** chemokines; ICAM-1; MAPK; NF- $\kappa$ B; spilanthol.

## INTRODUCTION

The airway inflammation associated with asthma is regulated by mutually interacting cytokines [1].

Asthma, a heterogeneous chronic inflammatory airway disease, is associated with interleukin-1 $\beta$  (IL-1 $\beta$ ), a pro-inflammatory cytokine that drives inflammation and induces airway smooth muscle (ASM)

Wen-Chung Huang and Ling-Yu Wu contributed equally to this work.

<sup>1</sup> Graduate Institute of Health Industry Technology, Research Center for Industry of Human Ecology, Research Center for Chinese Herbal Medicine, College of Human Ecology, Chang Gung University of Science and Technology, No.261, Wenhua 1st Rd., Guishan Dist., Taoyuan, 33303, Taiwan

<sup>2</sup> Division of Allergy, Asthma, and Rheumatology, Department of Pediatrics, Chang Gung Memorial Hospital, Linkou, Guishan Dist., Taoyuan, 33303, Taiwan

<sup>3</sup> Department of Nutrition and Health Sciences, Research Center for Food and Cosmetic Safety, and Research Center for Chinese Herbal Medicine, College of Human Ecology, Chang Gung University of Science and Technology, No.261, Wenhua 1st Rd., Guishan Dist., Taoyuan, 33303, Taiwan

<sup>4</sup> Aesthetic Medical Center, Department of Dermatology, Chang Gung Memorial Hospital, Guishan Dist., Taoyuan, 33303, Taiwan

<sup>5</sup> Department of Cosmetic Science, Research Center for Food and Cosmetic Safety, and Research Center for Chinese Herbal Medicine, College of Human Ecology, Chang Gung University of Science and Technology, No.261, Wenhua 1st Rd., Guishan Dist., Taoyuan, 33303, Taiwan

<sup>6</sup> To whom correspondence should be addressed at Department of Nutrition and Health Sciences, Research Center for Food and Cosmetic Safety, and Research Center for Chinese Herbal Medicine, College of Human Ecology, Chang Gung University of Science and Technology, No.261, Wenhua 1st Rd., Guishan Dist., Taoyuan, 33303, Taiwan. E-mail: sjwu@gw.cgust.edu.tw

responsiveness in asthma [2]. Studies have shown that IL-1 $\beta$  levels are elevated in the early phases of the inflammatory response and in the airways of patients with asthma, which show altered responsiveness [3]. IL-1 $\beta$  acts by upregulating adhesion molecules on endothelial cells and by inducing the synthesis of tumor necrosis factor- $\alpha$  (TNF- $\alpha$ ) and MCP-1, both of which are cytokines. Notably, TNF- $\alpha$  causes airway hyper-responsiveness and stimulates ASM cells, thereby playing an important role in the pathogenesis of asthma [4].

In inflamed airway epithelium, ICAM-1 upregulation mediates increased eosinophil adhesion to the endothelium [5]. Specifically, when endothelial cells are exposed to the pro-inflammatory mediators TNF- $\alpha$  and IL-1 $\beta$ , ICAM-1 is upregulated on the endothelial cell surface [6]. Studies indicate that the inflammatory response is mediated by phosphatidylinositol 3-kinase (PI3K), protein kinase (PKC), and reactive oxygen species (ROS), leading to NF- $\kappa$ B activation [7]. Lung endothelial cell ICAM-1 mRNA expression is induced by NF- $\kappa$ B activation, suggesting that the induction of ICAM-1 is mediated by NF- $\kappa$ B in the A549 cell by IL-1 $\beta$  [8]. Notably, NF- $\kappa$ B acts as an activator of multiple cytokines, chemokines, and adhesion molecules that play important roles in inflammatory diseases such as asthma. Consequently, NF- $\kappa$ B is considered as an attractive therapeutic target in asthma [9]. Indeed, airway epithelial NF- $\kappa$ B activation is observed in asthma patients, implying that NF- $\kappa$ B is a critical modulator of inflammation in the pathogenesis of this lung disease [10, 11].

Airway epithelial NF- $\kappa$ B is a central mediator in the inflammatory and immune responses to infections and environmental insults that modulate allergic sensitization and the severity of subsequent allergic airway disease [12]. Furthermore, MCP-1 is involved in mast cell, eosinophil, and macrophage recruitment and promotes PGE<sub>2</sub> generation. PGE<sub>2</sub> is biosynthesized from arachidonic acid, showing that COX-2 is primarily responsible [13]. COX-2 can be induced by cytokines IL- $\beta$  and TNF- $\alpha$ , which are involved in pathological processes such as cancer and inflammatory diseases and play important roles in the pathogenesis of asthma [14]. The MAPK pathways regulate the production of chemokines in primary epithelial cells [15]. Studies show that asthmatic patients have increased phosphorylated- (p)-ERK1/2, p-p38 (p-p38) and pJNK1/2/3 (pJNK) in their airway epithelium and smooth muscle cells [12]. Indeed, MAPK activity

is significantly higher in the lungs of asthmatic mice than in normal controls [16].

A previous study reported that spilanthol has an anti-inflammatory effect in lipopolysaccharide (LPS)-stimulated macrophages [17]. We assumed that spilanthol could inhibit IL-1 $\beta$ -induced inflammatory responses and suppress ICAM-1 expression to reduce leukocyte adherence to lung epithelial cells. Hence, in this study, we evaluated the anti-inflammatory effect of spilanthol and the signaling mechanism of the NF- $\kappa$ B and MAPK pathways in IL-1 $\beta$ -induced A549 human lung epithelial cells.

## MATERIALS AND METHODS

### Materials

Figure 1a shows the chemical structure of spilanthol (ChromaDex, Irvine, CA, USA) which was prepared as a 100 mM stock solution in dimethyl sulfoxide (DMSO) and stored at  $-20^{\circ}\text{C}$ . The final DMSO concentration was  $\leq 0.1\%$  in culture medium, as described previously. All chemicals and reagents were purchased from Sigma (St. Louis, MO, USA). Antibodies against  $\beta$ -actin, COX-2, and HO-1 were purchased from Santa Cruz Biotechnology (Santa Cruz, CA, USA). Antibodies against JNK, ERK, p38, phosphorylated (phospho)-JNK, phospho-ERK, and phospho-p38 were purchased from Millipore (Billerica, MA, USA). Enzyme-linked immunosorbent assay (ELISA) kits were obtained from R&D Systems (Minneapolis, MN, USA).

### Cell Line and Treatment

The A549 human lung epithelial cell line was purchased from the Bioresource Collection and Research Center (BCRC, Taiwan) and cultured in F12 medium (Invitrogen-Gibco™, Paisley, Scotland) supplemented with 10% heat-inactivated fetal bovine serum (Biological Industries, Haemek, Israel), penicillin (100 units/mL), streptomycin (100  $\mu\text{g/mL}$ ), and 2 mM L-glutamine. All cells were incubated under a humidified atmosphere of 5% CO<sub>2</sub> at 37  $^{\circ}\text{C}$ , and the cells were sub-cultured twice each week.

### Cell Viability Assay

The inhibitory effect of spilanthol on cell viability was assessed using 3-(4,5-dimethylthiazol -2-yl)-

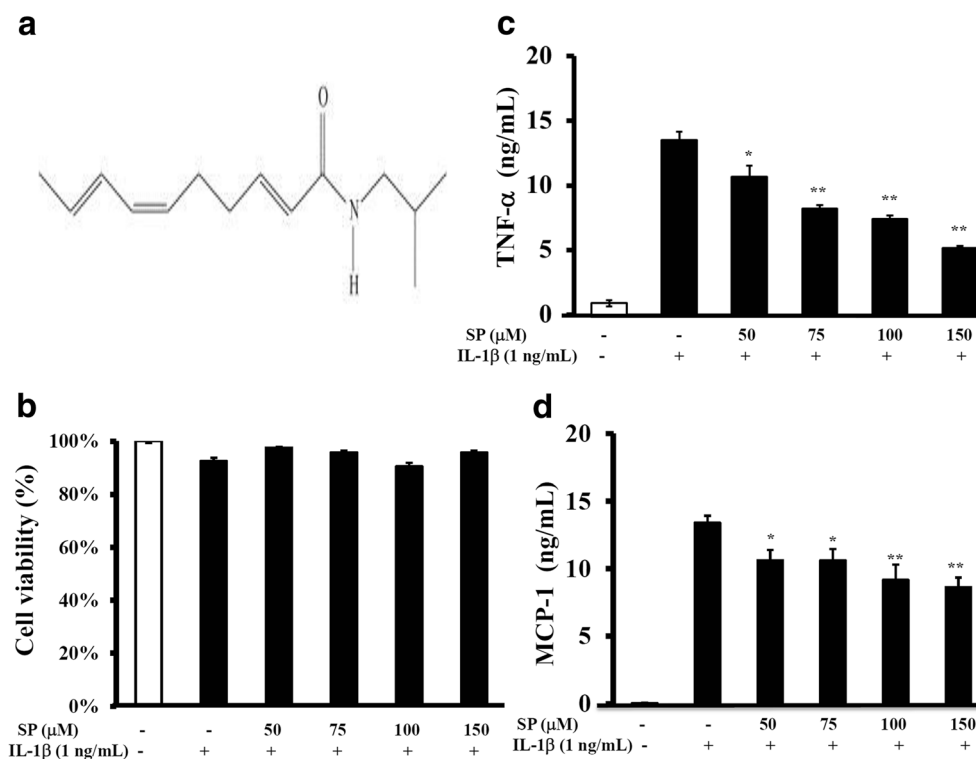


**Fig. 1.** The chemical structure (a) and cytotoxicity of spilanthol in A549 cells (b). The effects of spilanthol on IL-1 $\beta$ -induced production of TNF- $\alpha$  (c) and MCP-1 (d). Cells ( $10^6$  cells/well) were pretreated with the indicated concentrations of spilanthol (SP) for 1 h and then stimulated with IL-1 $\beta$  (1 ng/mL) for 24 h. The data are presented as the mean  $\pm$  SD; \* $p$  < 0.05, \*\* $p$  < 0.01 compared with the IL-1 $\beta$ -treated group.

2,5-diphenyltetrazolium bromide (MTT, Sigma) as described previously [18]. In brief, cells ( $10^4$  cells/well) were seeded in 96-well plates and treated with various concentrations of spilanthol for 24 h. After treatment, the supernatant was removed and incubated with 5 mg/mL MTT solution for 4 h. Then, the medium was removed, and isopropanol was added to dissolve the formazan crystals. Absorbance was measured at 570 nm with a microplate reader (Multiskan FC, Thermo Fisher Scientific, Waltham, MA, USA).

#### Measurement of Pro-inflammatory Cytokines, Chemokines, and PGE2

A549 cells ( $10^6$  cells/mL) were cultured and pretreated with different concentrations of spilanthol (50–150  $\mu$ M) in 24-well plates for 1 h, then IL-1 $\beta$  (1 ng/mL) was added and the cells were cultured for an additional 24 h. The supernatants were tested using ELISA kits specific for MCP-1, TNF- $\alpha$ , PGE2, and ICAM-1 (R&D Systems, Minneapolis, MN, USA). The OD was determined

spectrophotometrically at 450 nm in a microplate reader (Multiskan FC).

#### Preparation of Total and Nuclear Proteins

To assay the total protein and phosphorylated protein content, A549 ( $10^6$  cells/mL) cells were pretreated with or without spilanthol for 1 h in 6-well plates. Then, the cells were stimulated with or without IL-1 $\beta$  (1 ng/mL) for 30 min (before assaying for protein phosphorylation) or for 24 h (to evaluate total protein). The cells were harvested in 300  $\mu$ L protein lysis buffer (50 mM Tris-HCl, pH 8, 150 mM NaCl, 1 mM EDTA, 0.5% NP40, 0.1% SDS) containing protein inhibitor cocktail and phosphatase inhibitors (Sigma). Cells were also cultured for 1 h to detect NF- $\kappa$ B. To investigate the expression of nuclear proteins, cells were treated using the NE-PER® nuclear and cytoplasmic extraction reagent kits (Pierce, Rockford, IL, USA). All protein concentrations were measured with the BCA protein assay kit (Pierce).

## Western Blot Analysis

Protein samples (10–30  $\mu$ g) were loaded onto 10% SDS polyacrylamide gels, and the gels were transferred to polyvinylidene fluoride membranes (Millipore, Billerica, MA, USA). The membranes were blocked and incubated overnight at 4 °C with the following primary antibodies: antibodies to HO-1, COX-2, I $\kappa$ B- $\alpha$ , phosphorylated-I $\kappa$ B- $\alpha$ , and p65 (Santa Cruz, CA, USA); to ERK1/2, p38, JNK, phospho-ERK 1/2, phospho-p38, and phospho-JNK (Millipore); and to ICAM-1 and  $\beta$ -actin (Sigma). After the membranes were washed three times in Tris-buffered saline with Tween 20 (TBST) buffer (150 mM NaCl, 10 mM Tris-HCl pH 8.0, 0.1% Tween 20), they were incubated with secondary antibodies for 1 h at room temperature. Next, the membranes were incubated with HRP-conjugated secondary antibodies for 1 h at room temperature. Finally, the membranes were washed with TBST and incubated with Luminol/Enhancer Solution (Millipore), exposed to film, and bands were quantitated using the BioSpectrum 600 system (UVP, Upland, CA, USA).

## Real-Time PCR to Quantitate Gene Expression

The mRNA expression levels of ICAM-1 and MUC5AC were determined by real-time polymerase chain reaction (PCR) using the  $\beta$ -actin-encoding gene as an internal reference. Total RNA was prepared using TRIzol solution (Invitrogen, Carlsbad, CA, USA). RNA was isolated according to the manufacturer's instructions. TaqMan real-time quantitative PCR was performed and analyzed according to the manufacturer's instructions (Applied Biosystems, Foster City, CA, USA). The primers used for amplification were as follows: for ICAM-1, forward 5'-AGA CGC AGA GGA CCT TAA-3' and reverse 5'-CAC ACT TCA CAG TTA CTT GG-3'; for MUC5AC, forward 5'-CTG TTA CTA TGC GAT GTG TAG-3' and reverse 5'-GTG GCG TGG TAG ATG TAG-3'; and for  $\beta$ -actin, forward 5'-AAG ACC TCT ATG CCA ACA CAG T-3' and reverse 5'-AGC CAG AGC AGT AAT CTC CTT C-3'. The results are expressed as arbitrary units and normalized against  $\beta$ -actin mRNA expression.

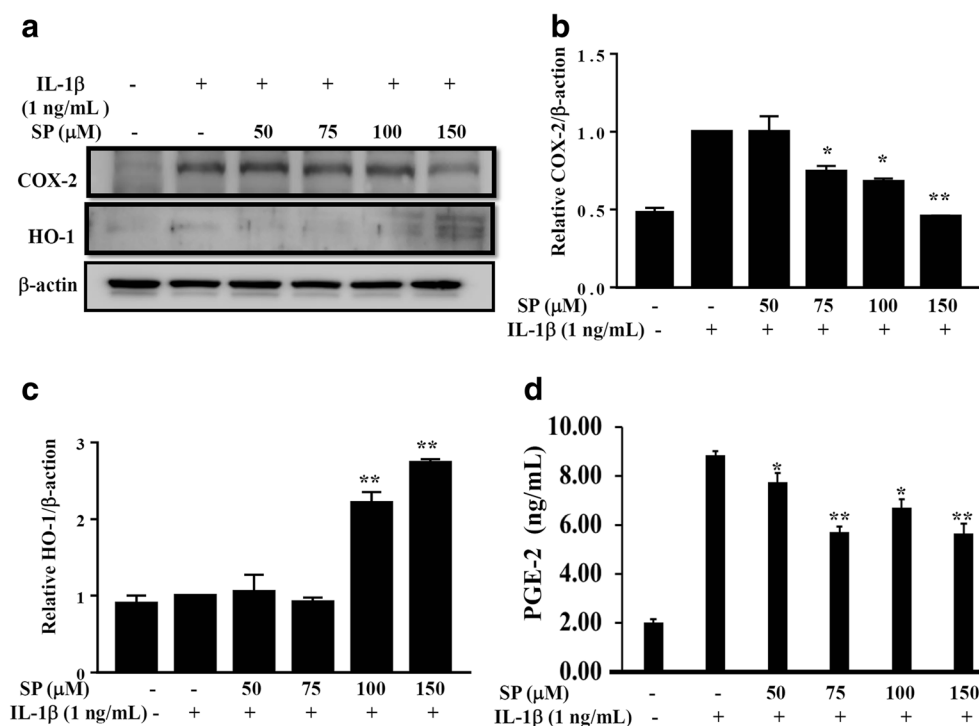


**Fig. 2.** The effects of spilanthol on IL-1 $\beta$ -induced production of COX-2 and HO-1 (a). COX-2 and HO-1 relative protein expressions were measured relative to the expression of  $\beta$ -actin were detected by Western blots ( $n = 3$  per group) in (b) (c), respectively. The effects of spilanthol on IL-1 $\beta$ -induced production of PGE<sub>2</sub> (d). Data are presented as the mean  $\pm$  SD; \* $p < 0.05$ , \*\* $p < 0.01$  compared with the IL-1 $\beta$ -treated group.



### Cell Adhesion Assay

A549 cells were treated with spilanthol for 1 h and incubated with 1 ng/mL IL-1 $\beta$  for 24 h. Then, human monocytic THP-1 cells in calcein AM solution (Sigma) were co-cultured with A549 cells for 1 h. Cells were washed and the adhesion of THP-1 cells to A549 cells was observed under fluorescence microscopy (Olympus, Tokyo, Japan).

### Statistical Analysis

Data are reported as the mean  $\pm$  standard deviation (SD). The significance of differences was assessed using one-way analysis of variance (ANOVA) and Tukey's test. Differences were considered statistically significant at  $p < 0.05$ .

## RESULTS

### The Effects of Spilanthol on the Viability of Human Lung Epithelial A549 Cells

To determine the cytotoxicity of spilanthol in A549 cells, the MTT assay was used to measure cell viability.

Spilanthol did not significantly affect cell viability at concentrations  $\leq 150 \mu\text{M}$  (Fig. 1b). Therefore, all subsequent experiments used concentrations of spilanthol that ranged from 50 to 150  $\mu\text{M}$ .

### Pretreatment with Spilanthol Efficiently Inhibits Pro-inflammatory Cytokines and Chemokines in IL-1 $\beta$ -Induced A549 Cells

Spilanthol is reported to have anti-inflammatory effects on LPS-induced macrophages [18]. Therefore, we investigated whether spilanthol could suppress the inflammatory response in terms of affecting IL-1 $\beta$ -induced pro-inflammatory cytokine and chemokine production. A549 cells were pretreated with 50, 75, 100, and 150  $\mu\text{M}$  spilanthol and stimulated with IL-1 $\beta$  (1 ng/mL) for 24 h. Analysis showed that IL-1 $\beta$  significantly induced the release of the inflammatory cytokine TNF- $\alpha$  and the chemokine MCP-1, and addition of spilanthol significantly suppressed the secretion of these inflammatory mediators at all concentrations of spilanthol compared with IL-1 $\beta$  alone. We found that 50–150  $\mu\text{M}$  spilanthol significantly decreased TNF- $\alpha$  and MCP-1 levels compared with IL-1 $\beta$

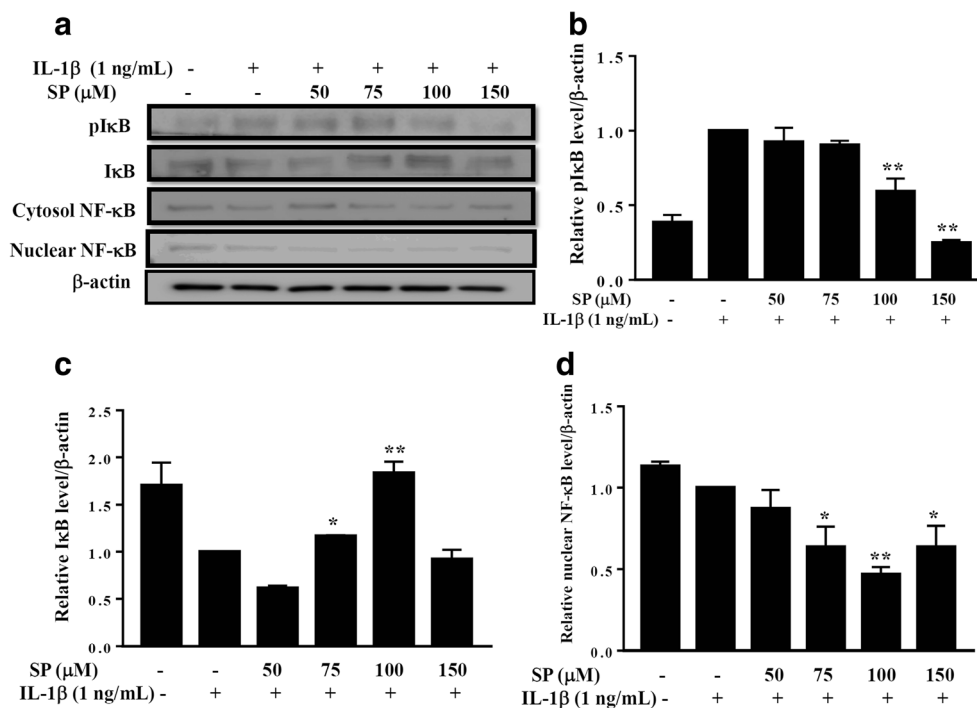


**Fig. 3.** The effects of spilanthol on IL-1 $\beta$ -induced the phosphorylation of I $\kappa$ B $\alpha$ , total I $\kappa$ B- $\alpha$  and NF- $\kappa$ B protein expressions (a). Phosphorylation of I $\kappa$ B $\alpha$ , total I $\kappa$ B- $\alpha$  and NF- $\kappa$ B relative protein expressions were measured relative to the expression of  $\beta$ -actin in (b) (c) (d), respectively. Phosphorylation of I $\kappa$ B $\alpha$ , total I $\kappa$ B $\alpha$  and NF- $\kappa$ B proteins were detected by western blots ( $n = 3$  per group). Data are presented as the mean  $\pm$  SD; \* $p < 0.05$ , \*\* $p < 0.01$  compared with the IL-1 $\beta$ -treated group.

alone (TNF- $\alpha$ ; SP50  $10.18 \pm 0.45$  ng/mL,  $p < 0.05$ ; SP75  $8.19 \pm 0.16$  ng/mL,  $p < 0.01$ ; SP100  $7.43 \pm 0.15$  ng/mL,  $p < 0.01$ ; SP150  $5.14 \pm 0.11$  ng/mL,  $p < 0.01$  versus IL-1 $\beta$  alone  $13.53 \pm 0.25$  ng/mL, respectively). MCP-1; SP50  $10.12 \pm 0.13$  ng/mL,  $p < 0.05$ ; SP75  $10.11 \pm 0.14$  ng/mL,  $p < 0.05$ ; SP100  $9.21 \pm 0.19$  ng/mL,  $p < 0.01$ ; SP150  $8.65 \pm 0.12$  ng/mL,  $p < 0.01$  versus IL-1 $\beta$  alone  $13.41 \pm 0.88$  ng/mL, respectively). Further, the inhibitory effects of spilanthol on TNF- $\alpha$  and MCP-1 levels were dose-dependent (Fig. 1c, d).

### Spilanthol Inhibits PGE<sub>2</sub> Production and Affects COX-2 and HO-1 Protein Expression in IL-1 $\beta$ -Induced A549 Cells

To investigate the effect of spilanthol on COX-2 protein expression, A549 cells were pretreated with spilanthol, followed by stimulation with IL-1 $\beta$  for 24 h. Pretreatment with 75–150  $\mu$ M spilanthol significantly inhibited COX-2 expression compared with IL-1 $\beta$ -stimulated cells that were

not treated with spilanthol (Fig. 2a, b). In addition, spilanthol modulated the expression of HO-1, which has anti-inflammatory and anti-oxidant activity [19]. Specifically,  $\geq 100$   $\mu$ M spilanthol concentrations increased HO-1 expression compared with IL-1 $\beta$  treatment alone (Fig. 2a, c). Spilanthol also significantly decreased the level of PGE<sub>2</sub> compared to IL-1 $\beta$  alone (Fig. 2d).

### The Effects of Spilanthol on I $\kappa$ B $\alpha$ Phosphorylation, and Suppression of I $\kappa$ B Degradation in IL-1 $\beta$ -Activated Human Lung Epithelial Cells

The NF- $\kappa$ B pathway plays a critical role in the inflammatory response by regulating the expression of inflammatory cytokines, including IL-1 $\beta$ , IL-6, and TNF- $\alpha$ . The rapid protease-mediated degradation of I $\kappa$ B $\alpha$  leads to NF- $\kappa$ B release from the cytoplasm into the nucleus [20]. Therefore, we investigated whether spilanthol could regulate NF- $\kappa$ B activity in A549 cells treated with IL-1 $\beta$  (Fig. 3a). Interestingly, spilanthol significantly decreased

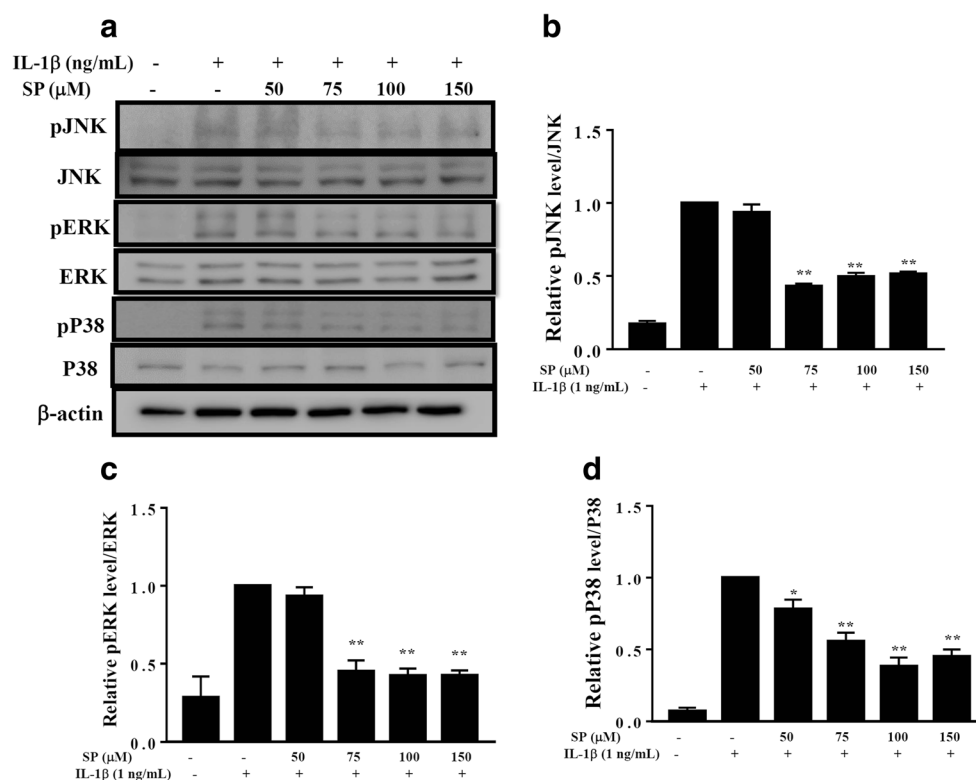


**Fig. 4.** The effects of spilanthol on the IL-1 $\beta$ -induced phosphorylation of MAPK. A549 cells were pretreated with varying concentrations of spilanthol (SP) for 1 h and then incubated with or without IL-1 $\beta$  (1 ng/mL) for 30 min. Protein samples were analyzed by Western blotting with phospho-specific antibodies (a). The phospho-specific JNK, ERK, and p38 relative protein expressions were measured relative to the expression of total MAPK levels were used as the internal control in (b) (c) (d), respectively. Data are presented as the mean  $\pm$  SD; \* $p < 0.05$ , \*\* $p < 0.01$  compared with the IL-1 $\beta$ -treated group.

I $\kappa$ B $\alpha$  phosphorylation, and suppression I $\kappa$ B degradation which is an indication that spilanthol suppresses NF- $\kappa$ B transcriptional activation and translocation to the nucleus induced by IL-1 $\beta$ -stimulated in A549 cells (Fig. 3b, c, d).

### Spilanthol Inhibits MAPK Phosphorylation in IL-1 $\beta$ -Activated Human Lung Epithelial Cells

The MAPK signaling pathways regulate cellular activities and the release of pro-inflammatory cytokines. We investigated whether spilanthol could modulate MAPK signaling pathways, including the ERK1/2, p38, and JNK proteins, in A549 cells treated with IL-1 $\beta$  (Fig. 4a). We found that spilanthol significantly decreased the phosphorylation of ERK1/2, p38, and JNK in a concentration-dependent manner compared with IL-1 $\beta$  treatment alone (Fig. 4b, c, d). These results indicated that spilanthol

modulated the activation of the MAPK signaling pathways in A549 cells that were treated with IL-1 $\beta$ .

### Spilanthol Inhibited ICAM-1 and MUC5AC Expression in IL-1 $\beta$ -Stimulated Human Lung Epithelial Cells

Previous studies have demonstrated that the expression of ICAM-1 by inflammatory endothelial cells results in eosinophil adhesion [11]. Here, we found that spilanthol significantly reduced ICAM-1 production compared to IL-1 $\beta$  treatment alone (Fig. 5a). In addition,  $\geq 50$   $\mu$ M spilanthol concentrations significantly suppressed ICAM-1 protein expression (Fig. 5b, c). Together, these results showed that spilanthol significantly decreased ICAM-1 production and suppressed its release into the cell culture medium. We used real-time PCR to assess gene expression and found that spilanthol

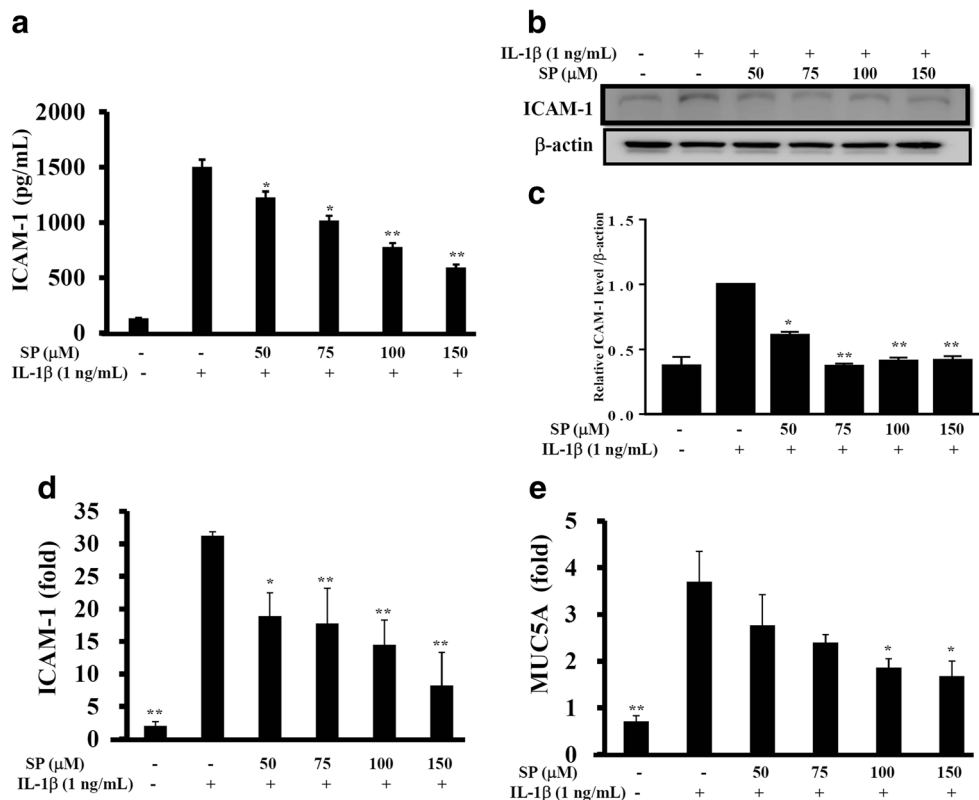


**Fig. 5.** The effects of spilanthol on the IL-1 $\beta$ -induced production of ICAM-1 and MUC5AC. A549 cells ( $10^6$  cells/mL) were stimulated with IL-1 $\beta$  for 24 h, then the level of ICAM-1 in the supernatant was assayed by ELISA (a), the level of ICAM-1 protein in the cells was assayed by Western blot ( $n = 3$  per group) (b), and ICAM-1 protein relative expressions were measured relative to  $\beta$ -actin (c). The cells were pretreated with the indicated concentrations of spilanthol (SP) for 1 h and then stimulated with IL-1 $\beta$  (1 ng/mL) for 4 h before assaying the ICAM-1 (d) and MUC5AC (e) gene expression levels, which were determined using real-time RT-PCR. Data are presented as the mean  $\pm$  SD; \* $p < 0.05$ , \*\* $p < 0.01$  compared with the IL-1 $\beta$ -treated group.

significantly decreased the mRNA levels of ICAM-1 and MUC5AC in A549 cells (Fig. 5d, e).

### Spilanthol Suppresses Monocyte Adhesion to Human Lung Epithelial Cells

The human cell line THP-1 with monocytic properties can be active to macrophage-like cells in the inflammatory response. Activated THP-1 release more inflammatory mediators and adhesion molecules and caused cells adherence [27]. We found that spilanthol significantly reduced ICAM-1 gene expression in IL-1 $\beta$ -stimulated A549 cells (Fig. 5d). Therefore, we further investigated whether spilanthol inhibited monocyte adhesion to IL-1 $\beta$ -stimulated A549 cells (Fig. 6a–f). THP-1 cells were stained with calcein AM and co-cultured with IL-1 $\beta$ -induced

A549 cells. We found that THP-1 cells adhered to IL-1 $\beta$ -activated A549 cells and that pretreatment with spilanthol significantly reduced this adhesion (Fig. 6g).

### DISCUSSION

When respiratory epithelial cells and macrophages are activated, they release pro-inflammatory cytokines increasing the secretion of chemokines and evoking an inflammatory response [20]. One study indicated that bacterial stimuli induce respiratory epithelial cells to secrete pro-inflammatory mediators such as IL-1 $\beta$  and TNF- $\alpha$ , which leads to upregulation of adhesion molecules [21]. There is also evidence that LPS-stimulated airway bronchiolar and alveolar epithelial cells induce NF- $\kappa$ B activation and

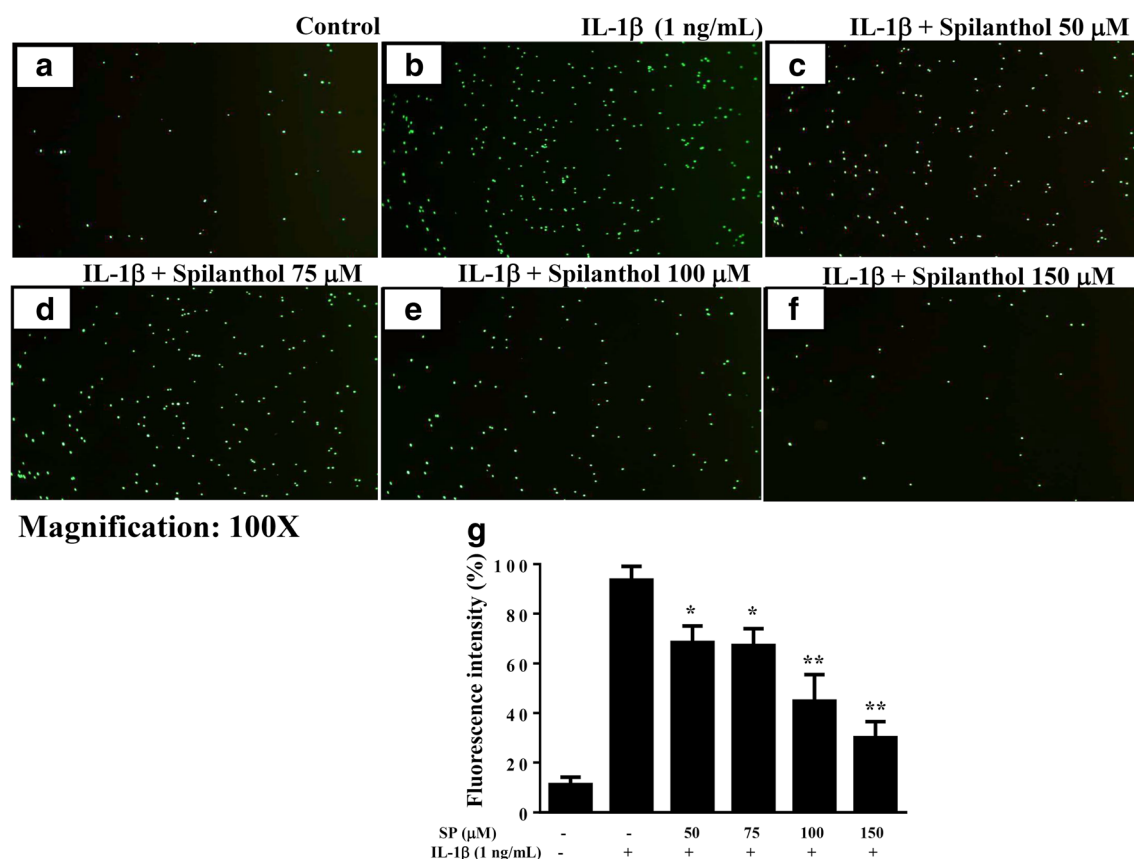


**Fig. 6.** Spilanthol inhibits the adherence of THP-1 cells to activated A549 cells. THP-1 cells were labeled with calcein AM, mixed with A549 cells, and observed using fluorescence microscopy. The adherence of THP-1 cells to normal (a) and IL-1 $\beta$ -activated A549 cells (b) is shown. THP-1 cells were treated with 50  $\mu$ M spilanthol (c), 75  $\mu$ M spilanthol (d), 100  $\mu$ M spilanthol (e), or 150  $\mu$ M spilanthol (f). Fluorescence intensity of THP-1 cell adhesion to A549 cells (g). THP-1 cell adhesion in spilanthol treated cells were detected by fluorescence microscope ( $n = 3$  per group). Data are presented as the mean  $\pm$  SD; \* $p < 0.05$ , \*\* $p < 0.01$  compared with the IL-1 $\beta$ -treated group.



increase ICAM-1 expression [22]. In adult respiratory distress syndrome (ARDS) the levels of pro-inflammatory cytokines  $\text{TNF-}\alpha$  and  $\text{IL-1}\beta$  are increased. Notably,  $\text{IL-1}\beta$  is the major cytokine that maintains lung inflammation in ARDS [23]. Studies show that  $\text{IL-1}\beta$  is an important factor in inflammatory responses as well as in fibroproliferative processes in the lungs of adult patients with ARDS [24].

Spilanthol is the compound (2E,6Z,8E)-N-isobutylamide-2,6,8-decatrienamide and a physiologically active substances from *Spilanthes acmella*, which is known as the anti-toothache plant and which has anti-bacterial effects [25]. An aqueous extract of *S. acmella* has important anti-inflammatory and analgesic properties in animal models [26]. One study suggested that spilanthol attenuates the LPS-induced inflammatory responses in murine RAW 264.7 macrophages, in part due to the inactivation of  $\text{NF-}\kappa\text{B}$ , which negatively regulates the production of proinflammatory mediators [27]. However, the anti-inflammatory effects of spilanthol have not been shown previously in human lung epithelial cells. In this study, we

found that spilanthol can downregulate COX-2 production and decrease  $\text{TNF-}\alpha$  and MCP-1 production in  $\text{IL-1}\beta$ -stimulated lung epithelial cells. In particular, spilanthol significantly decreased the phosphorylation of  $\text{I}\kappa\text{B}\alpha$  and MAPK pathways compared with  $\text{IL-1}\beta$  alone. These results indicated that spilanthol can inhibit the activation of  $\text{NF-}\kappa\text{B}$  and MAPK pathways in  $\text{IL-1}\beta$ -activated A549 cells. We demonstrated hypothesis that spilanthol dampen the inflammatory effects of  $\text{IL-1}\beta$  in stimulated lung epithelial cells.

Earlier studies showed that a hydroethanolic extract of *S. acmella* has anti-inflammatory properties that could decrease the levels of the lipid peroxidation product malondialdehyde (MDA) and increase antioxidant enzyme activity (catalase and superoxide dismutase) [26, 28]. We found that spilanthol enhanced heme oxygenase-1 (HO-1) protein expression. HO-1 can regulate the balance of anti-inflammatory mediators and has antioxidant properties [29], prompting us to evaluate the anti-inflammatory molecular mechanisms underlying the effects of spilanthol. Our results showed that spilanthol significantly reduced

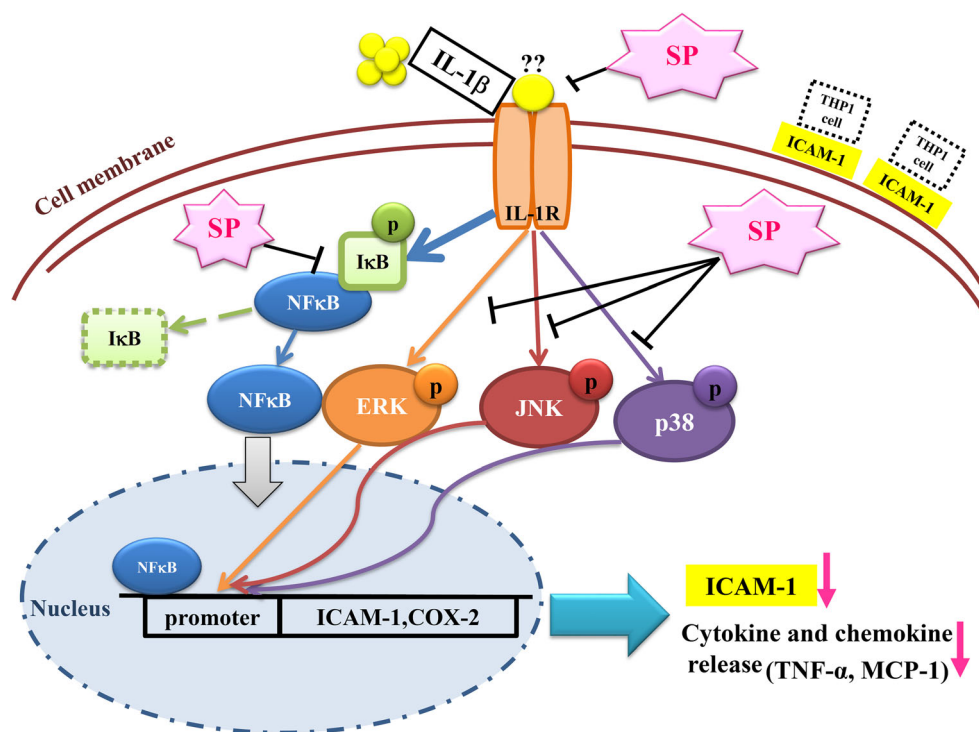


**Fig. 7.** Model explaining the mechanism underlying the anti-inflammatory effects of spilanthol (SP). Spilanthol decreased the levels of pro-inflammatory cytokine ( $\text{TNF-}\alpha$ ) and chemokine (MCP-1), and inhibited COX-2 and ICAM-1 expression *via* suppression of the  $\text{NF-}\kappa\text{B}$  and MAPK signaling in  $\text{IL-1}\beta$ -stimulated human lung epithelial cells. SP also inhibited leukocyte adherence to lung epithelial cells by reducing ICAM-1 expression *via* inhibition of the  $\text{IL-1}\beta$  pathway. Spilanthol is a potential anti-inflammatory compound that could ameliorate inflammatory in human lung epithelial cells.

COX-2 and PGE<sub>2</sub> production in LPS-stimulated macrophages and IL-1 $\beta$ -activated human lung epithelial cells. We suggest that spilanthol may be useful as a COX-2 inhibitor to attenuate the inflammatory response. In addition, bronchoalveolar lavage fluid from patients with interstitial lung disease contains more MCP-1, TNF- $\alpha$ , and IL-8 than normal tissue [4]. We found that spilanthol significantly decreased TNF- $\alpha$  and MCP-1 in IL-1 $\beta$ -stimulated lung epithelial cells, suggesting that spilanthol might suppress the inflammatory response of lung epithelial cells and improve lung disease symptoms.

As part of their response to inflammation of lung epithelial cells express cell adhesion molecules including ICAM-1 and VCAM-1, which induce monocyte adherence and lead to neutrophil migration and infiltration into lung tissue [5]. Inflammatory mediators are released from activated monocytes and neutrophils, thereby increasing lung inflammation. In this study, real-time PCR and Western blot analysis showed that spilanthol suppressed ICAM-1 gene and protein expression. In addition, inflammatory epithelial cells release “soluble” intercellular adhesion molecule-1 (sICAM-1), which is a marker of inflammation and promote the inflammatory responses. In inflammation-related diseases, as in autoimmune diseases, viral infections and bronchoalveolar lavage fluid of asthma patients serum sICAM-1 levels increase more than healthy individual. Inflammatory mediators (IL-1 $\beta$ , TNF- $\alpha$ , IL-6 and angiotensin II) could stimulate epithelial cells and endothelial cells to secrete sICAM-1 in circulating [30]. Inflammatory lung epithelial cells express ICAM-1 were cleaved to sICAM-1 and released into the supernatant. In this study, ELISA analysis showed that spilanthol decreased ICAM-1 levels. Although the roles of sICAM-1 have not been completely clear, the evidence suggests its implication in lung epithelial cells inflammatory progression at this works.

Further, to understand whether the spilanthol decrease in ICAM-1 expression could decrease lymphocyte adhesion to inflammatory lung epithelial cells, we co-cultured monocyte THP-1 cells with IL-1 $\beta$ -stimulated A549 cells. We found that spilanthol decreased THP-1 adherence to A549 cells compared with IL-1 $\beta$  treatment alone. Lung epithelial cells secrete excessive mucus as part of the inflammatory response, which obstructs the airway and leads to difficulty breathing and even to suffocation [6]. By preventing ICAM-1 expression, spilanthol decreases inflammatory leukocyte infiltration into lung tissue, possibly reducing mucus production. Comprehensive detections of sICAM-1, ICAM-1 gene and protein expression and THP-1 adherence to A549 cells indicated that spilanthol decreased ICAM-1 expression in

adherent monocytes as well. We confirmed hypothesis that spilanthol could suppress ICAM-1 expression to reduce leukocyte adherence to lung epithelial cells.

To summarize, we found that spilanthol not only inhibited the levels of TNF- $\alpha$  and MCP-1, but it also suppressed COX-2 protein expression and promoted HO-1 protein expression by suppressing NF- $\kappa$ B activation and MAPK pathways in IL-1 $\beta$ -activated human lung epithelial cells. In addition, we found evidence that spilanthol decreased ICAM-1 expression in these cells. Based on these results, we propose a model that explains the anti-inflammatory effects of spilanthol (Fig. 7).

## CONCLUSION

We conclude that spilanthol, which is a natural anti-inflammatory agent, acts as a regulatory factor in MAPK pathways and in NF- $\kappa$ B activation of COX-2 and ICAM-1 expression. Further studies are needed to investigate its effects *in vivo*.

**Authors' Contributions** Wen-Chung Huang and Ling-Yu Wu designed the study and performed the experiments. Sindy Hu searched the literature and performed the experiments. Shu-Ju analyzed interpretation of data and drafting the manuscript.

**Funding Information** This study was supported in part by grants from the Chang Gung Memorial Hospital (CMRPF1G0201), the Ministry of Science and Technology in Taiwan (MOST 105-2320-B-255-004), and Chang Gung University of Science and Technology (EZRP3FG0071).

## COMPLIANCE WITH ETHICAL STANDARDS

**Conflict of Interest.** The authors declare that they have no conflict of interest.



## REFERENCES

1. Adcock, I.M., and P.J. Barnes. 2008. Molecular mechanisms of corticosteroid resistance. *Chest* 134 (2): 394–401.
2. Gao, P., P.G. Gibson, K.J. Baines, I.A. Yang, J.W. Upham, P.N. Reynolds, S. Hodge, A.L. James, C. Jenkins, M.J. Peters, J. Zhang,

- and J.L. Simpson. 2015. Anti-inflammatory deficiencies in neutrophilic asthma: Reduced galectin-3 and IL-1RA/IL-1 $\beta$ . *Respiratory Research* 16: 5. <https://doi.org/10.1186/s12931-014-0163-5>.
3. Whelan, R., C. Kim, M. Chen, J. Leiter, M.M. Grunstein, and H. Hakonarson. 2004. Role and regulation of interleukin-1 molecules in pro-asthmatic sensitised airway smooth muscle. *The European Respiratory Journal* 24 (4): 559–567.
4. Schwingshack, A., M. Duszyk, N. Brown, and R. Moqbe. 1999. Human eosinophils release matrix metalloproteinase-9 on stimulation with TNF- $\alpha$ . *The Journal of Allergy and Clinical Immunology* 104 (5): 983–989.
5. Wegner, C.D., R.H. Gunde, P. Reilly, N. Haynes, L.G. Letts, and R. Rothlein. 1990. Intercellular adhesion molecule-1 (ICAM-1) in the pathogenesis of asthma. *Science* 247 (26): 456–459.
6. Min, J.K., Y.M. Kim, S.W. Kim, M.C. Kwon, Y.Y. Kong, and I.K. Hwang. 2005. TNF-related activation-induced cytokine enhances leukocyte adhesiveness: Induction of ICAM-1 and VCAM-1 via TNF receptor-associated factor and protein kinase C-dependent NF- $\kappa$ B activation in endothelial cells. *Journal of Immunology* 175 (1): 531–540.
7. Hoesel, B. Schmid, J. A. 2013. The complexity of NF- $\kappa$ B signaling in inflammation and cancer. <https://doi.org/10.1186/1476-4598-12-86>.
8. Fakler, C.R., B. Wu, H.W. McMicken, R.S. Geske, and S.E. Welty. 2000. Molecular mechanisms of lipopolysaccharide induced ICAM-1 expression in A549 cells. *Inflammation Research* 49 (2): 63–72.
9. Neil, S.H., C.C. Matthew, M.C. Lisa, J.B. Peter, and N. Robert. 2004. ICAM-1 expression is highly NF- $\kappa$ B-dependent in A549 cells No role for ERK and p38 MAPK. *European Journal of Biochemistry* 271 (4): 785–791.
10. Pantano, C., J.L. Ather, J.F. Alcorn, M.E. Poynter, A.L. Brown, and A.S. Guala. 2008. Nuclear factor- $\kappa$ B activation in airway epithelium induces inflammation and hyperresponsiveness. *American Journal of Respiratory and Critical Care Medicine* 177 (9): 959–969.
11. Kato, A., and R.P. Schleimer. 2007. Beyond inflammation: Airway epithelial cells are at the interface of innate and adaptive immunity. *Current Opinion in Immunology* 19 (6): 711–720.
12. Jennifer, L.A., R.H. Samantha, M.W. Yvonne, H. Janssen, and E.P. Matthew. 2011. Airway epithelial NF- $\kappa$ B activation promotes allergic sensitization to an innocuous inhaled antigen. *American Journal of Respiratory Cell and Molecular Biology* 44 (5): 631–638.
13. Conti, P., and M. DiGioacchino. 2001. MCP-1 and RANTES are mediators of acute and chronic inflammation. *Allergy and Asthma Proceedings* 22 (3): 133–137.
14. Min, T., D. Yunfei, and H.H. Tai. 2006. Reciprocal regulation of cyclooxygenase-2 and 15-hydroxyprostaglandin dehydrogenase expression in A549 human lung adenocarcinoma cells. *Carcinogenesis* 27 (11): 2170–2179.
15. Liu, W., Q. Liang, S. Balzar, S. Wenzel, M. Gorska, and R. Alam. 2008. Cell-specific activation profile of extracellular signal-regulated kinase 1/2, Jun N-terminal kinase, and p38 mitogen-activated protein kinases in asthmatic airways. *The Journal of Allergy and Clinical Immunology* 12 (4): 893–902.
16. Wei, D., H.P.C. Jasmine, H.W. Chui, P.L. Bernard, and W. Fred. 2004. Anti-inflammatory effects of mitogen-activated protein kinase inhibitor U0126 in an asthma mouse model. *Journal of Immunology* 172 (11): 7053–7059.
17. Diasa, A.M.A., P. Santosa, I.J. Seabraa, R.N.C. Júniorc, M.E.M. Bragaa, and H.C. de Sousaa. 2012. Spilanthol from *Spilantes acmella* flowers, leaves and stems obtained by selective supercritical carbon dioxide extraction. *Journal of Supercritical Fluids* 61: 62–70.
18. Wu, L.C., N.C. Fan, M.H. Lin, I.R. Chu, S.J. Huang, C.Y. Hu, and S.Y. Han. 2008. Anti-inflammatory effect of spilanthol from *Spilantes acmella* on murine macrophage by down regulating LPS-induced inflammatory mediators. *Journal of Agricultural and Food Chemistry* 56 (7): 2341–2349.
19. Wu, S.J. 2015. Osthole attenuates inflammatory responses and regulates the expression of inflammatory mediators in HepG2 cells grown in differentiated medium from 3T3-L1 Preadipocytes. *Journal of Medicinal Food* 18 (9): 972–979.
20. Yumi, Y., and B.G. Richard. 2001. Therapeutic potential of inhibition of the NF- $\kappa$ B pathway in the treatment of inflammation and cancer. *The Journal of Clinical Investigation* 107 (2): 35–42.
21. Richter, E., K. Ventz, M. Harms, J. Mostertz, and F. Hochgräfe. 2016. Induction of macrophage function in human THP-1 cells is associated with rewiring of MAPK signaling and activation of MAP3K7 (TAK1) protein kinase. *Frontiers in Cell and Development Biology*. <https://doi.org/10.3389/fcell.2016.00021>.
22. Moldoveanu, B., P. Otmishi, P. Jani, J. Walker, X. Sarmiento, J. Guardiola, M. Saad, and Y. Jerry. 2009. Inflammatory mechanisms in the lung. *Inflammation Research* 2 (16): 1–11.
23. I-Ta, L. 2013. Chuen-Mao, Y. Inflammatory signalings involved in airway and pulmonary diseases. *Mediat Inflamm*. Article ID 791231, 12 pages
24. Beck, S.B., C. Madjdpour, S. Kneller, U. Ziegler, T. Pasch, and R.P. Wuthrich. 2002. Role of alveolar epithelial ICAM-1 in lipopolysaccharide-induced lung inflammation. *The European Respiratory Journal* 19 (6): 1142–1150.
25. Suter, P.M., S. Suter, E. Girardin, P. Roux-Lombard, G.E. Grau, and J.M. Dayer. 1992. High bronchoalveolar levels of tumor necrosis factor and its inhibitors, interleukin-1, interferon, and elastase, in patients with adult respiratory distress syndrome after trauma, shock, or sepsis. *The American Review of Respiratory Disease* 145 (5): 1016–1022.
26. Park, W.Y., R.B. Goodman, and K.P. Steinberg. 2001. Cytokine balance in the lungs of patients with acute respiratory distress syndrome. *American Journal of Respiratory and Critical Care Medicine* 164 (15): 1896–1903.
27. Prachayasittikul, V., S. Prachayasittikul, S. Ruchirawat, and V. Prachayasittikul. 2013. High therapeutic potential of *Spilantes Acmella*, A Review. *Excli J* 12: 291–212.
28. Kevin, S., D. Delphine, M.C. Megan, M. Elisabeth, and G. Philippe. 2011. The traditional medicine *Spilantes acmella*, and the alkylamides spilanthol and undeca-2E -ene -8,10-diynoic acid isobutylamide, demonstrate in vitro and in vivo anti-malarial activity. *Phytotherapy Research* 25 (7): 1098–1101.
29. Ivones, H., M. Lucia, M. Ioanna, D. Rodrigo, D. Carla, P. Sylvia, M.T. Jorge, and G. Gabino. 2009. Anti-inflammatory effects of ethanolic extract and alkamides-derived from *Heliopsis longipes* roots. *Journal of Ethnopharmacology* 124 (3): 649–652.
30. Witkowska, A.M., and M.H. Borawska. 2004. Soluble intercellular adhesion molecule-1 (sICAM-1):an overview. *European Cytokine Network* 15 (2): 91–98.

## Article

# Chemical Constituents from the Stems of *Tinospora sinensis* and Their Bioactivity

Sio-Hong Lam <sup>1</sup>, Po-Hsun Chen <sup>2</sup>, Hsin-Yi Hung <sup>1</sup>, Tsong-Long Hwang <sup>3,4,5</sup> ,  
Chih-Chao Chiang <sup>6,7,8</sup>, Tran Dinh Thang <sup>9,10</sup>, Ping-Chung Kuo <sup>1,\*</sup>  and Tian-Shung Wu <sup>1,11,\*</sup>

<sup>1</sup> School of Pharmacy, College of Medicine, National Cheng Kung University, Tainan 701, Taiwan; shlam@mail.ncku.edu.tw (S.-H.L.); z10308005@email.ncku.edu.tw (H.-Y.H.)

<sup>2</sup> Department of Biotechnology, National Formosa University, Yunlin 632, Taiwan; pcckuo@gmail.com

<sup>3</sup> Graduate Institute of Natural Products, School of Traditional Chinese Medicine, College of Medicine, Chang Gung University, Taoyuan 333, Taiwan; htl@mail.cgu.edu.tw

<sup>4</sup> Research Center for Chinese Herbal Medicine, Research Center for Food and Cosmetic Safety, Graduate Institute of Health Industry Technology, College of Human Ecology, Chang Gung University of Science and Technology, Taoyuan 333, Taiwan

<sup>5</sup> Department of Anesthesiology, Chang Gung Memorial Hospital, Taoyuan 333, Taiwan

<sup>6</sup> Graduate Institute of Clinical Medical Sciences, College of Medicine, Chang Gung University, Taoyuan 338, Taiwan; moonlight0604@hotmail.com

<sup>7</sup> Supervisor Board, Taoyuan Chinese Medicine Association, Taoyuan 338, Taiwan

<sup>8</sup> Dazhu Fengze Chinese Medicine Clinic, Taoyuan 338, Taiwan

<sup>9</sup> School of Chemistry, Biology and Environment, Vinh University, Vinh City 44000, Vietnam; thangtd@vinhuni.edu.vn

<sup>10</sup> NTT Institute of High Technology, Nguyen Tat Thanh University, Ho Chi Minh City 700000, Vietnam

<sup>11</sup> Department of Pharmacy, College of Pharmacy and Health Care, Tajen University, Pingtung 907, Taiwan

\* Correspondence: z10502016@email.ncku.edu.tw (P.-C.K.); tswu@mail.ncku.edu.tw (T.-S.W.); Tel.: +886-6-2353535 (ext. 6806) (P.-C.K.); +886-6-2757575 (ext. 65333) (T.-S.W.)

Received: 27 August 2018; Accepted: 2 October 2018; Published: 5 October 2018



**Abstract:** Fifty-seven compounds were purified from the stems of *Tinospora sinensis*, including three new compounds characterized as a lignan (**1**), a pyrrole alkaloid (**11**), and a benzenoid (**17**), respectively. Their structures were elucidated and established by various spectroscopic and spectrometric analytical methods. Among the isolates, fifteen compounds were examined for their anti-inflammatory potential in vitro. The results showed that several compounds displayed moderate inhibition of *N*-formyl-methionyl-leucyl-phenylalanine/cytochalasin B (fMLP/CB)-induced superoxide anion generation and elastase release.

**Keywords:** Menispermaceae; lignan; pyrrole alkaloid; superoxide anion generation; elastase release

## 1. Introduction

Inflammation is the first response of the immune system to infection or irritation. Neutrophils play an important role in eliminating most of the exogenous pathogens. Various autoimmune diseases are linked to neutrophil overexpression, such as rheumatoid arthritis, ischemia, and asthma, etc. [1–3]. According to response of diverse stimuli, activated neutrophils will secrete a series of cytotoxins. The superoxide anions and neutrophil elastase are the major secreted products of stimulated neutrophils in infected tissues and organs, which contribute to the destruction of tissue in chronic inflammatory diseases [4–6]. Therefore, inhibition of superoxide anion generation and elastase release by natural compounds is considered to be an effective screening platform to evaluate anti-inflammatory drug candidates.



The genus *Tinospora*, belonging to family Menispermaceae, is composed of more than 20 species all over the tropical regions of the Eastern Hemisphere [7]. This genus is traditionally medical used in Southeast Asian countries for treating malaria, skin diseases, gout, and diabetes [8]. The majority of scientific reports of this genus state their physiological activities including antioxidation, anti-inflammation, and cytotoxicity, especially with the most extensively explored hypoglycemic activity [9–13]. However, the bioactive principles of *T. sinensis* remained poorly understood. Therefore, this plant was selected for study to discover novel anti-inflammatory lead compounds due to their relieving rigidity of muscles and activating collaterals effects in long-term folk medicine usage, which may be related to anti-inflammatory bioactivity. According to the preliminary screening results, the methanol extract of *T. sinensis* collected from Vietnam displayed half maximal inhibitory concentration (IC<sub>50</sub>) values of 6.66 µg/mL and 4.68 µg/mL in the inhibition of superoxide anion generation and elastase release, respectively (Table S1). Further chromatography purification resulted in the characterization of nine lignans (1–9), six pyrrole alkaloids (10–15), seventeen benzenoids (16–32), ten terpenoids (33–42), eight steroids (43–50), four amides (51–54), one coumarin (55), and two others (56–57), respectively. The chemical structures of new compounds 1, 11, and 17 (Figure 1) were established on the basis of nuclear magnetic resonance (NMR) and mass spectrometric analyses. Some of these purified compounds were examined for inhibition of superoxide anion generation and elastase release, thereby evaluating their in vitro anti-inflammatory potentials.

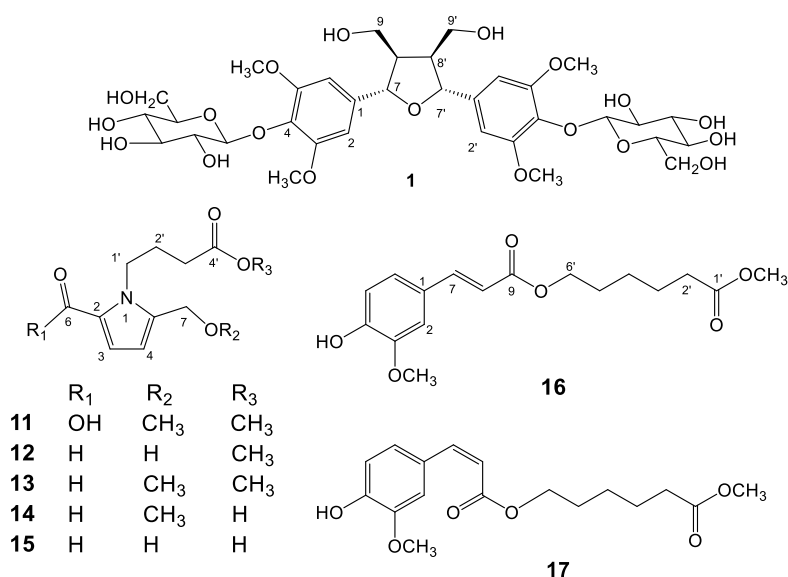


Figure 1. Structures of compounds 1 and 11–17.

## 2. Results and Discussion

The dried stems of *T. sinensis* were refluxed with methanol and the obtained extract was divided into chloroform (CHCl<sub>3</sub>) and water (H<sub>2</sub>O) soluble fractions by liquid–liquid partition. Further purification over silica gel column and preparative thin layer chromatography (pTLC) resulted in the isolation of fifty-seven compounds. Among the isolated compounds, 1, 11, and 17 were new compounds. The other fifty-four known compounds were identified, including eight lignans, (+)-pinosresinol (2) [14], syringaresinol (3) [15], medioresinol (4) [16], (+)-*epi*-syringaresinol (5) [15], (+)-pinosresinol monomethyl ether (6) [17], (+)-glaberride I (7) [18], sesamin (8) [19], and sesaminol (9) [20]; five pyrrole alkaloids, 5-(hydroxymethyl)-1*H*-pyrrole-2-carbaldehyde (10) [21], methyl 4-[formyl-5-(hydroxymethyl)-1*H*-pyrrol-1-yl] butanoate (12) [22,23], methyl 4-[formyl-5-(methoxymethyl)-1*H*-pyrrol-1-yl] butanoate (13) [22,23], 4-[formyl-5-(methoxymethyl)-1*H*-pyrrol-1-yl] butanoic acid (14) [22,23], and 4-[formyl-5-(hydroxymethyl)-1*H*-pyrrol-1-yl] butanoic acid (15) [23]; seventeen benzenoids, rhodiolate (16) [24], methyl ferulate (18) [25], β-hydroxypropiovanillone

(19) [26], 2-methyl-4,5-dimethoxybenzoic acid (20) [27], vanillic acid (21) [28], *p*-hydroxyl phenethanol (22) [29], tachioside (23) [30], icaraside D<sub>2</sub> (24) [31], salidroside (25) [32], syringin (26) [33], cordifolioside A (27) [34], *p*-hydroxybenzoic acid (28) [35], 4-(2-hydroxyethyl)benzoic acid (29) [36], syringic acid-4-*O*- $\alpha$ -L-rhamnoside (30) [37], isovanillic acid (31) [38], syringic acid (32) [39]; ten terpenoids, loliolide (33) [40], abscisic acid (34) [41], 3(17)-phytene 1,2-diol (35) [42], malabarolide (36) [43], lupeol (37) [44], 3-*O*-acetyloleanolic acid (38) [45], cycloeucalenol (39) [46], cycloabyssinone (40) [47], cycloartane-3 $\beta$ ,25-diol (41) [48], and cycloart-22-ene-3 $\beta$ ,25-diol (42) [49]; eight steroids,  $\beta$ -sitosterol (43) [50], stigmasterol (44) [50], 7 $\alpha$ -hydroxysitosterol (45) [51], 7 $\alpha$ -hydroxystigmasterol (46) [51], 6 $\beta$ -hydroxystigmast-4-en-3-one (47) [52], 6 $\beta$ -hydroxystigmasta-4,22-dien-3-one (48) [52], 7-ketositosterol (49) [53], and 3 $\beta$ -hydroxy-stigmasta-5,22-dien-7-one (50) [53]; four amides, 5,6-dimethoxy-*N*-methylphthalimide (51) [54], *N*-*trans*-feruloyldopamine (52) [55], *N*-*trans*-feruloyltyramine (53) [56], *N*-*cis*-feruloyltyramine (54) [57]; and one coumarin, scopoletin (55) [58]; and two others, lichexanthone (56) [59] and 2,6-dimethoxy-*p*-quinone (57) [60], respectively. The chemical structures of these new constituents were determined on the basis of 1D and 2D NMR and mass spectrometric analyses elucidated as follow.

The molecular formula of compound **1** was determined as C<sub>34</sub>H<sub>48</sub>O<sub>19</sub> by high resolution electrospray ionization mass spectrometry (HR-ESI-MS) which showed a quasi-molecular ion peak [M – H – H<sub>2</sub>O]<sup>–</sup> at *m/z* 741.2612. The <sup>1</sup>H and <sup>13</sup>C-NMR spectra (Table 1) revealed the presence of two sets of 1,3,4,5-tetrasubstituted symmetrical aromatic rings [ $\delta_{\text{H}}$  6.66 (H-2, 6, 2', 6') and  $\delta_{\text{C}}$  133.7 (C-1, 1'), 104.2 (C-2, 6, 2', 6'), 152.6 (C-3, 5, 3', 5'), 137.1 (C-4, 4')], two oxymethylenes [ $\delta_{\text{H}}$  4.18 (dd, *J* = 9.0, 6.7 Hz), 3.84 (dd, *J* = 9.0, 3.2 Hz) and  $\delta_{\text{C}}$  71.3 (C-9, 9')], two methines [ $\delta_{\text{H}}$  3.09 (m, H-8, 8') and  $\delta_{\text{C}}$  53.6 (C-8, 8')], two oxymethines [ $\delta_{\text{H}}$  4.66 (brd, *J* = 3.8, H-7, 7') and  $\delta_{\text{C}}$  85.0 (C-9, 9')], and two methoxy groups ( $\delta_{\text{H}}$  3.76 and  $\delta_{\text{C}}$  56.4). The correlation spectroscopy (COSY) spectrum provided key correlations between H-7 ( $\delta_{\text{H}}$  4.66) and H-8 ( $\delta_{\text{H}}$  3.09), and between H-8 ( $\delta_{\text{H}}$  3.09) and methylene H-9 protons ( $\delta_{\text{H}}$  4.18 and 3.84). Its heteronuclear multiple bond correlation (HMBC) spectrum provided further correlations from H-7 to C-1, C-2, C-6, and C-8 suggested the aromatic ring was attached to C-7 (Figure 2). From these spectral information, **1** was indicated as a 2,5-diaryl tetrahydrofuranoid type lignan. Two sets of  $\beta$ -glucopyranosyl unit [ $\delta_{\text{H}}$  4.90 (br d, *J* = 5.2 Hz) and  $\delta_{\text{C}}$  102.6 (G-1, 1'),  $\delta_{\text{H}}$  3.59, 3.40 and  $\delta_{\text{C}}$  102.6 (G-6, 6')] were also observed. The glucosylation shifts at C-9, -9' ( $\delta_{\text{C}}$  71.3) and C-8, -8' ( $\delta_{\text{C}}$  53.6) constructed the location of the glucosyl units at C-9 and C-9' of the aglycone, when compared with unbound C-9 ( $\delta_{\text{C}}$  61.2) and C-8 ( $\delta_{\text{C}}$  54.9) reported in the literature [61]. The relative configurations between C-7 and C-8 (also C-7' and C-8') were established as *trans*-configurations due to no nuclear Overhauser effect (NOE) correlations between H-7 and H-8 (also H-7' and H-8') in the nuclear Overhauser enhancement spectroscopy (NOESY) experiment (Figure 2). Thus, the structure of compound **1** was determined as dihydroxymethylbis(3,5-dimethoxy-4-hydroxyphenyl)tetrahydrofuran-9,9'-*O*- $\beta$ -diglucopyranoside and named trivially as tinosporide A.

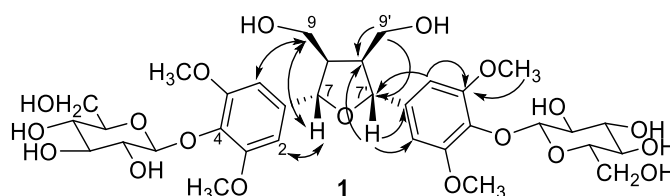


Figure 2. Diagnostic HMBC (→) and NOESY (↔) correlations of compound **1**.

Compounds **11**–**15** all exhibited similar ultraviolet (UV) and infrared (IR) absorption characteristics. Their UV spectra all displayed absorption maxima close to 293 nm, which are characteristic of the pyrrole-2-carbonyl basic skeleton [62]. The <sup>1</sup>H-NMR spectrum (Table 2) exhibited signals for two methine protons at  $\delta_{\text{H}}$  6.16 (d, *J* = 3.9 Hz, H-4) and 7.01 (d, *J* = 3.9 Hz, H-3). Chemical shifts at  $\delta_{\text{C}}$  110.8 (C-4), 119.0 (C-3), 121.6 (C-2), and 136.9 (C-5) in <sup>13</sup>C-NMR spectrum implied the

occurrence of a heterocyclic ring containing a nitrogen atom and their proton coupling constants also indicated the 2,5 di-substituted pyrrole ring (Table 2). The  $^1\text{H}$  and  $^{13}\text{C}$ -NMR spectra of **11** also evidenced the presence of a butanoic acid moiety which appeared at  $\delta_{\text{H}}$  4.37 (br t,  $J = 7.6$  Hz, H-1'), 2.36 (t,  $J = 7.3$  Hz, H-3'), and 2.04 (m, H-2'), confirmed by HMBC correlations from H-3' and H-2' to a carbonyl carbon ( $\delta_{\text{C}}$  173.4, C-4'). The connection of the butanoic acid moiety on the nitrogen atom was suggested by observing long range correlation peaks from  $\delta_{\text{H}}$  4.37 (H-1') to  $\delta_{\text{C}}$  136.9 (C-5) and  $\delta_{\text{C}}$  121.6 (C-2) in the HMBC spectrum (Figure 3). These spectral data clearly determined that a butanoic acid moiety was attached to N-1 of the pyrrole ring. An oxomethylene group connected to C-5 of pyrrole ring was proved by the HMBC correlation of  $\delta_{\text{H}}$  4.43 (H-7) and  $\delta_{\text{C}}$  136.9 (C-5). Two additional methoxy groups ( $\delta_{\text{H}}$  3.34,  $\delta_{\text{C}}$  51.6;  $\delta_{\text{H}}$  3.67,  $\delta_{\text{C}}$  57.7) were also observed and deduced to be located at C-7 and C-4' by HMBC analysis (Figure 3). However, the HR-ESI-MS analytical data was unavailable due to the sample lability. Therefore, the molecular formula of **11** was proposed as  $\text{C}_{12}\text{H}_{17}\text{NO}_5$  according to the above-mentioned NMR spectral analysis and gas chromatograph–mass spectrometer (GC–MS) analytical results which exhibited a molecular ion peak at  $m/z$  255 (see Supplementary Materials). On the basis of these data, the structure of **11** was determined as 1-(4-methoxy-4-oxobutyl)-5-(methoxymethyl)-1*H*-pyrrole-2-carboxylic acid and named trivially as tinosporin A.

Compound **12** displayed very similar  $^1\text{H}$  and  $^{13}\text{C}$ -NMR signals (Table 2) as those of **11** except an additional aldehyde signal ( $\delta_{\text{H}}$  9.42 (s, H-6) and  $\delta_{\text{C}}$  180.9 (C-6)) and one methoxy group ( $\delta_{\text{H}}$  3.66 (s,  $\text{OCH}_3$ ) and  $\delta_{\text{C}}$  52.2 ( $\text{OCH}_3$ )). Its HMBC spectrum exhibited the correlations from methoxy protons to butanoic acid C-4' ( $\delta_{\text{C}}$  175.1), as shown in Figure 3. The molecular formula of **12** was proposed as  $\text{C}_{11}\text{H}_{15}\text{NO}_4$  also based on the GC–MS analytical data of the molecular ion peak at  $m/z$  225 (see Supplementary Materials). Accordingly, the structure of **12** was established as methyl 4-[formyl-5-(hydroxymethyl)-1*H*-pyrrol-1-yl] butanoate. Compound **13** was shown to possess the molecular formula of  $\text{C}_{12}\text{H}_{17}\text{O}_4\text{N}$  by GC–MS measurement. An additional methoxy group ( $\delta_{\text{H}}$  3.36) was observed in **13** by comparison of its  $^1\text{H}$ -NMR spectra with that of **12**. The structure of compound **13** was elucidated as a methyl 4-[formyl-5-(methoxymethyl)-1*H*-pyrrol-1-yl] butanoate. Furthermore, compounds **14** and **15** were determined as 4-[formyl-5-(methoxymethyl)-1*H*-pyrrol-1-yl] butanoic acid and 4-[formyl-5-(hydroxymethyl)-1*H*-pyrrol-1-yl] butanoic acid, respectively, by comparison of their spectral data with those reported [22,23]. According to the above results, pyrrole alkaloids **10**–**15** were reported from *Tinospora* genus for the first time.

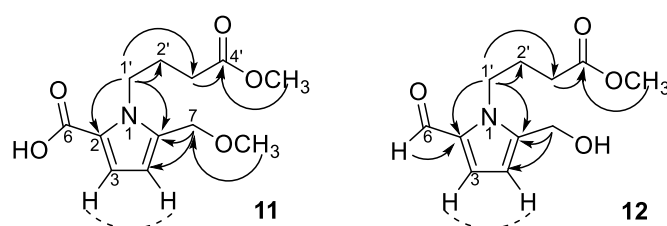


Figure 3. Diagnostic HMBC ( $\rightarrow$ )/COSY ( $\dashrightarrow$ ) correlations of compounds **11** and **12**.

Compounds **16** and **17** showed the same adduct ion peaks and were both assigned the same molecular formula  $\text{C}_{17}\text{H}_{22}\text{O}_6$ . The  $^1\text{H}$ -NMR spectrum of **16** revealed the existence of an aromatic protons at  $\delta_{\text{H}}$  7.07 (dd,  $J = 8.2, 1.8$  Hz, H-6), 7.04 (d,  $J = 1.8$  Hz, H-2), and 6.92 (d,  $J = 8.2$  Hz, H-5); five methylenes at  $\delta_{\text{H}}$  4.19 (t,  $J = 6.6$  Hz, H-6'), 2.34 (t,  $J = 7.4$  Hz, H-2'), 1.67 (m, H-3', 5'), and 1.47 (m, H-4'); and two methoxy singlets at  $\delta_{\text{H}}$  3.95 and 3.67. Additional signals at  $\delta_{\text{H}}$  7.59 (d,  $J = 16.0$  Hz, H-7) and 6.47 (d,  $J = 16.0$  Hz, H-8) suggested the presence of a *trans* double bond. The  $^{13}\text{C}$ -NMR spectrum revealed the existence of seventeen carbon atoms included an aromatic ring ( $\delta_{\text{C}}$  109.3, 112.7, 123.1, 127.0, 146.6, and 147.9), five methylenes ( $\delta_{\text{C}}$  64.0, 33.8, 28.1, 25.3, and 24.5), two methoxyls ( $\delta_{\text{C}}$  55.9 and 51.5), two carbonyls ( $\delta_{\text{C}}$  173.9 and 167.5), and a pair of olefinic carbons ( $\delta_{\text{C}}$  144.8 and 115.5). A 3,4-disubstituted cinnamoyl group linked with a hexanoyl alcohol was deduced from the

NMR data which described above (Table 1). This was further confirmed by the key HMBC correlations from  $\delta_H$  3.67 (OCH<sub>3</sub>) to 173.9 (C-1'), from  $\delta_H$  4.19 (H-6') to  $\delta_C$  167.5 (C-9), and 28.1 (C-5'), as shown in Figure 4. Therefore, compound **16** was confirmed as rhodiolate by comparison of its spectral data with those reported [24]. Compound **17** displayed closely related 1D NMR spectroscopic and mass spectrometric characteristics to **16** and was determined to have a similar structure to **16**. However, a pair of olefinic protons at  $\delta_H$  6.80 (d,  $J = 12.9$  Hz, H-7) and 5.81 (d,  $J = 12.9$  Hz, H-8) suggested the *cis* double bond feature. However, 2D NMR spectral analysis of **17** could not be furnished because of the rapid transformation of *cis*–*trans* double bond. Thus, the structure of compound **17** was concluded to be methyl 6-((Z)-3-(4-hydroxy-3-methoxyphenyl)acryloyloxy)-hexanoate and assigned the trivial name as tinosporin B.

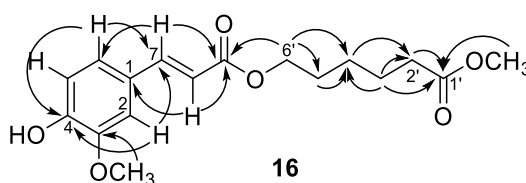


Figure 4. Diagnostic HMBC ( $\rightarrow$ ) correlations of compound **16**.

Table 1. NMR Spectroscopic Data of Compounds **1**, **16**, and **17**.

Position	<b>1</b> <sup>a</sup>			<b>17</b> <sup>b</sup>		<b>16</b> <sup>b</sup>	
	$\delta_H$	$\delta_C$	HMBC (H $\rightarrow$ C)	$\delta_H$	$\delta_H$	$\delta_C$	
1		133.7 s				127.0 s	
2	6.66 s	104.2 d	85.0, 104.2, 137.1, 152.6	7.76 d (1.9)	7.04 d (1.8)	109.3 d	
3		152.6 s				146.6 s	
4		137.1 s				147.9 s	
5		152.6 s		6.88 d (8.3)	6.92 d (8.2)	112.7 d	
6	6.66 s	104.2 d	85.0, 104.2, 137.1, 152.6	7.10 dd (8.3, 1.9)	7.07 dd (8.2, 1.8)	123.1 d	
7	4.66 br d (3.8)	85.0 d	53.6, 71.3, 104.2, 137.1	6.80 d (12.9)	7.59 d (16.0)	144.8 d	
8	3.09 m	53.6 d		5.81 d (12.9)	6.28 d (16.0)	115.5 d	
9	3.84 dd (9.0, 3.2)	71.3 t	53.6, 85.0			167.5 s	
	4.18 dd (9.0, 6.7)		53.6, 85.0, 104.2				
1'		133.7 s				173.9 s	
2'	6.66 s	104.2 d	85.0, 104.2, 137.1, 152.6	2.31 t (7.6)	2.34 t (7.4)	33.8 t	
3'		152.6 s		1.66 m	1.67 m	24.5 t	
4'		137.1 s		1.37 m	1.47 m	25.3 t	
5'		152.6 s		1.66 m	1.67 m	28.1 t	
6'	6.66 s	104.2 d	85.0, 104.2, 137.1, 152.6	4.12 t (6.6)	4.19 t (6.6)	64.0 t	
7'	4.66 br d (3.8)	85.0 d	53.6, 71.3, 104.2, 137.1				
8'	3.09 m	53.6 d					
9'	3.84 dd (9.0, 3.2)	71.3 t	53.6, 85.0				
	4.18 dd (9.0, 6.7)		53.6, 85.0, 104.2				
Bz-OMe	3.76 s	56.4 q		3.93 s	3.95 s	55.9 q	
OMe				3.67 s	3.67 s	51.5 q	
Glc H1, 1'	4.90 d (5.2)	102.6 d	76.5, 74.1				
Glc H2, 2'	3.17 m	76.5 d	74.1				
Glc H3, 3'	3.17 m	74.1 d	76.5				
Glc H4, 4'	3.11 m	69.9 d	76.5				
Glc H5, 5'	3.02 m	77.2 d	69.9				
Glc H6, 6'	3.40 m	60.9 t	77.2				
	3.59 m						

<sup>a</sup> <sup>1</sup>H and <sup>13</sup>C-NMR data measured in deuterated dimethyl sulfoxide (DMSO-*d*<sub>6</sub>) at 500 MHz and 125 MHz, respectively; <sup>b</sup> <sup>1</sup>H and <sup>13</sup>C-NMR data measured in deuterated chloroform (CDCl<sub>3</sub>) at 400 MHz and 100 MHz, respectively.



Fifteen purified compounds were examined for their inhibition bioactivity of superoxide anion generation and elastase release by human neutrophils in response to fMLP/CB (Table S2) [63,64]. However, most displayed weak inhibition percentages at the test concentration (10  $\mu$ M). Among these, **1**, **16**, and **17** displayed higher inhibitions of superoxide anion generation at 10  $\mu$ M with inhibition percentages ranged from  $10.2 \pm 7.1$  to  $20.2 \pm 5.1\%$ . In addition, compound **39** (10  $\mu$ M) also exhibited inhibitory effect on elastase release with inhibition percentage of  $22.3 \pm 10.0\%$  (Table S2). Columbin, an important furanoditerpenoid isolated from several *Tinosporae Radix*, exhibited significant anti-inflammatory activities in a dose-dependent manner [65]. However, based on our research data the related furanoid bisnorditerpenoid, malabarolide (**36**), was not the predominant component, maybe due to the different parts of plant materials. The conventional use of *T. sinensis* in traditional Chinese medicine is for relieving rigidity of muscles and activating collaterals, and the mechanism of action may be related to anti-inflammatory bioactivity. The present experimental data not only suggest that the extracts and purified compounds of the stems of *T. sinensis* have the potential to be developed as novel anti-inflammatory lead drugs or health foods, but also merit further investigation of the anti-inflammatory mechanism.

**Table 2.** NMR spectroscopic data of compounds **11**–**15**.

Position	<b>11</b> <sup>a</sup>		<b>12</b> <sup>b</sup>		<b>13</b> <sup>a</sup>	<b>14</b> <sup>c</sup>	<b>15</b> <sup>c</sup>
	$\delta_{\text{H}}$	$\delta_{\text{C}}$	$\delta_{\text{H}}$	$\delta_{\text{C}}$	$\delta_{\text{H}}$	$\delta_{\text{H}}$	$\delta_{\text{H}}$
2		121.6 s		133.5 s			
3	7.01 d (3.9)	119.0 d	6.98 d (4.0)	126.5 d	6.87 d (4.0)	6.96 d (4.0)	6.97 d (4.0)
4	6.16 d (3.9)	110.8 d	6.26 d (4.0)	111.5 d	6.23 d (4.0)	6.27 d (4.0)	6.25 d (4.0)
5		136.9 s		144.6 s			
6		162.2 s	9.42 s	180.9 d	9.50 s	9.45 s	9.40 s
7	4.43 s	65.8 t	4.63 s	56.4 t	4.45 s	4.52 s	4.65 s
1'	4.37 br t (7.6)	44.7 t	4.38 dd (7.4, 6.0)	45.7 t	4.36 br t (7.6)	4.35 br t (7.6)	4.37 dd (7.5, 6.0)
2'	2.04 m	26.5 t	2.01 m	27.5 t	2.01 m	1.96 m	1.98 m
3'	2.36 t (7.3)	31.0 t	2.35 t (7.3)	31.6 t	2.36 t (7.2)	2.23 t (7.5)	2.27 t (7.5)
4'		173.4 s		175.1 s			
OCH <sub>3</sub>	3.67 s	57.7 q	3.66 s	52.2 q	3.68 s		
CH <sub>2</sub> OCH <sub>3</sub>	3.34 s	51.6 q			3.36 s	3.36 s	

<sup>a</sup> <sup>1</sup>H and <sup>13</sup>C-NMR data measured in <sup>a</sup> CDCl<sub>3</sub> at 400 MHz and 100 MHz; <sup>b</sup> CD<sub>3</sub>OD at 400 MHz and 100 MHz;

<sup>c</sup> CD<sub>3</sub>OD at 500 MHz and 125 MHz, respectively.

### 3. Materials and Methods

#### 3.1. General Information

Optical rotations and UV spectra were measured using a Atago AP-300 digital polarimeter (Atago, Tokyo, Japan) and a GBC Cintra 101 spectrophotometer (GBC Scientific Equipment Ltd., Dandenong, Australia), respectively. IR spectra were obtained with a Shimadzu FT-IR Prestige-21 spectrophotometer (Shimadzu, Kyoto, Japan). <sup>1</sup>H and <sup>13</sup>C-NMR spectra were recorded on Bruker AV 700, AV 500, and Avance III 400 NMR spectrometers (Bruker, Billerica, MA, USA). Chemical shifts are shown in  $\delta$  values (ppm) with tetramethylsilane as an internal standard. GC–MS were analyzed using a Shimadzu GC-2010 gas chromatograph/mass spectrometer equipped with a quadrupole mass analyzer (Shimadzu, Kyoto, Japan). The HR-ESI-MS were taken on a Bruker Daltonics micrOTOF orthogonal ESI-TOF mass spectrometer (Bruker, Billerica, MA, USA). Column chromatography (CC) was performed on silica (70–230 mesh and 230–400 mesh, Merck, Darmstadt, Germany) and Diaion HP-20 (Mitsubishi, Tokyo, Japan) gels, and preparative thin-layer chromatography (TLC) was conducted on Merck precoated silica gel 60 F254 plates (Merck, Darmstadt, Germany), using UV light to visualize the spots. Methanol, chloroform (GR grade), *n*-hexane, ethyl acetate, benzene, and acetone (ACS grade) were purchased from Merck (Darmstadt,

Germany) and Mallinckrodt (St. Louis, MO, USA), respectively. DMSO-*d*<sub>6</sub>, CD<sub>3</sub>OD, and CDCl<sub>3</sub> were purchased from Sigma-Aldrich (St. Louis, MO, USA).

### 3.2. Materials

The stems of *T. sinensis* were collected from Vietnam in August 2009, and the plant material was identified and authenticated by Assoc. Prof. Dr. Vu Xuan Phuong, Institute of Ecology and Biological Resources, Vietnamese Academy of Science and Technology. A voucher specimen (Viet-TSWu-2009-1801-001) was deposited in the herbarium of the Institute of Ecology and Biological Resources, Vietnamese Academy of Science and Technology, Hanoi, Vietnam.

### 3.3. Extraction and Isolation

The dried stems of *T. sinensis* (10 kg) was refluxed with methanol (30 L × 8 × 8 h) and then filtered and concentrated under reduced pressure to obtain the methanol extract (400 g). The extract was suspended in distilled water and successively partitioned with chloroform to yield a chloroform layer (60 g) and water soluble (340 g). The chloroform layer was chromatographed directly on silica gel and eluted with a gradient of *n*-hexane and acetone to afford 10 fractions (CF 1-10). Fractions CF 1, 2, and 4 did not show any significant spots under TLC check and therefore were not purified further. Fraction CF 3 was isolated by CC on silica gel with a step gradient with benzene and acetone mixtures and the subfraction CF 3-6 was further purified by TLC using *n*-hexane-ethyl acetate (50:1) to yield cycloabysynone (**40**, 3 mg). Fraction CF 5 was purified using silica gel CC eluted with gradient mixtures of *n*-hexane and acetone to afford thirteen subfractions (CF 5-1 to 5-13). CF 5-2 was fractionated by silica gel CC eluted with benzene ethyl acetate and then lupeol (**37**, 8 mg), cycloeucalenol (**39**, 15 mg), and a mixture of β-sitosterol (**43**) and stigmasterol (**44**) (364 mg), respectively, was purified from the minor fractions by TLC using *n*-hexane-ethyl acetate (50:1). CF 5-5 was performed on silica gel CC with gradient mixtures of hexane and acetone to produce ten minor fractions. One minor fraction CF 5-5-7 was purified by silica gel CC with mixture of benzene and acetone and further purification by TLC using chloroform-acetone (9:1) yielded a mixture of 7α-hydroxysitosterol (**45**) and 7α-hydroxystigmasterol (**46**) (6 mg). CF 5-7 was subjected to silica gel CC eluted with a gradient mixture of benzene ethyl acetate to afford ten minor fractions. CF 5-7-4 was further isolated by silica gel CC, eluted with hexane ethyl acetate and subsequent TLC using hexane ethyl acetate (6:1) to afford 3-O-acetyloleanolic acid (**38**, 4 mg).

Fraction CF 6 was isolated by silica gel CC by gradient elution with mixture of *n*-hexane and ethyl acetate to result in eleven subfractions (CF 6-1 to 6-11). CF 6-4 was further purified by silica gel CC eluted with *n*-hexane-acetone to produce eight minor fractions (CF 6-4-1 to 6-4-8). Lichexanthone (**56**, 4 mg) was purified by TLC using chloroform-ethyl acetate (100:1) from CF 6-4-3. CF 6-4-4 was subjected to silica gel CC eluted by benzene-acetone gradient mixtures and further purified by TLC using chloroform:acetone (10:1) to afford 2-methyl-4,5-dimethoxybenzoic acid (**20**, 4 mg). CF 6-5 was subjected to silica gel CC with chloroform and methanol gradient mixtures to afford five minor fractions. CF 6-5-2 was isolated by silica gel CC eluted by chloroform:ethyl acetate gradient mixtures and subsequent TLC using hexane-ethyl acetate (10:1) to produce tinosporin A (**11**, 1 mg), 3(17)-phytene 1,2-diol (**35**, 3 mg), cycloart-22-ene-3β,25-diol (**42**, 4 mg), 5,6-dimethoxy-*N*-methyl-phthalimide (**51**, 8 mg), respectively. CF 6-6 was isolated by silica gel CC with chloroform and methanol gradient mixtures and further purified by TLC using hexane:acetone (10:1) to yield methyl 4-[formyl-5-(methoxymethyl)-1*H*-pyrrol-1-yl] butanoate (**13**, 2 mg).

Fraction CF 7 was chromatographed on silica gel column eluted with gradient mixtures of chloroform and ethyl acetate to afford seven subfractions (CF 7-1 to 7-7). CF 7-2 was purified by silica gel CC successively eluted with hexane:acetone, hexane ethyl acetate, and chloroform ethyl acetate and one minor fraction (CF 7-2-5-3) to afford methyl ferulate (**18**, 5 mg). Another minor fraction CF 7-2-5-4 was further isolated by silica gel CC with gradient elution of benzene and acetone, and subsequent purification by TLC using hexane ethyl acetate (5:1) to give rhodiolate (**16**, 2 mg) and tinosporin B

(17, 2 mg). CF 7-3 was also performed silica gel CC eluted with hexane ethyl acetate to afford ten minor fractions, and CF 7-3-7 was further isolated by silica gel CC eluted with hexane-ethyl acetate and subsequent TLC using benzene ethyl acetate (30:1) to afford (+)-pinoresinol monomethyl ether (6, 3 mg). CF 7-4 was isolated by silica gel CC eluted with hexane ethyl acetate to yield ten minor fractions. Of these, CF 7-4-5 was further purified by silica gel CC (hexane-acetone mixing eluents) and subsequent TLC using chloroform:acetone (20:1) to afford cycloartane-3 $\beta$ ,25-diol (41, 16 mg). CF 7-4-6 was also subjected into silica gel CC (hexane:acetone mixing eluents) to give seven minor fractions. Further purification of CF 7-4-6-4, CF 7-4-6-5, and CF 7-4-6-6 by silica gel CC eluted with chloroform:acetone (9:1) to yield loliolide (33, 5 mg), a mixture of 6 $\beta$ -hydroxystigmast-4-en-3-one (47) and 6 $\beta$ -hydroxystigmast-4,22-dien-3-one (48) (2 mg), and a mixture of 7-ketositosterol (49) and 3 $\beta$ -hydroxystigmast-5,22-dien-7-one (50) (6 mg), respectively.

Fraction CF 8 was isolated by silica gel CC eluted with gradient mixtures of hexane and acetone to afford six subfractions (CF 8-1 to 8-6). CF 8-4 was performed silica gel CC eluted with hexane ethyl acetate and further purified by TLC using benzene:acetone (20:1) to give *N-trans*-feruloyldopamine (52, 6 mg). Ten subfractions (CF 9-1 to 9-10) were obtained from CF 9 by silica gel CC eluted with gradient mixture of chloroform and acetone. CF 9-3 was further isolated by silica gel CC, eluted with benzene:ethyl acetate and, following TLC purification of minor fraction CF 9-3-6 using chloroform:acetone (30:1) to afford (+)-pinoresinol (2, 10 mg) and scopoletin (55, 3 mg), CF 9-3-7 was further purified by TLC using chloroform:acetone (10:1) to afford medioresinol (4, 4 mg), (+)-epi-syringaresinol (5, 3 mg), (+)-glaberide I (7, 3 mg), and 2,6-dimethoxy-p-quinone (57, 5 mg), respectively. CF 9-3-8 was isolated by silica gel CC eluted with gradient mixtures of chloroform-methanol and then purified by TLC using chloroform:methanol (300:1) to yield syringaresinol (3, 12 mg). CF 9-4 was divided to eight minor fractions by silica gel CC eluted with benzene:acetone solvent mixture. Of these, CF 9-4-5 was further fractionated by silica gel CC eluted with chloroform:acetone (30:1) to give  $\beta$ -hydroxypropiovanillone (19, 3 mg). CF 9-7 was isolated by silica gel CC (chloroform:acetone gradient mixture) to yield six minor fractions and one of these CF 9-7-4 was afforded *N-trans*-feruloyltyramine (53, 8 mg) and *N-cis*-feruloyltyramine (54, 5 mg) by further silica gel CC eluted with chloroform:acetone (30:1) and subsequent TLC using chloroform:methanol (50:1). The last fraction (CF 10) of the chloroform layer was also purified by silica gel CC eluted with gradient mixture of chloroform and acetone. The resulting subfraction CF 10-5 was divided to several minor fractions by silica gel CC eluted with chloroform:methanol (50:1) solvent mixture and further purified by TLC using chloroform:acetone (10:1) to give abscisic acid (34, 1 mg).

The water soluble fraction was subjected directly to Diaion HP-20 column chromatography, eluted by water and gradient with methanol, to afford seventeen fractions (WF 1-17). Fractions WF 1-5, 9, 11, and 14-16 did not show any significant spots under TLC check and therefore were not purified further. WF 6, 7, and 8 were purified by silica gel CC eluted with gradient mixture of chloroform and methanol and afforded tachioside (23, 10 mg); vanillic acid (21, 5 mg), *p*-hydroxyl phenethanol (22, 3 mg), icariside D<sub>2</sub> (24, 10 mg); and salidroside (25, 10 mg), respectively.

Fraction WF 10 was chromatographed on silica gel column eluted with gradient mixtures of chloroform and methanol to afford six subfractions (WF 10-1 to 10-6). WF 10-2 was purified by silica gel CC eluted with chloroform and methanol and one minor fraction (WF 10-2-3) affording 4-(2-hydroxyethyl)benzoic acid (29, 2 mg). WF 10-3 was also performed silica gel CC eluted with chloroform and methanol solvent mixture to afford ten minor fractions, and WF 10-3-4 was further isolated by silica gel CC eluted with chloroform and acetone (10:1) to afford *p*-hydroxybenzoic acid (28, 5 mg). WF 10-4 was isolated by silica gel CC eluted with chloroform and methanol solvent mixture to yield ten minor fractions. Of these, WF 10-4-5 was further purified by silica gel CC (chloroform:acetone mixing eluents) and subsequent TLC using chloroform:acetone (10:1) to afford 5-(hydroxymethyl)-1*H*-pyrrole-2-carbaldehyde (10, 1 mg). Recrystallization of WF 10-4-7 and 10-4-9 by chloroform:acetone produced syringin (26, 25 mg) and cordifolioside A (27, 30 mg), respectively. WF 10-6 was isolated by silica gel CC eluted with chloroform and methanol solvent mixture to yield

five minor fractions. Of these, WF 10-6-3 was further purified by silica gel CC eluted by chloroform and acetone (9:1) to afford syringic acid-4-*O*- $\alpha$ -L-rhamnoside (**30**, 8 mg).

Fractions WF 12, 13, and 17 were all chromatographed on silica gel column eluted with gradient mixtures of chloroform and methanol to produce several subfractions. WF 12-2 was purified by silica gel CC eluted with chloroform ethyl acetate to afford methyl 4-[formyl-5-(hydroxymethyl)-1*H*-pyrrol-1-yl] butanoate (**12**, 10 mg). Similarly, 4-[formyl-5-(methoxymethyl)-1*H*-pyrrol-1-yl] butanoic acid (**15**, 5 mg) and 4-[formyl-5-(methoxymethyl)-1*H*-pyrrol-1-yl] butanoic acid (**14**, 7 mg) resulted from the chromatographic elution of WF 12-5 and 12-12, respectively. WF 13-1 was isolated by silica gel CC eluted with chloroform and methanol solvent mixture to yield ten minor fractions. Of these, WF 13-1-7 was further purified by silica gel CC (chloroform-acetone mixing eluents) and subsequent TLC using chloroform:acetone (10:1) to syringic acid (**32**, 3 mg). Another subfraction WF 13-3 was further isolated by silica gel CC with gradient elution of chloroform and methanol, and subsequent purification by TLC using chloroform and methanol (9:1) to give isovanillic acid (**31**, 2 mg). Recrystallization of WF 13-4 and 13-13 by chloroform:acetone produced tinosporide A (**1**, 15 mg) and malabarolide (**36**, 10 mg), respectively. WF 17-2 was isolated by silica gel CC eluted with chloroform and methanol (9:1) and further purified by TLC using chloroform:acetone (20:1) to afford sesamin (**8**, 5 mg) and sesamolin (**9**, 2 mg).

**Tinosporide A (1):** colorless powder; UV (MeOH)  $\lambda_{\max}$  (log  $\epsilon$ ) 272 (2.87) nm; IR (neat)  $\nu_{\max}$  3258, 2862, 2358, 1592, 1457, 1418, 1235, 1131, 1045  $\text{cm}^{-1}$ ;  $^1\text{H-NMR}$  (500 MHz, DMSO- $d_6$ ) and  $^{13}\text{C-NMR}$  (125 MHz, DMSO- $d_6$ ), see Table 1; HR-ESI-MS  $m/z$  741.2612 ( $[\text{M} - \text{H} - \text{H}_2\text{O}]^-$ , calcd for  $\text{C}_{34}\text{H}_{45}\text{O}_{18}$ , 741.2611).

**Tinosporin A (11):** Pale yellow syrup; UV (EtOH)  $\lambda_{\max}$ : 319, 293, 220 nm;  $^1\text{H-NMR}$  (700 MHz,  $\text{CDCl}_3$ ) and  $^{13}\text{C-NMR}$  (175 MHz,  $\text{CDCl}_3$ ), see Table 2; GC-MS  $m/z$  255 ( $[\text{M}]^+$ ), 237, 210, 180, 136, 101, 59.

**Tinosporin B (17):** Colorless syrup; UV (MeOH)  $\lambda_{\max}$  (log  $\epsilon$ ): 323 (3.32), 299 (3.18, sh), 235(3.13), 218(3.20) nm; IR (neat)  $\nu_{\max}$ : 3410, 2926, 2853, 1729, 1709, 1632, 1595, 1515, 1464, 1432, 1376, 1270, 1162, 1126, 1033  $\text{cm}^{-1}$ ;  $^1\text{H-NMR}$  (400 MHz,  $\text{CDCl}_3$ ) see Table 1; HR-ESI-MS  $m/z$  345.1311 ( $[\text{M} + \text{Na}]^+$ , calcd for  $\text{C}_{17}\text{H}_{22}\text{O}_6\text{Na}$ , 345.1309).

### 3.4. Anti-inflammatory Bioactivity Examination

#### 3.4.1. Preparation of Human Neutrophils

The use of human neutrophils was approved by the Institutional Review Board at Chang Gung Memorial Hospital, Taoyuan, Taiwan, and the study was conducted according to the Declaration of Helsinki (2013). Written informed consent was obtained from each healthy donor before blood was drawn. The details of the preparation of human neutrophils are provided in the Supplementary Materials.

#### 3.4.2. Measurement of Superoxide Anion Generation and Elastase Release

The assay of the generation of superoxide anion was based on the superoxide dismutase (SOD)-inhibitable reduction of ferricytochrome c. Degranulation of azurophilic granules was determined by elastase release as described previously [63,64]. The details of measurement of superoxide anion generation and elastase release were provided in the Supplementary Materials.

**Supplementary Materials:** The following are available online. S1: Anti-inflammatory bioactivity experimental procedures; Tables S1 and S2: Inhibitory effects of extracts and compounds from *T. sinensis*; Figures S1–S16: NMR spectra of compounds **1**, **11**, **12**, **16**, and **17**.

**Author Contributions:** Conceptualization, P.-C.K. and T.-S.W.; Data curation, S.-H.L.; Investigation, P.-H.C.; Methodology, T.-L.H. and C.-C.C.; Resources, T.-D.T.; Writing—original draft, S.-H.L. and H.-Y.H.; Writing—review & editing, P.-C.K. and T.-S.W. All authors read and approved the final manuscript.

**Funding:** This research is sponsored by the Ministry of Science and Technology (MOST), Taiwan granted to S.-H.L. and T.-S.W. The authors are also thankful for partial financial support from Chang Gung Memorial Hospital (CMRPD1B0281~3, CMRPF1D0442~3, CMRPF1F0011~3, CMRPF1F0061~3 and BMRP450 granted to H.-L.H.).

**Conflicts of Interest:** The authors declare no conflicts of interest.



## References

1. Witko-Sarsat, V.; Rieu, P.; Descamps-Latscha, B.; Lesavre, P.; Halbwachs-Mecarelli, L. Neutrophils: Molecules, functions and pathophysiological aspects. *Lab. Investig.* **2000**, *80*, 617–653. [\[CrossRef\]](#) [\[PubMed\]](#)
2. Okajima, K.; Harada, N.; Uchiba, M. Ranitidine Reduces Ischemia/Reperfusion-Induced Liver Injury in Rats by Inhibiting Neutrophil Activation. *J. Pharmacol. Exp. Ther.* **2002**, *301*, 1157–1165. [\[CrossRef\]](#) [\[PubMed\]](#)
3. Ennis, M. Neutrophils in asthma pathophysiology. *Curr. Allergy Asthma Rep.* **2003**, *3*, 159–165. [\[CrossRef\]](#) [\[PubMed\]](#)
4. Hwang, T.L.; Li, G.L.; Lan, Y.H.; Chia, Y.C.; Hsieh, P.W.; Wu, Y.H.; Wu, Y.C. Potent inhibitors of superoxide anion production in activated human neutrophils by isopedicin, a bioactive component of the Chinese medicinal herb *Fissistigma oldhamii*. *Free Radic. Biol. Med.* **2009**, *46*, 520–528. [\[CrossRef\]](#) [\[PubMed\]](#)
5. Malech, H.L.; Gallin, J.I. Current concepts: Immunology: Neutrophils in human diseases. *N. Engl. J. Med.* **1987**, *317*, 687–694. [\[CrossRef\]](#) [\[PubMed\]](#)
6. Van Eeden, S.F.; Klut, M.E.; Walker, B.A.M.; Hogg, J.C. The use of flow cytometry to measure neutrophil function. *J. Immunol. Methods* **1999**, *232*, 23–43. [\[CrossRef\]](#)
7. Editorial Committee of the Flora of Taiwan. *Flora of Taiwan*, 2nd ed.; Department of Botany, National Taiwan University: Taipei, Taiwan, 1996; Volume 2, p. 605.
8. Krishna, K.L.; Jigar, B.; Jagruti, P. Guduchi (*Tinospora cordifolia*): Biological and Medicinal properties: A review. *Int. J. Altern. Med.* **2009**, *6*, 1–12.
9. Mishra, A.; Kumar, S.; Bhargava, A.; Sharma, B.; Pandey, A.K. Studies on in vitro antioxidant and antistaphylococcal activities of some important medicinal plants. *Cell Mol. Biol.* **2011**, *57*, 16–25. [\[PubMed\]](#)
10. Upadhyay, A.K.; Kumar, K.; Kumar, A.; Mishra, H.S. *Tinospora cordifolia* (Willd.) Hook. f. and Thoms. (*Guduchi*)—validation of the Ayurvedic pharmacology through experimental and clinical studies. *Int. J. Ayurveda Res.* **2010**, *1*, 112–121. [\[CrossRef\]](#) [\[PubMed\]](#)
11. Velazquez, E.A.; Kimura, D.; Torbati, D.; Ramachandran, C.; Totapally, B.R. Immunological response to (1,4)- $\alpha$ -D-glucan in the lung and spleen of endotoxin-stimulated juvenile rats. *Basic Clin. Pharmacol. Toxicol.* **2009**, *105*, 301–306. [\[CrossRef\]](#) [\[PubMed\]](#)
12. Lam, S.H.; Ruan, C.T.; Hsieh, P.H.; Su, M.J.; Lee, S.S. Hypoglycemic Diterpenoids from *Tinospora crispa*. *J. Nat. Prod.* **2012**, *75*, 153–159. [\[CrossRef\]](#) [\[PubMed\]](#)
13. Ruan, C.T.; Lam, S.H.; Lee, S.S.; Su, M.J. Hypoglycemic action of borapetoside A from the plant *Tinospora crispa* in mice. *Phytomedicine* **2013**, *20*, 667–675. [\[CrossRef\]](#) [\[PubMed\]](#)
14. Xie, L.H.; Akao, T.; Hamasaki, K.; Deyama, T.; Hattori, M. Biotransformation of pinoresinol diglucoside to mammalian lignans by human intestinal microflora, and isolation of *Enterococcus faecalis* strain PDG-1 responsible for the transformation of (+)-pinoresinol to (+)-lariciresinol. *Chem. Pharm. Bull.* **2003**, *51*, 508–515. [\[CrossRef\]](#) [\[PubMed\]](#)
15. Chen, C.Y.; Wu, T.Y.; Chang, F.R.; Wu, Y.C. Lignans and kauranes from the stems of *Annona cherimola*. *J. Chin. Chem. Soc.* **1998**, *45*, 629–634. [\[CrossRef\]](#)
16. Deyama, T. The constituents of *Eucommia ulmoides* Oliv. I. Isolation of (+)-medioresinol di-O- $\beta$ -D-glucopyranoside. *Chem. Pharm. Bull.* **1983**, *31*, 2993–2997. [\[CrossRef\]](#)
17. Kitagawa, S.; Nishibe, S.; Benecke, R.; Thieme, H. Phenolic compounds from *Forsythia* leaves. II. *Chem. Pharm. Bull.* **1988**, *36*, 3667–3670. [\[CrossRef\]](#)
18. Kinjo, J.; Higuchi, H.; Fukui, K.; Nohara, T. Lignoids from Albizziae cortex. II. A biodegradation pathway of syringaresinol. *Chem. Pharm. Bull.* **1991**, *39*, 2952–2955. [\[CrossRef\]](#)
19. Jong, T.T.; Jean, M.Y. Constituents of *Houttuynia cordata* and the crystal structure of vomifoliol. *J. Chin. Chem. Soc.* **1993**, *40*, 399–402. [\[CrossRef\]](#)
20. Haslam, E. The stereochemistry of sesamol. *J. Chem. Soc. C* **1970**, *17*, 2332–2334. [\[CrossRef\]](#)
21. Sudhakar, G.; Kadam, V.D.; Bayya, S.; Pranitha, G.; Jagadeesh, B. Total synthesis and stereochemical revision of acortatarins A and B. *Org. Lett.* **2011**, *13*, 5452–5455. [\[CrossRef\]](#) [\[PubMed\]](#)
22. Kim, S.B.; Chang, B.Y.; Hwang, B.Y.; Kim, S.Y.; Lee, M.K. Pyrrole alkaloids from the fruits of *Morus alba*. *Bioorg. Med. Chem. Lett.* **2014**, *24*, 5656–5659. [\[CrossRef\]](#) [\[PubMed\]](#)
23. Chin, Y.W.; Lim, S.W.; Kim, S.H.; Shin, D.Y.; Suh, Y.G.; Kim, Y.B.; Kim, Y.C.; Kim, J. Hepatoprotective Pyrrole Derivatives of *Lycium chinense* Fruits. *Bioorg. Med. Chem. Lett.* **2003**, *13*, 79–81. [\[CrossRef\]](#)

24. Zhou, J.T.; Li, C.Y.; Wang, C.H.; Wang, Y.F.; Wang, X.D.; Wang, H.T.; Zhu, Y.; Jiang, M.M.; Gao, X.M. Phenolic Compounds from the Roots of *Rhodiola crenulata* and Their Antioxidant and Inducing IFN- $\gamma$  Production Activities. *Molecules* **2015**, *20*, 13725–13739. [[CrossRef](#)] [[PubMed](#)]
25. Gopalakrishnan, S.; Subbarao, G.V.; Nakahara, K.; Yoshihashi, T.; Ito, O.; Maeda, I.; Ono, H.; Yoshida, M. Nitrification inhibitors from the root tissues of *Brachiaria humidicola*, a tropical grass. *J. Agric. Food Chem.* **2007**, *55*, 1385–1388. [[CrossRef](#)] [[PubMed](#)]
26. Okuyama, E.; Suzumura, K.; Yamazaki, M. Pharmacologically active components of Todopon Puok (*Fagraea racemosa*), a medicinal plant from Borneo. *Chem. Pharm. Bull.* **1995**, *43*, 2200–2204. [[CrossRef](#)] [[PubMed](#)]
27. Olesch, B.; Böhm, H. Abbau des 2-benzyl-isochinolin-alkaloids sendaverin. *Arch. Pharm.* **1972**, *305*, 222–229. [[CrossRef](#)]
28. Lee, S.Y.; Choi, S.U.; Lee, J.H.; Lee, D.U.; Lee, K.R. A new phenylpropane glycoside from the rhizome of *Sparganium stoloniferum*. *Arch. Pharm. Res.* **2010**, *33*, 515–521. [[CrossRef](#)] [[PubMed](#)]
29. Xu, Q.M.; Liu, Y.L.; Li, X.R.; Feng, Y.L.; Yang, S.L. Two new phenylglycol derivatives isolated from *Syringa reticulata* var. *mandshurica* and their antifungal activities. *Chem. Pharm. Bull.* **2009**, *57*, 863–866. [[PubMed](#)]
30. Zhong, X.N.; Otsuka, H.; Ide, T.; Hirata, E.; Takeda, Y. Hydroquinone diglycoside acyl esters from the leaves of *Myrsine seguinii*. *Phytochemistry* **1999**, *52*, 923–927. [[CrossRef](#)]
31. Miyase, T.; Ueno, A.; Takizawa, N.; Kobayashi, H.; Oguchi, H. Ionone and lignan glycosides from *Epimedium diphyllum*. *Phytochemistry* **1989**, *28*, 3483–3485. [[CrossRef](#)]
32. Kuwajima, H.; Takai, Y.; Takaishi, K.; Inoue, K. Synthesis of  $^{13}\text{C}$ -labeled possible intermediates in the biosynthesis of phenylethanoid derivatives, cornoside and renyosides. *Chem. Pharm. Bull.* **1998**, *46*, 581–586. [[CrossRef](#)]
33. Greca, M.D.; Ferrara, M.; Fiorentino, A.; Monaco, P.; Previtera, L. Antialgal compounds from *Zantedeschia aethiopica*. *Phytochemistry* **1998**, *49*, 1299–1304. [[CrossRef](#)]
34. Maurya, R.; Wazir, V.; Tyagi, A.; Kapil, R.S. Cordifoliosides A and B, two new phenylpropene disaccharides from *Tinospora cordifolia* possessing immunostimulant activity. *Nat. Prod. Lett.* **1996**, *8*, 7–10. [[CrossRef](#)]
35. Chen, C.Y.; Chang, F.R.; Teng, C.M.; Wu, Y.C. Cheritamine, a new *N*-fatty acyl tryptamine and other constituents from the stems of *Annona cherimola*. *J. Chin. Chem. Soc.* **1999**, *46*, 77–86. [[CrossRef](#)]
36. Li, A.; Mishra, Y.; Malik, M.; Wang, Q.; Li, S.; Taylor, M.; Reichert, D.E.; Luedtke, R.R.; Mach, R.H. Evaluation of *N*-phenyl homopiperazine analogs as potential dopamine D3 receptor selective ligands. *Bioorg. Med. Chem.* **2013**, *21*, 2988–2998. [[CrossRef](#)] [[PubMed](#)]
37. Wang, Y.L.; Li, Y.J.; Wang, A.M.; He, X.; Liao, S.G.; Lan, Y.Y. Two new phenolic glycosides from *Inula cappa*. *J. Asian Nat. Prod. Res.* **2010**, *12*, 765–769. [[CrossRef](#)] [[PubMed](#)]
38. Lee, C.K.; Lee, P.H.; Kuo, Y.H. The chemical constituents from the aril of *Cassia fistula* L. *J. Chin. Chem. Soc.* **2001**, *48*, 1053–1058. [[CrossRef](#)]
39. Chang, Y.C.; Chang, F.R.; Wu, Y.C. The constituents of *Lindera glauca*. *J. Chin. Chem. Soc.* **2000**, *47*, 373–380. [[CrossRef](#)]
40. Wada, T. Structure of digiprolactone. *Chem. Pharm. Bull.* **1965**, *13*, 43–49. [[CrossRef](#)] [[PubMed](#)]
41. Saxena, S.; Tripathi, J.; Chatterjee, S.; Gautam, S. Natural predominance of abscisic acid in *Pongamia pinnata* ("Karanj") honey contributed to its strong antimutagenicity. *J. Agric. Food Chem.* **2017**, *65*, 4624–4633. [[CrossRef](#)] [[PubMed](#)]
42. Rodríguez, A.D.; Acosta, A.L. New cembranoid diterpenes and a geranylgeraniol derivative from the common Caribbean sea whip *Eunicea succinea*. *J. Nat. Prod.* **1997**, *60*, 1134–1138. [[CrossRef](#)] [[PubMed](#)]
43. Atta-ur-Rahman; Ahmad, S.; Rycroft, D.S.; Prknyi, L.; Choudhary, M.I.; Clardy, J. Malabarolide, a novel furanoid bisnorditerpenoid from *Tinospora malabarica*. *Tetrahedron Lett.* **1988**, *29*, 4241–4244. [[CrossRef](#)]
44. Fotie, J.; Bohle, D.S.; Leimanis, M.L.; Georges, E.; Rukunga, G.; Nkengfack, A.E. Lupeol long-chain fatty acid esters with antimalarial activity from *Holarrhena floribunda*. *J. Nat. Prod.* **2006**, *69*, 62–67. [[CrossRef](#)] [[PubMed](#)]
45. Kim, N.C.; Desjardins, A.E.; Wu, C.D.; Kinghorn, A.D. Activity of triterpenoid glycosides from the root bark of *Mussaenda macrophylla* against two oral pathogens. *J. Nat. Prod.* **1999**, *62*, 1379–1384. [[CrossRef](#)] [[PubMed](#)]
46. Kocór, M.; St. Pyrek, J. Cyclotrichosantol, a new  $\text{C}_{31}$  31-nortriterpene. *J. Org. Chem.* **1973**, *38*, 3688–3690.
47. Baldé, A.M.; Apers, S.; Claeys, M.; Pieters, L.; Vlietinck, A.J. Cycloabyssinone, a new cycloterpene from *Harrisonia abyssinica*. *Fitoterapia* **2001**, *72*, 438–440. [[CrossRef](#)]

48. Kikuchi, T.; Toyoda, T.; Arimoto, M.; Takayama, M.; Yamano, M. Studies on the neutral constituents of *Pachysandra terminalis* Sieb. et Zucc. I. Isolation and characterization of sterols and triterpenes. *Yakugaku Zasshi* **1969**, *89*, 1358–1366. [[CrossRef](#)] [[PubMed](#)]
49. Öksüz, S.; Shieh, H.L.; Pezzuto, J.M.; Özhatay, N.; Cordell, G.A. Biologically active compounds from the Euphorbiaceae; part 1. Triterpenoids of *Euphorbia nicaeensis* subsp. *glareosa*. *Planta Med.* **1993**, *59*, 472–473.
50. Kuo, Y.H.; Li, Y.C. Constituents of the bark of *Ficus microcarpa* L. f. *J. Chin. Chem. Soc.* **1997**, *44*, 321–325. [[CrossRef](#)]
51. Kimura, Y.; Yasukawa, K.; Takido, M.; Akihisa, T.; Tamura, T. Inhibitory effect of some oxygenated stigmastane-type sterols on 12-O-tetradecanoylphorbol-13-acetate-induced inflammation in mice. *Biol. Pharm. Bull.* **1995**, *18*, 1617–1619. [[CrossRef](#)] [[PubMed](#)]
52. Katsui, N.; Matsue, H.; Hirata, T.; Masamune, T. Phytosterols and triterpenes in roots of the “kidney bean” (*Phaseolus vulgaris* L.). *Bull. Chem. Soc. Jpn.* **1972**, *45*, 223–226. [[CrossRef](#)]
53. Zhang, X.; Geoffroy, P.; Miesch, M.; Julien-David, D.; Raul, F.; Aoudé-Werner, D.; Marchioni, E. Gram-scale chromatographic purification of beta-sitosterol. Synthesis and characterization of beta-sitosterol oxides. *Steroids* **2005**, *70*, 886–895. [[CrossRef](#)] [[PubMed](#)]
54. Chen, J.J.; Tsai, I.L.; Ishikawa, T.; Wang, C.J.; Chen, I.S. Alkaloids from trunk bark of *Hernandia nymphaeifolia*. *Phytochemistry* **1996**, *42*, 1479–1484. [[CrossRef](#)]
55. Tseng, C.F.; Iwakama, S.; Mikajiri, A.; Shibuya, M.; Hanaoka, F.; Ebizuka, Y.; Padmawinata, K.; Sankawa, U. Inhibition of *in vitro* prostaglandin and leukotriene biosyntheses by cinnamoyl- $\beta$ -phenethylamine and *N*-acyldopamine derivatives. *Chem. Pharm. Bull.* **1992**, *40*, 396–400. [[CrossRef](#)] [[PubMed](#)]
56. Hsieh, T.J.; Chang, F.R.; Wu, Y.C. The constituents of *Cananga odorata*. *J. Chin. Chem. Soc.* **1999**, *46*, 607–611. [[CrossRef](#)]
57. Yoshihara, T.; Yamaguchi, K.; Takamatsu, S.; Sakamura, S. A new lignan amide, grossamide, from bell pepper (*Capsicum annuum* var. *grossum*). *Agric. Biol. Chem.* **1981**, *45*, 2593–2598.
58. Bayoumi, S.A.L.; Rowan, M.G.; Beeching, J.R.; Blagbrough, I.S. Constituents and secondary metabolite natural products in fresh and deteriorated cassava roots. *Phytochemistry* **2010**, *71*, 598–604. [[CrossRef](#)] [[PubMed](#)]
59. Harris, T.M.; Hay, J.V. Biogenetically modeled syntheses of heptaacetate metabolites. Alternariol and lichexanthone. *J. Am. Chem. Soc.* **1977**, *99*, 1631–1636. [[CrossRef](#)]
60. Nishina, A.; Hasegawa, K.; Uchibori, T.; Seino, H.; Osawa, T. 2,6-Dimethoxy-p-benzoquinone as an antibacterial substance in the bark of *Phyllostachys heterocycla* var. *pubescens*, a species of thick-stemmed bamboo. *J. Agric. Food Chem.* **1991**, *39*, 266–269. [[CrossRef](#)]
61. Kanchanapoom, T.; Kamel, M.S.; Kasai, R.; Yamasaki, K.; Picheansoonthon, C.; Hiraga, Y. Lignan glucosides from *Acanthus ilicifolius*. *Phytochemistry* **2001**, *56*, 369–372. [[CrossRef](#)]
62. Kim, S.B.; Chang, B.Y.; Jo, Y.H.; Lee, S.H.; Han, S.B.; Hwang, B.Y.; Kim, S.Y.; Lee, M.K. Macrophage activating activity of pyrrole alkaloids from *Morus alba* fruits. *J. Ethnopharmacol.* **2013**, *145*, 393–396. [[CrossRef](#)] [[PubMed](#)]
63. Yang, S.C.; Chung, P.J.; Ho, C.M.; Kuo, C.Y.; Hung, M.F.; Huang, Y.T.; Chang, W.Y.; Chang, Y.W.; Chan, K.H.; Hwang, T.L. Propofol Inhibits Superoxide Production, Elastase Release, and Chemotaxis in Formyl Peptide-Activated Human Neutrophils by Blocking Formyl Peptide Receptor 1. *J. Immunol.* **2013**, *190*, 6511–6519. [[CrossRef](#)] [[PubMed](#)]
64. Yu, H.P.; Hsieh, P.W.; Chang, Y.J.; Chung, P.J.; Kuo, L.M.; Hwang, T.L. 2-(2-Fluoro-benzamido)benzoate ethyl ester (EFB-1) inhibits superoxide production by human neutrophils and attenuates hemorrhagic shock-induced organ dysfunction in rats. *Free Radic. Biol. Med.* **2011**, *50*, 1737–1748. [[CrossRef](#)] [[PubMed](#)]
65. Moody, J.O.; Robert, V.A.; Connolly, J.D.; Houghton, P.J. Anti-inflammatory activities of the methanol extracts and an isolated furanoditerpene constituent of *Sphenocentrum jollyanum* Pierre (Menispermaceae). *J. Ethnopharmacol.* **2006**, *104*, 87–91. [[CrossRef](#)] [[PubMed](#)]

**Sample Availability:** Samples of all the isolated compounds are available from the authors.



© 2018 by the authors. Licensee MDPI, Basel, Switzerland. This article is an open access article distributed under the terms and conditions of the Creative Commons Attribution (CC BY) license (<http://creativecommons.org/licenses/by/4.0/>).



## Dual-targeted casein micelles as green nanomedicine for synergistic phytotherapy of hepatocellular carcinoma

Mona A. Abdelmoneem<sup>a,b</sup>, Mazen Mahmoud<sup>c</sup>, Amira Zaky<sup>c</sup>, Maged W. Helmy<sup>a,d</sup>, Marwa Sallam<sup>b</sup>, Jia-You Fang<sup>e,f,g,\*\*</sup>, Kadria A. Elkhodairy<sup>a,b</sup>, Ahmed O. Elzoghby<sup>a,b,h,i,\*</sup>

<sup>a</sup> Cancer Nanotechnology Research Laboratory (CNRL), Faculty of Pharmacy, Alexandria University, Alexandria 21521, Egypt

<sup>b</sup> Department of Industrial Pharmacy, Faculty of Pharmacy, Alexandria University, Alexandria 21521, Egypt

<sup>c</sup> Department of Biochemistry, Faculty of Science, Alexandria University, Alexandria 21511, Egypt

<sup>d</sup> Department of Pharmacology and Toxicology, Faculty of Pharmacy, Damanhur University, Damanhur, Egypt

<sup>e</sup> Pharmaceutics Laboratory, Graduate Institute of Natural Products, Chang Gung University, Taoyuan 333, Taiwan

<sup>f</sup> Research Center for Industry of Human Ecology, Research Center for Chinese Herbal Medicine, Chang Gung University of Science and Technology, Kweishan, Taoyuan 333, Taiwan

<sup>g</sup> Department of Anesthesiology, Chang Gung Memorial Hospital, Kweishan, Taoyuan 333, Taiwan

<sup>h</sup> Division of Engineering in Medicine, Department of Medicine, Brigham and Women's Hospital, Harvard Medical School, Boston, MA 02115, USA

<sup>i</sup> Harvard-MIT Division of Health Sciences and Technology, Cambridge, MA 02139, USA

### ARTICLE INFO

#### Keywords:

Green nanomedicine  
Hepatocellular carcinoma  
Casein micelles  
Dual-targeting  
Lactobionic acid  
Folic acid

### ABSTRACT

In recent years, green nanomedicines have made transformative difference in cancer therapy researches. Herein, we propose dual-functionalized spray-dried casein micelles (CAS-MCs) for combined delivery of two phytochemicals; berberine (BRB) and diosmin (DSN) as targeted therapy of hepatocellular carcinoma (HCC). The nanomicelles enabled parenteral delivery of the poorly soluble DSN via its encapsulation within their hydrophobic core. Moreover, sustained release of the water soluble BRB was attained by hydrophobic ion pairing with sodium deoxycholate followed by genipin crosslinking of CAS-MCs. Dual-active targeting of MCs, via conjugating both lactobionic acid (LA) and folic acid (FA), resulted in superior cytotoxicity and higher cellular uptake against HepG2 cells compared to single-targeted and non-targeted CAS-MCs. The dual-targeted DSN/BRB-loaded CAS-MCs demonstrated superior in vivo anti-tumor efficacy in HCC bearing mice as revealed by down regulation of cell necrosis markers (NF- $\kappa$ B and TNF- $\alpha$ ), inflammatory marker COX2, inhibition of angiogenesis and induction of apoptosis. Histopathological analysis and immunohistochemical Ki67 staining confirmed the superiority of the dual-targeted micelles. Ex-vivo imaging showed preferential liver-specific accumulation of dual-targeted CAS-MCs. Overall, this approach combined the benefits of traditional herbal medicine with nanotechnology via LA/FA-CAS-MCs loaded with BRB and DSN as a promising nanoplatform for targeted HCC therapy.

### 1. Introduction

Hepatocellular carcinoma (HCC) is the sixth most common cancer and the third cause of cancer-induced mortality in the world [1]. Patients with early HCC should be considered for curative treatments including surgical resection, liver transplantation, and percutaneous ablation that may cause complete cure and increase the patient survival [2]. Unfortunately, the patients with advanced progressive disease

accounts for > 80%, where only palliative approaches are suitable. The most commonly used therapeutic approach is the systemic chemotherapy for improving the survival of HCC-patients. However, conventional chemotherapeutic agents have many challenges in treatment of HCC due to their severe side effects and multidrug resistance [3].

Recently, green chemotherapy in combination with tumor-targeted nanocarriers have attracted much interest to enhance the efficacy and overcome the challenges of conventional chemotherapy [4].

\* Correspondence to: A.O. Elzoghby, Division of Engineering in Medicine, Department of Medicine, Brigham and Women's Hospital, Harvard Medical School, Boston, MA 02115, USA.

\*\* Correspondence to: J.-Y. Fang, Graduate Institute of Natural Products, Chang Gung University, Taoyuan 333, Taiwan.

E-mail addresses: [fajy@mail.cgu.edu.tw](mailto:fajy@mail.cgu.edu.tw) (J.-Y. Fang), [aelzoghby@bwh.harvard.edu](mailto:aelzoghby@bwh.harvard.edu) (A.O. Elzoghby).

<sup>1</sup> Division of Engineering in Medicine, Department of Medicine, Brigham and Women's Hospital, Harvard Medical School, Boston, MA 02115, USA

<sup>2</sup> Harvard-MIT Division of Health Sciences and Technology, Cambridge, MA 02139, USA

<https://doi.org/10.1016/j.jconrel.2018.08.026>

Received 21 April 2018; Received in revised form 22 July 2018; Accepted 16 August 2018

Available online 20 August 2018

0168-3659/ © 2018 Elsevier B.V. All rights reserved.



Accordingly, in our study, green phytochemistry was developed by co-encapsulating two phytochemicals with potential anti-cancer effects, diosmin (DSN) and berberine (BRB), in natural protein micelles for treatment of HCC [5–8]. DSN (diosmetin 7-O-rutinoside), a natural flavone glycoside, is known as a potent chemopreventive agent against hepatocarcinogenesis. It is reported as a supportive treatment for many cancer types such as hepatocellular and bladder with advantages of less toxicity and lower cost in comparison with cytotoxic chemotherapy [9]. DSN reduces tumor promotion through inhibiting the proliferation markers and also suppresses the expression of inflammatory markers such as COX-2 and iNOS through knock-down of NF- $\kappa$ B expression in HCC-induced rats [10]. Another herbal drug, berberine chloride (BRB), is an isoquinoline alkaloid with the ability to selectively reduce the viability of HCC cells without affecting normal hepatocytes. BRB has been shown to effectively induce cell cycle arrest at the G1/S phase [11]. Moreover, it causes autophagic death of hepatoma cells through inhibiting the expression of the anti-apoptotic factor Bcl-2 and knock-down of mTOR-signaling [12].

Combination strategies play a crucial role in cancer therapy, wherein multi-target therapy combines a cocktail of drugs, or other novel agents having different mechanisms of action. Based on the reported anticancer effects of DSN and BRB and their pharmacological pathways for the inhibition of liver cancer cells [10,12], we aimed to combine both natural phyto-medicines in a dual-targeted nano-formulation for targeting HCC.

Hence, single-targeted drug carriers may have unsatisfactory therapeutic responses due to the inefficient specific ligand-receptor interaction with the target tumor cells. For instance, HCC-patients usually suffer reduced binding efficacy for ASGPR-based single targeted therapy mainly because of the down-regulation of asialoglycoprotein receptors (ASGPRs) by hepatoma cells [13]. Therefore, in our study, we successfully developed dual-targeted CAS micelles using LA and FA as ligands for targeting ASGPR and FA-R, respectively.

However, DSN has poor solubility in water and most organic solvents resulting in its poor bioavailability [14]. On the other hand, BRB has aqueous solubility of 1 mg/ml, showing high initial burst release in water and aqueous buffers. To avoid premature berberine drug release in to circulation before reaching the tumor site it would be beneficial to develop an efficient controlled release nanoformulation. Therefore, novel tumor-targeted delivery systems are needed to enable i.v. administration of DSN and controlled release of BRB and enhance tumor-targeting efficiency resulting in decreased toxicity and improved clinical utility of both drugs. Among naturally occurring protein nanocarriers, casein (CAS), the major milk protein, has high self-assembling tendency into spherical nano-size micelles [15,16]. CAS micelles were successfully harnessed for delivering hydrophobic anticancer drugs including mitoxantrone, paclitaxel, and cisplatin [17]. In our laboratory, cross-linked CAS micelles have been successfully developed allowing controlled drug release via modulating the crosslinking density [18,19]. Recently, we have developed phospholipid bilayer-enveloped CAS micelles for combined delivery of the herbal drug resveratrol and the fungal-derived monascus yellow pigments as green therapy of breast cancer [20].

In this study, we propose LA/FA dual-targeted CAS micelles co-loaded with DSN and BRB as a completely green therapy of HCC. First, to overcome the high hydrophobicity and enable injection of the poorly soluble drug DSN, pH modulated loading approach was utilized to entrap the drug within micellar core. Second, to reduce the initial burst of BRB and prolong its release, both hydrophobic ion pairing with SDC and micellar crosslinking with genipin were exploited to increase the drug lipophilicity and hence facilitate its incorporation within the hydrophobic core of micelles. Third, both drugs were co-encapsulated within CAS micelles for improving their anti-tumor efficacy. Finally, for maximal tumor-targeting, the surface of CAS MCs was functionalized with LA and FA for respectively targeting asialoglycoprotein and folic acid receptors overexpressed HCC cells while reducing non-specific

uptake by normal hepatocytes. The developed delivery system was thoroughly investigated *in vitro* and *in vivo* to prove the anti-tumor superiority of the combined drug nanocarriers compared with free drugs.

## 2. Materials and methods

### 2.1. Materials

Casein (CAS), berberine hydrochloride (BRB), sodium deoxycholate (SDC), lactobionic acid (LA), N-hydroxysuccinimide (NHS), N-(3-dimethylaminopropyl)-N-ethyl carbodiimide hydrochloride (EDC), fetal bovine serum (FBS), 3-(4,5-dimethylthiazolyl-2)-2,5-diphenyltetrazolium bromide (MTT), bovine serum albumin, rhodamine B isothiocyanate (RBITC), dimethyl sulfoxide (DMSO), ethylene diamine tetraacetic acid (EDTA), Triton X100, haematoxylin solution, and eosin solution were from Sigma-Aldrich Co. Ltd., (USA). Folic acid (FA), genipin (GEN), diosmin were purchased from Xi'an Natural Field Bio-Technique Co., Ltd., (China). 1,1'-Diocetadecyl-3,3',3'-Tetramethylindocarbocyanine Perchlorate (DiI C<sub>18</sub>(3)) was obtained from Thermo Fisher Scientific (MA, USA). DPX mounting medium was obtained from Loba Chemie Pvt. Ltd. (Mumbai, India). Absolute ethanol, methanol, tertiary butyl alcohol (TBA) and orthophosphoric acid were from ADWIC Pharmaceutical Chemicals Co., (Cairo, Egypt). Methanol HPLC grade was obtained from JT Baker (Phillipsburg, NJ, USA). Human HepG2 liver cancer cells were supplied by the American Type Culture Collection (ATCC).

### 2.2. Preparation and characterization of BRB/SDC ion-pair complex

BRB-SDC complex was prepared via hydrophobic ion pairing technique [21]. An equimolar concentration of BRB. HCl and SDC were mixed with constant stirring for 30 min followed by centrifugation (3–30 KS Sigma, Germany) at 17000 rpm for 45 min, and lyophilization of the precipitate (Cryodos-50 lyophilizer, Telstar, Spain). The degree of BRB complexation was calculated by following equation:

%Complexation

$$= \frac{\text{Total amount of BRB added} - \text{amount of BRB in supernatant}}{\text{Total amount of BRB}} \times 100 \quad (1)$$

For determination of the drug content and uniformity of BRB-SDC complex, 10 mg of the complex was dissolved in 10 ml methanol and the solution was analyzed by HPLC method at 345 nm detailed in the supplementary section. The procedure was repeated three times to ensure the homogeneity of the complex [22].

### 2.3. Preparation & characterization of dual-targeted LA/FA-CAS conjugate

#### 2.3.1. For preparation of galactosylated casein (LA-CAS)

43 mg (0.12 mmol) LA was dissolved in 2 ml of purified water, 28 mg EDC and 17 mg NHS were added (LA:EDC:NHS; molar ratio 1:1.2:1.2) and stirred for 1 h [23]. Subsequently, 300 mg CAS was dissolved in 0.1 N NaOH solution, pH of solution was adjusted to 6.5 then added to activated LA solution followed by stirring for 24 h at room temperature. The mixture was dialyzed (12–14 kDa MWCO VISKING dialysis tubing, SERVA, Germany) against 0.2% sodium azide aqueous solution for 48 h. The product conjugate was purified by filtration, then lyophilized.

#### 2.3.2. For preparation of folic acid-conjugated casein (FA-CAS)

FA (53 mg, 0.12 mmol) was dissolved in 5 ml of 100 mM NaHCO<sub>3</sub> buffer, 60 mg EDC and 40 mg NHS were then added (FA:EDC:NHS molar ratio 1:2.4:2.4) [24]. After 1 h of activation, 300 mg CAS was dissolved in 0.1 N NaOH solution (pH adjusted to 6.5) was added to the

activated FA solution followed by stirring for 24 h at room temperature to allow conjugation of FA to CAS molecules. The mixture was purified and dried following the procedure described in the previous [Section 2.3.1](#).

### 2.3.3. For preparation of LA/FA-CAS conjugate

FA was activated by the same method described above and the resultant solution was added to LA-CAS solution followed by stirring for 24 h at room temperature to allow FA conjugation to LA-CAS molecules. The mixture was purified and dried following the procedure described above.

### 2.3.4. Galactose & folate content determination

Galactose content of LA-CAS conjugate was quantified by phenol/sulfuric acid method [25]. Briefly, 1 ml of 5% phenol solution was added to 1 ml aqueous solution of LA-CAS conjugate, followed by addition of 5 ml conc. Sulfuric acid and then kept at 25 °C for 20 min. For determination of galactose content, the absorbance of conjugate sample was measured at 490 nm based on a standard calibration curve developed using pure galactose. FA content of FA-CAS conjugate was determined spectrophotometrically at 364 nm by indirect method in the dialysate [26].

### 2.4. Preparation of non-targeted & dual-targeted BRB/SDC-DSN-loaded CAS MCs

Ten milligram DSN were added to 1% w/v CAS solution dissolved in 0.1 N NaOH followed by the addition of 5 ml methanol containing BRB or BRB-SDC (eq. to 15 mg). This solution was stirred for 2 h after which methanolic solution of genipin was added (2.5 or 5 mM). The solution was stirred till methanol evaporate, followed by pH adjustment to 9.5. The resultant micellar dispersion was then spray-dried using Büchi B-290 Mini-Spray Dryer (Flawil, Switzerland), equipped with a high-performance cyclone, with inlet temperature of 100 °C, outlet temperature of 50 °C, aspiration air of 90%, feed flow of 5 ml/min, spraying pressure of 5.0–5.8 mbar, and air flow rate of 320 l/h [18]. The spray-dried micelles were stored in a desiccator at 25 °C till further use. Dual-targeted LA/FA-CAS MCs were prepared following the same procedure described in [Section 2.4](#) except using LA/FA-CAS instead of CAS.

### 2.5. Physicochemical characterization of dual-drug loaded CAS MCs

The methodologies for assessing nanoparticle size and zeta potential [27], drug incorporation efficiency [28], FTIR spectra and DSC thermograms [29], drug release [30], morphology [31], hemolytic and serum stability [32,33] were performed as described previously and detailed in the Supporting Information.

### 2.6. In vitro cytotoxicity and uptake studies

The in vitro cytotoxicity of free BRB, free DSN, free BRB/DSN solution and different dual-drug loaded CAS-MCs against HepG2 human liver cancer cells were evaluated by MTT assay performed as described [34] and detailed in the Supporting Information. Combination Index (CI) and Dose Reduction Index (DRI) were calculated using CompuSyn software (version 1) to ensure the superiority of different nano-micelles compared to the free combination. Cellular uptake of (RBITC)-labeled targeted, non-targeted CAS-MCs and free dye into HepG2 liver cancer cells was evaluated using confocal microscopy as described previously [35] and detailed in the Supporting Information.

### 2.7. In vivo studies

#### 2.7.1. Animals

The anti-tumor efficacy of different dual-drug loaded CAS MCs were evaluated compared to free DSN, free BRB and BRB/DSN solution on

tumor-bearing mice housed in stainless steel mesh cages following standard protocol mentioned in the Supporting Information.

#### 2.7.2. HCC-induction in mice

The induction of HCC in mice was achieved chemically using diethyl nitrosamine (DEN) via weekly intraperitoneal (i.p.) injection for 6 weeks (at a dose 75 mg/kg for the first 3 weeks and followed by 100 mg/kg for another 3 weeks) as described and mentioned in the Supporting Information [36].

#### 2.7.3. In vivo anti-tumor efficacy

The in vivo anti-tumor efficacy was evaluated by dividing the animals randomly into nine groups (7 mice/group). The groups included negative control (healthy normal mice injected with saline), positive control (DEN-induced HCC mice), free BRB, free DSN, free combined BRB-DSN solution, combined dual drug-loaded non-targeted CAS-MCs, LA-CAS-MCs, FA-CAS-MCs and LA-FA-CAS-MCs treated groups. The HCC-induced mice were injected i.v. into the tail vein with the drugs either free or micelles eq. to 10 mg/kg BRB and 8 mg/kg DSN three times weekly for three weeks. Body weights were monitored throughout the treatment period. All the animals were sacrificed after treatment for 21 days. The excised livers were weighed and used for evaluation of tumor growth biomarkers and histopathological studies.

#### a) RT-PCR analysis of liver tissues

Semiquantitative RT-PCR was exploited to assess mRNA expression levels of COX-2, VEGF, TNF- $\alpha$  and NF- $\kappa$ B. The experimental method is detailed in the Supporting Information

#### b) Enzyme-linked immunosorbent assay (ELISA) of liver tissues

The tumor growth biomarkers were determined quantitatively using ELISA. The experimental method is detailed in the Supporting Information.

#### c) Histopathological and immunohistochemical analysis

The tumor samples were examined for histopathological changes as well as proliferation extent. The experimental method is detailed in the Supporting Information [37].

#### d) Measurement of serum hepatotoxicity markers

The serum hepatotoxicity markers including alanine aminotransferase (ALT) and aspartate aminotransferase (AST) were evaluated. The experimental method is detailed in the Supporting Information [38].

#### 2.7.4. Ex-vivo imaging of isolated livers

Three groups (each of 6) of tumor bearing mice were distinctively administered DiI C<sub>18</sub>(3) labeled non-targeted and dual-targeted CAS-MCs and free DiI C<sub>18</sub>(3) in physiological saline solution at a dose equivalent to 1 mg/kg body weight via tail vein injection [39]. At predetermined post-administration time points, the mice were sacrificed and excised livers were imaged using in vivo photon imager (Biospace lab, France).

### 2.8. Statistical analysis

Data analysis is detailed in the Supporting Information.

### 3. Results and discussion

#### 3.1. Fabrication & physicochemical characteristics of CAS MCs

By virtue of the hydrophobic and hydrophilic amino acids composing its structure, the amphiphilic nature of CAS induces its self-assembly into spherical micelles (CAS-MCs) [17]. Therefore, CAS MCs were successfully used to enable solubilization and i.v. injection of poorly soluble anti-cancer drugs by incorporation within their hydrophobic core. In our study, BRB and DSN were co-loaded into CAS-MCs via different mechanisms. First, for encapsulation of the poorly soluble DSN, the drug was solubilized together with CAS at alkaline pH followed by adjusting the working pH of CAS/DSN solution to 9.5, the lowest pH ensuring DSN is still soluble thus allowing its incorporation into the hydrophobic core of CAS-MCs. On another avenue, for entrapment of BRB, the carboxylic and phosphate groups of CAS become negatively charged at the preparation pH 9.5 (above isoelectric point pI of CAS 4.6–4.8), and hence can electrostatically interact the positively charged quaternary ammonium group of BRB. Thus, BRB was efficiently bound to CAS mainly via electrostatic interactions between the cationic drug molecules and the negatively charged CAS ones. Moreover, the hydrophobic binding between the remaining structure of BRB and the micellar core may be also involved. Similar results were observed for alfuzosin-loaded CAS MCs [40]. After spray-drying, the drug content was found to be 55.0 and 63.0% for BRB and DSN, respectively (Table 1, Fig. 1).

The spray-dried dual-drug loaded CAS-MCs exhibited a particle size of 186.7–295.4 nm with a relatively high polydispersity (0.34–0.45) which is in agreement with the previously reported size and composition of CAS micelles (50–500 nm) (Table 1) [40,41]. The micelles were negatively charged with a zeta potential range of  $-22$  to  $-29.6$  mV by virtue of the ionized carboxylic groups indicating a good colloidal stability (Table 1). These findings are in agreement with that reported for mitoxantrone loaded- $\beta$ -CAS micelles [41].

The release of DSN and BRB from spray-dried CAS-MCs in PBS (pH 7.4) at 37 °C is shown in Fig. 2a and b, respectively. Incorporation of the water insoluble DSN into the hydrophobic core of CAS-MCs enables its dispersion in a solubilized aqueous form; a property essential for its i.v. administration. This resulted in enhancement of its release where 23% of DSN was released from CAS MCs after 24 h compared to only 3.5% of pure DSN (Fig. 2a). In contrast, free BRB exhibited a fast release up to about 100% of the initial dose after only one hr, due to its water-soluble nature (1 mg/ml). Incorporation of BRB in CAS-MCs did not result in marked retardation of its release with about 70% was released after 2 h (Fig. 2b).

#### 3.2. Hydrophobic ion pairing

Among the approaches adopted for controlled release of water soluble drugs, hydrophobic ion-pairing (HIP) complex is developed via electrostatic interactions between ionizable drug groups with oppositely charged moieties of ion pairing agent (e.g. surfactant or polymer).

BRB has quaternary ammonium group making it a permanently positively charged compound irrespective to the pH of the medium. This allows its complexation with the negatively charged carboxylic group of sodium deoxycholate (SDC) without the need for specific pH adjustment [22]. Therefore, mixing equimolar concentrations of both BRB and SDC resulted in complex formation with 80% complexation efficiency and 60% w/w yield after freeze-drying.

The formed BRB-SDC HIP was observed to be highly soluble in organic solvents while practically insoluble in water. Therefore, BRB-SDC could be efficiently encapsulated into the hydrophobic core of CAS MCs (F2) with incorporating efficiency of 65.0 and 62.90% for BRB and DSN, respectively and a size of 225.6 nm (Table 1). Similar increase in entrapment of the water soluble drugs leuprolide acetate into PLGA microspheres and insulin into PLGA nanoparticles was reported upon HIP complexation with sodium oleate [42], and sodium deoxycholate (SDC) [43], respectively. Moreover, loading of BRB-SDC HIP complex into CAS MCs has significantly reduced the burst release of BRB from 70.0 to 57.0% in the first 2 h (Fig. 2b). However, further sustained drug release was still required to reside within the micellar system for a longer period and reach its target site of action.

#### 3.3. Crosslinking of CAS MCs

To further reduce the burst release of BRB, CAS MCs were cross-linked with genipin, a much less cytotoxic herbal crosslinker ( $\sim 10,000$  times less than glutaraldehyde). Genipin was reported to crosslink two free lysine amino groups of CAS macromolecule [40,44,45]. Upon adding genipin solution, the color of CAS micellar solution changed gradually from yellow to brown and finally to dark blue (Fig. S1). CAS MCs crosslinked using 2.5 (F3) and 5 mM (F4) genipin demonstrated size of 295.4 and 197.0 nm, respectively. Crosslinking of CAS-MCs with 2.5 and 5 mM genipin reduced the burst release of BRB from 57 to 45 and 30% after 2 h, respectively. After 24 h, 80.44% of BRB was released from un-crosslinked CAS-MCs (F2) compared to 55.5 and 45% from 2.5 mM (F3) and 5 mM (F4), genipin-crosslinked ones, respectively (Fig. 2b). At higher genipin concentration, the increased degree of protein crosslinking resulted in slower protein degradation and less available free space for drug diffusion [40]. Accordingly, the release behavior could be modulated by varying the degrees of micelles crosslinking.

#### 3.4. Decoration of CAS MCs with LA and FA

The surface of CAS was dually modified with galactose residues and FA to enhance the targeted delivery of BRB and DSN to liver cancer cells. The modification was accomplished through simple carbodiimide amidation reaction between amino groups of CAS and carboxylic groups of both LA [23] and FA [46]. To confirm the conjugation of FA to CAS MCs, UV spectra of FA, CAS MCs and FA-CAS MCs were recorded. As shown in Fig. S2, FA spectrum exhibited its characteristic peaks at 285 and 364 nm while the spectrum of CAS MCs showed only the characteristic protein peak at 280 nm. On the other hand, the

**Table 1**  
Composition and physicochemical characteristics of drug-loaded CAS MCs.

Formula	Genipin (mM)	Particle size (nm)	PDI	Zeta-potential (mv)	% Incorporation efficiency		% Yield
					BRB	DSN	
F1 BRB/DSN-CAS MCs	–	253.1 $\pm$ 0.38	0.340	$-26 \pm 0.23$	55.0	63.0	82.3
F2 BRB-SDC/DSN-CAS MCs	–	225.6 $\pm$ 0.23	0.391	$-26.9 \pm 0.36$	65.0	62.9	83.8
F3 BRB-SDC/DSN-CAS MCs	2.5	295.4 $\pm$ 0.36	0.310	$-26.0 \pm 0.41$	65.3	68.9	80.9
F4 BRB-SDC/DSN-CAS MCs (Non-targeted CAS MCs)	5	197.0 $\pm$ 0.50	0.346	$-27.9 \pm 0.20$	67.0	63.6	80.8
F5 BRB-SDC/DSN/LA-CAS MCs (LA-CAS MCs)	5	215.4 $\pm$ 0.42	0.380	$-22 \pm 0.50$	62.9	62.7	80.5
F6 BRB-SDC/DSN/FA-CAS MCs (FA-CAS MCs)	5	186.7 $\pm$ 0.70	0.327	$-26.9 \pm 0.40$	68.5	64.0	85.0
F7 BRB-SDC/DSN/LA-FA-CAS MCs (LA-FA CAS MCS)	5	208.3 $\pm$ 0.23	0.322	$-29.6 \pm 0.30$	65.6	63.0	87.7



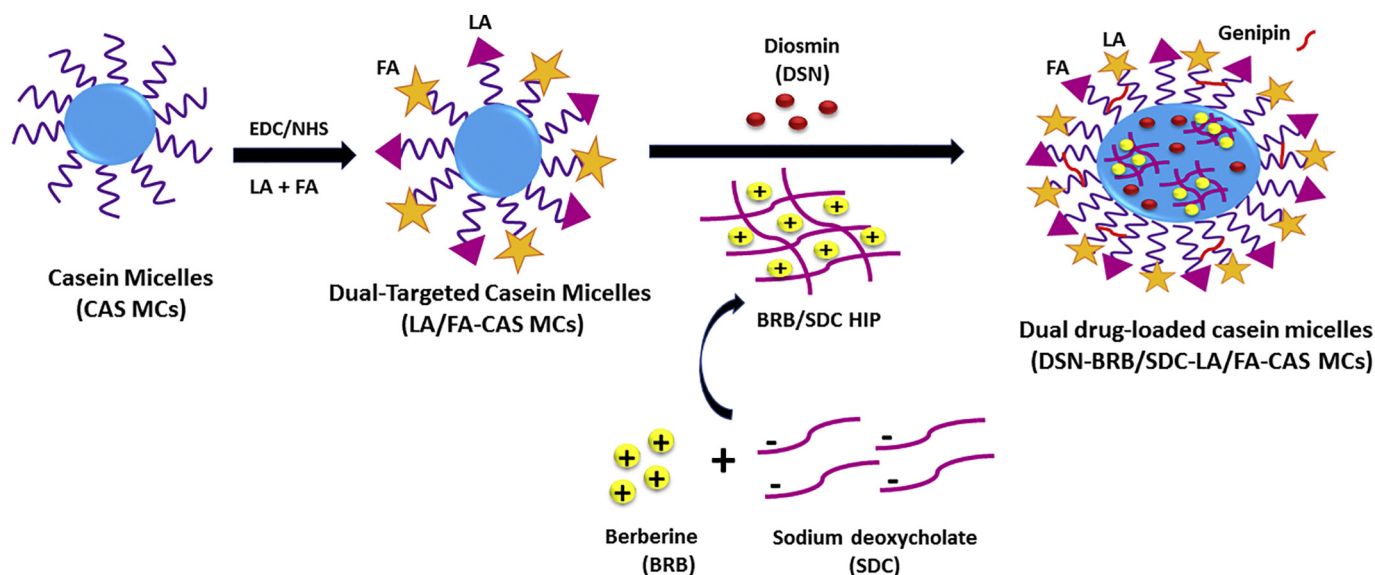


Fig. 1. Schematic diagram illustrates the preparation steps of dual-targeted LA-FA-CAS MCs.

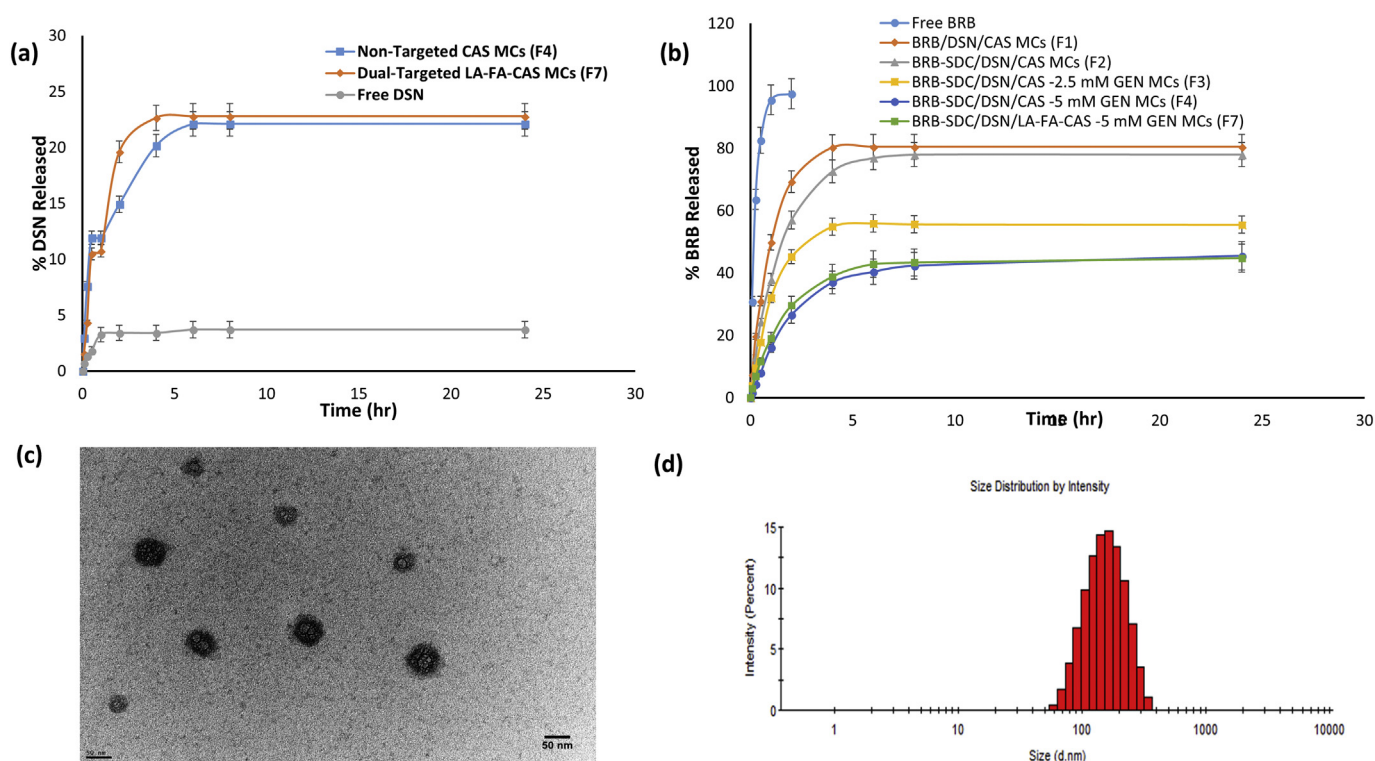


Fig. 2. In-vitro release profiles of (a) DSN and (b) BRB from different formulations in PBS (pH 7.4) at 100 rpm and 37°C using dialysis bag method, (c) TEM image showing the morphology of dual-targeted LA-FA-CAS MCs (F7), (d) Size distribution diagram of dual-targeted LA-FA-CAS MCs (F7) measured by DLS.

spectrum of our prepared FA-CAS MCs exhibited peaks at both 285 and 370 nm corresponding to folate moiety thus confirming successful conjugation [20]. The percentage of FA conjugated to CAS was determined to be 7.8% w/w assayed by UV at 364 nm (Fig. S3), while the coupled LA content was found to be 8.6% w/w assayed by phenol/sulfuric acid test at 490 nm (Fig. S4) [23]. The surface modification of CAS did not demonstrate a significant effect on the properties of the resultant micelles; BRB-SDC/DSN/LA-CAS (F5), BRB-SDC/DSN/FA-CAS (F6), BRB-SDC/DSN/LA-FA-CAS (F7) thus maintained the desired particle size range and controlled drug release pattern.

### 3.5. Spray-drying of CAS MCs

For long term stabilization, the dual drug-loaded CAS micellar dispersion was spray-dried into dry redispersible powder without drying adjuvant based on the thermal stabilizing characteristics of CAS [47]. The high thermal stability of CAS may be attributed to its proline-rich backbone with a relatively little secondary or tertiary structure [18]. Thus, high yield of the spray-dried CAS MCs powder (80.5–87.7 w/w) was enabled with the aid of high performance cyclone. The spray-dried BRB/DSN-CAS-MCs (F1) were easily reconstituted in aqueous medium demonstrating a size of 253.1 nm and zeta potential of −26 mV with no coagulation (Table 1).



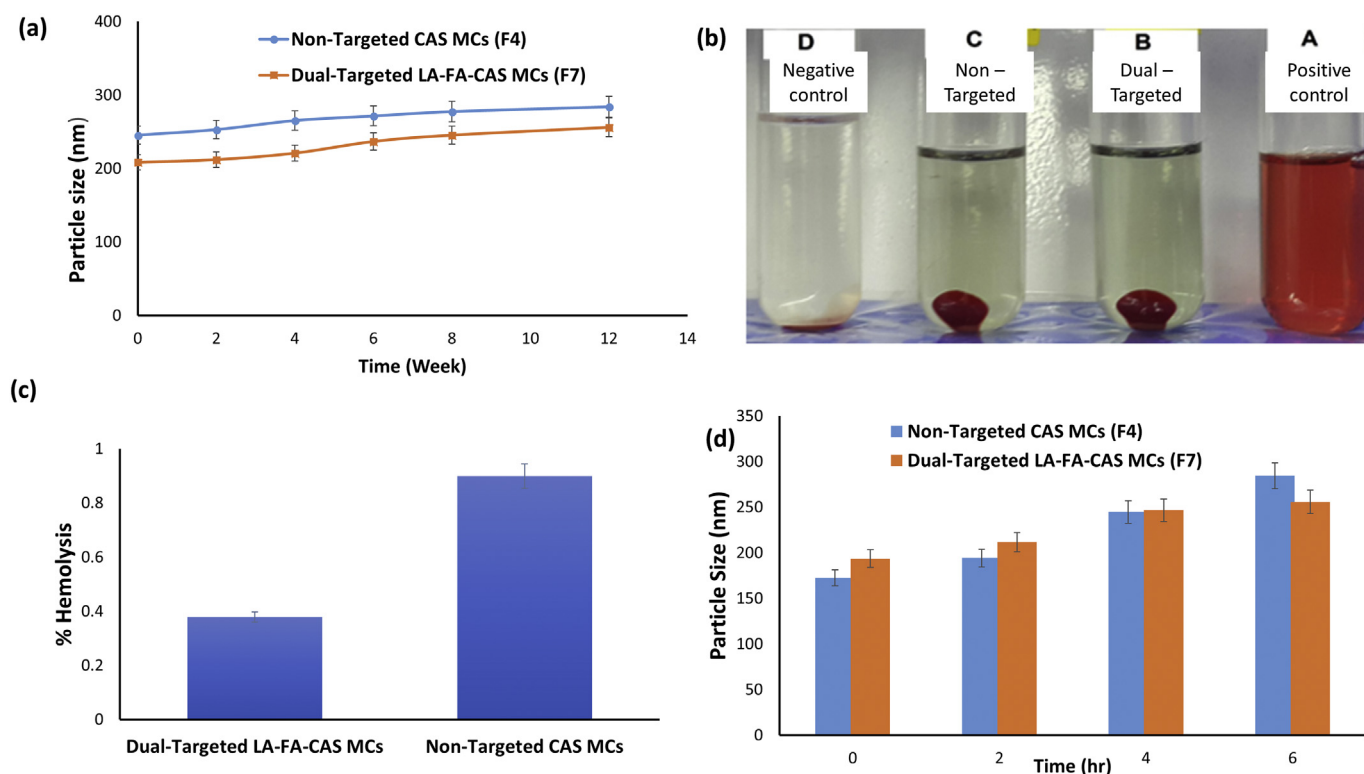


**Fig. 3.** (a) Physical stability of non-targeted CAS MCs (F4) and dual-targeted LA-FA-CAS MCs (F7) showing the change in particle size with time (b) Hemolytic potential of dual-drug loaded CAS MCs (F4 and F7) showing hemocompatibility image (b) and % hemolysis (c) after 1 h of incubation at 37 °C, (d) Particle size of F4 and F7 MCs after incubation in 10% fetal bovine serum (FBS) for 6 h at 37 °C.

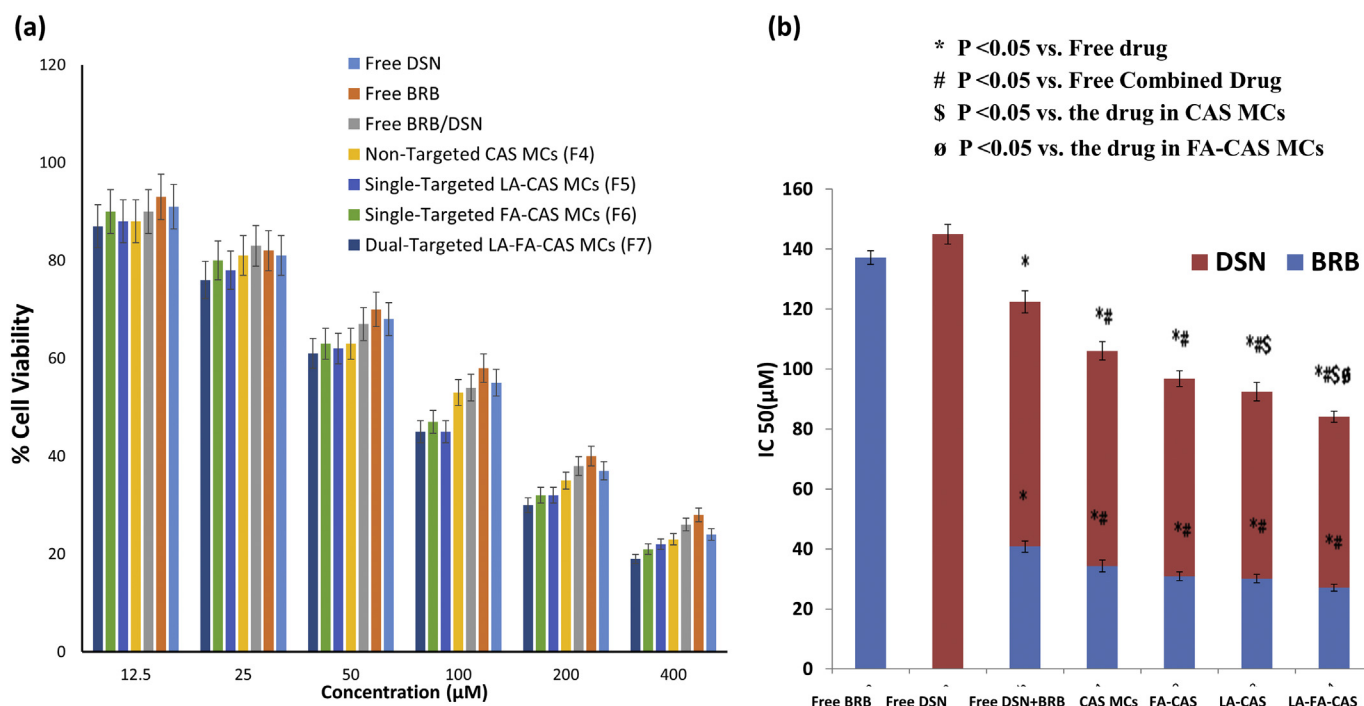


**Fig. 4.** (a) Cytotoxicity analysis of free BRB, free DSN and free BRB/DSN co-solvent compared to non-targeted CAS MCs (F4), targeted LA-CAS MCs (F5), targeted FA-CAS MCs (F6) and dual-targeted LA-FA-CAS MCs (F7) on HepG2 liver cancer cell line at the concentration of 0–400 μM after 48 h. (b) IC<sub>50</sub> of free drugs and different nano-micelles.

### 3.6. Solid state characteristics

The complexation of BRB with SDC was investigated by DSC. The thermograms of BRB, SDC, BRB-SDC complex as well as DSN and non-

targeted CAS MCs (F4) are illustrated in (Fig. S5). The thermogram of BRB exhibited a melting endothermic peak at 189 °C [22], while this peak was slightly shifted to lower temperature of 176 °C in the thermogram of BRB-SDC complex. This peak shift could be correlated to

**Table 2**  
IC<sub>50</sub> values of free drugs compared to the prepared drug-loaded CAS MCs on HepG2 liver cancer cells at the concentration of 0–400 μM after 48 h.

Drug/Combo	CI value	Total IC <sub>50</sub> of combination (μM)	Dose BRB (μM)	Dose DSN (μM)	DRI of BRB	DRI of DSN
Free BRB	–	–	137.146	–	–	–
Free DSN	–	–	–	144.961	–	–
Blank	–	–	–	–	–	66,516.0
Free BRB + DSN	0.921	122.31	40.79	81.58	3.36	1.77
Non-targeted CAS MCs (F4)	0.908	106.04	34.31	71.73	3.99	2.02
LA-CAS MCs (F5)	0.817	92.451	30.12	62.33	4.55	2.32
FA-CAS MCs (F6)	0.845	96.79	30.91	65.88	4.43	2.20
LA-FA-CAS MCs (F7)	0.782	84.08	27.12	56.96	5.05	2.54

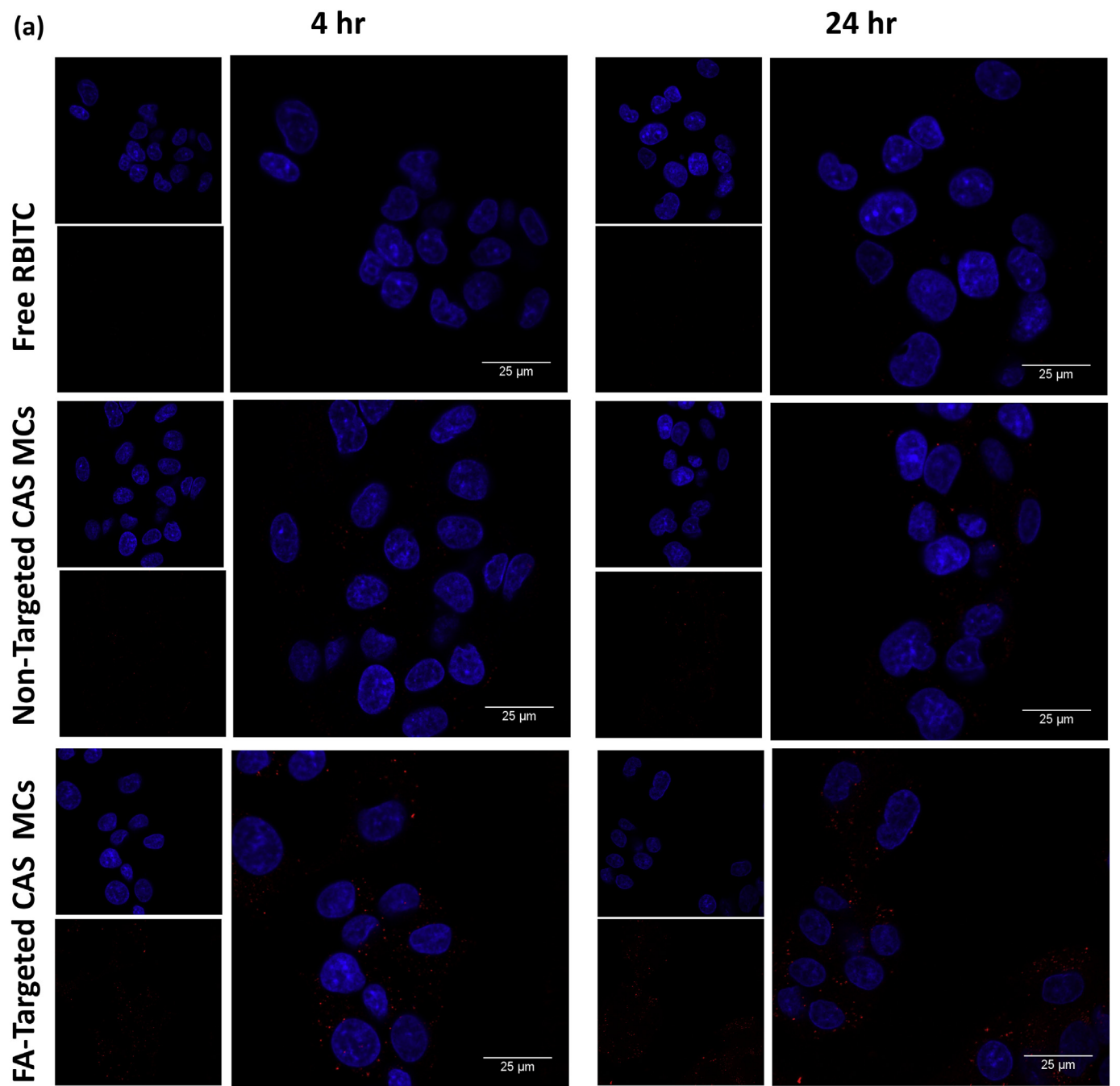


**Fig. 5.** Confocal images showing cellular uptake of (a) Free RBITC, non-targeted CAS MCs, targeted LA-CAS MCs (b) Targeted FA-CAS MCs and dual-targeted LA-FA-CAS MCs within HepG2 liver cancer cells after incubation for 4 h and 24 h.

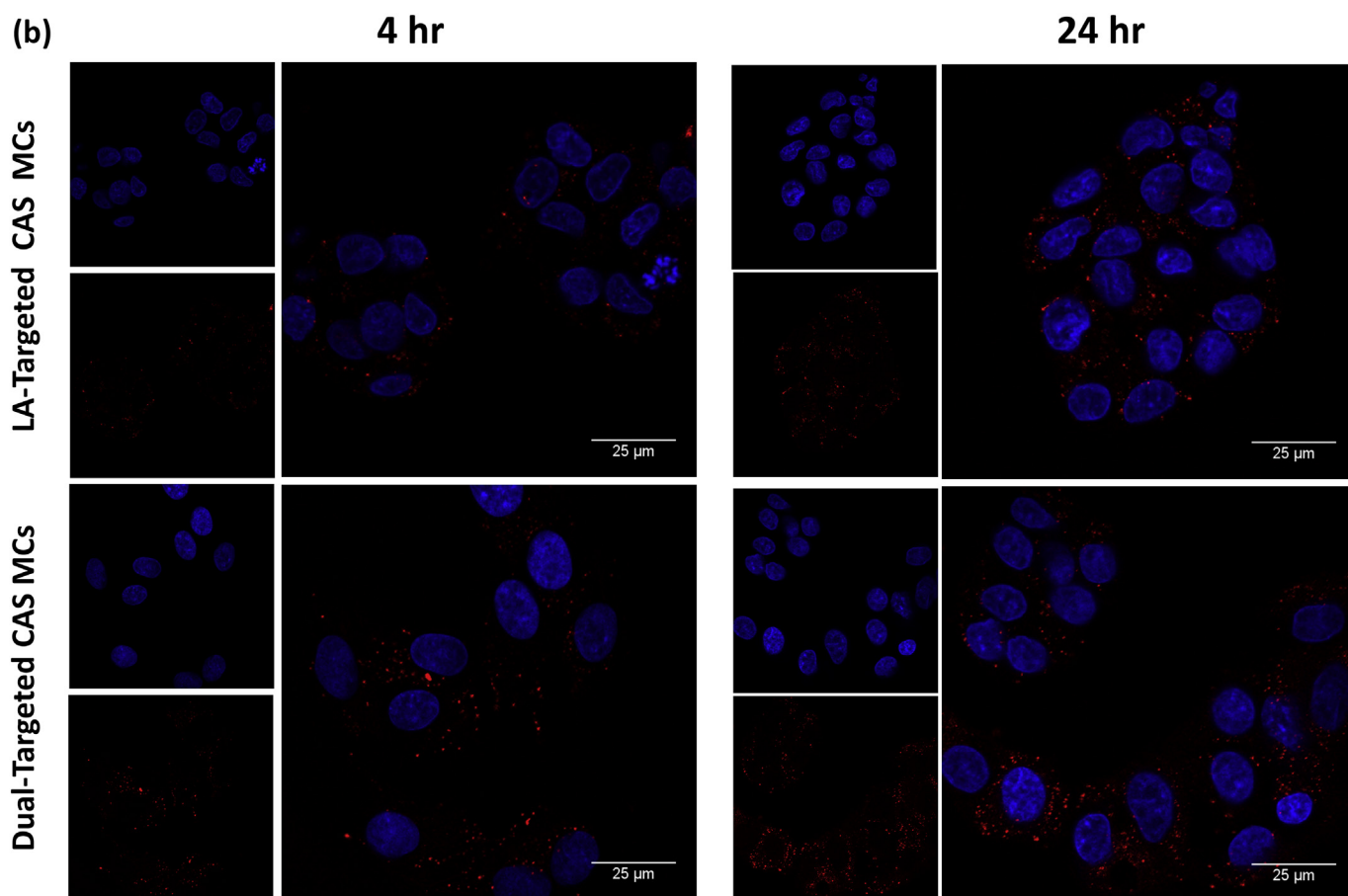


Fig. 5. (continued)

certain degree of transformation in the crystalline structure of BRB that occurred upon melting or complexation with SDC. DSN displayed an endothermic peak at 291 °C corresponding to its melting point which was disappeared in the thermogram of CAS-loaded MCs indicating amorphization of DSN upon solubilization within the micellar core [14]. On the other hand, the peak of BRB-SDC complex disappeared and a new sharp peak appeared at 127 °C which may indicate an interaction between the BRB-SDC complex and CAS MCs.

The FTIR spectra of BRB, SDC and BRB-SDC complex are shown in Fig. S6. It was observed that the absorption band of BRB at  $2844\text{ cm}^{-1}$  disappeared in the FTIR spectrum of BRB-SDC complex. Moreover, the FTIR absorption bands of SDC corresponding to CH stretching ( $2864.5$  and  $2938.2\text{ cm}^{-1}$ ) were still detected in the spectrum of BRB-SDC complex. Furthermore, the absorption peak at  $1565\text{ cm}^{-1}$  corresponding to COOH group of SDC was disappeared in BRB-SDC spectra. This demonstrated that the cationic ammonium group of BRB interacted with the  $\text{COO}^-$  group of SDC resulting in formation of a hydrophobic ion-pairing complex (HIP) [43]. The FTIR spectrum of the BRB-SDC/DSN/CAS-MCs (Fig. S7) showed peaks at  $2938.2$  and  $2864.5\text{ cm}^{-1}$  due to BRB-SDC complex but with lower intensity due to low drug content. Also, absorption bands were detected at  $1448$  and  $840\text{ cm}^{-1}$  which attributed to DSN absorption peaks. The characteristic band at  $1415.9\text{ cm}^{-1}$ , corresponding to  $\text{COO}^-$  group of CAS was shifted to  $1391\text{ cm}^{-1}$  in the spectrum of CAS MCs that could be attributed to ionic interaction between quaternary ammonium group of BRB and  $\text{COO}^-$  group of CAS [40] (More details in supplementary).

### 3.7. Morphological analysis & physical stability

Fig. 2c represents TEM photo of dual-targeted LA-FA-CAS-MCs showing spherical shape and with relatively smooth surface with no

aggregation. The apparent size measured by TEM was slightly less than that measured by DLS (Fig. 2d) due to dehydration-induced shrinkage of particles during preparation for TEM analysis [48,49].

Most polymeric micelles suffer from low colloidal stability particularly after drug loading. Moreover, the high tendency of micelles to dissociate in vivo after dilution in systemic circulation represents another stability challenge [50]. Therefore, in our study, the stability of CAS MCs could be enhanced via both genipin crosslinking and solidification by spray-drying technique. After 3 months storage, the MCs were physically stable and maintained their structural integrity upon reconstitution and dilution in aqueous medium. The particle size of CAS-MCs (F4) and LA-FA-CAS-MCs (F7) was increased to  $284.1 \pm 0.20$  and to  $255.8 \pm 0.52\text{ nm}$ , respectively still being in the desired size range (Fig. 3a) [51].

### 3.8. In vitro hemolysis & serum stability

Hemolytic activity was assessed through quantifying the release of hemoglobin from red blood cells (RBCs) after 1 h incubation with  $1\text{ mg/ml}$  of the dual drug-loaded CAS-MCs (F4 and F7) (Fig. 3b). The percentage hemolysis for CAS-MCs (F4) and dual-targeted LA-FA-CAS-MCs (F7) were  $0.90\%$  and  $0.38\%$ , respectively which were below  $5\%$  (Fig. 3c) [52]. This acceptable hemocompatibility may be attributed to the hydrated  $\kappa$ -CAS and the negative surface charge of the MCs that causes less damaging effect on the negatively charged outer membrane of RBCs [20]. This proves the blood compatibility of the CAS-MCs, indicating the possibility of using the system for i.v. administration applications. PLGA-CAS core/shell nanoparticles hemocompatibility effect was previously studied showing no hemolysis up to  $1\text{ mg/ml}$ , which is in agreement with our results [53].

To predict the feasibility of i.v. administration, the MCs stability in

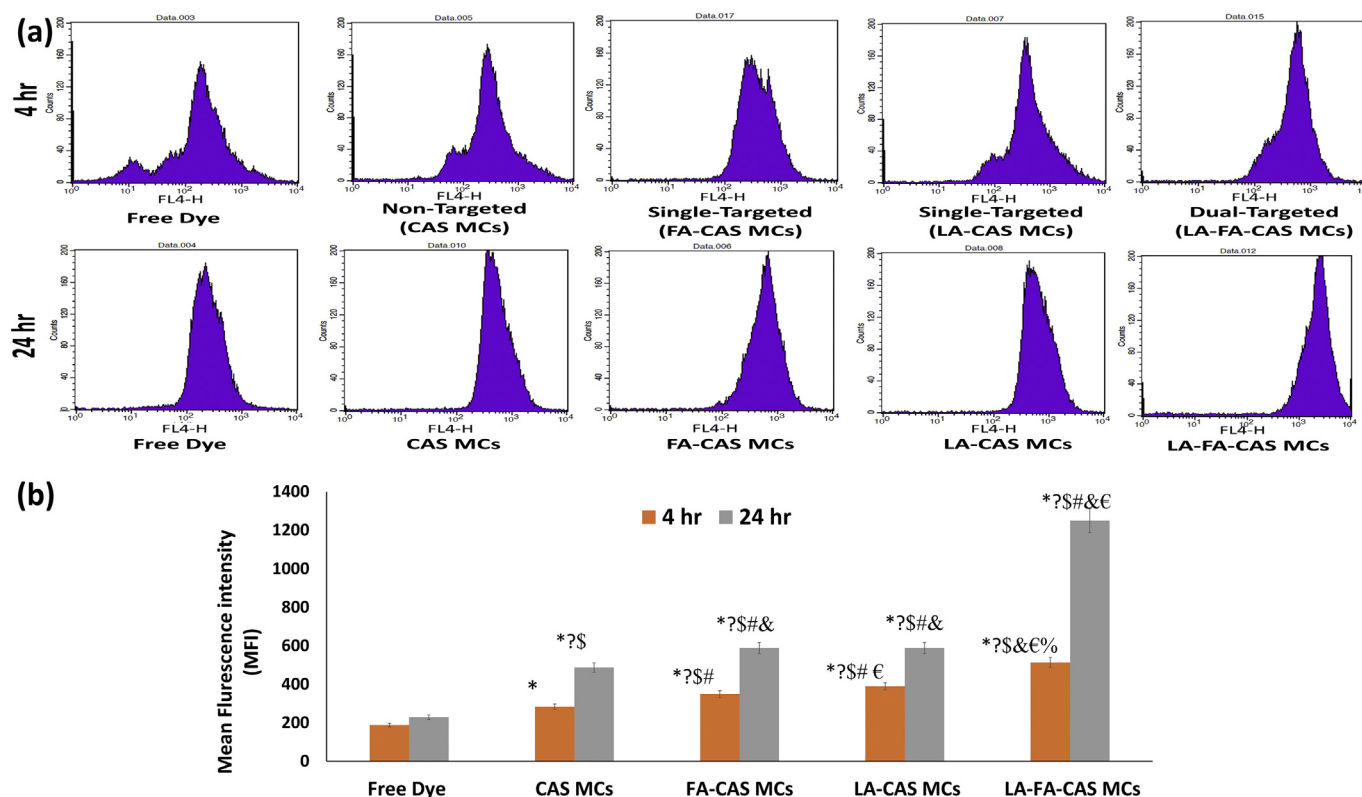


Fig. 6. (a) Flow cytometry histogram profiles of HepG2 cells after 4 and 24 h incubation with various RBITC-labeled CAS MCs. (b) Quantification of cellular level of mean fluorescence intensity in HepG2 cells after 4 h and 24 h incubation with various RBITC-labeled CAS MCs. (n = 3); (\*P < .05 vs Free dye after 4 h, ?P < .05 vs Free dye after 24 h, \$P < .05 vs Non-targeted CAS MCs after 4 h, #P < .05 vs Non-targeted CAS MCs after 24 h, &P < .05 vs FA-targeted CAS MCs after 4 h, €P < .05 vs FA-targeted CAS MCs after 24 h, %P < .05 vs Dual-targeted CAS MCs after 4 h).

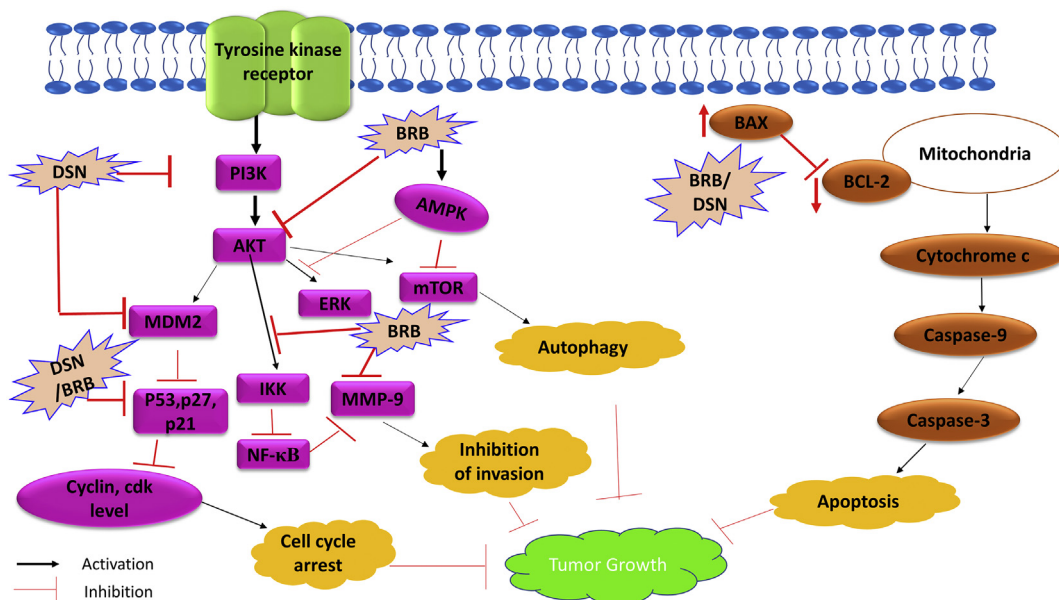
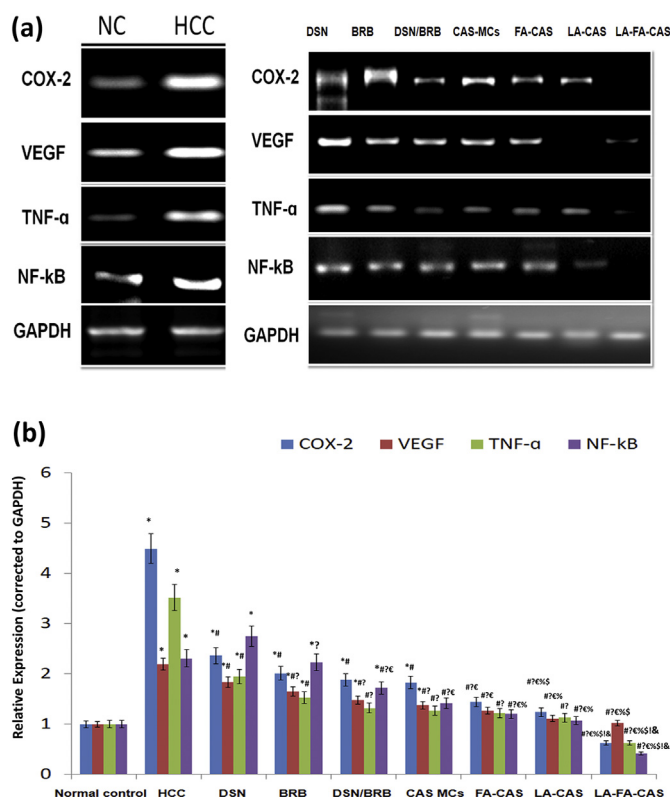


Fig. 7. A schematic representation showing the molecular mechanisms of BRB and DSN that involved in tumor growth suppression in HCC cells.

serum was evaluated. When mixed with 10% FBS, the dual-drug loaded CAS MCs (F4 and F7) showed obvious change in the size distribution compared with the initially prepared MCs (from  $172.6 \pm 0.430$  to  $194.2 \pm 0.23$  nm and from  $193.6 \pm 0.50$  to  $211.6 \pm 1.2$  nm, respectively). After 4 h of incubation with FBS, the particle size of non-targeted (F4) and dual-targeted CAS MCs (F7) reached  $244.5 \pm 1.3$  and  $246.5 \pm 0.6$  nm, respectively thus remain in the acceptable size

range required for tumor targeting (Fig. 3d). CAS-micelles possessed negative zeta potential which increased colloidal stability by electrostatic repulsive forces. Also, the polyelectrolyte layer of  $\kappa$ -CAS stabilizes the micelles by generating steric repulsion. The repulsive forces between the negatively charged serum proteins and CAS MCs may explain their high serum stability [20].





**Fig. 8.** (a) Expression profile for mRNA levels of COX-2, VEGF, TNF- $\alpha$  and NF- $\kappa$ B in groups treated with free BRB, free DSN, free combined, non-targeted CAS MCs, FA-CAS MCs and LA-FA-CAS MCs individual tissues was measured by (RT-PCR) and normalized to glyceraldehyde-3-phosphate dehydrogenase (GAPDH) ( $n = 7$ ). (b) Quantitative expression of VEGF, TNF- $\alpha$ , COX-2 and NF- $\kappa$ B levels quantified by RT-PCR for the studied groups, normalized according to GAPDH ( $n = 7$ ). (\* $P < .05$  vs Negative control, # $P < .05$  vs Positive control, ? $P < .05$  vs Free DSN, € $P < .05$  vs Free BRB, % $P < .05$  vs Free BRB/DSN, \$ $P < .05$  vs Non-targeted CAS MCs, & $P < .05$  vs LA-CAS MCs, ! $P < .05$  vs FA-CAS MCs).

### 3.9. In vitro cytotoxicity

The anticancer efficacy of the free combined BRB-DSN solution was compared to non-targeted and targeted micelles against human liver cancer HepG2 cells at 48 h (Fig. 4a, b). Blank CAS-MCs demonstrated very little toxicity to HepG2 cells (viability was  $> 95\%$  after 48 h) indicating their safety. The  $IC_{50}$  of free BRB alone and free DSN alone at 48 h was 137.146 and 144.961  $\mu$ M, respectively. On the other hand, the  $IC_{50}$  of the mixed free combined drugs solution at 48 h was 1.12- and 1.18-fold lower than that of BRB and DSN, respectively proving the synergistic cytotoxicity of this combination. Both LA-CAS and FA-CAS micelles enhanced the combination potency compared to free combined drugs solution and non-targeted micelles as demonstrated by the reduction of the  $IC_{50}$  to 92.45 and 96.7956  $\mu$ M, respectively (Table 2). Dual-targeted LA-FA-CAS micelles exhibited the most superior cytotoxic effect ( $IC_{50}$  84.09  $\mu$ M) against HepG2 cells. Further statistical analysis was done using CompuSyn software (version 1) described by Chou and Talalay where we used Combination Index (CI) and Dose Reduction Index (DRI) in comparing between the different MCs and the free combination [54–56]. The obtained results ensure the superiority of different drug-loaded MCs compared to the free combination, especially LA-CAS MCs & dual-targeted CAS MCs, where their CIs were 0.817 and 0.782, respectively revealing that they succeeded to achieve a synergy between BRB and DSN. Moreover, the Dose Reduction Indices (DRIs) of BRB were 4.55 and 5.05 in LA-CAS MCs and dual-targeted CAS MCs, respectively. While the DRIs of DSN were 2.32 and 2.54 in LA-CAS MCs

and dual-targeted CAS MCs, respectively. This could be directly correlated to their enhanced uptake into liver cancer cells by both over-expressed asialoglycoprotein and FA receptors resulting in higher drug accumulation inside the cancerous cells. The enhanced uptake could be proved via the cellular uptake study. In correlation with our results, galactose-decorated oridonin-loaded nanogels displayed higher anti-tumor efficacy against HepG2 cells through binding to ASGP-R with greater affinity [57].

### 3.10. Intracellular uptake

To visualize the cellular uptake of the micelles, RBITC was conjugated to the micelles through direct reaction of its thiocyanate group to the amino group of CAS. The uptake of RBITC-labeled non-targeted and targeted CAS-MCs compared to that of the free RBITC solution after 4 and 24 h incubation with HepG2 cells was examined by confocal laser scanning microscopy (Fig. 5a and b). Images revealed a bright red fluorescence signals in the cytoplasm of HepG2 cells, indicating that RBITC-conjugated micelles successfully entered the cells. Intracellular fluorescence signals in all groups increased with increasing the incubation time, indicating that the cellular uptake of micelles was time-dependent. At the same incubation time, we found that LA-CAS and FA-CAS-MCs demonstrated comparable fluorescence which was much higher than non-targeted CAS-MCs.

The intracellular uptake efficiency of RBITC-labeled MCs was also quantitatively evaluated by flow cytometry as shown in Fig. 6a. The cellular internalizations of MCs were assessed as a function of mean fluorescence intensity (MFI) calculated from flow cytometry data (Fig. 6b). The cellular levels of MFI demonstrated that there is a significant difference ( $P > .05$ ) between cellular uptake of non-targeted and single-targeted CAS MCs (FA- or LA-CAS MCs) after 4 h and 24 h incubation (Fig. 6b). On the other hand, there is no significant difference ( $P > .05$ ) between the cellular uptake of LA-CAS MCs and FA-CAS MCs after 4 h and 24 h incubation. More importantly, dual-targeted LA-FA-CAS-MCs have displayed the highest cellular levels of MFI ( $P > .001$ ) which was 2-fold higher than single-targeted CAS MCs (FA- or LA-CAS MCs) after 24 h incubation. The cellular uptake performance of dual-targeted LA-FA-CAS-MCs by HepG2 cells could be related with the receptor-mediated endocytosis through galactose and FA moieties due to high surface expression of ASGPR and folic acid receptors on HepG2 cells [36]. In agreement with the superior cytotoxicity displayed by dual-targeting strategy, glycyrrhethinic acid and LA dual-ligand modified chitosan NPs previously exhibited the best targeting efficiency against BEL-7402 cells compared to non-targeted and single-targeted NPs [13].

### 3.11. In vivo anti-tumor efficacy

#### 3.11.1. Measurement of cell necrosis markers expression level

**3.11.1.1. Nuclear factor-kappa B (NF- $\kappa$ B).** NF- $\kappa$ B signaling pathway is considered a valuable target for novel chemotherapeutic agents based on its inflammatory mechanistic contribution in tumor development [58]. DSN and BRB have been previously reported to downregulate NF- $\kappa$ B expression level in hepatoma cells (Fig. 7) [10,59]. In our study, we assessed the expression of NF- $\kappa$ B by RT-PCR (Fig. 8a and b). The group treated with free combined drugs (BRB + DSN) showed a significant inhibition in NF- $\kappa$ B expression level compared to the groups treated with either DSN ( $P < .001$ ) or BRB ( $P < .05$ ) thus confirming the synergistic effect. Moreover, there was a significant inhibition of NF- $\kappa$ B expression level in LA-CAS-MCs ( $P < .01$ ) and FA-CAS-MCs ( $P < .05$ ) treated groups relative to free combined drugs treated group. While single targeted LA-CAS-MCs and FA-CAS-MCs have demonstrated comparable inhibition of NF- $\kappa$ B expression level ( $P > .05$ ), dual-targeted LA-FA-CAS-MCs treated group has shown a significant inhibition in NF- $\kappa$ B expression level compared to groups treated with non-targeted ( $P < .001$ ), single targeted LA-CAS-MCs and FA-CAS-MCs

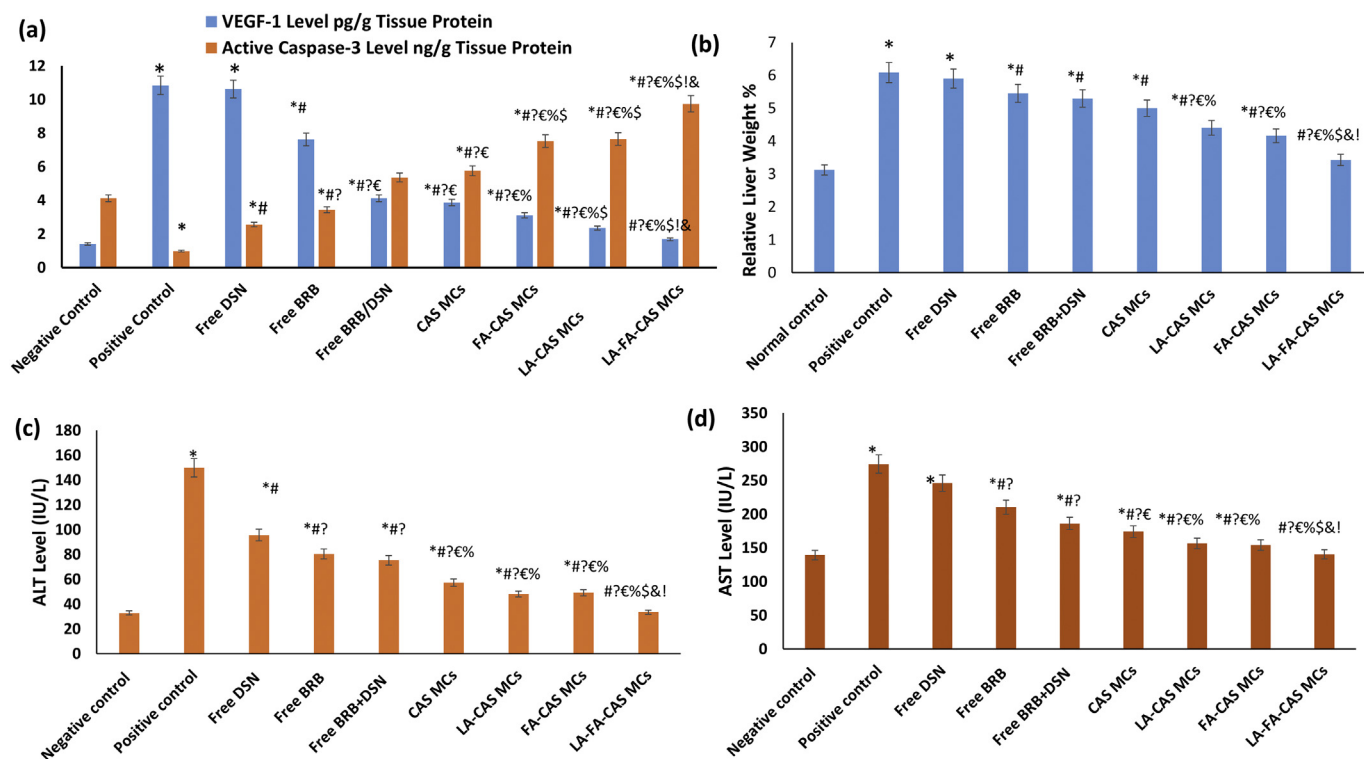


Fig. 9. Comparison between the studied groups (Free DSN, Free BRB, Free BRB/DSN co-solvent, F4(Non-targeted CAS MCs), F5 (Targeted LA-CAS MCs), F6 (Targeted FA-CAS MCs) and F7 (Dual-targeted LA-FA-CAS MCs) treated groups in addition to the positive control group according to (a) VEGF-1 level and active caspase-3, (b) Relative liver weight (RLW%), (c) ALT level and (d) AST level (n = 7). (\*P < .05 vs Negative control, #P < .05 vs Positive control, ?P < .05 vs Free DSN, €P < .05 vs Free BRB, %P < .05 vs Free BRB/DSN, \$P < .05 vs Non-targeted CAS MCs, &P < .05 vs LA-CAS MCs, !P < .05 vs FA-CAS MCs).

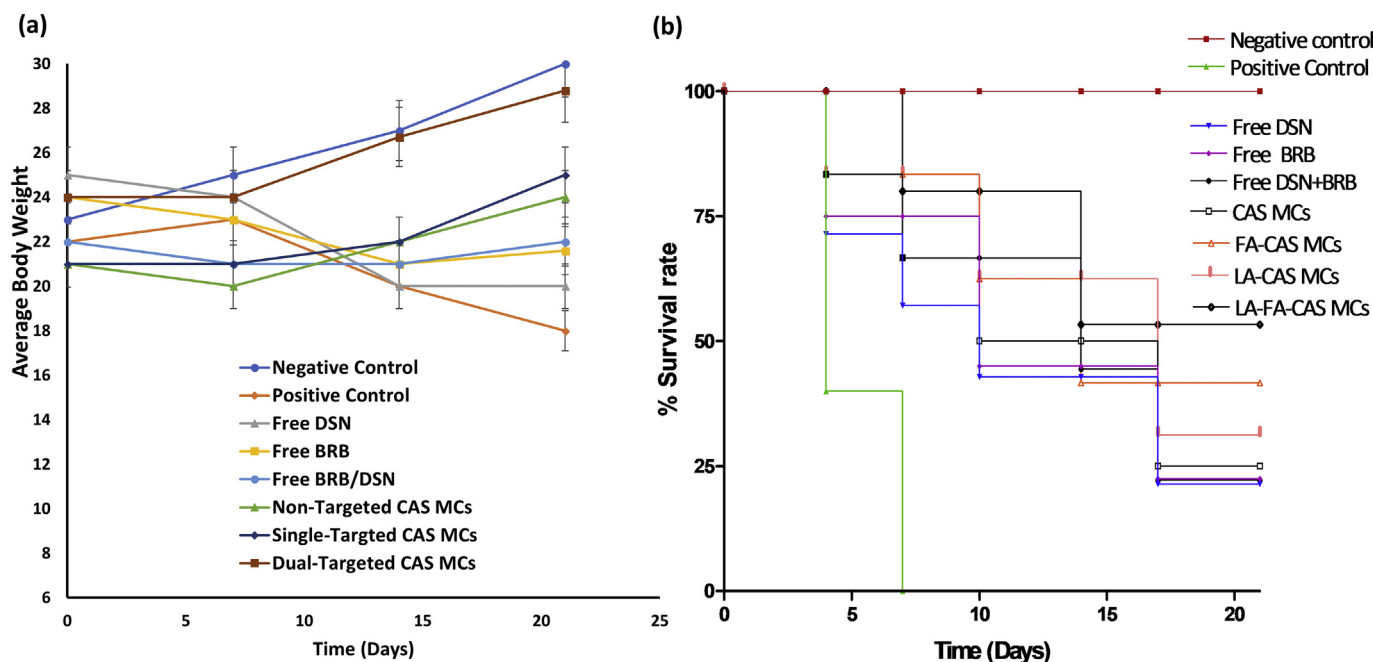
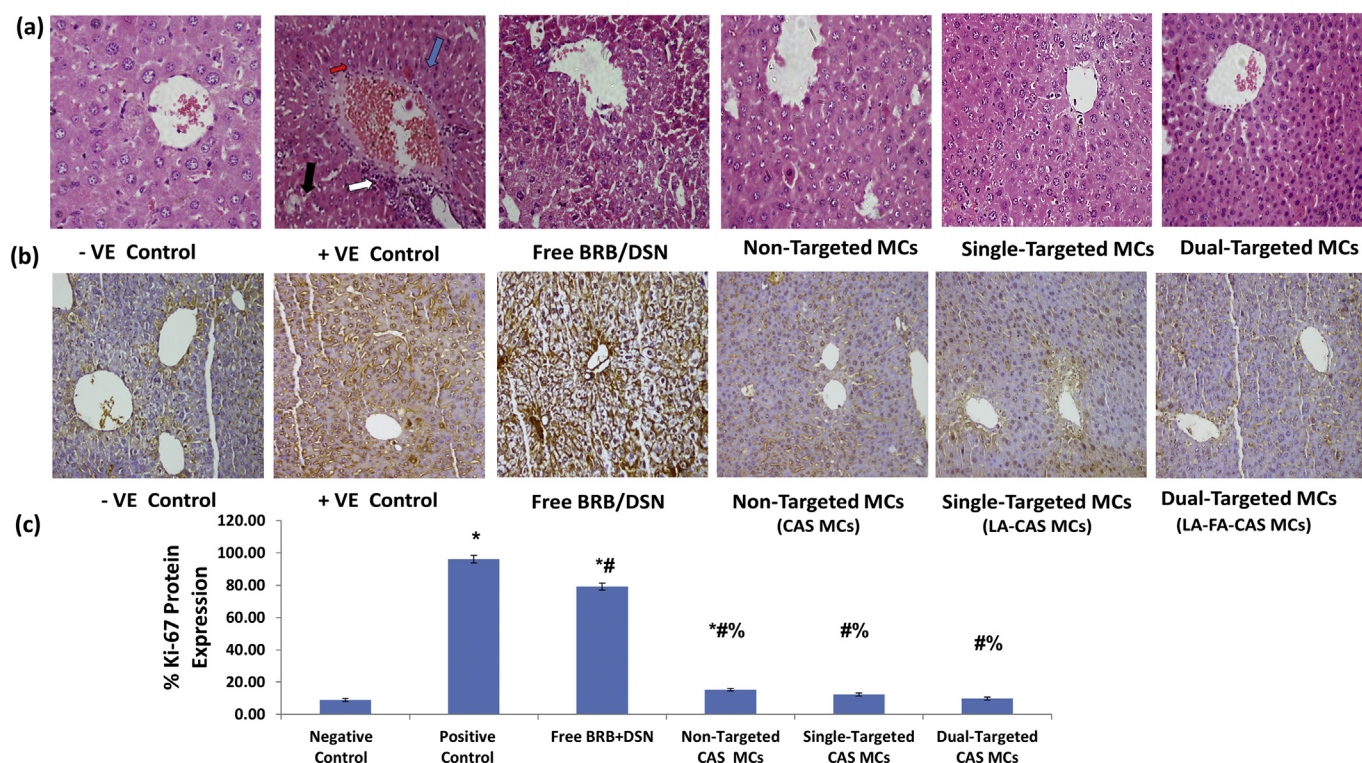


Fig. 10. Comparison between the studied groups (Free DSN, Free BRB, Free BRB/DSN co-solvent, F4(Non-targeted CAS MCs), F5 (Targeted LA-CAS MCs), F6 (Targeted FA-CAS MCs) and F7 (Dual-targeted LA-FA-CAS MCs) treated groups in addition to the positive control group according to (a) Average body weight (b) Kaplan-Meier survival curve.

(P < .05). This proves the synergistic action of our drug combination which was further augmented by their incorporation in dual-targeted LA-FA-CAS-MCs.

### 3.11.1.2. Tumor necrosis factor- $\alpha$ (TNF- $\alpha$ ). TNF- $\alpha$ promotes hepatocyte

apoptosis resulting in liver damage and activates the inflammatory and stress-related signaling pathways including NF- $\kappa$ B and p38MAPK pathways [60]. According to previous studies, DSN and BRB had effectively suppressed the expression of proinflammatory cytokines as TNF- $\alpha$  [10,59]. Therefore, in our study, the expression level of TNF- $\alpha$



**Fig. 11.** (a) H&E staining of liver cancer tissues of negative control, positive control group, free BRB/DSN combination, non-targeted CAS MCs (F4), single targeted LA-CAS MCs (F6) and dual-targeted LA-FA-CAS MCs (F7) treated groups (b) Immunohistopathological staining of the proliferative marker Ki-67 in liver cancer tissues of positive control group and free BRB/DSN combination, non-targeted CAS MCs (F4), single targeted LA-CAS MCs (F6) and dual-targeted LA-FA-CAS MCs (F7) treated groups and (c) % Ki-67 proliferation marker in positive control group and liver cancer tissues of free BRB/DSN combination, non-targeted F4 single targeted F6 and dual-targeted F7 treated groups (n = 7). (\*P < .05 vs Negative control, #P < .05 vs Positive control, %P < .05 vs Free BRB/DSN).

was assessed by RT-PCR (Fig. 8a and b). The group treated with the dual-targeted LA-FA-CAS-MCs has demonstrated the least expression level of TNF- $\alpha$  which was significantly ( $P < .05$ ) lower than that detected for the groups treated with non-targeted CAS-MCs, LA-CAS-MCs, FA-CAS-MCs and free combined drugs. Dual-targeted treated group succeeded in lowering the expression of TNF- $\alpha$  to a level comparable to that of negative control ( $P < .05$ ).

### 3.11.2. Measurement of cyclooxygenase-2 expression level

COX-2 enzyme has a potential role in HCC-associated angiogenesis through the induction of vascular endothelial growth factor (VEGF) and fibroblast growth factor 2 (FGF-2) that activate angiogenesis [61]. DSN and BRB were found to suppress COX-2 expression level in hepatoma cells [10,59]. Therefore, in our study, the expression level of COX-2 was assessed by RT-PCR (Fig. 8a and b). The group treated with dual targeted LA-FA-CAS-MCs showed 3-folds lowering in the COX-2 expression level relative to non-targeted CAS-MCs ( $P < .001$ ). Also, the dual-targeted treated group has demonstrated the least expression level of COX-2 which was significantly lower than that detected for the groups treated with LA-CAS-MCs ( $P < .05$ ) and FA-CAS-MCs ( $P < .01$ ).

### 3.11.3. Detection of anti-angiogenic effect

Angiogenesis is initiated by the release of angiogenic factors from tumor cells, the most potent of which is VEGF. Therefore, VEGF is widely considered as a potential target for cancer therapy [62,63]. The expression level of VEGF protein in the group treated with non-targeted CAS-MCs (3.87 pg/g tissue protein) was obviously lower than that detected for the group treated with the free drug combination (4.12 pg/g tissue protein). Moreover, the dual targeted LA-FA-CAS-MCs treated group has showed the least VEGF protein level (1.68 pg/g tissue protein) and the least the mRNA expression level of VEGF which was comparable to the negative control (Figs. 8a, b and 9a). This dual

targeted LA-FA-CAS-MCs treated group has shown a significant suppression in mRNA expression level of VEGF relative to non-targeted CAS-MCs ( $P < .05$ ). BRB was found to inhibit angiogenesis through down-regulating VEGF mRNA expression from hepatoma cells, hence suppresses tumor growth [64]. In our study, there was no significant difference ( $P > .05$ ) in the expression level of VEGF between group treated with BRB only and combination, as there is no data about the effect of DSN on VEGF expression level. These inhibitions have been augmented by incorporation of BRB in dual targeted MCs.

### 3.11.4. Measurement of apoptosis induction

BRB can induce mitochondrial apoptosis in liver cancer cells, demonstrated by a reduction in mitochondrial membrane potential and elevation in Bax expression in addition to activation of caspases 3 and 9 (Fig. 7) [11,12]. Moreover, DSN was reported to increase the expression of caspases 3 and 9, which confirmed its apoptotic induction potential (Fig. 7) [65]. Therefore, apoptosis in our study was evaluated by determining the expression level of caspase-3 in the liver tumor tissue of mice. Relative to positive control group, there was a 10-, 7.8-, 7.6- and 6.36-fold elevation in caspase-3 level in groups treated with LA-FA-CAS, LA-CAS, FA-CAS and CAS-MCs respectively, compared to 5.45-fold elevation for free BRB-DSN combination (Fig. 9a). This proves that the incorporation of both drugs in CAS MCs provided higher apoptotic activity than their administration in free form. Moreover, the decoration of the micelles by targeting ligands improved the apoptotic activity which was highest in case of the dual targeted LA-FA-CAS-MCs.

### 3.11.5. Measurement of serum AST and ALT levels and relative liver weight % (RLW)

The liver/body weight ratio (RLW %) in positive control group ( $6.08 \pm 0.2$  vs.  $3.12 \pm 0.2$ ,  $p < .05$ , Fig. 9b) was significantly elevated in comparison to normal mice. Also, serum ALT and AST levels



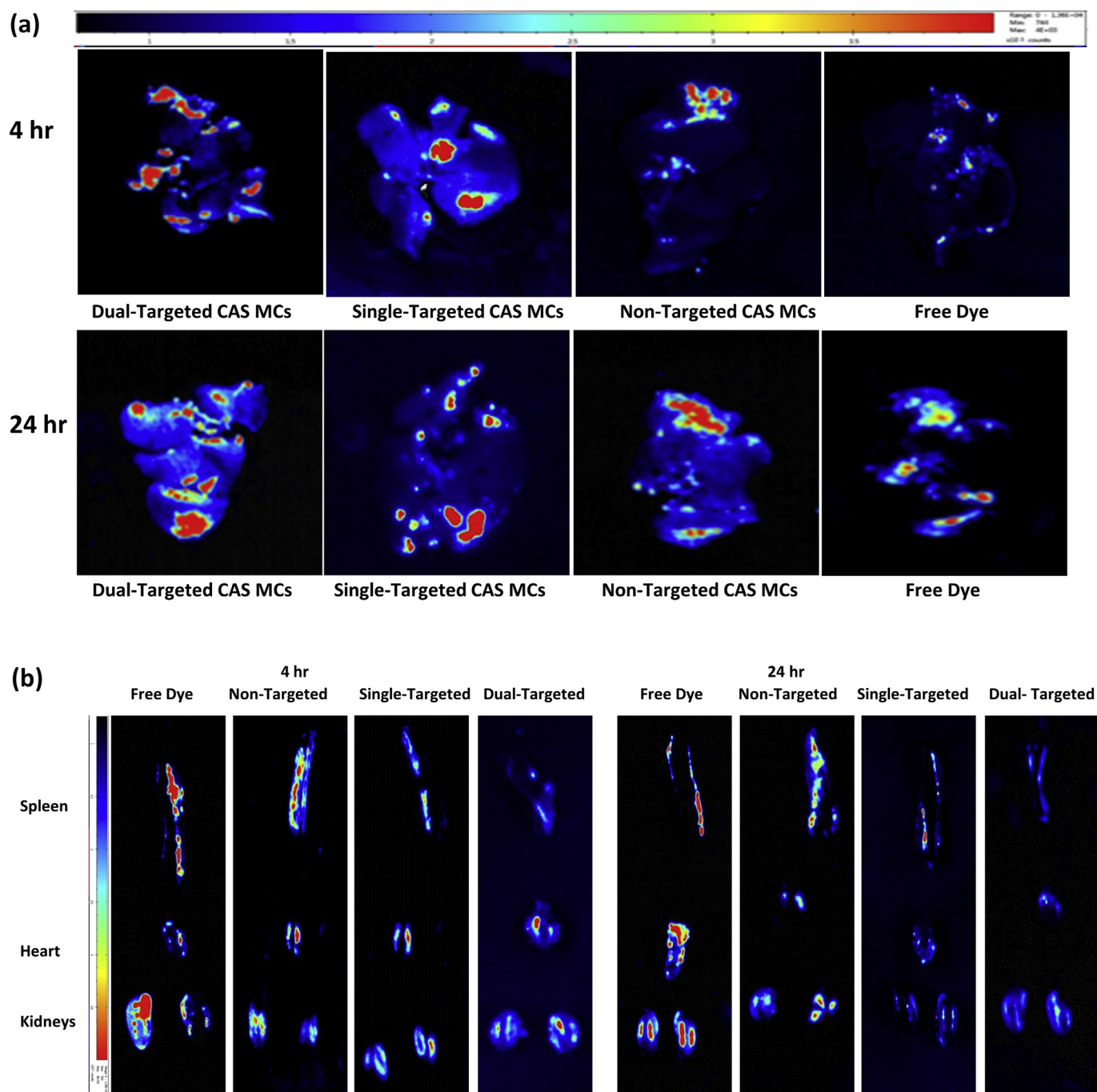


**Fig. 12.** (a) Ex vivo fluorescence images of dissected livers after 4 and 24 h post-injection. (b) Ex vivo fluorescence images of dissected organs (spleens, hearts, kidneys) after 4 and 24 h post-injection. (c) Quantitative estimation of relative fluorescence intensity acquired from different organs of mice after 4 and 24 h post injection ( $n = 3$ ). (\* $P < .05$  vs Livers of free dye treated group after 4 h,  $\$P < .05$  vs Livers of non-targeted CAS MCs treated group after 4 h, & $P < .05$  vs Livers of single-targeted CAS MCs treated group after 4 h, % $P < .05$  vs Livers of dual-targeted CAS MCs treated group after 4 h, ? $P < .05$  vs Livers of free dye treated group after 24 h, # $P < .05$  vs Livers of Non-targeted CAS MCs treated group after 24 h, € $P < .05$  vs Livers of single-targeted CAS MCs treated group after 24 h).

showed remarkable increase in positive control group compared with normal mice; revealing the damage of liver tissue induced by DEN [36,38]. Compared with group treated with free combined drugs, single targeted LA-CAS-MCs and FA-CAS-MCs both have shown about 1.2-fold reduction in the liver/body weight ratio and about 1.60- and 1.21-fold decrease in the expression levels of ALT and AST, respectively (Fig. 9c and d). The group treated with dual-targeted LA-FA-CAS-MCs caused about 1.55-fold decrease in liver/body weight ratio and 2.25- and 1.33-fold reduction in the expression levels of ALT and AST, respectively compared to free combined drugs treated group. Accordingly,

treatment with the dual-targeted LA-FA-CAS-MCs caused remarkable decrease in both the liver/body weight and serum ALT and AST levels which becomes comparable to normal control. These results indicated the potential capability of dual-targeted LA-FA-CAS-MCs to diminish the liver damage caused by DEN. Moreover, the average body weights of the mice monitored throughout the experiment period (Fig. 10a). It was observed that the positive control group demonstrated noticeable reduction in their body weights due to DEN-toxicity. This reduction was ameliorated in non-targeted MCs treated groups while body weights started to increase in single-targeted and dual-targeted MCs treated



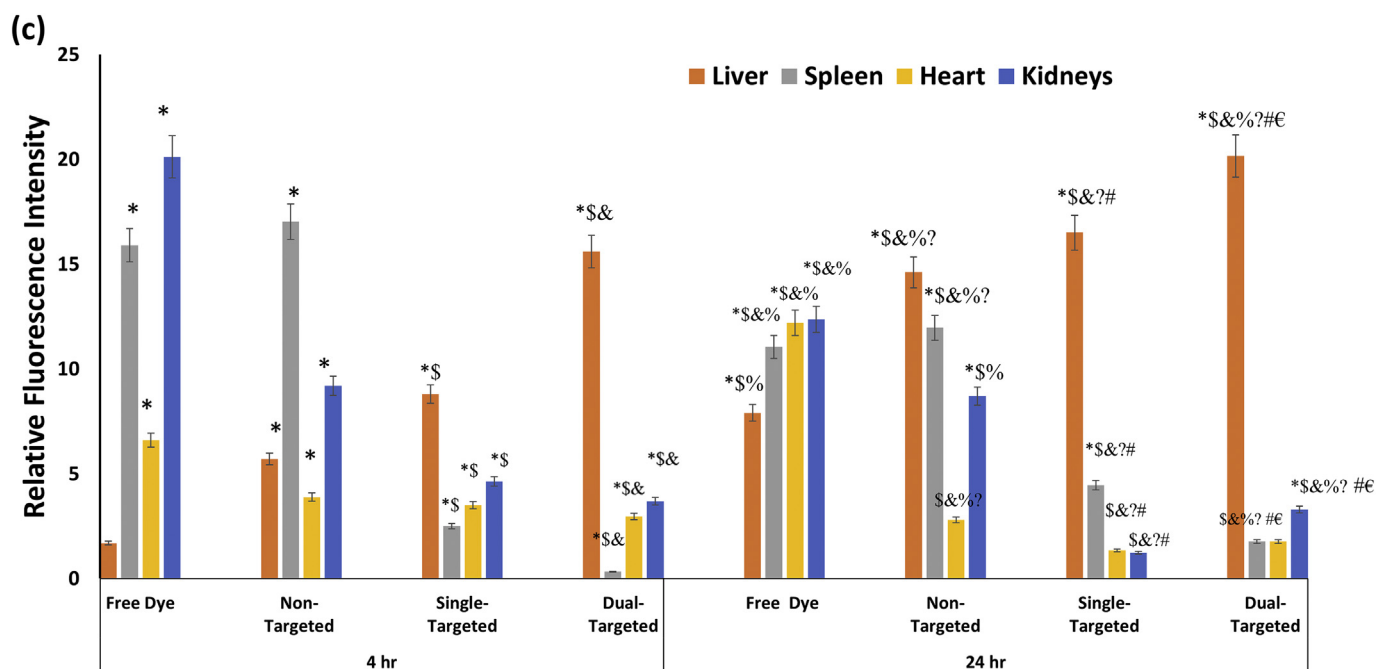


Fig. 12. (continued)

groups which become almost comparable to negative control. Finally, the Kaplan-Meier survival curve of HCC-induced mice was further investigated to evaluate the *in vivo* anti-tumor efficacy of the prepared MCs (Fig. 10b). It was noticed that non-targeted MCs treated group had an increase in survival by 50% while that of single-targeted MCs treated groups was improved by 65%. Furthermore, dual-targeted MCs treated group has shown the highest survival rate of about 75%. Thus, we can conclude that the prepared MCs succeeded to reduce the DEN-toxicity.

### 3.11.6. Histopathological study

Histological examination of H&E-stained liver sections of different treatment groups showed variable histological characters (Fig. 11a). The normal mice group (negative control) showed polyhydral hepatocytes with one or rarely two spherical-shaped nuclei and strongly eosinophilic cytoplasm. In contrast, DEN-treated mice livers showed areas of aberrant hepatocellular phenotype with variable nuclear size, hyperchromatinism and irregular sinusoids with prominent hyperbasophilic preneoplastic focal lesions. Other cells showed eosinophilic cytoplasm, large or bi-nucleated nuclei. Moreover, several evidences of inflammatory cells infiltration were further noticed [35,36,66,67]. Interestingly, the group treated with free combined drugs showed noticeable amelioration in all histopathological features of DEN-induced HCC, but to different extent, where the dual-targeted LA/FA-CAS-MCs showed remarked superiority over all other preparations. The liver sections from the group treated by LA/FA-CAS-MCs has a comparable cellular architecture with that of normal controls. The hepatocytes displayed a compact cytoplasm revealing the reduced hepatotoxicity.

### 3.11.7. Immunohistochemical analysis of cell proliferation (Ki-67 antigen)

Ki-67 is a nuclear protein that could be used as a prognostic marker to cancer cell proliferation [37]. Ki-67 was highly stained in the tissue specimens obtained from the positive control as well as the group treated with the free combined drugs compared to tumor specimens obtained from the groups treated with drug-loaded MCs (Fig. 11b). The results showed a significant elevation of % Ki-67 expression (96.10%) in liver cancer tissues of the positive control group compared to only 15.30 and 8.70% for non-targeted and dual-targeted LA-FA-CAS-MCs mice-treated groups (Fig. 11c). The reduced density of Ki-67 stained cells of the MCs-treated groups reflected the privilege of MCs in

inhibition of cancer cell proliferation thereby suppressing the tumor growth.

### 3.11.8. Ex-vivo imaging of isolated livers

The ex-vivo images of the isolated livers have demonstrated time-dependent accumulation of dual-targeted LA-FA-CAS-MCs in liver more than other organs (Fig. 12a and b). Dual-targeted CAS MCs displayed the highest fluorescence intensity in liver compared to non-targeted CAS MCs, single-targeted CAS MCs and free dye. The optical imaging signal of dual-targeted CAS MCs in the liver was increased by 9- and 2.5-folds compared to free dye 4 and 24 h after *i.v.* administration, respectively (Fig. 12c). These results ensured the effective targetability of dual-targeted CAS MCs to liver cancer cells [68].

## 4. Conclusion

In this study, a combination of two phyto-medicines BRB and DSN was formulated into a GRAS (generally recognized as safe) protein (CAS) micelles as a completely green HCC therapy. pH-modulation strategy was utilized for efficient solubilization of the poorly soluble drug DSN within the hydrophobic core of CAS MCs whereas combined strategies of both hydrophobic ion pairing and genipin-mediated chemical crosslinking of CAS MCs have been exploited to prolong the release of BRB from the nanocarriers. Dual functionalization of CAS-MCs by two targeting ligands LA and FA enhanced their cytotoxicity against HepG2 cells mediated by dual FA/ASGP receptor-mediated endocytosis. The superior *in vivo* antitumor efficacy of the dual-targeted dual loaded CAS MCs in liver cancer bearing mice was manifested as their ability to activate apoptotic enzyme, caspase 3 and inhibit VEGF, TNF-alpha, NF-kappa B, and COX2. The results were augmented by repairing the histopathological alterations and reducing the expression of tumor proliferation marker Ki67. Overall, these results confirmed the outstanding *in vivo* antitumor efficacy of combined delivery of BRB and DSN via dual-targeted LA/FA-CAS MCs.

## Appendix A. Supplementary data

Supplementary data to this article can be found online at <https://doi.org/10.1016/j.jconrel.2018.08.026>.

## References

- [1] S. Singh, P.P. Singh, L.R. Roberts, W. Sanchez, Chemopreventive strategies in hepatocellular carcinoma, *Nat. Rev. Gastroenterol. Hepatol.* 11 (2014) 45.
- [2] S. Lin, K. Hoffmann, P. Schemmer, Treatment of hepatocellular carcinoma: a systematic review, *Liver Cancer* 1 (2012) 144–158.
- [3] U. Asghar, T. Meyer, Are there opportunities for chemotherapy in the treatment of hepatocellular cancer? *J. Hepatol.* 56 (2012) 686–695.
- [4] S. Narayanan, N. Binulal, U. Mony, K. Manzoor, S. Nair, D. Menon, Folate targeted polymeric 'green' nanotherapy for cancer, *Nanotechnology* 21 (2010) 285107.
- [5] A. Elzoghby, M. Freag, H. Mamdouh, K. Elkhodairy, Zein-based nanocarriers as potential natural alternatives for drug and gene delivery: focus on cancer therapy, *Curr. Pharm. Des.* 23 (2017) 5261–5271.
- [6] S. Sabra, M. Abdelmoneem, M. Abdelwakil, M.M. Taha, D. Anwar, R. Mohamed, S. Khattab, A. Bekhit, K. Elkhodairy, M. Freag, Self-assembled nanocarriers based on amphiphilic natural polymers for anti-cancer drug delivery applications, *Curr. Pharm. Des.* 23 (35) (2017) 5213–5229.
- [7] H.M. Abdelaziz, M. Gaber, M.M. Abd-Elwakil, M.T. Mabrouk, M.M. Elgohary, N.M. Kamel, D.M. Kabary, M.S. Freag, M.W. Samaha, S.M. Mortada, Inhalable particulate drug delivery systems for lung cancer therapy: nanoparticles, micro-particles, nanocomposites and nanoaggregates, *J. Control. Release* 269 (2017) 374–392.
- [8] A. Elzoghby, Polymeric nanocarriers as robust platforms for cancer therapy, *Curr. Pharm. Des.* 23 (35) (2017) 5211–5212.
- [9] T.D. Dung, C.H. Day, T.V. Binh, C.-H. Lin, H.-H. Hsu, C.-C. Su, Y.-M. Lin, F.-J. Tsai, W.-W. Kuo, L.-M. Chen, PP2A mediates diosmin p53 activation to block HA22T cell proliferation and tumor growth in xenografted nude mice through PI3K–Akt–MDM2 signaling suppression, *Food Chem. Toxicol.* 50 (2012) 1802–1810.
- [10] M. Tahir, M.U. Rehman, A. Lateef, A.Q. Khan, R. Khan, W. Qamar, O. O'Hamiza, F. Ali, S.K. Hasan, S. Sultana, Diosmin abrogates chemically induced hepatocarcinogenesis via alleviation of oxidative stress, hyperproliferative and inflammatory markers in murine model, *Toxicol. Lett.* 220 (2013) 205–218.
- [11] N.K. Yip, W. Ho, Berberine induces apoptosis via the mitochondrial pathway in liver cancer cells, *Oncol. Rep.* 30 (2013) 1107–1112.
- [12] N. Wang, Y. Feng, M. Zhu, C.M. Tsang, K. Man, Y. Tong, S.W. Tsao, Berberine induces autophagic cell death and mitochondrial apoptosis in liver cancer cells: the cellular mechanism, *J. Cell. Biochem.* 111 (2010) 1426–1436.
- [13] H. Chen, M. Li, T. Wan, Q. Zheng, M. Cheng, S. Huang, Y. Wang, Design and synthesis of dual-ligand modified chitosan as a liver targeting vector, *J. Mater. Sci. Mater. Med.* 23 (2012) 431–441.
- [14] M.S. Freag, Y.S. Elnaggar, O.Y. Abdallah, Development of novel polymer-stabilized diosmin nanosuspensions: in vitro appraisal and ex vivo permeation, *Int. J. Pharm.* 454 (2013) 462–471.
- [15] A. Elzoghby, Editorial (thematic issue: nanocarriers based on natural polymers as platforms for drug and gene delivery applications), *Curr. Pharm. Des.* 22 (2016) 3303–3304.
- [16] A.O. Elzoghby, M.M. Elgohary, N.M. Kamel, Implications of protein- and peptide-based nanoparticles as potential vehicles for anticancer drugs, *Advances in Protein Chemistry and Structural Biology*, Elsevier, 2015, pp. 169–221.
- [17] A.O. Elzoghby, W.S.A. El-Fotoh, N.A. Elgindy, Casein-based formulations as promising controlled release drug delivery systems, *J. Control. Release* 153 (2011) 206–216.
- [18] A.O. Elzoghby, M.W. Helmy, W.M. Samy, N.A. Elgindy, Spray-dried casein-based micelles as a vehicle for solubilization and controlled delivery of flutamide: Formulation, characterization, and in vivo pharmacokinetics, *Eur. J. Pharm. Biopharm.* 84 (2013) 487–496.
- [19] A.O. Elzoghby, M.W. Helmy, W.M. Samy, N.A. Elgindy, Novel ionically crosslinked casein nanoparticles for flutamide delivery: formulation, characterization, and in vivo pharmacokinetics, *Int. J. Nanomedicine* 8 (2013) 1721.
- [20] S.W. El-Far, M.W. Helmy, S.N. Khattab, A.A. Bekhit, A.A. Hussein, A.O. Elzoghby, Phytosomal bilayer-enveloped casein micelles for codelivery of monascus yellow pigments and resveratrol to breast cancer, *Nanomedicine* 13 (5) (2018) 481–499.
- [21] L.M. Negi, M. Jaggi, V. Joshi, K. Ronodip, S. Talegaonkar, Hyaluronan coated liposomes as the intravenous platform for delivery of imatinib mesylate in MDR colon cancer, *Int. J. Biol. Macromol.* 73 (2015) 222–235.
- [22] S.K. Bhattu, M.A. Repka, S. Maddineni, A.G. Chittiboyina, M.A. Avery, S. Majumdar, Physicochemical characterization of berberine chloride: a perspective in the development of a solution dosage form for oral delivery, *AAPS PharmSciTech* 11 (2010) 1466–1475.
- [23] C. Li, D. Zhang, H. Guo, L. Hao, D. Zheng, G. Liu, J. Shen, X. Tian, Q. Zhang, Preparation and characterization of galactosylated bovine serum albumin nanoparticles for liver-targeted delivery of oridonin, *Int. J. Pharm.* 448 (2013) 79–86.
- [24] S. Liang, X. Jin, Y. Ma, J. Guo, H. Wang, Folic acid-conjugated BSA nanocapsule (n-BSA-FA) for cancer targeted radiotherapy and imaging, *RSC Adv.* 5 (2015) 88560–88566.
- [25] M. Dubois, K.A. Gilles, J.K. Hamilton, P.t. Rebers, F. Smith, Colorimetric method for determination of sugars and related substances, *Anal. Chem.* 28 (1956) 350–356.
- [26] B. Stella, S. Arpicco, M.T. Peracchia, D. Desmaële, J. Hoebeke, M. Renoir, J. D'Angelo, L. Cattel, P. Couvreur, Design of folic acid conjugated nanoparticles for drug targeting, *J. Pharm. Sci.* 89 (2000) 1452–1464.
- [27] S.N. Khattab, S.E.A. Naim, M. El-Sayed, A.A. Chittiboyina, M.A. Avery, S. Majumdar, Physicochemical characterization of berberine chloride: a perspective in the development of a solution dosage form for oral delivery, *AAPS PharmSciTech* 11 (2010) 1466–1475.
- [28] W. Lin, M.C. Garnett, S.S. Davis, E. Schacht, P. Ferruti, L. Illum, Preparation and characterisation of rose Bengal-loaded surface-modified albumin nanoparticles, *J. Control. Release* 71 (2001) 117–126.
- [29] A.O. Elzoghby, B.Z. Vranic, W.M. Samy, N.A. Elgindy, Swellable floating tablet based on spray-dried casein nanoparticles: near-infrared spectral characterization and floating matrix evaluation, *Int. J. Pharm.* 491 (2015) 113–122.
- [30] A.O. Elzoghby, S.A. El-Lakany, M.W. Helmy, M.M. Abu-Serie, N.A. Elgindy, Shell-crosslinked zein nanocapsules for oral codelivery of exemestane and resveratrol in breast cancer therapy, *Nanomedicine* 12 (2017) 2785–2805.
- [31] A.O. Elzoghby, N.I. Saad, M.W. Helmy, W.M. Samy, N.A. Elgindy, Ionically-cross-linked milk protein nanoparticles as flutamide carriers for effective anticancer activity in prostate cancer-bearing rats, *Eur. J. Pharm. Biopharm.* 85 (2013) 444–451.
- [32] A.O. Elzoghby, S.K. Mostafa, M.W. Helmy, M.A. Eldemellawy, S.A. Sheweita, Multi-reservoir phospholipid shell encapsulating protamine nanocapsules for co-delivery of letrozole and celecoxib in breast cancer therapy, *Pharm. Res.* 34 (2017) 1956–1969.
- [33] A.O. Elzoghby, S.K. Mostafa, M.W. Helmy, M.A. Eldemellawy, S.A. Sheweita, Superiority of aromatase inhibitor and cyclooxygenase-2 inhibitor combined delivery: hyaluronate-targeted versus PEGylated protamine nanocapsules for breast cancer therapy, *Int. J. Pharm.* 529 (2017) 178–192.
- [34] F. Ungaro, I. D'Angelo, C. Coletta, R.D.E. di Villa Bianca, R. Sorrentino, B. Perfetto, M.A. Tufano, A. Miro, M.I. La Rotonda, F. Quaglia, Dry powders based on PLGA nanoparticles for pulmonary delivery of antibiotics: modulation of encapsulation efficiency, release rate and lung deposition pattern by hydrophilic polymers, *J. Control. Release* 157 (2012) 149–159.
- [35] X. Zhen, X. Wang, C. Xie, W. Wu, X. Jiang, Cellular uptake, antitumor response and tumor penetration of cisplatin-loaded milk protein nanoparticles, *Biomaterials* 34 (2013) 1372–1382.
- [36] M. Nasr, N. Nafee, H. Saad, A. Kazem, Improved antitumor activity and reduced cardiotoxicity of epirubicin using hepatocyte-targeted nanoparticles combined with tocotrienols against hepatocellular carcinoma in mice, *Eur. J. Pharm. Biopharm.* 88 (2014) 216–225.
- [37] E. Kaczmarek, A. Gorna, P. Majewski, Techniques of image analysis for quantitative immunohistochemistry, *Rocz. Akad. Med. Białymst.* 49 (2004) 155–158.
- [38] X. Zhao, Q. Chen, Y. Li, H. Tang, W. Liu, X. Yang, Doxorubicin and curcumin co-delivery by lipid nanoparticles for enhanced treatment of diethylnitrosamine-induced hepatocellular carcinoma in mice, *Eur. J. Pharm. Biopharm.* 93 (2015) 27–36.
- [39] L. Zhang, J. Yao, J. Zhou, T. Wang, Q. Zhang, Glycyrrhetic acid-graft-hyaluronic acid conjugate as a carrier for synergistic targeted delivery of antitumor drugs, *Int. J. Pharm.* 441 (2013) 654–664.
- [40] A.O. Elzoghby, W.M. Samy, N.A. Elgindy, Novel spray-dried genipin-crosslinked casein nanoparticles for prolonged release of alfuzosin hydrochloride, *Pharm. Res.* 30 (2013) 512–522.
- [41] A. Shapira, Y.G. Assaraf, D. Epstein, Y.D. Livney, Beta-casein nanoparticles as an oral delivery system for chemotherapeutic drugs: impact of drug structure and properties on co-assembly, *Pharm. Res.* 27 (2010) 2175–2186.
- [42] S.H. Choi, T.G. Park, Hydrophobic ion pair formation between leuprolide and sodium oleate for sustained release from biodegradable polymeric microspheres, *Int. J. Pharm.* 203 (2000) 193–202.
- [43] S. Sun, N. Liang, Y. Kawashima, D. Xia, F. Cui, Hydrophobic ion pairing of an insulin-sodium deoxycholate complex for oral delivery of insulin, *Int. J. Nanomedicine* 6 (2011) 3049.
- [44] T. Imsoibut, Y. Srisuwan, P. Srihanam, Y. Baimark, Genipin-cross-linked silk fibroin microspheres prepared by the simple water-in-oil emulsion solvent diffusion method, *Powder Technol.* 203 (2010) 603–608.
- [45] H.C. Liang, W.H. Chang, K.J. Lin, H.W. Sung, Genipin-crosslinked gelatin microspheres as a drug carrier for intramuscular administration: in vitro and in vivo studies, *J. Biomed. Mater. Res.* A 65 (2003) 271–282.
- [46] Y.-J. Li, M. Dong, F.-M. Kong, J.-P. Zhou, Folate-decorated anticancer drug and magnetic nanoparticles encapsulated polymeric carrier for liver cancer therapeutics, *Int. J. Pharm.* 489 (2015) 83–90.
- [47] S. Wang, T. Langrish, M. Leszczynski, The effect of casein as a spray-drying additive on the sorption and crystallization behavior of lactose, *Dry. Technol.* 28 (2010) 422–429.
- [48] P. Shi, J.C. Goh, Release and cellular acceptance of multiple drugs loaded silk fibroin particles, *Int. J. Pharm.* 420 (2011) 282–289.
- [49] H.-z. Zhang, F.-p. Gao, L.-r. Liu, X.-m. Li, Z.-m. Zhou, Q.-q. Zhang, Pullulan acetate nanoparticles prepared by solvent diffusion method for epirubicin chemotherapy, *Colloids Surf. B: Biointerfaces* 71 (2009) 19–26.
- [50] N. Elgindy, K. Elkhodairy, A. Molokhia, A. Elzoghby, Biopolymeric microparticles combined with lyophilized monophase dispersions for controlled flutamide release, *Int. J. Pharm.* 411 (2011) 113–120.
- [51] C. De Kruijff, E.B. Zhulina,  $\kappa$ -Casein as a polyelectrolyte brush on the surface of casein micelles, *Colloids Surf. A Physicochem. Eng. Asp.* 117 (1996) 151–159.
- [52] R.F. Wallin, E. Arscott, A Practical Guide to ISO 10993-5: Cytotoxicity, Medical Device and Diagnostic Industry, vol. 20, (1998), pp. 96–98.
- [53] S. Narayanan, M. Pavithran, A. Viswanath, D. Narayanan, C.C. Mohan, K. Manzoor, D. Menon, Sequentially releasing dual-drug-loaded PLGA–casein core/shell nanomedicine: Design, synthesis, biocompatibility and pharmacokinetics, *Acta Biomater.* 10 (2014) 2112–2124.
- [54] T.-C. Chou, Drug combinations: from laboratory to practice, *J. Lab. Clin. Med.* 132 (1998) 6–8.
- [55] T. Chou, P. Talalay, Applications of the median-effect principle for the assessment of low-dose risk of carcinogens and for the quantitation of synergism and antagonism of chemotherapeutic agents, *New Avenues Dev. Cancer Chemother.* 8 (1987) 37–64.

- [56] T.-C. Chou, P. Talaly, A simple generalized equation for the analysis of multiple inhibitions of Michaelis-Menten kinetic systems, *J. Biol. Chem.* 252 (1977) 6438–6442.
- [57] C. Duan, J. Gao, D. Zhang, L. Jia, Y. Liu, D. Zheng, G. Liu, X. Tian, F. Wang, Q. Zhang, Galactose-decorated pH-responsive nanogels for hepatoma-targeted delivery of oridonin, *Biomacromolecules* 12 (2011) 4335–4343.
- [58] M. Karin, Nuclear factor- $\kappa$ B in cancer development and progression, *Nature* 441 (2006) 431–436.
- [59] T. Hamsa, G. Kuttan, Antiangiogenic activity of berberine is mediated through the downregulation of hypoxia-inducible factor-1, VEGF, and proinflammatory mediators, *Drug Chem. Toxicol.* 35 (2012) 57–70.
- [60] M.-K. Jang, H. Su Kim, Y.-H. Chung, Clinical aspects of tumor necrosis factor- $\alpha$  signaling in hepatocellular carcinoma, *Curr. Pharm. Des.* 20 (2014) 2799–2808.
- [61] C.S. Boosani, A.P. Mannam, D. Cosgrove, R. Silva, K.M. Hoidalva-Dilke, V.G. Keshamouni, A. Sudhakar, Regulation of COX-2-mediated signaling by  $\alpha$ 3 type IV noncollagenous domain in tumor angiogenesis, *Blood* 110 (2007) 1168–1177.
- [62] T. Feng, H. Yu, Q. Xia, Y. Ma, H. Yin, Y. Shen, X. Liu, Cross-talk mechanism between endothelial cells and hepatocellular carcinoma cells via growth factors and integrin pathway promotes tumor angiogenesis and cell migration, *Oncotarget* 8 (2017) 69577.
- [63] N. Nishida, H. Yano, T. Nishida, T. Kamura, M. Kojiro, Angiogenesis in cancer, *Vasc. Health Risk Manag.* 2 (2006) 213.
- [64] S. Jie, H. Li, Y. Tian, D. Guo, J. Zhu, S. Gao, L. Jiang, Berberine inhibits angiogenic potential of Hep G2 cell line through VEGF down-regulation in vitro, *J. Gastroenterol. Hepatol.* 26 (2011) 179–185.
- [65] T.D. Dung, C.-H. Lin, T.V. Binh, H.-H. Hsu, C.-C. Su, Y.-M. Lin, C.-H. Tsai, F.-J. Tsai, W.-W. Kuo, L.-M. Chen, Diosmin induces cell apoptosis through protein phosphatase 2A activation in HA22T human hepatocellular carcinoma cells and blocks tumour growth in xenografted nude mice, *Food Chem.* 132 (2012) 2065–2073.
- [66] Z. Mallat, A. Tedgui, Apoptosis in the vasculature: mechanisms and functional importance, *Br. J. Pharmacol.* 130 (2000) 947–962.
- [67] D. Chodon, S.M. Banu, R. Padmavathi, D. Sakthisekaran, Inhibition of cell proliferation and induction of apoptosis by genistein in experimental hepatocellular carcinoma, *Mol. Cell. Biochem.* 297 (2007) 73–80.
- [68] M. Wei, Y. Xu, Q. Zou, L. Tu, C. Tang, T. Xu, L. Deng, C. Wu, Hepatocellular carcinoma targeting effect of PEGylated liposomes modified with lactoferrin, *Eur. J. Pharm. Sci.* 46 (2012) 131–141.

## Article

# Components from the Leaves and Twigs of Mangrove *Lumnitzera racemosa* with Anti-Angiogenic and Anti-Inflammatory Effects

Szu-Yin Yu <sup>1,†</sup>, Shih-Wei Wang <sup>1,2,†</sup> , Tsong-Long Hwang <sup>3,4,5</sup> , Bai-Luh Wei <sup>6</sup>, Chien-Jung Su <sup>1</sup>, Fang-Rong Chang <sup>1,7,\*</sup>  and Yuan-Bin Cheng <sup>1,8,\*</sup> 

<sup>1</sup> Graduate Institute of Natural Products, College of Pharmacy, Kaohsiung Medical University, Kaohsiung 807, Taiwan; s91412232@gmail.com (S.-Y.Y.); shihwei@mmc.edu.tw (S.-W.W.); scj820826@gmail.com (C.-J.S.)

<sup>2</sup> Department of Medicine, Mackay Medical College, New Taipei City 252, Taiwan

<sup>3</sup> Graduate Institute of Natural Products, College of Medicine, and Chinese Herbal Medicine Research Team, Healthy Aging Research Center, Chang Gung University, Taoyuan 333, Taiwan; htl@mail.cgu.edu.tw

<sup>4</sup> Research Center for Chinese Herbal Medicine, Research Center for Food and Cosmetic Safety, and Graduate Institute of Health Industry Technology, College of Human Ecology, Chang Gung University of Science and Technology, Taoyuan 333, Taiwan

<sup>5</sup> Department of Anesthesiology, Chang Gung Memorial Hospital, Taoyuan 333, Taiwan

<sup>6</sup> Department of Life Science, National Taitung University, Taitung 950, Taiwan; blwei@nttu.edu.tw

<sup>7</sup> National Research Institute of Chinese Medicine, Ministry of Health and Welfare, Taipei 112, Taiwan

<sup>8</sup> Department of Medical Research, Kaohsiung Medical University Hospital, Kaohsiung 807, Taiwan

\* Correspondence: aaronfrc@kmu.edu.tw (F.-R.C.); jmb@kmu.edu.tw (Y.-B.C.); Tel.: +886-7-312-1101 (ext. 2162) (F.-R.C.); +886-7-312-1101 (ext. 2197) (Y.-B.C.)

† These authors contributed equally to this work.

Received: 5 October 2018; Accepted: 23 October 2018; Published: 25 October 2018



**Abstract:** One new neolignan, racelactone A (**1**), together with seven known compounds (**2**–**8**) were isolated from the methanolic extract of the leaves and twigs of *Lumnitzera racemosa*. The structure of racelactone A (**1**) was determined on the basis of the mass and NMR spectroscopic data interpretation. With respect to bioactivity, compound **1** displayed an anti-angiogenic effect by suppressing tube formation. Furthermore, compounds **1**, **4**, and **5** showed significant anti-inflammatory effects with IC<sub>50</sub> values of 4.95 ± 0.89, 1.95 ± 0.40, and 2.57 ± 0.23 μM, respectively. The plausible biosynthesis pathway of racelactone A (**1**) was proposed.

**Keywords:** neolignan; *Lumnitzera racemosa*; anti-angiogenesis; anti-inflammation

## 1. Introduction

Mangroves are unique plants growing in the intertidal zone of the tropical and subtropical climates; these species are salt-tolerant and have mechanisms which affect a variety of cellular metabolic processes [1]. Plants of the mangrove genus *Lumnitzera* (Combretaceae) comprise more than 600 species in Asia, Australia, and Africa. Among them, *Lumnitzera racemosa* Willd. is native to the seashore of southern Taiwan. *L. racemosa* can grow up to a five-meter height; its bark is dark brown and rough, the leaves are slightly concave top round, and the fruits are drupe and with an ellipsoid shape [2]. The woods of *L. racemosa* are hard and have a long shelf life; they can be used as building materials, equipment, or fuels. *L. racemosa* is also a fantabulous nectar plant, while the leaves are edible to date [3]. Traditionally, the sap of this plant is used to treat cutaneous pruritus, herpes, scabies, and thrush [4]. The chemical constituents of *L. racemosa* are fatty acids, flavonoids, polyisoprenoid alcohols, tannins, and triterpenoids [5]. Pharmacological studies of the extracts from *L. racemosa*



demonstrated antibacterial, antifungal, antihypertensive, antioxidant, cytotoxic, and hepatoprotective activities [6–9].

Inflammation is tightly associated with carcinogenesis and the disease progression of cancer [10]. Angiogenesis has been reported to facilitate the growth and dissemination of cancer cells in tumor microenvironments [11]. Plentiful studies reveal that inhibition of inflammation and angiogenesis is an effective therapeutic strategy to suppress cancer development and metastasis [12,13]. Our preliminary pharmacological investigation indicated that methanolic extract of the leaves and twigs of *L. racemosa* exerted promising anti-angiogenic and anti-inflammatory responses. Herein, we describe the isolation, structural elucidation, and bioactivities of one new neolignan, racelactone A (**1**), along with seven known compounds (**2–8**).

## 2. Results

In the present study, the methanolic extracted from *L. racemosa* was partitioned with ethyl acetate (EtOAc) and water (H<sub>2</sub>O). The EtOAc layer was further partitioned with *n*-hexane and 75% methanol (MeOH) in H<sub>2</sub>O to give a 75% MeOH<sub>(aq)</sub> layer. One new compound, racelactone A (**1**), and seven known compounds: Botulin (**2**) [14,15], 3,4,3'-tri-*O*-methyl ellagic acid (**3**) [16], methyl gallate (**4**) [17], myricitrin (**5**) [18], stigmasterol (**6**) [19], kaempferol (**7**) [20], and isoguaiacin (**8**) [21] were identified from the 75% MeOH<sub>(aq)</sub> layer. The structures of compounds (**1–8**) are shown in Figure 1.

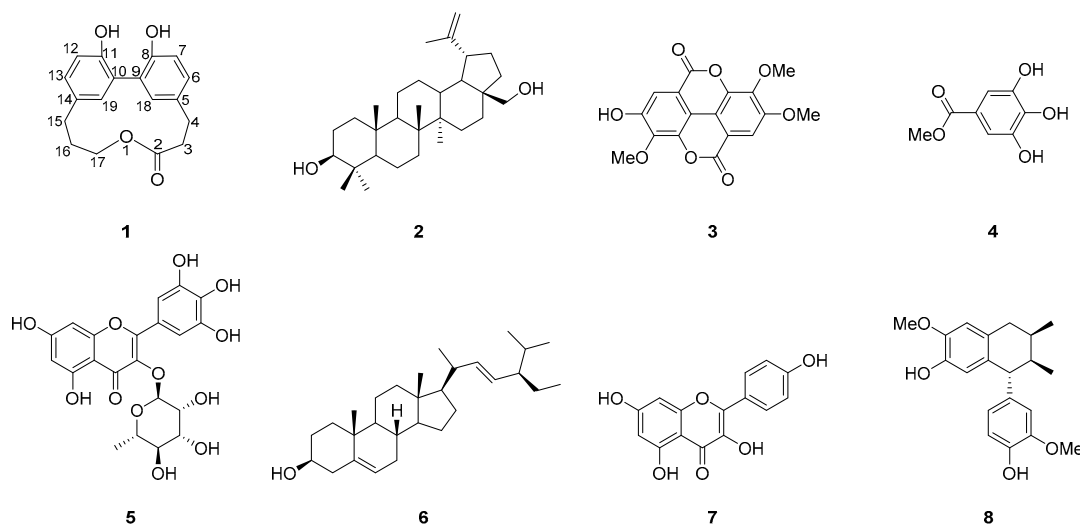


Figure 1. Structures of compounds **1–8**.

Racelactone A (**1**) was isolated as an amorphous powder, light yellow, having a molecular formula determined as C<sub>18</sub>H<sub>18</sub>O<sub>4</sub>. Ten indices of hydrogen deficiency were calculated, in accord with the high-resolution electrospray ionisation mass spectrometry (HRESIMS) data (*m/z* 321.10955 [M + Na]<sup>+</sup>) (Figure S1) and NMR spectrum. The IR spectrum (Figure S2) of **1** suggested the presence of hydroxy (3364 cm<sup>−1</sup>), carbonyl (1709 cm<sup>−1</sup>) and aromatic (1503, 1586 cm<sup>−1</sup>) functionalities. In <sup>1</sup>H NMR (Figure S3), data revealed six olefinic methines ( $\delta_{\text{H}}$  6.81, 6.87, 7.01, 7.03, 7.06, and 7.18), and five methylenes ( $\delta_{\text{H}}$  2.25, 2.58, 2.82, 2.98, and 4.29) (Table 1). The <sup>13</sup>C (Figure S4) and DEPT NMR spectrum (Table 1) of **1** noted eighteen carbon signals, including one carbonyl ( $\delta_{\text{C}}$  175.0), six olefinic methines ( $\delta_{\text{C}}$  113.3, 115.9, 116.4, 128.3, 129.2, and 133.1), six nonprotonated carbons ( $\delta_{\text{C}}$  126.6, 127.2, 131.4, 132.7, 151.9, and 152.7), and five methylenes ( $\delta_{\text{C}}$  25.2, 29.7, 30.7, 35.7, and 65.7). Analyses on a set of signals and coupling constants at  $\delta_{\text{H}}$  6.87 (d, 1H, *J* = 8.2 Hz, H-12), 7.03 (dd, 1H, *J* = 8.2, 2.4 Hz, H-13), and 7.06 (d, 1H, *J* = 2.5 Hz, H-18) as well as another set at  $\delta_{\text{H}}$  7.01 (dd, 1H, *J* = 8.2, 2.5 Hz, H-6), 6.81 (d, 1H, *J* = 8.1 Hz, H-7), and 7.19 (d, 1H, *J* = 2.5 Hz, H-19) led to the identification of two 1,3,4-trisubstituted phenyl moieties. From analyses of the NMR, UV (Figure S5), and IR data, compound **1** was determined to be a neolignan. Compound **1** showed similar <sup>1</sup>H and <sup>13</sup>C NMR signals (Table 1), partially similar to those

of corniculatolide A, which has an ether bridge between two propylphenyl moieties [22,23]—except for the presence of two unusual quaternary carbon signals at  $\delta_c$  126.6 and  $\delta_c$  127.2 instead of two signals at  $\delta_c$  149.0 and  $\delta_c$  154.2 in corniculatolide A. This indicated a new carbon–carbon linkage formation in the target molecule.

**Table 1.**  $^1\text{H}$  and  $^{13}\text{C}$  NMR data of **1**<sup>a</sup> in acetone- $d_6$ .

Position	$\delta_{\text{H}}$ , mult ( <i>J</i> in Hz)	$\delta_{\text{C}}$ , Type	HMBC ( $^1\text{H}$ - $^{13}\text{C}$ )
2	-	175.0, C	-
3	2.58, m	35.7, CH <sub>2</sub>	2, 4, 5
4	2.98, m	29.7, CH <sub>2</sub>	2, 3, 5, 6, 18
5	-	132.7, C	-
6	7.01, dd (8.1, 2.5)	128.3, CH	7, 8, 18
7	6.81, d (8.1)	115.9, CH	5, 6, 8, 9
8	-	152.7, C	-
9	-	127.2, C	-
10	-	126.6, C	-
11	-	151.9, C	-
12	6.87, d (8.2)	116.4, CH	10, 11, 14
13	7.03, dd (8.2, 2.5)	129.2, CH	11, 12, 15, 19
14	-	131.4, C	-
15	2.82, m	30.7, CH <sub>2</sub>	13, 14, 16, 17, 19
16	2.25, m	25.2, CH <sub>2</sub>	14, 15, 17
17	4.29, t (5.0)	65.7, CH <sub>2</sub>	2, 15, 16
18	7.06, d (2.5)	133.1, CH	4, 6, 8, 10
19	7.19, d (2.5)	133.3, CH	9, 11, 13

<sup>a</sup>  $^1\text{H}$  and  $^{13}\text{C}$  NMR data ( $\delta$ ) were measured at 400 and 100 MHz, respectively; chemical shifts are in ppm.

The planar structure of **1** was established by the correlation spectroscopy (COSY) (Figure S6) and heteronuclear multiple bond correlation (HMBC) (Figure S7) correlations (Figure 2). The COSY correlations established the fragments of H-3/H-4, H-6/H-7, H-12/H-13, and H-15/H-16/H-17 of compound **1**. The HMBC correlations of H-4/C-5, C-6, and C-18 and the correlations of H-15/C-13, C-14, and C-19 determined the linkages of two sets of propyl and phenyl functions, respectively. The macroring connection system of two phenylpropanoid moieties was completed on the basis of a key HMBC correlation between H-17/C-2, H-18/C-10, and H-19/C-9. As mentioned above, compound **1** was categorized as a macrolactone, and named racelactone A. The biosynthesis of racelactone A is proposed to be initiated by a PAL enzyme of phenylalanine to form dihydrocaffeic acid. The precursor was resonated to form intermediates A and B. Phenoxy radicals of intermediates A and B were linked to generate the intermediate C, which was structured as racelactone A during a cyclization (Figure 3).

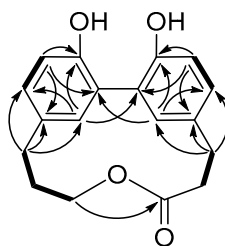


**Figure 2.** COSY (bold bond) and selected HMBC (arrow) correlations of **1**.

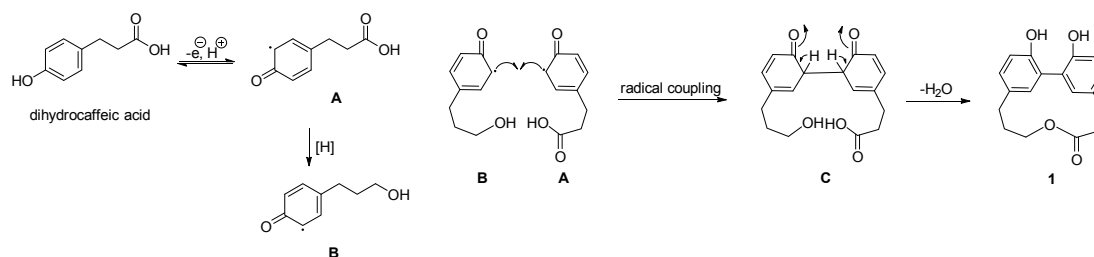


**Figure 3.** Plausible biosynthesis pathway of racelactone A (1).

Circulating endothelial progenitor cells (EPCs) have been reported to promote tumor angiogenesis and metastasis [24,25]. Tumors can secrete a variety of angiogenic factors to induce the recruitment of EPCs from bone marrow to the tumor site. Recruited EPCs enter the circulation system from their niche in bone marrow and extravasate with the chemotactic stimuli. After reaching the tumor site, EPCs differentiate into the structural part of the tumor vasculature, which contributes to tumor progression. Furthermore, EPCs have the ability to release pro-inflammatory cytokines that facilitate the growth and metastatic spread of tumors. Compelling evidence suggests that selective targeting of EPCs represents a novel therapeutic strategy for cancer treatment [26]. The differentiation and formation of capillary vessels is the most critical process during EPCs angiogenesis. Therefore, we performed tube formation assay to evaluate the anti-angiogenic activity of racelactone A in EPCs. As shown in Figure 4, the capillary tube-like structure was suppressed by racelactone A in a concentration-dependent manner. Sorafenib, a well-known angiogenesis inhibitor, was used as the positive control. To confirm this anti-angiogenic effect was not caused by the potential cytotoxicity of racelactone A, the release of lactate dehydrogenase (LDH) was measured in racelactone A-treated EPCs. We found that no statistical difference was observed between the control EPCs and EPCs treated with racelactone A. Collectively, these results reveal that the anti-angiogenic effect of racelactone A is not due to the cytotoxic action in human EPCs.

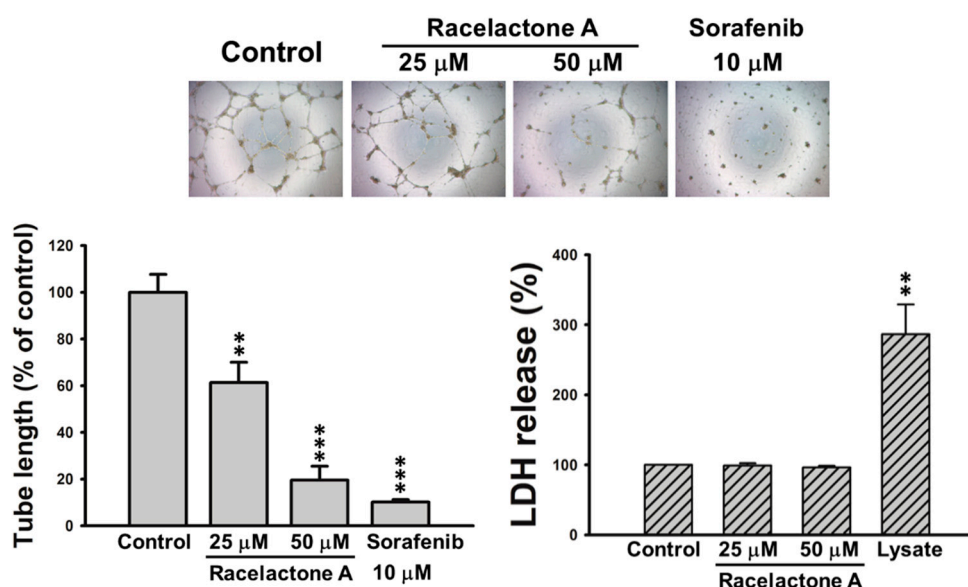


**Figure 4.** Effect of racelactone A (1) on tube formation and cytotoxicity of human endothelial progenitor cells (EPCs). EPCs were with the indicated concentrations of racelactone A and sorafenib for 24 h. The capillary-like structure formation and lactate dehydrogenase (LDH) release were determined by tube formation and cytotoxicity assay, respectively. Representative images of EPCs' tube formation were shown (phase contrast, 40 $\times$ ). Data represent the mean  $\pm$  SEM of five independent experiments. \*\*  $p < 0.01$ , \*\*\*  $p < 0.001$  compared with the control group.

All compounds were subjected to anti-inflammatory assays on superoxide anion generation and elastase release in fMLF/CB-induced human neutrophils inhibitory effects. Fortunately, the new compound **1** selectively displayed significant inhibitory activity on superoxide anion generation ( $IC_{50} = 4.95 \pm 0.89 \mu M$ ). The known compounds **4** and **5** also showed strong activity (Table 2).

**Table 2.** Inhibitory effects of isolates on superoxide anion generation and elastase release in fMLF/CB-induced human neutrophils.

Compound	Percentage of $IC_{50}$ ( $\mu M$ ) <sup>a</sup>			
	Superoxide Anion		Elastase Release	
<b>1</b>	$4.95 \pm 0.89$	**	>10	
<b>4</b>	$1.95 \pm 0.40$	***	>10	
<b>5</b>	$2.57 \pm 0.23$	***	>10	
genistein <sup>b</sup>	$1.54 \pm 0.37$	***	$17.47 \pm 2.80$	***

Percentage of inhibition (Inh %) at 10  $\mu M$  concentration. Results are presented as mean  $\pm$  SEM ( $n = 3\sim 5$ ). \*\*  $p < 0.01$ , \*\*\*  $p < 0.001$  compared with the control. <sup>a</sup> Concentration necessary for 50% inhibition ( $IC_{50}$ ). <sup>b</sup> positive control.

### 3. Materials and Methods

#### 3.1. General Experimental Procedures

Optical rotation was measured on a JASCO P-1020 digital polarimeter (Tokyo, Japan). UV data were recorded on a JASCO V-530 UV/VIS Spectrophotometer (Tokyo, Japan). High-resolution ESIMS data were obtained on a Bruker APEX II spectrometer (Billerica, MA, USA). The IR spectrum was measured on a Perkin Elmer system 2000 FT-IR spectrophotometer (Waltham, MA, USA). The NMR spectra were obtained by JEOL JNM-ECS 400 MHz NMR (Akishima, Japan). Merck (Darmstadt, Germany) silica gel 60 and GE Healthcare (Chicago, IL, USA) Sephadex LH-20 were used for column chromatography. The instrumentation for HPLC was composed of a Shimadzu LC-10AD pump (Kyoto, Japan) and a Shimadzu SPD-M10A PDA detector.

#### 3.2. Material

Specimens of *Lumnitzera racemosa* were collected in south Taiwan, in August 2015. The research samples were identified by Yuan-Bin Cheng. A voucher specimen (no. KMU-LR01) was deposited in the Graduate Institute of Natural Products, College of Pharmacy, Kaohsiung Medical University.

#### 3.3. Extraction and Isolation

The air-dry twigs and leaves (15.0 kg) of *L. racemosa* were ground and extracted thrice with MeOH (40 L) at room temperature. The solvent was concentrated under reducing pressure to yield crude extracts. The MeOH crude extracts were partitioned between H<sub>2</sub>O/EtOAc (1:1) to afford two portions. The EtOAc part was partitioned with *n*-hexane and 75% MeOH in water (1:1). The 75% MeOH<sub>(aq)</sub> layer (88.5 g) was subjected to a silica gel column stepwise eluted with *n*-hexane/EtOAc to yield botulin (221.1 mg), 3,4,3'-Tri-*O*-methyl ellagic acid (3330.0 mg), methyl gallate (4730.0 mg), myricitrin (5599.5 mg), and six fractions (A–J). Fraction C (830 mg) was isolated by silica gel column to give stigmaterol (63.4 mg). Fraction E (2.4 g) was chromatographed over a silica gel column to afford six subfractions (E.1–E.6). Subfraction E.4 (196.9 mg) was further separated by an LH-20 column, eluted with 100% MeOH to yield kaempferol (712.8 mg). Racelactone A (111.0 mg) and isoguaiacin (83.7 mg) were obtained from subfraction D.1 (144.7 mg) by LH-20 column, eluted with 100% MeOH and Phenyl-hexyl column (Luna phenyl-hexyl, 100 Å, 250  $\times$  10 mm, Phenomenex®) stepwise from 70% to 100% MeOH<sub>(aq)</sub>.

Racelactone A (1): Light yellow amorphous powder;  $[\alpha]_D^{26} -0.6$  ( $c$  0.05, MeOH); UV (MeOH)  $\lambda_{max}$  (log  $\epsilon$ ) 299 (2.85), 252 (2.95), 215 (3.34) nm; IR (neat)  $\nu_{max}$ : 3364, 1709, 1503, 1411  $cm^{-1}$ ; <sup>1</sup>H NMR and <sup>13</sup>C NMR data, see Table 1; HRESIMS  $m/z$  321.10955 [ $M + Na$ ]<sup>+</sup> (calcd for C<sub>18</sub>H<sub>18</sub>O<sub>4</sub>Na<sup>+</sup>: 321.10973).



### 3.4. Preparation of Human EPCs

The ethical approval for the collection of human EPCs was granted by the Institutional Review Board of Mackay Medical College, New Taipei City, Taiwan (P1000002). Prior to collecting the peripheral blood from healthy donors, informed consent was acquired. After density centrifugation Ficoll-Paque plus (Amersham Biosciences, Uppala, Sweden), peripheral blood mononuclear cells (PBMCs) were isolated from the fractionated blood components. CD34-positive progenitor cells were isolated from PMBCs with CD34 MicroBead kit and MACS Cell Separation System (Miltenyi Biotec, Bergisch Gladbach, Germany). Further isolation and preservation of CD34-positive EPCs were performed as described previously [27,28]. In the present study, all experiments were carried out on EPCs between passages 10 and 18. EPCs were cultured with 1% gelatin-coated plasticware and MV2 complete medium (PromoCell, Heidelberg, Germany) with 20% defined fetal bovine serum (FBS) (HyClone, Logan, UT, USA) in humidified incubator containing 5% CO<sub>2</sub> at 37 °C.

### 3.5. Tube Formation Assay

The capillary tube formation assay was carried out on Matrigel-coated 96-well plates. EPCs were seeded with the density of  $1.25 \times 10^4$  cells per well and incubated in an MV2 complete medium with 2% FBS and the indicated concentration of tested compounds for 24 h at 37 °C. Quantifications of EPCs differentiation and capillary-like tube formation were done with photomicrographs taken by an inverted phase contrast microscope. The long axis of each tube was measured with Image J software in 3 randomly chosen fields per well.

### 3.6. Cytotoxicity Assay

$5 \times 10^3$  of EPCs per well were seeded onto 96-well plates and incubated with an MV2 complete medium containing 2% FBS in the presence of vehicle (DMSO) or racelactone A. The quantification of LDH release in the medium was done with a cytotoxicity assay kit (Promega, Madison, WI, USA).

### 3.7. Superoxide Anion and Elastase Release Assays

The assay on superoxide anion generation and elastase release in response to fMLF stimulation of neutrophils were assayed by the same method as those of the reference published by co-author Professor Tsong-Long Hwang [29].

## 4. Conclusions

In summary, eight compounds, including one unusual macrolactone neolignan, were isolated and identified during a phytochemical investigation of the Taiwanese mangrove, *L. racemosa*. The new compound shows promising activities to anti-angiogenic and anti-inflammatory effects. Our findings suggest that racelactone A (**1**) may serve as a lead compound worthy of further development against angiogenesis-related diseases or inflammation-facilitated disorders, especially for the treatment of cancer.

**Supplementary Materials:** The following are available online at <http://www.mdpi.com/1660-3397/16/11/404/s1>, Figure S1: HRESIMS of racelactone A (**1**). Figure S2: IR spectrum of racelactone A (**1**). Figure S3: <sup>1</sup>H NMR Spectrum of racelactone A (**1**) in acetone-*d*<sub>6</sub>. Figure S4: <sup>13</sup>C NMR Spectrum of racelactone A (**1**) in acetone-*d*<sub>6</sub>. Figure S5: UV spectrum of racelactone A (**1**). Figure S6: COSY Spectrum of racelactone A (**1**) in acetone-*d*<sub>6</sub>. Figure S7: HMBC Spectrum of racelactone A (**1**) in acetone-*d*<sub>6</sub>.

**Author Contributions:** S.-Y.Y., S.-W.W., B.-L.W., F.-R.C., and Y.-B.C. contributed to manuscript preparation; Y.-B.C. designed the whole experiment; S.-W.W., T.-L.H., and C.-J.S. analyzed the data and performed data acquisition.

**Funding:** This research was funded by [Ministry of Science and Technology, Taiwan] grant number [MOST 105-2628-B-037-001-MY3, MOST 106-2320-B-037-008-MY2, MOST106-2320-B-037-016, and MOST 107-2628-B-037-001].

**Acknowledgments:** We appreciated the Ministry of Science and Technology, Taiwan (MOST 105-2628-B-037-001-MY3 and MOST 106-2320-B-037-008-MY2 award to F.-R. Chang; MOST106-2320-B-037-016 and MOST 107-2628-B-037-001 award to Y.-B. Cheng).

**Conflicts of Interest:** The authors declare no conflict of interest.

## References

1. Parida, A.L.; Jha, B. Salt tolerance mechanisms in mangroves: A review. *Trees* **2010**, *24*, 199–217. [\[CrossRef\]](#)
2. Chen, J. *Flora of China*; Missouri Botanical Garden: St. Louis, MO, USA; Harvard University Herbaria: Cambridge, MA, USA, 2007; Volume 13, p. 310.
3. Tomlinson, P.B. *The Botany of Mangroves*; Cambridge University Press: Cambridge, UK, 2016; p. 236, ISBN 9781107080676.
4. Chong, K.Y.; Tan, H.T.W.; Corlett, R.T. *A Checklist of the Total Vascular Plant Flora of Singapore Native, Naturalized and Cultivated Species*; National University of Singapore: Singapore, 2009; p. 273.
5. Anjaneyulu, A.S.R.; Murthy, Y.L.N.; Rao, V.L.; Sreedhar, K. A new aromatic ester from the mangrove plant *Lumnitzera racemosa* Willd<sup>+</sup>. *ARKIVOC* **2003**, *3*, 25–30. [\[CrossRef\]](#)
6. Lin, T.C.; Hsu, F.L.; Cheng, J.T. Antihypertensive activity of corilagin and chebulinic acid, tannins from *Lumnitzera racemosa*. *J. Nat. Prod.* **1993**, *56*, 629–632. [\[CrossRef\]](#)
7. D'Souza, L.; Wahidulla, S.; Devi, P. Antibacterial phenolics from the mangrove *Lumnitzera racemosa*. *Indian J. Mar. Sci.* **2010**, *39*, 294–298.
8. Ravikumar, S.; Gnanadesigan, M. Hepatoprotective and antioxidant activity of a mangrove plant *Lumnitzera racemosa*. *Asian Pac. J. Trop. Biomed.* **2011**, *1*, 348–352. [\[CrossRef\]](#)
9. Thao, N.P.; Luyen, B.T.T.; Diep, C.N.; Tai, B.H.; Kim, E.J.; Kang, H.K.; Lee, S.H.; Jang, H.D.; Cuong, N.T.; Thanh, N.V.; et al. In vitro evaluation of the antioxidant and cytotoxic activities of constituents of the mangrove *Lumnitzera racemosa* Willd. *Arch. Pharm. Res.* **2015**, *38*, 446–455. [\[CrossRef\]](#) [\[PubMed\]](#)
10. Clevers, H. At the crossroads of inflammation and cancer. *Cell* **2004**, *118*, 671–674. [\[CrossRef\]](#) [\[PubMed\]](#)
11. Chung, A.S.; Lee, J.; Ferrara, N. Targeting the tumour vasculature: Insights from physiological angiogenesis. *Nat. Rev. Cancer* **2010**, *10*, 505–514. [\[CrossRef\]](#) [\[PubMed\]](#)
12. Weis, S.M.; Cheresch, D.A. Tumor angiogenesis: Molecular pathways and therapeutic targets. *Nat. Med.* **2011**, *17*, 1359–1370. [\[CrossRef\]](#) [\[PubMed\]](#)
13. Zha, S.; Yegnashubramanian, V.; Nelson, W.G.; Isaacs, W.B.; Marzo, A.M.D. Cyclooxygenases in cancer: Progress and perspective. *Cancer Lett.* **2004**, *215*, 1–20. [\[CrossRef\]](#) [\[PubMed\]](#)
14. Liao, C.-R.; Kuo, Y.-H.; Ho, Y.-L.; Wang, C.-Y.; Yang, C.-S.; Lin, C.-W.; Chang, Y.-S. Studies on cytotoxic constituents from the leaves of *Elaeagnus oldhamii* Maxim. in non-small cell lung cancer A549 Cells. *Molecules* **2014**, *19*, 9515–9534. [\[CrossRef\]](#) [\[PubMed\]](#)
15. Schmidt, J.; Himmelreich, U.; Adam, G. Brassinosteroids, sterols and lup-20(29)-en-2 $\alpha$ ,3 $\beta$ ,28-triol from *Rheum Rhabarbarum*. *Phytochemistry* **1995**, *40*, 527–531. [\[CrossRef\]](#)
16. Begum, S.S.; Tauseef, S.; Siddiqui, B.S.; Nizami, S.S.; Ghulam, H.; Ahmad, A. In vitro antibacterial and antifungal activity of flower buds (clove) of *Syzygium aromaticum*. *J. Chem. Soc. Pak.* **2014**, *36*, 723–728.
17. Madikizela, B.; Aderogba, M.A.; Finnie, J.F.; Staden, J.V. Isolation and characterization of antimicrobial compounds from *Terminalia phanerophlebia* Engl. & Diels leaf extracts. *J. Ethnopharmacol.* **2014**, *156*, 228–234. [\[CrossRef\]](#) [\[PubMed\]](#)
18. Saldanha, L.L.; Vilegas, W.; Dokkedal, A.L. Characterization of flavonoids and phenolic acids in *Myrcia bella* Cambess. using FIA-ESI-IT-MS<sup>n</sup> and HPLC-PAD-ESI-IT-MS combined with NMR. *Molecules* **2013**, *18*, 8402–8416. [\[CrossRef\]](#) [\[PubMed\]](#)
19. Forgo, P.; Kövér, K.E. Gradient enhanced selective experiments in the <sup>1</sup>H NMR chemical shift assignment of the skeleton and side-chain resonances of stigmaterol, a phytosterol derivative. *Steroids* **2004**, *69*, 43–50. [\[CrossRef\]](#) [\[PubMed\]](#)
20. Moraes, L.S.; Donza, M.R.H.; Rodrigues, A.P.D.; Silva, B.J.M.; Brasil, A.S.B.; Zoghbi, M.G.B.; Andrade, E.H.A.; Guilhon, G.M.S.P.; Silva, E.O. Leishmanicidal activity of (+)-phyllanthidine and the phytochemical profile of *Margaritaria nobilis* (Phyllanthaceae). *Molecules* **2015**, *20*, 22157–22169. [\[CrossRef\]](#) [\[PubMed\]](#)

21. Wang, B.-G.; Hong, X.; Li, L.; Zhou, J.; Hao, Z.-J. Chemical constituents of two Chinese Magnoliaceae plants, *Tsoongiodendron odorum* and *Manglietiastrum sinicum*, and their inhibition of platelet aggregation. *Planta Med.* **2000**, *66*, 511–515. [[CrossRef](#)] [[PubMed](#)]
22. Vongvanich, N.; Kittakoop, P.; Charoensai, P.; Intamas, S.; Danwisetkanjana, K.; Thebtaranonth, Y. Combretastatins D-3 and D-4, new macrocyclic lactones from *Getonia floribunda*. *Planta Med.* **2005**, *71*, 191–193. [[CrossRef](#)] [[PubMed](#)]
23. Pettit, G.R.; Quistorf, P.D.; Fry, J.A.; Herald, D.L.; Hamel, E.; Chapuis, J.-C. Antineoplastic agents. 565. synthesis of combretastatin D-2 phosphate and dihydro-combretastatin D-2<sup>1</sup>. *J. Nat. Prod.* **2009**, *72*, 876–883. [[CrossRef](#)] [[PubMed](#)]
24. Carmeliet, P. Angiogenesis in life, disease and medicine. *Nature* **2005**, *438*, 932–936. [[CrossRef](#)] [[PubMed](#)]
25. Urbich, C.; Dimmeler, S. Endothelial progenitor cells: Characterization and role in vascular biology. *Circ. Res.* **2004**, *95*, 343–353. [[CrossRef](#)] [[PubMed](#)]
26. Moschetta, M.; Mishima, Y.; Sahin, I.; Manier, S.; Glavey, S.; Vacca, A.; Roccaro, A.M.; Ghobrial, I.M. Role of endothelial progenitor cells in cancer progression. *BBA-Rev. Cancer* **2014**, *1846*, 26–39. [[CrossRef](#)] [[PubMed](#)]
27. Chung, C.-H.; Chang, C.-H.; Chen, S.-S.; Wang, H.-H.; Yen, J.-Y.; Hsiao, C.-J.; Wu, N.-L.; Chen, Y.-L.; Huang, T.-F.; Wang, P.-C.; et al. Butein inhibits angiogenesis of human endothelial progenitor cells via the translation dependent signaling pathway. *Evid.-Based Complement. Altern. Med.* **2013**, *2013*, e943187. [[CrossRef](#)] [[PubMed](#)]
28. Lee, M.-S.; Wang, S.-W.; Wang, G.-J.; Pang, K.-L.; Lee, C.-K.; Kuo, Y.-H.; Cha, H.-J.; Lin, R.-K.; Lee, T.-H. Angiogenesis inhibitors and anti-inflammatory agents from *Phoma* sp. NT0U4195. *J. Nat. Prod.* **2016**, *79*, 2983–2990. [[CrossRef](#)] [[PubMed](#)]
29. Yang, S.-C.; Chung, P.-J.; Ho, C.-M.; Kuo, C.-Y.; Hung, M.-F.; Huang, Y.-T.; Chang, W.-Y.; Chang, Y.-W.; Chan, K.-H.; Hwang, T.-L. Propofol inhibits superoxide production, elastase release, and chemotaxis in formyl peptide-activated human neutrophils by blocking formyl peptide receptor 1. *J. Immunol.* **2013**, *190*, 6511–6519. [[CrossRef](#)] [[PubMed](#)]



© 2018 by the authors. Licensee MDPI, Basel, Switzerland. This article is an open access article distributed under the terms and conditions of the Creative Commons Attribution (CC BY) license (<http://creativecommons.org/licenses/by/4.0/>).

# The Constituents of the Stems of *Cissus assamica* and Their Bioactivities

Yu-Yi Chan <sup>1</sup>, Chiu-Yuan Wang <sup>1</sup>, Tsong-Long Hwang <sup>2,3,4</sup>, Shin-Hun Juang <sup>5</sup>, Hsin-Yi Hung <sup>6</sup>, Ping-Chung Kuo <sup>6</sup>, Po-Jen Chen <sup>7</sup> and Tian-Shung Wu <sup>5,6,\*</sup>

<sup>1</sup> Department of Biotechnology, Southern Taiwan University of Science and Technology, Tainan 71005, Taiwan; yuyichan@stust.edu.tw (Y.-Y.C.); m98h0104@gmail.com (C.-Y.W.)

<sup>2</sup> Graduate Institute of Natural Products, School of Traditional Chinese Medicine, College of Medicine, Chang Gung University, Taoyuan 333, Taiwan; htl@mail.cgu.edu.tw

<sup>3</sup> Research Center for Chinese Herbal Medicine, Research Center for Food and Cosmetic Safety, Graduate Institute of Health Industry Technology, College of Human Ecology, Chang Gung University of Science and Technology, Taoyuan 333, Taiwan

<sup>4</sup> Department of Anesthesiology, Chang Gung Memorial Hospital, Taoyuan 333, Taiwan

<sup>5</sup> Department of Pharmacy, Tajen University, Pingtung 90741, Taiwan; paul.juang@gmail.com

<sup>6</sup> School of Pharmacy, College of Medicine, National Cheng Kung University, Tainan 701, Taiwan; z10308005@email.ncku.edu.tw (H.-Y.H.); z10502016@email.ncku.edu.tw (P.-C.K.);

<sup>7</sup> Department of Cosmetic Science, Providence University, Taichung 433, Taiwan; littlep@hotmail.com

\* Correspondence: tswu@mail.ncku.edu.tw; Tel.: +886-6-2757575 (ext. 65333)

Received: 24 September 2018; Accepted: 26 October 2018; Published: 28 October 2018

**Abstract:** Fifty-five compounds were isolated from the fresh stems of *Cissus assamica*, including 14 benzenoids, 11 triterpenes, nine steroids, five tocopherols, five chlorophylls, four flavonoids, two benzoquinones, two tannins, and three other compounds. Their structures were constructed by 1D and 2D nuclear magnetic resonance (NMR) and mass spectral data, and were also identified by a comparison of their spectral data with those reported in the literature. Among these isolates, 1,2-bis-(5- $\gamma$ -tocopheryl) ethane (**51**) was reported for the first time from natural sources. Some purified compounds were examined for their anti-inflammatory and anticancer bioactivities. The results indicated that betulinic acid (**16**) exhibited strong inhibition of superoxide anion generation with IC<sub>50</sub> value of  $0.2 \pm 0.1$   $\mu$ M, while betulinic acid (**16**) and pheophytin-a (**47**) inhibited elastase release with IC<sub>50</sub> value of  $2.7 \pm 0.3$  and  $5.3 \pm 1.0$   $\mu$ M, respectively. In addition, betulinic acid (**16**) and *epi*-glut-5(6)-en-ol (**18**) exhibited potential cytotoxicity to non-small-cell lung carcinoma (NCI-H226) and colon cancer (HCT-116) cell lines with IC<sub>50</sub> values in the range of 1.6 to 9.1  $\mu$ M.

**Keywords:** Vitaceae; anti-inflammatory; anticancer; cytotoxicity

## 1. Introduction

*Cissus assamica* L. belong to the Vitaceae family and is distributed in mainland China, Vietnam, India, Thailand, Indonesia, the southern part of Taiwan, and Lanyu Island [1]. Traditional Chinese medical literature records that the stem of *C. assamica* can activate the circulation to remove blood stasis and treat bruises, fractures, and rheumatoid arthritis [2]. Moreover, several active constituents, such as quinolizidine alkaloids, triterpenes, sterols, flavonoids, stilbenes, and saponins, were isolated and reported from the *Cissus* genus [3–11]. Previous biological investigations indicated that the extract of *C. sicyoides* showed moderate cytostatic activity against HEP-2 cells [12] and a significant anti-inflammatory effect [13]. In addition, studies of biological activities also showed hypoglycemic, anti-dyslipidemic, and anti-allergic effects of this genus [14–26]. However, research related to the species *C. assamica* L. is scarce. Only a few reported the effects of antagonizing the vasoconstriction



induced by endothelin-1 [22–26]. Therefore, this study aimed at the purification and identification of anticancer and anti-inflammatory principles from the stem of *C. assamica*.

## 2. Results and Discussion

### 2.1. Isolation and Characterization of Compounds

The fresh stems of *C. assamica* L. were extracted with methanol and refluxed for 8 h. The filtrate was concentrated under reduced pressure to yield a dark brown syrup. The crude extract was suspended in water and then partitioned with chloroform and *n*-butanol successively to afford chloroform, *n*-butanol, and water layers, respectively. Purification of the three layers by column chromatography yielded a mixture of  $\beta$ -sitosterol (1) and stigmasterol (2) [27],  $\beta$ -sitosteryl glucoside (3) [28], a mixture of  $3\beta$ -hydroxyl stigmaster-5-en-7-one (4) and  $3\beta$ -hydroxystigmaster-5, 22-dien-7-one (5) [29], a mixture of  $\beta$ -sitostenone (6) [30] and stigmaster-4,22-dien-3-one (7) [31],  $6\beta$ -hydroxy- $\beta$ -sitostenone (8) [32], ergosterol peroxide (9) [33], 3,5,7,4'-tetramethoxyflavone (10) [34], 3',4',3,6,7-pentamethoxyflavone (11) [35], 3',4',5,6,7-pentamethoxyflavone (12) [35], 4',5,6,7-tetramethoxyflavone (13) [36], a mixture of oleanolic acid (14) [30] and ursolic acid (15) [28], betulinic acid (16) [37], friedelin (17) [38], *epi*-glut-5(6)-en-ol (18) [39], taraxerol (19) [9], *epi*-friedelinol (20) [40], glutinone (21) [41], lup-28-al-20(29)-en-3-ol (22) [42], a mixture of  $\alpha$ -amyrin (23) and  $\beta$ -amyrin (24) [43], bergenin (25) [44], *p*-hydroxybenzaldehyde (26) [45], vanillin (27) [30], methyl gallate (28) [46], gallic acid (29) [47], 4-methoxybenzoic acid (30) [48], vanillic acid (31) [30], a mixture of 4-hydroxy-*trans*-cinnamic acid methyl ester (32) and 4-hydroxy-*cis*-cinnamic acid methyl ester (33) [49], a mixture of octadecyl-*trans*-ferulate (34) and octadecyl-*cis*-ferulate (35) [50], 1-(4-methoxy-phenyl)undecan-1-one (36) [51], 3-hydroxy-4-methoxybenzoic acid (37) [52], hexadecyl ferulate (38) [45], 2-hydroxybenzoquinone (39) [53], 2,6-dimethoxybenzoquinone (40) [49], 3,3',4-tri-*O*-methyl-ellagic acid (41) [54], 3,3',4,4'-tetra-*O*-methylellagic acid (42) [55], methyl pheophorbide-a (43) [49], a mixture of methyl-21-hydroxy-(21S)-pheophorbide-a (44) and methyl-21-hydroxy-(21R)-pheophorbide-a (45) [49], methyl-21-hydroxyl-(21S)-pheophorbide-b (46) [49], pheophytin-a (47) [49],  $\alpha$ -tocopherol (48) [56], tocopherol trimer IVa (49) [57], tocopherol trimer IVb (50) [57], 1,2-bis-(5- $\gamma$ -tocopheryl)ethane (51) [58],  $\alpha$ -tocospirol B (52) [59], 5,6-dimethoxy-3-methyl-2-cyclohexa-2,5-dien-1,4-dione (53) [60], 3-methyl-8-hydroxy-3,4-dihydroisocoumarin (54) [61], and methyl linoleate (55) [62], respectively. Among them, 1,2-bis-(5- $\gamma$ -tocopheryl)ethane (51) (Figure 1) is reported from natural sources for the first time.

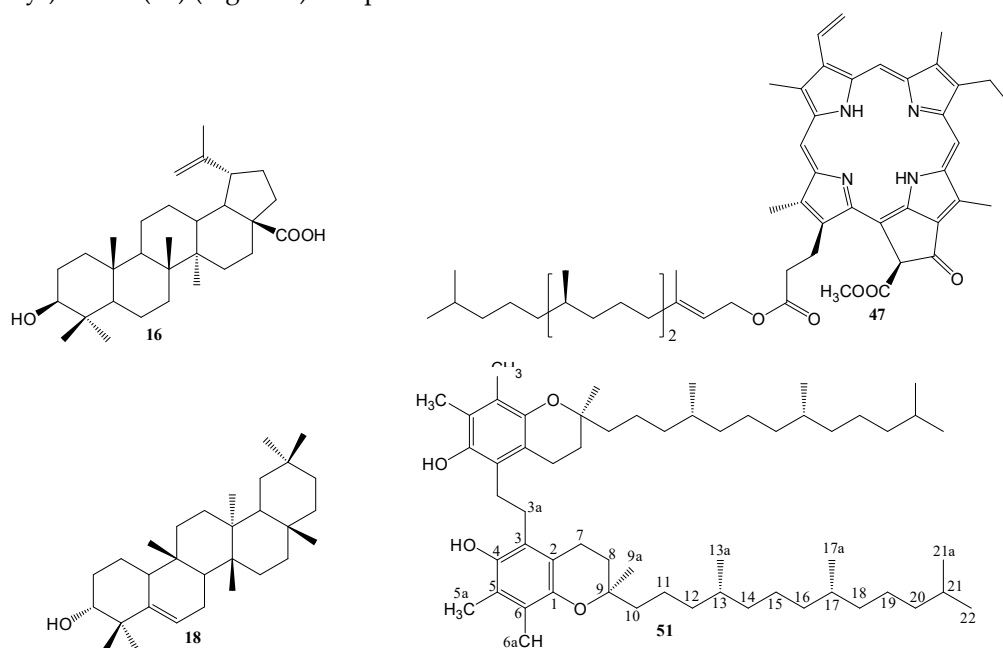


Figure 1. Structures of compounds 16, 18, 47 and 51.

## 2.2. Structural Elucidation of Compound 51

1,2-Bis-(5- $\gamma$ -tocopheryl)ethane (**51**) was isolated as a light yellow syrup. Its UV spectrum had an absorption maximum at 294 nm. The IR spectrum suggested the presence of hydroxyl ( $3444\text{ cm}^{-1}$ ) and an aromatic conjugated double bond ( $1458$  and  $1377\text{ cm}^{-1}$ ). The  $^{13}\text{C}$ -NMR and DEPT spectra exhibited a benzene ring partial structure that has two oxygenated substituents at  $\delta$  117.0 (s), 122.1 (s), 123.4 (s), 124.1 (s), 145.5 (s), and 146.3 (s). The  $^1\text{H}$ -NMR spectrum of **51** exhibited signals for two methyl and one methylene groups attached to a benzene ring at  $\delta$  2.13, 2.18, and 2.73. Comparing all the  $^1\text{H}$ - and  $^{13}\text{C}$ -NMR spectral signals carefully, the structure of **51** was similar to that of  $\alpha$ -tocopherol (**48**) [56]. It indicated that they are very closely related analogues, differing only in the presence of a methylene group ( $\delta_{\text{H}}$  2.73,  $\delta_{\text{C}}$  26.7) in **51**, instead of the methyl group ( $\delta_{\text{H}}$  2.17,  $\delta_{\text{C}}$  11.2) found in **48** (Table 1). To establish the structure of **51**, 2D NMR including correlation spectroscopy (COSY), nuclear Overhauser enhancement spectroscopy (NOESY), heteronuclear multiple quantum correlation (HMQC), and heteronuclear multiple bond correlation (HMBC) experiments were conducted. In the HMBC experiment, the correlations observed for H-5a ( $\delta_{\text{H}}$  2.18)/C-4, C-5, C-6 and H-6a ( $\delta_{\text{H}}$  2.13)/C-1, C-5, C-6 indicate that two methyl groups are located in the ortho position on the benzene ring. Moreover, the correlation of the methylene proton at  $\delta_{\text{H}}$  2.73 with C-3 in HMBC spectrum suggests that the location C-3a in the dimerization of  $\alpha$ -tocopherol forms the dimer **51**. Conclusively, the structure of **51** was assigned as 1,2-bis-(5- $\gamma$ -tocopheryl)ethane, which had been reported by synthesis [58], but is reported from natural sources for the first time. The NMR spectra are presented Figures S1–S6.

**Table 1.**  $^1\text{H}$ - and  $^{13}\text{C}$ -NMR spectra data of **48** and **51** ( $\text{CDCl}_3$ , 400 MHz).

Position	48		51	
	$\delta_{\text{H}}$ (mult., $J$ in Hz)	$\delta_{\text{C}}$	$\delta_{\text{H}}$ (mult., $J$ in Hz)	$\delta_{\text{C}}$
1		145.5		146.3
2		117.2		117.0
3		118.5		123.4
4		144.5		145.5
5		121.1		122.1
6		122.6		124.1
7	2.64 (t, 4.5)	21.0	2.74 (m)	21.7
8	1.79 (m)	31.5	1.83 (m)	32.3
9		74.5		75.3
10	1.56 (m)	39.8	1.56 (m)	40.7
11	1.54 (m)	22.6	1.54 (m)	21.3
12	1.26–1.25 (m)	37.4	1.28–1.25 (m)	38.2
13	1.31 (d, 7.4)	32.7	1.32 (d, 7.2)	33.4
14	1.26–1.25 (m)	37.2	1.28–1.25 (m)	37.9
15	1.26–1.25 (m)	24.8	1.28–1.25 (m)	25.5
16	1.26–1.25 (m)	37.5	1.28–1.25 (m)	38.2
17	1.31 (d, 7.4)	32.8	1.32 (d, 7.2)	33.5
18	1.16–1.13 (m)	37.4	1.16–1.13 (m)	38.2
19	1.16–1.13 (m)	25.1	1.16–1.13 (m)	25.2
20	1.16–1.13 (m)	39.4	1.16–1.13 (m)	40.1
21	1.52 (m)	27.9	1.52 (m)	28.7
22	0.91 (d, 6.4)	23.7	0.86 (d, 7.2)	23.4
3a	2.17 (s)	11.2	2.73 (s)	26.7
5a	2.22 (s)	12.8	2.18 (s)	12.8
6a	2.19 (s)	11.8	2.13 (s)	12.6
9a	1.28 (s)	24.4	1.24 (s)	24.5
13a	0.90 (d, 7.4)	20.3	0.85 (d, 7.2)	20.3
17a	0.89 (d, 7.4)	20.7	0.83 (d, 7.2)	20.5
21a	0.93 (d, 6.5)	22.7	0.87 (d, 7.2)	23.3
OH	4.25 (s)		5.41 (s)	

### 2.3. Anti-Inflammatory Activity

Neutrophils are the most abundant white blood cells and participate in the development of the inflammatory reactions in human body; they are important factors in the immune defense against various diseases. Some cytotoxins—for example, the superoxide anion radical, bioactive lipids, granule proteases, and elastase—can be secreted when the different stimuli activate neutrophils. Moreover, they are also major contributors to tissue destruction in chronic inflammatory diseases. It has been proposed that inhibiting neutrophil activation is a method of enhancing inflammatory disorders [63–66]. Most of the purified compounds in this study were inspected for the inhibition of elastase release and superoxide anion generation by human neutrophils in response to *N*-formyl-L-methionyl-phenylalanine/cytochalasin B (fMLP/CB). Only compound **16** (Figure 1) displayed significant inhibition of superoxide anion generation, with an  $IC_{50}$  value of  $0.2 \pm 0.1 \mu M$  (Table 2). In addition, compounds **16** and **47** also exhibited an inhibitory effect on elastase release with an  $IC_{50}$  value of  $2.7 \pm 0.3$  and  $5.3 \pm 1.0 \mu M$ , respectively (Table 2). The inhibitory effects of all the tested compounds on superoxide anion generation and elastase release by human neutrophils in response to fMLP/CB are presented in Table S1. The cytotoxicity of compounds **16**, **47**, and LY294002 (a PI3K inhibitor, as a positive control) was examined in human neutrophils using an LDH release assay (Figure S7). All these compounds did not induce LDH release, suggesting that the inhibitory effects did not result from cytotoxicity in human neutrophils.

**Table 2.** Inhibitory effects of isolated compounds on superoxide anion generation and elastase release by human neutrophils in response to fMLP/CB.

Compound	Superoxide Anion Generation	Elastase Release
	$IC_{50}$ ( $\mu M$ ) <sup>a</sup>	$IC_{50}$ ( $\mu M$ )
<b>16</b>	$0.2 \pm 0.1$ ***	$2.7 \pm 0.3$ ***
<b>47</b>	>10	$5.3 \pm 1.0$ ***
LY294002 <sup>b</sup>	$0.4 \pm 0.1$ ***	$1.5 \pm 0.3$ ***

Results are presented as mean  $\pm$  S.D. ( $n = 3\sim 4$ ). \*\*\*  $p < 0.001$  compared with the control (DMSO).<sup>a</sup> Concentration necessary for 50% inhibition ( $IC_{50}$ ).<sup>b</sup> A phosphatidylinositol-3-kinase inhibitor was used as a positive control.

### 2.4. Cytotoxicity

In order to evaluate the growth inhibitory activity of the purified compounds against cancer cells, this study selected three different cell lines from malignant tumors including human nasopharyngeal carcinoma (NPC-TW01), non-small-cell lung carcinoma (NCI-H226), and colon cancer cell lines (HCT116). The results showed that betulinic acid (**16**) and *epi*-glut-5(6)-en-ol (**18**) (Figure 1) exhibited significant cytotoxicity with  $IC_{50}$  values ranged from 1.6 to 9.1  $\mu M$  (Table 3). Moreover, betulinic acid (**16**) exhibited powerful inhibitory activity against NCI-H226 and HCT116 with  $IC_{50}$  values of 2.0 and 1.6  $\mu M$ , respectively. Our study suggested the stem extracts of *C. assamica* and the purified compounds are potential candidates for the development of anti-cancer drugs. The preliminary growth inhibitory activity of all the tested compounds is presented in Table S2.

**Table 3.** Cytotoxicity of compounds **16**, **18**, **20**, **21**, **41** and **52**.

Compounds	Cell Lines	
	NCI-H226	HCT-116
	$IC_{50}$ ( $\mu M$ )	$IC_{50}$ ( $\mu M$ )
<b>16</b>	2.0	1.6
<b>18</b>	9.1	6.0
<b>20</b>	15.8	16.7
<b>21</b>	38.0	24.0
<b>41</b>	31.6	30.3
<b>52</b>	>50	39.4

### 3. Materials and Methods

#### 3.1. General Information

UV spectra were obtained with a Hitachi UV-3210 and UV-3010 spectrophotometer (Hitachi, Tokyo, Japan), and IR spectra were measured with a Shimadzu FTIR Prestige-21 spectrometer (Shimadzu, Kyoto, Japan). Optical rotations were measured with a HORIBA SEPA-300 digital polarimeter in a 0.5 dm cell (Horiba, Kyoto, Japan). The ESIMS and HRESIMS were taken on a Bruker Daltonics APEX II 30e spectrometer (Bruker, Billerica, MA, USA).  $^1\text{H}$ - and  $^{13}\text{C}$ -NMR spectra were measured using Bruker Avance-300, AMX-400, and AV-500 spectrometers (Bruker, Billerica, MA, USA) with TMS as the internal reference, and chemical shifts are expressed in  $\delta$  (ppm). Silica gel (70–230 and 230–400 mesh; Merck, Darmstadt, Germany) and Spherical C18 100 Å reversed phase silica gel (RP-18; particle size 20–40  $\mu\text{m}$ ; Silicycle, Quebec City, QC, Canada) were used for column chromatography (CC), and silica gel 60 F<sub>254</sub> and RP-18 F<sub>254S</sub> thin-layer chromatography (TLC) plates (Merck, Darmstadt, Germany) were used for preparative TLC, respectively.

#### 3.2. Materials

The fresh stems of *C. assamica* L. were collected from Taitung Hsien, Taiwan, in October 2009 and verified by Prof. Chang-Sheng Kuoh (Department of Biology, National Cheng Kung University, Tainan, Taiwan). A voucher specimen (TSWu 20091016) has been deposited in the Herbarium of School of Pharmacy, National Cheng Kung University, Tainan, Taiwan.

#### 3.3. Extraction and Isolation

The fresh stems of *C. assamica* L. (15 kg) were extracted with methanol (15  $\times$  20 L) and refluxed for 8 h. The filtrate was evaporated under reduced pressure to yield a dark brown syrup (418 g). The residue was suspended in water and then partitioned with chloroform (5  $\times$  2 L) and *n*-butanol (5  $\times$  2 L) successively to afford chloroform (63 g), *n*-butanol (145 g) and water (210 g) soluble fractions respectively.

The chloroform soluble extracts were fractionated via silica gel column chromatography eluting with *n*-hexane/acetone (9:1) to afford seven fractions, on the basis of TLC monitoring. Fraction 1 was subjected to silica gel column chromatography eluted with *n*-hexane/acetone (79:1) to yield a mixture of  $\beta$ -sitosterol (**1**) and stigmasterol (**2**) (3.1 g), 3,5,7,4'-tetramethoxyflavone (**10**, 2.9 mg), 3',4',3,6,7-pentamethoxyflavone (**11**, 12.2 mg), 3',4',5,6,7-pentamethoxyflavone (**12**, 6.1 mg), 4',5,6,7-tetramethoxyflavone (**13**, 3.1 mg), friedelin (**17**, 1.8 g), taraxerol (**19**, 3.9 mg), glutinone (**21**, 3.2 mg) and methyl linoleate (**55**, 20.7 mg).

Purification of fraction 2 by column chromatography with silica gel was eluted by a gradient of benzene/ethyl acetate (79:1) to afford *epi*-glut-5(6)-en-ol (**18**, 23.2 mg),  $\alpha$ -tocopherol (**48**, 200 mg), tocopherol trimer IVa (**49**, 24.3 mg), tocopherol trimer IVb (**50**, 28.1 mg), 1,2-bis-(5- $\gamma$ -tocopheryl)-ethane (**51**, 15.4 mg),  $\alpha$ -tocospirol B (**52**, 6.1 mg) and 5,6-dimethoxy-3-methyl-2-cyclohexa-2,5-dien-1,4-dione (**53**, 52.2 mg).

Separation of fraction 3 by column chromatography with silica gel eluted by *n*-hexane/ethyl acetate (9:1) yielded a mixture of 3 $\beta$ -hydroxystigmast-5-en-7-one (**4**) and 3 $\beta$ -hydroxystigmast-5,22-dien-7-one (**5**, 4.5 mg), a mixture of  $\beta$ -sitostenone (**6**) and stigmasta-4,22-dien-3-one (**7**, 13.7 mg), 6 $\beta$ -hydroxy- $\beta$ -sitostenone (**8**, 16.9 mg), ergosterol peroxide (**9**, 35 mg), *epi*-friedelinol (**20**, 200 mg), lup-28-al-20(29)-en-3-ol (**22**, 3.2 mg), a mixture of  $\alpha$ -amyrin (**23**) and  $\beta$ -amyrin (**24**, 60 mg), a mixture of 4-hydroxy-*trans*-cinnamic acid methyl ester (**32**) and 4-hydroxy-*cis*-cinnamic acid methyl ester (**33**, 190 mg), a mixture of octadecyl-*trans*-ferulate (**34**) and octadecyl-*cis*-ferulate (**35**, 45.3 mg), hexadecyl ferulate (**38**, 20.7 mg) and 3-methyl-8-hydroxy-3,4-dihydroisocoumarin (**55**, 3.5 mg).

Fraction 4 was chromatographed over silica gel eluted with a benzene/acetone gradient (49:1) to give a mixture of oleanolic acid (**14**) and ursolic acid (**15**, 49.6 mg), betulinic acid (**16**, 63.6 mg), 4-methoxybenzoic acid (**30**, 4.7 mg), 1-(4-methoxyphenyl)undecan-1-one (**36**, 2.3 mg) and pheophytin-a (**47**, 11.2 mg).



Purification of fraction 5 by column chromatography with silica gel was eluted by a gradient of chloroform/acetone (49:1) to afford 2-hydroxybenzoquinone (**39**, 3.5 mg), methyl pheophorbide-a (**43**, 3.1 mg), a mixture of methyl-21-hydroxy-(21S)-pheophorbide-a (**44**) and methyl-21-hydroxy-(21R)-pheophorbide-a (**45**, 3.5 mg).

Separation of fraction 6 by column chromatography with a silica gel eluted by chloroform/acetone (49:1) yielded *p*-hydroxybenzaldehyde (**26**, 4.0 mg), 3,3',4-tri-*O*-methylellagic acid (**41**, 37.7 mg), 3,3',4,4'-tetra-*O*-methylellagic acid (**42**, 1.5 mg) and methyl-21-hydroxy-(21S)-pheophorbide-b (**46**, 3.6 mg).

Fraction 7 was subjected to silica gel column chromatography eluted with chloroform/methanol (49:1) to yield  $\beta$ -sitosterol glucoside (**3**, 700 mg), vanillin (**27**, 7.8 mg), vanillic acid (**31**, 1.7 mg), 3-hydroxy-4-methoxybenzoic acid (**37**, 3.2 mg), 2, 6-dimethoxybenzoquinone (**40**) (3.5 mg).

The *n*-butanol layer was subjected directly to Diaion HP-20 column chromatography, eluted with water containing increasing proportions of methanol, to give six fractions. Fraction 1 was chromatographed over Sephadex LH-20 eluted with gradient of water/methanol to give gallic acid (**29**, 600 mg). Fraction 2 was chromatographed on Sephadex LH-20 eluted with gradient of water/methanol to afford bergenin (**25**, 6.2 g). Fraction 4 was chromatographed on Sephadex LH-20 with water/methanol to give methyl gallate (**28**, 32.1 mg).

1,2-Bis-(5- $\gamma$ -tocopheryl)ethane (**51**): light yellow syrup; UV  $\lambda_{\max}$  (MeOH) nm (log  $\epsilon$ ) 294; IR (KBr)  $\nu_{\max}$  cm<sup>-1</sup> 3444, 2920, 2850, 1458, 1377, 1257, 1087; <sup>1</sup>H- and <sup>13</sup>C-NMR data, see Table 1.

### 3.4. Anti-Inflammatory Bioactivity Examination

#### 3.4.1. Preparation of Human Neutrophils

Human neutrophils study was approved by Chang Gung Memorial Hospital Institutional Review Board, Taoyuan, Taiwan. It was conducted according to the Declaration of Helsinki. Blood was obtained from healthy donors (20–32 years old) who provided written informed consent before blood was drawn. Briefly, neutrophils were isolated by dextran sedimentation, Ficoll-Hypaque gradient centrifugation, and hypotonic lysis of the erythrocytes [67].

#### 3.4.2. Measurement of Superoxide Anion Generation and Elastase Release

The superoxide anion generation and elastase release were measured using the reduction of ferricytochrome *c* and elastase substrate, methoxysuccinyl-Ala-Ala-Pro-Val-*p*-nitroanilide, respectively, as described previously [68–70]. Human neutrophils were suspended in HBSS containing ferricytochrome *c* (0.6 mg/mL) or elastase substrate (100  $\mu$ M) at 37 °C and treated with DMSO or tested compounds for 5 min. The cells were then activated using fMLF (0.1  $\mu$ M)/cytochalasin B (CB, 1  $\mu$ g/mL for superoxide generation and 0.5  $\mu$ g/mL for elastase release) and the change of absorbance was continually measured at 550 nm and 405 nm by a spectrophotometer (U-3010, Hitachi) to determine the superoxide anion generation and elastase release, respectively.

#### 3.4.3. Detection of Cytotoxicity

Human neutrophils were treated with DMSO or tested compounds and incubated at 37 °C for 15 min. The supernatant was assayed to detect the released LDH using CytoTox 96 non-radioactive cytotoxicity assay (Promega, Madison, WI, USA). The results are presented in Figure S7.

### 3.5. Determination of Anticancer Bioactivity

#### 3.5.1. Cell Lines

Human cancer cell lines, non-small cell lung carcinoma (NCI-H226) and colon cancer cell line (HCT116) were obtained from the American Type Culture Collection (Rockville, MD, USA). A nasopharyngeal carcinoma (NPC-TW01) cell line was purchased from Food Industry Research and

Development Institute (Hsinchu, Taiwan). Tumor cells were maintained in proper medium supplemented with 10% fetal bovine serum (FBS) at 37 °C in a humidified atmosphere of 5% CO<sub>2</sub>.

### 3.5.2. Growth Inhibition Assay

The evaluation of cell growth and survival was carried out according to Hansen et al. [71] with some modifications.

## 4. Conclusions

In summary, 55 compounds were characterized from the fresh stems of *C. assamica*, including 14 benzenoids, 11 triterpenes, nine steroids, five tocopherols, five chlorophylls, four flavonoids, two benzoquinones, two tannins, and three other compounds. Among these isolates, 1,2-bis-(5-γ-tocopheryl)ethane was reported for the first time from natural sources. Furthermore, the inhibitory activity on superoxide anion generation and elastase release and the cytotoxicity on three cancer cells were analyzed. The present study suggests that the stems of *C. assamica* and several compounds of its isolation could be further developed as candidates for the treatment or prevention of cancer and various inflammatory diseases. Thus, the detailed mechanism of action of these compounds appears worthy of follow-up investigation.

**Supplementary Materials:** The following are available online at [www.mdpi.com/1420-3049/23/11/2799/s1](http://www.mdpi.com/1420-3049/23/11/2799/s1), Tables S1 and S2: Anti-inflammatory and cytotoxic effects of all the tested compounds from *C. assamica*; Figures S1–S6: NMR spectra of compound **51**; Figure S7: Cytotoxicity of compounds **16**, **47** and LY294002.

**Author Contributions:** Conceptualization, T.-S.W.; Data curation, Y.-Y.C.; Investigation, C.-Y.W., H.-Y.H., P.-C.K.; Methodology, T.-L.H., S.-H.J., and P.-J.C.; Writing—original draft, Y.-Y.C., H.-Y.H.; Writing—review & editing, P.-C.K. and T.-S.W. All authors read and approved the final manuscript.

**Funding:** This study was sponsored by the Ministry of Science and Technology, Taiwan via a grant to T.-S.W. and Y.-Y.C. (NSC97-2320-B-218-001-MY3). The authors are also thankful to Chang Gung Memorial Hospital [CMRPD1B0281~3, CMRPF1D0442~3, CMRPF1F0011~3, CMRPF1F0061~3 and BMRP450 granted to T.-L.H.] for the partial financial support for the present research.

**Acknowledgments:** Authors were thankful to the Instruments Center of NCKU and the Joint Center for High Valued Instruments at NSYSU of the Ministry of Science and Technology, Taiwan for the assistance of recording NMR and MS spectra.

**Conflicts of Interest:** The authors declare no conflict of interest.

## References

1. Yang, T.Y. *Flora of Taiwan*, 2nd ed.; Editorial Committee of the Flora of Taiwan: Taipei, Taiwan, 1998; pp. 701–703.
2. Zhang, Y.Q.; Xie, Y.H.; Huang, L.P. Studies on the chemical constituents and biological activities from *Cissus L.* *Lishizhen Medicine and Materia Medica Research* **2006**, *17*, 107–114.
3. Otshudi, A.L.; Foriers, A.; Vercruysse, A.; Van, Z.A.; Lauwers, S. In vitro antimicrobial activity of six medicinal plants traditionally used for the treatment of dysentery and diarrhoea in Democratic Republic of Congo. *Phytomedicine* **2000**, *7*, 167–172.
4. Beltrame, F.L.; Sartoretto, J.L.; Bazotte, R.B.; Cuman, R.N.; Cortez, D.A.G. Phytochemical study and evaluation of the antidiabetic potential of *Cissus sicyoides* L. *Quim. Nova* **2001**, *24*, 783–785.
5. Beltrame, F.L.; Ferreira, A.G.; Cortez, D.A. Coumarin glycoside from *Cissus sicyoides*. *Nat. Prod. Lett.* **2002**, *16*, 213–216.
6. Adesanya, S.A.; Nia, R.; Martin, M.T.; Boukamcha, N.; Montagnac, A.; Pais, M. Stilbene derivatives from *Cissus quadrangularis*. *J. Nat. Prod.* **1999**, *62*, 1694–1695.
7. Bhutani, K.K.; Kapoor, R.; Atal, C.K. Two unsymmetric tetracyclic triterpenoids from *Cissus quadrangularis*. *Phytochemistry* **1984**, *23*, 407–410.
8. Gupta, M.M.; Verma, R.K. Unsymmetric tetracyclic triterpenoid from *Cissus quadrangularis*. *Phytochemistry* **1990**, *29*, 336–337.
9. Gupta, M.M.; Verma, R.K. Lipid constituents of *Cissus quadrangularis*. *Phytochemistry* **1991**, *30*, 875–878.

10. Khan, M.A.; Nabi, S.G.; Prakash, S.; Zaman, A. Pallidol, a resveratrol dimer from *Cissus pallida*. *Phytochemistry* **1986**, *25*, 1945–1948.
11. Al-Said, M.S.; Khalifa, A.S.; Al-Azizi, M.M. Flavonoids from *Cissus digitat*. *Int. J. Pharm.* **1991**, *29*, 281–283.
12. Saenz, M.T.; Garcia, M.D.; Quilez, A.; Ahumada, M.C. Cytotoxic activity of *Agave intermixta* L. (Agavaceae) and *Cissus sicyoides* L. (Vitaceae). *Phytother. Res.* **2000**, *14*, 552–554.
13. Garcia, M.D.; Quilez, A.M.; Saenz, M.T.; Martinez, D.M.E.; De, P.R. Anti-inflammatory activity of agave intermixta trel and *Cissus sicyoides* L., species used in the caribbean traditional medicine. *J. Ethnopharmacol.* **2000**, *71*, 395–400.
14. Atawodi, S.E.; Arneh, D.A.; Ibrahim, S.; Andrew, J.N.; Nzelibe, H.C.; Onyike, E.O.; Anigo, K.M.; Abu, E.A.; James, D.B.; Njoku, G.C.; Sallau, A.B. Indigenous knowledge system for treatment of trypanosomiasis in Kaduna state of Nigeria. *J. Ethnopharmacol.* **2002**, *79*, 279–282.
15. Jainu, M.; Devi, C.S.S. Effect of *Cissus quadrangularis* on gastric mucosal defensive factors in experimentally induced gastric ulcer—A comparative study with sucralfate. *J. Med. Food* **2004**, *7*, 372–376.
16. Quilez, A.M.; Saenz, M.T.; Garcia, M.D.; de la Puerta, R. Phytochemical analysis and anti-allergic study of agave intermixta trel and *Cissus sicyoides* L. *J. Pharm. Pharmacol.* **2004**, *56*, 1185–1189.
17. Viana, G.S.; Medeiros, A.; Lacerda, A.M.; Leal, L.K.; Vale, T.G.; Matos, F.J. Hypoglycemic and anti-lipemic effects of the aqueous extract from *Cissus sicyoides*. *BMC Pharmacol.* **2004**, *4*, 9–15.
18. Chidambara, M.K.N.; Vanitha, A.; Mahadeva, S.M.; Ravishankar, G.A. Antioxidant and antimicrobial activity of *Cissus quadrangularis* L. *J. Med. Food* **2003**, *6*, 99–105.
19. Pepato, M.T.; Baviera, A.M.; Vendramini, R.C.; Perez, M.P.M.S.; Kettelhut, I.C.; Brunetti, I.L. *Cissus sicyoides* in the long-term treatment of streptozotocin-diabetic rats. *Biotechnol. Appl. Biochem.* **2003**, *37*, 15–20.
20. Alzoreky, N.S.; Nakahara, K. Antibacterial activity of extracts from some edible plants commonly consumed in Asia. *Int. J. Food. Microbiol.* **2003**, *80*, 223–230.
21. Garcia, X.; Cartas, H.L.; Lorenzana, J.M.; Gijon, E. Vasoconstrictor effect of *Cissus sicyoides* on guinea Pig aortic rings. *Gen. Pharmacol.* **1997**, *29*, 457–462.
22. Mori, T.; Nishikawa, Y.; Takata, Y.; Kashuichi, N.; Ishihara, N. Effect of insulina leaf extract on development of diabetes comparison between normal, streptozotocin-induced diabetic rats and hereditary diabetic mice. *Nippon Eiyo Shokuryo Gakkaishi* **2001**, *54*, 197–203.
23. Yang, L.; Wang, F.; Liu, M.; Lu, M.; Jia, H.; Fang, X.; Li, Z. Isolation of resveratrol and its antagonistic effects on endothelin-1. *Huaxi Yaoxue Zazhi* **2000**, *15*, 81–84.
24. Wang, F.; Yang, L.; Cheng, Y.; Lu, M.; Liu, M.; Ji, X.; Jia, H. Antagonism effects of extracts of Chinese herb *Cissus assamica* and monomer CA-1201 on endothelin-1 responses. *Zhongguo Yaoxue Zazhi* **1998**, *33*, 337–340.
25. Yang, L.C.; Wang, F.; Liu, M. A study of an endothelin antagonist from a Chinese anti-snake venom medicinal herb. *J. Cardiovasc. Pharmacol.* **1998**, *31*, S249–S250.
26. Wang, F.; Yang, L.; Liu, M.; Lu, M.; Cheng, Y.; Jia, H. A primary study on antagonizing effects of anti-snake venom Chinese herb on endothelin-1 and sarafotoxin 6b. *Zhongguo Zhong Yao Za Zhi* **1997**, *22*, 620–622.
27. Shen, D.Y.; Juang, S.H.; Kuo, P.C.; Huang, G.J.; Chan, Y.Y.; Damu, A.G.; Wu, T.S. Chemical constituents from *Andrographis echinoides* and their anti-inflammatory activity. *Int. J. Mol. Sci.* **2013**, *14*, 496–514.
28. Wu, T.S.; Chan, Y.Y. Constituents of leaves of *Uncaria hirsuta* Haviland. *J. Chin. Chem. Soc.* **1994**, *41*, 209–212.
29. Kuo, Y.H.; Chu, P.H. Studies on the constituents from the bark of *Bauhinia purpurea*. *J. Chin. Chem. Soc.* **2002**, *49*, 269–274.
30. Wu, S.J.; Chan, Y.Y. Five New Iridoids from Roots of *Salvia digitaloides*. *Molecules* **2014**, *19*, 15521–15534.
31. Kuo, P.C.; Yang, M.L.; Hwang, T.L.; Lai, Y.Y.; Li, Y.C.; Thang, T.D.; Wu, T.S. Anti-inflammatory Diterpenoids from *Croton tonkinensis*. *J. Nat. Prod.* **2013**, *76*, 230–236.
32. Chang, Y.C.; Chang, F.R.; Wu, Y.C. The Constituents of *Lindera Glauca*. *J. Chin. Chem. Soc.* **2000**, *47*, 373–380.
33. Thang, T.D.; Kuo, P.C.; Hwang, T.L.; Yang, M.L.; Ngoc, T.B.; Han, T.N.; Lin, C.W.; Wu, T.S. Triterpenoids and steroids from *Ganoderma mastoporum* and their inhibitory effects on superoxide anion generation and elastase release. *Molecules* **2013**, *18*, 14285–14292.
34. Dong, H.; Gou, Y.L.; Cao, S.G.; Chen, S.X.; Sim, K.Y. Eicosenones and methylated flavonols from *Amomum koenigii*. *Phytochemistry* **1999**, *50*, 899–902.
35. Machida, K.; Osawa, K. On the flavonoid constituents from the peels of *Citrus hassaku* Hort.ex Tanaka. *Chem. Pharm. Bull.* **1989**, *37*, 1092–1094.

36. Weber, B.; Hartmann, B.; Stockigt, D.; Schreiber, K.; Roloff, M.; Bertram, H.J.; Schmidt, C.O. Liquid chromatography/mass spectrometry and liquid chromatography nuclear magnetic resonance as complementary analytical techniques for unambiguous identification of polymethoxylated flavones in residues from molecular distillation of orange peel oils (*Citrus sinensis*). *J. Agric. Food Chem.* **2006**, *54*, 274–278.
37. Chatterjee, P.; Kouzi, S.A.; Pezzuto, J.P.; Hamann, M.T. Biotransformation of the antimelanoma agent betulinic acid by *Bacillus megaterium* ATCC 13368. *Appl. Environ. Microbiol.* **2000**, *66*, 3850–3855.
38. Wu, T.S.; Chan, Y.Y.; Liou, M.J.; Lin, F.W.; Shi, L.S.; Chen, K.T. Platelet aggregation inhibitor from *Murraya euchrestifolia*. *Phytother. Res.* **1998**, *12*, S80–S82.
39. Tanabe, Y.; Sinoda, R.; Horikoshi, Y.; Takahashi, K. Studies on constituents of medicinal plants. XVI. The constituents of *Spiraea* species. *Yakugaku Zasshi* **1976**, *96*, 248–250.
40. Li, K.H.; Chang, C.R.; Chang, Y.S. Chemical components from *Triumfetta bartramia*. *J. Chin. Chem. Soc.* **1995**, *42*, 93–95.
41. Zhang, J.; Yin, Z.Q.; Cao, P.; Li, Y.B.; Duan, J.A. A new flavonol derivative from *Fagopyrum dibotrys*. *Chem. Nat. Compd.* **2008**, *44*, 701–703.
42. Hata, K.; Hori, K.; Takahashi, S. Differentiation and apoptosis-inducing activities by pentacyclic triterpenes on a mouse melanoma cell line. *J. Nat. Prod.* **2009**, *65*, 645–648.
43. Bolleddula, J.; Mulabagal, V.; Yanjun, Z.; David, L.D.; Muraleedharan, G.N. Impact of alkyl esters of caffeic and ferulic acids on tumor cell proliferation cyclooxygenase enzyme and lipid peroxidation. *J. Agric. Food Chem.* **2006**, *54*, 5375–5381.
44. Xie, Y.H.; Zhang, Y.Q.; Deng, P.; Yu, W.S. Determination of bergenin in *Cissus assamica* by HPLC. *Shizhen Guoyi Guoyao* **2009**, *20*, 1086–1087.
45. Chiang, C.Y.; Leu, Y.L.; Chan, Y.Y.; Wu, T.S. Sodium aristolochates from the flowers and fruits of *Aristolochia zollingeriana*. *J. Chin. Chem. Soc.* **1998**, *45*, 93–97.
46. Choi, S.E.; Yoon, J.H.; Choi, H.K.; Lee, M.W. Phenolic compounds from the root of *Phragmites communis*. *Chem. Nat. Compd.* **2009**, *45*, 893–895.
47. Jun, X.L.; Duo, L.D.; Yan, P.S. Diversity of chemical constituents from *Saxifraga montana* H. *J. Chin. Chem. Soc.* **2008**, *55*, 863–870.
48. Cui, L.Q.; Liu, K.; Zhang, C. Effective oxidation of benzylic and alkane C–H bonds catalyzed by sodium O-iodobenzenesulfonate with oxone as a terminal oxidant under phase-transfer conditions. *Org. Biomol. Chem.* **2011**, *9*, 2258–2265.
49. Wu, T.S.; Tsanga, Z.J.; Wu, P.L.; Lin, F.W.; Li, C.Y.; Temg, C.M.; Lee, K.H. New constituents and antiplatelet aggregation and anti-HIV principles of *Artemisia capillaris*. *Bioorg. Med. Chem.* **2001**, *9*, 77–83.
50. Wei, H.; Wen, D.X.; Liu, X.S.; Tang, R.J. Constituents in petroleum ether and ethyl acetate extract fractions of *Dracaena cochinchinensis*. (Lour.) *Zhong Guo Zhong Yao Za Zhi* **1998**, *23*, 616–618.
51. Loupy, A.; Chatti, S.; Delamare, S.; Lee, D.-Y.; Chung, J.-H.; Jun, C.-H. Solvent-free chelation-assisted hydroacylation of olefins rhodium(I) catalyst under microwave irradiation. *J. Chem. Soc.* **2002**, *10*, 1280–1285.
52. Ding, H.Y.; Lin, H.C.; Teng, C.M.; Wu, Y.C. Phytochemical and pharmacological studies on Chinese *Paeonia* species. *J. Chin. Chem. Soc.* **2000**, *47*, 381–388.
53. Magdziak, D.; Rodriguez, A.A.; Van, D.W.; Ryan, W.; Pettus, T.R.R. Regioselective oxidation of phenols to O-quinones with O-iodoxybenzoic Acid (IBX). *Org. Lett.* **2002**, *4*, 285–288.
54. Gao, X.; Wu, J.; Zou, W.; Dai, Y. Two ellagic acids isolated from roots of *Sanguisorba officinalis* L. promote hematopoietic progenitor cell proliferation and megakaryocyte differentiation. *Molecules* **2014**, *19*, 5448–5458.
55. Reitze, J.D.; Przewloka, S.R.; Shearer, B.J. The further chemistry of ellagic acid: I. synthesis of tetramethylellagic acid and associated polymer precursors. *Holzforschung* **2005**, *55*, 171–175.
56. Almeida, E.R.D.; Rafael, K.R.D.O.; Couto, G.B.L.; Ishigmi, A.B. Anxiolytic and anticonvulsant effects on mice of flavonoids, linalool, and  $\alpha$ -tocopherol presents in the extract of leaves of *Cissus sicyoides* L. *J. Biomed. Biotechnol.* **2009**, *1*, 1–6.
57. Lie, C.R.; Jiau, C.H.; Chiu, M.C. Cerebrosides and tocopherol trimers from the seeds of *Euryale ferox*. *J. Nat. Prod.* **2007**, *70*, 1214–1217.



58. Rosenau, T.; Kloser, E.; Gille, L.; Mazzini, F.; Netscher, T. Vitamin E chemistry. studies into initial oxidation intermediates of  $\alpha$ -tocopherol: disproving the involvement of 5a-C-centered chromanol methide radicals. *J. Org. Chem.* **2007**, *72*, 3268–3281.
59. Chiang, Y.M.; Kuo, Y.H. Two novel  $\alpha$ -tocopheroids from the aerial roots of *Ficus microcarpa*. *Tetrahedron Lett.* **2003**, *44*, 5125–5128.
60. Lipshutz, B.H.; Butler, T.; Lower, A. Controlling regiochemistry in negishi carboaluminations fine tuning the ligand on zirconium. *J. Am. Chem. Soc.* **2006**, *128*, 15396–15398.
61. Zeng, Z.X.; Ma, W.H.; Li, Y.L.; Han, T.; Zheng, C.J.; Qin, L.P. Two new diterpenes from *Solidago canadensis*. *Helv. Chim. Acta.* **2012**, *95*, 1121–1125.
62. Zeng, Z.X.; Li, Y.L.; Dong, L.L.; Fan, G.X.; Fei, D.Q. Chemical constituents of the roots of *Ligularia lapathifolia*. *Chem. Nat. Compd.* **2015**, *51*, 375–377.
63. Witko-Sarsat, V.; Rieu, P.; Descamps-Latscha, B.; Lesavre, P.; Halbwachs-Mecarelli, L. Neutrophils: Molecules, functions and pathophysiological aspects. *Lab. Investig.* **2000**, *80*, 617–653.
64. Borregaard, N. The human neutrophil. Function and dysfunction. *Eur. J. Haematol.* **1998**, *41*, 401–413.
65. Roos, D.; van Bruggen, R.; Meischl, C. Oxidative killing of microbes by neutrophils. *Microbes Infect.* **2003**, *5*, 1307–1315.
66. Faurschou, M.; Borregaard, N. Neutrophil granules and secretory vesicles in inflammation. *Microbes Infect.* **2003**, *5*, 1317–1327.
67. Chen, P.J.; Wang, Y.L.; Kuo, L.M.; Lin, C.F.; Chen, C.Y.; Tsai, Y.F.; Shen, J.J.; Hwang, T.L. Honokiol suppresses TNF- $\alpha$ -induced neutrophil adhesion on cerebral endothelial cells by disrupting polyubiquitination and degradation of IkappaB $\alpha$ . *Sci. Rep.* **2016**, *6*, 26554.
68. Yang, S.C.; Chung, P.J.; Ho, C.M.; Kuo, C.Y.; Hung, M.F.; Huang, Y.T.; Chang, W.Y.; Chang, Y.W.; Chan, K.H.; Hwang, T.L. Propofol inhibits superoxide production, elastase release, and chemotaxis in formyl peptide-activated human neutrophils by blocking formyl peptide receptor 1. *J. Immunol.* **2013**, *190*, 6511–6519.
69. Babior, B.M.; Kipnes, R.S.; Curnutte, J.T. Biological defense mechanisms. The production by leukocytes of superoxide, a potential bactericidal agent. *J. Clin. Investig.* **1973**, *52*, 741–744.
70. Hwang, T.L.; Li, G.L.; Lan, Y.H.; Chia, Y.C.; Shieh, P.W.; Wu, Y.H.; Wu, Y.C. Potent inhibition of superoxide anion production in activated human neutrophils by isopedicin, a bioactive component of the Chinese medicinal herb *Fissistigma oldhamii*. *Free Radic. Biol. Med.* **2009**, *46*, 520–528.
71. Hansen, M.B.; Nielsen, S.E.; Berg, K. Re-examination and further development of a precise and rapid dye method for measuring cell growth/cell kill. *J. Immunol. Methods* **1989**, *119*, 203–210.

**Sample Availability:** Samples of all the isolated compounds are available from the authors.



© 2018 by the authors. Licensee MDPI, Basel, Switzerland. This article is an open access article distributed under the terms and conditions of the Creative Commons Attribution (CC BY) license (<http://creativecommons.org/licenses/by/4.0/>).



# Carbon monoxide ameliorates *Staphylococcus aureus*-elicited COX-2/IL-6/MMP-9-dependent human aortic endothelial cell migration and inflammatory responses

Ming-Horng Tsai<sup>a,b,1</sup>, Chuen-Mao Yang<sup>c,d,e,1</sup>, Kuo-Ting Chang<sup>f</sup>, Chu-Chun Chuang<sup>g</sup>, Wei-Ning Lin<sup>h</sup>, Rong-San Jiang<sup>i</sup>, Cheng-Hsun Wu<sup>j,\*\*</sup>, I-Ta Lee<sup>i,k,\*</sup>

<sup>a</sup> Department of Pediatrics, Division of Neonatology and Pediatric Hematology/Oncology, Chang Gung Memorial Hospital, Yunlin, Taiwan

<sup>b</sup> Graduate Institute of Clinical Medical Science, College of Medicine, Chang Gung University, Kwei-San, Tao-Yuan, Taiwan

<sup>c</sup> Department of Physiology and Pharmacology and Health Ageing Research Center, College of Medicine, Chang Gung University, Kwei-San, Tao-Yuan, Taiwan

<sup>d</sup> Department of Anesthetics, Chang Gung Memorial Hospital at Linkuo and Chang Gung University, Kwei-San, Tao-Yuan, Taiwan

<sup>e</sup> Research Center for Chinese Herbal Medicine and Research Center for Food and Cosmetic Safety, College of Human Ecology, Chang Gung University of Science and Technology, Tao-Yuan, Taiwan

<sup>f</sup> Translational Medicine Center, Taoyuan General Hospital, Ministry of Healthy and Welfare, Taoyuan, Taiwan

<sup>g</sup> Department of Physical Therapy, China Medical University, Taichung, Taiwan

<sup>h</sup> Graduate Institute of Biomedical and Pharmaceutical Science, Fu Jen Catholic University, New Taipei City, Taiwan

<sup>i</sup> Department of Medical Research, Taichung Veterans General Hospital, Taichung, Taiwan

<sup>j</sup> School of Medicine, College of Medicine, China Medical University, Taichung, Taiwan

<sup>k</sup> Department of Nursing, College of Nursing, Hungkuang University, Taichung, Taiwan

## ARTICLE INFO

### Keywords:

*Staphylococcus aureus*

Cyclooxygenase-2

Matrix metalloproteinase-9

Carbon monoxide

Interleukin-6

## ABSTRACT

*Staphylococcus aureus* (*S. aureus*) can often lead to many life-threatening diseases. It has the ability to invade normal endovascular tissue. Acute inflammation and its resolution are important to ensure bacterial clearance and limit tissue injury. Carbon monoxide (CO) has been shown to exert anti-inflammatory effects in various tissues and organ systems. In our study, we investigated the effects and the mechanisms of carbon monoxide releasing molecule-2 (CORM-2) on *S. aureus*-induced inflammatory responses in human aortic endothelial cells (HAECs). We proved that *S. aureus* induced cyclooxygenase-2 (COX-2)/prostaglandin E<sub>2</sub> (PGE<sub>2</sub>)/interleukin-6 (IL-6)/matrix metalloproteinase-9 (MMP-9) expression and cell migration, which were decreased by CORM-2. Moreover, CORM-2 had no effects on TLR2 mRNA levels in response to *S. aureus*. Interestingly, we proved that *S. aureus* decreased intracellular ROS generation, suggesting that the inhibition of ROS further promoted inflammatory responses. However, CORM-2 significantly inhibited *S. aureus*-induced inflammation by increasing intracellular ROS generation. *S. aureus*-induced NF-κB activation was also inhibited by CORM-2. Finally, we proved that *S. aureus* induced levels of the biomarkers of inflammation in cardiovascular diseases, which were inhibited by CORM-2. Taken together, these results suggest that CORM-2 inhibits *S. aureus*-induced COX-2/PGE<sub>2</sub>/IL-6/MMP-9 expression and aorta inflammatory responses by increasing the ROS generation and reducing the inflammatory molecules levels.

## 1. Introduction

*Staphylococcus aureus* (*S. aureus*) is a common pathogen causing human skin and other soft tissues, bloodstream, and respiratory tract bacterial infections [1]. In addition, *S. aureus* often causes endocarditis, bacteremia, and endovascular infections [2]. The interactions between

*S. aureus* and endothelial cells are considered to be the most important interactions in the pathogenesis of cardiovascular infection [3]. However, these interactions can cause damage to heart valves in endocarditis or induce multi-organ dysfunction [3]. Recently, Venza et al. proved that *S. aureus* can trigger interleukin-8 (IL-8) activation by increasing cyclooxygenase-2 (COX-2) levels and prostaglandin E<sub>2</sub> (PGE<sub>2</sub>)

\* Corresponding author at: Department of Medical Research, Taichung Veterans General Hospital, 1650 Taiwan Boulevard Sect. 4, 40705 Taichung, Taiwan.

\*\* Corresponding author.

E-mail addresses: [chsunwu@mail.cmu.edu.tw](mailto:chsunwu@mail.cmu.edu.tw) (C.-H. Wu), [ita700128@vghtc.gov.tw](mailto:ita700128@vghtc.gov.tw) (I.-T. Lee).

<sup>1</sup> These authors contributed equally to this work.

<https://doi.org/10.1016/j.imlet.2018.09.010>

Received 14 June 2018; Received in revised form 28 August 2018; Accepted 14 September 2018

Available online 17 September 2018

0165-2478/ © 2018 European Federation of Immunological Societies. Published by Elsevier B.V. All rights reserved.

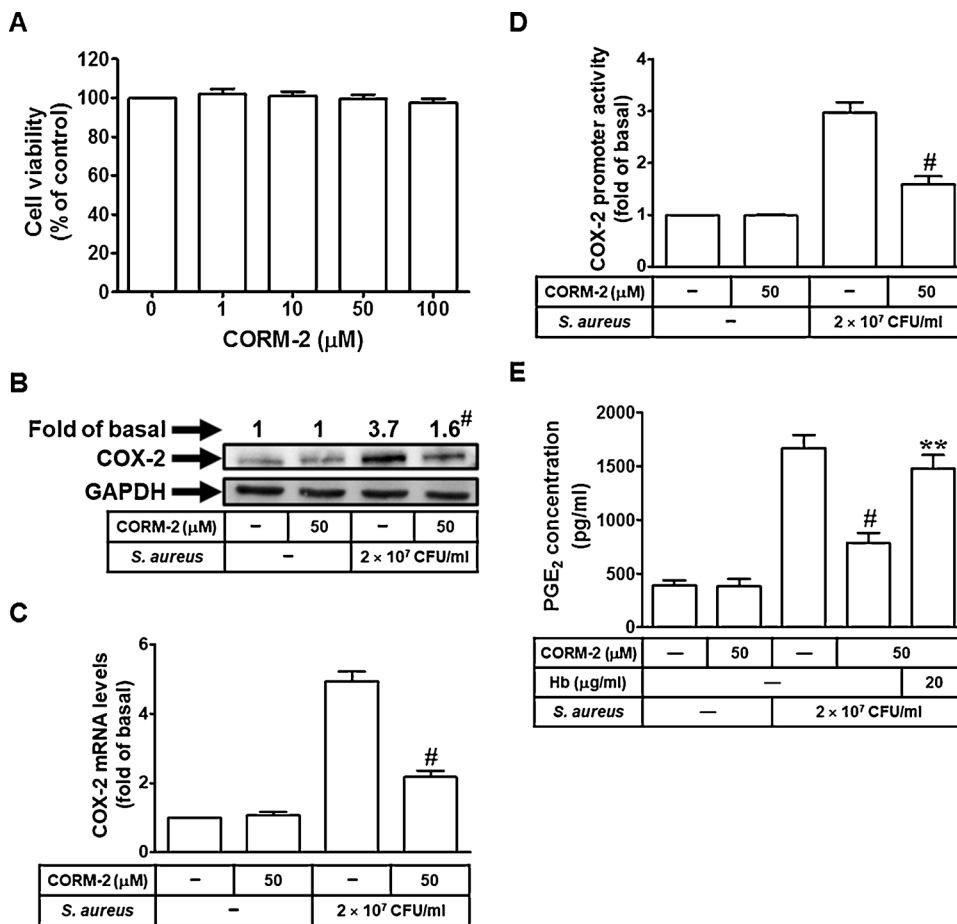


**Fig. 1.** CORM-2 inhibits *S. aureus*-induced COX-2/PGE<sub>2</sub> expression. (A) Cells were incubated with CORM-2 for the indicated times, and then the cell viability was determined. (B) Cells were pretreated with CORM-2 (50 μM) for 2 h, and then treated with *S. aureus* for 24 h. The COX-2 expression was determined by Western blot. (C) Cells were pretreated with CORM-2 (50 μM) for 2 h, and then treated with *S. aureus* for 6 h. The COX-2 mRNA levels were determined by real-time PCR. (D) Cells were pretreated with CORM-2 (50 μM) for 2 h, and then treated with *S. aureus* for 6 h. The COX-2 promoter activity was determined by promoter assay. (E) Cells were pretreated with CORM-2 (50 μM) in the presence or absence of 20 μg/ml hemoglobin (Hb), and then treated with *S. aureus* for 24 h. The PGE<sub>2</sub> production was measured. Data are expressed as mean ± S.E.M. of five independent experiments. <sup>#</sup>*P* < 0.01, as compared with the cells exposed to *S. aureus* alone. <sup>\*\*</sup>*P* < 0.05, as compared with the cells exposed to CORM-2 + *S. aureus*.

production in *S. aureus*-infected human conjunctival cells [4]. Moreover, Klemm et al. proved that interleukin-6 (IL-6), a marker of severe disease, was up-regulation during *S. aureus* infection [5]. Matrix metalloproteinase-9 (MMP-9) is thought to be involved in extracellular matrix degeneration and inflammation [6].

Carbon monoxide (CO) is currently known to be generated in cells or tissues as a byproduct of heme oxygenase (HO) after heme catalytic activity [7,8]. Even though CO is toxic to humans at high concentration, many studies have documented that low-dose exogenous CO (approximately 250–500 ppm) have protective effects against various human diseases [9–12]. Previous studies have confirmed that low concentrations of CO or CO-releasing molecules (CORMs) can eliminate microorganisms, regulate cell death, and resist inflammation [8,10,13]. However, the lipid-soluble tricarbonyldichlororuthenium (II) dimer (CORM-2) is the most characterized CO-RMs [14]. In this study, we hypothesized that CORM-2 may be effective as an anti-inflammatory modulator and a therapeutic agent for aorta inflammation.

Increased oxidative stress often causes cell damage and leads to inflammation [15]. Oxidative stress may occur due to increased generation and/or reduced ROS destruction [15]. It is known that NADPH oxidase is the critical enzyme for the generation of ROS under various pathological conditions. The balance between destruction and production of ROS depends on the NADPH oxidase activity and endogenous cellular antioxidants levels. Studies have confirmed that bacteria may be killed by a variety of deadly stressors, some of which facilitate a ROS cascade [16]. Bacteria have multiple protective proteins to detoxify ROS [16]. On the other hand, Tavares et al. proved that CORM-2 could promote intracellular ROS generation, and then cause DNA lesions to bacterial cells [17]. Thus, in the present study, we intend to establish whether the generation of ROS by CORM-2 may indeed result in the inhibition of *S. aureus*-induced inflammation in human aortic

endothelial cells (HAECs) and mice. We report here for the first time that in HAECs, CORM-2 inhibits *S. aureus*-induced COX-2/IL-6/MMP-9 expression and inflammatory responses by increasing the ROS generation and reducing the NF-κB activity.

## 2. Materials and methods

### 2.1. Materials

We purchased anti-COX-2, anti-GAPDH, anti-p65, and anti-COX-1 antibodies from Santa Cruz Biotechnology Inc (SantaCruz, CA, USA). Anti-phospho-p65 antibody was purchased from Cell Signaling (Danvers, MA, USA). SC-51322, MCI-186, and diphenyleneiodonium (DPI) were purchased from Calbiochem (San Diego, CA, USA). CORM-2, hemoglobin (Hb), H<sub>2</sub>O<sub>2</sub>, lipoteichoic acid (LTA), MitoTEMPO, N-acetyl-L-cysteine (NAC), enzymes, and other chemicals were purchased from Sigma (St. Louis, MO, USA). NF-κB(p65) transcription factor assaykit and helenalin (HLN) were purchased from Cayman (Ann Arbor, MI, USA).

### 2.2. Cell culture

HAECs were purchased from Cascade Biologics (Portland, OR). The cells were grown in culture flasks in endothelial cell growth medium, M200 (Cascade Biologics, Inc.) supplemented with fetal bovine serum (FBS, 5%), human basic fibroblast growth factor (3 ng/ml), human epidermal growth factor (10 ng/ml), streptomycin (100 pg/ml), penicillin (100 U/ml), insulin (10 mg/ml), and Fungizone (1.25 mg/ml) at 37 °C in a humidified 5% CO<sub>2</sub> atmosphere. Cells were used between passages 3 and 7 in this study.

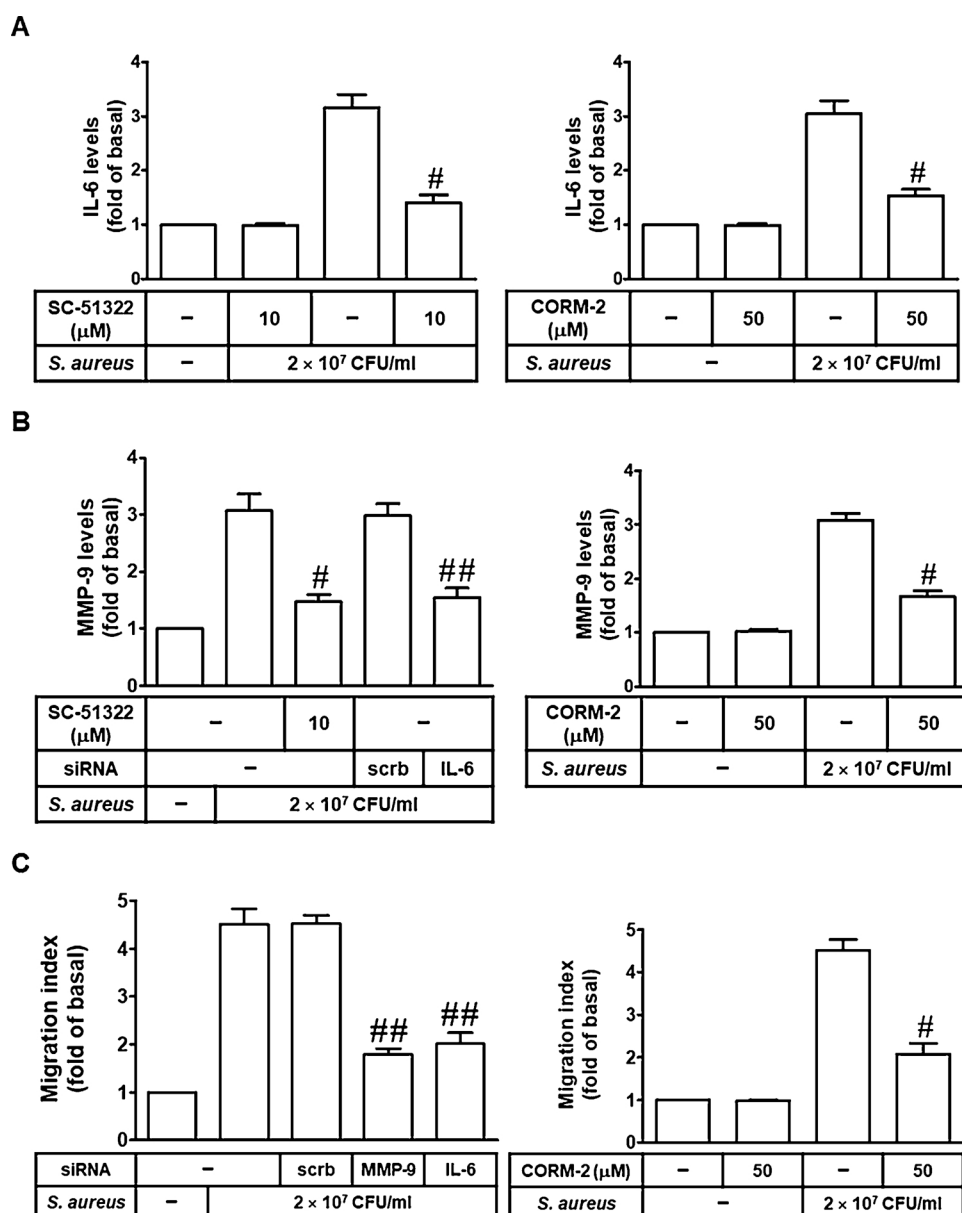


**Fig. 2.** CORM-2 inhibits *S. aureus*-induced MMP-9-dependent cell migration. **(A)** Cells were pretreated with SC-51322 for 1 h or pretreated with CORM-2 for 2 h, and then treated with *S. aureus* for 24 h. The IL-6 production was measured. **(B)** Cells were pretreated with SC-51322 for 1 h or CORM-2 for 2 h or transfected with siRNA of scrambled or IL-6, and then treated with *S. aureus* for 24 h. The MMP-9 production was measured. **(C)** Cells were transfected with siRNA of scrambled, IL-6, or MMP-9 or preincubated with CORM-2 for 2 h, and then treated with *S. aureus* for 24 h. The cell migration was determined by migration assay. Data are expressed as mean ± S.E.M. of three independent experiments. #*P* < 0.01, as compared with the cells exposed to *S. aureus* alone. ##*P* < 0.01, as compared with the cells exposed to *S. aureus* + scrambled siRNA.

### 2.3. Preparation of *S. aureus*

*S. aureus* (strain 12,598; a gift from Dr J. C. Shu, Department of Medical Biotechnology and Laboratory Science, Chang Gung University, Tao-Yuan, Taiwan) was maintained in BHI (brain heart infusion) broth (Sigma). However, the preparation of *S. aureus* can refer to our previous study [18]. In each experiment, approximately 2 × 10<sup>7</sup> bacteria, representing a bacteria/epithelial cell ratio of 20:1, were added in 1 ml of RPMI 1640 medium (Gibco) to each well.

### 2.4. Transient transfection with siRNAs

Scrambled, IL-6, MMP-9, p65, p50, TLR2, and TLR4 human siRNAs were purchased from Sigma (St. Louis, MO, USA). We transiently transfected siRNA (100 nM) using a Lipofectamine™ RNAiMAX reagent according to the manufacturer's instructions.

### 2.5. Real-Time PCR

We used TRIzol reagent to extract total RNA. We then reverse-transcribed mRNA into cDNA and analyzed by real-time PCR using

SYBR Green PCR reagents (Applied Biosystems, Branchburg, NJ, USA) and primers specific for human GAPDH, COX-2, TLR2, and TLR4 and mouse GAPDH, COX-1, and COX-2 mRNAs. Finally, COX-1, COX-2, TLR2, and TLR4 mRNA levels were determined by normalizing to that of GAPDH expression.

### 2.6. Migration assay

HAECs were cultured to confluence in 10-cm dishes and starved with serum-free M200 for one day. We then scratched the monolayer cells with a blade, creating extended and definite scratches in the center of the dishes with a bright and clear field. The cells were washed once with PBS to remove the detached cells. After pretreatment with the inhibitors for 2 h, serum-free M200 with or without *S. aureus* was added to each dish containing the DNA synthesis inhibitor hydroxyurea (10 μM) during the period of incubation. We counted the number of migratory cells from the resulting four phase images for each point and then averaged for each experimental condition. The final data came from three separate assays.



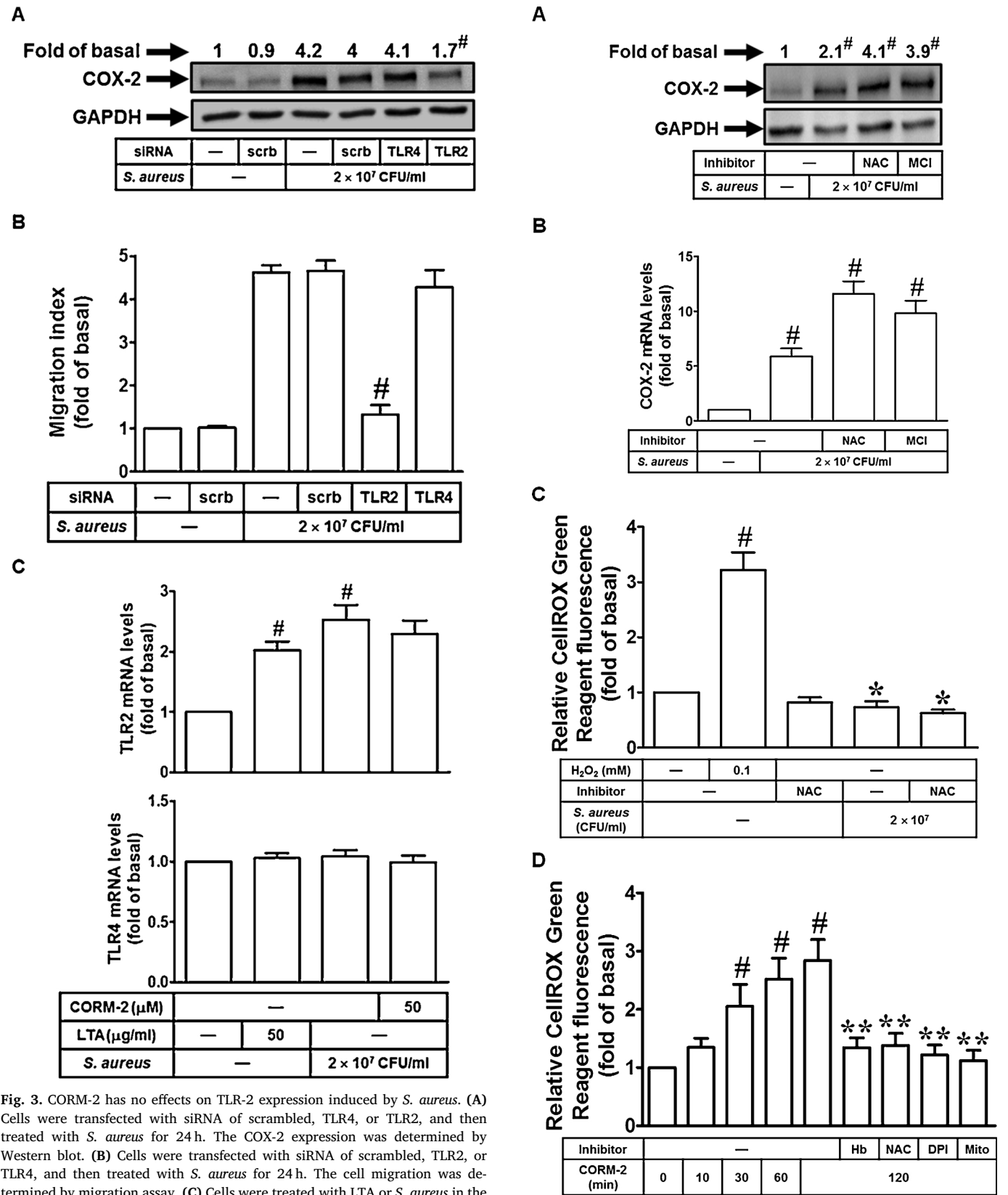


**Fig. 3.** CORM-2 has no effects on TLR-2 expression induced by *S. aureus*. (A) Cells were transfected with siRNA of scrambled, TLR4, or TLR2, and then treated with *S. aureus* for 24 h. The COX-2 expression was determined by Western blot. (B) Cells were transfected with siRNA of scrambled, TLR2, or TLR4, and then treated with *S. aureus* for 24 h. The cell migration was determined by migration assay. (C) Cells were treated with LTA or *S. aureus* in the presence or absence of CORM-2. The TLR2 and TLR4 mRNA levels were determined by real-time PCR. Data are expressed as mean ± S.E.M. of four independent experiments. #*P* < 0.01, as compared with the cells exposed to *S. aureus* + scrambled siRNA (A, B). #*P* < 0.01, as compared with the basal level (C).

(caption on next page)

**Fig. 4.** *S. aureus* reduces ROS generation in HAECs. (A) Cells were pretreated with NAC (10 mM) or MCI-186 (10  $\mu$ M) for 2 h, and then treated with *S. aureus* for 24 h. The COX-2 expression was determined by Western blot. (B) Cells were pretreated with NAC (10 mM) or MCI-186 (10  $\mu$ M) for 2 h, and then treated with *S. aureus* for 6 h. The COX-2 mRNA levels were determined by real-time PCR. (C) Cells were treated with H<sub>2</sub>O<sub>2</sub> or *S. aureus* in the presence or absence of NAC (10 mM), and then the intracellular ROS generation was determined. (D) Cells were treated with CORM-2 for the indicated times or pretreated with Hb (20  $\mu$ g/ml), NAC (10 mM), DPI (1  $\mu$ M), or MitoTEMPO (10  $\mu$ M) for 2 h, and then incubated with CORM-2 for 2 h. The intracellular ROS generation was determined. Data are expressed as mean  $\pm$  S.E.M. of three independent experiments. \* $P$  < 0.05; # $P$  < 0.01, as compared with the basal level. \*\* $P$  < 0.05, as compared with the cells exposed to CORM-2 alone.

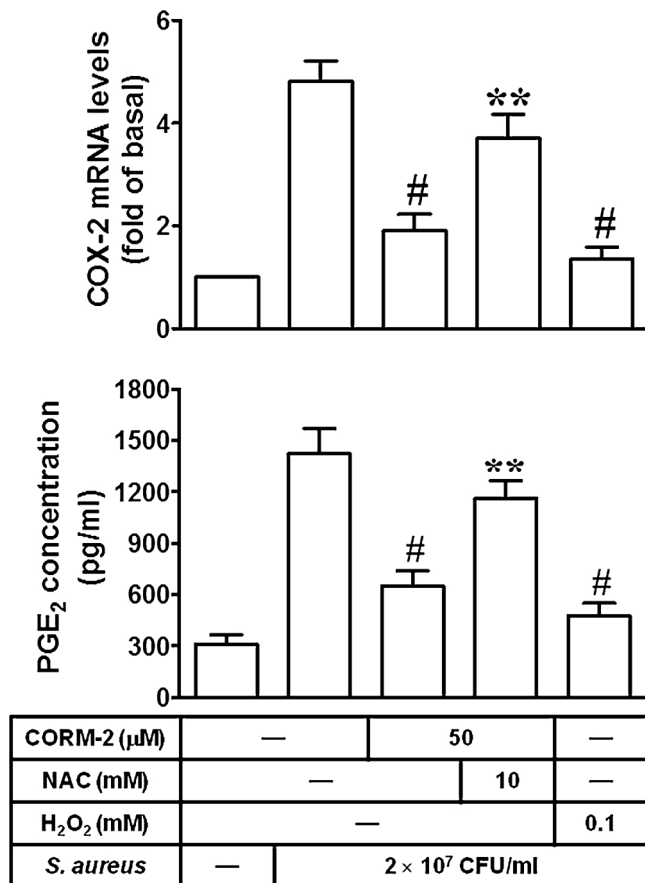


**Fig. 5.** CORM-2 inhibits *S. aureus*-induced inflammation by increasing intracellular ROS generation. Cells were pretreated with CORM-2 in the presence or absence of NAC, and then treated with *S. aureus* for 6 h or 24 h. In addition, cells were pretreated with H<sub>2</sub>O<sub>2</sub>, and then treated with *S. aureus* for 6 h or 24 h. The COX-2 mRNA levels were determined by real-time PCR. The PGE<sub>2</sub> production was measured. Data are expressed as mean  $\pm$  S.E.M. of four independent experiments. # $P$  < 0.01, as compared with the cells exposed to *S. aureus* alone. \*\* $P$  < 0.05, as compared with the cells exposed to CORM-2 + *S. aureus*.

## 2.7. Measurement of intracellular ROS accumulation

We used CellROX Green Reagent (Molecular Probes, Eugene, OR, USA) to measure oxidative stress in live cells. The fluorescence for CellROX Green Reagent staining was detected at 485/520 nm. HAECs were washed with warm Hank's Balanced Salt Solution (HBSS) and incubated in HBSS containing 5  $\mu$ M CellROX Green Reagent at 37 °C for 30 min. Subsequently, HBSS containing CellROX Green Reagent was removed and replaced with fresh medium. HAECs were then incubated with *S. aureus* for the indicated times. Finally, HAECs were washed

twice with PBS and detached with trypsin/EDTA, and the fluorescence intensity of the cells was analyzed using a FACScan flow cytometer (BD Biosciences, San Jose, CA) at 485 nm excitation and 520 nm emission.

## 2.8. Measurement of MMP-9 and IL-6 generation

HAECs were cultured in 12-well culture plates. After reaching confluence, HAECs were incubated with *S. aureus* for the indicated times at 37 °C. The media were gathered and IL-6 and MMP-9 levels were assayed by using an IL-6 ELISA kit (BioSource International, Camarillo, CA, USA) and MMP-9 ELISA kit (Thermo scientific, Rockford, USA), respectively, following the instructions of the manufacturers.

## 2.9. Measurement of PGE2 generation

HAECs were cultured in 12-well culture plates. After reaching confluence, HAECs were incubated with *S. aureus* for the indicated times at 37 °C. The media were gathered and PGE<sub>2</sub> levels were assayed by using a PGE<sub>2</sub> ELISA kit (Enzo Life Sciences, Farmingdale, NY, USA) following the instructions of the manufacturers.

## 2.10. Western blot

We cultured HAECs in 6-well culture plates. After reaching confluence, HAECs were incubated with *S. aureus* for the indicated times at 37 °C. Western blot analysis methods have been described [18]. Finally, membranes were incubated with the anti-COX-2 antibody for one day, and then incubated with the anti-mouse horseradish peroxidase antibody for 60 min. We used enhanced chemiluminescence (ECL) reagents to detect immunoreactive bands.

## 2.11. Measurement of COX-2 luciferase promoter activity

We cloned the human COX-2 promoter (a region spanning —459 to +9 bp) into pGL3-basic vector (Promega, Madison, WI, USA) to construct a COX-2-luc plasmid. The COX-2 luciferase promoter assay was performed as we have described [19]. Firefly luciferase activities were finally normalized to  $\beta$ -gal activity.

## 2.12. Gelatin zymography

HAECs were plated onto 6-well culture plates and made quiescent at confluence by incubation in serum-free M200 for 24 h, and then incubated with *S. aureus* at 37 °C for the indicated time intervals. The culture medium was collected and centrifuged at 10,000g for 5 min at 4 °C to remove cell debris. The MMP-9 expression was analyzed as previously described [6].

## 2.13. Animal care and experimental procedures

Male ICR mice aged 6–8 weeks were from the National Laboratory Animal Centre (Taipei, Taiwan) and were handled according to NIH Guides for the Care and Use of Laboratory Animals. We used 100  $\mu$ l bacterial suspension (2  $\times$  10<sup>7</sup> CFU/mouse) into ICR mice using the i.p. injection. Control mice were administered BHI. ICR mice were given i.p. (intraperitoneally) one dose of NAC, MCI-186, or CORM-2 for 2 h before *S. aureus* (2  $\times$  10<sup>7</sup> CFU/mouse) treatment. The animals were killed after 48 h. Plasma MPO and serum CRP, IL-6, and TNF- $\alpha$  were measured.

## 2.14. Statistical software and analysis

We analyzed the data with the GraphPad Prism program (GraphPad, San Diego, CA, USA). Quantitative data were expressed as the mean  $\pm$  S.E.M. and analyzed with one-way ANOVA followed with

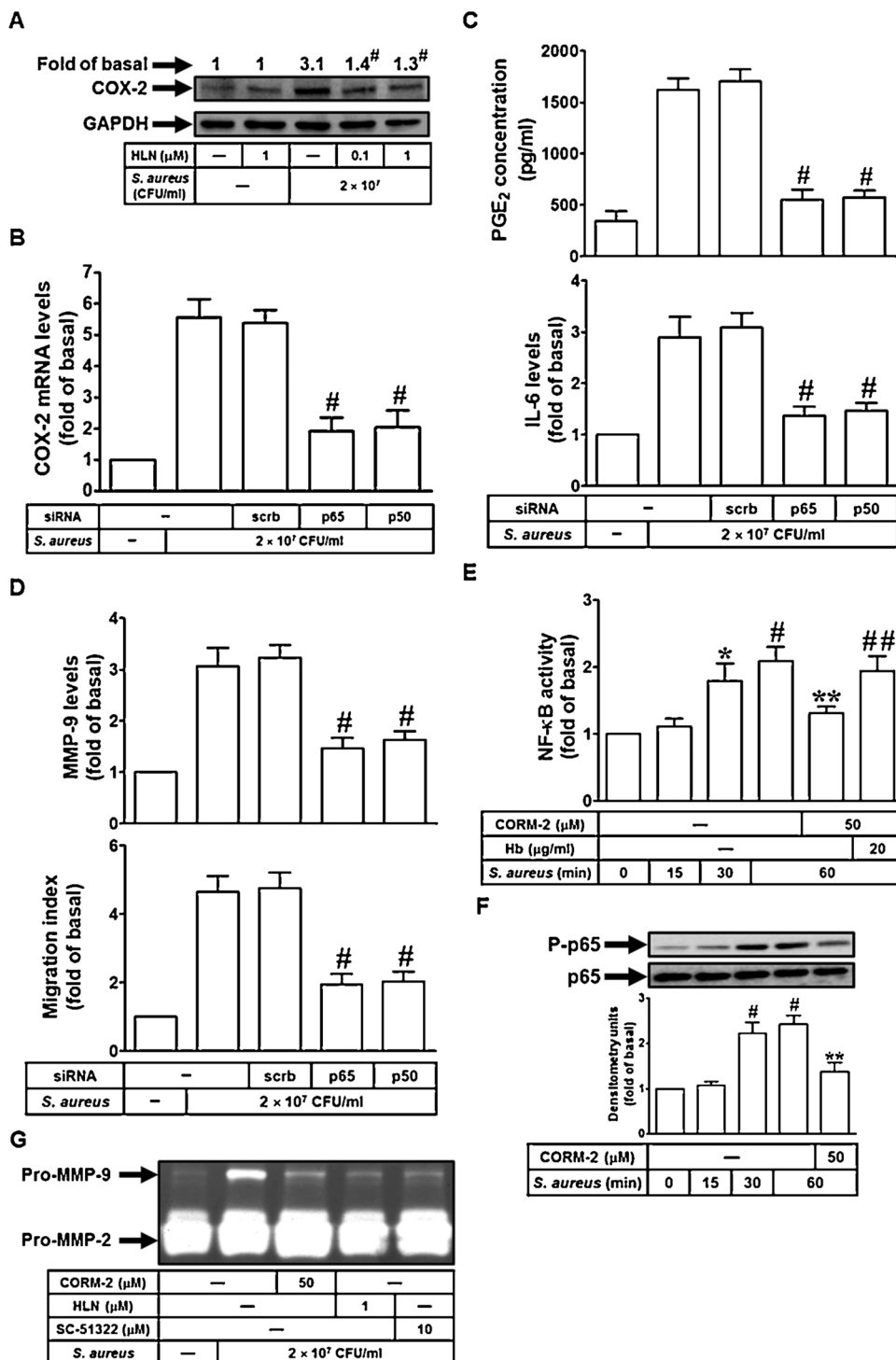


**Fig. 6.** CORM-2 inhibits *S. aureus*-induced COX-2 expression via the reduction of NF-κB activity. (A) Cells were pretreated with HLN for 1 h, and then treated with *S. aureus* for 24 h. The COX-2 expression was determined by Western blot. (B) Cells were transfected with siRNA of scrambled, p65, or p50, and then treated with *S. aureus* for 6 h. The COX-2 mRNA levels were determined by real-time PCR. (C) Cells were transfected with siRNA of scrambled, p65, or p50, and then treated with *S. aureus* for 24 h. The PGE<sub>2</sub> and IL-6 production was measured. (D) Cells were transfected with siRNA of scrambled, p65, or p50, and then treated with *S. aureus* for 24 h. The MMP-9 production was measured. The cell migration was determined by migration assay. (E) Cells were treated with *S. aureus* (2 × 10<sup>7</sup> CFU/ml) for the indicated times or pretreated with CORM-2 in the presence or absence of Hb, and then treated with *S. aureus* for 1 h. The NF-κB activity was determined. (F) Cells were treated with *S. aureus* (2 × 10<sup>7</sup> CFU/ml) for the indicated times or pretreated with CORM-2, and then treated with *S. aureus* for 1 h. The expression of phospho-p65 was determined by Western blot. (G) Cells were pretreated with CORM-2, HLN, or SC-51322, and then incubated with *S. aureus* for 24 h. Pro-MMP-9 and pro-MMP-2 levels were determined by gelatin zymography. Data are expressed as mean ± S.E.M. of three independent experiments. #*P* < 0.01, as compared with the cells exposed to *S. aureus* alone (A) or *S. aureus* + scrambled siRNA (B, C, D). \**P* < 0.05; #*P* < 0.01, as compared with the basal level (E, F). \*\**P* < 0.05, as compared with the cells exposed to *S. aureus* alone (E, F). ##*P* < 0.05, as compared with the cells exposed to CORM-2 + *S. aureus* (E).

Tukey's post-hoc test. We defined *P* < 0.05 as a significant difference.

### 3. Results

#### 3.1. CORM-2 inhibits *S. aureus*-induced COX-2/PGE<sub>2</sub> expression

*S. aureus* has been shown to promote COX-2 or PGE<sub>2</sub> expression in various cell types [4,18]. In addition, CO can perform the anti-inflammatory effects in various tissues [8–10]. First, we examined the effects of CORM-2 on the cell viability of HAECs. As shown in Fig. 1A, we proved that various concentrations of CORM-2 (1, 10, 50, and 100 μM) had no effects on the cell viability of HAECs. Pretreatment

with CORM-2 (50 μM) markedly inhibited *S. aureus*-induced COX-2 protein and mRNA levels and promoter activity (Fig. 1B–D). COX-2 converts arachidonic acid to bioactive lipids, including PGE<sub>2</sub> which could be used as a marker of COX-2 activity [19]. Moreover, as shown in Fig. 1E, we proved that *S. aureus* significantly promoted PGE<sub>2</sub> release, which was reduced by CORM-2 (50 μM). However, the addition of CO scavenger, hemoglobin (Hb), significantly reversed the attenuating effects of CORM-2 on PGE<sub>2</sub> secretion induced by *S. aureus* (Fig. 1E). Taken together, we suggest that CORM-2 can reduce inflammatory responses via the inhibition of COX-2/PGE<sub>2</sub> expression in HAECs.

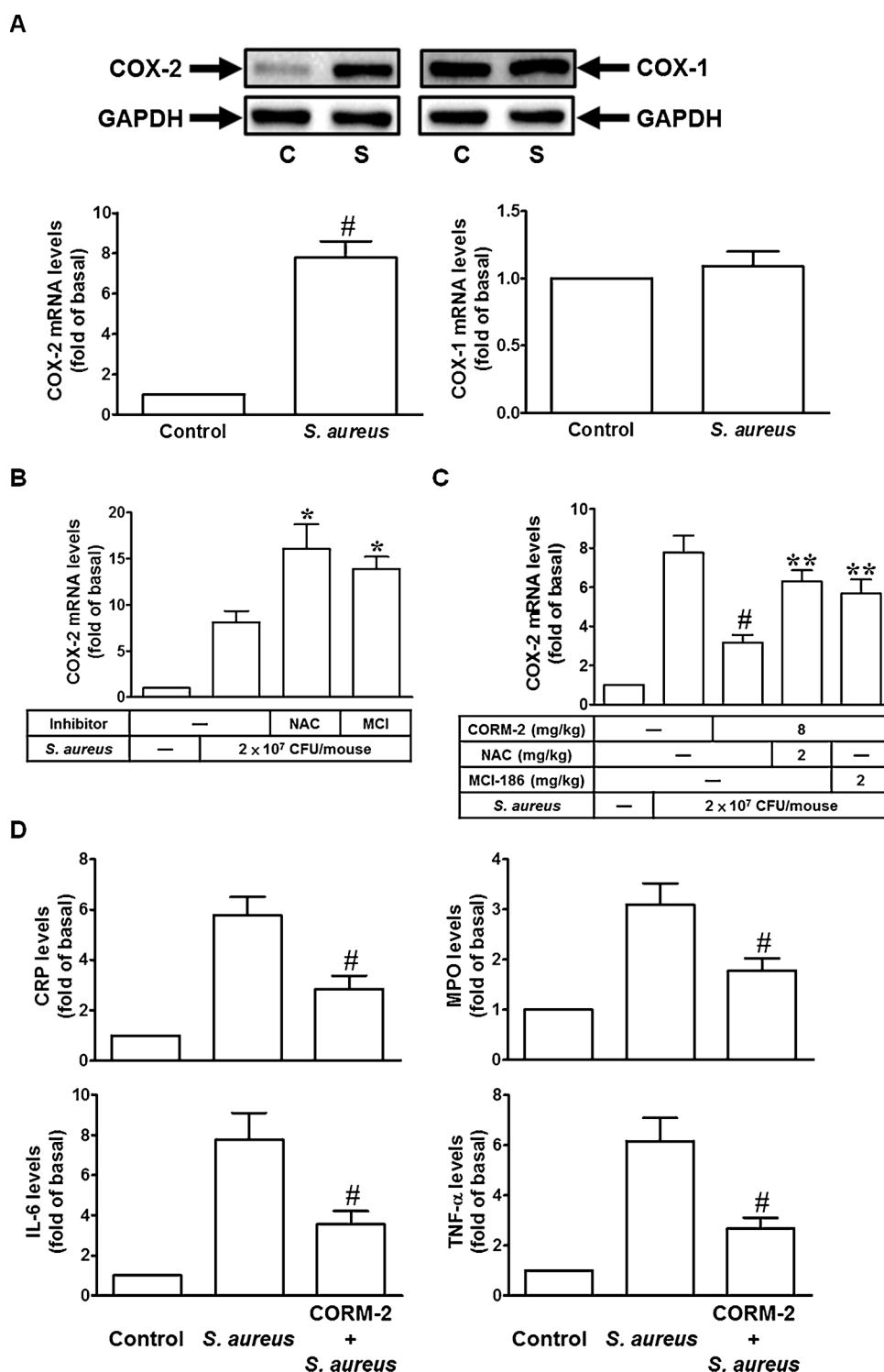


**Fig. 7.** CORM-2 inhibits *S. aureus*-induced COX-2 expression and aorta inflammation in mice. **(A)** Mice were treated with *S. aureus* ( $2 \times 10^7$  CFU/mouse), and then killed after 48 h. Preparation of aorta tissues was analysed by Western blot and real-time PCR to determine the levels of COX-2 and COX-1 protein and mRNA respectively. **(B)** Mice were given i.p. one dose of NAC or MCI-186 for 2 h before *S. aureus* ( $2 \times 10^7$  CFU/mouse) treatment, and then killed after 48 h. Preparation of aorta tissues was analysed by real-time PCR to determine the levels of COX-2 mRNA. **(C)** Mice were pretreated with CORM-2 in the presence or absence of NAC or MCI-186, and then treated with *S. aureus* ( $2 \times 10^7$  CFU/mouse) for 48 h. Preparation of aorta tissues was analysed by real-time PCR to determine the levels of COX-2 mRNA. **(D)** Mice were pretreated with CORM-2, and then treated with *S. aureus* ( $2 \times 10^7$  CFU/mouse) for 48 h. Levels of CRP, MPO, IL-6, and TNF- $\alpha$  were measured. Data are expressed as mean  $\pm$  S.E.M. of five independent experiments. # $P < 0.01$ , as compared with the basal level (A). \* $P < 0.05$ ; # $P < 0.01$ , as compared with the mice exposed to *S. aureus* alone (B, C, D). \*\* $P < 0.05$ , as compared with the mice exposed to CORM-2 + *S. aureus* (C).

### 3.2. CORM-2 inhibits *S. aureus*-induced PGE<sub>2</sub>/IL-6/MMP-9-dependent cell migration

When IL-6 binds to its soluble receptor sIL-6R $\alpha$ , it can affect the transition from acute to chronic inflammation by regulating the properties of leukocyte infiltrate [20]. We previously proved that PGE<sub>2</sub> could enhance IL-6 release in human tracheal smooth muscle cells (HTSMCs) [21]. In this study, we proved that *S. aureus* also induced IL-6 production, which was reduced by pretreatment with SC-51322 (the inhibitor of PGE<sub>2</sub>) (Fig. 2A). On the other hand, preincubation with CORM-2 decreased *S. aureus*-induced IL-6 release in HAECs (Fig. 2A).

IL-6 has been shown to regulate cell migration in various cell types [22,23]. MMP-9 induction plays a key role in regulating cell migration [24]. We proved that *S. aureus* enhanced MMP-9 levels in HAECs, which was inhibited by pretreatment with SC-51322 or transfection with IL-6 siRNA (Fig. 2B). CORM-2 also had the inhibitory effects on *S. aureus*-enhanced MMP-9 levels (Fig. 2B). Finally, we proved that *S. aureus* promoted cell migration, which was reduced by transfection with siRNA of IL-6 or MMP-9 or pretreatment with CORM-2 (Fig. 2C). Taken together, we suggest that CORM-2 can reduce inflammatory responses through the inhibition of PGE<sub>2</sub>/IL-6/MMP-9-dependent cell migration.



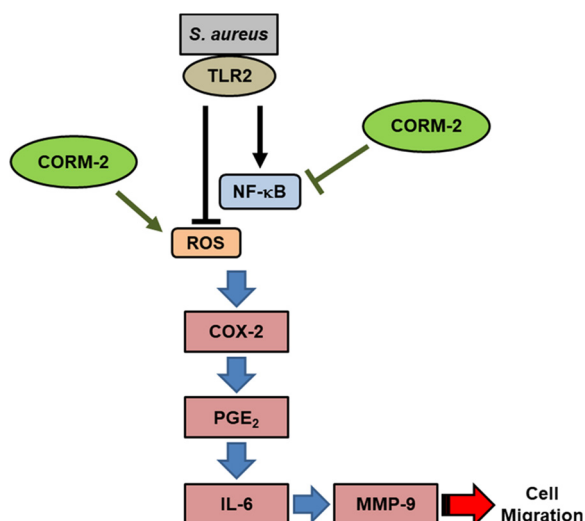


**Fig. 8.** Schematic diagram illustrating the proposed signaling pathway involved in the inhibitory effects of CORM-2 on *S. aureus*-induced COX-2/PGE<sub>2</sub>/IL-6/MMP-9-dependent cell migration. In HAECs, CORM-2 inhibits *S. aureus*-induced COX-2 expression and inflammatory responses by increasing the ROS generation and reducing the NF-κB activity.

### 3.3. CORM-2 has no effects on *S. aureus*-induced TLR-2 expression

TLR2 plays an important role in the immune system and inflammatory responses. It can identify staphylococcal lipoteichoic acid (LTA) [25]. Here, we proved that *S. aureus*-induced COX-2 expression was reduced by transfection with TLR2 siRNA, but not TLR4 siRNA in HAECs (Fig. 3A). On the other hand, *S. aureus*-induced cell migration was also reduced by transfection with TLR2 siRNA, but not TLR4 siRNA (Fig. 3B). We further examined whether CORM-2 could inhibit COX-2 expression via the inhibition of TLRs expressions. As shown in Fig. 3C, CORM-2 had no effects on *S. aureus*-induced TLR2 mRNA levels. These data suggest that CORM-2 does not reduce *S. aureus*-induced inflammation via the inhibition of TLR2 expression in HAECs.

### 3.4. CORM-2 inhibits *S. aureus*-induced inflammation by increasing intracellular ROS generation

ROS can not only directly kill pathogens by causing oxidative damage, but also indirectly kill pathogens through many nonoxidative mechanisms, such as pattern recognition receptors signaling [26]. Therefore, ROS production may inhibit bacterial infection. However, in this study, we proved that *S. aureus*-induced COX-2 expression was further enhanced by pretreatment with the inhibitor of ROS (NAC or MCI-186) (Fig. 4A and B). On the other hand, we also proved that *S. aureus* could decrease ROS generation in HAECs (Fig. 4C). We demonstrated that CORM-2 could enhance intracellular ROS production, which was inhibited by pretreatment with Hb, NAC, DPI (an inhibitor of NADPH oxidase), or MitoTEMPO (a mitochondria-targeted antioxidant) (Fig. 4D). Therefore, we suppose that *S. aureus* decreases ROS generation, and then promotes downstream inflammatory responses. Finally, we proved that pretreatment with NAC reversed the attenuating effects of CORM-2 on COX-2 mRNA levels and PGE<sub>2</sub> secretion induced by *S. aureus* (Fig. 5). We suppose that CORM-2 can enhance ROS generation, and then kill pathogens directly by causing oxidative damage.

### 3.5. CORM-2 inhibits *S. aureus*-induced COX-2 expression via the reduction of NF-κB activity in HAECs

NF-κB activation has been shown to mediate COX-2 expression and PGE<sub>2</sub> release [21]. Here, we observed that *S. aureus*-induced COX-2 protein and mRNA levels were inhibited by the inhibitor of NF-κB

(HLN) or siRNA of p65 or p50 (Fig. 6A and B). On the other hand, *S. aureus*-induced PGE<sub>2</sub>/IL-6/MMP-9 levels and cell migration were also decreased by transfection with siRNA of p65 or p50 (Fig. 6C and D). We further proved that *S. aureus* time-dependently induced NF-κB activity, which was reduced by CORM-2 (Fig. 6E). However, preincubation with Hb reversed the attenuating effects of CORM-2 on NF-κB activity induced by *S. aureus* (Fig. 6E). We proved that CORM-2 decreased *S. aureus*-induced NF-κB p65 phosphorylation in HAECs (Fig. 6F). Finally, we observed that *S. aureus* markedly induced pro-MMP-9 expression by using gelatin zymography, which was inhibited by pretreatment with CORM-2, HLN, or SC51322 (Fig. 6G). However, *S. aureus* had no effects on pro-MMP-2 levels in these cells (Fig. 6G). Taken together, these data suppose that CORM-2 inhibits *S. aureus*-induced COX-2 expression via the reduction of NF-κB activity in HAECs.

### 3.6. CORM-2 inhibits *S. aureus*-induced COX-2 expression and aorta inflammation in mice

In an *in vivo* study, mice were treated with *S. aureus* ( $2 \times 10^7$  CFU/mouse), and then killed after 48 h. Preparation of aorta tissues was analysed by Western blot and real-time PCR to examine the levels of COX-2 and COX-1 protein and mRNA respectively. As shown in Fig. 7A, we proved that *S. aureus* induced COX-2, but not COX-1 protein and mRNA levels in the aorta tissues. Mice were given i.p. one dose of NAC or MCI-186 for 2 h before *S. aureus* ( $2 \times 10^7$  CFU/mouse) treatment, and then killed after 48 h. Preparation of aorta tissues was analysed by real-time PCR to determine the levels of COX-2 mRNA. We showed that *S. aureus* induced COX-2 mRNA levels, which were further enhanced by NAC or MCI-186 (Fig. 7B). On the other hand, CORM-2 could markedly inhibit *S. aureus*-induced COX-2 mRNA levels, which was reversed by NAC or MCI-186 (Fig. 7C). C-reactive protein (CRP) is the biomarker of inflammation in cardiovascular diseases. Myeloperoxidase (MPO) also plays a key role in the inflammatory responses [27]. Here, we showed that *S. aureus* enhanced the levels of plasma MPO and serum CRP, IL-6, and TNF-α, which were inhibited by CORM-2 (Fig. 7D). Thus, we suggest that CORM-2 can inhibit aorta inflammation via the reduction of COX-2 up-regulation and inflammatory responses induced by *S. aureus*.

## 4. Discussion

*S. aureus* is a common bacterium that is often found in the body's nose, throat, hair, and skin without causing discomfort. In addition, they will also be present in large numbers on inflamed or purulent wounds. *S. aureus* invades blood circulation through damaged skin, mucous membranes, sputum, pneumonia, or otitis media, and then derives bacteremia. *S. aureus* infection can also lead to lethal sepsis [25,28]. Endovascular *S. aureus* infection is very difficult to treat. This may be related to the complex pathogenesis of many host and bacterial factors [28]. Several lines of evidence suppose that high levels of PGE<sub>2</sub> and COX-2 are involved in the inflammatory responses [29]. CO is currently known to be generated in cells or tissues as a byproduct of HO after heme catalytic activity [7,8]. Moreover, the anti-inflammatory effects of CORMs and CO have been demonstrated. Thus, they could be used as a therapeutic for various inflammatory diseases. The molecular mechanisms by which CORM-2 inhibits *S. aureus*-induced aorta inflammation are not fully understood. Here, we showed for the first time that in HAECs, *S. aureus* decreases ROS generation, and then promotes inflammatory responses. Moreover, COX-2/PGE<sub>2</sub> up-regulation can further promote IL-6/MMP-9-dependent cell migration. CORM-2 inhibits *S. aureus*-induced COX-2 expression and inflammatory responses by increasing the ROS generation and reducing the NF-κB activity.

Recently, more and more investigations have been initiated due to the role of CO in cell protection and anti-inflammation [30]. CORM-2 is a CO-releasing agent. Due to its chemical structure, it has superior and more effective drug traits than gaseous CO [30]. However, many

previous studies have demonstrated the therapeutic potential of CORMs [30,31]. In addition, researchers have also observed that the biological effects of CORMs and CO are regulated by the HO-1 gene [31]. IL-6 is a pro-inflammatory cytokine and the elevation of IL-6 levels is often associated with various chronic diseases and inflammation [21]. Previous studies have demonstrated that IL-6 can mediate cell migration in many cell types [22]. On the other hand, previous studies have also found a positive correlation between the PGE<sub>2</sub> up-regulation and the release of IL-6 [21]. In HAECs, we proved that *S. aureus* induced cell migration through a COX-2/PGE<sub>2</sub>/MMP-9 pathway. Moreover, we also observed that CORM-2 markedly inhibited *S. aureus*-induced inflammatory proteins up-regulation and cell migration in HAECs and mice. TLRs are the very important receptors in the mammalian immune system. Their main function is to detect the invasion of foreign pathogens. Once the invasion of a pathogen is detected, the TLRs activate the signal transmission and induce innate immunity, which affects the subsequent adaptive immunity [32]. TLR2 plays an important role in the immune system and inflammatory responses. It can identify staphylococcal LTA (a major constituent of the cell wall of gram-positive bacteria) [25]. Indeed, in this study, we proved that *S. aureus* induced COX-2 expression and cell migration via TLR2, but not TLR4 in HAECs. However, CORM-2 had no effects on *S. aureus*-enhanced TLR2 mRNA levels, suggesting that CORM-2 could not reduce *S. aureus*-induced inflammation via the inhibition of TLR2 expression in HAECs.

Increased oxidative stress often causes cell damage and leads to inflammation. Oxidative stress may occur due to increased generation and/or reduced ROS destruction. It is known that NADPH oxidase is the critical enzyme for the generation of ROS under various pathological conditions [29]. However, ROS have been shown to be a deadly weapon used by many cell types to fight pathogens [26]. ROS can not only directly kill pathogens by causing oxidative damage, but also indirectly kill pathogens through many nonoxidative mechanisms, such as pattern recognition receptors signaling [17,26]. Therefore, ROS production may inhibit bacterial infection. Indeed, in HAECs, *S. aureus* markedly decreased ROS generation. We suggested that *S. aureus* promoted the inflammatory responses via the inhibition of ROS production and oxidative damage in HAECs. Moreover, we proved that CORM-2 inhibited *S. aureus*-induced inflammation by increasing intracellular ROS generation in HAECs. Altogether, these results revealed that the bactericidal action of CORM-2 relies on the generation of deleterious intracellular ROS.

NF- $\kappa$ B is an extremely important molecule in the process of inflammation. When cells receive extracellular stimulation, NF- $\kappa$ B is activated and translocated from the cytosol to the nucleus, which can further cause inflammation [29]. In addition, NF- $\kappa$ B plays a critical role in mediating LTA-induced inflammation [29]. This is confirmed by our observation that *S. aureus*-induced COX-2/PGE<sub>2</sub>/IL-6/MMP-9 expression was decreased by transfection with p65 or p50 siRNA. NF- $\kappa$ B is retained in the cytoplasm via interaction with I $\kappa$ Bs [33]. Upon stimulation, I $\kappa$ Bs are phosphorylated by the activated IKK complex, and then ubiquitin-dependently degraded by the 26S proteasome [33]. This cascade allows NF- $\kappa$ B to translocate to the nucleus, where they induce target genes up-regulation. In our study, it was also found that *S. aureus* markedly stimulated p65 phosphorylation and NF- $\kappa$ B activity in HAECs. Moreover, CORM-2 had the inhibitory effects on *S. aureus*-induced NF- $\kappa$ B activation, and then further reduced the inflammatory responses. On the other hand, we used gelatin zymography to observe that *S. aureus* could enhance pro-MMP-9, but not pro-MMP-2 levels in HAECs. Pretreatment with CORM-2 or the inhibitor of NF- $\kappa$ B or PGE<sub>2</sub> could reduce *S. aureus*-induced pro-MMP-9 expression. Although activity of MMP-2 has also been associated with severity of chronic inflammatory diseases, in our study, we did not find any changes in the expression of MMP-2 in response to *S. aureus* within 24 h in HAECs. We will increase the infected duration of *S. aureus* to observe whether the levels of MMP-2 change or not in the further research.

In the process of inflammation, various inflammatory biomarkers

are increased. CRP is the most commonly studied inflammatory biomarker in cardiovascular diseases [34]. MPO is also an inflammatory biomarker that has been studied extensively in the past few years [27]. IL-6 is a pro-inflammatory cytokine and the elevation of IL-6 levels is often associated with various chronic diseases and inflammation. Previous studies have demonstrated that IL-6 can mediate cell migration in many cell types. When IL-6 binds to its soluble receptor sIL-6R $\alpha$ , it can affect the transition from acute to chronic inflammation by regulating the properties of leukocyte infiltrate [35]. The pathogen-recognition receptors (PRRs) including TLRs stimulate many signaling pathways including NF- $\kappa$ B, and then promote inflammatory cytokines such as IL-6, TNF- $\alpha$ , and IL-1 $\beta$  mRNA transcription [36,37]. In addition, TNF- $\alpha$  and IL-1 $\beta$  also activate various transcription factors to generate IL-6 [37]. Here, in an *in vivo* study, we observed that *S. aureus* induced levels of plasma MPO and serum CRP, IL-6, and TNF- $\alpha$ . Interestingly, pretreatment with the ROS inhibitors enhanced *S. aureus*-induced COX-2 mRNA levels in the aorta tissues of mice. Pretreatment with CORM-2 could inhibit *S. aureus*-induced levels of plasma MPO and serum CRP, IL-6, and TNF- $\alpha$ . In addition, CORM-2 also reduced *S. aureus*-induced COX-2 mRNA levels, which was reversed by the ROS inhibitors.

Indeed, various agents can stimulate or inhibit MMPs expression. Li et al. indicated that epigallocatechin-3-gallate (EGCG) could inhibit MMP-9 expression via the TLR4/MAPK/NF- $\kappa$ B signaling pathway in lipopolysaccharide (LPS)-enhanced macrophages [38]. Cao et al. also proved that *Ginkgo biloba* exocarp extract could inhibit MMP-9 expression via the PI3K/Akt/NF- $\kappa$ B signaling pathway [39]. On the other hand, Shin et al. indicated that phorbol myristate acetate (PMA) could induce MMP-9 expression via PKC $\alpha$ /NF- $\kappa$ B in human lung epithelial cells [40]. Cao et al. further found that curcumin could reduce PMA-induced MMP-9 expression via AMPK-MAPK and PKC signaling [41]. Thus, we hypothesize that CORM-2 can inhibit MMP-9 expression induced by *S. aureus* through other signaling pathways. Moreover, in this study, even though CO is toxic to humans at high concentration, we mainly focus on the cytoprotective role of CORM-2 in *S. aureus*-treated HAECs. In the future, we will investigate the detailed mechanisms involved in the antibacterial effects of CORM-2.

In summary, as depicted in Fig. 8, our results demonstrate that in HAECs, *S. aureus* induces COX-2 expression via the activation of NF- $\kappa$ B and reduction of ROS generation. COX-2/PGE<sub>2</sub> can further promote IL-6/MMP-9-dependent cell migration. Moreover, CORM-2 inhibits *S. aureus*-induced COX-2 expression and inflammatory responses by increasing the ROS generation and reducing the NF- $\kappa$ B activity. Altogether, the results of this study provide molecular mechanisms for the antibacterial effects of CORM-2.

## Conflict of interest

The authors declare no conflict of interest.

## Acknowledgments

This work was supported by the Chang Gung Medical Research Foundation, grant number CMRPGMF0022 and CMRPGMF0023; the China Medical University, grant number CMU106-S-14 and CMU105-S-46.

## References

- [1] M.Z. David, R.S. Daum, Treatment of *Staphylococcus aureus* Infections, *Curr. Top. Microbiol. Immunol.* 409 (2017) 325–383.
- [2] H. Asgerisson, A. Thalme, M. Kristjansson, O. Weiland, Incidence and outcome of *Staphylococcus aureus* endocarditis—a 10-year single-centre northern European experience, *Clin. Microbiol. Infect.* 21 (8) (2015) 772–778.
- [3] S.W. Kerrigan, C. McDonnell, Dysregulation of the endothelium following *Staphylococcus aureus* infection, *Biochem. Soc. Trans.* 43 (4) (2015) 715–719.
- [4] I. Venza, M. Visalli, M. Cucinotta, D. Teti, M. Venza, NOD2 triggers PGE<sub>2</sub> synthesis leading to IL-8 activation in *Staphylococcus aureus*-infected human conjunctival epithelial cells, *Biochem. Biophys. Res. Commun.* 440 (4) (2013) 551–557.

- [5] C. Klemm, C. Bruchhagen, A. van Krüchten, S. Niemann, B. Löffler, G. Peters, et al., Mitogen-activated protein kinases (MAPKs) regulate IL-6 over-production during concomitant influenza virus and *Staphylococcus aureus* infection, *Sci. Rep.* 7 (2017) 42473.
- [6] H. Li, H. Zheng, L. Li, X. Shen, W. Zang, Y. Sun, The effects of matrix metalloproteinase-9 on dairy goat mastitis and cell survival of goat mammary epithelial cells, *PLoS One* 11 (8) (2016) e0160989.
- [7] S.W. Ryter, J. Alam, A.M. Choi, Heme oxygenase-1/carbon monoxide: from basic science to therapeutic applications, *Physiol. Rev.* 86 (2) (2006) 583–650.
- [8] S.W. Ryter, A.M. Choi, Heme oxygenase-1/carbon monoxide: from metabolism to molecular therapy, *Am. J. Respir. Cell Mol. Biol.* 41 (3) (2009) 251–260.
- [9] K. Nakahira, A.M. Choi, Carbon monoxide in the treatment of sepsis, *Am. J. Physiol. Lung. Mol. Physiol.* 309 (12) (2015) L1387–L1393.
- [10] S.W. Ryter, A.M. Choi, Targeting heme oxygenase-1 and carbon monoxide for therapeutic modulation of inflammation, *Transl. Res.* 167 (1) (2016) 7–34.
- [11] K. Katada, T. Takagi, K. Uchiyama, Y. Naito, Therapeutic roles of carbon monoxide in intestinal ischemia-reperfusion injury, *J. Gastroenterol. Hepatol.* 30 (2015) S46–S52.
- [12] M.M. Al-Owais, J.L. Scragg, M.L. Dallas, H.E. Boycott, P. Warburton, A. Chakrabarty, J.P. Boyle, C. Peers, Carbon monoxide mediates the anti-apoptotic effects of heme oxygenase-1 in medulloblastoma DAOY cells via  $K^+$  channel inhibition, *J. Biol. Chem.* 287 (2012) 24754–24764.
- [13] R. Motterlini, L.E. Otterbein, The therapeutic potential of carbon monoxide, *Nat. Rev. Drug Discov.* 9 (9) (2010) 728–743.
- [14] S. Lian, Y. Xia, T.T. Ung, P.N. Khoi, H.J. Yoon, N.H. Kim, et al., Carbon monoxide releasing molecule-2 ameliorates IL-1 $\beta$ -induced IL-8 in human gastric cancer cells, *Toxicology* 12 (361–362) (2016) 24–38.
- [15] K.L. Siu, Q. Li, Y. Zhang, J. Guo, J.Y. Youn, J. Du, et al., NOX isoforms in the development of abdominal aortic aneurysm, *Redox. Biol.* 11 (2017) 118–125.
- [16] X. Zhao, K. Drlica, Reactive oxygen species and the bacterial response to lethal stress, *Curr. Opin. Microbiol.* 21 (2014) 1–6.
- [17] A.F. Tavares, M. Teixeira, C.C. Romão, J.D. Seixas, L.S. Nobre, L.M. Saraiva, Reactive oxygen species mediate bactericidal killing elicited by carbon monoxide-releasing molecules, *J. Biol. Chem.* 286 (30) (2011) 26708–26717.
- [18] I.T. Lee, C.W. Lee, W.H. Tung, S.W. Wang, C.C. Lin, J.C. Shu, C.M. Yang, Cooperation of TLR2 with MyD88, PI3K, and Rac1 in lipoteichoic acid-induced cPLA<sub>2</sub>/COX-2-dependent airway inflammatory responses, *Am. J. Pathol.* 176 (2010) 1671–1684.
- [19] I.T. Lee, C.C. Lin, W.N. Lin, W.L. Wu, L.D. Hsiao, C.M. Yang, Lung inflammation caused by adenosine-5'-triphosphate is mediated via  $Ca^{2+}$ /PKCs-dependent COX-2/PGE<sub>2</sub> induction, *Int. J. Biochem. Cell Biol.* 45 (8) (2013) 1657–1668.
- [20] C. Gabay, Interleukin-6 and chronic inflammation, *Arthritis Res. Ther.* 8 (2006) S3.
- [21] C.C. Lin, I.T. Lee, Y.L. Yang, C.W. Lee, Y.R. Kou, C.M. Yang, Induction of COX-2/PGE<sub>2</sub>/IL-6 is crucial for cigarette smoke extract-induced airway inflammation: role of TLR4-dependent NADPH oxidase activation, *Free Radic. Biol. Med.* 48 (2) (2010) 240–254.
- [22] W. Chen, T. Xia, D. Wang, B. Huang, P. Zhao, J. Wang, et al., Human astrocytes secrete IL-6 to promote glioma migration and invasion through upregulation of cytomembrane MMP14, *Oncotarget* 7 (38) (2016) 62425–62438.
- [23] J. Meng, X.T. Zhang, X.L. Liu, L. Fan, C. Li, Y. Sun, WSTF promotes proliferation and invasion of lung cancer cells by inducing EMT via PI3K/Akt and IL-6/STAT3 signaling pathways, *Cell. Signal.* 28 (11) (2016) 1673–1682.
- [24] C.C. Lin, C.T. Kuo, C.Y. Cheng, C.Y. Wu, C.W. Lee, H.L. Hsieh, et al., IL-1 $\beta$  promotes A549 cell migration via MAPKs/AP-1- and NF- $\kappa$ B-dependent matrix metalloproteinase-9 expression, *Cell. Signal.* 21 (11) (2009) 1652–1662.
- [25] B. Fournier, D.J. Philpott, Recognition of *Staphylococcus aureus* by the innate immune system, *Clin. Microbiol. Rev.* 18 (3) (2005) 521–540.
- [26] C.N. Paiva, M.T. Bozza, Are reactive oxygen species always detrimental to pathogens? *Antioxid. Redox Signal.* 20 (6) (2014) 1000–1037.
- [27] N. Anantliotakis, S. Deftereos, G. Bouras, G. Giannopoulos, D. Tsounis, C. Angelidis, et al., Myeloperoxidase: expressing inflammation and oxidative stress in cardiovascular disease, *Curr. Top. Med. Chem.* 13 (2) (2013) 115–138.
- [28] B. Sinha, M. Herrmann, Mechanism and consequences of invasion of endothelial cells by *Staphylococcus aureus*, *Thromb. Haemost.* 94 (2) (2005) 266–277.
- [29] I.T. Lee, C.M. Yang, Inflammatory signalings involved in airway and pulmonary diseases, *Mediators Inflamm.* 2013 (2013) 791231.
- [30] K. Ling, F. Men, W.C. Wang, Y.Q. Zhou, H.W. Zhang, D.W. Ye, Carbon monoxide and its controlled release: therapeutic application, detection, and development of carbon monoxide releasing molecules (CORMs), *J. Med. Chem.* 61 (7) (2018) 2611–2635.
- [31] S. García-Gallego, G.J. Bernardes, Carbon-monoxide-releasing molecules for the delivery of therapeutic CO in vivo, *Angew. Chem. Int. Ed. Engl.* 53 (37) (2014) 9712–9721.
- [32] M. Nemati, T. Larussa, H. Khorramdelazad, M. Mahmoodi, A. Jafarzadeh, Toll-like receptor 2: an important immunomodulatory molecule during *Helicobacter pylori* infection, *Life Sci.* 178 (2017) 17–29.
- [33] B. Kaltschmidt, J.F.W. Greiner, H.M. Kadhim, C. Kaltschmidt, Subunit-specific role of NF- $\kappa$ B in cancer, *Biomedicines* 6 (2) (2018) pii: E44.
- [34] S. Li, Y. Jiao, H. Wang, Q. Shang, F. Lu, L. Huang, et al., Sodium tanshinone IIA sulfate adjunct therapy reduces high-sensitivity C-reactive protein level in coronary artery disease patients: a randomized controlled trial, *Sci. Rep.* 7 (1) (2017) 17451.
- [35] T. Tanaka, M. Narazaki, T. Kishimoto, IL-6 in inflammation, immunity, and disease, *Cold Spring Harb. Perspect. Biol.* 6 (10) (2014) a016295.
- [36] T. Tanaka, M. Narazaki, A. Ogata, T. Kishimoto, A new era for the treatment of inflammatory autoimmune diseases by interleukin-6 blockade strategy, *Semin. Immunol.* 26 (1) (2014) 88–96.
- [37] T. Tanaka, M. Narazaki, T. Kishimoto, Anti-interleukin-6 receptor antibody, tocilizumab, for the treatment of autoimmune diseases, *FEBS Lett.* 585 (23) (2011) 3699–3709.
- [38] Y.F. Li, H. Wang, Y. Fan, H.J. Shi, Q.M. Wang, B.R. Chen, M.R. Khurwolah, Q.Q. Long, S.B. Wang, Z.M. Wang, L.S. Wang, Epigallocatechin-3-gallate inhibits matrix metalloproteinase-9 and monocyte chemotactic protein-1 expression through the 67-kDa laminin receptor and the TLR4/MAPK/NF- $\kappa$ B signalling pathway in lipopolysaccharide-induced macrophages, *Cell. Physiol. Biochem.* 43 (3) (2017) 926–936.
- [39] C. Cao, Y. Su, Y. Gao, C. Luo, L. Yin, Y. Zhao, H. Chen, A. Xu, *Ginkgo biloba* extract inhibits the metastasis of B16-F10 melanoma involving PI3K/Akt/NF- $\kappa$ B/MMP-9 signaling pathway, *Evid. Complement. Alternat. Med.* 2018 (2018) 4969028.
- [40] Y. Shin, S.H. Yoon, E.Y. Choe, S.H. Cho, C.H. Woo, J.Y. Rho, J.H. Kim, PMA-induced up-regulation of MMP-9 is regulated by a PKC $\alpha$ -NF- $\kappa$ B cascade in human lung epithelial cells, *Exp. Mol. Med.* 39 (1) (2007) 97–105.
- [41] J. Cao, Z. Han, L. Tian, K. Chen, Y. Fan, B. Ye, W. Huang, C. Wang, Z. Huang, Curcumin inhibits EMT and MMP-9 expression through AMPK-MAPK and PKC signaling in PMA induced macrophages, *J. Transl. Med.* 12 (2014) 266.



# The active compounds derived from *Psoralea corylifolia* for photochemotherapy against psoriasis-like lesions: The relationship between structure and percutaneous absorption

Ahmed Alalaiwe<sup>a</sup>, Chi-Feng Hung<sup>b</sup>, Yann-Lii Leu<sup>c,d,e</sup>, Kohei Tahara<sup>f</sup>, Hi-Han Chen<sup>c</sup>, Kai-Yin Hu<sup>c</sup>, Jia-You Fang<sup>c,d,g,h,\*</sup>

<sup>a</sup> Department of Pharmaceutics, College of Pharmacy, Prince Sattam Bin Abdulaziz University, Al Kharj, Saudi Arabia

<sup>b</sup> School of Medicine, Fu Jen Catholic University, New Taipei City, Taiwan, Taiwan

<sup>c</sup> Graduate Institute of Natural Products, Chang Gung University, Taoyuan, Taiwan

<sup>d</sup> Chinese Herbal Medicine Research Team, Healthy Aging Research Center, Chang Gung University, Taoyuan, Taiwan

<sup>e</sup> Center for Traditional Chinese Medicine, Chang Gung Memorial Hospital at Linkou, Taoyuan, Taiwan

<sup>f</sup> Laboratory of Pharmaceutical Engineering, Gifu Pharmaceutical University, Gifu, Japan

<sup>g</sup> Department of Anesthesiology, Chang Gung Memorial Hospital at Linkou, Taoyuan, Taiwan

<sup>h</sup> Research Center for Industry of Human Ecology and Research Center for Chinese Herbal Medicine, Chang Gung University of Science and Technology, Taoyuan, Taiwan

## ARTICLE INFO

### Keywords:

PUVA  
Skin  
Psoriasis  
*Psoralea corylifolia*  
Percutaneous absorption

## ABSTRACT

8-Methoxypsoralen (8-MOP) in combination with ultraviolet A (PUVA) is a photochemotherapy for management of psoriasis. 8-MOP is a natural compound from *Psoralea corylifolia*. The present work was undertaken to evaluate the percutaneous absorption of five compounds derived from *P. corylifolia*, and to further explore the inhibitory effect on psoriasis-like lesions generated by imiquimod stimulation in a mouse model. 8-MOP, psoralen, isopsoralen, psoralidin, and bakuchiol were comparatively tested for in vitro skin permeation, keratinocyte apoptosis, and in vivo antipsoriatic potency. The pig ear skin deposition of 8-MOP, isopsoralen, and bakuchiol at an equimolar dose was 0.47, 0.58, and 0.50 nmol/mg, respectively, which was comparable and higher than that of psoralen (0.25 nmol/mg) and psoralidin (0.14 nmol/mg). Psoralidin and bakuchiol were absorbed into the skin without further penetration across the skin. Besides experimental data of physicochemical properties, the hydrogen bond number, total polarity surface, and stratum corneum lipid docking calculated could explain the correlation of the penetrant structure with the skin permeability. The antiproliferative activity against keratinocytes was stronger for 8-MOP and isopsoralen than the others. Topical application of PUVA by using 8-MOP and isopsoralen on imiquimod-induced plaque significantly reduced transepidermal water loss from 55 to 33 and 38 g/m<sup>2</sup>/h, respectively. The epidermal thickening elicited by imiquimod (117 μm) was decreased to 62 and 26 μm by 8-MOP and isopsoralen application. IL-6 expression in psoriasisform skin was downregulated by isopsoralen but not 8-MOP. Isopsoralen may be a potential candidate for PUVA therapy.

## 1. Introduction

Psoriasis, an autoimmune disorder, is a common inflammatory skin disease (Griffiths et al., 2017). The lesional psoriasis skin is characterized by silvery scales over the thickened skin. According to histological observation, psoriasis produced keratinocyte proliferation, immune cell infiltration, and elongated rete pegs due to the interplay among genetics, the environment, immune modulation, and cutaneous barrier disruption (Raychaudhuri et al., 2014). Until now, an effective and

long-term regimen for psoriasis eradication has been lacking, especially for moderate-to-severe psoriasis. Recently, the biologics such as etanercept, ixekizumab, and adalimumab are widely used for psoriasis treatment with successful outcomes (Rønholt and Iversen, 2017). However, the need of invasive injection can cause the low patient compliance, as well as economic burden and mental stress for patients and their caregivers. Photochemotherapy, one of the oldest therapies for psoriasis, employs psoralens plus ultraviolet A exposure (PUVA). It is useful for treating psoriasis because of the direct antiproliferative

\* Corresponding author at: Pharmaceutics Laboratory, Graduate Institute of Natural Products, Chang Gung University, 259 Wen-Hwa 1st Road, Kweishan, Taoyuan 333, Taiwan.

E-mail address: [fajy@mail.cgu.edu.tw](mailto:fajy@mail.cgu.edu.tw) (J.-Y. Fang).

<https://doi.org/10.1016/j.ejps.2018.08.031>

Received 28 May 2018; Received in revised form 7 August 2018; Accepted 23 August 2018

Available online 25 August 2018

0928-0987/ © 2018 Elsevier B.V. All rights reserved.



effect on keratinocytes (Farahnik et al., 2016). The psoralens bind to the DNA, in which pyrimidine bases are the targets for photochemical apoptosis (Singh et al., 2010).

8-Methoxypsoralen (8-MOP) is the predominant psoralen used for PUVA as approved by the USFDA. The structure of 8-MOP is categorized as furocoumarin, largely found in the seeds of *Psoralea corylifolia*. The extract of *P. corylifolia* shows several bioactivities such as cytotoxic, anticancer, antimicrobial, and immunomodulatory properties (Zhang et al., 2016). The dried seeds of this plant for external use are successful in mitigating the lesions of psoriasis, vitiligo, eczema, and alopecia (Hussain et al., 2016; Alam et al., 2018). The coumarins and terpenes in the extract of *P. corylifolia* seeds may contribute to the amelioration of these cutaneous diseases. Although 8-MOP is commonly utilized as the agent for photochemotherapy, the unsatisfied delivery to the nidus and the adverse effects of burning, pigmentation, and blisters have limited its application (Doppalapudi et al., 2017). The undesirable systemic photosensitivity may occur by 8-MOP transport into the circulation (Der-Petrossian et al., 2000). The intervention of new treatments for psoriasis causing greater skin targeting and less irritation would be necessary. In this study, we aimed to search the alternative compounds in *P. corylifolia* for PUVA therapy. We attempted to compare the percutaneous absorption, antiproliferative activity, and the ability to improve the psoriasis-like lesions of the compounds derived from *P. corylifolia*. These included 8-MOP, psoralen, isopsoralen, psoralidin, and bakuchiol (Fig. 1).

The exploration of how the structure and physicochemical characteristics influence the skin absorption of penetrants is the principle used to choose or design a suitable active for topical administration. The structure-permeation relationship (SPR) involves the elucidation of a series of compounds affecting skin permeation and targeting (Geinoz et al., 2004). The second aim of this study was to organize the possible SPR of the compounds in *P. corylifolia* after cutaneous delivery. All compounds tested in our work were extracted and isolated from the seeds of *P. corylifolia*. The 20% polyethylene glycol (PEG)400 in pH 7.4 buffer was used as the vehicle of these compounds for in vitro and in vivo tests since several attempts for SPR establishment employ the in vitro models obtained from penetrant delivery from aqueous solution (Riviere and Brooks, 2011). The molecular modeling was conducted to achieve the information pertaining to the hydrogen bond acceptor and donor, the total polarity surface, the molecular volume, as well as the interaction to the stratum corneum (SC) lipids for building the SPR. To estimate the in vivo efficiency of these compounds for PUVA regimen,

transepidermal water loss (TEWL), cytokine expression, and proliferation were evaluated using a BALB/c mouse model with psoriasisiform skin. Whether the skin was tolerant to topically applied penetrants was also measured in vivo.

## 2. Materials and methods

### 2.1. Extraction of *P. corylifolia*

Seeds of *P. corylifolia* were supplied and authenticated by Chuang Song Zong Pharmaceutical Company (Pingtung, Taiwan). A voucher specimen (CGU-PC-1) was deposited in the herbarium of Chang Gung University. The seeds (5.4 kg) were extracted with EtOH (11 l × 9) and concentrated to yield a brown syrup (1.4 kg). The syrup was suspended in H<sub>2</sub>O and partitioned with *n*-hexane and EtOAc. The *n*-hexane extract (515.6 g) was subjected to column chromatography over silica gel and eluted with *n*-hexane and EtOAc stepwise gradients to afford eleven fractions. The repeated column chromatography of the first fraction, over silica gel with *n*-hexane and EtOAc (20:1) mixtures yielded (+)-bakuchiol (1870 mg). The third fraction was applied on a silica gel column and eluted with a gradient of *n*-hexane and EtOAc (10:1) to give isopsoralen (3120 mg). The fourth fraction was subjected to column chromatography over silica gel and eluted with *n*-hexane and EtOAc (7:1) to afford psoralen (2873 mg). The seventh fraction was repeatedly chromatographed over silica gel with *n*-hexane and EtOAc (1:1) to get psoralidin (1249 mg). The structures of these compounds were identified by comparison of their spectral data with corresponding literature values (Guo et al., 2005; Pahari and Rohr, 2009). The data of <sup>1</sup>H NMR and <sup>13</sup>C-NMR for these compounds are summarized in the Supplementary data.

### 2.2. Partition coefficient (log *P*)

The compounds in 1-ml methanol (0.5 mg/ml) were positioned in the test tube. The organic solvent was evaporated under vacuum. Water (1 ml) and *n*-octanol (1 ml) were pipetted into the tube, respectively. The tube was shaken at 37 °C for 24 h, then centrifuged at 10,000 × *g* for 10 min. The amount of compounds in *n*-octanol and water was determined by high-performance liquid chromatography (HPLC). The value of log *P* was estimated as log (compound content in *n*-octanol/compound content in water).

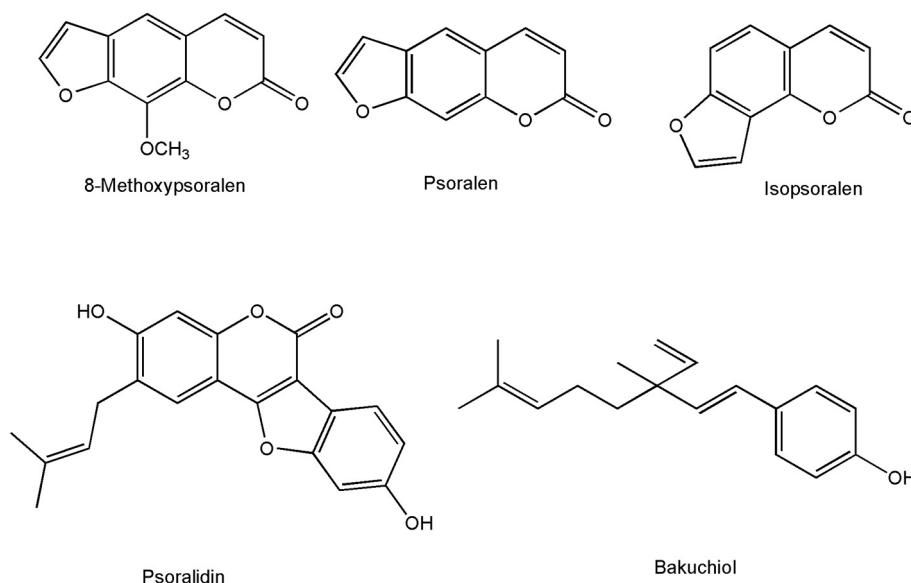


Fig. 1. The chemical structures of 8-MOP, psoralen, isopsoralen, psoralidin, and bakuchiol.

### 2.3. Capacity factor ( $\log K'$ )

The  $\log K'$  was determined based on the retention time of the compounds in HPLC chromatography. The HPLC setup was an HPLC system (7-series, Hitachi, Tokyo, Japan) with a LiChrospher® RP-18 column (200 × 4.6 mm, Merck, Darmstadt, Germany). The mobile phase consisted of methanol and double-distilled water at a ratio of 65:35. The flow rate and detection wavelength were 1 ml/min and 246 nm, respectively. The  $\log K'$  was estimated as  $\log [t_r - t_0 / t_0]$ , where  $t_r$  and  $t_0$  were the retention time of the compound and the non-retained solvent peak, respectively.

### 2.4. Melting point

The melting point of the compounds in free form was determined using a calorimeter (Q2000, TA Instruments, New Castle, DE, USA). The compounds were weighed and sealed in the calorimeter. The heating curve was detected (0 to 350 °C) at a scan rate of 20 °C/min under nitrogen.

### 2.5. Saturated solubility in 20% PEG400 vehicle

The test compounds at 5 mM were prepared by using PEG400/pH 7.4 buffer (1:4) as the medium. This compound-containing vehicle was shaken at 37 °C for 2 h. The compound-containing vehicle was subsequently centrifuged at 10,000 × g for 10 min. The supernatant was then filtered through the polyvinylidene fluoride membrane (pore size = 0.45 µm). The saturated solubility of the compounds was quantified by HPLC.

### 2.6. Animals

The eleven-month-old pigs were obtained from Doctor Pig Animal Technology (Miaoli, Taiwan). The eight-week-old female nude mice and BALB/c hairy mice were purchased from the National Laboratory Animal Center (Taipei, Taiwan). All animal experiments were performed in strict accordance with the recommendation in the Guidelines for the Care and Use of Laboratory Animals of Chang Gung University. The protocol was approved by the Institutional Animal Care and Use Committee.

### 2.7. In vitro percutaneous absorption

The compound absorption into and across the animal skins was conducted with the Franz cell assembly. The pig ear or nude mouse dorsal skin was positioned between the donor and receptor compartments. The volume of the donor and receptor was 0.5 and 5 ml, respectively. The receptor compartment was loaded with ethanol/pH 7.4 buffer (3:7). The topically applied vehicle was tailored to contain the penetrants at saturated solubility or equimolar concentration (5 mM). The penetration region available for Franz cell was 0.785 cm<sup>2</sup>. At the determined duration, a 300-µl receptor medium was withdrawn to analyze the compound penetration across the skin. The skin was removed from the cell 24 h post-application. The skin was then cleaned by water and dried. The compound deposition within the skin reservoir was detected by homogenization of the skin (MagNA Lyser, Roche, Indianapolis, IN, USA). The homogenate was then centrifuged at 10,000 × g for 10 min. The penetrant concentration in the receptor and skin was quantified by HPLC.

### 2.8. Molecular modeling

The parameters including Alog P, hydrogen bond number, total polarity surface, and molecular volume of the test compounds were computed by Discovery Studio® 4.1 workstation (Accelrys, San Diego, CA, USA). The superimposition of the compounds interacted with SC

lipids was sketched for visualizing the ligand-binding effect and conformation. The negative CDOCKER energy was measured by Discovery Studio® through the conduction of the docking simulation with SC lipids.

### 2.9. Keratinocyte apoptosis assay

Cultured HaCaT cells were cultivated in DMEM with 10% fetal calf serum, 100 mg/ml streptomycin, and 100 U/ml penicillin. HaCaT cells cultured in the plate were treated with the compounds (0.1–2.0 µM) and a 365-nm UVA irradiation (15 J/cm<sup>2</sup>, Bio-Sun Illuminator, Vilber Lourmat, France). In another protocol, the UVA was irradiated after a 2-h pretreatment of the compounds. The length between the plate and UVA light resource was 10 cm. MTT assay was used to detect the cell viability by 24 h post-treatment of the compounds. The detailed procedures of the MTT assay were described previously (Wu et al., 2010).

### 2.10. In vivo psoriasis-like model

The method for the induction of psoriasiform skin in the back of BALB/c mice was modified from the process by van der Fits et al. (2009). The imiquimod cream (Aldara®, 3 M, Leicestershire, UK) with a dose amount of 62.5 mg was applied on the shaved dorsal skin each day for 6 days. From Days 3 to 6, the PEG400/pH 7.4 buffer (1:4) containing the compounds (0.2 mg) was administered on the imiquimod-treated area of 3 × 2 cm<sup>2</sup>. After 30 min of compound intervention, UVA (2.5 J/cm<sup>2</sup>) was irradiated on the mouse back for PUVA management. On Day 7, the appearance of the back skin was monitored by the handheld digital magnifier (Mini Scope-V, M&T Optics, Taipei, Taiwan). TEWL had been examined by Tewameter (TM300, Courage and Khazaka, Köln, Germany).

### 2.11. Measurement of cytokines

On Day 7, the mice were sacrificed after the determination of TEWL. The biopsies were obtained from the back skin, and then frozen immediately in liquid nitrogen. The cytokines including IL-1β, IL-6, and TNF-α within the treated skin area were analyzed using the ELISA method. The 5-mm punch biopsy was acquired from the mouse back, incubating in PBS (1 ml) with complete protease inhibitors. The fragments of the biopsy were homogenized at 6500 rpm for 30 s and then cooled down for 1 min. The supernatant was withdrawn after a centrifugation at 13,000 rpm and 4 °C for 10 min. The protein concentration of skin tissue lysate was determined by a total protein assay (Bio-Rad, Hercules, CA, USA). Each sample was calibrated to the same amount of total protein for each assay. The cytokine concentration was determined by the commercial kits (BioLegend, San Diego, CA, USA) according to the instructions provided by the manufacturer.

### 2.12. Histology

The skin specimen was deposited into a 10% buffered formaldehyde using ethanol, embedded in paraffin wax, and sliced at 3 µm for hematoxylin and eosin (H&E) staining. The unstained specimens were prepared for immunohistochemistry (IHC). After dewaxing and rehydration, the paraffin-embedded sections were subjected to heat-induced epitope retrieval according to the manufacturer's instructions, followed by blocking with diluted normal serum. The sections were incubated with anti-mouse Ki67 antibody for 1 h at room temperature; washed with saline containing 0.5% Tween 20, and subsequently incubated at ambient temperature with biotinylated donkey anti-goat IgG for 20 min. Photographs were obtained using a Leica DMi8 microscopy (München, Germany).

### 2.13. In vivo skin tolerance

The PEG400/pH 7.4 buffer (1:4) containing the compounds (5 mM) was applied (0.2 ml) on the dorsal region ( $1.5 \times 1.5 \text{ cm}^2$ ) of the BALB/c mice daily for 7 consecutive days. On Day 7, the treated skin region was examined via handheld digital magnifier, TEWL, and erythema (CD100 spectrophotometer, Yokogawa, Tokyo, Japan).

### 2.14. Data analysis

To analyze percutaneous absorption of the compounds, the skin deposition was measured as the molar content per mg of skin (nmol/mg) as the penetrants were administered as the equimolar dose. In the experiment of using the saturated dose, the calibrated skin deposition (CSD) was calculated as the skin deposition divided by the saturated solubility. The flux (nmol/cm<sup>2</sup>/h) was measured by the slope of the cumulative amount-time profile. The permeability coefficient (cm/h) was estimated from the flux divided by the saturated solubility. To predict the therapeutic consequence of topically applied photochemotherapy, the therapeutic index (TI) was rated by the skin deposition divided by keratinocyte viability in the presence of UVA irradiation.

The statistical measurement was conducted using GraphPad Prism 5 software. Dual comparisons were made with unpaired Student's *t*-test. Groups of three or more were analyzed by ANOVA with Tukey or Dunnett posttests. The significance was indicated as \* for  $p < 0.05$ , \*\* for  $p < 0.01$ , and \*\*\* for  $p < 0.001$  in the figures.

## 3. Results

### 3.1. Physicochemical properties of the compounds

The physicochemical characteristics of the compounds derived from *P. corylifolia* are presented in Table 1. With respect to the experimental log *P* value, isopsoralen showed the greater level as compared to 8-MOP and psoralen. Psoralidin and bakuchiol revealed an extremely high lipophilicity since all molecules were detected in the *n*-octanol phase. The theoretical log *P* (Alog *P*) measured by molecular modeling demonstrated a similar trend as experimental log *P*. The log *K'* is another indicator of lipophilicity based on the chromatographic retention in the stationary column of HPLC. The log *K'* of the compounds varied from 0.18 to 0.73. The sequence of bakuchiol > psoralidin > isopsoralen > 8-MOP > psoralen was noticed as the rank of log *K'*. The molecular weight (MW) ranged between 186 and 336 g/mol, with psoralidin showing the highest molecular size. The melting point (MP) was in the sequence of psoralidin > psoralen > 8-MOP > isopsoralen. The morphology of bakuchiol was the yellow oil. Although

the lipophilicity of the furocoumarins (8-MOP, psoralen, and isopsoralen) was approximate, the aqueous solubility was quite different. Psoralen and isopsoralen were the isomers; however, the latter compound showed less solubility (1.47 versus 1.21 mM). The extra methoxyl moiety of 8-MOP compared to psoralen contributed to a lower solubility. Both psoralidin and bakuchiol displayed a negligible solubility in 20% PEG400 solution because of the extremely high lipophilicity of both compounds.

### 3.2. In vitro percutaneous absorption

At first, the pig ear skin was dosed with saturated compound solubility to evaluate the CSD and permeability coefficient. The saturated solution was applied as a scenario to achieve a constant diffusion with maximum thermodynamic activity. Pig ear skin is extensively employed as a model barrier for human skin. In the left panel of Fig. 2A, the CSD of bakuchiol (4.00 nmol/mg/solubility) was much higher than that of furocoumarins. The CSD for pig ear skin in the case of 8-MOP, psoralen, and isopsoralen was 0.13, 0.08, and 0.13 nmol/mg/solubility, respectively. The CSD of psoralidin was found below the determination limit of HPLC after a 24-h application. This could be due to psoralidin being practically insoluble in the donor vehicle. The right panel of Fig. 2A indicates a significant furocoumarin penetration across the pig ear skin. The permeability coefficient of the three psoralens showed no significant difference after statistical analysis. No psoralidin and bakuchiol molecules were detected in the receptor, although the sink condition was maintained for both compounds.

The donor vehicle was prepared at a concentration that was the molar equivalent to 5 mM. The equimolar dosing was found to more closely mimic the “in use” status. This compound concentration was much higher as compared to the saturated solubility. The results in the left panel of Fig. 2B demonstrated that isopsoralen was the compound with the highest skin deposition. However, the difference of cutaneous isopsoralen deposition was not statistically significant as compared to 8-MOP and bakuchiol. The capability of psoralidin to accumulate in the skin reservoir was the lowest among all the penetrants tested. Similar to the results of the saturated solubility dose, psoralidin and bakuchiol at an equimolar concentration tended to accumulate in the skin with no transport across the skin (the right panel of Fig. 2B). The mouse skin was also chosen as the permeation barrier in the absorption study. The cutaneous deposition and flux trends of various penetrants were similar to those of pig skin (Fig. 2C).

### 3.3. Molecular modeling

To further understand the impact of molecular structure on percutaneous delivery of the penetrants, the structural parameters such as

**Table 1**  
Physicochemical properties of the compounds derived from *Psoralea corylifolia*.

Compound	log <i>P</i> <sup>a</sup>	Alog <i>P</i> <sup>b</sup>	log <i>K'</i> <sup>c</sup>	MW <sup>d</sup> (g/mol)	MP <sup>e</sup> (°C)	Solubility in 20% PEG400 <sup>f</sup> (mM)
8-MOP <sup>g</sup>	2.66 ± 0.002	2.19	0.20	216.19	148.35	0.69 ± 0.01
Psoralen	2.66 ± 0.01	2.20	0.18	186.16	164.30	1.47 ± 0.01
Isopsoralen	2.88 ± 0.01	2.20	0.22	186.16	141.10	1.21 ± 0.01
Psoralidin	— <sup>h</sup>	4.92	0.65	336.34	318.11	N.D. <sup>i</sup>
Bakuchiol	—	5.35	0.73	256.38	Oil type	0.02 ± 0.002

<sup>a</sup> log *P*, *n*-octanol/water partition coefficient.

<sup>b</sup> Alog *P*, partition coefficient measured by molecular modeling.

<sup>c</sup> log *K'*, logarithm of  $t_r - t_0 / t_0$ ,  $t_r$  is the retention time of compound peak,  $t_0$  is the retention time of solvent peak.

<sup>d</sup> MW, molecular weight.

<sup>e</sup> MP, melting point determined by differential scanning calorimetry.

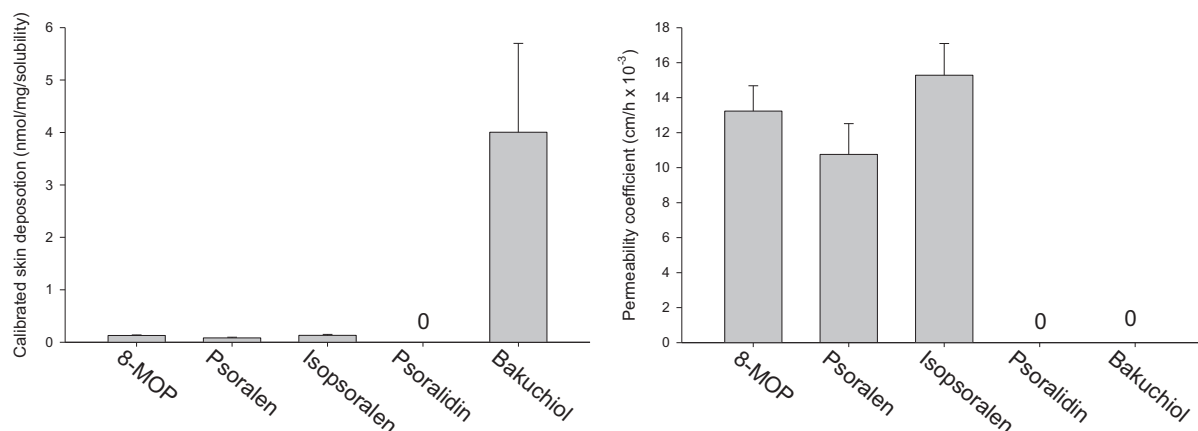
<sup>f</sup> PEG400, polyethylene glycol 400.

<sup>g</sup> 8-MOP, 8-methoxypsoralen.

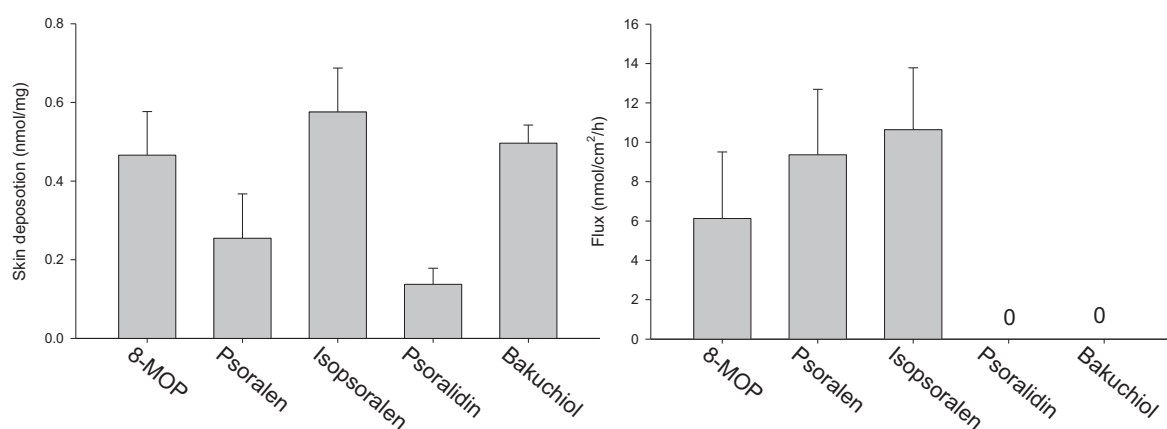
<sup>h</sup> —, all molecules were found in *n*-octanol layer.

<sup>i</sup> N.D., not determined.

## (A) Pig ear skin/saturated dose



## (B) Pig ear skin/equimolar dose



## (C) Nude mouse skin/equimolar dose

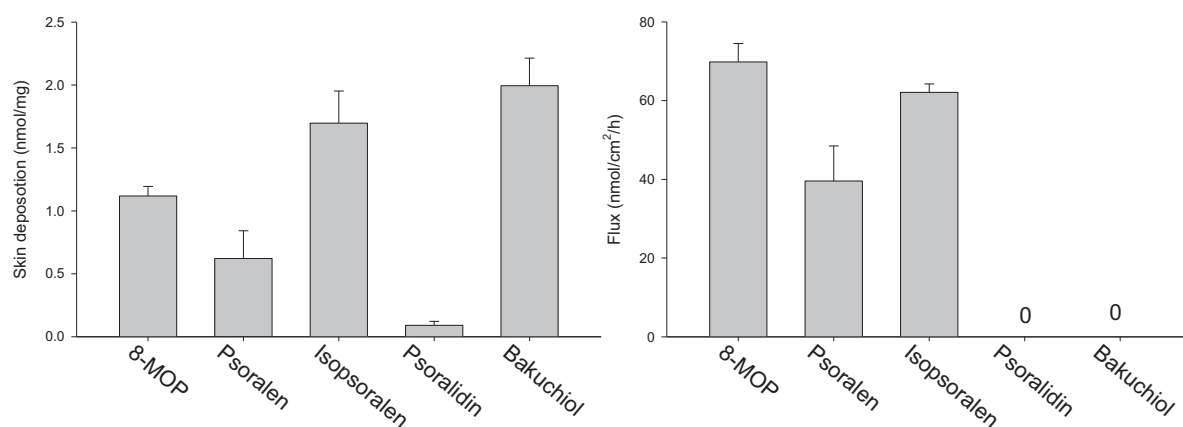


**Fig. 2.** Skin deposition, permeability coefficient, and flux of the compounds derived from *P. corylifolia* after topical treatment on pig ear and nude mouse dorsal skins: (A) a dose at saturated solubility for penetrating into and across pig ear skin, (B) a dose at equimolar concentration (5 mM) for penetrating into and across pig ear skin, and (C) a dose at equimolar concentration (5 mM) for penetrating into and across nude mouse dorsal skin. The donor vehicle is 20% PEG400 in pH 7.4 buffer. All data are presented as the mean of four experiments  $\pm$  S.D.

hydrogen bond number, total polarity surface, and molecular volume were computed as summarized in Table 2. Because of the two hydroxyl groups, psoralidin revealed the greatest hydrogen bond acceptor (4) and donor (2) numbers among the compounds tested. The furocoumarins possessed 2 or 3 hydrogen bond acceptors, whereas bakuchiol had only one. No hydrogen bond donor was given by the

furocoumarins. The total polarity surface of the compounds demonstrated a correlation with the hydrogen bond acceptor number, with psoralidin offering the greatest surface polarity. The molecular volume of the compounds correlated well with the MW. The molecular volume of isopsoralen is slightly smaller than that of psoralen although they have the same MW.



**Table 2**

The hydrogen bond number, total polarity surface, and molecular volume of the compounds derived from *Psoralea corylifolia* determined by molecular modeling.

Compound	Hydrogen bond accept number	Hydrogen bond donor number	Total polarity surface	Molecular volume
8-MOP <sup>a</sup>	3	0	48.67	156.75
Psoralen	2	0	39.44	128.96
Isopsoralen	2	0	39.44	128.28
Psoralidin	4	2	79.90	259.99
Bakuchiol	1	1	20.23	238.38

<sup>a</sup> 8-MOP, 8-methoxypsoralen.

The computational molecular docking can be used to anticipate the interaction between the penetrants and SC lipids. It is advantageous to conceive the ability of penetrant partitioning into the SC layer. Table 3 details the best docking scores of the compounds interacting with SC lipids. The interactions calculated by docking score were van der Waals, hydrogen bonding, and electrostatic forces. The higher value of negative CDOCKER energy shown in Table 3 suggests the stronger interaction. Cholesterol and cholesteryl sulfate more favorably interacted with the compounds than ceramides and fatty acid. The differences of negative CDOCKER energy among the compounds were minimal, except for the absence of interaction between psoralidin and palmitic acid. Although the docking energy was approximate for all compounds, psoralidin was the penetrant showing the lowest interaction with SC lipids. Fig. 3 depicts the best docking poses of the compounds interacting with cholesteryl sulfate, the lipid having the superior interaction with the penetrants than the others. The imaging was computed employing an in silico calculation by using the three-dimensional lipid model. Different compounds have various conformations to interact with cholesteryl sulfate although the docking score was similar.

### 3.4. Keratinocyte apoptosis assay

Fig. 4A shows the antiproliferative activity of the compounds in cultures of grown HaCaT. These compounds generally evoked a concentration-dependent cytotoxicity. Furocoumarins demonstrated the greater cytotoxicity, followed by psoralidin and bakuchiol. There was no significant difference among the HaCaT death induced by the three furocoumarins. As shown in Fig. 4B, the cell viability was reduced following the increase of UVA fluence. We further combined the compound treatment and UVA (15 J/cm<sup>2</sup>) for simulating the photochemotherapy. In the simultaneous protocol, the treatment of the compounds and UVA at the same time dose-dependently decreased the cell numbers as illustrated in Fig. 4C. An enhanced cytotoxic activity in the keratinocytes of the compounds in combination with UVA irradiation was detected. 8-MOP and isopsoralen were among the most potent compounds. Both compounds at the concentrations of > 0.25 μM could completely inhibit keratinocyte growth. We also tested the cell viability by the pretreatment protocol. The keratinocytes were pretreated with the compounds for 2 h and then the UVA irradiation started. As

**Table 3**

The negative CDOCKER energy of the compounds derived from *Psoralea corylifolia* determined by molecular modeling.

Compound	Ceramide II	Ceramide III	Ceramide VI	Cholesterol	Cholesteryl sulfate	Palmitic acid
8-MOP <sup>a</sup>	−9.37	−12.74	−11.44	56.4715	120.94	−13.30
Psoralen	−6.42	−15.60	−10.53	59.5761	130.09	−11.66
Isopsoralen	−5.97	−8.67	−14.59	60.2852	128.11	−12.14
Psoralidin	−12.81	−20.54	−18.86	56.3096	119.08	N.I. <sup>b</sup>
Bakuchiol	−8.06	−14.63	−11.36	60.099	128.79	−11.24

<sup>a</sup> 8-MOP, 8-methoxypsoralen.

<sup>b</sup> N.I., no interaction.

compared to the simultaneous protocol, the pretreatment strategy did not increase keratinocyte susceptibility to UVA (Fig. 4D). The rank of the apoptosis level of different compounds was the same for both protocols.

TI was calculated to appraise the possible antipsoriatic activity by topical application. The TI based on simultaneous protocol and pretreatment protocol is shown in Fig. 4E and F, respectively. In contrast, 8-MOP and isopsoralen were expected to markedly suppress proliferative keratinocytes after skin delivery. The high cutaneous uptake and cytotoxicity against cultured HaCaT of 8-MOP and isopsoralen contributed to the greater TI compared to the other compounds. In the case of the pretreatment approach, isopsoralen manifested a higher index than 8-MOP. The TI for isopsoralen was 2 times higher than that of 8-MOP. Because of the ideal TI and percutaneous absorption of 8-MOP and isopsoralen, both agents were used for further in vivo study.

### 3.5. In vivo psoriasis-like model

The mouse skin was treated with repetitive PUVA during the induction of psoriasis-like lesions through the topical imiquimod administration. Fig. 5A shows the appearance of the skin surface. With the repeated challenge by imiquimod, scaling, erythema, and thickening of the mouse skin could be visualized. The signs and symptoms of the psoriatic lesions in the 8-MOP- and isopsoralen-treated groups were significantly reduced compared with those of the imiquimod-treated group, with isopsoralen showing better improvement than 8-MOP. Fig. 5B illustrates the close-up view of the skin observed using a handheld digital magnifier. A significant scaling and inflammation activated by imiquimod could be diminished by the furocoumarins. The skin's appearance of the furocoumarin-treated groups could not be recovered to the healthy condition (sham). TEWL is associated with the level of barrier function impairment. The psoriasiform skin demonstrates a significantly greater degree of TEWL (55.5 g/m<sup>2</sup>/h) as compared to the sham group (8.8 g/m<sup>2</sup>/h). Both the furocoumarin-treated groups could decrease TEWL (33.3 and 37.5 g/m<sup>2</sup>/h) to ameliorate the barrier deficiency though the level could not be recovered to the control baseline.

The Th17 axis is linked to the psoriatic condition. The production of IL-1β, IL-6, and TNF-α is the downstream effect of IL-17. The results of the cytokine assay are exhibited in Fig. 5D to F. Upon treatment with imiquimod, IL-1β, IL-6, and TNF-α was significantly increased with by 2.4-, 2.2-, and 2.5-fold compared with the healthy control, respectively. Our result indicated that 8-MOP and isopsoralen suppressed IL-1β expression induced by imiquimod in parallel to the sham group (Fig. 5D). Isopsoralen significantly downregulated the abnormally elevated IL-6 level activated by imiquimod (Fig. 5E). The decrease in IL-6 production was not achieved by PUVA of 8-MOP because of the high intersubject variation. Both furocoumarins were unable to suppress TNF-α in psoriasiform lesions.

Analysis of H&E sections from the lesional skin showed typical psoriasis symptoms, such as hyperkeratosis, epidermal hyperplasia, elongation of rete ridges, and excess immune cell migration in the dermis as shown in Fig. 6A. The thickness of epidermis increased from 24.5 ± 6.8 to 117.1 ± 8.2 μm after imiquimod stimulation. 8-MOP

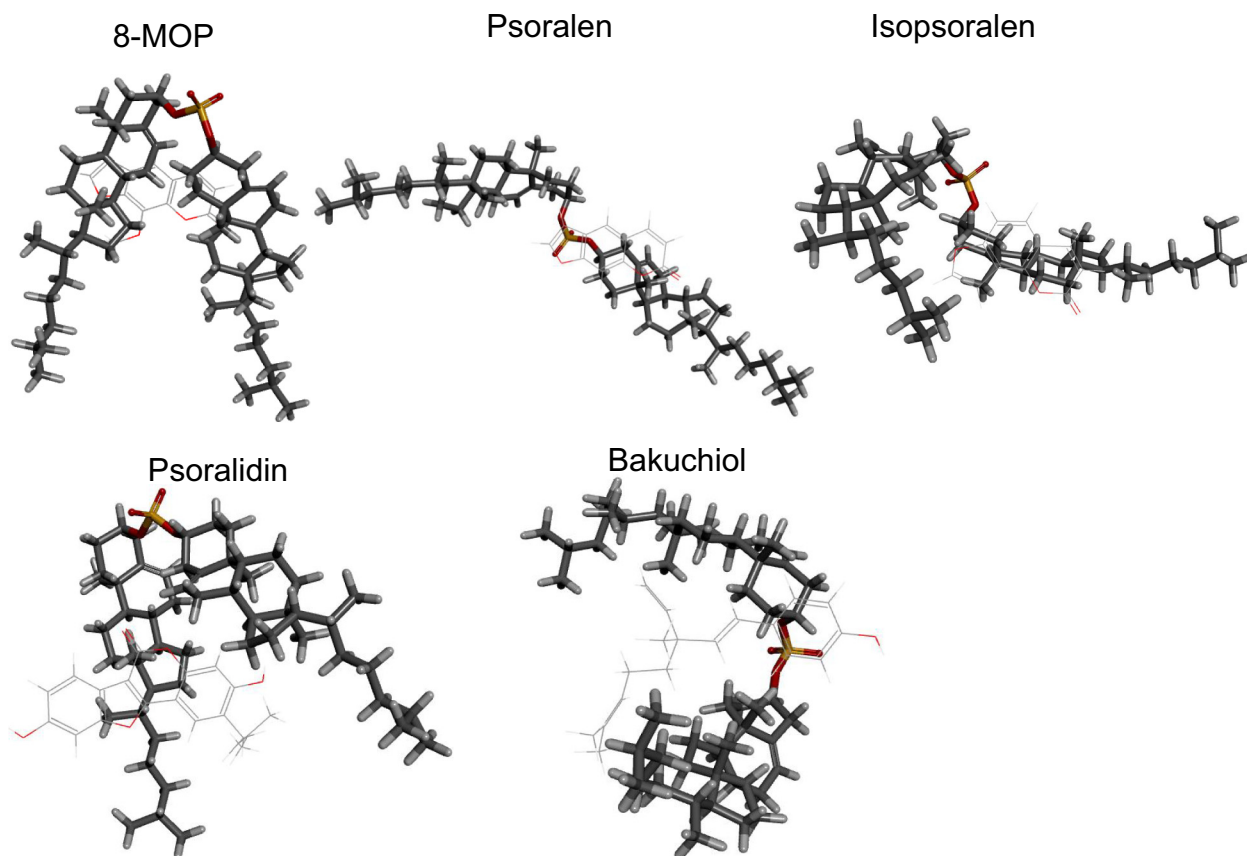


Fig. 3. Superimposition of the computed poses for the compounds derived from *P. corylifolia* with cholesteryl sulfate.

and isopsoralen significantly improved the severity of the lesions. The histological improvement was paralleled with the macroscopic visualization. The epidermal thickness could be reduced to  $61.5 \pm 17.0$  and  $25.9 \pm 8.2 \mu\text{m}$  by 8-MOP and isopsoralen, respectively. The nucleus loss of skin cells in the epidermis indicated the apoptosis by PUVA. There was still some immune cell infiltration in the dermis after PUVA application. Ki-67 is a protein associated with proliferation. IHC staining with Ki-67 revealed that the basal layer of the epidermis stained positive in the sham mice (Fig. 6B). Ki-67 largely appeared in the basal layer of the imiquimod-treated group, suggesting the cell proliferation. PUVA depressed Ki-67 positivity in the epidermis.

### 3.6. In vivo skin tolerance

8-MOP and isopsoralen in 20% PEG400 suspension were topically applied on healthy mouse skin each day for 7 days. Fig. 7A and B illustrate the gross and close-up appearance of the skin surface, respectively. When the mouse skin was administered with the vehicle without the compounds, a slight exfoliation and erythema occurred. The incorporation of the compounds did not further worsen the symptoms. This suggests that the peeling and redness resulted from the repetitive application of PEG400 or water to soften the skin's architecture. As shown in Fig. 7C, TEWL remains unchanged by furocoumarin treatment compared to the vehicle control. The erythema ( $a^*$ ) recorded after a 7-day management also did not exhibit any alteration by the topically applied compounds (Fig. 7D).

## 4. Discussion

We aimed to compare the percutaneous absorption and antipsoriatic activity of the actives in *P. corylifolia* to find a way to improve the current photochemotherapy. Coumarins in *P. corylifolia* can be divided

into furocoumarins and coumestrols. 8-MOP, psoralen, and isopsoralen are classified as furocoumarins, whereas psoralidin is a molecule with a coumestrol skeleton. Furocoumarins are the compounds with planar and tricyclic structures consisting of a furan ring. Bakuchiol is a meroterpene largely found in *P. corylifolia* seeds (Wu et al., 2018). The five compounds demonstrated different natures penetrating into and across the skin. 8-MOP, isopsoralen, and bakuchiol generally manifested superior in vitro skin deposition compared to psoralen and psoralidin. The ability of furocoumarins to pass the skin into the receptor was comparable. Psoralidin and bakuchiol were mainly located in the skin reservoir without further passage into the receptor. Isopsoralen and bakuchiol were capable of targeting the skin with minimal transport across the skin, leading to the efficacious topical application. Although psoralidin penetrated into the skin with no receptor accumulation, the low skin deposition may be insufficient to trigger the pharmacological action after topical delivery. We proposed to unravel the effect of the structure on percutaneous absorption and antipsoriatic activity of the compounds. The physicochemical properties of the penetrants showed a significant impact on the skin absorption. Among the chemical natures, lipophilicity was the major determinant of percutaneous permeation (Thors et al., 2016). The ability of passive permeation depends upon the penetrant partitioning into the SC. The penetrants with higher lipophilicity facily partition into the SC lipid bilayers as compared to those with less lipophilicity. The previous study (Fang et al., 2016) also indicated the importance of SC partitioning for cutaneous 8-MOP delivery. The lipophilicity index can be judged by  $\log P$  and  $\log K'$ . The highest lipophilicity of bakuchiol had led to the high skin deposition, especially in the case of a saturated dose.

It should be pointed out that the skin penetration is predominated not only by the SC, but also by the barrier function of viable skin. Considering the presence of microcirculation in the upper dermis, viable skin is crucial to controlling the flux of penetrants into the systemic

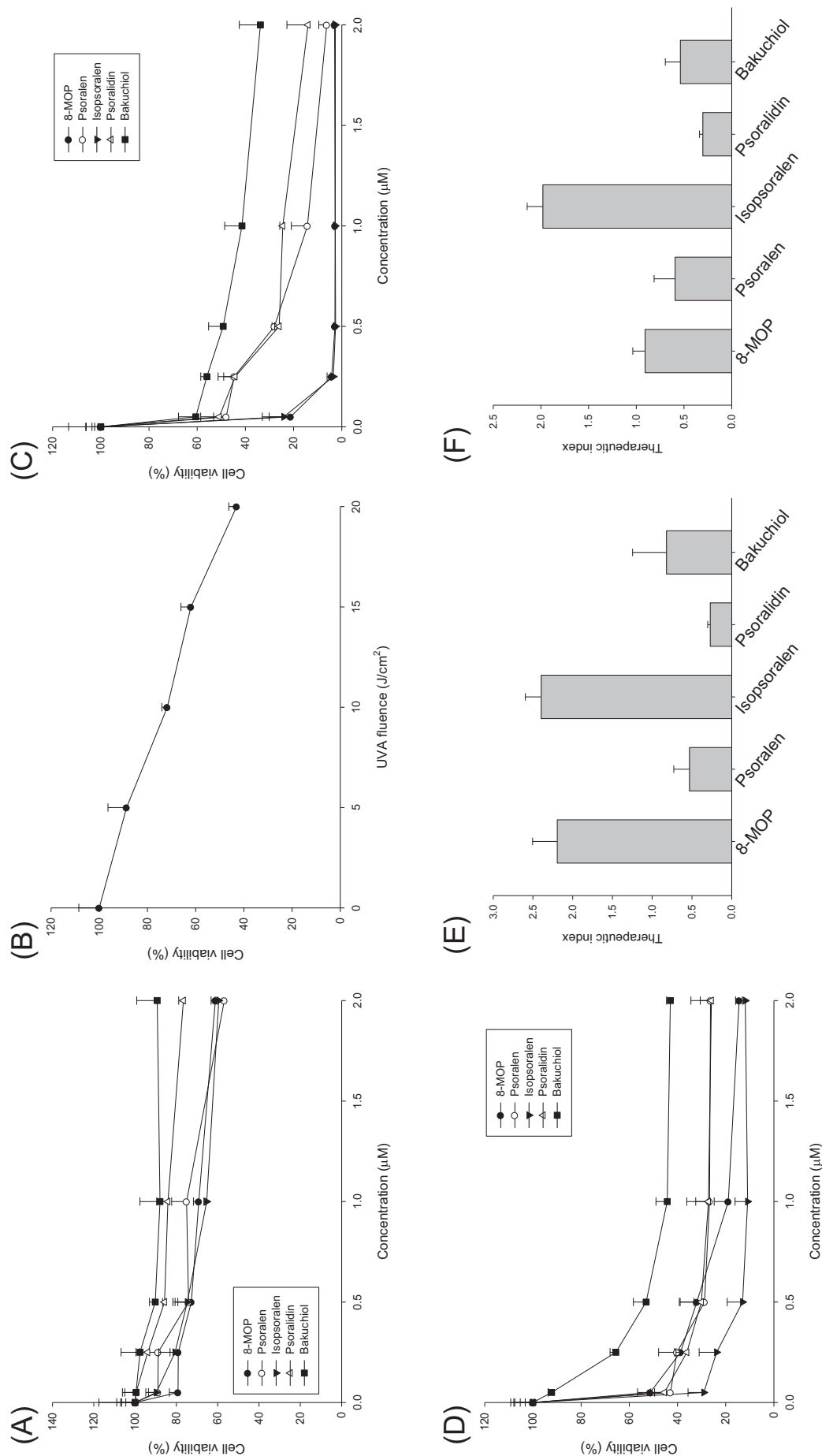


**Fig. 4.** The keratinocyte apoptosis and calculation of therapeutic index (TI) by the compounds derived from *P. corylifolia*: (A) keratinocyte viability after the treatment of the compounds at different concentrations, (B) keratinocyte viability after the treatment of UVA at different fluences, (C) keratinocyte viability after the simultaneous treatment of the compounds and UVA exposure at 15 J/cm<sup>2</sup>, (D) keratinocyte viability after the pretreatment of the compounds for 2 h followed by UVA exposure at 15 J/cm<sup>2</sup>, (E) TI values of the compounds in the simultaneous protocol, and (F) TI values of the compounds in the pretreatment protocol. All data are presented as the mean of six experiments ± S.D.

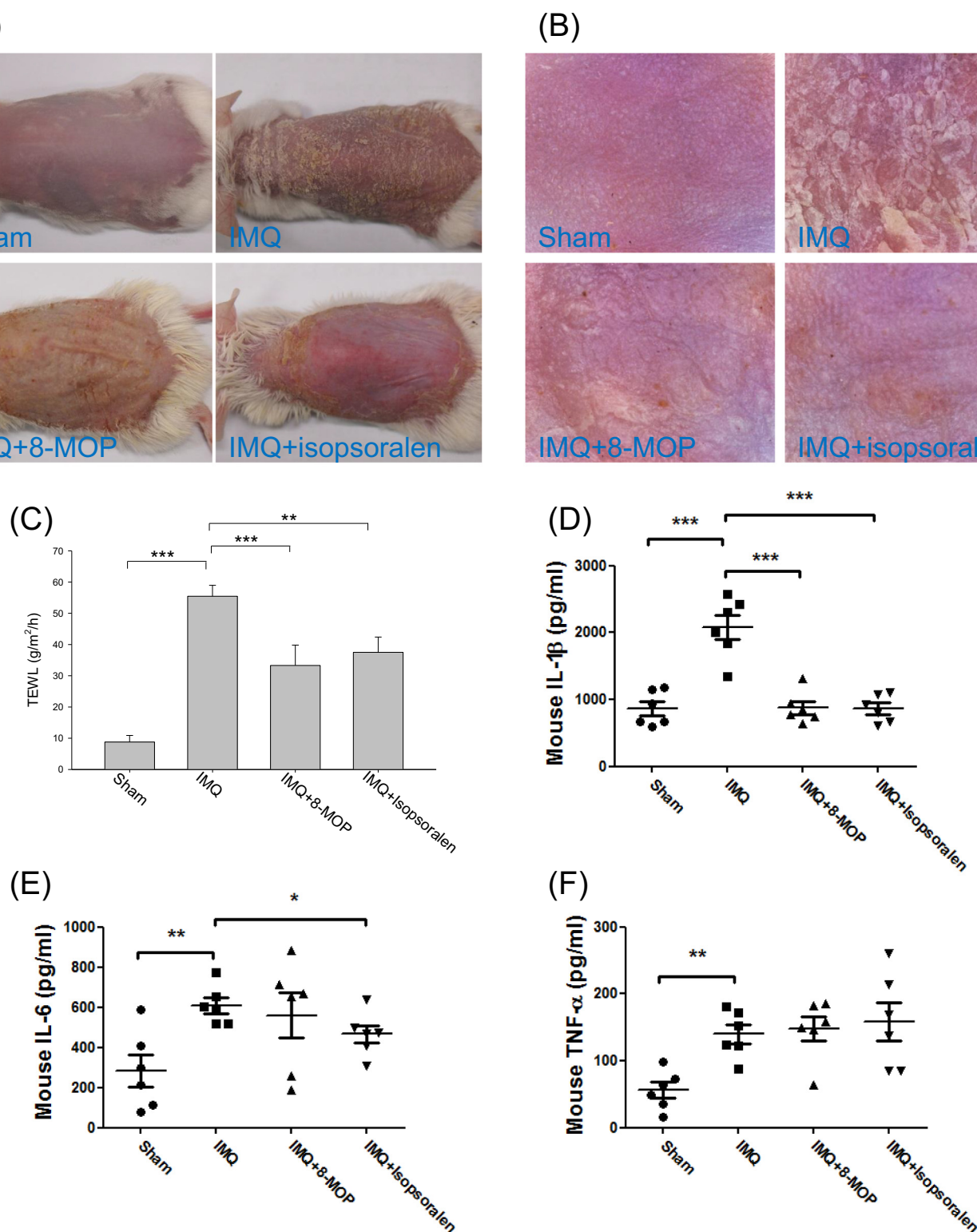


**Fig. 5.** The effect of topically applied 8-MOP and isopsoralen to attenuate imiquimod-induced mouse psoriatic skin inflammation: (A) the gross images of mouse back skin were represented on Day 7 by digital camera, (B) the close-up imaging by handheld digital magnifier, (C) transepidermal water loss (TEWL) measurement, (D) IL-1 $\beta$ , (E) IL-6, and (F) TNF- $\alpha$ . All data are presented as the mean of six experiments  $\pm$  S.D.

circulation. Although the high lipophilicity is critical to diffuse into the skin, a hydrophilic nature is also important for release from the skin into the aqueous medium or circulation (Song et al., 2011). There exists a parabolic relationship between log  $P$  and flux, with the log  $P$  of 2–3 displaying the greatest permeability across the skin (Liu et al., 2011;

Riviere and Brooks, 2011). Our result is consistent with this theory. The compounds with an extremely high log  $P$  even showed no penetration into the receptor compartment. The furocoumarins with a feasible log  $P$  (2.7–2.9) may preferentially reside in the viable epidermis and dermis, inhabited by the psoriatic nidus. Solubility is an important factor for



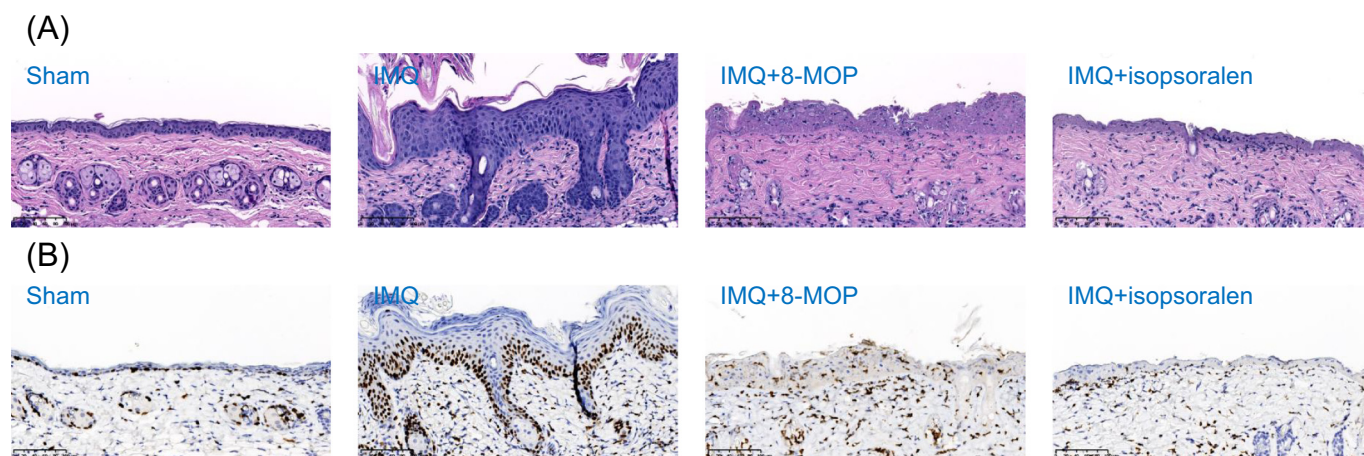


Fig. 6. Skin sections removed from psoriasis-like lesion treated with or without PUVA represented by H&E staining and IHC analysis: (A) H&E histology, and (B) Ki-67 IHC.

skin transport. The penetrants should be in the solubilized form to pass the biomembrane (Liu et al., 2017). The very low solubility of psoralidin and bakuchiol in the vehicle led to the negligible flux. The low bakuchiol solubility was the reason for this meroterpene showing a much higher deposition when applied at the saturated dose but not in the case of equimolar suspension.

Different from experimental log *P* and log *K'*, the total polarity surface is a parameter offering a molecular estimation to picture the level of lipophilicity. This value is measured based on the sum of the surface area involving in nitrogen and oxygen, as well as the hydrogen binding to electronegative atoms (Ertl et al., 2000). It is generally inversely correlated with the penetrant transport across biomembranes such as gastrointestinal membrane and skin (Schaftenaar and de Vlieg, 2012). The greatest polar surface area of psoralidin could prove to have insignificant skin absorption. The large molecular size of psoralidin as approved by MW and molecular volume suggested the difficulty of penetrating into the skin. The other parameters calculated from molecular modeling such as negative CDOCKER energy and hydrogen bond number also confirmed the poor absorption of this coumestrol. Molecular docking was used to predict the possible interaction of the penetrants with the SC lipids. A higher affinity to the lipid bilayers could produce a greater SC uptake for facile skin absorption (Chuang et al., 2017). Psoralidin showed the least interaction force compared to the other compounds according to the negative CDOCKER score.

The hydrogen bond number is a parameter related to skin retention of the penetrants, but less important to exhibiting the relation with flux (Grice and Benson, 2013). Previous reports (Alikhan et al., 2009; Zhang et al., 2009) suggested that the increase in the hydrogen bond acceptor or total hydrogen bond number (acceptor and donor) caused a decrease in SC diffusion. This is because the SC sheet is mainly a hydrogen bond acceptor (N'Da, 2014). Psoralidin was the compound revealing the highest hydrogen bond acceptor and donor numbers in this study. The feature retarded psoralidin permeation into the SC. Contrary to this result, the compound with the lowest hydrogen bond number (bakuchiol) was preferable to retain in the uppermost skin layer and unavailable in the receptor compartment. The penetrants showing a high hydrogen bond number may adsorb the water molecules in the aqueous vehicle to generate a solvation cage. The large solvation complex is harmful if absorbed into the skin (Mohammed et al., 2014). Though the MW of psoralidin fell into a suitable level for percutaneous delivery (< 500 g/mol), the attraction of water molecules to produce a solvation cage may produce a complex of > 500 g/mol. This is unfavorable for skin transport.

The melting point of the penetrants is related to the molecular association with the SC. The decrease of the melting point would enhance the penetrant solubility in the SC and hence promote the SC

partitioning (Bijaya et al., 2010; N'Da, 2014). The high melting point of 318 °C for psoralidin impeded the SC partitioning and the subsequent cutaneous diffusion. Among the furocoumarins tested, psoralen gave the lowest skin absorption, although its structure was similar to isopsoralen. This indicates that the isomers can demonstrate quite different absorption features. Although psoralen had a small molecular size, the higher melting point than 8-MOP and isopsoralen contributed to the difficult penetration into the SC. The lowest log *K'* and highest solubility of psoralen among the furocoumarins indicated the hydrophilic character, which was also detrimental for SC partitioning.

We examined the inhibitory effect of combined *P. corylifolia* compounds and UVA on keratinocyte growth. UVA light is proved to delay the rapid expansion of keratinocytes in psoriatic patients (Farahnik et al., 2016). The UVA wavelength was set at 365 nm, which is the peak UVA emission used in clinical PUVA (Al-Ismael et al., 2016). Our results showed that UVA could assist the apoptosis induced by the compounds. Photochemotherapy elicits both apoptotic and immunomodulatory functions, which are responsible for psoriasis amelioration. 8-MOP can quickly penetrate the keratinocytes and intercalate between nucleic acids (Stern, 2007). Subsequently UVA generates 8-MOP linkage to pyrimidine bases, forming adducts. The adducts inhibit DNA replication and cell proliferation. PUVA also produces reactive oxygen species to evoke apoptosis. All compounds tested in the present study were previously reported to demonstrate significant apoptosis against tumors (Lee et al., 2011; Kim et al., 2016; Zhang et al., 2016). The similar action might occur in the proliferative keratinocytes. It is evidenced that strong apoptosis was attributed to the compounds with furocoumarin structure (psoralens). Psoralidin and bakuchiol only showed a moderate cell growth inhibition. This implies a superior candidate of furocoumarins for PUVA therapy. In contrast to psoralen, 8-MOP and isopsoralen are the preferable candidates for topical photochemotherapy due to the high TI. Moreover, 8-MOP and isopsoralen could be advantageous for topical administration with respect to cutaneous targeting but less transport across skin. Bakuchiol seems to be appropriate for the targeted skin treatment due to its minimum penetration into the receptor. Nevertheless, it only exerted a moderate TI because of the low keratinocyte apoptosis.

Topical imiquimod stimulation of mouse skin would induce the psoriasis-like lesions, which resemble the symptoms of human psoriasis (Lin et al., 2015). We employed this model to test the effect of PUVA on antipsoriatic ability. The dose exposure of UVA was 2.5 J/cm<sup>2</sup> in this study. This energy was similar to the dose suggestion in clinical photochemotherapy (Farahnik et al., 2016). Psoriasis can cause skin barrier disruption and increased TEWL, which is proportional to clinical severity. Our result suggested that 8-MOP or isopsoralen in combination with UVA significantly restored the skin barrier defect induced by

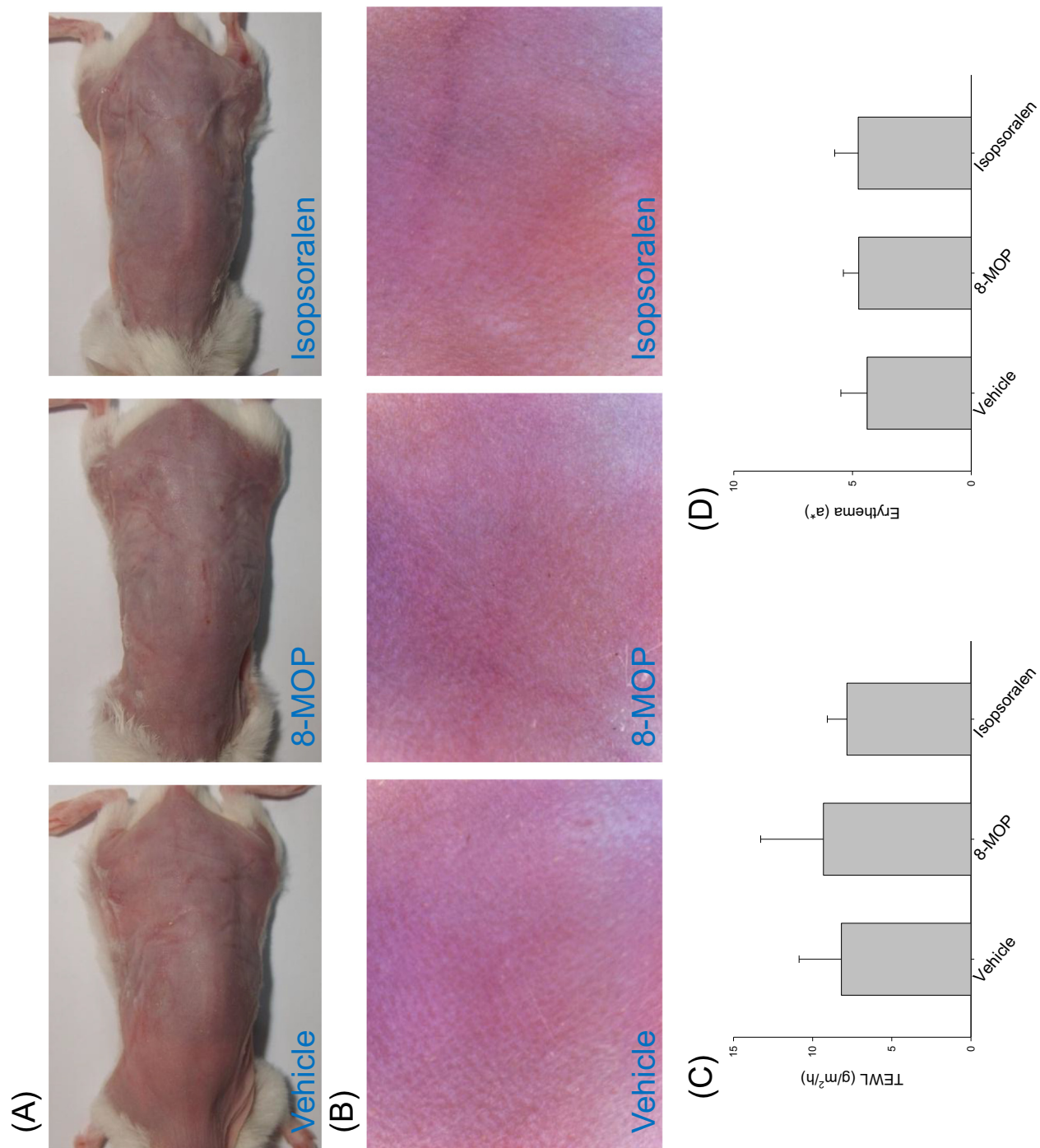


Fig. 7. The in vivo skin tolerance of topically applied 8-MOP and isoprosoralen after a 7-day consecutive application: (A) the gross images of mouse back skin were represented on Day 7 by digital camera, (B) the close-up imaging by handheld digital magnifier, (C) transepidermal water loss (TEWL) measurement, and (D) erythema ( $a^*$ ) measurement. All data are presented as the mean of six experiments  $\pm$  S.D.

imiquimod. Epidermal hyperproliferation is a consequence of barrier deficiency (Wolf et al., 2012). Analysis of sections taken from the mouse skin showed that the proliferation marker Ki-67 was decreased by furocoumarins. The reduced proliferation could result in the decrease of epidermal thickening induced by imiquimod.

The development of psoriasis leads to the keratinocyte proliferation to activate cytokine production (Johnson-Huang et al., 2012). IL-1 $\beta$ , IL-6, and TNF- $\alpha$  have been linked to the psoriatic pathogenesis in the inflammatory regulation. IL-1 $\beta$  and IL-6 are increased in the epidermal layer after barrier disruption. Both cytokines are able to elevate keratinocyte proliferation and epidermal thickening (Hänel et al., 2013). TNF- $\alpha$  produced by the activated keratinocytes is important in psoriatic lesion maintenance through the induction of proliferation and survival (Chen et al., 2017). The results indicated that the expression of IL-1 $\beta$  and IL-6 was markedly inhibited after treatment of combined isopsoralen and UVA as compared to the imiquimod-treated mice. The suppression of IL-1 $\beta$  and IL-6 regulated keratinocyte proliferation and differentiation, attenuating the inflammation in psoriasiform lesions. 8-MOP only inhibited IL-1 $\beta$  upregulation by imiquimod. This compound showed no effect on IL-6 and TNF- $\alpha$  in our case. Besides the cytokines, the profiles of gross appearance and epidermal thickness demonstrated a superior lesion inhibition by isopsoralen compared to 8-MOP. The higher mouse skin deposition and limited diffusion across skin of isopsoralen compared to 8-MOP might improve the efficacy of topical PUVA in imiquimod-induced injury. This corroborates that topical application can deliver isopsoralen to the viable epidermis, which is the targeted site for psoriasis treatment. The psoriasiform skin is more permeable to the penetrants than the normal skin (Gattu and Maibach, 2010; Lin et al., 2015). The decreased skin integrity can increase penetrant delivery across the skin to the circulation.

The in vivo tolerance study verified that 8-MOP and isopsoralen did not damage the skin barrier. Both furocoumarins were proved to be safe and nonirritant for 7-day use. Nevertheless, we could see that PUVA on mouse skin caused excessive apoptosis in the epidermis compared to the sham group. It might be due to an exposure UVA dose of 2.5 J/cm<sup>2</sup> being too high for the mouse, though this exposure and influence is feasible for humans. The common adverse effects of photochemotherapy are erythema, pruritus, dry skin, and hyperpigmentation (Coelho and Apetato, 2016). The protocol of PUVA should be further optimized to accomplish the therapy with a balance between efficiency and safety.

## 5. Conclusions

We investigated the skin permeation and psoriasiform lesion inhibition of the compounds from *P. corylifolia* in combination with phototherapy. The in vitro results suggested that the chemicals with more hydrophilic property (furocoumarins) initially formed a reservoir in the skin, and some molecules in the reservoir diffused out of the skin to the receptor. The more-lipophilic compounds (psoralidin and bakuchiol) were mainly located in the cutaneous reservoir. We could distinguish that the parameters estimated from molecular modeling were useful to establish the SPR of these compounds. The antipsoriatic potency of these chemicals resulted from the suppression of keratinocyte proliferation, with 8-MOP and isopsoralen showing greater inhibition than the others. 8-MOP and isopsoralen could attenuate psoriasis-like lesions via the reduction of epidermal thickening, cytokine release, and barrier defect in the presence of UVA. Both furocoumarins could be considered safe for topical application. This study indicated that isopsoralen can be a potential alternative to 8-MOP due to the satisfied skin accumulation and TI. This compound can proceed to the next stage of clinical testing in order to elucidate possible antipsoriatic therapy.

## Acknowledgements

The authors are grateful for the financial support from Chang Gung Memorial Hospital (CMRPD1F0231-3 and CMRPD1F0331-3).

## Appendix A. Supplementary data

Supplementary data to this article can be found online at <https://doi.org/10.1016/j.ejps.2018.08.031>.

## References

- Alam, F., Khan, G.N., Bin Asad, M.H.H., 2018. *Psoralea corylifolia* L: ethnobotanical, biological, and chemical aspects: a review. *Phytother. Res.* 32, 597–615.
- Alikhan, A., Farahmand, S., Maibach, H.I., 2009. Correlating percutaneous absorption with physicochemical parameters in vivo in man: agricultural, steroid, and other organic compounds. *J. Appl. Toxicol.* 29, 590–596.
- Al-Ismael, D., Edwards, C., Anstey, A.V., 2016. Erythema action spectrum of topical 8-methoxypsoralen-sensitized skin re-evaluated: implications for routine clinical practice. *Br. J. Dermatol.* 174, 131–135.
- Bijaya, G., Kaushal, D., Sonal, D., Pallavi, K., 2010. Synthesis and evaluation of esmolol prodrugs for transdermal delivery. *Drug Deliv.* 17, 532–540.
- Chen, H., Lu, C., Liu, H., Wang, M., Zhao, H., Yan, Y., Han, L., 2017. Quercetin ameliorates imiquimod-induced psoriasis-like skin inflammation in mice via the NF- $\kappa$ B pathway. *Int. Immunopharmacol.* 48, 110–117.
- Chuang, S.Y., Lin, Y.K., Lin, C.F., Wang, P.W., Chen, E.L., Fang, J.Y., 2017. Elucidating the skin delivery of aglycone and glycoside flavonoids: how the structures affect cutaneous absorption. *Nutrients* 9, 1304.
- Coelho, M.M.V., Apetato, M., 2016. The dark side of the light: phototherapy adverse effects. *Clin. Dermatol.* 34, 556–562.
- Der-Petrossian, M., Seeber, A., Höningmann, H., Tanew, A., 2000. Half-side comparison study on the efficacy of 8-methoxypsoralen bath-PUVA versus narrow-band ultra-violet B phototherapy in patients with severe chronic atopic dermatitis. *Br. J. Dermatol.* 142, 39–43.
- Doppalapudi, S., Jain, A., Chopra, D.K., Khan, W., 2017. Psoralen loaded liposomal nanocarriers for improved skin penetration and efficacy of topical PUVA in psoriasis. *Eur. J. Pharm. Sci.* 96, 515–529.
- Ertl, P., Rohde, B., Selzer, P., 2000. Fast calculation of molecular polar surface area as a sum of fragment-based contributions and its application of drug transport properties. *J. Med. Chem.* 43, 3714–3717.
- Fang, Y.P., Yang, S.H., Lee, C.H., Aljuffali, I.A., Kao, H.C., Fang, J.Y., 2016. What is the discrepancy between drug permeation into/across intact and diseased skins? Atopic dermatitis as a model. *Int. J. Pharm.* 497, 277–286.
- Farahnik, B., Nakamura, M., Singh, R.K., Abrouk, M., Zhu, T.H., Lee, K.M., Jose, M.V., Dalovisio, R., Koo, J., Bhutani, T., Liao, W., 2016. The patient's guide to psoriasis treatment. Part 2: PUVA phototherapy. *Dermatol. Ther.* 6, 315–324.
- Gattu, S., Maibach, H.I., 2010. Enhanced absorption through damaged skin: an overview of the in vitro human model. *Skin Pharmacol. Physiol.* 23, 171–176.
- Geinoz, S., Guy, R.H., Testa, B., Carrupt, P.A., 2004. Quantitative structure-permeation relationships (QSPeRs) to predict skin permeation: a critical evaluation. *Pharm. Res.* 21, 83–92.
- Grice, J., Benson, H.A.E., 2013. Analysing the skin barrier from down under. *Skin Pharmacol. Physiol.* 26, 254–262.
- Griffiths, C.E.M., van de Kerkhof, P., Czarnecka-Operacz, M., 2017. Psoriasis and atopic dermatitis. *Dermatol. Ther.* 7 (Suppl. 1), S31–S41.
- Guo, J., Weng, X., Wu, H., Li, Q., Bi, K., 2005. Antioxidants from a Chinese medicinal herb – *Psoralea corylifolia* L. *Food Chem.* 91, 287–292.
- Hänel, K.H., Cornelissen, C., Lüscher, B., Baron, J.M., 2013. Cytokines and the skin barrier. *Int. J. Mol. Sci.* 14, 6720–6745.
- Hussain, I., Hussain, N., Manan, A., Rashid, A., Khan, B., Bakhsh, S., 2016. Fabrication of anti-vitiligo ointment containing *Psoralea corylifolia*: in vitro and in vivo characterization. *Drug Des. Devel. Ther.* 10, 3805–3816.
- Johnson-Huang, L.M., Lowes, M.A., Krueger, J.G., 2012. Putting together the psoriasis puzzle: an update on developing targeted therapies. *Dis. Model. Mech.* 5, 423–433.
- Kim, J.E., Kim, J.H., Lee, Y., Yang, H., Heo, Y.S., Bode, A.M., Lee, K.W., Dong, Z., 2016. Bakuchiol suppresses proliferation of skin cancer cells by directly targeting Hck, Btk, and p38 MAP kinase. *Oncotarget* 7, 14616–14627.
- Lee, S.J., Nam, K.W., Mar, W., 2011. Effects of psoralen from *Psoralea corylifolia* on quinone reductase, ornithine decarboxylase, and JB6 cells transformation promotion. *Arch. Pharm. Res.* 34, 31–36.
- Lin, Y.K., Yang, S.H., Chen, C.C., Kao, H.C., Fang, J.Y., 2015. Using imiquimod-induced psoriasis-like skin as a model to measure the skin penetration of anti-psoriatic drugs. *PLoS One* 10, e0137890.
- Liu, X., Testa, B., Fahr, A., 2011. Lipophilicity and its relationship with passive drug permeation. *Pharm. Res.* 28, 962–977.
- Liu, K.S., Huang, T.H., Aljuffali, I.A., Chen, E.L., Wang, J.J., Fang, J.Y., 2017. Exploring the structure-permeation relationship of topical tricyclic antidepressants used for skin analgesia. *Int. J. Pharm.* 523, 386–397.
- Mohammed, D., Matts, P.J., Hadgraft, J., Lane, M.E., 2014. In vitro-in vivo correlation in skin permeation. *Pharm. Res.* 31, 394–400.
- N'Da, D.D., 2014. Prodrug strategies for enhancing the percutaneous absorption of drugs. *Molecules* 19, 20780–20787.



- Pahari, P., Rohr, J., 2009. Total synthesis of psoralidin, an anticancer natural product. *J. Org. Chem.* 74, 2750–2762.
- Raychaudhuri, S.K., Maverakis, E., Raychaudhuri, S.P., 2014. Diagnosis and classification of psoriasis. *Autoimmun. Rev.* 13, 490–495.
- Riviere, J.E., Brooks, J.D., 2011. Predicting skin permeability from complex chemical mixtures: dependency of quantitative structure permeation relationships on biology of skin model used. *Toxicol. Sci.* 119, 224–232.
- Rønholt, K., Iversen, L., 2017. Old and new biological therapies for psoriasis. *Int. J. Mol. Sci.* 18, 2297.
- Schaftenaar, G., de Vlieg, J., 2012. Quantum mechanical polar surface area. *J. Comput. Aided Mol. Des.* 26, 311–318.
- Singh, T.P., Schön, M.P., Wallbrecht, K., Michaelis, K., Rinner, B., Mayer, G., Schmidbauer, U., Strohmaier, H., Wang, X.J., Wolf, P., 2010. 8-Methoxypsoralen plus ultraviolet A therapy acts via inhibition of the IL-23/Th17 axis and induction of Foxp3<sup>+</sup> regulatory T cells involving CTLA4 signaling in a psoriasis-like skin disorder. *J. Immunol.* 184, 7257–7267.
- Song, K., An, S.M., Kim, M., Koh, J.S., Boo, Y.C., 2011. Comparison of the anti-melanogenic effects of *p*-coumaric acid and its methyl ester and their permeabilities. *J. Dermatol. Sci.* 63, 17–22.
- Stern, R.S., 2007. Psoralen and ultraviolet A light therapy for psoriasis. *N. Engl. J. Med.* 357, 682–690.
- Thors, L., Koch, B., Koch, M., Häggglund, L., Bucht, A., 2016. In vitro human skin penetration model for organophosphorus compounds with different physicochemical properties. *Toxicol. in Vitro* 32, 198–204.
- van der Fits, L., Mourits, S., Voerman, J.S.A., Kant, M., Boon, L., Laman, J.D., Cornelissen, F., Mus, A.M., Florencia, E., Prens, E.P., Lubberts, E., 2009. Imiquimod-induced psoriasis-like skin inflammation in mice is mediated via the IL-23/IL-17 axis. *J. Immunol.* 182, 5836–5845.
- Wolf, R., Orion, E., Ruocco, E., Ruocco, V., 2012. Abnormal epidermal barrier in the pathogenesis of psoriasis. *Clin. Dermatol.* 30, 323–328.
- Wu, N.L., Chiang, Y.C., Huang, C.C., Fang, J.Y., Chen, D.F., Hung, C.F., 2010. Zeaxanthin inhibits PDGF-BB-induced migration in human dermal fibroblasts. *Exp. Dermatol.* 19, 173–181.
- Wu, C.Z., Liu, D.C., Guo, X., Dai, Y., Ma, T., Li, H.M., Huo, Q., 2018. Synthesis and evaluation of bakuchiol derivatives as potential anticancer agents. *Molecules* 23, 515.
- Zhang, Q., Grice, J.E., Li, P., Jepps, O.G., Wang, G.J., Roberts, M.S., 2009. Skin solubility determines maximum transepidermal flux for similar size molecules. *Pharm. Res.* 26, 1974–1985.
- Zhang, X., Zhao, W., Wang, Y., Lu, J., Chen, X., 2016. The chemical constituents and bioactivities of *Psoralea corylifolia* Linn.: a review. *Am. J. Chin. Med.* 44, 35–60.





Contents lists available at ScienceDirect

Journal of Dermatological Science

journal homepage: [www.jdsjournal.com](http://www.jdsjournal.com)



## The atopic dermatitis-like lesion and the associated MRSA infection and barrier dysfunction can be alleviated by 2,4-dimethoxy-6-methylbenzene-1,3-diol from *Antrodia camphorata*

Shih-Chun Yang<sup>a</sup>, Tse-Hung Huang<sup>b,c,d</sup>, Chun-Hui Chiu<sup>e,f</sup>, Wei-Ling Chou<sup>b</sup>,  
Ahmed Alalaiwe<sup>g</sup>, Yuan-Chieh Yeh<sup>b,h</sup>, Kuan-Wen Su<sup>i,j</sup>, Jia-You Fang<sup>f,k,l,m,\*</sup>

<sup>a</sup> Department of Cosmetic Science, Providence University, Taichung, Taiwan

<sup>b</sup> Department of Traditional Chinese Medicine, Chang Gung Memorial Hospital, Keelung, Taiwan

<sup>c</sup> School of Traditional Chinese Medicine, Chang Gung University, Kweishan, Taoyuan, Taiwan

<sup>d</sup> School of Nursing, National Taipei University of Nursing and Health Sciences, Taipei, Taiwan

<sup>e</sup> Graduate Institute of Health Industry Technology, Chang Gung University of Science and Technology, Kweishan, Taoyuan, Taiwan

<sup>f</sup> Research Center for Food and Cosmetic Safety and Research Center for Chinese Herbal Medicine, Chang Gung University of Science and Technology, Kweishan, Taoyuan, Taiwan

<sup>g</sup> Department of Pharmaceutics, College of Pharmacy, Prince Sattam Bin Abdulaziz University, Al Kharj, Saudi Arabia

<sup>h</sup> Program in Molecular Medicine, School of Life Sciences, National Yang Ming University, Taipei, Taiwan

<sup>i</sup> Graduate Institute of Clinical Medical Science, Chang Gung University, Kweishan, Taoyuan, Taiwan

<sup>j</sup> Department of Pediatrics, Chang Gung Memorial Hospital, Keelung, Taiwan

<sup>k</sup> Pharmaceutics Laboratory, Graduate Institute of Natural Products, Chang Gung University, Kweishan, Taoyuan, Taiwan

<sup>l</sup> Chinese Herbal Medicine Research Team, Healthy Aging Research Center, Chang Gung University, Kweishan, Taoyuan, Taiwan

<sup>m</sup> Department of Anesthesiology, Chang Gung Memorial Hospital, Kweishan, Taoyuan, Taiwan

### ARTICLE INFO

#### Article history:

Received 24 May 2018

Received in revised form 21 August 2018

Accepted 4 September 2018

#### Keywords:

2,4-dimethoxy-6-methylbenzene-1,3-diol

*Antrodia camphorata*

Atopic dermatitis

Barrier function

Bacterial infection

### ABSTRACT

**Background:** Atopic dermatitis (AD) is an inflammatory skin disease with an associated barrier dysfunction and *Staphylococcus aureus* infection. The mainstay steroid and calcineurin inhibitor therapy shows some adverse effects. 2,4-Dimethoxy-6-methylbenzene-1,3-diol (DMD) is a benzenoid isolated from *Antrodia camphorata*.

**Objective:** We investigated the inhibitory effect of DMD on methicillin-resistant *S. aureus* (MRSA), the chemokine production in stimulated keratinocytes, and the AD-like lesion found in ovalbumin (OVA)-sensitized mice.

**Methods:** The antimicrobial effect and cutaneous barrier function were evaluated using an in vitro culture model and an in vivo mouse model of AD-like skin.

**Results:** DMD exhibited a comparative minimum inhibitory concentration (MIC) and minimum bactericidal concentration (MBC) against MRSA with nalidixic acid, a conventional antibiotic. The MIC and MBC for DMD was 78.1 and 156.3 µg/ml, respectively. DMD also showed the ability to eliminate the clinical bacteria isolates with resistance to methicillin and vancomycin. The DNA polymerase and gyrase inhibition evoked by DMD for bacterial lethality was proposed. In the activated keratinocytes, DMD stopped the upregulation of chemokines (CCL5 and CCL17) and increased the expression of differentiation proteins (filaggrin, involucrin, and integrin β-1). Topical application of DMD readily penetrated into the skin, with AD-like skin displaying 2.5-fold greater permeation than healthy skin. The in vivo assessment using the mouse model with OVA sensitization and MRSA inoculation revealed a reduction of transepidermal water loss (TEWL) and bacterial burden by DMD by about 2- and 100-fold, respectively. Differentiation proteins were also restored after topical DMD delivery.

**Conclusion:** Our data demonstrated an advanced concept of AD treatment by combined barrier repair and bacterial eradication with a sole agent for ameliorating the overall complications.

© 2018 Japanese Society for Investigative Dermatology. Published by Elsevier B.V. All rights reserved.

\* Corresponding author at: Pharmaceutics Laboratory, Graduate Institute of Natural Products, Chang Gung University, 259 Wen-Hwa 1st Road, Kweishan, Taoyuan 333, Taiwan.

E-mail address: [fajy@mail.cgu.edu.tw](mailto:fajy@mail.cgu.edu.tw) (J.-Y. Fang).

## 1. Introduction

Atopic dermatitis (AD) is an inflammatory disease characterized by erythema, edema, vesicles, and lichenification. The prevalence of AD has increased 3-fold over the past 30 years [1]. Two features associated with AD are the compromised skin barrier and increased risk of cutaneous infection. The reduced barrier function leads to *Staphylococcus aureus* invasion and the eczema's exacerbation [2]. More than 90% of AD patients are colonized with *S. aureus* [3]. The occurrence of methicillin-resistant *S. aureus* (MRSA) has emerged as a predominant threat for AD treatment. Efficient AD management requires multiple drug treatments. The anti-AD drugs such as coal tar, doxepin, calcineurin inhibitors, and steroids are reported to cause skin itching and stinging [4]. Several investigations assessing anti-AD therapy based on natural sources reveal a potential activity [5]. *Antrodia camphorata* is a fungal parasite on the inner cavity of *Cinnamomum kaehirae* Hayata. It has long served as the traditional medicine for the treatment of skin itching, abdominal pain, hypertension, influenza, and cancers [6]. *A. camphorata* also displays a potential for inhibiting and eradicating the pathogenic bacteria [7,8].

The present study attempted to purify the chemicals from this mycelium to evaluate the anti-AD potency. MRSA was used as the model pathogen to examine the antibacterial activity of the crude extract and compounds. We found that 2,4-dimethoxy-6-methylbenzene-1,3-diol (DMD) was superior in showing the anti-MRSA effect compared to the other compounds. We detected the chemokines in the stimulated keratinocytes by DMD treatment. To assess the in vivo efficiency of DMD, the MRSA burden, transepidermal water loss (TEWL), and differentiation proteins were estimated using a mouse model of AD plus bacterial implantation.

## 2. Materials and methods

### 2.1. Extraction and isolation of *A. camphorata*

The agar-cultured mycelium of *A. camphorata* (500 g) was used to prepare the extract in 95% ethanol (1.5:1) for 3 days at room temperature. The extract supernatant (AC) was further partitioned with ethyl acetate as the fractions. The fractions were separated by silica gel column chromatography using the gradient mixtures (400 ml) of *n*-hexane:acetone (9:1, 7:1, 5:1, 3:1, 1:1, total acetone, and total methanol) as eluents to obtain seven fractions.

### 2.2. Liquid chromatography-mass spectrometry (LC–MS) analysis

The system included a Dionex UltiMate 3000 equipped with a pump, column compartment, autosampler, and a Thermo Finnigan LXQ linear ion trap mass spectrometer operated in positive electrospray ion mode. The Acquity UPLC BEH Shield RP18 column was employed and maintained at 35 °C with a flow rate of 0.3 ml/min. The mobile phase consisted of water and methanol, both containing 0.1% formic acid. The data analysis was performed using Xcalibur 2.0.7 software.

### 2.3. Bacterial strains

MRSA (ATCC 33591) and vanomycin-intermediate *S. aureus* (VISA, ATCC 700699) were obtained from American Type Culture Collection. Ten drug-resistant clinical isolates were used, five of which were MRSA (KM-1 to KM-5). The others were VISA (KV-1 to KV-5).

### 2.4. Disk diffusion test

Disk diffusion test was performed according to EUCAST instruction (<http://www.eucast.org>) with Müller-Hinton agar

plate, a MRSA or VISA suspension in TSB solution at a density equivalent to a 0.5 McFarland barium standard ( $1-2 \times 10^8$  CFU/ml) as detected by a McFarland densitometer, and the disk loaded with the compounds or crude extract (500 µg). After incubation for 20 h, the inhibition zone diameter was measured.

### 2.5. Minimum inhibitory concentration (MIC) and minimum bactericidal concentration (MBC)

A broth twofold serial dilution method was utilized to measure the MIC [9]. The bacterial population was exposed to several dilutions of the compounds ranging from 1.22 to 2500 µg/ml with TSB and incubated at 37 °C for 20 h. For the MBC assay, the bacterial suspension was diluted in PBS and plated on TSB plates. MBC was defined as the lowest concentration that killed  $\geq 99.9\%$  of bacteria.

### 2.6. The bacterial morphology

The morphology of MRSA after DMD treatment was observed by Jeol JEM-1200 EX transmission electron microscopy (TEM) based on previous study [9].

### 2.7. Biofilm determined by confocal microscopy

The biofilm was treated by DMD, ciprofloxacin, or CPC at a concentration of 500 µg/ml for 24 h. The three-dimensional structure and thickness of biofilm were detected by Leica TSC SP2 confocal microscopy [10].

### 2.8. Intracellular MRSA killing

The HaCaT keratinocytes and macrophages differentiated from THP-1 monocytes by phorbol myristate acetate (0.1 µM) were used as the host cells to determine the DMD activity toward intracellular MRSA. The detailed information was shown in the previous report [11].

### 2.9. Genomic DNA preparation and agarose gel analysis of MRSA

The detailed procedure is shown in Supplementary Materials.

### 2.10. Anti-Taq DNA polymerase activity

The detailed procedure is shown in Supplementary Materials.

### 2.11. DNA binding ability of Taq DNA polymerase

The detailed procedure is shown in Supplementary Materials.

### 2.12. Wrapping assay

The detailed procedure is shown in Supplementary Materials.

### 2.13. Keratinocyte viability

To estimate the effect of DMD on HaCaT cells, the cell viability was examined using the tetrazolium assay. The detailed process of this assay was described previously [12].

### 2.14. Determination of chemokines in keratinocytes

HaCaT cells ( $1 \times 10^5$  cells/well) were trypsinized into 24-well plates. After incubation in DMEM without FBS for 24 h, tumor necrosis factor (TNF)-α and interferon (IFN)-γ (20 ng/ml of each) were added with or without AC or DMD for 24 h. The supernatant was harvested after 24 h and subjected to ELISA with a murine

monoclonal antibody against human chemokines CC motif ligand 5 and 17 (CCL5 and CCL17). ELISA was performed according to the manufacturer's directions.

### 2.15. *In vitro* cutaneous absorption test

The *in vitro* cutaneous absorption of DMD was conducted using Franz diffusion cell. DMD penetration into the receptor was quantified by HPLC. The other procedures were the same as in the previous research [13].

### 2.16. Ovalbumin (OVA)-induced AD-like mouse and MRSA infection

The AD-like skin was induced by a method modified from the previous study [14]. On Day 14 of OVA treatment, 100  $\mu$ l MRSA with an OD<sub>600</sub> of 1 was pipetted onto the gauze, which was administered to the dorsal skin. On Day 15 and 16, 10 mg/ml DMD was spread onto the 1  $\times$  1 cm gauze. At the end of the experiment, the skin was excised to count MRSA CFU and analyze the differentiation protein gene expression by real-time PCR. Total RNA was extracted with ZYMO Direct-zol<sup>®</sup> reagent. The cDNA was synthesized by reverse transcription by using an iScript<sup>®</sup> cDNA synthesis kit. The real-time PCR was performed using iQ SYBR Green Supermix according to the manufacturer's instructions. The primers used to analyze mRNA were the same as in the previous report [15].

### 2.17. *In vivo* cutaneous tolerance

The 10% methanol/PBS containing 1 mg/ml DMD was applied daily (0.2 ml) on the dorsal area of the healthy mouse for 5 consecutive days. The DMD vehicle was replaced with a new one every day. After the vehicle removal, the treated skin region was assessed by TEWL and surface pH using Cutometer<sup>®</sup> MPA 580.

### 2.18. Statistical analysis

The statistical analysis was carried out using GraphPad Prism 5 software. Dual comparisons were made with unpaired Student's *t*-test. Groups of three or more were analyzed by analysis of variance (ANOVA) with Tukey or Dunnett posttests. The significance was indicated as \* for *p* < 0.05, \*\* for *p* < 0.01, and \*\*\* for *p* < 0.001 in the figures.

## 3. Results

### 3.1. LC–MS determination of *A. camphorata* extract

An LC profile of the ethanolic extract exhibits many peaks as shown in Fig. 1A. Investigation using chromatography led to the identification of five compounds. Fig. 1B illustrates the structures of these compounds. Suppl. Table 1 summarizes the MS analysis of the compounds derived from ethanolic extract. The five

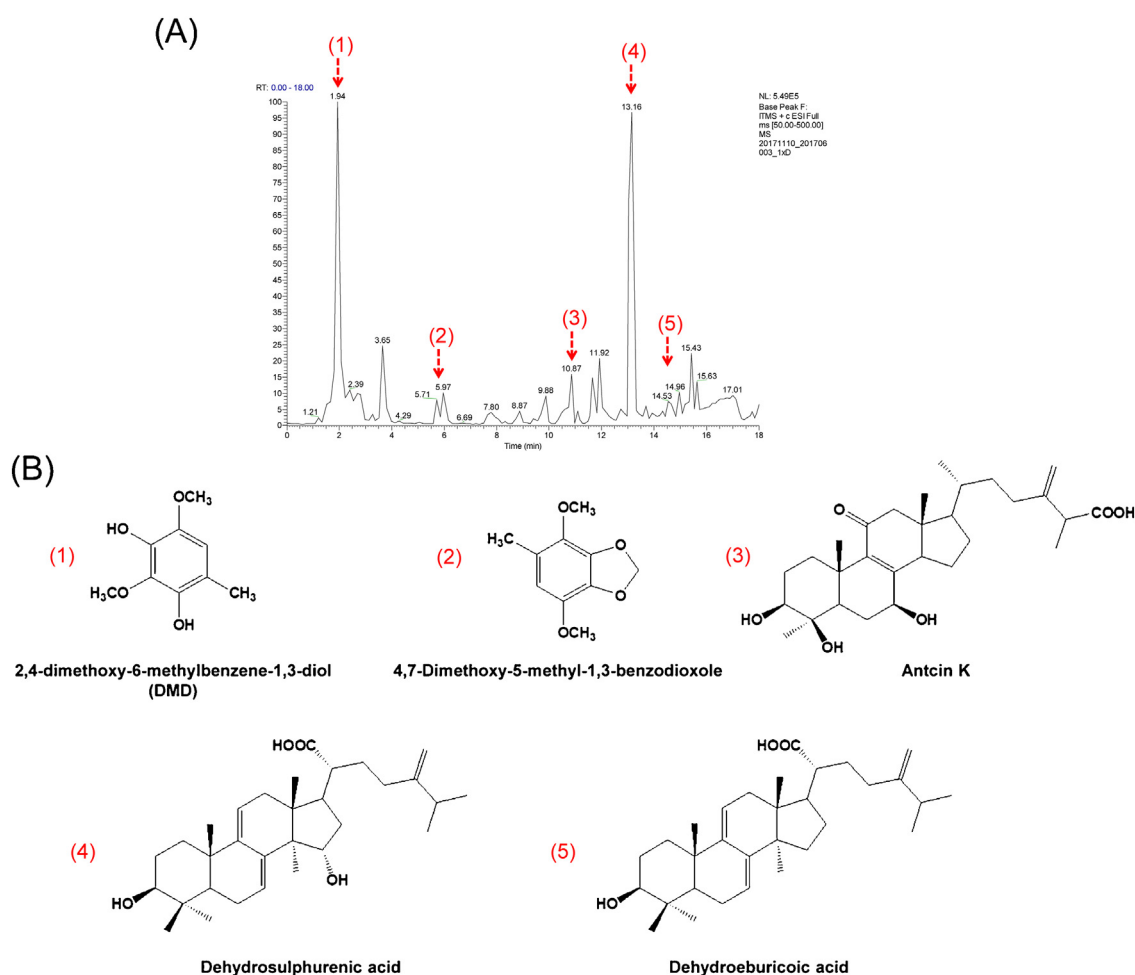


**Fig. 1.** Structural characterization of *A. camphorata*. (A) LC–MS chromatograms of *A. camphorata* extract. (B) Index compounds of *A. camphorata* mycelium.

compounds were previously found in *A. camphorata* based on the references [16,17].

### 3.2. DMD inhibits MRSA growth

The ethanolic extract was further separated by column chromatography with different eluents to yield 7 fractions as shown in Suppl. Table 2. The agar diffusion inhibition zone demonstrated the susceptibility of MRSA to the eluents of *n*-hexane:acetone 7:1, 3:1, and 1:1. DMD, antcin B, and 4-hydroxy-benzaldehyde were isolated from these three fractions, respectively. To examine the effect of these compounds on MRSA eradication, the MIC and MBC were measured as compared to the ethanolic extract (AC) as depicted in Suppl. Table 3. DMD demonstrated the strongest MRSA and VISA growth inhibition. The inhibition capability of DMD was comparable to nalidixic acid, a positive control. Nalidixic acid was used because of the similarity of physicochemical properties with DMD. Another positive control was vancomycin, which is the antibiotic used for eliminating MRSA infection in clinics. As expected, vancomycin revealed very low MIC and MBC values to MRSA with efficient growth inhibition. A panel

of drug-resistant clinical isolates was employed to test the MIC and MBC of DMD (Suppl. Table 4). The results showed that DMD was able to inhibit the growth of these isolates to a determined amount.

The MRSA and VISA inhibition was recognized by the agar diffusion assay (Fig. 2A). The trend of inhibition zone for inhibiting MRSA and VISA is DMD > antcin B > 4-hydroxy-benzaldehyde. Flow cytometry was used to determine the MRSA death rate. DMD shows a dose-dependent fashion for MRSA killing (Suppl. Fig. 1). Fig. 2B presents the TEM imaging of MRSA appearance. The intact bacteria exhibited a smooth morphology on the surface. DMD produced no influence on the MRSA shape. As a positive control, CPC disrupted bacterial surface and released cytoplasm. Fig. 2C presents the effect of DMD and CPC on the suppression of MRSA in the biofilm form. DMD significantly reduced CFU inside and outside the biofilm by about  $10^3$ -fold.

Fig. 2D shows the anti-biofilm activity of DMD, ciprofloxacin, and CPC against MRSA under confocal microscopy. The green signal was faded after treatment of the antibacterial agents, with CPC showing the weakest intensity. CPC is proved to be a strong biofilm inhibitor via the mechanism of disrupting bacterial membrane [18]. DMD, ciprofloxacin, and CPC restricted the biofilm thickness

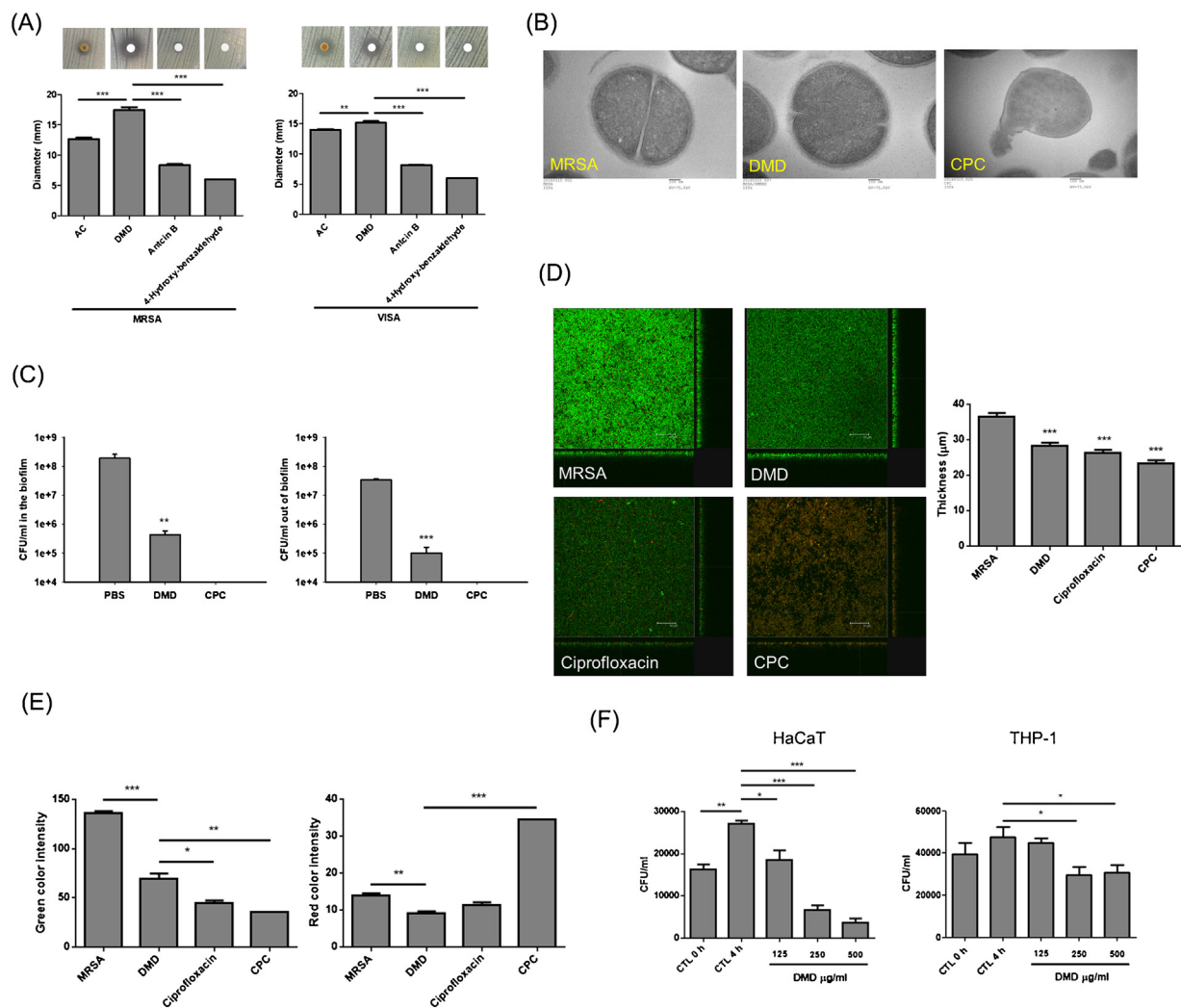


**Fig. 2.** Determination of the antibacterial activity of *A. camphorata* extracted compound DMD. (A) Zone of inhibition of MRSA and VISA measured from EUCAST guideline. (B) Morphological changes of MRSA viewed under TEM. (C) Measurement of MRSA counts for planktonic and biofilm. (D) The three-dimensional images and corresponding biofilm thickness analyzed by CLSM. (E) Quantification of fluorescence intensity of MRSA biofilm. (F) Intracellular MRSA killing in HaCaT keratinocytes and macrophages (THP-1). Each value represents the mean  $\pm$  SEM ( $n=3$ ). \*\*\*  $p < 0.001$ ; \*\*  $p < 0.01$ ; \*  $p < 0.05$ . The statistical methods used for comparing the data of different groups are unpaired *t*-test and ANOVA.



from 36.4 to 28.4, 26.4, and 23.2  $\mu\text{m}$ , respectively. The quantification of biofilm fluorescence intensity shows that CPC markedly reduced the green signal (Fig. 2E). The green fluorescence was significantly decreased by DMD and ciprofloxacin. The MRSA burden in the mammalian cells increased after a 4-h incubation (Fig. 2F). Treatment with DMD dose-dependently reduced the MRSA production. DMD at a dose of 500  $\mu\text{g}/\text{ml}$  could reduce MRSA CFU in keratinocytes by 7.5-fold as compared to the control (4 h).

### 3.3. Antibacterial mechanism of DMD

We explored the antibacterial mechanism of DMD by genomic DNA detection (Fig. 3A). DMD and ciprofloxacin revealed a similar pattern diminishing DNA concentration. Taq DNA polymerase is important to replicating DNA in MRSA. We further examined the ability of DMD to inhibit DNA polymerase (left panel of Fig. 3B). The PCR products were reduced by DMD in a dose-dependent manner,

confirming the role of DMD as a DNA polymerase inhibitor. Mitomycin C is an antitumor drug with a capability to elicit DNA damage via an interstrand DNA crosslink. This drug may not affect the activity of DNA polymerase. The right panel of Fig. 3B demonstrates a significant presence of PCR products after mitomycin C treatment.

As shown in Fig. 3C, DMD at different concentrations can decrease the polymerase-DNA complex (red arrows) in the ssDNA type but not in dsDNA. We further tested the effect of DMD on the inhibition of the supercoiling activity of DNA gyrase and the relaxing activity of DNA topoisomerase I. The assay demonstrates that DMD exhibited a capacity to deactivate gyrase (left panel of Fig. 3D). However, this effect was not observed in the case of topoisomerase I. Based on the aforementioned experiments, we suggest that during the process of DNA replication, DMD may inhibit the activity of DNA polymerase and gyrase. Fig. 3E illustrates the possible action mechanisms for DMD.

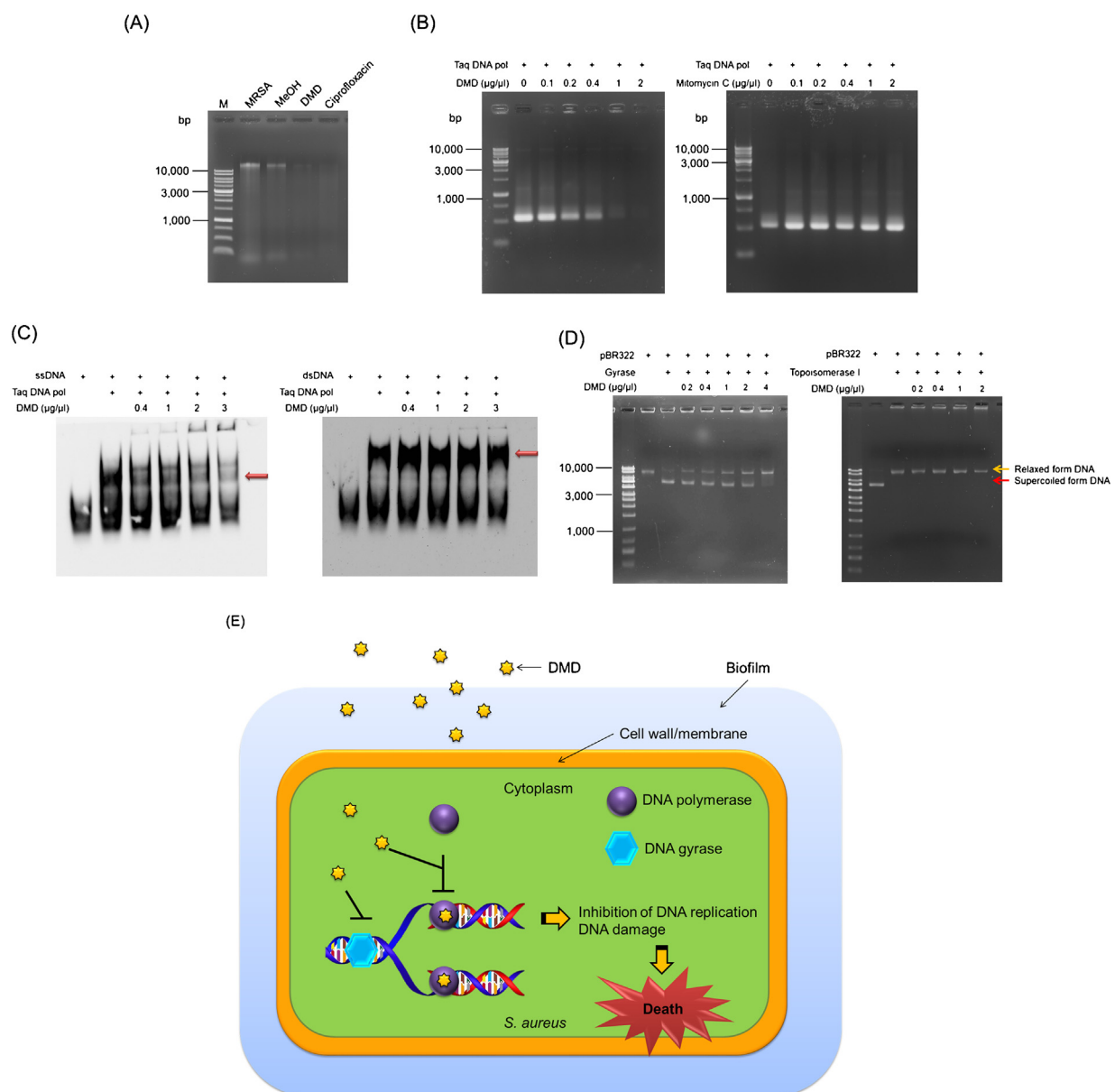


**Fig. 3.** Antibacterial mechanisms of DMD. (A) Analysis the quality of MRSA genomic DNA after treated with DMD by 0.8% agarose gel electrophoresis. (B) Effects of DMD and mitomycin C on Taq DNA polymerases in PCR. (C) A mobility shift assay for Taq DNA polymerase with ssDNA and dsDNA. (D) Effect of DMD on *E. coli* gyrase and topoisomerase I in wrapping assay. (E) Illustration for antibacterial mechanism of DMD on reduced biofilm production, inhibited DNA polymerase and gyrase activity.

### 3.4. DMD reduced chemokines in activated keratinocytes

As shown in Fig. 4A, the DMD concentrations of 10 and 50  $\mu\text{g/ml}$  indicate no cytotoxicity. The higher doses of  $>100 \mu\text{g/ml}$  further decreased the keratinocyte viability. We next assessed the effect of AC and DMD on the levels of CCL5 and CCL17. The expressions of CCL5 and CCL17 were elevated 4.2- and 30.1-fold with treatment of TNF- $\alpha$ /IFN- $\gamma$  (Fig. 4B and C). The TNF- $\alpha$ /IFN- $\gamma$ -induced chemokine increase was significantly inhibited by AC and DMD. DMD at the lower concentration (10  $\mu\text{g/ml}$ ) was sufficient to return CCL17 expression to the control baseline.

### 3.5. DMD ameliorates AD-like lesion

In vitro DMD permeation across pig, BALB/c mouse, and AD-like skins was investigated using Franz cell as depicted in Fig. 5A. DMD penetration across mouse skin was greater as compared to that across pig skin because of the thinner and more-permeable features of rodent skin compared to pig skin. We also compared the cutaneous DMD delivery in intact and AD-like skin after a 12-h application. OVA sensitization significantly increased DMD absorption by 2.5-fold compared to healthy skin. An AD-like skin lesion with MRSA infection developed in the mouse. The application of MRSA or OVA on the back skin displayed the symptoms of erythema, edema, scaling, and epidermal excoriation according to the gross and microscopic appearances of the skin surface (Fig. 5B and C). The severity of these lesions was worsened by the combined OVA and MRSA. The signs of AD-like lesion in the DMD-treated groups were significantly lessened compared with MRSA alone or OVA plus MRSA.

In Fig. 5D, we see that MRSA application induced a 1000-fold increase of bacterial CFU in the skin. DMD treatment could decrease the MRSA burden by 10-fold. The combined OVA and MRSA further drove the increase of MRSA inoculation. The antibacterial activity of DMD significantly mitigated the progression of MRSA by about 100-fold. TEWL was measured to evaluate the skin barrier function as shown in Fig. 5E. The water evaporation was increased to 3-fold by combined OVA and MRSA compared to normal skin. The topical administration of DMD significantly reduced TEWL to 8.0 g/cm<sup>2</sup>/h, approximating the baseline. As illustrated in Fig. 5F, the mRNA level was downregulated by

combined OVA and MRSA. The AD-like skin with MRSA exposure even exhibited a minimized or negligible gene expression of the proteins. DMD markedly enhanced the mRNA of the proteins tested.

### 3.6. DMD elicits no irritation on intact skin

The repeated treatment of DMD for 5 days generally showed no change in the appearance visualized by a digital camera and handheld microscope (Fig. 6A and B). TEWL was significantly increased after a 4-day treatment of PBS and vehicle (Fig. 6C). This could be due to the methanol and water excessively hydrating the SC and disturbing the barrier property. DMD could reverse the increased TEWL produced by the vehicle effect. This may imply a protective capability of DMD on barrier function. No skin pH change was detected by vehicle and DMD treatments (Fig. 6D).

## 4. Discussion

AD produces lesions with low antimicrobial peptides [19], leading to the increased bacterial colonization and the following inflammation and barrier disruption exacerbation. Our results demonstrated that DMD had the anti-MRSA activity as evaluated in the forms of planktonic bacteria, biofilm mass, and intracellular infection. According to the TEM imaging and biofilm visualization, the anti-MRSA activity of DMD was not mediated by membrane disturbance. The results of biofilm imaging and genomic DNA assay inferred that DMD might represent a mechanism which traps DNA gyrase and topoisomerase and disarranges DNA replication. We found that DMD could interfere with ssDNA binding capacity to create an unstable polymerase-DNA complex. The DNA replication efficiency was thus lessened. DNA gyrase appears to be an ideal target for bacterial killing [20]. We provided evidence of the gyrase sensitivity toward the inhibition by DMD.

Our skin absorption data showed that topically applied DMD could penetrate the skin, assuring the subsequent anti-AD activity. The cutaneous absorption can be facilitated by the more lipophilic penetrants [21]. DMD revealed a lipophilic characteristic according to a partition coefficient log *P* of 1.8. Another possibility elucidating the absorption of DMD was the low molecular weight (184 g/mol) for preferentially penetrating into the SC. Inflammatory skin

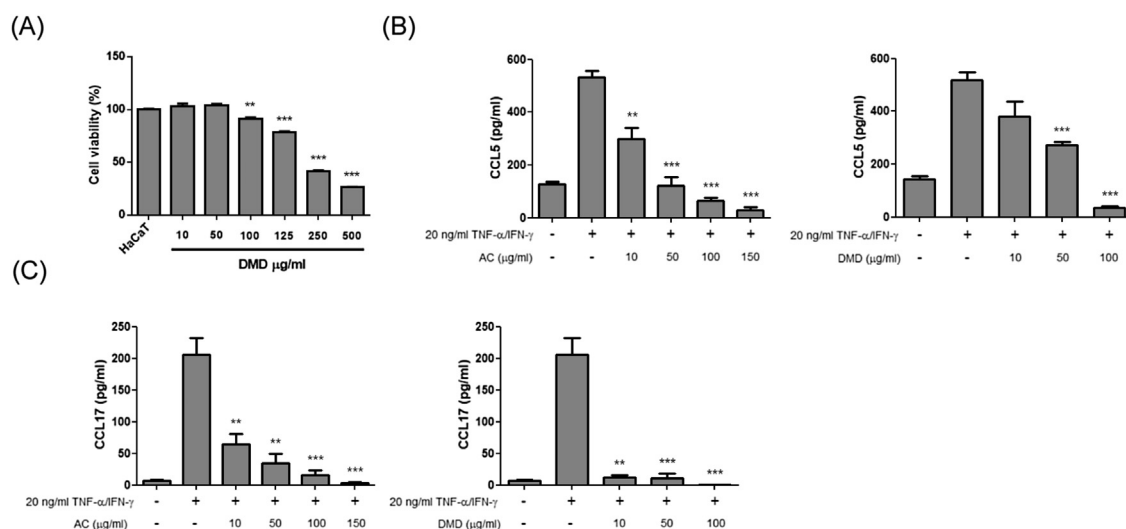


**Fig. 4.** The effects of crude extract (AC) and DMD on HaCaT keratinocytes. (A) Cell viability of DMD-treated HaCaT cells with respect to untreated control. (B), (C) AC and DMD reduced AD inflammation chemokines marker CCL5 and CCL17. Each value represents the mean  $\pm$  SEM ( $n = 6$ ). \*\*\*  $p < 0.001$ ; \*\*  $p < 0.01$ ; \*  $p < 0.05$ . The statistical methods used for comparing the data of different groups are unpaired *t*-test and ANOVA.

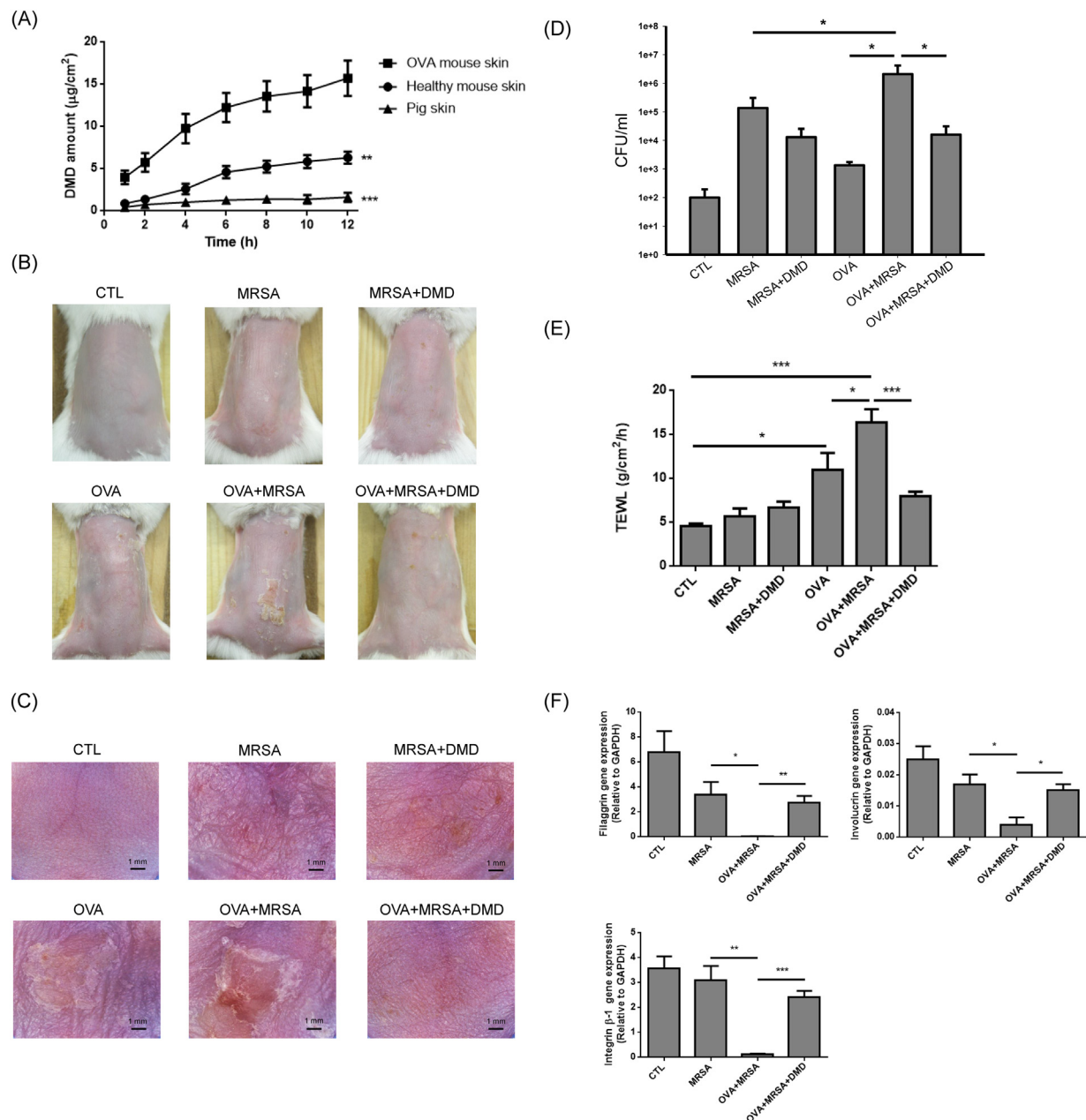


**Fig. 5.** In vitro absorption-time profiles of DMD and in vivo topical application of DMD against MRSA infection AD-like mouse. (A) In vitro permeation profile of DMD in Franz Cell using OVA mouse, healthy mouse, and pig skins. (B) The skin surface of mouse after treatment of OVA induction or MRSA infection with and without DMD condition at day 17. (C) The magnified images of panel (B). The scale bar is 1 mm. (D) Survival of MRSA in mouse skin treated with DMD. Seventeen days after OVA induction and MRSA infection, skin were cut, homogenized, and bacterial count was determined by CFU assay. (E) Transepidermal water loss (TEWL) of mice skin treated with DMD. (F) qPCR analysis of mouse skin RNA for differentiation markers filaggrin, involucrin and integrin β-1. Each value represents the mean ± SEM (n = 6). \*\*\* p < 0.001; \*\* p < 0.01; \* p < 0.05. The statistical methods used for comparing the data of different groups are unpaired t-test and ANOVA.

diseases are always associated with impaired SC integrity and tight junction (TJ) function for the greater drug transport compared to intact skin [22]. Our results confirmed a superior DMD penetration across the lesional skin as compared to healthy skin. The limitation of the present work was the use of murine model but not human skin as the permeation barrier. It is known that human skin exhibits stronger barrier characteristic than murine skin. Whether the topical DMD application is advantageous for skin penetration and AD therapy in humans remains to be elucidated.

*S. aureus* infiltrates into the skin to trigger keratinocyte stimulation, leading to inflammation. The inflammation produces further barrier defect and hence a vicious cycle [3]. The skin barrier impairment parallels the increased TEWL [23,24]. Not only the skin

inflammation but also the bacteria themselves interact with the SC and TJ to cause barrier damage [25]. Topically applied DMD attenuated the increased TEWL level induced by OVA and MRSA. This compound could even maintain the TEWL at the baseline level to ignore the effect of vehicle disruption on the barrier's nature in the in vivo tolerance study. The upregulation of differentiation proteins in skin tissue suggests that DMD strengthened the SC and TJ barriers. The AD production is partly driven by the terminal keratinocyte differentiation defect [26]. DMD was useful for raising this TJ for barrier function restoration. There is a relationship between the barrier function and microbial infection by estimating the TEWL increase following the decrease of antimicrobial peptides in AD patients [27]. Both the direct bacterial killing

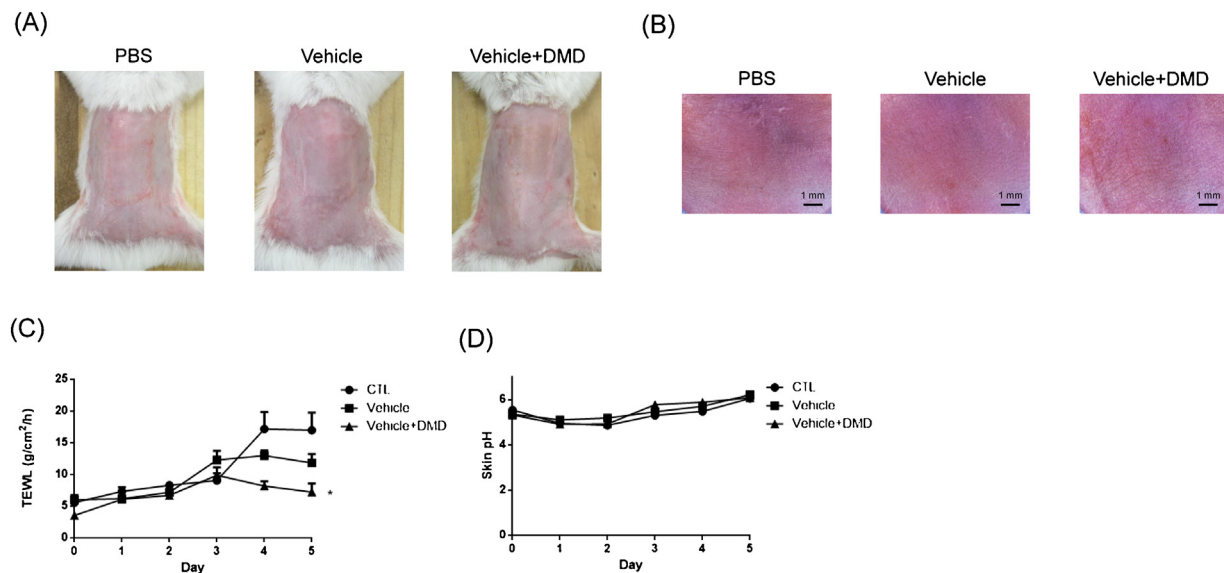


**Fig. 6.** Skin tolerance examination of mouse skin by a 5-day treatment of topically applied DMD: (A) Macroscopic appearance and (B) magnified images. (C) Transepidermal water loss (TEWL) of mouse skin treated with DMD; and (D) skin surface pH value. Each value represents the mean  $\pm$  SEM ( $n=6$ ). \*  $p < 0.05$ . The statistical methods used for comparing the data of different groups are unpaired  $t$ -test and ANOVA.

and improvement of epidermis disruption for preventing infection by DMD were helpful for reducing the overall risk of pathogen invasion in AD.

The previous work [28] suggests the anti-inflammatory effect of *A. camphorata* against the production of nitric oxide, IL-1 $\beta$ , COX-2, and TNF- $\alpha$  in the lipopolysaccharide-activated macrophages. Some benzenoids isolated from *A. camphorata* have attracted attention due to the anti-inflammatory activity in T cells and macrophages [29,30]. The keratinocytes of AD patients indicate a propensity to produce cytokines and chemokines [31], both of which can be employed as the clinical markers. Chemokines are the signaling peptides regulating immune cell trafficking. The inflammatory cell infiltration in AD skin is commonly observed. A previous study [32] demonstrated that *A. camphorata* lowered inflammatory cell infiltration in the epidermis in a mouse skin ischemia model. CCL5 is a chemokine that induces leukocyte infiltration in response to bacterial toxins. The barrier damage elicits the production of CCL17 from keratinocytes, resulting in the attraction of T lymphocytes via CC chemokine receptor 4 (CCR4). Both chemokines are highly associated with the occurrence of AD [23,33]. Our results showed that DMD significantly decreased CCL5 and CCL17 induced by the activated keratinocytes, suggesting that DMD might play a role in the inhibition of T lymphocyte migration into AD lesions.

The in vivo safety rating through topical DMD application manifested a minimal adverse event on normal skin. Although DMD caused in vitro cytotoxicity against HaCaT at the concentrations of  $>100 \mu\text{g/ml}$ , the in vivo tolerance study demonstrated no irritation of topically applied DMD at 1 mg/ml. The use of topical therapy is beneficial in comparison with systemic therapy as it generally exhibits less adverse risk and increases compliance. Our data proved the feasibility of DMD for topical use because of the capability to penetrate the skin and the improvement of AD symptoms and complications. Topical therapy of bacterial skin infection provides advantages over systemic therapy, including the minimization of systemic toxicity and reduced cost [34]. Chlorhexidine is a topical antiseptic employed in outpatient settings to control MRSA outbreak and prevention of skin infection [35]. The anti-MRSA agent developed in this study achieved similar aims to chlorhexidine. However, the structures and antimicrobial mechanisms of both compounds are quite different. Chlorhexidine is a

cationic disinfectant with broad-spectrum biocide activity against Gram-positive bacteria, Gram-negative bacteria, and fungi [36]. The main mechanism of action is the destabilization of cell wall to interfere osmosis. On the other hand, DMD showed specific antibacterial activity against Gram-positive bacteria but limited activity against Gram-negative bacteria such as *E. coli* and *P. aeruginosa* (data not shown). The mechanism of DMD was the protein synthesis inhibition but not cell membrane damage. The study of AD patient compliance has suggested that use of the anti-inflammatory therapy is too late once the flare-up has started [37]. Currently, there is no primary preventive intervention established for AD [38]. DMD may be developed as a preventative agent because it is safe and even protects the barrier feature in healthy skin.

## Conflict of interest

The authors have no conflict of interest to declare.

## Acknowledgement

The authors are grateful to the financial support by Ministry of Science and Technology of Taiwan (MOST-105-2320-B-182-010-MY3) and Chang Gung Memorial Hospital (CMRPG2G0661-3 and CMRPG2E0062).

## Appendix A. Supplementary data

Supplementary material related to this article can be found, in the online version, at doi:<https://doi.org/10.1016/j.jdermsci.2018.09.002>.

## References

- [1] T.E. Shaw, G.P. Currie, C.W. Koudelka, E.L. Simpson, Eczema prevalence in the United States: data from the 2003 National Survey of Children's Health, *J. Invest. Dermatol.* 131 (2011) 67–73.
- [2] J. van Smeden, J.A. Bouwstra, Stratum corneum lipids: their role for the skin barrier function in healthy subjects and atopic dermatitis patients, *Curr. Probl. Dermatol.* 49 (2016) 8–26.
- [3] P.Y. Ong, Recurrent MRSA skin infections in atopic dermatitis, *J. Allergy Clin. Pract.* 2 (2014) 396–399.
- [4] H.C. Williams, Atopic dermatitis, *N. Engl. J. Med.* 352 (2005) 2314–2324.



- [5] Y. Yun, K. Kim, I. Choi, S.G. Ko, Topical herbal application in the management of atopic dermatitis: a review of animal studies, *Mediat. Inflamm.* 2014 (2014) 752103.
- [6] M. Geethangili, Y.M. Tzeng, Review of pharmacological effects of *Antrrodia camphorata* and its bioactive compounds, *Evid. Complement. Altern. Med.* 2011 (2011) 212641.
- [7] M. Geethangili, S.H. Fang, C.H. Lai, Y.K. Rao, H.M. Lien, Y.M. Tzeng, Inhibitory effect of *Antrrodia camphorata* constituents on the *Helicobacter pylori*-associated gastric inflammation, *Food Chem.* 119 (2010) 149–153.
- [8] S.S. Chiang, L.T. Wang, S.Y. Chen, J.L. Mau, Antibacterial and anti-inflammatory activities of mycelia of a medicinal mushroom from Taiwan, *Taiwanofungus salmoneus* (higher basidiomycetes), *Int. J. Med. Mushrooms* 15 (2013) 39–47.
- [9] S.C. Yang, I.A. Aljuffali, C.T. Sung, C.F. Lin, J.Y. Fang, Antimicrobial activity of topically-applied soyaethyl morpholinium ethosulfate micelles against *Staphylococcus* species, *Nanomedicine* 11 (2016) 657–671.
- [10] S.C. Yang, C.H. Tseng, P.W. Wang, P.L. Lu, Y.H. Weng, F.L. Yen, J.Y. Fang, Pterostilbene, a methoxylated resveratrol derivative, efficiently eradicates planktonic, biofilm, and intracellular MRSA by topical application, *Front. Microbiol.* 8 (2017) 1103.
- [11] C.Y. Hsu, C.T. Sung, I.A. Aljuffali, C.H. Chen, K.Y. Hu, J.Y. Fang, Intravenous anti-MRSA phosphatidylserine mediate enhanced affinity to pulmonary surfactants for effective treatment of infectious pneumonia, *Nanomed.-Nanotechnol. Biol. Med.* 14 (2017) 215–225.
- [12] T.L. Pan, P.W. Wang, I.A. Aljuffali, C.T. Huang, C.W. Lee, J.Y. Fang, The impact of urban particulate pollution on skin barrier function and the subsequent drug absorption, *J. Dermatol. Sci.* 78 (2015) 51–60.
- [13] C.F. Lin, C.F. Hung, I.A. Aljuffali, Y.L. Huang, W.C. Liao, J.Y. Fang, Methylation and esterification of magnolol for ameliorating cutaneous targeting and therapeutic index by topical application, *Pharm. Res.* 33 (2016) 2152–2167.
- [14] Y.P. Fang, S.H. Yang, C.H. Lee, I.A. Aljuffali, H.C. Kao, J.Y. Fang, What is the discrepancy between drug permeation into/across intact and diseased skins? Atopic dermatitis as a model, *Int. J. Pharm.* 497 (2016) 277–286.
- [15] C.F. Hung, W.Y. Chen, I.A. Aljuffali, Y.K. Lin, H.C. Shih, J.Y. Fang, Skin aging modulates percutaneous drug absorption: the impact of ultraviolet irradiation and ovariectomy, *Age* 37 (2015) 21.
- [16] H.M. Lien, C.H. Chiu, C.C. Chen, W.L. Chang, C.C. Chyau, R.Y. Peng, Comparison of the apoptotic effects of supercritical fluid extracts of *Antrrodia cinnamomea* mycelia on hepatocellular carcinoma cells, *Molecules* 19 (2014) 9033–9050.
- [17] C.Y. Chen, S.C. Chien, N.W. Tsao, C.S. Lai, Y.Y. Wang, W.W. Hsiao, et al., Metabolite profiling and comparison of bioactivity in *Antrrodia cinnamomea* and *Antrrodia salmonea* fruiting bodies, *Planta Med.* 82 (2016) 244–249.
- [18] W.C. Nance, S.E. Dowd, D. Samarian, J. Chludzinski, J. Delli, J. Battista, A.H. Rickard, A high-throughput microfluidic dental plaque biofilm system to visualize and quantify the effect of antimicrobials, *J. Antimicrob. Chemother.* 68 (2013) 2550–2560.
- [19] P.Y. Ong, D.Y.M. Leung, Bacterial and viral infections in atopic dermatitis: a comprehensive review, *Clin. Rev. Allergy Immunol.* 51 (2016) 329–337.
- [20] S. Alt, L.A. Mitchenall, A. Maxwell, L. Heide, Inhibition of DNA gyrase and DNA topoisomerase IV of *Staphylococcus aureus* and *Escherichia coli* by aminocoumarin antibiotics, *J. Antimicrob. Chemother.* 66 (2011) 2061–2069.
- [21] J.Y. Fang, T.H. Huang, C.F. Hung, Y.L. Huang, I.A. Aljuffali, W.C. Liao, et al., Derivatization of honokiol by integrated acetylation and methylation for improved cutaneous delivery and anti-inflammatory potency, *Eur. J. Pharm. Sci.* 114 (2018) 189–198.
- [22] F. Rancan, M. Giubudagian, J. Jurisch, U. Blume-Peytavi, M. Calderón, A. Vogt, Drug delivery across intact and disrupted skin barrier: identification of cell populations interacting with penetrated thermoresponsive nanogels, *Eur. J. Pharm. Biopharm.* 116 (2017) 4–11.
- [23] K. Kabashima, New concept of the pathogenesis of atopic dermatitis: interplay among the barrier, allergy, and pruritus as a trinity, *J. Dermatol. Sci.* 70 (2013) 3–11.
- [24] F.F. Sahle, T. Gebre-Mariam, B. Dobner, J. Wohlrab, R.H.H. Neubert, Skin diseases associated with the depletion of stratum corneum lipids and stratum lipid substitution therapy, *Skin Pharmacol. Physiol.* 28 (2015) 42–55.
- [25] K. Bäsler, J.M. Brandner, Tight junction in skin inflammation, *Eur. J. Appl. Physiol. Occup. Physiol.* 469 (2017) 3–14.
- [26] L.M. Roesner, T. Werfel, A. Heratizadeh, The adaptive immune system in atopic dermatitis and implications on therapy, *Expert Rev. Clin. Immunol.* 12 (2016) 787–796.
- [27] K.Y. Park, D.H. Kim, M.S. Jeong, K. Li, S.J. Seo, Changes of antimicrobial peptides and transepidermal water loss after topical application of tacrolimus and ceramide-dominant emollient in patients with atopic dermatitis, *J. Korean Med. Sci.* 25 (2010) 766–771.
- [28] Y.C. Hseu, F.Y. Wu, J.J. Wu, J.Y. Chen, W.H. Chang, F.J. Lu, et al., Anti-inflammatory potential of *Antrrodia camphorata* through inhibition of iNOS, COX-2 and cytokines via the NF- $\kappa$ B pathway, *Int. Immunopharmacol.* 5 (2005) 1914–1925.
- [29] M. Buccini, K.A. Punch, B. Kaskow, G.R. Flematti, B.W. Skelton, L.J. Abraham, et al., Ethynylbenzenoid metabolites of *Antrrodia camphorata*: synthesis and inhibition of TNF expression, *Org. Biomol. Chem.* 12 (2014) 1100.
- [30] P.H. Shie, S.Y. Wang, H.L. Lay, G.J. Huang, 4,7-Dimethoxy-5-methyl-1,3-benzodioxole from *Antrrodia camphorata* inhibits LPS-induced inflammation via suppression of NF- $\kappa$ B and induction HO-1 in RAW264.7 cells, *Int. Immunopharmacol.* 31 (2016) 186–194.
- [31] R. Asahina, S. Maeda, A review of the roles of keratinocyte-derived cytokines and chemokines in the pathogenesis of atopic dermatitis in humans and dogs, *Vet. Dermatol.* 28 (2017) 16–e5.
- [32] T.C. Tsai, Y.T. Tung, Y.H. Kuo, J.W. Liao, H.C. Tsai, K.Y. Chong, et al., Anti-inflammatory effects of *Antrrodia camphorata*, a herbal medicine, in a mouse skin ischemia model, *J. Ethnopharmacol.* 159 (2015) 113–121.
- [33] B. Nedoszytko, M. Sokołowska-Wojdyło, K. Ruckemann-Dziurdzińska, J. Roszkiewicz, R.J. Nowicki, Chemokines and cytokines network in the pathogenesis of the inflammatory skin diseases: atopic dermatitis, psoriasis and skin mastocytosis, *Postep. Dermatol. Alergol.* 31 (2014) 84–91.
- [34] M. Niebuhr, U. Mai, A. Kapp, T. Werfel, Antibiotic treatment of cutaneous infections with *Staphylococcus aureus* in patients with atopic dermatitis: current antimicrobial resistances and susceptibilities, *Exp. Dermatol.* 17 (2008) 953–957.
- [35] S.D. Schlett, E.V. Millar, K.B. Crawford, T. Cui, J.B. Lanier, D.R. Tribble, M.W. Ellis, Prevalence of chlorhexidine-resistant methicillin-resistant *Staphylococcus aureus* following prolonged exposure, *Antimicrob. Agents Chemother.* 58 (2014) 4404–4410.
- [36] A.M. Milstone, C.L. Passaretti, T.M. Perl, Chlorhexidine: expanding the armamentarium for infection control and prevention, *Clin. Infect. Dis.* 46 (2008) 274–281.
- [37] T. Bieber, Atopic dermatitis, *Ann. Dermatol.* 22 (2010) 125–137.
- [38] M. Kelleher, A. Dunn-Galvin, J.O. Hourihane, D. Murray, L.E. Campbell, W.H.I. McLean, et al., Skin barrier dysfunction measured by transepidermal water loss at 2 days and 2 months predates and predicts atopic dermatitis at 1 year, *J. Allergy Clin. Immunol.* 135 (2015) 930–935.



# Infection with *Staphylococcus aureus* elicits COX-2/PGE<sub>2</sub>/IL-6/MMP-9-dependent aorta inflammation via the inhibition of intracellular ROS production

Ming-Horng Tsai<sup>a,b,1</sup>, Cheng-Hsun Wu<sup>c,1</sup>, Wei-Ning Lin<sup>d</sup>, Ching-Yi Cheng<sup>e,f</sup>, Chu-Chun Chuang<sup>g</sup>, Kuo-Ting Chang<sup>h</sup>, Rong-San Jiang<sup>i</sup>, Jen-Fu Hsu<sup>j</sup>, I-Ta Lee<sup>i,k,\*</sup>

<sup>a</sup> Department of Pediatrics, Division of Neonatology and Pediatric Hematology/Oncology, Chang Gung Memorial Hospital, Yunlin, Taiwan

<sup>b</sup> Graduate Institute of Clinical Medical Science, College of Medicine, Chang Gung University, Taiwan

<sup>c</sup> School of Medicine, College of Medicine, China Medical University, Taichung, Taiwan

<sup>d</sup> Graduate Institute of Biomedical and Pharmaceutical Science, Fu Jen Catholic University, New Taipei City, Taiwan

<sup>e</sup> Graduate Institute of Health Industry Technology, Research Center for Chinese Herbal Medicine and Research Center for Food and Cosmetic Safety, Chang Gung University of Science and Technology, Taoyuan, Taiwan

<sup>f</sup> Department of Ophthalmology, Chang Gung Memorial Hospital at Linkou, Taoyuan, Taiwan

<sup>g</sup> Department of Physical Therapy of China Medical University, Taichung, Taiwan

<sup>h</sup> Translational Medicine Center, Taoyuan General Hospital, Ministry of Health and Welfare, Taoyuan, Taiwan

<sup>i</sup> Department of Medical Research, Taichung Veterans General Hospital, Taichung, Taiwan

<sup>j</sup> Department of Pediatrics, Division of Neonatology, Chang Gung Memorial Hospital at Linkou, Taoyuan, Taiwan

<sup>k</sup> Department of Nursing, College of Nursing, Hungkuang University, Taichung, Taiwan

## ARTICLE INFO

### Keywords:

*Staphylococcus aureus*  
Cyclooxygenase-2  
Matrix metalloproteinase-9  
Aorta inflammation  
Interleukin-6

## ABSTRACT

*Staphylococcus aureus* (*S. aureus*) can lead to many life-threatening diseases. It has the ability to invade normal endovascular tissue. The molecular mechanisms and pathological changes of endothelial cells after *S. aureus* infection are of interest, but the basic understanding of how *S. aureus* destroys this barrier is not clear. Here, we showed that *S. aureus* enhanced COX-2 expression and prostaglandin E<sub>2</sub> (PGE<sub>2</sub>) secretion in human aortic endothelial cells (HAECs). In addition, *S. aureus* induced PGE<sub>2</sub>/interleukin-6 (IL-6)/matrix metalloproteinase-9 (MMP-9)-dependent cell migration. *S. aureus*-induced COX-2, IL-6, and MMP-9 levels were inhibited by transfection with siRNA of Toll-like receptor 2 (TLR2), p38, p42, p44, p50, or p65. *S. aureus* also induced p38 MAPK, ATF2, ERK1/2, and NF-κB p65 activation. Interestingly, we proved that *S. aureus* decreased intracellular generation of reactive oxygen species (ROS), which suggests that the inhibition of ROS production promoted inflammatory responses. Finally, we showed that *S. aureus* enhanced a variety of biomarkers of inflammation in cardiovascular diseases. However, the free radical scavenger (MCI-186) or antioxidant (N-acetyl-L-cysteine, NAC) markedly enhanced *S. aureus*-induced COX-2 mRNA levels in the aorta tissues. Taken together, these findings established that *S. aureus* promoted aorta inflammation via activation of p38 MAPK, ERK1/2, and NF-κB and inhibition of ROS generation.

## 1. Introduction

*Staphylococcus aureus* (*S. aureus*) is a common pathogen that can cause infection of human skin and other soft tissues, blood, and the respiratory tract [1]. In addition, *S. aureus* often causes endocarditis, bacteremia, and endovascular infections [2]. The interactions between *S. aureus* and endothelial cells are considered the most important interactions in the pathogenesis of cardiovascular infection [3], and the

interactions can damage heart valves in endocarditis or induce multi-organ dysfunction [3]. Recently, Venza et al. found that *S. aureus* can trigger interleukin-8 (IL-8) activation by increasing cyclooxygenase-2 (COX-2) levels and prostaglandin E<sub>2</sub> (PGE<sub>2</sub>) production in *S. aureus*-infected human conjunctival cells [4]. Moreover, Klemm et al. found that interleukin-6 (IL-6), a marker of severe disease, was up-regulated during *S. aureus* infection [5]. Matrix metalloproteinase-9 (MMP-9) is thought to be involved in extracellular matrix degeneration and

\* Corresponding author at: Department of Medical Research, Taichung Veterans General Hospital, 1650 Taiwan Boulevard Sect. 4, Taichung, Taiwan.  
E-mail address: [itl700128@gmail.com](mailto:itl700128@gmail.com) (I.-T. Lee).

<sup>1</sup> These authors contributed equally to this work.

inflammation [6]. However, the relationship between *S. aureus* and these pro-inflammatory mediators, including COX-2/PGE<sub>2</sub>, IL-6, and MMP-9, in human aortic endothelial cells (HAECs) and the detailed mechanisms involved in *S. aureus*-induced vascular inflammation are still unknown. Thus, in this study, we explored how *S. aureus* causes vascular inflammation.

Many studies have shown that *S. aureus* promotes inflammatory responses through Toll-like receptor 2 (TLR2)-dependent signaling molecules, including mitogen-activated protein kinases (MAPKs) and NF-κB [5,7,8]. Induction and mediation of the inflammatory response is controlled by MAPKs, a well-studied, important family of kinases, among various mechanisms [5]. MAPK signaling pathways encompass cascades of kinases, which convert extracellular signals into cellular responses [5]. Isoforms of MAPKs JNK, p38, and ERK1/2 are the best-studied of the kinases in mammalian cells [5]. Upon pathogen challenge, MAPKs are activated and then cause the up-regulation of chemokines, inflammatory proteins, and cytokines [9]. NF-κB regulates inflammation by inducing many genes, including those coding for chemokines and cytokines [9]. Many studies have demonstrated that NF-κB activation/translocation and inflammatory responses can be mediated by TLR2 [10]. However, whether these signaling molecules involved in inflammatory responses induced by *S. aureus* in HAECs is unknown. Thus, we investigated the detailed mechanisms involved in *S. aureus*-induced vascular inflammation.

Studies have shown that the physiological flux of reactive oxygen species (ROS) mediates cell survival, differentiation, proliferation, and migration. Increased oxidative stress often causes cell damage and leads to inflammation [11]. Oxidative stress may occur due to increased generation and/or reduced ROS destruction [11]. Therefore, levels of endogenous cellular antioxidants and antioxidant enzymes and activation of ROS-producing systems affect the balance between ROS production and destruction. Several mechanisms in the body resist oxidative stress by producing antioxidants. Nonetheless, oxidant inhibitors and antioxidant strategies are not always beneficial for the treatment of diseases. Therefore, a lack of necessary ROS is detrimental to cells, and redox imbalance due to an excess of oxidizing or reducing equivalents creates oxidative stress or reductive stress states (redox stress states) that are harmful to biological systems [12]. Previous reports have indicated that bacteria are destroyed by various deadly stressors, some of which facilitate cascades of ROS [13]. Bacteria have protective proteins that can be used to counter damage and detoxify ROS [13]. Therefore, in this study, we also explored the role of ROS in *S. aureus*-mediated inflammation in HAECs and in rats. In this way, the results of this study can help clarify how *S. aureus* causes vascular inflammation, which could be helpful in designing clinical treatment of *S. aureus* infections.

## 2. Materials and methods

### 2.1. Materials

We purchased anti-COX-2 (sc-376861), anti-GAPDH (sc-365062), anti-TLR2 (sc-21759), anti-TLR4 (sc-293072), anti-p38α/β (sc-7972), anti-ATF2 (sc-187), anti-p65 (sc-8008), and anti-COX-1 (sc-19998) antibodies from Santa Cruz Biotechnology Inc (Santa Cruz, CA, USA). Anti-phospho-p65 (#3033), anti-phospho-ATF2 (#9221), anti-phospho-p38 MAPK (#9211), and anti-phospho-ERK1/2 (#9101) antibodies were purchased from Cell Signaling (Danvers, MA, USA). MCI-186, SC-51322, U0126, SB202190, and N-acetyl-L-cysteine (NAC) were purchased from Calbiochem (San Diego, CA, USA). H<sub>2</sub>O<sub>2</sub>, enzymes, and other chemicals were purchased from Sigma (St. Louis, MO, USA). Helenalin (HLN) was purchased from Cayman (Ann Arbor, MI, USA).

### 2.2. Cell culture

Human aortic endothelial cells (HAECs) (C00625PA) were purchased from Cascade Biologics (Portland, OR). The cells were grown in

culture flasks in endothelial cell growth medium, M200 (Cascade Biologics, Inc.) supplemented with fetal bovine serum (FBS, 5%), human basic fibroblast growth factor (3 ng/ml), human epidermal growth factor (10 ng/ml), streptomycin (100 pg/ml), penicillin (100 U/ml), insulin (10 mg/ml), and Fungizone (1.25 mg/ml) at 37 °C in a humidified 5% CO<sub>2</sub> atmosphere. Cells were used between passages 3 and 7 in this study.

### 2.3. Preparation of *S. aureus*

*S. aureus* (strain 12598, a gift from Dr J. C. Shu, Department of Medical Biotechnology and Laboratory Science, Chang Gung University, Tao-Yuan, Taiwan) was maintained in BHI (brain heart infusion) broth (Sigma). The method of preparation of *S. aureus* is described in our previous study [10]. In each experiment, approximately  $2 \times 10^7$  bacteria, representing a bacteria/epithelial cell ratio of 20:1, were added in 1 ml of RPMI 1640 medium (Gibco) to each well.

### 2.4. Transient transfection with siRNAs

Scrambled, COX-2, IL-6, MMP-9, p42, p44, p38, p65, p50, TLR2, and TLR4 human siRNAs were purchased from Sigma (St. Louis, MO, USA). We transiently transfected siRNA (100 nM) by use of a Lipofectamine™ RNAiMAX reagent, according to the manufacturer's instructions.

### 2.5. Real-Time PCR

We used TRIzol reagent to extract total RNA. We then reverse-transcribed mRNA into cDNA and analyzed it by real-time PCR, using SYBR Green PCR reagents (Applied Biosystems, Branchburg, NJ, USA) and primers specific for human GAPDH, COX-2, TLR2, and TLR4 and mouse GAPDH, COX-1, and COX-2 mRNAs. Finally, COX-1, COX-2, TLR2, and TLR4 mRNA levels were determined by normalizing to levels of GAPDH expression.

Real time RT-PCR primer sequences were as follows:

Rat COX-1:

5'-TCCTGTTCCGAGCCCAGTT-3' (forward)

5'-CTTGAAGGAATCAGGCATGA-3' (reverse)

Rat COX-2:

5'-GGCACAAATATGATGTTTCGCA-3' (forward)

5'-CCTCGCTTCTGATCTGTCTTGA-3' (reverse)

Rat GAPDH:

5'-AAGGTGGTGAAGCAGGCGGC-3' (forward)

5'-GAGCAATGCCAGCCCCAGCA-3' (reverse)

Human COX-2:

5'-ATCATTACCAGGCAAATTGC-3' (forward)

5'-GGCTTCAGCATAAAGCGTTTG-3' (reverse)

Human TLR2:

5'-CAGGTGACTGCTCGGAGTTC-3' (forward)

5'-CACAACTACCAGTTGAAAGCAGTGA-3' (reverse)

Human TLR4:

5'-TGGAAGTTGAACGAATGGAATGTG-3' (forward)

5'-ACCAGAACTGCTACAACAGATACT-3' (reverse)

Human GAPDH:

5'-TCATCCCTGAGCTGAACGG-3' (forward)

5'-GTCAAAGGTGGAGGAGTGGG-3' (reverse)

### 2.6. Migration assay

HAECs were cultured to confluence in 10-cm dishes and starved with serum-free M200 for one day. We then scratched the monolayer cells with a blade, creating extended and definite scratches in the center of the dishes with a bright and clear field. The cells were washed once with PBS to remove the detached cells. After pretreatment with the inhibitors for 2 h, serum-free M200 with or without *S. aureus* was added

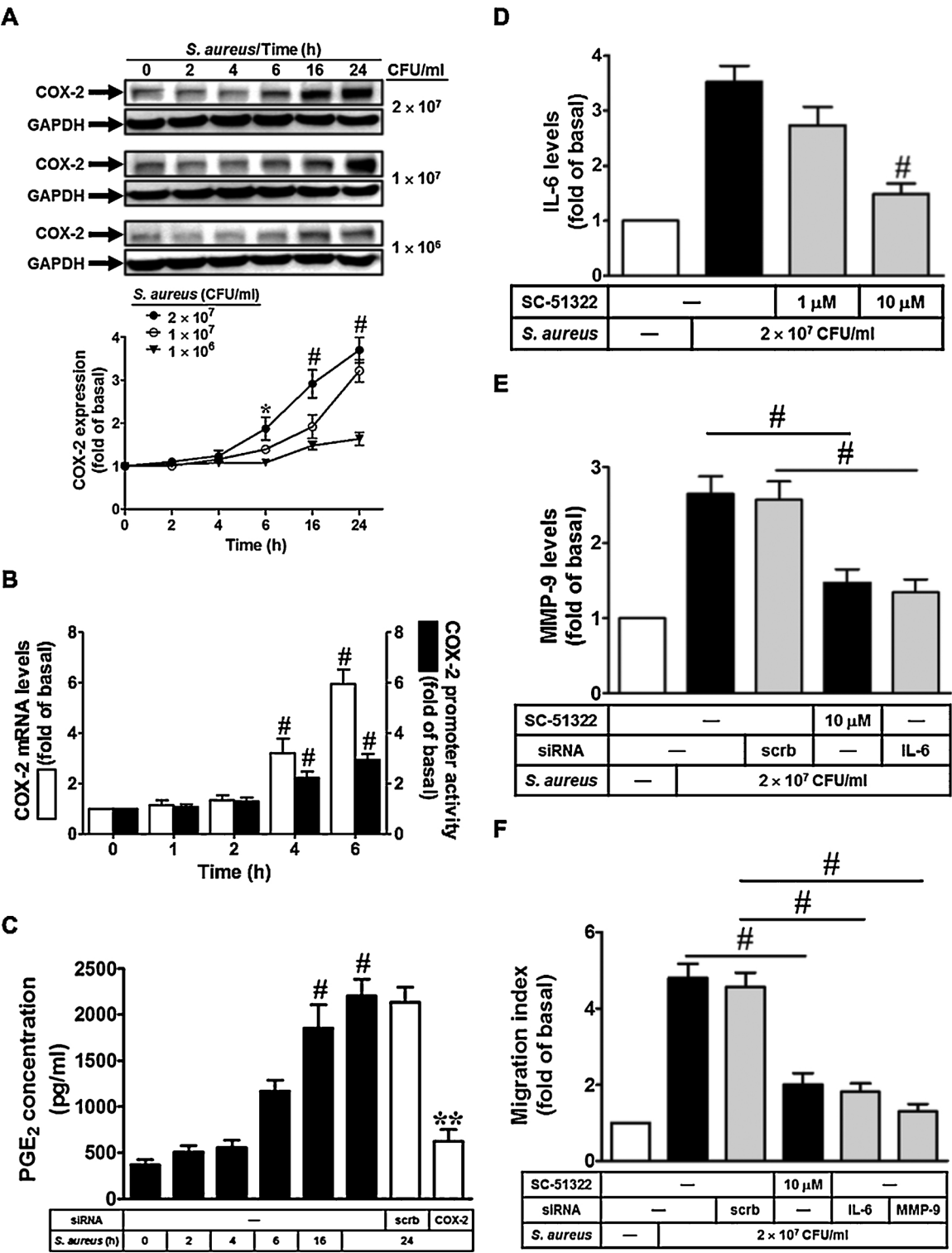


**Fig. 1.** *S. aureus* induces MMP-9-dependent cell migration. (A) Cells were treated with *S. aureus* for the indicated times. The COX-2 expression was determined. (B) Cells were treated with *S. aureus* (2 × 10<sup>7</sup> CFU/ml) for the indicated times. The COX-2 mRNA levels and promoter activity were determined. (C) Cells were treated with *S. aureus* (2 × 10<sup>7</sup> CFU/ml) for the indicated times or transfected with siRNA of scrambled or COX-2, then treated with *S. aureus* for 24 h. PGE<sub>2</sub> production was measured. (D) Cells were pretreated with SC-51322, and then treated with *S. aureus* for 24 h. IL-6 production was measured. (E) Cells were pretreated with SC-51322 or transfected with siRNA of scrambled or IL-6, and then treated with *S. aureus* for 24 h. The MMP-9 production was measured. (F) Cells were pretreated with SC-51322 or transfected with siRNA of scrambled, IL-6, or MMP-9, then treated with *S. aureus* for 24 h. Cell migration was determined. n = 3–4, \*P < 0.05; #P < 0.01, as compared with the basal level (A, B, C). \*\*P < 0.01, as compared with the cells exposed to *S. aureus* + scrambled siRNA (C). #P < 0.01, as compared with the cells exposed to *S. aureus* alone (D). #P < 0.01 for significant difference between the groups (E, F).



to each dish containing the DNA synthesis inhibitor, hydroxyurea (10  $\mu$ M), during the period of incubation. We counted the number of migratory cells from the resulting four-phase images for each point and averaged for each experimental condition. The final data came from three separate assays.

## 2.7. Measurement of intracellular ROS accumulation

We used CellROX Green Reagent (Molecular Probes, Eugene, OR, USA) to measure oxidative stress in live cells. The fluorescence for CellROX Green Reagent staining was detected at 485/520 nm. HAECs were washed with warm Hank's Balanced Salt Solution (HBSS) and incubated in HBSS containing 5  $\mu$ M CellROX Green Reagent at 37 °C for 30 min. The HBSS containing CellROX Green Reagent then was removed and replaced with fresh medium. HAECs were incubated with *S. aureus* for the indicated times. Finally, HAECs were washed twice with PBS and detached with trypsin/EDTA. The fluorescence intensity of the cells was analyzed with a FACSscan flow cytometer (BD Biosciences, San Jose, CA) at 485 nm excitation and 520 nm emission.

## 2.8. Measurement of MMP-9 and IL-6 expression

HAECs were cultured in 12-well culture plates. After reaching confluence, HAECs were incubated with *S. aureus* for the indicated times at 37 °C. The media were gathered, and IL-6 and MMP-9 were measured with an IL-6 ELISA kit (BioSource International, Camarillo, CA, USA) and MMP-9 ELISA kit (Thermo scientific, Rockford, USA), respectively, according to instructions of the manufacturers.

## 2.9. Measurement of PGE<sub>2</sub> release

HAECs were cultured in 12-well culture plates. After reaching confluence, HAECs were incubated with *S. aureus* for the indicated times at 37 °C. The media were gathered, and PGE<sub>2</sub> were measured with a PGE<sub>2</sub> ELISA kit (Enzo Life Sciences, Farmingdale, NY, USA), according to instructions of the manufacturers.

## 2.10. Western blot analysis

We cultured HAECs in 6-well culture plates. After reaching confluence, HAECs were incubated with *S. aureus* for the indicated times at 37 °C. Western blot analysis methods have been described [10]. Finally, membranes were incubated with the anti-COX-2 antibody for one day and then incubated with the anti-mouse horseradish peroxidase antibody for 60 min. We used enhanced chemiluminescence (ECL) reagents to detect immunoreactive bands.

## 2.11. COX-2 luciferase promoter assay

We cloned the human COX-2 promoter (a region spanning —459 to +9 bp) [14–16] into pGL3-basic vector (Promega, Madison, WI, USA) to construct a COX-2-luc plasmid. The COX-2 luciferase promoter assay was performed as we have described [10]. Firefly luciferase activities were finally normalized to  $\beta$ -gal activity.

## 2.12. Animal care and experimental procedures

Male Sprague Dawley rats aged 6–8 weeks were obtained from the National Laboratory Animal Centre (Taipei, Taiwan) and were handled according to NIH Guides for the Care and Use of Laboratory Animals. We injected 100  $\mu$ l of bacterial suspension intraperitoneally ( $2 \times 10^7$  CFU/mouse) into Sprague Dawley rats; control rats were injected with BHI. Sprague Dawley rats were given one dose of NAC, MCI-186, U0126, SB202190, or HLN (2 mg/kg of body weight) intraperitoneally 2 h before *S. aureus* ( $2 \times 10^7$  CFU/rat) treatment. The animals were killed after 48 h. Plasma myeloperoxidase (MPO) and serum C-reactive

protein (CRP), IL-6, and TNF- $\alpha$  were measured.

## 2.13. Statistical software and analysis

We analyzed the data with the GraphPad Prism program (GraphPad, San Diego, CA, USA). Quantitative data were expressed as the mean  $\pm$  S.E.M. and analyzed with one-way ANOVA followed with Tukey's post-hoc test. We defined  $P < 0.05$  as a significant difference.

## 3. Results

### 3.1. *S. aureus* induces COX-2/PGE<sub>2</sub>/IL-6/MMP-9-dependent cell migration

Many studies have pointed out that *S. aureus* induces COX-2 or PGE<sub>2</sub> expression [10,17] in various cell types. Here, we investigated whether *S. aureus* could induce COX-2 expression in HAECs. Cells were treated with various concentrations of *S. aureus* for 2, 4, 6, 16, or 24 h. The protein expression of COX-2 was determined with Western blot. As shown in Fig. 1A, *S. aureus* induced COX-2 protein levels in a dose- and time-dependent manner. *S. aureus*-induced COX-2 expression was significantly increased within 6 h and continued to increase over 24 h. In addition, we observed that *S. aureus* ( $2 \times 10^7$  CFU/ml) induced COX-2 mRNA levels and promoter activity in a time-dependent manner, with a maximal response within 4–6 h ( $P < 0.01$ ) (Fig. 1B). We have already known that COX-2 can convert arachidonic acid to PGE<sub>2</sub>, which can be used as a marker of COX-2 activity [17]. Moreover, as shown in Fig. 1C, we demonstrated that *S. aureus* time-dependently induced PGE<sub>2</sub> generation ( $< 5$ -fold,  $P < 0.01$ ), which was decreased by transfection with COX-2 siRNA ( $P < 0.01$ ). When IL-6 binds to its soluble receptor, sIL-6R $\alpha$ , it can affect the transition from acute to chronic inflammation by regulating the properties of leukocyte infiltrate [18]. We previously demonstrated that PGE<sub>2</sub> could induce IL-6 release in human tracheal smooth muscle cells [19]. In this study, we pointed out that *S. aureus* induced IL-6 release ( $< 4$ -fold,  $P < 0.01$ ), which was reduced by pretreatment with the inhibitor of PGE<sub>2</sub>, SC-51322 (10  $\mu$ M) ( $P < 0.01$ ) (Fig. 1D). Studies have shown that IL-6 can mediate cell migration in various cell types [20]. Moreover, we showed that *S. aureus* enhanced MMP-9 levels ( $< 3$ -fold,  $P < 0.01$ ) in HAECs, which was reduced by pretreatment with 10  $\mu$ M SC-51322 ( $P < 0.01$ ) or transfection with IL-6 siRNA ( $P < 0.01$ ) (Fig. 1E). Finally, we showed that *S. aureus* promoted cell migration ( $< 6$ -fold,  $P < 0.01$ ), which was inhibited by transfection with siRNA of IL-6 or MMP-9 ( $P < 0.01$ ) or pretreatment with SC-51322 ( $P < 0.01$ ) (Fig. 1F). These results prompt us to suggest that *S. aureus* induces HAECs migration via a COX-2/PGE<sub>2</sub>/IL-6/MMP-9-dependent pathway.

### 3.2. *S. aureus* induces COX-2 expression via TLR2, but not TLR4 in HAECs

Staphylococcal lipoteichoic acid (LTA) triggers a cascade of inflammatory responses through TLR2. After stimulation, TLR2 can promote production of inflammatory cytokines [21]. On the other hand, TLR4 is most known for recognizing lipopolysaccharide (LPS), a component present in Gram-negative bacteria [22]. Here, we found that *S. aureus*-induced COX-2 expression was reduced by transfection with TLR2 siRNA ( $P < 0.01$ ), but not with transfection of TLR4 siRNA (Fig. 2A). *S. aureus* and LTA also increased TLR2 protein levels directly ( $< 4$ -fold,  $P < 0.01$ ) (Fig. 2B). We further demonstrated that *S. aureus* ( $< 7$ -fold,  $P < 0.01$ ) and LTA ( $< 3$ -fold,  $P < 0.01$ ) could induce TLR2 mRNA levels, but not TLR4 mRNA levels, in HAECs (Fig. 2C). Finally, we showed that *S. aureus*-induced MMP-9 and IL-6 levels were reduced by transfection with TLR2 siRNA ( $P < 0.01$ ) (Fig. 2D). Thus, we suggest that *S. aureus* induces COX-2 expression via TLR2 in HAECs.

### 3.3. *S. aureus* induces COX-2 expression via p38 MAPK in HAECs

p38 MAPK has been shown to regulate COX-2 expression and PGE<sub>2</sub>

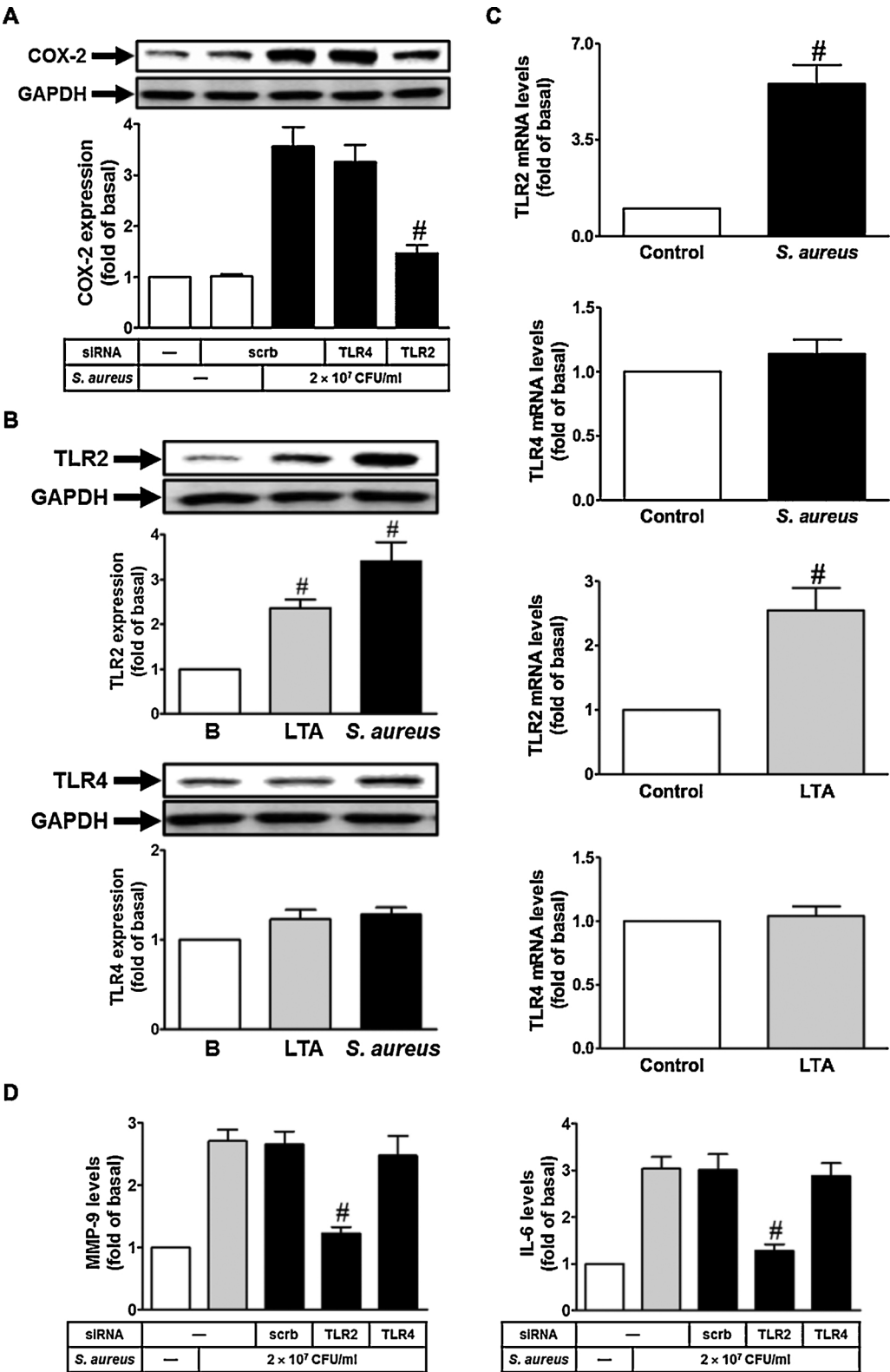


**Fig. 2.** *S. aureus* induces COX-2 expression via TLR2, but not TLR4 in HAECs. (A) Cells were transfected with siRNA of scrambled, TLR4, or TLR2, and then treated with *S. aureus* for 24 h. The COX-2 expression was determined. (B) Cells were treated with LTA (50 µg/ml) or *S. aureus* for 24 h. TLR2 and TLR4 expression was determined. (C) Cells were treated with *S. aureus* or LTA for 6 h. TLR2 and TLR4 mRNA levels were determined. (D) Cells were transfected with siRNA of scrambled, TLR2, or TLR4, and then treated with *S. aureus* for 24 h. MMP-9 and IL-6 production was measured. n = 4–5, #*P* < 0.01, as compared with the cells exposed to *S. aureus* + scrambled siRNA (A, D). \**P* < 0.01, as compared with the basal level (B, C).

release [23]. Indeed, we found that *S. aureus*-induced COX-2 protein and mRNA were inhibited by the inhibitor of p38 MAPK, SB202190 (*P* < 0.01) or p38 siRNA (*P* < 0.01) (Fig. 3A and B). On the other hand, *S. aureus*-induced PGE<sub>2</sub>/IL-6/MMP-9 and cell migration were also reduced by transfection with siRNA of p38 (*P* < 0.01) (Fig. 3C and D). The ATF2 transcription factor is phosphorylated by the stress-activated p38 MAPK [24]. Moreover, *S. aureus* markedly induced p38 MAPK

activation in a time-dependent manner with a maximal response within 15–30 min (< 3-fold), which was reduced by SB202190 (*P* < 0.01) (Fig. 3E). Finally, we showed that *S. aureus* induced ATF2 phosphorylation in a time-dependent manner in these cells, with a maximal response within 15–30 min (< 4-fold, *P* < 0.01) (Fig. 3F). Thus, we suggest that *S. aureus* induces COX-2 expression and cell migration via p38 MAPK in HAECs.

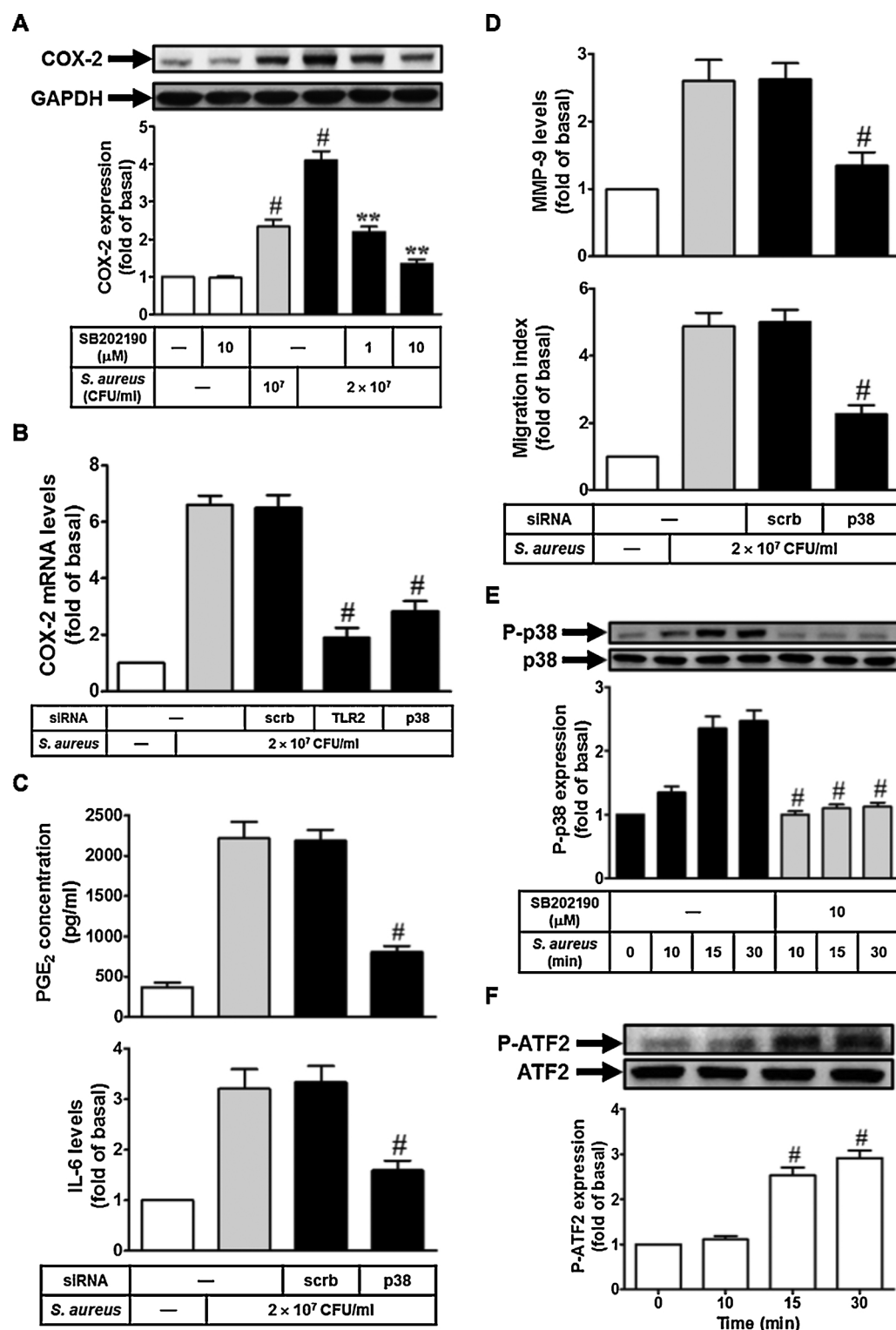


**Fig. 3. *S. aureus* induces COX-2 expression via p38 MAPK.** (A) Cells were pretreated with SB202190, and then treated with *S. aureus*. COX-2 expression was determined. (B) Cells were transfected with siRNA of scrambled, TLR2, or p38, then treated with *S. aureus* for 6 h. COX-2 mRNA levels were determined. (C, D) Cells were transfected with siRNA of scrambled or p38, then treated with *S. aureus* for 24 h. PGE<sub>2</sub>, IL-6, and MMP-9 production and cell migration were measured. (E) Cells were pretreated without or with SB202190, then treated with *S. aureus* for the indicated times. Expression of phospho-p38 MAPK was determined. (F) Cells were treated with *S. aureus* for the indicated times. Expression of phospho-ATF2 was determined. n = 3, \**P* < 0.01, as compared with the cells exposed to *S. aureus* alone (A). #*P* < 0.01, as compared with the cells exposed to *S. aureus* + scrambled siRNA (B, C, D). #*P* < 0.01, as compared with the cells exposed to *S. aureus* alone (E).

### 3.4. *S. aureus* induces COX-2 expression via ERK1/2 in HAECs

ERK1/2 has been shown to regulate COX-2 expression and PGE<sub>2</sub> release [10]. We found that *S. aureus*-induced COX-2 protein and mRNA levels were inhibited by the inhibitor of MEK1/2, U0126 (*P* < 0.01), or siRNA of p42 or p44 (*P* < 0.01) (Fig. 4A and B). *S. aureus*-induced PGE<sub>2</sub>/IL-6/MMP-9 levels and cell migration were also reduced by transfection with siRNA of p42 or p44 (*P* < 0.01) (Fig. 4C and D). Finally, we showed that *S. aureus* induced ERK1/2 phosphorylation in a

time-dependent manner, with a maximal response within 10–15 min (< 3-fold) in these cells, which was reduced by U0126 (*P* < 0.01) (Fig. 4E). Thus, we suggest that *S. aureus* induces COX-2 expression and cell migration via ERK1/2 in HAECs.

### 3.5. *S. aureus* induces COX-2 expression via NF-κB in HAECs

NF-κB has been shown to regulate COX-2 expression and PGE<sub>2</sub> release [10]. We found that *S. aureus*-induced COX-2 protein and mRNA

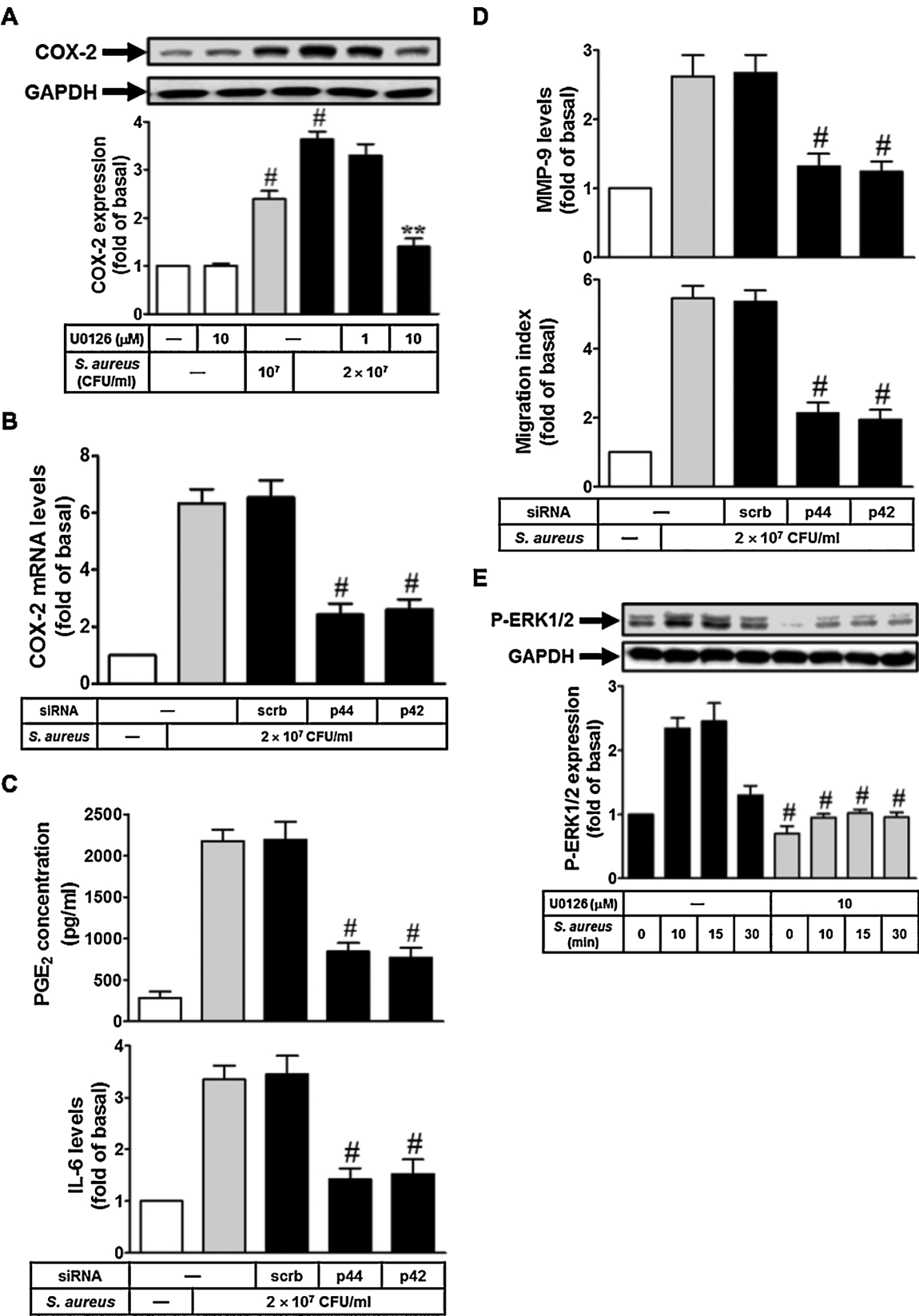


**Fig. 4.** *S. aureus* induces COX-2 expression via ERK1/2. (A) Cells were pretreated with U0126, and then treated with *S. aureus*. COX-2 expression was determined. (B) Cells were transfected with siRNA of scrambled, p44, or p42, and then treated with *S. aureus* for 6 h. COX-2 mRNA levels were determined. (C, D) Cells were transfected with siRNA of scrambled, p44, or p42, and treated with *S. aureus* for 24 h. PGE<sub>2</sub>, IL-6, and MMP-9 production and cell migration were measured. (E) Cells were pretreated without or with U0126, then treated with *S. aureus* for the indicated times. Expression of phospho-ERK1/2 was determined. n = 3, <sup>#</sup>P < 0.01, as compared with the basal level (A). <sup>\*\*</sup>P < 0.01, as compared with the cells exposed to *S. aureus* alone (A). <sup>#</sup>P < 0.01, as compared with the cells exposed to *S. aureus* + scrambled siRNA (B, C, D). <sup>#</sup>P < 0.01, as compared with the cells exposed to *S. aureus* alone (E).



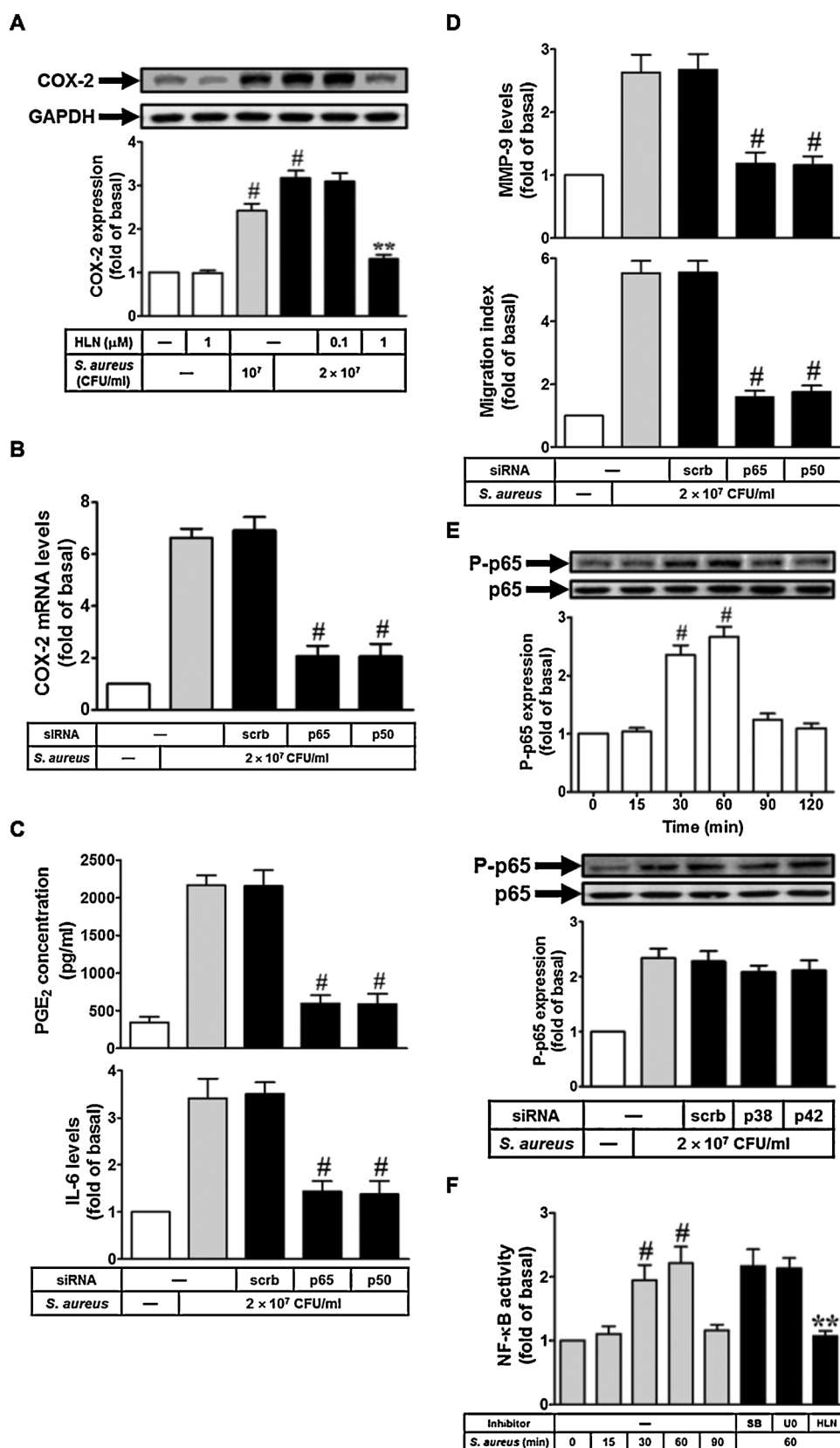


**Fig. 5.** *S. aureus* induces COX-2 expression via NF- $\kappa$ B. (A) Cells were pretreated with HLN, and then treated with *S. aureus*. COX-2 expression was determined. (B) Cells were transfected with siRNA of scrambled, p65, or p50, and then treated with *S. aureus* for 6 h. COX-2 mRNA levels were determined. (C, D) Cells were transfected with siRNA of scrambled, p65, or p50, and then treated with *S. aureus* for 24 h. PGE<sub>2</sub>, IL-6, and MMP-9 production and cell migration were measured. (E) Cells were treated with *S. aureus* for the indicated times or transfected with siRNA of scrambled, p38, or p42, then treated with *S. aureus* for 60 min. Expression of phospho-p65 was determined. (F) Cells were treated with *S. aureus* for the indicated times or pretreated with SB202190, U0126, or HLN, then treated with *S. aureus*. NF- $\kappa$ B activity was determined.  $n = 3$ ,  $^{\#}P < 0.01$ , as compared with the basal level (A, E, F).  $^{**}P < 0.01$ , as compared with the cells exposed to *S. aureus* alone (A, F).  $^{\#}P < 0.01$ , as compared with the cells exposed to *S. aureus* + scrambled siRNA (B, C, D).

levels were inhibited by the inhibitor of NF- $\kappa$ B, (HLN) ( $P < 0.01$ ), or siRNA of p65 or p50 ( $P < 0.01$ ) (Fig. 5A and B). *S. aureus*-induced PGE<sub>2</sub>/IL-6/MMP-9 levels and cell migration were also reduced by transfection with siRNA of p65 or p50 ( $P < 0.01$ ) (Fig. 5C and D). However, we found that *S. aureus* induced NF- $\kappa$ B p65 activation in a

time-dependent manner with a maximal response within 30–60 min ( $< 3$ -fold,  $P < 0.01$ ), which was not reduced by siRNA of p38 or p42 (Fig. 5E). Finally, we showed that *S. aureus* time-dependently induced NF- $\kappa$ B activity ( $< 3$ -fold,  $P < 0.01$ ), which was reduced by HLN ( $P < 0.01$ ), but not by SB202190 or U0126 (Fig. 5F). Taken together,

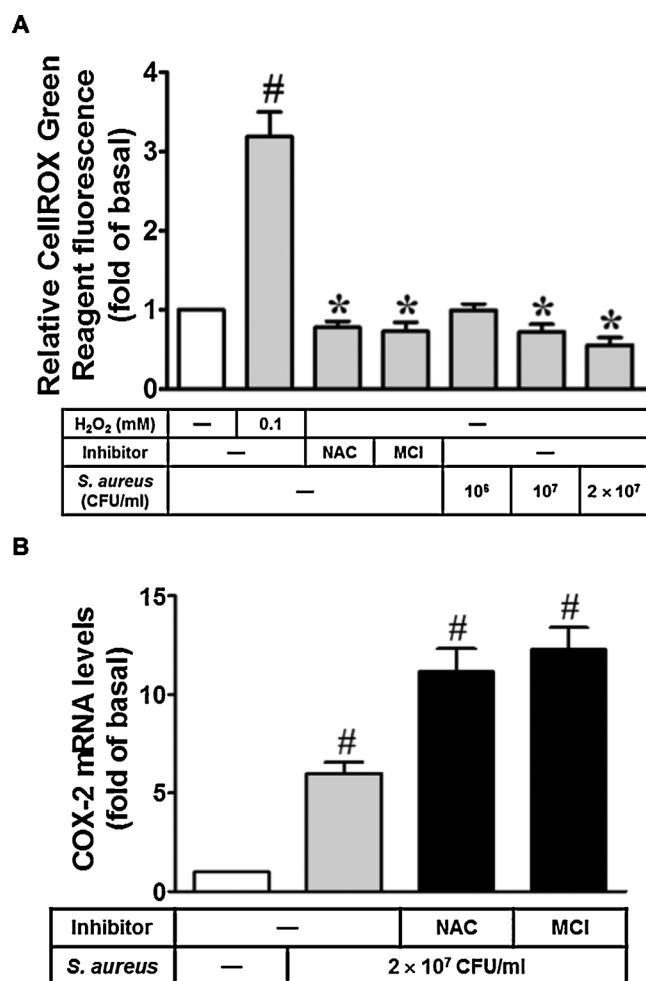


Fig. 6. *S. aureus* reduces ROS generation in HAECs. (A) Cells were treated with H<sub>2</sub>O<sub>2</sub>, NAC, MCI-186, or *S. aureus* for 2 h. ROS generation was determined. (B) Cells were pretreated without or with NAC or MCI-186 for 2 h, and then treated with *S. aureus* for 6 h. COX-2 mRNA levels were determined. n = 5, \*P < 0.05; #P < 0.01, as compared with the basal level.

these data suggest that *S. aureus* induces COX-2 expression via p38 MAPK- and ERK1/2-independent NF- $\kappa$ B activation in HAECs.

### 3.6. *S. aureus* reduces ROS generation, and then promotes infection in HAECs

ROS are deadly weapons used by phagocytes and other cell types against pathogens [25]. On the other hand, ROS can kill pathogens directly by causing oxidative damage to biocompounds or indirectly by stimulating pathogen elimination through various nonoxidative mechanisms [25]. Thus, one would expect that the inhibition of ROS production would promote infection. Increasing evidence indicates that in certain infections, antioxidants decrease and prooxidants increase pathogen burden [26]. Interestingly, in this study, we found that *S. aureus* (2 × 10<sup>7</sup> CFU/ml and 10<sup>7</sup> CFU/ml) markedly decreased intracellular ROS generation in these cells (P < 0.05) (Fig. 6A). On the other hand, the free radical scavenger (MCI-186) or antioxidant (NAC) further enhanced *S. aureus*-induced COX-2 mRNA levels (< 15-fold, P < 0.01) (Fig. 6B). Taken together, the results suggest that *S. aureus* decreases ROS generation and then promotes inflammatory responses.

### 3.7. *S. aureus* induces COX-2 expression and aorta inflammation in rats

In an in vivo study, Sprague Dawley rats were treated with *S. aureus*

(2 × 10<sup>7</sup> CFU/rat) and killed after 48 h. Preparation of aorta tissues was analyzed with Western blot and real-time PCR to determine the levels of COX-2 and COX-1 protein and mRNA, respectively. As shown in Fig. 7A, we found that *S. aureus* induced COX-2, but not COX-1 protein (< 6-fold, P < 0.01) and mRNA levels (< 20-fold, P < 0.01), in the aorta tissues. The most extensively studied biomarker of inflammation in cardiovascular diseases is CRP [27]. MPO is one of the most studied molecules during the last decade that plays a crucial role in inflammation at the cellular level [28]. MPO-catalyzed reactions have been ascribed to potentially proatherogenic biological activities throughout the evolution of cardiovascular disease [28]. Here, we also showed that *S. aureus* induced plasma MPO (< 5-fold, P < 0.01), serum CRP (< 8-fold, P < 0.01), IL-6 (< 10-fold, P < 0.01), and TNF- $\alpha$  (< 8-fold, P < 0.01) (Fig. 7B). Finally, Sprague Dawley rats were given one dose of NAC, MCI-186, U0126, SB202190, or HLN intraperitoneally 2 h before *S. aureus* (2 × 10<sup>7</sup> CFU/rat) treatment and killed after 48 h. Preparation of aorta tissues was analyzed with real-time PCR to determine the levels of COX-2 mRNA. We showed that *S. aureus* induced COX-2 mRNA levels (< 15-fold), which were reduced by U0126, SB202190, or HLN (P < 0.01) (Fig. 7C). However, NAC or MCI-186 further enhanced *S. aureus*-induced COX-2 mRNA levels (P < 0.05) (Fig. 7C).

## 4. Discussion

*S. aureus* is a major pathogen responsible for a variety of diseases, ranging from minor skin infections to life-threatening conditions, such as sepsis. Endovascular *S. aureus* infections are among the most difficult to treat, which probably is due to the complex pathogenesis involving a numerous host and bacterial factors [29]. Cell wall-associated and secreted proteins and cell-wall components, such as peptidoglycan, have been shown to be inflammatory, and these staphylococcal components may contribute to sepsis [21]. Several lines of evidence suggest that high levels of PGE<sub>2</sub>, synthesized by COX-2, are also involved in inflammatory responses [10]. However, little has been known about the molecular mechanisms involved in *S. aureus*-induced aorta inflammation. Here, we established for the first time that in HAECs, *S. aureus* decreases ROS generation and then promotes inflammatory responses. Moreover, COX-2/PGE<sub>2</sub> up-regulation can further promote IL-6/MMP-9-dependent cell migration. This study provided a better understanding of the inflammatory mechanisms and a putative therapeutic strategy for endovascular *S. aureus* infections.

TLRs are transmembrane proteins that detect invading pathogens by binding conserved, microbially derived molecules and that induce signaling cascades for proinflammatory gene expression [30]. TLR2 has been shown to function as the transmembrane component involved in the detection of staphylococcal lipoteichoic acid and phenol-soluble modulins, and is involved in the synthesis of inflammatory cytokines by monocytes/macrophages in response to these components [21]. Indeed, we documented that *S. aureus* induced COX-2 expression via TLR2, but not TLR4 in HAECs. *S. aureus* may also promote inflammatory responses via the up-regulation of TLR2 expression. IL-6 is the predominant mediator of the acute-phase response, which is an innate immune mechanism triggered by inflammation [19]. Previous studies have shown a positive association between endogenous PGE<sub>2</sub> production and IL-6 synthesis [31]. IL-6 has been shown to regulate cell migration in various cell types [20]. Here, we demonstrated in HAECs that *S. aureus* induced cell migration through a COX-2/PGE<sub>2</sub>/MMP-9 pathway. The MAPKs family consists of three major members: ERK1/2, p38 MAPK, and JNK [32]. MAPKs are important for intracellular signal transduction and play critical roles in regulating inflammatory responses [9]. In this study, we proved that *S. aureus* induced COX-2/PGE<sub>2</sub>/IL-6/MMP-9 expression via ERK1/2 and p38 MAPK by using siRNA of p42, p44, or p38. However, transfection with JNK1 or JNK2 siRNA had no effects on *S. aureus*-induced COX-2/PGE<sub>2</sub>/IL-6/MMP-9 expression (data not shown). Thus, we suggest that *S. aureus* induced COX-2/PGE<sub>2</sub>/IL-6/MMP-9-

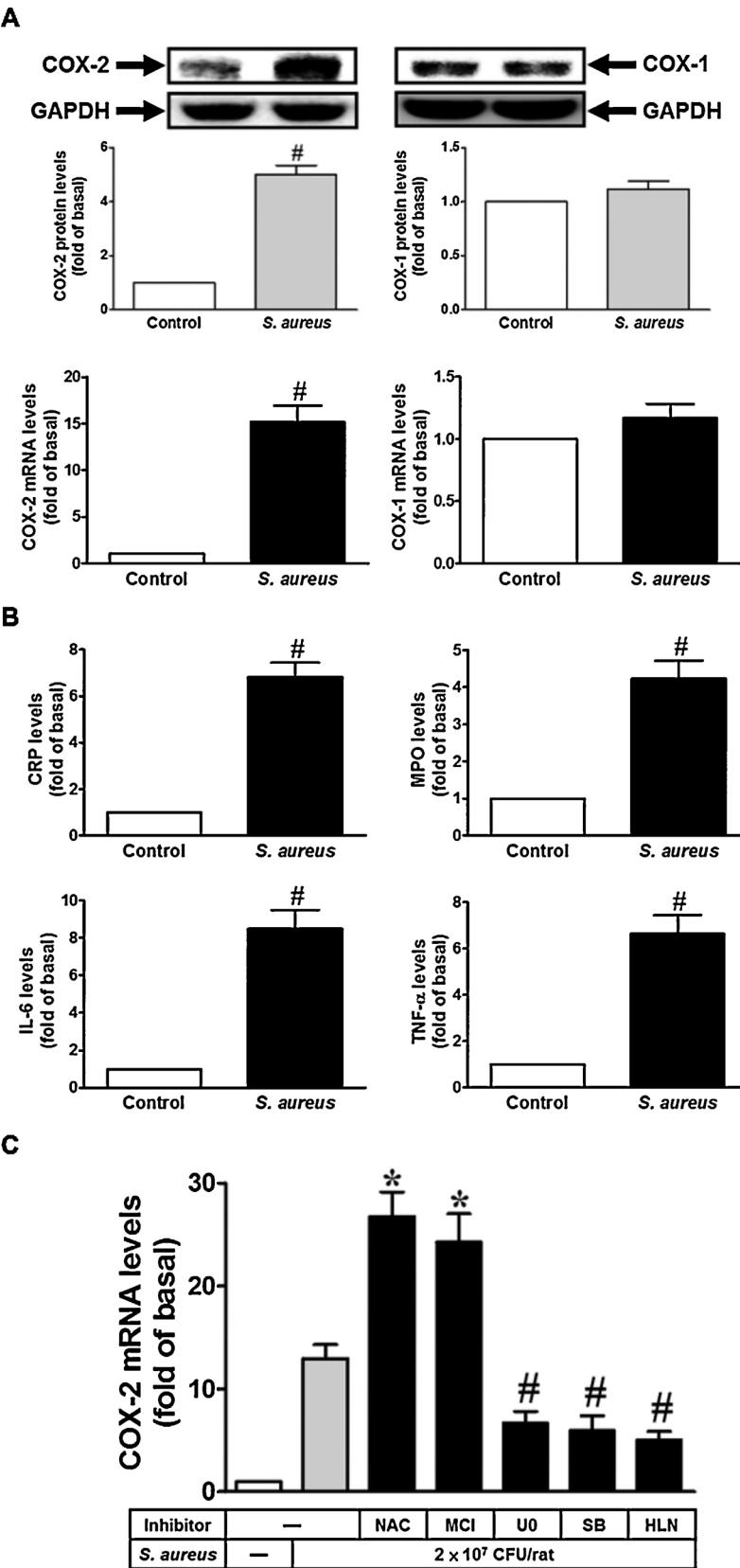


**Fig. 7.** *S. aureus* induces COX-2 expression and aorta inflammation in rats. (A) Rats were treated with *S. aureus* ( $2 \times 10^7$  CFU/rat), then killed after 48 h. Preparation of aorta tissues was analyzed by Western blot and real-time PCR to determine the levels of COX-2 and COX-1 protein and mRNA, respectively. (B) Rats were treated with *S. aureus* ( $2 \times 10^7$  CFU/rat), then killed after 48 h. Levels of CRP, MPO, IL-6, and TNF- $\alpha$  were measured. (C) Rats were given one dose of NAC, MCI-186, U0126, SB202190, or HLN intraperitoneally 2 h before *S. aureus* ( $2 \times 10^7$  CFU/rat) treatment, then killed after 48 h. Preparation of aorta tissues was analyzed by real-time PCR to determine the levels of COX-2 mRNA.  $n = 7-8$ ,  $^{\#}P < 0.01$ , as compared with the basal level (A, B).  $^*P < 0.05$ ;  $^{\#}P < 0.01$ , as compared with the rats exposed to *S. aureus* alone (C).

dependent cell migration through ERK1/2 and p38 MAPK, but not through JNK, in HAECs. Although in various cell types, an elevation in COX-2/PGE<sub>2</sub> levels is often associated with an increase in ERK1/2, JNK, or p38 MAPK activation, our results show for the first time a novel role of ERK1/2 or p38MAPK in *S. aureus*-induced COX-2/PGE<sub>2</sub>/IL-6/MMP-

9-dependent cell migration in HAECs.

The transcription factor NF- $\kappa$ B is a key regulator of immune responses and inflammation through the induction of numerous genes, including those coding for cytokines, chemokines, and adhesion molecules [33]. Moreover, NF- $\kappa$ B is one of the major mediators of the

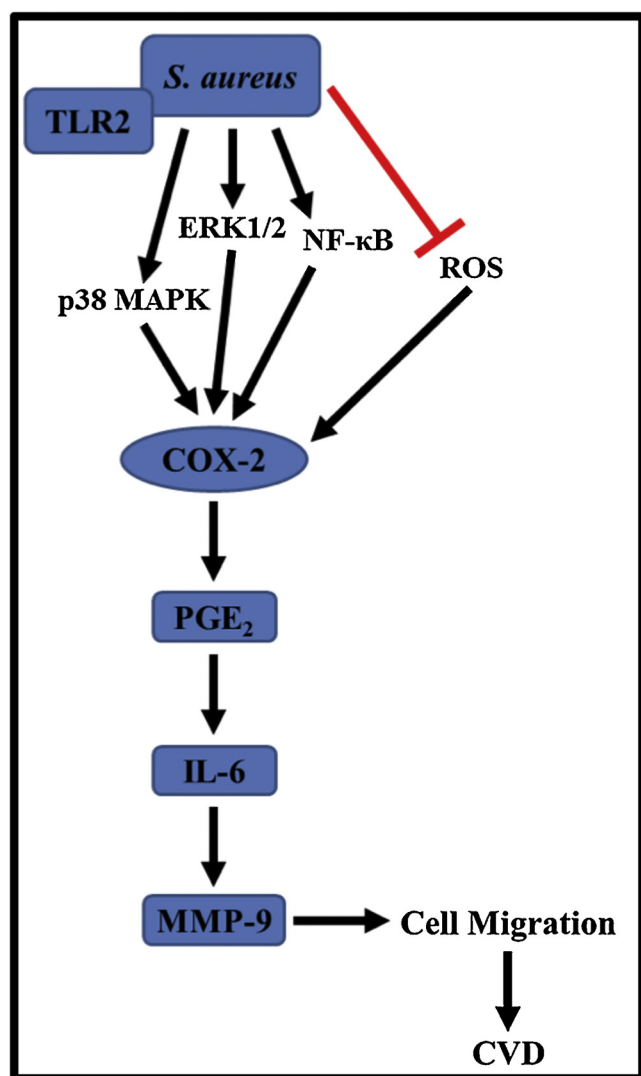


**Fig. 8.** Schematic diagram illustrating the proposed signaling pathway involved in *S. aureus*-induced COX-2/PGE<sub>2</sub>/IL-6/MMP-9-dependent cell migration. In HAECs, *S. aureus* induces COX-2 expression via the activation of p38 MAPK, ERK1/2, and NF-κB and reduction of ROS generation. Moreover, COX-2/PGE<sub>2</sub> can further promote IL-6/MMP-9-dependent cell migration. CVD, cardiovascular disease.

intracellular functions of LTA [9]. This activity is confirmed by our observation that *S. aureus*-induced COX-2/PGE<sub>2</sub>/IL-6/MMP-9 expression was decreased by transfection with p65 or p50 siRNA. NF-κB dimers containing RelA or c-Rel are retained in the cytoplasm through interaction with the inhibitors of NF-κB (IκBs). In response to various stimuli, IκBs are phosphorylated by the activated IκB kinase (IKK) complex, followed by rapid ubiquitin-dependent degradation by the 26S proteasome [34]. This activity allows NF-κB dimers to translocate to the nucleus, where they stimulate expression of target genes. In this study, we found also that *S. aureus* markedly stimulated p65 phosphorylation and NF-κB activity in HAECs. However, p38 MAPK and ERK1/2 were not involved in *S. aureus*-induced NF-κB activation in these cells. A major challenge for future research is elucidation of the mechanisms involved in regulation of NF-κB activation and the physiological relevance of NF-κB-targeted genes in various cells. This information may lead to the development of therapeutic inhibitors that selectively block NF-κB-regulated inflammatory responses.

ROS are generated by living organisms as a result of normal cellular metabolism and environmental factors. ROS are highly reactive molecules that can damage cell structures and alter their functions. The shift

in the balance between oxidants and antioxidants in favor of oxidants is termed “oxidative stress” [35]. Mediation of reducing and oxidizing (redox) state is critical for cell viability, activation, proliferation, and organ function [35]. Nonetheless, manipulation of oxidant inhibitors and antioxidants are not always beneficial for the treatment of diseases. Therefore, a lack of necessary ROS may be detrimental to cells, and redox imbalance, with an excess of oxidizing or reducing equivalents, creates oxidative stress or reductive stress states, (redox stress states) that are harmful to biological systems [12]. In addition, ROS are deadly weapons used by phagocytes and other cell types, such as lung epithelial cells, against pathogens [25]. ROS can kill pathogens directly by causing oxidative damage to biocompounds or indirectly by stimulating pathogen elimination by various nonoxidative mechanisms. Thus, one would expect that the inhibition of ROS production would promote infection [25]. Aerobic organisms have integrated antioxidant systems, which include enzymatic and non-enzymatic antioxidants that are usually effective in blocking the harmful effects of ROS [13]. Interestingly, in HAECs, *S. aureus* markedly decreased ROS generation. Thus, we suggest that *S. aureus* promoted inflammatory responses via the inhibition of ROS production in HAECs. In the future, we will investigate the relationship between ROS and MAPKs or NF-κB in *S. aureus*-treated HAECs.

The most extensively studied biomarker of inflammation in cardiovascular diseases is CRP [27]. MPO is one of the most widely studied during the last decade molecule that plays a crucial role in inflammation in the cellular level [28]. MPO-catalyzed reactions have been attributed to potentially proatherogenic biological activities throughout the evolution of cardiovascular disease [28]. IL-6 is a soluble mediator with a pleiotropic effect on inflammation, immune response, and hematopoiesis. IL-6 functions as a mediator for notification of some emergent event [36]. IL-6 is generated in an infectious lesion and sends out a warning signal to the entire body [36]. The signature of exogenous pathogens, known as pathogen-associated molecular patterns, is recognized in the infected lesion by pathogen-recognition receptors (PRRs) of immune cells, such as monocytes and macrophages [37]. These PRRs comprise TLRs, retinoic acid-inducible gene-1-like receptors, nucleotide-binding oligomerization domain-like receptors, and DNA receptors [37]. They stimulate a range of signaling pathways, including NF-κB, and enhance the transcription of the mRNA of inflammatory cytokines, such as IL-6, tumor necrosis factor TNF-α, and IL-1β. TNF-α and IL-1β also activate transcription factors to produce IL-6 [38]. Indeed, in an in vivo study, we also showed that *S. aureus* induced levels of plasma MPO and serum CRP, IL-6, and TNF-α. Interestingly, pretreatment with the free radical scavenger (MCI-186) or antioxidant (NAC) enhanced *S. aureus*-induced COX-2 mRNA levels in the aorta tissues of rats. This response demonstrated that *S. aureus* promoted infection via the inhibition of ROS production and oxidative damage.

In summary, as depicted in Fig. 8, our results demonstrate that in HAECs, *S. aureus* induces COX-2 expression via the activation of p38 MAPK, ERK1/2, and NF-κB and reduced ROS generation. Moreover, COX-2/PGE<sub>2</sub> can further promote IL-6/MMP-9-dependent cell migration. These results indicate a role for HAECs as inflammatory cells involved in the production of chemical mediators that may contribute to the inflammatory response seen in cardiovascular diseases.

#### Conflict of interest

The authors declare no conflict of interest.

#### Acknowledgment

This work was supported by the Chang Gung Medical Research Foundation, grant number CMRPGMF0022 and CMRPGMF0023; the China Medical University, grant number CMU106-S-14 and CMU105-S-46.



## References

- [1] M.Z. David, R.S. Daum, Treatment of *Staphylococcus aureus* Infections, Curr. Top. Microbiol. Immunol. 409 (2017) 325–383.
- [2] H. Asgeirsson, A. Thalme, M. Kristjansson, O. Weiland, Incidence and outcome of *Staphylococcus aureus* endocarditis—a 10-year single-centre northern European experience, Clin. Microbiol. Infect. 21 (2015) 772–778.
- [3] S.W. Kerrigan, C. McDonnell, Dysregulation of the endothelium following *Staphylococcus aureus* infection, Biochem. Soc. Trans. 43 (2015) 715–719.
- [4] I. Venza, M. Visalli, M. Cucinotta, D. Teti, M. Venza, NOD2 triggers PGE<sub>2</sub> synthesis leading to IL-8 activation in *Staphylococcus aureus*-infected human conjunctival epithelial cells, Biochem. Biophys. Res. Commun. 440 (2013) 551–557.
- [5] C. Klemm, C. Bruchhagen, A. van Krüchten, S. Niemann, B. Löffler, G. Peters, S. Ludwig, C. Ehrhardt, Mitogen-activated protein kinases (MAPKs) regulate IL-6 over-production during concomitant influenza virus and *Staphylococcus aureus* infection, Sci. Rep. 7 (2017) 42473–42487.
- [6] K.Y. Deleon-Pennell, R. Altara, A. Yabluchanskiy, A. Modesti, M.L. Lindsey, The circular relationship between matrix metalloproteinase-9 and inflammation following myocardial infarction, IUBMB Life 67 (2015) 611–618.
- [7] K.F. Jiang, G. Zhao, G.Z. Deng, H.C. Wu, N.N. Yin, X.Y. Chen, C.W. Qiu, X.L. Peng, Polydatin ameliorates *Staphylococcus aureus*-induced mastitis in mice via inhibiting TLR2-mediated activation of the p38 MAPK/NF-κB pathway, Acta Pharmacol. Sin. 38 (2017) 211–222.
- [8] H. Wang, C. Bi, Y. Wang, J. Sun, X. Meng, J. Li, Selenium ameliorates *Staphylococcus aureus*-induced inflammation in bovine mammary epithelial cells by inhibiting activation of TLR2, NF-κB and MAPK signaling pathways, BMC Vet. Res. 14 (2018) 197–204.
- [9] I.T. Lee, C.M. Yang, Inflammatory signalings involved in airway and pulmonary diseases, Mediators Inflamm. (2013) 791231–791242 2013.
- [10] I.T. Lee, C.W. Lee, W.H. Tung, S.W. Wang, C.C. Lin, J.C. Shu, C.M. Yang, Cooperation of TLR2 with MyD88, PI3K, and Rac1 in lipoteichoic acid-induced cPLA<sub>2</sub>/COX-2-dependent airway inflammatory responses, Am. J. Pathol. 176 (2010) 1671–1684.
- [11] K.L. Siu, Q. Li, Y. Zhang, J. Guo, J.Y. Youn, J. Du, H. Cai, NOX isoforms in the development of abdominal aortic aneurysm, Redox Biol. 11 (2017) 118–125.
- [12] D.E. Handy, J. Loscalzo, Responses to reductive stress in the cardiovascular system, Free Radic. Biol. Med. 109 (2017) 114–124.
- [13] X. Zhao, K. Drlica, Reactive oxygen species and the bacterial response to lethal stress, Curr. Opin. Microbiol. 21 (2014) 1–6.
- [14] R. Tazawa, X.M. Xu, K.K. Wu, L.H. Wang, Characterization of the genomic structure, chromosomal location and promoter of human prostaglandin H synthase-2 gene, Biochem. Biophys. Res. Commun. 203 (1994) 190–199.
- [15] W.J. Lukiw, R.P. Pelaez, J. Martinez, N.G. Bazan, Budesonide epimer R or dexamethasone selectively inhibit platelet-activating factor-induced or interleukin 1β-induced DNA binding activity of cis-acting transcription factors and cyclooxygenase-2 gene expression in human epidermal keratinocytes, Proc. Natl. Acad. Sci. U. S. A. 95 (1998) 3914–3919.
- [16] N.G. Bazan, W.J. Lukiw, Cyclooxygenase-2 and presenilin-1 gene expression induced by interleukin-1β and amyloid β42 peptide is potentiated by hypoxia in primary human neural cells, J. Biol. Chem. 277 (2002) 30359–30367.
- [17] Y. Wang, B. Ren, X. Zhou, S. Liu, Y. Zhou, B. Li, Y. Jiang, M. Li, M. Feng, L. Cheng, Growth and adherence of *Staphylococcus aureus* were enhanced through the PGE<sub>2</sub> produced by the activated COX-2/PGE<sub>2</sub> pathway of infected oral epithelial cells, PLoS ONE 12 (2017) e0177166–e0177186.
- [18] S.P. Didion, Cellular and oxidative mechanisms associated with interleukin-6 signaling in the vasculature, Int. J. Mol. Sci. 18 (2017) 2563–2585.
- [19] C.C. Lin, I.T. Lee, Y.L. Yang, C.W. Lee, Y.R. Kou, C.M. Yang, Induction of COX-2/PGE<sub>2</sub>/IL-6 is crucial for cigarette smoke extract-induced airway inflammation: role of TLR4-dependent NADPH oxidase activation, Free Radic. Biol. Med. 48 (2010) 240–254.
- [20] W. Chen, T. Xia, D. Wang, B. Huang, P. Zhao, J. Wang, X. Qu, X. Li, Human astrocytes secrete IL-6 to promote glioma migration and invasion through upregulation of cytomembrane MMP14, Oncotarget 7 (2016) 62425–62438.
- [21] G. Zhao, K. Jiang, H. Wu, C. Qiu, G. Deng, X. Peng, Polydatin reduces *Staphylococcus aureus* lipoteichoic acid-induced injury by attenuating reactive oxygen species generation and TLR2-NFκB signaling, J. Cell. Mol. Med. 21 (2017) 2796–2808.
- [22] F. Cochet, F. Peri, The role of carbohydrates in the lipopolysaccharide (LPS)/Toll-like receptor 4 (TLR4) signaling, Int. J. Mol. Sci. 18 (2017) 2318–2333.
- [23] M.H. Tsai, L.F. Hsu, C.W. Lee, Y.C. Chiang, M.H. Lee, J.M. How, C.M. Wu, C.L. Huang, I.T. Lee, Resveratrol inhibits urban particulate matter-induced COX-2/PGE<sub>2</sub> release in human fibroblast-like synoviocytes via the inhibition of activation of NADPH oxidase/ROS/NF-κB, Int. J. Biochem. Cell Biol. 88 (2017) 113–123.
- [24] H. Zhou, L. Cai, X. Zhang, A. Li, Y. Miao, Q. Li, X. Qiu, E. Wang, ARHGEF39 promotes tumor progression via activation of Rac1/P38 MAPK/ATF2 signaling and predicts poor prognosis in non-small cell lung cancer patients, Lab. Invest. 98 (2017) 670–681.
- [25] C.N. Paiva, M.T. Bozza, Are reactive oxygen species always detrimental to pathogens? Antioxid. Redox Signal. 20 (2014) 1000–1037.
- [26] A. Rahal, A. Kumar, V. Singh, B. Yadav, R. Tiwari, S. Chakraborty, K. Dhama, Oxidative stress, prooxidants, and antioxidants: the interplay, Biomed Res. Int. (2014) 7612642014.
- [27] S. Li, Y. Jiao, H. Wang, Q. Shang, F. Lu, L. Huang, J. Liu, H. Xu, K. Chen, Sodium tanshinone IIA sulfate adjunct therapy reduces high-sensitivity C-reactive protein level in coronary artery disease patients: a randomized controlled trial, Sci. Rep. 7 (2017) 17451.
- [28] Y. Aratani, Myeloperoxidase: its role for host defense, inflammation, and neutrophil function, Arch. Biochem. Biophys. 640 (2018) 47–52.
- [29] B. Sinha, M. Herrmann, Mechanism and consequences of invasion of endothelial cells by *Staphylococcus aureus*, Thromb. Haemost. 94 (2005) 266–277.
- [30] M. Nemati, T. Larussa, H. Khorramdelazad, M. Mahmoodi, A. Jafarzadeh, Toll-like receptor 2: an important immunomodulatory molecule during *Helicobacter pylori* infection, Life Sci. 178 (2017) 17–29.
- [31] D. Che, S. Zhang, Z. Jing, L. Shang, S. Jin, F. Liu, J. Shen, Y. Li, J. Hu, Q. Meng, Y. Yu, Macrophages induce EMT to promote invasion of lung cancer cells through the IL-6-mediated COX-2/PGE<sub>2</sub>/β-catenin signalling pathway, Mol. Immunol. 90 (2017) 197–210.
- [32] B. Yao, S. Wang, P. Xiao, Q. Wang, Y. Hea, Y. Zhang, MAPK signaling pathways in eye wounds: multifunction and cooperation, Exp. Cell Res. 359 (2017) 10–16.
- [33] L. Chen, H. Deng, H. Cui, J. Fang, Z. Zuo, J. Deng, Y. Li, X. Wang, L. Zhao, Inflammatory responses and inflammation-associated diseases in organs, Oncotarget 9 (2017) 7204–7218.
- [34] T. Liu, L. Zhang, D. Joo, S.C. Sun, NF-κB signaling in inflammation, Signal Transduct. Target. Ther. 2 (2017) e17023–e17031.
- [35] A.B. García-Redondo, A. Aguado, A.M. Briones, M. Salas, NADPH oxidases and vascular remodeling in cardiovascular diseases, Pharmacol. Res. 114 (2016) 110–120.
- [36] M. Mesquida, B. Molins, V. Llorenç, M.S. de la Maza, A. Adán, Targeting interleukin-6 in autoimmune uveitis, Autoimmun. Rev. 16 (2017) 1079–1089.
- [37] S. Tarte, O. Takeuchi, Pathogen recognition and Toll-like receptor targeted therapeutics in innate immune cells, Int. Rev. Immunol. 36 (2017) 57–73.
- [38] T. Tanaka, M. Narazaki, T. Kishimoto, Anti-interleukin-6 receptor antibody, tocilizumab, for the treatment of autoimmune diseases, FEBS Lett. 585 (2011) 3699–3709.

## Regular Article

# Echinacoside, an Active Constituent of *Cistanche Herba*, Exerts a Neuroprotective Effect in a Kainic Acid Rat Model by Inhibiting Inflammatory Processes and Activating the Akt/GSK3 $\beta$ Pathway

Cheng Wei Lu,<sup>a,b</sup> Hsi Lung Hsieh,<sup>c,d</sup> Tzu Yu Lin,<sup>a,b</sup> Ting Yang Hsieh,<sup>e</sup> Shu Kuei Huang,<sup>a</sup> and Su Jane Wang<sup>\*f,g</sup>

<sup>a</sup>Department of Anesthesiology, Far-Eastern Memorial Hospital; New Taipei 22060, Taiwan; <sup>b</sup>Department of Mechanical Engineering, Yuan Ze University; Taoyuan 320, Taiwan; <sup>c</sup>Department of Nursing, Division of Basic Medical Sciences, Research Center for Chinese Herbal Medicine, and Graduate Institute of Health Industry Technology, Chang Gung University of Science and Technology; Taoyuan 33303, Taiwan; <sup>d</sup>Department of Neurology, Chang Gung Memorial Hospital; Taoyuan 33303, Taiwan; <sup>e</sup>P.H.D. Program in Nutrition & Food Science, Fu Jen Catholic University; New Taipei, Taiwan; <sup>f</sup>School of Medicine, Fu Jen Catholic University; New Taipei 24205, Taiwan; and <sup>g</sup>Research Center for Chinese Herbal Medicine, College of Human Ecology, Chang Gung University of Science and Technology; Taoyuan 33303, Taiwan.

Received May 30, 2018; accepted August 29, 2018; advance publication released online September 8, 2018

Echinacoside is a major compound of *Cistanche Herb* and has glutamate release-inhibiting activity in the brain. Given the involvement of excitotoxicity caused by massive glutamate in the pathophysiology of epilepsy, we explored the antiepileptic effect of echinacoside on kainic acid-induced seizures in rats. The rats were intraperitoneally administered echinacoside for 30 min prior to intraperitoneal injection with kainic acid. The results showed that kainic acid induced seizure-like behavioral patterns, increased glutamate concentrations, caused neuronal loss and microglial activation, and stimulated proinflammatory cytokine gene expression in the hippocampus. These kainic acid-induced alternations were found to be attenuated by echinacoside pretreatment. Furthermore, decreased Akt and glycogen synthase kinase 3 $\beta$  (GSK3 $\beta$ ) phosphorylation as well as Bcl-2 expression in the hippocampus was reversed by the echinacoside pretreatment. These results demonstrate that echinacoside exerts its antiepileptic and neuroprotective actions in a kainic acid rat model through suppressing inflammatory response and activating the Akt/GSK3 $\beta$  signaling. Therefore, the present study suggests that echinacoside is the potentially useful in the prevention of epilepsy.

**Key words** echinacoside; kainic acid; epilepsy; neuroprotective effect; hippocampus

Epilepsy is a prevalent brain disorder worldwide. It affects more than 65 million people, nearly 1% of the world's population.<sup>1)</sup> Synthetic antiepileptic drugs are widely available in the pharmaceutical market; however, these drugs are only effective in 60–70% of patients and have adverse side effects.<sup>2–4)</sup> Thus, there is an unmet need to search a drug with more efficacious and safer. Medicinal plants represent a potential source of such compounds.<sup>5,6)</sup>

In traditional Chinese herbal medicine, *Cistanche Herba* has long been used for the treatment of epilepsy.<sup>7,8)</sup> Echinacoside is a major component of *Cistanche Herba*<sup>9)</sup> and has many pharmacological properties, such as antioxidant, anti-inflammatory, antineoplastic, hepatoprotective, and immune modulatory activity.<sup>10,11)</sup> Moreover, it has been reported that echinacoside can enter the brain and elicit neuroprotection.<sup>12–16)</sup> We previously demonstrated that echinacoside reduces glutamate release in rat cerebrocortical nerve terminals.<sup>17)</sup> Because glutamate is a major excitatory neurotransmitter in the mammalian brain and plays a crucial role in the pathophysiology of epilepsy,<sup>18,19)</sup> we suggested that echinacoside has antiepileptic activity. To elucidate this hypothesis, a kainic acid rat model was used in this study.

Kainic acid is a glutamate derivative and its single systemic injection to rodents results in seizures, neuroinflammation, and neuronal degeneration or death on selective population of neurons in the brain.<sup>20–22)</sup> These pathological alternations are similar to human temporal lobe epilepsy.<sup>23,24)</sup> Administering

kainic acid to rodents is generally considered to induce an adequate model of epilepsy. To date, no study has investigated the antiepileptic and neuroprotective properties of echinacoside in a kainic acid-injected animal model. Therefore, our study aims to evaluate the effect and its possible mechanism of echinacoside preadministration in kainic acid-treated rats.

## MATERIALS AND METHODS

**Animals and Seizure Activity** Male Sprague–Dawley rats (BioLASCO, Taipei, Taiwan) weighing 150–200 g were used throughout the study. The rats were randomly assigned to four groups as follows: i) Group 1: dimethylsulfoxide-treated group (control); ii) Group 2: kainic acid-treated group; iii) Group 3: echinacoside 10 mg/kg+kainic acid group; iv) Group 4: echinacoside 50 mg/kg+kainic acid group. Echinacoside (ChemFaces, Wuhan, P.R.C.) was injected (intraperitoneal administration) 30 min prior to kainic acid (15 mg/kg) intraperitoneal injection. Seizure activity was rated during a 4 h period after kainic acid injection according to the Racine's scale.<sup>25)</sup> The dose and schedule of administration were chosen on the basis of previous studies.<sup>22,26,27)</sup> The experiments on animals were approved by the Institutional Animal Care and Use Committee at the Fu Jen Catholic University, and carried out in accordance with the protocols issued, which followed National Institutes of Health Guide for the Care and Use of Laboratory (NAC 2011).

\* To whom correspondence should be addressed. e-mail: med0003@mail.fju.edu.tw

**Glutamate Levels Determination** Four hours after the kainic acid treatment, the rats were sacrificed by decapitation. The whole brain was dissected and the hippocampus of each rat was collected for analysis. The glutamate concentration of brain hippocampus tissue was determined according to the methods described by previous studies.<sup>28,29)</sup>

**Neutral Red and Fluoro-Jade B Staining** Three days after the kainic acid injection, rats were anesthetized using chloral hydrate (650 mg/kg) and perfused transcardially with fixative solution containing 4% paraformaldehyde in 0.1 M phosphate buffer solution (PBS, pH 7.4). Brains were removed immediately after perfusion and stored in 4% paraformaldehyde overnight at 4°C. After post-fixation, the brains were immersed with 30% sucrose at 4°C for 24 h. The specimens were frozen rapidly and 30- $\mu$ m-thick sections were cut by using a frozen microtome. Free-floating sections were stained with neutral red (Sigma-Aldrich, St. Louis, MO, U.S.A.) and Fluoro-Jade B (Millipore, CA, U.S.A.). Fluoro-Jade B-positive cells in the CA3 region of hippocampus was determined as previously described.<sup>30,31)</sup>

**Immunohistochemistry** The sections were washed with 0.1 M PBS and blocked with 0.5% normal goat serum in 0.1 M PBS for 1 h at room temperature. Primary antibody (mouse monoclonal anti-OX-42 antibody, 1:1000; AbD Serotec, Oxford, U.K.) incubation was performed two overnight at 4°C. After repeated washes with PBS, the sections were incubated with biotinylated anti-mouse immunoglobulin G (IgG) (1:200) for 90 min, treated with the avidin-biotin complex (ABC) solution (1:1000) for 1 h at room temperature, and reacted with 0.025% 3,3'-diaminobenzidine and 0.0025% H<sub>2</sub>O<sub>2</sub> until the desired stain intensity was achieved. Sections were mounted on slides using standard protocols. The stained slides were examined and imaged under a microscope (Olympus, Tokyo, Japan).<sup>31)</sup> Analysis of microglial cell body and process length was carried out with ImageJ.<sup>32)</sup>

**Transmission Electron Microscopy** Transmission electron microscopy was performed as previously described.<sup>33)</sup> Briefly, the CA3 region of hippocampus was removed and fixed in a buffer containing 4% paraformaldehyde and 2.5% glutaraldehyde at 4°C for 24–36 h. After washes with PBS, CA3 regions were postfixed in 1% osmium tetroxide for 2 h, dehydrated with ethanol, and embedded in epoxy resin. Ultrathin sections (70 nm) were prepared by using an ultramicrotome (EM UC7, Leica Microsystems, Wetzlar, Germany). The sections were stained with uranyl acetate and lead citrate, and observed through transmission electron microscopy (Model JEM-1400, JEOL Ltd., Tokyo, Japan).

**Quantitative Real-Time PCR** RNA extraction and real-time quantitative PCR were performed as previously described.<sup>34,35)</sup> Total RNA was extracted from the hippocampus using *mirVana*<sup>TM</sup> miRNA Isolation Kit (Life Technologies, Grand Island, NY, U.S.A.) following the manufacturer's protocol. Genomic DNA was removed by incubation with deoxyribonuclease (DNase) I. The cDNA was synthesized by (GoScript reverse transcription system kit; Promega, Madison, WI, U.S.A.) and used for the SYBR Green (Roche Diagnostics, Mannheim, Germany) quantitative real-time PCR amplification with specific primers using the LightCycler 480 System (Roche Diagnostics). The protocol consisted of an initial denaturation step at 95°C for 3 min, followed by 45 cycles of denaturing at 95°C for 10 s, annealing at 56°C for 30 s. The

mRNA levels of each target gene were normalized to that of glyceraldehyde-3-phosphate dehydrogenase (GAPDH) mRNA. Fold-induction was calculated using the 2<sup>- $\Delta\Delta$ CT</sup> method as described in a previous study.<sup>34)</sup>

**Immunoblotting** Twenty micrograms of protein extracts from the hippocampi were separated by 10% sodium dodecyl sulphate-polyacrylamide gel electrophoresis (SDS-PAGE) followed by electrophoretic transfer onto polyvinylidene difluoride (PVDF) membrane. Membrane was blocked using 5% skimmed milk for 1 h at room temperature and incubated with the appropriate antibodies in 1% skimmed milk overnight at 4°C, followed by incubation with a secondary antibody for 1 h. Primary antibodies were rabbit monoclonal antibodies directed against Akt (1:2000), pAkt<sub>Ser473</sub> (1:2000), glycogen synthase kinase 3 $\beta$  (GSK3 $\beta$ ) (1:2000), pGSK3 $\beta$ <sub>Ser9</sub> (1:500), Bcl-2 (1:1000), and  $\beta$ -actin (1:2000) obtained from Cell Signaling Technology (MA, U.S.A.). The secondary peroxidase-conjugated goat anti-rabbit antibody (1:5000) was obtained from Santa Cruz (CA, U.S.A.). Bands were visualized with enhanced chemiluminescence (Amersham, Buckinghamshire, U.K.) using a gel imaging analysis system. The intensity of each band was measured using the Syngene software (SynGene, Cambridge, U.K.).

**Statistical Analysis** Data are presented as the mean  $\pm$  standard error of the mean (S.E.M.). Statistical analysis was carried out by the two-tailed Student's *t* test when comparing two groups and by one-way ANOVA with Tukey's multiple comparisons *post hoc* tests when comparing more than two groups. Analysis was completed using SPSS software (Version 17.0; SPSS Inc., Chicago, IL, U.S.A.). *p* < 0.05 was considered statistically significant.

## RESULTS

**Effect of Echinacoside on Kainic Acid-Induced Seizures and Elevation of Hippocampal Glutamate Levels** To evaluate the neuroprotective effect of echinacoside against kainic acid-induced excitotoxicity, rats were pretreated with echinacoside (5, 10 and 50 mg/kg, intraperitoneal administration) for 30 min before kainic acid (15 mg/kg) intraperitoneal injection. Kainic acid (15 mg/kg) intraperitoneal injection resulted in seizures with latency and score of 92.5  $\pm$  5.3 min and 4.9  $\pm$  0.1, respectively (Figs. 1A, B). A significant increase in seizure latency [*F*(2, 43) = 40.2, *p* < 0.01; Fig. 1A] and a significant decrease in seizure score [*F*(2, 40) = 21.5, *p* < 0.001; Fig. 1B] were observed in echinacoside (10 or 50 mg/kg)-pretreated rats. However, echinacoside at 5 mg/kg had no significant effect on seizure latency and score (*p* > 0.05; Figs. 1A, B). Given the robust attenuation of seizure activity that was seen with 10 or 50 mg/kg echinacoside, these two dose of echinacoside were used in subsequent experiments to evaluate the mechanisms that underlie the ability of echinacoside to inhibit kainic acid-induced seizures. Figure 1C shows that elevation of hippocampal glutamate levels was noted in kainic acid-treated rats at 4 h when compared with dimethylsulfoxide-treated group (control; *p* < 0.001). However, decreased hippocampal glutamate levels were obtained in the echinacoside group (10 or 50 mg/kg) [*F*(3, 16) = 6.1, *p* < 0.01; Fig. 1C].

**Effect of Echinacoside on Kainic Acid-Induced Neuronal Injury in the CA3 Region of Hippocampus** The degree of neuronal damage was evaluated 3 d after kainic acid injection

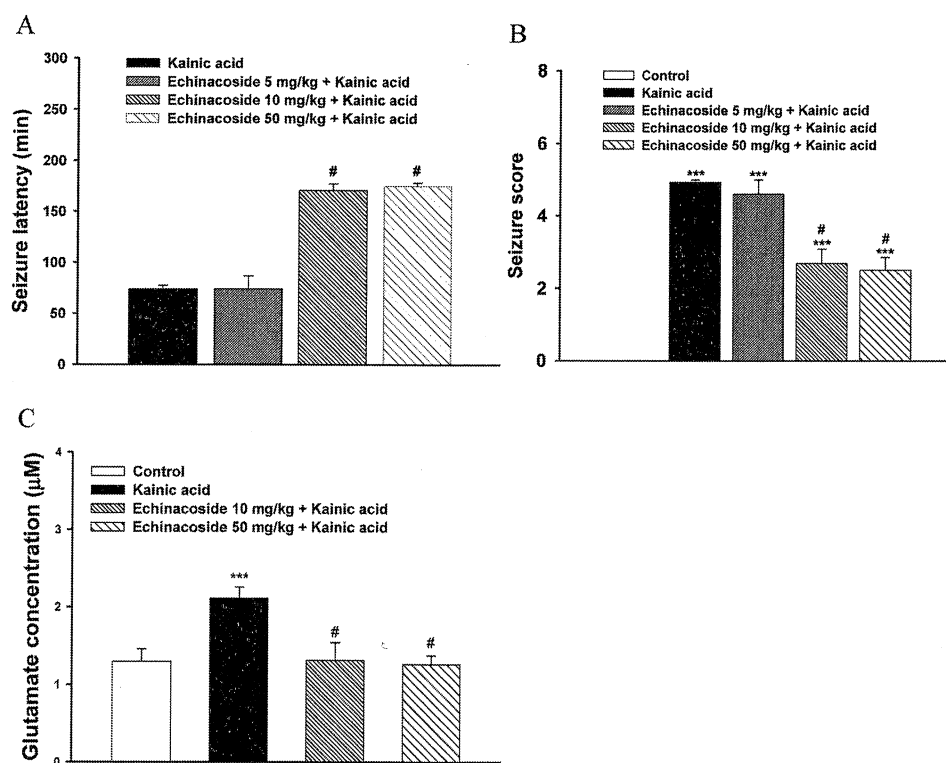


Fig. 1. Echinacoside Attenuates Kainic Acid-Induced Seizure Behavior in Rats

Echinacoside (5, 10 or 50 mg/kg) was intraperitoneally administered 30 min prior to kainic acid (15 mg/kg) intraperitoneal injection. The seizure behavior tests [seizure latency (A) and seizure score (B)] were evaluated during 1–4 h after kainic acid injection. (C) Glutamate levels in the hippocampus were measured with HPLC at 4 h after kainic acid treatment. Data are expressed as mean  $\pm$  S.E.M. \*\*\* $p$  < 0.001 compared with the control group. # $p$  < 0.05 compared with the kainic acid-treated group.

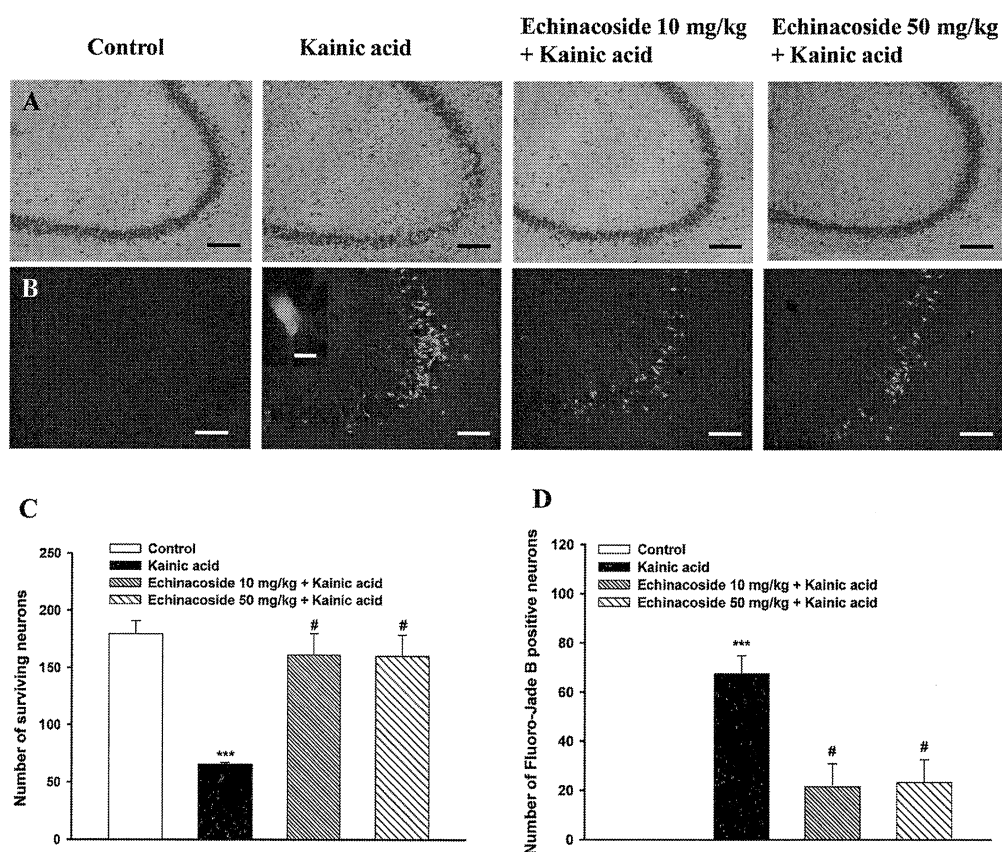


Fig. 2. Protective Action of Echinacoside against Kainic Acid-Induced Neuronal Damage in CA3 Region of Hippocampus

Determination of neuronal damage was examined by neutral red (A) and Fluoro-Jade B (B) staining. Scale bar, 100  $\mu$ m. The insets are high magnification micrographs of neurons. Scale bar, 25  $\mu$ m. Numbers of surviving neurons (C) and Fluoro-Jade B-positive neurons (D) were counted in the CA3 regions of hippocampus and presented as mean  $\pm$  S.E.M. ( $n$  = 6–11). \*\*\* $p$  < 0.001 compared with the control group. # $p$  < 0.05 compared with the kainic acid-treated group. (Color figure can be accessed in the online version.)



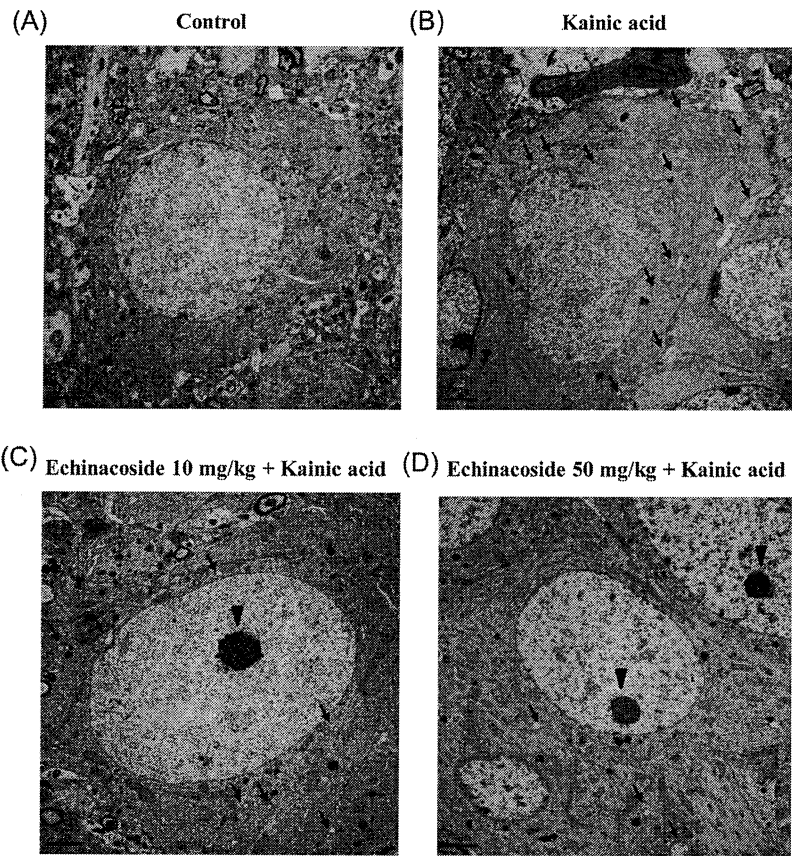


Fig. 3. The Hippocampal CA3 Nerve Cell Injury Measured by Transmission Electron Micrograph  
(A) The control group, (B) the kainic acid group, (C, D) the echinacoside group. Arrows indicate autophagosomes and arrowheads indicate nucleolus. Scale bar, 2 μm.

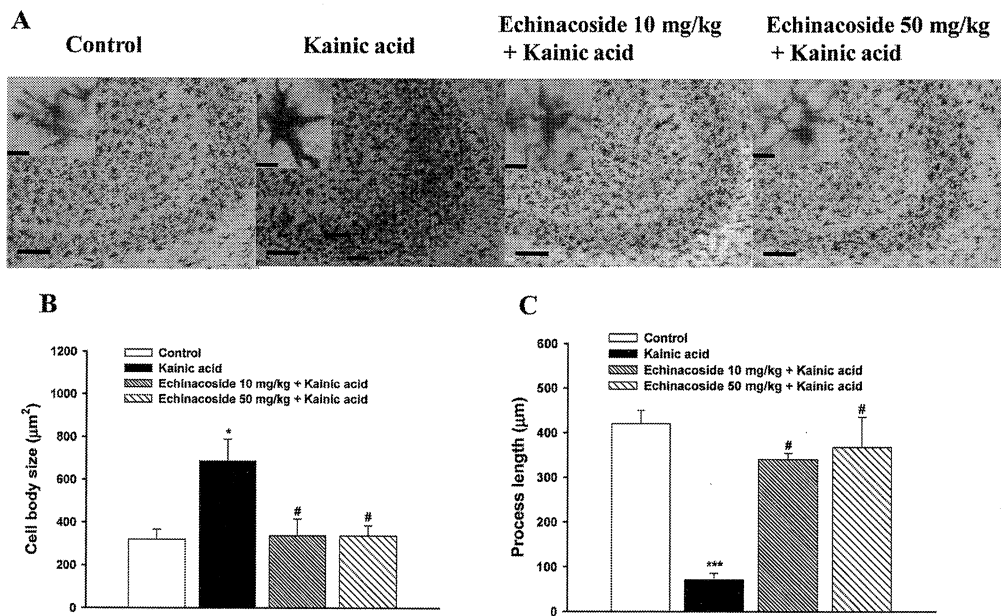


Fig. 4. Echinacoside Suppresses Kainic Acid-Induced Microglial Activation in the Hippocampal CA3 Region  
(A) Representative coronal sections of the hippocampal CA3 region following OX-42 immunostaining 3 d after kainic acid treatment. Representative picture from five independent experiments were presented. Scale bar, 100 μm. The insets are high magnification micrographs of microglial cells. Scale bar, 25 μm. Measurements of cell body size (B) and longest processes (C) and presents as mean ± S.E.M. ( $n=5-11$ ). \*\*\*  $p<0.001$ , \*  $p<0.01$  as compared with the control group. #  $p<0.05$  as compared with the kainic acid-treated group. (Color figure can be accessed in the online version.)

through neutral red staining or Fluoro-Jade B to detect surviving neurons and degenerating neurons, respectively. Neutral red staining revealed an apparent neuronal loss in CA3 of kainic acid-injected rats, compared with dimethylsulfoxide-treated rats (control;  $p<0.001$ ; Figs. 2A, C). However, echinacoside pretreatment (10 or 50 mg/kg) effectively reduced kainic acid-induced neuronal loss in CA3 [ $F(2, 13)=11.6$ ,  $p<0.001$ ; Figs. 2A, C]. Similarly, echinacoside-treated animals presented a

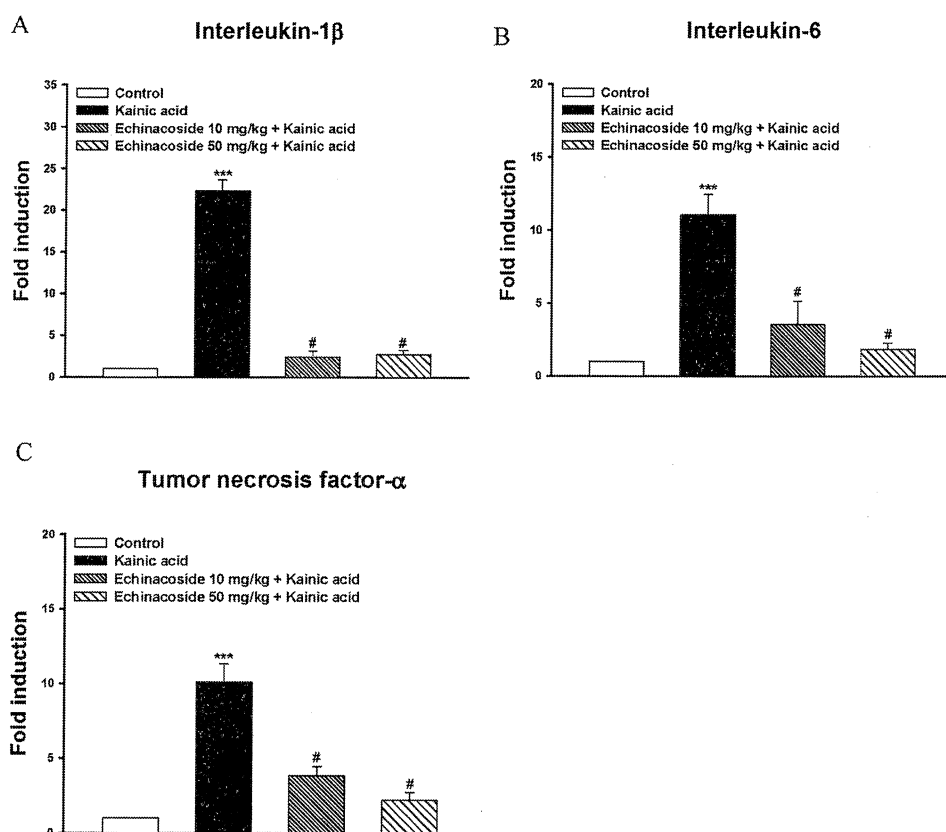


Fig. 5. Echinacoside Reduces Kainic Acid-Induced Proinflammatory Cytokine Expression in the Hippocampus

Relative quantification of interleukin-1 $\beta$  (A), interleukin-6 (B), and tumor necrosis factor- $\alpha$  (C) mRNA expression in the hippocampus were measured at 1 d after kainic acid treatment with RT-PCR. The expression levels of interleukin-1 $\beta$ , interleukin-6, and tumor necrosis factor- $\alpha$  were normalized to that of control. Data are expressed as mean  $\pm$  S.E.M. \*\*\* $p$ <0.001 compared with the control group. # $p$ <0.05 compared with the kainic acid-treated group.

diminished Fluoro-Jade B fluorescence in the CA3 regions of hippocampus after kainic acid injection ( $p$ <0.001), compared with the strong damage observed in kainic acid-injected rats [ $F(2, 24)$ =6.9,  $p$ <0.001; Figs. 2B, D]. In addition, transmission electron microscopy shows that neuronal injury in CA3 was not obvious in the dimethylsulfoxide-treated (control) group. However, in the kainic acid-treated group, nerve cells had ultrastructural changes. Nerve cells exhibited autophagosome formations, deformed nuclei with condensed, and disruptive cell plasma membrane. In contrast, the neuronal injury in the echinacoside-pretreated group was apparently attenuated compared with the kainic acid-injected rats (Fig. 3).

**Effect of Echinacoside on Kainic Acid-Induced Microglia Activation and Gene Expression of Proinflammatory Cytokines in the Hippocampus** In the model for kainic acid-induced seizures and hippocampal neuronal death, microglia activation and proinflammatory cytokine production are increased in the hippocampus.<sup>36,37</sup> In order to investigate whether echinacoside affected inflammatory response in the hippocampus of kainic acid-injected rats, microglia activation was analyzed using the anti-OX42 antibody. In dimethylsulfoxide-treated rats (control group), the microglial cell bodies in the CA3 regions were small and their processes were long and thin (Fig. 4A). However, the number of activated microglial cells in the CA3 area of KA injected rats increased significantly, the microglial cell bodies were enlarged ( $p$ <0.01; Figs. 4A, B), and their cellular processes became shorter and thicker ( $p$ <0.001; Figs. 4A, C). In the animals pretreated with echinacoside (10 or 50 mg/kg)-pretreated rats, the number of

activated microglial cells was significantly decreased, and the microglial cell bodies were thin [ $F(2, 13)$ =6.2,  $p$ <0.01; Fig. 4B] and their cytoplasmic processes were ramified [ $F(2, 28)$ =47.5,  $p$ <0.001; Fig. 4C]. In addition, the expression levels of interleukin-1 $\beta$ , interleukin-6, and tumor necrosis factor- $\alpha$  mRNA in the hippocampus were apparently elevated at 1 d after kainic acid injection, compared to dimethylsulfoxide-injected animals (control) ( $p$ <0.001). However, decreased mRNA levels for these proinflammatory cytokines were obtained in the echinacoside group [interleukin-1 $\beta$ ,  $F(3, 18)$ =154.7,  $p$ <0.001; interleukin-6,  $F(3, 17)$ =17.9,  $p$ <0.001; tumor necrosis factor- $\alpha$ ,  $F(3, 16)$ =31.1,  $p$ <0.001; Figs. 5A–C].

**Effect of Echinacoside on Kainic Acid-Induced Decrease in the Levels of Hippocampal Phospho-Akt, Phospho-Glycogen Synthase Kinase 3 $\beta$ , and Bcl-2** The levels of phosphorylated Akt (pAkt) (Ser473), phosphorylated GSK3 $\beta$  (pGSK3 $\beta$ ) (Ser9), and Bcl-2, was assayed in the hippocampus (Fig. 6). A substantial lowering in pAkt, pGSK3 $\beta$ , and Bcl-2 expression in the hippocampus were observed in kainic acid-treated rats at 4 h when compared with dimethylsulfoxide-treated rats (control) ( $p$ <0.001). However, pretreatment with echinacoside (10 or 50 mg/kg) significantly increased the levels of pAkt, pGSK3 $\beta$ , and Bcl-2 compared with kainic acid treatment alone [pAkt,  $F(3, 19)$ =69.5,  $p$ <0.001; pGSK3 $\beta$ ,  $F(3, 17)$ =60.3,  $p$ <0.001; Bcl-2,  $F(3, 18)$ =26.1,  $p$ <0.001; Figs. 6A–C].

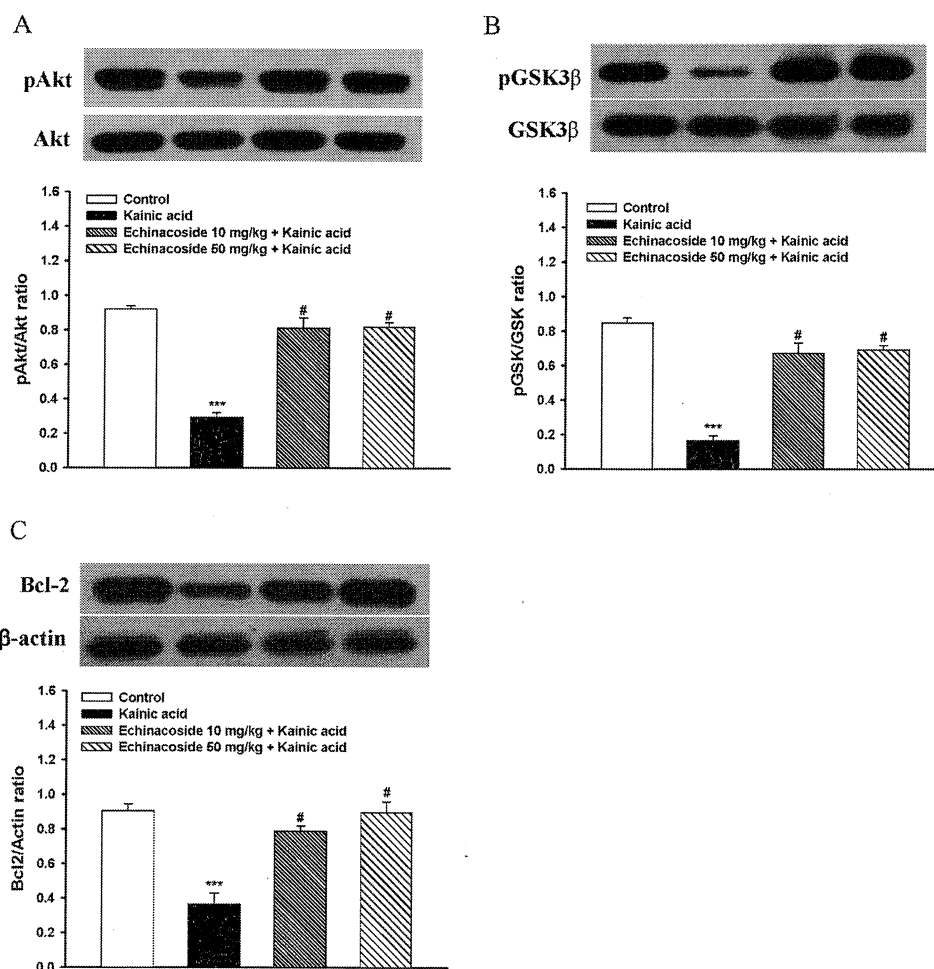


Fig. 6. Echinacoside Rescues Kainic Acid-Induced Inhibition of pAkt, pGSK3 $\beta$ , and Bcl-2 Expression in the Hippocampus

The expression levels of pAkt (A), pGSK3 $\beta$  (B), and Bcl-2 (C) in the whole hippocampus were determined with immunoblotting at 4 h after kainic acid treatment. Data are expressed as mean  $\pm$  S.E.M. \*\*\* $p$  < 0.001 compared with the control group. # $p$  < 0.05 compared with the kainic acid-treated group.

## DISCUSSION

Evidences indicated that glutamate plays a crucial role in the pathophysiology of epilepsy.<sup>17,18)</sup> The glutamatergic hypothesis of epilepsy suggests that epileptogenic process is related to an increased glutamate concentration in the brain and a reduction in the concentration of this neurotransmitter is able to produce antiepileptic action.<sup>38–40)</sup> Study from our laboratory demonstrated that echinacoside can reduce glutamate release from nerve terminals and suggested that echinacoside is likely to have an antiepileptic effect.<sup>17)</sup> This suggestion was confirmed in the current study using a kainic acid-injected rat model. Kainic acid, a glutamate derivative, is widely used for inducing epilepsy in animal studies, because its neuropathological and biochemical characteristics are similar to those in humans.<sup>23,24)</sup>

Intraperitoneal injection of kainic acid into rats causes seizures and neuronal damage, particularly in the CA3 regions of the hippocampus.<sup>41–43)</sup> Furthermore, these pathological alternations produced by kainic acid are related to the massive release of glutamate.<sup>41,44,45)</sup> In agreement with these findings, we observed that the intraperitoneal administration of kainic acid (15 mg/kg) induced seizure behavior, increased glutamate levels in the hippocampus, and caused pyramidal cell loss in the hippocampal CA3 region. These kainic acid-induced

pathological alternations were attenuated by intraperitoneal pretreatment with echinacoside (10 or 50 mg/kg). Furthermore, the hippocampal CA3 nerve cell injury evaluated by ultrastructural alteration with transmission electron microscopy was alleviated by echinacoside in the kainic acid rats. In addition, an increased number of autophagosomes was observed in CA3 cells after kainic acid administration. Pretreatment with echinacoside suppressed the increased formation of autophagosomes. Previous studies have suggested that autophagy activation is involved in kainic acid-induced neuronal death and inhibition of autophagy process seems to be neuroprotective.<sup>46,47)</sup> Although the mechanism underlying the antiepileptic effect of echinacoside requires further exploration, the neuroprotective effect of echinacoside in the kainic acid animal model may be resulted from antiepileptic activity through inhibition of glutamate excitotoxicity and autophagy activation.

Neuroinflammation contributes considerably to delayed brain damage after acute injury and exerts a detrimental effect on a neurological outcome.<sup>27)</sup> Inflammatory responses, such as microglia activation and inflammatory cytokine production, has been described in human epilepsy and in experimental models of epilepsy.<sup>36,48)</sup> Moreover, the release of these pro-inflammatory cytokines from the activated microglial cells promotes kainic acid-induced neuronal damage in the hippocampus.<sup>36,37)</sup> We showed that, while kainic acid increased the

activation of microglia and gene expression of proinflammatory cytokines (interleukin-1 $\beta$ , interleukin-6, and tumor necrosis factor- $\alpha$ ) in the hippocampus, these effects were suppressed by echinacoside pretreatment. Therefore, we suggest that echinacoside through suppressing inflammatory processes, may contribute to its antiepileptic and neuroprotective effects in the kainic acid animal model. As already observed by our previous studies, several drugs and natural products also exert antiepileptic effects and neuroprotection against kainic acid-induced seizures, by means of their anti-inflammatory effect.<sup>31,33,35)</sup>

Numerous protein kinase signaling cascades are known to be activated by kainic acid that play important roles in neuroprotection. Among those that appear to have a particularly significant participation is Akt.<sup>49,50)</sup> Akt mediates its neuroprotective effects by activating various downstream substrates, including GSK-3 $\beta$  and Bcl-2. Akt phosphorylates GSK-3 $\beta$  at Ser9, leading to its inactivation and the reinforcement of neuronal cell survival<sup>51)</sup> because the active form of GSK-3 $\beta$  activates the mitochondrial death pathway.<sup>52,53)</sup> Bcl-2 is a key member of the anti-apoptotic Bcl-2 family and plays a key role in suppressing mitochondrial-mediated apoptotic cell death. For example, Bcl-2 can protect the integrity of mitochondrial membrane and block cytochrome C release from mitochondria, leading to cell survival and the inhibition of apoptosis.<sup>54)</sup> It has also reported that the overexpression of Bcl-2 protects neurons against excitotoxic insults *in vitro* and *in vivo*.<sup>54,55)</sup> The present study observed a decreased Akt (Ser473) and GSK3 $\beta$  (Ser9) phosphorylation as well as Bcl-2 expression in the hippocampus of rats following kainic acid exposure, which is in accordance with previous studies.<sup>56,57)</sup> Furthermore, echinacoside pretreatment rescued kainic acid-induced decrease in pAkt and pGSK3 $\beta$  as well as Bcl-2 expression. Thus, the neuroprotective effects of echinacoside in the kainic acid animal model might be partly mediated by preventing the down-regulation of the Akt/GSK-3 $\beta$ /Bcl-2 pathway, thus increasing neuron survival.

Echinacoside is a potential new therapeutic candidate. This is because echinacoside can entry the brain and exhibits numerous benefits.<sup>58)</sup> Numerous studies have demonstrated that echinacoside attenuates brain damage and alleviates motor or memory impairment in several experimental models *in vivo*.<sup>12,14,15,59)</sup> Although the mechanisms that underlie the neuroprotective effects of echinacoside in the brain require elucidation, inhibited neuroinflammation, antioxidation, oxygen-free radical scavenging, and increased neurogenesis have been implicated.<sup>14–16)</sup> In addition to these possible mechanisms, our previous<sup>17)</sup> and present results suggest that the inhibition of glutamate-mediated overexcitation may partly contribute to the neuroprotective and antiepileptic effects of echinacoside in the brain. This is supported by the fact that kainic acid-induced seizure activity, neuroinflammation and brain damage are associated with the excessive release of glutamate and activation of glutamate receptors.<sup>44,45)</sup> Furthermore, several clinically used antiepileptic drugs have been shown to attenuate the seizure activity induced by kainic acid<sup>60,61)</sup> and decrease the glutamate release in human and rat brain tissues.<sup>62,63)</sup> These findings pointed out that reduced glutamate levels is important for pharmacotherapeutic effects of antiepileptic drugs.

In conclusion, our results demonstrate that echinacoside, through suppressing inflammatory processes, decreasing

glutamate-mediated overexcitation, as well as increasing Akt/GSK-3 $\beta$  activation and Bcl-2 expression, have a significant antiepileptic and neuroprotective effect in kainic acid-injected rats. Although the role of echinacoside on patients with epilepsy requires further evaluation, our findings suggest that it could be a valuable approach in epilepsy therapy.

**Acknowledgments** The authors would like to thank Mr. Yen-Sheng Wu of the Electron Microscope Laboratory of Tzong Jwo Jang, College of Medicine, Fu Jen Catholic University. This work was supported by the Ministry of Science and Technology (MOST 103-2320-B-030-001 MY3).

**Conflict of Interest** The authors declare no conflict of interest.

## REFERENCES

- 1) Hesdorffer DC, Beck V, Begley CE, Bishop ML, Cushner-Weinstein S, Holmes GL, Shafer PO, Sirven JI, Austin JK. Research implications of the Institute of Medicine Report, epilepsy across the spectrum: promoting health and understanding. *Epilepsia*, **54**, 207–216 (2013).
- 2) Patsalos PN. Some new developments in therapeutic drug monitoring of antiepileptic drugs. *Ther. Drug Monit.*, **21**, 139 (1999).
- 3) Löscher W. Current status and future directions in the pharmacotherapy of epilepsy. *Trends Pharmacol. Sci.*, **23**, 113–118 (2002).
- 4) Rogawski MA, Löscher W. The neurobiology of antiepileptic drugs. *Nat. Rev. Neurosci.*, **5**, 553–564 (2004).
- 5) Grunze H, Langosch J, von Loewenich C, Walden J. Modulation of neural cell membrane conductance by the herbal anxiolytic and antiepileptic drug aswal. *Neuropsychobiology*, **42** (Suppl. 1), 28–32 (2000).
- 6) Sucher NJ, Carles MC. A pharmacological basis of herbal medicines for epilepsy. *Epilepsy Behav.*, **52** (Pt B), 308–318 (2015).
- 7) Tu PF, Wang B, Deyama T, Zhang ZG, Lou ZC. Analysis of phenylethanoid glycosides of *Herba cistanchis* by RP-HPLC. *Yao Xue Bao*, **32**, 294–300 (1997).
- 8) Wang F, Wang WK. Chinese medicinal composition for treating epilepsy and preparation method thereof. Chinese Patent CN 101797352 B, 2012.
- 9) Zhao LX, Zhang CL, Zhao JX. Experience of WANG Guo-san in treating epilepsy. *China J. Trad. Chin. Med. Pharm.*, **6**, 25 (2011).
- 10) Karalliedde LD, Kappagoda CT. The challenge of traditional Chinese medicines for allopathic practitioners. *Am. J. Physiol. Heart Circ. Physiol.*, **297**, H1967–H1969 (2009).
- 11) Lei L, Song ZH, Tu PF, Li YZ, Wu LJ, Chen FK. Metabolic regulation of phenylethanoid glycosides from *Herba cistanches* in dogs' gastrointestinal. *Yao Xue Bao*, **36**, 432–435 (2001).
- 12) Shiao YJ, Su MH, Lin HC, Wu CR. Echinacoside ameliorates the memory impairment and cholinergic deficit induced by amyloid beta peptides *via* the inhibition of amyloid deposition and toxicology. *Food Funct.*, **8**, 2283–2294 (2017).
- 13) Wu CR, Lin HC, Su MH. Reversal by aqueous extracts of *Cistanche tubulosa* from behavioral deficits in Alzheimer's disease-like rat model: relevance for amyloid deposition and central neurotransmitter function. *BMC Complement. Altern. Med.*, **14**, 202 (2014).
- 14) Zhang J, Zhang Z, Xiang J, Cai M, Yu Z, Li X, Wu T, Cai D. Neuroprotective effects of echinacoside on regulating the stress-active p38MAPK and NF- $\kappa$ B p52 signals in the mice model of Parkinson's disease. *Neurochem. Res.*, **42**, 975–985 (2017).
- 15) Zhao Q, Gao J, Li W, Cai D. Neurotrophic and neurorescue effects of Echinacoside in the subacute MPTP mouse model of Parkinson's disease. *Brain Res.*, **1346**, 224–236 (2010).
- 16) Zhu M, Lu C, Li W. Transient exposure to echinacoside is sufficient



- to activate Trk signaling and protect neuronal cells from rotenone. *J. Neurochem.*, **124**, 571–580 (2013).
- 17) Lu CW, Lin TY, Huang SK, Wang SJ. Echinacoside inhibits glutamate release by suppressing voltage-dependent  $\text{Ca}^{2+}$  entry and protein kinase C in rat cerebrocortical nerve terminals. *Int. J. Mol. Sci.*, **17**, 1006 (2016).
  - 18) Cavus I, Pan JW, Hetherington HP, Abi-Saab W, Zaveri HP, Vives KP, Krystal JH, Spencer SS, Spencer DD. Decreased hippocampal volume on MRI is associated with increased extracellular glutamate in epilepsy patients. *Epilepsia*, **49**, 1358–1366 (2008).
  - 19) Lason W, Chlebicka M, Rejdak K. Research advances in basic mechanisms of seizures and antiepileptic drug action. *Pharmacol. Rep.*, **65**, 787–801 (2013).
  - 20) Ben-Ari Y. Limbic seizure and brain damage produced by kainic acid: mechanisms and relevance to human temporal lobe epilepsy. *Neuroscience*, **14**, 375–403 (1985).
  - 21) Ben-Ari Y, Cossart R. Kainate, a double agent that generates seizures: two decades of progress. *Trends Neurosci.*, **23**, 580–587 (2000).
  - 22) Friedman LK, Pellegrini-Giampietro DE, Sperber EF, Bennett MV, Moshé SL, Zukin RS. Kainate-induced status epilepticus alters glutamate and GABA<sub>A</sub> receptor gene expression in adult rat hippocampus: an *in situ* hybridization study. *J. Neurosci.*, **14**, 2697–2707 (1994).
  - 23) Van Nieuwenhuysse B, Raedt R, Sprengers M, Dauwe I, Gadeyne S, Carrette E, Delbeke J, Wadman WJ, Boon P, Vonck K. The systemic kainic acid rat model of temporal lobe epilepsy: long-term EEG monitoring. *Brain Res.*, **1627**, 1–11 (2015).
  - 24) Lévesque M, Avoli M. The kainic acid model of temporal lobe epilepsy. *Neurosci. Biobehav. Rev.*, **37**, 2887–2899 (2013).
  - 25) Racine RJ. Modification of seizure activity by electrical stimulation. II. Motor seizure. *Electroencephalogr. Clin. Neurophysiol.*, **32**, 281–294 (1972).
  - 26) Chang Y, Lu CW, Lin TY, Huang SK, Wang SJ. Baicalein, a constituent of *Scutellaria baicalensis*, reduces glutamate release and protects neuronal cell against kainic acid-induced excitotoxicity in rats. *Am. J. Chin. Med.*, **44**, 943–962 (2016).
  - 27) Spigolon G, Veronesi C, Bonny C, Vercelli A. c-Jun N-terminal kinase signaling pathway in excitotoxic cell death following kainic acid-induced status epilepticus. *Eur. J. Neurosci.*, **31**, 1261–1272 (2010).
  - 28) Chang CY, Lin TY, Lu CW, Huang SK, Wang YC, Chou SS, Wang SJ. Hesperidin inhibits glutamate release and exerts neuroprotection against excitotoxicity induced by kainic acid in the hippocampus of rats. *Neurotoxicology*, **50**, 157–169 (2015).
  - 29) Morishima Y, Miyakawa T, Furuyashiki T, Tanaka Y, Mizuma H, Nakanishi S. Enhanced cocaine responsiveness and impaired motor coordination in metabotropic glutamate receptor subtype 2 knockout mice. *Proc. Natl. Acad. Sci. U.S.A.*, **102**, 4170–4175 (2005).
  - 30) Schmued LC, Hopkins KJ. Fluoro-Jade B: a high affinity fluorescent marker for the localization of neuronal degeneration. *Brain Res.*, **874**, 123–130 (2000).
  - 31) Lin TY, Huang WJ, Wu CC, Lu CW, Wang SJ. Acacetin inhibits glutamate release and prevents kainic acid-induced neurotoxicity in rats. *PLOS ONE*, **9**, e88644 (2014).
  - 32) Young K, Morrison H. Quantifying microglia morphology from photomicrographs of immunohistochemistry prepared tissue using ImageJ. *J. Vis. Exp.*, **136**, e57648 (2018).
  - 33) Lin TY, Lu CW, Wang SJ. Luteolin protects the hippocampus against neuron impairments induced by kainic acid in rats. *Neurotoxicology*, **55**, 48–57 (2016).
  - 34) Livak KJ, Schmittgen TD. Analysis of relative gene expression data using real-time quantitative PCR and the  $2^{-\Delta\Delta C_T}$  method. *Methods*, **25**, 402–408 (2001).
  - 35) Chiu KM, Wu CC, Wang MJ, Lee MY, Wang SJ. Protective effects of bupivacaine against kainic acid-induced seizure and neuronal cell death in the rat hippocampus. *Biol. Pharm. Bull.*, **38**, 522–530 (2015).
  - 36) Avignone E, Ulmann L, Levavasseur F, Rassendren F, Audinat E. Status epilepticus induces a particular microglial activation state characterized by enhanced purinergic signaling. *J. Neurosci.*, **28**, 9133–9144 (2008).
  - 37) Shin EJ, Koh YH, Kim AY, Nah SY, Jeong JH, Chae JS, Kim SC, Yen TP, Yoon HJ, Kim WK, Ko KH, Kim HC. Ginsenosides attenuate kainic acid-induced synaptosomal oxidative stress via stimulation of adenosine A(2A) receptors in rat hippocampus. *Behav. Brain Res.*, **197**, 239–245 (2009).
  - 38) Chapman AG, Elwes RD, Millan MH, Polkey CE, Meldrum BS. Role of glutamate and aspartate in epileptogenesis; contribution of microdialysis studies in animal and man. *Epilepsy Res. Suppl.*, **12**, 239–246 (1966).
  - 39) Meldrum BS. The role of glutamate in epilepsy and other CNS disorders. *Neurology*, **44** (Suppl. 8), S14–S23 (1994).
  - 40) Carlson H, Ronne-Engström E, Ungerstedt U, Hillered L. Seizure related elevations of extracellular amino acids in human focal epilepsy. *Neurosci. Lett.*, **140**, 30–32 (1992).
  - 41) Sperk G. Kainic acid seizures in the rat. *Prog. Neurobiol.*, **42**, 1–32 (1994).
  - 42) Coyle JT. Neurotoxic action of kainic acid. *J. Neurochem.*, **41**, 1–11 (1983).
  - 43) Bahn S, Volk B, Wisden W. Kainate receptor gene expression in the developing rat brain. *J. Neurosci.*, **14**, 5525–5547 (1994).
  - 44) Ferkany JW, Coyle JT. Kainic acid selectively stimulates the release of endogenous excitatory acidic amino acids. *J. Pharmacol. Exp. Ther.*, **225**, 399–406 (1983).
  - 45) Chittajallu R, Vignes M, Dev KK, Barnes JM, Collingridge GL, Henley JM. Regulation of glutamate release by presynaptic kainate receptors in the hippocampus. *Nature*, **379**, 78–81 (1996).
  - 46) Wang Y, Han R, Liang ZQ, Wu JC, Zhang XD, Gu ZL, Qin ZH. An autophagic mechanism is involved in apoptotic death of rat striatal neurons induced by the non-N-methyl-D-aspartate receptor agonist kainic acid. *Autophagy*, **4**, 214–226 (2008).
  - 47) Dong XX, Wang YR, Qin S, Liang ZQ, Liu BH, Qin ZH, Wang Y. p53 mediates autophagy activation and mitochondria dysfunction in kainic acid-induced excitotoxicity in primary striatal neurons. *Neuroscience*, **207**, 52–64 (2012).
  - 48) Kim DH, Yoon BH, Jung WY, Kim JM, Park SJ, Park DH, Huh Y, Park C, Cheong JH, Lee KT, Shin CY, Ryu JH. Sinapic acid attenuates kainic acid-induced hippocampal neuronal damage in mice. *Neuropharmacology*, **59**, 20–30 (2010).
  - 49) Piermartiri TC, Vandresen-Filho S, de Araújo Herculano B, Martins WC, Dal'agnolo D, Stroeh E, Carqueja CL, Boeck CR, Tasca CI. Atorvastatin prevents hippocampal cell death due to quinolinic acid-induced seizures in mice by increasing Akt phosphorylation and glutamate uptake. *Neurotox. Res.*, **16**, 106–115 (2009).
  - 50) Lee SH, Chun W, Kong PJ, Han JA, Cho BP, Kwon OY, Lee HJ, Kim SS. Sustained activation of Akt by melatonin contributes to the protection against kainic acid-induced neuronal death in hippocampus. *J. Pineal Res.*, **40**, 79–85 (2006).
  - 51) Jope RS, Johnson GV. The glamour and gloom of glycogen synthase kinase-3. *Trends Biochem. Sci.*, **29**, 95–102 (2004).
  - 52) Frame S, Cohen P, Biondi RM. A common phosphate binding site explains the unique substrate specificity of GSK3 and its inactivation by phosphorylation. *Mol. Cell*, **7**, 1321–1327 (2001).
  - 53) Crespo-Biel N, Canudas AM, Camins A, Pallàs M. Kainate induces AKT, ERK and cdk5/GSK3 $\beta$  pathway deregulation, phosphorylates tau protein in mouse hippocampus. *Neurochem. Int.*, **50**, 435–442 (2007).
  - 54) Cory S, Huang DC, Adams JM. The Bcl-2 family: roles in cell survival and oncogenesis. *Oncogene*, **22**, 8590–8607 (2003).
  - 55) Howard S, Bottino C, Brooke S, Cheng E, Giffard RG, Sapolsky R. Neuroprotective effects of bcl-2 overexpression in hippocampal

- cultures: interactions with pathways of oxidative damage. *J. Neurochem.*, **83**, 914–923 (2002).
- 56) Wang ZH, Mong MC, Yang YC, Yin MC. Astatic acid and maslinic acid attenuated kainic acid-induced seizure through decreasing hippocampal inflammatory and oxidative stress. *Epilepsy Res.*, **139**, 28–34 (2018).
- 57) Kim YS, Choi MY, Lee DH, Jeon BT, Roh GS, Kim HJ, Kang SS, Cho GJ, Choi WS. Decreased interaction between FoxO3a and Akt correlates with seizure-induced neuronal death. *Epilepsy Res.*, **108**, 367–378 (2014).
- 58) Wei L, Chen H, Jiang Y, Tu P, Zhong M, Liu F, Liu C. Determination of ECH on cerebral ischemia injury rat plasma and brain tissue by HPLC method. *Chin. Pharm. Bull.*, **27**, 737–738 (2011).
- 59) Geng X, Tian X, Tu P, Pu X. Neuroprotective effects of echinacoside in the mouse MPTP model of Parkinson's disease. *Eur. J. Pharmacol.*, **564**, 66–74 (2007).
- 60) Halonen T, Miettinen R, Toppinen A, Tuunanen J, Kotti T, Riekkinen PJ Sr. Vigabatrin protects against kainic acid-induced neuronal damage in the rat hippocampus. *Neurosci. Lett.*, **195**, 13–16 (1995).
- 61) Park HJ, Kim HJ, Park HJ, Ra J, Zheng LT, Yim SV, Chung JH. Protective effect of topiramate on kainic acid-induced cell death in mice hippocampus. *Epilepsia*, **49**, 163–167 (2008).
- 62) Kammerer M, Brawek B, Freiman TM, Jackisch R, Feuerstein TJ. Effects of antiepileptic drugs on glutamate release from rat and human neocortical synaptosomes. *Naunyn Schmiedeberg's Arch. Pharmacol.*, **383**, 531–542 (2011).
- 63) Sitges M, Guarneros A, Nekrassov V. Effects of carbamazepine, phenytoin, valproic acid, oxcarbazepine, lamotrigine, topiramate and vinpocetine on the presynaptic  $\text{Ca}^{2+}$  channel-mediated release of  $[^3\text{H}]\text{glutamate}$ : comparison with the  $\text{Na}^{+}$  channel-mediated release. *Neuropharmacology*, **53**, 854–862 (2007).

RESEARCH ARTICLE

Open Access



# Study of the anti-allergic and anti-inflammatory activity of *Brachychiton rupestris* and *Brachychiton discolor* leaves (Malvaceae) using in vitro models

Amany A. Thabet<sup>1†</sup>, Fadia S. Youssef<sup>1†</sup>, Michal Korinek<sup>2,3,4,5</sup>, Fang-Rong Chang<sup>2,6</sup>, Yang-Chang Wu<sup>2,7,8</sup>, Bing-Hung Chen<sup>3,8,9</sup>, Mohamed El-Shazly<sup>1,10\*</sup>, Abdel Nasser B. Singab<sup>1\*</sup> and Tsong-Long Hwang<sup>4,5,11,12,13\*</sup> 

## Abstract

**Background:** *Brachychiton rupestris* and *Brachychiton discolor* (Malvaceae) are ornamental trees native to Australia. Some members of *Brachychiton* and its highly related genus, *Sterculia*, are employed in traditional medicine for itching, dermatitis and other skin diseases. However, scientific studies on these two genera are scarce. Aiming to reveal the scientific basis of the folk medicinal use of these plants, the cytotoxicity, anti-inflammatory and anti-allergic activities of *Brachychiton rupestris* and *Brachychiton discolor* leaves extracts and fractions were evaluated. Also, phytochemical investigation of *B. rupestris* was performed to identify the compounds exerting the biological effect.

**Methods:** Extracts as well as fractions of *Brachychiton rupestris* and *Brachychiton discolor* were tested for their cytotoxicity versus hepatoma HepG2, lung A549, and breast MDA-MB-231 cancer cell lines. Assessment of the anti-allergic activity was done using degranulation assay in RBL-2H3 mast cells. Anti-inflammatory effect was tested by measuring the suppression of superoxide anion production as well as elastase release in fMLF/CB-induced human neutrophils. Phytochemical investigation of the *n*-hexane, dichloromethane and ethyl acetate fractions of *B. rupestris* was done using different chromatographic and spectroscopic techniques.

**Results:** The tested samples showed no cytotoxicity towards the tested cell lines. The nonpolar fractions of both *B. rupestris* and *B. discolor* showed potent anti-allergic potency by inhibiting the release of  $\beta$ -hexosaminidase. The dichloromethane fraction of both species exhibited the highest anti-inflammatory activity by suppressing superoxide anion generation and elastase release with IC<sub>50</sub> values of 2.99 and 1.98  $\mu$ g/mL, respectively for *B. rupestris*, and 0.78 and 1.57  $\mu$ g/mL, respectively for *B. discolor*. Phytochemical investigation of various fractions of *B. rupestris* resulted in the isolation of  $\beta$ -amyrin acetate (1),  $\beta$ -sitosterol (2) and stigmasterol (3) from the *n*-hexane fraction. Scopoletin (4) and  $\beta$ -sitosterol-3-*O*- $\beta$ -D-glucoside (5) were obtained from the dichloromethane fraction. Dihydrodehydrodiconiferyl alcohol 4-*O*- $\beta$ -D-glucoside (6) and dihydrodehydrodiconiferyl alcohol 9-*O*- $\beta$ -D-glucoside (7) were separated from the ethyl acetate fraction. Scopoletin (4) showed anti-allergic and anti-inflammatory activity.

**Conclusions:** It was concluded that the nonpolar fractions of both *Brachychiton* species exhibited anti-allergic and anti-inflammatory activities.

**Keywords:** Anti-allergic, Anti-inflammatory, *Brachychiton discolor*, *Brachychiton rupestris*, Cytotoxicity, Phytochemistry

\* Correspondence: [mohamed.elshazly@pharma.asu.edu.eg](mailto:mohamed.elshazly@pharma.asu.edu.eg); [dean@pharma.asu.edu.eg](mailto:dean@pharma.asu.edu.eg); [htl@mail.cgu.edu.tw](mailto:htl@mail.cgu.edu.tw)

<sup>†</sup>Amany A. Thabet and Fadia S. Youssef contributed equally to this work.

<sup>1</sup>Department of Pharmacognosy, Faculty of Pharmacy, Ain Shams University, African Union Organization Street, Abbassia, Cairo 11566, Egypt

<sup>4</sup>Graduate Institute of Natural Products, College of Medicine, Chang Gung University, Taoyuan 33302, Taiwan

Full list of author information is available at the end of the article



© The Author(s). 2018 **Open Access** This article is distributed under the terms of the Creative Commons Attribution 4.0 International License (<http://creativecommons.org/licenses/by/4.0/>), which permits unrestricted use, distribution, and reproduction in any medium, provided you give appropriate credit to the original author(s) and the source, provide a link to the Creative Commons license, and indicate if changes were made. The Creative Commons Public Domain Dedication waiver (<http://creativecommons.org/publicdomain/zero/1.0/>) applies to the data made available in this article, unless otherwise stated.

## Background

Allergy is one of the most popular diseases worldwide and its great prevalence makes allergic disorder a growing global concern [1]. Allergic reaction can be defined as the development of signs and symptoms of hypersensitivity reactions upon exposure to certain allergenic substances resulting in massive production of allergen-specific IgE and allergen-specific T-cell populations [2]. Allergic reaction can be a life-threatening condition especially in anaphylaxis and severe asthma or it can be a chronic condition that interferes with the quality of life such as in eczema and allergic rhinitis [3].

Inflammation is another common disorder which is an innate immune response from the host defense mechanism. It consists of a series of complex biological processes aiming to combat infection and tissue injury. These processes lead to accumulation of plasma and blood cells in the tissue in addition to the release of inflammatory mediators aiming to reestablish tissue structures and function [4, 5]. Untreated inflammation can lead to a chronic condition which is characterized as a very long-term inflammation affecting the remodeling of tissue for many weeks and even years. It is considered as a main cause in the development of a various life threatening disorders, such as neurodegenerative diseases and cancers [4].

Non-steroidal anti-inflammatory drugs (NSAIDs) constitute the commonly adopted classes for the alleviation of inflammation and related conditions. Meanwhile, their intolerable side effects represented by gastrointestinal ulcers, and perforation with concomitant bleeding are the main obstacles facing their therapeutic usage [6]. On the contrary, nature continues to serve as a rich and appealing source of novel, safer, and cheaper bioactive molecules in comparison to many synthetic drugs. A plethora of plant extracts, as well as isolated compounds, possess notable anti-allergic and anti-inflammatory activities, as previously reported [5, 7–11].

Malvaceae, the mallows, is a family that comprises more than 200 genera and 2300 species. A great diversity of phytoconstituents such as triterpenes, flavonoids, coumarins, as well as alkaloids was previously reported in the members of this family [12, 13]. *Brachychiton* (Malvaceae) is a small genus native to Australia comprising of 30 species [14, 15]. Recently, *Brachychiton* has been considered as a separate genus from *Sterculia* as proved by the detailed investigation of its follicles, seed coats and embryo [14]. Members of the *Brachychiton* genus were used as food by Australian Aborigines and some are used as ornamental trees or shrubs [16, 17]. Different members of the genus possess several interesting biological effects such as antioxidant, antibacterial, anti-hyperglycemic, hepatoprotective and anti-schistosomal activities [18–21]. Phytochemical studies of various members of *Brachychiton* sp.

resulted in the identification of various classes of compounds such as flavonoids, coumarins, triterpenes, sterols, and alkaloids [22–24]. *Brachychiton rupestris* is commonly known as “Queensland bottle tree” because it is native to Queensland and has a bottle shaped trunk. *B. discolor* (synonym *B. luridus*) is commonly called the lacebark tree [25–27]. The mucilage and ethyl acetate fraction of *B. rupestris* leaves were previously investigated for their in vivo anti-hyperglycemic effect and the phytochemical investigation of this species led to the isolation and identification of flavonoid aglycones and glycosides from the leaves [20, 28]. However, no complete phytochemical study was done on this species. Regarding *B. discolor*, two complete phytochemical studies were reported on this species where many classes of compounds were reported from the leaves, seeds and roots including triterpenes, flavonoids, phenolic acids, coumarins and alkaloids [23, 24].

Tracing current literature, nothing was found regarding the anti-allergic and anti-inflammatory effects of *B. rupestris*. However, different studies were carried out confirming the anti-allergic and anti-inflammatory activities of several triterpenes such as  $\beta$ -amyrin, oleanolic acid and lupeol [29–33] which were also isolated from *B. discolor* [23, 24]. Another species (*B. populneus*) was reported to be effective in relieving pain and skin diseases in folk medicine [34]. Furthermore, many members of the related genus, *Sterculia*, are popular in folk medicine for alleviating itching, dermatitis, boils, inflammations and other skin diseases [35–40]. Herein, we investigated the anti-allergic and anti-inflammatory activities of the methanol extracts and fractions of both *B. rupestris* and *B. discolor* leaves. The cytotoxic effect of *B. rupestris* and *B. discolor* leaves extracts and fractions was also evaluated to ascertain their safety. Additionally, the isolation and structural elucidation of the major constituents from the bioactive fractions of *B. rupestris* was achieved within this work.

## Methods

### Plant materials

The leaves of *B. rupestris* (T.Mitch.ex Lindl) K.Schum and *B. discolor* F.Muell were obtained from El-Orman Botanical Garden, Giza, Egypt, in summer 2014. The plants were generously authenticated by Prof. Dr. Mohamed El-Gibaly, Department of Botany, National Research Center (NRC), Giza, Egypt. Voucher specimens (PHG-P-BR-248 and PHG-P-BL-249) for *B. rupestris* and *B. discolor* (*B. luridus*), respectively were kept at the Pharmacognosy Department, Faculty of Pharmacy, Ain Shams University.

### Extraction and fractionation

Total amount of 3.05 kg of *B. rupestris* air-dried leave were crushed, macerated in 29 L of distilled methanol



for three times and filtered. Subsequently, the obtained filtrate was evaporated in vacuo at low temperature (45 °C) till dryness and then subjected to lyophilization to give 333.56 g of the total methanol extract. A portion of the extract (300 g) was successively partitioned with *n*-hexane (37.9 L), dichloromethane (4.8 L) and ethyl acetate (5.2 L) to give 54.35, 8.54 and 5.91 g, respectively along with the remaining hydromethanolic fraction estimated as 191.5 g.

Similarly, for *B. discolor*, the crushed air-dried leaves 600 g were macerated in distilled methanol (6 L × 3), filtered, and evaporated at 45 °C under reduced pressure till dryness to yield 36 g of the total methanol extract. Then, 11 g of the total extract were fractionated using 430 mL of *n*-hexane, 300 mL of dichloromethane and 300 mL of ethyl acetate successively to give 1.3, 1.2, and 0.9 g of the dried residues, respectively.

## Biological investigations

### *In vitro* assessment of the cytotoxic activity

**Cell culture** The cytotoxicity of *B. rupestris* and *B. discolor* total extracts as well as their obtained fractions was examined on A549 (adenocarcinoma human alveolar basal epithelial cells), HepG2 (human liver cancer cell line) and MDA-MB-231 (invasive ductal carcinoma) cells. Cells were preserved in Dulbecco's modified Eagle's medium-high glucose powder (DMEM) containing 10% heat-inactivated fetal bovine serum (FBS), 1 mM sodium pyruvate, 100 µg/mL streptomycin, 100 U/mL penicillin, and 2 mM L-glutamine. Cells were cultured in culture dishes (Cellstar) that were kept in a humidified chamber supplied with 5% (v/v) CO<sub>2</sub> at 37 °C. Then the cells were maintained as a monolayer culture adopting serial sub-culturing. Cells growing in the logarithmic phase were employed in all experiments [41].

**Cytotoxicity assay** MTT (methylthiazoltetrazolium) assay was employed to evaluate the cytotoxic activity of the tested samples against human cancer cells [42, 43]. Trypsinized cell suspensions were freshly prepared and then planted in a 96-well culture plate followed by overnight incubation. Tested samples were prepared in dimethyl sulfoxide (DMSO) to form stock solutions of 1 mg/mL. Cells were treated with the tested samples using different concentrations (2.5–20 µg/mL) then incubated for 72 h at 37 °C under 5% CO<sub>2</sub>. After the incubation, and removal of the cells medium, 100 µL of MTT solution was added to each well followed by incubation of the cells for 1 h. The formed formazan crystals were dissolved in DMSO after the removal of the medium to measure absorbance at 550 nm. The percentage of cell viability was calculated by the following formula:

$$\% \text{cell viability} = \frac{\text{O.D of treated cells} - \text{O.D of culture medium}}{\text{O.D of untreated cells} - \text{O.D of culture medium}} \times 100$$

Where O.D = optical density

Cytotoxicity was expressed as % cell inhibition. Doxorubicin was used as the positive control.

### *In vitro* assessment of the anti-allergic activity

**Chemicals and reagents** DMEM, dexamethasone, *p*-nitrophenyl-*N*-acetyl-D-glucosaminide (*p*-NAG), MTT (3-(4,5-dimethylthiazol-2-yl)-2,5-diphenyltetrazolium bromide), penicillin and streptomycin, calcium ionophore A23187, mouse anti-DNP (dinitrophenyl) IgE antibody, and DMSO were purchased from Sigma-Aldrich (St. Louis, MO, USA). Moreover, FBS was obtained from Hyclone (Logan, UT, USA). Dinitrophenyl-conjugated bovine serum albumin (DNP-BSA) was purchased from Merck (Kenilworth, NJ, USA). Additional chemicals as well as reagents were purchased at the highest possible purity.

**Cell culture** The mucosal mast cell-derived rat basophilic leukemia (RBL-2H3) cell line was obtained from the American Type Culture Collection. Cells were grown in DMEM medium accompanied with 10% FBS in addition to 100 U/mL penicillin plus 100 µg/mL streptomycin. Cells were cultured in 10 cm cell culture dishes (Cellstar) at 37 °C with 5% CO<sub>2</sub> in air.

**Cell viability assay** MTT assay was used to assess the toxic effects of samples on RBL-2H3 cells [44] and was done as previously mentioned [42, 43]. All experiments were done in triplicates. DMSO served as the negative control not affecting the growth of RBL-2H3 cells. Triton X-100 (0.5% solution) was employed as the positive control resulting in the death of all cells in a well.

**Degranulation β-hexosaminidase assay induced by A23187** A23187-induced degranulation in RBL-2H3 cells was evaluated by a β-hexosaminidase activity assay as previously reported employing certain modifications [45, 46]. RBL-2H3 cells were seeded into 96-wells plate using a density of 2 × 10<sup>4</sup> cells/well and were incubated at 37 °C for 5 h in 5% CO<sub>2</sub>. Cells were washed with PBS (phosphate buffered saline) and then various concentrations of samples or medium (untreated control) were added to each well (100 µL), and the treated cells were incubated at 37 °C in 5% CO<sub>2</sub> for 20 h. The cells were stimulated by calcium ionophore A23187 (1 µM) diluted in Tyrode's buffer (135 mM NaCl, 1.8 mM CaCl<sub>2</sub>, 5 mM KCl, 1.0 mM MgCl<sub>2</sub>, 5.6 mM glucose, 20 mM HEPES at pH 7.4), and kept at 37 °C in 5% CO<sub>2</sub> for 1 h. For the total amount of β-hexosaminidase release, the unstimulated cells were lysed using 0.5% Triton X-100. Untreated unstimulated

cells represented spontaneous  $\beta$ -hexosaminidase release. The control wells were represented by the stimulated untreated cells. The cells supernatants (50  $\mu$ L) were incubated with equal volume of 1  $\mu$ M of p-NAG (50  $\mu$ L), a substrate for  $\beta$ -hexosaminidase, prepared in 0.05 M citrate buffer (pH 4.5) for 1 h at 37 °C. The reaction was stopped by 100  $\mu$ L of stop buffer (0.1 M  $\text{Na}_2/\text{NaHCO}_3$ , pH 10.0). Microplate reader was used to measure the absorbance at 405 nm. The inhibition percentage of  $\beta$ -hexosaminidase release from RBL-2H3 cells was calculated using the following equation:

$$\text{Inhibition (\%)} = \left[ 1 - \frac{(\text{OD}_{\text{sample}} - \text{OD}_{\text{spontaneous}})}{(\text{OD}_{\text{control}} - \text{OD}_{\text{spontaneous}})} \right] \times 100$$

Dexamethasone (10 nM) was employed as the positive control.

**Degranulation  $\beta$ -hexosaminidase assay induced by IgE**  $\beta$ -Hexosaminidase release from the activated RBL-2H3 cells was measured as previously reported [45, 47], with some modifications. The inhibition percentage of antigen-induced  $\beta$ -hexosaminidase release from RBL-2H3 cells was assessed in a similar way as described above in the degranulation A23187-induced  $\beta$ -hexosaminidase assay, except of the stimulation process. The cells were sensitized with anti-DNP IgE (0.1  $\mu$ g/mL) for at least 2 h and then washed with pre-warmed Tyrode's buffer, followed by stimulation by antigen DNP-BSA (100 ng/mL). Dexamethasone (10 nM) was employed as the positive control.

#### *In vitro assessment of the anti-inflammatory activity*

**Preparation of human neutrophils** Blood was withdrawn from 20 to 35 years old healthy human donors adopting a protocol approved by the institutional review board at Chang Gung Memorial Hospital. Isolation of neutrophils was done employing a standard method which was previously reported [48].

#### **Measurement of superoxide generation**

Ferricytochrome *c* (0.5 mg/mL) and  $\text{Ca}^{2+}$  (1 mM) were incubated with neutrophils at 37 °C for 2 min, followed by the treatment with the tested samples for 5 min. Cells activation was done using formyl-methionyl-leucyl-phenylalanine (fMLF, 100 nM)/cytochalasin B (CB, 1  $\mu$ g/mL) for 10 min. The absorbance was detected at 550 nm in a double-beam spectrophotometer Hitachi U-3010. Superoxide inhibition was determined by lowering ferricytochrome *c* as reported previously [48, 49]. The differences in absorbance between the measurements in the presence of superoxide (100 U/mL) and its absence divided by the extinction coefficient for the reduction of

ferricytochrome *c* ( $\epsilon = 21.1/\text{mM}/10 \text{ mm}$ ) were used as the basis for calculations. Genistein was adopted as the positive control [50, 51].

#### **Measurement of elastase release**

The release of elastase was determined by assessing the degranulation of azurophilic granules [48, 49]. An elastase substrate MeO-Suc-Ala-Ala-Pro-Val-*p*-nitroanilide (100  $\mu$ M) was equilibrated with neutrophils at 37 °C for 2 min, followed by incubation with drugs for 5 min. Activation of the cells was done using 100 nM fMLF and 0.5  $\mu$ g/mL CB, and then the variations in absorbance were detected at 405 nm. The results are shown as the percentage of the initial rate of elastase release in the fMLF/CB-activated, drug-free control system. Genistein was employed as the positive control [50, 51].

#### **Statistical analysis**

Results are represented as mean  $\pm$  SD value of at least three independent measurements unless otherwise specified. The 50% inhibitory concentration ( $\text{IC}_{50}$ ) was determined using the dose-response curve which was constructed by plotting the percentage of inhibition versus concentrations (linear function, Microsoft Office). Statistical analysis was done using one-way analysis of variance (ANOVA) followed by Dunnett's test (GraphPad Prism 6.0, GraphPad Software, San Diego, CA, USA, anti-allergic assay) or Student's *t*-test (Sigma Plot, Systat software, Systat Software Inc., San Jose, CA, USA, anti-inflammatory assay). Values which show  $*p < 0.05$ ,  $**p < 0.001$  are statistically significant.

#### **Phytochemical investigations**

##### **General experimental procedures**

$^1\text{H}$  and  $^{13}\text{C}$  (APT) NMR analyses were done using a Bruker Ascend 400/R spectrometer (Bruker Avance III, Fallanden Switzerland) at the Center for Drug Discovery, Research and Development, Faculty of Pharmacy, Ain Shams University using 400 and 100 MHz the operating frequencies. Chemical shifts were reported in  $\delta$  ppm and were related to that of the solvents. Dissolution of the tested samples was done using various deuterated solvents (Sigma Aldrich, Germany) in 3 mm NMR tubes (Bruker). Spectra were recorded at 25 °C;  $\delta$  ppm relative to tetramethylsilane ( $\text{Me}_4\text{Si}$ ) as the internal standard. Two-dimensional (2D) NMR experiments ( $^1\text{H}$ ,  $^1\text{H}$ - $^1\text{H}$  COSY;  $^1\text{H}$ - $^{13}\text{C}$  HSQC;  $^1\text{H}$ - $^{13}\text{C}$  HMBC) were done using the pulse sequences from the Bruker user library. Waters Xevo TQD mass spectrometer supplied with UPLC Acquity mode (Milford, USA) was employed to carry out ESI-MS analysis. Normal phase column chromatography was done using silica gel (Kieselgel 60, 70–230, and 230–400 mesh, Merck KGaA, Darmstadt, Germany). TLC analysis was done utilizing normal phase silica gel

precoated plates F<sub>254</sub> (Merck, Germany). Detection of TLC spots was done using UV light at 254 nm and 365 nm as well as by spraying with 10% H<sub>2</sub>SO<sub>4</sub> with subsequent heating on a hot plate at 100 °C.

#### Isolation of the secondary metabolites from the bioactive fractions

The *n*-hexane fraction (33 g) of *B. rupestris* was chromatographed on silica gel (600 g) employing *n*-hexane:EtOAc with increasing polarity to give 23 major fractions. Fraction II was further eluted with a mixture of *n*-hexane: EtOAc (9.0:1.0) from which compound **1** (40 mg) was precipitated as a white amorphous powder. A mixture of compounds **2** and **3** (60 mg) was precipitated from fraction III as white crystalline needles using the solvent system *n*-hexane:EtOAc (9.0:1.0) as illustrated in Fig. 1.

The dichloromethane fraction of *B. rupestris* (6 g) was chromatographed on silica gel (300 g) using mixtures of CH<sub>2</sub>Cl<sub>2</sub>:CH<sub>3</sub>OH with increasing polarity as eluents to afford 26 major fractions. Fraction VI (70 mg) was further eluted with dichloromethane and was subjected to silica gel column using a mixture of CH<sub>2</sub>Cl<sub>2</sub>:CH<sub>3</sub>OH to give seven subfractions. Subfraction 7 (30 mg) was eluted with a mixture of CH<sub>2</sub>Cl<sub>2</sub>:CH<sub>3</sub>OH (9.9:0.1) and purified over preparative TLC which resulted in the separation of compound **4** (8 mg) that showed strong fluorescent yellow color. Fraction XV

was eluted using a mixture of CH<sub>2</sub>Cl<sub>2</sub>:CH<sub>3</sub>OH (9.6:0.4) from which compound **5** (50 mg) was precipitated as a yellow powder as shown in Fig. 2.

The EtOAc fraction (4 g) was applied on the top of 150 g Diaion HP column using water, 50% methanol, 100% methanol as the mobile phases. The 50% methanol fraction (2 g) was the most promising fraction after comparing its TLC with the other fractions and was applied on the top of 40 g Sephadex® LH 20 and eluted using water and methanol of decreasing polarity to give 16 fractions. Fraction V (70 mg) and fraction VI (50 mg) were eluted using water 100% and were purified over preparative TLC using CH<sub>2</sub>Cl<sub>2</sub>:CH<sub>3</sub>OH (8.5:1.5) as the mobile phase to separate compounds **6** (6 mg) and **7** (5 mg), respectively (Fig. 3).

#### Spectroscopic data of compounds 1–7

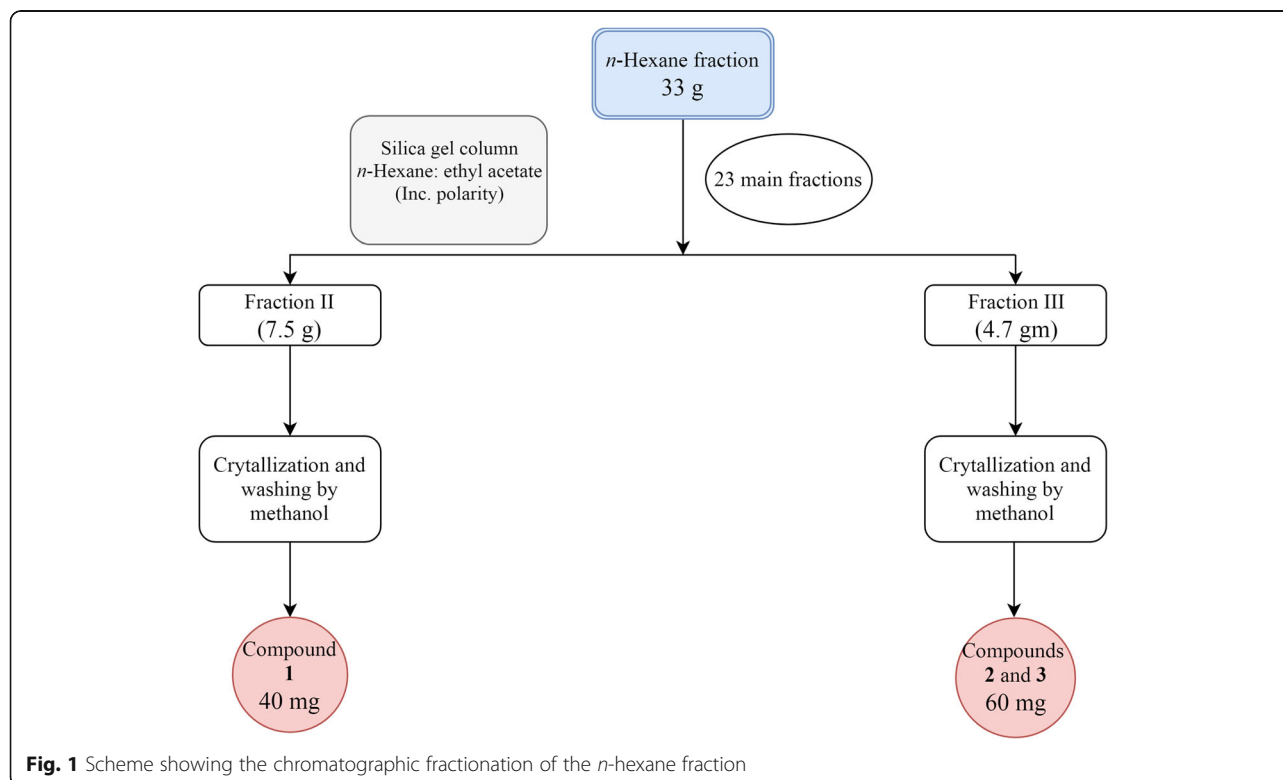
##### β-Amyrin acetate (**1**)

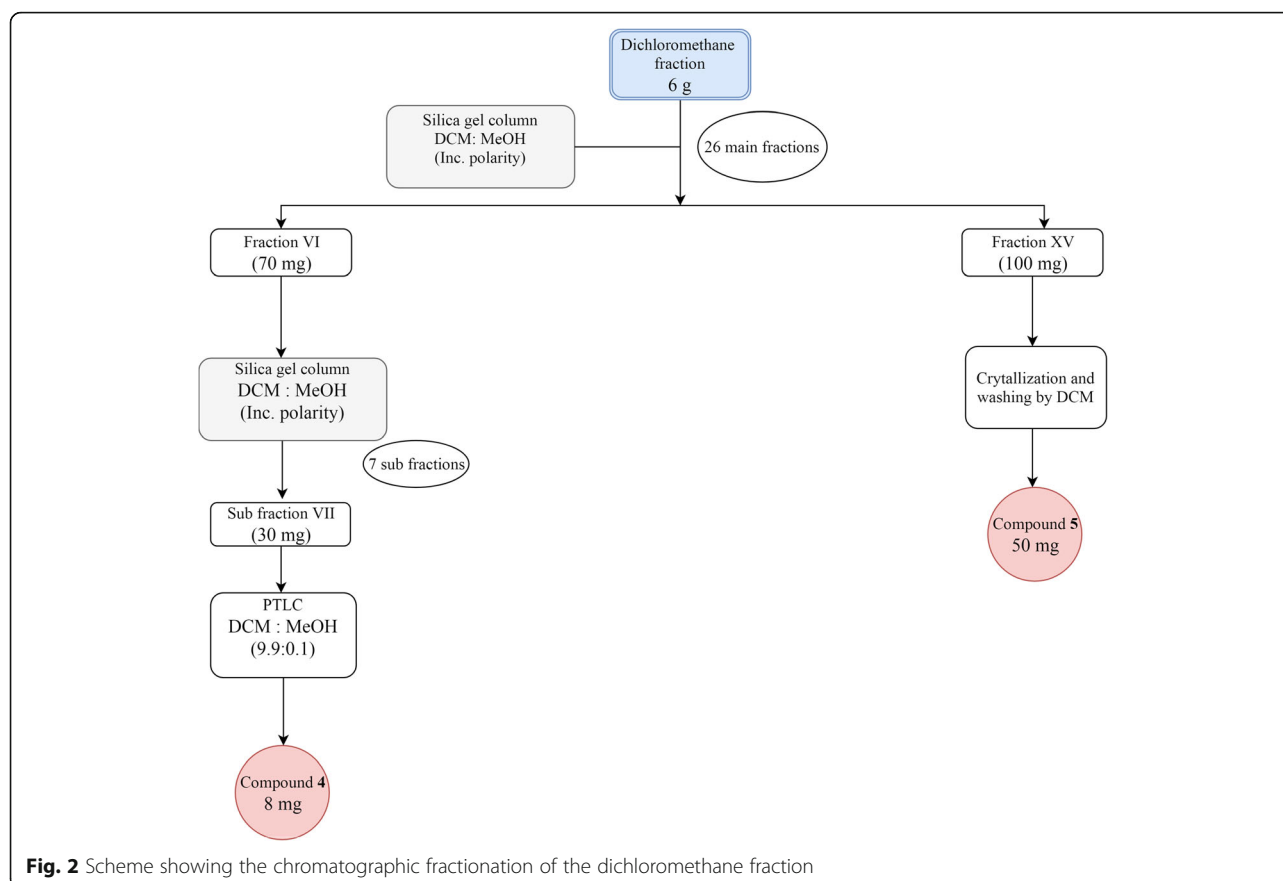
It was isolated as a white amorphous powder; with R<sub>f</sub>= 0.530 in *n*-hexane:EtOAc (9.5:0.5). <sup>1</sup>H NMR (400 MHz, CDCl<sub>3</sub>), <sup>13</sup>C NMR (100 MHz, CDCl<sub>3</sub>) and 2D NMR spectroscopic data are displayed in the Additional file 1: Figure S1).

##### β-Sitosterol (**2**) and Stigmasterol (**3**)

They were isolated as white crystalline needles; showing R<sub>f</sub>= 0.206 in *n*-hexane:EtOAc (9:1). <sup>1</sup>H-NMR (400 MHz, CDCl<sub>3</sub>), <sup>13</sup>C NMR (100 MHz, CDCl<sub>3</sub>) and 2D NMR spectral data are displayed in the Additional file 1: Figure S2.

##### Scopoletin (**4**)





It was obtained as a yellow powder; with  $R_f = 0.630$  in  $\text{CH}_2\text{Cl}_2:\text{CH}_3\text{OH}$  (9.9:0.1).  $^1\text{H-NMR}$  (400 MHz,  $\text{CD}_3\text{OD}$ ) ( $\delta$  ppm): 7.75 (1H,  $d$ ,  $J = 9.1$ , H-4), 6.80 (1H,  $s$ , H-5), 6.45 (1H,  $s$ , H-8), 5.85 (1H,  $d$ ,  $J = 9.1$  Hz, H-3), 3.81 (3H,  $s$ , 6- $\text{OCH}_3$ ).  $^{13}\text{C}$  NMR data (100 MHz,  $\text{CD}_3\text{OD}$ ) ( $\delta$  ppm): 166.26 (C-2), 153.86 (C-7), 151.4 (C-6), 146.99 (C-4), 107.65 (C-5), 105.50 (C-3), 104.59, (C-8), 56.03 (6- $\text{OCH}_3$ ). It exhibited a deprotonated molecular ion peak at  $m/z$  190.8  $[\text{M-H}]^-$  in ESI-MS negative ion mode, corresponding to the molecular formula  $\text{C}_{10}\text{H}_8\text{O}_4$  (Additional file 1: Figure S3).

#### $\beta$ -Sitosterol-3-O- $\beta$ -D-glucoside (5)

It was isolated as a buff amorphous powder; with  $R_f = 0.630$  in  $\text{CH}_2\text{Cl}_2:\text{CH}_3\text{OH}$  (9.2:0.8).  $^1\text{H-NMR}$  (400 MHz,  $\text{DMSO}-d_6$ ),  $^{13}\text{C}$  NMR (100 MHz,  $\text{DMSO}-d_6$ ) and 2D NMR spectroscopic data are displayed in the Additional file 1: Figure S4.

#### Dihydrodehydrodiconiferyl alcohol 4-O- $\beta$ -D-glucoside (6)

It was obtained as a yellowish white amorphous powder; with  $R_f = 0.259$  in  $\text{CH}_2\text{Cl}_2:\text{CH}_3\text{OH}$  (8.5:1.5).  $^1\text{H-NMR}$  (400 MHz,  $\text{CD}_3\text{OD}$ ),  $^{13}\text{C}$  NMR data (100 MHz,  $\text{CD}_3\text{OD}$ ) are illustrated in Table 4, (Additional file 1: Figure S5).

#### Dihydrodehydrodiconiferyl alcohol 9-O- $\beta$ -D-glucoside (7)

It was obtained as a yellowish white amorphous powder; with  $R_f = 0.304$  in  $\text{CH}_2\text{Cl}_2:\text{CH}_3\text{OH}$  (8.5:1.5).  $^1\text{H-NMR}$

(400 MHz,  $\text{CD}_3\text{OD}$ ),  $^{13}\text{C}$  NMR (100 MHz,  $\text{CD}_3\text{OD}$ ) and 2D NMR spectroscopic data are displayed in Table 4 and the Additional file 1: Figure S6.

## Results

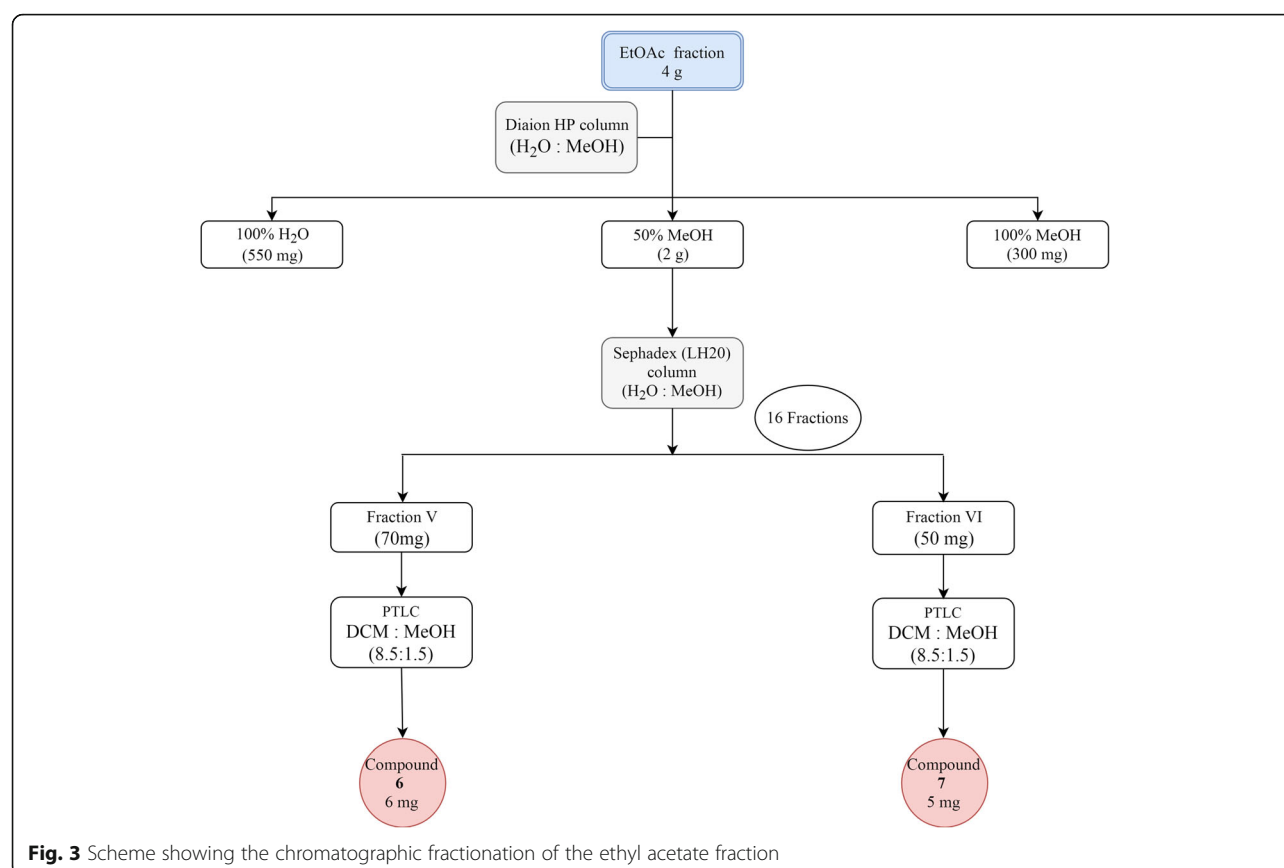
### In vitro assessment of the cytotoxic activity of *B. rupestris* and *B. discolor*

The cytotoxicity of the total methanol extracts and fractions of both *B. rupestris* and *B. discolor* was evaluated versus HepG2, A549 and MDA-MB-231 cancer cells using doxorubicin as the positive control. Extracts and fractions of both species at 20  $\mu\text{g/mL}$  exhibited no cytotoxic activity against any of the tested cell lines. Noteworthy to mention that doxorubicin showed 91.28, 97.69 and 98.05% cell growth inhibition against HepG2, MDA-MB-231 and A549, respectively at 2  $\mu\text{g/mL}$ . The results are illustrated in Table 1. Together with the nontoxic effects of all samples towards RBL-2H3 mast cells (see the following section, and Table 2) the results suggested that both species extracts and fractions exhibited no cytotoxicity against the tested cancer cell lines.

### In vitro assessment of the anti-allergic activity of *B. rupestris* and *B. discolor*

The anti-allergic activity of the total methanol extracts and fractions of both *B. rupestris* and *B. discolor* was





assessed using degranulation assay in RBL-2H3 mast cell model and the results are presented in Table 2. Initially, the cytotoxic effect of all samples was tested against RBL-2H3 cells using MTT viability assay. All samples were found to be nontoxic at 100  $\mu\text{g/mL}$ . The samples were subjected to the anti-allergic assay by evaluating their inhibitory effect on  $\beta$ -hexosaminidase release in RBL-2H3 cells induced by calcium ionophore, A23187. According to our results, *B. rupestris* and *B. discolor* crude methanol extracts (BRT 25.7% and BDT 16.0% inhibition) and nonpolar *n*-hexane (BRH 39.0%, BDH 30.3% inhibition) and dichloromethane fractions (BRD 19.0%; and BDD 44.0% inhibition) exhibited significant inhibition of  $\beta$ -hexosaminidase release in A23187-induced degranulation assay at 100  $\mu\text{g/mL}$  (Table 2). Dexamethasone, a

positive control, showed 62.0% inhibition of  $\beta$ -hexosaminidase release at 10 nM.

#### In vitro assessment of the anti-inflammatory activity of *B. rupestris* and *B. discolor*

Similarly, the anti-inflammatory activity was determined for the total methanol extracts and fractions of *B. rupestris* and *B. discolor* and the results are presented in Table 3. Both *Brachychiton* species exhibited a promising inhibitory activity on superoxide anion production as well as elastase release in fMLF-activated human neutrophils indicating their potential applications for the alleviation of both acute and chronic inflammatory disorders. All samples inhibited superoxide anion generation showing  $\text{IC}_{50}$  values between 0.78 and 6.25  $\mu\text{g/mL}$  in addition

**Table 1** In vitro cytotoxicity of different extracts and fractions of *B. rupestris* and *B. discolor* against HepG2, MDA-MB-231 and A549 cell lines

Cell line	BRT	BRH	BRD	BRE	BRR	BDT	BDH	BDD	BDE	doxorubicin
HepG2	1.28	-2.078	-8.02	-8.43	-13.74	1.66	-7.43	-16.18	-6.62	91.28 $\pm$ 0.3
MDA-MB-231	-15.86	-9.70	-18.83	-25.52	-23.30	-6.19	-6.73	13.17	-20.64	97.69 $\pm$ 0.4
A549	0.44	-0.81	7.85	-8.37	-0.89	12.59	8.18	14.99	-6.52	98.05 $\pm$ 0.0

Results are presented as growth inhibition percentage at concentration of 20  $\mu\text{g/mL}$ , mean ( $n = 1$ ). Doxorubicin (2  $\mu\text{g/mL}$ ) was used as the reference drug, mean  $\pm$  SD ( $n = 2$ ). BRT: *B. rupestris* total methanol extract; BHT: *B. rupestris* *n*-hexane fraction; BRD: *B. rupestris* dichloromethane fraction; BRE: *B. rupestris* ethyl acetate fraction; BRR: *B. rupestris* remaining MeOH(aq) fraction; BDT: *B. discolor* total methanol extract; BDH: *B. discolor* *n*-hexane fraction; BDD: *B. discolor* dichloromethane fraction; BDE: *B. discolor* ethyl acetate fraction

**Table 2** Anti-allergic activity of *B. rupestris* and *B. discolor* extracts and fractions

Sample	% viability, RBL-2H3 <sup>a</sup>	% inhibition of A23187-induced $\beta$ -hexosaminidase release <sup>b</sup>	
	100 $\mu$ g/mL	10 $\mu$ g/mL	100 $\mu$ g/mL
BRT	99.0 $\pm$ 1.7	3.0 $\pm$ 5.2	25.7 $\pm$ 2.1**
BRH	96.7 $\pm$ 4.0	3.3 $\pm$ 5.8	39.0 $\pm$ 13.1**
BRD	95.3 $\pm$ 8.1	4.3 $\pm$ 7.5	19.0 $\pm$ 4.4*
BRE	97.7 $\pm$ 4.0	2.0 $\pm$ 3.5	7.0 $\pm$ 5.2
BRR	99.0 $\pm$ 1.7	4.3 $\pm$ 5.1	3.7 $\pm$ 6.4
BDT	99.0 $\pm$ 1.7	3.7 $\pm$ 6.4	16.0 $\pm$ 5.0*
BDH	99.7 $\pm$ 0.6	4.3 $\pm$ 7.5	30.3 $\pm$ 3.1**
BDD	100.0 $\pm$ 0.0	0.0 $\pm$ 0.0	44.0 $\pm$ 7.8**
BDE	100.0 $\pm$ 0.0	1.7 $\pm$ 2.9	0.3 $\pm$ 0.6

<sup>a</sup>The cytotoxicity of samples towards RBL-2H3 cells was evaluated using MTT viability assay and none of the samples showed any toxicity; results are presented as mean  $\pm$  SD ( $n = 3$ )

<sup>b</sup>Dexamethasone (10 nM) was used as the positive control and inhibited  $62.0 \pm 9.5\%$  of A23187-induced  $\beta$ -hexosaminidase release in RBL-2H3 cells. Results are presented as mean  $\pm$  SD ( $n = 3$ ); \* $p < 0.05$ , \*\* $p < 0.001$  compared with the control value (A23187 only)

BRT *B. rupestris* total methanol extract, BRH *B. rupestris* *n*-hexane fraction, BRD *B. rupestris* dichloromethane fraction, BRE *B. rupestris* ethyl acetate fraction, BRR *B. rupestris* remaining MeOH(aq) fraction, BDT *B. discolor* total methanol extract, BDH *B. discolor* *n*-hexane fraction, BDD *B. discolor* dichloromethane fraction, BDE *B. discolor* ethyl acetate fraction

**Table 3** Effect of the total extracts and fractions of *B. rupestris* and *B. discolor* on superoxide anion generation and elastase release in fMLF/CB-induced human neutrophils

Sample	Superoxide anion generation <sup>a</sup>	Elastase release <sup>a</sup>
	IC <sub>50</sub> ( $\mu$ g/mL) <sup>b</sup>	IC <sub>50</sub> ( $\mu$ g/mL) <sup>b</sup>
BRT	4.92 $\pm$ 1.47	3.82 $\pm$ 0.55
BRH	5.69 $\pm$ 0.80	3.73 $\pm$ 1.16
BRD	2.99 $\pm$ 0.73	1.98 $\pm$ 1.54
BRE	6.25 $\pm$ 3.10	2.71 $\pm$ 0.79
BRR	3.01 $\pm$ 1.91	> 10 <sup>c</sup>
BDT	4.73 $\pm$ 0.97	5.37 $\pm$ 1.23
BDH	6.25 $\pm$ 2.18	6.04 $\pm$ 2.32
BDD	0.78 $\pm$ 0.29	1.57 $\pm$ 0.84
BDE	5.22 $\pm$ 1.35	2.95 $\pm$ 1.08
genistein	0.41 $\pm$ 0.09	4.41 $\pm$ 1.99

<sup>a</sup>IC<sub>50</sub> values, results are presented as mean  $\pm$  SD ( $n = 3$ ), compared with the control value (formyl-methionyl-leucyl-phenylalanine/cytochalasin B, fMLF/CB)

<sup>b</sup>Concentration necessary for 50% inhibition (IC<sub>50</sub>)

<sup>c</sup>BRR exerted significant inhibitory activity in superoxide anion generation ( $49.6 \pm 2.9\%$ , \*\* $p < 0.001$ ) at 10  $\mu$ g/mL. BRT *B. rupestris* total methanol extract, BRH *B. rupestris* *n*-hexane fraction, BRD *B. rupestris* dichloromethane fraction, BRE *B. rupestris* ethyl acetate fraction, BRR *B. rupestris* remaining MeOH(aq) fraction, BDT *B. discolor* total methanol extract, BDH *B. discolor* *n*-hexane fraction, BDD *B. discolor* dichloromethane fraction, BDE *B. discolor* ethyl acetate fraction

to inhibition of elastase release showing IC<sub>50</sub> values ranging from 1.57 to > 10  $\mu$ g/mL (Table 3). The most potent fractions, dichloromethane fractions of *B. rupestris* (BRD) and *B. discolor* (BDD) inhibited superoxide anion generation with IC<sub>50</sub> values 2.99  $\mu$ g/mL (BRD) and 0.78  $\mu$ g/mL (BDD), and inhibited elastase release with IC<sub>50</sub> values 1.98  $\mu$ g/mL (BRD) and 1.57  $\mu$ g/mL (BDD). Such activities indicated comparable or even better inhibitory potential than that of genistein (superoxide IC<sub>50</sub> 0.41  $\mu$ g/mL and elastase IC<sub>50</sub> 4.41  $\mu$ g/mL), a known anti-inflammatory natural product [50, 51]. The dichloromethane fractions (BRD and BDD) were capable of almost completely abolishing oxidative burst and degranulation in fMLF-activated human neutrophils at 10  $\mu$ g/mL (data not shown). Meanwhile, the ethyl acetate fraction of both species showed anti-inflammatory activity by inhibiting elastase release showing IC<sub>50</sub> values of 2.71  $\mu$ g/mL for *B. rupestris* (BRE) and 2.95  $\mu$ g/mL for *B. discolor* (BDE).

### Phytochemical investigations

In-depth phytochemical investigation was performed on the most bioactive fractions of *B. rupestris* leaves including the *n*-hexane, the dichloromethane and ethyl acetate fractions that showed the highest anti-allergic and anti-inflammatory activities. Three compounds were isolated and structurally elucidated from the *n*-hexane fraction which were  $\beta$ -amyrin acetate (1) [29],  $\beta$ -sitosterol (2) [52], stigmasterol (3) [52]. Meanwhile, two compounds were obtained from the dichloromethane fraction including scopoletin (4) [53, 54] and  $\beta$ -sitosterol-3-O- $\beta$ -D-glucoside (5) [55] which were isolated for the first time from *B. rupestris* leaves. Furthermore, two neolignans were obtained from the ethyl acetate fraction, dihydrodehydrodiconiferyl alcohol 4-O- $\beta$ -D-glucoside (6) [56] and dihydrodehydrodiconiferyl alcohol 9-O- $\beta$ -D-glucoside (7) [57] which were isolated for the first time from the genus (Fig. 4). Their structures were fully elucidated using 1D and 2D NMR techniques and they were further ascertained by comparing their data with previously reported data in literature.

Dihydrodehydrodiconiferyl alcohol 4-O- $\beta$ -D-glucoside (6) was isolated as a yellowish white amorphous powder. <sup>1</sup>H-NMR of (6) revealed the presence of a 1,2,4-trisubstituted benzene ring with signals at  $\delta_H$  7.03 (*d*,  $J = 1.84$  Hz), 7.14 (*d*,  $J = 8.43$  Hz) and 6.93 (*dd*,  $J = 8.31, 2.03$  Hz) for H-2, H-5 and H-6, respectively, each integrated for one proton. Also, a 1,2,3,5-tetrasubstituted benzene ring was presented by two broad singlet signals at  $\delta_H$  6.73 (H-2') and 6.72 (H-6'). The spectrum revealed the existence of a hydroxypropyl group showing three signals at  $\delta_H$  2.63 (*t*, H-7'), 1.82 (*m*, H-8'), 3.57 (*t*, H-9'). Furthermore, a methine-methine-methylene group (CH-CH-CH<sub>2</sub>) appeared at  $\delta_H$  5.56 (*d*,  $J = 5.85$ , H-7), 3.44 (*m*, H-8), 3.80, 3.75 (*m*, *m*, H-9). The presence of  $\beta$ -D-glucose was

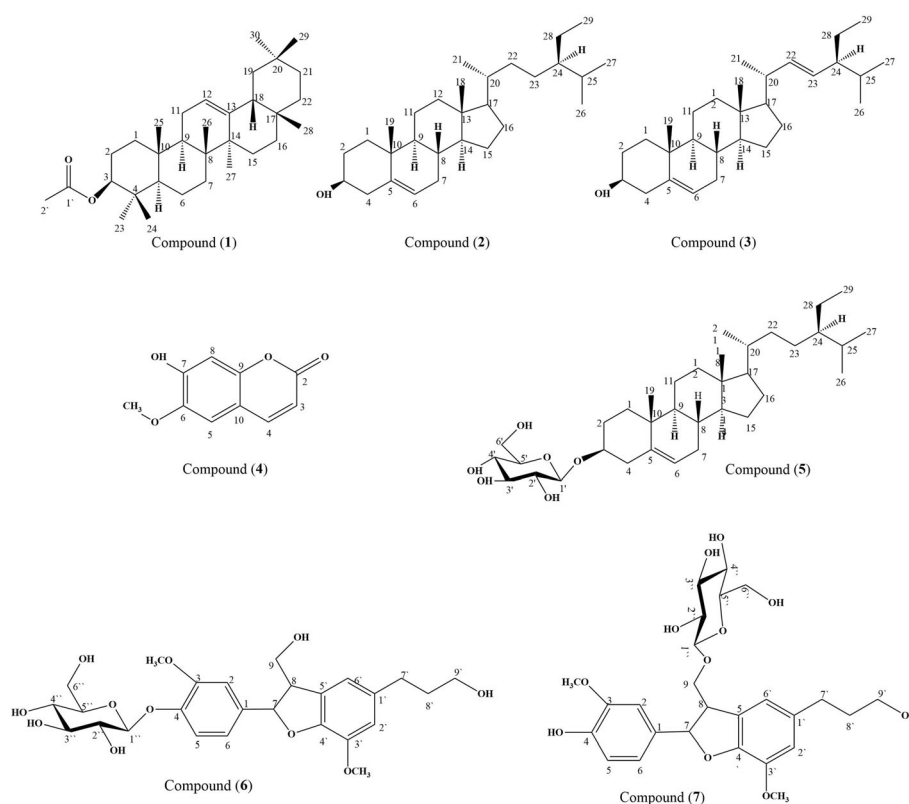


**Fig. 4** Structures of identified compounds from *n*-hexane, dichloromethane and ethyl acetate fractions of *B. rupestris*

proposed by the appearance of anomeric proton at  $\delta_H$  4.88 and other sugar protons at 3.39–3.85. Two singlet signals each integrated for three protons at  $\delta_H$  3.87 and 3.83 were attributed to two methoxy groups.  $^{13}C$ -NMR spectrum of compound (6) showed the presence of five aromatic methines and seven quaternary aromatic carbons signals attributed to two benzene rings at  $\delta_C$  111.19, 117.95, 119.37, 114.19, 118.04, 137.09, 150.9, 147.6, 138.37, 145.24, 147.6, 129.58. Downfield shifts of C-3 (150.9), C-4 (147.6), C-3' (145.24), C-4' (147.6) indicated their attachment to oxygenated functional groups. A signal at  $\delta_C$  102.78 was attributed to the anomeric carbon of glucose unit and the other sugar carbons appeared at 74.90, 77.84, 71.34, 78.19 and 62.51. The two signals at  $\delta_C$  56.79 and 56.71 represented two methoxy groups. Other aliphatic signals appeared at  $\delta_C$  88.48, 65.07, 62.22, 55.68, 35.84 and 32.89. The HMBC spectrum showed that the methoxy group at  $\delta_C$  56.79 was placed at C-3 (150.9) and the methoxy group at  $\delta_C$  56.71 was placed at C-3' (145.24). Also, it showed a correlation between C-6, C-2 with H-7; C-6', C-2' with H-7'; and C-9' with H-7'. The correlation between C-4 with H-1'' supported the presence of the sugar at C-4. From the displayed data (Table 4) and through comparison with the previously reported literature [56], compound (6) was identified as

dihydrodehydrodiconiferyl alcohol 4-*O*- $\beta$ -D-glucoside which was the first time to be reported in the genus.

Dihydrodehydrodiconiferyl alcohol 9-*O*- $\beta$ -D-glucoside (7) was isolated as a yellowish white amorphous powder. The  $^1H$ -NMR and  $^{13}C$ -NMR data for this compound were similar to compound (6) suggesting the same neolignan nucleus; the two compounds differ in the position of the glucose moiety. The HMBC spectrum revealed the correlation between C-9 with H-1'' which supported the attachment of the sugar at C-9. The downfield shift of C-9 at  $\delta_C$  72.46 also supported the attachment of the sugar at C-9 [57] (Table 4).

#### In vitro assessment of the cytotoxic activity of the isolated compounds

Additionally, the cytotoxic activity of the compounds obtained from the *n*-hexane and dichloromethane fractions of *B. rupestris* was examined using different concentrations (20, 10, 5, 2.5  $\mu$ g/mL) of these compounds on the same cell lines utilized in the determination of the cytotoxic effect of the total extracts and subsequent fractions. The isolated compounds showed no cytotoxicity against hepatoma HepG2, breast MDA-MB-231 and lung A549 cancer cell lines with growth inhibition below 20%. The results are illustrated in Table 5.

**Table 4**  $^1\text{H}$ - and  $^{13}\text{C}$ -NMR spectroscopic data for 6 and 7

	Dihydrodehydrodiconiferyl alcohol 4-O- $\beta$ -D-glucoside (6)		Dihydrodehydrodiconiferyl alcohol 9-O- $\beta$ -D-glucoside (7)	
	$\delta_{\text{C}}$	$\delta_{\text{H}}$ (Mult, Int), J in Hz	$\delta_{\text{C}}$	$\delta_{\text{H}}$ (Mult, Int), J in Hz
1	137.09		134.67	
2	111.19	7.03 (d, 1H), 1.84	110.71	7.02 (d, 1H), 2.01
3	150.9		149.05	
4	147.6		147.48	
5	117.95	7.14 (d, 1H), 8.43	116.08	6.78 (d, 1H), 8.09
6	119.37	6.93 (dd, 1H), 8.31, 2.03	119.72	6.89 (dd, 1H), 8.28, 2
7	88.48	5.56 (d, 1H), 5.85	88.98	5.62 (d, 1H), 6.21
8	55.68	3.44 (m, 1H)	53.28	3.69 (m, 1H)
9	65.07	3.80, 3.75 (m, m, 2H)	72.46	4.23, 3.79 (dd, m, 2H)
3-OCH <sub>3</sub>	56.79	3.87 (s, 3H)	56.44	3.85 (s, 3H)
1'	138.37		136.64	
2'	114.19	6.73 (s, 1H)	114.19	6.75 (s, 1H)
3'	145.24		145.21	
4'	147.6		147.48	
5'	129.58		129.56	
6'	118.04	6.72 (s, 1H)	118.21	6.80 (s, 1H)
7'	32.89	2.63 (t, 2H)	32.89	2.65 (t, 2H)
8'	35.84	1.82 (m, 2H)	35.82	1.84 (m, 2H)
9'	62.22	3.57 (t, 2H)	62.23	3.59 (t, 2H)
3'-OCH <sub>3</sub>	56.71	3.83 (s, 3H)	56.77	3.88 (s, 3H)
1''	102.78	4.88 (covered by solvent, 1H)	104.57	4.38 (d, 1H), 7.79
2''	74.90	3.48 (m, 1H)	75.18	3.25 (m, 1H)
3''	77.84	3.39 (m, 1H)	78.07	3.31 (m, 1H)
4''	71.34	3.39 (m, 1H)	71.66	3.31 (m, 1H)
5''	78.19	3.39 (m, 1H)	78.26	3.31 (m, 1H)
6''	62.51	3.85, 3.69 (m, 2H)	62.81	3.88, 3.70 (m 2H)

NMR data ( $\delta$ ) were measured  $^1\text{H}$ -NMR (400 MHz, CD<sub>3</sub>OH) and  $^{13}\text{C}$ -NMR data (100 MHz, CD<sub>3</sub>OH)

Doxorubicin was employed as a positive control and exhibited a strong cytotoxic effect against HepG2 (IC<sub>50</sub> 0.49  $\mu\text{g/mL}$ ), MDA-MB-231 (IC<sub>50</sub> 0.68  $\mu\text{g/mL}$ ) and A549 (IC<sub>50</sub> 0.13  $\mu\text{g/mL}$ ) cells.

#### In vitro assessment of the anti-allergic activity of the isolated compounds

To ascertain, whether the isolated compounds might be responsible for the anti-allergic activity observed in *Bra-chychiton* sp. crude extracts and nonpolar fractions, the isolated compounds were subjected to degranulation assay in RBL-2H3 mast cell model. The results are presented in Table 6. MTT viability assay was used to evaluate the potential toxic effects against RBL-2H3 cells. A mixture of  $\beta$ -sitosterol (2) and stigmasterol (3) (200 and 100  $\mu\text{g/mL}$ ) was considered toxic (viability below 85%). According to our results, scopoletin (4) showed 23.0% inhibition of A23187-induced and 30.0% of antigen-

induced degranulation at 500  $\mu\text{M}$ . Dihydrodehydrodiconiferyl alcohol 9-O- $\beta$ -D-glucoside (7) showed only weak inhibitory effect in the A23187-induced assay (16.3% at 100  $\mu\text{M}$  and 18.0% at 500  $\mu\text{M}$ ). Dexamethasone (10 nM) was utilized as the positive control and inhibited  $\beta$ -hexosaminidase release by 93.7%.

#### In vitro assessment of the anti-inflammatory activity of the isolated compounds

The anti-inflammatory effect of the isolated compounds was determined to understand whether any of these compounds might be accountable for the potent activity of *B. rupestris* crude extract and its fractions. The results are illustrated in Table 7. According to the results, scopoletin (4) was found to significantly inhibit elastase release in fMLF-induced human neutrophils by 22.8% at 10  $\mu\text{M}$ . Genistein, natural tyrosine kinase inhibitor [50, 51], was used as the positive control and caused significant



**Table 5** Cytotoxic activity of the isolated compounds

Cell line	Conc. ( $\mu\text{g}/\text{mL}$ )	% Inhibition	
		$\beta$ -amyrin acetate (1)	Scopoletin (4)
HepG2	20	12.1 $\pm$ 3.4	11.4 $\pm$ 2.1
	10	16.0 $\pm$ 0.3	6.5 $\pm$ 1.2
	5	20.4 $\pm$ 2.3	0.9 $\pm$ 0.1
	2.5	8.23 $\pm$ 0.7	5.9 $\pm$ 1.2
MDA-MB-231	20	-19.6 $\pm$ 1.2	8.2 $\pm$ 1.0
	10	-13.9 $\pm$ 1.2	6.0 $\pm$ 0.3
	5	-5.5 $\pm$ 1.2	10.7 $\pm$ 9.8
	2.5	7.0 $\pm$ 0.1	15.5 $\pm$ 0.3
A549	20	2.2 $\pm$ 0.5	7.9 $\pm$ 0.4
	10	9.0 $\pm$ 1.0	14.9 $\pm$ 0.4
	5	10.8 $\pm$ 0.5	14.6 $\pm$ 0.5
	2.5	0.4 $\pm$ 0.7	14.3 $\pm$ 0.7

Results are presented as cell growth inhibition percentage at concentrations of 2.5 to 20  $\mu\text{g}/\text{mL}$ , mean  $\pm$  SD ( $n = 3$ ). Doxorubicin was used as the positive control and exerted significant cell viability inhibitory effects against HepG2 ( $\text{IC}_{50}$  0.49  $\mu\text{g}/\text{mL}$ ), MDA-MB-231 ( $\text{IC}_{50}$  0.68  $\mu\text{g}/\text{mL}$ )

suppression of superoxide anion generation ( $\text{IC}_{50}$  1.16  $\mu\text{M}$ ) and elastase release ( $\text{IC}_{50}$  21.51  $\mu\text{M}$ ).

## Discussion

RBL-2H3 are mast cells that greatly affect the development of allergic response [58]. Upon activation by antigen or A23187 (calcium ionophore), mast cells produce histamine in addition to other mediators that immediately initiate hypersensitivity reactions.  $\beta$ -Hexosaminidase represents an important mast cells degranulation marker that is commonly used for the assessment of anti-allergic activity [59].

The anti-allergic activity of the crude extracts as well as *n*-hexane and dichloromethane fractions of *B. rupestris* and *B. discolor* leaves (Table 2) might be attributed

to the presence of many active constituents from their non-polar fractions. Sterols, sterol glycosides, coumarin, and triterpenes were isolated and identified in *B. rupestris* leaves. Lanosterol, lupeol,  $\beta$ -amyrin,  $\beta$ -amyrin acetate and oleanolic acid were previously reported from *B. discolor* leaves by Kassem et al. [23]. These triterpenes were reported to exert a potent anti-allergic activity [60–62] including  $\beta$ -amyrin that was previously documented to exhibit mast cell membrane stabilization [30]. The anti-allergic activity of triterpenes might be attributed to the suppression of secretion of histamine and interleukins (IL-2, IL-4) from mast cells [62]. Also,  $\beta$ -sitosterol was reported to possess anti-allergic activity and might have therapeutic potential in allergic asthma [63, 64]. It was suggested that  $\beta$ -sitosterol and its glycoside inhibited the release of IL-4 so it could act as an immune modulator to relieve symptoms associated with seasonal allergic response [65]. However, we did not observe any significant effect of either  $\beta$ -amyrin acetate (1), the mixture of  $\beta$ -sitosterol (2) and stigmasterol (3) or  $\beta$ -sitosterol glycoside (5) in degranulation assay using the RBL-2H3 mast cell model (Table 6). Meanwhile, scopoletin (4) and dihydrodehydrodiconiferyl alcohol 9-*O*- $\beta$ -D-glucoside (7) showed inhibitory activity on degranulation in RBL-2H3 cells.

Regarding the in vitro anti-inflammatory activity, neutrophils exert a vital role in host's defenses versus the attack by microorganisms and in the pathogenesis of various inflammatory diseases [66]. In response to stimuli, such as fMLF, the activated neutrophils secrete a series of inflammatory mediators such as superoxide anion ( $\text{O}_2^{\cdot-}$ ) and elastase which are major contributors to the destruction of tissue in inflammatory response [67]. We observed that the crude extracts and fractions of *B. rupestris* and *B. discolor* leaves (Table 3) exerted potent anti-inflammatory activity in human neutrophils. Many studies supported the anti-inflammatory activity

**Table 6** Anti-allergic activity of compounds isolated from *B. rupestris*

Sample	% viability, RBL-2H3 <sup>a</sup>		% inhibition of A23187-induced $\beta$ -hexosaminidase release <sup>b</sup>		
	100 $\mu\text{M}$	500 $\mu\text{M}$	10 $\mu\text{M}$	100 $\mu\text{M}$	500 $\mu\text{M}$
$\beta$ -amyrin acetate (1)	98.3 $\pm$ 2.9	<sup>c</sup>	0.3 $\pm$ 0.6	0.7 $\pm$ 1.2	<sup>c</sup>
scopoletin (4)	96.0 $\pm$ 4.0	93.7 $\pm$ 6.5	3.7 $\pm$ 4.7	13.7 $\pm$ 8.0	23.0 $\pm$ 8.0 <sup>**d</sup>
$\beta$ -sitosterol-3- <i>O</i> - $\beta$ -D-glucoside (5)	96.0 $\pm$ 1.0	<sup>c</sup>	5.0 $\pm$ 5.6	7.7 $\pm$ 3.8	<sup>c</sup>
dihydrodehydrodiconiferyl alcohol 4- <i>O</i> - $\beta$ -D-glucoside (6)	97.3 $\pm$ 2.5	<sup>e</sup>	7.0 $\pm$ 10.4	12.7 $\pm$ 7.6	<sup>e</sup>
dihydrodehydrodiconiferyl alcohol 9- <i>O</i> - $\beta$ -D-glucoside (7)	97.7 $\pm$ 2.1	95.3 $\pm$ 4.2	3.3 $\pm$ 4.2	16.3 $\pm$ 5.5*	18.0 $\pm$ 8.7*

A mixture of  $\beta$ -sitosterol (2) and stigmasterol (3) was toxic towards RBL-2H3 cells at the concentration of 200  $\mu\text{g}/\text{mL}$  (73.7  $\pm$  11.7% viability) and 100  $\mu\text{g}/\text{mL}$  (78.7  $\pm$  11.6% viability) and inactive at the concentration of 10  $\mu\text{g}/\text{mL}$  (5.0%  $\pm$  5.0% inhibition) in A23187-induced degranulation assay

<sup>a</sup>The cytotoxicity of samples to RBL-2H3 was evaluated using MTT viability assay; results are presented as mean  $\pm$  SD ( $n = 3$ )

<sup>b</sup>Dexamethasone (10 nM) was used as the positive control and inhibited 93.7  $\pm$  1.5%<sup>\*\*</sup> of A23187-induced  $\beta$ -hexosaminidase release in RBL-2H3 cells. Results are presented as mean  $\pm$  SD ( $n = 3$ ); \* $p < 0.05$ , \*\* $p < 0.001$  compared with the control value (A23187 only)

<sup>c</sup>Precipitate was formed upon the addition into the medium at the concentration of 500  $\mu\text{M}$ , therefore the result could not be justified

<sup>d</sup>Scopoletin (500  $\mu\text{M}$ ) exerted 30.0  $\pm$  7.1% inhibition of antigen-induced  $\beta$ -hexosaminidase release (mean  $\pm$  SD,  $n = 2$ )

<sup>e</sup>Dihydrodehydrodiconiferyl alcohol 4-*O*- $\beta$ -D-glucoside was not tested at the concentration of 500  $\mu\text{M}$ , however, it was nontoxic towards RBL-2H3 cells (96.0  $\pm$  6.9% viability) and inactive in A23187-induced degranulation assay (10.0  $\pm$  4.6% inhibition) at the concentration of 200  $\mu\text{M}$

**Table 7** Effect of pure compounds on superoxide anion generation and elastase release in fMLF/CB-induced human neutrophils

Sample	Superoxide anion generation <sup>a</sup>	Elastase release <sup>a</sup>
	IC <sub>50</sub> (μM) <sup>b</sup>	IC <sub>50</sub> (μM) <sup>b</sup>
β-amyrin acetate (1)	> 10	> 10
scopoletin (4)	> 10	> 10 <sup>c</sup>
β-sitosterol-3-O-β-D-glucoside (5)	> 10	> 10
dihydrodehydrodiconiferyl alcohol 4-O-β-D-glucoside (6)	> 10	> 10
dihydrodehydrodiconiferyl alcohol 9-O-β-D-glucoside (7)	> 1 <sup>d</sup>	> 1 <sup>d</sup>
genistein	1.16 ± 0.12	21.51 ± 6.50

<sup>a</sup>IC<sub>50</sub> values, results are presented as mean ± SD (*n* = 3–4), compared with the control value (formyl-methionyl-leucyl-phenylalanine/cytochalasin B, fMLF/CB)

<sup>b</sup>Concentration necessary for 50% inhibition (IC<sub>50</sub>)

<sup>c</sup>Scopoletin (4) exerted significant inhibitory activity in elastase release assay (22.8 ± 15.3%, \**p* < 0.05) at 10 μM

<sup>d</sup>Dihydrodehydrodiconiferyl alcohol 9-O-β-D-glucoside (10) was used at the final concentration of 1 μM due to solubility issues

of sterols and their glycosides [68–70]. They induce immunomodulatory response that affects inflammatory mediators [71, 72]. They were also reported to possess potent in vivo anti-inflammatory activity with the concomitant reduction of edema and inflammation in rats [73]. Various studies confirmed the anti-inflammatory activity of triterpenes including β-amyrin and β-amyrin acetate [29, 74–76]. Coumarins also were found to have anti-inflammatory activity by inhibiting different inflammatory mediators such as cyclooxygenase-2, nitric oxide, tumor necrosis factor-α and interleukins [77–79]. Neolignans were reported to exert anti-inflammatory effects by suppressing superoxide anion generation and elastase release [80], they also exhibited nitric oxide (NO) and tumor necrosis factor-α (TNF-α) inhibitory effects [81]. However, according to our results, only scopoletin (4) exerted mild inhibition of elastase release. All other isolated compounds including dihydrodehydrodiconiferyl alcohol glycosides (6 and 7) were inactive in fMLF-activated human neutrophils.

## Conclusions

The total extract and fractions of *B. rupestris* and *B. discolor* were nontoxic against hepatoma, breast and lung cancer cell lines. The crude extracts as well as the *n*-hexane and dichloromethane fractions of *B. rupestris* and *B. discolor* exhibited significant anti-allergic as well as anti-inflammatory activities. The phytochemical study of the leaves of *B. rupestris* resulted in the isolation of compounds from different chemical classes, including triterpene, sterols, sterol glycoside, coumarin and neolignans. All the tested compounds were nontoxic against the tested cancer cell lines. Among the isolated

compounds, scopoletin exerted anti-allergic effects and mild anti-inflammatory activity by reducing elastase release in human neutrophils. However, the bioactivity of *B. rupestris* extracts and fractions was much more potent compared with any of the isolated compounds. Thus, leaves of *B. rupestris* and *B. discolor* are worth to be considered for further development and research based on their anti-allergic and anti-inflammatory activities. In vivo evaluation of the anti-allergic and anti-inflammatory activities is highly recommended for the active fractions of both *Brachychiton* species.

## Additional file

**Additional file 1:** Supplementary data contains supplementary figures (Figures S1–S6) showing the spectroscopic data of isolated compounds 1–7 from *n*-hexane, dichloromethane and ethyl acetate fractions of *B. rupestris*. (DOCX 2306 kb)

## Abbreviations

ANOVA: One-way analysis of variance; APT: Attached proton test; *B*: *Brachychiton*; BHT: tert-Butyl-1-hydroxytoluene; BDD: *Brachychiton discolor* leaves dichloromethane fraction; BDE: *Brachychiton discolor* leaves ethyl acetate fraction; BDH: *Brachychiton discolor* leaves *n*-hexane fraction; BDT: *Brachychiton discolor* leaves total extract; BRD: *Brachychiton rupestris* leaves dichloromethane fraction; BRE: *Brachychiton rupestris* leaves ethyl acetate fraction; BRH: *Brachychiton rupestris* leaves *n*-hexane fraction; BRR: *B. rupestris* remaining fraction; BRT: *Brachychiton rupestris* leaves total extract; CDCL<sub>3</sub>: Deuterated chloroform; CD<sub>3</sub>OD: Deuterated methanol; <sup>13</sup>C-NMR: Carbon-13 Nuclear Magnetic Resonance; *d*: doublet; *dd*: doublet of doublet; DMEM: Dulbecco's modified Eagle's medium; DMSO: Dimethylsulfoxide; DMSO-*d*<sub>6</sub>: Deuterated dimethylsulfoxide-*d*<sub>6</sub>; 2D-NMR: Two-dimensional nuclear magnetic resonance spectroscopy; DNP: Dinitrophenyl; DNP-BSA: Dinitrophenyl-conjugated bovine serum albumin; ESI-MS: Electro-Spray Ionization Mass Spectrometry; EtOAc: Ethyl acetate; FBS: Fetal bovine serum; fMLF/CB: formyl-methionyl-leucyl-phenylalanine/cytochalasin B; <sup>1</sup>H-<sup>1</sup>H COSY: <sup>1</sup>H-<sup>1</sup>H Correlated spectroscopy; HMB: Heteronuclear Multiple-Bond Correlation Spectroscopy; <sup>1</sup>H-NMR: Proton Nuclear Magnetic Resonance; HSQC: Heteronuclear Single Quantum Coherence; IC<sub>50</sub>: The half maximal inhibitory concentration; *m*: multiplet; MTT: (3-(4,5-dimethylthiazol-2-yl)-2,5-diphenyltetrazolium bromide); *p*-NAG: *p*-Nitrophenyl-*N*-acetyl-D-glucosaminide; PTLC: Preparative thin layer chromatography; *q*: quartet; *R*<sub>f</sub>: Retardation factor; *s*: Singlet; S.D.: Standard deviation; SEM: Standard error of mean; *t*: Triplet; TLC: Thin Layer Chromatography; UPLC: Ultra Performance Liquid Chromatography

## Acknowledgements

We are grateful to the Center for Research Resources and Development, Kaohsiung Medical University for providing instrumentation support and to Ms. Shu-Li Chen for kind assistance in cytotoxicity measurements. Also, we would like to thank the Center for Drug Discovery, Research and Development at Faculty of Pharmacy, Ain Shams University for the analyses of the isolated compounds.

## Funding

This research was financial supported by the grants from the Ministry of Science and Technology (MOST 107–2911-I-037-502, MOST 106–2320-B-037-007-MY3, MOST 106–2320-B-255-003-MY3 and MOST 104–2320-B-255-004-MY3), Ministry of Education (EMRPD1G0231), Kaohsiung Medical University (106CM-KMU-02, KMU-DK107003, KMU-M106009), and Chang Gung Memorial Hospital (CMRPF1F0011~3, CMRPF1F0061~3, CMRPF1G0241~3, and BMRP450), Taiwan. The funders had no role in study design, data collection and analysis, decision to publish, or preparation of the manuscript.

**Availability of data and materials**

The datasets used and/or analysed during the current study are available from the corresponding author on reasonable request.

**Authors' contributions**

AAT and FSU performed extraction, isolation and identification of pure compounds and shared writing the whole manuscript. MK, YCW, and BHC carried out the cytotoxic and anti-allergic studies, interpreted the results and edited the manuscript. ME, FRC and ANBS formulated the research hypothesis, supervised the biological part and shared in critical revision of the manuscript and the whole work. TLH contributed to the anti-inflammatory assays. All authors participated in interpretations of results, read and approved the final manuscript.

**Ethics approval and consent to participate**

Not applicable.

**Consent for publication**

Not applicable.

**Competing interests**

The authors declare that they have no competing interests.

**Publisher's Note**

Springer Nature remains neutral with regard to jurisdictional claims in published maps and institutional affiliations.

**Author details**

<sup>1</sup>Department of Pharmacognosy, Faculty of Pharmacy, Ain Shams University, African Union Organization Street, Abbassia, Cairo 11566, Egypt. <sup>2</sup>Graduate Institute of Natural Products, College of Pharmacy, Kaohsiung Medical University, Kaohsiung 80708, Taiwan. <sup>3</sup>Department of Biotechnology, College of Life Science, Kaohsiung Medical University, Kaohsiung 80708, Taiwan. <sup>4</sup>Graduate Institute of Natural Products, College of Medicine, Chang Gung University, Taoyuan 33302, Taiwan. <sup>5</sup>Research Center for Chinese Herbal Medicine, Research Center for Food and Cosmetic Safety, and Graduate Institute of Health Industry Technology, College of Human Ecology, Chang Gung University of Science and Technology, Taoyuan 33302, Taiwan. <sup>6</sup>National Research Institute of Chinese Medicine, Ministry of Health and Welfare, Taipei 11221, Taiwan. <sup>7</sup>Research Center for Natural Products & Drug Development, Kaohsiung Medical University, Kaohsiung 80708, Taiwan. <sup>8</sup>Department of Medical Research, Kaohsiung Medical University Hospital, Kaohsiung 80708, Taiwan. <sup>9</sup>The Institute of Biomedical Sciences, National Sun Yat-sen University, Kaohsiung 80424, Taiwan. <sup>10</sup>Department of Pharmaceutical Biology, Faculty of Pharmacy and Biotechnology, German University in Cairo, Cairo 11835, Egypt. <sup>11</sup>Department of Anesthesiology, Chang Gung Memorial Hospital, Taoyuan 33305, Taiwan. <sup>12</sup>Chinese Herbal Medicine Research Team, Healthy Aging Research Center, Chang Gung University, Taoyuan 33302, Taiwan. <sup>13</sup>Department of Chemical Engineering, Ming Chi University of Technology, New Taipei City 24301, Taiwan.

Received: 26 June 2018 Accepted: 24 October 2018

Published online: 09 November 2018

**References**

- Kawai M, Hirano T, Higa S, Arimitsu J, Maruta M, Kuwahara Y, et al. Flavonoids and related compounds as anti-allergic substances. *Allergol Int*. 2007;56:113–23.
- Galli SJ, Tsai M, Piliponsky AM. The development of allergic inflammation. *Nature* 2008;454:445–454.
- Broide DH. Immunomodulation of allergic disease. *Annu Rev Med*. 2009;60:279–91.
- Baek K-S, Yi Y-S, Son Y-J, Yoo S, Sung NY, Kim Y, et al. *In vitro* and *in vivo* anti-inflammatory activities of Korean red ginseng-derived components. *J Ginseng Res*. 2016;40:437–44.
- Wang Y-T, Zhu L, Zeng D, Long W, Zhu S-M. Chemical composition and anti-inflammatory activities of essential oil from *Trachydium roylei*. *J Food Drug Anal*. 2016;24:602–9.
- Shaikh RU, Pund MM, Gacche RN. Evaluation of anti-inflammatory activity of selected medicinal plants used in Indian traditional medication system *in vitro* as well as *in vivo*. *J Tradit Complement Med*. 2016;6:355–61.
- Andhare RN, Raut MK, Naik SR. Evaluation of antiallergic and anti-anaphylactic activity of ethanolic extract of *Sanseveiria trifasciata* leaves (EEST) in rodents. *J Ethnopharmacol*. 2012;142:627–33.
- Sato A, Zhang T, Yonekura L, Tamura H. Antiallergic activities of eleven onions (*Allium cepa*) were attributed to quercetin 4'-glucoside using QuEChERS method and Pearson's correlation coefficient. *J Funct Foods*. 2015;14:581–9.
- Shi Y-H, Zhu S, Ge Y-W, He Y-M, Kazuma K, Wang Z, et al. Monoterpene derivatives with anti-allergic activity from red peony root, the root of *Paonia lactiflora*. *Fitoterapia*. 2016;108:55–61.
- Singh B, Nadkarni JR, Vishwakarma RA, Bharate SB, Nivsarkar M, Anandjiwala S. The hydroalcoholic extract of *Cassia alata* (Linn.) leaves and its major compound rhein exhibits antiallergic activity via mast cell stabilization and lipoxigenase inhibition. *J Ethnopharmacol*. 2012;141:469–73.
- Tian J, Che H, Ha D, Wei Y, Zheng S. Characterization and anti-allergic effect of a polysaccharide from the flower buds of *Lonicera japonica*. *Carbohydr Polym*. 2012;90:1642–7.
- Silva FV, Oliveira IS, Figueiredo KA, Melo Júnior FB, Costa DA, Chaves MH, et al. Anti-inflammatory and antinociceptive effects of *Sterculia striata* a. St-Hil. & Naudin (Malvaceae) in rodents. *J Med Food*. 2014;17:694–700.
- Dai Y, Harinantenaina L, Brodie PJ, Callmender MW, Randrianasolo S, Rakotobe E, et al. Isolation and synthesis of two antiproliferative calamenene-type sesquiterpenoids from *Sterculia tavia* from the Madagascar rain forest. *Bioorg Med Chem*. 2012;20:6940–4.
- Guymer GP. A taxonomic revision of *Brachychiton* (Sterculiaceae). *Aust Syst Bot*. 1988;1:199–323.
- Wilkie P, Clark A, Pennington RT, Cheek M, Bayer C, Wilcock CC. Phylogenetic relationships within the subfamily Sterculioideae (Malvaceae/Sterculiaceae-Sterculieae) using the chloroplast gene *ndhF*. *Syst Bot*. 2006;31:160–70.
- Salem MZM, Ali HM, Mansour MM. Fatty acid methyl esters from air-dried wood, bark, and leaves of *Brachychiton diversifolius* R. Br: antibacterial, antifungal, and antioxidant activities. *Bioresources*. 2014;9:3835–45.
- Rao KS. Characteristics and fatty acid composition of *Brachychiton* species seeds and the oils (Sterculiaceae). *J Agric Food Chem*. 1991;39:881–2.
- Abdel-Megeed A, Salem MZ, Ali HM, Gohar YM. *Brachychiton diversifolius* as a source of natural products: antibacterial and antioxidant evaluation of extracts of wood branches. *J Pure Appl Microbiol*. 2013;7:1843–50.
- Yousif F, Hifnawy MS, Soliman G, Boulos L, Labib T, Mahmoud S, et al. Large-scale *in vitro* screening of Egyptian native and cultivated plants for schistosomicidal activity. *Pharm Biol*. 2007;45:501–10.
- Thabet AA, Youssef FS, El-Shazly M, El-Beshbishy HA, Singab ANB. Validation of the antihyperglycaemic and hepatoprotective activity of the flavonoid rich fraction of *Brachychiton rupestris* using *in vivo* experimental models and molecular modelling. *Food Chem Toxicol*. 2018;114:302–10.
- Kassem HA, Eid HH, Abdel-Latif HA. Phytochemical and hypoglycemic studies of the leaves of *Brachychiton australis* (Schott & Endl.) a. Terrac. Grown in Egypt. *Bull Fac Pharm Cairo Univ*. 2001;40:85–91.
- De Laurentis N, Armenise D, Milillo M, Matrella R. Chemical investigation of *Sterculia acerifolia* leaves. *Riv Ital EPPOS*. 2003;13:21–30.
- Kassem HA. Study of further phytoconstituents of *Brachychiton discolor* F.J. Muell. cultivated in Egypt. *Bull Fac Pharm Cairo Univ*. 2007;45:155–60.
- Kassem HA, Aziz WM. A Pharmacognostical study of *Brachychiton discolor* F. J. Muell. Cultivated in Egypt. *Az Pharm Sci*. 2002;29:196–219.
- Chapman AD. Australian plant name index: Australian Biological Resources Study Canberra; 1991.
- The International Plant Names Index. 2012. <http://www.ipni.org>. Accessed 24 Sept 2018.
- The Plant List. Version 1. 2010. <http://www.theplantlist.org>. Accessed 24 Sept 2018.
- Desoky E, Youssef S. Hypoglycaemic effect of *Sterculia rupestris* and a comparative study of its flavonoids with *Sterculia diversifolia*. *Bull Fac Pharm Cairo Univ*. 1997;35:257–61.
- Okoye NN, Ajaghaku DL, Okeke HN, Ilodigwe EE, Nworu CS, Okoye FB. Beta-Amyrin and alpha-amyrin acetate isolated from the stem bark of *Alstonia boonei* display profound anti-inflammatory activity. *Pharm Biol*. 2014;52:1478–86.
- Oliveira FA, Lima-Junior RCP, Cordeiro WM, Vieira-Júnior GM, Chaves MH, Almeida FRC, et al. Pentacyclic triterpenoids,  $\alpha$ ,  $\beta$ -amyrins, suppress the scratching behavior in a mouse model of pruritus. *Pharmacol Biochem Behav*. 2004;78:719–25.
- Ayeleso TB, Matumba MG, Mukwevho E. Oleanolic acid and its derivatives: biological activities and therapeutic potential in chronic diseases. *Molecules*. 2017;22:1915.

32. Córdova C, Gutiérrez B, Martínez-García C, Martín R, Gallego-Muñoz P, Hernández M, et al. Oleonic acid controls allergic and inflammatory responses in experimental allergic conjunctivitis. *PLoS One*. 2014;9:e91282.
33. Geetha T, Varalakshmi P. Anti-inflammatory activity of lupeol and lupeol linoleate in rats. *J Ethnopharmacol*. 2001;76:77–80.
34. Khan AS. Antipyretic and analgesic activities of some economically important woody plants. In: *Medicinally important trees*: Springer; 2017. p. 159–85.
35. Mujumdar AM, Naik DG, Waghole RJ, Kulkarni DK, Kumbhojka MS. Pharmacological studies on *Sterculia foetida* leaves. *Pharm Biol*. 2000;38:13–7.
36. Raja T. Evaluation of anticonvulsant effect of *Sterculia foetida* (Pinari) in pentylenetetrazole (PTZ) and MES induced convulsions in albino rats. *World J Pharm Pharm Sci*. 2014;3:1898–907.
37. Babalola IT, Adelakun EA, Wang Y, Shode FO. Anti-TB activity of *Sterculia setigera* Del., leaves (Sterculiaceae). *J Pharmacogn. Phytochemistry*. 2012;1: 19–26.
38. Tor-Anyiin T, Akpuaka M, Oluma H. Phytochemical and antimicrobial studies on stem bark extract of *Sterculia setigera*, Del. *Afr J Biotechnol*. 2011;10: 11011–5.
39. Hossain MM, AIH E, Akbar MA, Ganguly A, Rahman SA. Evaluation of analgesic activity of *Sterculia villosa* Roxb. (Sterculiaceae) bark in swiss-albino mice. *Dhaka Univ J Pharm Sci*. 2013;12:125–9.
40. Hossain MF, Talukder B, Rana MN, Tasnim R, Nipun TS, Uddin SN, et al. *In vivo* sedative activity of methanolic extract of *Sterculia villosa* Roxb. Leaves. *BMC Complement Altern Med*. 2016;16:398.
41. Sobeh M, Mamadaliya NZ, Mohamed T, Krstin S, Youssef FS, Ashour ML, et al. Chemical profiling of *Phlomis thapsoides* (Lamiaceae) and *in vitro* testing of its biological activities. *Med Chem Res*. 2016;25:2304–15.
42. Van de Loosdrecht AA, Nennie E, Ossenkoppele GJ, Beelen RH, Langenhuijsen MM. Cell mediated cytotoxicity against U 937 cells by human monocytes and macrophages in a modified colorimetric MTT assay: a methodological study. *J Immunol Methods*. 1991;141:15–22.
43. Marks DC, Belov L, Davey MW, Davey RA, Kidman AD. The MTT cell viability assay for cytotoxicity testing in multidrug-resistant human leukemic cells. *Leuk Res*. 1992;16:1165–73.
44. Chen B-H, Wu P-Y, Chen K-M, Fu T-F, Wang H-M, Chen C-Y. Antiallergic potential on RBL-2H3 cells of some phenolic constituents of *Zingiber officinale* (ginger). *J Nat Prod*. 2009;72:950–3.
45. Korinek M, Tsai YH, El-Shazly M, Lai KH, Backlund A, Wu SF, et al. Anti-allergic hydroxy fatty acids from *Typhonium blumei* explored through ChemGPS-NP. *Front Pharmacol*. 2017;8:356.
46. Matsuda H, Tewtrakul S, Morikawa T, Nakamura A, Yoshikawa M. Anti-allergic principles from Thai zedoary: structural requirements of curcuminoids for inhibition of degranulation and effect on the release of TNF- $\alpha$  and IL-4 in RBL-2H3 cells. *Bioorg Med Chem*. 2004;12:5891–8.
47. Chen B-H, Hung M-H, Chen JY-F, Chang H-W, Yu M-L, Wan L, et al. Anti-allergic activity of grape seed extract (GSE) on RBL-2H3 mast cells. *Food Chem*. 2012;132:968–74.
48. Chung Y-M, Chang F-R, Tseng T-F, Hwang T-L, Chen L-C, Wu S-F, et al. A novel alkaloid, aristopyridinone A and anti-inflammatory phenanthrenes isolated from *Aristolochia manshuriensis*. *Bioorg Med Chem Lett*. 2011;21: 1792–4.
49. Yang SC, Chung PJ, Ho CM, Kuo CY, Hung MF, Huang YT, et al. Propofol inhibits superoxide production, elastase release, and chemotaxis in formyl peptide-activated human neutrophils by blocking formyl peptide receptor 1. *J Immunol*. 2013;190:6511–9.
50. Mócsai A, Jakus Z, Tibor Vántus T, Berton G, Lowell GA, Ligeti E. Kinase pathways in chemoattractant-induced degranulation of neutrophils: the role of p38 mitogen-activated protein kinase activated by Src family kinases. *J Immunol*. 2000;164:4321–31.
51. Liou JR, El-Shazly M, Du YC, Tseng CN, Hwang TL, Chuang YL, et al. 1,5-Diphenylpent-3-en-1-ynes and methyl naphthalene carboxylates from *Lawsonia inermis* and their anti-inflammatory activity. *Phytochemistry*. 2013; 88:67–73.
52. Youssef FS, Ashour ML, Sobeh M, El-Beshbishy HA, Singab ANB, Wink M. *Eremophila maculata*- isolation of a rare naturally-occurring lignan glycoside and the hepatoprotective activity of the leaf extract. *Phytomedicine*. 2016; 23:1484–93.
53. Dubey H, Ticari J. Flavonoids and other constituents of *Sterculia* genus. *J Indian Chem Soc*. 1991;68:426–7.
54. Anjaneyulu A, Raju S. Terpenoids and phenolics from the bark and heartwood of *Sterculiaurens* ROXB. *J Indian Chem Soc*. 1987;64:323–4.
55. Khan NMU, Hossain MS. Scopoletin and  $\beta$ -sitosterol glucoside from roots of *Ipomoea digitata*. *J Pharmacogn. Phytochemistry*. 2015;4:05–7.
56. H-x K, Y-g X, B-y Y, Wang Q-h, S-w L. Lignan constituents from *Chloranthus japonicus* Sieb. *Arch Pharm Res*. 2009;32:329–34.
57. Lee S, Song I-H, Lee J-H, Yang W-Y, Oh K-B, Shin J. Sortase A inhibitory metabolites from the roots of *Pulsatilla koreana*. *Bioorg Med Chem Lett*. 2014;24:44–8.
58. De Souza Santos M, Jonis Andrioli W, Freire de Moraes Del Lama MP, Kenupp Bastos J, NPD N, Zumstein Georgetto Naal RM. *In vitro* anti-allergic activity of the fungal metabolite pyridovericin. *Int Immunopharmacol*. 2013; 15:532–8.
59. Korinek M, Chen KM, Jiang YH, El-Shazly M, Stocker J, Chou CK, et al. Anti-allergic potential of *Typhonium blumei*: inhibition of degranulation via suppression of PI3K/PLC $\gamma$ 2 phosphorylation and calcium influx. *Phytomedicine*. 2016;23:1706–15.
60. Ryu SY, Oak MH, Yoon SK, Cho DI, Yoo GS, Kim TS, et al. Anti-allergic and anti-inflammatory triterpenes from the herb of *Prunella vulgaris*. *Planta Med*. 2000;66:358–60.
61. Yoshikawa M, Nakamura S, Kato Y, Matsuhira K, Matsuda H. Medicinal flowers. XIV. New acylated oleanane-type triterpene oligoglycosides with antiallergic activity from flower buds of chinese tea plant (*Camellia sinensis*). *Chem Pharm Bull*. 2007;55:598–605.
62. Chen M-L, Hsieh C-C, Chiang B-L, Lin B-F. Triterpenoids and polysaccharide fractions of *Ganoderma tsugae* exert different effects on antiallergic activities. *Evid Based Complement Altern Med*. 2015;2015:1–10.
63. Nirmal SA, Patel AP, Bhawar SB, Pattan SR. Antihistaminic and antiallergic actions of extracts of *Solanum nigrum* berries: possible role in the treatment of asthma. *J Ethnopharmacol*. 2012;142:91–7.
64. Mahajan SG, Mehta AA. Suppression of ovalbumin-induced Th2-driven airway inflammation by beta-sitosterol in a Guinea pig model of asthma. *Eur J Pharmacol*. 2011;650:458–64.
65. Bouic P, Lamprecht JH. Plant sterols and sterolins: a review of their immune-modulating properties. *Altern Med Rev*. 1999;4:170–7.
66. Hwang TL, Yeh SH, Leu YL, Chern CY, Hsu HC. Inhibition of superoxide anion and elastase release in human neutrophils by 3'-isopropoxychalcone via a cAMP-dependent pathway. *Br J Pharmacol*. 2006;148:78–87.
67. Mantovani A, Cassatella MA, Costantini C, Jaillon S. Neutrophils in the activation and regulation of innate and adaptive immunity. *Nat Rev Immunol*. 2011;11:519–31.
68. Kim JA, Son JH, Song SB, Yang SY, Kim YH. Sterols isolated from seeds of *Panax ginseng* and their antiinflammatory activities. *Pharmacogn Mag*. 2013;9:182.
69. Kaith BS, Kaith NS, Chauhan NS. Anti-inflammatory effect of *Arnebia euchroma* root extracts in rats. *J Ethnopharmacol*. 1996;55:77–80.
70. Vassallo A, De Tommasi N, Merfort I, Sanogo R, Severino L, Pelin M, et al. Steroids with anti-inflammatory activity from *Vernonia nigritiana* Oliv. & Hiern. *Phytochemistry*. 2013;96:288–98.
71. Bouic PJ. The role of phytosterols and phytosterolins in immune modulation: a review of the past 10 years. *Curr Opin Clin Nutr Metab Care*. 2001;4:471–5.
72. Lee J-H, Lee JY, Park JH, Jung HS, Kim JS, Kang SS, et al. Immunoregulatory activity by daucosterol, a  $\beta$ -sitosterol glycoside, induces protective Th1 immune response against disseminated candidiasis in mice. *Vaccine*. 2007; 25:3834–40.
73. Correa G, Abreu VDC, Martins D, Takahashi JA, Fontoura H, Cara DC, et al. Antiinflammatory and antimicrobial activities of steroids and triterpenes isolated from aerial parts of *Justicia acuminatissima* (Acanthaceae). *Int J Pharm Pharm Sci*. 2014;6:75–81.
74. de Almeida PD, Boleti AP, Rudiger AL, Lourenco GA, da Veiga Junior VF, Lima ES. Anti-inflammatory activity of triterpenes isolated from *Protium paniculatum* oil-resins. *Evid Based Complement Altern Med*. 2015;2015:293768.
75. Romero-Estrada A, Maldonado-Magaña A, González-Christen J, Bahena SM, Garduño-Ramírez ML, Rodríguez-López V, et al. Anti-inflammatory and antioxidative effects of six pentacyclic triterpenes isolated from the Mexican copal resin of *Bursera copallifera*. *BMC Complement Altern Med*. 2016;16:422.
76. Thirupathi A, Silveira PC, Nesi RT, Pinho RA. Beta-Amyrin, a pentacyclic triterpene, exhibits anti-fibrotic, anti-inflammatory, and anti-apoptotic effects on dimethyl nitrosamine-induced hepatic fibrosis in male rats. *Hum Exp Toxicol*. 2017;36:113–22.
77. Wei W, Wu X-W, Deng G-G, Yang X-W. Anti-inflammatory coumarins with short- and long-chain hydrophobic groups from roots of *Angelica dahurica* cv. Hangbaizhi. *Phytochemistry*. 2016;123:58–68.



78. Azelmat J, Fiorito S, Taddeo VA, Genovese S, Epifano F, Grenier D. Synthesis and evaluation of antibacterial and anti-inflammatory properties of naturally occurring coumarins. *Phytochem Lett.* 2015;13:399–405.
79. Kang K-H, Kong C-S, Seo Y, Kim M-M, Kim S-K. Anti-inflammatory effect of coumarins isolated from *Corydalis heterocarpa* in HT-29 human colon carcinoma cells. *Food Chem Toxicol.* 2009;47:2129–34.
80. Shih H-C, Kuo P-C, Wu S-J, Hwang T-L, Hung H-Y, Shen D-Y, et al. Anti-inflammatory neolignans from the roots of *Magnolia officinalis*. *Bioorg Med Chem.* 2016;24:1439–45.
81. Peng Y, Lou L-L, Liu S-F, Zhou L, Huang X-X, Song S-J. Antioxidant and anti-inflammatory neolignans from the seeds of hawthorn. *Bioorg Med Chem Lett.* 2016;26:5501–6.

**Ready to submit your research? Choose BMC and benefit from:**

- fast, convenient online submission
- thorough peer review by experienced researchers in your field
- rapid publication on acceptance
- support for research data, including large and complex data types
- gold Open Access which fosters wider collaboration and increased citations
- maximum visibility for your research: over 100M website views per year

**At BMC, research is always in progress.**

Learn more [biomedcentral.com/submissions](https://biomedcentral.com/submissions)



## RESEARCH

# Thyroid hormone negatively regulates tumorigenesis through suppression of BC200

Yang-Hsiang Lin<sup>1,2</sup>, Meng-Han Wu<sup>1</sup>, Ya-Hui Huang<sup>2</sup>, Chau-Ting Yeh<sup>2</sup>, Hsiang-Cheng Chi<sup>1,3</sup>, Chung-Ying Tsai<sup>4</sup>, Wen-Yu Chuang<sup>5</sup>, Chia-Jung Yu<sup>6,7,8,9</sup>, I-Hsiao Chung<sup>1</sup>, Ching-Ying Chen<sup>1</sup> and Kwang-Huei Lin<sup>1,2,7,10</sup>

<sup>1</sup>Department of Biochemistry, College of Medicine, Chang Gung University, Taoyuan, Taiwan

<sup>2</sup>Liver Research Center, Chang Gung Memorial Hospital, Linkou, Taoyuan, Taiwan

<sup>3</sup>Radiation Biology Research Center, Institute for Radiological Research, Chang Gung University/Chang Gung Memorial Hospital, Linkou, Taoyuan, Taiwan

<sup>4</sup>Kidney Research Center and Department of Nephrology, Chang Gung Memorial Hospital, Taoyuan, Taiwan

<sup>5</sup>Department of Pathology, Chang Gung Memorial Hospital and Chang Gung University College of Medicine, Taoyuan, Taiwan

<sup>6</sup>Molecular Medicine Research Center, Chang Gung University, Taoyuan, Taiwan

<sup>7</sup>Graduate Institute of Biomedical Sciences, College of Medicine, Chang Gung University, Taoyuan, Taiwan

<sup>8</sup>Department of Cell and Molecular Biology, College of Medicine, Chang Gung University, Taoyuan, Taiwan

<sup>9</sup>Department of Thoracic Medicine, Chang Gung Memorial Hospital, Linkou, Taoyuan, Taiwan

<sup>10</sup>Research Center for Chinese Herbal Medicine, College of Human Ecology, Chang Gung University of Science and Technology, Taoyuan, Taiwan

Correspondence should be addressed to K-H Lin: [khlin@mail.cgu.edu.tw](mailto:khlin@mail.cgu.edu.tw)

## Abstract

Thyroid hormone ( $T_3$ ) and its receptor (TR) are involved in cancer progression. While deregulation of long non-coding RNA (lncRNA) expression has been detected in many tumor types, the mechanisms underlying specific involvement of lncRNAs in tumorigenicity remain unclear. Experiments from the current study revealed negative regulation of BC200 expression by  $T_3$ /TR. BC200 was highly expressed in hepatocellular carcinoma (HCC) and effective as an independent prognostic marker. BC200 promoted cell growth and tumor sphere formation, which was mediated via regulation of cell cycle-related genes and stemness markers. Moreover, BC200 protected cyclin E2 mRNA from degradation. Cell growth ability was repressed by  $T_3$ , but partially enhanced upon BC200 overexpression. Mechanistically, BC200 directly interacted with cyclin E2 and promoted CDK2–cyclin E2 complex formation. Upregulation of cell cycle-related genes in hepatoma samples was positively correlated with BC200 expression. Our collective findings support the utility of a potential therapeutic strategy involving targeting of BC200 for the treatment of HCC.

## Key Words

- thyroid hormone
- non-coding RNA
- tumor-initiating cell
- mRNA stability
- overall survival

Endocrine-Related Cancer  
(2018) 25, 967–979

## Introduction

Thyroid hormone ( $T_3$ ) and its receptor (TR) are involved in cell growth, metabolism, autophagy and cancer progression (Wu *et al.* 2013, Chi *et al.* 2016). Two TR genes, TR $\alpha$ 1 and TR $\beta$ 1, have been identified on chromosomes 17 and 3, respectively. The receptors function as ligand-dependent transcriptional factors through binding to specific regions known as thyroid hormone response elements (TREs) that are usually located in the promoter

region of target genes.  $T_3$ /TR has been shown to reduce tumor formation in various cancer types, including hepatocellular carcinoma (HCC) (Chi *et al.* 2013) and breast cancer (Martinez-Iglesias *et al.* 2009), suggestive of a tumor suppressor function.

According to the tumor-initiating cell (TIC) concept, a subset of cancer cells possesses stem cell features that are indispensable for tumor formation (Plaks *et al.* 2015).

TICs are generally characterized by their capacity for self-renewal and generate progeny to create the tumor bulk. Accumulating evidence supports the involvement of TICs in perpetuation of various cancers, including liver (Zhu *et al.* 2016), breast (Nadal *et al.* 2013), prostate (Vander Griend *et al.* 2008), brain (Brescia *et al.* 2013) and colon (Jing *et al.* 2015). In liver cancers, CD133/Prominin-1, a transmembrane hematopoietic stem cell antigen, has been identified as a putative marker of TICs. Notably, CD133 promotes tumorigenic capacity in cancer stem cells through activation of PI3K/AKT/mTOR (Xia & Xu 2015) or  $\beta$ -catenin signaling pathways (Mak *et al.* 2012).

Long non-coding RNAs (lncRNAs) are a class of non-protein coding transcripts longer than 200 nucleotides that regulate complex cellular functions, such as cell growth, differentiation, metabolism and metastasis (Rinn & Chang 2012). Recently, dysregulation of many HCC-related lncRNAs such as lncRNA-ATB (Yuan *et al.* 2014), NEAT1 (Mang *et al.* 2017), HOTAIR (Gao *et al.* 2016) and MALAT1 (Malakar *et al.* 2017) have been identified. Brain cytoplasmic RNA 1 (BCYRN1 or BC200), hereafter referred to as BC200, is overexpressed in several tumor types, including esophageal squamous cell carcinoma (Zhao *et al.* 2016), breast (Iacoangeli *et al.* 2004) and lung cancer (Hu & Lu 2015). However, the mechanisms underlying functional impairment and specific involvement of BC200 in HCC remain to be established.

Here, we aimed to elucidate the involvement of specific deregulated lncRNAs and target genes mediated by  $T_3$ /TR in tumor formation. Experiments from the current study revealed BC200 as a target gene downregulated by  $T_3$ /TR. BC200 promoted cell growth and oncogenic sphere formation of hepatocarcinoma cells through upregulation of cell cycle-related genes. Furthermore,  $T_3$ /TR signaling inhibited cell growth through suppression of BC200. Our results collectively demonstrate novel associations among  $T_3$ /TR, BC200, cyclin E2 and cyclin-dependent kinases (CDK) 2 that are involved in regulation of the tumor formation.

## Materials and methods

### Cell culture

The human hepatoma cell lines, HepG2, Hep3B, SK-Hep1 (obtained from American Type Culture Collection), Huh7 (gift from Dr. T.Y Hsieh, Tri-Service General Hospital, Taiwan) (Shiu *et al.* 2013) and J7 (gift from Dr. C S Yang, National Taiwan University, Taiwan) (Chen *et al.* 2002)

were cultured in Dulbecco's modified Eagle's medium (DMEM) containing 10% (v/v) fetal bovine serum (FBS). Cells were grown at 37°C in a humidified atmosphere of 95% air and 5% CO<sub>2</sub>. The cell lines were authenticated using the Promega StemElite ID System, which is a short tandem repeat-based assay (Supplementary Fig. 1, see section on [supplementary data](#) given at the end of this article). All experiments were conducted with cells from passage numbers 5–20. Serum was depleted of  $T_3$ , as described previously (Chen *et al.* 2008).

### lncRNA profiling

Human Disease-Related lncRNA Profiler (System Biosciences, Mountain View, CA, USA) consisting of 83 lncRNAs was used. Briefly, total RNA was isolated from HepG2-TR $\alpha$ 1 cells treated with/without  $T_3$  for 24 h and two paired HCC specimens. The detection of lncRNA was performed according to the manufactory's instructions. Values are expressed as log 2-transformed relative fold increase or decrease in lncRNA expression, relative to that in without  $T_3$  treatment or adjacent non-tumorous tissues after normalization to the internal control. A positive log 2-transformed fold-change indicates higher expression in  $T_3$  treatment and tumor specimens, whereas a negative value signifies relatively decreased expression. A Student's *t*-test was performed to identify significantly and differentially expressed lncRNAs with a fold-change  $\geq 2.0$  or  $\leq 0.5$ ,  $P < 0.05$ .

### Human hepatoma specimens

Hepatoma samples from Taiwan Liver Cancer Network (TLCN) were selected for study and subjected to qRT-PCR and western blot analyses (Chang *et al.* 2016). These analyses were carried out under informed consent. The protocol was approved by the Medical Ethics and Human Clinical Trial Committee at Chang Gung Memorial Hospital (Institutional Review Board, No: 103-4866B).

### Quantitative reverse transcription-PCR (qRT-PCR)

To quantify lncRNA transcripts, total RNA was extracted from cells with TRIzol reagent kit (Life Technologies Inc.) and converted into cDNA using reverse transcriptase (Life Technologies). qRT-PCR was conducted in a total reaction volume of 15  $\mu$ L containing forward and reverse primers and 1X SYBR Green mix (Applied Biosystems). The ABI

Prism 7500 Fast Real-Time PCR system (Life Technologies) was employed for qRT-PCR analysis. The primer sequences were listed in Supplementary Table 1.

### RNA *in situ* hybridization (RNA-ISH)

*In situ* detection of BC200 expression was performed on formalin-fixed paraffin-embedded HCC samples. BC200 anti-sense RNA probes were labeled with digoxigenin (DIG) using a DIG RNA labeling kit (Roche). Before the labeling reaction, BC200 plasmid was digested with restriction enzymes for linearization. Further, *in vitro* transcription from plasmid was carried out using SP6 RNA polymerase. After de-paraffinization and rehydration, samples were treated with proteinase K (20 µg/mL) to digest tissues before hybridization, which was conducted at 37°C for 30 min. Sections were prehybridized in buffer containing 4×SSC and 50% deionized formamide for at least 10 min at 37°C and hybridized overnight with DIG-labeled probe at 62°C in solution containing 40% deionized formamide, 10% dextran sulfate, 1× Denhardt's solution, 4× SSC, 10 mM DTT and 1 µg/mL yeast t-RNA. After stringent washing, signals were detected using anti-DIG-AP antibodies (1:800 dilution, Roche) and NBT/BCIP substrate (Roche).

### Immunoblot analysis

The immunoblot procedure was performed as described previously (Wu *et al.* 2011). Antibodies specific for cyclin E1, cyclin E2 and CDK2 (Santa Cruz Biotechnology Inc.), p21 (Thermo Fisher Scientific Inc.), p27 (Sigma-Aldrich), CD133 (Miltenyi Biotec, Auburn, CA, USA), CD44, Sox2, Nanog (GeneTex, Inc., Irvine, CA, USA) and GAPDH (Merck Millipore) were used. Band intensities were calculated using Image Gauge software (Fujifilm, Tokyo, Japan). The PVDF membranes were reprobed for different antibodies after using TOOLStripping Buffer (BIOTOOLS CO., LTD. Taiwan). The signal intensities of expression of target genes were normalized to those of GAPDH.

### Establishment of overexpression and knockdown stable cell lines

For ectopic expression of BC200 ncRNA, the sequences were amplified via PCR and cloned into pLKO-TRC001 vector. BC200 shRNAs (shBC200#1 and shBC200#2) were designed and cloned into pLKO-TRC001 vector. The shRNA sequences were shown below:

shBC200#1-F: 5'-CCGGGAGACCTGCCTGGGCAATATACTCGAGTATATTGCCCAGGCAGGTCTCTTTT-3'  
shBC200#1-R: 5'-CTCTGGACGGACCCGTTATATGAGCTCATATAACGGGTCCGTCCAGAGAAAAATTAA-3'  
shBC200#2-F: 5'-CCGGACTTCCCTCAAAGCAACAACCCTCGAGGGTTGTTGCTTTGAGGGAAGTTTTT-3'  
shBC200#2-R: 5'-TGAAGGGAGTTTCGTTGTTGGGAGCTCCCAACAACGAACTCCCTTCAAAAAATTAA-3'

Single shRNA plasmid and virus package plasmids (pCMV-ΔR8.91 and pMD.G) were co-transfected into 293FT, and the virus harvested after 72 h of transfection. A pool of stably infected cells was selected in medium containing puromycin.

### Cell proliferation

Cells ( $1 \times 10^5$ ) were grown on 6 cm dishes. At the indicated time-points, cell growth rates were determined with trypan blue exclusion and quantitated using the LUNA Automated Cell Counter.

### Soft agar assay

Stable cells (10,000/well) were seeded in 12-well plates for layer agar cultures. Cells were resuspended in 0.33% agar in DMEM containing 10% FBS, and the upper layer replaced once a week in complete medium. After 3 weeks, colonies were stained with 0.01% (w/v) crystal violet. Images of all plates were obtained under a microscope (Olympus IX71), and colony numbers scanned and counted with Image J.

### RNA immunoprecipitation assay

The RNA immunoprecipitation (RIP) assay was performed as described previously (Hsieh *et al.* 2014). Antibodies for RIP assay against cyclin E2 (Santa Cruz) were used.

### Cell sorting and flow cytometry

Cell sorting via flow cytometry was performed on HCC cells using PE-conjugated monoclonal mouse anti-human CD133/1 (Miltenyi Biotec). Isotype control mouse IgG1k-PE (eBioscience, San Diego, CA, USA) served as the negative control.

### Sphere formation assay

For the sphere formation assay, cells ( $1 \times 10^3$ ) were plated to the ultralow attachment 6-well plate (Corning Inc., Corning, NY, USA) with DMEM/F12 medium containing



20 ng/mL basic fibroblast growth factor, 20 ng/mL epidermal growth factor and B27. Two weeks later, the whole image of each well was taken and the number of spheres larger than 100  $\mu$ m was manually counted using ImageJ software.

### Animal models

**Model I:** Five-week-old male nude mice were subcutaneously injected with BC200-overexpressing Hep3B cells ( $5 \times 10^6$ ,  $n=3$  per group) and BC200-depleted SK-Hep1 cells ( $2 \times 10^6$ ,  $n=4$  per group) to assess the effects of the lncRNA on tumor formation ability. Tumor volumes ( $\text{mm}^3$ ) were measured using the formula:  $(W^2 \times L)/2$  ( $W$ , smallest diameter;  $L$ , longest diameter). All animals were killed at the indicated time-points after tumor inoculation. **Model II:** Hyper- and eu-thyroid mice ( $n=8$  per group) were generated and samples preparations were described in our previous report (Chi *et al.* 2016). Briefly, the effects of  $T_3$  repressed diethylnitrosamine (DEN)-induced liver injury were determined in C57BL/6 male mice. Mice were treated with  $T_3$  (10  $\mu$ g/100 g body weight) before intraperitoneal injection of DEN (100 mg/kg). All groups of mice received continued  $T_3$  after DEN injection. Animal experiments were approved by the committee and performed according to the guidelines of the Chang Gang Institutional Animal Care and Use Committee Guide for the Care and Use of Laboratory animals (CGU13-106).

### Statistical analysis

Results are presented as means  $\pm$  S.D. of three independent experiments. Statistical analysis was performed with SPSS version 15 software (SPSS Inc., Chicago, IL, USA) using the Mann–Whitney test for comparison of two groups and one-way ANOVA, followed by Tukey's *post hoc* test, for two or more groups. Kaplan–Meier survival curves were employed to analyze survival outcomes. Overall survival (OS) with death as an event was analyzed using the log-rank test.  $P$  values  $<0.05$  were considered significant.

## Results

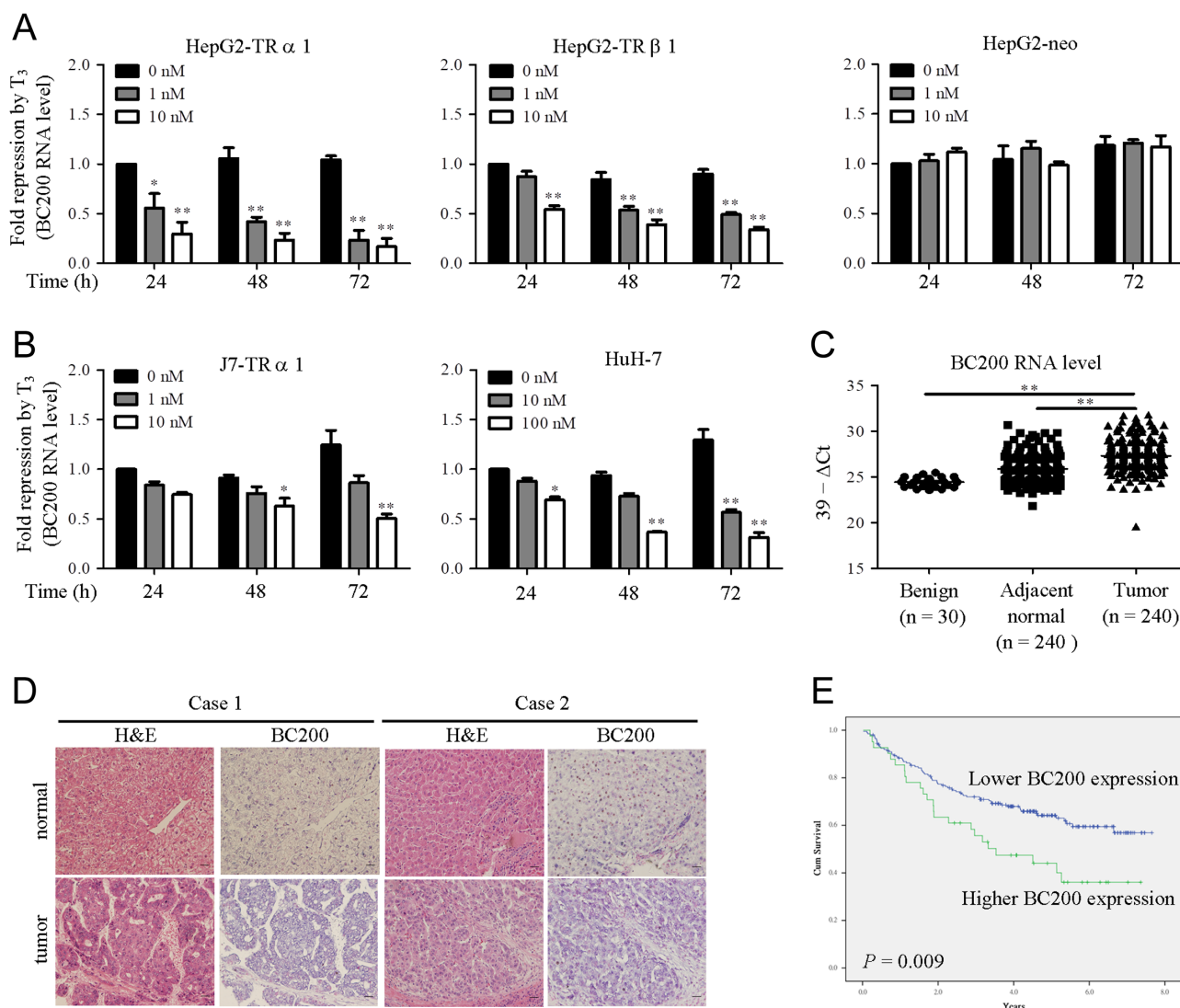
### BC200 is downregulated by $T_3$ /TR

To identify  $T_3$ /TR-related lncRNAs that are differentially expressed in HCC, lncRNA expression profile screening was performed using the SYBR Green-based qRT-PCR array in TR-overexpressing HepG2 cell lines and HCC specimens. Candidate lncRNAs that were simultaneously

downregulated by  $T_3$ /TR and upregulated in HCC were selected for further study, leading to the identification of BC200 (Supplementary Fig. 2A). Expression levels of BC200 decreased by 50–80% after incubation of HepG2-TR $\alpha$ 1 and HepG2-TR $\beta$ 1 with  $T_3$  for 24–72 h (Fig. 1A). In contrast, BC200 expression levels were only marginally regulated by  $T_3$  in HepG2-neo cells (Fig. 1A). In other hepatoma cell lines, including J7-TR $\alpha$ 1 and Huh7 expressing exogenous and endogenous TR protein,  $T_3$  suppressed BC200 expression (Fig. 1B), similar to results obtained with HepG2-TR cells. These findings indicate that  $T_3$ /TR signaling negatively regulates BC200 expression in a dose- and time-dependent manner *in vitro*. Promoter activity analysis was further performed to determine whether BC200 is regulated by  $T_3$  at the transcriptional level. Putative negative TREs (nTRE) in the BC200 promoter region (I–VI), based on the sequences from nTRE-thyroid-stimulating hormone (TSH) (Nakano *et al.* 2004) or nTRE-Nm23-H1 (Lin *et al.* 2000), were identified with bioinformatics tools (Supplementary Fig. 2B). In the presence of  $T_3$ , luciferase activity was decreased by 30–40% in constructs I, II, III and IV. Repression of luciferase activity was alleviated upon deletion of region d (–305/–289) in constructs V and VI (Supplementary Fig. 2B), indicating that potential nTRE of the BC200 promoter is located within this region. TR binding to promoter fragment VI of BC200 *in vivo* was validated using the ChIP assay. Specific binding of TR to the BC200 promoter fragment was confirmed based on pulldown with the TR antibody, but not mopc21 (immunoglobulin) antibody (Supplementary Fig. 2C).

### BC200 expression is upregulated in HCC

qRT-PCR and ISH were performed to validate the profiling results. Notably, BC200 expression was significantly upregulated in HCC tissues compared with benign and adjacent normal tissues (Fig. 1C). Consistently, the ISH assay revealed high expression of BC200 in HCC (Fig. 1D). Furthermore, BC200 expression in HCC was positively correlated with tumor type, tumor size, vascular invasion and pathological stage (Table 1). Kaplan–Meier survival analysis showed association of high BC200 expression with poor OS rate in HCC patients (Fig. 1E). Multivariate Cox proportional hazard regression analysis revealed that BC200 is an independent prognostic factor associated with survival (Table 2). These data clearly support a critical role of BC200 in hepatocarcinogenesis.

**Figure 1**

BC200 is downregulated by  $T_3$ /TR and highly expressed in HCC. (A and B) HepG2-TR, HepG2-neo, J7-TR and Huh-7 cells were treated with  $T_3$  for 24–72 h, and BC200 levels measured using qRT-PCR. 18S rRNA was used as the internal control. (C) qRT-PCR analysis of BC200 expression in human HCC. 18S rRNA was used as the internal control. (D) ISH analysis of BC200 expression in human HCC. (E) Kaplan–Meier analysis of overall survival based on BC200 expression in HCC specimens. Mean expression of BC200 was used as the cutoff. Overall survival was analyzed using the log-rank test.

### BC200 promotes cell growth and transformation *in vitro* and *in vivo*

The precise functions of the majority of lncRNAs are still unknown. The co-expression network analysis has been used to predict function of unknown non-coding RNA since genes regulated by the specific regulator or a set of genes with the same function would be co-expressed (Lee *et al.* 2004, Gong *et al.* 2016, Shang *et al.* 2016). This type of approach may be effectively used for exploring the roles of lncRNAs in cancer progression (Lee *et al.* 2004). The Oncomine database ([www.oncomine.com](http://www.oncomine.com)) was used

to systematically assess the relative BC200 expression in different cancer types. However, only one publicly available dataset contains information of BC200 was found to exhibit a significant upregulation of BC200 in lung cancer (Supplementary Fig. 2D). In our study, co-expression analysis for BC200-involved pathway was performed using Pearson correlation in a publicly available dataset (GSE32863). Pathway analysis was further carried out by Gene Set Enrichment Analysis tool after genes obtained from co-expression network analysis. The results indicate that cell cycle mitotic and DNA replication pathway are significantly enhanced and positively correlated with

**Table 1** Clinicopathological correlations of BC200 in HCC specimens.

Parameters	Cases (n=240)	Mean $\pm$ s.e.	P <sup>a</sup>
Age (years)			
<65	148	7.971 $\pm$ 1.838	0.4403
$\geq$ 65	92	5.122 $\pm$ 0.6504	
Gender			
Male	131	4.340 $\pm$ 0.4438	0.1600
Female	109	3.721 $\pm$ 0.3843	
Cirrhosis			
No	142	5.891 $\pm$ 1.106	0.3239
Yes	98	8.310 $\pm$ 2.354	
AFP			
Low	107	5.059 $\pm$ 1.400	0.1404
Medium	49	5.485 $\pm$ 1.438	
High	84	10.1 $\pm$ 2.654	
Viral status			
NBNC	32	5.206 $\pm$ 1.452	0.9081
HBV	122	7.812 $\pm$ 1.890	
HCV	81	6.335 $\pm$ 1.859	
HBV & HCV	5	3.629 $\pm$ 1.146	
Tumor type			
Solitary	181	5.460 $\pm$ 0.9396	0.0322
Multiple	59	11.23 $\pm$ 3.715	
Tumor size			
<5 cm	137	5.172 $\pm$ 1.192	0.0343
$\geq$ 5 cm	103	9.150 $\pm$ 2.183	
Vascular invasion			
No	128	4.090 $\pm$ 0.6392	0.01
Yes	112	10.07 $\pm$ 2.351	
Pathological stage			
I	116	4.185 $\pm$ 0.6977	0.0376
II	71	7.686 $\pm$ 2.102	
III	53	11.69 $\pm$ 4.126	
Grading			
1	11	2.173 $\pm$ 0.5413	0.2778
2	166	5.898 $\pm$ 1.047	
3	63	10.28 $\pm$ 3.444	

<sup>a</sup>Mann–Whitney *U* test (for two groups) or Kruskal–Wallis test (for > two groups).

BC200 expression (Supplementary Fig. 2E). Based on the indirect pathway analysis data, we examined BC200 potential effects on cell growth via cell counting and soft agar assay in hepatoma cells. Based on indirect pathway analysis data, we examined BC200 potential effects on cell growth via cell counting and soft agar assay in hepatoma cells. Notably, BC200 showed low expression in well and moderately differentiated cell lines (HepG2, Huh7 and Hep3B) but high expression in poorly differentiated cell lines (J7, Mahlavu and SK-Hep1) (Supplementary Fig. 3A, upper panel). Interestingly, poorly differentiated cell lines exhibited a higher growth rate than well-differentiated cell lines (Supplementary Fig. 3A, lower panel), suggesting that expression of BC200 is positively correlated with cell growth ability. Stable BC200 knockdown or

overexpression in J7, SK-Hep1, Hep3B and Huh7 cell lines was subsequently established (Supplementary Fig. 3B). Cell growth and soft agar assay were suppressed in J7 and SK-Hep1 cells after depletion of endogenous BC200 (Fig. 2A and B). Conversely, increased proliferation was observed in BC200-overexpressing Hep3B and Huh7 cells (Fig. 2A and B). To confirm whether the *in vitro* phenotype can be recapitulated *in vivo*, tumor formation was examined in nude mice. To this end, stable cells were subcutaneously injected into nude mice and tumor growth rates were determined. Overexpression of BC200 significantly promoted tumor growth and tumor weights, compared with the control group (Fig. 2C). Conversely, tumor growth curves and tumor weights were markedly reduced in BC200-depleted SK-Hep1 cells, compared with the control group (Fig. 2C). Our collective findings support a tumor promoter role of BC200 in HCC, both *in vitro* and *in vivo*.

### BC200 is required for self-renewal maintenance of liver cancer stem cells

Our findings suggest that BC200 is responsible for conferring growth advantages at an early stage of tumor development. As specified earlier, TICs have the capacity to self-renew and regenerate new tumors. To determine the association between TIC behavior and BC200, flow cytometry of the CD133<sup>+</sup> TIC population in HCC cell lines was performed. The data revealed the presence of the CD133<sup>+</sup> population in HepG2 and Huh7 cells, with expression ranging from 8 to 68% (Supplementary Fig. 4A). HepG2 and Huh7 cell lines were further sorted into CD133<sup>-</sup> and CD133<sup>+</sup> populations and confirmed via western blot (Supplementary Fig. 4B). BC200 was upregulated in CD133<sup>+</sup> HepG2 cells (Supplementary Fig. 4C). To determine whether BC200 functions in liver TIC self-renewal, the sphere formation assay was performed. Knockdown of BC200 dramatically reduced the tumor sphere formation frequencies of CD133<sup>+</sup> subsets of HepG2 and Huh7 cells, compared with sh-luc cells (Fig. 2D). To ascertain the role of T<sub>3</sub>/TR in liver TIC self-renewal, CD133<sup>+</sup> HepG2 cells were infected with Adenovirus-TR $\alpha$ 1 (Ad-TR $\alpha$ 1) or Adenovirus-TR $\beta$ 1 (Ad-TR $\beta$ 1) and tumor sphere formation with/without T<sub>3</sub> examined. T<sub>3</sub> clearly suppressed tumor sphere formation in CD133<sup>+</sup> HepG2 cells overexpressing Ad-TR $\alpha$ 1 or Ad-TR $\beta$ 1 relative to non-treated cells (Fig. 2E). In view of these results, we propose that BC200 is required for maintaining stemness ability in HCC.

**Table 2** Univariate and multivariate Cox regression analyses for overall survival.

Variable	Univariate analysis	P	Multivariate analysis	P
	HR (95% CI)		HR (95% CI)	
BC200 (high vs low)	1.838 (1.156–2.922)	0.01	1.618 (1.011–2.589)	0.045
Age (≥50 vs <50)	1.154 (0.767–1.736)	0.493	–	–
Gender (male vs female)	0.912 (0.608–1.366)	0.654	–	–
Cirrhosis (yes vs no)	1.206 (0.804–1.808)	0.366	–	–
AFP (high vs medium vs low)	1.310 (1.046–1.640)	0.019	1.080 (0.858–1.360)	0.51
Tumor size (≥5 vs <5 cm)	2.717 (1.796–4.108)	<0.001	1.705 (1.035–2.810)	0.036
Tumor type (multiple vs solitary)	2.135 (1.415–3.223)	<0.001	1.170 (0.627–2.181)	0.622
Vascular invasion (present vs absent)	1.824 (1.519–2.191)	<0.001	1.561 (1.124–2.166)	0.008
Pathological stage (III vs II vs I)	2.176 (1.695–2.794)	<0.001	1.043 (0.549–1.980)	0.898
Grading (3 vs 2 vs 1)	1.147 (0.777–1.694)	0.49	–	–

CI, confidence interval; HR, hazard ratio.

### BC200 is involved in T<sub>3</sub>/TR-mediated repression of cell growth ability

CDKs and cyclin-dependent kinase inhibitors play important roles in control of cell growth (Abbas & Dutta 2009, Malumbres 2014). Deregulation of these proteins is a hallmark of several diseases, including cancers. To assess the contributory role of BC200 in cell growth, its effects on the mRNA levels of cell cycle-related genes were examined. The p21 transcript levels were increased in SK-Hep1 cells after knockdown of BC200 expression while mRNA levels of CDK2, cyclin E1 and cyclin E2 were reduced (Fig. 3A, left panel). Conversely, overexpression of BC200 led to opposite effects (Fig. 3A, right panel). As expected, levels of the corresponding proteins were consistent with mRNA results, both *in vitro* and *in vivo* (Fig. 3B and C). In addition, BC200 depletion in CD133<sup>+</sup> HepG2 cells led to reduced expression of pluripotent transcription factors (Nanog and Sox2), CD44 and cell cycle-related genes, compared with control (sh-luc) cells (Fig. 3D). To confirm the involvement of BC200 in T<sub>3</sub>/TR-regulated cell growth, HepG2-TRβ1 cells were transfected with BC200-expressing or control (vc) plasmid and proliferation examined in the presence or absence of T<sub>3</sub>. T<sub>3</sub> clearly repressed HepG2-TRβ1 cell growth. Interestingly, this effect was partially rescued by BC200 in the presence of T<sub>3</sub> (Fig. 3E). Notably, protein levels of cyclin E2 and CDK2 were clearly increased in BC200-overexpressing HepG2-TRβ1 cells treated with T<sub>3</sub>, compared with their T<sub>3</sub>-treated control counterparts (Fig. 3E, lanes 2 vs 4). Our results collectively demonstrate that T<sub>3</sub>/TR suppresses BC200 expression, leading to modulation of cell cycle-related genes, and ultimately, inhibition of cell proliferation.

### BC200 protects cyclin E2 mRNA from degradation

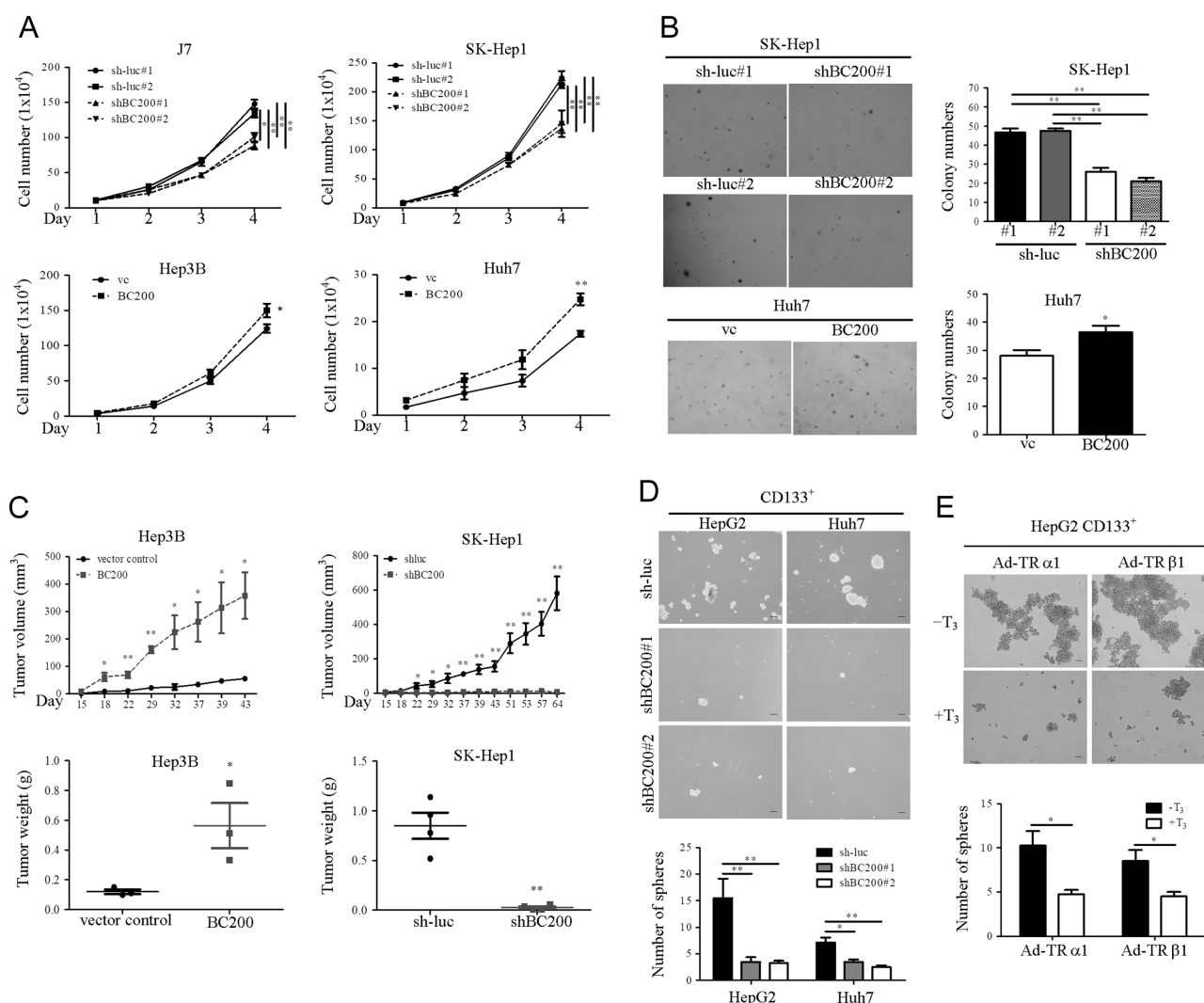
To clarify the regulatory mechanism of cyclin E2, its expression was measured using qRT-PCR after treatment

with actinomycin D (ActD, a transcriptional inhibitor). Knockdown of BC200 promoted cyclin E2 mRNA degradation in SK-Hep1 cells (Fig. 4A), suggesting a protective effect of BC200 against degradation. To determine the functional sequence of BC200, we established stable expression of BC200-wt (1–200), BC200-F1 (1–119), BC200-F2 (122–200) and BC200-F3 (51–119) in BC200 knockdown cell lines. Overexpression of BC200-wt and BC200-F1 partially delayed cyclin E2 mRNA degradation, compared to the control group, while overexpression of BC200-F2 and BC200-F3 had no effect on the stability of these mRNAs (Fig. 4B). These findings suggest that a functional sequence of 1–50 nucleotides participates in regulation of cyclin E2 mRNA stability. Previously, cyclin E-CDK2 complex has been considered an essential and master regulator of progression through G1 phase of the cell cycle (Koff *et al.* 1992). To test this hypothesis, co-immunoprecipitation assay was performed in BC200 stable cell lines. We found BC200 promoted association with CDK2-cyclin E2, but not CDK2-cyclin E1 (Fig. 4C). These findings indicated that the critical role of BC200 in cyclin E2-CDK2 activity in HCC cells. Next, the physical interaction of BC200 and cyclin E2 was examined using RIP assay. The results showed a specific enrichment of BC200 (but not GAPDH mRNA) coprecipitated within the cyclin E2 (Fig. 4D), indicating BC200 associated with cyclin E2 through direct binding and enhanced CDK2–cyclin E2 complex formation. Furthermore, levels of the p27 and p21 were decreased in cyclin E2-overexpressing cells compared to control cells (Fig. 4E).

### Cyclin E2 and CDK2 are highly expressed in HCC and positively correlated with BC200

T<sub>3</sub> protects hepatocyte from DEN-induced HCC-like liver tumors in mice model (Chi *et al.* 2016). To further

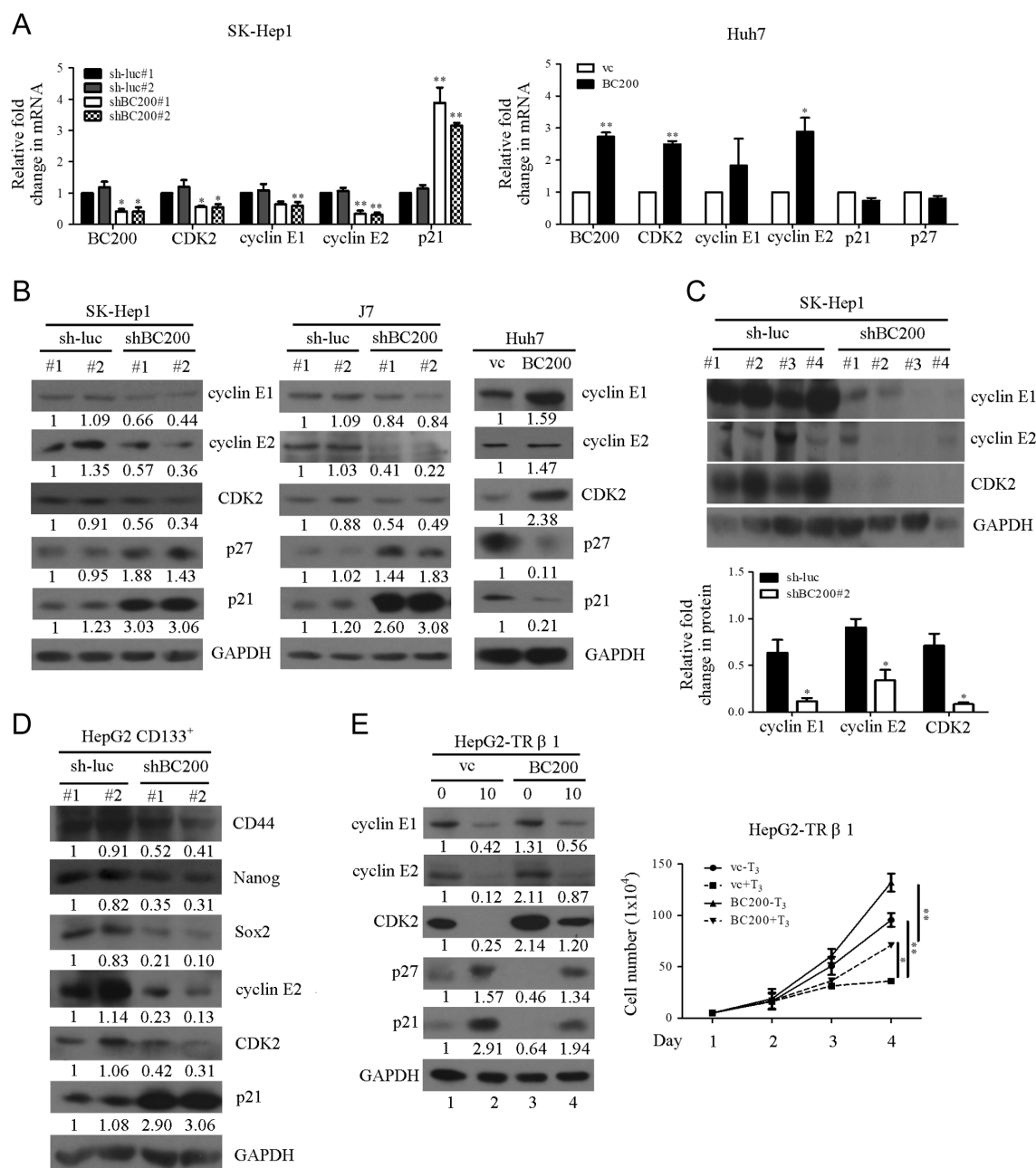


**Figure 2**

BC200 promotes cell growth and transformation ability. Effects of BC200 on cell growth (A) and soft agar colony formation (B). (C) Comparison of tumor volumes between hepatoma xenografts in BC200 stable cell lines. Xenografts were derived from Hep3B ( $5 \times 10^6$ ,  $n=3$  per group) and SK-Hep1 cells ( $2 \times 10^6$ ,  $n=4$  per group). Tumor volumes and weights were measured in xenografts after subcutaneous injection of cells. (D) Sphere formation assay of BC200-silenced stable cells. (E) CD133<sup>+</sup> HepG2 cells treated with T<sub>3</sub> or left untreated were infected with adenovirus-TRα1 (Ad-TRα1) and adenovirus-TRβ1 (Ad-TRβ1), and the sphere formation assay performed.

determined T<sub>3</sub> represses this phenotype through BC200/cyclin E2/CDK2 cascade, the expression levels of these genes were determined in DEN/hyper- and DEN/euthyroid mice. The expression levels of BC200 and cell cycle-related genes were repressed in DEN/hyperthyroid group, compared with DEN/euthyroid group (Fig. 5A and B). Our results suggest that T<sub>3</sub> suppresses DEN-induced hepatocarcinogenesis through BC200/cyclin E2/CDK2 cascade. To determine whether cyclin E2 and CDK2 are associated with tumor formation, mRNA levels of these molecules were determined in HCC specimens using qRT-PCR. The markers were significantly expressed in HCC compared with the corresponding adjacent

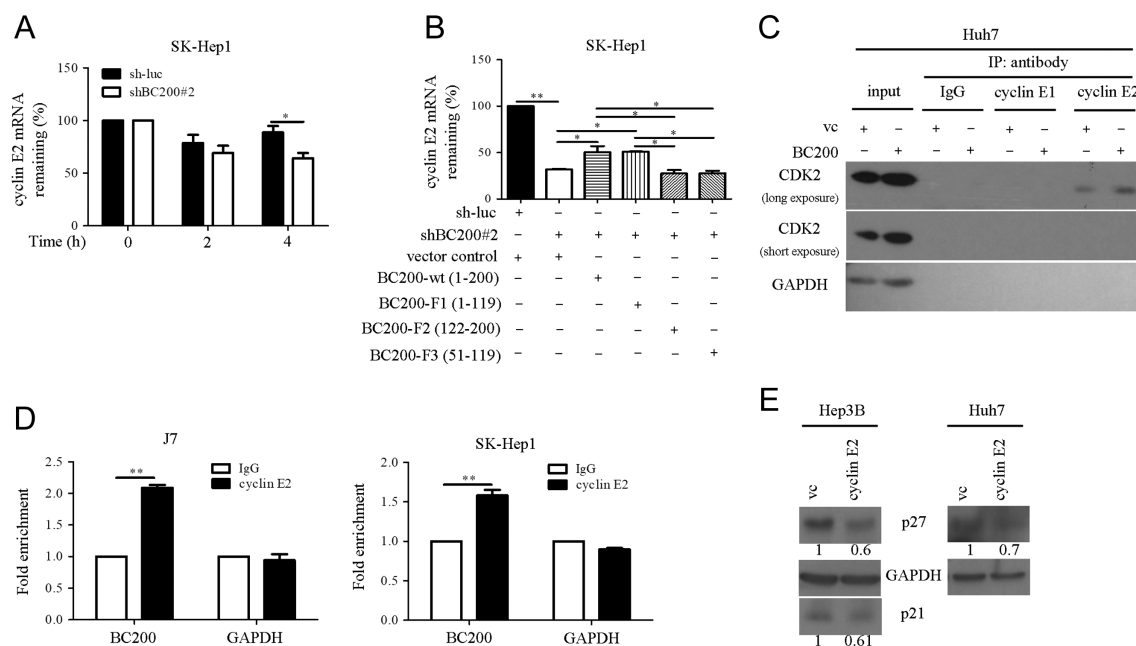
non-tumor counterparts (Fig. 5C and Supplementary Fig. 5A), consistent with high expression in HCC reported earlier from two publicly available datasets (Supplementary Fig. 5B and C). Furthermore, both TRα1 and TRβ1 were downregulated in HCC relative to the normal control group (Supplementary Fig. 5B and C). Notably, cyclin E2 and CDK2 expression were significantly correlated with OS of HCC patients (Supplementary Fig. 6A), similar to findings from the public dataset (Supplementary Fig. 6B). Spearman's correlation coefficient analysis revealed significant positive correlation of BC200 with cyclin E2 and CDK2 (Supplementary Table 2). Considering the positive correlation between these markers in HCC

**Figure 3**

BC200 regulates cell cycle-related genes and is involved in T<sub>3</sub>/TR-mediated cell growth function. (A) qRT-PCR analysis of total RNA in the indicated cell lines using 18S rRNA as a loading control to determine the mRNA expression levels of cell cycle-related genes. (B and C) Western blot analysis of cyclin E, CDK2, p21 and p27 expression in the indicated cell lines and tissues. (D) Immunoblot analysis of the expression patterns of CD44, Nanog, Sox2 and cell cycle-related genes in the indicated cell lines. GAPDH was used as the loading control. (E) Left panel: Western blot analysis of expression of cell cycle-related genes in the presence and absence of T<sub>3</sub>. Right panel: Vector control (vc) and BC200 cell lines stably expressing in HepG2-TRβ1 were grown in 6 cm dishes, and cell growth detected in the presence and absence of T<sub>3</sub>.

tumors, their combined influence on patient outcomes were evaluated. Patients were classified into three groups (I–III) using the median value as cutoff. Patients in group III (higher expression of both genes) showed significantly

poorer OS than those in group I (lower expression of both genes) (Fig. 5D). Our findings clearly support an important regulatory function of the BC200/cyclin E2/CDK2 axis in hepatoma (Fig. 5E).

**Figure 4**

BC200 promotes cyclin E2-CDK2 complex formation. (A and B) Half-life of cyclin E mRNA was calculated in the indicated cell lines after adding actinomycin D (ActD), normalizing to 18S rRNA. (C) Lysates from indicated cells were immunoprecipitated with IgG, anti-cyclin E1 and anti-cyclin E2 antibody, respectively. The immunoprecipitates were analyzed by Western blotting with an anti-CDK2 antibody. (D) RIP experiments were performed in J7 and SK-Hep1 cells and the coprecipitated RNA was subjected to qRT-PCR for BC200. GAPDH was used as negative controls. (E) Immunoblot analysis of the expression patterns of p27 and p21 in the indicated cell lines.

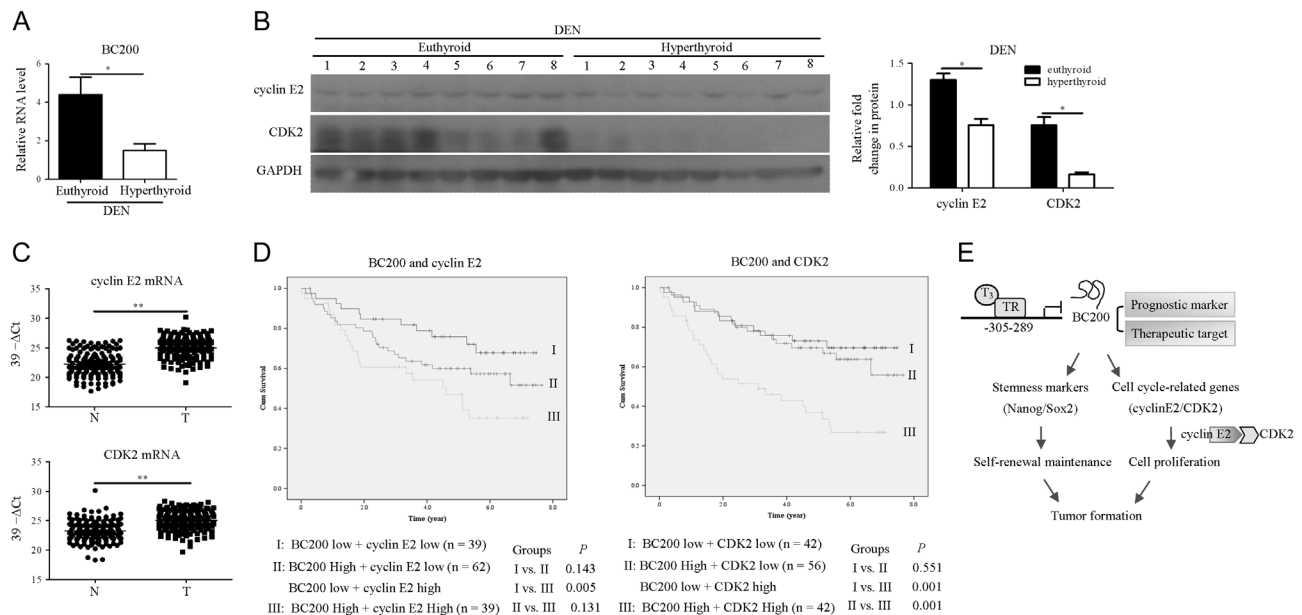
## Discussion

Previous studies have confirmed that lncRNAs and transcriptional factors form feedback or feed-forward loops, which play critical roles in biological processes. For example, the MYC-induced long non-coding RNA (MINCR) is activated by MYC and modulates the MYC transcription network (Doose *et al.* 2015). LincRNA-p21 is upregulated by HIF1 $\alpha$  and essential for hypoxia-enhanced glycolysis (Yang *et al.* 2014). In view of these associations, it is proposed that deregulation of lncRNAs by transcriptional factors could cause disease or cancer progression. Therefore, transcriptional factor-mediated lncRNA regulation is a significant focus of cancer biology research. In the current study, BC200 was identified as a novel gene downregulated by T<sub>3</sub>/TR that modulates thyroid hormone-mediated functions.

BC200 is reported to be expressed at high levels in invasive carcinoma of the breast (Iacoangeli *et al.* 2004). Earlier receiver-operating characteristics analysis of sensitivity and specificity confirmed the diagnostic power of BC200 RNA as a molecular marker of invasive breast cancer. However, the functional and clinical significance of BC200 in HCC remains to be established. Here, we showed that BC200 promotes cancer cell growth,

both *in vitro* and *in vivo* and is positively correlated with tumor type, tumor size, vascular invasion and pathological stage, supporting its utility as an independent prognostic factor associated with OS. Additionally, BC200 is known to act as a translational regulator in neurons (Iacoangeli & Tiede 2013). Data from the current study support a novel role of BC200 in regulation of cyclin E2 mRNA stability. Functional sequences of BC200 1–50 nucleotides in length were responsible for regulating cyclin E2 mRNA stability. On the other hand, BC200 expression appeared positively correlated with the cell proliferation rate. These results were similar to previous findings (Booy *et al.* 2017). Interestingly, BC200 was upregulated in CD133<sup>+</sup> HepG2 cells and stimulated stemness marker expression (Sox2 and Nanog), in turn, promoting sphere-formation capacity. Accordingly, we concluded that BC200 regulates early-stage HCC formation.

In our experiments, several genes that are positively or negatively regulated by T<sub>3</sub> were identified in the HepG2-TR $\alpha$ 1 cell line, including endoglin (Lin *et al.* 2013), pituitary tumor-transforming 1 (PTTG1) (Chen *et al.* 2008), Dickkopf 4 (DKK4) (Liao *et al.* 2012), Ubiquitin-like with PHD and ring finger domains 1 (UHRF1) (Wu *et al.* 2015) and Death-associated protein kinase 2 (DAPK2) (Chi *et al.* 2016), proposed to suppress

**Figure 5**

The BC200/cyclin E2/CDK2 axis is correlated with poor prognosis in HCC patients. QRT-PCR (A) and immunoblot analysis (B) of hepatic levels of BC200, cyclin E2 and CDK2 in the numbers of mice receiving DEN treatment ( $n=8$  per group). The quantitative results of western blot were shown. (C) qRT-PCR analysis of cyclin E2 and CDK2 expression in 140 pairs of human HCC (T) and adjacent normal (N) tissues using 18S rRNA as the loading control. (D) Kaplan-Meier overall survival analysis curve for high- or low-risk survival groups were measured in 140 paired HCC patients. High BC200 and simultaneous high the other genes were significantly associated with poorest overall survival. *P* values were determined via the log-rank test. (E) Proposed model for the  $T_3$ /TR/BC200/stemness marker/cell cycle-related gene pathway in regulation of tumor formation and self-renewal of hepatoma.

tumor formation. Previously, hypothyroidism was shown to be associated with significantly elevated risk for HCC (Hassan *et al.* 2009). A recent study by our group suggests that the  $T_3$ /PTEN-induced kinase 1/Parkin pathway plays an important role in protecting hepatocytes from HBx-induced HCC (Chi *et al.* 2017). Catalano and co-workers demonstrated that  $T_3$  reduces the tumorigenic potential of colorectal cancer-CSC to a significant extent through regulating Wnt and BMP signaling (Catalano *et al.* 2016). In contrast, the group of Wang showed that the thyroid hormone ( $T_4$ ) promotes cell self-renewal in HCC cells through TR $\alpha$ , but not TR $\beta$  (Wang *et al.* 2016). Kress and colleagues reported that TR $\alpha$ 1 overexpression and Wnt pathway activation enhance colorectal cancer formation (Kress *et al.* 2010). Specifically, the group demonstrated that TR $\alpha$ 1 promotes tumorigenesis in APC $^{+}/1638N$  mice with a Wnt-activated genetic background but TR $\alpha$ 1 overexpression alone is unable to trigger tumor formation. Thus,  $T_3$ /TRs may perform a dual function as an oncogene or tumor suppressor in different genetic backgrounds.

In conclusion, we have made conceptual progress toward advancing the theory that  $T_3$ /TR suppresses tumor growth and tumor sphere formation via reduction of BC200. Mechanistically, BC200 promotes

cyclin E2 expression via regulation of mRNA stability. The identification of a novel pathway interlinking  $T_3$ /TR, BC200, cyclin E2 and CDK2, which regulates proliferation and tumor sphere formation of hepatoma cells, presents potential therapeutic strategies involving targeting of BC200 and associated molecules for treatment of HCC.

#### Supplementary data

This is linked to the online version of the paper at <https://doi.org/10.1530/ERC-18-0176>.

#### Declaration of interest

The authors declare that there is no conflict of interest that could be perceived as prejudicing the impartiality of the research reported.

#### Funding

This work was supported by grants from Chang Gung Memorial Hospital, Taoyuan, Taiwan (CMRPD1D0383; CMRPD1G0421, CMRPD1G0422, CRRPD1F0011, CRRPD1F0012, CRRPD1F0013, NMRPD1G0951 to K-H L) and from the Ministry of Science and Technology of the Republic of China (MOST 103-2320-B-182-017-MY3; 106-2320-B-182-031-MY3, 106-2320-B-182-032-MY3 to K-H L; MOST 106-2321-B-182-003-MY3 to Y-H L).



**Author contribution statement**

Conception and design of the study: Yang-Hsiang Lin, Meng-Han Wu, Kwang-Huei Lin; Acquisition of data: Yang-Hsiang Lin, Meng-Han Wu, Ya-Hui Huang, Hsiang-Cheng Chi, Wen-Yu Chuang, Chia-Jung Yu, Ching-Ying Chen; Analysis and interpretation of data: Yang-Hsiang Lin, Ya-Hui Huang, Chau-Ting Yeh, Chung-Ying Tsai, I-Hsiao Chung; Drafting of the manuscript: Yang-Hsiang Lin, Meng-Han Wu, Kwang-Huei Lin; Statistical analysis: Yang-Hsiang Lin, Ya-Hui Huang, Chau-Ting Yeh; Study supervision: Kwang-Huei Lin.

**Acknowledgments**

The authors would like to thank Taiwan Liver Cancer Network (TLCN) for providing the hepatoma tissue samples and related clinical data (all are anonymous) for our research work. They thank Chuen Hsueh for helping to improve RNA-ISH detection.

**References**

- Abbas T & Dutta A 2009 p21 in cancer: intricate networks and multiple activities. *Nature Reviews Cancer* **9** 400–414. (<https://doi.org/10.1038/nrc2657>)
- Booy EP, McRae EK, Koul A, Lin F & McKenna SA 2017 The long non-coding RNA BC200 (BCYRN1) is critical for cancer cell survival and proliferation. *Molecular Cancer* **16** 109. (<https://doi.org/10.1186/s12943-017-0679-7>)
- Brescia P, Ortensi B, Fornasari L, Levi D, Broggi G & Pelicci G 2013 CD133 is essential for glioblastoma stem cell maintenance. *Stem Cells* **31** 857–869. (<https://doi.org/10.1002/stem.1317>)
- Catalano V, Dentice M, Ambrosio R, Luongo C, Carollo R, Benfante A, Todaro M, Stassi G & Salvatore D 2016 Activated thyroid hormone promotes differentiation and chemotherapeutic sensitization of colorectal cancer stem cells by regulating Wnt and BMP4 signaling. *Cancer Research* **76** 1237–1244. (<https://doi.org/10.1158/0008-5472.CAN-15-1542>)
- Chang IC, Huang SF, Chen PJ, Chen CL, Chen CL, Wu CC, Tsai CC, Lee PH, Chen MF, Lee CM, *et al.* 2016 The hepatitis viral status in patients with hepatocellular carcinoma: a study of 3843 patients from Taiwan Liver Cancer Network. *Medicine* **95** e3284. (<https://doi.org/10.1097/MD.0000000000003284>)
- Chen CJ, Tsai NM, Liu YC, Ho LI, Hsieh HF, Yen CY & Harn HJ 2002 Telomerase activity in human hepatocellular carcinoma: parallel correlation with human telomerase reverse transcriptase (hTERT) mRNA isoform expression but not with cell cycle modulators or c-Myc expression. *European Journal of Surgical Oncology* **28** 225–234. (<https://doi.org/10.1053/ejso.2001.1237>)
- Chen RN, Huang YH, Yeh CT, Liao CH & Lin KH 2008 Thyroid hormone receptors suppress pituitary tumor transforming gene 1 activity in hepatoma. *Cancer Research* **68** 1697–1706. (<https://doi.org/10.1158/0008-5472.CAN-07-5492>)
- Chi HC, Chen CY, Tsai MM, Tsai CY & Lin KH 2013 Molecular functions of thyroid hormones and their clinical significance in liver-related diseases. *BioMed Research International* **2013** 601361. (<https://doi.org/10.1155/2013/601361>)
- Chi HC, Chen SL, Tsai CY, Chuang WY, Huang YH, Tsai MM, Wu SM, Sun CP, Yeh CT & Lin KH 2016 Thyroid hormone suppresses hepatocarcinogenesis via DAPK2 and SQSTM1-dependent selective autophagy. *Autophagy* **12** 2271–2285. (<https://doi.org/10.1080/15548627.2016.1230583>)
- Chi HC, Chen SL, Lin SL, Tsai CY, Chuang WY, Lin YH, Huang YH, Tsai MM, Yeh CT & Lin KH 2017 Thyroid hormone protects hepatocytes from HBx-induced carcinogenesis by enhancing mitochondrial turnover. *Oncogene* **36** 5274–5284. (<https://doi.org/10.1038/onc.2017.136>)
- Doose G, Haake A, Bernhart SH, Lopez C, Duggimpudi S, Wojciech F, Bergmann AK, Borkhardt A, Burkhardt B, Claviez A, *et al.* 2015 MINCR is a MYC-induced lncRNA able to modulate MYC's transcriptional network in Burkitt lymphoma cells. *PNAS* **112** E5261–E5270. (<https://doi.org/10.1073/pnas.1505753112>)
- Gao JZ, Li J, Du JL & Li XL 2016 Long non-coding RNA HOTAIR is a marker for hepatocellular carcinoma progression and tumor recurrence. *Oncology Letters* **11** 1791–1798. (<https://doi.org/10.3892/ol.2016.4130>)
- Gong X, Wei W, Chen L, Xia Z & Yu C 2016 Comprehensive analysis of long non-coding RNA expression profiles in hepatitis B virus-related hepatocellular carcinoma. *Oncotarget* **7** 42422–42430. (<https://doi.org/10.18632/oncotarget.13796>)
- Hassan MM, Kaseb A, Li D, Patt YZ, Vauthey JN, Thomas MB, Curley SA, Spitz MR, Sherman SI, Abdalla EK, *et al.* 2009 Association between hypothyroidism and hepatocellular carcinoma: a case-control study in the United States. *Hepatology* **49** 1563–1570. (<https://doi.org/10.1002/hep.22793>)
- Hsieh CL, Liu H, Huang Y, Kang L, Chen HW, Chen YT, Wee YR, Chen SJ & Tan BC 2014 ADAR1 deaminase contributes to scheduled skeletal myogenesis progression via stage-specific functions. *Cell Death and Differentiation* **21** 707–719. (<https://doi.org/10.1038/cdd.2013.197>)
- Hu T & Lu YR 2015 BCYRN1, a c-MYC-activated long non-coding RNA, regulates cell metastasis of non-small-cell lung cancer. *Cancer Cell International* **15** 36. (<https://doi.org/10.1186/s12935-015-0183-3>)
- Iacoangeli A & Tiedge H 2013 Translational control at the synapse: role of RNA regulators. *Trends in Biochemical Sciences* **38** 47–55. (<https://doi.org/10.1016/j.tibs.2012.11.001>)
- Iacoangeli A, Lin Y, Morley EJ, Muslimov IA, Bianchi R, Reilly J, Weedon J, Diallo R, Bocker W & Tiedge H 2004 BC200 RNA in invasive and preinvasive breast cancer. *Carcinogenesis* **25** 2125–2133. (<https://doi.org/10.1093/carcin/bgh228>)
- Jing F, Kim HJ, Kim CH, Kim YJ, Lee JH & Kim HR 2015 Colon cancer stem cell markers CD44 and CD133 in patients with colorectal cancer and synchronous hepatic metastases. *International Journal of Oncology* **46** 1582–1588. (<https://doi.org/10.3892/ijo.2015.2844>)
- Koff A, Giordano A, Desai D, Yamashita K, Harper JW, Elledge S, Nishimoto T, Morgan DO, Franza BR & Roberts JM 1992 Formation and activation of a cyclin E-cdk2 complex during the G1 phase of the human cell cycle. *Science* **257** 1689–1694. (<https://doi.org/10.1126/science.1388288>)
- Kress E, Skah S, Sirakov M, Nadjar J, Gadot N, Scoazec JY, Samarut J & Plateroti M 2010 Cooperation between the thyroid hormone receptor TRalpha1 and the WNT pathway in the induction of intestinal tumorigenesis. *Gastroenterology* **138** 1863–1874. (<https://doi.org/10.1053/j.gastro.2010.01.041>)
- Lee HK, Hsu AK, Sajdak J, Qin J & Pavlidis P 2004 Coexpression analysis of human genes across many microarray data sets. *Genome Research* **14** 1085–1094. (<https://doi.org/10.1101/gr.1910904>)
- Liao CH, Yeh CT, Huang YH, Wu SM, Chi HC, Tsai MM, Tsai CY, Liao CJ, Tseng YH, Lin YH, *et al.* 2012 Dickkopf 4 positively regulated by the thyroid hormone receptor suppresses cell invasion in human hepatoma cells. *Hepatology* **55** 910–920. (<https://doi.org/10.1002/hep.24740>)
- Lin KH, Shieh HY & Hsu HC 2000 Negative regulation of the antimetastatic gene Nm23-H1 by thyroid hormone receptors. *Endocrinology* **141** 2540–2547. (<https://doi.org/10.1210/endo.141.7.7570>)
- Lin YH, Huang YH, Wu MH, Wu SM, Chi HC, Liao CJ, Chen CY, Tseng YH, Tsai CY, Tsai MM, *et al.* 2013 Thyroid hormone suppresses cell proliferation through endoglin-mediated promotion of p21 stability. *Oncogene* **32** 3904–3914. (<https://doi.org/10.1038/onc.2013.5>)

- Mak AB, Nixon AM, Kittanakom S, Stewart JM, Chen GI, Curak J, Gingras AC, Mazitschek R, Neel BG, Stagljar I, *et al.* 2012 Regulation of CD133 by HDAC6 promotes beta-catenin signaling to suppress cancer cell differentiation. *Cell Reports* **2** 951–963. (<https://doi.org/10.1016/j.celrep.2012.09.016>)
- Malakar P, Shilo A, Mogilevsky A, Stein I, Pikarsky E, Nevo Y, Benyamini H, Elgavish S, Zong X, Prasanth KV, *et al.* 2017 Long noncoding RNA MALAT1 promotes hepatocellular carcinoma development by SRSF1 upregulation and mTOR activation. *Cancer Research* **77** 1155–1167. (<https://doi.org/10.1158/0008-5472.CAN-16-1508>)
- Malumbres M 2014 Cyclin-dependent kinases. *Genome Biology* **15** 122. (<https://doi.org/10.1186/gb4184>)
- Mang Y, Li L, Ran J, Zhang S, Liu J, Li L, Chen Y, Liu J, Gao Y & Ren G 2017 Long noncoding RNA NEAT1 promotes cell proliferation and invasion by regulating hnRNP A2 expression in hepatocellular carcinoma cells. *OncoTargets and Therapy* **10** 1003–1016. (<https://doi.org/10.2147/OTT.S116319>)
- Martinez-Iglesias O, Garcia-Silva S, Tenbaum SP, Regadera J, Larcher F, Paramio JM, Vennstrom B & Aranda A 2009 Thyroid hormone receptor beta1 acts as a potent suppressor of tumor invasiveness and metastasis. *Cancer Research* **69** 501–509. (<https://doi.org/10.1158/0008-5472.CAN-08-2198>)
- Nadal R, Ortega FG, Salido M, Lorente JA, Rodriguez-Rivera M, Delgado-Rodriguez M, Macia M, Fernandez A, Corominas JM, Garcia-Puche JL, *et al.* 2013 CD133 expression in circulating tumor cells from breast cancer patients: potential role in resistance to chemotherapy. *International Journal of Cancer* **133** 2398–2407. (<https://doi.org/10.1002/ijc.28263>)
- Nakano K, Matsushita A, Sasaki S, Misawa H, Nishiyama K, Kashiwabara Y & Nakamura H 2004 Thyroid-hormone-dependent negative regulation of thyrotropin beta gene by thyroid hormone receptors: study with a new experimental system using CV1 cells. *Biochemical Journal* **378** 549–557. (<https://doi.org/10.1042/bj20031592>)
- Plaks V, Kong N & Werb Z 2015 The cancer stem cell niche: how essential is the niche in regulating stemness of tumor cells? *Cell Stem Cell* **16** 225–238. (<https://doi.org/10.1016/j.stem.2015.02.015>)
- Rinn JL & Chang HY 2012 Genome regulation by long noncoding RNAs. *Annual Review of Biochemistry* **81** 145–166. (<https://doi.org/10.1146/annurev-biochem-051410-092902>)
- Shang C, Zhu W, Liu T, Wang W, Huang G, Huang J, Zhao P, Zhao Y & Yao S 2016 Characterization of long non-coding RNA expression profiles in lymph node metastasis of early-stage cervical cancer. *Oncology Reports* **35** 3185–3197. (<https://doi.org/10.3892/or.2016.4715>)
- Shiu TY, Huang TY, Huang SM, Shih YL, Chu HC, Chang WK & Hsieh TY 2013 Nuclear factor kappaB down-regulates human UDP-glucuronosyltransferase 1A1: a novel mechanism involved in inflammation-associated hyperbilirubinaemia. *Biochemical Journal* **449** 761–770. (<https://doi.org/10.1042/BJ20121055>)
- Vander Griend DJ, Karthaus WL, Dalrymple S, Meeker A, DeMarzo AM & Isaacs JT 2008 The role of CD133 in normal human prostate stem cells and malignant cancer-initiating cells. *Cancer Research* **68** 9703–9711. (<https://doi.org/10.1158/0008-5472.CAN-08-3084>)
- Wang T, Xia L, Ma S, Qi X, Li Q, Xia Y, Tang X, Cui D, Wang Z, Chi J, *et al.* 2016 Hepatocellular carcinoma: thyroid hormone promotes tumorigenicity through inducing cancer stem-like cell self-renewal. *Scientific Reports* **6** 25183. (<https://doi.org/10.1038/srep25183>)
- Wu SM, Cheng WL, Lin CD & Lin KH 2013 Thyroid hormone actions in liver cancer. *Cellular and Molecular Life Sciences* **70** 1915–1936. (<https://doi.org/10.1007/s00018-012-1146-7>)
- Wu SM, Cheng WL, Liao CJ, Chi HC, Lin YH, Tseng YH, Tsai CY, Chen CY, Lin SL, Chen WJ, *et al.* 2015 Negative modulation of the epigenetic regulator, UHRF1, by thyroid hormone receptors suppresses liver cancer cell growth. *International Journal of Cancer* **137** 37–49. (<https://doi.org/10.1002/ijc.29368>)
- Wu SM, Huang YH, Yeh CT, Tsai MM, Liao CH, Cheng WL, Chen WJ & Lin KH 2011 Cathepsin H regulated by the thyroid hormone receptors associate with tumor invasion in human hepatoma cells. *Oncogene* **30** 2057–2069. (<https://doi.org/10.1038/onc.2010.585>)
- Xia P & Xu XY 2015 PI3K/Akt/mTOR signaling pathway in cancer stem cells: from basic research to clinical application. *American Journal of Cancer Research* **5** 1602–1609.
- Yang F, Zhang H, Mei Y & Wu M 2014 Reciprocal regulation of HIF-1alpha and lincRNA-p21 modulates the Warburg effect. *Molecular Cell* **53** 88–100. (<https://doi.org/10.1016/j.molcel.2013.11.004>)
- Yuan JH, Yang F, Wang F, Ma JZ, Guo YJ, Tao QF, Liu F, Pan W, Wang TT, Zhou CC, *et al.* 2014 A long noncoding RNA activated by TGF-beta promotes the invasion-metastasis cascade in hepatocellular carcinoma. *Cancer Cell* **25** 666–681. (<https://doi.org/10.1016/j.ccr.2014.03.010>)
- Zhao RH, Zhu CH, Li XK, Cao W, Zong H, Cao XG & Hu HY 2016 BC200 lncRNA a potential predictive marker of poor prognosis in esophageal squamous cell carcinoma patients. *OncoTargets and Therapy* **9** 2221–2226. (<https://doi.org/10.2147/OTT.S99401>)
- Zhu P, Wang Y, Wu J, Huang G, Liu B, Ye B, Du Y, Gao G, Tian Y, He L, *et al.* 2016 LncBRM initiates YAP1 signalling activation to drive self-renewal of liver cancer stem cells. *Nature Communications* **7** 13608. (<https://doi.org/10.1038/ncomms13608>)

Received in final form 22 June 2018

Accepted 10 July 2018

RESEARCH ARTICLE

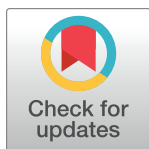
# Development of sandwich ELISA and lateral flow strip assays for diagnosing clinically significant snakebite in Taiwan

Chien-Chun Liu<sup>1☯</sup>, Jau-Song Yu<sup>1,2,3,4☯</sup>, Po-Jung Wang<sup>5</sup>, Yung-Chin Hsiao<sup>1,3</sup>, Chien-Hsin Liu<sup>6</sup>, Yen-Chia Chen<sup>7,8</sup>, Pei-Fang Lai<sup>9</sup>, Chih-Po Hsu<sup>10</sup>, Wen-Chih Fann<sup>11</sup>, Chih-Chuan Lin<sup>5\*</sup>

**1** Molecular Medicine Research Center, Chang Gung University, Tao-Yuan, Taiwan, **2** Department of Cell and Molecular Biology, College of Medicine, Chang Gung University, Tao-Yuan, Taiwan, **3** Liver Research Center, Chang Gung Memorial Hospital, Linkou, Tao-Yuan, Taiwan, **4** Research Center for Food and Cosmetic Safety, Research Center for Chinese Herbal Medicine, College of Human Ecology, Chang Gung University of Science and Technology, Tao-Yuan, Taiwan, **5** Department of Emergency Medicine, Chang Gung Memorial Hospital, Tao-Yuan, Taiwan, **6** Center for Research, Diagnostics and Vaccine Development, Centers for Disease Control, Ministry of Health and Welfare, Taipei, Taiwan, **7** Department of Emergency medicine, Taipei Veterans General Hospital, Taipei, Taiwan, **8** Department of Emergency Medicine, School of Medicine, National Yang-Ming University, Taipei, Taiwan, **9** Department of Emergency, Buddhist Tzu Chi Hospital, Hualien, Taiwan, **10** Department of Trauma and Emergency Surgery, Chang Gung Memorial Hospital, Chang Gung University, Tao-Yuan, Taiwan, **11** Department of Emergency Medicine, Chia-Yi Chang Gung Memorial Hospital, Chiayi, Taiwan

☯ These authors contributed equally to this work.

\* [bearuncle@yahoo.com](mailto:bearuncle@yahoo.com)



## OPEN ACCESS

**Citation:** Liu C-C, Yu J-S, Wang P-J, Hsiao Y-C, Liu C-H, Chen Y-C, et al. (2018) Development of sandwich ELISA and lateral flow strip assays for diagnosing clinically significant snakebite in Taiwan. *PLoS Negl Trop Dis* 12(12): e0007014. <https://doi.org/10.1371/journal.pntd.0007014>

**Editor:** Elda Sanchez, Texas A&M University Kingsville, UNITED STATES

**Received:** August 15, 2018

**Accepted:** November 21, 2018

**Published:** December 3, 2018

**Copyright:** © 2018 Liu et al. This is an open access article distributed under the terms of the [Creative Commons Attribution License](https://creativecommons.org/licenses/by/4.0/), which permits unrestricted use, distribution, and reproduction in any medium, provided the original author and source are credited.

**Data Availability Statement:** All relevant data are within the manuscript and its Supporting Information files.

**Funding:** This work was supported by the Ministry of Science and Technology, Taiwan (grants MOST 106-2632-B-182-002 and 106-2320-B-182-029-MY3 to JSY), by Chang Gung Memorial Hospital, Taiwan (grants CMRPG3F0241, 242 and 243 to CCLin, CIRPD3B0013, CRRPD1F0051, 52 and 53, CLRPD190018 and BMRP208 to JSY), and by the "Molecular Medicine Research Center, Chang Gung

## Abstract

Taiwan is an island located in the south Pacific, a subtropical region that is home to 61 species of snakes. Of these snakes, four species—*Trimeresurus stejnegeri*, *Protobothrops mucrosquamatus*, *Bungarus multicinctus* and *Naja atra*—account for more than 90% of clinical envenomation cases. Currently, there are two types of bivalent antivenom: hemorrhagic antivenom against the venom of *T. stejnegeri* and *P. mucrosquamatus*, and neurotoxic antivenom for treatment of envenomation by *B. multicinctus* and *N. atra*. However, no suitable detection kits are available to precisely guide physicians in the use of antivenoms. Here, we sought to develop diagnostic assays for improving the clinical management of snakebite in Taiwan. A two-step affinity purification procedure was used to generate neurotoxic species-specific antibodies (NSS-Abs) and hemorrhagic species-specific antibodies (HSS-Abs) from antivenoms. These two SSABs were then used to develop a sandwich ELISA (enzyme-linked immunosorbent assay) and a lateral flow assay comprising two test lines. The resulting ELISAs and lateral flow strip assays could successfully discriminate between neurotoxic and hemorrhagic venoms. The limits of quantification (LOQ) of the ELISA for neurotoxic venoms and hemorrhagic venoms were determined to be 0.39 and 0.78 ng/ml, respectively, and the lateral flow strips were capable of detecting neurotoxic and hemorrhagic venoms at concentrations lower than 5 and 50 ng/ml, respectively, in 10–15 min. Tests of lateral flow strips in 21 clinical snakebite cases showed 100% specificity and 100% sensitivity for neurotoxic envenomation, whereas the sensitivity for detecting hemorrhagic envenomation samples was 36.4%. We herein presented a feasible strategy for

University” from The Featured Areas Research Center Program within the framework of the Higher Education Sprout Project by the Ministry of Education (MOE) in Taiwan. The funders had no role in study design, data collection and analysis, decision to publish, or preparation of the manuscript.

**Competing interests:** The authors have declared that no competing interests exist.

developing a sensitive sandwich ELISA and lateral flow strip assay for detecting and differentiating venom proteins from hemorrhagic and neurotoxic snakes. A useful snakebite diagnostic guideline according to the lateral flow strip results and clinical symptoms was proposed to help physicians to use antivenoms appropriately. The two-test-line lateral flow strip assay could potentially be applied in an emergency room setting to help physicians diagnose and manage snakebite victims.

## Author summary

Snakebite is a public health issue that causes life-threatening medical emergencies. Rapid diagnosis of snakebite in the clinic is a critical necessity in many tropical and subtropical countries, where various venomous snakes are common. Venoms from different snake species contain distinct protein components that require treatment with different antivenoms. However, given the similarity in clinical symptoms among some snake envenomations, it is often challenging for physicians to precisely define the snake species responsible for envenomation. Thus, a reliable method or assay for rapidly diagnosing envenoming species is urgently needed. Here, we present a two-step affinity purification procedure for generating species-specific antibodies (SSAbs) from antivenom, followed by the development of a sandwich ELISA (enzyme-linked immunosorbent assay) and lateral flow strip assay using these SSAbs. This feasible and cost-effective strategy allowed us to develop workable assays for distinguishing between venom proteins from hemorrhagic and neurotoxic snakes in Taiwan. The usefulness of this strategy was demonstrated in the clinic, where both diagnostic assays were shown capable of detecting venoms in blood samples from snakebite patients. Together with the observation of clinical symptoms, the two-test-line lateral flow strip assay is potentially applicable in an emergency room setting to improve snakebite diagnosis and management.

## Introduction

Envenoming resulting from snakebites is a significant public health issue in many regions of the world, particularly in tropical and subtropical countries and some poor rural communities [1]. An estimated 1,800,000–2,700,000 envenoming cases and 81,410–137,880 associated deaths occur each year globally owing to snakebite [2]. The regions with the highest burden are South Asia, Southeast Asia, and Africa [2, 3].

Administration of antivenom is the standard treatment for snake envenomation. In most countries, multiple types of antivenom are clinically available, but uncertainty regarding the appropriate antivenom to use in any given situation remains an important issue. To date, the species responsible for envenomation of snakebite victims referred for medical treatment is initially identified primarily based on the shape of the wound or identification of dead snakes brought to the hospital. Thereafter, the physician monitors local symptoms to confirm which antivenom should be used. However, some clinical symptoms caused by envenomation are similar among species, and non-venomous snakes are often responsible for the patient’s snakebite [4]. Additionally, physicians are often misled by incorrect descriptions of the snake by victims or their family members [5]. Identification of venomous snake species is important for optimal clinical management, because it allows physicians to use the correct antivenom for effective treatment, thereby improving patients’ prognosis and preventing the waste of



expensive antivenoms and exposing victims to antivenom-induced adverse reactions [6]. Although identification of snake species is important for the management of snakebite-related injuries worldwide, there are currently no developed standard platforms or guidelines for snakebite diagnosis globally.

Detection of venom proteins using antibodies is a simple and effective approach for identifying the species responsible for snakebite. To date, various immunoassays for detecting venom proteins in body fluids have been described [7–13], including radioimmunoassay [14], agglutination assays [9, 15], enzyme-linked immunosorbent assays (ELISAs) [10–12, 16, 17], and fluorescence immunoassays [18, 19]. In addition to immunoassays, immunology-based biosensors have been explored for detection of snakebite [20, 21]. ELISAs and lateral flow assays [22, 23] are arguably the best choice of immunoassays for snakebite identification. ELISAs, the most common and general immunoassays in clinical use, are sensitive to their target at pictogram per milliliter levels [18]. Although the antibodies are relatively costly, ELISA devices and reagents are affordable for routine diagnosis. Compared with ELISAs, lateral flow assays offer advantages in terms of detection time and required equipment: it takes only ~5–20 min to obtain assay results and no supporting instrumentation is needed [24, 25]. Although lateral flow assays mainly provide qualitative results, their simple design and operation compared with quantitative ELISAs make them the most user-friendly for the public, allowing rapid adoption in rural countries.

Snake venoms contain many proteins, and closely related snake species have some of the same or similar venom components, causing cross-reactions in immunoassays applied to detect venom proteins [11, 12, 26]. The venom antigens responsible for the observed cross-reactivity would further cause ambiguities and false-positive results in snake species detection [11, 27]. Hence, the direct use of polyclonal antibodies against whole venoms for snake species detection is inappropriate, and elimination of cross-reactive antibodies is critical for generating an immunoassay with high specificity for discriminating snake species [11, 12, 28]. Solving the problem of cross-reaction and improving the specificity of immunoassays might most efficiently be achieved through purification of species-specific antibodies (SSAbs) on affinity columns immobilized with venom proteins cross-reactive to the polyclonal antibodies or antisera [11, 12].

Six venomous snakes—*Deinagkistrodon acutus*, *Trimeresurus stejnegeri*, *Protobothrops mucrosquamatus*, *Daboia russelii formosensis*, *Bungarus multicinctus* and *Naja atra*—are indigenous to Taiwan, a subtropical island in East Asia [29]. Four kinds of antivenom had been produced by the Vaccine Center, Center for Disease Control, Taiwan, to treat envenomation by these six venomous snakes and effectively limit snakebite mortality [30]. Freeze-dried hemorrhagic antivenom (FHAV) is used to treat envenomation by *T. stejnegeri* and *P. mucrosquamatus*, and freeze-dried neurotoxic antivenom (FNAV) neutralizes venom of *B. multicinctus* and *N. atra*. Envenomation by the other two snake species is treated by monovalent antivenoms. A population-based study of venomous snakebites in Taiwan from 2005 to 2009 reported a total of 4647 snakebite cases, of which 380 (8.1%) received at least two types of antivenoms, mainly because of similarities in the clinical presentations of different snakebites and the inability of some patients to identify the culprit snake [31]. In some studies, such unidentified cases accounted for 12–45% of total cases [32–35]. In addition, according to a clinical survey of antivenom usage in Taiwan, more than 99% of snakebite patients that had received FHAV or FNAV treatment were rescued [36], indicating that most snakebite cases in Taiwan represent envenomation by *T. stejnegeri*, *P. mucrosquamatus*, *B. multicinctus* or *N. atra*. Unfortunately, there have been very few efforts to develop sensitive assays for detecting snake venom in Taiwan. Currently, only one ELISA-based blood assay has been developed to detect the *N. atra* venom, but it is not commercially available [7], and no laboratory test can be used to identify other types of venoms.

In the present study, we designed a workflow to develop immunoassays for snakebite detection based on clinical antivenom usage in Taiwan. We used FHAV and FNAV as resources for purification of hemorrhagic species-specific antibodies (HSS-Ab) and neurotoxic species-specific antibodies (NSS-Ab), and applied these two critical reagents to develop ELISAs and lateral flow strip assays. These assays hold the potential for use in identification of snake species responsible for snakebites in Taiwan.

## Materials and methods

### Snake venoms and hyper-immunized horse plasma

Lyophilized venoms of *T. stejnegeri*, *P. mucrosquamatus*, *B. multicinctus* and *N. atra* were obtained from the Center for Disease Control, R.O.C (Taiwan). The venoms were collected from several adult specimens, then freeze-dried and stored at -20°C before use. Hemorrhagic venom (*T. stejnegeri* and *P. mucrosquamatus*)-immunized and neurotoxic venom (*B. multicinctus* and *N. atra*)-immunized horse plasma were also donated by the Center for Disease Control, R.O.C (Taiwan). The plasma was stored at -80°C before use.

### Affinity purification of SSABs

For coupling of venom proteins onto Sepharose beads, CNBr-activated Sepharose 4B was swollen in 1.0 mM HCl (pH 3.0), then incubated with 10 mg hemorrhagic or neurotoxic snake venoms dissolved in coupling buffer (0.1 M NaHCO<sub>3</sub> pH 8.3) overnight at 4°C on a round rotator. After washing with coupling buffer, any remaining active sites on beads were blocked by incubating overnight at 4°C with blocking buffer (1.0 M diethanolamine pH 8.0) on a rotator. The beads were then alternately washed three times with an acidic buffer (0.1 M C<sub>2</sub>H<sub>3</sub>NaO<sub>2</sub> pH 4.0, 0.5 M NaCl) and basic buffer (0.1 M Tris pH 8.0, 0.5 M NaCl) and packed into a column. The resulting venom affinity columns were equilibrated with binding buffer (10 mM Tris-HCl pH 7.5) and stored at 4°C before use.

To purify HSS-Ab, 2 ml FHAV was diluted in 30 ml of binding buffer and the diluted sample was pumped into the neurotoxic venom affinity column at 4°C for 3 h. The flow-through fraction was then pumped into the hemorrhagic venom affinity column at 4°C for another 3 h. The hemorrhagic venom affinity column was then washed with 60 ml binding buffer and 60 ml wash buffer (10 mM Tris-HCl pH 7.5, 0.5 M NaCl). After washing, each affinity column was eluted with 20 ml of acidic (100 mM glycine pH 2.5) or basic (100 mM triethylamine pH 11.5) elution buffer, and eluted fractions (1 ml/fraction) were collected into microcentrifuge tubes containing 100 µl of neutralized buffer (1.5 M Tris-HCl pH 8.0). Finally, all eluted fractions were pooled, concentrated, and exchanged into phosphate-buffered saline (PBS) by dialysis overnight. The concentrated antibodies in PBS were diluted with an equal volume of glycerol and stored at -20°C. Similar protocol was used to purify NSS-Ab from 2 ml FNAV, in which the diluted FNAV was passed through the hemorrhagic venom affinity column first, and the flow-through fraction containing NSS-Ab was further purified using the neurotoxic venom affinity column.

### Indirect ELISA assays

Snake venom proteins (100 ng) were diluted in 100 µl PBS and coated onto 96-well polystyrene microplates (Corning, USA) by incubating at 4°C overnight. The plates were washed six times with 200 µl of PBST (PBS contain 0.1% Tween-20) and blocked by incubating with 200 µl of 1% ovalbumin in PBS at room temperature for 2 h. After washing wells six times with PBST, antivenom or purified Ab (1 mg/ml) was serially diluted (from 1:2000 to 1:16000) and added to

individual wells, then the plate was incubated at room temperature for 2 h. Wells were again washed six times with PBST, and then alkaline phosphatase-conjugated anti-horse IgG antibody (Santa Cruz Biotechnology, USA) was added to each well and the plate was incubated at room temperature for 1 h. After washing six times with PBST, the substrate 4-methyl umbelliferyl phosphate (100  $\mu$ M, 100  $\mu$ l/well; Molecular Probes) was added to each well, and fluorescence was measured with a SpectraMax M2 microplate reader (Molecular Devices, USA) at excitation and emission wavelengths of 355 and 460 nm, respectively.

### Western blot analysis

Snake venom proteins (5  $\mu$ g) were separated by sodium dodecyl sulfate-polyacrylamide gel electrophoresis (SDS-PAGE), transferred onto PVDF (polyvinylidene difluoride) membranes (Millipore, USA), and probed with antivenom or purified Ab. Immunoreactive proteins in PVDF membranes were detected by incubating for 1 h with the appropriate alkaline phosphatase-conjugated anti-horse IgG antibodies (Santa Cruz Biotechnology, USA) and visualized using the CDP-Star Western Blot Chemiluminescence Reagent (PerkinElmer, USA).

### Biotinylation of SSABs

Antibodies were biotinylated using a Lightning-Link biotinylation kit (Innova Biosciences, USA) according to the protocol provided by the manufacturer. Briefly, 100  $\mu$ l of SSAB (2 mg/ml) was mixed with 10  $\mu$ l of modifier reagent, then added to the tube containing biotinylation powder and incubated for 15 min in the dark. After the biotinylation reaction, 10  $\mu$ l of quencher reagent was added and the reaction mixture was stored at -20°C until use.

### Sandwich ELISA assays

SSAB (100  $\mu$ l at 2 mg/ml), diluted 1:1000 in PBS, was coated onto 96-well polystyrene microplates. Thereafter, wells were blocked by incubating with 1% bovine serum albumin (BSA) in PBS for 1 h, then washed six times with 200  $\mu$ l PBST. Test samples (100  $\mu$ l) were added into individual wells and incubated at room temperature for 2 h. After washing six times with PBST, 100  $\mu$ l of biotin-labeled SSAB, diluted 1:16000 in PBS, was added and plates were incubated for 2 h. Plates were again washed six times with PBST, then alkaline phosphatase-conjugated streptavidin was added and allowed to interact with biotin. The alkaline phosphatase substrate, 4-methyl umbelliferyl phosphate (100  $\mu$ M, 100  $\mu$ l/well), was then added to each well, and fluorescence was measured with a SpectraMax M5 microplate reader at excitation and emission wavelengths of 355 and 460 nm, respectively.

### Snakebite animal model and plasma sample collection

Experiments were performed on male 7-wk-old littermate mice (C57BL/6Narl strain). Mice were maintained under specific pathogen-free conditions with a 12:12 h light-dark cycle at a temperature of 22°C and a humidity level of 60–70%. Animals had ad libitum access to food and water. Mice ( $n = 3$ /group) within a defined weight range (20–25 g) were subcutaneously (*B. multicinctus* and *N. atra* venom) or intraperitoneally (*T. stejnegeri* and *P. mucrosquamatus* venom) injected with a precise 0.1 ml volume of sterile saline solution containing a minimal lethal dose (MLD) of venom. Blood samples from each mouse were collected using a heparinized capillary blood collection system (Kent Scientific, USA) 0.5, 1, 1.5 and 2 h after venom injection. Collected blood was centrifuged at 3000  $\times$  g for 20 min. The resulting supernatant (plasma) was collected into a microcentrifuge tube and stored at -80°C before use.

## Preparation of colloidal gold-labeled SSAbs

A colloidal gold (40 nm) solution (REGA Biotechnology Inc., Taipei, Taiwan) was adjusted to pH 8.0 with 0.1 M potassium carbonate. The optimal concentration of SSAb (10 mg) was added to 2 ml of colloidal gold solution and incubated at room temperature for 10 min with gentle mixing. The mixture was blocked by incubating with 0.5 ml of 5% BSA in PBS at room temperature for 15 min with gentle mixing, and then centrifuged at  $10,000 \times g$  at 4°C for 30 min. The gold pellets were suspended in PBST containing 1% BSA, and washed by repeated centrifugation and suspension in the same solution. The final precipitates were suspended in 1 ml PBST containing 1% BSA and stored at 4°C until use.

## Development of lateral flow strips

The strips were manufactured by REGA Biotechnology Inc. (Taipei, Taiwan). Nitrocellulose membranes, sample pads, conjugate pads and absorbent pads were all from REGA Biotechnology Inc. Conjugate pads were saturated with HSS-Ab-or NSS-Ab-conjugated colloidal gold, then dried at 37°C for 1 h before assembling. The nitrocellulose membrane was pasted to the cardboard, after which conjugated and absorbent pads were also pasted to the cardboard such that they overlapped with each side of the nitrocellulose membrane by about 2 mm. The sample pad was also laid over the absorbent pad (2 mm overlap) and pasted onto the cardboard. The AGISMART RP-1000 rapid test immuno-strip printer (REGA Biotechnology Inc.) was used to dispense HSS-Abs and NSS-Abs (2 mg/ml) onto hemorrhagic and neurotoxic test lines, respectively, and goat anti-horse IgG antibody (2 mg/mL) (REGA Biotechnology Inc.) onto the control line on the nitrocellulose membrane. The distance between each line was 5 mm. The strips were prepared and assembled in a low-humidity environment, packaged into an aluminum pouch, and stored at room temperature before use.

## Clinical sample collection

Patients with suspected snakebite were admitted directly to the Emergency Departments of Taipei Veteran General Hospital, Linkou Chang Gung Memorial Hospital, Chiayi Chang Gung Memorial Hospital or Hualien Tzu Chi Hospital, and did not receive antivenom treatment before being enrolled in this study. After obtaining signed, informed consent forms from patients, 5 ml of blood was collected in SST blood collection tubes (BD, Franklin Lakes, New Jersey, USA) and centrifuged at 4°C for 10 min to obtain serum samples. A 100–200  $\mu$ l aliquot of serum sample was immediately applied to lateral flow strip test in the emergency room, and results were determined by clinical physicians. The remainder of each sample was sent to the laboratory in Chang Gung University and stored at -80°C. All samples were re-analyzed using the lateral flow strip test in the laboratory to confirm emergency room result; samples were also analyzed by sandwich ELISA to measure the concentrations of venom proteins.

## Venom detection with lateral flow strips

Each serum sample (100–200  $\mu$ l) was diluted with 1 volume of reaction buffer (100 mM borax, 250 nM polyvinylpyrrolidone (PVP)-40 and 1% Triton X-100) in a microcentrifuge tube. The strips were directly soaked in the samples, and results were recorded after a 10-min reaction.

## Agreement between lateral flow strip and sandwich-ELISA methods

The Cohen's kappa coefficient ( $\kappa$ ) statistic [37, 38] was used to assess the strength of inter-method agreement for diagnosis results. The value of kappa coefficient statistic over 0.75,



between 0.75 to 0.40, or below 0.40 indicates excellent agreement, good to fair agreement, and poor agreement, respectively [39, 40].

## Ethics statement

All clinical serum samples were collected and obtained at Taipei Veteran General Hospital, Linkou Chang Gung Memorial Hospital, Chiayi Chang Gung Memorial Hospital or Hualien Tzu Chi Hospital from February 2017 to February 2018. All study subjects are adult participants and signed an informed consent form approved by the Institutional Review Board (IRB) of Taipei Veteran General Hospital (Approval No: 2017-06-013BCF) and Linkou Chang Gung Memorial Hospital (Approval No: 201800098B0) permitting the use of plasma samples for this study. Experiments involving the care, bleeding, and injection of mice with various venoms were reviewed and approved by the Institutional Animal Care and Use Committee of Chang Gung University (Permit Number: CGU14-024). The protocol for mouse studies was based on guidelines provided by the Council for International Organizations of Medical Sciences (CIOMS) [41].

## Results

### Immunoreactivity and cross-reactivity among four venoms and two antivenoms

To assess the cross-reactivity among four venoms and two antivenoms, we performed indirect ELISAs and immunoblotting. The results of indirect ELISAs showed that cross-reactivity of FHAV towards *B. multicinctus* and *N. atra* venom was very low (Fig 1A); however, FNAV strongly cross-reacted with *T. stejnegeri* and *P. mucrosquamatus* venom (Fig 1B). Cross-reaction signals increased gradually with increases in antivenom concentration, and both antivenoms showed stronger reactivity toward homologous venoms than heterologous venoms. As shown in Western blot profiling data, FHAV primarily cross-reacted with protein bands in the high molecular weight region (55–70 kDa) of *N. atra* venom (Fig 1C), whereas FNAV cross-reacted with multiple bands in *T. stejnegeri* and *P. mucrosquamatus* venoms, predominantly towards protein bands in the 15–25 kDa range in *P. mucrosquamatus* venom (Fig 1D). A comparison of the protein profiles of the four venoms (S1 Fig) showed that, generally, most venom components of these venoms were recognized by the corresponding homologous antivenom.

### HSS-Ab and NSS-Ab specificity

In this study, we used an affinity purification procedure to eliminate cross-reactive antibodies from antivenoms. Heterologous venom-immobilized affinity columns were prepared and used to remove cross-reactive antibodies from antivenoms, after which the remaining antibodies were purified using a homologous venom-immobilized affinity column, yielding SSAbs. SDS-PAGE analysis of the affinity-purified HSS-Abs and NSS-Abs showed a typical pattern of IgG heavy and light chains (S2 Fig). Indirect ELISAs and Western blotting assays were performed to evaluate the specificity of affinity-purified SSAbs, HSS-Abs and NSS-Abs. The results of indirect ELISAs showed that both SSAbs possessed high specificity toward the homologous venoms, and showed significantly decreased cross-reactivity with heterologous venoms compared with the original antivenoms (Fig 2A & 2B). The immunoreactivity of HSS-Ab towards *P. mucrosquamatus* venom was stronger than that towards *T. stejnegeri* venom, whereas NSS-Ab preferentially reacted with venom proteins from *N. atra* compared with those from *B. multicinctus*. Consistent with the ELISA data, Western blot analyses also showed the high specificity of HSS-Ab and NSS-Ab towards their homologous venoms (Fig

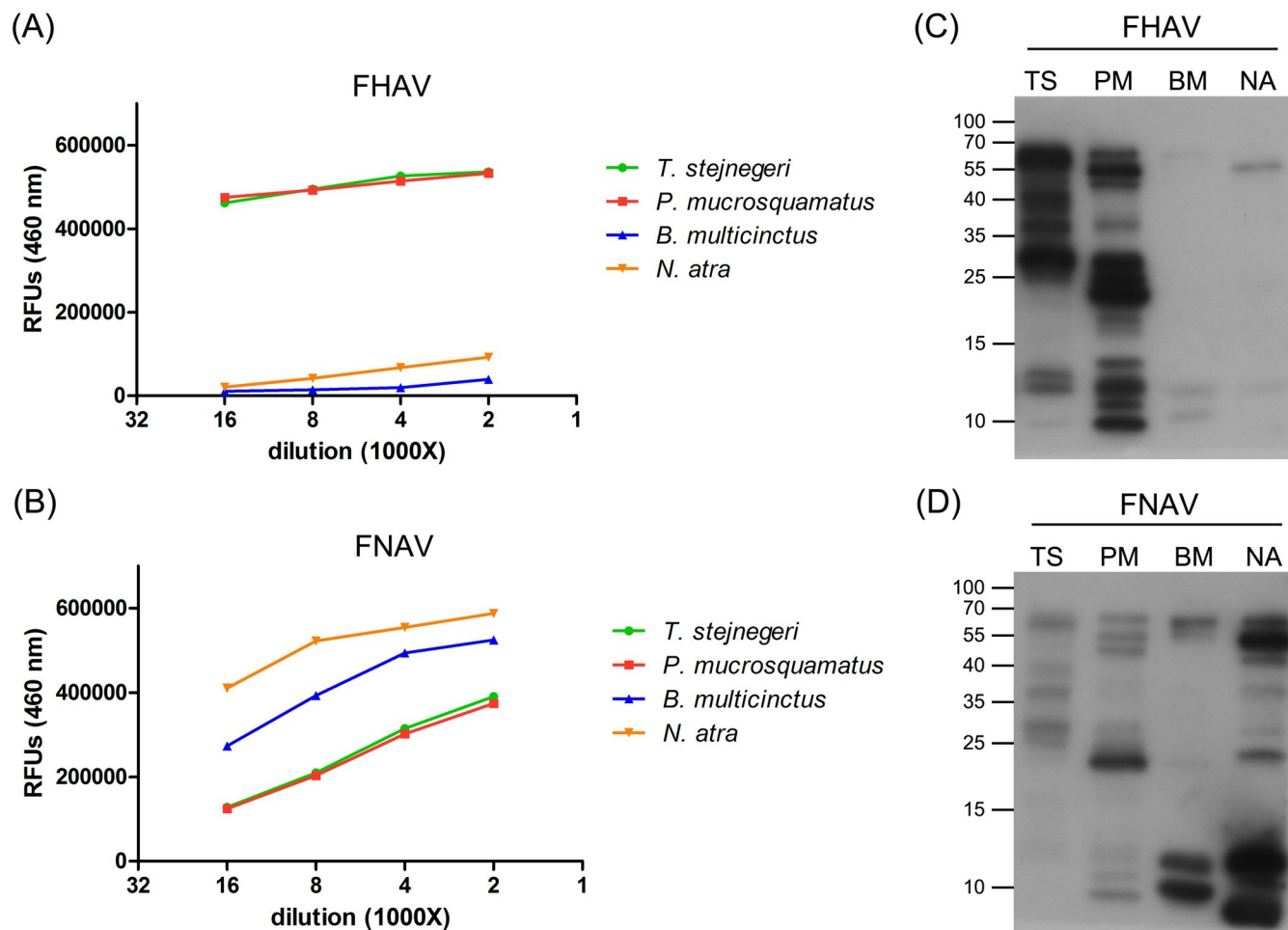


**Fig 1. The cross-reactivity of FHAV and FNAV.** (A, B) FHAV (A) and FNAV (B) were serially diluted from 1:2000 to 1:16000 and used as primary antibodies to detect four snake venoms. The assay was performed in duplicate, and results are presented as average values in relative fluorescence units (RFUs). (C, D) Venom proteins (5 µg) from *T. stejnegeri* (TA), *P. mucrosquamatus* (PM), *B. multicinctus* (BM), and *N. atra* (NA) were resolved by SDS-PAGE on 15% gels, transferred to PVDF membranes, and probed with FHAV (C) and FNAV (D) (2 µg/ml) as primary antibodies.

<https://doi.org/10.1371/journal.pntd.0007014.g001>

2C & 2D), although NSS-Ab did weakly react with high-molecular-weight proteins (55–70 kDa) in the two hemorrhagic venoms (Fig 2D). Proteins in the high molecular weight region (25–70 kDa) of *T. stejnegeri* and *P. mucrosquamatus* venom represented the dominant targets of HSS-Ab (Fig 2C); in contrast, NSS-Ab mainly recognized lower molecular weight proteins (<15 kDa) in the two neurotoxic venoms (Fig 2D).

### Development of sandwich ELISA assays for detecting four snake venoms

To form sandwich complexes for ELISA measurements, we used HSS-Ab (or NSS-Ab) as the capture antibody and biotinylated HSS-Ab (or NSS-Ab) as the detection antibody. Antibody concentrations, buffers, and incubation times used for these sandwich ELISAs were optimized based on the ELISA development guide provided by the manufacturer (R&D Systems, Inc.). To determine the sensitivity of sandwich ELISA assays for snake venom detection, we serially diluted the four snake venoms in plasma and measured their reactivity by sandwich ELISA, generating standard curves for each venom (Fig 3). The limits of detection (LODs) of

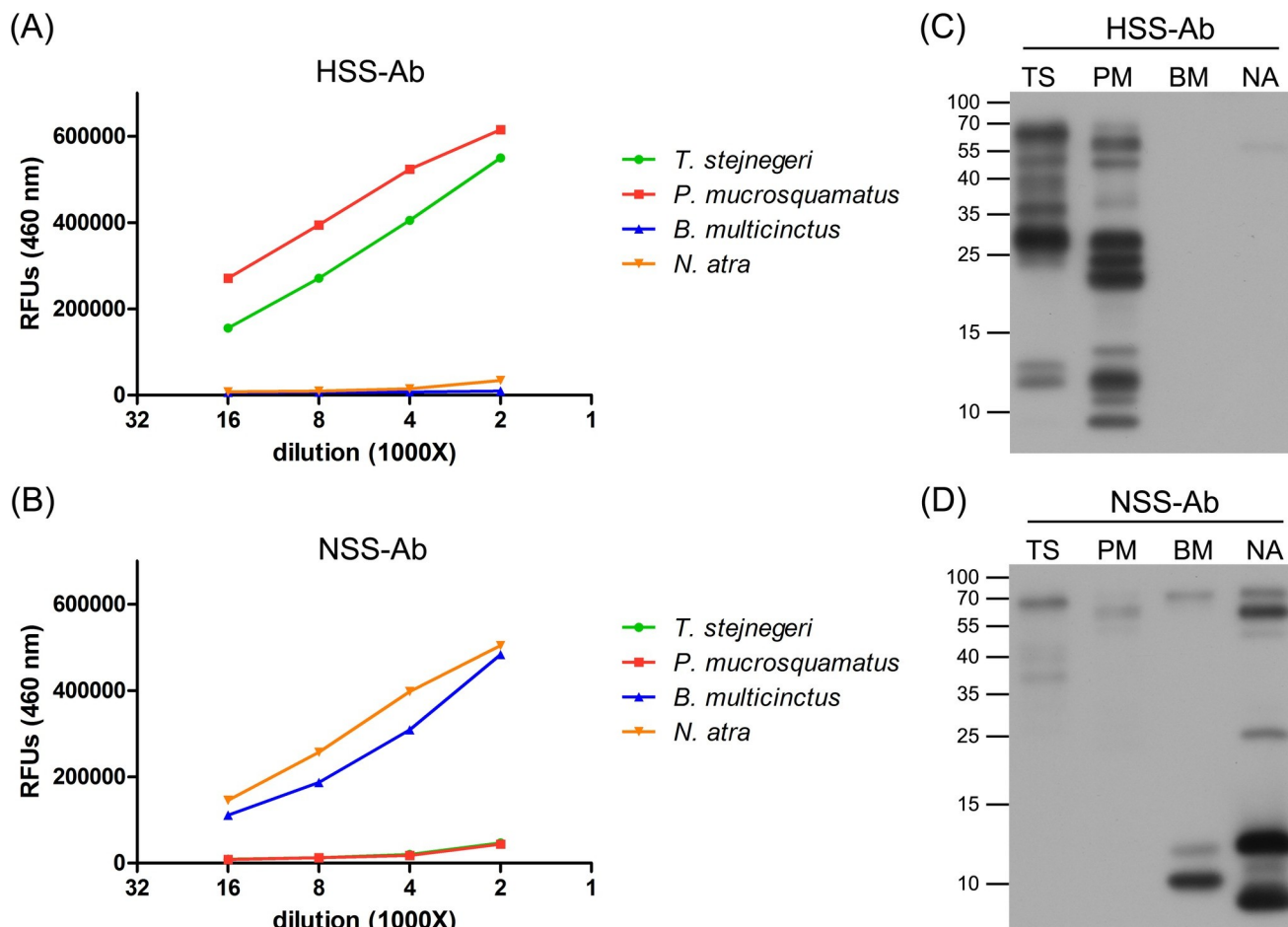


**Fig 2. The specificity of HSS-Ab and NSS-Ab.** (A, B) HSS-Ab (A) and NSS-Ab (B) were serially diluted from 1:2000 to 1:16000 and used as primary antibodies to detect four snake venoms. The assay was performed in duplicate, and results are presented as average values in relative fluorescence units (RFUs). (C, D) Venom proteins (5 $\mu$ g) from *T. stejnegeri* (TA), *P. mucrosquamatus* (PM), *B. multicinctus* (BM), and *N. atra* (NA) were resolved by SDS-PAGE on 15% gels, transferred to PVDF membranes, and probed with HSS-Ab (C) and NSS-Ab (D) (2  $\mu$ g/ml) as primary antibodies.

<https://doi.org/10.1371/journal.pntd.0007014.g002>

sandwich ELISAs for detecting *T. stejnegeri*, *P. mucrosquamatus*, *B. multicinctus* and *N. atra* venom were 0.39, 0.14, 0.56 and 0.23 ng/ml, respectively. In all cases,  $R^2$  values of standard curves were greater than 0.99. Taken together, these results suggest that our sandwich ELISA has the potential to identify snake species and quantify venom proteins in body fluids. For further application of this snakebite sandwich ELISA, the four venoms were used as the gold standards for venom quantification, and the LOD value determined as described above was set as the cutoff for detecting each venom.

To determine whether snake venoms are still detectable after neutralization by antivenoms, we individually neutralized a fixed amount of venom with serially diluted antivenoms and then performed sandwich ELISAs. ELISA signals produced by 10 ng of *T. stejnegeri* (Fig 4A) and *P. mucrosquamatus* (Fig 4B) venom were completely eliminated by 8–40 nl of FHAV. Similarly, 40–200 and 8–40 nl of FNAV totally blocked ELISA signals derived from 10 ng of *B. multicinctus* (Fig 4C) and *N. atra* (Fig 4D) venom, respectively. These observations show that our sandwich ELISA assays only detects “free” venom proteins, and not antivenom-neutralized venoms. Importantly, they also suggest that our assays are suitable for evaluating the amount

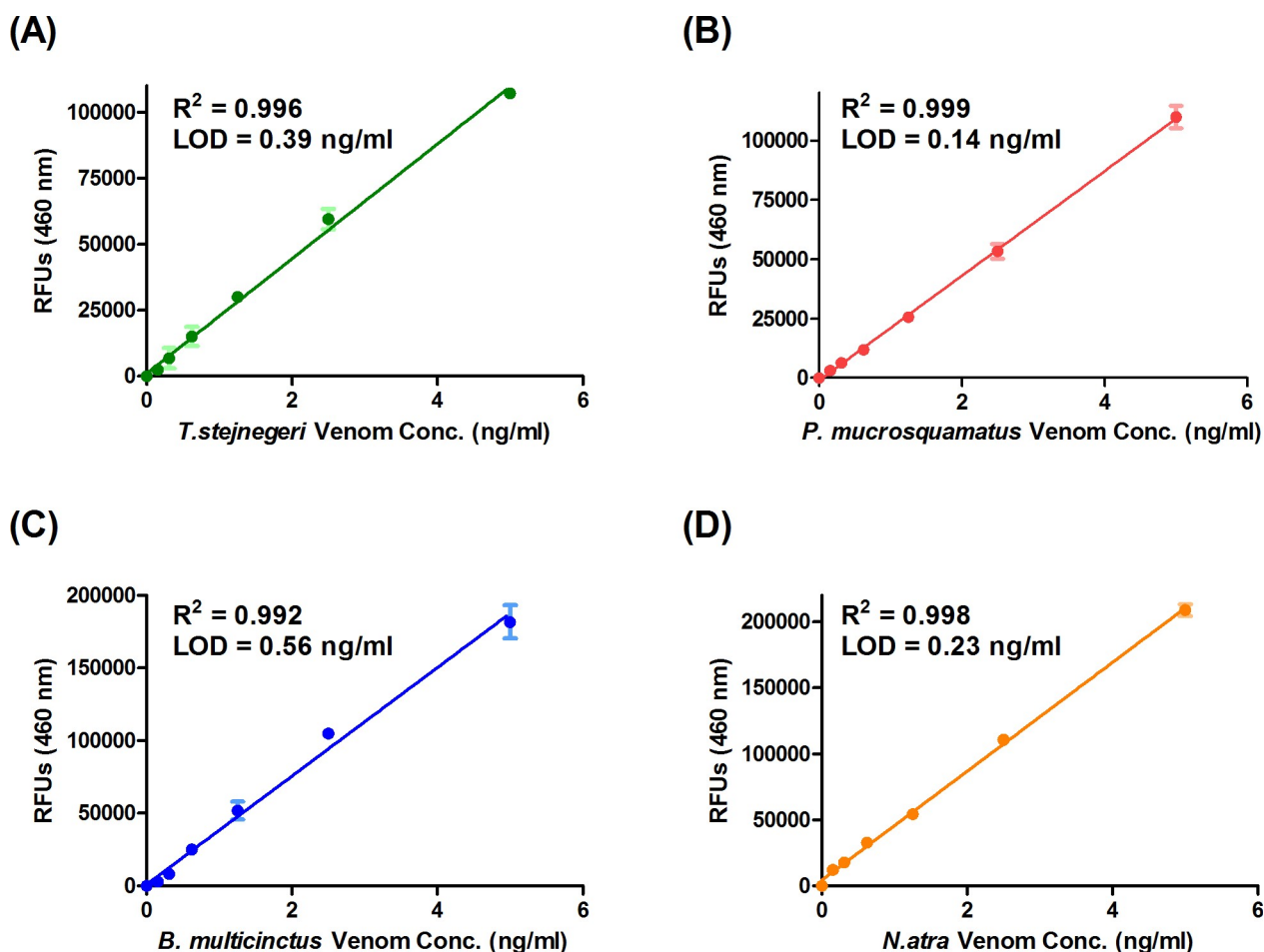


**Fig 3. Calibration curves of sandwich ELISAs for detecting four snake venoms.** Serially diluted venom proteins from (A) *T. stejnegeri*, (B) *P. mucrosquamatus*, (C) *B. multicinctus* and (D) *N. atra* were subjected to HSS-Ab-based (A and B) or NSS-Ab-based (C and D) sandwich ELISAs in triplicate. Shown here are the assay results used to generate the standard curves for measuring venom protein concentrations in snakebite patients.

<https://doi.org/10.1371/journal.pntd.0007014.g003>

of free venom proteins remaining in a snakebite victim, making it possible to determine whether the dosage of antivenom delivered is sufficient to treat the patient.

### Venom detection by sandwich ELISA in an experimental envenomation animal model

The MLD of each venom was determined using an experimental envenomation animal model. The MLD of *T. stejnegeri*, *P. mucrosquamatus*, *B. multicinctus* and *N. atra* were 1.5, 3, 0.3 and 0.65  $\mu$ g/g, respectively. All mice developed local symptoms within 10–20 min after injection of a lethal dose of venom. As soon as 30 min post injection, all four venoms could be detected by sandwich ELISA in plasma samples from mice injected with venom; as expected, none of the saline-injected control mice showed a positive reaction in these assays (Fig 5). The plasma concentrations of *T. stejnegeri* (Fig 5A), *P. mucrosquamatus* (Fig 5B) and *N. atra* (Fig 5D) venom proteins in these mice gradually increased during a 2-h period post injection. In contrast, the plasma concentrations of venom proteins in mice injected with *B. multicinctus* venom decreased dramatically during this period (Fig 5C). Collectively, these results demonstrate that the newly developed sandwich ELISA can successfully identify and quantify these four Taiwanese snake venoms *in vivo*.



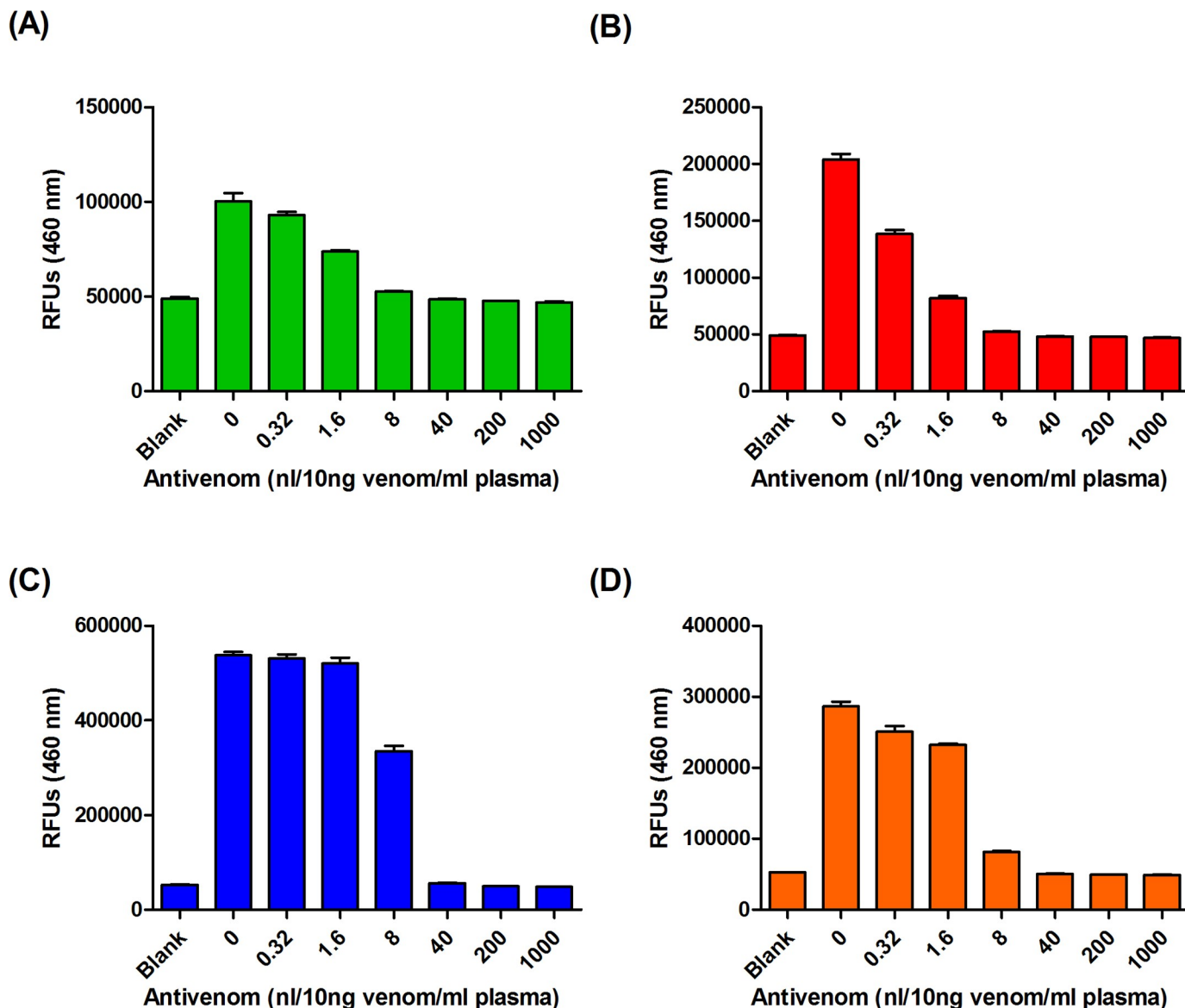


**Fig 4. Pre-incubation of venom-containing human plasma with FHAV or FNAV diminishes HSS-Ab- and NSS-Ab-reactive ELISA signals.** (A, B) Venom proteins of (A) *T. stejnegeri* and (B) *P. mucrosquamatus* were diluted in human plasma (10 ng venom protein per ml of plasma) and then mixed with serially diluted FHAV (0.32 to 1000 nL) at room temperature for 30 min. The mixtures were then subjected to HSS-Ab-based sandwich ELISA assay. (C, D) Venom proteins of (C) *B. multicinctus* and (D) *N. atra* were diluted in human plasma (10 ng venom protein per ml of plasma) and then mixed with serially diluted FHAV (0.32 to 1000 nL) at room temperature for 30 min. The mixtures were then subjected to NSS-Ab-based sandwich ELISA assay.

<https://doi.org/10.1371/journal.pntd.0007014.g004>

### Assay performance of lateral flow strips

Although the newly developed sandwich ELISA assay exhibited high specificity and sensitivity, the assay time in its current format is too long for use in clinical practice. To reduce the operation time and simplify the platform for snakebite diagnosis, we sought to develop another assay using a lateral flow strip format with two test lines (Fig 6A). To assess the specificity and sensitivity of this lateral flow strip, we tested it on the four venoms serially diluted (from 500 ng/ml to 5 ng/ml) in human plasma. The assay was evaluated based on the appearance of a control line, a hemorrhagic test line (H line), or a neurotoxic test line (N line) (Fig 6B). All

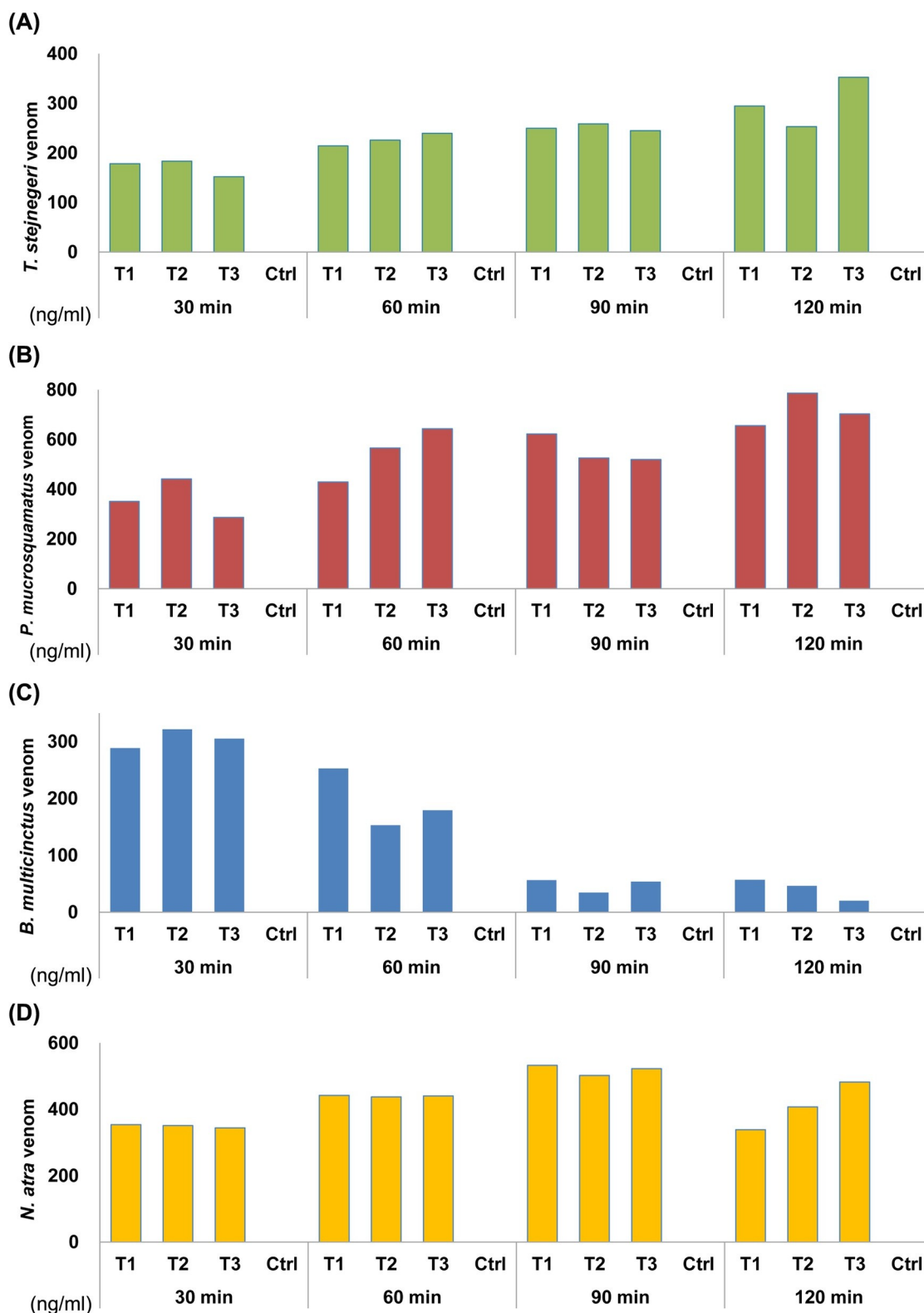


**Fig 5. Detection of snake venom proteins in plasma samples from an animal model of snakebite.** Each mouse was injected with the MLD of venom proteins from (A) *T. stejnegeri*, (B) *P. mucrosquamatus*, (C) *B. multicinctus* or (D) *N. atra*, and plasma samples were collected from venous blood at four time-points (30 min, 1 h, 1.5 h and 2 h) post injection. Venom concentrations were determined by analyzing the collected plasma samples using HSS-Ab-based (A and B) or NSS-Ab-based (C and D) sandwich ELISAs.

<https://doi.org/10.1371/journal.pntd.0007014.g005>

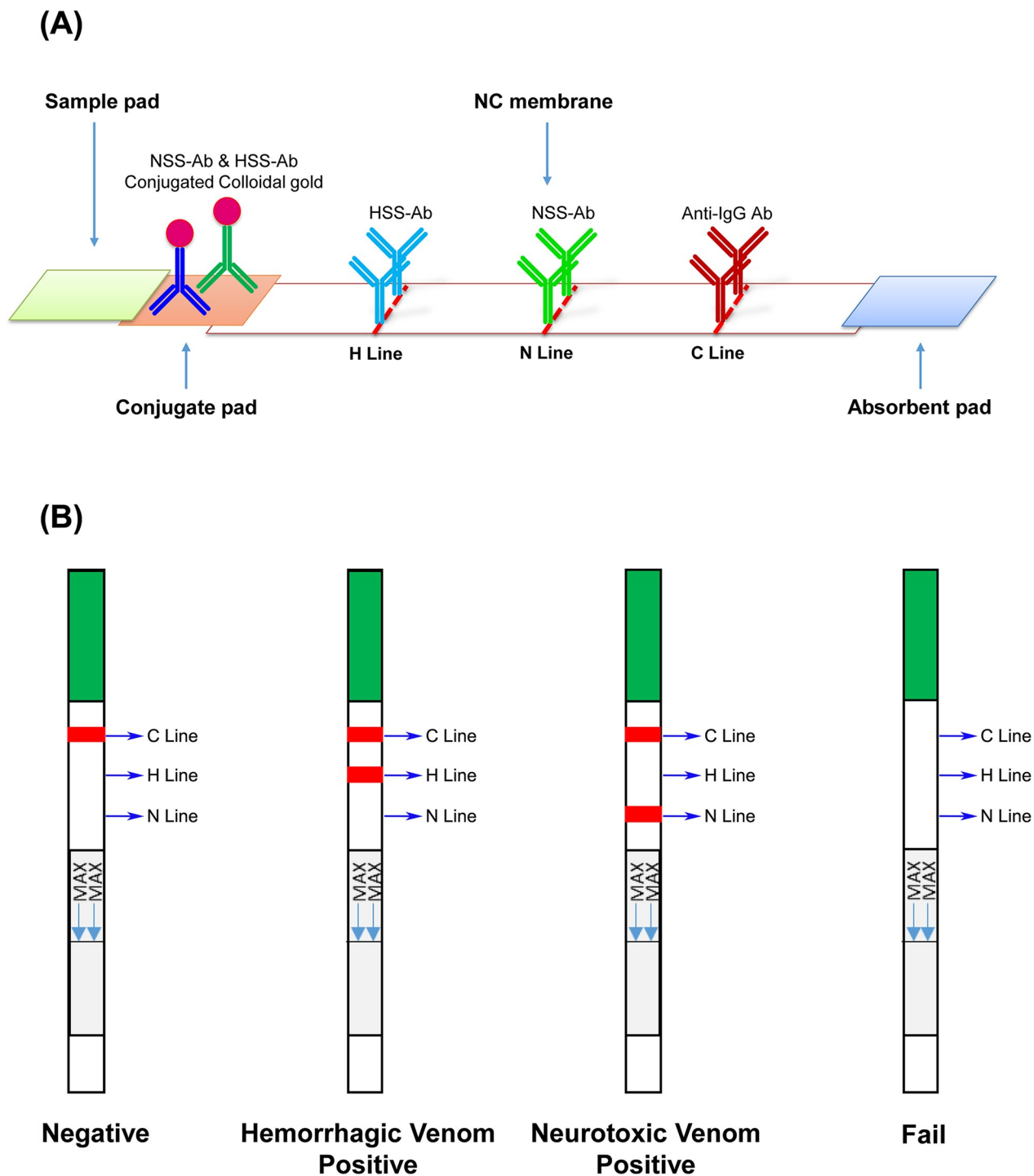


**Fig 6. Schematic diagram of the lateral flow strips for detecting snake venom proteins.** (A) The design of the lateral flow strip constructed on the basis of HSS-Ab and NSS-Ab and (B) a schematic depiction of predicted results are shown. C line, control line; H line, hemorrhagic test line; N line, neurotoxic test line.

<https://doi.org/10.1371/journal.pntd.0007014.g006>

strips showed a visible control line, confirming that all test samples were successfully flowed onto the strips (Fig 7). An H line was only observed in those strips used to test *T. stejnegeri* and *P. mucrosquamatus* venom (Fig 7A & 7B), and the N line appeared only in assays of *N.*

*atra* and *B. multicinctus* venom proteins (Fig 7C & 7D). These results indicate that this newly developed strip assay does not exhibit sufficient cross-reactivity to cause ambiguous results. In assays of hemorrhagic venom, the H line was still detectable after reducing the concentration of *T. stejnegeri* and *P. mucrosquamatus* venom proteins to 50 ng/ml (Fig 7A & 7B). For neurotoxic venom detection, the N line was still visible when both venom protein levels were reduced to 5 ng/ml (Fig 7C & 7D).

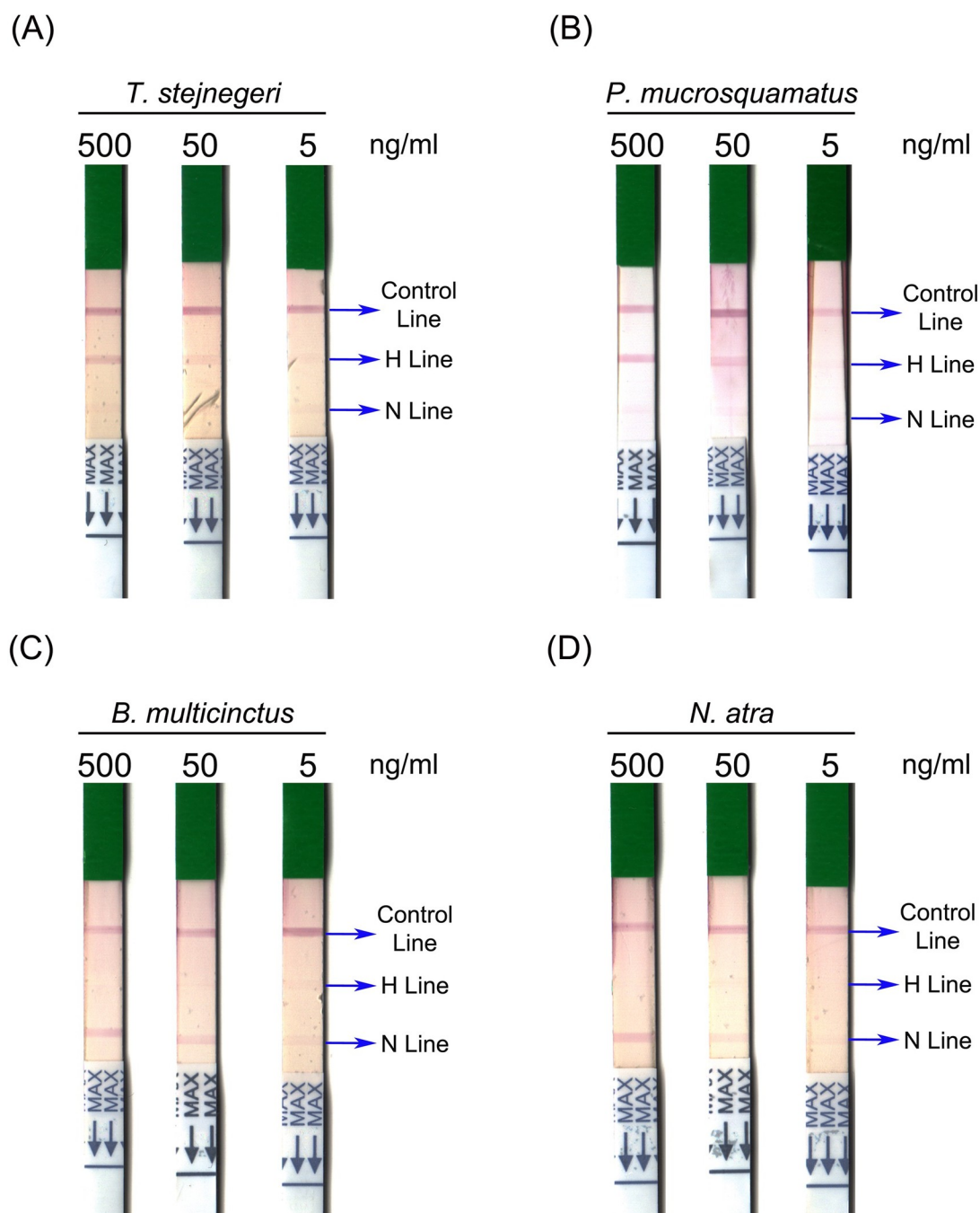


**Fig 7. Performance of lateral flow strip assays in the detection of four snake venoms.** Venom proteins of (A) *T. stejnegeri*, (B) *P. mucrosquamatus*, (C) *B. multicinctus* and (D) *N. atra* were serially diluted to 500, 50 and 5 ng/ml in human plasma, and then subjected to the lateral flow strip assay.

<https://doi.org/10.1371/journal.pntd.0007014.g007>



Table 1. Correlation between sandwich ELISAs and lateral flow strips for snakebite diagnosis.

Lateral flow strip	ELISA				Total
	FH (+)	FN (+)	Negative	Kappa	
FH (+)	4	0	0	0.53	4
FN (+)	0	5	0		5
Negative	7	0	5		12
Total	11	5	5		21

<https://doi.org/10.1371/journal.pntd.0007014.t001>

## Venom detection in clinical samples by sandwich ELISA and lateral flow strip assays

Thirty-two victims of snakebite sent to Emergency Departments of the four participating hospitals from May 2017 to February 2018 were enrolled in this study. Among them, eleven patients were excluded because they had been treated with the appropriate antivenom before arrival in the Emergency Department ( $n = 9$ ) or displayed no symptoms ( $n = 2$ ). The serum samples obtained from the remaining 21 cases were analyzed by sandwich ELISA and lateral flow strip assay (Table 1). The lateral flow strip assay showed 100% (5/5) specificity and 100% sensitivity (5/5) for the detection of neurotoxic envenomation samples. However, the sensitivity for detecting hemorrhagic envenomation samples was only 36.4% (4/11). We used the kappa statistic to assess the strength of agreement between the two assays, and this analysis indicated good to fair agreement ( $\kappa = 0.53$ ) between snakebite sandwich-ELISA and lateral flow strip assay (Table 1).

The clinical information of these 21 patients were summarized in Table 2. Most of the culprit snakes were initially identified by patients' description or recognition of snake photograph (17/21), and 2 of them were definitely confirmed according to the killed snakes brought to the hospital. The aggressor snakes of case 18–21 cannot be identified at scenes of ED. In the laboratory identification, both ELISA and lateral flow strip assay were shown hemorrhagic venom positive results for case 18 and 19, and venom negative result for case 20 and 21. All patients were presented with local swelling except case 11 who was initially identified as *B. multicinctus* envenomation, and no neurologic symptoms appeared in all. Case 16, 18 and 19, who were performed surgery, have higher level of venom concentration than other victims. Seven cases with hemorrhagic venom-positive ELISA results appeared with negative lateral flow strip results. The venom concentration of them was ranged from 2.2 to 10.6 ng/ml, which are lower than other cases detected by lateral flow strip assay. Among them, five cases were shown mild clinical severity, and 2 cases shown moderate severity. Case 11, 15, 17, 20 and 21 have ELISA undetectable venom level. All of them have mild clinical severity that the local swelling restricted in fang mark area, or even did not have local swelling. The sample time after bite for the majority of the victims (15/21) was  $\leq 3.5$  h. Overall, there was no significant correlation between the blood venom concentration and sampling time after snakebite or the bitten area according to this small-scale clinical study.

## Discussion

The presence of common antigens in heterologous venoms has been demonstrated to be a major source of bias for the development of snakebite detection assays [26, 42]. The appearance of widespread cross-reactivity between heterologous snake venoms and polyvalent or monovalent antivenoms considerably hampers the specificity of such assays [11, 12, 28, 43]. Consistent with these previous observations, the current study also found that FHAV and FNAV cross-reacted towards heterologous venoms, as evidenced by the detection of 3–5

Table 2. The clinical information of 21 snakebite cases enrolled in this study.

Initial identification <sup>a</sup>	Case No.	Sex	Sampling time after bite (h)	Bitten area	Local swelling	Surgery	Clinical severity <sup>b</sup>	Antivenom dosage	ELISA	Lateral flow strip	
									Venom Conc. (ng/ml)	FH	FN
<i>T. stejnegeri</i>	1	M	1	Foot	Foot	-	Mild	1 FHAV	3.2 (TS)	-	-
	2	M	1.5	Hand	Forearm	-	Moderate	1 FHAV	2.2 (TS)	-	-
	3	F	0.5	Finger	Finger	-	Mild	2 FHAV	10.6 (TS)	-	-
	4	M	1	Finger	Forearm	-	Moderate	5 FHAV	19.7 (TS)	+	-
<i>P. mucrosquamatus</i>	5	F	6	Wrist	Elbow	-	Moderate	1 FHAV	3.9 (PM)	-	-
	6	M	1	Toe	Calf	-	Moderate	2 FHAV	141 (PM)	+	-
	7	F	0.5	Ankle	Ankle	-	Mild	2 FHAV	9.1 (PM)	-	-
	8	F	1.5	Finger	Hand	-	Mild	1 FNAV	14.3 (NA)	-	+
	9*	M	1	Ankle	Ankle	-	Mild	1 FHAV	2.6 (PM)	-	-
	10	F	0.5	Foot	Ankle	-	Mild	1 FHAV	6 (PM)	-	-
<i>B. multicinctus</i>	11	M	14	Finger	-	-	Mild	1 FNAV	ND <sup>c</sup>	-	-
<i>N. atra</i>	12	M	3.5	Foot	Ankle	-	Mild	-	21.2 (NA)	-	+
	13*	M	1	Foot	Foot	-	Mild	2 FNAV	93.6 (NA)	-	+
	14	M	1	Finger	Wrist	-	Moderate	5FNAV	147.3 (NA)	-	+
	15	M	10.5	Toe	Toe	-	Mild	-	ND	-	-
	16	M	1.5	Toe	Ankle	Debridement	Severe	4 FNAV	297.8 (NA)	-	+
	17	M	1.5	Finger	Finger	-	Mild	4 FNAV	ND	-	-
Unidentified	18	M	12.5	Finger	Shoulder	Debridement/ Fasciotomy	Severe	4 FHAV	210.6 (TS)/77.6 (PM)	+	-
	19	M	Unknown	Forearm	Upper arm	Debridement/ Fasciotomy	Severe	4 FHAV	90.3 (TS)/59.4 (PM)	+	-
	20	M	2.5	Ankle	Ankle	-	Mild	1 FHAV	ND	-	-
	21	M	34	Thumb	Forearm	-	Mild	2 FHAV	ND	-	-

<sup>a</sup> Initial identification: it is shown the envenoming snake species which was initially identified by patients' description or recognition of snake photograph.

<sup>b</sup> Clinical severity: the definition of each level of severity is shown in Supplemental Table 1.

<sup>c</sup> Non-detected: The level of venom concentration is lower than the LOD of ELISA, or even no venom is existed in the clinical sample.

\*: The envenoming species was confirmed from the culprit snake brought to the ER.

<https://doi.org/10.1371/journal.pntd.0007014.t002>

protein bands in Western blot analyses (Fig 2A & 2B). However, snake venoms are known to comprise multiple (10–100) proteins, many of which have the same or similar epitope(s), but with different molecular weights. At present, it is difficult to predict the venom components that contribute to this cross-reactivity. Immunoaffinity purification appears capable of removing antibodies in antiserum that recognize common epitopes of venom components. Even though the identity of the species-specific antigens and common epitopes that contribute to the cross-reactivity remain largely unknown, we were still able to successfully obtain venom protein antibodies with high specificity (i.e., low cross-reactivity among different snake species). In addition, detection of snake envenomation by monoclonal antibodies generated using a single species-specific venom protein can considerably improve assay specificity [44–47]. However, the sensitivity of these antibodies may not be high enough, because venoms contain numerous protein components and a mAb can only react with a single epitope on its target protein. Moreover, the targeted venom component may become degraded through metabolic processes in biological systems. Thus, the application of monoclonal antibodies to the development of snakebite kits remains a considerable challenge. The promising data shown in the

present study suggest that purification of SSABs from antivenoms could be a feasible and cost-effective strategy for generating effective probes for snake venom detection and species discrimination.

Sandwich ELISAs, which have been widely used in snake venom detection and snakebite diagnosis [10, 11, 44, 48], are capable of measuring venom proteins at the level of a few nanograms per milliliter. In conjunction with the biotin-streptavidin amplification system, the detection limit can be further improved, reducing the lower limit to less than 1 ng/ml [10]. Generally, two different antibodies are used for sandwich ELISA assay development. Because we used the same SSAB as both capture and detection antibody in our sandwich ELISA, the capture SSABs in the solid phase only occupied one binding site on their cognate antigen molecules. Thus, the detection SSAB was still capable of recognizing the remaining epitopes on the captured antigens. With this approach, how to pair two suitable antibodies to form the sandwich complex for detection is not a concern, making it easy to adapt for snake venom detection. Although the sandwich ELISA assay is time consuming, and thus is likely not the most appropriate assay for use in emergency rooms, it is still a good tool for snakebite epidemiology and prognosis studies.

The usefulness of our sandwich ELISA assay was demonstrated by detecting venoms in blood samples from an experimentally envenomed mouse model (Fig 5). These experiments showed that this assay is capable of identifying the envenoming species and quantifying venom concentrations in blood. Application of this ELISA to the snakebite animal model revealed that concentrations of *T. stejnegeri*, *P. mucrosquamatus* and *N. atravenom* proteins gradually increased in mouse plasma during a 2-h period post-injection; in contrast, the concentration of *B. multicinctus* venom proteins dramatically decreased over this same time period (Fig 5). A previous study reported that more than half (nearly 60–80%) of *B. multicinctus* venom components are neurotoxins, including  $\beta$ -bungarotoxin,  $\alpha$ -bungarotoxin and  $\gamma$ -bungarotoxin [49]. These bungarotoxins bind to specific receptor(s) on presynaptic and postsynaptic membranes, leading to paralysis and neurotoxicity [50–52]. Our findings suggest that, when injected into the victim, these bungarotoxins rapidly interact with specific receptors, and thus are immobilized in the neuromuscular junctions; this, in turn, causes a significant decrease in their bioavailability, accounting for the rapid decrease in their concentration in blood plasma.

The lateral flow strip assay is a sandwich-based immunostrip used to rapidly (5–20 min) examine whether target molecules are present in a sample [53]. This type of assay is appropriate for use in snakebite detection and diagnosis, and can offer guidance to physicians in administering antivenom [22, 23]. Furthermore, the visual diagnosis format of this assay is simple, making it desirable for use in developing countries, where snakebites are most prevalent. However, some factors and sampling conditions may profoundly affect strip assay results. For example, a high concentration of serum proteins and high viscosity of the test sample could interfere with the formation of the red line in test and control zones, and samples containing high concentrations of salt, such as urine, often cause false-positive results. Thus, in some situations, sample pretreatment is required. The lateral flow strip assay developed here has two test lines for discriminating hemorrhagic and neurotoxic snake envenomation in Taiwan. This strip assay successfully detected and identified snake venom in serum samples from snakebite patients.

Our small-scale clinical study demonstrated that the lateral flow strip assay is useful for assessing neurotoxic envenomation, exhibiting a sensitivity/specificity of 100%. It is suggested that the newly developed strip assay holds promise for the diagnosis of neurotoxic snakebite. However, the sensitivity of this assay for hemorrhagic envenomation was nearly 40%. ELISA results of these 11 hemorrhagic envenomation samples showed that the *T. stejnegeri* or *P.*

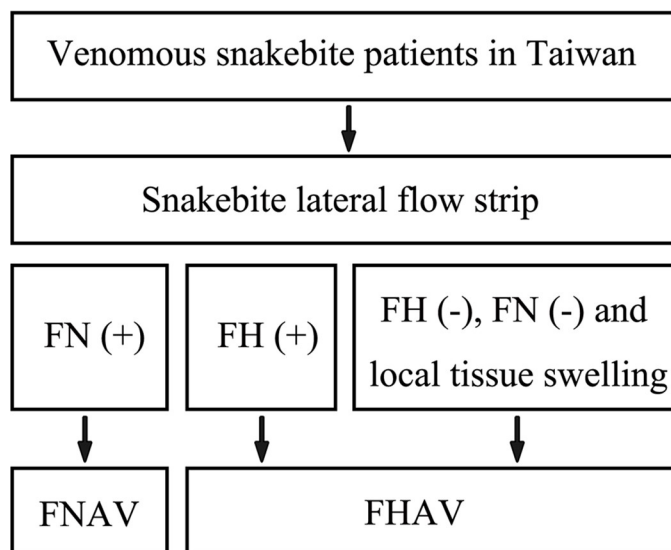


**Fig 8. A proposed diagnosis flowchart for venomous snakebite patients in Taiwan by incorporating the newly developed lateral flow strip assay.**

<https://doi.org/10.1371/journal.pntd.0007014.g008>

*mucrosquamatus* venom protein concentrations in 7 lateral flow strip-negative samples were less than 10 ng/ml (Table 2), suggesting that this assay is not sensitive enough to detect snakebite cases with low blood concentration of hemorrhagic venom in clinical practice. Although, at this point, we cannot definitively establish the appropriateness of our lateral flow strip assay for precise diagnosis of all clinical snakebites, the combination of clinical symptoms and the results of lateral flow strip could improve the clinical utility of our lateral flow strip, especially in the weak aspect of diagnosis of hemorrhagic snake envenomation. A diagnosis flowchart which composed of clinical symptoms and the result of lateral flow strip was therefore proposed (Fig 8). Because of the relative high sensitivity and specificity of our lateral flow strip in diagnosis of neurotoxic snake envenoming, cases with negative lateral flow strip results have a great possibility of hemorrhagic snake envenoming when they have developed local tissue swelling. This diagnosis flowchart may further enhance the ability of our lateral flow strip to guide the usage of antivenom. Because only 21 snakebite cases were included, further study using a larger sample set is needed to verify the sensitivity, specificity, stability, and feasibility of this strip assay.

Seven of the 21 clinical samples examined in this study showed positive ELISA result but negative on the lateral flow strip test. All of them were identified as hemorrhagic snake envenomation with low venom concentration level accompanying with mild or moderate clinical severity. Even though these patients have been transferred to hospital and sampled nearly within 1–2 hrs, their blood venom concentrations were still lower than the others. It is highly possible that the amount of venom injected into these victims was originally low, which is hard to detect by lateral flow strip assay after dilution in the systemic circulation, and only induced mild clinical symptoms. Despite initial identification of envenoming species is almost the same as the test results in our small-scale study (Table 2), sometimes, envenoming species identified by patients or their family may mislead the physicians. Take case 8 as an example, this patient was initially identified as *P. mucrosquamatus* envenomation according to family members' recognition of the snake pictures, however, both ELISA and lateral flow strip assay showed positive result of neurotoxic snake envenomation, indicating the culprit snake is *N. atra*. Furthermore, few cases with negative result of both assays may be bitten by non-



venomous snakes. There are more than 50 snake species in Taiwan. It is hard for citizens to correctly recognize and distinguish all of them. Bringing the envenoming snake to the hospital, like cases 9 and 13, is the most reliable way for species identification.

In the present study, all five cases (case 11, 15, 17, 20 and 21) with negative quantification of venom displayed the mild clinical severity. These patients may be bitten by non-venomous snakes, or the dry bite. As mentioned above, snakebite victims have the chance to misidentify the envenoming species, and slight swelling usually occurred around the fang mark even if they were bitten by non-venomous snakes. It is one of the reasons leading to the negative results in both assays. In addition, although we did not observe a close relationship between the transcurrent time from the bites to the ER consult and the results of the diagnostic test, 3 of the 5 cases with negative ELISA result had longer transcurrent time. Case 11, 15 and 21 had their transcurrent time for 14, 10.5 and 34 hrs, respectively. The metabolism time more than 10 hours may allow the venom to be eliminated from patients' body and resulted in negative test result. The delay in seeking medical help may be another reason leading to the negative test results. On the other hand, case 18 had 12.5 hours of transcurrent time, but displayed severe clinical symptoms and positive test results. It is reasonable to assume that the type and amount of venom injected into patients is the main factor to determine the outcome of the test results, and the effect of transcurrent time could be minor.

The current study used serum samples from snakebite patients to evaluate the performance of the snakebite lateral flow strip assay. Other types of specimen, such as urine, wound exudate and blister fluid, have been reported as alternatives for venom detection [7, 12]. The highest amounts of venom proteins (>100 ng/ml) are found in wound exudates and blister fluid; thus, venom proteins are more easily detected and measured in these types of specimens [12]. However, cases with blister fluid are very rare; in the current study, only one patient formed blister fluids after envenomation. Wound exudates are easier to obtain than blister fluids, but obtaining untreated wound exudates for pre-clinical trials is another challenge. Because people have been taught to perform first aid when bitten by snakes, snake venom remaining in the wound will typically have been washed out or swabbed out. Furthermore, fang marks have usually clotted by the time victims arrive at the Emergency Department. Thus, although wound exudate maybe the best sample type for venom detection, how to collect good quality samples for survey remains a daunting challenge.

Countries in tropical and subtropical regions have various indigenous venomous snake species. Two or more antivenoms are currently available for clinical treatment of snake envenomation. Directly using these antivenoms as a resource for the development of snakebite diagnostic assays could be a cost-effective approach for snakebite management. The use of an affinity purification strategy makes it possible to obtain SSABs from antivenoms, thereby eliminating cross-reactive antibodies and preventing false-positive results in assays of snake venoms. This approach obviates the need to produce additional polyclonal or monoclonal antibodies, and alleviates concerns regarding whether the antigens targeted by the polyclonal or monoclonal antibodies produced are species specific. SSABs purified from antivenoms are suitable for use in developing sandwich ELISAs and lateral flow assays for rapid detection of snake venoms. The ability of these purified SSABs to detect venom in the blood of animal models as well as in blood samples taken from snakebite patients validates the usefulness of this strategy.

In conclusion, our data indicate the feasibility of a cost-effective approach (i.e. preparation of SSABs from specific antivenoms available in Taiwan) to develop the snakebite diagnostic assay for discriminating hemorrhagic and neurotoxic snake envenomation in Taiwan. When combining the clinical observation of patient's symptom, this assay would aid in the clinical decision of the appropriate antivenom to be used where the signs and symptoms of the envenoming did not

allow a precise diagnosis by the clinician responsible to treat the envenomed patient. Although our present results are promising, further studies including improvement of detection sensitivity/specificity of the assays and application of the optimized assays to a larger sample set are needed to validate the clinical utility of the assays for snakebite management.

## Supporting information

**S1 Fig. Protein profiles of the four snake venoms.** Venom proteins (5 µg) from each of the four snakes were resolved by SDS-PAGE on 15% gels and visualized by Coomassie blue staining.  
(TIF)

**S2 Fig. SDS-PAGE analysis of affinity-purified HSS- and NSS-Abs.** Affinity-purified HSS-Abs and NSS-Abs (1 ml for each) were resolved by SDS-PAGE on 15% gels and visualized by Coomassie blue staining.  
(TIF)

**S1 Table. The definition of Clinical severity of Snakebite.**  
(XLSX)

## Acknowledgments

We wish to acknowledge Emergency Department staffs of Taipei Veteran General Hospital, Linkou Chang Gung Memorial Hospital, Chiayi Chang Gung Memorial Hospital and Hualien Tzu Chi Hospital for their excellent assistance with the collection of clinical samples evaluated in this investigation.

## Author Contributions

**Conceptualization:** Chien-Chun Liu, Jau-Song Yu, Yung-Chin Hsiao.

**Data curation:** Chien-Chun Liu.

**Formal analysis:** Chien-Chun Liu, Po-Jung Wang, Yung-Chin Hsiao.

**Funding acquisition:** Jau-Song Yu, Chih-Chuan Lin.

**Investigation:** Chien-Chun Liu, Po-Jung Wang.

**Methodology:** Chien-Chun Liu, Jau-Song Yu, Yung-Chin Hsiao.

**Project administration:** Chien-Chun Liu, Jau-Song Yu.

**Resources:** Chien-Hsin Liu, Yen-Chia Chen, Pei-Fang Lai, Chih-Po Hsu, Wen-Chih Fann.

**Supervision:** Jau-Song Yu, Chih-Chuan Lin.

**Validation:** Jau-Song Yu.

**Visualization:** Jau-Song Yu.

**Writing – original draft:** Chien-Chun Liu, Jau-Song Yu, Chih-Chuan Lin.

**Writing – review & editing:** Chien-Chun Liu, Jau-Song Yu, Chih-Chuan Lin.

## References

1. Harrison RA, Hargreaves A, Wagstaff SC, Faragher B, Laloo DG. Snake envenoming: a disease of poverty. *PLoS neglected tropical diseases*. 2009; 3(12):e569. <https://doi.org/10.1371/journal.pntd.0000569> PMID: 20027216

2. Gutierrez JM, Calvete JJ, Habib AG, Harrison RA, Williams DJ, Warrell DA. Snakebite envenoming. *Nat Rev Dis Primers*. 2017; 3:17079. Epub 2017/10/06. <https://doi.org/10.1038/nrdp.2017.79> PMID: 28980622
3. Kasturiratne A, Wickremasinghe AR, de Silva N, Gunawardena NK, Pathmeswaran A, Premaratna R, et al. The global burden of snakebite: a literature analysis and modelling based on regional estimates of envenoming and deaths. *PLoS medicine*. 2008; 5(11):e218. <https://doi.org/10.1371/journal.pmed.0050218> PMID: 18986210
4. Alirol E, Sharma SK, Bawaskar HS, Kuch U, Chappuis F. Snake bite in South Asia: a review. *PLoS neglected tropical diseases*. 2010; 4(1):e603. <https://doi.org/10.1371/journal.pntd.0000603> PMID: 20126271
5. Harris JB, Faiz MA, Rahman MR, Jalil MM, Ahsan MF, Theakston RD, et al. Snake bite in Chittagong Division, Bangladesh: a study of bitten patients who developed no signs of systemic envenoming. *Trans R Soc Trop Med Hyg*. 2010; 104(5):320–7. <https://doi.org/10.1016/j.trstmh.2009.12.006> PMID: 20096910
6. Isbister GK, Shahmy S, Mohamed F, Abeysinghe C, Karunathilake H, Ariaratnam A. A randomised controlled trial of two infusion rates to decrease reactions to antivenom. *PloS one*. 2012; 7(6):e38739. <https://doi.org/10.1371/journal.pone.0038739> PMID: 22719932
7. Hung DZ, Liao MY, Lin-Shiau SY. The clinical significance of venom detection in patients of cobra snakebite. *Toxicon: official journal of the International Society on Toxinology*. 2003; 41(4):409–15.
8. Stone SF, Isbister GK, Shahmy S, Mohamed F, Abeysinghe C, Karunathilake H, et al. Immune response to snake envenoming and treatment with antivenom; complement activation, cytokine production and mast cell degranulation. *PLoS neglected tropical diseases*. 2013; 7(7):e2326. <https://doi.org/10.1371/journal.pntd.0002326> PMID: 23936562
9. Amuy E, Alape-Giron A, Lomonte B, Thelestam M, Gutierrez JM. Development of immunoassays for determination of circulating venom antigens during envenomations by coral snakes (*Micrurus* species). *Toxicon: official journal of the International Society on Toxinology*. 1997; 35(11):1605–16.
10. Kulawickrama S, O'Leary MA, Hodgson WC, Brown SG, Jacoby T, Davern K, et al. Development of a sensitive enzyme immunoassay for measuring taipan venom in serum. *Toxicon: official journal of the International Society on Toxinology*. 2010; 55(8):1510–8.
11. Van Dong L, Quyen le K, Eng KH, Gopalakrishnakone P. Immunogenicity of venoms from four common snakes in the South of Vietnam and development of ELISA kit for venom detection. *Journal of immunological methods*. 2003; 282(1–2):13–31. PMID: 14604537
12. Dong le V, Eng KH, Quyen le K, Gopalakrishnakone P. Optical immunoassay for snake venom detection. *Biosensors & bioelectronics*. 2004; 19(10):1285–94.
13. Selvanayagam ZE, Gopalakrishnakone P. Tests for detection of snake venoms, toxins and venom antibodies: review on recent trends (1987–1997). *Toxicon: official journal of the International Society on Toxinology*. 1999; 37(4):565–86.
14. Pukrittayakamee S, Ratcliffe PJ, McMichael AJ, Warrell DA, Bunnag D. A competitive radioimmunoassay using a monoclonal antibody to detect the factor X activator of Russell's viper venom. *Toxicon: official journal of the International Society on Toxinology*. 1987; 25(7):721–9.
15. Chinonavanig L, Karnchanachetane C, Pongsettakul P, Ratanabanangkoon K. Diagnosis of snake venoms by a reverse latex agglutination test. *Journal of toxicology Clinical toxicology*. 1991; 29(4):493–503. PMID: 1749056
16. Sjostrom L, Karlson-Stiber C, Persson H, Al-Abdulla IH, Smith DC. Development and clinical application of immunoassays for European adder (*Vipera berus berus*) venom and antivenom. *Toxicon: official journal of the International Society on Toxinology*. 1996; 34(1):91–8.
17. Bucher B, Canonge D, Thomas L, Tyburn B, Robbe-Vincent A, Choumet V, et al. Clinical indicators of envenoming and serum levels of venom antigens in patients bitten by *Bothrops lanceolatus* in Martinique. Research Group on Snake Bites in Martinique. *Trans R Soc Trop Med Hyg*. 1997; 91(2):186–90. PMID: 9196765
18. Gilliam LL, Ownby CL, McFarlane D, Canida A, Holbrook TC, Payton ME, et al. Development of a double sandwich fluorescent ELISA to detect rattlesnake venom in biological samples from horses with a clinical diagnosis of rattlesnake bite. *Toxicon: official journal of the International Society on Toxinology*. 2013; 73:63–8.
19. Lomonte B, Kahan L. Production and partial characterization of monoclonal antibodies to *Bothrops asper* (terciopelo) myotoxin. *Toxicon: official journal of the International Society on Toxinology*. 1988; 26(7):675–89.
20. Bogdanovskaya VA, Tarasevich MR. Electrochemical biosensors for medicine and ecology. *Biosensors & bioelectronics*. 1996; 11(9):853–61.

21. Selvanayagam ZE, Neuzil P, Gopalakrishnakone P, Sridhar U, Singh M, Ho LC. An ISFET-based immunosensor for the detection of beta-Bungarotoxin. *Biosensors & bioelectronics*. 2002; 17(9):821–6.
22. Hung DZ, Lin JH, Mo JF, Huang CF, Liao MY. Rapid diagnosis of *Naja atra* snakebites. *Clin Toxicol (Phila)*. 2014; 52(3):187–91. Epub 2014/03/04.
23. Pawade BS, Salvi NC, Shaikh IK, Waghmare AB, Jadhav ND, Wagh VB, et al. Rapid and selective detection of experimental snake envenomation—Use of gold nanoparticle based lateral flow assay. *Toxicon: official journal of the International Society on Toxinology*. 2016; 119:299–306. Epub 2016/07/06.
24. Wong RC, Tse HY. *Lateral flow immunoassay*. New York, NY: Springer; 2009. xii, 223 p. p.
25. Wild D. *The immunoassay handbook: theory and applications of ligand binding, ELISA, and related techniques*. 4th ed. Oxford; Waltham, MA: Elsevier; 2013. xxi, 1013 p. p.
26. Steuten J, Winkel K, Carroll T, Williamson NA, Ignjatovic V, Fung K, et al. The molecular basis of cross-reactivity in the Australian Snake Venom Detection Kit (SVDK). *Toxicon: official journal of the International Society on Toxinology*. 2007; 50(8):1041–52.
27. Ho M, Warrell MJ, Warrell DA, Bidwell D, Voller A. A critical reappraisal of the use of enzyme-linked immunosorbent assays in the study of snake bite. *Toxicon: official journal of the International Society on Toxinology*. 1986; 24(3):211–21.
28. Gao JF, Wang J, Qu YF, Ma XM, Ji X. Immunoreactivity between venoms and commercial antisera in four Chinese snakes and venom identification by species-specific antibody. *Journal of immunological methods*. 2013; 387(1–2):211–8. Epub 2012/11/13. <https://doi.org/10.1016/j.jim.2012.10.016> PMID: 23142457
29. Hung DZ. Taiwan's venomous snakebite: epidemiological, evolution and geographic differences. *Trans R Soc Trop Med Hyg*. 2004; 98(2):96–101. Epub 2004/02/18. PMID: 14964809
30. Liao MY, Huang RJ. Toxoids and antivenoms of venomous snakes in Taiwan. *J Toxicol-Toxin Rev*. 1997; 16(3):163–75.
31. Chun-Kuei Chen C-CL, Fuh-Yuan Shih, Chung-Hsien Chaou, Jasper Chia-Cheng Lin, Ting-I Lai, Chiung-Yao Tseng, Cheng-Chung Fang. Population-based study of venomous snakebite in Taiwan. *Journal of Acute Medicine*. 2015; 5(2):38–42.
32. Liu CH JD, Lian WC, Liu DP. Epidemiological analysis of antivenin usage in Taiwan Area, 2002–2005. *Epidemiol Bull*. 2009; 25:510–25.
33. Chen JC LS, Bullard MJ, Chiu TF. Treatment of poisonous snakebites in northern Taiwan. *J Formos Med Assoc*. 2000; 99:135–9. PMID: 10770028
34. Liao WB L, Tsai YS, Liu BM, Chung KJ. Influential factors affecting prognosis of snakebite patients management: Kaohsiung Chang Gung Memorial Hospital experience. *Chang Gung Med J*. 2000; 23:577–83. PMID: 11126148
35. Liang WJ TY, Wang HJ. Treatment of snakebite in Taiwan-analysis of 100 cases. *J Med Sci*. 1992; 13:51–6.
36. Lin CC, Chaou CH, Tseng CY. An investigation of snakebite antivenom usage in Taiwan. *J Formos Med Assoc*. 2016; 115(8):672–7. <https://doi.org/10.1016/j.jfma.2015.07.006> PMID: 26250942
37. Sim J, Wright CC. The kappa statistic in reliability studies: use, interpretation, and sample size requirements. *Phys Ther*. 2005; 85(3):257–68. Epub 2005/03/01. PMID: 15733050
38. Viera AJ, Garrett JM. Understanding interobserver agreement: the kappa statistic. *Fam Med*. 2005; 37(5):360–3. Epub 2005/05/11. PMID: 15883903
39. Pottumarthy S, Morris AJ, Harrison AC, Wells VC. Evaluation of the tuberculin gamma interferon assay: potential to replace the Mantoux skin test. *J Clin Microbiol*. 1999; 37(10):3229–32. Epub 1999/09/17. PMID: 10488182
40. Chen K, Zhao K, Song D, He W, Gao W, Zhao C, et al. Development and evaluation of an immunochromatographic strip for rapid detection of porcine hemagglutinating encephalomyelitis virus. *Virology*. 2012; 9:172. Epub 2012/08/28. <https://doi.org/10.1186/1743-422X-9-172> PMID: 22920192
41. Howard-Jones N. A CIOMS ethical code for animal experimentation. *WHO Chron*. 1985; 39(2):51–6. PMID: 4090462
42. Theakston RD, Laing GD. Diagnosis of snakebite and the importance of immunological tests in venom research. *Toxins (Basel)*. 2014; 6(5):1667–95. Epub 2014/05/27.
43. Prieto da Silva AR, Yamagushi IK, Morais JF, Higashi HG, Raw I, Ho PL, et al. Cross reactivity of different specific *Micrurus* antivenom sera with homologous and heterologous snake venoms. *Toxicon: official journal of the International Society on Toxinology*. 2001; 39(7):949–53. Epub 2001/02/27.
44. Theakston RD. The application of immunoassay techniques, including enzyme-linked immunosorbent assay (ELISA), to snake venom research. *Toxicon: official journal of the International Society on Toxinology*. 1983; 21(3):341–52. Epub 1983/01/01.



45. Lee CH, Lee YC, Liang MH, Leu SJ, Lin LT, Chiang JR, et al. Antibodies against Venom of the Snake *Deinagkistrodon acutus*. *Appl Environ Microbiol*. 2016; 82(1):71–80. Epub 2015/10/18. <https://doi.org/10.1128/AEM.02608-15> PMID: 26475102
46. Lee CH, Lee YC, Leu SJ, Lin LT, Chiang JR, Hsu WJ, et al. Production and Characterization of Neutralizing Antibodies against *Bungarus multicinctus* Snake Venom. *Appl Environ Microbiol*. 2016. Epub 2016/09/25.
47. Lee CH, Lee YC, Lee YL, Leu SJ, Lin LT, Chen CC, et al. Single Chain Antibody Fragment against Venom from the Snake *Daboia russelii formosensis*. *Toxins (Basel)*. 2017; 9(11). Epub 2017/10/28.
48. Huang YP, Yu YJ, Hung DZ. Sandwich enzyme-linked immunosorbent assay for Taiwan cobra venom. *Vet Hum Toxicol*. 2002; 44(4):200–4. Epub 2002/07/26. PMID: 12136964
49. Shan LL, Gao JF, Zhang YX, Shen SS, He Y, Wang J, et al. Proteomic characterization and comparison of venoms from two elapid snakes (*Bungarus multicinctus* and *Naja atra*) from China. *Journal of proteomics*. 2016; 138:83–94. Epub 2016/03/01. <https://doi.org/10.1016/j.jprot.2016.02.028> PMID: 26924299
50. Young HS, Herbette LG, Skita V. Alpha-bungarotoxin binding to acetylcholine receptor membranes studied by low angle X-ray diffraction. *Biophys J*. 2003; 85(2):943–53. Epub 2003/07/30. [https://doi.org/10.1016/S0006-3495\(03\)74533-0](https://doi.org/10.1016/S0006-3495(03)74533-0) PMID: 12885641
51. Wu PF, Chang LS. Expression of A chain and B chain of beta-bungarotoxin from taiwan banded krait: the functional implication of the interchain disulfide bond between A chain and B chain. *J Protein Chem*. 2001; 20(5):413–21. Epub 2001/12/06. PMID: 11732693
52. Wu PF, Wu SN, Chang CC, Chang LS. Cloning and functional expression of B chains of beta-bungarotoxins from *Bungarus multicinctus* (Taiwan banded krait). *Biochem J*. 1998; 334 (Pt 1):87–92. Epub 1998/08/07.
53. Sajid M, Kawde AN, Daud M. Designs, formats and applications of lateral flow assay: A literature review. *J Saudi Chem Soc*. 2015; 19(6):689–705.



## Review article

## Protein-polysaccharide nanohybrids: Hybridization techniques and drug delivery applications



Mohamed Gaber<sup>a,b</sup>, Mostafa T. Mabrouk<sup>a,c,d</sup>, May S. Freag<sup>a,e,f,g</sup>, Sachin K. Khiste<sup>f,g</sup>,  
Jia-You Fang<sup>h,i,j,\*</sup>, Kadria A. Elkhodairy<sup>a,c</sup>, Ahmed O. Elzoghby<sup>a,c,f,g,\*</sup>

<sup>a</sup> Cancer Nanotechnology Research Laboratory (CNRL), Faculty of Pharmacy, Alexandria University, Alexandria 21521, Egypt

<sup>b</sup> Department of Cancer Biology, Wake Forest School of Medicine, Winston-Salem, NC 27157, USA

<sup>c</sup> Department of Industrial Pharmacy, Faculty of Pharmacy, Alexandria University, Alexandria 21521, Egypt

<sup>d</sup> Department of Biomedical Engineering, University at Buffalo, State University of New York, Buffalo, NY 14260, USA

<sup>e</sup> Department of Pharmaceutics, Faculty of Pharmacy, Alexandria University, Alexandria 21521, Egypt

<sup>f</sup> Division of Engineering in Medicine, Department of Medicine, Brigham and Women's Hospital, Harvard Medical School, Boston, MA 02115, USA

<sup>g</sup> Harvard-MIT Division of Health Sciences and Technology, Cambridge, MA 02139, USA

<sup>h</sup> Pharmaceutics Laboratory, Graduate Institute of Natural Products, Chang Gung University, Taoyuan 333, Taiwan

<sup>i</sup> Research Center for Industry of Human Ecology and Research Center for Chinese Herbal Medicine, Chang Gung University of Science and Technology, Kweishan, Taoyuan 333, Taiwan

<sup>j</sup> Department of Anesthesiology, Chang Gung Memorial Hospital, Kweishan, Taoyuan 333, Taiwan

## ARTICLE INFO

## Keywords:

Nanohybrids

Proteins

Polysaccharides

Drug delivery

Electrostatic nanocomplexes

Maillard conjugates

Electrospinning

## ABSTRACT

Complex nanosystems fabricated by hybridization of different types of materials such as lipids, proteins, or polysaccharides are usually superior to simple ones in terms of features and applications. Proteins and polysaccharides hold great potential for development of nanocarriers for drug delivery purposes based on their unique biocompatibility, biodegradability, ease of functionalization, improved biodistribution and minimal toxicity profiles. Protein-polysaccharide nanohybrids have gained a lot of attention in the past few years particularly for drug delivery applications. In this review, different hybridization techniques utilized in the fabrication of such nanohybrids including electrostatic complexation, Maillard conjugation, chemical coupling and electrospinning were thoroughly reviewed. Moreover, various formulation factors affecting the characteristics of the formed nanohybrids were discussed. We also reviewed in depth the outcomes of such hybridization ranging from stability enhancement, to toxicity reduction, improved biocompatibility, and drug release modulation. We also gave an insight on their limitations and what hinders their clinical translation and market introduction.

## 1. Introduction

The advanced progress of research in the fabrication of different

nanosystems for drug delivery applications gives an insight about their added benefit in that area. The scope of benefits includes enhanced drug solubility, modulated drug release, enhanced targeting efficacy

**Abbreviations:** 5-FU, 5-Fluorouracil;  $\alpha$ -La,  $\alpha$ -lactalbumin;  $\beta$ -Lg,  $\beta$ -lactoglobulin; BSA, Bovine serum albumin; CMC, Carboxymethyl cellulose; CMCS, Carboxymethyl chitosan; CPs, Cocoa procyanidins; CS, Chondroitin sulfate; DHA, Docosahexaenoic acid; DOX, Doxorubicin; DTX, Docetaxel; EGCG, Epigallocatechin-3-gallate; EPR, Enhanced permeation and retention; FDA, Food and drugs administration; FSP, Fish sarcoplasmic protein; GEM, Gemcitabine; GFP-ODN, Green fluorescent protein antisense oligodeoxynucleotide; GRAS, Generally recognized as safe; HA, Hyaluronic acid; HAF, 5-hexadecanoylamino fluorescein; HMP, High methoxyl pectin; HYL, Hyaluronidase; i-Carrageenan, iota Carrageenan; ITC, Isothermal titration calorimetry; KC,  $\kappa$ -carrageenan; LDL, low density lipoprotein; Lf, Lactoferrin; LMP, Low methoxyl pectin; MCCh, Microcrystalline chitosan; miR-34a, a potent endogenous tumor suppressor microRNA; MD, Maltodextrin; MRI, Magnetic resonance imaging; MTX, Methotrexate; NPs, Nanoparticles; OPA, ortho-phthalaldehyde; PDI, polydispersity index; PEG, polyethylene glycol; pEGFP, Plasmid for enhanced green fluorescent protein; pI, isoelectric point; pMUC5AC, Plasmid for gel-forming mucin; psiRNA-hH1GFPzeo, vector for generating shRNA targeting GL3 luciferase; Pt(II) complex, Bipyridine ethyl dithiocarbamate Pt(II) nitrate; QDs, Quantum dots; SPARC, Secreted Protein, Acidic and Rich in Cysteine; STP, Sodium tripolyphosphate; TFA, Trifluoroacetic acid; TMX, Tamoxifen; TOC, Tocopherol; TPP, Tea polyphenol; TRAIL, Tumor necrosis factor-related apoptosis-inducing ligand; WPI, Whey protein isolate

\* Corresponding authors at: Division of Engineering in Medicine, Department of Medicine, Brigham and Women's Hospital, Harvard Medical School, Boston, MA 02115, USA (A. Elzoghby). Graduate Institute of Natural Products, Chang Gung University, Taoyuan 333, Taiwan (J.-Y. Fang).

E-mail addresses: [fajy@mail.cgu.edu.tw](mailto:fajy@mail.cgu.edu.tw) (J.-Y. Fang), [aelzoghby@bwh.harvard.edu](mailto:aelzoghby@bwh.harvard.edu), [ahmed\\_elzoghby@alexu.edu.eg](mailto:ahmed_elzoghby@alexu.edu.eg) (A.O. Elzoghby).

<https://doi.org/10.1016/j.ejpb.2018.10.001>

Received 2 July 2018; Received in revised form 28 September 2018; Accepted 1 October 2018

Available online 06 October 2018

0939-6411/ © 2018 Elsevier B.V. All rights reserved.

and better uptake by cells, enhanced drug stability and reduced toxicity, enhanced biocompatibility, among others [1–4]. A variety of materials, including natural and synthetic ones, have been used in the fabrication of these nanosystems [5,6]. Natural biopolymers, in-specific, including proteins and polysaccharides have become an interesting alternative to synthetic ones in the fabrication of different nano-sized drug delivery systems [7–9]. Among these synthetic polymers, polyethylene glycol (PEG) has been widely used, if not being the most one, in products approved by the food and drugs administration (FDA) or products undergoing clinical trials. PEG is well known for its biocompatibility, however, toxicities occurring from its accumulation *in vivo* as well as some immunogenic reactions are still being discussed. In contrast, proteins and polysaccharides are generally safer, especially when their physicochemical properties are finetuned for the biological safety, with many being “generally recognized as safe” (GRAS) by FDA, which makes them a better candidate for the fabrication of different drug-loaded nanocarriers [10–12]. Moreover, proteins and polysaccharides carry intrinsic biological properties which can be exploited for a wide array of applications [13–15]. For example, albumin can be used for targeting certain tissues overexpressing its receptors e.g. tumor and inflamed tissues, reducing recognition by the mononuclear phagocytic system (MPS), among other applications [16–18]. Chitosan and alginate can be exploited for their mucoadhesive properties, thus increasing the residence time of loaded drugs and interaction with intestinal cells, and subsequently increasing drug absorption [19]. Hyaluronan can be exploited for targeting chondrocytes and certain tumors overexpressing its receptors [9,20,21].

Proteins and polysaccharides are major components in biological systems with different roles ranging from structural ones to enzymatic activity, or energy production [22–24]. Many can be even found interacting specifically *in vivo* such as the interaction between lysozyme and glycosaminoglycans in cartilages, or the interaction between heparin and antithrombin in the inhibition of coagulation. These natural interactions inspired the fabrication of protein-polysaccharide nanohybrids which were superior to their individual components showing features not usually attained individually. Different proteins such as albumin, gelatin,  $\alpha$ -lactalbumin ( $\alpha$ -La),  $\beta$ -lactoglobulin ( $\beta$ -Lg), casein, lactoferrin (Lf), and lysozyme; and polysaccharides such as chitosan, carrageenans, pectins, chondroitin sulfate, and alginate were used in the fabrication of those protein-polysaccharide nanohybrids. Thus, the choice of the right partners for fabrication of protein-polysaccharide nanohybrids is important in creating certain sizes, hydrophilicities, surface charges, release patterns, etc. [21,25,26]. These different features have changed the scope of applications of these materials which is discussed in depth in our review. The wide array of applications of such nanocomplexes include enhanced stability of many unstable drugs such

as vitamin D, curcumin, and insulin, improved biocompatibility, and stability of the nanosystem itself, enhanced targeting ability, and modulated drug release. Also discussed are the different hybridization techniques used in the fabrication of these nanohybrids and the different factors affecting their physicochemical properties. Last, but not least, the limitations hindering the clinical translation of these nanohybrids and the future prospects looming in the horizon.

## 2. Hybridization techniques

Protein-polysaccharide nanohybrids for drug delivery applications could be fabricated via many techniques including electrostatic complexation, chemical conjugation and electrospinning.

### 2.1. Electrostatic complexation

As mixing of the macromolecules results in low entropy gain, proteins and polysaccharides are rarely miscible and their thermodynamically stable mixtures exist only under certain conditions such as low concentrations and/or being structurally and chemically very similar. The protein-polysaccharide interactions determine their phase behavior whether being attractive interaction which in general will lead to associative phase separation or repulsive interaction leading to segregative phase separation. Associative phase separation results from oppositely charged protein/polysaccharide condensation in the same phase leaving the solvent phase depleted yielding an insoluble complex. The driving forces for associative phase separation are the electrostatic interactions between protein and polysaccharide and the entropic gain by releasing counterions upon complex formation. In general, associative phase separation is observed between negatively charged polysaccharides carrying groups such as sulphate or carboxylates and positively charged proteins at pHs below their isoelectric points (PIs) [27,28].

In the light of the previous information, the formation of a protein-polysaccharide electrostatic complex will depend mainly on making the protein and polysaccharide bear opposite charges to avoid segregative phase separation thus favouring electrostatic attraction which will lead to a size increment. According to the stability of the formed particles, these particles will either continue to aggregate resulting in associative phase separation and finally precipitate or will remain colloidal in the nanosized range. Tian et al. established a phase diagram and structural transitions of protein/polysaccharide where bovine serum albumin (BSA) represents the protein and sugar beet pectin represents the polysaccharide (Fig. 1). The phase diagram shows five regions where different structures of protein/polysaccharide complexes are formed: (I) individual soluble molecules with no interactions; (II) the

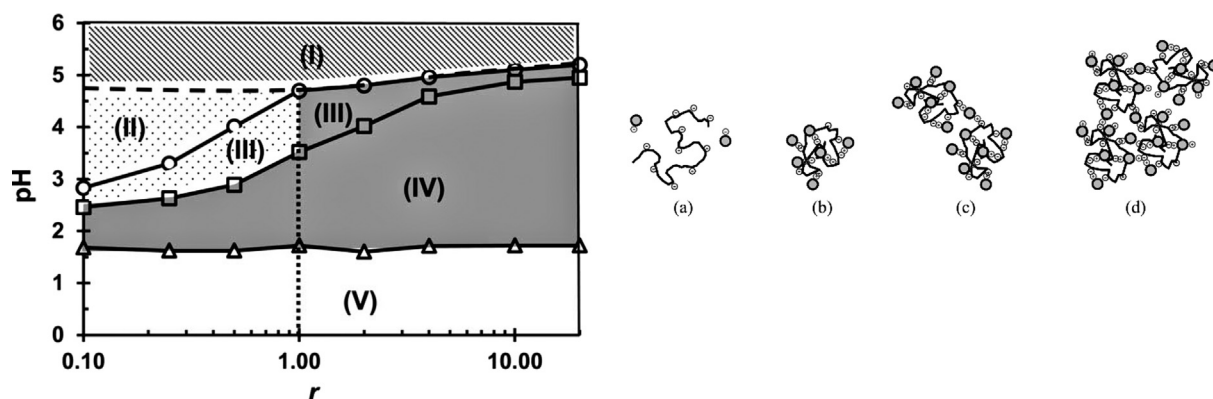


**Fig. 1.** Phase diagram showing 5 regions (I–V) and structural transitions showing 4 different structures of protein/polysaccharide complexes (a–d). (a) shows individual soluble polymers corresponding to regions I and V of phase diagram. (b) is the soluble intramolecular complex corresponding to region II. (c) is the soluble intermolecular complex corresponding to region III. (d) is the insoluble intermolecular complex corresponding to region IV. pH<sub>c</sub> (circle) and pH<sub>o</sub> (square), and pH<sub>d</sub> (triangle) are going to be discussed later on in this review [28].

**Table 1**  
Protein-polysaccharide nanohybrids prepared by electrostatic complexation.

Protein-Polysaccharide	Drug	Key Outcomes	Ref.
Albumin-CMC	DTX	Enhanced antitumor activity was demonstrated via an active targeting mechanism	[36]
Albumin-Chitosan	DOX	Significant cytotoxicity enhancement in HepG2 cells for retinoic acid-targeted nanohybrids in comparison to non-targeted ones	[29]
Albumin-Chitosan, Alginate and Dextran	Insulin	Enhanced stability of insulin, release modulation according to pH, and enhanced intestinal permeability	[37]
BSA-Chitosan	GEM	Higher cytotoxicity in A549 and H460 lung adenocarcinoma cell lines in comparison to sole albumin nanoparticles	[33]
BSA-Chitosan	psiRNA-hH1GFPzeo	Higher biocompatibility in comparison to chitosan alone	[34]
BSA- i-Carrageenan	Curcumin	Enhanced the stability and the antioxidant activity of curcumin	[38]
BSA- i-Carrageenan	EGCG	Enhanced stability and antioxidant activity of EGCG	[31]
BSA-Alginate	TRAIL and DOX	Synergistic cytotoxic activity was achieved even in the DOX-resistant L929 cell line	[39]
BSA-Gum acacia	–	Successful fabrication of nanohybrids with a size of 108 nm	[40]
BSA-Chitosan-Dextran	DOX	Significant prolongation in the survival of hepatoma (H22)-bearing mice in comparison to free DOX	[41]
Egg albumin-Chitosan	Aceclofenac	Enhanced skin permeation and higher anti-inflammatory activity in comparison to the marketed gel	[30]
Ovalbumin- Chitosan	–	Enhanced nanohybrid stability upon long term storage with pH responsiveness	[42]
Gelatin-Chitosan	CPs	Higher apoptotic activity was achieved against THP-1 leukemic cells in comparison to free CPs	[43]
Gelatin-Chitosan	Fluorescein	The intravenous administration was found optimum for achieving higher tissue concentrations rather than the intraperitoneal one	[44]
Gelatin-Chitosan	5-FU and HYL	Release modulation of 5-FU and HYL to COLO-205 and HT-29 colon cancer cells	[45]
Gelatin-CMC	alpha amylase	Efficient carrier systems for the immobilization of alpha amylase	[46]
Gelatin-Alginate	Curcumin	Enhanced cytotoxic activity against MCF-7 cell line	[47]
Gelatin-Gum arabic	Jasmine oil	Stability enhancement against humid heat	[48]
Cationized gelatin- Dextran or CS	pEGFP	Enhanced plasmid ocular delivery	[49]
Cationized gelatin- Dextran or CS	pMUC5AC	Enhanced MUC5AC protein expression in conjunctival cells	[50]
$\alpha$ -La or $\beta$ -Lg-Chitosan	–	Successful fabrication of the nanohybrid system with potential applications for drug, food, cosmetic or nutraceutical delivery	[51]
$\beta$ -Lg-Alginate	Quercetin	Enhanced the stability of quercetin 3-folds and modulated its release profile	[52]
$\beta$ -Lg-Pectin	DHA	Transparent nanohybrid systems with stability for DHA against oxidation	[53]
$\beta$ -Lg-Pectin	–	Cosolvents as glycerol and sorbitol could modulate nanohybrid properties formed by heat treatment	[54]
$\beta$ -Lg- Pectin	Pt(II) complex	Enhanced cytotoxicity against the colon cancer HCT116 cell line	[55]
$\beta$ -Lg-Pectin or Carrageenan	–	$\beta$ -Lg-Pectin nanohybrids were more stable than their $\beta$ -Lg-Carrageenan counterparts against pH changes	[56]
$\beta$ -Lg-KC or $\beta$ -Lg-Sodium alginate	–	Enhanced stability against aggregation	[57,58]
$\beta$ -Lg-LMP	Oxali-palladium	A pH-sensitive targeted colon delivery of oxali-palladium was achieved	[59]
$\beta$ -Lg-Gum Arabic or CMC	–	Enhanced stability against aggregation	[60]
WPI-Inulin	Resveratrol	Intrinsic prebiotic activity with efficient encapsulation of resveratrol	[61]
WPI-Alginate	–	Successful fabrication of the nanohybrid system with higher hydrophobic patches exposed for binding lipophilic drugs	[62]
Soy protein-Soy polysaccharide	Curcumin	The nanohybrids enhanced the thermal stability of curcumin and modulated its release	[63]
Soy protein-Soy polysaccharide	Folic acid	Enhanced folic acid protection and delivery in food and beverages	[64,65]
Soy protein-CMCS	Vitamin D <sub>3</sub>	Enhanced vitamin D <sub>3</sub> loading, encapsulation efficiency and release profile	[66]
Soy protein-KC	Quercetagenin	Improved light stability and the antioxidant properties of quercetagenin	[67]
Lf-Pectin	–	Higher nanosystem thermal stability in comparison Lf alone	[68]
Lf-Pectin, Carrageenan or Alginate	–	Improved stability at pH range 5 to 8	[35]
Lf-Alginate or i-Carrageenan	–	Alginate and i-Carrageenan endowed Lf nanoparticles with higher stability against gastric digestion	[69]
Lf-Pectin, i-Carrageenan or Alginate	–	Enhanced stability against gastric digestion was demonstrated especially with i-carrageenan	[70]
Lysozyme-CS	–	CS endowed lysozyme with stability against degradation and biocompatibility	[71]
Lysozyme-CMC	5-FU	A more sustained drug release was achieved in simulated gastric fluid than in intestinal fluid	[72]
Lysozyme-CMC	MTX and QDs	Concomitant cancer imaging and therapy “theranostic nanohybrids” were developed	[73]
Lysozyme-CMC	–	The higher the substitution degree on CMC, the more is the negative charge and the stronger is the electrostatic interaction	[74]
Lysozyme-Alginate	$\beta$ -lactamase	Prevention of the irreversible destruction of the enzyme with stimuli-responsive release	[75]
Casein-Pectin	Vitamins	Successful incorporation of both hydrophilic and hydrophobic vitamins	[76]
Casein-Pectin	Rutin	Enhanced stability in gastric conditions while releasing rutin in intestinal conditions	[77]
Casein-Chitosan	–	Successful fabrication of stable soluble nanohybrid systems in the pH range 4.8 to 6.0	[78]
Protamine-HA	GFP-ODN	Enhanced cellular uptake and transfection efficiency of the GFP-ODNs	[79]
Protamine-HA	miR-34a	Enhanced delivery of miR-34a to breast tumor tissues	[80]
Protamine-Heparin	Ferumoxylol	Enhanced cell-labelling capability facilitating MRI-monitoring	[81]
FSP-Alginate	–	Successful fabrication of non-toxic stable nanohybrids	[82]
Zein-Pectin	–	Successful fabrication of nanohybrids with potential emulsion stabilizing properties	[83]
Egg yolk LDL-Pectin	Curcumin	Successful fabrication of nanohybrids with modulated curcumin release	[84]
Lactoferrin-chondroitin	DOX/Ellagic acid	Superior internalization of the nanocomplex into lung cancer cells and hence enhanced anti-tumor efficacy <i>in vitro</i> and <i>in vivo</i>	[32]

**CMC:** Carboxymethyl cellulose, **DTX:** Docetaxel, **DOX:** Doxorubicin, **psiRNA-hH1GFPzeo:** vector for generating shRNA targeting GL3 luciferase, **EGCG:** Epigallocatechin-3-gallate, **TRAIL:** Tumor necrosis factor-related apoptosis-inducing ligand, **CPs:** Cocoa procyanidins, **5-FU:** 5-Fluorouracil, **HYL:** Hyaluronidase, **CS:** Chondroitin sulfate, **pEGFP:** Plasmid for enhanced green fluorescent protein, **pMUC5AC:** Plasmid for gel-forming mucin, **DHA:** Docosahexaenoic acid, **Pt(II) complex:** Bipyridine ethyl dithiocarbamate Pt(II) nitrate, **KC:**  $\kappa$ -carrageenan, **LMP:** Low methoxyl pectin, **WPI:** Whey protein isolate, **CMCS:** Carboxymethyl chitosan, **Lf:** Lactoferrin, **i-Carrageenan:** iota Carrageenan, **MTX:** Methotrexate, **QDs:** Quantum dots, **HA:** Hyaluronic acid, **MRI:** Magnetic resonance imaging, **GFP-ODN:** Green fluorescent protein antisense oligodeoxynucleotide, **miR-34a:** a potent endogenous tumor suppressor microRNA, **FSP:** Fish sarcoplasmic protein, **LDL:** low density lipoprotein.

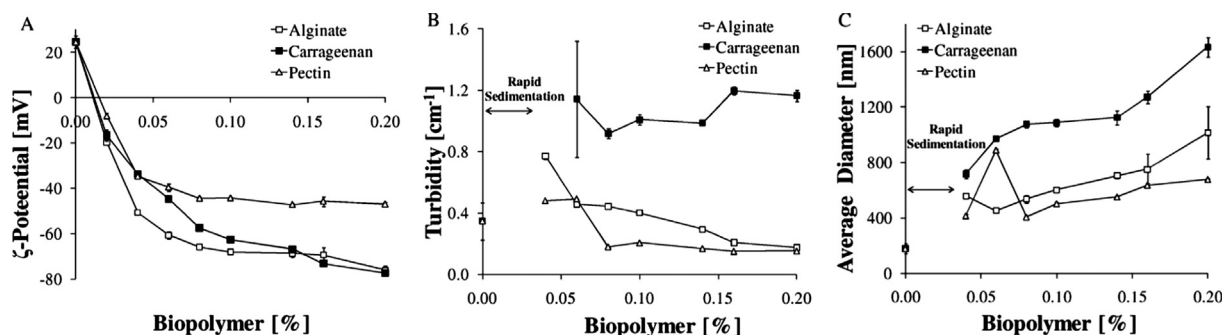


Fig. 2. The effect of increasing the polysaccharide (biopolymer) concentration on the zeta potential (A), turbidity (B), and mean particle size (C) of Lf nanoparticles [35].

intramolecular soluble complex at the molecular state; (III) the intermolecular soluble complex where colloidal stability will determine whether the complex will be in nanosized range; or (IV) aggregates resulting in an intermolecular insoluble complex; and finally phase (V) where individual soluble molecules appear again [28].

The electrostatic protein-polysaccharide nanocomplexes are fabricated by one of two main methods. The **first** method is a single-step strategy depending on matrix formation between the protein and polysaccharide where the nanoparticles are prepared by mixing their pH adjusted aqueous solutions. The **second** method is a two-step core/shell method where the core is formed in an independent step from either polymers and subsequently coated by the other. All the protein-polysaccharide nanohybrids prepared by electrostatic complexation, to our knowledge, are summarized in Table 1.

#### 2.1.1. Single-step nanocomplexes

The **single-step approach** utilizes the electrostatic/ionic interaction between the two polymers forming a matrix nanoparticle. This aqueous ionic coacervation method is preferred since it eliminates the need of an organic solvent or a toxic crosslinking agent such as glutaraldehyde that dictates their subsequent removal. Thus, this method reduces the production costs, and increases the safety of the formed drug delivery system. In a study by Varshosaz et al., cationic chitosan (pKa 6.5) and anionic albumin (pI 4.7) were utilized to fabricate nanoparticles by direct mixing of both solutions under stirring to induce aqueous coacervation. The polysaccharide here, chitosan, unlike most polysaccharides, carried out a positive charge because of the abundance of amino groups that get protonated at pH of 2.49 which is lower than its pKa. Albumin, however, carried out a net negative charge since it was dissolved in deionized water with a pH above its pI. The prepared chitosan-albumin nanoparticles were subsequently decorated with retinoic acid showing an optimum size of 286 nm for the targeted delivery of doxorubicin to hepatocellular carcinoma [29]. In another study, Jana et al. also fabricated chitosan/albumin complexes by adding chitosan-aceclofenac mixtures into egg albumin solutions followed by pH adjustment to 5.4 and heating at 80 °C for 30 min, thus forming nanoparticles via electrostatic attraction/heat coagulation. The nanoparticles were then further stabilized by tripolyphosphate crosslinking, showing a size of 352.90 nm, and then incorporated into a transdermal Carbopol gel for sustained skin permeation of aceclofenac and enhanced its *in vivo* anti-inflammatory activity [30]. On the other hand, BSA-Carrageenan nanocomplexes were prepared by mixing BSA and i-carrageenan solutions at pH 7 and then heating them. Although BSA and i-carrageenan are both anionic at pH 7, the formation of BSA/i-carrageenan complexes might be attributed to an electrostatic interaction between the cationic amino patches on BSA and the anionic sulphate groups on i-carrageenan [31]. In a recent study, an electrostatic nanocomplex was formed based on ionic interaction between cationic lactoferrin and anionic chondroitin [32]. Adjusting the pH of protein solution at 3.5 (below its isoelectric point 8.6) increased the positive

charge density on the macromolecule resulting in strong interaction with the polysaccharide leading to small size nanoparticles (192.3 nm) with high colloidal stability.

#### 2.1.2. Core-shell nanocomplexes

In this **two-step approach**, nanoparticles are initially fabricated from one of the polymers and then electrostatically coated by the other one. Tekade and Chougule have formulated albumin-chitosan hybrid nanocarriers for efficient cancer-specific delivery of a model anticancer drug, Gemcitabine (GEM). First, GEM-loaded BSA nanoparticles were prepared as core by modified desolvation method where diluted ethanol was used to induce coacervation instead of pure ethanol. Then, the surface of preformed GEM-loaded albumin nanoparticles were coated with chitosan shell through electrostatic interactions. This was concluded through the increase in size from approximately 25 nm to 46 nm upon the addition of chitosan and the charge reversal from −24.88 mV to 15.05 mV. Then, this was followed by crosslinking the chitosan shell with the polyanionic crosslinker, tripolyphosphate, instead of glutaraldehyde due to its superior safety and biocompatibility. The use of diluted ethanol instead of pure ethanol was anticipated to impart milder conditions for desolvation and nanofabrication; thereby allowing mild folding of BSA polymer to generate nanocarriers in the size range of 50 nm in contrast to that of reported methodologies that generate nanocarriers in the size range between 150 and 300 nm [33].

In another study, Karimi et al. used cationic chitosan to condense the negatively charged DNA which was then used to coat a plasmid (shRNA targeting GL3 luciferase)-loaded albumin nanoparticles prepared by desolvation. The experiment was carried out at a pH of 5–6; and so imparting chitosan and albumin opposite charges; thus facilitating the electrostatic interaction between the two polymers [34]. Similarly, Peinado et al. fabricated nanosized lactoferrin (Lf)-polysaccharide nanoparticles by an electrostatic interaction of heat-denatured (91 °C, 20 min) Lf nanoparticles (200–400 nm) with different negatively charged polysaccharides (carrageenan, alginate, or pectin). Lowering the pH from 8 to 5 has promoted electrostatic deposition of the anionic polysaccharides onto the surface of protein nanoparticles since Lf has a pI of 8.5. The charge inversion and the size increase of Lf nanoparticles upon the addition the three polysaccharides as shown in Fig. 2 proves such electrostatic complexation [35].

Another interesting approach includes the use of oppositely charged alternative layers of proteins and polysaccharide for coating of previously prepared nanocarriers. Those layers can provide controlled drug release, enable tumor targeting or enhance the physical stability of nanocarriers. In our laboratory, the tumor targeting properties of the cationic lactoferrin (Lf) and anionic hyaluronate were exploited to coat lipid nanoparticles co-loaded with rapamycin and berberine for efficient targeting of lung cancer cells [85,86]. The layer-by-layer (LbL)-coated NPs showed enhanced uptake and cytotoxicity against A549 lung cancer cells via binding to CD44 receptors overexpressed by tumor cells. In another study, a cationic layer of gelatin type A was used to



coat the negatively charged chondroitin sulfate-based oily core nanocapsules co-encapsulating celecoxib and rapamycin for synergistic killing of breast cancer cells [87]. The outer gelatin corona helped to inhibit the nonspecific binding of chondroitin nanocapsules with normal cells expressing CD44 receptors. At the tumor microenvironment, the gelatin layer would be degraded by matrix metalloproteinase (MMP-2) thus exposing the tumor-targeting chondroitin nanocapsules resulting in enhanced internalization into tumor cells and hence superior antitumor efficacy. Moreover, coupling of quantum dots to the gelatin layer displayed strong fluorescence which enabled imaging of the nanocarriers after their internalization into cancer cells.

### 2.1.3. Drug loading mechanisms

A variety of mechanisms could be used for drug encapsulation into electrostatic protein-polysaccharide nanohybrids; the simplest of which is the physical encapsulation through desolvation of the core polymer with the drug, or through mixing the drug with the protein and polysaccharide and then heating them to form stable nanohybrid systems through a thermal coagulation process. Other mechanisms for drug encapsulation including electrostatic, hydrophobic, or covalent interactions can be also considered depending on the characteristics of drug molecules.

In a study by Tekade et al., albumin nanoparticles were physically loaded with GEM through desolvation process, which were then electrostatically coated with chitosan. In this approach, an aqueous solution of GEM was slowly injected into albumin solution for under stirring followed by desolvation using a diluted ethanol solution. After complete removal of ethanol, a high entrapment efficiency of GEM (80%) in the hybrid nanoparticles was achieved [33]. For loading of the water insoluble cocoa procyanidins (CPs), a solution of CPs in acetone was gradually added to an aqueous gelatin solution inducing the formation of nanoparticles which were then electrostatically coated with chitosan. A high loading capacity (about 20%) of CPs into the nanohybrids was obtained [43]. In a study by Jana et al., aceclofenac-loaded albumin-chitosan nanohybrids were prepared by a heat coagulation process. A homogenized aceclofenac-chitosan solution was added to aqueous albumin solution under stirring. The pH of solution was finally adjusted to 5.4; and the dispersions were then heated at 80 °C for 30 min resulting in formation of aceclofenac-loaded nanohybrids with a significantly high entrapment efficiency of aceclofenac (96.32%) [30]. In another approach, the water insoluble herbal drug, ellagic acid was first pre-formulated as water dispersible nanocrystals by anti-solvent precipitation to facilitate its physical encapsulation into the hydrophilic electrostatic Lf-chondroitin nanocomplex [32].

Other mechanisms for drug encapsulation include hydrophobic, electrostatic, or covalent interactions based on the properties of drug molecules. In a study by Li et al., (-)-epigallocatechin-3-gallate (EGCG) was found to be hydrophobically bound to albumin in the albumin-i-carrageenan nanocomplexes. Blank nanocomplexes without EGCG showed a characteristic fluorescence peak at 345 nm due to tryptophan residues (Trp 214) in the hydrophobic pockets of albumin. Addition of EGCG to the nanocomplexes resulted in remarked decrease of the fluorescence peak intensity with a red shift. This could be attributed to the fluorescence quenching induced by the hydrophobic binding of phenolic rings of EGCG to the hydrophobic groups near Trp 214 residues of albumin. In a similar study, docosahexaenoic acid (DHA) was hydrophobically bound to the tryptophan residue 19 (Trp 19) in  $\beta$ -lactoglobulin ( $\beta$ LG) before the formation of  $\beta$ LG-pectin electrostatic nanocomplexes. About 2.67 mol of DHA were bound to each mole of  $\beta$ LG which suggests the presence of other binding sites in the protein rather than the Trp 19 which could be the dimer interface and crevice next to the alpha helix in the  $\beta$ LG structure [53]. On the other hand, a plasmid psiRNA-hH1GFPzeo (vector for generating shRNA targeting GL3 luciferase) was electrostatically complexed with chitosan. The abundant cationic amino groups of chitosan can strongly interact with the negatively charged phosphate groups in the backbone of genetic

materials; thus protecting them from endonuclease degradation. The electrostatic complex was further electrostatically coated with albumin to form a nanohybrid with a small size of about 176 nm and a high loading efficiency of approximately 80% [34].

### 2.1.4. Factors affecting characteristics of electrostatic nanocomplexes

Many factors affect the electrostatic complexation and physiochemical properties of protein-polysaccharide nanohybrids resulting in the formation of coacervates or soluble complexes.

#### (a) pH

Being the main factor for formation of the ionic complex, the pH of the complexation medium affects nearly all physiochemical characteristics of the formed nanocomplex. For the ionic complex to be formed, both protein and polysaccharide should bear opposite surface charges. Polysaccharides having only either negative or positive ionizable groups will oblige the charge to be possessed by the protein which, thanks to its zwitterionic nature, can possess either positive or negative charge depending on its pI; the protein will be negatively charged above its pI and positively charged below it. Three pH regions are to be identified for each electrostatic complex where each region will correspond to a phase as previously described in the protein/polysaccharide phase diagram (Fig. 1). pH<sub>c</sub> is regarded as the critical point for the formation of protein-polysaccharide soluble complexes. pH<sub>φ</sub> is the pH where the formation of protein-polysaccharide insoluble complexes takes place. Finally, pH<sub>d</sub> is attributed to the dissociation of protein-polysaccharide complexes due to the reduction of negative charges on the polysaccharide by protonation at low pHs. In general, for a nanocomplex to be formed, the pH should lie between pH<sub>c</sub> and pH<sub>φ</sub> [28].

By tracking the pH during gelatin/gum arabic complex formation by measuring turbidity at 600 nm upon acidification, Lv et al. found that the soluble nanocomplexes were formed within a narrow window of pH range and the nanoparticles specifically were favorably formed at pH 4.80 under a mixing ratio of 1:1 (gelatin/gum arabic, w/w). Once the turbidity changed from 0 to 0.001, the pH of 5.47 which triggered such change was considered the pH<sub>c</sub> which denoted the onset of soluble complexes formation in the nanosize. Upon further lowering of pH, the turbidity started to rise gradually until reaching the pH<sub>φ</sub> of 4.68, which denoted the halting of soluble complex formation and the beginning of microparticles formation. Turbidity results were supported with size results where soluble complexes of a 100 nm size were formed with a more unimodal size distribution in comparison to an evident bimodal pattern accompanied with a narrow peak at 10000 nm at pHs below pH of 5.10 indicating the beginning of microparticles formation. Interestingly enough, at pH of 4.8 and a mixing ratio of 1:1, the nanoparticles showed a unimodal size of around 100 nm with a homogeneous distribution [48].

#### (b) Ionic strength

To further understand the effect of salt concentration, Teng et al. prepared hybrid nanoparticles from carboxymethyl chitosan (CMCS) and soy protein isolate (SPI) by ionic co-gelation with Ca<sup>2+</sup> at a concentration range of 0.2–1.6 mg/ml. Comparing the nanoparticle forming ability, the hybrid nanoparticles exhibited 46% and 190% higher count rates than the maximum achieved by SPI or CMCS alone, respectively. Moreover, complex nanoparticles showed the smallest particle size of 265.5 nm in comparison to 267.4 nm and 417.6 nm for SPI and CMCS, respectively. Regarding the CaCl<sub>2</sub> concentration, hybrid nanoparticles were formed at concentrations lower than 0.1 mg/ml in the pH range of 6.0 to 8.5. These concentrations were similar to the concentrations needed for SPI to form nanoparticles but were approximately one tenth the concentrations needed for CMCS. The differences in the nanoparticle forming ability between SPI and CMCS

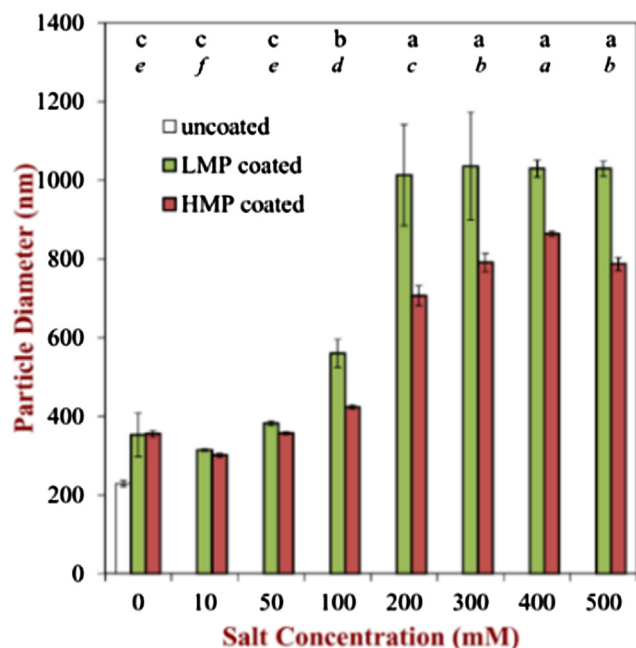


Fig. 3. The effect of increasing NaCl salt concentration (mM) on HMP and LMP-coated gliadin nanoparticles diameter (nm) [88].

could not be attributed to the zeta potential which was minorly different, being -19.4 and -23.2 mV, respectively, at pH 7.5. Rather, the difference was attributed to two main factors; the hydrophobicity and chain rigidity. Unlike polysaccharides, proteins are known for their hydrophobic side chains on their surface. Moreover, polysaccharides have bulky sugar rings that tend to make polysaccharides more linearly conformed, whereas globulins such as SPI tend to be more convoluted in conformation with higher chain flexibility. It could be concluded that the higher  $\text{CaCl}_2$  concentration needed in nanoparticle formation by CMCS could be attributed to the weaker hydrophobic interactions and higher rigidity and linearity that need to be overcome by  $\text{CaCl}_2$  to bring CMCS molecules in proximity and crosslink them into spherical nanoparticles. Thus, the SPI presence in the nanohybrid system is critical since it lowers the  $\text{CaCl}_2$  concentration needed preventing an overdose of  $\text{CaCl}_2$ , decreases the size of nanoparticles, and maintains nanoparticles stable over a wide range of pH. The nanohybrids had a diameter of 163 nm at pH 6.5 and were stable maintaining a nanosize of about 250 nm upon increasing pH from 7.0 to 9.5 [66].

In a study by Joye et al., gliadin-pectin nanohybrids were found more stable to salt in comparison to uncoated gliadin nanoparticles which precipitated even in low salt concentrations i.e. 10 mM NaCl. As can be seen in Fig. 3, the nanohybrids fabricated with two types of pectin; the low (LMP) and high methoxyl pectin (HMP), were stable in the NaCl concentration range from 0 to 50 mM where their size did not appreciably change. This could be attributed not only to the electrostatic repulsion but also to the steric hindrance imposed by pectin, since pectin enhanced the stability of nanoparticles against gravitational separation in NaCl concentrations up to 500 mM [88].

The influence of pH and ionic strength on the stability of different LF-polysaccharide nanohybrids formed by electrostatic interaction of heat-denatured LF and negatively charged polysaccharides was examined by Peinado et al. through observing the zeta potential, turbidity, and mean particle size upon changing pH or addition of different amounts of NaCl in separate experiments, as shown in Fig. 4A & B.

Due to electrostatic screening effects, the zeta potential of all nanohybrids became less negative with rising salt concentrations as shown in Fig. 4(iiA). However, the authors observed that Lf-alginate and Lf-pectin nanohybrids were relatively homogenous and turbid at all salt concentrations, denoting their stability, whereas Lf-carrageenan

nanohybrids formed a thin white sediment layer at all salt concentrations indicating at least a partial instability. The particle size of Lf-pectin nanohybrids decreased with rising salt concentrations which could be ascribed to the charge screening of similarly charged groups preventing their repulsion, and so becoming more compact. However, Lf-alginate nanohybrids showed a more dependent behavior on salt concentration whereas an increase in size and turbidity was observed with an increase in salt concentration up to 100 mM, after which a decrease in size and turbidity was observed. The results suggested that flocculation was promoted at intermediate salt concentrations, whereas higher levels promoted the de-flocculation of the aggregates. All nanohybrids showed high stability across a pH range of 8 to 4, due to the high negative zeta potential. However, upon further reduction of pH from 4 to 2, Lf-alginate and Lf-pectin nanohybrids showed a remarkable decrease of surface charge, whereas Lf-carrageenan showed a slight decrease in zeta potential. This was ascribed to the protonation of carboxyl groups of alginate and pectin when the pH approached their pKa, however, the sulfate groups of carrageenan conferred a lower pKa, and thus the extent of protonation was lower. Flocculation occurred at low pHs because of charge neutralization. As the charge density on the nanohybrids decreased, the electrostatic repulsion decreased, thus promoting aggregation [35].

### (c) Biopolymers ratio

Evidence from literature have shown that the nanocomplexes composition or better stoichiometric ratios between proteins and the poly-acid polysaccharides depends mainly on their charge density. Each component; either the protein or the poly-acid polysaccharide, have their own pH at which their charge neutralizes depending on their pI or pKa, respectively, as mentioned previously. At a pH below the pI of the protein where the formation of nanocomplexes becomes possible, the ratio between the protein and the poly-acid polysaccharide decreases as the pH decreases until reaching a point where the poly-acid stops dissociation and so suppressing the electrostatic complexation (usually at a pH below 2.0 which was previously described as pHd). This is true for weak poly-acids; however, the situation is different for strong ones. First of all, proteins tend to precipitate upon complexation with strong poly-acids. Secondly, strong poly-acids never get neutralized at low pHs. When the strong poly-acid is titrated with a protein at a pH below its pI, the poly-acid may adsorb protons as to impose charge neutrality of the complex; which as a result causes an increase in pH in the beginning before sufficient protein gets added [89].

Luo et al. formulated zein nanoparticles coated with chitosan to encapsulate tocopherol (TOC) based on the hydrophobic properties of zein [90,91]. Different weight ratios between zein and chitosan were tested; 20/1, 10/1, and 5/1. Interestingly, the particle size of the uncoated zein nanoparticles was around 800 nm and decreased significantly to around 211 nm after coating with chitosan at 20/1 ratio. This reduction in particle size indicated an interaction between TOC-loaded zein nanoparticles and chitosan has taken place. However, the size increased significantly to 364 nm and 862 nm upon lowering the ratios to 10/1 and 5/1, respectively, which was attributed to the excess chitosan increasing the thickness of the coat layer [92]. Similar findings were observed upon coating of Lf nanoparticles with different concentrations of the anionic polysaccharides (alginate, carrageenan, or pectin). As shown in Fig. 2, the increase of polysaccharide concentration resulted in increase of the size and zeta potential of the nanohybrids that became increasingly negative until reaching a plateau indicating surface saturation of Lf nanoparticles with polysaccharide coat. At very low polysaccharide concentrations, large aggregates were formed that rapidly sedimented which could be attributed to their instability; having no enough coating with high zeta potential to act as an electrostatic or steric barrier for aggregation [35].

However, in another study by Karimi et al., the protein concentration had more prominent effect on the size of fabricated nanohybrid

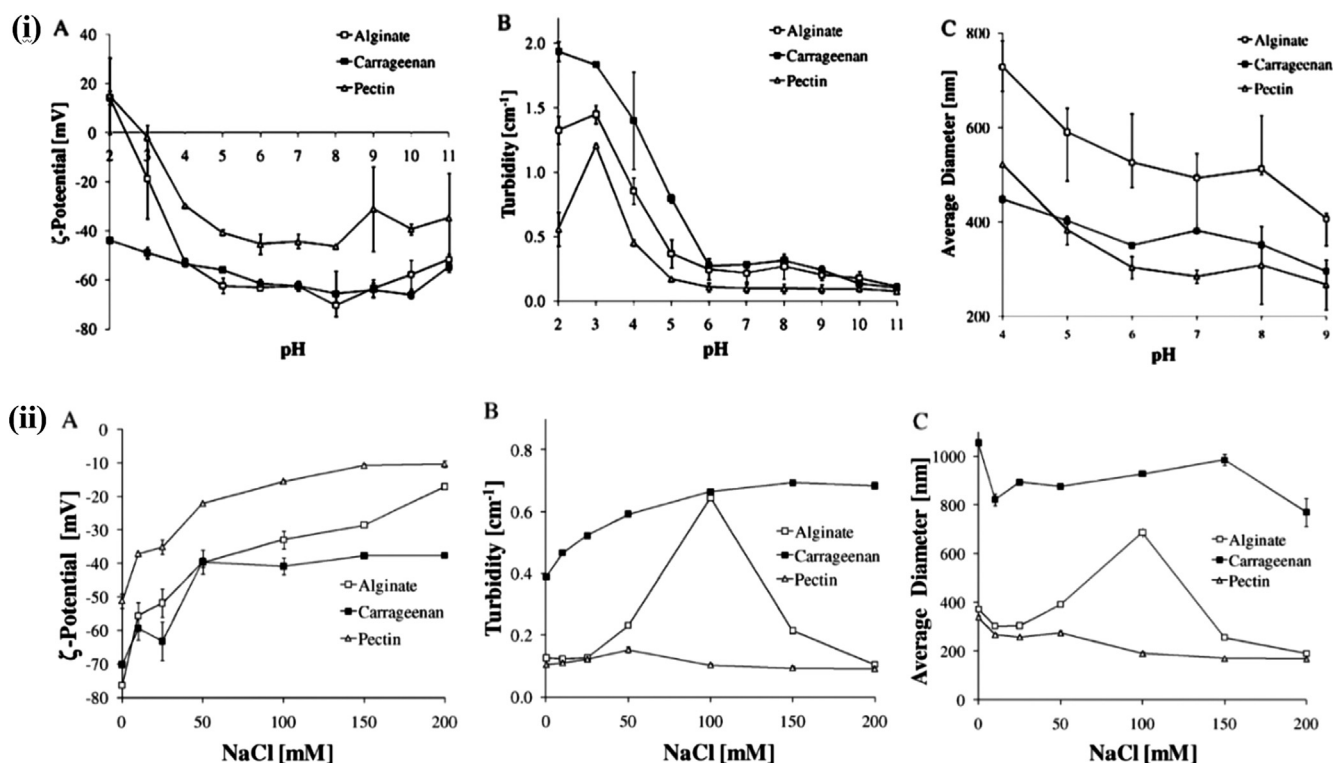


Fig. 4. Change in zeta potential (A), turbidity (B), and mean particle size (C) upon changing pH (i) or addition of different amounts of NaCl (ii) [35].

rather than the protein/polysaccharide ratio. Chitosan-coated albumin nanohybrid system was found to be more affected by the concentration of albumin which was kept at a low level of 0.1 mg/ml in further studies. This was attributed to albumin; being the constituting polymer of the core of the nanohybrid, and thus affecting its size [34].

#### (d) Sonication

Hosseini et al. studied the effect of ultrasound irradiation of  $\kappa$ -carrageenan (KC) solution on its interaction with  $\beta$ LG. There was a great reduction in the viscosity of KC solution (0.5% w/w) from 19 to 3 mPa.s after sonication for 30 min with an amplitude 100% at 25 °C. This was attributed to the cleavage of the polysaccharide backbone into smaller chains with lower molecular weight. The depolymerization process is a result of cavitation forces which could have involved one of two mechanisms: the mechanical polymer degradation as a result of collapsed cavitation bubbles, or chemical degradation mediated by interaction between the polysaccharide with high energy hydroxyl groups formed by the cavitation process. Comparing the turbidimetry results of nanohybrids produced from either intact KC or ultrasonicated KC with  $\beta$ LG; intact KC produced more turbid solutions than the ultrasonicated counterpart which was attributed to formation of hybrids with low molecular weight KC in case of ultrasonication. The interaction was further investigated by isothermal titration calorimetry (ITC), and the results have shown that ultrasonicated KC showed a significantly lower affinity constant of  $535 \pm 137 \text{ g}^{-1}$  in comparison to  $10476 \pm 6032 \text{ g}^{-1}$  for the intact KC. This lower affinity could be ascribed to the lower charge density on the ultrasonicated KC and the changes in its helical structure. Using ultrasonicated KC, the nanohybrids showed a more homogenous size distribution in comparison to intact KC. For instance, using a weight ratio of 0.75, intact KC produced nanohybrids with a polydispersity index (PDI) of 0.313 which is significantly higher than the PDI for the nanohybrids produced from ultrasonicated KC; being 0.151. Such results were attributed to the effect of sonication on the unification polysaccharide chains' sizes [57]. The authors found nearly the same findings when the study was performed

on alginate instead of KC [58].

#### (e) Thermal treatment

Nanocomplexes between proteins and polysaccharides could be created by heating of the electrostatic nanocomplexes between proteins and polysaccharides to a temperature higher than the protein's thermal denaturation temperature. Unlike native proteins, native polysaccharides, or electrostatic complexes without thermal treatment, the thermally-treated nanocomplexes have shown great stability against dissociation or aggregation upon changes in pH, temperature, or salt concentration. Therefore, the thermally-treated nanocomplexes hold great potential as vehicles for encapsulation and stabilization of foods and drugs [93].

In addition to the studies held on  $\beta$ LG-based nanohybrids, ovalbumin-chitosan nanogels were fabricated by heating their mixed solution at a pH where both polymers were oppositely charged. Upon thermal gelation of ovalbumin, the chitosan macromolecular chains were partially frozen within the gelled protein core, whereas the remaining chitosan chain fragments have extended out forming a shell. The nanogels maintained their size during storage over a broad pH range of 2–10.5 even when both polymers carried the same charge due to crosslinking of the protein core [42].

Jones et al. examined the thermal treatment of electrostatic nanocomplexes formed between pectins (HMP and LMP) and carrageenan as negatively charged polysaccharides, and  $\beta$ LG as a cationic protein. Pectins are characterized by a linear anionic backbone with regions of no side chains and regions with non-ionic side chains. The electrical characteristics of pectins depend on the number and location of carboxylic groups; either in the free or methyl esterified form, with a pKa value at about 3.5. Carrageenans have a linear anionic backbone without side chains, and their electrical characteristics depend on the sulfate groups ( $-\text{OSO}_3$ ) which have a pKa around pH 2 thus carrageenans possess a higher charge density compared to pectins. Therefore, strong aggregation took place above Tm for  $\beta$ LG-pectin, but not for  $\beta$ LG-carrageenan complexes. This difference was ascribed to the

**Table 2**  
Protein-polysaccharide nanohybrids prepared by chemical conjugation.

Protein-Polysaccharide	Drug	Chemical conjugation technique	Key Outcomes	Ref.
BSA-Dextran	Ibuprofen	Maillard coupling	Simultaneous formation of nanohybrids and ibuprofen loading was achieved through a simple green process	[103]
BSA-Dextran	DOX	Maillard coupling	Improved toxicity profile of DOX, thus allowing the usage of a higher dose	[105]
BSA-Alginate	TMX	Thiol coupling	- Enhanced anti-tumor activity while minimizing TMX levels in non-target tissues - Modulation of TMX release by changing the protein-polysaccharide ratio - Folic acid-targeted nanohybrids caused tumor remission which was not achieved by the non-targeted ones	[94,95,106,107]
BSA-Alginate	5-FU	Thiol coupling	Enough stability for the nanohybrids to reach the blood stream after oral administration	[96]
BSA-Dextran or BSA-Chitosan-Dextran	DOX	Maillard coupling	Survival prolongation of hepatoma H22-bearing mice in comparison to free DOX	[41,108]
Ovalbumin- Dextran	Curcumin	Maillard coupling	Enhanced oral bioavailability of curcumin	[109]
Casein-Dextran	EGCG	Maillard coupling	Sustained EGCG release profile and stability against degradation in gut conditions	[110]
Casein-Dextran	$\beta$ -carotene	Maillard coupling	Enhanced stability against ionic strength and pH changes, oxidation and dilution	[111,112]
Casein-Dextran	Curcumin	Maillard coupling	Enhanced curcumin loading and stability	[113]
Casein-MD	Vitamin D	Maillard coupling	Improved vitamin D stability and enhanced solution transparency	[100]
$\alpha$ -La-Dextran	Curcumin	Maillard coupling	Improved oxidative stability of curcumin	[114]
WPI-Chitosan	Catechin	Maillard coupling	Improved stability and controlled release behavior in gastric conditions	[102]
WPI-MD	Eugenol	Maillard coupling	Enhanced thermal stability and dispersion transparency	[98]
Lysozyme-Dextran	HAF	Maillard coupling	Enhanced uptake by their target endothelial cells while preventing phagocytic uptake	[99]
Lysozyme-Dextran	Ibuprofen	Maillard coupling	Successful fabrication through a green process with high loading and encapsulation efficiencies	[101]
Gelatin-Dextran	TPP	Maillard coupling	Comparable or even higher cytotoxicity than free TPP in MCF-7	[104]

TMX: Tamoxifen, HAF: 5-hexadecanoylamino fluorescein, TPP: Tea polyphenol.

stronger electrostatic attraction between  $\beta$ LG and carrageenan, rather than with pectin molecules. Moreover, the formed  $\beta$ LG-carrageenan complexes had the highest charge density which might have impeded the complexes from approaching each other, and thus preventing aggregation [56].

## 2.2. Chemical conjugation

Protein-polysaccharide nanocomplexes could be also prepared via chemical coupling rather than electrostatic complexation. Natural polymers such as proteins and polysaccharides are rich in reactive functional groups such as amino, carboxylic, and thiol groups which can be used in chemical conjugation under certain conditions. Therefore, protein-polysaccharide nanohybrids could be developed by various chemical bonding strategies or Maillard conjugation process. The protein-polysaccharide nanohybrids prepared by chemical conjugation are summarized in Table 2.

### 2.2.1. Chemical coupling

BSA-alginate hybrid nanoparticles were prepared using chemical conjugation for the delivery of tamoxifen [94,95] and 5-fluorouracil (5-FU) [96]. In order to facilitate a disulfide bond formation between alginic acid and BSA, L-cysteine was first used to introduce thiol groups onto alginic acid via an amide linkage between the carboxylic moieties of alginate and cysteine's primary amino groups. Then, a disulfide bond-reduced BSA was prepared by incubating BSA with 2-mercaptoethanol at pH 8.0. For the preparation of hybrid nanoparticles, a mixture of each polymer was dissolved in 1 mM HCl and left to stir vigorously for 12 hrs for disulphide bonds to form. Results have shown that the nanohybrid particles were cubic in shape with spherical tendency. The size of the different formulations made were always below 300 nm. Tamoxifen loading was 2–4  $\mu$ g per mg of nanoparticle with a modulated release behaviour depending on the percentage of alginate [94]. No many researches have been reported concerning chemical coupling between proteins and polysaccharides, such as BSA-alginate conjugate nanohybrids discussed above. Therefore, we focused on

discussing Maillard conjugates' drug loading mechanisms, factors affecting their stability, or characteristics in the coming sections.

### 2.2.2. Maillard conjugates

A special form of chemical conjugation is Maillard reaction which is an ubiquitous condensation reaction that occurs naturally between the amino groups a peptide or a protein and the reducing end carbonyl moieties of a reducing sugar or a polysaccharide upon heating. The primary glycation site is the  $\epsilon$ -amino group of the lysine residues, however other groups like the indole group of tryptophan, the guanidine group of arginine and the imidazole group of histidine residues also involve in the reaction with a lesser extent. According to Hodge et al., Maillard reaction can be classified into 3 stages: initial, intermediate, and final as seen in Fig. 5. Conjugation is based on the Amadori rearrangement of the Maillard reaction and finally reaching for melanoidins in the final step. Maillard reaction can occur in powder and solutions. The glycation rate is affected by the presence of water as it slows down the initial Amadori reaction and the consequent reactions in aqueous solutions. Therefore, in all the following studies, Maillard conjugates were prepared by heating the lyophilized powder mixture of protein and polysaccharide [97].

Generally, 0.1 N NaOH is used to adjust the pH of the aqueous solution of proteins and polysaccharides to 7–8. The mixture solution is then dried by either spray-drying or lyophilization. The reaction of dried powder is performed at 60–90 °C and 78.9% relative humidity. Shah et al. successfully prepared whey protein isolate-maltodextrin (WPI-MD) Maillard conjugate encapsulating eugenol by spray-drying of the aqueous solution containing both WPI and MD; and then the spray-dried powders was heated at 90 °C for 2 h [98].

In some cases, Maillard product may be used without separation of the unreacted proteins and polysaccharides. Instead, to obtain the pure glycosylated protein, two simple techniques were successfully used, namely, centrifugal filtration and isoelectric point precipitation. In **centrifugal filtration**, Maillard conjugate was first allowed to cool-down to room temperature after its formation and then it was purified by centrifugation using centrifugal filter devices for reactant removal.



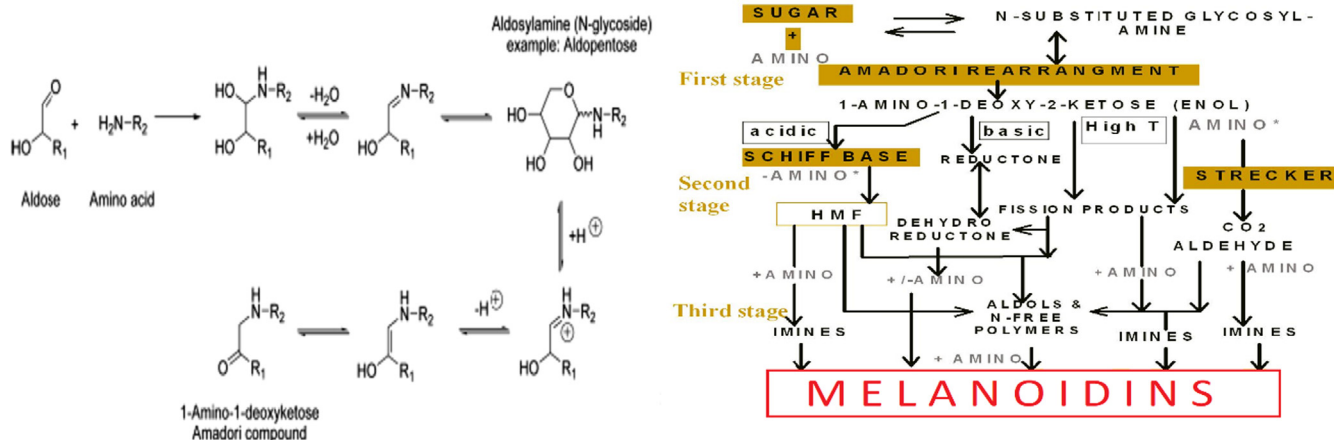


Fig. 5. A schematic diagram of the Maillard reaction with modification from Hodge et al. [97].

In a study by Ferrer et al. the individual lysozyme (14.3 kDa) or dextran (64–76 kDa) molecules not taking part in the dextran-lysozyme Maillard conjugate formation flowed through the membrane (100 kDa molecular weight cutoff) as an ultrafiltrate, while the conjugate was retained on the membrane as a retentate which was collected, freeze-dried and, then stored at 4 °C [99]. In **isoelectric point precipitation**, fractionation of the conjugate can be performed by sedimentation of the protein at its pI. In the study of Markman et al., after the precipitation of the unreacted casein at its isoelectric point, the supernatant containing the Maillard casein–MD (CN–MD) conjugate was found to be soluble at such pH owing to the superior solubility of the saccharide parts at this pH, which was then collected, and freeze-dried. Vitamin D (VD)-ethanolic solution was added to those solutions while vortexing. It is observed that the majority of the VD-containing supernatant conjugates maintained a size less than 30 nm without precipitation, even at the pI of CN at pH 4.6 [100].

Different approaches were attempted for stabilization of Maillard conjugates including thermal gelation, chemical crosslinking, and electrostatic interaction. In thermal gelation, the pH of Maillard conjugate aqueous solution is adjusted to be around its pI and then heated above the denaturation temperature of secondary and tertiary structures of the protein. This heat gelation process causes partial denaturation of the protein followed by protein–protein interactions involving hydrophobic, electrostatic interactions, disulfide-sulfhydryl interchange reactions, and hydrogen bonding with subsequent formation of stable nanogels having a protein-rich core and polysaccharide shell. The increase in the time of heating may lead to further denaturation and aggregation/gelation of protein, inducing higher degree of crosslinking to the nanoparticles.

In the study of Li et al., the pH of the aqueous solution of lysozyme-dextran Maillard conjugate was adjusted to 10.7 (near pI of lysozyme), where the solution was further reacted at 80 °C for 30 min to form the nanogel. While a physical mixture of lysozyme and dextran at pH 10.7 showed aggregation/coagulation upon heating at 80 °C, the solution of lysozyme-dextran Maillard conjugates constituted of the same mixture turned into a homogeneous particulate solution of 200 nm in diameter at the same temperature conditions, indicating the nanogels formation where dextran shell could suppress lysozyme coagulation. The lysozyme-dextran nanogels demonstrated excellent stability as indicated by the unchanged nanogel size either in solution or lyophilized form up to 7 months or even after dilution indicating that the cross-linked structure of the nanogels could hinder the dissociation due to dilution [101].

Another approach is the stabilization of the Maillard conjugate via an electrostatic interaction. Qi et al. prepared BSA–dextran–chitosan nanoparticles through the combination of the ionic interaction between negatively charged BSA (above pI 4.8) and cationic chitosan (pKa 6.2–7.0) as well as the thermal gelation of BSA. Upon heating chitosan

and BSA–dextran Maillard conjugate solutions mixture at 80 °C for 1 h after pH adjustment to 5.6, the molecules of BSA gelate constituting the nanoparticles core while chitosan chains become partly trapped in the core of the nanoparticle as illustrated in Fig. 6. The remaining chitosan and the dextran conjugated to BSA extended in the nanoparticles shell, hence stabilizing them [41].

Chemical crosslinking strategy was also utilized for stabilizing Maillard conjugates via formation of covalent or ionic bonding. Nanoparticles made of the catechin-loaded chitosan–whey protein isolate Maillard conjugate were spontaneously formed by the ionic crosslinking between the positively charged chitosan's amino groups and anionic sodium tripolyphosphate (STP) [102]. Glutaraldehyde was also used to prepare crosslinked ibuprofen-loaded BSA–dextran conjugate nanoparticles via covalent linking of the amino groups of BSA [103]. Similarly, gelatin-dextran conjugates encapsulating tea polyphenols were successfully crosslinked by genipin via the reaction of the aldehyde groups of genipin with the amine groups of gelatin [104].

### 2.2.3. Drug loading mechanisms

Maillard conjugates have been exploited for the loading of both hydrophilic and hydrophobic drugs. **Water soluble drugs** such as ibuprofen [103] and doxorubicin hydrochloride [108] were added to the aqueous BSA–dextran Maillard conjugate solution before pH adjustment and heat gelation process at 80 °C for at least 30–60 min to produce nanogels fixing the drug in the core. Binding of drug with BSA via electrostatic and hydrophobic interactions as well as the gelation of BSA could suppress the drug precipitation. The free unloaded drug was separated from the nanogels by ultrafiltration. DOX has a pKa of 8.2 while the pI of BSA is at pH 4.8. Increasing the pH of the solution from 5.4 to 7.4 facilitated the electrostatic interactions between the positively charged DOX and the negatively charged BSA. Moreover, the uncharged DOX molecules formed at this higher pH can bind with BSA via hydrophobic interactions with the lipid binding domain of BSA [103]. Similar findings were observed with ibuprofen (pKa 5.2–5.6), where drug precipitation did not take place after setting the solution pH to 5.2 at 10 mg/mL BSA concentration and ibuprofen/BSA weight ratio of 0.4 or less via electrostatic and hydrophobic interactions with BSA. However, precipitation occurred when the weight ratio became larger than 0.4. Such behavior could be attributed to either the hydrophobicity of BSA being insufficient for stabilizing the nanocomplexes and/or the saturation of the binding sites in BSA making it unable to accommodate more ibuprofen. To increase the hydrophobicity of BSA and accommodate more ibuprofen, BSA–dextran Maillard conjugates were formulated. The conjugates have prevented precipitation for all weight ratios below 1.6 at pH 5.2 showing that BSA binding sites have not reached saturation [108].

On the other hand, for loading of **water insoluble drugs**, the high



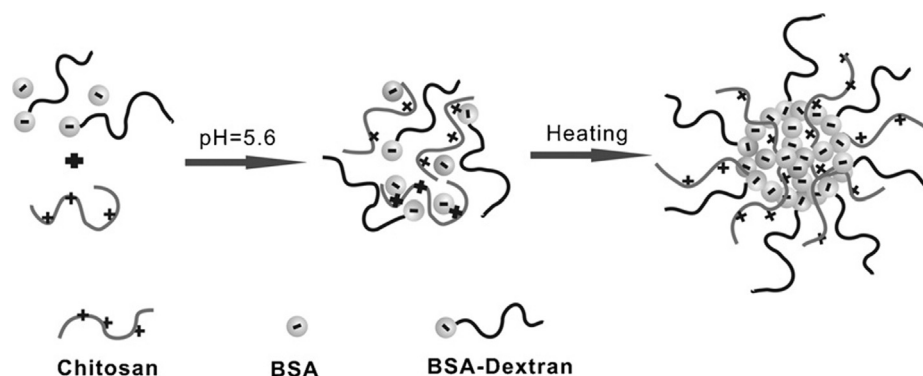


Fig. 6. A schematic diagram showing the formation and the final structure of the hybrid BSA–dextran–chitosan nanoparticles [41].

hydrophobicity of some drugs and nutraceuticals enabled the interaction with the hydrophobic segments of proteins. Particularly, the milk protein, casein is known for its great capacity for encapsulation of hydrophobic drugs within its hydrophobic core [115–118]. Different techniques including solvent evaporation, dialysis or emulsification were used for encapsulation of the water insoluble drug or nutraceuticals into Maillard conjugates. In solvent evaporation method, ethanolic solution of  $\beta$ -carotene was stirred with the aqueous solution of casein-g-dextran conjugate (pH 7.0) for 24 h, followed by solvent evaporation under vacuum at 0 °C. In dialysis method, the mixture of prepared conjugate and  $\beta$ -carotene was dialyzed against a gradually increasing water concentration in water ethanol solvent from 70 to 80 to 90 and then finally reaching 100%. Increasing the percentage of water up to 100%, resulted in formation of particles with a hydrodynamic diameter of 200 nm, which inferred that increasing water concentration was essential for nanoparticles formation. When either dialysis or evaporation method was utilized, water dispersion decreases the solubility of the hydrophobic casein/ $\beta$ -carotene complex and gradually increases the solubility of dextran which lead to subsequent formation of nanoparticles with  $\beta$ -carotene and casein in the core with dextran shell [112]. In emulsification technique, an oily phase of eugenol was emulsified into an aqueous solution of whey protein isolate-maltodextrin conjugates then the emulsion was subjected to spray-drying [98].

#### 2.2.4. Factors affecting characteristics of Maillard conjugates

Different factors such as temperature, time, relative humidity (RH), pH, and reactant protein/polysaccharide molar ratio affect the extent and rate of the Maillard reaction, hence, the nature of the products formed and their functional properties.

##### (a) Maillard reaction time

Analysis of lysozyme-dextran conjugate using SDS-PAGE showed that lysozyme was a single band before the reaction and appearance of a new smear band with much higher molecular weight after the Maillard reaction with dextran, denoting lysozyme-dextran conjugates formation. With increasing time of the reaction, the smear band became more evident and the band of lysozyme became fainter, denoting that more lysozyme-dextran conjugates were formed. Ortho-phthalaldehyde (OPA) assay, which expressed the loss in free amino groups per gram of protein following Maillard reaction, revealed the decrease in free amino groups with increasing reaction time. With a dextran to lysozyme molar ratio of 1:2, about 0.5 mol or more of amino groups was lost after a reaction time of 72 h or longer, indicating some crosslinking and other side reactions taking place in the final stages of the Maillard reaction. To get a grip the Amadori rearrangements in their early stages, the time of Maillard reaction was set as 24 h or less; the reaction products were white and well-dissolved in water, denoting that the side reactions were nominal. In this study, to prepare the conjugates, the

authors selected a reaction time of 18 h, where about 0.3 mol of dextran was linked to 1.0 mol of lysozyme; and lysozyme kept its native-like secondary and tertiary structures. The conjugates formed at different reaction times as mentioned above were utilized for nanogels preparation by adjusting the pH of conjugate solutions to 10.7 followed by heating at 80 °C for 30 min. The intensity (kcounts/sec) and hydrodynamic diameter (nm) decreased whereas the PDI increased with longer reaction times. For instance, as the reaction time increased from 6 to 168 h, the hydrodynamic diameter decreased from 217 to 160 nm, the PDI increased from 0.11 to 0.18, and the intensity decreased 79–32 kcounts/sec. The longer reaction time resulted in more dextran chains linked to the lysozyme; hence stabilizing a larger surface area and resulting in nanogels of smaller sizes. On the other hand, when the time of Maillard reaction exceeded 24 h, crosslinking and other side reactions took place which resulted in aggregate formation [101].

In the study of Pan et al., Casein-g-dextran Maillard conjugate was fabricated after a Maillard reaction time of 8 or 20 h with casein: dextran molar ratio of 1:8 and pH adjusted to 7.0 (38). Similarly, in the study of Hiller et al., conjugates were prepared with reaction times of 4, 6, or 8 h, so controlling the reaction in its early stages; the Amadori rearrangements, without significant advancement of the Maillard reaction towards melanoidin formation [119].

##### (b) Molecular weight and molar ratio

Li et al. studied the effect of different dextran molar ratios (1:8, 1:4, 1:2, 1:1, 2:1, 4:1, and 8:1) and molecular weights (10,000, 35,000, and 62,000) in the formation of nanohybrids with lysozyme. As the dextran molar ratio and molecular weight were increased, a reduction of the nanogel size with more homogeneity (low PDI) was observed. This was attributed to the increased hydrophilicity endowed upon the nanogel by dextran which stabilized a larger surface area as a result, producing a smaller size. Using dextran with molecular weights of 10,000 and 35,000, aggregates appeared at low molar ratios which indicated the absence of enough hydrophilicity to prevent aggregation. However, using a higher molecular weight of 62000, a nanosize of 140–210 nm with a PDI of 0.1 was obtained for the molar ratio range 1:8–2:1. Further increase in the molar ratio to 4:1 or 8:1, produced nanogel with higher PDI and lower intensity indicating that too much of hydrophilicity disturbs the formation of the nanogel. Thus, a molecular weight of 62,000 with a molar ratio of 1:2 was selected as the optimum one [101].

Different molar ratios of maltodextrin:casein (10, 20, 40, and 80) were used in the formation of Maillard nanohybrids and their effect on the conjugation efficiency was studied. Using OPA assay, a maximum of 8–9 lysine residues from a total of 13.6 lysine residues in casein were conjugated to maltodextrin producing a conjugation efficiency of 62% at a molar ratio of 40. There was no further increase in the conjugation efficiency by increasing the molar ratio to 80, which could be attributed to two main factors. The first of which is the steric hindrance produced

by the conjugated maltodextrin preventing the approach of any further maltodextrin molecules. The second attribute could be the phase separation due to the thermodynamic instability between the two polymers especially during freeze-drying; owing to the effect of freeze-concentration. Both attributes diminished the contact between the two polymers affecting the conjugation efficiency. In an attempt to possibly increase the conjugation efficiency, freeze drying could be conducted by quench freezing of the polymer solution under liquid nitrogen [100].

#### (c) Heating temperature and time in the second heating process

The lysozyme denaturation temperatures are 75 and 60 °C at pHs of 7.0 and 10.3, respectively. Therefore, to prepare the nanogels, Li et al. heated the dextran-lysozyme conjugate solutions for 30 min at 80 °C. After 10 min of heating, the change of turbidity at 500 nm absorbance levelled off indicated that the nanogels have been fabricated in the first 10 min of the process of heating. Circular dichroism spectra showed that the lysozyme's secondary and tertiary structures in the nanogels were vanished, indicating the denaturation of the lysozyme molecules in the nanogels [101].

#### (d) pH and polymer concentration in the second heating process

It was found by Li et al. that by increasing the pH from 9.5 to 10.5, the size and intensity of the formed dextran-lysozyme nanohybrids increased while the PDI decreased indicating an increase in homogeneity. This could be attributed to the decrease in charge of lysozyme as the pH approached its pI of 10.7, thus decreasing the electrostatic repulsion. A balance between the hydrophobic association and electrostatic repulsion is achieved in this process of gelation. When the pH decreases from 10.5 to 9.5, lysozyme carries more positive charge which makes the molecules apart from each other; unfavouring nanogel formation. Regarding lysozyme concentration, a higher concentration favours nanogel formation overcoming the electrostatic repulsion between lysozyme molecules. Increasing the concentration from 1 to 10 mg/ml at pH 9.5 increased the conjugation efficiency from 55 to 100% [101]. In another study, casein-g-dextran copolymer was found to have a pH-dependent behaviour, where no particles were formed over a broad range of pH except at the pI of casein (pH 4.6). A hydrodynamic diameter of 80 nm was obtained at a pH of 4.6; however, no peak was obtained at higher or lower pH values. These results are in line with what Li et al. findings indicating that the charge endowed upon casein at higher or lower pH values caused an electrostatic repulsion between casein molecules preventing the formation of nanoparticles. Moreover, the hydrophilicity of dextran makes the copolymer soluble in aqueous solutions [112].

### 2.3. Electrospinning

Although the term “electrospinning” recently appeared in 1994 which stands for “electrostatic spinning”, electrospinning as a process dates way back to 1934 when Formulas started patenting the apparatus and the process of filament production using an electric field. Electrospinning is the uniaxial stretching of a viscoelastic jet of a charged polymer solution under the effect of an electric field [120,121]. The process relies on three fundamental stages; (1) the formation and the extension of the jet, (2) the formation of a whipping/bending instability and further elongation of the jet, and (3) the solidification of the formed nanofibers [122].

To fully understand the process and the parameters upon which the characteristics of the formed nanofibers vary, a schematic diagram of the apparatus is shown in Fig. 7A. The apparatus consists of three main partitions; (1) a polymer reservoir (a capillary tube) with a nozzle, (2) a high voltage supplier, and (3) a collector. First, an electric field is applied to the polymer reservoir which causes mutual charge repulsion and ions to accumulate in the solution droplet at the tip of the nozzle.

The droplet starts then to act as an electrode which only gets held back from falling by its surface tension. As the voltage starts to increase, the droplet elongates taking the shape of a hyperbolic cone, called the Taylor cone. At a certain point, the electric force overcomes the surface tension and drives a thin jet to the nearest electrode of an opposite polarity; the collector. In many cases, the collector is just grounded as shown in Fig. 7. Although most frequently a solvent is used to dissolve the polymer which subsequently evaporates during the jet ejection in the air, electrospinning could be performed without solvents through using a polymer melt in a vacuum chamber, which in both cases, leave nanofibers in the form of a non-woven web on the collector [121,122].

Regarding protein-polysaccharide nanohybrids, few have exploited them in the formation of nanofibers by electrospinning; a summary of which is presented in Table 3. In an attempt to electrospin egg albumin, cellulose acetate was used by Wongsasulak et al. to form an electrospinnable protein-polysaccharide hybrid nanofibers. The globular structure of egg albumin lacked the sufficient entanglement and the low surface tension to be electrospinnable. The hybridization of egg albumin with cellulose acetate and the addition of tween 80 have decreased both its surface tension and electrical conductivity which in turn facilitated its electrospinning [124]. In another study, the antimicrobial property of chitosan was to be exploited in the formation of a biocidal nanofiber mat. However, chitosan has been long known for its difficulty to electrospin due to its high surface tension and viscosity. By hybridization with zein, chitosan-zein hybrid system has been rendered electrospinnable up to 10 wt.% chitosan; after which electro-spraying phenomena started to appear where small droplets were sprayed instead of a continuous jet. As shown in Fig. 7B, more beads start to appear in the structure of nanofibers with increasing concentrations of chitosan. This could be attributed to the high molecular weight of chitosan (50 to 190 KDa) which in turn increases the viscosity and surface tension of the formed solution causing the formation of beaded fibers. Zein also rendered the formed nanofibers water-resistant which is desirable for moisture contact applications [123]. Similarly, silver nanoparticles-microcrystalline chitosan composites could be electrospun by the use of gelatin (10% wt/wt) for wound dressing applications [125].

#### 2.3.1. Factors affecting characteristics of electrospun nanofibers

Factors affecting the electrospinning process and the characteristics of the formed protein-polysaccharide hybrid nanofibers could be divided into: (a) solution properties, (b) apparatus parameters, and (c) environmental factors.

##### (a) Solution properties

Solution properties such as the concentration, viscosity, surface tension, or the molecular weight of the used polymers have great impact on the electrospinnability and the morphology of the formed nanofibers. It has been observed that electrospinning of a polymer solution usually can not occur below a molecular weight of 10,000 g/mole which could be explained by the lack of sufficient polymer entanglement needed for electrospinning. Below such molecular weight, the electro-spraying phenomenon has been observed. Another important remark has to be made to the molecular structure of the polymer which also affects the entanglement of the polymeric chains. Branched globular polymers are difficult to electrospin and need to be in higher concentrations or hybridized with another polymer in order to render it electrospinnable as has been observed with Wongsasulak et al. in the electrospinning of egg albumin [124].

Another important factor that affects the morphology of the formed nanofibers is the polymer solution concentration. As the polymer concentration increases, the nanofiber diameter increases and bead formation decreases. The addition of salt has been observed to decrease the diameter of the formed fibers. This could be ascribed to the increase in the charge density of the solution that would increase the elongation

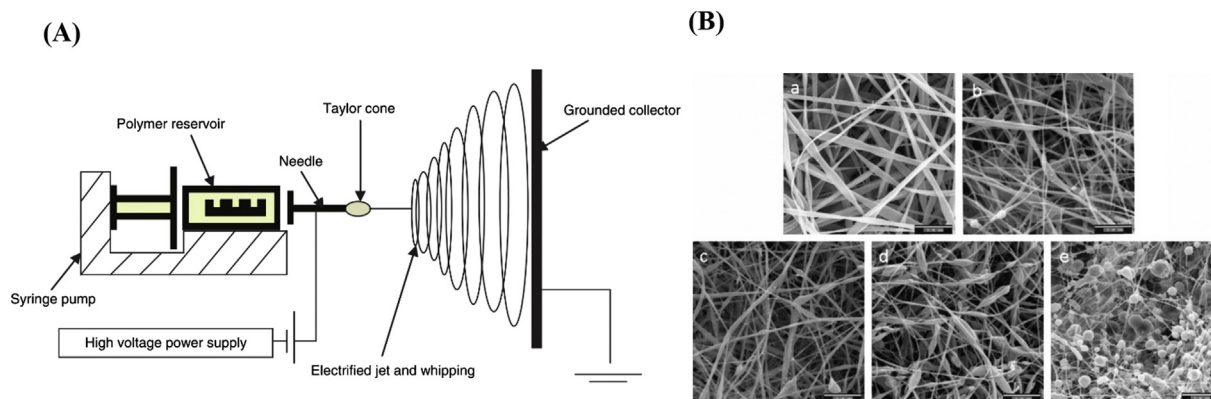


**Fig. 7.** (A) A schematic diagram of the electrospinning apparatus setup [122], (B) Scanning electron microscope images of zein-chitosan nanofibers made with increasing concentrations of chitosan: (a) 0 wt.% chitosan (pure zein), (b) 1 wt.% chitosan, (c) 3 wt.% chitosan (d) 5 wt.% chitosan (e) 10 wt.% chitosan [123].

**Table 3**  
Protein-polysaccharide nanohybrids prepared by electrospinning.

Protein-Polysaccharide	Drug	Key Outcomes	Ref.
Egg albumin-Cellulose acetate	–	Edible hybrid nanofibers were formulated with potential to act as carriers for drugs or nutraceuticals.	[124]
Gelatin-MCCh	Silver NPs	Hybrid nanofibers encapsulating silver NPs were prepared for wound dressing applications.	[125]
Zein-Chitosan	–	An intrinsic antibacterial activity for the nanohybrid was observed.	[123]

**MCCh:** Microcrystalline chitosan, **NPs:** Nanoparticles.

forces acting on the solution causing thinner more straight fibers to form. Viscosity is another important factor that needs to be taken in consideration. A certain critical range of viscosity for each polymer or hybrid of polymers allows electrospinning, above which the solution cohesiveness causes jet instability and below which the jet breaks into small droplets. Thus, in electrospinning, the concentration needs to be maintained above a critical point and below a certain viscosity that would allow the process to occur. Lastly, as explained previously, the surface tension needs to be low enough for the electric forces to overcome it and allow a thin jet to be formed. An emphasis on the impact of surface tension and viscosity has been made by Torres-Giner et al. in the electrospinning of zein-chitosan hybrid. Increasing chitosan concentration from up to 10% wt/wt in the hybrid has caused a significant increase of surface tension from 44.8 to 63.1 mN/m and a significant increase in viscosity from 118.5 to 475.1 cP which made it impossible to electrospin the hybrid solution at chitosan concentrations above 10% [123].

With regards to the polymers' solvent, generally a solvent with low surface tension that evaporates rapidly is more preferred, however, this is not always the case. Acetone with a surface tension of 23.7 dyne/cm was found to produce short fibres of cellulose acetate with 1  $\mu$ m size and beaded morphology. However, when a mixture with dimethylacetamide (surface tension of 32.4 dyne/cm) was used, a uniform size of 700 nm with no beads was obtained [126].

#### (b) Apparatus parameters

Many apparatus-related parameters affect the characteristics of the formed nanofibers including voltage, needle diameter, and distance. There has been some discrepancies about the effect of voltage on the diameter of the obtained fibers. Electrospinning of polyurethane solution showed an increase in diameter with increased voltage [127] which was the reverse to that observed upon electrospinning of poly (lactic-co-glycolic acid) (PLGA) [128]. Needle diameter is another

parameter that affects the size of the formed nanofibers. When smaller needles are used, the diameter of the formed nanofibers decreases due to a smaller Taylor cone base and so a thinner jet to be produced. Distance between the needle tip and the collector screen is another important parameter that needs to be controlled, since shorter distances do not allow for complete solvent evaporation and so sticky beaded fibres get formed [122].

#### (c) Environmental factors

One of the most important environmental factors that affect the electrospinning process is the temperature. Increased solution temperature would result in decreased viscosity which may affect the morphology of the formed fibers. Although a higher concentration of polyurethane (21.2 wt.%) was used at 70 °C, the diameter of the formed fibers was smaller and more uniform than that produced at room temperature and a lower concentration (12.8 wt.%) [127]. Humidity is another important factor that affects the morphology of the formed fibers as the presence of humidity induces the formation of pores in the nanofibers [122].

Comparing the three techniques used for preparation of protein-polysaccharide nanohybrids, the electrostatic complexation is a mild technique based on the ionic interaction between oppositely charged proteins and polysaccharides. Therefore, the physicochemical properties of those mild complexes can be easily tailored by modulating pH or ionic strength. Moreover, various drug categories can be physically encapsulated within the complexes that can be further stabilized via crosslinking approach. On the other hand, chemical conjugation requires specific chemical linkers, reducing end polysaccharides, or relatively harsh conditions (such as alkaline pH and heating at high temperature). Although more stable nanohybrids can be generated, many sensitive drugs cannot withstand those harsh conditions. Electrospinning seems to be a promising technique for fabrication of protein-polysaccharide nanohybrids in the form of nanofibers. However, some limitations exist concerning the nature of polymers (e.g. being non-electrospinnable) or the apparatus parameters. Therefore, more optimization of the preparation conditions is required to include more proteins and polysaccharides and elucidate more advanced applications of the resultant electrospun nanofibers.

### 3. Implications of protein-polysaccharide nanohybrids

#### 3.1. Enhanced colloidal stability

It would be of no value to obtain a nanohybrid system without assuring its stability to maintain such nanosize whether on-shelf or *in vivo* till reaching its target site. In a study developed by X. Pan et al., the impact of dilution on the stability of casein-dextran Maillard conjugate

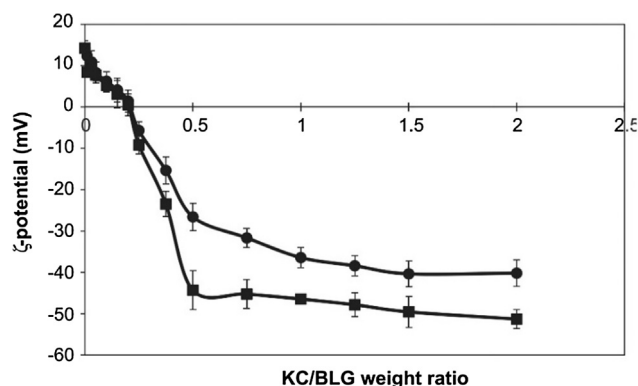


Fig. 8. Change in zeta potential of  $\alpha$ -carrageenan- $\beta$ -Lg nanohybrid upon increasing concentration of  $\alpha$ -carrageenan; intact (●) and ultrasonicated (■) [57].

micelles was investigated. The casein-dextran nanohybrids maintained their nanometric size of 80 nm without disassociation after dilution to 10 mg/L indicating their thermodynamic stability. This dissociation concentration could be further reduced to 1 mg/L after incorporation of  $\beta$ -carotene within the casein core of the micelles. This could be explained by the strong hydrophobicity induced by  $\beta$ -carotene preventing the copolymer system from dissociation in water. Compared to the dissociation concentration of some copolymers such as polylactic acid-b-poly(ethylene oxide) (35 mg/L) and poly( $\beta$ -benzyl-L-aspartate)-b-poly(ethylene oxide) (5–18 mg/L), casein-dextran copolymer was at least as stable or even showed higher stability against dilution. Moreover, the nanohybrids showed stability over a broad range of pH (2.0–12.0) and over a long period of storage as long as 91 days [111,112].

In another study, aggregates of  $\beta$ -Lg were formed at pH 4–5 due to strong self-association of the protein around its isoelectric point (pI). However, there was a significant decrease in the pH that caused aggregation of  $\beta$ -Lg in the presence of alginate which could be attributed to the stabilization effect imparted by alginate presumably due to an increase in both, electrostatic repulsion and steric hindrance of the nanohybrids [58]. A similar stabilizing effect of  $\beta$ -Lg to aggregation was induced by  $\alpha$ -carrageenan as revealed by the increasing negative zeta potential of the nanohybrids upon increasing concentration of  $\alpha$ -carrageenan as shown in Fig. 8 [57].

### 3.2. Enhanced targeting efficacy

Certain proteins and polysaccharides such as albumin and hyaluronic acid (HA) could target anti-cancer drugs to certain tumors overexpressing their receptors such as SPARC (Secreted Protein, Acidic and Rich in Cysteine) and CD44 receptors, respectively [129]. Albumin-coated Cellax, which is a docetaxel-carboxymethylcellulose (DTX-CMC) conjugate, had enhanced the cellular uptake by more than 2-folds in SPARC-positive 4T1 cells in comparison to uncoated Cellax. However, there was no significant difference in cellular uptake between albumin-coated and uncoated Cellax when using SPARC-negative MDA-MB-231 cells which clearly demonstrates the importance of SPARC receptors in mediating the internalization of albumin-coated nanohybrids. *In vivo*, the expression level of SPARC receptors showed a positive linear correlation with the level of inhibition of tumor growth. Moreover, prior to this active targeting mechanism, the nanosize of the hybrids played a vital role in targeting the leaky vasculature of tumor blood vessels mediated by enhanced permeability and retention (EPR) effect. An illustration of these targeting mechanisms is shown in Fig. 9 [36].

CD44 receptors are known for their overexpression on some cancerous cells in addition to chondrocytes which could serve as a viable target for treating cancer and osteoarthritis. However, the high

clearance rate by the synovium which necessitates repeated injections that might cause infection and disability. Therefore, Chen et al. developed HA-coated BSA nanohybrids for chondrocyte-targeted drug delivery. HA-coated brucine-loaded BSA nanohybrids have shown a 2- and 4-fold increase in uptake by chondrocytes after 1 h in comparison to BSA nanoparticles and brucine solution, respectively. Upon addition of free HA, a significant inhibition in cellular uptake of HA-coated nanohybrids was observed but not with uncoated BSA nanoparticles indicating the critical role of HA interaction with CD44 receptors for the internalization of the nanohybrids. When intra-articularly injected into rats, the near infrared dye (NIRD)-loaded HA-coated BSA nanohybrids have shown little distribution into systemic circulation and continued to show fluorescence from joints for more than 14 days which clearly indicated their prolonged retention [130].

Protamine is a cationic polypeptide that forms electrostatic nano-complexes with anionic polysaccharides [131,132]. CD44 receptors overexpressed on triple-negative breast cancer cells (MDA-MB-231) were successfully targeted by miR-34a-loaded HA-protamine nanohybrid complexes via receptor-mediated endocytosis. *In vivo*, smaller tumor sizes and higher miRNA expression levels (200-folds) were achieved [80].

Proteins and polysaccharides, not only they inherently target their overexpressed receptors in certain tissues, but also provide functionalities ( $-\text{OH}$ ,  $-\text{COOH}$ ,  $-\text{NH}_2$ , and  $-\text{SH}$ ) that aid ligand attachment for targeting purposes [133]. In a study reported by Martínez et al., folic acid-albumin conjugate was formed via a carbodiimide chemistry which was then used to form albumin-alginate nanohybrids as tamoxifen carriers for breast cancer treatment. When the BSA to alginate ratio was 50:50 (B-50-50), 3.5-folds higher cellular uptake into MCF-7 cells after 24 hr and hence higher cytotoxicity in comparison to B-30-70 which was attributed to the provision of more folate to interact with folate receptors overexpressed on MCF-7 cells. *In vivo*, higher tamoxifen tumor accumulation and tumor volume regression was also observed for folate-targeted nanohybrids in comparison to non-targeted ones. Similar enhanced targeting was observed with folate-conjugated DOX-loaded BSA-dextran nanohybrids in hepatoma H22-bearing mice [105].

Another targeting moiety, retinoic acid, was exploited for conjugation with abundant amines on chitosan via carbodiimide chemistry. The conjugate was then exploited to form chitosan-albumin nanohybrids loaded with DOX for targeting hepatocellular carcinoma. Targeted nanohybrids have shown a significant reduction in the  $\text{IC}_{50}$  values of DOX in comparison to non-targeted nanohybrids or free DOX, respectively. Such enhancement in activity was attributed to the receptor-mediated internalization of the nanohybrids by retinoic acid [29].

### 3.3. Enhanced biocompatibility

One of the prerequisites for the clinical translation of any nano-system is the avoidance of non-target cell interactions and opsonization by fibronectin, complement proteins, and immunoglobulins to avoid phagocytosis and in order to ultimately increase the chances for target site interaction. In a study developed by Ferrer et al., rhodamine-labelled dextran-lysozyme nanogels showed “stealth” properties against phagocytosis. The dextran shell increased the hydrophilicity of nanohybrids and sterically hindered their opsonisation thus reducing their uptake by the MPSF. After 24 hr of exposure, a slow uptake with only 41.1% of THP-1 phagocytic cells containing the nanohybrids was stably transduced with green fluorescent protein (GFP) even in the presence of 10% serum in the culture medium (19).

Several studies have reported that albumin showed an enhancement in the biocompatibility of chitosan [33,34,37]. Albumin-chitosan nanohybrids showed lower toxicity than chitosan nanoparticles against HeLa cells, H460 and A549 cells which was attributed to the lower positive charge induced by albumin on the nanohybrids, being +28.9 mV, in comparison to +53.9 for their chitosan counterparts (Fig. 10) [34].



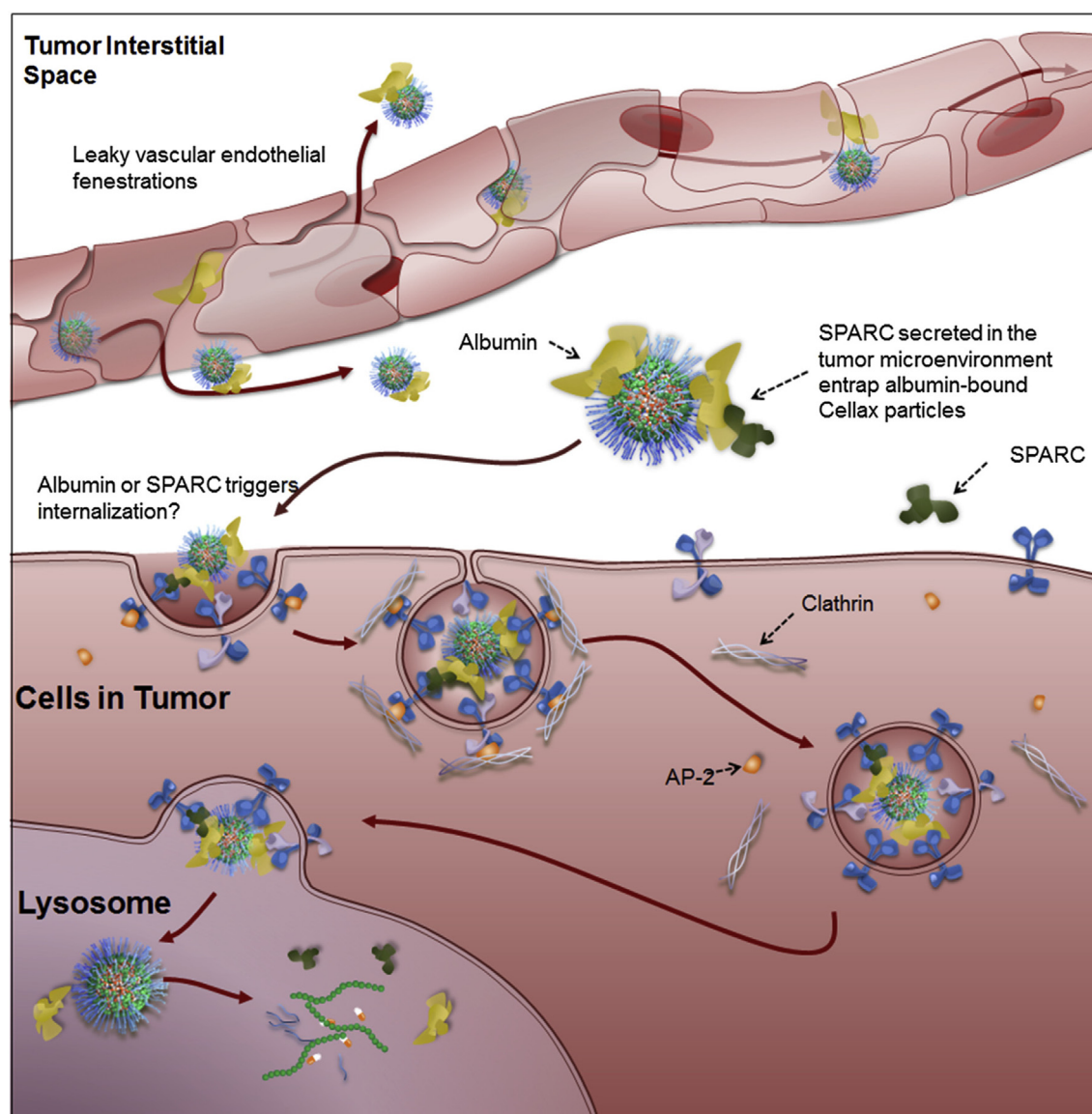


Fig. 9. Mechanisms proposed for the targeting of albumin-coated Cellax to tumor cells [36].

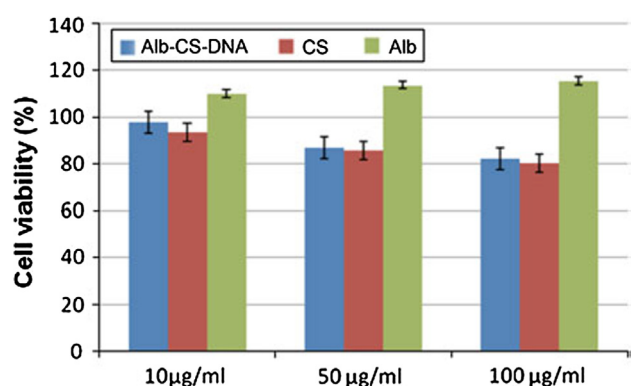


Fig. 10. MTT assay on HeLa cells at three different concentrations of the Albumin-Chitosan nanohybrid (Blue), Chitosan (Red), and Albumin (Green) [34]. (For interpretation of the references to colour in this figure legend, the reader is referred to the web version of this article.)

### 3.4. Modulated release profile

Protein-polysaccharide nanohybrids showed sustained release of drugs via different mechanisms. In a study by Chen et al., 56–60% curcumin was released from soy polysaccharide-soy protein nanohybrids at pH 4 or 7 in comparison to ~90% from soy protein nanoparticles after 20 hr. This sustained release could be ascribed to the core-shell structure of the nanohybrids resulting in a longer distance for curcumin to pass [63]. On another avenue, the hydrogen bonding interaction between EGCG and casein, and the protection of casein against gastric digestion by the dextran shell seem to be the possible mechanisms responsible for sustained release of EGCG from dextran-casein nanohybrids [110].

Besides controlled release, protein-polysaccharide nanohybrids can also induce stimuli-responsive drug release. A pH-sensitive curcumin release was observed upon incorporation into cationized gelatin-sodium alginate nanohybrids. 87% curcumin was released at pH 5 compared to ~64% at pH 7.4 after 48 hr. The charge density on sodium alginate decreases as acidity increases due to the protonation of its carboxylic groups, thus disrupting the electrostatic complex and releasing curcumin. Such pH-sensitive release is desired in targeting the acidic



tumour microenvironment where accumulation of the acidic metabolic products favours the nanohybrid disruption and curcumin release [47]. Oppositely, a slower release of rutin (20%) from pectin-casein nanohybrids was observed in simulated gastric fluid (pH 2) in the first 2 hr followed by a faster release of 80% in simulated intestinal fluid (pH 7) after 4 hr. While the pectin shell protected casein core from gastric enzymes, it was dissociated as the pH increased from 2 to 7 due to the loss of the electrostatic interaction between the negative charge of pectin's carboxylic groups and the positive charge of casein's protonated amines. Surpassing its pI of 4.6, the casein charge was inverted from positive to negative through the deprotonation of its carboxylic groups, thus repelling the similarly-charged pectin and increasing rutin release [77].

Ionic strength can be also exploited as the stimulus that trigger the cargo release as in the case of  $\beta$ -lactamase-loaded alginate-lysozyme nanohybrids. Increasing the ionic strength by increasing NaCl concentration caused a decrease in light scattering till complete fading at a concentration of 150 mM. Accompanied with such decrease in scattering, an increase in  $\beta$ -lactamase activity, becoming 4-fold at 150 mM concentration. These results demonstrated the screening effect of the electrolyte on the electrostatic interaction between alginate and lysozyme overcoming it completely and causing its dissociation at 150 mM concentration [75].

### 3.5. Enhanced drug stability

Encapsulation of sensitive drugs within the matrix of protein-polysaccharide nanohybrids was found to improve their stability. Since clinical application of curcumin was hampered by its high instability in neutral/basic conditions and limited aqueous solubility, extensive research was done curcumin and was loaded into different protein-polysaccharide nanohybrid systems including i-carrageenan-albumin [38],  $\alpha$ -lactalbumin-dextran [114], and soy polysaccharide-soy protein [63] nanohybrids to overcome these instabilities. Its encapsulation within i-carrageenan-albumin nanohybrids reduced its decomposition to 16, 12, and 10% after 1000 min of incubation at pH 7 upon using increasing concentrations of i-carrageenan of 0.5, 1.0, and 1.5 g/L, respectively. In comparison, 53 and 24% of curcumin was decomposed for free curcumin and BSA nanoparticles, respectively. Moreover, loading of curcumin into  $\alpha$ -lactalbumin-dextran nanohybrids enhanced its DPPH (2,2-diphenyl-1-picryl-hydrazil) scavenging ability to 64.1% compared to only 25.4% for free curcumin. Even the thermal stability of curcumin has been enhanced where 14.5% of free curcumin was retained after 4 hr of thermal treatment at 95 °C in comparison to 29.1 and 35.5% for  $\alpha$ -lactalbumin nanoparticles and  $\alpha$ -lactalbumin-dextran nanohybrids, respectively. The stabilizing mechanisms of nanohybrids include stronger hydrophobic binding of curcumin to the nanohybrids with high binding constant ( $K_b$ ) which in turn decreases the interaction with water and suppresses the proton donation from the activated carbon in the ketone group causing curcumin degradation [38].

The incorporation of folic acid into soy polysaccharide-soy protein nanohybrids protected it from photodegradation that breaks the C<sub>9</sub>–N<sub>10</sub> bond yielding pteridine and (p-aminobenzoyl)-l-glutamic acid. UV irradiation of free folic acid caused a 100% degradation in compared to only 17% for soy polysaccharide-soy protein nanohybrids. Such result could be ascribed to the prevention of interaction between folic acid and dissolved oxygen during UV irradiation through the intrinsic ability of the soy proteins and polysaccharides to react with oxygen [64]. Also, the immobilization of vitamin D in the hydrophobic core of casein-maltodextrin nanohybrids caused a marked reduction of its reactivity. As a result, 90% of the vitamin survived gastric-like conditions comparison to 75% and 30% for the casein-maltodextrin mixture and the free vitamin, respectively. Another important stabilization mechanism involves the products of Maillard reaction itself which conferred an antioxidant activity [100]. The protection of EGCG against oxidation was enabled by its incorporation within the matrix of

dextran-casein [110] and i-carrageenan-albumin [31] nanohybrids by preventing the destruction of its galloyl group. This was ascribed to the strong hydrophobic binding of EGCG with the hydrophobic pockets of albumin, thus effectively retarding the contact between its galloyl groups and water [31]. Similarly, the strong binding of quercetagenin to the hydrophobic pockets in soy protein- $\alpha$ -carrageenan nanohybrids enhanced its stability which was indicated by the longer half-life in comparison to the free form, soy protein, or  $\alpha$ -carrageenan nanoparticles [67].

### 3.6. Reduced drug toxicity

Chemotherapeutic drugs are suffering from severe toxicity to normal tissues. Therefore, some anti-cancer drugs were incorporated into protein-polysaccharide nanohybrids with the aim of reducing their toxicity. Encapsulation of DOX into albumin-dextran nanohybrids showed a marked increase in the average body weight (from 20.7 to 24.4 g after 7 days) and 35.4% increase in survival rate of hepatoma H22 bearing-mice compared to free doxorubicin (body weight changed from 20.7 to 16.1 g) with only 1.24% increase of survival rate. Moreover, the nanohybrids allowed an increase in doxorubicin dose to 8 mg/Kg which further increased the survival rate to 55.7%. These results implied the enhancement in the safety profile of doxorubicin endowed by the nanohybrids which could be attributed to the better retention, enhanced targeting, and extended release of doxorubicin [108]. Further attachment of folic acid as a targeting ligand to the BSA-dextran nanohybrids caused a higher increase in body weight and survival rate which confirms that better targeting together with a better release profile are the main factors for enhancing the toxicity profile of doxorubicin [105]. Similar conclusions were drawn from doxorubicin loading into albumin-dextran-chitosan nanohybrids [41].

### 3.7. Intrinsic activity

Novel zein-chitosan hybrid nanofibers electrospun from trifluoroacetic acid (TFA) solutions showed intrinsic antimicrobial activity resulting in complete death of *S. aureus* in a period of 24 hr. The antimicrobial activity of nanofibers was not caused by the acidity of TFA but rather to the intrinsic antimicrobial activity of chitosan. This was proved when control TFA solutions showed no activity upon titration to the same pH of chitosan-containing nanofibers. The biocidal activity of chitosan could be attributed to the release of protonated glucosamine fractions which bind the DNA and subsequently inhibit RNA and protein synthesis, or the formation of an impervious layer on bacterial cells causing their death [123].

Based on the well-known prebiotic effects of inulin, Ha et al. tested whether the whey protein isolate-inulin nanohybrids will preserve the prebiotic effects of inulin on *L. acidophilus* ATCC 43121. As shown in Fig. 11, 1% whey protein isolate showed a higher number of viable cells in comparison to negative control (minimum media), however, this was significantly lower than the positive control (1% inulin). The

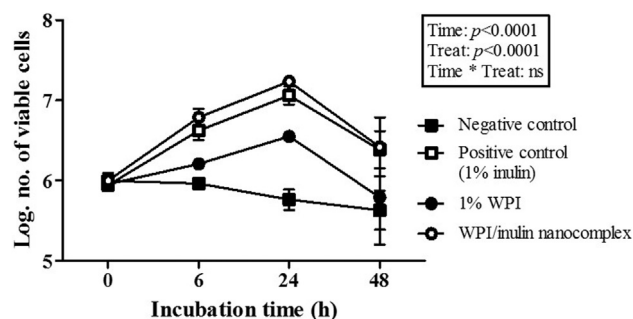


Fig. 11. The potential prebiotic effect of different treatments on the viability of *L. acidophilus* ATCC 43121 [61].

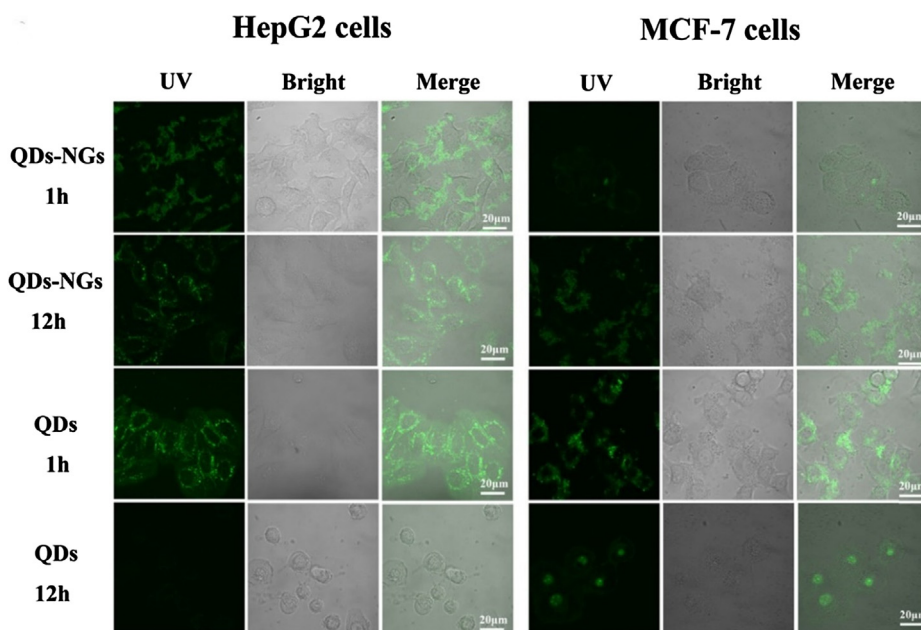


Fig. 12. The fluorescence of free QDs (QDs) and the QD-loaded nanohybrid system (QDs-NGs) on HepG2 and MCF-7 cell lines after 1 and 12 hr of incubation [73].

nanohybrids, however, showed similar viability to the positive control indicating that inulin, as reported, is the component responsible for the prebiotic properties and that the nanohybrid did not quench such property. Such nanohybrids can be used as a delivery system as well as conferring an intrinsic prebiotic activity [61].

### 3.8. Theranostic applications

In recent years, polymeric-inorganic nanohybrids have been emerged for drug delivery, tissue engineering and theranostic applications [134,135]. Theranostic nanohybrids based on lysozyme-carboxymethylcellulose complexes were used for the co-delivery of the therapeutic agent, methotrexate, and the imaging agent, CdTe quantum dots (QDs). The nanohybrids maintained their fluorescence in HepG2 and MCF-7 cells for longer time showing higher fluorescence after 12 hr of incubation compared to free QDs (Fig. 12). This could be attributed to the protective effect endowed upon QDs by the nanohybrids preventing their quick degradation. Moreover, the nanohybrids showed enhanced anti-cancer activity in comparison to free methotrexate. The ability of nanohybrids to reduce the p-glycoprotein efflux mechanism as well as the gradual drug release over a prolonged period contributed to the enhanced efficacy compared to the free drug. Moreover, the nanohybrids enhanced the biocompatibility of the QDs reducing their cytotoxicity [73].

### 3.9. Improved transparency for food applications

For food application purposes, the visual appearance of the nanosystem is of utmost importance where transparent systems are needed for enhancement of the sensorial characteristics of the final product especially for beverages. However, protein nanosystems aggregate and become turbid when the pH is near their pI where the electrostatic repulsion is weakened especially at high ionic strength. Moreover, the nanosystem should be stable enough to allow the mandate thermal treatment of food for the prevention of spoilage by pathogenic microorganisms. In a study by Shah et al., whey protein isolate-maltodextrin nanohybrids showed enhanced transparency for the encapsulation of eugenol in comparison to the corresponding mixture. A whey protein isolate-maltodextrin mass ratio of 1:2 showed lower turbidity before or after heating than mass ratios of 1:1 or 2:1. This was attributed to the

higher conjugation efficiency at higher maltodextrin concentration resulting in lower particle size, lower scattering of light, and enhanced transparency. As shown in Fig. 13, the non-conjugated whey protein isolate-maltodextrin mixture was more turbid than the nanohybrids especially at pH 5 which is near the pI of the most abundant whey protein,  $\beta$ -lactoglobulin (pI = 5.2), which led to its aggregation. Moreover, eugenol encapsulation decreased the dispersibility of the mixture leading to the formation of more translucent samples. Similar observation was seen after heating which could be attributed to the increase in the size of the mixture yielding more turbid samples in comparison to a decrease in the size of the nanohybrids after heating yielding more transparent ones [98]. Similar results were obtained by encapsulation of vitamin D,  $\omega$ -3 fatty acids and rutin into casein-maltodextrin [100],  $\beta$ -lactoglobulin-pectin [53] and casein-pectin [77] nanohybrids showing enhanced transparency.

### 3.10. Miscellaneous applications

#### 3.10.1. Enhanced oral bioavailability

Numerous approaches have been exploited to improve the oral bioavailability of drugs such as nanoencapsulation, phospholipid complexation and solid dispersions [136–139]. Particularly, lots of research have been made to overcome the impediments standing against the oral delivery of protein drugs such as insulin. In a study by Lopes et al., albumin/chitosan-coated alginate/dextran sulfate nanohybrids have been developed to enhance the oral bioavailability of insulin. In simulated gastric fluid (pH = 1.2), 35% of insulin was released from the nanohybrids after 2 hr in comparison to 80% for free insulin which preserved insulin from degradation by gastric proteases. The retention of insulin by the nanohybrids could be attributed to the high positive charge conferred by insulin at this acidic environment enhancing its interaction with the alginate/dextran sulfate core. Moreover, the calcium in simulated gastric fluid crosslinked the alginate causing a sol-gel transition, thus making insulin release more of a cumbersome. However, a shift to intestinal conditions (pH = 5.5) caused a complete release of insulin to 100% from the nanohybrids while maintaining its solubility. This in contrast to free insulin which precipitated completely during such shift that could be attributed to the rapid release of insulin and its accumulation at a pH near its pI making it uncharged. Beside this stabilizing effect, the nanohybrids enhanced the interaction with

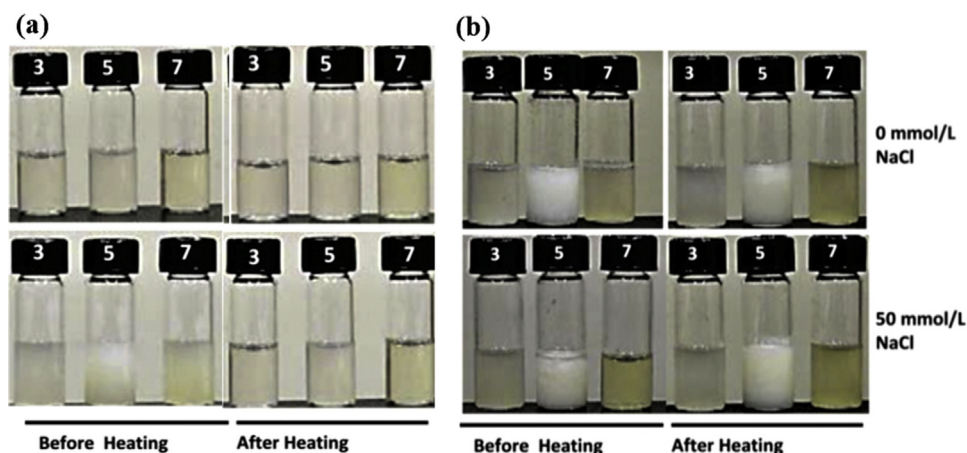


Fig. 13. Photographs of whey protein isolate-maltodextrin nanohybrids (a) and mixture (b) at three different pHs (3, 5, and 7) and at two different NaCl concentrations (0 mmol/L and 50 mmol/L) before and after heat treatments [98].

Caco-2:HT29-MTX co-cultures and hence demonstrated higher apparent permeability in both intestinal (pH = 5.5) and colonic conditions (pH 7.4) than free insulin. This could be attributed to chitosan which beside its mucoadhesive properties, its positive charge enhances the interaction with the negatively charged proteoglycans on the cellular surfaces. All in all, the ability of the nanohybrids to protect insulin from degradation and improve its intestinal permeation would definitely enhance its oral bioavailability [37].

In another study, the stability and bioavailability of curcumin has been enhanced via its encapsulation into ovalbumin-dextran nanohybrids. The nanohybrids protected > 90% of curcumin after simulated gastrointestinal digestion in comparison to 74.22 and 56.17% for ovalbumin nanoparticles and free curcumin, respectively. This simply could be attributed to the physical barrier provided by the nanohybrids preventing the contact of curcumin with the surrounding aqueous environment. The dextran shell acts as an extra barrier, preventing the access of aqueous environment to curcumin inside the hydrophobic ovalbumin core. Moreover, the steric hindrance provided by the dextran shell resulted in reduction of ovalbumin proteolysis. The stability enhancement endowed upon curcumin by the nanohybrid did not compromise its bioaccessibility to intestinal cells. The percentage of curcumin available in the micellar form was in the range of 50–53% for both, the nanohybrids and the ovalbumin nanoparticles, in comparison to 18.9% for free curcumin. These results demonstrate the ability of nanohybrids to enhance the stability of curcumin without compromising its bioavailability in comparison to nonhybrid nanoparticles [109].

### 3.10.2. Enhanced skin permeation

The transdermal route of delivery has become very attractive since it reduces side effects, avoids first pass metabolism, increases patient compliance, and sustains drug release over a longer period maintaining a steady blood concentration [140]. Non-steroidal anti-inflammatory drugs (NSAIDs) such as aceclofenac are known for their side effects as gastric irritation, ulceration, flatulence, and abdominal pain when used chronically. A topical gel formulation containing aceclofenac-loaded chitosan-albumin nanohybrids was fabricated to overcome such problems. The formulation showed a significantly higher *ex vivo* permeation of 0.0681  $\mu\text{g}/\text{cm}^2/\text{hr}$  using excised mouse skin in comparison to 0.0316  $\mu\text{g}/\text{cm}^2/\text{hr}$  for the marketed aceclofenac gel. This correlated well with the *in vivo* anti-inflammatory results in carrageenan-induced rat-paw edema where the nanohybrid gel formulation showed a higher percentage of paw edema inhibition over a period of 4 hr in comparison to the marketed aceclofenac gel [30].

### 3.10.3. Enhanced ocular delivery

Ocular gene delivery has attracted interest recently due to the immune-privileged nature of the eye and easy accessibility. Moreover, the local gene delivery could provide low and continuous concentrations enhancing the efficacy and safety of these biologically active compounds. In a study by Zorzi et al., two nanohybrid systems, cationized gelatin-chondroitin sulfate and cationized gelatin-dextran sulfate, were investigated for enhancing the ocular delivery of plasmid DNA. The nanohybrids conferred higher plasmid protection against degradation by DNase I for at least 1 hr in comparison to complete degradation after 5 min for naked plasmid DNA. This was ascribed to the spermine content in cationized gelatin which is known for its inhibition of endonucleases such as DNase I. Moreover, the nanohybrid systems enhanced the toxicity profile of cationized gelatin nanoparticles against human corneal epithelial (HCE) cells where the  $\text{IC}_{50}$  of cationized gelatin-chondroitin sulfate and cationized gelatin-dextran sulfate

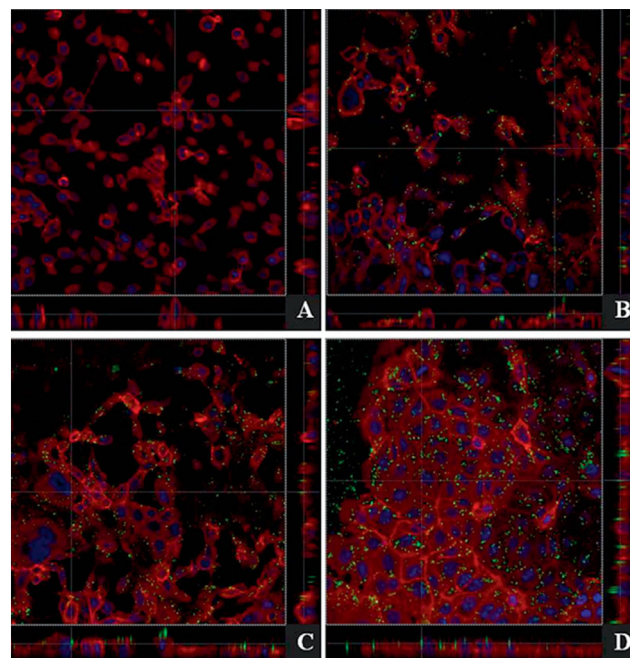


Fig. 14. Confocal microscopy images showing cellular uptake of free Cy3-labelled plasmid DNA (A), Cy3-labelled plasmid DNA-loaded cationized gelatin nanoparticles (B), Cy3-labelled plasmid DNA-loaded cationized gelatin-chondroitin sulfate nanohybrids (C), and Cy3-labelled plasmid DNA-loaded cationized gelatin-dextran sulfate nanohybrids (D) by HCE cells [49].



nanohybrids were 107 and 79  $\mu\text{g}/\text{cm}^2$ , respectively, being 3- and 2-folds higher than that of cationized gelatin nanoparticles. The cellular uptake by HCE cells has been also enhanced by the nanohybrid systems where Cy3-labelled plasmid DNA-loaded nanohybrids showed a more intense green fluorescence in comparison to cationized gelatin nanoparticles (Fig. 14). These results were reflected well on the transfection study where the nanohybrids surpassed its cationized gelatin counterpart [49].

#### 4. *In vivo* fate of protein-polysaccharide nanohybrids following administration

Protein based carrier systems for drug delivery are gaining interest because of their advantages like biocompatibility and biodegradability [24]. Fate of the protein delivery system is very crucial, as ultimately it will affect the fate of the drug following physiological administration. One study by Yang et al. has shown distribution of self-assembled protein nanoparticles in xenografted mice. In this study, they used tumor targeting bombesin peptide to radiolabel with technetium tricarbonyl, which is hydrophilic in nature. The resulting nanoparticles were monodispersed and had particles size of 33–36 nm. The biodistribution study showed that nanoparticles mostly accumulated in the liver and immune organ spleen of mice, following the intravenous administration [141].

On the other hand, polysaccharides are safe, biocompatible, cheap and biodegradable. Because of these merits polysaccharides are increasingly used as drug delivery systems [142]. Chitosan based drug delivery is one the common polysaccharide used in drug delivery. Nascimento et al. studied the biodistribution of Mad2 siRNA-loaded EGFR targeting chitosan nanoparticles in xenografted mice. When injected by i.v. route, nanoparticles were mainly accumulated in tumor, liver and kidney for the first 48 hr. Tumor targeting efficiency for EGFR in tumor was increased for these nanoparticles, as compared with other tissues [143].

In a study by Yi-Mu et al., the fate of the protein-polysaccharide nanohybrid systems was studied after oral administration in Kunming rats. 5-FU-loaded  $^{125}\text{I}$ -labelled sodium alginate-BSA nanohybrids were shown to be distributed mainly to organs rich in phagocytes; the liver and the spleen. Radioactivity after 8 h in the liver, spleen and lungs were 2.08, 2.32 and 1.60 times as that in blood which decreased to 1.18, 1.22 and 0.87 times after 24 h, respectively. The micro-radioautographical results denoted the accumulation of the nanohybrids in the Kupffer liver cells and the parenchymal ones. Pharmacokinetic parameters showed that the  $T_{1/2} = 9.42$  hr,  $T_{\text{max}} = 2.18$  hr,  $C_{\text{max}} = 2.45 \times 10^7$  Becquerel (Bq), and  $\text{AUC} = 148 \times 10^9$  Bq [96]. Further research should be conducted in order to investigate the fate of protein-polysaccharide nanohybrids in the body after *in vivo* administration.

Interestingly, in a study by Fuenzalida et al., the physicochemical properties of alginate, the molecular weight and composition, were examined for their effect on protein (lysozyme) association. Alginate is composed of alternating blocks of homopolymeric (1/4)-linked poly-D- $\beta$ -mannuronate (poly-M), poly-L- $\alpha$ -guluronate (poly-G), and heteropolymeric section of poly-MG; and the overall composition is expressed as an M/G ratio. The increase in M/G ratio or molecular weight of alginate interacting with lysozyme was associated with higher enthalpy, and thus higher lysozyme association. This could explain the increase in non-specific binding to immune system proteins associated with higher binding enthalpies. It has been shown in previous studies that alginates of high M-content elicit the immune response via cytokine production in monocytes, and CD14 stimulation on innate immune cells [75,144]. The level of impurities in alginate samples is another potential cause for immunogenic responses. Alginate, depending on the source and the purification method, could end up being contaminated with polyphenols, endotoxins and proteins, which were shown to play a role in alginate immunogenicity. What applied on alginate could apply, by

varying degrees, on other polymers; thus it is of big importance to fine tune the polymer properties according to the intended goals, such as an alginate with a high G-content (> 50%) or an alginate with high purity which had shown to elicit no immune responses [75,145]. And, although, knowledge about the sole polymers could give us cues, their immunological properties should be studied in their nanosized forms and when hybridized with other polymers, which might bring new properties that were not evident in either polymer alone. Evidently, the lack of research on the pharmacokinetics and the biological fate of the nanohybrid systems ensues further studies to be conducted in order to reach a more conclusive picture.

#### 5. Limitations and future prospects

The field of nanotechnology is rapidly growing with 77 nanotechnology-based products have been granted approval by FDA and 40% of clinical trials registered in 2014 or 2015 being nanotechnology-based. Needless to say, the obvious increase in basic research in this field has led to such hike up in product approvals and clinical trials in different phases. What can be noticed is that the vast majority of these nanosystems are simple ones, with no hybrid nanosystems being granted approval up till now. Specifically speaking, no protein-polysaccharide nanohybrids have been approved, nor currently being in clinical trials which raises many questions regarding the efficacy, toxicity and/or financial causes. Generally, efficacy issues are the main reason comprising 51% of Phase II failures according to a review published in 2011 while strategic problems and toxicity issues comprise 29 and 19%, respectively. Similar results were obtained for phase III failures which might give an insight of what might be hindering their clinical translation. The complexity of nanohybrids undoubtedly increases costs and proposes difficulties in the scaling up of these systems which grants further research. Moreover, nanohybrids might show features that are totally different from their respective constituting materials which raises questions regarding their toxicity and/or immunogenicity. Last, but not least, the translation of such research requires funding from industry which is only willing to do so in promising products that have obtained a “proof of concept in man” that itself requires big funding. All this poses restriction for the translation of the recently introduced protein-polysaccharide nanohybrids which, in the end, often face less support and guidance from drug regulatory authorities that lack experience in hybrid systems making their translation even more difficult. It is also important to say that 25% of approved products and 80% of clinical trials are aimed at cancer which itself faces its own challenges. The heterogeneity of tumors, the difficulty in extrapolating *in vitro* results and animal studies into human trials, and the great dependency on the EPR effect which is currently doubted by many for being a passive targeting strategy are the main reasons hindering cancer nanotechnology research. Moreover, regulatory authorities find it difficult to classify these newly introduced hybrid systems and take a precautionary stand in their progress. All in all, extensive research needs to be directed towards the scalability and toxicity of these hybrid systems before any progress can be seen in this area, especially for protein-polysaccharide nanohybrids [111,146–148].

#### References

- [1] P. Tyagi, J.A. Subramony, Nanotherapeutics in oral and parenteral drug delivery: key learnings and future outlooks as we think small, *J. Control. Release* 272 (2018) 159–168.
- [2] A. Elzoghby, Polymeric nanocarriers as robust platforms for cancer therapy, *Curr. Pharm. Des.* 23 (2017) 5211–5212.
- [3] C.-H. Chen, T.-H. Huang, A.O. Elzoghby, P.-W. Wang, C.-W. Chang, J.-Y. Fang, Squarticles as the nanoantidotes to sequester the overdoes antidepressant for detoxification, *Int. J. Nanomed.* 12 (2017) 8071–8083.
- [4] M.A. Sallam, A.O. Elzoghby, Flutamide-loaded zein nanocapsule hydrogel, a promising dermal delivery system for pilosebaceous unit disorders, *AAPS Pharm. Sci. Tech.* 19 (2018) 2370–2382.
- [5] S.N. Khattab, S.E.A. Naim, M. El-Sayed, A.A. El Bardan, A.O. Elzoghby,



- A.A. Bekhit, A. El-Faham, Design and synthesis of new s-triazine polymers and their application as nanoparticulate drug delivery systems, *New J. Chem.* 40 (2016) 9565–9578.
- [6] F. Danhier, E. Ansorena, J.M. Silva, R. Coco, A. Le Breton, V. Préat, PLGA-based nanoparticles: an overview of biomedical applications, *J. Control. Release* 161 (2012) 505–522.
- [7] A.O. Elzoghby, M.M. Abd-Elwakil, K. Abd-El salam, M.T. Elsayed, Y. Hashem, O. Mohamed, Natural polymeric nanoparticles for brain-targeting: implications on drug and gene delivery, *Curr. Pharm. Des.* 22 (2016) 3305–3323.
- [8] H.M. Abdelaziz, M. Gaber, M.M. Abd-Elwakil, M.T. Mabrouk, M.M. Elgohary, N.M. Kamel, D.M. Kabary, M.S. Freag, M.W. Samaha, S.M. Mortada, K.A. Elkhodairy, J.Y. Fang, A.O. Elzoghby, Inhalable particulate drug delivery systems for lung cancer therapy: nanoparticles, microparticles, nanocomposites and nanoaggregates, *J. Control. Release: Off. J. Control. Release Soc.* 269 (2018) 374–392.
- [9] S. Sabra, M. Abdelmoneem, M. Abdelwakil, M.M. Taha, D. Anwar, R. Mohamed, S. Khatlab, A. Bekhit, K. Elkhodairy, M. Freag, Self-assembled nanocarriers based on amphiphilic natural polymers for anti-cancer drug delivery applications, *Curr. Pharm. Des.* (2017).
- [10] G. Pasut, F.M. Veronese, State of the art in PEGylation: the great versatility achieved after forty years of research, *J. Control. Release* 161 (2012) 461–472.
- [11] F. Seidi, R. Jenjob, T. Phakkeeree, D. Crespy, Saccharides, oligosaccharides, and polysaccharides nanoparticles for biomedical applications, *J. Control. Release: Off. J. Control. Release Soc.* 284 (2018) 188–212.
- [12] R. Ahmad, Y. Deng, R. Singh, M. Hussain, M.A.A. Shah, S. Elingarami, N. He, Y. Sun, Cutting edge protein and carbohydrate-based materials for anticancer drug delivery, *J. Biomed. Nanotechnol.* 14 (2018) 20–43.
- [13] S.A. Sabra, A.O. Elzoghby, S.A. Sheweita, M. Haroun, M.W. Helmy, M.A. Eldemellawy, Y. Xia, D. Goodale, A.L. Allan, S. Rohani, Self-assembled amphiphilic zein-lactoferrin micelles for tumor targeted co-delivery of rapamycin and wogonin to breast cancer, *Eur. J. Pharm. Biopharm.* 128 (2018) 156–169.
- [14] D.M. Anwar, S.N. Khattab, M.W. Helmy, M.K. Kamal, A.A. Bekhit, K.A. Elkhodairy, A.O. Elzoghby, Lactobionic/folate dual-targeted amphiphilic maltodextrin-based micelles for targeted co-delivery of sulfasalazine and resveratrol to hepatocellular carcinoma, *Bioconjug. Chem.* 19 (2018) 3026–3041.
- [15] S.W. El-Far, M.W. Helmy, S.N. Khattab, A.A. Bekhit, A.A. Hussein, A.O. Elzoghby, Folate conjugated vs PEGylated phytosomal casein nanocarriers for codelivery of fungal- and herbal-derived anticancer drugs, *Nanomedicine* 13 (2018) 1463–1480.
- [16] A. Elzoghby, Editorial (thematic issue: nanocarriers based on natural polymers as platforms for drug and gene delivery applications), *Curr. Pharm. Des.* 22 (2016) 3303–3304.
- [17] N. Elgindy, K. Elkhodairy, A. Molokhia, A. ElZoghby, Biopolymeric nanoparticles for oral protein delivery: design and in vitro evaluation, *J. Nanomedicine & Nanotechnol.* 02 (2011).
- [18] A.O. Elzoghby, M.M. Elgohary, N.M. Kamel, Implications of protein- and Peptide-based nanoparticles as potential vehicles for anticancer drugs, *Adv. Protein Chem. Struct. Biol.* 98 (2015) 169–221.
- [19] M.S. Freag, W.M. Saleh, O.Y. Abdallah, Exploiting polymer blending approach for fabrication of buccal chitosan-based composite sponges with augmented mucoadhesive characteristics, *Eur. J. Pharm. Sci.* 120 (2018) 10–19.
- [20] M. Gaber, W. Medhat, M. Hany, N. Saher, J.Y. Fang, A. Elzoghby, Protein-lipid nanohybrids as emerging platforms for drug and gene delivery: challenges and outcomes, *J. Control. Release: Off. J. Control. Release Soc.* 254 (2017) 75–91.
- [21] J.P. Fuenzalida, F.M. Goycoolea, Polysaccharide-protein nanoassemblies: novel soft materials for biomedical and biotechnological applications, *Curr. Protein Pept. Sci.* 16 (2015) 89–99.
- [22] M.A. Abdelmoneem, M. Mahmoud, A. Zaky, M.W. Helmy, M. Sallam, J.-Y. Fang, K.A. Elkhodairy, A.O. Elzoghby, Dual-targeted casein micelles as green nanomedicine for synergistic phytotherapy of hepatocellular carcinoma, *J. Control. Release* 287 (2018) 78–93.
- [23] Y. Luo, Q. Wang, Recent development of chitosan-based polyelectrolyte complexes with natural polysaccharides for drug delivery, *Int. J. Biol. Macromol.* 64 (2014) 353–367.
- [24] M.J. Hawkins, P. Soon-Shiong, N. Desai, Protein nanoparticles as drug carriers in clinical medicine, *Adv. Drug. Deliv. Rev.* 60 (2008) 876–885.
- [25] O.G. Jones, D.J. McClements, Recent progress in biopolymer nanoparticle and microparticle formation by heat-treating electrostatic protein-polysaccharide complexes, *Adv. Colloid Interface Sci.* 167 (2011) 49–62.
- [26] S.L. Turgeon, C. Schmitt, C. Sanchez, Protein-polysaccharide complexes and coacervates, *Curr. Opin. Colloid Interface Sci.* 12 (2007) 166–178.
- [27] Y. Fang, L. Li, C. Inoue, L. Lundin, I. Appelqvist, Associative and segregative phase separations of gelatin/kappa-carrageenan aqueous mixtures, *Langmuir ACS J. Surf. Colloids* 22 (2006) 9532–9537.
- [28] D.Z. Tian, Y.P. Fang, K. Nishinari, G.O. Phillips, Protein-polysaccharide interactions: phase behaviour and applications (2014) 52–63.
- [29] J. Varshosaz, F. Hassanzadeh, H. Sadeghi, Z. Ghelich Khan, M. Rostami, Retinoic acid decorated albumin-chitosan nanoparticles for targeted delivery of doxorubicin hydrochloride in hepatocellular carcinoma, *J. Nanomaterials* 2013 (2013) 1–12.
- [30] S. Jana, S. Manna, A.K. Nayak, K.K. Sen, S.K. Basu, Carbopol gel containing chitosan-egg albumin nanoparticles for transdermal aceclofenac delivery, *Colloids Surf. B* 114 (2014) 36–44.
- [31] J. Li, X. Wang, Binding of (–)-epigallocatechin-3-gallate with thermally-induced bovine serum albumin/iota-carrageenan particles, *Food Chem.* 168 (2015) 566–571.
- [32] M.M. Abd Elwakil, M.T. Mabrouk, M.W. Helmy, E.-Z.A. Abdelfattah, S.K. Khiste, K.A. Elkhodairy, A.O. Elzoghby, Inhalable lactoferrin-chondroitin nanocomposites for combined delivery of doxorubicin and ellagic acid to lung carcinoma, *Nanomedicine* 13 (2018).
- [33] R.K. Tekade, M.B. Chougule, Formulation development and evaluation of hybrid nanocarrier for cancer therapy: Taguchi orthogonal array based design, *Biomed. Res. Int.* 2013 (2013) 712678.
- [34] M. Karimi, P. Avci, R. Mobasser, M.R. Hamblin, H. Naderi-Manesh, The novel albumin-chitosan core-shell nanoparticles for gene delivery: preparation, optimization and cell uptake investigation, *J. Nanoparticle Res.: An Interdisciplinary Forum Nanoscale Sci. Technol.* 15 (2013) 1651.
- [35] I. Peinado, U. Lesmes, A. Andres, J.D. McClements, Fabrication and morphological characterization of biopolymer particles formed by electrostatic complexation of heat treated lactoferrin and anionic polysaccharides, *Langmuir ACS J. Surf. Colloids* 26 (2010) 9827–9834.
- [36] B. Hoang, M.J. Ernstring, A. Roy, M. Murakami, E. Undzys, S.D. Li, Docetaxel-carboxymethylcellulose nanoparticles target cells via a SPARC and albumin dependent mechanism, *Biomaterials* 59 (2015) 66–76.
- [37] M. Lopes, N. Shrestha, A. Correia, M.A. Shahbazi, B. Sarmento, J. Hirvonen, F. Veiga, R. Seica, A. Ribeiro, H.A. Santos, Dual chitosan/albumin-coated alginate/dextran sulfate nanoparticles for enhanced oral delivery of insulin, *J. Control. Release: Off. J. Control. Release Soc.* 232 (2016) 29–41.
- [38] M. Yang, Y. Wu, J. Li, H. Zhou, X. Wang, Binding of curcumin with bovine serum albumin in the presence of iota-carrageenan and implications on the stability and antioxidant activity of curcumin, *J. Agric. Food. Chem.* 61 (2013) 7150–7155.
- [39] W. Cui, A. Wang, J. Zhao, X. Yang, P. Cai, J. Li, Layer by layer assembly of albumin nanoparticles with selective recognition of tumor necrosis factor-related apoptosis-inducing ligand (TRAIL), *J. Colloid Interface Sci.* 465 (2016) 11–17.
- [40] R. Hedayati, M. Jahanshahi, H. Attar, Fabrication and characterization of albumin-acacia nanoparticles based on complex coacervation as potent nanocarrier, *J. Chem. Technol. Biotechnol.* 87 (2012) 1401–1408.
- [41] J. Qi, P. Yao, F. He, C. Yu, C. Huang, Nanoparticles with dextran/chitosan shell and BSA/chitosan core-doxorubicin loading and delivery, *Int. J. Pharm.* 393 (2010) 176–184.
- [42] S. Yu, J. Hu, X. Pan, P. Yao, M. Jiang, Stable and pH-sensitive nanogels prepared by self-assembly of chitosan and ovalbumin, *Langmuir ACS J. Surfaces Colloids* 22 (2006) 2754–2759.
- [43] T. Zou, S.S. Percival, Q. Cheng, Z. Li, C.A. Rowe, L. Gu, Preparation, characterization, and induction of cell apoptosis of cocoa procyanidins-gelatin-chitosan nanoparticles, *Eur. J. Pharm. Biopharm.: Official J. Arbeitsgemeinschaft fur Pharmazeutische Verfahrenstechnik e.V* 82 (2012) 36–42.
- [44] A.N. Jatauri Cadinoiu, M.N. Holban, C.A. Peptu, A. Sava, M. Costuleanu, M. Popa, Double crosslinked interpenetrated network in nanoparticle form for drug targeting-preparation, characterization and biodistribution studies, *Int. J. Pharm.* 436 (2012) 66–74.
- [45] M. Rajan, V. Raj, A.A. Al-Arfaj, A.M. Murugan, Hyaluronidase enzyme core-5-fluorouracil-loaded chitosan-PEG-gelatin polymer nanocomposites as targeted and controlled drug delivery vehicles, *Int. J. Pharm.* 453 (2013) 514–522.
- [46] V. Singh, S. Ahmad, Carboxymethyl cellulose-gelatin-silica nanohybrid: an efficient carrier matrix for alpha amylase, *Int. J. Biol. Macromol.* 67 (2014) 439–445.
- [47] P.R. Sarika, N.R. James, Polyelectrolyte complex nanoparticles from cationised gelatin and sodium alginate for curcumin delivery, *Carbohydr. Polym.* 148 (2016) 354–361.
- [48] Y. Lv, F. Yang, X. Li, X. Zhang, S. Abbas, Formation of heat-resistant nanocapsules of jasmine essential oil via gelatin/gum arabic based complex coacervation, *Food Hydrocolloids* 35 (2014) 305–314.
- [49] G.K. Zorzi, J.E. Parraga, B. Seijo, A. Sanchez, Hybrid nanoparticle design based on cationized gelatin and the polyanions dextran sulfate and chondroitin sulfate for ocular gene therapy, *Macromol. Biosci.* 11 (2011) 905–913.
- [50] G. Konat Zorzi, L. Contreras-Ruiz, J.E. Parraga, A. Lopez-Garcia, R. Romero Bello, Y. Diebold, B. Seijo, A. Sanchez, Expression of MUC5AC in ocular surface epithelial cells using cationized gelatin nanoparticles, *Mol. Pharm.* 8 (2011) 1783–1788.
- [51] A.-C. Lee, Y.-H. Hong, Coacervate formation of  $\alpha$ -lactalbumin-chitosan and  $\beta$ -lactoglobulin-chitosan complexes, *Food Res. Int.* 42 (2009) 733–738.
- [52] S.F. Mirpoor, S.M.H. Hosseini, A.R. Nekoei, Efficient delivery of quercetin after binding to beta-lactoglobulin followed by formation soft-condensed core-shell nanostructures, *Food Chem.* 233 (2017) 282–289.
- [53] P. Zimet, Y.D. Livney, Beta-lactoglobulin and its nanocomplexes with pectin as vehicles for  $\omega$ -3 polyunsaturated fatty acids, *Food Hydrocolloids* 23 (2009) 1120–1126.
- [54] W. Chanasattru, O.G. Jones, E.A. Decker, D.J. McClements, Impact of cosolvents on formation and properties of biopolymer nanoparticles formed by heat treatment of  $\beta$ -lactoglobulin-Pectin complexes, *Food Hydrocolloids* 23 (2009) 2450–2457.
- [55] Z. Izadi, A. Divsalar, A.A. Saboury, L. Sawyer, beta-lactoglobulin-pectin nanoparticle-based oral drug delivery system for potential treatment of colon cancer, *Chem. Biol. Drug Des.* 88 (2016) 209–216.
- [56] O. Jones, E.A. Decker, D.J. McClements, Thermal analysis of  $\beta$ -lactoglobulin complexes with pectins or carrageenan for production of stable biopolymer particles, *Food Hydrocolloids* 24 (2010) 239–248.
- [57] S.M. Hosseini, Z. Emam-Djomeh, S.H. Razavi, A.A. Moosavi-Movahedi, A.A. Saboury, M.A. Mohammadifard, A. Farahnaky, M.S. Atri, P. Van der Meer, Complex coacervation of beta-lactoglobulin - kappa-carrageenan aqueous mixtures as affected by polysaccharide sonication, *Food Chem.* 141 (2013) 215–222.
- [58] S.M.H. Hosseini, Z. Emam-Djomeh, S.H. Razavi, A.A. Moosavi-Movahedi, A.A. Saboury, M.S. Atri, P. Van der Meer,  $\beta$ -Lactoglobulin-sodium alginate

- interaction as affected by polysaccharide depolymerization using high intensity ultrasound, *Food Hydrocolloids* 32 (2013) 235–244.
- [59] B. Ghalandari, A. Divsalar, A.A. Saboury, K. Parivar, The new insight into oral drug delivery system based on metal drugs in colon cancer therapy through beta-lactoglobulin/oxali-palladium nanocapsules, *Journal of photochemistry and photobiology, B, Biology* 140 (2014) 255–265.
- [60] S.M. Hosseini, Z. Emam-Djomeh, M. Negahdarifar, M. Sepeidnameh, S.H. Razavi, P. Van der Meer, Polysaccharide type and concentration affect nanocomplex formation in associative mixture with beta-lactoglobulin, *Int. J. Biol. Macromol.* 93 (2016) 724–730.
- [61] H.K. Ha, N.E. Jeon, J.W. Kim, K.S. Han, S.S. Yun, M.R. Lee, W.J. Lee, Physicochemical characterization and potential prebiotic effect of whey protein isolate/inulin nano complex, *Korean J. Food Sci. Anim. Resour.* 36 (2016) 267–274.
- [62] S.A. Fioramonti, A.A. Perez, E.E. Aringoli, A.C. Rubiolo, L.G. Santiago, Design and characterization of soluble biopolymer complexes produced by electrostatic self-assembly of a whey protein isolate and sodium alginate, *Food Hydrocolloids* 35 (2014) 129–136.
- [63] F.P. Chen, S.Y. Ou, C.H. Tang, Core-shell soy protein-soy polysaccharide complex (nano)particles as carriers for improved stability and sustained release of curcumin, *J. Agric. Food. Chem.* 64 (2016) 5053–5059.
- [64] X. Ding, P. Yao, Soy protein/soy polysaccharide complex nanogels: folic acid loading, protection, and controlled delivery, *Langmuir ACS J. Surf. Colloids* 29 (2013) 8636–8644.
- [65] B. Yin, W. Deng, K. Xu, L. Huang, P. Yao, Stable nano-sized emulsions produced from soy protein and soy polysaccharide complexes, *J. Colloid Interface Sci.* 380 (2012) 51–59.
- [66] Z. Teng, Y. Luo, Q. Wang, Carboxymethyl chitosan-soy protein complex nanoparticles for the encapsulation and controlled release of vitamin D(3), *Food Chem.* 141 (2013) 524–532.
- [67] W. Wang, F. Liu, Y. Gao, Quercetin loaded in soy protein isolate- $\kappa$ -carrageenan complex: fabrication mechanism and protective effect, *Food Res. Int.* 83 (2016) 31–40.
- [68] C. Bengoechea, O.G. Jones, A. Guerrero, D.J. McClements, Formation and characterization of lactoferrin/pectin electrostatic complexes: impact of composition, pH and thermal treatment, *Food Hydrocolloids* 25 (2011) 1227–1232.
- [69] G. Shimoni, C. Shani Levi, S. Levi Tal, U. Lesmes, Emulsions stabilization by lactoferrin nano-particles under in vitro digestion conditions, *Food Hydrocolloids* 33 (2013) 264–272.
- [70] T. David-Birman, A. Mackie, U. Lesmes, Impact of dietary fibers on the properties and proteolytic digestibility of lactoferrin nano-particles, *Food Hydrocolloids* 31 (2013) 33–41.
- [71] E.S. Lee, K.H. Park, D. Kang, I.S. Park, H.Y. Min, D.H. Lee, S. Kim, J.H. Kim, K. Na, Protein complexed with chondroitin sulfate in poly(lactide-co-glycolide) microspheres, *Biomaterials* 28 (2007) 2754–2762.
- [72] K. Zhu, T. Ye, J. Liu, Z. Peng, S. Xu, J. Lei, H. Deng, B. Li, Nanogels fabricated by lysozyme and sodium carboxymethyl cellulose for 5-fluorouracil controlled release, *Int. J. Pharm.* 441 (2013) 721–727.
- [73] Z. Li, W. Xu, Y. Wang, B.R. Shah, C. Zhang, Y. Chen, Y. Li, B. Li, Quantum dots loaded nanogels for low cytotoxicity, pH-sensitive fluorescence, cell imaging and drug delivery, *Carbohydr. Polym.* 121 (2015) 477–485.
- [74] Z. Li, Y. Wang, Y. Pei, W. Xiong, W. Xu, B. Li, J. Li, Effect of substitution degree on carboxymethylcellulose interaction with lysozyme, *Food Hydrocolloids* 62 (2017) 222–229.
- [75] J.P. Fuenzalida, P.K. Nareddy, I. Moreno-Villoslada, B.M. Moerschbacher, M.J. Swamy, S. Pan, M. Ostermeier, F.M. Goycoolea, On the role of alginate structure in complexing with lysozyme and application for enzyme delivery, *Food Hydrocolloids* 53 (2016) 239–248.
- [76] T. Wang, S. Soyama, Y. Luo, Development of a novel functional drink from all natural ingredients using nanotechnology, *LWT - Food Sci. Technol.* 73 (2016) 458–466.
- [77] Y. Luo, K. Pan, Q. Zhong, Casein/pectin nanocomplexes as potential oral delivery vehicles, *Int. J. Pharm.* 486 (2015) 59–68.
- [78] A.K. Anal, A. Tobiassen, J. Flanagan, H. Singh, Preparation and characterization of nanoparticles formed by chitosan-caseinate interactions, *Colloids Surf., B* 64 (2008) 104–110.
- [79] H. Mok, J.W. Park, T.G. Park, Antisense oligodeoxynucleotide-conjugated hyaluronic acid/protamine nanocomplexes for intracellular gene inhibition, *Bioconjug. Chem.* 18 (2007) 1483–1489.
- [80] S. Wang, M. Cao, X. Deng, X. Xiao, Z. Yin, Q. Hu, Z. Zhou, F. Zhang, R. Zhang, Y. Wu, W. Sheng, Y. Zeng, Degradable hyaluronic acid/protamine sulfate interpolyelectrolyte complexes as miRNA-delivery nanocapsules for triple-negative breast cancer therapy, *Adv. Healthcare Mater.* 4 (2015) 281–290.
- [81] M.S. Thu, L.H. Bryant, T. Coppola, E.K. Jordan, M.D. Budde, B.K. Lewis, A. Chaudhry, J. Ren, N.R. Varma, A.S. Arbab, J.A. Frank, Self-assembling nanocomplexes by combining ferumoxyl, heparin and protamine for cell tracking by magnetic resonance imaging, *Nat. Med.* 18 (2012) 463–467.
- [82] K. Stephansen, M. Mattheij, J. Wattjes, A. Milisavljevic, F. Jessen, K. Qvortrup, F.M. Goycoolea, I.S. Chronakis, Design and characterization of self-assembled fish sarcoplasmic protein-alginate nanocomplexes, *Int. J. Biol. Macromol.* 76 (2015) 146–152.
- [83] S. Piriyaprasarth, M. Juttulapa, P. Sriamornsak, Formation and characterization of polyelectrolyte complexes containing pectin and zein, *Walailak J. Sci. Technol. (WJST)* 13 (10) (2016) Special Issue on Pharmacy and Pharmaceutical Sciences, (2016).
- [84] M. Zhou, T. Wang, Q. Hu, Y. Luo, Low density lipoprotein/pectin complex nanogels as potential oral delivery vehicles for curcumin, *Food Hydrocolloids* 57 (2016) 20–29.
- [85] D.M. Kabary, M.W. Helmy, K.A. Elkhodairy, J.-Y. Fang, A.O. Elzoghby, Hyaluronate/lactoferrin layer-by-layer-coated lipid nanocarriers for targeted co-delivery of rapamycin and berberine to lung carcinoma, *Colloids Surf., B* 169 (2018) 183–194.
- [86] D.M. Kabary, M.W. Helmy, E.-Z.A. Abdelfattah, J.-Y. Fang, K.A. Elkhodairy, A.O. Elzoghby, Inhalable multi-compartmental phospholipid enveloped lipid core nanocomposites for localized mTOR inhibitor/herbal combined therapy of lung carcinoma, *Eur. J. Pharm. Biopharm.* 130 (2018) 152–164.
- [87] A.S. Abdelhamid, M.W. Helmy, S.M. Ebrahim, M. Bahey-El-Din, D.G. Zayed, E.A. Zein El Dein, S.A. El-Gizawy, A.O. Elzoghby, Layer-by-layer gelatin/chondroitin quantum dots-based nanotheranostics: combined rapamycin/celecoxib delivery and cancer imaging, *Nanomedicine* 13 (2018).
- [88] I.J. Joye, V.A. Nelis, D.J. McClements, Gliadin-based nanoparticles: Stabilization by post-production polysaccharide coating, *Food Hydrocolloids* 43 (2015) 236–242.
- [89] C.G. de Kruij, F. Weinbreck, R. de Vries, Complex coacervation of proteins and anionic polysaccharides, *Curr. Opin. Colloid Interface Sci.* 9 (2004) 340–349.
- [90] A. Elzoghby, M. Freag, H. Mamdouh, K. Elkhodairy, Zein-based nanocarriers as potential natural alternatives for drug and gene delivery: focus on cancer therapy, *Curr. Pharm. Des.* (2017).
- [91] A.O. Elzoghby, S.A. El-Lakany, M.W. Helmy, M.M. Abu-Serie, N.A. Elgindy, Shell-crosslinked zein nanocapsules for oral codelivery of exemestane and resveratrol in breast cancer therapy, *Nanomedicine* 12 (2017) 2785–2805.
- [92] Y. Luo, B. Zhang, M. Whent, L.L. Yu, Q. Wang, Preparation and characterization of zein/chitosan complex for encapsulation of alpha-tocopherol, and its in vitro controlled release study, *Colloids Surf. B* 85 (2011) 145–152.
- [93] O.G. Jones, U. Lesmes, P. Dubin, D.J. McClements, Effect of polysaccharide charge on formation and properties of biopolymer nanoparticles created by heat treatment of  $\beta$ -lactoglobulin-pectin complexes, *Food Hydrocolloids* 24 (2010) 374–383.
- [94] A. Martínez, I. Iglesias, R. Lozano, J.M. Teijón, M.D. Blanco, Synthesis and characterization of thiolated alginate-albumin nanoparticles stabilized by disulfide bonds, *Eval. Drug Delivery Syst. Carbohydr. Polym.* 83 (2011) 1311–1321.
- [95] A. Martinez, E. Muniz, I. Iglesias, J.M. Teijon, M.D. Blanco, Enhanced preclinical efficacy of tamoxifen developed as alginate-cysteine/disulfide bond reduced albumin nanoparticles, *Int. J. Pharm.* 436 (2012) 574–581.
- [96] Y.M. Yi, T.Y. Yang, W.M. Pan, Preparation and distribution of 5-fluorouracil (125I) sodium alginate-bovine serum albumin nanoparticles, *World J. Gastroenterol.* 5 (1999) 57–60.
- [97] J.E. Hodge, Dehydrated foods, chemistry of browning reactions in model systems, *J. Agric. Food. Chem.* 1 (1953) 928–943.
- [98] B. Shah, P.M. Davidson, Q. Zhong, Encapsulation of eugenol using Maillard-type conjugates to form transparent and heat stable nanoscale dispersions, *LWT - Food Sci. Technol.* 49 (2012) 139–148.
- [99] M. Carme Coll Ferrer, P. Sobolewski, R.J. Composto, D.M. Eckmann, Cellular uptake and intracellular cargo release from dextran based nanogel drug carriers, *J. Nanotechnol. Eng. Med.* 4 (2013) 110021–110028.
- [100] G. Markman, Y.D. Livney, Maillard-conjugate based core-shell co-assemblies for nanoencapsulation of hydrophobic nutraceuticals in clear beverages, *Food Funct.* 3 (2012) 262–270.
- [101] J. Li, S. Yu, P. Yao, M. Jiang, Lysozyme-dextran core-shell nanogels prepared via a green process, *Langmuir ACS J. Surf. Colloids* 24 (2008) 3486–3492.
- [102] L. Zhang, A. Dudhani, L. Lundin, S.L. Kosaraju, Macromolecular conjugate based particles: preparation, characterisation and evaluation of controlled release properties, *Eur. Polym. J.* 45 (2009) 1960–1969.
- [103] J. Li, P. Yao, Self-assembly of ibuprofen and bovine serum albumin-dextran conjugates leading to effective loading of the drug, *Langmuir ACS J. Surf. Colloids* 25 (2009) 6385–6391.
- [104] H. Zhou, X. Sun, L. Zhang, P. Zhang, J. Li, Y.N. Liu, Fabrication of biopolymeric complex coacervation core micelles for efficient tea polyphenol delivery via a green process, *Langmuir ACS J. Surf. Colloids* 28 (2012) 14553–14561.
- [105] H. Hao, Q. Ma, C. Huang, F. He, P. Yao, Preparation, characterization, and in vivo evaluation of doxorubicin loaded BSA nanoparticles with folic acid modified dextran surface, *Int. J. Pharm.* 444 (2013) 77–84.
- [106] A. Martinez, E. Muniz, C. Teijon, I. Iglesias, J.M. Teijon, M.D. Blanco, Targeting tamoxifen to breast cancer xenograft tumours: preclinical efficacy of folate-attached nanoparticles based on alginate-cysteine/disulphide-bond-reduced albumin, *Pharm. Res.* 31 (2014) 1264–1274.
- [107] A. Martinez, R. Olmo, I. Iglesias, J.M. Teijon, M.D. Blanco, Folate-targeted nanoparticles based on albumin and albumin/alginate mixtures as controlled release systems of tamoxifen: synthesis and in vitro characterization, *Pharm. Res.* 31 (2014) 182–193.
- [108] W. Deng, J. Li, P. Yao, F. He, C. Huang, Green preparation process, characterization and antitumor effects of doxorubicin-BSA-dextran nanoparticles, *Macromol. Biosci.* 10 (2010) 1224–1234.
- [109] J. Feng, S. Wu, H. Wang, S. Liu, Improved bioavailability of curcumin in ovalbumin-dextran nanogels prepared by Maillard reaction, *J. Funct. Foods* 27 (2016) 55–68.
- [110] J. Xue, C. Tan, X. Zhang, B. Feng, S. Xia, Fabrication of epigallocatechin-3-gallate nanocarrier based on glycosylated casein: stability and interaction mechanism, *J. Agric. Food. Chem.* 62 (2014) 4677–4684.
- [111] X. Pan, M. Mu, B. Hu, P. Yao, M. Jiang, Micellization of casein-graft-dextran copolymer prepared through Maillard reaction, *Biopolymers* 81 (2006) 29–38.
- [112] X. Pan, P. Yao, M. Jiang, Simultaneous nanoparticle formation and encapsulation

- driven by hydrophobic interaction of casein-graft-dextran and beta-carotene, *J. Colloid Interface Sci.* 315 (2007) 456–463.
- [113] Y. Wu, X. Wang, Binding, stability, and antioxidant activity of curcumin with self-assembled casein–dextran conjugate micelles, *Int. J. Food Prop.* 20 (2017) 3295–3307.
- [114] J. Yi, Y. Fan, Y. Zhang, Z. Wen, L. Zhao, Y. Lu, Glycosylated  $\alpha$ -lactalbumin-based nanocomplex for curcumin: physicochemical stability and DPPH-scavenging activity, *Food Hydrocolloids* 61 (2016) 369–377.
- [115] S.W. El-Far, M.W. Helmy, S.N. Khattab, A.A. Bekhit, A.A. Hussein, A.O. Elzoghby, Phytosomal bilayer-enveloped casein micelles for codelivery of monascus yellow pigments and resveratrol to breast cancer, *Nanomedicine (London, Engl.)* 13 (2018) 481–499.
- [116] A.O. Elzoghby, M.W. Helmy, W.M. Samy, N.A. Elgindy, Micellar delivery of flutamide via milk protein nanovehicles enhances its anti-tumor efficacy in androgen-dependent prostate cancer rat model, *Pharm. Res.* 30 (2013) 2654–2663.
- [117] A.O. Elzoghby, N.I. Saad, M.W. Helmy, W.M. Samy, N.A. Elgindy, Ionically-crosslinked milk protein nanoparticles as flutamide carriers for effective anticancer activity in prostate cancer-bearing rats, *Eur. J. Pharm. Biopharma.: Official J. Arbeitsgemeinschaft fur Pharmazeutische Verfahrenstechnik e.V* 85 (2013) 444–451.
- [118] A.O. Elzoghby, B.Z. Vranic, W.M. Samy, N.A. Elgindy, Swellable floating tablet based on spray-dried casein nanoparticles: near-infrared spectral characterization and floating matrix evaluation, *Int. J. Pharm.* 491 (2015) 113–122.
- [119] B. Hiller, P.C. Lorenzen, Functional properties of milk proteins as affected by Maillard reaction induced oligomerisation, *Food Res. Int.* 43 (2010) 1155–1166.
- [120] Z.-M. Huang, Y.Z. Zhang, M. Kotaki, S. Ramakrishna, A review on polymer nanofibers by electrospinning and their applications in nanocomposites, *Compos. Sci. Technol.* 63 (2003) 2223–2253.
- [121] A. Valizadeh, S. Mussa Farkhani, Electrospinning and electrospun nanofibres, *IET Nanobiotechnology* 8 (2014) 83–92.
- [122] N. Ashammakhi, I. Wimpenny, L. Nikkila, Y. Yang, Electrospinning: methods and development of biodegradable nanofibres for drug release, *J. Biomed. Nanotechnol.* 5 (2009) 1–19.
- [123] S. Torres-Giner, M.J. Ocio, J.M. Lagaron, Novel antimicrobial ultrathin structures of zein/chitosan blends obtained by electrospinning, *Carbohydr. Polym.* 77 (2009) 261–266.
- [124] S. Wongsasulak, M. Patapeejumrongsong, J. Weiss, P. Supaphol, T. Yoovidhya, Electrospinning of food-grade nanofibers from cellulose acetate and egg albumen blends, *J. Food Eng.* 98 (2010) 370–376.
- [125] X. Zhuang, B. Cheng, W. Kang, X. Xu, Electrospun chitosan/gelatin nanofibers containing silver nanoparticles, *Carbohydr. Polym.* 82 (2010) 524–527.
- [126] H. Liu, Y.-L. Hsieh, Ultrafine fibrous cellulose membranes from electrospinning of cellulose acetate, *J. Polym. Sci., Part B: Polym. Phys.* 40 (2002) 2119–2129.
- [127] M.M. Demir, I. Yilgor, E. Yilgor, B. Erman, Electrospinning of polyurethane fibers, *Polymer* 43 (2002) 3303–3309.
- [128] D.S. Katti, K.W. Robinson, F.K. Ko, C.T. Laurencin, Bioresorbable nanofiber-based systems for wound healing and drug delivery: optimization of fabrication parameters, *J. Biomed. Mater. Res.* 70B (2004) 286–296.
- [129] M.S. Freag, Hyaluronate-lipid nanohybrids: fruitful harmony in cancer targeting, *Curr. Pharm. Des.* 23 (2017) 5283–5291.
- [130] Z. Chen, J. Chen, L. Wu, W. Li, J. Chen, H. Cheng, J. Pan, B. Cai, Hyaluronic acid-coated bovine serum albumin nanoparticles loaded with brucine as selective nanovectors for intra-articular injection, *Int. J. Nanomed.* 8 (2013) 3843–3853.
- [131] A.O. Elzoghby, S.K. Mostafa, M.W. Helmy, M.A. ElDemellawy, S.A. Sheweita, Multi-reservoir phospholipid shell encapsulating protamine nanocapsules for co-delivery of letrozole and celecoxib in breast cancer therapy, *Pharm. Res.* 34 (2017) 1956–1969.
- [132] A.O. Elzoghby, S.K. Mostafa, M.W. Helmy, M.A. ElDemellawy, S.A. Sheweita, Superiority of aromatase inhibitor and cyclooxygenase-2 inhibitor combined delivery: hyaluronate-targeted versus PEGylated protamine nanocapsules for breast cancer therapy, *Int. J. Pharm.* 529 (2017) 178–192.
- [133] M.S. Freag, W.M. Saleh, O.Y. Abdallah, Laminated chitosan-based composite sponges for transmucosal delivery of novel protamine-decorated tripterine phytosomes: ex-vivo mucopenetration and in-vivo pharmacokinetic assessments, *Carbohydr. Polym.* 188 (2018) 108–120.
- [134] M. Freag, A. Elzoghby, Protein-inorganic nanohybrids: A potential symbiosis in tissue engineering, *Curr. Drug Targets* 19 (2018) 1897–1904.
- [135] A.O. Elzoghby, A.L. Hemasa, M.S. Freag, Hybrid protein-inorganic nanoparticles: from tumor-targeted drug delivery to cancer imaging, *J. Control. Release* 243 (2016) 303–322.
- [136] M.S. Freag, W.M. Saleh, O.Y. Abdallah, Self-assembled phospholipid-based phytosomal nanocarriers as promising platforms for improving oral bioavailability of the anticancer celestrol, *Int. J. Pharm.* 535 (2017) 18–26.
- [137] N. Elgindy, K. Elkhodairy, A. Molokhia, A. Elzoghby, Biopolymeric microparticles combined with lyophilized monophase dispersions for controlled flutamide release, *Int. J. Pharm.* 411 (2011) 113–120.
- [138] N. Elgindy, K. Elkhodairy, A. Molokhia, A. Elzoghby, Lyophilization monophase solution technique for preparation of amorphous flutamide dispersions, *Drug Dev. Ind. Pharm.* 37 (2011) 754–764.
- [139] N. Elgindy, K. Elkhodairy, A. Molokhia, A. Elzoghby, Lyophilized flutamide dispersions with polyols and amino acids: preparation and in vitro evaluation, *Drug Dev. Ind. Pharm.* 37 (2011) 446–455.
- [140] A.S. Torky, M.S. Freag, M.M.A. Nasra, O.Y. Abdallah, Novel skin penetrating berberine oleate complex capitalizing on hydrophobic ion pairing approach, *Int. J. Pharm.* 549 (2018) 76–86.
- [141] Y. Yang, T. Neef, C. Mittelholzer, E. Garcia Garayoa, P. Blauenstein, R. Schibli, U. Aebi, P. Burkhard, The biodistribution of self-assembling protein nanoparticles shows they are promising vaccine platforms, *J. Nanobiotechnology* 11 (2013) 36.
- [142] H. Kaur, M. Ahuja, S. Kumar, N. Dilbaghi, Carboxymethyl tamarind kernel polysaccharide nanoparticles for ophthalmic drug delivery, *Int. J. Biol. Macromol.* 50 (2012) 833–839.
- [143] A.V. Nascimento, F. Gattaccea, A. Singh, H. Bousbaa, D. Ferreira, B. Sarmento, M.M. Amiji, Biodistribution and pharmacokinetics of Mad2 siRNA-loaded EGFR-targeted chitosan nanoparticles in cisplatin sensitive and resistant lung cancer models, *Nanomedicine (London, Engl.)* 11 (2016) 767–781.
- [144] T. Andersen, B.L. Strand, K. Formo, E. Alsberg, B.E. Christensen, Chapter 9 Alginates as biomaterials in tissue engineering, *Carbohydrate Chemistry, The Royal Society of Chemistry*, 2012, pp. 227–258.
- [145] M. Menard, J. Dusseault, G. Langlois, W.E. Baille, S.K. Tam, L. Yahia, X.X. Zhu, J.P. Halle, Role of protein contaminants in the immunogenicity of alginates, *J. Biomed. Mater. Res. Part B, Appl. Biomaterials* 93 (2010) 333–340.
- [146] D. Bobo, K.J. Robinson, J. Islam, K.J. Thurecht, S.R. Corrie, Nanoparticle-based medicines: a review of fda-approved materials and clinical trials to date, *Pharm. Res.* 33 (2016) 2373–2387.
- [147] P. Satalkar, B.S. Elger, P. Hunziker, D. Shaw, Challenges of clinical translation in nanomedicine: a qualitative study, *Nanomedicine: Nanotechnol. Biol. Med.* 12 (2016) 893–900.
- [148] C.A. Schutz, L. Juillerat-Jeanneret, H. Mueller, I. Lynch, M. Riediker, Therapeutic nanoparticles in clinics and under clinical evaluation, *Nanomedicine (London, Engl.)* 8 (2013) 449–467.

ARTICLE

Open Access

# Discovery of Enterovirus A71-like nonstructural genomes in recent circulating viruses of the *Enterovirus A* species

Kuo-Ming Lee<sup>1</sup>, Yu-Nong Gong<sup>1</sup>, Tzu-Hsuan Hsieh<sup>2</sup>, Andrew Woodman<sup>3</sup>, Nynke H. Dekker<sup>4</sup>, Craig E. Cameron<sup>3</sup> and Shin-Ru Shih<sup>1,2,5,6</sup>

## Abstract

Enterovirus A71 (EV-A71) is an important nonpolio enterovirus that causes severe neurological complications. In 1998, Taiwan experienced an EV-A71 outbreak that caused 78 deaths. Since then, periodic epidemics of EV-A71 associated with newly emerging strains have occurred. Several of these strains are known to be recombinant; however, how these strains arose within such a short period of time remains unknown. Here, we sequenced 64 full-length genomes from clinical isolates collected from 2005 to 2016 and incorporated all 91 Taiwanese genomes downloaded from the Virus Pathogen Resource to extensively analyze EV-A71 recombination in Taiwan. We found that the B3 subgenotype was a potential recombinant parent of the EV-A71 C2-like and C4 strains by intratypic recombination. Such B3-similar regions were also found in many cocirculating coxsackieviruses belonging to *Enterovirus A* species (EV-A) through a series of intertypic recombinations. Therefore, locally enriched outbreaks of cocirculating viruses from different genotypes/serotypes may facilitate recombination. Most recombination breakpoints we found had nonrandom distributions and were located within the region spanning from the boundary of P1 (structural gene) and P2 (nonstructural) to the *cis*-acting replication element at P2, indicating that specific genome reassembly of structural and nonstructural genes may be subject to natural selection. Through intensive recombination, 11 EV-A71-like signatures (including one in 3A, two in 3C, and eight in 3D) were found to be present in a variety of recently cocirculating EV-A viruses worldwide, suggesting that these viruses may be targets for wide-spectrum antiviral development.

## Introduction

Enterovirus A71 (EV-A71), a member of the nonpolio enterovirus family, belongs to the *Enterovirus A* species (EV-A) of Picornaviridae<sup>1</sup>. Notably, infection with EV-A71 in children under 5 years of age sometimes leads to severe neurological complications (e.g., brainstem encephalitis, meningitis, and acute flaccid paralysis) and

even death owing to cardiopulmonary failure<sup>1–3</sup>. EV-A71 is a nonenveloped small RNA virus with a positive, single-stranded RNA genome<sup>1</sup>. The viral genome can be directly translated into a polyprotein consisting of the structural (P1) and nonstructural (P2 and P3) regions; this polyprotein is subjected to a series of proteolytic cleavages to generate functional proteins, including structural proteins (VP1–4) functioning in capsid assembly and nonstructural proteins (2A–C, 3A–D) required for viral replication<sup>1</sup>. Based on the nucleotide sequence of the VP1 protein, EV-A71 is classified into seven genotypes (A–G)<sup>4–6</sup>. Genotypes B and C can be further divided into subgenotypes

Correspondence: Shin-Ru Shih (srshih@mail.cgu.edu.tw)

<sup>1</sup>Research Center for Emerging Viral Infections, College of Medicine, Chang Gung University, Taoyuan, Taiwan

<sup>2</sup>Department of Medical Biotechnology and Laboratory Science, College of Medicine, Chang Gung University, Taoyuan, Taiwan

Full list of author information is available at the end of the article.

These authors contributed equally: Kuo-Ming Lee, Yu-Nong Gong

© The Author(s) 2018



**Open Access** This article is licensed under a Creative Commons Attribution 4.0 International License, which permits use, sharing, adaptation, distribution and reproduction in any medium or format, as long as you give appropriate credit to the original author(s) and the source, provide a link to the Creative Commons license, and indicate if changes were made. The images or other third party material in this article are included in the article's Creative Commons license, unless indicated otherwise in a credit line to the material. If material is not included in the article's Creative Commons license and your intended use is not permitted by statutory regulation or exceeds the permitted use, you will need to obtain permission directly from the copyright holder. To view a copy of this license, visit <http://creativecommons.org/licenses/by/4.0/>.



from B0 to B5 and from C1 to C5, respectively<sup>7</sup>. Outbreaks caused by these variable genotypes have been reported<sup>8</sup>.

In 1969 and the early 1970s, EV-A71 genotype A caused outbreaks in the United States of America (USA). However, genotype A did not recur until 2008, and the intervening worldwide epidemics were found to be caused by other genotypes<sup>8</sup>. From the 1970s to the late 1980s, genotype B dominated and led to outbreaks in the USA, Japan, Australia, and Europe. In the late 1980s, the prevalent genotype changed to genotype C, which is currently active outside the Asia-Pacific region. However, after the 1975 Bulgaria and 1978 Hungary outbreaks, no severe outbreaks occurred until 1997<sup>7,8</sup>; since then, several EV-A71 outbreaks have accompanied fatal hand-foot-mouth disease (HFMD) cases in various countries in the Western Pacific region, and the threat continues<sup>8</sup>. Thus, EV-A71 has been selected by the World Health Organization as one of the top five viruses in the post-polio eradication era<sup>9</sup>. These recent outbreaks were associated with newly emerging strains, including the recombinant B3, B4, C2, and C4 subgenotypes<sup>7,8</sup>. Notably, recombination is believed to play a more important role than that of mutations in the evolution of EV-A71<sup>7,10</sup>. Although clinical trials of the EV-A71 vaccine are currently ongoing<sup>11</sup>, novel vaccine-resistant strains might appear as a result of recombination. Therefore, characterization of the mechanisms of viral recombination remains essential.

In Taiwan, EV-A71 has become a long-term pathogen and can be traced back to as early as 1980<sup>3</sup>; however, the first severe outbreak occurred in 1998, and Taiwan experienced the most severe EV-A71 outbreak on record. In a subsequent outbreak in 2000–2002, 846 severe cases and 129 deaths were reported<sup>2,3</sup>. Thus, enterovirus infection has been evaluated as an important infectious disease in Taiwan. From 1989 to 2009, physicians and hospitals used sentinel surveillance systems to monitor highly infectious diseases; now, computerized systems carry this responsibility. Additionally, a laboratory-based virological surveillance system was established in 2000 to focus on influenza virus and enterovirus infections<sup>3</sup>, and reporting of severe cases is now mandatory in Taiwan.

Here, we evaluated the evolution and recombination of different genotypes of EV-A71 and several cocirculating EV-A viruses in Taiwan based on full-genome sequence analyses. Our results provide insights into the crucial role of the similar nonstructural regions via a series of recombination events associated with various serotypes, which may be triggered by the emergence of the temporal EV-A71 B3 strain. These results may facilitate the development of wide-spectrum antivirals against cocirculating EV-A strains.

## Results

### Molecular epidemiological analysis of EV-A71 from 2005 to 2016 in Taiwan

We summarized epidemiological reports of enterovirus infections from the Taiwan Centre for Disease Control in Fig. 1. More than 1000 enterovirus infection cases have been reported annually since 2005 in Taiwan, and both EV-A and EV-B viruses were common (Fig. 1a). No dominant serotype has been observed since 2005, and EV-A71 infections (Fig. 1a, marked in red) had a lower prevalence than those of the other cocirculating types, except in 2012. However, most severe cases were associated with EV-A71 infections (Fig. 1b), and much higher numbers of severe cases were reported in 2005, 2008, 2011, and 2012, correlated with EV-A71 outbreaks<sup>12,13</sup>.

Sixty-four clinical isolates collected from 2005 to 2016 were sequenced to investigate EV-A71 recombination. Yearly counts are presented in Table 1. For the purpose of recombination analysis, all of the 91 full-length genomes isolated from Taiwan were downloaded from the Virus Pathogen Resource (ViPR) and subjected to the following examinations. A maximum likelihood (ML) tree was inferred using all Taiwanese genomes and published reference sequences with known subgenotypes (EV-A71 A, B0–B5, and C1–C5; Fig. 1c). The genotype distribution of the Taiwanese strains is summarized in Table 1. Except for one C5 strain collected in 2007, all our clinical isolates belonged to the B5 and C4 subgenotypes. The B5 and C4 subtrees are shown in Fig. 1d, e, respectively. The B5 strain showed a ladder-like distribution in the phylogenetic tree (Fig. 1d). The strains collected in each year formed a distinct clade, and the consecutive replacement of the older clades with the more recent clades indicated the continuous evolution of the B5 strain after its divergence from the B4 strain. However, the most recent B5 strains seemed to represent a new branch (Fig. 1d, upper), which is further discussed in Fig. 2b. The EV-A71 C4 strains collected in different years also belonged to different clades (Fig. 1e). In contrast, these clades showed a scattered distribution, meaning that multiple lineages of the C4 strain may coexist and be transmitted over time.

Interestingly, a periodic switching between the EV-A71 C4 and B5 strains occurred in Taiwan during the years from 2005 to 2016 (Table 1). To elucidate whether this genotype switching may be caused by the transmission of different EV-A71 strains from other countries, the VP1 genes of genomes collected worldwide were obtained from ViPR and phylogenetically analyzed (Fig. 2a). The details of each analyzed sequence can be found in Supplementary Table 1. Since B5 and C4 were the dominant circulating EV-A71 strains in Taiwan, we examined their relationships with the same strains circulating in nearby countries, including China, Cambodia, Thailand, and Vietnam (Fig. 2b, c). In the B5 tree, most sequences came from Taiwan; indeed, Taiwan

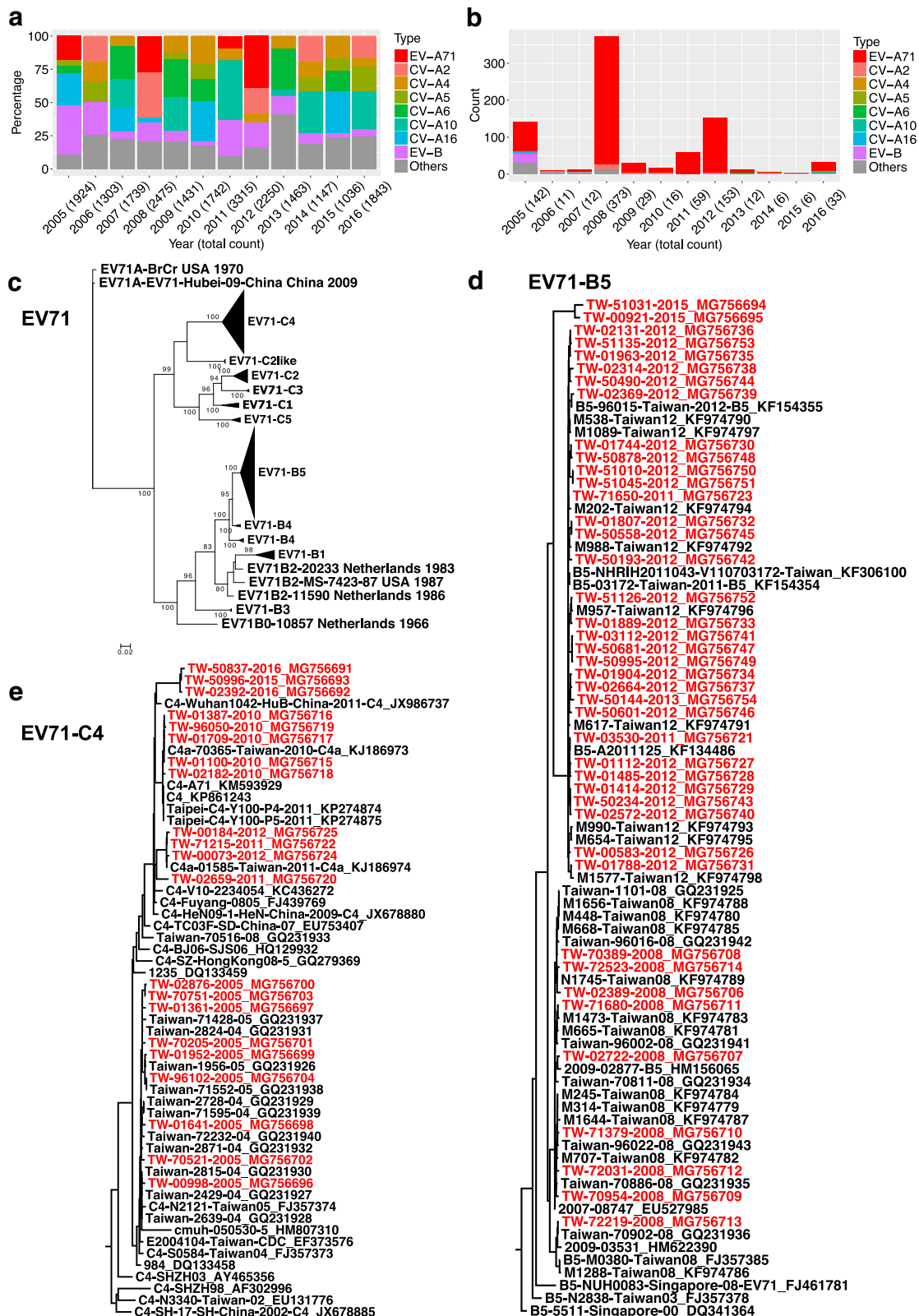


Fig. 1 (See legend on next page.)

(see figure on previous page)

**Fig. 1 Enterovirus surveillance reports in Taiwan since 2005 and phylogenetic tree of Taiwanese EV-A71 full-genome sequences.**

**a** Percentages of enterovirus infections since 2005, including EV-A71 (marked in red), six CV types (A2, A4, A5, A6, A10, and A16 in different colors), EV-B (purple), and other species (gray) in Taiwan. EV-B included CV types (B1–6 and A9) and echovirus types 3, 6, 11, 18, and 30. Counts of total cases reported in each year are also shown in parentheses. **b** Counts of severe complications are further summarized. **c** Compressed ML tree of Taiwanese strains in various subgenotypes (A, B0–5, and C1–5). Significant bootstrap support values greater than 70% are indicated at major nodes. **d** B5 and **e** C4 subtrees are shown. The tip labels of the 63 strains in B5 and C4 sequenced in this study are colored in red

**Table 1 Taiwanese genomes of EV-A71 analyzed in this study**

Year	Counts (genotype) of sequences acquired in this study	Counts (genotype) of sequences downloaded from ViPR
1986		6 (B1)
1998		6 (C2)
1999		1 (B4)
2000		1 (B4)
2001		1 (B4)
2002		1 (C4)
2003		1 (B5)
2004		11 (C4)
2005	9 (C4)	5 (C4)
2007	1 (C5)	1 (B5), 1 (C5)
2008	9 (B5)	19 (B5), 3 (C2-like), 1 (C4)
2009		2 (B5)
2010	5 (C4)	1 (C4)
2011	2 (B5), 2 (C4)	8 (B5), 6 (B4), 4 (C4)
2012	28 (B5), 2 (C4)	10 (B5), 1 (C2)
2013	1 (B5)	1 (C2)
2014		
2015	2 (B5), 1 (C4)	
2016	2 (C4)	
Total	64	91

has been the only country to suffer from EV-A71 outbreaks caused by the B5 strain. Sequences from other countries collected at similar times formed clusters with Taiwanese sequences (Fig. 2b, marked in red). For example, Taiwanese strains in 2003 (TW/2003) were closely related to strains from Malaysia in the same year. TW/2011–13 were clustered together, but they also clustered with two Vietnam/2012–13 strains and one China/2009 strain. In contrast, the new B5 branch may be derived from recent sequences found in Thailand. Two TW/2015 strains were closely related to the Thailand/2012–14 strains (Fig. 2b, upper), and the older Thailand strains (before 2012) were within the other cluster containing the TW/2003 strains rather than

that containing the TW/2007–11 strain (Fig. 2b, lower). Thus, the B5 strain may have first been transmitted from Taiwan to Thailand, where the virus independently evolved. Later, the locally evolved Thailand B5 strain was transferred back to Taiwan. Regarding the C4 strain, Taiwanese strains isolated after 2005 showed higher similarity to those isolated from China (Fig. 2c). Unlike that of the B5 strains, a scattered distribution of the C4 strains was observed (Fig. 2c). This result indicated that their genetic clades were not correlated with isolation year, despite the close relationships between strains from Taiwan and China in similar isolation years. Considering the different antigenicities of the B5 and C4 strains, which could alter herd immunity<sup>13</sup>, genotype switching in Taiwan may be related to the frequent transmission of different strains outside the Taiwan region.

**Interconnection of circulating EV-A71 by intratypic recombination**

Recent EV-A71 outbreaks have been characterized by an association with newly emerging subgenotypes<sup>8</sup>. Both the C2 and C4 strains are recombinogenic and carry partial genomes derived through intertypic recombination with coxsackievirus (CV)-A8 and CV-A16, respectively<sup>13,14</sup>. Furthermore, the B4 strain is an example of intratypic recombination within EV-A71 genotype B<sup>13</sup>. The emergence of various EV-A71 strains within a decade may be attributable to regionally enriched, large-scale outbreaks that can increase the risk of coinfection, a key requirement for recombination<sup>15</sup>. To examine this possibility, we evaluated Taiwanese full-genome sequences that consisted of a variety of genotypes/subgenotypes (Table 1) and explored the relationships among these newly emerging strains. EV-A71 and prototype CV (including types A2–A8, A10, A12, A14, and A16) sequences of EV-A were compared to reveal their recombinogenic properties. Breakpoints in EV-A71 recombination are usually located in the P2 and P3 regions<sup>16</sup>. Therefore, we first reconstructed ML phylogenetic trees of the P1, P2, and P3 regions (Fig. 3a–c, respectively). Possible recombination events were revealed by changes in the tree positions of analyzed sequences in the subgenomic phylogenies<sup>17</sup>.

In the phylogenetic tree constructed via the P1 region and rooted with the oldest strain (CVA2-Fleetwood), distinct clades representative of each genotype/subgenotype were observed, and all sequences of prototype

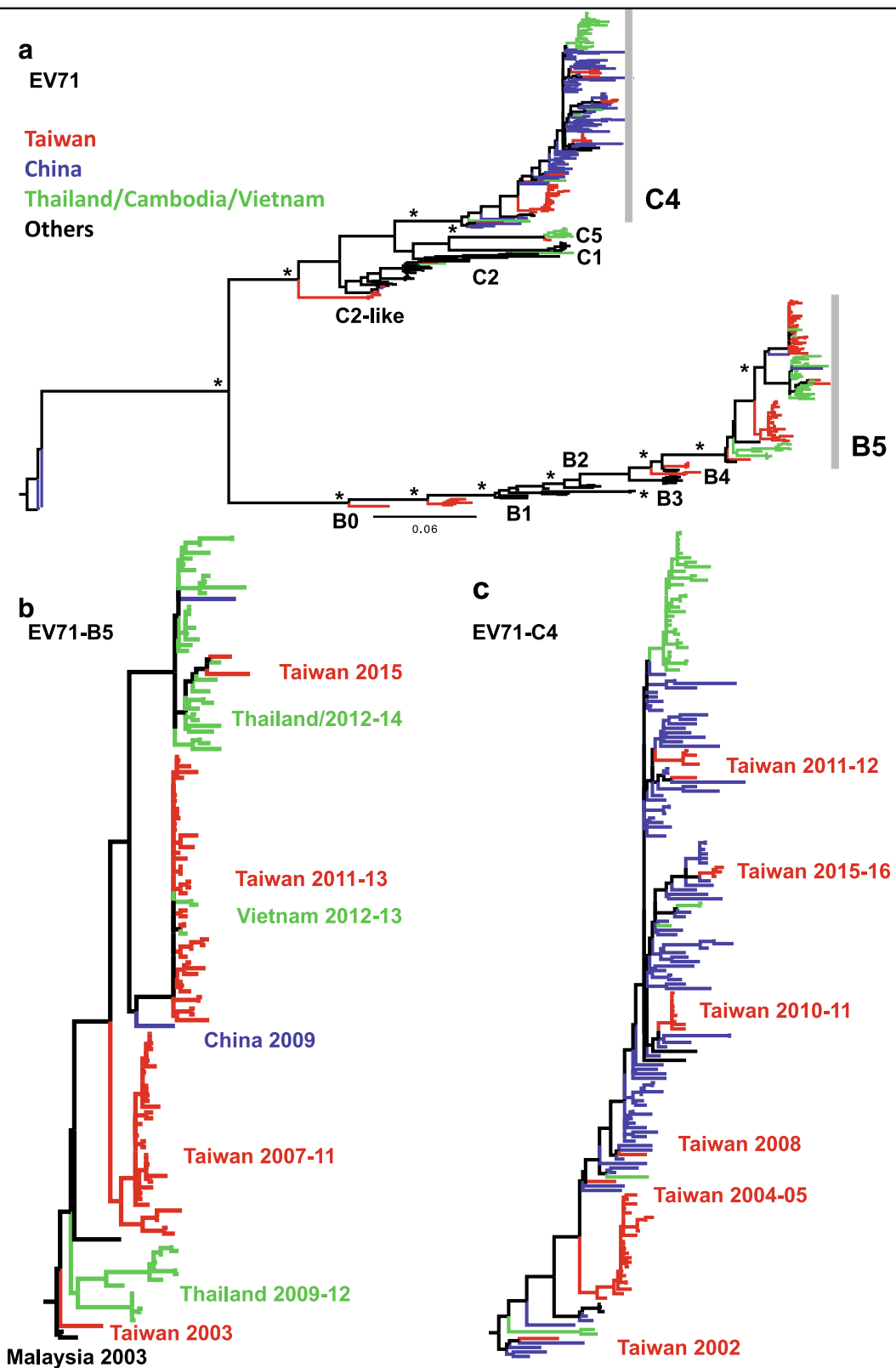
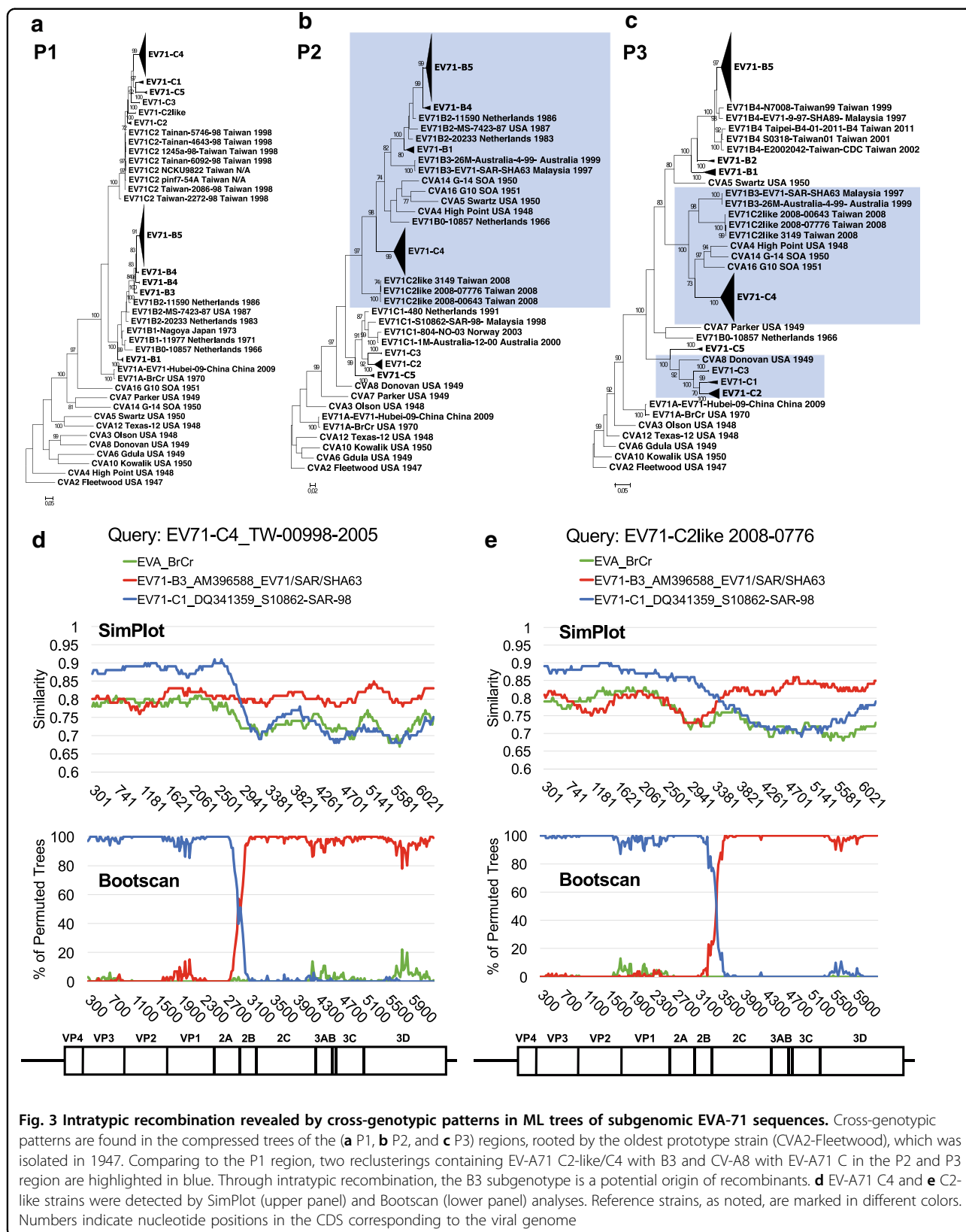


**Fig. 2** ML tree of the VP1 gene in Taiwanese and worldwide EV-A71 strains. **a** Compressed tree, including Taiwanese and worldwide strains. Significant bootstrap support values greater than 70% are indicated by asterisks at the major nodes. Strains isolated from Taiwan, China, Cambodia/Thailand/Vietnam, and other countries are marked in different colors. **b** B5 and **c** C4 subtrees are shown





CV appeared as an outgroup (Fig. 3a). In contrast, cross-genotypic patterns in the CV-A and EV-A71 sequences were identified in the P2 and P3 phylogenetic trees (Fig. 3b, c). The inconsistency of these phylogenies reflected recombination events. For example, CV-A8 was reported as the recombination parent of EV-A71 C2<sup>13</sup>, and this result is reflected by their coclustering in the P3 region (Fig. 3c, highlighted in blue), indicating that the high sequence similarity between CV-A8 and EV-A71 genotype C may have facilitated the recombination and emergence of the EV-A71 C2 strain. Similar reclustering also occurred in the C2-like and C4 strains. In the P2 phylogenetic tree, the C2-like strain was an outlier of genotype C of EV-A71, and the C4 cluster was closely related to genotype B and several prototype CVs (Fig. 3b). The clustering pattern changed again in the P3 phylogenetic tree, and a new cluster containing EV-A71 B3, C2-like, and C4 was formed. Additionally, prototypes CV-A4, CV-A14, and CV-A16 were redistributed into the same cluster (Fig. 3c). Given that the EV-A71 C4 strain was regarded as a double-recombinant virus containing EV-A71 genotype B-like P2 and CV-A16-like P3 regions and that the B3 strain was a recombinant with a CV-A16-like 3D region<sup>14,18,19</sup>, our results suggested that the EV-A71 B3 strain may be the possible recombination parent of the C4 strain. Similarly, the C2-like strain may be an uncharacterized recombinant EV-A71 that also originated from the B3 strain. These predictions were confirmed by SimPlot analysis (Fig. 3d, e). When comparing the C4 strain to reference strains including the EV-A71 genotypes A, B3, and C1, its 5' region showed a higher similarity (approximately 88%) to that of EV-A71 genotype C1; however, the similarity decreased at the boundary of the 2A/2B coding region, and this effect was accompanied by an increased similarity (approximately 80%) to B3 toward the 3' half of the viral genome. The recombinant breakpoint was mapped to approximately nucleotide position 2881 of the coding sequence (CDS) (Fig. 3d). The shift of predominant similarity from one reference strain to another in different genomic regions was also observed when we queried C2-like strain sequences. The C2-like genome contained genotype C- and B3-similar sequences at the 5' and 3' regions, respectively. However, the breakpoint of the C2-like strain was mapped to the downstream 2C coding region (approximately nucleotide 3481 of the CDS), near the structural *cis*-acting replication element (Fig. 3e). Since the EV-A71 B3 strain was also the recombination parent of the B4 strain<sup>13</sup>, our data suggested that a temporally circulating EV-A71 strain B3 may serve as an important intermediate leading to the emergence of diverse EV-A71 strains. Although we attempted to remove sample size limitations in the interpretation of the phylogenetic trees (by downloading all of the full-length genomes isolated in

Taiwan for the current study), some differences may still exist between the published full-length genomes and the actual viral population.

### Extensive genomic recombinations among the cocirculating enteroviruses

Various viruses belonging to EV-A continuously cocirculate with EV-A71 in Taiwan (Fig. 1a), and many of these non-EV-A71 viruses are recombinant with unknown parents<sup>16</sup>. Thus, we next examined whether EV-A71 may be involved in the recombination of non-EV-A71 viruses of EV-A. To prevent sampling bias, we collected all of the historical EV-A full-genome sequences worldwide for the following analyses. Since most recombinations in other EV-A viruses also occur outside the P1 region<sup>16</sup>, we evaluated EV-A71 and CV sequences in the P2/P3 coding region. We utilized Bayesian evolutionary analysis to specify the spatial-temporal relationships among these sequences. When sequences spanning from P2 to the 3' end of the viral genome were analyzed, several clusters were observed, most of which contained clades corresponding to different serotypes of EV-A and subgenotypes of EV-A71 (Fig. 4a). One cluster of particular interest contained the EV-A71 B3, C2-like, and C4 strains as well as several currently circulating viruses (Fig. 4a, red rectangle). The details of this cluster are shown in Fig. 4b. Notably, this cluster was proximal to a second cluster containing the prototype sequences of CV-A4, CV-A14, and CV-A16, indicating a potential role of these viruses as recombination parents. Because the evolutionary paths of the circulating strains in phylogenies might be biased by a series of recombination events, we emphasized the detection of incongruous genetic clusters<sup>20</sup>. Considering the times at which the viruses distributed in this cluster arose, EV-A71 B3 represented the oldest strain among all the branches and may represent the possible origin of the other viruses (Fig. 4b). However, more genomes (particularly of historical EV-A strains) are required to strengthen this conclusion.

We next compared the locations of these recombinant viruses within the phylogenies constructed using either the P2 or P3 sequence. In the P2 phylogeny, the prototype strains of CV-A4, CV-A14, and CV-A16 were redistributed to another cluster consisting of most strains of genotype B (Fig. 4c, lower), indicating the high sequence similarity among these viruses, which may have promoted the emergence of the EV-A71 B3 strain through intertypic recombination. In the EV-A71 B3-containing cluster, currently circulating rather than prototype strains of CV-A2, CV-A6, CV-A8, and CV-A12 were found. The majority of currently circulating CV-A4 was distributed to another EV-A71 C4-containing cluster, suggesting that additional recombination events involving EV-A71 C4 may occur (Fig. 4c, upper). In contrast, all viruses mixed

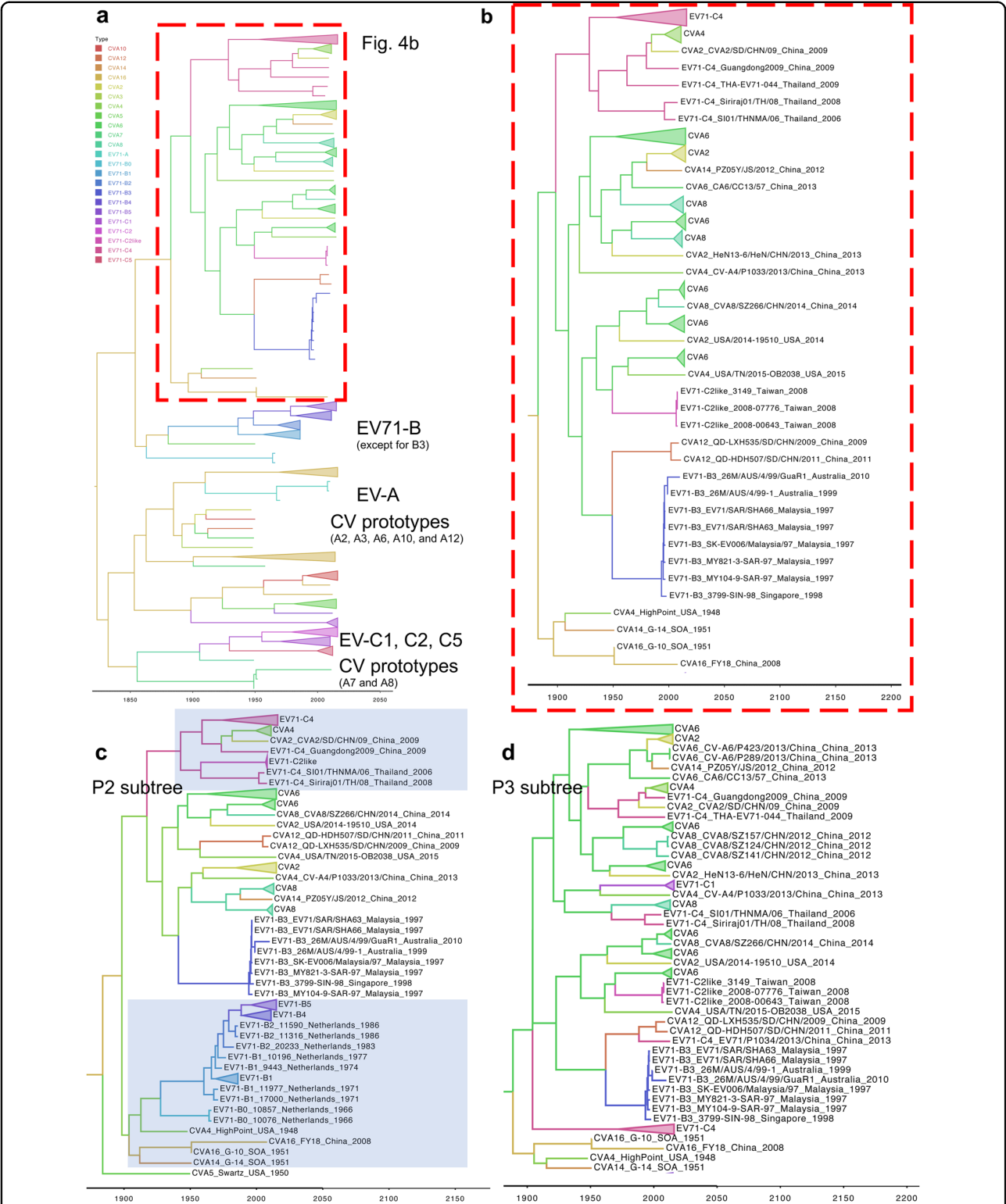


**Fig. 4** Bayesian phylogenetic tree of currently circulating EV-A viruses. Bayesian phylogenetic trees based on (a) and b. P2/P3, c P2 and d P3 regions. Genotypes/subgenotypes of EV-A71 and CVs are marked in different colors. The subtrees in (b–d) contain mixed clusters, showing intra- and intertypic recombination events among EV-A71 B3/C4 and CVs. Highlights in c represent the reclustering of the prototype CVs with EV-A71 B and of EV-A71 C4 with the currently circulating CV-A4

together without clear assortment in the P3 phylogeny (Fig. 4d). This sporadic distribution indicated that most viruses may have similar P3 regions. Thus, recombination may occur among the cocirculating viruses in the P2 region, which could result in a common P3 region shared by these viruses. To verify this hypothesis, SimPlot analyses were carried out to examine the recombination of currently circulating CVs (Fig. 5). When EV-A71 B3 was incorporated as the reference strain, a single crossover was found in the P1/P2 boundary when CV-A2, CV-A6, CV-A8, and CV-A12 were analyzed (Fig. 5a–d). The role of EV-A71 C4 in the recombinant CV-A4 and an additional intertypic recombination between CV-A4 and CV-A2 were also confirmed (Fig. 5e, f). To eliminate sampling bias, consensus sequences of these recombinant strains from EV-A71 B3, B5, C2-like, and C4, and CV-A2, CV-A4, CV-A6, CV-A8, CV-A12, and CV-A16 were further generated for comparison to the prototype strains of EV-A71 and CVs. Eleven EV-A71-like signatures were identified in the circulating strains of EV-A71 C2-like and C4 and CV-A2, CV-A4, CV-A6, and CV-A12, but not their prototype strains, except for CV-A4 and CV-A16 (Table 2). Thus, in addition to CV-A16<sup>14,18,19,21</sup>, CV-A4 might be another potential recombination parent of these currently circulating viruses. Consistent with the results of the Bayesian phylogenetic tree (Fig. 4d) and SimPlot predictions (Fig. 5), all signatures were located in the P3 region (Table 2), which might be caused by the intensive recombinations in the P2 region. Such signatures cannot be found in the circulating CV-A16 strain, which has been reported to be recombinant with EV-A71 genotype A<sup>16</sup>, or in the EV-A71 B5 strain, which evolves independently of other viruses. Both strains carry sequences similar to those of the EV-A71 prototype strain.

## Discussion

In this study, we found that many currently circulating EV-A strains have undergone recombination and that EV-A71 B3 may have played a central role in this process, based on the latest published database of EV-A full-length genomes (Fig. 6). It is expected that more genomes will be published and will be added to this simplified flowchart. Through a series of intra- and intertypic recombinations, EV-A71-like signatures were found to be widely present in many currently circulating EV-A viruses (Table 2). Although the impact of these signatures on viral replication remains unclear, their prevalence in various EV-A viruses may have applications in the development of broad-spectrum antivirals.

### Role of recombination in the evolution of EV-A71

The classification of various EV-A71 strains was based on the nucleotide sequence diversity of the VP1 gene (genetic variation less than 12 and 19% for subgenotype

and genotype, respectively). The overall identity of amino acid sequences among these viruses still reached 94%<sup>5</sup>. The effects of mutations and recombinations on EV-A71 evolution have been extensively discussed, and although several VP1 amino acids are under positive selection, EV-A71 may be subjected to strong negative selection, which theoretically should result in a stabilized and purified virus<sup>7,10</sup>. Thus, recombination may have played an important role in the appearance of diverse EV-A71 strains such as B3, B4, C2, and C4 since 1997<sup>13,14,18,19</sup>. Intratypic recombinations have also occurred in different EV species, with a higher frequency in EV-B species than in EV-A and EV-C<sup>22</sup>. Here, by analysis of full-genome sequences collected in Taiwan from 1998 to 2016, we determined when and where recombination occurred and how these events could have led to the emergence of the different strains associated with EV-A71 outbreaks. Although published genomes have limited value as a proxy for the actual viral population, several recombination events can be revealed by analyzing the phylogenetic relationships among EV-A71 subgenotypes. We did not rule out the importance of mutation during EV-A71 evolution<sup>23</sup>. Instead, a combination of both recombination and mutation may result in the rapid switching between different EV-A71 strains within a short time period. In the future, more genomes will be needed to decipher the evolutionary history of EV-A71.

### Extensive recombination in cocirculating viruses

Sequences with high similarity to those of the prototype strains CV-A8 and CV-A16 were found in the EV-A71 C2 and B3/C4 strains, respectively<sup>13,14,18,19</sup>. However, considering the requirement of coinfection for recombination, it is possible to obtain the “non-self” genome from cocirculating viruses<sup>15</sup>. In addition, as one of the countries having cocirculation of multiple EV-A71 subgenotypes and several EV-A viruses, Taiwan represents a good niche for clarifying the relationships among cocirculating viruses<sup>8</sup>. In this study, we proposed that the emergence of the EV-A71 C2-like and C4 strains may be explained by intratypic recombination with the B3 strain. Although the presence of the B3 strain in Taiwan has not been previously documented, it was involved in the recombination of the B4 strain, which caused severe outbreaks in the early 2000s<sup>12,13</sup>. The intensive recombinations were not EV-A71-specific and could also be found in several currently circulating EV-A viruses through intertypic recombinations. Among these viruses, only CV-A2, CV-A4, and CV-A6 have been documented in Taiwan. However, all these viruses have been reported to be common causes of HFMD in China and are recombinogenic with EV-A71<sup>24</sup>. Interestingly, a novel EV-A71 genotype C strain with a mosaic genome structure has been identified in Germany and Denmark<sup>25,26</sup>. This new strain had a



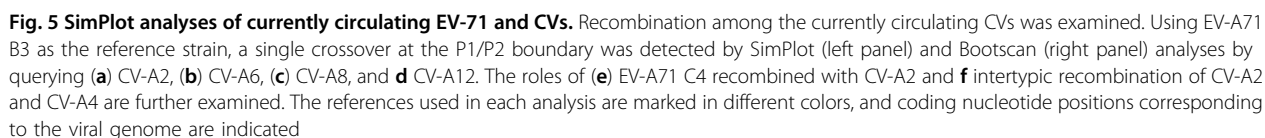


**Table 2 Amino acid positions of 11 signatures carried by circulating strains of recombinant EV-A viruses**

Gene	3A	3C	3D								
Position	39	36	95	44	76	94	134	138	368	428	451
<b>Consensus sequence of circulating strains</b>											
EV-A71 B3	D	V	S	H	E	Q	T	V	N	Q	Y
EV-A71 C2-like	.	.	.	.	.	.	.	.	.	.	.
EV-A71 C4	.	.	.	.	.	.	.	.	.	.	.
CVA2	.	.	.	.	.	.	.	.	.	.	.
CVA4	.	.	.	.	.	.	.	.	.	.	.
CVA6	.	.	.	.	.	.	.	.	.	.	.
CVA8	.	.	.	.	.	.	.	.	.	.	.
CVA12	.	.	.	.	.	.	.	.	.	.	.
CVA16	E	I	T	T	Q	K	V	T	T	E	F
EV-A71 B5	E	.	.	T	Q	K	V	.	T	D	F
<b>Prototype strains (Strain, Country, Year)</b>											
EV-A71 A (BrCr, USA, 1970)	E	I	T	T	Q	K	V	T	T	E	L
CVA2 (Fleetwood, USA, 1947)	E	I	T	T	Q	K	V	T	T	E	F
CVA4 (HighPoint, USA, 1948)	.	.	.	.	.	.	.	.	.	.	.
CVA6 (Gdula, USA, 1949)	E	I	T	T	Q	K	A	T	T	E	F
CVA8 (Donovan, USA, 1949)	.	.	.	T	.	K	.	.	T	E	F
CVA12 (Texas-12, USA, 1948)	E	I	T	T	Q	K	V	T	T	E	F
CVA16 (G-10, SOA, 1951)	.	.	.	.	.	.	.	.	.	.	.

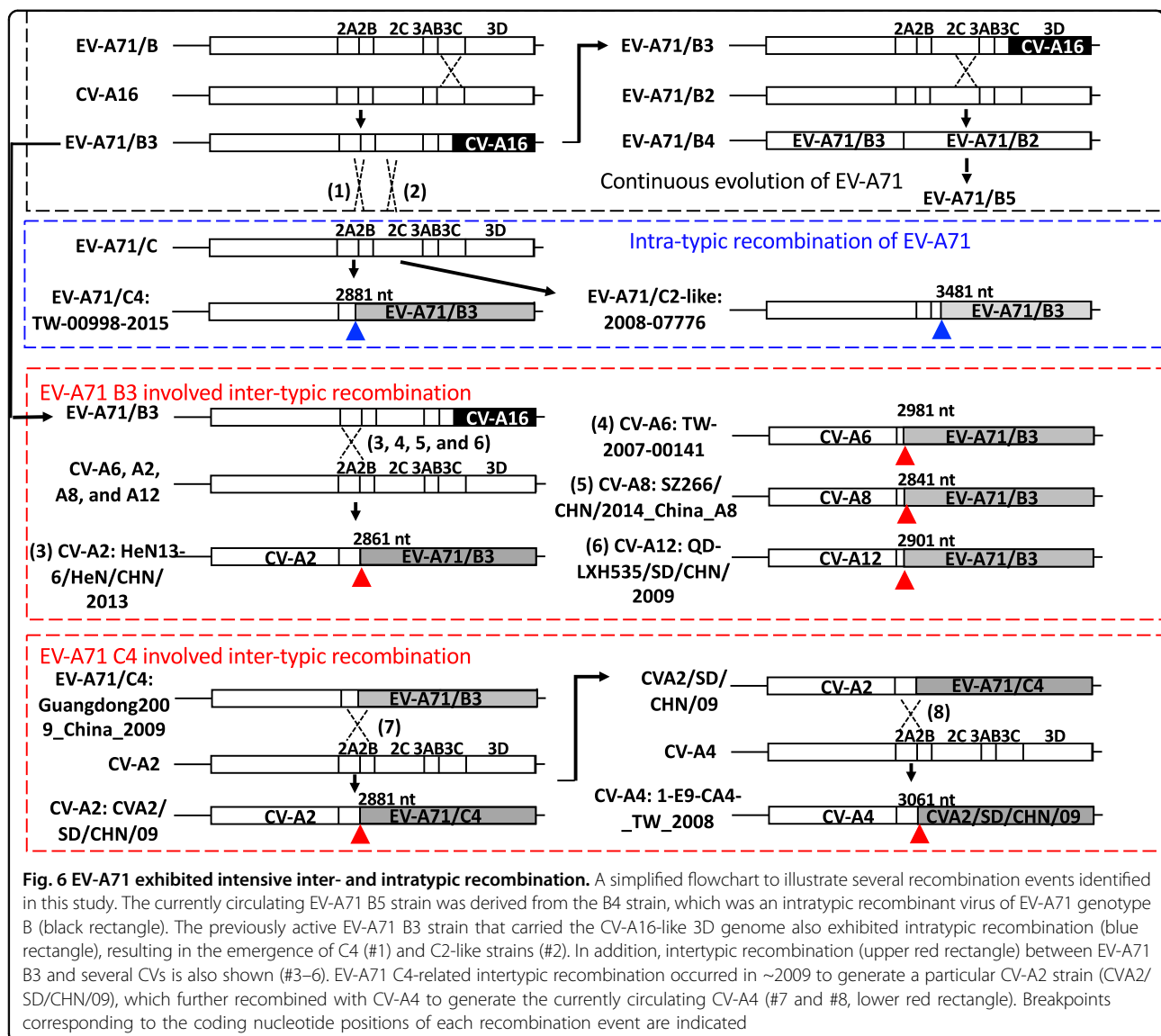
Signatures identified from the EV-A71 B3 strain were found in consensus sequences of circulating strains in EV-A71 genotypes C2-like and C4, and CV serotypes A2, A4, A6, and A12

C1-like VP1 region; however, the 5' untranslated region and the P2/P3 region showed higher similarity to EV-A71 B3/C2-like and C4, respectively. This new EV-A71 strain may have been generated by recombination of the locally circulating C1 strain with the imported C4 strain that became dominant recently<sup>27</sup>. Although intensive recombination of cocirculating EV-A viruses with EV-A71 has been observed, there are some exceptions. Both CV-A5 and CV-A10 are commonly detected by the Taiwan enterovirus surveillance system; however, no recombination with EV-A71 has been observed. Instead, a close relationship in the nonstructural region, possibly caused by intertypic recombination between circulating CV-A5 and CV-A10, has been reported<sup>28</sup>. Therefore, recombination between cocirculating viruses may be more common than expected, and full-genome sequencing rather than sequencing of VP1 only should be considered when encountering a new epidemic.

#### Hot spots for recombination: functional impact of genome reassembly

In all recombination events identified in this study, breakpoints were mapped to the region extending from

the P1/P2 boundary to the 2C region (Fig. 6a), suggesting the existence of recombination hot spots. Thus, recombination can result in genome reassembly of the structural and nonstructural regions. The restricted location of the breakpoints may have resulted from natural selection. Delicate cooperation among picornavirus viral proteins and genomes is required for productive viral replication<sup>29</sup>. Because the genome of EV-A can be directly translated into a polyprotein and then undergo proteolytic cleavage, changes in the functional entities by recombination could be deleterious to the virus. For example, viral 3D<sup>pol</sup> is required for viral replication and recognizes several *cis*-elements throughout the genome<sup>29</sup>. In the case of EV-A71 B3, due to the presence of the CV-A16-like 3D<sup>pol</sup>, the virulence was decreased when compared with those of EV-A71 B4 and CV-A16 in mouse model infections<sup>21</sup>. Therefore, the EV-A71-like signatures that consist of EV-A71 genotype B-like P2 and CV-A16-like P3 regions may have been less favored and discarded in the evolution of EV-A71 genotype B (Fig. 6a, black rectangle). However, as we have shown here, EV-A71-like signatures are tolerated by EV-A71 genotype C and several CVs of EV-A, and the numbers of appropriate



recombination acceptors could keep increasing<sup>25,26</sup>. Because a high sequence similarity is preferred for copy-choice recombination, as detailed in the widely accepted model of RNA virus recombination<sup>15</sup>, the sequence identity between the EV-A71 C4 and B5 strains should definitely be higher than that between the EV-A71 and EV-A viruses. Restricted recombination under natural selection may explain why EV-A71 C4 and B5 cocirculated but did not recombine, exhibiting independent evolution. We currently have no evidence to conclude whether recombination may be beneficial for the virus; however, the ratio of recombinant CV-A6-associated HFMD has increased worldwide<sup>24,30</sup>. Here, we provide only evidence demonstrating the shared nonstructural proteins of cocirculating EV-A viruses. Through the establishment of sequence databases that integrate complete sets of full-genome sequences, we might able to

predict what kinds of genome assembly and possible recombinants might appear in the future.

## Materials and methods

### Specimen collection and sequencing of EV-A71

All of the 64 EV-A71 clinical specimens isolated from 2005 to 2016 were provided by the Linkou Chang Gung Memorial Hospital, Taiwan. Regardless of the illness diagnosed, we randomly picked clinical samples from epidemics in this time span. To prevent contamination, amplified viral stocks from human rhabdomyosarcoma cells were used for full-genome sequencing. Viral genomes were recovered using TRIzol LS reagent (Thermo Fisher Scientific, Waltham, MA, USA) according to the manufacturer's instructions. The 59 samples collected before 2014 were sequenced by Sanger sequencing. Oligo-(dT)<sub>20</sub> was used to prepare poly(A)-containing viral

cDNA using a ReverTra Ace  $\alpha$ - kit (Toyobo, Osaka, Japan). Overlapping amplicons covering the entire viral genome were amplified by different sets of primers<sup>18,31</sup>, and genome assembly was carried out using SeqMan software (DNASTAR, Inc., Madison, WI, USA). The five samples collected after 2014 were sequenced using the Illumina HiSeq platform for next-generation sequencing (NGS). NGS data preprocessing included the removal of low-quality and host reads. Using the Taiwanese B5 and C4 strains as an initial template, the viral genomes were assembled by an iterative mapping approach<sup>32</sup>. A total of 64 genomes obtained in this study were deposited in GenBank with accession numbers MG756691–MG756754.

#### Data collection for EV-A genomes from ViPR and recombination analysis

Eight hundred thirty-one EV-A71 genomes worldwide were initially retrieved from ViPR in September 2017. Sequences with ambiguous nucleotides or without known sampling dates and countries were removed. To reduce redundancy, we randomly selected 10 sequences with the same genotype and isolation year from each country. We then collected 427 EV-A71 sequences including all Taiwanese strains for analysis (Supplementary Table 1). Moreover, 780 complete CV genomes (belonging to EV-A) were downloaded from ViPR. After data preprocessing, 351 CV genomes were collected. Details of the analyzed sequences are shown in Supplementary Table 2. Recombination between the EV-A71 and CV genomes in this study was detected using SimPlot (version 3.5.1) with a sliding window size of 600 nt and a step size of 20 nt<sup>33</sup>. To identify genomic signatures associated with detected recombination in this study, a consensus sequence for each of the serotypes/genotypes was generated by using the Cons tool with the default setting from EMBOSS<sup>31</sup>.

#### Phylogenetic tree analysis

The ML method based on the Hasegawa–Kishino–Yano (HKY) model was performed to infer the evolutionary history<sup>34</sup>. The percentage of replicate trees in which the associated taxa clustered together in a bootstrap test with 1000 replicates was calculated. All positions with less than 95% site coverage were eliminated. Evolutionary analyses were conducted in MEGA7<sup>35</sup>. Furthermore, the Bayesian phylogenetic tree was inferred by BEAST<sup>36</sup> with BEAGLE<sup>37</sup> to estimate the maximum clade credibility (MCC) tree under the HKY model. Based on our collected sequences, we generated 50 million Markov chain Monte Carlo (MCMC) chains with 10% burn-in. One MCC tree was constructed for every 25,000 chains, and a single consensus tree was summarized from these MCC trees. MCMC was also used in BEAST to estimate the time of divergence for each alignment.

#### Acknowledgements

This work was financially supported by a grant from the Human Frontier Science Program (RGP0011/2015), the Ministry of Science and Technology (MOST), Taiwan (MOST 107-3017-F-182-001), and the Research Center for Emerging Viral Infections from The Featured Areas Research Center Program within the framework of the Higher Education Sprout Project by the Ministry of Education (MOE) in Taiwan.

#### Authors' contributions

K.-M.L. and S.-R.S. conceptualized and designed the study in collaboration with N.H.D. and C.E.C. K.-M.L. drafted the manuscript and participated in the collection of sequence data, phylogenetic and recombination analyses, and figure preparation. Y.-N.G. collected sequence data, performed the next-generation sequencing of clinical isolates and phylogenetic and recombination analyses, and prepared the figures. T.-H.H. prepared and stored the virus stock of all clinical isolates and performed the Sanger sequencing of clinical isolates. A.W., N.H.D., and C.E.C. were involved in conceptualization of the study and contributed to the writing of the manuscript. All authors have critically reviewed the manuscript.

#### Author details

<sup>1</sup>Research Center for Emerging Viral Infections, College of Medicine, Chang Gung University, Taoyuan, Taiwan. <sup>2</sup>Department of Medical Biotechnology and Laboratory Science, College of Medicine, Chang Gung University, Taoyuan, Taiwan. <sup>3</sup>Department of Biochemistry and Molecular Biology, The Pennsylvania State University, University Park, PA 16802, USA. <sup>4</sup>Department of Bionanoscience, Kavli Institute of Nanoscience, Delft University of Technology, Van der Maasweg 9, Delft 2629 HZ, The Netherlands. <sup>5</sup>Department of Laboratory Medicine, Linkou Chang Gung Memorial Hospital, Taoyuan, Taiwan. <sup>6</sup>Research Center for Chinese Herbal Medicine, Research Center for Food and Cosmetic Safety, and Graduate Institute of Health Industry Technology, College of Human Ecology, Chang Gung University of Science and Technology, Taoyuan, Taiwan

#### Conflict of interest

The authors declare that they have no conflict of interest.

**Supplementary Information** accompanies this paper at (<https://doi.org/10.1038/s41426-018-0107-0>).

Received: 13 February 2018 Revised: 27 April 2018 Accepted: 29 April 2018  
Published online: 21 June 2018

#### References

- Solomon, T. et al. Virology, epidemiology, pathogenesis, and control of enterovirus 71. *Lancet Infect. Dis.* **10**, 778–790 (2010).
- Ho, M. et al. An epidemic of enterovirus 71 infection in Taiwan. Taiwan Enterovirus Epidemic Working Group. *N. Engl. J. Med.* **341**, 929–935 (1999).
- Chang, L. Y. Enterovirus 71 in Taiwan. *Pediatr. Neonatol.* **49**, 103–112 (2008).
- Bessaud, M. et al. Molecular comparison and evolutionary analyses of VP1 nucleotide sequences of new African human enterovirus 71 isolates reveal a wide genetic diversity. *PLoS ONE* **9**, e90624 (2014).
- Brown, B. A., Oberste, M. S., Alexander, J. P. Jr, Kennett, M. L. & Pallansch, M. A. Molecular epidemiology and evolution of enterovirus 71 strains isolated from 1970 to 1998. *J. Virol.* **73**, 9969–9975 (1999).
- Saxena, V. K., Sane, S., Nadkarni, S. S., Sharma, D. K. & Deshpande, J. M. Genetic diversity of enterovirus A71, India. *Emerg. Infect. Dis.* **21**, 123–126 (2015).
- Tee, K. K. et al. Evolutionary genetics of human enterovirus 71: origin, population dynamics, natural selection, and seasonal periodicity of the VP1 gene. *J. Virol.* **84**, 3339–3350 (2010).
- McMinn, P. C. Recent advances in the molecular epidemiology and control of human enterovirus 71 infection. *Curr. Opin. Virol.* **2**, 199–205 (2012).
- Christian, K. A. et al. What we are watching—five top global infectious disease threats, 2012: a perspective from CDC's Global Disease Detection Operations Center. *Emerg. Health Threats J.* **6**, 20632 (2013).



10. Chen, X. et al. Analysis of recombination and natural selection in human enterovirus 71. *Virology* **398**, 251–261 (2010).
11. Mao, Q., Wang, Y., Bian, L., Xu, M. & Liang, Z. EV-A71 vaccine licensure: a first step for multivalent enterovirus vaccine to control HFMD and other severe diseases. *Emerg. Microbes Infect.* **5**, e75 (2016).
12. Wang, S. F. An epidemiological analysis of enterovirus 71: Taiwan, 1998–2004. *Taiwan Epidemiol. Bull.* **21**, 125–153 (2005).
13. Huang, S. W. et al. Reemergence of enterovirus 71 in 2008 in Taiwan: dynamics of genetic and antigenic evolution from 1998 to 2008. *J. Clin. Microbiol.* **47**, 3653–3662 (2009).
14. Yip, C. C. et al. Emergence of enterovirus 71 “double-recombinant” strains belonging to a novel genotype D originating from southern China: first evidence for combination of intratypic and intertypic recombination events in EV71. *Arch. Virol.* **155**, 1413–1424 (2010).
15. Simon-Loriere, E. & Holmes, E. C. Why do RNA viruses recombine? *Nat. Rev. Microbiol.* **9**, 617–626 (2011).
16. Kyriakopoulou, Z., Pliaka, V., Amoutzias, G. D. & Markoulatos, P. Recombination among human non-polio enteroviruses: implications for epidemiology and evolution. *Virus Genes* **50**, 177–188 (2015).
17. Posada, D., Crandall, K. A. & Holmes, E. C. Recombination in evolutionary genomics. *Annu. Rev. Genet.* **36**, 75–97 (2002).
18. Yoke-Fun, C. & AbuBakar, S. Phylogenetic evidence for inter-typic recombination in the emergence of human enterovirus 71 subgenotypes. *BMC Microbiol.* **6**, 74 (2006).
19. Chan, Y. F. et al. Comparative genetic analysis of VP4, VP1 and 3D gene regions of enterovirus 71 and coxsackievirus A16 circulating in Malaysia between 1997–2008. *Trop. Biomed.* **29**, 451–466 (2012).
20. Biek, R., Pybus, O. G., Lloyd-Smith, J. O. & Didelot, X. Measurably evolving pathogens in the genomic era. *Trends Ecol. Evol.* **30**, 306–313 (2015).
21. Chan, Y. F. & AbuBakar, S. Human enterovirus 71 subgenotype B3 lacks coxsackievirus A16-like neurovirulence in mice infection. *Virol. J.* **2**, 74 (2005).
22. Simmonds, P. & Welch, J. Frequency and dynamics of recombination within different species of human enteroviruses. *J. Virol.* **80**, 483–493 (2006).
23. Huang, S. W. et al. Mutations in the non-structural protein region contribute to intra-genotypic evolution of enterovirus 71. *J. Biomed. Sci.* **21**, 33 (2014).
24. Guo, W. P. et al. Fourteen types of co-circulating recombinant enterovirus were associated with hand, foot, and mouth disease in children from Wenzhou, China. *J. Clin. Virol.* **70**, 29–38 (2015).
25. Bottcher, S., Obermeier, P. E., Neubauer, K. & Diedrich, S., Laboratory Network for Enterovirus, D. Recombinant enterovirus A71 subgenogroup C1 strains, Germany, 2015. *Emerg. Infect. Dis.* **22**, 1843–1846 (2016).
26. Midgley, S. E. et al. Co-circulation of multiple subtypes of enterovirus A71 (EV-A71) genotype C, including novel recombinants characterised by use of whole genome sequencing (WGS), Denmark 2016. *Euro. Surveill.* **22**. <https://doi.org/10.2807/1560-7917.ES.2017.22.26.30565> (2017).
27. Fischer, T. K. et al. Emergence of enterovirus 71 C4a in Denmark, 2009 to 2013. *Eur. Surveill.* **19**, 20911 (2014).
28. Hu, Y. F. et al. Complete genome analysis of coxsackievirus A2, A4, A5, and A10 strains isolated from hand, foot, and mouth disease patients in China revealing frequent recombination of human enterovirus A. *J. Clin. Microbiol.* **49**, 2426–2434 (2011).
29. Paul, A. V. & Wimmer, E. Initiation of protein-primed picornavirus RNA synthesis. *Virus Res.* **206**, 12–26 (2015).
30. Cabrerizo, M. et al. Molecular epidemiology of enterovirus 71, coxsackievirus A16 and A6 associated with hand, foot and mouth disease in Spain. *Clin. Microbiol. Infect.* **20**, O150–O156 (2014).
31. Zhang, Y. et al. Complete genome analysis of the C4 subgenotype strains of enterovirus 71: predominant recombination C4 viruses persistently circulating in China for 14 years. *PLoS ONE* **8**, e56341 (2013).
32. Gong, Y. N. et al. A next-generation sequencing data analysis pipeline for detecting unknown pathogens from mixed clinical samples and revealing their genetic diversity. *PLoS ONE* **11**, e0151495 (2016).
33. Lole, K. S. et al. Full-length human immunodeficiency virus type 1 genomes from subtype C-infected seroconverters in India, with evidence of inter-subtype recombination. *J. Virol.* **73**, 152–160 (1999).
34. Hasegawa, M., Kishino, H. & Yano, T. Dating of the human-ape splitting by a molecular clock of mitochondrial DNA. *J. Mol. Evol.* **22**, 160–174 (1985).
35. Kumar, S., Stecher, G. & Tamura, K. MEGA7: Molecular Evolutionary Genetics Analysis Version 7.0 for bigger datasets. *Mol. Biol. Evol.* **33**, 1870–1874 (2016).
36. Drummond, A. J. & Rambaut, A. BEAST: Bayesian evolutionary analysis by sampling trees. *BMC Evol. Biol.* **7**, 214 (2007).
37. Suchard, M. A. & Rambaut, A. Many-core algorithms for statistical phylogenetics. *Bioinformatics* **25**, 1370–1376 (2009).

# Topical application of anthranilate derivatives ameliorates psoriatic inflammation in a mouse model by inhibiting keratinocyte-derived chemokine expression and neutrophil infiltration

Zih-Chan Lin,\* Pei-Wen Hsieh,<sup>†,‡,§,¶</sup> Tsong-Long Hwang,<sup>†,‡,§,¶,||</sup> Chi-Yuan Chen,<sup>‡,§,¶,\*\*</sup> Calvin T. Sung,<sup>††</sup> and Jia-You Fang<sup>†,‡,§,¶,||,1</sup>

\*Graduate Institute of Biomedical Sciences, <sup>†</sup>Graduate Institute of Natural Products, and <sup>||</sup>Healthy Aging Research Center, Chang Gung University, Kweishan, Taoyuan, Taiwan; <sup>‡</sup>Research Center for Food and Cosmetic Safety and <sup>§</sup>Research Center for Chinese Herbal Medicine and <sup>¶</sup>Graduate Institute of Health Industry Technology, Chang Gung University of Science and Technology, Kweishan, Taoyuan, Taiwan; <sup>¶</sup>Department of Anesthesiology and <sup>\*\*</sup>Tissue Bank, Chang Gung Memorial Hospital, Kweishan, Taoyuan, Taiwan; and <sup>††</sup>School of Medicine, University of California, Riverside, Riverside, California, USA

**ABSTRACT:** Psoriasis is an inflammatory autoimmune skin disorder possessing a complex etiology related to genetic and environmental triggers. Keratinocytes show a potential role for the origin of psoriasis. In this study, we estimated the efficiency of 2 anthranilate derivatives—(E)-4-(N-[2-[1-(hydroxyimino)ethyl]phenyl]sulfamoyl)phenyl pivalate (HFP031) and butyl 2-[2-(2-fluorophenyl)acetamido]benzoate (HFP034)—on psoriasis amelioration in a mouse model. The results showed that topical treatment with both compounds could attenuate epidermal thickness and scaling in an imiquimod (IMQ)-induced psoriasis mouse model *via* decreased expression of cytokines and chemokines [C-X-C chemokine ligand (CXCL)1 and CXCL2], leading to the reduction of neutrophilic abscess in the skin. The *in vivo* cutaneous absorption of HFP034 was 7.6-fold greater than that of HFP031. Both compounds caused negligible irritation on healthy mouse skin. In addition, we examined the effect of the anthranilate derivatives on chemokine expression in IMQ-treated HaCaT keratinocytes. Our results elucidated a mechanism for anti-inflammatory activity of HFP034 that involved the elevation of intracellular cAMP concentration, suppression of NF- $\kappa$ B activity, and attenuation of neutrophil chemoattractant expression. These results suggest that HFP034 could increase the cutaneous concentration of cAMP to suppress neutrophil infiltration into the skin. Topically applied HFP034 may demonstrate a potential for future clinical application as a novel therapy for psoriasis treatment.—Lin, Z.-C., Hsieh, P.-W., Hwang, T.-L., Chen, C.-Y., Sung, C. T., Fang, J.-Y. Topical application of anthranilate derivatives ameliorates psoriatic inflammation in a mouse model by inhibiting keratinocyte-derived chemokine expression and neutrophil infiltration. *FASEB J.* 32, 000–000 (2018). www.fasebj.org

**KEY WORDS:** psoriasis • imiquimod • anthranilic acid • skin disease • phosphodiesterase-4 inhibitor

Psoriasis is a chronic, multifactorial, inflammatory skin disorder displaying a complex etiology involving in both genetic and environmental causes (1). It affects people of

all ages, making psoriasis a serious global problem with 125 million individuals affected worldwide (2). The psoriasis pathogenesis involves the crosstalk between multiple cell types and numerous cytokines and chemokines in response to internal and external triggers (3). The immunologic capacity of keratinocytes in epidermis for both acute and chronic stages of skin inflammation is maintained by permanent crosstalk among particular epidermal keratinocytes and immune cells recruited in the skin (4, 5). For the treatment of mild-to-moderate psoriasis, topical therapy is generally the most appropriate option (6). Frustration with medication efficacy, inconvenience, time constraints, and fear of adverse effects are among the most common reasons behind patients not using topical medication as directed (7). There is a great need for the continuous development of novel, safe, and effective treatment modalities for psoriasis.

**ABBREVIATIONS:** CXCL, C-X-C chemokine ligand; CXCR, C-X-C chemokine receptor; GAPDH, glyceraldehyde-3-phosphate dehydrogenase; H&E, hematoxylin and eosin; HFP031, (E)-4-(N-[2-[1-(hydroxyimino)ethyl]phenyl]sulfamoyl)phenyl pivalate; HFP034, butyl 2-[2-(2-fluorophenyl)acetamido]benzoate; IHC, immunohistochemical/immunohistochemistry; IMQ, imiquimod; Ly6G, lymphocyte antigen 6 complex locus G6D; m, mouse; MPO, myeloperoxidase; MTT, 3-(4,5-dimethylthiazol-2-yl)-2,5-diphenyltetrazolium bromide; PASI, Psoriasis Area Severity Index; PDE, phosphodiesterase; PEG, polyethylene glycol; SC, stratum corneum; TEWL, transepidermal water loss

<sup>1</sup> Correspondence: Pharmaceuticals Laboratory, Graduate Institute of Natural Products, Chang Gung University, 259 Wen-Hua 1st Rd., Kweishan, Taoyuan 333, Taiwan. E-mail: fajy@mail.cgu.edu.tw

doi: 10.1096/fj.201800354

This article includes supplemental data. Please visit <http://www.fasebj.org> to obtain this information.

Mahil *et al.* (8) highlighted the significance of neutrophil-keratinocyte interaction in the early pathogenesis of psoriasis, showing the importance of neutrophils in the early phase of psoriasis, because they are involved in T-cell recruitment and keratinocyte proliferation/differentiation. A previous clinical study had shown that depletion of activated neutrophils by adsorptive apheresis, as a nonpharmacological intervention, was associated with a significant improvement of psoriasis lesion (9). Neutrophils are mainly observed in the viable skin affected by psoriasis and are migrated by the chemokines (10, 11). The chemokines C-X-C chemokine ligand (CXCL1)/growth-related protein- $\alpha$  and CXCL2 (growth-related protein- $\beta$ /macrophage inflammatory protein 2 $\alpha$ ) are produced by macrophages, mast cells, and keratinocytes (12, 13). They mediate the function by signaling *via* C-X-C chemokine receptor (CXCR)2 on the neutrophils. CXCL8 (IL-8) is a member of the chemokine family that acts on CXCR1 and CXCR2. CXCL8 is constitutively produced by macrophages, hepatocytes, keratinocytes, and endothelial cells (14). CXCL1, CXCL2, and CXCL8 are considered to show an essential position in the psoriasis evolution. The previous report had indicated that the expression of CXCL1, CXCL2, and CXCL8 is elevated in psoriatic skin but not in healthy skin (15).

Anthranilate-related compounds have been recognized as having biologic activities, in particular, anticancer, -platelet, -bacterial, and -inflammatory activities (16–18). The 2 anthranilate derivatives—(E)-4-(N-[2-[1-(hydroxyimino)ethyl]phenyl]sulfamoyl)phenyl pivalate (HFP031) and butyl 2-[2-(2-fluorophenyl)acetamido]benzoate (HFP034)—have been reported to have anti-inflammatory potency. HFP031 (in our previous study) showed dual inhibitory effects on human neutrophil elastase and proteinase 3 (19). HFP034 (in our previous study) exhibited a potent inhibitory effect on the *N*-formyl-L-methionyl-L-leucyl-phenylalanine-induced release of O<sub>2</sub><sup>•−</sup> and phosphodiesterase (PDE)4 activity by using human neutrophils as the inflammation cell models (20). PDE4 is a cAMP-metabolizing enzyme, exhibiting a major role in inflammatory regulation. PDE4 inhibitors have been investigated as anti-inflammatory agents as a result of the repressed activity on immune cells (21). Apremilast is a PDE4 inhibitor approved by the U.S. Food and Drug Administration for oral administration to treat psoriasis. However, oral PDE4 inhibitors can cause a low therapeutic index and adverse effects, such as nausea and headache. We aimed to examine the anti-psoriatic activity of HFP031 and HFP034 using the imiquimod (IMQ)-induced mouse, as well as human keratinocytes and neutrophils, as the models. The topical route was used in this work to avoid the side effects caused by oral PDE4 inhibitors. The possible mechanisms of the anti-psoriatic potency of both compounds were also explored.

## MATERIALS AND METHODS

### IMQ-induced psoriasis mouse model

All animal experiments were conducted in strict accordance with the recommendation set forth in the Guidelines for the

Institutional Animal Care and Use Committee of Chang Gung University. BALB/c mice, at 8 wk of age, received a daily topical dose of 62.5 mg Aldara cream (3M Pharmaceuticals, St Paul, MN, USA) containing 5% IMQ on their shaved backs for 5 consecutive days. The control mice were also shaved and left untreated. The treatment group of mice was additionally pretreated with 100  $\mu$ l of 10 mg/ml compounds in a polyethylene glycol (PEG)400-ethanol mixture (4:6). HFP031 and HFP034 were synthesized based on the methods reported previously (19, 20). The mice were euthanized on d 4 and 7. The samples from the dorsal skin were taken for mRNA or protein extraction and histologic visualization. According to the objective scoring system—Psoriasis Area and Severity Index (PASI)—erythema, scaling, and thickness were recorded independently, with a score from 0 to 4 (0 no infection, 1 mild, 2 intermediate, 3 severe, 4 very severe). The total scoring (erythema, scaling, and thickness) presented as the estimation of the psoriatic severity degree (score 0–12).

### Immunohistochemical staining of skin sections

The dorsal skin sample was fixed in 10% formalin, buffered in the phosphate saline, and processed for hematoxylin and eosin (H&E) staining. The unstained slices of formalin-fixed, paraffin-embedded skin samples were prepared for immunohistochemistry (IHC). After dewaxing and rehydration, the paraffin-embedded sections were subjected to heat-induced epitope retrieval using Bond Epitope Retrieval Solution 2 (Leica Biosystems, Wetzlar, Germany), according to the manufacturer's instructions, followed by blocking with diluted normal serum. Sections were incubated with rabbit polyclonal anti-mouse (m)CXCL1 antibody, anti-mCXCL2 antibody, anti-mLy6G antibody, or anti-mouse myeloperoxidase (anti-mMPO) antibody for 1 h at room temperature; washed with saline containing 0.5% Tween 20, and subsequently incubated at ambient temperature with biotinylated donkey anti-goat IgG (Jackson ImmunoResearch Laboratories, West Grove, PA, USA) for 20 min. Color reaction was visualized using a Vectastain Elite avidin-biotin complex kit (Vector Laboratories, Burlingame, CA, USA). Photomicrographs were obtained using an Olympus DP72 digital color camera for microscopy (Tokyo, Japan).

### Real-time quantitative RT-PCR

After the mice were euthanized, 5 mm punch biopsies were acquired from the dorsal region. The total RNA was isolated by the Direct-zol RNA MiniPrep Kit (Zymo Research, Irvine, CA, USA). The mRNA concentration was rated, using a Nanodrop spectrophotometer (Thermo Fisher Scientific, Waltham, MA, USA) before conversion to cDNA using iScript Reverse Transcription Supermix (Bio-Rad, Hercules, CA, USA). The real-time PCR primers for relative expression analyses of mCXCL1, CXCL2, and glyceraldehyde-3-phosphate dehydrogenase (GAPDH) are described elsewhere. The assay of real-time PCR was set up in microcapillary tubes (10  $\mu$ l), consisting of cDNA solution (3  $\mu$ l), iQ SYBR Green Supermix (5  $\mu$ l; Bio-Rad), and 0.5 mM each with sense and antisense primers. We carried out the PCR program as follows: denaturation at 95°C for 3 min and 40 amplification cycles consisting of denaturation at 95°C for 15 s, annealing, and extension at 60°C for 30 s. GAPDH levels were used for normalization of the mRNA level. The sequences of the PCR primers were as follows: 5'-CAAACCGAAGTCATAGCCACAC-3' (forward) and 5'-TGGGGACACCTTTTAGCATCTTT-3' (reverse) for mCXCL1; 5'-ACTCTCAAGGGCGGTCAAAA-3' (forward) and 5'-AGGCACATCAGGTACGATCCA-3' (reverse) for mCXCL2; and 5'-AAGGTCATCCCAGAGCTGAA-3' (forward) and 5'-CTGCTTACCACCTTCTTGA-3' (reverse) for mGAPDH (22).

## Measurement of cytokines and chemokines

The amounts of cytokines and chemokines in the skin or cell supernatant were determined by the ELISA method. The 5 mm punch biopsies were acquired from the dorsal area of the mouse, incubating in a 1 ml PBS with complete protease inhibitors (Roche, Basel, Switzerland). The fragments of biopsy were homogenized at 6500 rpm for 30 s and cooled down for 1 min. After a centrifugation at 13,000 rpm and 4°C for 10 min, the supernatant was pipetted. The protein was quantified with Protein Assay Dye (Bio-Rad). For *in vitro* samples, HaCaT cells ( $1 \times 10^5$ /well) were seeded at least in triplicate into 12-well plates in a 1 ml medium with 10% fetal bovine serum. After reaching confluence, the cells were treated with different experimental conditions for 24 h. The culture supernatants were harvested for analysis. The concentrations of cytokines IL-1 $\beta$ , IL-6, and TNF- $\alpha$  and chemokines CXCL1, CXCL2, and CXCL8 were measured using the commercial kits (BioLegend, San Diego, CA, USA), based on the manufacturer's instructions.

## *In vitro* absorption of HFP031 and HFP034

The skin absorption experiment was conducted with the Franz diffusion cell. Nude mice, BALB/c mice, and pig skins were used as the model permeation barriers in this study. The available diffusion area was 0.785 cm<sup>2</sup>. The medium loaded in the receptor compartment was 30% ethanol in pH 7.4 buffer to facilitate examining the absorption of HFP031 and HFP034. The donor compartment (0.5 ml) was loaded with 1 mg/ml HFP031 or HFP034 in a PEG400-ethanol mixture (4:6). At determined intervals, a 300  $\mu$ l medium was withdrawn from the receptor. The skin was removed from the Franz cell after a 24 h treatment. The cutaneous reservoir was extracted by methanol. The receptor medium and skin extract were analyzed by HPLC. A 25 cm-long, 4 mm inner-diameter, stainless-steel C18 column (Merck, Kenilworth, NJ, USA) was used for the stationary phase. The mobile phase consisted of methanol-water (80:20) for HFP031; methanol-water (90:10) for HFP034 was used at a flow rate of 0.7 ml/min. The wavelength of the UV detector was set at 264 and 248 nm for HFP031 and HFP034, respectively.

## *In vivo* absorption of HFP031 and HFP034

A glass, hollow cylinder, with an available region of 0.785 cm<sup>2</sup>, was attached to the BALB/c mouse back, with or without 5% Aldara cream treatment. A 0.2 ml PEG400-ethanol mixture (4:6), containing HFP031 or HFP034, was pipetted into the cylinder. The administration duration was 6 h. The extraction method to detect the cutaneous reservoir of the anthranilate compounds was the same as the *in vitro* absorption study.

## *In vivo* skin tolerance of HFP031 and HFP034

The PEG400-ethanol vehicle containing HFP031 or HFP034, at the concentration of 10 mg/ml, was applied daily (0.6 ml) on the dorsal skin of the mouse for 6 consecutive days. The compound vehicle was replaced by a new one each 24 h. The treated skin was examined each day for physiologic parameters. These included transepidermal water loss (TEWL), erythema, and skin surface pH every day after the vehicle removal. A Tewameter (TM300; Courage and Khazaka, Köln, Germany) was used to measure TEWL (g/ m<sup>2</sup>/h). A spectrophotometer (CD100; Yokogawa, Tokyo, Japan) was used to estimate skin erythema. The skin surface pH was detected by Cutometer MPA580 (Courage and Khazaka).

## Cell culture

HaCaT cells were routinely cultured in DMEM (Thermo Fisher Scientific), supplemented with 10% fetal bovine serum and 1% penicillin-streptomycin in 5% CO<sub>2</sub> at 37°C. Cells from passages 5–12 were used for the experiments. In some experiments, the HaCaT was serum starved for the determined periods. For the activation of inflammatory condition, the cells were stimulated with IMQ (5  $\mu$ g/ml) for the determined times.

## Cytotoxicity

The 3-(4,5-dimethylthiazol-2-yl)-2,5-diphenyltetrazolium bromide (MTT) assay was used for the evaluation of HaCaT viability. HaCaT ( $10^5$  cells/ml) was added to 96-well plates overnight. After incubation with the compounds at different concentrations for 24 h, MTT solution (5 mg/ml in PBS) was added into the wells. After the incubation at 37°C for 4 h, the cellular MTT was resolved with DMSO. The plates were read by a spectrophotometer at 550 nm. All experiments were performed in 4 repeats.

## Measurement of cAMP concentration

HaCaT was added in 6-well plates ( $3 \times 10^6$  cells/well), pretreated with 10  $\mu$ M forskolin or compounds at 37°C for 1 h and subsequently treated with 5  $\mu$ g/ml IMQ for another 30 min. The cAMP level was measured by using a commercial Enzyme Immunoassay Kit (Amersham Biosciences, Little Chalfont, United Kingdom), based on the manufacturer's instruction.

## Immunoblotting analysis

The HaCaT was seeded onto 12-well plates with serum for a 12-h starvation. After the incubation with IMQ (5  $\mu$ g/ml), in the presence or absence of inhibitors or compounds for different periods, HaCaT was collected and pipetted into the lysis buffer. The nuclear pellet was obtained after a centrifugation at 400 g and 4°C for 5 min. After probe sonication, the nuclear protein fractions were obtained by centrifugation at 8000 g and 4°C for 10 min. The Protein Assay Dye (Bio-Rad) was used to quantify the protein concentration. The proteins were separated and analyzed by SDS-PAGE. The proteins were treated with various antibodies overnight at 4°C after the transfer onto the nitrocellulose membranes. These antibodies included phospho-P65 secondary anti-rabbit or anti-mouse horseradish peroxidase antibodies (1:2000 dilution), which were subsequently incorporated for 1 h. Bound antibodies were observed by the ECL reagent (PerkinElmer, Waltham, MA, USA).

## Chemotaxis assay

A chemotaxis assay was conducted in 24-chamber Transwell plates with a pore size of 3  $\mu$ m (Corning, Corning, NY, USA). The neutrophils were separated from the blood of healthy volunteers, aged between 20 and 30 yr old, based on the protocol approved by the Institutional Review Board of Chang Gung Memorial Hospital. The procedures for neutrophil purification were the same as for the previous study (23). The isolated human neutrophils were incorporated in DMEM, supplemented with 0.25% bovine serum albumin. The cells were added into the upper wells ( $5 \times 10^4$  cells/well), and conditioned medium harvested from HaCaT cells was added to the lower wells. The plates were stored at 37°C for 1.5 h before being placed on ice, and 0.5 M EDTA (100  $\mu$ l) was pipetted into each well at 4°C 10 min. The well insert was



removed, and then the cell suspension was collected for washing. Absolute counts were obtained using a Moxi Z Mini-Automated Cell Counter Kit (Orflo, Ketchum, ID, USA).

## Statistical analysis

The statistical analysis was carried out using GraphPad Prism 5 software. Dual comparisons were made with an unpaired Student's *t* test. Groups of 3 or more were analyzed by ANOVA with Tukey or Dunnett posttests.

## RESULTS

### Topical application of anthranilate derivatives prevents the development and severity of IMQ-induced psoriasis-like skin inflammation

**Figure 1A** shows the MW and partition coefficient ( $\log P$ ) of the compounds tested in this study. The physicochemical characteristics revealed that the molecular size of HFP031 was greater than HFP034. A lower  $\log P$  of HFP031 than HFP034 demonstrated a more hydrophilic nature of HFP031. This could be a result of the greater number of oxide double bonds in the HFP031 structure. To assess whether anthranilate derivatives were able to improve psoriatic pathogenesis, mice were topically pretreated with HFP031 or HFP034 for 7 d, and the IMQ cream was applied daily, 2 d post-treatment of the anthranilate compounds (Fig. 1B). The mice were euthanized on d 7. The application of IMQ cream on the back skin displayed the symptoms of erythema, scaling, and thickening of the skin, following a significant inflammation, according to the gross and microscopic appearances of the skin surface (Fig. 1C, D). The signs and symptoms of the psoriatic erythema, scaling, and thickening in the HFP031- and HFP034-treated groups were significantly reduced compared with those of the IMQ-treated group. The H&E staining of the IMQ-induced skin showed a dramatic increase of epidermal thickness in the back skin (Fig. 1E). IHC staining of lymphocyte antigen 6 complex locus G6D (Ly6G) revealed the infiltration of neutrophils into the dermis and epidermis, known as Munro's microabscesses, in IMQ-treated skin (Fig. 1F). During the process of neutrophil recruitment, MPO was rapidly created upon IMQ stimulation (Fig. 1G). IHC staining of the epidermal proliferation marker Ki67<sup>+</sup> showed the increased epidermal thickness (acanthosis) and elongated finger-like epidermal projections into the dermis (rete ridges; Fig. 1H). The anthranilate derivative-treated groups showed a significant decrease in epidermal thickness, neutrophil infiltration, and keratinocyte proliferation. Notably, the PASI score and epidermal thickness estimated by histopathology were significantly reduced in the compound-treated groups compared with the IMQ group (Fig. 1I, J). HFP034-treated mice showed a significantly stronger inhibition of microabscesses compared with HFP031-treated mice (Fig. 1K). TEWL is associated with the level of barrier-function impairment.

The psoriasiform skin of the IMQ-treated group revealed a significantly greater degree of TEWL (Fig. 1L). Both of the anthranilate derivative-treated groups could reduce TEWL to ameliorate the barrier disruption, although the level could not be recovered to the control baseline.

### Skin absorption and safety of anthranilate derivatives

After the determination of the efficacy of the anthranilate derivatives in the IMQ-induced psoriatic mouse model, we next examined the deposition of these 2 compounds in mouse and pig skins to speculate on the ability of the topically applied compounds to penetrate into the skin. As there is an ester moiety in the HFP031 and HFP034 structures, the esterases in the skin may hydrolyze the compounds to produce an inactive form. **Figure 2A**, left, is the HPLC chromatogram of HFP031 and HFP034 in standard solution. We found only 1 peak in the graph, indicating a high purity. The anthranilate compounds in the skin after extraction were monitored by HPLC, as illustrated in Fig. 2A, right. There was still 1 peak of the compounds after penetration into the skin, suggesting that no hydrolysis occurred after absorption. The cutaneous permeation of HFP031 and HFP034 was first compared using the *in vitro* Franz cell. The skin deposition and the flux across the skin were estimated. The permeant deposition within the skin indicates the uptake by the skin tissue. The flux predicts the possible delivery into systemic circulation. When anthranilate derivatives were applied to the different animal skins for 24 h, the diffusion amount into the receptor was below the detection limit of the analytical method. This demonstrated good targeting of HFP031 and HFP034 in the skin reservoir without further penetration into the circulation. We investigated the *in vitro* skin absorption of the anthranilate derivatives in nude mice, BALB/c mice, and pig skins (Fig. 2B). Topical application of HFP034 resulted in much greater mouse skin accumulation than HFP031. In the case of pig skin, HFP031 and HFP034 exerted a comparable cutaneous uptake. We also compared the *in vivo* skin delivery of both compounds in intact and psoriasis-like skins after a 6 h administration (Fig. 2C, D). IMQ sensitization significantly increased HFP034 accumulation, from 0.27 to 1.29 nmol/mg. A similarly increased trend by IMQ was observed in HFP031 absorption. This indicated a weak barrier property of psoriasis-like skin, as proven by TEWL.

Safety is a vital issue for the new agent development for skin-disease therapy. It was our attempt to know the possible skin irritation by anthranilate derivatives. Topically applied HFP031 and HFP034 treatments generally showed no change in appearance, visualized by a digital camera and a handheld microscope (Fig. 2E, F). The skin histology also revealed no epidermal or dermal damage after compound treatment for a consecutive 5 d challenge (Fig. 2G). The skin physiology, such as TEWL, erythema, and skin-surface pH, was evaluated each day by a 5 d administration of the

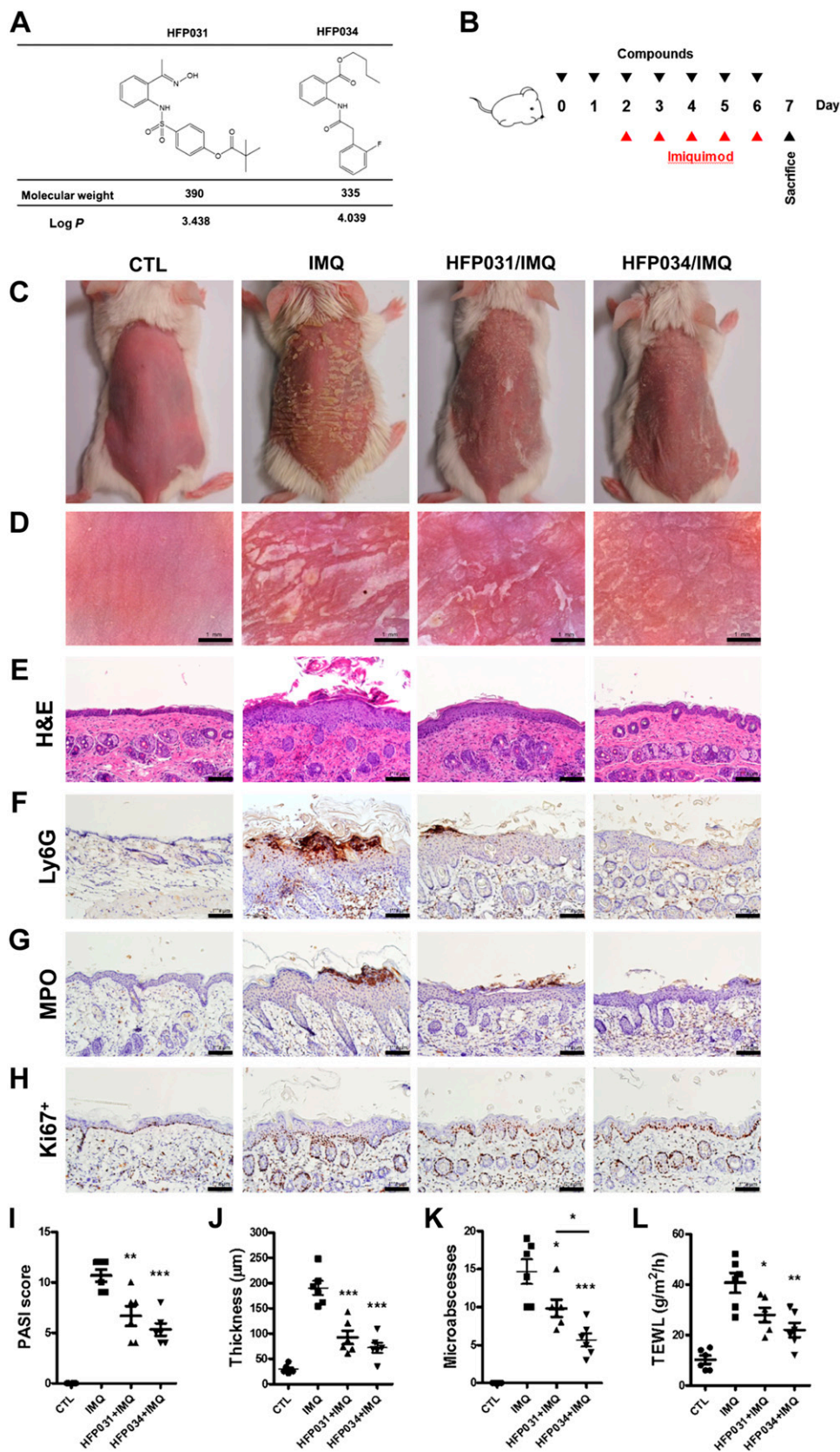


**Figure 1.** The anthranilate derivatives attenuate IMQ-induced mouse psoriatic skin inflammation. **A)** The chemical structures, MWs, and log *P* of compounds HFP031 and HFP034. **B)** Timeline for IMQ-induced psoriasis-like skin inflammation model. The mice were topically treated with or without compounds from d 0 to 6, and then the psoriasis-like skin was induced by IMQ cream from d 2 to 6. Mouse back skin was collected on d 7. **C)** The gross images of mouse back skin were represented on d 7 by digital camera. **D)** The close-up imaging by hand-held digital microscopy. **E–H)** Skin sections were represented by H&E staining (**E**) and IHC analysis for Ly6G (**F**), MPO (**G**), and Ki67<sup>+</sup> (**H**). **I)** Quantification of mouse skin histology examined using the PASI score. **J)** Epidermal thickness quantified by H&E staining. **K)** Total counts of abscesses by H&E staining. **L)** TEWL measurement. CTL, control. \**P* < 0.05, \*\**P* < 0.01, \*\*\**P* < 0.001.

compounds (Fig. 2H–J). TEWL was slightly increased after a 4 d treatment of the control vehicle, HFP031, and HFP034. This could be a result of the ethanol in the vehicle disrupting the skin barrier. The treatment of

anthranilate derivatives did not further elicit the barrier defect. The profiles of erythema and the skin surface pH detection indicated no skin rash and irritation in any of the groups.

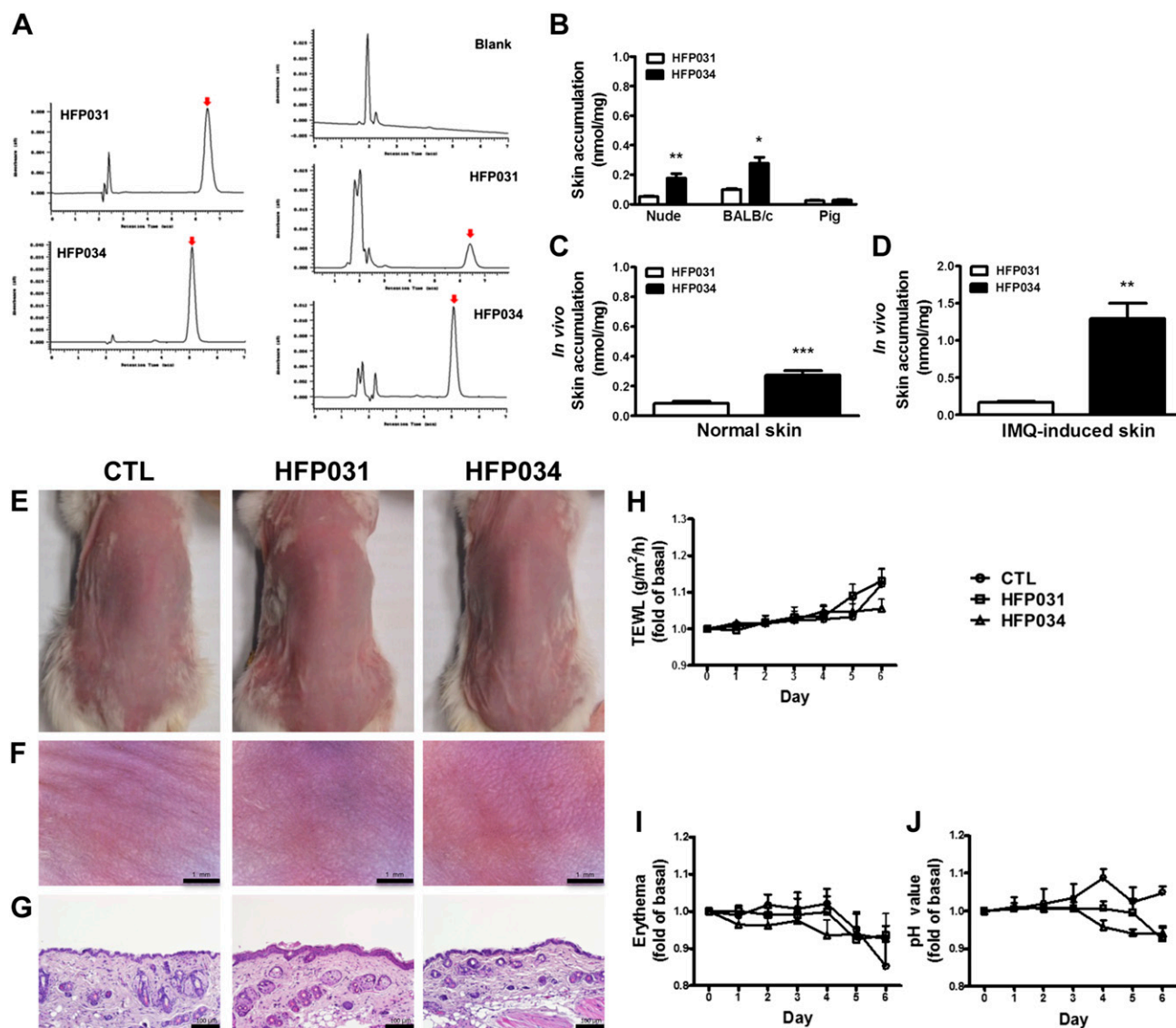


**Figure 2.** *In vitro* and *in vivo* cutaneous absorption of the anthranilate derivatives. *A*) HPLC chromatogram of HFP031 and HFP034 in standard solution and psoriasis-like skin extract. *B*) *In vitro* skin absorption of HFP031 and HFP034 in 40% PEG400-ethanol solution, measured by the Franz diffusion cell in nude mouse, BALB/c mouse, and pig skins. *C*, *D*) *In vivo* skin absorption of HFP031 and HFP034 in 40% PEG400-ethanol solution (1 mg/ml) using BALB/c mouse skin induced without (*C*) and with (*D*) IMQ cream. *In vivo* skin tolerance examination after a 6 d application of topically applied 0.6 ml anthranilate derivatives (10 mg/ml in 40% PEG400-ethanol solution). *E*) The gross images of mouse back skin were represented on d 6 by digital camera. *F*) The close-up imaging by hand-held digital microscopy. *G*) Skin sections represented by H&E staining. *H–J*) TEWL (*H*); erythema (*I*); and skin surface pH value (*J*). \* $P < 0.05$ , \*\* $P < 0.01$ , \*\*\* $P < 0.001$ .

## Anthranilate derivatives inhibit chemokines in psoriasis-like skin

It is apparent that neutrophils are involved in regulatory networks underlying the psoriasis pathophysiology. IMQ induces the CXCR2 ligand expression in HaCaT cell lines and primary human keratinocytes *in vitro* (22, 24), suggesting that IMQ-stimulated keratinocytes may initiate neutrophil recruitment. This result prompted us to hypothesize that anthranilate derivatives inhibit the production of these ligands, contributing to decreased early neutrophil infiltration in the initial stage of psoriasis. The location of CXCL1 and CXCL2 expression in the skin was determined by IHC, 3 d after IMQ treatment (Fig. 3*A*, *B*).

The histology showed clouds of chemokine expression in the epidermis by IMQ application. We also observed the neutrophil recruitment in the dermis in the early stage of the psoriasis-like mouse skin by Ly6G and MPO staining (Fig. 3*C*, *D*). HFP031 and HFP034 inhibited chemokine expression in the epidermis and neutrophil infiltration in the dermis. We also analyzed the mRNA expression and protein levels of CXCL1 and CXCL2, 3 d post-IMQ stimulation (Fig. 3*E*, *F*). These chemokines were highly expressed in the IMQ-irritated mouse skin. Treatment with HFP034 downregulated the chemokine expression more significantly than HFP031. The mRNA and protein expression demonstrated a consistent result. IMQ is known to reduce anti-inflammatory cAMP and then to



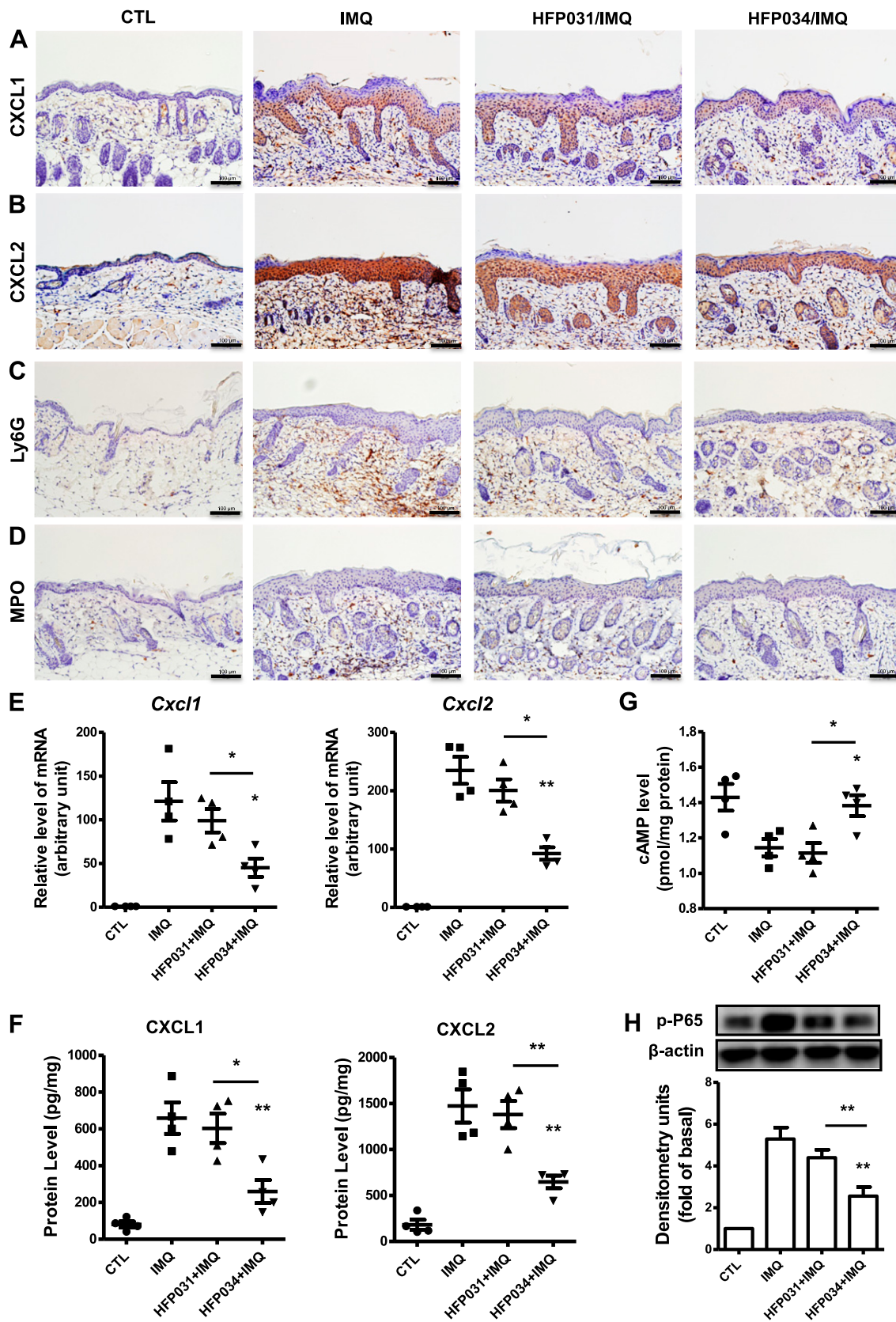


**Figure 3.** A–D) The anthranilate derivatives suppress IMQ-induced, neutrophil-related chemokine expression and neutrophil infiltration in mouse skin at the early stage of psoriasis-like skin. IHC analysis represents neutrophil-related chemokines CXCL1 (A) and CXCL2 (B) and neutrophil markers Ly6G (C) and MPO (D) on d 4. E, F) The mRNA (E) and protein (F) levels of neutrophil-related chemokines CXCL1 and CXCL2 in psoriasis-like skin. G, H) The effect of HFP031 and HFP034 on IMQ-induced cAMP level (G) and NF- $\kappa$ B phosphorylation (H) in psoriasis-like skin. \* $P < 0.05$ , \*\* $P < 0.01$ .



elicit the stimulation of NF- $\kappa$ B and the downstream production of proinflammatory cytokines through the adenosine receptor-dependent mechanism. The mRNA and protein levels of cytokines, such as IL-1 $\beta$ , IL-6, and TNF- $\alpha$ , were also examined (Supplemental Fig. S1). There was a significant inhibition of cutaneous cytokines in the psoriasis-like skin treated by both compounds. Beside these cytokines, it is well known, at the present time, that the T-helper 17-derived IL-17 and IL-22 cytokines are strongly enhanced in psoriasis and mainly involved in its physiopathology (25). We also determined IL-17A, IL-17E, and IL-22 protein expression in IMQ mice skin (Supplemental Fig. S2). The results showed that HFP034 could significantly reduce the IL-17A and IL-17E expression. However, there was no significant inhibition of IL-22 protein expression in the psoriasis-like skin treated by both compounds. We then evaluated the effect of anthranilate derivatives on the cAMP level in the psoriasis-like skin (Fig. 3G). The experimental data exhibited that the cAMP level was higher in the tissue of the HFP034-treated group compared with the IMQ and HFP031 groups. This suggested that HFP034, but not HFP031, elevated the cAMP concentration arrested by IMQ. The phosphorylation of NF- $\kappa$ B was increased after IMQ treatment (Fig. 3H). The

HFP034-treated group significantly downregulated the phosphorylation level of NF- $\kappa$ B compared with HFP031.

### HFP034 but not HFP031 enhances the cAMP level in HaCaT cells

The cAMP level is the result of the balance between synthesis by adenylyl cyclases and degradation by PDEs. PDE inhibition displays an efficient mechanism for enhancing intracellular cAMP, resulting in the targeted immune suppression. The immunosuppressive and anti-inflammatory impacts of cAMP are also attributed to its inhibitory downstream activity on the NF- $\kappa$ B function. Next, we examined the mechanisms underlying the effects of anthranilate derivatives on the intracellular concentration of cAMP and activation of NF- $\kappa$ B in the IMQ-stimulated HaCaT model. Before the determination of the cAMP level and NF- $\kappa$ B phosphorylation, the cytotoxicity of anthranilate derivatives should be known. The data showed that there was no significant cell death under the concentration of 20  $\mu$ M (Fig. 4A). The cAMP concentration in HaCaT was assessed by different treatments (Fig. 4B). Rolipram is a selective PDE4 inhibitor used as a positive control. Forskolin is demonstrated to raise the cAMP level

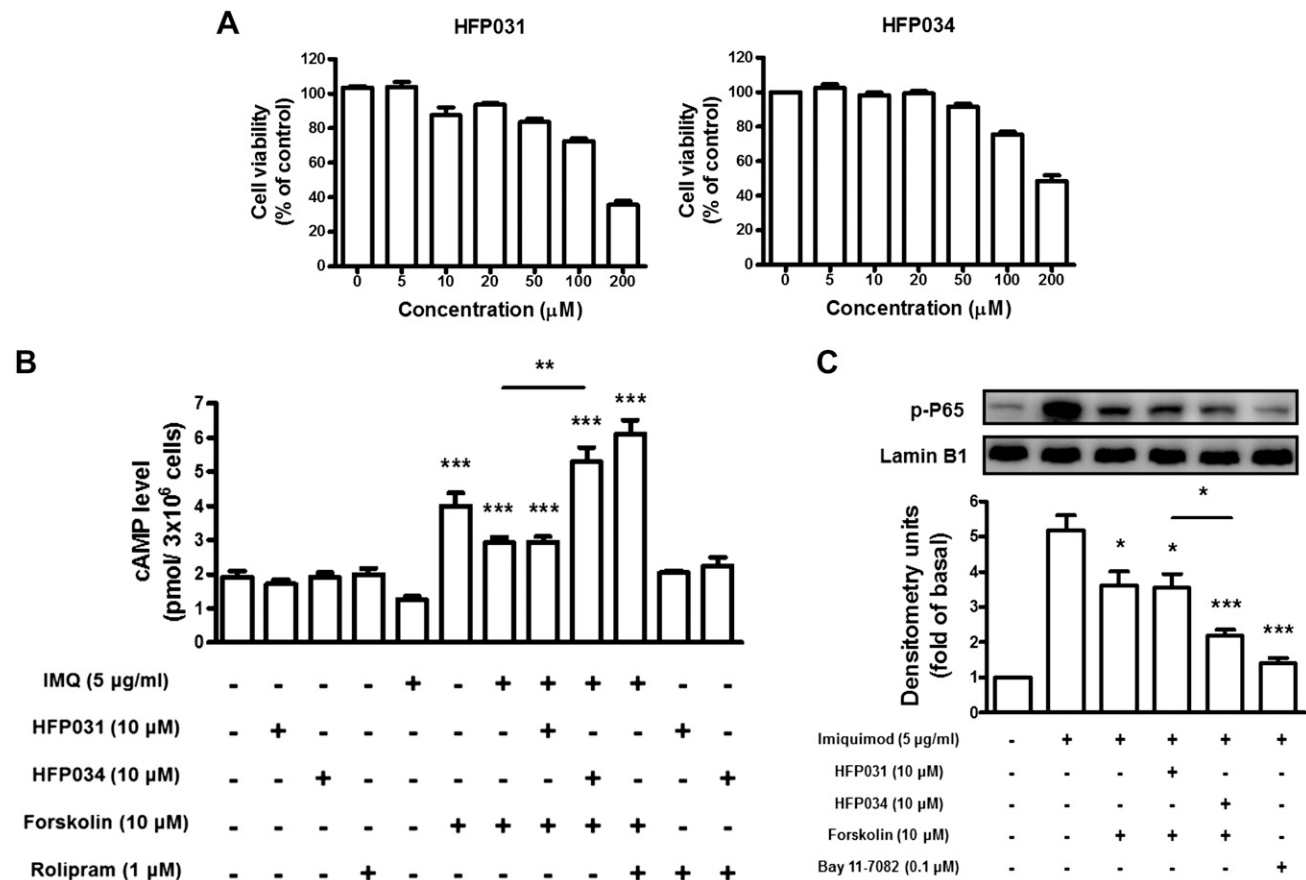


**Figure 4.** The anthranilate derivatives mediate cAMP concentration and NF- $\kappa$ B phosphorylation in IMQ-induced HaCaT keratinocytes. **A**) HaCaT keratinocytes were treated with various concentrations of anthranilate derivatives for 24 h. The cell viability of the cells was determined by MTT assay. **B, C**) HaCaT keratinocytes were pretreated with HFP031 (10  $\mu$ M), HFP034 (10  $\mu$ M), forskolin (10  $\mu$ M), and rolipram (1  $\mu$ M) or forskolin combined with anthranilate derivatives and then stimulated with IMQ (5  $\mu$ g/ml) for 30 min. The cAMP levels were measured using enzyme immune assay kits. The phosphorylation status of P65 was determined by Western blotting. All data are expressed as the means  $\pm$  SEM ( $n = 4$ ). \* $P < 0.05$ , \*\* $P < 0.01$ , \*\*\* $P < 0.001$ .

via the activation of adenylyl cyclase. HFP031, HFP034, and rolipram induced no increase in the cAMP concentration in the absence of IMQ activation. IMQ treatment slightly, but insignificantly, decreased cAMP expression. Forskolin promoted the cAMP level in the conditions, with or without IMQ treatment. With the presence of IMQ, forskolin promoted a higher cAMP level when HFP034 was added rather than HFP031. Additionally, forskolin and IMQ promoted a similar level of cAMP in the presence and absence of HFP031. Forskolin produced the highest cAMP level in the presence of IMQ and rolipram.

HFP034 and rolipram induced a significant increase in the cAMP level in the forskolin-induced cAMP formation. This phenomenon was not detectable for HFP031. On the other hand, HFP034 combined with rolipram did not demonstrate an additive effect on cAMP formation, which confirmed the role of HFP034 as a PDE4 inhibitor. P65 is a subunit of NF- $\kappa$ B. HFP034 and rolipram markedly attenuated the phosphorylation of NF- $\kappa$ B in IMQ-stimulated HaCaT keratinocytes (Fig. 4C). These results suggested that cAMP/NF- $\kappa$ B was involved in HFP034-mediated inhibition on IMQ-induced, neutrophil-related chemokine expression in HaCaT cells. The inhibitory capability of HFP031 on psoriasis and chemokines was not based on the PDE4 pathway.

### Involvement of anthranilate derivatives in forskolin-induced inhibition of chemokine production in HaCaT cells

We subsequently examined whether anthranilate derivatives enhanced forskolin-induced inhibition of chemokine production in HaCaT cells activated with IMQ. As shown in Fig. 5A, B, HFP034 greatly enhanced forskolin-induced inhibition of IMQ-induced secretion of CXCL1, CXCL2, and CXCL8 in the mRNA and protein levels. The results indicated that adenylyl cyclase is required for the forskolin-induced inhibition of these chemokines. However, HFP031 did not significantly alter forskolin-induced inhibition of these chemokines. Bay 11-7082 is a positive control for suppressing the production of chemokines. The key proinflammatory cytokines in psoriasis, such as IL-1 $\beta$ , IL-6, and TNF- $\alpha$ , also showed a reduction in the activated HaCaT treated with anthranilate derivatives and rolipram (Supplemental Fig. S3). The expression of CXCL1, CXCL2, and CXCL8 prompted us to hypothesize that these factors regulated neutrophil infiltration in psoriasis. To test this hypothesis, we performed an *in vitro* chemotaxis assay of neutrophils. Migration toward the conditioned medium of the IMQ-induced group was significantly reduced after forskolin treatment (Fig. 5C). Moreover, the migration of neutrophils induced by the conditioned medium of forskolin plus HFP034 was significantly decreased compared with forskolin alone and forskolin plus the HFP031 group. Figure 5D illustrates the proposed pathway of HFP034 for inhibiting the inflammatory response induced by IMQ.

## DISCUSSION

IMQ is shown to stimulate the cells through a number of separate mechanisms, including: 1) TLR7-dependent

stimulation of the myeloid differentiation primary response 88 pathway in immune cells, 2) neuronal apoptosis inhibitor protein, class 2 transcription activator, heterokaryon incompatibility, telomerase-associated protein 1; leucine-rich repeat; and PYRIN domain-containing protein 3 activation of the inflammasomes, 3) direct cytotoxic effect of high-concentration IMQ leading to the preformed IL-1 $\alpha$  release, and 4) antagonism of adenosine receptor signaling, resulting in decreased levels of anti-inflammatory cAMP on keratinocytes, leading to the induction of proinflammatory cytokines (26). As HaCaT cells lack the TLR7/8, the HaCaT activation by IMQ, observed in our study, could be mainly a result of the cAMP-related pathways.

Development of novel medication for psoriasis therapy is urgently needed. Anthranilic acid analogs are a group of nonsteroidal anti-inflammatory drugs, including tolfe-namic acid, flufenamic acid, and mefenamic acid. They are derived from fenamic acid or anthranilic acid and are called anthranilate derivatives or fenamates (27). The anti-inflammatory effects of our anthranilate derivatives have been recently shown to be mediated through the inhibition of elastase and reactive oxygen species production in *N*-formyl-L-methionyl-L-leucyl-phenylalanine-induced human neutrophils. Moreover, HFP034 inhibited O<sub>2</sub><sup>•-</sup> production in human neutrophils associated with an elevation in cellular cAMP levels through the selective inhibition of PDE. PDE4 is an enzyme to degrade cAMP. It is centrally related to the cytokine production of inflammatory cells, angiogenesis, and the functional properties of keratinocytes. Inhibitors of PDE4 have been shown to ameliorate symptoms in patients with atopic dermatitis and psoriasis (28). The anthranilate compounds exhibited a mild inhibition of Ki67<sup>+</sup>, based on IHC profiles. This result could reflect the insufficient effect of HFP031 and HFP034 in ameliorating hyperplasia. The epidermal thickness of psoriasis-like skin was not restored to its normal status after compound treatment. This may demonstrate that keratinocyte apoptosis was not the predominant mechanism for the anti-psoriatic action of HFP031 and HFP034.

In human skin, keratinocytes act as a physical barrier to the external environment. In addition, the keratinocytes are major producers of inflammatory cytokines and chemokines. This phenomenon has also been hypothesized to play a role in vitiligo, atopic dermatitis, and psoriasis (29–31). In this study, we evaluated whether the anthranilate derivatives may suppress the inflammatory response in human keratinocytes exposed to IMQ. Neutrophils are proven to connect important pathogenic actions of both innate and adaptive immune systems. This immune cell shows the intricate relationship with the regulatory networks underlying the psoriasis pathology (32, 33). Chemokines are signaling peptides that regulate cell trafficking and provide control of the tissue-specific cell homing. In the skin, chemokines are secreted both by the resident cells, such as keratinocytes, melanocytes, fibroblasts, dendritic cells, and mast cells, as well as by infiltrated cells, such as lymphocytes, eosinophils, and monocytes, which allows increased downstream effects and cytokine release, leading to the proliferation and

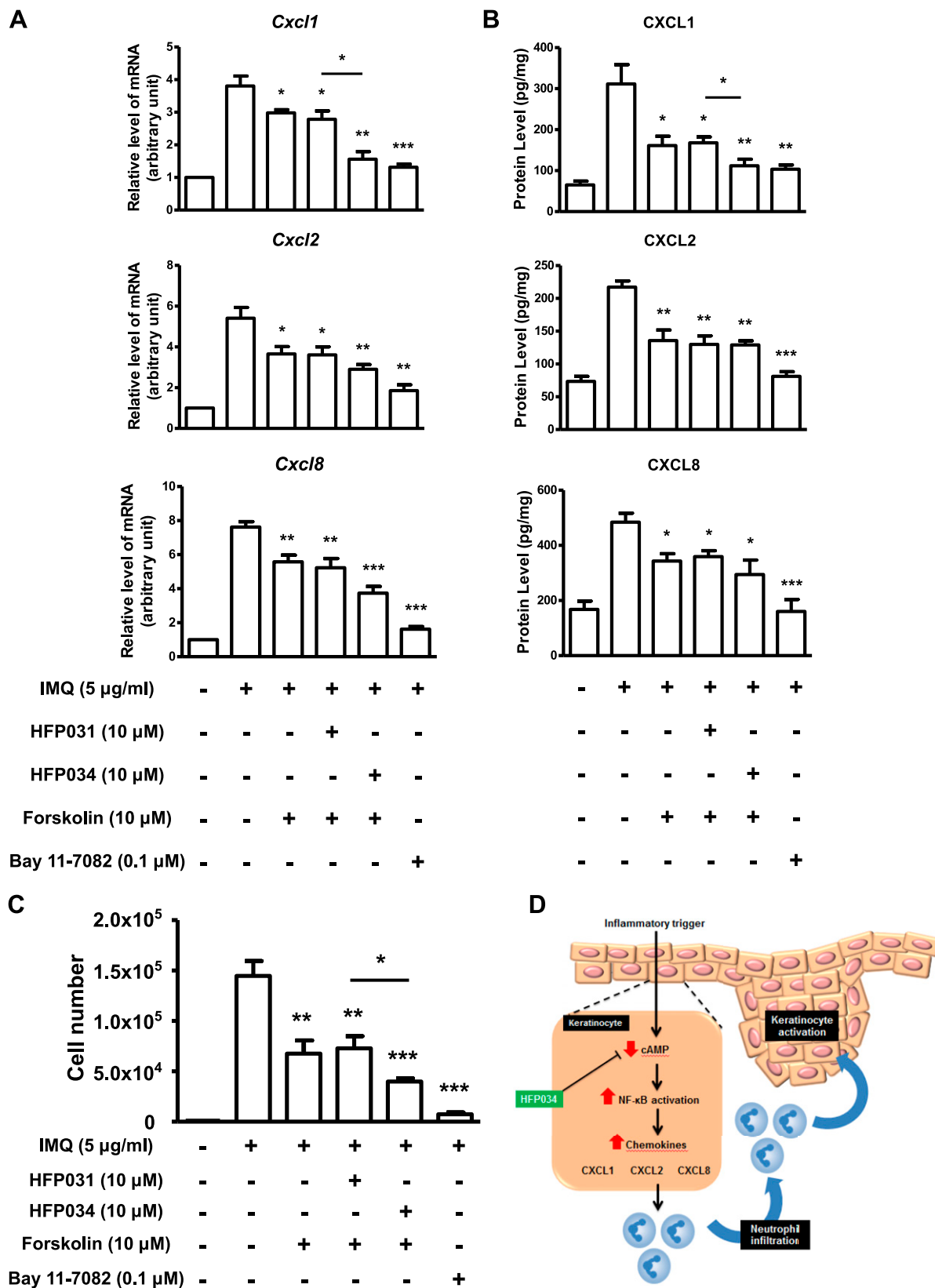


**Figure 5.** The effect of the anthranilate derivatives on neutrophil-related chemokine expression in IMQ-induced HaCaT keratinocytes. *A*) HaCaT keratinocytes were pretreated with forskolin (10 µM) and Bay 11-7082 (0.1 µM) or forskolin (10 µM), combined with anthranilate, for 1 h before the addition of IMQ (5 µg/ml). The mRNA level was examined using quantitative PCR after 4 h. *B*) HaCaT keratinocytes were incubated with IMQ for 24 h, after which, chemokine expression was examined using ELISA. *C*) Chemotaxis assay of neutrophils from IMQ-induced HaCaT keratinocyte condition medium pretreated with forskolin, forskolin-combined anthranilate derivatives, or Bay 11-7082 before stimulation with IMQ ( $n = 4$ ). *D*) The proposed mechanisms of the anti-psoriatic activity of HFP034. \* $P < 0.05$ , \*\* $P < 0.01$ , \*\*\* $P < 0.001$ .

differentiation of keratinocytes. Chemokines, together with cytokines, contribute to local and systemic inflammation in patients with psoriasis (34). The chemokines target cells of the immune system that have all been implicated in the immunopathology of psoriasis, including T cells, dendritic cells, macrophages, neutrophils, NK cells, and mast cells. (35, 36) Therefore, chemokines and chemokine receptors can be novel therapeutic targets in psoriasis.

The neutrophil chemoattractants, including CXCL1, CXCL2, and CXCL8, are upregulated in psoriatic skin and the IMQ-induced psoriasis mouse model (34, 37). The results of this study showed that anthranilate derivatives inhibited the chemokine subsets in the IMQ-induced psoriasis mouse model. The neutrophil migration into the skin would be blocked after chemokine subset suppression, resulting in the inflammation attenuation by anthranilate compounds. The reduction of biomarkers Ly6G and MPO in psoriasis-like skin proved the ability of anthranilate compounds to impede the neutrophil recruitment.

The preclinical and clinical studies have demonstrated that the adenylyl cyclase-cAMP network has anti-inflammatory characters, both *in vitro* and *in vivo* (38). For example, an elevated cAMP can decrease TNF- $\alpha$  plus IFN- $\gamma$ -induced CCL17 and CCL22 expression at the transcriptional and post-transcriptional level in HaCaT cells (39). The activator of adenylyl cyclase that synthesizes intracellular cAMP can reduce CXCL1, CXCL2, and CXCL8 release from keratinocytes (24). The PDE4 inhibitors manifest *in vivo* and clinical anti-inflammatory activities in atopic dermatitis and psoriasis (28, 40). Forskolin is a ligand for adenylyl cyclase to increase cAMP in keratinocytes (41). We found that HFP034 markedly enhanced the inhibitory effect of forskolin on CXCL1, CXCL2, and CXCL8 expression in HaCaT cells induced by IMQ. This synergistic effect was not observed in the absence of IMQ. This suggested a cAMP/PDE4-dependent inhibition of chemokines and cytokines for HFP034. HFP034, but not HFP031, enhanced the inhibition by forskolin. Although HFP031 did not modulate the cAMP pathway, this compound was effective in improving the psoriasis pathology in mice and in reducing chemokine and cytokine expression in cultured keratinocytes. The previous study (19) suggested that HFP031 could inhibit neutrophil elastase and proteinase 3, which are 2 major neutrophil serine proteases. Activated neutrophils liberate elastase and proteinase 3 that can cleavage IL-36 family cytokines to an active form, leading to the emphasis of psoriatic inflammation (42). Accordingly, we hypothesize that HFP031 may demonstrate the different mechanisms from HFP034 in the IMQ-induced models. HFP031 may play a role with activated keratinocytes in inflammatory inhibition.

We next explored the potential mechanisms of HFP034 by which the adenylyl cyclase-cAMP system suppresses immune responses in HaCaT cells. Chemokine promoters contain NF- $\kappa$ B-binding sequences (43). IMQ stimulated activation of NF- $\kappa$ B, an important transcription factor and upstream regulator of many cytokines. Therefore, the transcription factor may mediate the transcription of these

chemokine genes (44). The use of the NF- $\kappa$ B-specific inhibitor (Bay 11-7082) in our study demonstrated that NF- $\kappa$ B inhibition is responsible for the suppression of CXCL1, CXCL2, and CXCL8 by HFP034.

The T-helper 17-derived IL-17 and IL-22 cytokines are also key factors in the IMQ murine model for psoriasis (25). In the skin, IL-17A and IL-22 are produced mainly by T cells and innate lymphoid cells, a part of IL-17A produced by neutrophils, whereas IL-17E is highly produced in psoriasis by keratinocytes. IL-6 is known as an upstream cytokine of IL-17A to exacerbate neutrophil microabscess development in psoriasiform lesions (45). From our results, the inhibitory effect of IL-6 and the keratinocyte-derived chemokine of HFP034 was stronger than HFP031. A same manner was observed in IL-17A expression in psoriatic skin. Both of the compounds only showed a slightly inhibitory effect on IL-22 expression, but the protein expression of IL-22 was totally lower than IL-17A and -E. We hypothesized that the tested compounds could attenuate the neutrophil recruitment in the early phase of psoriasis, decreasing the adaptive T-cell activation in the late phase. Moreover, HFP034 showed an inhibitory effect on IL-17E in IMQ-treated skin. This result broadened the current views on psoriatic pathogenesis by revealing a new mechanism of the PDE4 inhibitor in keratinocyte-derived IL-17E.

An ideal topical application represents a much greater accumulation of the drugs in the skin compared with that in the systemic circulation and is a more efficient method for targeting to bypass systemic toxicity (46). Our skin absorption data showed that both HFP031 and HFP034 were absent in the Franz cell receptor, implying a targeting capability to the skin with minimal systemic absorption. The stratum corneum (SC) represents a major lipid barrier for topical delivery. The cutaneous transport can be facilitated by making more lipophilic analogs of the permeant (47). HFP034 showed a greater lipophilicity than HFP031 according to log *P*. This contributed to the higher cutaneous reservoir of HFP034 compared with HFP031. Another possibility elucidating the higher absorption of HFP034 was the lower MW of this compound for facilely penetrating into the SC. Although HFP031 revealed less skin penetration than HFP034, the *in vivo* study demonstrated a similar level of inflammatory inhibition in psoriasis-like skin between both compounds. This suggests a potent activity of HFP031 to prevent inflammation. The accumulation of anthranilate compounds in psoriasis-like skin was higher than that in healthy skin. This confirms a weak barrier characteristic of SC in inflamed skin.

The limitation of this study is that HaCaT is a TLR7- and TLR8-negative cell. The effect of the compounds on the TLR-related pathways could not be detected in our model. It has been reported that IMQ, independent of TLR7, stimulates cytokine production in HaCaT possibly through inhibition of adenylyl cyclase, adenosine receptor signaling, and cAMP on the transcription of proinflammatory mediators (48). We could only reveal the partial keratinocyte-intrinsic mechanism linking cAMP, NF- $\kappa$ B, and chemokine signaling to disease initiation. Further study is warranted to elucidate the detailed pathways. Another limitation of this study is that



we believe there were some discrepancies between skin physiology and histopathology of the experimental psoriasis-like skin and the psoriasis skin in humans (49, 50). Although a successful result was achieved in this report, it should be cautious to reflect the clinical condition by these data using the mouse as the animal model. Whether the results from mice can be correlated with humans needs further examination.

## CONCLUSIONS

The findings of this study indicated that anthranilate derivatives exert potential anti-psoriatic effects on skin keratinocytes exposed to IMQ by inhibiting CXCL1, CXCL2, and CXCL8 in the skin. HFP034 showed PDE4 inhibitory activity by enhancing forskolin-induced intracellular cAMP generation and inhibiting NF- $\kappa$ B phosphorylation in keratinocytes exposed to IMQ. The anti-inflammatory action of HFP034 but not HFP031 may be mediated by reversing the decreased cAMP concentration and down-regulation of NF- $\kappa$ B signaling. Although HFP031 and HFP034 possessed similar structures containing anthranilate moiety, the anti-psoriatic mechanisms were quite different for both compounds. The topical treatment with anthranilate derivatives attenuated chemokine expression in the epidermal keratinocytes of IMQ-induced psoriasis-like skin for prohibiting neutrophil recruitment. The novel PDE4 inhibitor may be potentially applicable in the future treatment or prevention of psoriasis. F

## ACKNOWLEDGMENTS

The authors are grateful to the financial support from the Ministry of Science and Technology of Taiwan (MOST-105-2320-B-182-010-MY3) and Chang Gung Memorial Hospital (CMRPD1G0411). The authors declare no conflicts of interest.

## AUTHOR CONTRIBUTIONS

Z.-C. Lin initiated the study and drafted the manuscript; J.-Y. Fang was involved in the design of all experiments; Z.-C. Lin and P.-W. Hsieh carried out the experiments; T.-L. Hwang and J.-Y. Fang analyzed data and wrote the manuscript; C.-Y. Chen supervised the entire project; C. T. Sung reviewed critically and approved the final manuscript; and all authors read and approved the final manuscript.

## REFERENCES

- Harden, J. L., Krueger, J. G., and Bowcock, A. M. (2015) The immunogenetics of psoriasis: a comprehensive review. *J. Autoimmun.* **64**, 66–73
- Greb, J. E., Goldminz, A. M., Elder, J. T., Lebwohl, M. G., Gladman, D. D., Wu, J. J., Mehta, N. N., Finlay, A. Y., and Gottlieb, A. B. (2016) Psoriasis. *Nat. Rev. Dis. Primers* **2**, 16082
- Tschachler, E. (2007) Psoriasis: the epidermal component. *Clin. Dermatol.* **25**, 589–595
- Bernard, F. X., Morel, F., Camus, M., Pedretti, N., Barrault, C., Garnier, J., and Lecron, J. C. (2012) Keratinocytes under fire of proinflammatory cytokines: bona fide innate immune cells involved in the physiopathology of chronic atopic dermatitis and psoriasis. *J. Allergy (Cairo)* **2012**, 718725
- Sah, S. K., Park, K. H., Yun, C. O., Kang, K. S., and Kim, T. Y. (2016) Effects of human mesenchymal stem cells transduced with superoxide dismutase on imiquimod-induced psoriasis-like skin inflammation in mice. *Antioxid. Redox Signal.* **24**, 233–248
- Murphy, G., and Reich, K. (2011) In touch with psoriasis: topical treatments and current guidelines. *J. Eur. Acad. Dermatol. Venerol.* **25** (Suppl 4), 3–8
- Feldman, S. R., Horn, E. J., Balkrishnan, R., Basra, M. K., Finlay, A. Y., McCoy, D., Menter, A., and van de Kerkhof, P. C.; International Psoriasis Council. (2008) Psoriasis: improving adherence to topical therapy. *J. Am. Acad. Dermatol.* **59**, 1009–1016
- Mahil, S. K., Capon, F., and Barker, J. N. (2016) Update on psoriasis immunopathogenesis and targeted immunotherapy. *Semin. Immunopathol.* **38**, 11–27
- Ikeda, S., Takahashi, H., Suga, Y., Eto, H., Etoh, T., Okuma, K., Takahashi, K., Kanbara, T., Seishima, M., Morita, A., Imai, Y., and Kanekura, T. (2013) Therapeutic depletion of myeloid lineage leukocytes in patients with generalized pustular psoriasis indicates a major role for neutrophils in the immunopathogenesis of psoriasis. *J. Am. Acad. Dermatol.* **68**, 609–617
- Zlotnik, A., and Yoshie, O. (2012) The chemokine superfamily revisited. *Immununity* **36**, 705–716
- Lima, X. T., Oliveira, R. T., Braga, F. G., Magalhães, R. F., Mamoni, R. L., and Blotta, M. H. (2015) Circulating levels of chemokines in psoriasis. *Autoimmunity* **48**, 57–60
- De Filippo, K., Dudeck, A., Hasenberg, M., Nye, E., van Rooijen, N., Hartmann, K., Gunzer, M., Roers, A., and Hogg, N. (2013) Mast cell and macrophage chemokines CXCL1/CXCL2 control the early stage of neutrophil recruitment during tissue inflammation. *Blood* **121**, 4930–4937
- Lowes, M. A., Russell, C. B., Martin, D. A., Towne, J. E., and Krueger, J. G. (2013) The IL-23/T17 pathogenic axis in psoriasis is amplified by keratinocyte responses. *Trends Immunol.* **34**, 174–181
- Russo, R. C., Garcia, C. C., Teixeira, M. M., and Amaral, F. A. (2014) The CXCL8/IL-8 chemokine family and its receptors in inflammatory diseases. *Expert Rev. Clin. Immunol.* **10**, 593–619
- Johnston, A., Xing, X., Wolterink, L., Barnes, D. H., Yin, Z., Reingold, L., Kahlenberg, J. M., Harms, P. W., and Gudjonsson, J. E. (2017) IL-1 and IL-36 are dominant cytokines in generalized pustular psoriasis. *J. Allergy Clin. Immunol.* **140**, 109–120
- Shi, L., Hu, R., Wei, Y., Liang, Y., Yang, Z., and Ke, S. (2012) Anthranilic acid-based diamides derivatives incorporating arylisoxazoline pharmacophore as potential anticancer agents: design, synthesis and biological evaluation. *Eur. J. Med. Chem.* **54**, 549–556
- Shou, Q., Banbury, L. K., Maccarone, A. T., Renshaw, D. E., Mon, H., Griesser, S., Griesser, H. J., Blanksby, S. J., Smith, J. E., and Wohlmuth, H. (2014) Antibacterial anthranilic acid derivatives from *Geijera parviflora*. *Fitoterapia* **93**, 62–66
- Rio, G. F., Silva, B. V., Martínez, S. T., and Pinto, A. C. (2015) Anthranilic acids from isatin: an efficient, versatile and environmentally friendly method. *An. Acad. Bras. Cienc.* **87**, 1525–1529
- Hwang, T. L., Wang, W. H., Wang, T. Y., Yu, H. P., and Hsieh, P. W. (2015) Synthesis and pharmacological characterization of 2-aminobenzaldehyde oxime analogs as dual inhibitors of neutrophil elastase and proteinase 3. *Bioorg. Med. Chem.* **23**, 1123–1134
- Cheng, Y. D., Hwang, T. L., Wang, H. H., Pan, T. L., Wu, C. C., Chang, W. Y., Liu, Y. T., Chu, T. C., and Hsieh, P. W. (2011) Anthranilic acid-based inhibitors of phosphodiesterase: design, synthesis, and bioactive evaluation. *Org. Biomol. Chem.* **9**, 7113–7125
- Suzuki, O., Goto, T., Yoshino, T., Nakamura, S., and Maeda, H. (2015) The role of phosphodiesterase 4B in IL-8/LTB<sub>4</sub>-induced human neutrophil chemotaxis evaluated with a phosphodiesterase 4B inhibitor. *Acta Pharm.* **65**, 191–197
- Sumida, H., Yanagida, K., Kita, Y., Abe, J., Matsushima, K., Nakamura, M., Ishii, S., Sato, S., and Shimizu, T. (2014) Interplay between CXCR2 and BLT1 facilitates neutrophil infiltration and resultant keratinocyte activation in a murine model of imiquimod-induced psoriasis. *J. Immunol.* **192**, 4361–4369
- Tsai, Y. F., Yu, H. P., Chung, P. J., Leu, Y. L., Kuo, L. M., Chen, C. Y., and Hwang, T. L. (2015) Osthol attenuates neutrophilic oxidative stress and hemorrhagic shock-induced lung injury via inhibition of phosphodiesterase 4. *Free Radic. Biol. Med.* **89**, 387–400
- Uribe-Herranz, M., Lian, L. H., Hooper, K. M., Milora, K. A., and Jensen, L. E. (2013) IL-1R1 signaling facilitates Munro's microabscess formation in psoriasiform imiquimod-induced skin inflammation. *J. Invest. Dermatol.* **133**, 1541–1549

25. Van der Fits, L., Mourits, S., Voerman, J. S., Kant, M., Boon, L., Laman, J. D., Cornelissen, F., Mus, A. M., Florencia, E., Prens, E. P., and Lubberts, E. (2009) Imiquimod-induced psoriasis-like skin inflammation in mice is mediated via the IL-23/IL-17 axis. *J. Immunol.* **182**, 5836–5845
26. Flutter, B., and Nestle, F. O. (2013) TLRs to cytokines: mechanistic insights from the imiquimod mouse model of psoriasis. *Eur. J. Immunol.* **43**, 3138–3146
27. Asif, M. (2014) Study of anthranilic acid derivatives: mefenamic acid and its various analogues. *Am. J. Med. Studies* **2**, 24–32
28. Schett, G., Sloan, V. S., Stevens, R. M., and Schafer, P. (2010) Apremilast: a novel PDE4 inhibitor in the treatment of autoimmune and inflammatory diseases. *Ther. Adv. Musculoskelet. Dis.* **2**, 271–278
29. Kim, J., and Krueger, J. G. (2015) The immunopathogenesis of psoriasis. *Dermatol. Clin.* **33**, 13–23
30. Asahina, R., and Maeda, S. (2017) A review of the roles of keratinocyte-derived cytokines and chemokines in the pathogenesis of atopic dermatitis in humans and dogs. *Vet. Dermatol.* **28**, 16–e5
31. Richmond, J. M., Bangari, D. S., Essien, K. I., Currimbhoy, S. D., Groom, J. R., Pandya, A. G., Youd, M. E., Luster, A. D., and Harris, J. E. (2017) Keratinocyte-derived chemokines orchestrate T-cell positioning in the epidermis during vitiligo and may serve as biomarkers of disease. *J. Invest. Dermatol.* **137**, 350–358
32. Reich, K., Papp, K. A., Matheson, R. T., Tu, J. H., Bissonnette, R., Bourcier, M., Gratton, D., Kunyetz, R. A., Poulin, Y., Rosoph, L. A., Stingl, G., Bauer, W. M., Salter, J. M., Falk, T. M., Blödmann-Schlicht, N. A., Hueber, W., Sommer, U., Schumacher, M. M., Peters, T., Kriehuber, E., Lee, D. M., Wiczorek, G. A., Kolbinger, F., and Bleul, C. C. (2015) Evidence that a neutrophil-keratinocyte crosstalk is an early target of IL-17A inhibition in psoriasis. *Exp. Dermatol.* **24**, 529–535
33. Schön, M. P., Broekaert, S. M., and Erpenbeck, L. (2017) Sexy again: the renaissance of neutrophils in psoriasis. *Exp. Dermatol.* **26**, 305–311
34. Nedoszytko, B., Sokołowska-Wojdyło, M., Ruckemann-Dziurdzińska, K., Roszkiewicz, J., and Nowicki, R. J. (2014) Chemokines and cytokines network in the pathogenesis of the inflammatory skin diseases: atopic dermatitis, psoriasis and skin mastocytosis. *Postępy Dermatol. Alergol.* **31**, 84–91
35. Mabuchi, T., Chang, T. W., Quinter, S., and Hwang, S. T. (2012) Chemokine receptors in the pathogenesis and therapy of psoriasis. *J. Dermatol. Sci.* **65**, 4–11
36. Singh, T. P., Lee, C. H., and Farber, J. M. (2013) Chemokine receptors in psoriasis. *Expert Opin. Ther. Targets* **17**, 1405–1422
37. Pohl, D., Andrys, C., Borská, L., Fiala, Z., Hamáková, K., Ettler, K., and Krejsek, J. (2009) CC and CXC chemokines patterns in psoriasis determined by protein array method were influenced by Goeckerman's therapy. *Acta Med. (Hradec Kralove)* **52**, 9–13
38. Zippin, J. H., Chadwick, P. A., Levin, L. R., Buck, J., and Magro, C. M. (2010) Soluble adenylyl cyclase defines a nuclear cAMP microdomain in keratinocyte hyperproliferative skin diseases. *J. Invest. Dermatol.* **130**, 1279–1287
39. Qi, X. F., Kim, D. H., Yoon, Y. S., Li, J. H., Song, S. B., Jin, D., Huang, X. Z., Teng, Y. C., and Lee, K. J. (2009) The adenylyl cyclase-cAMP system suppresses TARC/CCL17 and MDC/CCL22 production through p38 MAPK and NF-kappaB in HaCaT keratinocytes. *Mol. Immunol.* **46**, 1925–1934
40. Andoh, T., and Kuraishi, Y. (2014) Antipruritic mechanisms of topical E6005, a phosphodiesterase 4 inhibitor: inhibition of responses to proteinase-activated receptor 2 stimulation mediated by increase in intracellular cyclic AMP. *J. Dermatol. Sci.* **76**, 206–213
41. Amaro-Ortiz, A., Yan, B., and D'Orazio, J. A. (2014) Ultraviolet radiation, aging and the skin: prevention of damage by topical cAMP manipulation. *Molecules* **19**, 6202–6219
42. Henry, C. M., Sullivan, G. P., Clancy, D. M., Afonina, I. S., Kulms, D., and Martin, S. J. (2016) Neutrophil-derived proteases escalate inflammation through activation of IL-36 family cytokines. *Cell Reports* **14**, 708–722
43. Burke, S. J., Lu, D., Sparer, T. E., Masi, T., Goff, M. R., Karlstad, M. D., and Collier, J. J. (2014) NF-κB and STAT1 control CXCL1 and CXCL2 gene transcription. *Am. J. Physiol. Endocrinol. Metab.* **306**, E131–E149
44. Wu, P., Ma, G., Zhu, X., Gu, T., Zhang, J., Sun, Y., Xu, H., Huo, R., Wang, B., Shen, B., Chen, X., and Li, N. (2017) Cyr61/CCN1 is involved in the pathogenesis of psoriasis vulgaris via promoting IL-8 production by keratinocytes in a JNK/NF-κB pathway. *Clin. Immunol.* **174**, 53–62
45. Croxford, A. L., Karbach, S., Kurschus, F. C., Wörtge, S., Nikolaev, A., Yögev, N., Klebow, S., Schüller, R., Reissig, S., Piotrowski, C., Brylla, E., Bechmann, L., Scheller, J., Rose-John, S., Thomas Wunderlich, F., Münzel, T., von Stebut, E., and Waisman, A. (2014) IL-6 regulates neutrophil microabscess formation in IL-17A-driven psoriasiform lesions. *J. Invest. Dermatol.* **134**, 728–735
46. Sawamura, R., Sakurai, H., Wada, N., Nishiya, Y., Honda, T., Kazui, M., Kurihara, A., Shinagawa, A., and Izumi, T. (2015) Bioactivation of loxoprofen to a pharmacologically active metabolite and its disposition kinetics in human skin. *Biopharm. Drug Dispos.* **36**, 352–363
47. Lin, C. F., Hung, C. F., Aljuffali, I. A., Huang, Y. L., Liao, W. C., and Fang, J. Y. (2016) Methylation and esterification of magnolol for ameliorating cutaneous targeting and therapeutic index by topical application. *Pharm. Res.* **33**, 2152–2167
48. Schön, M. P., Schön, M., and Klotz, K. N. (2006) The small antitumoral immune response modifier imiquimod interacts with adenosine receptor signaling in a TLR7- and TLR8-independent fashion. *J. Invest. Dermatol.* **126**, 1338–1347
49. Lin, Y. K., Yang, S. H., Chen, C. C., Kao, H. C., and Fang, J. Y. (2015) Using imiquimod-induced psoriasis-like skin as a model to measure the skin penetration of anti-psoriatic drugs. *PLoS One* **10**, e0137890
50. Chuang, S. Y., Lin, C. H., Sung, C. T., and Fang, J. Y. (2018) Murine models of psoriasis and their usefulness for drug discovery. *Expert Opin. Drug Discov.* **13**, 551–562

Received for publication February 22, 2018.

Accepted for publication June 4, 2018.

Original Paper

# Protective Effects of Morus Root Extract (MRE) Against Lipopolysaccharide-Activated RAW264.7 Cells and CCl<sub>4</sub>-Induced Mouse Hepatic Damage

Tsui-Hwa Tseng<sup>a,b</sup> Wea-Lung Lin<sup>c</sup> Che-Kai Chang<sup>d</sup> Ko-Chao Lee<sup>e</sup>  
Shui-Yi Tung<sup>f,g</sup> Hsing-Chun Kuo<sup>h,i,j</sup>

<sup>a</sup>Department of Medical Applied Chemistry, Chung Shan Medical University, Taichung, <sup>b</sup>Department of Medical Education, Chung Shan Medical University Hospital, Taichung, <sup>c</sup>Department of Pathology, Chung Shan Medical University Hospital, Taichung, <sup>d</sup>Institute of Biochemistry, Microbiology and Immunology, Chung Shan Medical University, Taichung, <sup>e</sup>Division of Colorectal Surgery, Department of Surgery, Chang Gung Memorial Hospital, Kaohsiung Medical Center, Chang Gung University College of Medicine, Kaohsiung, <sup>f</sup>Department of Hepato-Gastroenterology, Chang Gung Memorial Hospital, Chiayi, <sup>g</sup>Chang Gung University College of Medicine, Taoyuan, <sup>h</sup>Department of Nursing, Chang Gung University of Science and Technology, Chia-Yi Campus, Chiayi, <sup>i</sup>Research Fellow, Chang Gung Memorial Hospital, Chiayi, Taiwan, <sup>j</sup>Chronic Diseases and Health Promotion Research Center, CGUST, Research Center for Industry of Human Ecology and Research Center for Chinese Herbal Medicine, College of Human Ecology, Chang Gung University of Science and Technology, Taoyuan, Taiwan

## Key Words

Lipopolysaccharide • Carbon tetrachloride • *Morus australis* • Morusin

## Abstract

**Background/Aims:** Inflammation is one of the main contributors to chronic diseases such as cancer. It is of great value to identify the potential activity of various medicinal plants for regulating or blocking uncontrolled chronic inflammation. We investigated whether the root extract of *Morus australis* possesses antiinflammatory and antioxidative stress potential and hepatic protective activity. **Methods:** The microwave-assisted extraction was used to prepare the ethanol extract from the dried root of *Morus australis* (MRE), including polyphenolic and flavonoid contents. Lipopolysaccharide (LPS)-stimulated RAW264.7 cells was examined the anti-inflammatory and anti-oxidative potential of MRE. CCl<sub>4</sub>-induced mouse hepatic damage were performed to detect the hepatic protective potential *in vivo*. Immunohistochemistry (IHC) and western blot assays were used to detect target proteins. **Results:** MRE contained approximately 23% phenolic compounds and 3% flavonoids. The major flavonoid component of MRE was morusin. MRE and morusin inhibited lipopolysaccharide-induced production of nitrite and prostaglandin E<sub>2</sub> in RAW264.7 cells. MRE and morusin also suppressed the formation of intracellular reactive oxygen species and the expression of iNOS and COX-2. In an *in vivo* study, a thiobarbituric acid reactive substances assay showed that MRE inhibited CCl<sub>4</sub>-induced

Shui-Yi Tung  
and Hsing-Chun Kuo, Ph.D

Chang Gung Memorial Hospital, Chiayi;  
Chang Gung University of Science and Technology, Chia-Yi Campus, Chiayi (Taiwan)  
Tel. +886-5-3628800, Fax 886-5-3628866, E-Mail guscsi@gmail.com

oxidative stress and expression of nitrotyrosine. MRE also decreased  $\text{CCl}_4$ -induced hepatic iNOS and COX-2 expression, as well as  $\text{CCl}_4$ -induced hepatic inflammation and necrosis in mice. **Conclusion:** MRE exhibited antiinflammatory and hepatic protective activity.

© 2018 The Author(s)  
Published by S. Karger AG, Basel

## Introduction

Inflammation is a complex biological immune response of the body to harmful stimuli, such as pathogens, damaged cells, and other irritants. Acute inflammation is a short-term process that usually lasts for a few hours up to several days and ceases upon the removal of the injurious stimuli. If the progressive destruction persists for months and years, chronic inflammation can be triggered. This degenerative process creates cellular stress and metabolic disorder, thus causing chronic diseases, such as cancer, ageing, and atherosclerosis. Because many inflammatory mediators lead to a wide range of pathological changes, it is difficult to treat inflammation [1]. Therefore, medicinal plants have received great attention and are expected to provide efficacious disease-prevention agents. In pathogenic conditions, abnormally activated macrophages produce excessive amounts of various pro-inflammatory mediators and cytokines that eventually aggravate inflammatory conditions. Lipopolysaccharides (LPSs), a component of the outer membrane of Gram-negative bacteria, are the most common cause of macrophage activation [2-3]. LPS-induced activation of macrophages causes a wide range of pro-inflammatory responses, such as production of pro-inflammatory mediators. Therefore, suppressing aberrant macrophage activation might be a valuable therapeutic target for treating inflammatory disorders.

Liver inflammation is usually attributed to the intensive exposure to endogenous and exogenous reactive oxygen species (ROS) [4]. Trichloromethyl radicals, derived from  $\text{CCl}_4$ , can initiate oxidative stress, resulting in hepatotoxicity [5, 6]. In addition, trichloromethyl radicals can be biotransformed into peroxynitrite, a strong oxidant capable of disrupting the physiological cellular structure and function through peroxidation of cellular lipids, proteins, and DNA. Therefore,  $\text{CCl}_4$ -induced liver injury has been widely used as a rodent model for the development of hepatic protective agents.

The root bark of the mulberry tree (*Morus* spp., Moraceae) is used in traditional Chinese medicine as an antiinflammatory, antipyretic, antiheadache, and diuretic. From these species, a series of prenylated flavonoids, stilbenes, 2-arylbenzofurans, and other phenolic compounds have been extracted with various biological activities, including antioxidant, anticancer, and antiinflammatory properties [7–12]. Among them, *Morus australis*, one of the major species, is commonly distributed in Taiwan. Its leaves are used to feed silkworms, and its fruit is used as a raw food or to make juice, wine, vinegar, and jam. Moreover, it has been suggested that the extracts from the leaves and fruits have great biological potential for preventing hepatic lipogenesis and obesity [13–14]. The *M. australis* root extract, which contains some flavonoids and stilbenes, has been proposed for use in foods as an antibrowning agent and in cosmetics as a skin-whitening agent [15]. However, the other biological activities of the *M. australis* root have not yet been clarified. In the present study, the antiinflammatory effect of the ethanol extract of the dried root of *M. australis* (MRE) was evaluated *in vitro* and *in vivo*. It was demonstrated that MRE exhibits a hepatic protective effect through antiinflammatory and antioxidative stress potential.



## Materials and Methods

### Chemicals

RPMI medium, phosphate-buffered saline (PBS), fetal bovine serum, penicillin/streptomycin/neomycin (PSN), and trypsin-EDTA were purchased from Gibco Ltd. (Grand Island, NY, USA). Antibodies against COX-2, iNOS, and actin were obtained from Santa Cruz Biotechnology, Inc., CA, USA. Morusin was synthesized in our laboratory [16]. The dried root of *M. australis* was purchased from a reputable folk medicine store in Taiwan. A prostaglandin E2 and IL-6 immunoassay kit was obtained from R&D Systems (Minneapolis, MN, USA) and a protein assay kit was obtained from Bio-Rad Laboratories (Watford, Herts, UK). LPS (endotoxin from *Escherichia coli*, serotype 0127: B8) and other chemicals were purchased from Sigma Chemical Co. (St. Louis, MO, USA).

### Preparation of MRE

MRE was prepared from the dried root of *M. australis*, which was shredded and ground. Then it was extracted with 10 volumes of 95% ethanol using a microwave extractor (Milestone) equipped with a reflux unit and with a nominal maximum power of 300W for 20 min. The mixture was filtered through filter paper (5 µm pore size), and the filtrate was dried using rotary evaporation under vacuum at 40°C. The percentage yield was 9.5% (w/w).

### Assay of total phenolic content

The total phenolic compound content of MRE was spectrophotometrically determined in accordance with the Folin-Ciocalteu procedure by reading the absorbance at 725 nm against a methanol blank. Briefly, samples (20 µL, water added to 1.6 mL) were placed in the test tubes, to which 100 µL Folin-Ciocalteu reagent and 300 µL of sodium carbonate (20%) were then added. The contents were mixed and incubated at 40°C for 40 min. The absorbance at 725 nm was measured. The total phenolic content was expressed as milligrams per gram of MRE for gallic acid.

### Assay of total flavonoid content

The total flavonoid content was analyzed by using AlCl<sub>3</sub>. Briefly, 0.5 mL of MRE was mixed with 0.1 mL of AlCl<sub>3</sub> (10%, w/v), 1.5 mL of ethanol, and 0.1 mL of 1M CH<sub>3</sub>COOK. The total volume of the mixture was adjusted to 5 mL with distilled water and then mixed well. After 40 min, absorbance at 415 nm was measured and the flavonoid content was estimated by calibration curves using quercetin. The percentage of flavonoid was expressed as quercetin equivalents in milligrams per 100g of fresh weight.

### HPLC Analysis

MRE was analyzed using a Hitachi L7100 HPLC system with a 5-µm ODS-Hypersil column (250 x 4.6 mm). The mobile phase was generated from solvent A (acetonitrile) and solvent B (water) using the following gradient program: 5% solvent A and 95% solvent B at 0 min, 90% solvent A and 10% solvent B at 20 min, 95% solvent A and 5% solvent B at 45 min. The detection wavelength was 270 nm.

### Cell Culture

Rat macrophage RAW 264.7 cells were cultured in a humidified atmosphere of 95% air-5% carbon dioxide at 37°C and using RPMI 1640 containing 10% heat-inactivated fetal bovine serum, 1% glutamine, and 1% penicillin-streptomycin. To investigate whether the root extract of *Morus australis* possessed anti-inflammatory and anti-oxidative stress potential and hepatic protective activity, we pretreated RAW264.7 cells to MRE and morusin for 30 min and then co-treated them with the LPS for 24 h.

### Cell Viability Assay

RAW 264.7 cells were plated in 24-well plates at 5 × 10<sup>4</sup> cells per well and allowed to adhere to the plate overnight, after which the medium was refreshed. Cells underwent a 24-h treatment with MRE (0–80 µg/mL), and then treatment medium was replaced with fresh medium containing 5 mg/mL 3-(4, 5-dimethylthiazol-2-yl)-2, 5-diphenyltetrazolium bromide (MTT) and incubated for 4 h. Medium was then removed, and 1 mL of 2-propanol was added to the wells to solubilize the crystals. The optical density of each sample was read at 563 nm against the blank prepared from cell-free wells.

## *Intracellular reactive oxygen species measurement*

Relative changes in intracellular ROS were monitored using the fluorescent probe  $H_2DCF\text{-}DA$ , which diffused through the cell membrane readily and was hydrolyzed by intracellular esterase to nonfluorescent  $DCFH_2$ , which was then rapidly oxidized to fluorescent 2',7'-dichlorofluorescein (DCF) in the presence of ROS. DCF fluorescence intensity was proportional to the amount of intracellular ROS. After treatment with MRE and LPS, the RAW 264.7 cells were achieved by incubation with  $H_2DCF\text{-}DA$  for 30 min at a final concentration of 10  $\mu M$  at 37°C in the dark. Fluorescence was monitored by fluorophotometer (excitation, 485 nm; emission, 528 nm).

## *Nitrite measurement*

Total nitrite in the culture medium was measured using the Griess reagent as described [17]. After incubation of RAW 264.7 cells with or without LPS and/or MRE at 37°C for 24 h, 100  $\mu L$  of each culture medium was mixed with an equal volume of Griess reagent and incubated at room temperature for 10 min. Absorbance at 550 nm was then read and compared with known standard solutions of  $NaNO_2$ .

## *Determination of PGE2*

RAW 264.7 cells were plated in 24-well plates at  $1 \times 10^6$  cells per well, after the cells had been allowed to adhere to the plate and the medium had been refreshed without phenol red. After incubation with or without LPS and/or MRE (0–40  $\mu g/mL$ ) at 37°C for 24 h, the production of prostaglandin E2 (PGE2) of each culture medium was determined with a commercial ELISA kit.

## *Preparation of total cell extracts and immunoblots analysis*

The cells were collected using trypsin-EDTA and lysed in RIPA buffer (50 mM Tris-HCl, 1 mM EDTA, 150 mM NaCl, 1% NP-40) containing protease inhibitors. After mixing for 30 min at 4°C, the mixtures were centrifuged (10,000 $\times g$ ) for 10 min at 4°C and the supernatants were collected as whole-cell extracts. The protein content was determined using the Bio-Rad protein assay reagent and bovine serum albumin as a standard. An equal amount of protein from the total cell extracts was boiled for 8 min. The extracts were separated by SDS-polyacrylamide gels and transferred to an NC membrane (Whatman). The blots were blocked in 5% nonfat dry milk/PBS for 1 h at room temperature. The blots then were incubated overnight with primary antibodies, followed by horseradish peroxidase-conjugated goat anti-mouse (or anti-rabbit) IgG for 1 h. The immunoreactive bands were revealed by enhanced chemiluminescence with a commercially available ECL kit.

## *Animal treatment*

Male ICR mice (body weight 19–21 g) were purchased from GlycoNex Inc. (Taiwan) and maintained in cage housing in a specifically designed pathogen-free isolation facility with a 12/12 h light/dark cycle. Animal care and the general protocols for animal use were approved by the Institutional Animal Care and Use Committee of Chung Shan Medical University Animal Ethics Research Board. The mice were intragastric with 150 and 300 mg/kg of MRE thrice weekly for 7 weeks. After MRE treatment for 1 week, the mice of the  $CCl_4$ -treated-alone group or the co-treatment with MRE group were given 0.1 mL/mice of  $CCl_4$  (20%  $CCl_4$  in olive oil) via intragastric procedure twice a week for 6 weeks. Those in the control and the MRE-treated-alone groups were given an equal volume of olive oil. The mice were divided randomly into five groups of six mice each. Then, the mice were sacrificed 24 h after the last treatment of  $CCl_4$ . The livers were divided into two portions: (1) preserved in 10% formalin for histological and immunohistochemistry examination; (2) frozen for immunoblotting analysis at -80°C.

## *Liver lipid peroxidation and inflammatory mediator analysis*

For the preparation of liver cytosol, 50 mg of liver tissues were homogenized at 4°C in 1 mL RIPA lysis buffer containing 2 mM phenylmethylsulfonyl fluoride, 1 mM sodium orthovanadate, and 2  $\mu g/mL$  of each leupeptin and pepstatin. A modified thiobarbituric acid reactive species (TBARS) assay was performed to determine the lipid peroxides. Briefly, 100  $\mu L$  of liver cytosol was added to 200  $\mu L$  of 10% TCA and then centrifuged at 14,000 rpm for 10 min. 100  $\mu L$  of supernatant was reacted with 200  $\mu L$  0.67% TBA

at 100°C for 30min and detected at 532 nm, then compared with known standard solutions of 1, 1, 3, 3-tetramethoxypropane. In addition, a volume equivalent to 80 µg proteins of liver cytosol was analyzed by Western immunoblotting assay against anti- COX-2 and anti-iNOS as previously described.

#### Histopathological and immunohistochemistry analysis

Liver tissues from each mouse were rapidly removed, fixed in 10% neutral-buffered formalin, and processed routinely. Paraffin-embedded sections were cut into sections 4 µm thick. The sections were stained with hematoxylin and eosin (H&E), then examined under a light microscope. Immunohistochemistry (IHC) staining was performed using the primary antibody F4/80 (a global marker for murine macrophages) and nitrotyrosine (oxidative stress marker) and a biotinylated secondary antibody (Vectastain Universal Elite ABC Kit, Burlingame, CA, USA) according to the manufacturer's instruction. Digital images were captured using a digital camera (100× magnification) for each slide.

#### Statistical Analysis

Statistical significance was determined using one-way analysis of variance (ANOVA) followed by Dunnett's or Tukey's post hoc test. *P* values less than 0.05 were considered statistically significant.

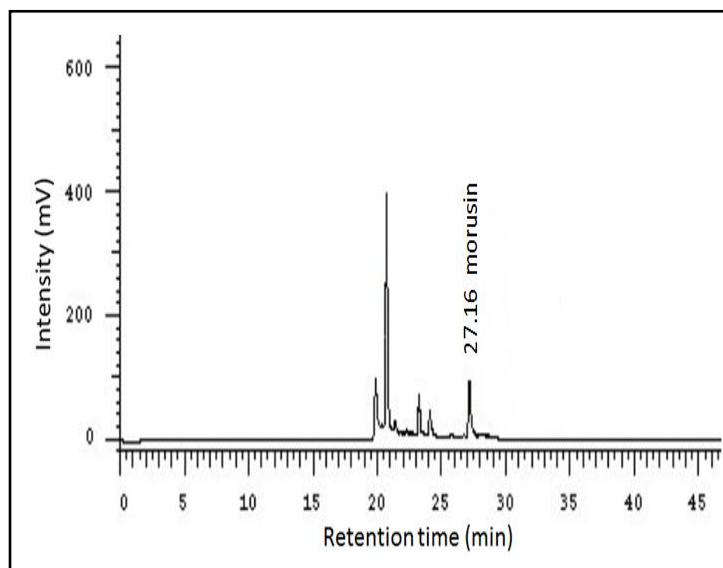
## Results

#### Analysis of total phenolic and flavonoid content in MRE and HPLC

Microwave-assisted extraction has received increasing attention as an alternative to traditional solid-liquid extraction methods, mainly due to considerable savings in processing time and solvent consumption. Our preliminary extraction study showed that the yield of microwave-assisted extraction was higher than that of Soxhlet extraction. Thereafter, we used the microwave-assisted extraction to prepare MRE. The polyphenolic compounds, including flavonoids, in the roots of *Morus* spp. exhibit biological activity [7–14]. Thus, we assessed the total polyphenolic and flavonoid content. MRE contained approximately 23% phenolic components (gallic acid as the standard) and 3% flavonoids (quercetin as the standard). Morusin had a retention time of 27.16 min (Fig. 1).

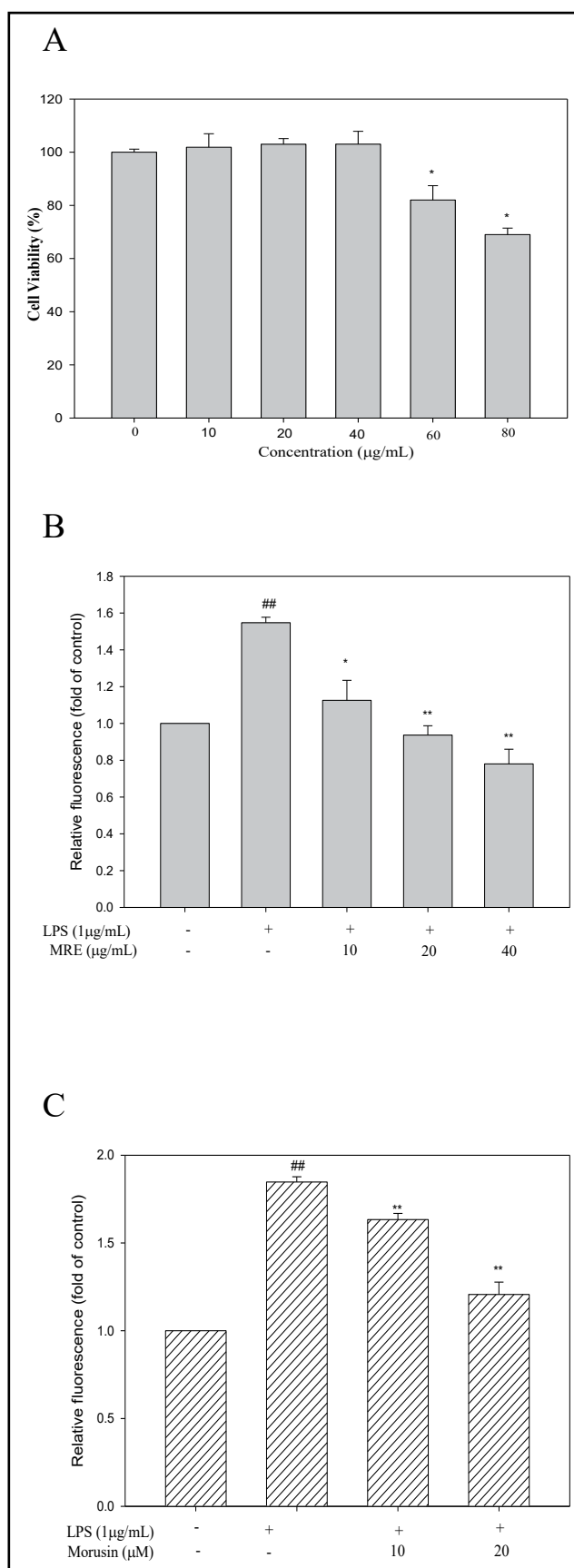
#### MRE reduces LPS-induced intracellular ROS

To evaluate the antioxidative and antiinflammatory effect of MRE, we used an *in vitro* model with the murine RAW264.7 macrophage cell line. Because MRE showed no cytotoxicity toward RAW264.7 macrophages at concentrations up to 40 µg/mL (Fig. 2A), we used 10, 20, and 40 µg/mL MRE for the rest of the *in vitro* experiments. First, we determined the effect MRE on the production of intracellular ROS induced by LPS. LPS-induced intracellular ROS were reduced significantly by 20



**Fig. 1.** HPLC analysis of *Morus australis* extract. For the conditions, see the section of Methods. Retention time peak at 20.82 min is oxyresveratrol and at 27.16 min is morusin.

**Fig. 2.** Effects of MRE on cell viability and LPS-promoted intracellular ROS in RAW-264.7 cells. (A) RAW264.7 cells were treated with 0- 80  $\mu\text{g/mL}$  of MRE for 24 h, after which the cell viability was determined by MTT assay as described in Methods section. The results are reported as the mean $\pm$ SD of three independent experiments. Data presented as mean  $\pm$  S.D of three independent experiments. \* $p < 0.05$ , compared with control (lane 1). RAW-264.7 cells were treated with indicated concentrations of (B) MRE or (C) morusin for 30 min and stimulated with or without LPS for 24 h. Intracellular ROS were determined by the DCF fluorescence intensity as described in the text. Data presented as mean  $\pm$  S.D of three independent experiments. ## $p < 0.01$ , compared with control (lane 1). \* $p < 0.05$ , \*\* $p < 0.01$ , compared with LPS treated alone.





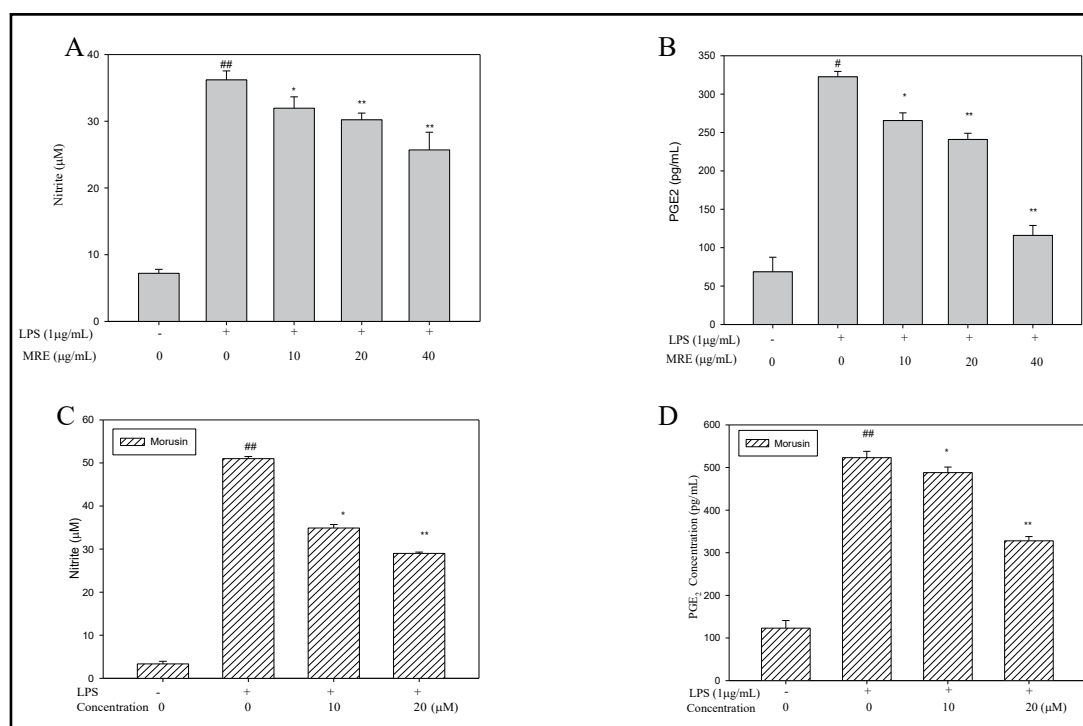


**Fig. 3.** Effects of MRE and morusin on LPS-stimulated production of nitrite and PGE<sub>2</sub> in RAW-264.7 cells. (A) RAW-264.7 cells ( $5 \times 10^5$  cells/mL) were treated with indicated concentrations of MRE for 30 min and stimulated with or without LPS for 24 h. Supernatants were collected for nitrite analysis by Griess reagent and determined at 550 nm. (B) PGE<sub>2</sub> analysis was performed by ELISA assay determined at 450 nm respectively. (C) RAW-264.7 cells were treated with indicated concentrations of morusin for 30 min and stimulated with or without LPS for 24 h. Supernatants were collected for nitrite analysis and (D) PGE<sub>2</sub> analysis. Data presented as mean  $\pm$  S.D of three independent experiments. ## $p < 0.01$ , compared with control (lane 1). \* $p < 0.05$ , \*\* $p < 0.01$ , compared with LPS stimulation alone.

and 40  $\mu\text{g/mL}$  MRE (Fig. 2B). In addition, because the antioxidant and antiinflammatory properties of oxyresveratrol, one of the major components of MRE, have been assessed [10], we determined the antioxidant and antiinflammatory activity of morusin. We found that 10 and 20  $\mu\text{M}$  morusin was noncytotoxic (data not shown) and exhibited a significant inhibitory effect on the LPS-induced intracellular ROS (Fig. 2C).

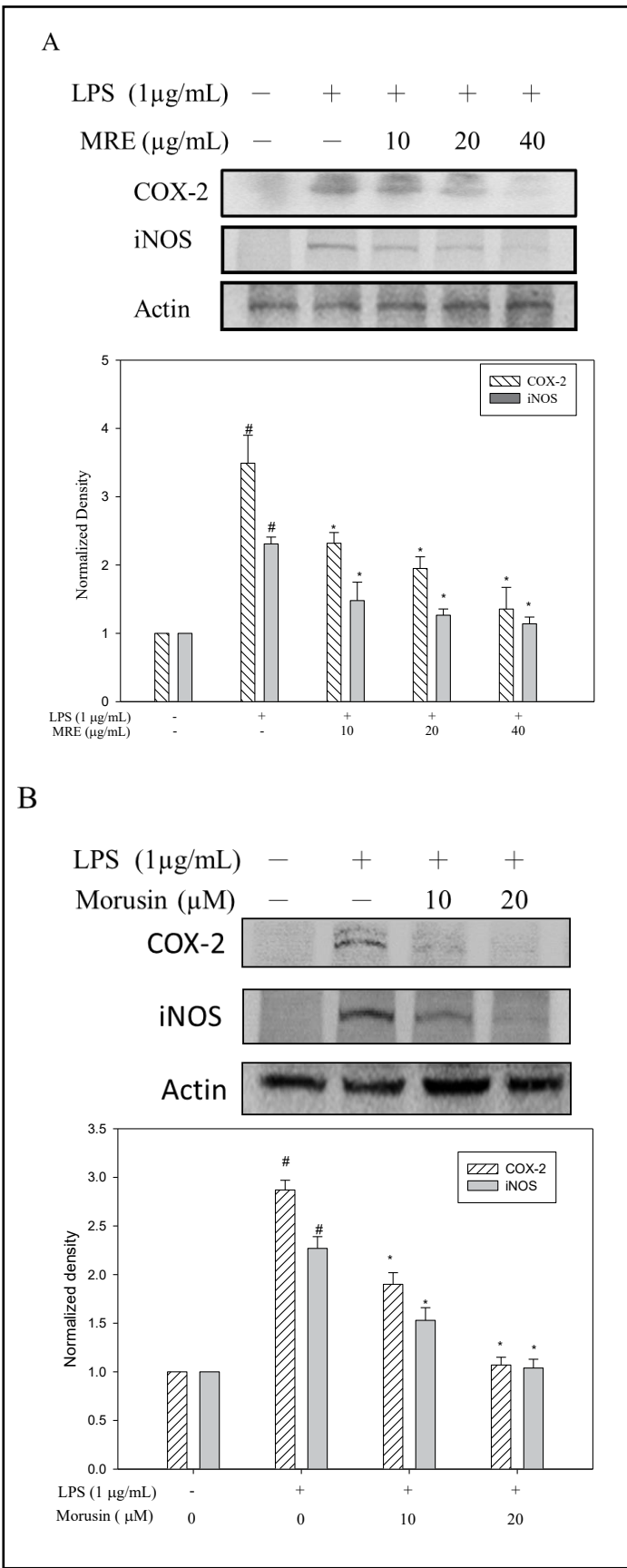
#### MRE inhibits LPS-stimulated production of inflammatory mediators

Chronic inflammation is associated with many diseases, such as cardiovascular and hepatic disease. We determined the effect of MRE on the LPS-stimulated production of nitrite and prostaglandin E<sub>2</sub> (PGE<sub>2</sub>) by RAW264.7 cells. MRE inhibited LPS-induced nitrite and PGE<sub>2</sub> production in a dose-dependent manner (Fig. 3A and 3B). In addition, morusin (10 and 20  $\mu\text{M}$ ) significantly inhibited LPS-induced nitrite and PGE<sub>2</sub> production (Fig. 3C and 3D). Consistent with the findings for PGE<sub>2</sub> and nitrite production, immunoblotting analysis showed that LPS-stimulated COX-2 and iNOS expression in RAW264.7 cells was also reduced by MRE treatment (Fig. 4A). In addition, morusin significantly inhibited LPS-stimulated COX-2 and iNOS expression (Fig. 4B).

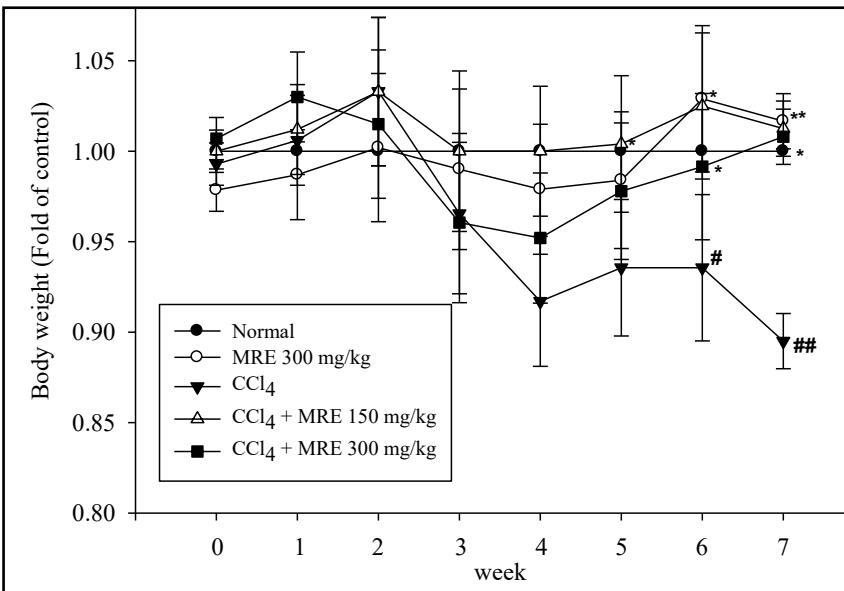
#### Body weight examination

Fig. 5 shows the variation of relative changes in body weight during the 7-week experiment. The body weights of the group that received MRE treatment alone were similar to those of the control group (Fig. 5). In addition, the weights of the livers and kidneys from the group treated with MRE alone were similar to those in the control group (data

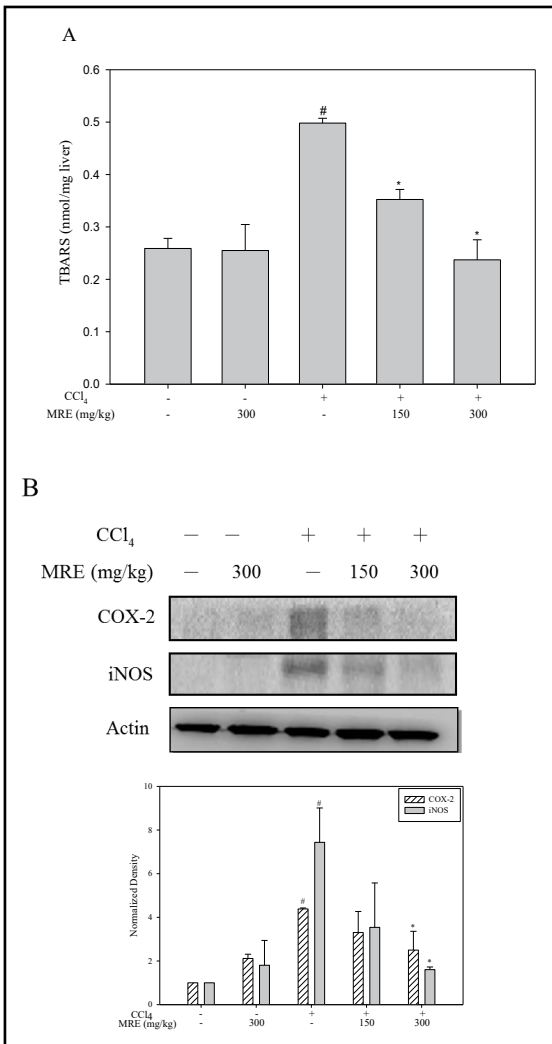
**Fig. 4.** Effect of MRE and morusin on LPS-stimulated COX-2 and iNOS proteins expression in RAW-264.7 cells by western blotting analysis. Cells were treated with various concentration of MRE or morusin for 30 min and then incubated with LPS (1 $\mu$ g/mL) for 24 h, and the cells were collected for protein extraction. Protein extract from (A) MRE or (B) morusin pretreatment was subjected to SDS-PAGE, and immunoblotting was performed against anti-COX-2 and anti-iNOS antibodies, and actin as internal control. The average densitometric values of three independent experiments is shown below as means  $\pm$  SD. #p<0.05, compared with control (lane 1). \*p<0.05, compared with LPS stimulation.



**Fig. 5.** Effect of MRE on the relative changes in body weight of mice with liver injury induced by  $\text{CCl}_4$ . # $p < 0.05$ , ## $p < 0.01$ , compared with control. \* $p < 0.05$ , \*\* $p < 0.01$ , compared with  $\text{CCl}_4$  treated alone.



**Fig. 6.** Effect of MRE on  $\text{CCl}_4$  induced hepatic lipid peroxidation and expression of COX-2 and iNOS in the mice. The hepatic homogenates of mice were analyzed as described in the Methods section. (A) The absorbance of TBARS was determined at 532 nm. Data presented as mean  $\pm$  S.D (n=6). # $p < 0.05$ , compared with the control group (lane 1). \* $p < 0.05$ , compared with the  $\text{CCl}_4$  stimulation alone. (B) The representative immunoblotting was performed against anti-COX-2 and anti-iNOS antibodies, and actin as internal control. The average densitometric values was shown below as means  $\pm$  SD. # $p < 0.05$ , compared with control (lane 1). \* $p < 0.05$ , compared with  $\text{CCl}_4$  treated alone.



not shown). This suggests that the treatment with MRE resulted in no toxicity. During the 6- and 7-week experiments,  $\text{CCl}_4$  treatment significantly suppressed the increase in body weight compared with the control group, indicating that the growth of  $\text{CCl}_4$ -treated mice was strongly suppressed. In addition, the  $\text{CCl}_4$ -induced body weight loss was alleviated in the MRE-treated groups.

#### *MRE ameliorates $\text{CCl}_4$ -induced hepatic lipid peroxidation and inflammatory mediator expression*

MRE prevented the increase of thiobarbituric acid reactive substances in the liver homogenates of the mice treated with  $\text{CCl}_4$  in a dose-dependent manner (Fig. 6A). In addition, Western blot analyses of the iNOS and COX-2 protein levels in the liver showed that treatment with  $\text{CCl}_4$  induced expression of both proteins that were undetectable in the control group and the group dosed with MRE alone. The expression of the iNOS and COX-2 protein in the liver was decreased by co-treatment with a low dose of MRE (150 mg/kg), and it was almost abolished by a high dose of MRE (300 mg/kg) (Fig. 6B).

#### *Effect of MRE on $\text{CCl}_4$ -induced histopathology and oxidative stress*

The morphological changes in liver injury caused by  $\text{CCl}_4$  were visualized in H&E stained liver sections. The changes included necrosis and inflammation with neutrophil infiltration (Fig. 7). The degree of necrosis and inflammation were decreased in animals treated with both MRE and  $\text{CCl}_4$  compared with those treated with  $\text{CCl}_4$  alone. MRE treatment alone did not cause visible changes in the liver. To evaluate the impact of MRE on inflammation and oxidative stress, hepatic macrophages and nitrotyrosine were assessed in the mouse liver using an immunohistochemistry assay. The intensities of F4/80 and nitrotyrosine were higher in the  $\text{CCl}_4$ -treated group than in the control group. However, co-treatment with MRE decreased the staining of F4/80 and nitrotyrosine, and the high-dose co-treatment of MRE (300 mg/kg) almost abolished both stainings (Fig. 7). These data suggest that MRE protects the liver against  $\text{CCl}_4$ -induced injury by attenuating inflammation and oxidative stress.

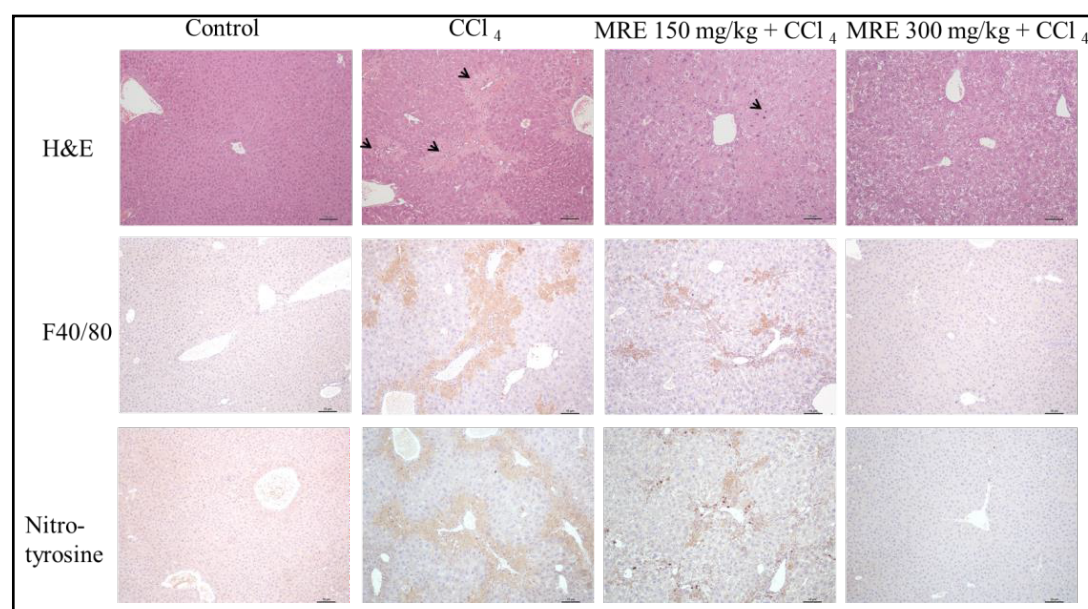


**Fig. 7.** Effect of MRE on histologic changes and liver Inflammation and oxidative stress induced by  $\text{CCl}_4$  in mice. The sections of mouse liver were stained with hematoxylin-eosin (original magnification 100x). Macrophage and oxidative stress were revealed as indicated by immunohistochemical staining of anti-F40/80 and anti-nitrotyrosine.



## Discussion

Much attention has been devoted to identifying phytochemicals in medicinal plants and the diet that have preventive or therapeutic effects against various chronic diseases. *M. australis* exhibits beneficial effects, such as antileukemia, antiinflammatory, and antiobesity activities, as well as tyrosinase inhibition. Twenty-two compounds were isolated from the root extract of *M. australis* by Zheng et al. [15]. Nineteen of the compounds were flavonoids, one was a stilbene (oxyresveratrol), and two were arylbenzofuran derivatives. These compounds have a polyphenolic structure that contributes to many of their bioactivities [18]. Our results showed that the total phenolic content was 23% and the total flavonoid content was 3%. The major components were oxyresveratrol and morusin. Oxyresveratrol has possesses a wide variety of biological activities, such as skin-whitening, antiviral, and neuroprotective effects [15, 19–20]. Soonthornsit et al. reported that oxyresveratrol at concentrations of 5 and 10 µg/mL inhibited LPS-induced nitrite production and the expression of iNOS and COX-2 [12]. Morusin, a prenylated flavonoid, potentially has neuroprotective, anticancer, antioxidative, and ant-colitis activities [21–24]. In this study, the anti-inflammatory effect of ethanol extract from the dried root of *M. australis* (MRE) was evaluated *in vitro* and *in vivo*. In the present study, it showed about one fourth active phenolic components in MRE was morusin, 2% by HPLC analysis while in the following studies we investigate that 40 µg/mL of MRE exhibits a hepatic protection effect through anti-inflammatory and anti-oxidative stress potential as noncytotoxic concentrations. Morusin is one of the major components of MRE, we determined the used concentrations of morusin correlate with its content one tenth. The 4.2 µg/mL (10 µM) of morusin was noncytotoxic concentrations and exhibited a significantly inhibitory effect on the LPS-induced inflammatory effect in RAW264.7 cells. Our data show that morusin also inhibited LPS-induced nitrite production and the expression of iNOS and COX-2. Because pure phytochemicals are expensive, bioactive mixtures may be a realistic alternative for consumers. Our data demonstrated that MRE potently inhibited an LPS-activated inflammatory effect in RAW264.7 cells and CCl<sub>4</sub>-induced liver injury in mice. The phenolic constituents, such as oxyresveratrol and morusin, exerted these effects. Therefore, MRE may be valuable as a preventive agent for inflammation-associated chronic disease.

Increased gene expression of iNOS and COX-2 is associated with inflammatory responses [25–26]. NO is synthesized from the amino acid arginine by nitric oxide synthase and induces tissue injury at the inflammatory site. COX-2 catalyses the conversion of arachidonic acid to prostaglandins, which contribute to chronic inflammatory conditions and oxidative stress [27]. Therefore, reduction of iNOS and COX-2 protein expression may be associated with the prevention and treatment of chronic inflammatory disease. In the present study, MRE inhibited iNOS and COX-2 expression induced by LPS stimulation in RAW264.7 cells or by CCl<sub>4</sub> treatment in mouse liver. In addition, a preliminary experiment showed that MRE scavenged free radicals (data not shown). Thus, MRE exerted its antioxidative stress potential by scavenging free radicals and decreasing the expression of iNOS and COX-2. Furthermore, increased nitrotyrosine and lipid peroxidation are indicators of oxidative stress-induced tissue injury. Our animal study demonstrated that MRE decreased CCl<sub>4</sub>-induced oxidative stress, resulting in the mitigation of CCl<sub>4</sub>-induced liver injury.

Many studies suggest a regular diet of fruit and vegetables as an antioxidative defence as part of a preventive strategy to inhibit, delay, or reverse human carcinogenesis using naturally extracted or synthetic chemical agents, including various phytochemicals [28]. Chemoprevention is an active hepatocellular carcinoma preventive strategy that aims to inhibit, delay, or reverse metabolic function disorders and hepatic injury using naturally extracted or synthetic chemical agents. Our study indicates that *M. australis* root extract may prevent liver damage. We have shown that t-BHP-induced apoptosis, the unfolded protein response, and oxidative stress correspond to the effects of mitochondrial respiratory-chain electron transport [29]. However, further studies of daily consumption of natural MRE products and studies of Chinese herbs, considered as blocking or suppressing agents, are still required to validate these mechanisms of unfolded protein response and oxidative stress corresponding to the effects of mitochondrial respiratory-chain electron transport [30].

## Conclusion

We showed that iNOS/COX-2/PGE2 inflammation level and oxidative stress were moderated by morusin. An *in vivo* study demonstrated that MRE decreased the mouse hepatocyte cell loss and macrophages. MRE inhibited liver cell damage based on the oxidative stress levels and the expression of iNOS/COX-2/PGE2 (Fig. 8). These results imply that MRE possesses antiinflammatory and hepatic protective activity. However, the use of MRE in humans needs further clinical investigation.

## Acknowledgements

This study was supported by grants from the Ministry of Science and Technology, Taiwan (MOST 106-2320-B-040-027, MOST 103-2622-B-255-001-CC3, MOST 103-2313-B-255-001 and MOST 104-2320-B-255-003-MY3). Densitometry was performed at the Instrument Center of Chung Shan Medical University, which is supported by the Ministry of Science and Technology, Ministry of Education and Chung Shan Medical University. Funding for this study was provided in part by research grants BMRPD42, CLRPG8G0591, CMRPF6G0011, CMRPF6G0012, CMRPF6G0013, CMRPG6H0261, CMRPG6H0262, CMRPG6H0263 from Chang Gung Memorial Hospital, Chiayi, Taiwan, and Chang Gung University of Science and Technology, Chia-Yi Campus, Taiwan.

## Disclosure Statement

There is no financial/commercial conflict of interest.

## References

- 1 Libby P. Inflammatory mechanisms: the molecular basis of inflammation and disease. *Nut Rev* 2007;65:S140-146.
- 2 Rehman MU, Yoshihisa Y, Miyamoto Y, Shimizu T: The anti-inflammatory effects of platinum nanoparticles on the lipopolysaccharide-induced inflammatory response in RAW 264.7 macrophages. *Inflamm Res*. 2012;61:1177-1185.
- 3 Rietschel ET, Brade H: Bacterial endotoxins. *Sci Am*. 1992;267:54-61.
- 4 Vitaglione P, Morisco F, Caporaso N, Fogliano V: Dietary antioxidant compounds and liver health. *Crit Rev Food Sci Nutr* 2004;44:575-586.
- 5 Hsu YW, Tsai CF, Chang WH, Ho YC, Chen WK, Lu FJ: Protective effects of Dunaliella salina--a carotenoids-rich alga, against carbon tetrachloride-induced hepatotoxicity in mice. *Food Chem Toxicol*. 2008;46:3311-3317.
- 6 Geetha S, Jayamurthy P, Pal K, Pandey S, Kumar R, Sawhney RC: Hepatoprotective effects of sea buckthorn (*Hippophae rhamnoides* L.) against carbon tetrachloride induced liver injury in rats. *J Sci Food Agric*. 2008;88:1592-1597.
- 7 Ko HH, Yu SM, Ko FN, Teng CM, Lin CN: Bioactive constituents of Morus australis and Broussonetia papyrifera. *J Nat Prod*. 1997;60:1008-1011.

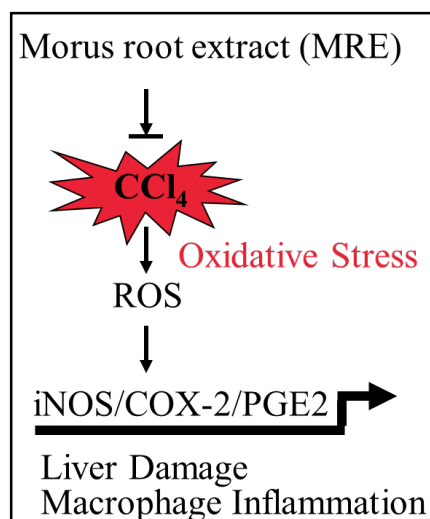


**Fig. 8.** Schematic presentation of the pathway depicting  $\text{CCl}_4$  uptake and intracellular oxidative stress signaling inhibited by MRE leading to decrease of iNOS, COX-2, and their respective secreted metabolites in liver and RAW264.7 cells. The inhibition of effects of  $\text{CCl}_4$  on the oxidative stress triggering production of ROS activates iNOS/COX-2/PGE2 complex formation, which was prevented the cells inflammation and increases liver injury in hepatocyte cells.

- 8 Ko HH, Wang JJ, Lin HC, Wang JP, Lin CN: Chemistry and biological activities of constituents from *Morus australis*. *Biochim Biophys Acta*. 1999;1428:293-299.
- 9 Zelová H, Hanáková Z, Čermáková Z, Šmejkal K, Dalí Acqua S, Babula P, Cvačka J, Hošek J: Evaluation of anti-inflammatory activity of prenylated substances isolated from *Morus alba* and *Morus nigra*. *J Nat Prod*. 2014;77:1297-1303.
- 10 Venkatesh Kumar R, Chauhan S. Mulberry: life enhancer. *JMPR*. 2008;2:271-278.
- 11 Choi SW, Jang YJ, Lee YJ, Leem HH, Kim EO: Analysis of Functional Constituents in Mulberry (*Morus alba* L.) Twigs by Different Cultivars, Producing Areas, and Heat Processings. *Prev Nutr Food Sci*. 2013;18:256-262.
- 12 Soonthornsit N, Pitaksutheepong C, Hemstapat W, Utaisincharoen P, Pitaksuteepong T: *In vitro* Anti-Inflammatory Activity of *Morus alba* L. Stem Extract in LPS-Stimulated RAW 264.7 Cells. *Evid. Based Complement Alternat Med*. 2017;2017:3928956.
- 13 Ann JY, Eo H, Lim Y: Mulberry leaves (*Morus alba* L.) ameliorate obesity-induced hepatic lipogenesis, fibrosis, and oxidative stress in high-fat diet-fed mice. *Genes Nutr*. 2015;10:46.
- 14 Wu T, Qi X, Liu Y, Guo J, Zhu R, Chen W, Zheng X, Yu T: Dietary supplementation with purified mulberry (*Morus australis* Poir) anthocyanins suppresses body weight gain in high-fat diet fed C57BL/6 mice. *Food Chem*. 2013;141:482-487.
- 15 Zheng ZP, Tan HY, Wang M: Tyrosinase inhibition constituents from the roots of *Morus australis*. *Fitoterapia*. 2012;83:1008-1013.
- 16 Tseng TH, Chuang SK, Hu CC, Chang CF, Huang YC, Lin CW, Lee YJ: The synthesis of morusin as a potent antitumor agent. *Tetrahedron*. 2010;66:1335-1340.
- 17 Green L, Wanger DA, Glogowski J, Skipper P L, Wishnok J S, Tannenbaum SR: Analysis of nitrate, nitrite, and [15N]nitrite in biological fluids. *Anal Biochem*. 1982;126:131-138.
- 18 Pandey KB, Rizvi SI: Plant polyphenols as dietary antioxidants in human health and disease. *Oxid Med Cell Longev*. 2009;2:270-278.
- 19 Chatsumpun N, Chuanasa T, Sritularak B, Lipipun V, Jongbunprasert V, Ruchirawat S, Ploypradith P, Likhitwitayawuid K: Oxyresveratrol: Structural Modification and Evaluation of Biological Activities. *Molecules*. 2016;21:489.
- 20 Chao J, Yu MS, Ho YS, Wang M, Chang RC: Dietary oxyresveratrol prevents parkinsonian mimetic 6-hydroxydopamine neurotoxicity. *Free Radic Biol Med*. 2008;45:1019-1026.
- 21 Lee HJ, Lyu da H, Koo U, Nam KW, Hong SS, Kim KO, Kim KH, Lee D, Mar W: Protection of prenylated flavonoids from Mori Cortex Radicis (Moraceae) against nitric oxide-induced cell death in neuroblastoma SH-SY5Y cells. *Arch Pharm Res*. 2012;35:163-170.
- 22 Lin WL, Lai DY, Lee YJ, Chen NF, Tseng TH: Antitumor progression potential of morusin suppressing STAT3 and NF-κB in human hepatoma SK-Hep1 cells. *Toxicol Lett*. 2015;232:490-498.
- 23 Cheng PS, Hu CC, Wang CJ, Lee YJ, Chung WC, Tseng TH: Involvement of the antioxidative property of morusin in blocking phorbol ester-induced malignant transformation of JB6 P+ mouse epidermal cells. *Chem Biol Interact*. 2017;264:34-42.
- 24 Vochyánová Z, Pokorná M, Rotrekl D, Smékal V, Fictum P, Suchý P, Gajdziok J, Smejkal K, Hosek J: Prenylated flavonoid morusin protects against TNBS-induced colitis in rats. *PLoS ONE*. 2017;12:e0182464.
- 25 Salerno L, Sorrenti V, Di Giacomo C, Romeo G, Siracusa MA: Progress in the development of selective nitric oxide synthase (NOS) inhibitors. *Curr Pharm Des*. 2002;8:177-200.
- 26 Griswold DE, Adams JL: Constitutive cyclooxygenase (COX-1) and inducible cyclooxygenase (COX-2): rationale for selective inhibition and progress to date. *Med Res Rev*. 1996;16:181-206.
- 27 Uchida K: A lipid-derived endogenous inducer of COX-2: a bridge between inflammation and oxidative stress. *Mol Cells*. 2008;25:347-351.
- 28 Zhang T, Song N, Fang Y, Teng J, Xu X, Hu J Zhang P, Chen R, Lu Z, Yu X, Ding X: Delayed Ischemic Preconditioning Attenuated Renal Ischemia-Reperfusion Injury by Inhibiting Dendritic Cell Maturation. *Cell Physiol Biochem*. 2018;46:1807-1820.
- 29 Shen CH, Tung SY, Huang WS, Lee KF, Hsieh YY, Hsieh MC, Chen CN, Kuo HC: Comparative Proteomic Identification of Protein Disulphide Isomerase A6 Associated with Tert-Butylhydroperoxide-Induced Liver Injury in Rat. Hepatocytes. *Cell Physiol Biochem*. 2018;45:1915-1926.
- 30 Shen CH, Tung SY, Huang WS, Lu CC, Lee KC, Hsieh YY, Chang PJ, Liang HF, Chen JH, Lin TH, Hsieh MC, Kuo HC: Exploring the effects of tert-butylhydroperoxide induced liver injury using proteomic approach. *Toxicology*. 2014;316:61-70.



# Lysophosphatidylcholine induces cyclooxygenase-2-dependent IL-6 expression in human cardiac fibroblasts

Hui-Ching Tseng<sup>1,2</sup> · Chih-Chung Lin<sup>3</sup> · Chen-Yu Wang<sup>2</sup> · Chien-Chung Yang<sup>4,5</sup> · Li-Der Hsiao<sup>3</sup> · Chuen-Mao Yang<sup>1,2,3,6</sup>

Received: 30 March 2018 / Revised: 8 August 2018 / Accepted: 4 September 2018  
© Springer Nature Switzerland AG 2018

## Abstract

Lysophosphatidylcholine (LysoPC) has been shown to induce the expression of inflammatory proteins, including cyclooxygenase-2 (COX-2) and interleukin-6 (IL-6), associated with cardiac fibrosis. Here, we demonstrated that LysoPC-induced COX-2 and IL-6 expression was inhibited by silencing NADPH oxidase 1, 2, 4, 5; p65; and FoxO1 in human cardiac fibroblasts (HCFs). LysoPC-induced IL-6 expression was attenuated by a COX-2 inhibitor. LysoPC-induced responses were mediated via the NADPH oxidase-derived reactive oxygen species-dependent JNK1/2 phosphorylation pathway, leading to NF- $\kappa$ B and FoxO1 activation. In addition, we demonstrated that both FoxO1 and p65 regulated COX-2 promoter activity stimulated by LysoPC. Overexpression of wild-type FoxO1 and S256D FoxO1 enhanced COX-2 promoter activity and protein expression in HCFs. These results were confirmed by ex vivo studies, where LysoPC-induced COX-2 and IL-6 expression was attenuated by the inhibitors of NADPH oxidase, NF- $\kappa$ B, and FoxO1. Our findings demonstrate that LysoPC-induced COX-2 expression is mediated via NADPH oxidase-derived reactive oxygen species generation linked to the JNK1/2-dependent pathway leading to FoxO1 and NF- $\kappa$ B activation in HCFs. LysoPC-induced COX-2-dependent IL-6 expression provided novel insights into the therapeutic targets of the cardiac fibrotic responses.

**Keywords** COX-2 · Lysophosphatidylcholine · IL-6 · NOX · ROS · NF- $\kappa$ B · FoxO1

**Electronic supplementary material** The online version of this article (<https://doi.org/10.1007/s00018-018-2916-7>) contains supplementary material, which is available to authorized users.

✉ Chuen-Mao Yang  
chuenmao@mail.cgu.edu.tw

- <sup>1</sup> Graduate Institute of Biomedical Sciences, College of Medicine, Chang Gung University, 259 Wen-Hwa 1st Road, Kwei-San, Tao-Yuan, Taiwan
- <sup>2</sup> Department of Physiology and Pharmacology and Health Ageing Research Center, Chang Gung University, Kwei-San, Tao-Yuan, Taiwan
- <sup>3</sup> Department of Anesthetics, Chang Gung Memorial Hospital at Linkuo and Chang Gung University, Kwei-San, Tao-Yuan, Taiwan
- <sup>4</sup> Department of Traditional Chinese Medicine, Chang Gung Memorial Hospital at Tao-Yuan, Kwei-San, Tao-Yuan, Taiwan
- <sup>5</sup> School of Traditional Chinese Medicine, Chang Gung University, Kwei-San, Tao-Yuan, Taiwan
- <sup>6</sup> Research Center for Chinese Herbal Medicine and Research Center for Food and Cosmetic Safety, College of Human Ecology, Chang Gung University of Science and Technology, Tao-Yuan, Taiwan

## Abbreviations

COX-2	Cyclooxygenase-2
DPI	Diphenyleneiodonium chloride
DUOX	Dual oxidase
EP	Prostaglandin E <sub>2</sub> receptor
FoxO	FoxO Forkhead box protein O
HCFs	Human cardiac fibroblasts
IL	Interleukin
LysoPC	Lysophosphatidylcholine
NOX	NADPH oxidase
PC	Phosphatidylcholine
PGE <sub>2</sub>	Prostaglandin E <sub>2</sub>
PLA <sub>2</sub>	Phospholipase A <sub>2</sub>
ROS	Reactive oxygen species
TGF- $\beta$	Transforming growth factor- $\beta$
TNF	Tumor necrosis factor

## Introduction

Heart diseases involve the pathological development of several functional and structural defects in the heart [1]. Cardiac fibroblasts (CFs) play a major role in the repair



and remodeling of the heart during myocardial injury [2]. However, over-secretion of cytokines from CFs, such as interleukin (IL)-1 $\beta$ , tumor necrosis factor (TNF)- $\alpha$ , IL-6, and transforming growth factor- $\beta$  (TGF- $\beta$ ) [3], amplifies inflammatory cascades, contributing to cardiac fibrosis and hypertrophy [4]. Lysophosphatidylcholine (LysoPC) is produced by phospholipase A<sub>2</sub> (PLA<sub>2</sub>) via the hydrolysis of cell membrane-derived phosphatidylcholine (PC). It regulates several cellular events including oxidative stress, differentiation, and inflammation [5–7]. The levels of LysoPC are also increased in ischemic and insulin-resistant hearts [8, 9], suggesting its association with cardiomyocyte apoptosis in fibrosis [8, 10], providing important evidence for an association between LysoPC and pathogenesis of various cardiovascular diseases [11]. Previous reports have indicated that IL-6 is a key mediator in tissue remodeling that promotes acute inflammation to chronic fibrotic state and induces recurrent inflammatory cascades [4]. Induction of IL-6 in rat CFs is associated with fibroblast proliferation and differentiation via a TGF- $\beta$ -mediated pathway [12–14]. LysoPC is a potential inducer to stimulating the release of pro-inflammatory cytokines including IL-6 [6]. Nevertheless, the pathological relationship between LysoPC-induced inflammatory cytokines and cardiac fibrosis remains unclear.

LysoPC has been shown to induce intracellular generation of reactive oxygen species (ROS) in various cell types [15, 16]. ROS is a group of highly reactive molecules, including hydrogen peroxide (H<sub>2</sub>O<sub>2</sub>), hydroxyl radical (OH $\cdot$ ), and superoxide anion (O<sub>2</sub><sup>-</sup>). NADPH oxidase (NOX) is a major source of ROS generation such as H<sub>2</sub>O<sub>2</sub> and O<sub>2</sub><sup>-</sup> via an NADPH-dependent one- or two-electron reduction of oxygen [17]. Activation of NOX is hypothesized to increase oxidative stress, contributing to pathogenesis of cardiac remodeling and heart failure [18, 19]. NOX-derived ROS are recognized as major second messengers involved in activation of various signaling components leading to COX-2 expression via NF- $\kappa$ B [20]. Upregulation of COX-2 is linked to the development of heart failure involving macrophage infiltration and fibroblast proliferation [21, 22]. Brkic et al. indicated that LysoPC induced COX-2 expression in endothelial cells [23]. However, whether COX-2 further induced IL-6 secretion in human cardiac fibroblasts (HCFs) is still unknown.

Forkhead transcription factors of the O class 1 (FoxO1) have been shown to be involved in COX-2 expression induced by IL-1 $\beta$  [24], whereas FoxO1 negatively regulates COX-2 expression by sphingosine-1-phosphate [25]. FoxO1 is a critical player in the development of physiological heart and cardiac remodeling during heart failure [26, 27]. FoxO1 also regulates cellular energy metabolism, cell survival, and autophagy in the heart [28–30]. Moreover, accumulation of nuclear FoxO1 increases the expression of pro-inflammatory cytokines, including IL-6 [31, 32]. Based on these findings,

the functional roles of FoxO1 in physiological and pathological processes are still controversial. Therefore, we aimed to investigate the mechanisms by which LysoPC primed NOX/ROS-JNK1/2-dependent NF- $\kappa$ B and FoxO1 activation, leading to COX-2-induced IL-6 expression in HCFs.

## Methods

### Antibodies and reagents

CM-H<sub>2</sub>DCFDA and M-MLV Reverse Transcriptase kit were obtained from Invitrogen (Carlsbad, CA, USA). Human cytokine antibody array C3 was obtained from Ray Biotech (Norcross, GA, USA). Anti-phospho-FoxO1 (Ser<sup>256</sup>) (#9461) was obtained from Cell signaling (Danvers, MA, USA). Anti-COX-2 (ab62331), anti-FoxO1 (ab52857), and anti-phospho-p65 (ab86299) were obtained from Abcam (Cambridge, UK). Anti-FoxO1 (sc-11350), anti-p65 (sc-398442), anti-lamin A (sc-20680), and  $\beta$ -actin (sc-47778) antibodies were obtained from Santa Cruz (Santa Cruz, CA, USA). Anti-GAPDH (#MCA-1D4) was obtained from EnCor Biotechnology (Gainesville, FL, USA). LysoPC (L-0906) and TRIzol were obtained from Sigma-Aldrich (St. Louis, MO, USA). LysoPC was dissolved in 50% ethanol and filtered through a 0.22  $\mu$ m syringe filter. A final concentration of 0.25% ethanol was used for cell culture treatment. Celecoxib and diphenyleneiodonium chloride (DPI) were obtained from Biomol (Plymouth Meeting, PA, USA). AS1842856 was obtained from EMD Millipore (Billerica, MA, USA). Helenalin was obtained from Cayman Chemicals (Ann Arbor, MI, USA). Kapa Probe Fast qPCR Kit was obtained from KAPA Biosystems (Wilmington, MA, USA). GenMute<sup>TM</sup> siRNA Transfection Reagent was obtained from SignaGen Lab (Gaithersburg, MD, USA). X-tremeGENE<sup>TM</sup> HP DNA Transfection Reagent and  $\beta$ -gal reporter assay kit were obtained from Roche Applied Sciences (Indianapolis, IN, USA). SDS-PAGE supplies and BSA were obtained from MDBio Inc (Taipei, Taiwan). DMEM/F-12 medium was obtained from Corning (Manassas, VA, USA). FBS was obtained from Gibco (Grand Island, NY, USA).

### Ethics of animal experimentation

Male ICR mice (25–30 g, 8 weeks old) were purchased from the National Laboratory Animal Centre (Taipei, Taiwan). All animal experiments were conducted in accordance with the Institutional Animal Care and Use Committee (IACUC) guidelines and approved by the IACUC committee of Chang Gung University (CGU 16-046), and were carried out in accordance with the guidelines of the National Institute of Health for the Care and Use of Laboratory Animal.

## Collection and incubation of ex vivo tissues

ICR mice were anesthetized with one injection of Zoletil (40 mg/kg i.p.) and xylazine (10 mg/kg i.p.). After anesthesia, mice were withdrawn with lined forceps on the paws, and then the chests were opened and the hearts were quickly removed for experiments. The slices of cardiac apexes were pretreated with the respective inhibitors for 1 h and then exposed to LysoPC for 6 h while in Krebs solution (119 mM NaCl, 25 mM NaHCO<sub>3</sub>, 4.7 mM KCl, 11 mM glucose, 2.5 mM CaCl<sub>2</sub>, 1.2 mM KH<sub>2</sub>PO<sub>4</sub>, 1.2 mM MgSO<sub>4</sub>, pH 7.4) bubbled with 95% O<sub>2</sub> and 5% CO<sub>2</sub> at 37 °C. The homogenates of cardiac apexes were prepared and lysed in a lysis buffer (25 mM Tris-HCl (pH 7.4), 25 mM NaCl, 25 mM NaF, 25 mM sodium pyrophosphate, 1 mM sodium vanadate, 2.5 mM EDTA, 2.5 mM EGTA, 0.05% (w/v) Triton X-100, 0.5% (w/v) SDS, 0.5% (w/v) deoxycholate, 0.5% (w/v) NP-40, 10 µg/ml leupeptin, 10 µg/ml aprotinin, and 1 mM PMSF) and subjected to western blot analysis and RT/qPCR.

## Cell culture

Human cardiac fibroblasts were purchased from ScienCell Research Laboratories (San Diego, CA, USA) and maintained in DMEM/F-12 medium supplemented with 10% FBS, as previously described [33].

## Preparation of samples and western blot analysis

Growth-arrested HCFs were incubated without or with different concentrations of LysoPC at 37 °C for the indicated time intervals. When pharmacological inhibitors were used, they were added 1 h prior to the exposure of LysoPC. After incubation, the cells were rapidly washed with ice-cold PBS and lysed with a sample buffer containing 125 mM Tris-HCl, 1.25% SDS, 6.25% glycerol, 3.2% β-metacaproethanol, and 7.5 nM bromophenol blue with pH 6.8. Samples were denatured, subjected to SDS-PAGE using a 10% (w/v) running gel, and transferred to nitrocellulose membrane (BioTrace™ NT membrane, Pall Life Sciences, Ann Arbor, MI, USA). The membranes were immunoblotted with one of the primary antibodies (1:1000 dilution) overnight at 4 °C, followed by incubation with a peroxidase-conjugated secondary antibody at room temperature for 2 h. The immunoreactive bands were visualized by enhanced chemiluminescence reagent (Western Lighting Plus; Perkin Elmer, Waltham, MA, USA). The images of the immunoblots were acquired by using a UVP BioSpectrum 500 imaging system (Upland, CA, USA) and densitometry analysis was conducted using UN-SCAN-IT gel software (Orem, UT, USA).

## cDNA microarray analysis

Growth-arrested HCFs were incubated with LysoPC for either 6 h or 12 h. Total RNA was extracted with TRIzol (Sigma-Aldrich, St. Louis, MO, USA) which was used to prepare aRNA amplification (Amino Allyl MessageAmp II aRNA Amplification Kit; Ambion) and labeled with Cy5. The labeled aRNAs were hybridized to the Human Whole Genome OneArray™ (HOA 6.2; Phalanx Biotech Group, Hsinchu, Taiwan) according to Phalanx OneArray™ Plus protocol and examined using Agilent 0.1 XDR protocol (Phalanx Biotech Group, Hsinchu, Taiwan). The raw fluorescence intensities of each spot were analyzed by GenePix software and subsequently loaded into Rosetta Resolver System (version 7.2, Rosetta Biosoftware, Seattle, WA, USA) to process analyzed data. Normalized data are expressed as log<sub>2</sub> of LysoPC-treatment relative to the control group.

## Reverse-transcription PCR and qPCR analyses

Total RNA was extracted with TRIzol reagent according to the protocol of the manufacturer.

First-strand cDNA synthesis was performed with 5 µg of total RNA using Oligo(dT)<sub>15</sub> as primers in a final volume of 20 µl [25 ng/µl Oligo(dT)<sub>15</sub>, 0.5 mM dNTPs, 10 mM DTT, 2 units/µl RNase inhibitor, and 10 unit/µl of superscript II reverse transcriptase (Invitrogen, Carlsbad, CA, USA)]. The synthesized cDNAs were used as templates for PCR reaction using Q-Amp™ 2× screeningFire Taq master mix (Bio-Genesis Technologies, Taipei, Taiwan) and primers for the target genes. qPCR was performed by using Kapa Probe Fast qPCR Kit Master Mix Universal (KAPA Biosystems, Wilmington, MA, USA) on a StepOnePlus™ real-time PCR system (ThermoScientific-Applied Biosystems). The relative amount of the target gene was calculated using  $2^{(C_i \text{ test gene} - C_i \text{ GAPDH})}$  ( $C_i$  = threshold cycle). The primer sequences are given in Supplementary Tables 1 and 2.

## Determination of NADPH oxidase activity by chemiluminescence assay

Human cardiac fibroblasts were seeded in six-well plates, reaching about 90% confluence, and then transferred to fresh DMEM/F-12 medium for 24 h. Cells were then exposed to LysoPC for the indicated time intervals, gently scraped, and then centrifuged at 8000×g for 12 min at 4 °C. The cell pellet was resuspended in 100 µl ice-cold PBS containing 150 mM sucrose and 1 mM EGTA. To a final 200 µl volume of pre-warmed (37 °C) PBS containing either NAD(P)H (0.1 mM) or lucigenin (0.2 mM), 10 µl of cell suspension was added to initiate the reaction followed by immediate measurement of chemiluminescence using a luminometer (Synergy H1 Hybrid Reader, BioTek) in an out-of-coincidence mode.

Appropriate blanks and controls were established, and chemiluminescence was recorded. Neither NAD(P)H nor NADH enhanced the background chemiluminescence of lucigenin alone (30–40 counts/min). Chemiluminescence was continuously measured for 12 min, and the activity of NADPH oxidase was expressed as counts per million cells.

### Evaluation of ROS generation

Human cardiac fibroblasts were stimulated with LysoPC and then incubated in DMEM/F-12 medium containing 5  $\mu$ M CM-H<sub>2</sub>DCFDA. The fluorescent intensity was detected by using a fluorescence microplate reader (Synergy H1 Hybrid Reader, BioTek) with EX495 nm and EM529 nm.

### Transient transfection with siRNAs

Human cardiac fibroblasts were plated in 12-well, 6-well plates or 10-cm dish, reaching about 90% confluence, and transferred to fresh DMEM/F-12 medium before transfection. p65 siRNA (HSS109161) was obtained from Invitrogen Life Technologies (Carlsbad, CA, USA), and siRNAs of NOX1 (SASI\_Hs02\_00342845), NOX2 (SASI\_Hs01\_00086110, NOX4 (SASI\_Hs02\_00349918), FoxO1 (SASI\_Hs01\_00076732), and scramble siRNA were obtained from Sigma-Aldrich (St. Louis, MO, USA). NOX5 siRNA (1070614\_8103) was obtained from MDBio Inc (Taipei, Taiwan) [34]. The siRNA sequences are shown in Supplementary Table 3. Transient transfection of siRNA was carried out using GenMute™ siRNA Transfection Reagent according to the instructions of the manufacturer (SignaGen Lab. Gaithersburg, MD, USA). The siRNA (100 nM) was added to each well and then incubated at 37 °C for 6 h. The cells were transferred to DMEM/F-12 medium containing 10% FBS for an additional 6 h, washed twice with PBS, and then maintained in serum-free DMEM/F-12 medium for 24 h before treatment with LysoPC.

### Construction of FoxO1 plasmid DNA

For the construction of pCMV-Tag2B, the FoxO1 protein-encoding sequence was amplified by PCR using the following primer sequences: sense 5'-GGGGA TAT CATGGCCGAGGCGCCTCAGGTGGTGGAGA-3' and antisense 5'-GGGAAGCTTTCAGCCTGACACCCA GCTATGTG-3'. Ser<sup>256</sup>-to-Ala<sup>256</sup> FoxO1 mutant (S256A FoxO1), Ser<sup>256</sup>-to-Asp<sup>256</sup> FoxO1 mutant (S256D FoxO1), Ser<sup>319</sup>-to-Ala<sup>319</sup> FoxO1 mutant (S319A FoxO1), and Ser<sup>319</sup>-to-Asp<sup>319</sup> FoxO1 mutant (S319D FoxO1) were cloned. The Ser<sup>256</sup> and Ser<sup>319</sup> residues of FoxO1 were replaced with an alanine and aspartic acid residue, respectively, by priming with oligonucleotide 5'-CTCCTAGGAG AAGAGCTGCATGCAATGGACAACAACAGTAAATTT

GCT-3' (S256A), 5'-CTCCT AGGAGAAGAGCTGCAT GACATGGACAACAACAGTAAATTTGCT-3' (S256D), 5'-TACTATTAGTGGGAGACTCGCACCCATTATGACC GAACAG-3' (S319A), and 5'-TACTATTAGTGGGAGACT CGACCCATTATGACCGAACAG-3' (S319D). The PCR products were cloned into the *EcoRV-HindIII* site of the pCMV-Tag2B vector.

### Transient transfection of plasmid DNA

Human cardiac fibroblasts were seeded in six-well plates or 10-cm dishes, reaching 90% confluence, transferred to serum-free DMEM/F-12 medium, and transiently transfected with plasmid DNA using an X-tremeGENE™ HP DNA Transfection Reagent (Roche Applied Science, Indianapolis, IN, USA). Briefly, 3  $\mu$ g of plasmid DNA (pCMV-Tag2B-FoxO1, -FoxO1 mutants, or pCMV-Tag2B) into six-well or 15  $\mu$ g of plasmid DNA into 10-cm dish was diluted with Opti-MEM (200  $\mu$ l/well or 500  $\mu$ l/dish) (Gibco, Life Technologies, Gaithersburg, MD, USA) and incubated at 25 °C for 15 min. The X-tremeGENE™ HP DNA Transfection Reagent was added to the DNA diluents [3:1 ratio of reagent ( $\mu$ l) to DNA ( $\mu$ g)] and incubated at 25 °C for 20 min. Subsequently, the transfection complex was added into each well and incubated at 37 °C in a humidified 5% CO<sub>2</sub> atmosphere. After 48 h of transfection, the cells were incubated with LysoPC and harvested.

### Measurement of COX-2 promoter activity

For construction of the COX-2-luc plasmid, human COX-2 promoter, a region spanning from –484 to +37 was cloned into pGL3-basic vector, as previously described [35]. HCFs were co-transfected with pGL3b-cox-2, pCMV-Tag2B-FoxO1, pCMV-Tag2B (as a control group), or pCMV- $\beta$ -gal plasmid (as an internal control). Promoter activities of COX-2 were determined using a luciferase-e assay HIT kit (BioThema, Handen, Sweden) and normalized with  $\beta$ -Gal reporter gene.

### Assessment of cytokine secretion

Human cardiac fibroblasts were starved and exposed to LysoPC in the presence or absence of pharmacological inhibitors for the indicated time durations. The media were collected and the levels of cytokines and chemokines were determined using a human cytokine antibody array (Ray Biotech Inc., Norcross, GA, USA). The dot intensities of different cytokines were semi-quantified using UN-SCAN-IT and normalized to the intensity of internal positive control.

## Immunofluorescence staining

Human cardiac fibroblasts were seeded on coverslips in six-well culture plates, reaching 90% confluence, transferred to serum-free DMEM/F-12 medium overnight, and then stimulated with 40  $\mu$ M LysoPC for the indicated time durations. After washing twice with ice-cold PBS, the cells were fixed with 4% (w/v) paraformaldehyde in PBS for 30 min, and then permeabilized with 0.1 % Triton X-100 in PBS for 15 min. The staining was performed by incubating with 5% BSA for 2 h at 37 °C, followed by incubation with a primary anti-phospho-FoxO1<sup>S256</sup> polyclonal antibody (1:100 dilution) overnight in PBS with 1% BSA. The cells were washed thrice with PBS and incubated for 2 h with a fluorescein isothiocyanate (FITC)-conjugated goat anti-rabbit antibody (1:100 dilution; Jackson Immunoresearch) in PBS with 1% BSA. Finally, cells were washed thrice with PBS and then mounted with aqueous mounting medium containing DAPI (H1200; Vector Lab, Burlingame, CA, USA). Images were captured with a fluorescence microscope (Axiovert 200 M; Carl Zeiss, Thornwood, NY, USA).

## Chromatin immunoprecipitation assay

Human cardiac fibroblasts were transfected with FoxO1 plasmid or incubated with LysoPC. Samples were prepared and chromatin immunoprecipitation (ChIP) assay was performed. Protein–DNA complexes were fixed by 1% formaldehyde in DMEM/F-12 medium and the reaction was stopped by 0.125 M glycine. The fixed cells were washed and lysed in a lysis buffer (1% SDS, 10 mM EDTA, 1 mM PMSF, 50 mM Tris–HCl, pH 8.1). The cell lysates were sonicated using a Misonix Sonicator S-4000 (pulse on for 20 s and off for 15 s at amplitude 20 for 90 cycles; Farmingdale, NY, USA) at 4 °C until the chromosome DNA was broken to approximately 200–500 base pairs. The samples were centrifuged, and the soluble chromatin was pre-cleared by incubation with salmon sperm DNA–protein agarose A slurry (Upstate, Billerica, MA, USA) for 30 min at 4 °C with rotation. The samples were then centrifuged at 4000 $\times$ g for 2 min and the supernatant was transferred to a new tube. The samples were quantified and adjusted to the same protein concentrations. One portion of the sample was used as DNA input control. Soluble chromatin was immunoprecipitated either without (control) or with an anti-FoxO1, anti-p65, or anti-Flag M2 antibody for 3 h at 4 °C, and then incubated with salmon sperm DNA–protein agarose A slurry overnight at 4 °C with rotation. The samples were successively washed with low-salt buffer (0.1% SDS, 1% Triton X-100, 2 mM EDTA, 150 mM NaCl, 20 mM Tris–HCl, pH 8.1), high-salt buffer (same as low-salt buffer but with 500 mM NaCl), LiCl buffer (0.25 M LiCl, 1% NP-40, 1% deoxycholate, 1 mM EDTA, 10 mM Tris–HCl, pH 8.1), and Tris–EDTA (10 mM

Tris–HCl and 1 mM EDTA, pH 8.0), prior to elution (1% SDS, 100 mM NaHCO<sub>3</sub>). The cross-linked protein–DNA complexes were reversed by incubation at 65 °C overnight. DNA fragments were purified by using an EasyPure PCR/Gel Extraction kit (Bioman, Taiwan). The purified DNA was subjected to PCR amplification. The primer sequences were as follows—FoxO1: forward primer 5'-AAGACATCTGGC GGAAACC-3', reverse primer 5'-ACAATTGGTCGCTAA CCGAG-3' (–299 to +7); proximal NF- $\kappa$ B: forward primer 5'-GGCAAAGACTGCGAAGAAGA-3', reverse primer 5'-AAAATCGGAAACCCAGGAAG-3'; and distal NF- $\kappa$ B: forward primer 5'-CCTCGACCCTCTAAAGACGTA-3', reverse primer 5'-AGCCAGTTCTGGACTGATCG-3', which were specifically designed from the COX-2 promoter region (–320 to –171) and (–499 to –335), respectively. PCR fragments were analyzed on 3% agarose in 1 $\times$  TAE gel containing ethidium bromide. In addition, qPCR was performed with KAPA SYBR FAST qPCR Kit Master Mix Universal (KAPA Biosystems, Wilmington, MA, USA) on a StepOnePlus™ real-time PCR system.

## Isolation of subcellular fractions

Human cardiac fibroblasts were seeded in 10-cm dishes, reaching 90% confluence, transferred to serum-free DMEM/F-12 medium for 24 h, and then incubated with LysoPC for the indicated time durations. The subcellular fractions were prepared by using a NE-PER nuclear and cytoplasmic extraction kit according to the instructions of the manufacturer (Thermo Scientific, Rockford, IL, USA). Cells were gently scraped and then centrifuged at 2000 $\times$ g for 12 min at 4 °C. The pellet was suspended in 300  $\mu$ l CRE I, and then vortexed for 15 s. After incubation for 10 min, 25  $\mu$ l CRE II was added to the sample, sonicated for 10 s at level of amplitude 10 (Misonix Sonicator S-4000), and then incubated for 30 min. The samples were centrifuged at 16,000 $\times$ g for 5 min. The supernatants (cytoplasmic extracts) were transferred to new tubes. The pellets (nuclear extracts) were lysed with 150  $\mu$ l NER and sonicated for 10 s at level of amplitude 10. All the reagents contained protease inhibitor cocktails (1 mM PMSF, 10  $\mu$ g/ml aprotinin, and 10  $\mu$ g/ml leupeptin) and the procedures were carried out at 4 °C. Protein concentration was determined by a BCA assay, and 20  $\mu$ g of protein from each sample was analyzed by western blot analysis.

## Co-immunoprecipitation assay

Human cardiac fibroblasts were seeded in 10-cm dishes, reaching 90% confluence, transferred to serum-free DMEM/F-12 medium for 24 h, and then incubated with LysoPC for the indicated time durations. The nuclear extracts were isolated and lysed in a RIPA buffer (20 mM



Tris-HCl, 150 mM NaCl, 1 mM EDTA, 1% Triton X-100, 1% NP40, 10 µg/ml leupeptin, 10 µg/ml aprotinin, and 1 mM PMSF, pH 8.0). The supernatants containing 1 mg of protein were incubated without (input) or with anti-FoxO1 or anti-p65 antibody under gentle rocking at 4 °C for 2 h, and after addition of 50 µl of 50% protein A-agarose beads tumbled overnight at 4 °C. The agarose beads were extensively washed with a lysis buffer without Triton X-100 and NP40. The samples were added to 2× western blot loading buffer and the western blot analysis was performed.

## Data and statistical analysis

All the data were estimated using a GraphPad Prism Program (GraphPad, San Diego, CA, USA). Quantitative data were expressed as the mean ± SEM of at least three individual experiments ( $n \geq 3$ ), and analyzed with a one-way ANOVA followed by Tukey's post hoc test at a  $*p < 0.01$  or  $^{\#}p < 0.05$  level of significance. Error bars were omitted when they fell within the dimensions of the symbols.

## Results

### LysoPC enhances COX-2 expression and promoter activity

To determine the effect of LysoPC on COX-2 expression, as shown in Fig. 1a, LysoPC-induced COX-2 protein expression in a time- and concentration-dependent manner was studied and a maximal response was observed within 16 h. Next, the results of RT/qPCR analysis showed that LysoPC induced an approximate 13.6-fold increase in *cox-2* mRNA expression within 6 h (Fig. 1b). To explore the LysoPC-regulated COX-2 transcription, LysoPC induction was studied and an approximate 2.3-fold increase in COX-2 promoter activity was observed within 4 h (Fig. 1b). These data suggested that LysoPC regulates COX-2 expression at the transcriptional level in HCFs.

### LysoPC induces COX-2-mediated IL-6 expression

The expression of potential fibrotic genes in HCFs induced by LysoPC was determined by cDNA microarray analysis. The data showed that the pro-fibrotic cytokine genes (*illa*, *illb*, *il6*, *il33*, and *TNF-α*) and *PTGS2* (encoding COX-2 protein) were upregulated in HCFs treated with LysoPC (Supplementary Table 4). To confirm the effects of LysoPC on the profile of cytokines, the conditioned media were subjected to a human inflammatory cytokine array. The levels of IL-1α, IL-β, and IL-6 were predominately increased in the LysoPC-treated HCFs (Fig. 1c). Our previous study demonstrated that sphingosine-1-phosphate induces COX-2

expression, contributing to IL-6 production via a PGE<sub>2</sub>/EP autocrine pathway [35]. Thus, we determined whether LysoPC-induced IL-6 secretion shared a similar mechanism in HCFs. We found that pretreatment with celecoxib (a selective COX-2 inhibitor) attenuated LysoPC-induced IL-6 secretion (Fig. 1c) and mRNA expression (Fig. 1d). These results suggested that LysoPC-induced IL-6 secretion is mediated via a COX-2-dependent mechanism in HCFs.

### NADPH oxidase/ROS is involved in LysoPC-induced COX-2 expression

Previous studies have demonstrated that LysoPC increased intracellular ROS production in various cell types [5, 10, 15]. Thus, we explored whether LysoPC induced intracellular ROS generation in HCFs. Our results showed that the levels of ROS generation in cells induced by LysoPC were elevated in a time-dependent manner ranging from 30 to 60 min (Fig. 2a). We further determined whether the ROS generation was due to promotion of NOX activity by LysoPC. As shown in Fig. 2a, LysoPC induced NOX activity in a time-dependent manner with a maximal response within 5–60 min. Moreover, pretreatment with either edaravone (a scavenger of ROS) or DPI (a NOX inhibitor) inhibited the LysoPC-induced ROS generation as well as NOX activation (Fig. 2b), suggesting that LysoPC primes NOX activation leading to ROS generation. The family of NOX comprises seven members: NOX1–5 and DUOX1–2, although, DUOX1/2 is not expressed in the cardiovascular system [36]. Previous studies have demonstrated that ROS are involved in COX-2 expression via NOX2 activation [20]. Our results also demonstrated that pretreatment with DPI attenuated LysoPC-induced COX-2 protein expression in a concentration-dependent manner (Fig. 2c). Moreover, we identified the expression of NOX isoforms in HCFs using RT/PCR. The isoforms of NOX that expressed in HCFs were NOX1, 2, 4, and 5 (Supplementary Fig. 1A). To ensure the roles of NOX isoforms in COX-2 expression, specific NOX siRNAs were used to knock down their respective mRNA targets (Supplementary Fig. 1B–E). Transfection with NOX1, NOX2, NOX4, or NOX5 reduced LysoPC-induced COX-2 expression in HCFs (Fig. 2d). Although NOX/ROS-dependent IL-6 expression has been confirmed in human vascular smooth muscle cells [25], the role of NOX/ROS in COX-2-mediated IL-6 expression was not well defined for HCFs. RT/qPCR analysis showed that IL-6 mRNA expression was downregulated after transfection with NOX1, NOX2, NOX4, or NOX5 siRNA (Fig. 2e). These results suggested that LysoPC-induced IL-6 expression is mediated via a NOX/ROS-dependent cascade in HCFs.

LysoPC has been shown to stimulate phosphorylation of MAPKs, including JNK1/2 [10, 37]. Therefore, we tested the role of JNK1/2 in COX-2 expression using the inhibitor

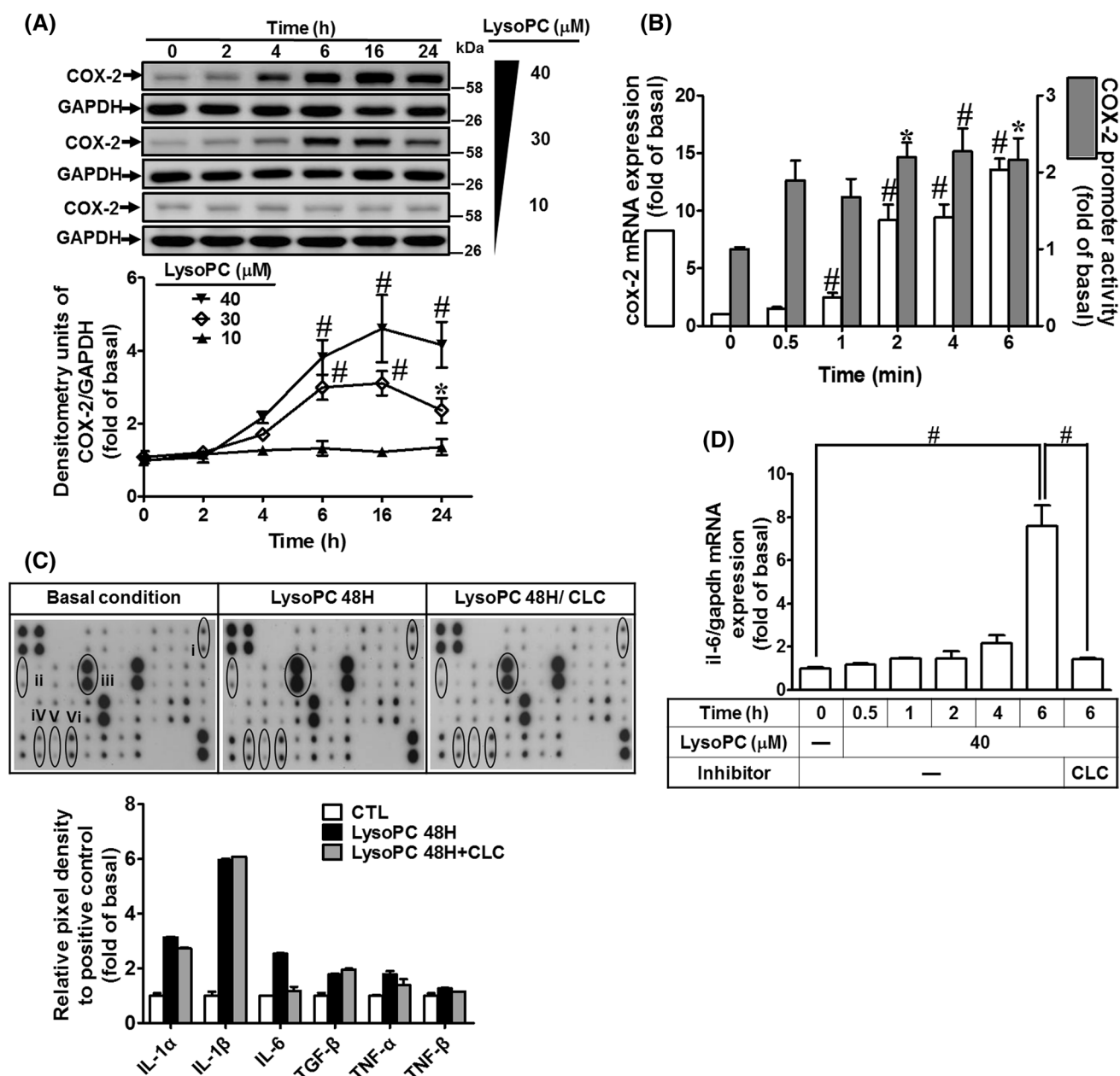


**Fig. 1** LysoPC induces COX-2-mediated IL-6 expression. **a** HCFs were treated with various concentrations of LysoPC for the indicated time intervals. The levels of COX-2 and GAPDH proteins were determined by western blot ( $n=6$ ). **b** HCFs were incubated with LysoPC (40  $\mu$ M) for the indicated time points. The levels of COX-2 and GAPDH mRNA were determined by RT/qPCR (open bars;  $n=7$ ). Cells were co-transfected with a pGL3b-COX-2-luc and pCMV- $\beta$ -gal plasmids with LysoPC (40  $\mu$ M) for the indicated time intervals (black bars;  $n=5$ ). **c** HCFs were pretreated with celecoxib (10  $\mu$ M)

for 1 h and then incubated with or without LysoPC (40  $\mu$ M) for 48 h. The conditioned media were analyzed by cytokine antibody arrays. (1) IL-1 $\alpha$ , (2) IL-1 $\beta$ , (3) IL-6, (4) TGF- $\beta$ , (5) TNF- $\alpha$ , (6) TNF- $\beta$ . **d** HCFs were incubated with LysoPC for the indicated time intervals in the absence or presence of celecoxib (10  $\mu$ M). The levels of IL-6 and GAPDH mRNA expression were determined by RT/qPCR ( $n=6$ ). Data are presented with mean  $\pm$  SEM, and analyzed by one-way ANOVA with Tukey's post hoc tests. \* $p<0.05$ ; # $p<0.01$

of JNK1/2 (SP600125) which attenuated LysoPC-induced COX-2 expression in a concentration-dependent manner (Supplementary Fig. 2A). We further examined whether NOX/ROS played a role in LysoPC-mediated JNK1/2 activation. The results showed that pretreatment with either

DPI or SP600125 attenuated JNK1/2 phosphorylation stimulated by LysoPC (Fig. 2f; Supplementary Fig. 2B and C), suggesting that LysoPC-induced COX-2 expression is mediated via activation of NOX/ROS-dependent JNK1/2 pathway in HCFs.

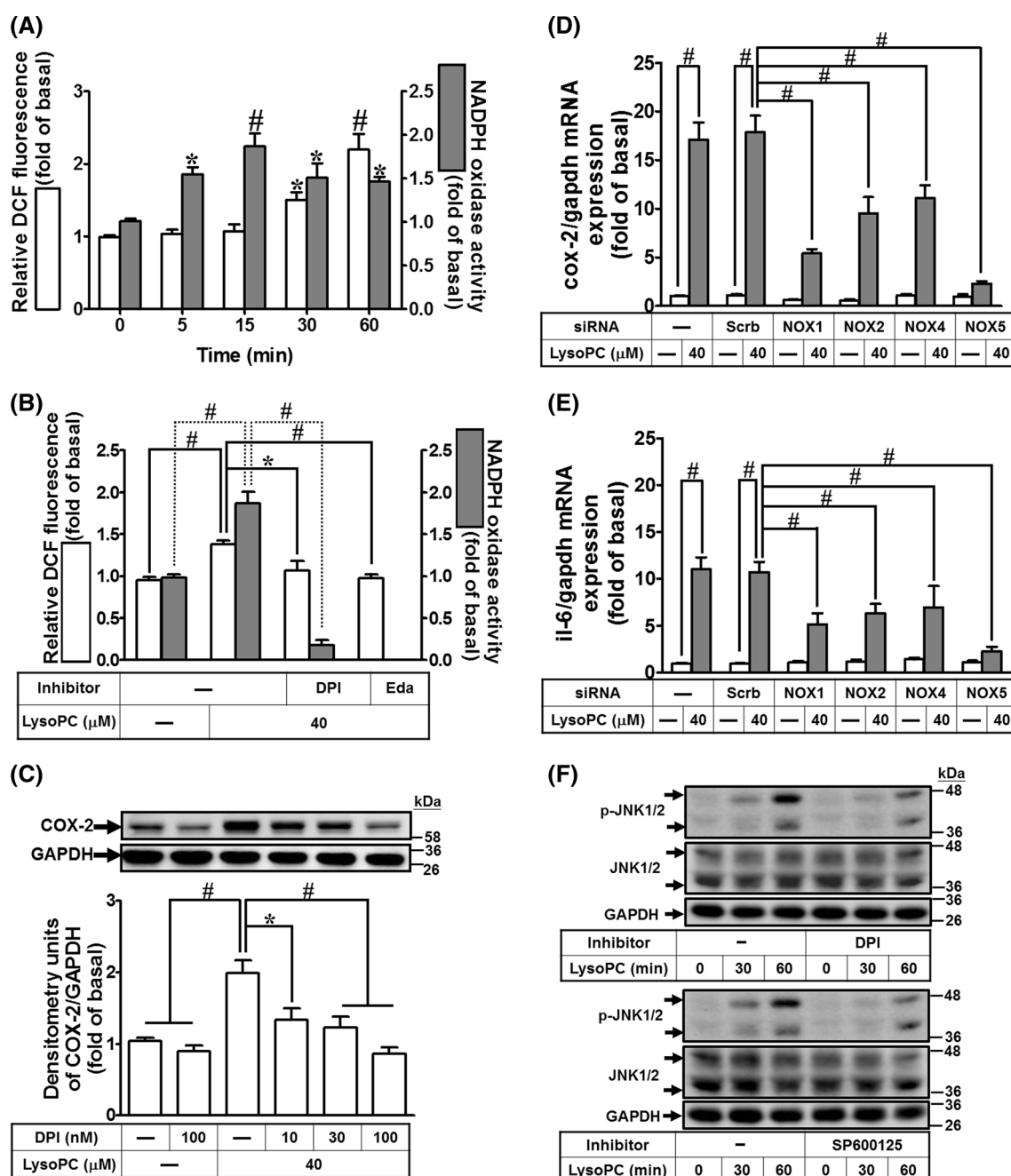


**Fig. 2** NADPH oxidase/ROS are involved in LysoPC-induced COX-2 and IL-6 expression. **a** HCFs were treated with LysoPC (40  $\mu$ M) for the indicated time intervals. The generation of ROS and activity of NADPH oxidase were determined using a CM-H<sub>2</sub>DCFDA probe (open bars;  $n=10$ ) and lucigenin chemiluminescence analysis (black bars;  $n=10$ ), respectively. **b** HCFs were pretreated with either DPI (100 nM) or edaravone (Eda; 100 nM) for 1 h and then incubated with LysoPC for 30 min. The cell lysates were subjected to determine the ROS generation (open bars;  $n=5$ ) and NADPH oxidase activity (black bars;  $n=7$ ). **c** HCFs were pretreated with DPI for 1 h and then incubated with LysoPC for 6 h. The levels of COX-2

and GAPDH protein were determined by western blot ( $n=6$ ). **d**, **e** HCFs were transfected with siRNA of scramble, NOX1, NOX2, NOX4, or NOX5 and then incubated with LysoPC for 6 h. The levels of COX-2, IL-6, and GAPDH mRNA were determined by RT/qPCR (**d**,  $n=5$ ; **e**,  $n=5$ ). **f** HCFs were pretreated with either DPI (100 nM) or SP600125 (1  $\mu$ M) for 1 h and then treated with LysoPC for the indicated time intervals. The levels of JNK1/2, phospho-JNK1/2, and GAPDH protein were determined by western blot ( $n=5$ ). The densitometry measurements are presented in Supplementary Fig. 2B and C. Data are presented with mean  $\pm$  SEM and analyzed by one-way ANOVA with Tukey's post hoc tests. \* $p < 0.05$ ; # $p < 0.01$

### NF- $\kappa$ B is involved in LysoPC-mediated COX-2 and IL-6 expression

Previous studies have demonstrated that activation of NF- $\kappa$ B leads to expression of pro-inflammatory cytokines and COX-2 induced by LysoPC [23, 38]. To investigate the role of NF- $\kappa$ B in LysoPC-mediated COX-2 expression, the HCFs were transfected with p65 siRNA, which knocked down p65 protein and attenuated LysoPC-induced COX-2 protein and mRNA expression (Fig. 3a, b). In addition, LysoPC-stimulated p65 phosphorylation, with a maximal response at 60 min, was reduced after p65 siRNA transfection (Fig. 3c; Supplementary Fig. 3A). While investigating NOX/ROS-mediated p65 activation, our data indicated that LysoPC-stimulated p65 phosphorylation was attenuated by DPI, SP600125, or helenalin (an inhibitor of NF- $\kappa$ B) (Fig. 3d; Supplementary Fig. 3B–D), suggesting that LysoPC-induced COX-2 expression is mediated via NOX/ROS-JNK1/2-dependent NF- $\kappa$ B p65 activation in HCFs.

COX-2 contains two NF- $\kappa$ B binding elements in its promoter regions, specifically at –449 to –437 and –225 to –214 [39]. Thus, we determined which NF- $\kappa$ B binding elements of the COX-2 promoter was manipulated by LysoPC, which led to COX-2 expression. The results of ChIP revealed that the binding activity of p65 was increased after flanking of proximal NF- $\kappa$ B elements using an anti-p65 or anti-phospho-p65 antibody (Supplementary Fig. 4B and C). Moreover, we investigated the interaction between activated NF- $\kappa$ B and COX-2 promoter stimulated by LysoPC via NOX/ROS pathways. Our results showed that LysoPC-stimulated binding of p65 to the proximal NF- $\kappa$ B-binding element on COX-2 promoters was attenuated by either DPI or helenalin (Fig. 3e). These results suggested that NOX/ROS-stimulated phosphorylated p65 binds to a proximal NF- $\kappa$ B-binding element, leading to COX-2 expression in HCFs. While determining whether LysoPC-activated p65 affected IL-6 expression in HCFs, we found that transfection with p65 siRNA knocked down p65 protein expression and markedly suppressed LysoPC-induced IL-6 gene expression (Fig. 3f). Together, these results suggested that LysoPC-primed NOX/ROS signaling regulates NF- $\kappa$ B activation, leading to COX-2-dependent IL-6 expression in HCFs.

### FoxO1 is involved in LysoPC-mediated COX-2 and IL-6 expression

While determining the role of FoxO1 in the LysoPC-induced COX-2 expression, we found that knockdown of FoxO1 protein after transfection with FoxO1 siRNA reduced LysoPC-induced COX-2 protein and mRNA expression in HCFs (Fig. 4a, b). Next, we determined whether FoxO1 bound to COX-2 promoter in HCFs treated with LysoPC. ChIP analysis showed that LysoPC stimulated the binding of FoxO1 to the

COX-2 promoter in a time-dependent manner, with a maximal response within 30–60 min (Fig. 4c). Furthermore, transfection with FoxO1 siRNA attenuated the LysoPC-induced IL-6 mRNA expression (Fig. 4d). These results suggested that LysoPC-mediated FoxO1-dependent COX-2 induction leads to IL-6 expression in HCFs.

### LysoPC-mediated phosphorylation of FoxO1 at Ser<sup>256</sup> enhances nuclear localization and binding activity with COX-2 promoter

Phosphorylation at Ser<sup>256</sup> of human FoxO1 results in differential transcriptional activities [40], including, increase in transcriptional activity of nuclear FoxO1, leading to expression of pro-inflammatory genes [31, 32, 41]. While investigating whether LysoPC stimulated phosphorylation at Ser<sup>256</sup> of FoxO1, the immunofluorescence images showed that LysoPC induced FoxO1 phosphorylation at Ser<sup>256</sup> residue and its nuclear accumulation (Fig. 5a). The nuclear accumulation of phosphorylated FoxO1<sup>S256</sup> was also confirmed by western blot (Fig. 5b), and was attenuated after transfection with FoxO1 siRNA (Fig. 5c; Supplementary Fig. 5A). Indeed, nuclear accumulation of FoxO1 increases transcriptional activity in response to oxidative stresses [42]. Thus, we investigated whether LysoPC-stimulated phosphorylation of FoxO1<sup>S256</sup> was mediated through NOX/ROS signaling. LysoPC-stimulated phosphorylation of FoxO1<sup>S256</sup> was attenuated by DPI, SP600125, or AS1842856 (an inhibitor of FoxO1) (Fig. 5d; Supplementary Fig. 5B–D). To further validate the binding between JNK1/2 and FoxO1, the cell lysates were immunoprecipitated with an anti-FoxO1 antibody after LysoPC stimulation and then analyzed by western blot using an antibody as indicated. The results showed that the levels of JNK1/2 and phosphorylation of FoxO1<sup>S256</sup> were increased after treatment with LysoPC within 30–60 min (Fig. 5e), suggesting that phosphorylation of FoxO1 is regulated by a NOX/ROS-JNK1/2 pathway. Moreover, we investigated whether phosphorylation of FoxO1<sup>S256</sup> was associated with LysoPC-induced COX-2 gene expression. The interaction between FoxO1 and COX-2 promoter was determined by a ChIP analysis. As shown in Fig. 5f, LysoPC-induced phosphorylation of FoxO1<sup>S256</sup> enhanced the binding activity of FoxO1 with COX-2 promoter, which was attenuated by either DPI or AS1842856. These results suggested that LysoPC-stimulated phosphorylated FoxO1<sup>S256</sup> interacts with COX-2 promoter, contributing to increase in the transcriptional activity via NOX/ROS-JNK1/2 pathways in HCFs.

### FoxO1 coordinates with NF- $\kappa$ B in regulating COX-2 promoter activity

While investigating the association of FoxO1 with p65 in response to LysoPC in HCFs, the results of



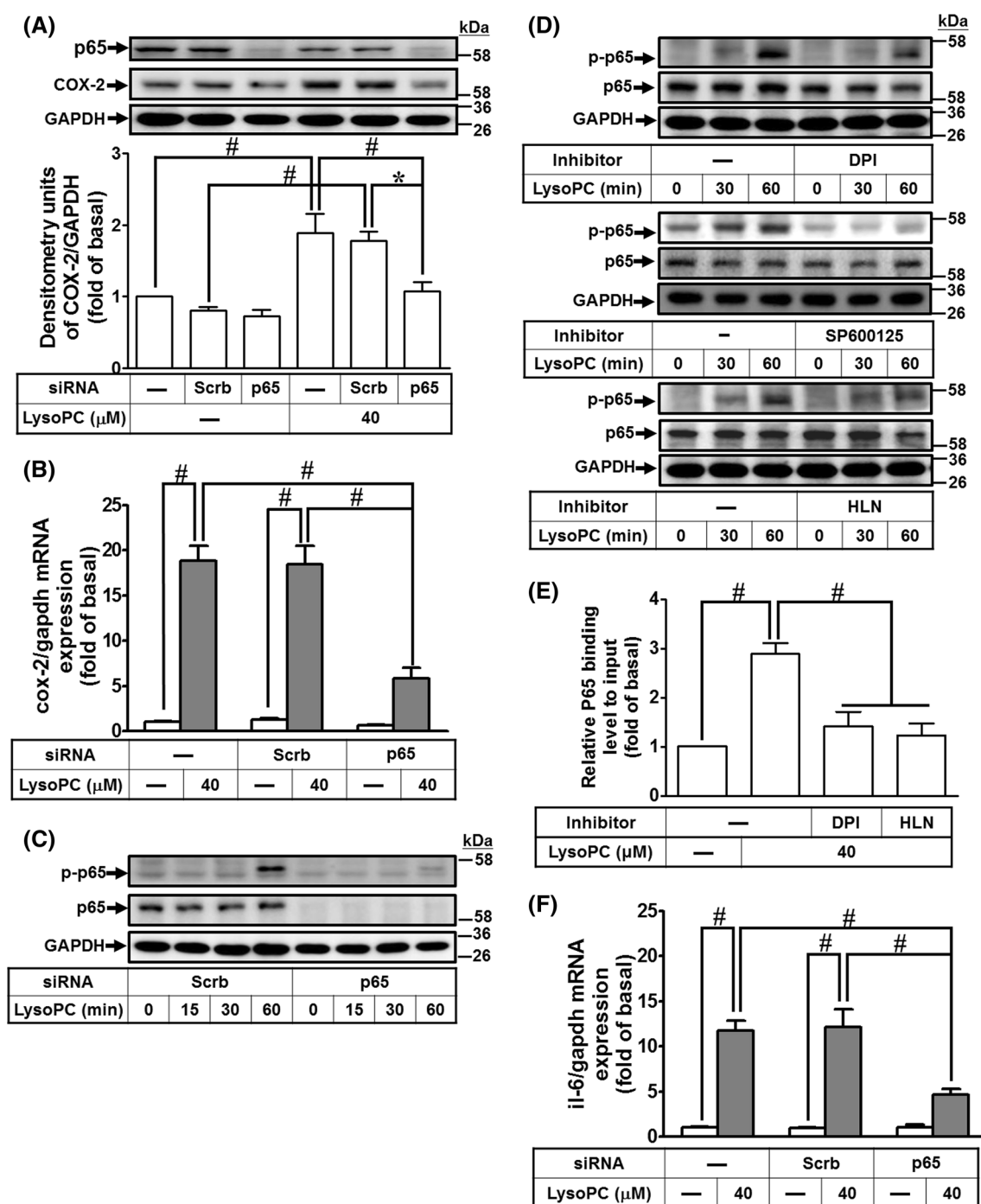


**Fig. 3** NF- $\kappa$ B is involved in LysoPC-induced COX-2 and IL-6 expression. **a, b** HCFs were transfected with siRNA of scramble or p65 and then treated with LysoPC for 6 h. **a** The levels of p65, COX-2, and GAPDH protein were determined by western blot ( $n=6$ ). **b** The levels of COX-2 and GAPDH mRNA were determined by RT/qPCR ( $n=6$ ). **c** HCFs were transfected with siRNA of scramble or p65, and then treated with LysoPC for the indicated time intervals. The levels of p65, phospho-p65, and GAPDH protein were determined by western blot ( $n=6$ ). The densitometry measurements of phospho-p65 are presented in Supplementary Fig. 3A. **d** HCFs were pretreated with DPI (100 nM;  $n=7$ ), SP600125 (1  $\mu$ M;  $n=5$ ), or helenalin (HLN, 1  $\mu$ M;  $n=7$ ) for 1 h, and then treated with LysoPC for the indicated time interval. The levels of p65, phospho-p65, and

GAPDH protein were determined by western blot. The densitometry measurements of phospho-p65 are presented in Supplementary Fig. 3B–D. **e** HCFs were pretreated with DPI (100 nM) or helenalin (1  $\mu$ M) for 1 h, and then incubated with LysoPC for 1 h. The DNA binding activity of NF- $\kappa$ B was determined by a ChIP assay. Quantification of p65 immunoprecipitated DNA was performed by an SYBR system for qPCR, and the results are shown as the fold change normalized to input control ( $n=4$ ). **f** HCFs were transfected with siRNA of scramble or p65, and then treated with LysoPC for 6 h. The levels of IL-6 and GAPDH mRNA were determined by RT/qPCR ( $n=6$ ). Data are presented as mean  $\pm$  SEM, and analyzed by one-way ANOVA with Tukey's post hoc tests. \* $p < 0.05$ ; # $p < 0.01$

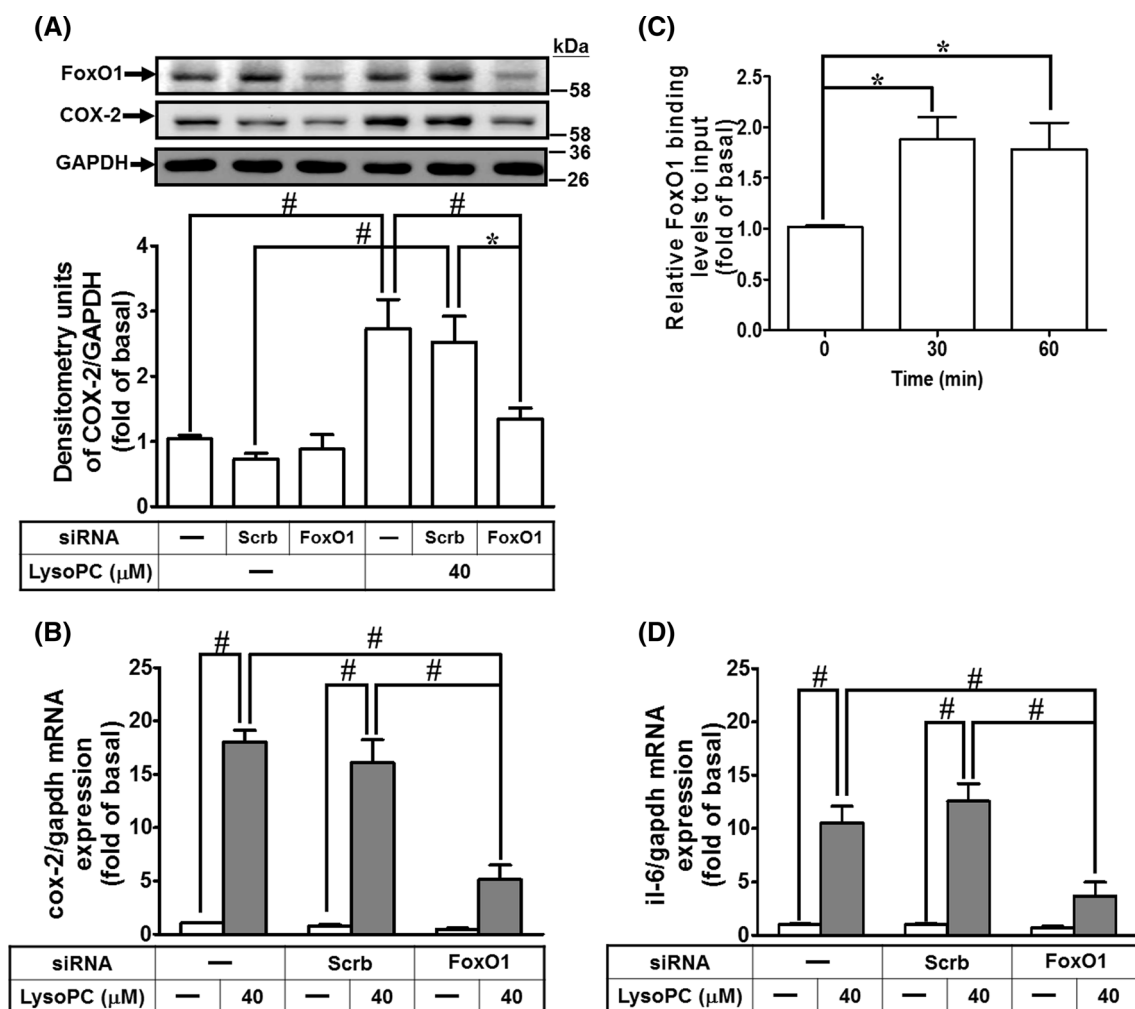


**Fig. 4** FoxO1 is involved in LysoPC-mediated COX-2 expression and IL-6 expression. **a**, **b** HCFs were transfected with siRNA of scramble or FoxO1 and then treated with LysoPC for 6 h. **a** The levels of COX-2, FoxO1 and GAPDH protein were determined by western blot ( $n=6$ ). **b** The levels of COX-2 and GAPDH mRNA expression were determined by RT/qPCR ( $n=7$ ). **c** HCFs were treated with LysoPC for the indicated time intervals. DNA binding activity of FoxO1 was

determined by a ChIP assay. Quantification of data was performed by an SYBR system for qPCR, and the results are shown as the fold change normalized to input control ( $n=5$ ). **d** HCFs were transfected with siRNA of scramble or FoxO1 and then treated with LysoPC for 6 h. The levels of IL-6 and GAPDH mRNA were determined by RT/qPCR ( $n=6$ ). Data are presented as mean  $\pm$  SEM, and analyzed by one-way ANOVA with Tukey's post hoc tests. \* $p < 0.05$ ; # $p < 0.01$

co-immunoprecipitation showed that LysoPC enhanced p65 translocation and its interaction with FoxO1 (Fig. 6a). Similarly, the nuclear FoxO1 enhanced p65 activity upon LysoPC stimulation in a time-dependent manner (Fig. 6b). Next, we examined whether activation of FoxO1 enhanced p65 binding to COX-2 promoters. The ChIP results showed that knockdown of either FoxO1 or p65 expression by FoxO1 or p65 siRNA, respectively (Fig. 6c), attenuated immunoprecipitated DNA with an anti-p65 or anti-phospho-FoxO1<sup>S256</sup> antibody (Fig. 6d). These findings suggested that LysoPC-induced FoxO1 interacts with p65 and coordinately enhances its binding to COX-2 promoters, leading to COX-2 gene expression in HCFs.

### Overexpression of wild-type or S256D FoxO1 enhances COX-2 promoter activity

To corroborate our findings above, we explored the effects of overexpression of FoxO1 on COX-2 expression. Exposure of HCFs to LysoPC induced approximately 2.3-fold increase in the COX-2 promoter activity (Fig. 7a). Co-transfection of pCMV Tag-2B FoxO1 (wild-type) further increased the COX-2 promoter activity by approximately 2.7-fold as compared to that of empty vector alone (Fig. 7a). The ChIP results showed that overexpression of FoxO1 or treatment with LysoPC significantly increased the binding activity of FoxO1 on COX-2 promoters (Fig. 7b). FoxO1 is also

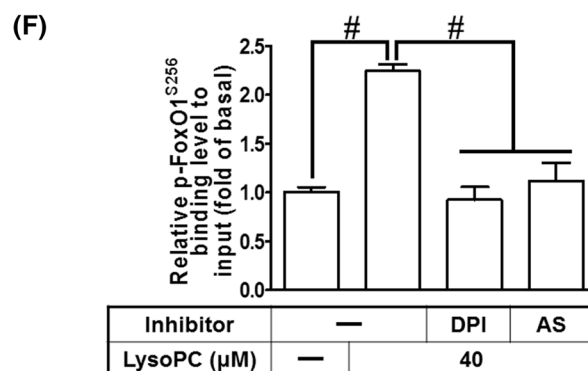
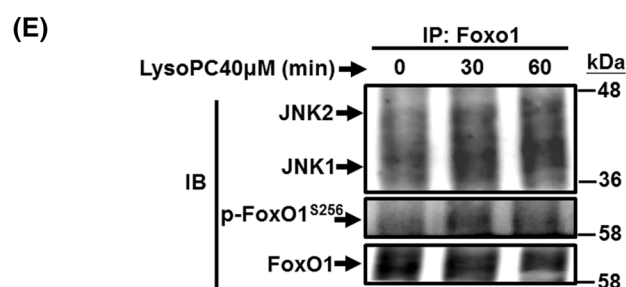
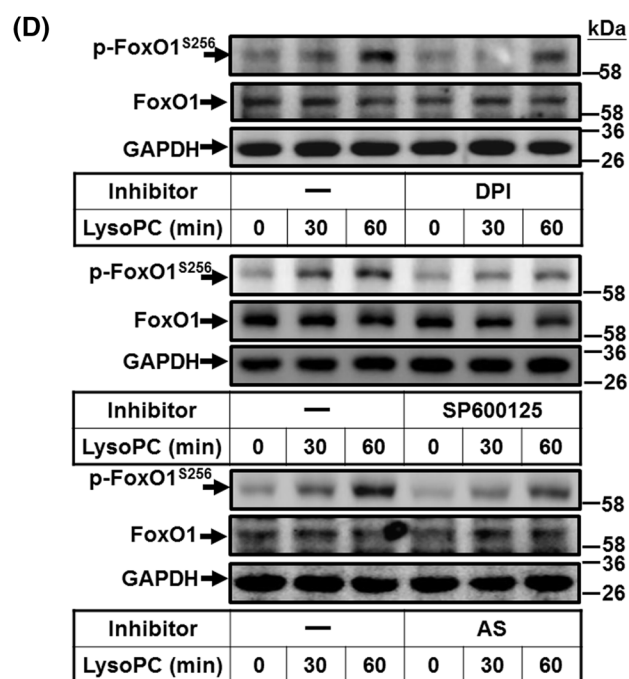
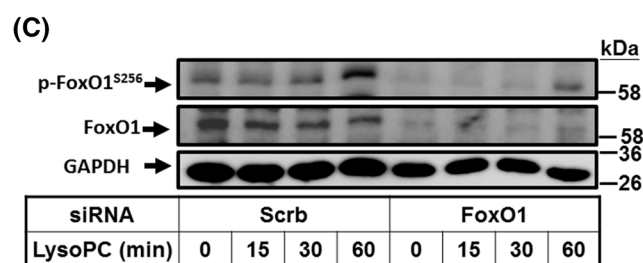
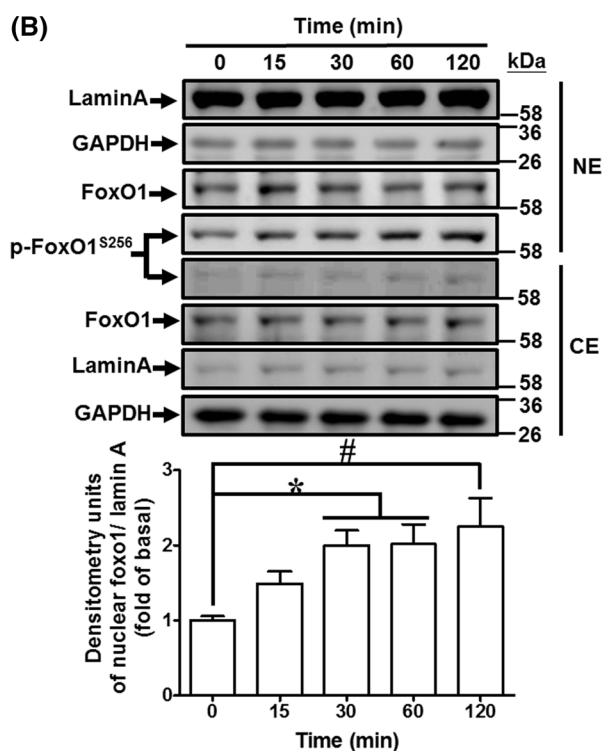
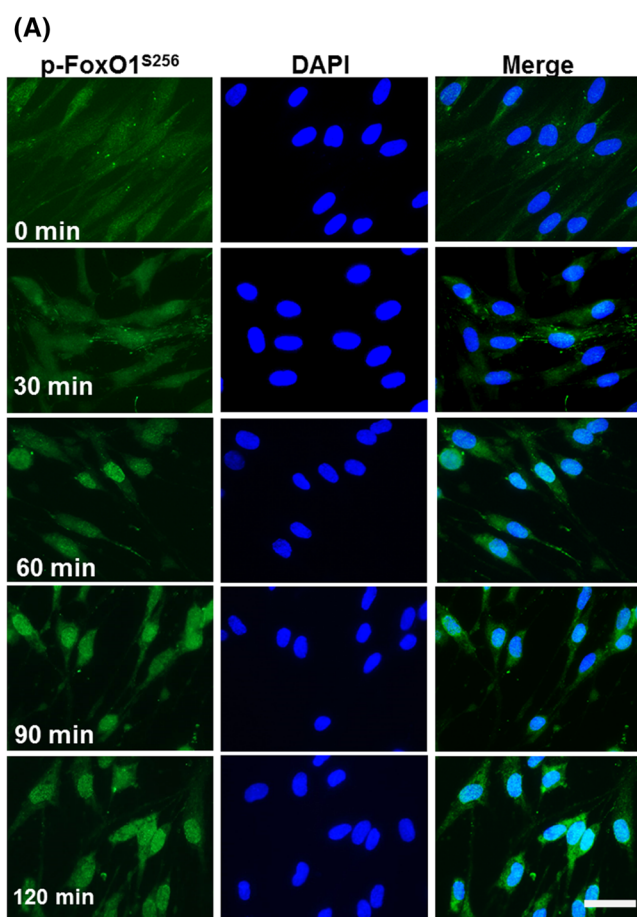


**Fig. 5** LysoPC-mediated phosphorylation at Ser256 of FoxO1 increases nuclear localization and DNA binding activity on COX-2 promoter. **a, b** HCFs were incubated with LysoPC (40  $\mu$ M) for the indicated time points. **a** Immunofluorescence staining was performed with an anti-phospho-FoxO1<sup>S256</sup> antibody, labeled with FITC (green) and DAPI (blue), and observed by using a fluorescence microscope (scale bar, 100  $\mu$ m). **b** The cytosolic and nuclear fractions were prepared and subjected to western blot analysis. Lamin A and GAPDH were used as a marker protein for the nuclear and cytosolic fractions, respectively. Quantification data of nuclear phospho-FoxO1<sup>S256</sup> data is presented in the bottom panel ( $n=6$ ). **c** HCFs were transfected with siRNA of scramble or FoxO1 and then treated with LysoPC for the indicated time intervals. The levels of FoxO1, phospho-FoxO1<sup>S256</sup>, and GAPDH protein were determined by western blot ( $n=7$ ). The densitometry measurements of phospho-FoxO1<sup>S256</sup> are presented in Supplementary Fig. 5A. **d** HCFs were pretreated with DPI (100 nM;  $n=7$ ), SP600125 (1  $\mu$ M;  $n=5$ ), or AS1842856 (AS, 100 nM;  $n=7$ ) for 1 h, and then treated with LysoPC for the indicated time intervals. The levels of phospho-FoxO1<sup>S256</sup>, FoxO1, and GAPDH protein were determined by western blot. The densitometry measurements of phospho-FoxO1<sup>S256</sup> are presented in Supplementary Fig. 5B–D. **e** HCFs were treated with LysoPC for the indicated time intervals and subjected to immunoprecipitation assay using an anti-FoxO1 antibody. The immunoprecipitates were analyzed by western blot using an anti-JNK1/2, anti-phospho-FoxO1<sup>S256</sup>, or anti-FoxO1 (as an internal control) antibody. Data are representative of three independent experiments ( $n=3$ ). **f** HCFs were pretreated with DPI (100 nM) or AS1842856 (100 nM) for 1 h and then incubated with LysoPC for 1 h. The DNA binding activity of phospho-FoxO1<sup>S256</sup> was determined by a ChIP assay. Quantification of data was performed by an SYBR system for qPCR, and the results are shown as the fold change normalized to input control ( $n=5$ ). Data are presented as mean  $\pm$  SEM, and analyzed by one-way ANOVA with Tukey's post hoc tests. \* $p<0.05$ ; # $p<0.01$ . NE nuclear extract, CE cytosolic extract

phosphorylated by Akt at Tyr<sup>24</sup>, Ser<sup>256</sup>, or Ser<sup>319</sup>, while post-transcriptional modification independently regulates FoxO1 transcriptional activity [27, 40, 43]. To directly assess the impact of FoxO1 phosphorylation on COX-2 expression, we modified the Flag-tagged FoxO1 to encode phospho-silencing mutants (S256A and S319A FoxO1) and phospho-mimic mutants (S256D and S319D FoxO1). Overexpression of wild-type FoxO1 and S256D FoxO1 was associated with a 1.6- and 1.7-fold increase in COX-2 expression, respectively (Fig. 7c). The levels of chimeric Flag-FoxO1 were expressed as the levels of mRNA, determined by RT/PCR analysis. However, overexpression of S256D FoxO1 significantly enhanced COX-2 expression as compared with that of S256A FoxO1. In contrast, neither S319A nor S319D FoxO1 mutant affected COX-2 expression. Immunoprecipitation of Flag was used to determine the DNA binding activity of FoxO1 mutants on COX-2 promoter. Consistently, ChIP analysis demonstrated that the interaction of FoxO1 with the COX-2 promoter was enhanced in HCFs overexpressing either wild-type FoxO1 or S256D FoxO1 (Fig. 7d). These results suggested that phosphorylation at Ser<sup>256</sup> residue of FoxO1 is sufficient to upregulate COX-2 gene expression in HCFs.

## LysoPC induces COX-2 and IL-6 expression in ex vivo mouse heart tissue

We investigated whether LysoPC induced COX-2 expression in ex vivo mouse heart tissues. LysoPC-induced COX-2 protein and mRNA expressions were reduced by DPI, helenalin, or AS1842856 (Fig. 8a, b). Moreover, our results demonstrated that LysoPC-induced IL-6 expression was inhibited by DPI, helenalin, AS1842856, or celecoxib, as determined by RT/qPCR analysis (Fig. 8c). These results suggested that induction of COX-2 by LysoPC is associated with IL-6 expression in ex vivo mouse heart tissues and is mediated through NOX/ROS, FoxO1, and NF- $\kappa$ B in the heart.

## Discussion

LysoPC induced COX-2-dependent IL-6 expression in HCFs, which may be associated with pro-fibrotic responses. Our findings showed that LysoPC-induced COX-2-dependent IL-6 expression is mediated through NOX/ROS/JNK1/2 leading to FoxO1<sup>S256</sup> and NF- $\kappa$ B activation (Fig. 8d). These results were confirmed by ex vivo studies, indicating the involvement of NOX, NF- $\kappa$ B, or FoxO1 in LysoPC-mediated responses. We found that nuclear accumulation of phospho-FoxO1<sup>S256</sup> was significantly increased and it was bound to the COX-2 promoter. In contrast with previous reports, the phosphorylation of FoxO1 at Ser256 strongly promoted nuclear exclusion [43]. Moreover, overexpression of S256D FoxO1, but not of S256A FoxO1, promoted DNA binding activity and turned on COX-2 expression in HCFs. These data suggested that interaction between FoxO1 and p65 may coordinately regulate COX-2 gene expression in HCFs. Our findings provided new insights into the mechanisms underlying LysoPC-induced COX-2-dependent IL-6 expression through phosphorylated p65 and FoxO1<sup>S256</sup>-mediated transcriptional activation in HCFs.

Induction of COX-2 could enhance macrophage infiltration and fibroblast activation during myocardial infarction in patients and experimental animals [21, 22]. COX-2 catalyzes the conversion of arachidonic acid into PGs, which activate their specific receptors. For example, PGE<sub>2</sub> enhances IL-6 production through EP1, EP2, or EP4 in various cell types [44, 45]. Our previous study also demonstrated that S1P induces COX-2 expression associated with PGE<sub>2</sub>/IL-6 production in human tracheal smooth muscle cells [25, 35]. In this study, we found that inhibition of COX-2 activity attenuated LysoPC-induced IL-6 expression in HCFs and ex vivo mouse heart tissues. IL-6 has been shown to either enhance collagen synthesis leading to cardiac fibrosis via activation of CFs [13] or induce TGF- $\beta$  expression leading to tissue remodeling via TGF- $\beta$ /smad3 activation [12, 14]. Therefore, we speculated that activation of the COX-2/



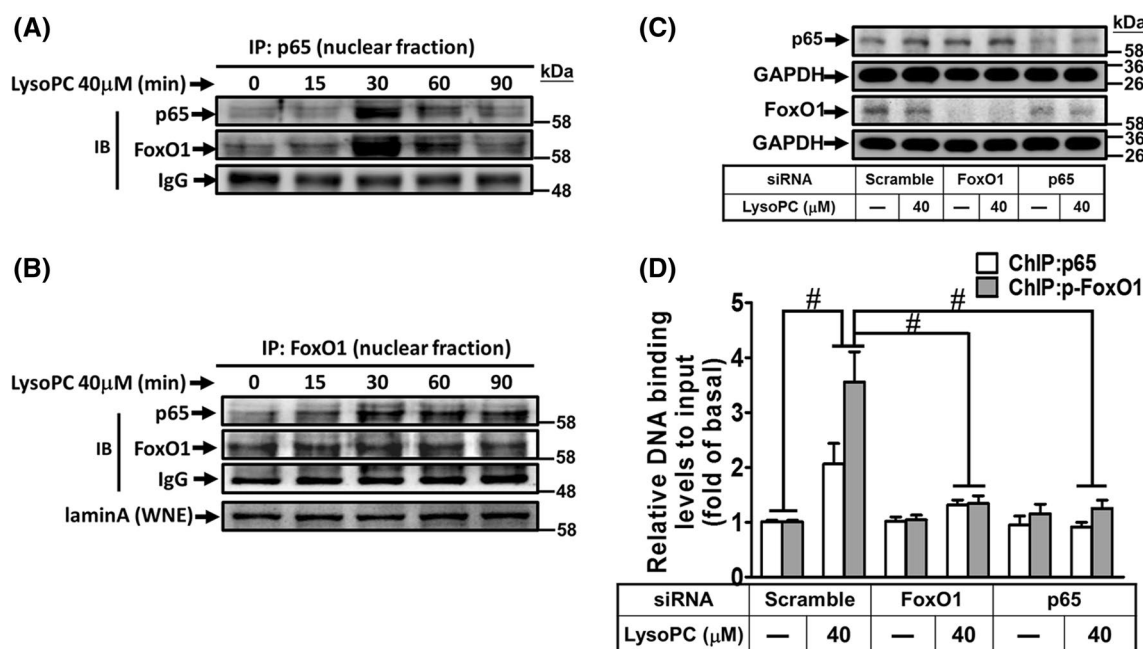


**Fig. 6** FoxO1 coordinates with NF- $\kappa$ B in regulating COX-2 promoter activity. **a, b** HCFs were treated with LysoPC for the indicated time intervals, and then the nuclear fraction was prepared. Nuclear fractions were subjected to immunoprecipitation assay using the indicated antibodies. Immunoprecipitates were analyzed by western blot using an anti-p65, anti-FoxO1, or anti-laminA (as an internal control) antibody. *IP* immunoprecipitation, *IB* immunoblotting, *WNE* whole nuclear extract. Data are representative of three independent experi-

ments. **c, d** HCFs were transfected with siRNA of scramble, FoxO1, or p65 and then treated with LysoPC for 1 h. The cells lysates were subjected to western blot analysis (**c**) and a ChIP analysis (**d**). The DNA binding activity of FoxO1 and NF- $\kappa$ B was determined by a ChIP assay, using an anti-phospho-FoxO1<sup>S256</sup> or anti-p65 antibody. Quantification of data is shown as fold change after normalizing to input control ( $n=5$ ). Data are presented as mean  $\pm$  SEM and analyzed by one-way ANOVA with Tukey's post hoc tests. \* $p < 0.05$ ; # $p < 0.01$

PG axis promotes IL-6 production and further triggers profibrotic responses in CFs, which is an important issue to be considered for future studies.

LysoPC stimulates NOX-derived ROS generation in various types of cells [15, 16]. Consistent with these findings, LysoPC stimulated NOX activation and increased ROS generation in HCFs. ROS are believed to activate various signaling molecules, leading to COX-2 expression [20, 25]. Our findings confirmed that LysoPC-induced COX-2 expression was dependent on NOX/ROS generation. NOX1, 2, 4, and 5 were involved in LysoPC-mediated responses as confirmed after transfection of cells with their respective siRNAs. In mouse heart, knockout of either NOX2 or NOX4 reduces ROS production, hypertrophy, interstitial fibrosis, and apoptosis [18, 19]. Moreover, JNK1/2 can be activated by ROS signaling [46]. Our results supported the NOX-derived ROS generation mediated JNK1/2 activation, contributing to LysoPC-induced COX-2 expression in HCFs.

NF- $\kappa$ B is a key player in the regulation of COX-2 transcription [39]. LysoPC has been shown to mediate phosphorylation and degradation of I $\kappa$ B, resulting in the nuclear translocation of NF- $\kappa$ B p65 in endothelial cells [38]. LysoPC-activated NF- $\kappa$ B is also involved in the expression of endothelial adhesion molecules and COX-2 expression

[5, 23]. Consistent with these findings, our results supported that LysoPC-induced COX-2 and IL-6 expressions were mediated through NF- $\kappa$ B activation.  $\kappa$ B sites are highly conserved among species [39]. The human COX-2 promoter contains two NF- $\kappa$ B binding elements, which are different from those of rodents [39]. The rodent COX-2 promoter lacks the proximal NF- $\kappa$ B binding element, whereas the proximal NF- $\kappa$ B-binding element of the human COX-2 promoter is a major regulatory element, contributing to COX-2 promoter activation upon treatment with LysoPC in HCFs. Nguyen et al. mentioned that the COX-2 promoter is differentially regulated between mice and humans [39]. We found that LysoPC regulated COX-2-dependent IL-6 expression via the proximal NF- $\kappa$ B-binding element in the COX-2 promoter. Redox signaling has been shown to activate NF- $\kappa$ B through various signaling pathways and thereby enhance the expression of its targeted proteins [5]. Our previous results demonstrated that ATP $\gamma$ S-induced COX-2 expression is mediated via NOX/ROS generation-dependent NF- $\kappa$ B activation in human pulmonary alveolar epithelial cells [20]. Here, we demonstrated that activated p65 interacted with the COX-2 promoter and initiated its gene transcription, which was inhibited by DPI, or helenalin in HCFs. In addition, increase in NF- $\kappa$ B activity is mediated

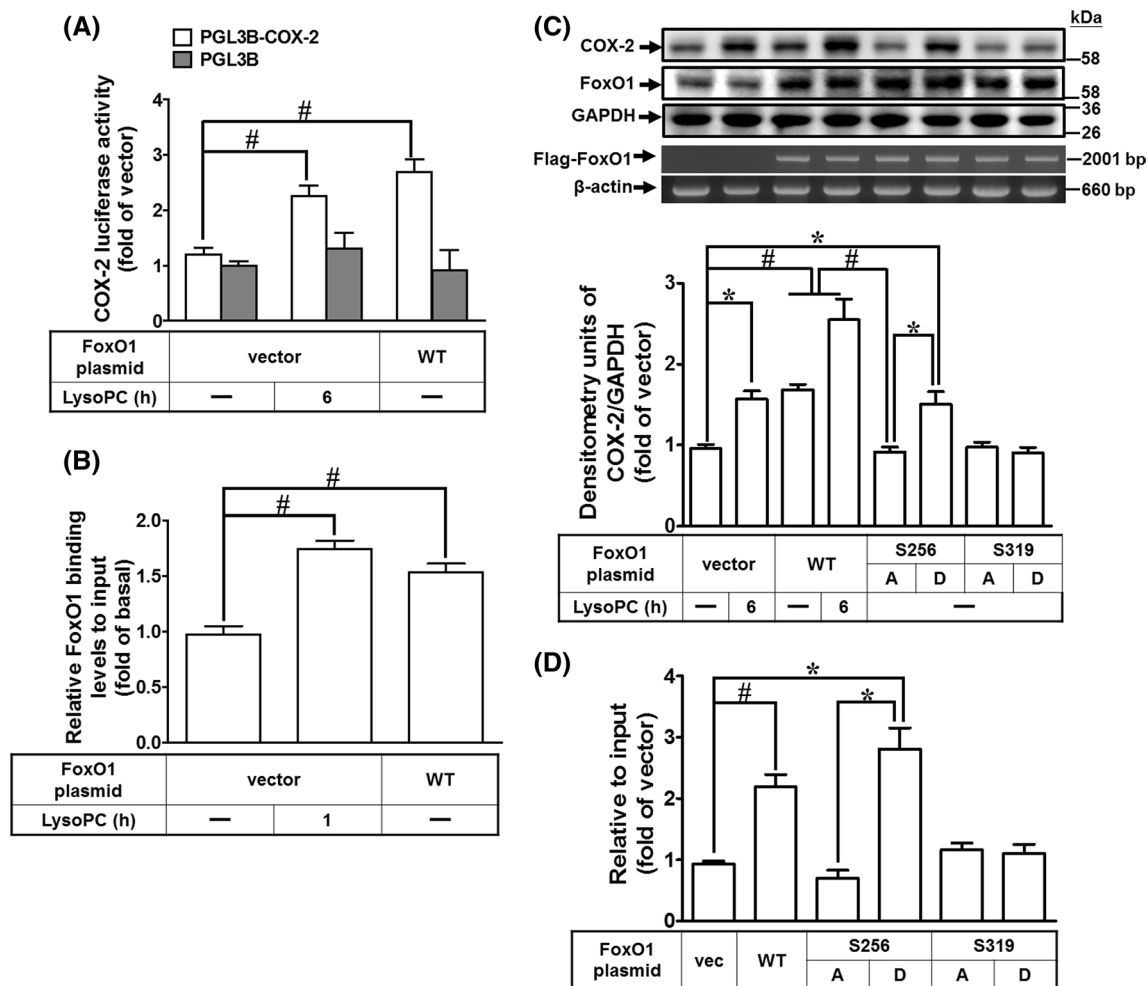


**Fig. 7** Overexpression of wild-type FoxO1 and S256D FoxO1 enhances DNA binding activity on COX-2 promoter. **a** HCFs were co-transfected with pGL3b, pGL3b-cox-2-luc, pCMV- $\beta$ -gal, pCMV-Tag2B, or pCMV-Tag2B-FoxO1 (WT) plasmid for 48 h and treated with LysoPC (40  $\mu$ M) for 6 h. The luciferase activity was determined and normalized to the respective  $\beta$ -gal activity ( $n=4$ ). **b** HCFs were transfected with pCMV-Tag2B or pCMV-Tag2B-FoxO1 (WT) for 48 h and then treated with LysoPC (40  $\mu$ M) for 1 h. Quantification of data were determined by an SYBR system for qPCR, and the results are shown as the fold change normalized to input control ( $n=5$ ). **c, d** HCFs were transfected with pCMV-Tag2B-FoxO1, S256A

FoxO1, S256D FoxO1, S319A FoxO1 or S319D FoxO1 for 48 h and then treated with LysoPC (40  $\mu$ M) for 6 h. **c** The levels of COX-2, FoxO1 and GAPDH protein were analyzed by western blot. Expressions of chimeric Flag-FoxO1 and  $\beta$ -actin were determined by RT/PCR. Quantification of data is shown in the bottom panel ( $n=7$ ). **d** DNA binding activity of FoxO1 constructs on COX-2 promoter was determined by a ChIP assay using an anti-Flag M2 antibody and analyzed by an SYBR system for qPCR ( $n=7$ ). Data are presented as mean  $\pm$  SEM and analyzed by one-way ANOVA with Tukey's post hoc tests. \* $p<0.05$ ; # $p<0.01$

via JNK1/2-dependent phosphorylation at Ser<sup>176</sup> of IKK $\alpha$ , contributing to I $\kappa$ B degradation and subsequent NF- $\kappa$ B activation [47]. Consistent with previous reports, inhibition of JNK1/2 by SP600125 attenuated LysoPC-stimulated p65 phosphorylation. Thus, we concluded that NOX-derived ROS resulted in an increase of NF- $\kappa$ B activity and upregulation of COX-2 and IL-6 gene expression via a NOX/ROS-JNK1/2-dependent pathway in HCFs.

FoxO1 is a multifunctional transcription factor [24, 25, 31, 32]. Knockdown of FoxO1 attenuates the IL-1 $\beta$ -induced COX-2 expression in primary human myometrial cells [24]. In contrast, IL-1 $\beta$ -induced COX-2 expression is not altered

by knockdown of either FoxO1 or FoxO3 in human chondrocytes [48]. However, regulation of FoxOs' downstream targets is highly cell lineage dependent in response to oxidative stress [49]. In this study, we found the involvement of FoxO1 in COX-2 expression by transfection of cells with FoxO1 siRNA. The interaction between FoxO1 and COX-2 promoter was confirmed using a ChIP assay, demonstrating that induction of COX-2 by LysoPC was mediated via an increase in the binding activity of FoxO1 on the COX-2 promoters. In particular, overexpression of FoxO1 enhanced either COX-2 promoter activity or FoxO1 DNA association. We found that the FoxO1 binding element of the COX-2 promoter was

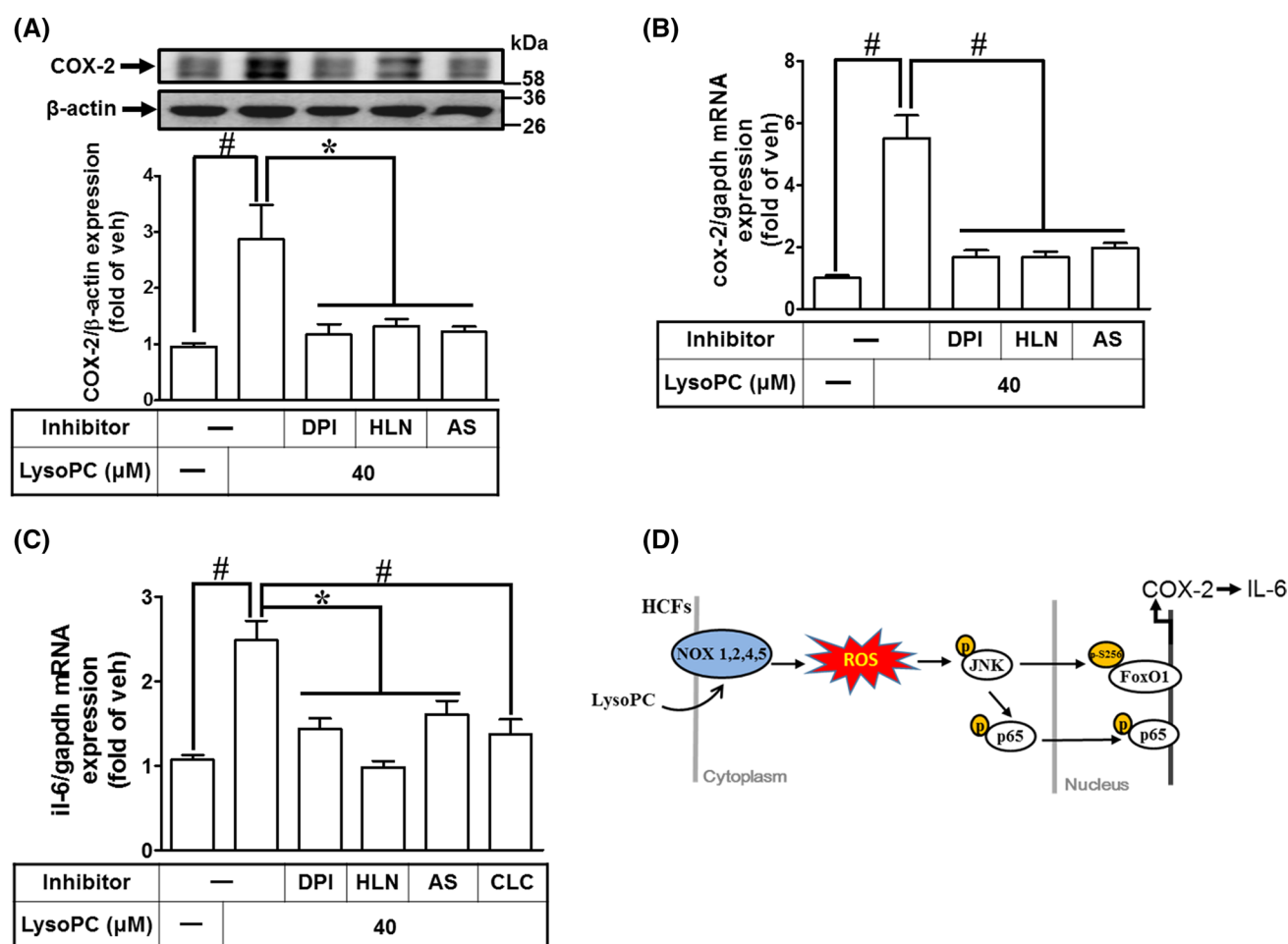


**Fig. 8** LysoPC induces COX-2 and IL-6 expression in ex vivo mouse heart tissue. **a–c** Mouse heart segments were pretreated with DPI (100 nM), AS1842856 (100 nM), helenalin (1  $\mu$ M), or celecoxib (10  $\mu$ M) for 1 h and then exposed to LysoPC (40  $\mu$ M) for 6 h while in Krebs solution bubbled with 95%  $O_2$  and 5%  $CO_2$  at 37  $^{\circ}C$ . The heart tissues were homogenized and subjected to western blot analysis or RT/qPCR to determine the levels of COX-2 protein (**a**;  $n=6$ ) and

mRNA (**b**;  $n=7$ ) or the levels of IL-6 mRNA (**c**;  $n=7$ ). **d** Schematic diagram illustrates that LysoPC activated FoxO1 and NF- $\kappa$ B mediated a COX-2-dependent IL-6 expression via NOX/ROS-JNK1/2-dependent pathway in HCFs. Data are presented as mean  $\pm$  SEM and analyzed by one-way ANOVA with Tukey's post hoc tests. \* $p < 0.05$ ; # $p < 0.01$

located between positions  $-299$  and  $+7$ . FoxO1 has been shown to be involved in IL-6 expression induced by IL-1 $\beta$ , LPS, and TNF- $\alpha$  [24, 31, 32]. In this study, knockdown of FoxO1 attenuated LysoPC-induced COX-2-dependent IL-6 expression in HCFs. These results suggested that FoxO1 is involved in LysoPC-induced COX-2-dependent IL-6 expression associated with cardiac inflammation.

On the basis of previous studies, cooperative regulation of inflammatory genes by NF- $\kappa$ B and FoxO1 is controversial. Several genes such as the IL-1 $\beta$  promoter contain both FoxO1 and NF- $\kappa$ B response elements [31, 50]. Fan et al. mentioned that NF- $\kappa$ B potentially interacted with FoxO1 because response motifs of NF- $\kappa$ B were significantly enriched across the FoxO1 cistrome [31]. For the chemotactic ligand CCL20, overexpression of FoxO1 increased the binding of the active NF- $\kappa$ B dimer, whereas FoxO1

silencing decreased NF- $\kappa$ B binding to its response element. Since FoxO1 does not directly bind to the CCL20 promoter, FoxO1 may serve as a coactivator of NF- $\kappa$ B in the nucleus to amplify NF- $\kappa$ B signaling [51]. Thus, in some cases such as IL-1 $\beta$ , FoxO1 binds to a response element nearby the NF- $\kappa$ B binding element to enhance transcription, whereas, in CCL20, FoxO1 is speculated to physically interact with NF- $\kappa$ B and enhance NF- $\kappa$ B-mediated CCL20 transcription. Our data revealed that FoxO1 can associate with nuclear p65, a component of NF- $\kappa$ B, and knockdown of FoxO1 attenuated p65 binding to the proximal NF- $\kappa$ B binding element of the COX-2 promoter in HCFs. We speculated that the spatial conformation of proximal NF- $\kappa$ B binding element is close to the FoxO1 binding element, inferring that p65 and FoxO1 coordinately regulated COX-2 gene expression in HCFs.

The transcriptional activity of FoxO1 is dependent on its phosphorylation status and subcellular localization. Akt-mediated FoxO1 activation has been shown to promote nuclear exclusion of FoxO1 and negatively regulate IRS-dependent gene expression in response to IGF signaling [43]. Therefore, nuclear accumulation of FoxO1 increases DNA binding activity and results in CCL20 induction in keratinocytes and mouse models [41]. Kinase-dead mutation of Akt blocks FoxO1 phosphorylation at Tyr<sup>24</sup>, Ser<sup>256</sup>, and Ser<sup>319</sup>, which restricts FoxO1 expression in the cytoplasm [27] and enhances the expression of pro-inflammatory genes including TNF- $\alpha$ , IL-1 $\beta$ , and IL-6 [31, 32]. Our novel findings indicated that LysoPC-stimulated FoxO1<sup>S256</sup> phosphorylation increased the nuclear accumulation of FoxO1 and its binding activity on COX-2 promoter. Previous reports have indicated that under oxidative stress, phosphorylated JNK1/2 accelerates FoxO1 nuclear localization, leading to its target gene expression [42]. Here, we demonstrated that blocking of NOXs and JNK1/2 activity attenuated LysoPC-stimulated phosphorylation of FoxO1<sup>S256</sup>. In addition, our data also demonstrated that overexpression of S256D FoxO1 enhanced COX-2 induction, whereas S256A, S319D, and S319A FoxO failed to alter COX-2 gene expression. These results suggested that phosphorylation of FoxO1 at Ser<sup>256</sup> is required for COX-2 expression in HCFs, leading to cardiac inflammation.

With respect to the limitations of the present study, we recognized the inhibition of COX-2 activity as a target may also incur side effects on the cardiovascular system. Increase in COX-2 activation leads to metabolism and production of various prostanoids by cell-dependent isomerases of different tissues, which may also be involved in pathological and physiological regulation. It is crucial to further investigate the modulation of these prostanoids and their receptors in response to LysoPC. Nevertheless, our results provide new insights into COX-2 gene expression, involving a synergistic regulation of FoxO1 and p65 in HCFs. In fact, our previous data demonstrated FoxO1 as a transcription repressor for COX-2 gene expression in human tracheal smooth muscle cells [25]. We suggest that FoxO1-mediated COX-2 regulation is a key mechanism and represents different patterns in various tissues exposed to different stimuli.

**Acknowledgements** We thank Ms. Yu-Wen Chen for her technical assistance. This work was supported by the Ministry of Education, Taiwan, Grant numbers: EMRPD1H032 and EMRPD1H055; the Ministry of Science and Technology, Taiwan, Grant numbers: MOST104-2320-B-182A-003-MY3, MOST105-2320-B-182-005-MY3, MOST107-2320-B-182A-011, and MOST107-2320-B-182-020-MY2; Chang Gung Medical Research Foundation, Taiwan, Grant numbers: CMRPD1F0022, CMRPD1F0023, CMRPD1F0551, CMRPD1F0552, CMRPG3E2232, CMRPG3F1532, CMRPG3F1533, CMRPG3H0061, and CMRPG5F0202.

## References

- Metra M, Teerlink JR (2017) Heart failure. *Lancet* 390:1981–1995
- Fan D, Takawale A, Lee J, Kassiri Z (2012) Cardiac fibroblasts, fibrosis and extracellular matrix remodeling in heart disease. *Fibrogenesis Tissue Repair* 5:15
- Sziksz E, Pap D, Lippai R, Beres NJ, Fekete A, Szabo AJ, Vannay A (2015) Fibrosis related inflammatory mediators: role of the IL-10 cytokine family. *Mediators Inflamm* 2015:764641
- Belperio J, Horwich T, Abraham WT, Fonarow GC, Goresan J 3rd, Bersohn MM, Singh JP, Sonel A, Lee LY, Halilovic J, Kadish A, Shalaby AA (2016) Inflammatory mediators and clinical outcome in patients with advanced heart failure receiving cardiac resynchronization therapy. *Am J Cardiol* 117:617–625
- Li X, Fang P, Li Y, Kuo YM, Andrews AJ, Nanayakkara G, Johnson C, Fu H, Shan H, Du F, Hoffman NE, Yu D, Eguchi S, Madesh M, Koch WJ, Sun J, Jiang X, Wang H, Yang X (2016) Mitochondrial reactive oxygen species mediate lysophosphatidylcholine-induced endothelial cell activation. *Arterioscler Thromb Vasc Biol* 36:1090–1100
- Qin X, Qiu C, Zhao L (2014) Lysophosphatidylcholine perpetuates macrophage polarization toward classically activated phenotype in inflammation. *Cell Immunol* 289:185–190
- Scholz H, Eder C (2017) Lysophosphatidylcholine activates caspase-1 in microglia via a novel pathway involving two inflammasomes. *J Neuroimmunol* 310:107–110
- Huang JP, Cheng ML, Wang CH, Shiao MS, Chen JK, Hung LM (2016) High-fructose and high-fat feeding correspondingly lead to the development of lysoPC-associated apoptotic cardiomyopathy and adrenergic signaling-related cardiac hypertrophy. *Int J Cardiol* 215:65–76
- Nam M, Jung Y, Ryu DH, Hwang GS (2017) A metabolomics-driven approach reveals metabolic responses and mechanisms in the rat heart following myocardial infarction. *Int J Cardiol* 227:239–246
- Chen HM, Hsu JH, Liou SF, Chen TJ, Chen LY, Chiu CC, Yeh JL (2014) Baicalein, an active component of *Scutellaria baicalensis* Georgi, prevents lysophosphatidylcholine-induced cardiac injury by reducing reactive oxygen species production, calcium overload and apoptosis via MAPK pathways. *BMC Complement Altern Med* 14:233
- Goncalves I, Edsfieldt A, Ko NY, Grufman H, Berg K, Bjorkbacka H, Nitulescu M, Persson A, Nilsson M, Prehn C, Adamski J, Nilsson J (2012) Evidence supporting a key role of Lp-PLA2-generated lysophosphatidylcholine in human atherosclerotic plaque inflammation. *Arterioscler Thromb Vasc Biol* 32:1505–1512
- Ma F, Li Y, Jia L, Han Y, Cheng J, Li H, Qi Y, Du J (2012) Macrophage-stimulated cardiac fibroblast production of IL-6 is essential for TGF beta/Smad activation and cardiac fibrosis induced by angiotensin II. *PLoS One* 7:e35144
- Melendez GC, McLarty JL, Levick SP, Du Y, Janicki JS, Brower GL (2010) Interleukin 6 mediates myocardial fibrosis, concentric hypertrophy, and diastolic dysfunction in rats. *Hypertension* 56:225–231
- Wang JH, Zhao L, Pan X, Chen NN, Chen J, Gong QL, Su F, Yan J, Zhang Y, Zhang SH (2016) Hypoxia-stimulated cardiac fibroblast production of IL-6 promotes myocardial fibrosis via the TGF-beta1 signaling pathway. *Lab Invest* 96:1035
- Chaudhuri P, Rosenbaum MA, Birnbaumer L, Graham LM (2017) Integration of TRPC6 and NADPH oxidase activation in lysophosphatidylcholine-induced TRPC5 externalization. *Am J Physiol Cell Physiol* 313:C541–C555
- Kelher MR, McLaughlin NJ, Banerjee A, Elzi DJ, Gamboni F, Khan SY, Meng X, Mitra S, Silliman CC (2017) LysoPCs induce Hck- and PKCdelta-mediated activation of PKCgamma causing



- p47phox phosphorylation and membrane translocation in neutrophils. *J Leukoc Biol* 101:261–273
17. Teixeira G, Szyndralewicz C, Molango S, Carnesecchi S, Heitz F, Wiesel P, Wood JM (2017) Therapeutic potential of NADPH oxidase 1/4 inhibitors. *Br J Pharmacol* 174:1647–1669
  18. Zhao QD, Viswanadhapalli S, Williams P, Shi Q, Tan C, Yi X, Bhandari B, Abboud HE (2015) NADPH oxidase 4 induces cardiac fibrosis and hypertrophy through activating Akt/mTOR and NFkappaB signaling pathways. *Circulation* 131:643–655
  19. Parajuli N, Patel VB, Wang W, Basu R, Oudit GY (2014) Loss of NOX2 (gp91phox) prevents oxidative stress and progression to advanced heart failure. *Clin Sci (Lond)* 127:331–340
  20. Lin CC, Lee IT, Wu WL, Lin WN, Yang CM (2012) Adenosine triphosphate regulates NADPH oxidase activity leading to hydrogen peroxide production and COX-2/PGE2 expression in A549 cells. *Am J Physiol Lung Cell Mol Physiol* 303:L401–L412
  21. Wong SC, Fukuchi M, Melnyk P, Rodger I, Giaid A (1998) Induction of cyclooxygenase-2 and activation of nuclear factor-kappaB in myocardium of patients with congestive heart failure. *Circulation* 98:100–103
  22. Scheuren N, Jacobs M, Ertl G, Schorb W (2002) Cyclooxygenase-2 in myocardium stimulation by angiotensin-II in cultured cardiac fibroblasts and role at acute myocardial infarction. *J Mol Cell Cardiol* 34:29–37
  23. Brkic L, Riederer M, Graier WF, Malli R, Frank S (2012) Acyl chain-dependent effect of lysophosphatidylcholine on cyclooxygenase (COX)-2 expression in endothelial cells. *Atherosclerosis* 224:348–354
  24. Lappas M (2013) Forkhead box O1 (FOXO1) in pregnant human myometrial cells: a role as a pro-inflammatory mediator in human parturition. *J Reprod Immunol* 99:24–32
  25. Hsu CK, Lin CC, Hsiao LD, Yang CM (2015) Mevastatin ameliorates sphingosine 1-phosphate-induced COX-2/PGE2-dependent cell migration via FoxO1 and CREB phosphorylation and translocation. *Br J Pharmacol* 172:5360–5376
  26. Kappel BA, Stohr R, De Angelis L, Mavilio M, Menghini R, Federici M (2016) Posttranslational modulation of FoxO1 contributes to cardiac remodeling in post-ischemic heart failure. *Atherosclerosis* 249:148–156
  27. Wilhelm K, Happel K, Eelen G, Schoors S, Oellerich MF, Lim R, Zimmermann B, Aspalter IM, Franco CA, Boettger T, Braun T, Fruttiger M, Rajewsky K, Keller C, Bruning JC, Gerhardt H, Carmeliet P, Potente M (2016) FOXO1 couples metabolic activity and growth state in the vascular endothelium. *Nature* 529:216–220
  28. Hariharan N, Ikeda Y, Hong C, Alcindor RR, Usui S, Gao S, Maejima Y, Sadoshima J (2013) Autophagy plays an essential role in mediating regression of hypertrophy during unloading of the heart. *PLoS One* 8:e51632
  29. Puthanveetil P, Wan A, Rodrigues B (2013) FoxO1 is crucial for sustaining cardiomyocyte metabolism and cell survival. *Cardiovasc Res* 97:393–403
  30. Gopal K, Saleme B, Al Batran R, Aburasayn H, Eshreif A, Ho KL, Ma WK, Almutairi M, Eaton F, Gandhi M, Park EA, Sutendra G, Ussher JR (2017) FoxO1 regulates myocardial glucose oxidation rates via transcriptional control of pyruvate dehydrogenase kinase 4 expression. *Am J Physiol Heart Circ Physiol* 313:H479–H490
  31. Fan W, Morinaga H, Kim JJ, Bae E, Spann NJ, Heinz S, Glass CK, Olefsky JM (2010) FoxO1 regulates Tlr4 inflammatory pathway signalling in macrophages. *EMBO J* 29:4223–4236
  32. Brown J, Wang H, Suttles J, Graves DT, Martin M (2011) Mammalian target of rapamycin complex 2 (mTORC2) negatively regulates Toll-like receptor 4-mediated inflammatory response via FoxO1. *J Biol Chem* 286:44295–44305
  33. Lin CC, Yang CC, Wang CY, Tseng HC, Pan CS, Hsiao LD, Yang CM (2015) NADPH oxidase/ROS-dependent VCAM-1 induction on TNF-alpha-challenged human cardiac fibroblasts enhances monocyte adhesion. *Front Pharmacol* 6:310
  34. Rizvi F, Heimann T, O'Brien WJ (2012) Expression of NADPH oxidase (NOX) 5 in rabbit corneal stromal cells. *PLoS One* 7:e34440
  35. Hsu CK, Lee IT, Lin CC, Hsiao LD, Yang CM (2015) Sphingosine-1-phosphate mediates COX-2 expression and PGE2/IL-6 secretion via c-Src-dependent AP-1 activation. *J Cell Physiol* 230:702–715
  36. Griendling KK (2004) Novel NAD(P)H oxidases in the cardiovascular system. *Heart* 90:491–493
  37. Watanabe N, Zmijewski JW, Takabe W, Umez-Goto M, Le Goffe C, Sekine A, Landar A, Watanabe A, Aoki J, Arai H, Kodama T, Murphy MP, Kalyanaraman R, Darley-Usmar VM, Noguchi N (2006) Activation of mitogen-activated protein kinases by lysophosphatidylcholine-induced mitochondrial reactive oxygen species generation in endothelial cells. *Am J Pathol* 168:1737–1748
  38. Bi X, Song J, Gao J, Zhao J, Wang M, Scipione CA, Koschinsky ML, Wang ZV, Xu S, Fu G (2016) Activation of liver X receptor attenuates lysophosphatidylcholine-induced IL-8 expression in endothelial cells via the NF-kappaB pathway and SUMOylation. *J Cell Mol Med* 20:2249–2258
  39. Nguyen LK, Cavadas MA, Kholodenko BN, Frank TD, Cheong A (2015) Species differential regulation of COX2 can be described by an NFkappaB-dependent logic AND gate. *Cell Mol Life Sci* 72:2431–2443
  40. Langlet F, Haeusler RA, Linden D, Ericson E, Norris T, Johansson A, Cook JR, Aizawa K, Wang L, Buettner C, Accili D (2017) Selective inhibition of FOXO1 activator/repressor balance modulates hepatic glucose handling. *Cell* 171(824–835):e818
  41. Zhang C, Ponugoti B, Tian C, Xu F, Tarapore R, Batres A, Alsadun S, Lim J, Dong G, Graves DT (2015) FOXO1 differentially regulates both normal and diabetic wound healing. *J Cell Biol* 209:289–303
  42. Kawamori D, Kaneto H, Nakatani Y, Matsuoka TA, Matsuhisa M, Hori M, Yamasaki Y (2006) The forkhead transcription factor Foxo1 bridges the JNK pathway and the transcription factor PDX-1 through its intracellular translocation. *J Biol Chem* 281:1091–1098
  43. Zhang X, Gan L, Pan H, Guo S, He X, Olson ST, Mesecar A, Adam S, Unterman TG (2002) Phosphorylation of serine 256 suppresses transactivation by FKHR (FOXO1) by multiple mechanisms. Direct and indirect effects on nuclear/cytoplasmic shuttling and DNA binding. *J Biol Chem* 277:45276–45284
  44. Gomi K, Zhu FG, Marshall JS (2000) Prostaglandin E2 selectively enhances the IgE-mediated production of IL-6 and granulocyte-macrophage colony-stimulating factor by mast cells through an EP1/EP3-dependent mechanism. *J Immunol* 165:6545–6552
  45. Inoue H, Takamori M, Shimoyama Y, Ishibashi H, Yamamoto S, Koshihara Y (2002) Regulation by PGE2 of the production of interleukin-6, macrophage colony stimulating factor, and vascular endothelial growth factor in human synovial fibroblasts. *Br J Pharmacol* 136:287–295
  46. Son Y, Kim S, Chung HT, Pae HO (2013) Reactive oxygen species in the activation of MAP kinases. *Methods Enzymol* 528:27–48
  47. Tsai KH, Wang WJ, Lin CW, Pai P, Lai TY, Tsai CY, Kuo WW (2012) NADPH oxidase-derived superoxide anion-induced apoptosis is mediated via the JNK-dependent activation of NF-kappaB in cardiomyocytes exposed to high glucose. *J Cell Physiol* 227:1347–1357
  48. Akasaki Y, Alvarez-Garcia O, Saito M, Carames B, Iwamoto Y, Lotz MK (2014) FoxO transcription factors support oxidative stress resistance in human chondrocytes. *Arthritis Rheumatol* 66:3349–3358

49. Paik JH, Kollipara R, Chu G, Ji H, Xiao Y, Ding Z, Miao L, Tothova Z, Horner JW, Carrasco DR, Jiang S, Gilliland DG, Chin L, Wong WH, Castrillon DH, DePinho RA (2007) FoxOs are lineage-restricted redundant tumor suppressors and regulate endothelial cell homeostasis. *Cell* 128:309–323
50. Harant H, Eldershaw SA, Lindley IJ (2001) Human macrophage inflammatory protein-3 $\alpha$ /CCL20/LARC/Exodus/SCYA20 is transcriptionally upregulated by tumor necrosis factor- $\alpha$  via a non-standard NF- $\kappa$ B site. *FEBS Lett* 509:439–445
51. Miao H, Zhang Y, Lu Z, Yu L, Gan L (2012) FOXO1 increases CCL20 to promote NF- $\kappa$ B-dependent lymphocyte chemotaxis. *Mol Endocrinol* 26:423–437